

ICL Contribution to Landslide Disaster Risk Reduction

Binod Tiwari
Kyoji Sassa
Peter T. Bobrowsky
Kaoru Takara
Editors

Understanding and Reducing Landslide Disaster Risk

Volume 4 Testing, Modeling
and Risk Assessment



 Springer

The Springer logo is located in the bottom right corner. It features a white chess knight piece on a pedestal, followed by the word 'Springer' in a white, serif font.

ICL Contribution to Landslide Disaster Risk Reduction

Series Editor

Kyoji Sassa, The International Consortium on Landslides, ICL, Kyoto, Japan

The ICL Contribution to Landslide Disaster Risk Reduction book-series publishes integrated research on all aspects of landslides. The volumes present summaries on the progress of landslide sciences, disaster mitigation and risk preparation. The contributions include landslide dynamics, mechanisms and processes; volcanic, urban, marine and reservoir landslides; related tsunamis and seiches; hazard assessment and mapping; modeling, monitoring, GIS techniques; remedial or preventive measures; early warning and evacuation and a global landslide database.

More information about this series at <http://www.springer.com/series/16332>

Binod Tiwari • Kyoji Sassa •
Peter T. Bobrowsky • Kaoru Takara
Editors

Understanding and Reducing Landslide Disaster Risk

Volume 4 Testing, Modeling and Risk
Assessment

 Springer

Editors

Binod Tiwari
Civil and Environmental Engineering
California State University Fullerton
Fullerton, CA, USA

Peter T. Bobrowsky
Geological Survey of Canada
Sidney, BC, Canada

Kyoji Sassa
International Consortium on Landslides
Sakyo-ku, Kyoto, Japan

Kaoru Takara
Graduate School of Advanced Integrated
Studies in Human Survivability (Shishu-kan)
Kyoto University
Sakyo-ku, Kyoto, Japan

Associate Editors

Beena Ajmera
North Dakota State University, USA

Ryosuke Uzuoka
Kyoto University, Japan

Sabatino Cuomo
University of Salerno, Italy

Katsuo Sasahara
Kochi University, Japan

ISSN 2662-1894 ISSN 2662-1908 (electronic)
ICL Contribution to Landslide Disaster Risk Reduction
ISBN 978-3-030-60705-0 ISBN 978-3-030-60706-7 (eBook)
<https://doi.org/10.1007/978-3-030-60706-7>

© Springer Nature Switzerland AG 2021

This work is subject to copyright. All rights are reserved by the Publisher, whether the whole or part of the material is concerned, specifically the rights of translation, reprinting, reuse of illustrations, recitation, broadcasting, reproduction on microfilms or in any other physical way, and transmission or information storage and retrieval, electronic adaptation, computer software, or by similar or dissimilar methodology now known or hereafter developed.

The use of general descriptive names, registered names, trademarks, service marks, etc. in this publication does not imply, even in the absence of a specific statement, that such names are exempt from the relevant protective laws and regulations and therefore free for general use.

The publisher, the authors and the editors are safe to assume that the advice and information in this book are believed to be true and accurate at the date of publication. Neither the publisher nor the authors or the editors give a warranty, expressed or implied, with respect to the material contained herein or for any errors or omissions that may have been made. The publisher remains neutral with regard to jurisdictional claims in published maps and institutional affiliations.

Cover illustration: Portuguese Bend Landslide, located in the city of Rancho Palos Verdes, California, USA (International Consortium on Landslides. All Rights Reserved)

This Springer imprint is published by the registered company Springer Nature Switzerland AG
The registered company address is: Gewerbestrasse 11, 6330 Cham, Switzerland

ICL and Springer created a new book series “ICL Contribution to Landslide Disaster Risk Reduction” in 2019 which is registered as ISSN 2662-1894 (print version) and ISSN 2662-1908 (electronic version). The first books in this series are six volume of books “Understanding and Reducing Landslide Disaster Risk” containing the recent progress of landslide science and technologies from 2017 to 2020.

Editor-in-Chief: Kyoji Sassa

Assistant Editor-in-Chief: Željko Arbanas

Organizational Structure of the Fifth World Landslide Forum

Organizers

International Consortium on Landslides (ICL)

Global Promotion Committee of International Programme on Landslides (IPL-GPC), including: United Nations Educational, Scientific and Cultural Organization (UNESCO), World Meteorological Organization (WMO), Food and Agriculture Organization (FAO), United Nations Office for Disaster Risk Reduction (UNDRR), United Nations University (UNU), International Science Council (ISC), World Federation of Engineering Organizations (WFEO), International Union of Geological Sciences (IUGS), International Union of Geodesy and Geophysics (IUGG)

Kyoto University (KU), Japan Landslide Society (JLS), Japanese Geotechnical Society (JGS), Japan Society for Natural Disaster Science (JSNDS) and Japan Association for Slope Disaster Management (JASDiM)

Co-sponsors

Cabinet Office (Disaster Management Bureau) of Japan; Ministry of Foreign Affairs of Japan (MOFA); Ministry of Education, Culture, Sports, Science and Technology-Japan (MEXT); Ministry of Land Infrastructure, Transport and Tourism (MLIT); Ministry of Agriculture, Forestry and Fisheries (MAFF); Science Council of Japan (SCJ); Japan International Cooperation Agency (JICA); Japan Society of Civil Engineers (JSCE); Japanese Society of Irrigation, Drainage and Rural Engineering (JSIDRE); Japan Society of Erosion Control Engineering; Japan Society of Engineering Geology.

Supporting Organizations with Finance

Tokyo Geographical Society

International Union of Geological Sciences (IUGS)

Association for Disaster Prevention Research, Kyoto, Japan

Organizing Committee

Honorary Chairpersons

Audrey Azoulay, Director-General of UNESCO*

Mami Mizutori, Special Representative of the United Nations Secretary-General for Disaster Risk Reduction*

Petteri Taalas, Secretary-General of WMO*
 Qu Dongyu, Director-General of FAO*
 David Malone, Under-Secretary General of the United Nations and Rector of UNU
 Daya Reddy, President of ISC
 Gong Ke, President of WFEO
 Qiuming Cheng, President of IUGS
 Kathryn Whaler, President of IUGG
 Qunli Han, Executive Director of Integrated Research on Disaster Risk (IRDR)
 Walter Ammann, President and CEO of Global Risk Forum GRF Davos, Switzerland
 Juichi Yamagiwa, President of Kyoto University, Japan
 Angelo Borrelli, Head of the National Civil Protection Department, Italian Presidency of the Council of Ministers, Italy
 Darko But, Director General of the Administration for Civil Protection and Disaster Relief of the Republic of Slovenia, Slovenia
 Akifumi Nakao, Director, International Cooperation Division, Disaster Management Bureau, Cabinet Office, Japan
 Kazuyuki Imai, Director General of Sabo Department, Ministry of Land Infrastructure, Transport and Tourism, Japan*
 Chungsik Yoo, President of the International Geosynthetics Society
 Rafiq Azzam, President of the International Association for Engineering Geology and the Environment
 (*to be confirmed)

Chairpersons

Kyoji Sassa, Professor Emeritus, Kyoto University; Secretary General of ICL
 Peter T. Bobrowsky, Geological Survey of Canada; President of ICL
 Kaoru Takara, Kyoto University, Japan; Executive Director of ICL

Members

Željko Arbanas (University of Rijeka, Croatia)
 Snježana Mihalić Arbanas (University of Zagreb, Croatia)
 Nicola Casagli (University of Firenze, Italy)
 Fausto Guzzetti (Department of Civil Protection, Italy)
 Matjaž Mikoš (University of Ljubljana, Slovenia)
 Paola Reichenbach (Research Institute for Geo-Hydrological Protection, National Research Council, Italy)
 Shinji Sassa (Port and Airport Research Institute, Japan)
 Alexander Strom (Geodynamics Research Center LLC, Russia)
 Binod Tiwari (California State University, Fullerton, USA)
 Veronica Tofani (University of Firenze, Italy)
 Vít Vilímek (Charles University in Prague, Czech Republic)
 Fawu Wang (Tongji University, China)

Chairpersons of Local Organizing Committee

Kaoru Takara (Kyoto University)
 Daisuke Higaki (Japan Landslide Society)
 Ikuo Towhata (Japanese Geotechnical Society)

Secretary Generals

Ryosuke Uzuoka (Disaster Prevention Research Institute, Kyoto University)
 Kazuo Konagai (International Consortium on Landslides)
 Khang Dang (International Consortium on Landslides)

International Scientific Committee

Beena Ajmera, North Dakota State University, USA
Snježana Mihalić Arbanas, University of Zagreb, Croatia
Željko Arbanas, Faculty of Civil Engineering, University of Rijeka, Croatia
Amin Askarinejad, Technische Universiteit Delft, Delft, The Netherlands
Peter T. Bobrowsky, Geological Survey of Canada, Sidney, Canada
Michele Calvello, University of Salerno, Italy
Giovanna Capparelli, Università degli Studi della Calabria, Rende, Italy
Nicola Casagli, University of Florence, Italy
Yifei Cui, Tsinghua University, Beijing, China
Sabatino Cuomo, University of Salerno, Fisciano, Italy
Khang Dang, International Consortium on Landslides, Kyoto, Japan
Elias Garcia-Urquia, National Autonomous University of Honduras, Tegucigalpa, Honduras
Stefano Luigi Gariano, Research Institute for Geo-Hydrological Protection, CNR, Perugia, Italy
Daniele Giordan, Research Institute for Geo-Hydrological Protection, CNR, Italy
Fausto Guzzetti, Department of Civil Protection, Italy
Baator Has, Asia Air Survey, Tokyo, Japan
Hans-Balder Havenith, Universite de Liege, Liege, Belgium
D. P. Kanungo, Central Building Research Institute (CBRI), Roorkee, Uttarakhand, India
Oded Katz, Geological Survey of Israel, Jerusalem, Israel
Kazuo Konagai, International Consortium on Landslides, Kyoto, Japan
Doan Huy Loi, International Consortium on Landslides, Kyoto, Japan
Ping Lu, Tongji University, Shanghai, China
Olga Mavrouli, University of Twente, Enschede, The Netherlands
Matjaž Mikoš, Faculty of Civil and Geodetic Engineering, University of Ljubljana, Slovenia
Alessandro C. Mondini, Research Institute for Geo-Hydrological Protection, CNR, Italy
Veronica Pazzi, Department of Earth Science, University of Florence, Florence, Italy
Dario Peduto, Department of Civil Engineering, University of Salerno, Fisciano, Italy
Paola Reichenbach, Research Institute for Geo-Hydrological Protection, CNR, Italy
Paola Salvati, Research Institute for Geo-Hydrological Protection, CNR, Italy
Katsuo Sasahara, Kochi University, Japan
Kyoji Sassa, International Consortium on Landslides, Kyoto, Japan
Shinji Sassa, Port and Airport Research Institute, Japan
Andrea Segalini, University of Parma, Italy
Hendy Setiawan, Universitas Gadjah Mada, Yogyakarta, Indonesia
Alexander Strom, Geodynamics Research Center LLC, Moscow, Russia
Kaoru Takara, Kyoto University, Japan
Faraz Tehrani, Deltares, Delft, The Netherlands
Binod Tiwari, California State University, Fullerton, California, USA
Veronica Tofani, University of Florence, Italy
Ryosuke Uzuoka, Kyoto University, Kyoto, Japan
Vít Vilímek, Faculty of Science, Charles University, Prague, Czech Republic
Fawu Wang, College of Civil Engineering, Tongji University, Shanghai, China
Gonghui Wang, Kyoto University, Kyoto, Japan
Mike Winter, Winter Associates Limited, Kirknewton, UK
Hiromitsu Yamagishi, Hokkaido Research Center of Geology (HRCG), Sapporo, Japan

Local Organizing Committee

Shinro Abe, Okuyama Boring Co., Ltd.
Kiminori Araiba, Fire and Disaster Management College
Shiho Asano, Forestry and Forest Products Research Institute
Has Baator, Asia Air Survey Co., Ltd.

Hiromu Daimaru, Forestry and Forest Products Research Institute
Khang Dang, International Consortium on Landslides
Mitsuya Enokida, Japan Conservation Engineers & Co., Ltd.
Kumiko Fujita, International Consortium on Landslides
Kazunori Hayashi, Okuyama Boring Co., Ltd.
Daisuke Higaki, The Japan Landslide Society
Kiyoharu Hirota, Kokusai Kogyo Co., Ltd.
Kazuo Konagai, International Consortium on Landslides
Taketoshi Marui, MARUI & Co., Ltd.
Satoshi Nishikawa, Nagoya University
Keisuke Oozone, OYO Corporation
Katsuo Sasahara, Kochi University
Kyoji Sassa, International Consortium on Landslides
Shinji Sassa, Port and Airport Research Institute
Go Sato, Teikyo Heisei University
Nobuyuki Shibasaki, Nippon Koei Co., Ltd.
Nobuo Sugiura, Japan Association for Slope Disaster Management
Kaoru Takara, Kyoto University
Keisuke Takimoto, GODAI KAIHATSU Corporation
Yoko Tomita, Public Works Research Institute
Ikuo Towhata, The Japanese Geotechnical Society
Kenichi Tsukahara, Kyushu University
Ryosuke Tsunaki, Sabo & Landslide Technical Center
Taro Uchida, Saitama University
Mie Ueda, International Consortium on Landslides
Ryosuke Uzuoka, Kyoto University
Fawu Wang, Tongji University
Hiroshi Yagi, Yamagata University
Hiromitsu Yamagishi, Shin Engineering Consultants Co., Ltd.
Maki Yano, OSASI Technos Inc.

Foreword by Mami Mizutori

More landslides can be expected as climate change exacerbates rainfall intensity. The long-term trend of the last 40 years has seen the number of major recorded extreme weather events almost double, notably floods, storms, landslides, and wildfires.

Landslides are a serious geological hazard. Among the host of natural triggers are intense rainfall, flooding, earthquakes or volcanic eruption, and coastal erosion caused by storms that are all too often tied to the El Niño phenomenon. Human triggers including deforestation, irrigation or pipe leakage, and mine tailings, or stream and ocean current alteration can also spark landslides. Landslides can also generate tsunamis, as Indonesia experienced in 2018.

Globally, landslides cause significant economic loss and many deaths and injuries each year. Therefore, it is important to understand the science of landslides: why they occur, what factors trigger them, the geology associated with them, and where they are likely to happen.

Landslides with high death tolls are often a result of failures in risk governance, poverty reduction, environmental protection, land use and the implementation of building codes. Understanding the interrelationships between earth surface processes, ecological systems, and human activity is the key to reducing landslide risk.

The Sendai Framework for Disaster Risk Reduction, the global plan to reduce disaster losses adopted in 2015, emphasizes the importance of tackling these risk drivers through improved governance and a better understanding of disaster risk.

One important vehicle for doing that is the Sendai Landslide Partnerships 2015–2025 for global promotion of understanding and reduction of landslide risk facilitated by the International Consortium on Landslides (ICL) and signed by the leaders of 22 global stakeholders, including the UN Office for Disaster Risk Reduction (UNDRR), during the Third UN World Conference on Disaster Risk Reduction in Sendai, Japan.

The Sendai Landslide Partnerships—featured on the Sendai Framework Voluntary Commitments online platform—helps to provide practical solutions and tools, education, and capacity building, to reduce landslide risks.

The work done by the Sendai Partnerships can be of value to many stakeholders including civil protection, planning, development and transportation authorities, utility managers, agricultural and forest agencies, and the scientific community.

UNDRR fully supports the work of the Sendai Landslide Partnerships and ICL and looks forward to an action-oriented outcome from the 5th World Landslide Forum to be held in November 2020 in Kyoto, Japan. Successful efforts to reduce disaster losses are a major contribution to achieving the overall 2030 Agenda for Sustainable Development.



Mami Mizutori
United Nations Special Representative of the
Secretary-General for Disaster Risk Reduction

Foreword by the Assistant Director-General for the Natural Sciences Sector of UNESCO for the Book of the 5th World Landslide Forum

As the world slowly recovers from the COVID-19 global pandemic, and looking back at the way this crisis developed, it becomes evident that as a global community we were not prepared for an event of this scale. Although not commonly perceived as such, biological hazards such as epidemics are included in the Sendai Framework for Disaster Risk Reduction 2015–2030. In that sense, the preparedness approach for a pandemic is very similar to that of a geophysical natural hazard such as landslides.

Although natural hazards are naturally occurring phenomena, the likelihood of their occurrence and of associated disasters is rising. Climate change, urban pressure, under-development and poverty and lack of preparedness are increasingly transforming these natural hazards into life-threatening disasters with severe economic impacts. Therefore, Disaster Risk Reduction (DRR) is gaining momentum on the agenda of the UN system of Organizations including UNESCO. While the Sendai Framework for Disaster Risk Reduction 2015–2030 is the roadmap for DRR, other global agendas including the Sustainable Development Goals, the Paris Climate Agreement and the New Urban Agenda have targets which cannot be attained without DRR.

In shaping its contribution to those global agendas, UNESCO is fully committed in supporting its Member States in risk management, between its different mandates and disciplines and with relevant partners. The International Consortium on Landslides (ICL) is UNESCO's key partner in the field of landslide science. The Organization's support to the Consortium is unwavering. Since ICL was established in 2002, the two organizations have a long history of cooperation and partnership and UNESCO has been associated with almost all of ICL activities. I am very glad that ICL and UNESCO are mutually benefitting from their collaboration.

The 5th World Landslide Forum (WLF5) is expected to represent a milestone in the history of landslide science particularly for scientists and practitioners. One of the major outcomes of WLF5 will be the Kyoto 2020 Commitment for global promotion of understanding and reducing landslide disaster risk (KLC2020). This commitment is expected to strengthen and expand the activities of the Sendai Landslide Partnership 2015–2025. With UNESCO already engaged as a partner, the adoption of this international commitment will raise global awareness on landslide risk and mobilize wider partnerships that draw together stakeholders from all levels of society, across different regions, sectors and disciplines.

It is my great pleasure to congratulate the organizers for holding this event and assure you that UNESCO is fully committed in contributing to its success. As part of that contribution, our Organization is proud to host a session on landslides and hazard assessment at UNESCO-designated sites such as natural World Heritage sites, biosphere reserves and UNESCO Global Geoparks. This session aims to assess landslide impacts on our shared cultural and natural heritage, providing the best opportunity to generate public awareness and capacity development for landslide disaster reduction.

I am confident that WLF5 will contribute to further advance the knowledge of both scientists and practitioners regarding landslide disaster risk reduction. This book paves the way for the science, knowledge and know-how which will feature in the deliberations of the Forum. UNESCO commends all of the contributors to this publication. I look forward to an enhanced collaboration between UNESCO and ICL in future activities and undertakings.



Shamila Nair-Bedouelle
Assistant Director-General for Natural Sciences
UNESCO

Preface I

Understanding and Reducing Landslide Disaster Risk

Book Series: ICL Contribution to Landslide Disaster Risk

The International Consortium on Landslides (ICL) was established in pursuance of the 2002 Kyoto Declaration “Establishment of an International Consortium on Landslides,” with its Statutes adopted in January 2002. The Statutes define the General Assembly of ICL as follows: in order to report and disseminate the activities and achievements of the Consortium, a General Assembly shall be convened every 3 years by inviting Members of the International Consortium on Landslides, individual members within those organizations, and all levels of cooperating organizations and individual researchers, engineers, and administrators. The General Assembly developed gradually prior to, during and after its first meeting in 2005. In the light of the 2006 Tokyo Action Plan, the Assembly was further facilitated at, and following the First World Landslide Forum held in November 2008. On the occasion of each of its triennial forums, ICL publishes the latest progress of landslide science and technology for the benefit of the whole landslide community including scientists, engineers, and practitioners in an understandable form. Full color photos of landslides and full color maps are readily appreciated by those from different disciplines. We have published full color books on landslides at each forum. In 2019, ICL created a new book series “ICL Contribution to Landslide Disaster Risk Reduction” ISSN 2662-1894 (print version) and ISSN 2662-1908 (electronic version). Six volumes of full color books *Understanding and Reducing Landslide Disaster Risk* will be published in 2020 as the first group of books of this series.

The Letter of Intent 2005 and the First General Assembly 2005

The United Nations World Conference on Disaster Reduction (WCDR) was held in Kobe, Japan, 18–22 January 2005. At this Conference, ICL organized session 3.8 “New international Initiatives for Research and Risk Mitigation of Floods (IFI) and Landslides (IPL)” on 19 January 2005 and adopted a “Letter of Intent” aimed at providing a platform for a holistic approach in research and learning on ‘Integrated Earth System Risk Analysis and Sustainable Disaster Management’. This Letter was agreed upon and signed, during the first semester of 2005, by heads of seven global stakeholders including the United Nations Educational, Scientific and Cultural Organization (UNESCO), the World Meteorological Organization (WMO), the Food and Agriculture Organization of the United Nations (FAO), the United Nations International Strategy for Disaster Risk Reduction (UNISDR-currently UNDRR), the United Nations University (UNU), the International Council for Science (ICSU-currently ISC), and the World Federation of Engineering Organizations (WFEO).

The first General Assembly of ICL was held at the Keck Center of the National Academy of Sciences in Washington D.C., USA, on 12–14 October 2005. It was organized after the aforementioned 2005 World Conference on Disaster Reduction (WCDR). ICL published the

first full color book reporting on Consortium activities for the initial 3 years, 2002–2005 titled “Landslides-Risk analysis and sustainable disaster management”. In the preface of this book, the Letter of Intent for Integrated Earth System Risk Analysis and Sustainable Disaster Management was introduced. Results of the initial projects of the International Programme on Landslides (IPL) including IPL C101-1 Landslide investigation in Machu Picchu World Heritage, Cusco, Peru and previous agreements and MoU between UNESCO, ICL and the Disaster Prevention Research Institute of Kyoto University including UNESCO/KU/ICL UNITWIN Cooperation programme were published as well in this book.

The 2006 Tokyo Action Plan and the First World Landslide Forum 2008

Based on the Letter of Intent, the 2006 Tokyo Round-Table Discussion—“Strengthening Research and Learning on Earth System Risk Analysis and Sustainable Disaster Management within UN-ISDR as Regards Landslides”—towards a dynamic global network of the International Programme on Landslides (IPL) was held at the United Nations University, Tokyo, on 18–20 January 2006. The 2006 Tokyo Action Plan—Strengthening research and learning on landslides and related earth system disasters for global risk preparedness—was adopted. The ICL exchanged Memoranda of Understanding (MoUs) concerning strengthening cooperation in research and learning on earth system risk analysis and sustainable disaster management within the framework of the United Nations International Strategy for Disaster Reduction regarding the implementation of the 2006 Tokyo action plan on landslides with UNESCO, WMO, FAO, UNISDR (UNDRR), UNU, ICSU (ISC) and WFEO, respectively in 2006. A set of these MoUs established the International Programme on Landslides (IPL) as a programme of the ICL, the Global Promotion Committee of IPL to manage the IPL, and the triennial World Landslide Forum (WLF), as well as the concept of the World Centres of Excellence on Landslide Risk Reduction (WCoE).

The First World Landslide Forum (WLF1) was held at the Headquarters of the United Nations University, Tokyo, Japan, on 18–21 November 2008. 430 persons from 49 countries/regions/UN entities were in attendance. Both Hans van Ginkel, Under Secretary-General of the United Nations/Rector of UNU who served as chairperson of the Independent Panel of Experts to endorse WCoEs, and Salvano Briceno, Director of UNISDR who served as chairperson of the Global Promotion Committee of IPL, participated in this Forum. The success of WLF1 paved the way to the successful second and third World Landslide Forum held in Italy and China respectively.

The Second World Landslide Forum 2011 and the Third World Landslide Forum 2014

The Second World Landslide Forum (WLF2)—Putting Science into Practice—was held at the Headquarters of the Food and Agriculture Organization of the United Nations (FAO) on 3–9 October 2011. It was jointly organized by the IPL Global Promotion Committee (ICL, UNESCO, WMO, FAO, UNDRR, UNU, ISC, WFEO) and two ICL members from Italy: the Italian Institute for Environmental Protection and Research (ISPRA) and the Earth Science Department of the University of Florence with support from the Government of Italy and many Italian landslide-related organizations. It attracted 864 participants from 63 countries.

The Third World Landslide Forum (WLF3) was held at the China National Convention Center, Beijing, China, on 2–6 June 2014. A high-level panel discussion on an initiative to create a safer geoenvironment towards the UN Third World Conference on Disaster Risk Reduction (WCDRR) in 2015 and forward was moderated by Hans van Ginkel, Chair of Independent Panel of Experts for World Centers of Excellence (WCoE). In a special address to this high-level panel discussion, Irina Bokova, Director-General of UNESCO, underlined that

countries should be united to work against natural disasters and expressed commitment that UNESCO would like to further deepen cooperation with ICL. Ms. Bokova awarded certificates to 15 World Centres of Excellence.

The Sendai Landslide Partnerships 2015 and the Fourth World Landslide Forum 2017

The UN Third World Conference on Disaster Risk Reduction (WCDRR) was held in Sendai, Japan, on 14–18 March 2015. ICL organized the Working Session “Underlying Risk Factors” together with UNESCO, the Japanese Ministry of Land, Infrastructure, Transport and Tourism (MLIT) and other competent organizations. The session adopted ISDR-ICL Sendai Partnerships 2015–2025 (later changed to Sendai Landslide Partnerships) for global promotion of understanding and reducing landslide disaster risk as a Voluntary Commitment to the World Conference on Disaster Risk Reduction, Sendai, Japan, 2015 (later changed to Sendai Framework for Disaster Risk Reduction). After the session on 16 March 2015, the Partnerships was signed by Margareta Wahlström, Special Representative of the UN Secretary-General for Disaster Risk Reduction, Chief of UNISDR (UNDDR), and other representatives from 15 intergovernmental, international, and national organizations. Following the Sendai Landslide Partnerships, the Fourth World Landslide Forum was held in Ljubljana, Slovenia from 29 May to 2 June in 2017. On that occasion, five volumes of full color books were published to disseminate the advances of landslide science and technology. The high-level panel discussion on 30 May and the follow-up round table discussion on 31 May adopted the 2017 Ljubljana Declaration on Landslide Risk Reduction. The Declaration approved the outline of the concept of “Kyoto 2020 Commitment for global promotion of understanding and reducing landslide disaster risk” to be adopted at the Fifth World Landslide Forum in Japan, 2020.

The Fifth World Landslide Forum 2020 and the Kyoto Landslide Commitment 2020

The Fifth World Landslide Forum was planned to be organized on 2–6 November 2020 at the National Kyoto International Conference Center (KICC) and the preparations for this event were successfully ongoing until the COVID-19 pandemic occurred over the world in early 2020. The ICL decided to postpone the actual Forum to 2–6 November 2021 at KICC in Kyoto, Japan. Nevertheless, the publication of six volumes of full color books *Understanding and Reducing Landslide Disaster Risk* including reports on the advances in landslide science and technology from 2017 to 2020 is on schedule. We expect that this book will be useful to the global landslide community.

The Kyoto Landslide Commitment 2020 will be established during the 2020 ICL-IPL Online Conference on 2–6 November 2020 on schedule. Joint signatories of Kyoto Landslide Commitment 2020 are expected to attend a dedicated session of the aforementioned Online Conference, scheduled on 5 November 2020 which will also include and feature the Declaration of the launching of KLC2020. *Landslides: Journal of the International Consortium on Landslides* is the common platform for KLC2020. All partners may contribute and publish news and reports of their activities such as research, investigation, disaster reduction administration in the category of News/Kyoto Commitment. Online access or/and hard copy of the Journal will be sent to KLC2020 partners to apprise them of the updated information from other partners. As of 21 May 2020, 63 United Nations, International and national organizations have already signed the KLC2020.

Call for Partners of KLC2020

Those who are willing to join KLC2020 and share their achievements related to understanding and reducing landslide disaster risk in their intrinsic missions with other partners are invited to inform the ICL Secretariat, the host of KLC2020 secretariat (secretariat@iclhq.org). The ICL secretariat will send the invitation to the aforementioned meeting of the joint signatories and the declaration of the launching of the KLC2020 on 5 November 2020.

Eligible Organizations to be Partners of the KLC2020

1. ICL member organizations (full members, associate members and supporters)
2. ICL supporting organization from UN, international or national organizations and programmes
3. Government ministries and offices in countries having more than 2 ICL on-going members
4. International associations /societies that contribute to the organization of WLF5 in 2021 and WLF6 in 2023
5. Other organizations having some aspects of activities related to understanding and reducing landslide disaster risk as their intrinsic missions.



Kyoji Sassa
Chair of WLF5/
Secretary-General of ICL
Kyoto, Japan



Peter T. Bobrowsky
President of ICL
Sidney, Canada



Kaoru Takara
Executive Director of ICL
Kyoto, Japan

Appendix: World Landslide Forum Books

WLF	Place/participants	Title	Editors	Publisher/pages
WLF0 (1st General Assembly) 2005	Washington D.C., USA 59 from 17 countries/UNs	Landslides-Risk Analysis and Sustainable Disaster Management	Kyoji Sassa, Hiroshi Fukuoka, Fawu Wang, Goghui Wang	Springer/377 pages ISBN: 978-3-540-2864-6
WLF1 2008	Tokyo, Japan 430 from 49 countries/regions/UNs	Landslides-Disaster Risk Reduction	Kyoji Sassa, Paolo Canuti	Springer/649 pages ISBN: 978-3-540-69966-8
WLF2 2011	Rome, Italy 864 from 63 countries	Landslide Science and Practice Vol. 1 Landslide inventory and Sustainability and Hazard Zoning	Claudia Margottini, Paolo Canuti, Kyoji Sassa	Springer/607 pages ISBN: 978-3-642-31324-0
		Vol. 2 Early Warning, Instrumentation and Monitoring		Springer/685 pages ISBN: 978-3-642-31444-5
		Vol. 3 Spatial Analysis and Modelling		Springer/440 pages ISBN: 978-3-642-31309-7
		Vol. 4 Global Environmental Change		Springer/431 pages ISBN: 978-3-642-31336-3
		Vol. 5 Complex Environment		Springer/354 pages ISBN: 978-3-642-31426-1
		Vol. 6 Risk Assessment, Management and Mitigation		Springer/789 pages ISBN: 978-3-642-31318-9
		Vol. 7 Social and Economic Impact and Policies		Springer/333 pages ISBN: 978-3-642-31312-7
WLF3 2014	Beijing, China 531 from 45 countries/regions/UNs	Landslide Science for a Safer Geoenvironment Vol. 1 The International Programme on Landslides (IPL)	Kyoji Sassa, Paolo Canuti, Yueping Yin	Springer/493 pages ISBN: 978-3-319-04998-4
		Vol. 2 Methods of Landslide Studies		Springer/851 pages ISBN: 978-3-319-05049-2
		Vol. 3 Targeted Landslides		Springer/717 pages ISBN: 978-3-319-04995-3
WLF4 2017	Ljubljana, Slovenia 588 from 59 countries/regions/UNs	Advancing Culture of Living with Landslides Vol. 1 ISDR-ICL Sendai Partnerships 2015-2025	Kyoji Sassa, Matjaž Mikoš, Yueping Yin	Springer/585 pages ISBN: 978-319-53500-5

(continued)

WLF	Place/participants	Title	Editors	Publisher/pages
		Vol. 2 Advances in Landslide Science	Matjaž Mikoš, Binod Tiwari, Yueping Yin, Kyoji Sassa	Springer/1197 pages ISBN: 978-319-53497-8
		Vol. 3 Advances in Landslide Technology	Matjaž Mikoš, Željko Arbanas, Yueping Yin, Kyoji Sassa	Springer/621 pages ISBN: 978-3-319-53486-2
		Vol. 4 Diversity of Landslide Forms	Matjaž Mikoš, Nicola Casagli, Yueping Yin, Kyoji Sassa	Springer/707 pages ISBN: 978-3-319-53484-8
		Vol. 5 Landslides in Different Environments	Matjaž Mikoš, Vít Vilímek, Yueping Yin, Kyoji Sassa	Springer/557 pages ISBN: 978-3-319-53482-4
WLF5	2020 (publication) 2021 (Forum)	Understanding and Reducing Landslide Disaster Risk Vol. 1 Sendai Landslide Partnerships and Kyoto Landslide Commitment	Kyoji Sassa, Matjaž Mikoš, Shinji Sassa, Peter T. Bobrowsky, Kaoru Takara, Khang Dang	Springer In Process
		Vol. 2 From mapping to hazard and risk zonation	Fausto Guzzetti, Snježana Mihalić Arbanas, Paola Reichenbach, Kyoji Sassa, Peter T. Bobrowsky, Kaoru Takara	
		Vol. 3 Monitoring and early Warning	Nicola Casagli, Veronica Tofani, Kyoji Sassa, Peter T. Bobrowsky, Kaoru Takara	
		Vol. 4 Testing, modelling and risk assessment	Binod Tiwari, Kyoji Sassa, Peter T. Bobrowsky, Kaoru Takara	
		Vol. 5 Catastrophic landslides and Frontier of Landslide Science	Vít Vilimek, Fawu Wang, Alexander Strom, Kyoji Sassa, Peter T. Bobrowsky, Kaoru Takara	
		Vol. 6 Specific topics in landslide science and applications	Željko Arbanas, Peter T. Bobrowsky, Kazuo Konagai, Kyoji Sassa, Kaoru Takara	

Preface II

Landslides, among the most devastating natural disasters in the world, have been, annually, killing thousands of lives, affecting millions of people, and causing billions of dollars of property damage globally. Understanding the causes of specific landslides and their failure mechanisms will help us developing appropriate mitigation measures. Specifically, as landslides directly affect our lifeline infrastructures, applying appropriate engineering judgement while designing sustainable and suitable prevention works using locally available manpower and resources is very important for any strategic landslide management planning. With the advancement of new technology and knowledge, there has been a significant enhancement in the resources available for the analyses of landslides and debris flow disasters, prior to developing their mitigation measures. Dissemination of such information through scientific platforms such as publication, conferences, and global lecture series play an important role in reducing the impact of landslide disasters globally and developing resilient community. More importantly, methods pertinent to in situ and laboratory testing, numerical and experimental as well as physical modeling, and tools available for landslide risk assessment advance very quickly and utilization of globally available resources for landslide testing, modeling, and risk assessment help in promoting global partnership on landslide hazard mitigation. This volume of the book series is intended to compile articles from all over the world, specifically related to recent development on testing, analyzing, modeling, and risk assessment techniques to reduce landslide hazards.

Divided into six parts, this volume includes 5 keynote lectures and 45 peer-reviewed papers in five different research areas pertinent to the theme of this volume, namely, recent development in physical modeling of landslides, recent development in numerical modeling of landslides, recent development in soil and rock testing techniques, application and analysis methods, recent advancements in the methods of slope stability and deformation analyses, and recent development in disaster risk assessment.

The Keynote lectures have been authored by global experts on numerical and physical modeling of landslides, laboratory, and in situ testing of soil and rock, stability and deformation analysis, and landslide risk assessment and cover case studies associated with each topics including but not limited to the seismically induced landslides such as due to the 2015 Gorkha earthquake 1994 Northridge Earthquake, rainfall-induced landslides such as the 2014 Oso Landslide in Washington, and large landslides that occurred along the Jinsha River in China.

Eight different articles authored by lead scientists in physical modeling of landslides from seven countries in four different continents, such as from New Zealand, Indonesia, Malaysia, Japan, China, the USA, and Italy, cover the topics ranging from laboratory-based modeling of rock blocks to saturated as well as partially saturated soils, engineered to natural as well as tailings and submarine slopes, flume based to full scale as well centrifuge modeling, and caused by construction practices to wildfire as well as rainfall and earthquakes. Likewise, 17 different articles authors by global leaders on numerical modeling of landslides and debris flows, specifically from Taiwan, the UK, Belgium, Spain, Austria, Japan, Italy, Vietnam, and Serbia, cover various aspects of numerical modeling ranging from 1D to 3D, rock slope to soil slope, locally developed to commercially available software as well as GIS and remote sensing

techniques, simple rendering to virtual reality techniques, rockfall to debris flows as well as dam break, natural to submarine slopes, finite element to discrete element as well as constitutive modeling, and saturated to unsaturated slopes. Moreover, nine articles authored by global scientific research leads from Italy, Sri Lanka, China, Indonesia, Japan, and the USA, on various aspects of soil and rock testing techniques as well as application and analysis methods, cover testing methods ranging from direct shear to ring shear as well as cyclic or monotonic simple shear tests, simple to customized tests, and laboratory to field tests. On the other hand, four papers authored by scientists from Turkey, Japan, and the UK on recent advancements in the methods of slope stability and deformation analyses cover topics ranging from 2D to 3D analyses methods, analysis techniques for movement mechanism to counter-measure design, soil to rock slopes, limit equilibrium to finite element as well as deformation analyses, and effects on shallow landslides to tsunami generating coastal slopes. Likewise, eight articles authored by global experts on landslide disaster risk assessment from Canada, India, Italy, Indonesia, Slovenia, New Zealand, Hong Kong, and Japan, cover various aspects of disaster risk assessment techniques ranging from saturated to unsaturated slopes, soil to rock slopes, and various causative factors spanning from wildfires to rainfall as well as earthquakes.

All papers published in this volume went through rigorous peer review process and were accepted with at least one affirmative review decision. The author would like to acknowledge the tireless work of the associate editors of this volume, Drs. Beena Ajmera, Sabatino Cuomo, Katsuo Sasahara, and Ryosuke Uzuoka for effectively handling the review process, specifically assigning the manuscripts to appropriate reviewers, and making decisions based on the reviewers' suggestion and their own judgement. Moreover, the author thanks over 50 reviewers who dedicated their time and effort to go over the manuscripts, review them, and provide constructive suggestions to improve the quality of the manuscripts.

Fullerton, CA, USA

Binod Tiwari

Contents

Introduction—Testing, Modeling and Risk Assessment	1
Binod Tiwari, Beena Ajmera, Sabatino Cuomo, Katsuo Sasahara, and Ryosuke Uzuoka	
Part I Keynote Lectures	
Recent Developments in the Evaluation and Application of Residual and Fully Softened Shear Strengths for the Stability Analyses of Landslides	11
Binod Tiwari and Beena Ajmera	
Oso Landslide: Failure Mechanism and Runout Analyses	47
Timothy D. Stark and Zhengdan Xu	
Numerical Modelling for Slope Stabilizations in Modern Geotechnical Practice	65
Daniel Pradel	
Recent Advances in the Methods of Slope Stability and Deformation Analyses	81
Beena Ajmera and Binod Tiwari	
Engineering Risk Mitigation for Landslide Hazard Chains: The Baige Landslides on the Jinsha River in 2018	109
Limin M. Zhang, Jian He, and Te Xiao	
Part II Recent Development in Physical Modeling of Landslides	
Application of Magnetic Tracking System in Laboratory-Scale Rock Avalanche Model Tests	123
Xiaoyu Chen and Rolando P. Orense	
A Simple Physically-Based Distributed Translational Landslide Model	131
Yanto, Sumiyanto, and Arwan Apriyono	
Study on the Behaviour of Slope Instability Using Physical Modelling	137
Mastura Azmi, Harris Ramli, Muhammad Azril Hezmi, Siti Aimi Nadia Mohd Yusoff, and Hazwan Zaki	
Centrifuge Modelling of Slope Failure Due to Groundwater During Excavation	147
Nobutaka Hiraoka, Naotaka Kikkawa, and Kazuya Itoh	
Effects of Relative Density in Progressive Sliding of Tailing	157
Wei Hu, Xiaoyan Zhang, and Huawei Hu	
Experimental Studies on the Effect of Vegetation Density to Change Underground Seepage Rate and Stability of Slopes	165
Binod Tiwari	

Laboratory Simulations of Submarine Landslide Failure Mechanisms	173
Jonathan M. Carey, Joshu J. Mountjoy, Gareth J. Crutchley, Barbara Lyndsell, and David N. Petley	
Laboratory Tests to Simulate the Rainfall Infiltration Process of Pyroclastic Soils Subject to Instability	179
Gennaro Spolverino, Giovanna Capparelli, and Pasquale Versace	
Part III Recent Development in Numerical Modeling of Landslides	
3D Analysis of a Fragmental Rockfall	187
Roger Ruiz-Carulla, Gerard Matas, Jordi Corominas, and Nieves Lantada	
3D Landslide Models in VR	195
Hans-Balder Havenith	
A Coupled Discrete Element and Depth-Averaged Model for Flow-Like Landslide Simulations	205
Xiaoli Su, Xilin Xia, and Qihua Liang	
Advanced Methods for Simulating Complex Landslides	211
Martin Mergili and Shiva P. Pudasaini	
Application of Reciprocal Green's Functions on the Forecast of Submarine Landslide Tsunamis	217
Guan-Yu Chen, Chin-Chih Liu, and Yi-Fung Wang	
Deformation Characteristics with Porewater Pressure Development of Shallow Landslide Triggered by Rainfall Infiltration	227
Kuo-Hsin Yang, Thanh Son Nguyen, Harianto Rahardjo, and Der-Guey Lin	
Debris Flow Simulations Due to Landslide Dam Outburst and Considering Effective Countermeasures	235
Kana Nakatani, Ken'ichirou Kosugi, and Yoshifumi Satofuka	
Preliminary Results from the SMART-SED Basin Scale Sediment Yield Model	241
Federico Gatti, Luca Bonaventura, Alessandra Menafoglio, Monica Papini, and Laura Longoni	
Hazard Assessment of a Rainfall-Induced Deep-Seated Landslide in Hakha City, Myanmar	249
Khang Dang, Doan Huy Loi, Kyoji Sassa, Do Minh Duc, and Nguyen Duc Ha	
Landslide Hazard Zoning Based on the Integrated Simulation Model (LS-Rapid)	259
Doan Huy Loi, Kyoji Sassa, Khang Dang, and Hong Le Luong	
Numerical Models of Debris Flows with Entrainment Analysis-Case Studies from the Republic of Serbia	267
Jelka Krušić, Biljana Abolmasov, and Miloš Marjanović	
Numerical Simulation of a Creeping Landslide Case in Japan	273
Akihiko Wakai, Deepak Raj Bhat, Kenta Kotani, and Soichiro Osawa	
Numerical Simulation of Debris Flows After Ash Fall at Mt. Fuji	281
Takashi Kitazume, Takahiro Abe, and Satoshi Goto	

On the Progression of Slope Failures Using Inverse Velocity of Surface Movements in an Undercut Slope Model	293
Thirapong Pipatpongsa, Krit Aroonwattanaskul, and Kun Fang	
Rainfall Boundary Condition in a Multiphase Material Point Method	303
Mario Martinelli, Wei-Lin Lee, Chjeng-Lun Shieh, and Sabatino Cuomo	
Response of Slopes to Earthquakes and Rainfall	311
Jiawei Xu, Ryosuke Uzuoka, and Kyohei Ueda	
Reproduction of Sedimentation State During Rock Slope Failure Using the Simplified DEM Model	321
Hitoshi Nakase and Yukio Nakata	
Part IV Recent Development in Soil and Rock Testing Techniques, Application and Analysis Methods	
Analysis of Shear Strength Variability of Ash-Fall Pyroclastic Soils Involved in Flow-Like Landslides	329
Rita Tufano, Luigi Annunziata, Enrico Di Clemente, Giovanni Falgiano, Francesco Fusco, and Pantaleone De Vita	
Comparison of Soil Parameters and Soil Moduli E_{50} and E_{70} of Residual Soils Used in Stability Analysis	335
L. K. N. S. Kulathilake, E. H. N. Premasiri, and A. A. Virajh Dias	
Influence of Plant Root Asperities and Architectural Traits on Soil Shear Resistance	341
Qi Liu, Lijun Su, and Jun Zhang	
Modelling of Creep Behavior of Claystone in Mae Moh Open-Pit Mine Using the Soft Soil Creep Model	349
Pongsakorn Wongchana, Peerapong Jitsangiam, Suriyah Thongmune, and Tawatchai Tanchaisawat	
Monotonic and Cyclic Behaviour of Tephra Layer Landslide at Takanodai from the 2016 Kumamoto Earthquake	357
Satoshi Goto and Kento Okada	
Shearing Rate Effect on Residual Strength of Typical Clay Soils in Ring Shear Test	365
Deepak Raj Bhat	
Simple Shear Tests for Unsaturated Soils	371
Mariagiovanna Moscariello and Sabatino Cuomo	
Simplest Methods of Determining Dynamic Soil Properties for Use in Co-seismic Hazard Analysis	379
Beena Ajmera and Binod Tiwari	
The Acoustic Emission Characteristics and Shear Behaviour During Granular Shearing	385
Yao Jiang and Gonghui Wang	

Part V Recent Advancements in the Methods of Slope Stability and Deformation Analyses

- Prediction of Deformation of Caisson Type Piles in Open cut Works and Countermeasures Employing Early Closure Method** 393
Masahiro Katayama, Tsuyoshi Nakade, Tetsuji Yamaguchi, and Masafumi Okawara
- Slope Stability Assessment of Weak and Weathered Rocks with BQ System** 401
Timur Ersöz, Merve Özköse, and Tamer Topal
- Soil Databases to Assist Slope Stability Assessments in the Eastern Caribbean** 407
Paul J. Vardanega, Elizabeth A. Holcombe, Myrto Savva, Casey J. Shephard, Rose Hen-Jones, and Flavia De Luca
- The Mt Gamalama Instability Level in Generating Landslide-Induced Tsunami in Ternate Island, Indonesia** 415
Saaduddin, Jurgen Neuberg, Mark E. Thomas, and Jon Hill
- ## **Part VI Recent Development in Disaster Risk Assessment**
- Effect of Pore Pressure Dynamics on Progressive Failure in a Clayey Glaciolacustrine Landslide** 423
Kelvin Sattler, David Elwood, Michael T. Hendry, David Huntley, Jessica Holmes, and Paul B. Wilkinson
- Engineering Geological Investigation and Slope Stability Analysis for Landslide Hazard Assessment in Indian Himalayas** 431
Shantanu Sarkar and Koushik Pandit
- First Consideration About Post 2017 Wildfire Erosion Response and Debris Flow in Susa Valley (NW Italy)** 443
Damiano Vacha, Giuseppe Mandrone, Matteo Garbarino, and Donato Morresi
- Identification of Sliding Surface and Crack Pattern in the Soil Creep, Case Study: Unika Soegijapranata Campus, Semarang, Central Java, Indonesia** 451
Wahyu Wilopo, Hendy Setiawan, Doni Prakasa Eka Putra, and Teuku Faisal Fathani
- Preliminary Result of Real-Time Landslide Monitoring in the Case of the Hinterland of Koroška Bela, NW Slovenia** 459
Tina Peternel, Ela Šegina, Matija Zupan, Mateja Jemec Auflič, and Jernej Jež
- Quantitative Risk Analysis of Earthquake-Induced Landslides** 465
Saskia de Vilder, Chris Massey, Tony Taig, Biljana Lukovic, Garth Archibald, and Regine Morgenstern
- Role of Remote Sensing Technology in Landslide Risk Management of Hong Kong** 471
Julian S. H. Kwan, W. K. Leung, and Clarence E. Choi
- The Characteristics of the Vegetation Distribution Related to the Slope Failure Caused by the Earthquake** 479
Yoshikazu Tanaka, Kyohei Ueda, and Ryosuke Uzuoka

Cutting-Edge Technologies Aiming for Better Outcomes of Landslide Disaster Mitigation	485
Kazuo Konagai	
International Consortium on Landslides	507



2020 Kyoto Japan

Introduction—Testing, Modeling and Risk Assessment

Binod Tiwari, Beena Ajmera, Sabatino Cuomo, Katsuo Sasahara, and Ryosuke Uzuoka

Abstract

There has been a significant progress in landslide mitigation strategies in recent years. Recent advancement in physical or experimental and numerical modelling, testing methods to evaluate soil properties, and computing capabilities for slope and deformation analyses as well as landslide risk assessment lead the global scientists to prepare in advance for landslide hazard mitigation. The papers collected in this volume, authored by global leaders in scientific research pertinent to landslide hazard mitigation, provide testament of the progress we made recently on landslide hazard mitigation, specifically on recent development in testing, modelling and risk assessment methods.

Keywords

In-situ testing • Laboratory testing • Experimental modeling • Numerical modeling • Slope stability • Deformation analysis • Risk assessment

Background

While evaluating mass movement such as landslides and debris flows, properties of materials involved in the process play an important role. The material testing methods, instrumental as well as computational sensitivities, and accuracy levels have progressively been improved with the development of newer technology. Moreover, with the development of better technology every year, mass movement modeling techniques, both numerical and experimental, have significantly been improved in the past decade. Such modeling capabilities help researchers significantly to understand the mass movement behavior and perform sensitivity analyses at significantly lower cost compared to full scale models. One area that has significantly improved with the development of robust technology and efficient modeling techniques is landslide or debris flow risk assessment. Recent advancement in testing, modeling and risk assessment have been discussed routinely in various conferences and forums in the past, including the World landslide Forum 4 (Mikos et al. 2017a, b). Volume 4 of this book series (Tiwari et al. 2020) incorporates papers by leading scientists in the world who are making tireless efforts in research pertinent to the recent development and advancement in testing, modeling, and risk assessment for the mitigation of hazards caused by landslides, debris flows and other mass movements. This volume includes five keynote lectures and 45 peer reviewed papers in five different research areas pertinent to the theme of this volume. The entire volume is divided into six parts—(I) Keynote Lectures, (II) Recent Development in Physical Modeling of Landslides,

B. Tiwari (✉)

California State University, Fullerton, Office of Research and Sponsored Projects, 1121 N. State College Blvd., Fullerton, CA 92831, USA
e-mail: btiwari@fullerton.edu

B. Ajmera

Department of Civil and Environmental Engineering, North Dakota State University, CIE Building Room 201Q, Fargo, ND 58108, USA
e-mail: beena.ajmera@ndsu.edu

S. Cuomo

Department of Civil Engineering, University of Salerno, 84084 Fisciano, Italy
e-mail: scuomo@unisa.it

K. Sasahara

Science and Technology Unit, Natural Sciences Cluster, Research and Education Faculty, Kochi University, 2-5-1, Akebonocho, Kochi, 780-8520, Japan
e-mail: sasahara@kochi-u.ac.jp

R. Uzuoka

Disaster Prevention Research Institute, Kyoto University, Gokasho, Uji, Kyoto, 611-0011, Japan
e-mail: uzuoka.ryosuke.6z@kyoto-u.ac.jp

© Springer Nature Switzerland AG 2021

B. Tiwari et al. (eds.), *Understanding and Reducing Landslide Disaster Risk*, ICL Contribution to Landslide Disaster Risk Reduction, https://doi.org/10.1007/978-3-030-60706-7_1

(III) Recent Development in Numerical Modeling of Landslides, (IV) Recent Development in soil and rock testing techniques, application and analysis methods, (V) Recent advancements in the methods of slope stability and deformation analyses, and (VI) Recent Development in Disaster Risk Assessment. Presented in the subsequent sections are the brief descriptions of the papers covered in each part. All of these papers were peer reviewed and accepted with at least one affirmative review decision. The editors of this volume express their appreciation to the reviewers who have provided their valuable time to review the manuscript submitted in this volume.

Part I—Keynote Lectures

Tiwari and Ajmera (2020) has compiled state of the practice knowledge regarding shearing behavior and resistance of soil, specifically fully softened and residual shear strength, and recommended the procedure for utilizing residual and fully softened shear strengths for slope stability analysis in practice. In this key-note paper, the authors outlined the details regarding currently available testing methods and their benefits as well as limitations, regression equations to estimate such strengths with easily measurable index properties, and the influence of pore water chemistry as well as mineralogical compositions on these shear strengths. The authors also outlined various interpretation techniques to obtain shear strength parameters from laboratory test results and their influence in slope stability analysis results.

Stark and Xu (2020) describes the 2014 Oso Landslide in Washington focusing on the use of three computer programs to estimate the runout characteristics with the intent of comparing the results obtained with the field observations. The paper describes the two-phase failure of the landslide in which significant strength losses occur resulting in 1.4 km of movement and destroying a residential community. The material is described to undergo brittle failure during the second phase. Stark and Xu (2020) also describe the previous landslide history in the region. From their comparison of the runout results obtained from DAN3D, FLO-2D and Anura3D models, the authors find the runout zone is under-predicted by the FLO-2D model. The results from DAN3D and Anura3D were both found to be in good agreement with the field observations.

Pradel (2020) presents recent advancements geomechanical modelling, specifically in slope and deformation analysis, and provided some guidelines to use the results of such modelling in landslide stabilization practice. Two applications are considered in the key-note paper, which suit well for slope stability modelling. In the analysis of slope repairs and landslide stabilizations that combine multiple structural elements (e.g., several rows of piles with tiebacks),

numerical modelling can enhance understanding. The seismic performance of slopes also greatly benefits from modelling, especially in the cases where dynamic amplification and permanent seismic displacements are a major concern.

Ajmera and Tiwari (2020) provided an extensive review on slope stability and deformation analysis methods available in practice. Such analyses range from easily developable excel spreadsheets to specific software programs as well as GIS software. This key-note paper details with the methods commonly used in practice for slope stability analysis both for natural as well as engineered slopes and outlines the importance of back analysis method to analyze stability of landslides. In this paper, the authors have included case studies available in the literature to illustrate some of the slope stability and deformation analysis methods.

The study by Zhang et al. (2020) presents a protocol for managing the risk of landslide hazard chains. This protocol is stated to quantify the amplification and overlapping effects of multiple hazards. This protocol is applied to landslide hazard chains for two large landslides that occurred along the Jinsha River. For these landslides, the measures implemented to reduce short and long-term risks and consequences are also described in the paper. The paper also presents an extensive list of future research avenues associated with landslide hazard chain risk management.

Part II—Recent Development in Physical Modeling of Landslides

Chen and Orense (2020) investigated the use of a magnetic tracking system applied at the laboratory-scale to measure the behaviour of the blocks as they propagate downslope. The system consists of permanent magnets as trackers and magnetometers as receivers. For various combinations of pile height, block volume and surface inclination, the displacements and orientations of the permanent magnet, representing one of the blocks undergoing movement, are monitored from which kinematic quantities are captured to highlight the behaviour of the blocks as they flow down the chute. The results obtained coincide very well with image analysis from video camera.

Yanto and Apriyono (2020) presents a new physically-based method for translational landslides to calculate the factor of safety. The proposed method was used to calculate the factor of safety for unsaturated and saturated materials. It is stated that unlike the previous methods, the method proposed in this study estimates the depth of the sliding surface as a function of the bearing capacity. Yanto and Apriyono (2020) compared the results from their method against field observations of landslides in the Sirampog and Kandang Serang subdistrict in Western Central Java. It was stated that there was good agreement.

Azmi et al. (2020) carried out an integrated analysis of rainfall-induced landslides through a laboratory test, as well as laboratory and numerical analyses. A set of laboratory-scale soil slopes was subjected to instability through different modes of rainfall intensities and slope inclination to clarify the process of failure initiation. A numerical analysis was also performed to confirm the effect of these factors on landslide occurrence. The results of the experiment and analyses concluded that the unsaturated slope stability analysis, setting the initial conditions and boundary condition, is important in dealing with the issues presented in their experiments.

Centrifuge model slope experiments with the increase of groundwater level were implemented by Hiraoka et al. (2020) to develop warning and evacuation alerts for workers in construction sites for slope excavation. Three cases of model slope with different slope angles were set up for the experiment. The results showed that the model slopes collapsed with groundwater while they did not collapse without groundwater under same slope angle. Shear deformation was measured by strain meters installed at the surface layers of the slopes. The deformation showed accelerative increase prior to the failure. Standard deviation of the increase of the deformation could be the criteria for alert. The slope might collapse soon when the increase of the deformation velocity exceeded the criteria based on the standard deviation.

To study the failure of tailing dam slopes, Hu et al. (2020) conducted a series of flume tests. The model slopes were constructed using iron waste deposits from the An-Nigh tailing pond in China and prepared to various relative densities. Hu et al. (2020) found that the failure mechanism varied based on the relative density with sudden collapses occurring when the relative density was less than 35% and progressive failures occurring when the relative density was greater. Specifically, sudden failure resulted when the saturation of caused densification of the soil mass resulting in the formation of crack that increased the pore pressure at the toe of slope. The authors also noted that multiple sliding surfaces initiating at the toe of the slope extending further upslope were characteristic of the progressive failures observed in their tests.

Tiwari (2020) measured velocity of infiltration of rainwater in model slope with different vegetation cover density under artificial rainfall to examine the influence of vegetation on surface runoff or infiltration during rainfall. Definition of vegetation cover, that the author considered, was ratio of area covered with leaves of a plant to that of slope surface area. Velocity of vertical infiltration of rainwater was larger until a certain value of vegetation cover density and it was almost constant above that threshold value. The result showed that the vegetation encouraged rainwater infiltration into the slope. Factor of safety of the slope was lower in the slope with vegetation cover of more density according to the

slope stability analysis conducted by modelling the effect of a degree of saturation and vegetation cover density on shear strength of the soil in the slope.

Carey et al. (2020) studied potential failure mechanisms of submarine landslides in the laboratory. Specifically, the study evaluates mechanisms for both shallow and deep submarine landslides considering both the impacts of earthquakes and elevated pore pressures, separately. The experimentation is performed in a modified dynamic back pressure shear box using soils collected from the Tuaheni Landslide Complex off the east coast of New Zealand. From the results obtained, Carey et al. (2020) observed several different failure patterns. These observations were used to describe two potential failure mechanisms that submarine landslides may be subjected to.

The effect of rainfall infiltration on the stability of layered slopes were studied using flume tests in Capparelli et al. (2020). The study presents the results from three tests modeling slopes with (a) one layer comprised entirely of volcanic ash, (b) two layers consisting of pumice and volcanic ash and (c) three layers consisting of pumice between two layers of volcanic ash. Based on the results obtained, the authors conclude that the stability of the slope depended on the pumice layers in the models. The behavior of the pumice was noted to be dependent on the initial humidity and the intensity and duration of the rainfall applied. Capparelli et al. (2020) found that the ash hampered the drainage of pore pressures generated during the rainfall events, which will result in a reduction in the soil suction and the associated shear strength. As a result, localized shallow slope failures were observed in the one and three layer models., but not in the two layer model.

Part III—Recent Development in Numerical Modeling of Landslides

Ruiz-Carulla et al. (2020) proposes a model to replicate the fragmentation of a rockfall event. This model is, then, implemented in RockGIS, which is a three-dimensional trajectory rockfall simulator. To verify the proposed model, the authors used UAV surveys and digital photogrammetry to determine the block size distribution of a fragmented rockfall in Mallorca, Spain. The results from RockGIS were verified with the field observations finding good agreement between the two. It is also found that some of the smaller fragments are deposited along the path taken by the rockfall, while larger fragments reach a protection gallery causing a multi-impact effect.

Havenith (2020) discusses the use of virtual reality to visualize landslides. To do so, three-dimensional surface and geological models for several landslides sites with the intent of using them to perform slope stability analyses were

developed. In the paper, the author uses virtual reality technology to study the internal structure of a landslide site. Require inputs for the development of this visualization along with the issues encountered during the process are described within the paper. Havenith (2020) notes that the acceptance of virtual reality will require the integration of its environment with existing computers and requires further critical evaluation for the applications in which it is employed.

Su et al. (2020) introduced a novel landslide model developed by coupling a DEM model with DAM for simulation of flow-like landslides, in which the DEM was employed in the landslide initiation area to better simulate the failure mechanism of slope, and the DAM was adopted in the landslide runout and deposition phase, where the landslide has developed into flow-like landslide with fluid-like behaviour. Finally, the new coupled model was validated against an experimental test case. The coupled model was able to accurately capture the detailed dynamics of flow-like landslides.

Mergili and Pudasaini (2020) deal with the challenges in modelling complex cascading landslides. The focus is put on the propagation and interaction of flow processes, with special reference to the physical processes, the numerical implementation, and model parameterization. Some important cases are treated such as landslide-reservoir interactions; entrainment, deposition, and stopping; improved numerical schemes; guiding parameter sets; and dynamic adaptation of key parameters to flow dynamics. Promising approaches are presented for most of these aspects, and the need for further research is outlined.

Chen et al. (2020) demonstrated an application of reciprocal Green's functions on the forecast of submarine landslide tsunami. Some precautions that should be taken in applying this approach in submarine landslide tsunamis different from seismic tsunamis were included. Possible solutions to overcome difficulties using this approach were also recommended. Finally, suggestions based on reciprocal Green's functions were advanced to build a practical forecast system for submarine landslide tsunamis.

Fully coupled flow-deformation analysis using finite element method framework PLAXIS 2D were adopted by Yang et al. (2020) to simulate hydraulic response and deformation of slopes. Shear strength of an unsaturated soil was modelled by combining Bishop's effective stress and extended Mohr–Coulomb criterion by Vanapali. They simulated model slope deformation in previous literature to validate the applicability of the model at first. And then they applied to simulate rainfall infiltration and deformation of assumed slope with shallow depth under constant rainfall intensity. The simulation revealed that slope displacement could be divided into three stages, namely constant, accelerated and critical deformation stages.

Nakatani et al. (2020) investigate the case of landslide dam formations in mountainous regions, with special reference to the case when landslide dam outburst occurs, and large scale debris flow devastates the downstream area. For a case history, the pre- and post-event digital terrain models are used, and the landslide dam outburst scenario is numerically simulated by comparing the results with the downstream deposition. Then, the installation of one closed type Sabo dam is considered in the torrent, and this prevents the sediments from moving downstream.

Gatti et al. (2020) described a first version of the simulation tool developed within the SMART-SED project. The two main components of the SMART-SED model consist in a data preprocessing tool and in a robust numerical solver, which does not require a priori identification of river beds and other surface run-off areas, thus being especially useful to provide accurate input data to more localized landslide and debris-flow models. The results of a complete numerical simulation were reported and possible future developments of the model were discussed.

The paper by Dang et al. (2020) examines the potential of additional landslides formed from the blocks remaining from the Mr. Rung Landslide in Myanmar in July 2015. The study focuses on rainfall-induced slope failures, whose stability is assessed with the use of results from ring shear tests inputted into LS-RAPID simulations. For their study, Dang et al. (2020) evaluate various groundwater table levels to determine the volume of any induced landslides and their associated velocities for the development of plans for landslide disaster mitigation. From the results obtained, it was concluded that the potential landslides would occur when the pore pressure ratio reached between 0.35 and 0.39. A rise in the groundwater table was found to correspond to an increase in the likelihood of deeper landslides. Dang et al. (2020) stated that the results could be used to develop real-time early warning systems to determine the need for excavations of individuals that may be affected by potential failures.

Loi et al. (2020), based on site investigation and multi-temporal satellite images, presented the adverse effects of urbanization and estimated hazard zoning caused by a potential landslide using the ring shear tests and integrated simulation model. The 2014.8.20 landslide disasters in Hiroshima, Japan was selected as the case study to examine the adverse effect of urbanization. The results of hazard assessment of rainfall induced landslides in Midori and Yagi area may give effective information for the local government authorities in Hiroshima city.

Krušić et al. (2020) presented material entrainment analyses in RAMMS debris flow software, as well as numerical models of final flow heights for two case studies from the Republic of Serbia. Results of the analyses showed

that entrainment materials affected final results of transportation model, runout distance, deposition area and volume of debris flow. In both cases entrainment volume was very huge, but it was much less than initial volume. The final results were validated with pre- and post- event DEMs and analysis of ERT geophysical results.

New elasto-viscoplastic constitutive equation was proposed by Wakai et al. (2020) for 2D-FEM to simulate creeping displacement of landslides and applied to Tomuro landslide with snowmelt water in Japan. Two new control constitutive parameters were incorporated in the equation. They were based on the relationship between total factor of safety derived by existing slope stability analysis methods and displacement velocity measured in the field for actual landslides. The simulation proved the validity of the model to simulate horizontal displacement of Tomuro landslide if not only rainfall intensity but also snowmelt water intensity was adopted in the simulation.

Kitazume et al. (2020) simulated debris flows caused by rainfall after an eruption with ash fall at Mt. Fuji using a method that combines Cellular Automaton (CA) and Multi Agent (MA) Systems. The CA/MA method can realize high-speed calculations because large-scale simultaneous equations do not need to be solved and the results can be easily imaged. Although local rules must be set experimentally and calibrated, the CA/MA method can easily reflect knowledge and experiences of experts such as geologists, geomorphologists, and geotechnical engineers.

Measurement of displacement on the surface of undercutting for a centrifuge model slope was implemented by Pipatpongsa et al. (2020) in order to examine the validity of inverse velocity method proposed by Fukuzono for predicting failure time of undercutting wall in open-pit coal mining area. Displacement on the model slope was recorded by a high-speed VDO camera and analyzed by image processing software. The result suggested that the inverse velocity method was valid for prediction of failure time of the model experiment.

Martinelli et al. (2020) provided a new solution to estimate the true velocity of the liquid phase at the node of the boundary layer and implemented a coupled hydro-mechanical model using MPM. The validation of such implementation was achieved by simulating a 1D infiltration problem and comparing with the MPM results with those obtained through the commercial software PLAXIS. With the help of this newly implemented boundary condition, rainfall-induced landslides could be better investigated using MPM.

Centrifuge model slope experiments subjected to earthquake shaking and following rainfall were implemented by Xu et al. (2020) to reveal the effect of cracks in the slope generated by earthquake on instability of the slope at following rainfall event. Cracks were not generated on the slope by shaking due to insufficient shaking intensities and

only small displacements were induced unfortunately in the experiments. While this kind of challenging experiment might be necessary to reveal the mechanism of rainfall-induced landslides after generating cracks on the slope by earthquakes and their trial should be appreciated.

Nakase and Nakata (2020) propose a model using the discrete element method to evaluate the traveling distance of a collapsed rock mass when slope collapse occurs. A new model parameter to evaluate the reach distance and accumulation state of collapsed soil called rotational friction is introduced. To determine the range of appropriate values for the rotational friction, numerical simulations are conducted to reproduce laboratory experiments for finding the repose angle of various sands. A parametric study for a bedrock slope collapse is also presented under various hypotheses.

Part IV—Recent Development in Soil and Rock Testing Techniques, Application and Analysis Methods

Given the occurrence of several deadly debris flow events in pyroclastic soil deposits in southern Italy, Tufano et al. (2020) noted the need to characterize the shear strength of these deposits. To do so, they conducted nearly 100 direct shear tests from soils collected from different strata in four landslide sites. The tests were used to determine the Mohr–Coulomb shear strength parameters. Tufano et al. (2020) found a linear relationship between the drained friction angle and the sum of the sand and gravel contents of the mixtures. They further found that the materials tested high cohesion values which they attributed to the effects of reinforcement by roots, soil crushing and/or the interlocking and angularity of the soil grains. The study also examined the inherent variability in the shear strength parameters by estimating the lower bound values corresponding to the 10th percentile data.

The impact of void ratio, dry density and moisture content on the Young's modulus of elasticity of residual soils was studied by Nimani et al. (2020). To do so, the authors conducted triaxial tests on 29 silty clay and sandy clay residual soil samples from several landslide sites in Sri Lanka. In this study, the secant Young's modulus of elasticity values corresponding to 50 and 70% of the maximum deviator stress were examined. The authors found that the moduli values depend on the void ratio, dry density and moisture content. Specifically, they noted that the void ratio had a strong influence on the moduli values than the dry density. Furthermore, Nimani et al. (2020) found that higher moduli values could be expected in soils with lower water contents.

Liu et al. (2020) conducted a series of pull-out friction tests and triaxial shear tests on soil-root composites to

evaluate the impact of the friction between the soil-root interface. From the results, the authors find that the root diameter has a little influence on the surface roughness. Additionally, it is noted that an increase in the soil moisture content results in a reduction in the pull-out shear stress. Liu et al. (2020) use the generalized equivalent confining pressure to further discuss friction of the soil-root interface. The generalized equivalent confining pressure is defined as the difference between the confining pressure between the reinforced and unreinforced soil at a constant shear strength. The paper concludes that the generalized equivalent confining pressure will be larger for horizontal roots as opposed to vertical roots.

The long-term stability of the Mae Moh lignite mine, which is the largest open pit mine in Thailand, was studied by Wongchana et al. (2020). This stability is dependent on the creep behavior of the claystone material found at this mine, which was stated to behave like a rock when dry and like a soil when the moisture content is high. To study the creep behavior of this material, the authors performed a series of customized triaxial creep tests. The creep behavior at the open-pit mine was then modeled using Plaxis 3D. The results found that the behavior of the claystone at the open pit mine was better simulated using the soft soil creep model than the Mohr–Coulomb model.

Istiyanti et al. (2020) evaluated the relationship between the water content and the shear strength of tephra layers from the Aso Volcano in Japan. They measured the shear strength using a Yamanaka-type soil hardness and direct shear box. Both disturbed and undisturbed samples collected from two sites were tested in the study. The authors conclude that the shear strength results from both tests were the same. They found that the maximum shear stress varies with the moisture content. Furthermore, the authors conclude that higher shear strengths were obtained from the undisturbed samples than the reconstituted samples.

In Bhat (2020), four clayey soils were used to perform ring shear tests at six different strain rates. The four clayey soils tested in this study consisted of a commercial kaolin clay and three soils collected from landslide sites in Japan and Nepal. The author studies the effect of strain rate on the residual shear strengths of the soils. The author found that the residual shear strength was not affected by the strain rate when the strain rate is between 0.073 and 0.162 mm/min. However, when the strain rate is between 0.162 and 0.586 mm/min, the residual shear strength was found to increase with an increase in the strain rate. This impact was found to be greater in soils with higher plasticity indices.

Loose unsaturated pyroclastic soil deposits experience static liquefaction and collapse upon shearing. To study the impact of soil suction on the changes in shear strength, Moscariello and Cuomo (2020) conducted suction controlled simple shear tests. They stated that these tests allow for the

coupling of hydro-mechanical behavior better reproducing the in-situ conditions. The results obtained were compared with those from direct shear and triaxial tests. From the results, the authors observed dilative behavior when the pyroclastic soils were in the unsaturated condition, while contractive behavior was observed when the soils were saturated. Moscariello and Cuomo (2020) found that the suction rate had an impact on the stress ratio obtained at failure.

The paper of Amjera and Tiwari (2020) deal with soil cyclic mobility, that is the loss of shear strength in a soil subjected to cyclic loading resulting from a reduction in the effective stress. Several mixtures of powdered montmorillonite and kaolinite clay minerals mixed with ground quartz are prepared in the laboratory and used to perform static and cyclic simple shear tests. A relationship between the normalized undrained strength ratio and the post-cyclic effective stress ratio is thus obtained. The latter is used to assess the reduction in the factor of safety of a slope affected by landslide in a site of the Lokanthali region of Nepal after the 2015 Gorkha earthquake.

The fluctuations in the shear strength as a result of acoustic emissions were studied by Jiang and Wang (2020). The relationship between these parameters was studied with the use of a customized servo-hydraulic controlled ring shear tests using glass beads of different sizes to represent the granular materials. The study found that shear strength was strongly correlated with acoustic emissions. Furthermore, it was concluded that the rate of acoustic emissions increased with an increase in the shear velocity. These increases were further stated to depend on the particle size. Jiang and Wang (2020) also concluded that they were unable to establish a relationship between the magnitude of the stress drops and the frequency-size distribution of acoustic emissions.

Part V—Recent Advancements in the Methods of Slope Stability and Deformation Analyses

3D FEM analysis was performed by Katayama et al. (2020) to validate the effect of caisson type piles to stabilize open cut walls in landslide area. The early closer method was adopted in open cut works in the project and appropriate construction method against large deformations was examined by the analysis. The analysis showed not only the rebound of the excavated bottom was suppressed but also displacement of the pile and increase in rebar stress could be restricted.

Ersöz et al. (2020) assessed the stability of fifty-five rock slopes in the Western Black Sea Region, Turkey using limit equilibrium procedures and basic quality system, which was developed in China. The rock slopes studied had a variety of different rock types, whose strengths were primarily categorized as weak to medium. The paper stated that most of

the rock materials encountered in the studied slopes were moderately weathered. Ersöz et al. (2020) found that the results from the limit equilibrium analyses matched well with the field observations, from which it was noted that the majority of the slopes were stable except for the occurrence of surficial failures. However, the results from the basic quality system did not agree with the field observations unless the strength was larger than 50 MPa. This was stated to be a consequence of the fact that the basic quality system relied more heavily on unconfined compressive strengths and rock soundness than the discontinuity features.

Analysis of updated database for shear tests results of soils in Saint Lucie, in the Caribbean, was carried out by Vardanega et al. (2020) and combined them with the results by the Government of Saint Lucia. Existing regression equation for internal friction angle with physical properties such as liquid limit, plastic limit, plasticity index, silt–clay fraction and water content were re-examined using updated database and improved correlations were proposed. These equations were derived to decide soil strength parameters for simple slope stability analysis for road construction projects in Saint Lucia.

The possibility of tsunami generation because of landslides occurring in the steep flanks of Mt. Gamalama volcanic island in the Molucca Sea were studied by Saaduddin et al. (2020). The paper focuses primarily on the stability of the flanks considering both static and seismic conditions. The pressure of magma is also considered in the stability analyses. The study finds that all four sections analyzed in the study were stable under static conditions. However, the combination of seismic loads and pressure from the magma were noted to lead to instability of the sections. Saaduddin et al. (2020) found that massive landslides were triggered.

Part VI—Recent Development in Disaster Risk Assessment

Sattler et al. (2020) note that slope stability calculations typically ignore the impacts of fluctuations in the matric suction and unsaturated soil mechanics, but that these considerations can significantly influence the stability of a slope. To demonstrate this, they consider the Ripley Landslide in the Thompson River Valley as a case study describing the changes in its movement rates as a function of weather patterns, soil moisture deficit, and matric suction. Their results indicated that the downslope movement is correlated with soil moisture deficit values with greater movements occurring in wetter years. The study further finds that a delay in the matric suction values behind the soil moisture deficit values. The authors find that river elevation has an impact on stabilizing the Ripley Landslide with higher river elevations corresponding to more stable conditions. They also noted

that the river elevation was not solely responsible for the varying displacement rates find that rapid snowmelt can lead to unstable conditions due to the delay in time between the snowmelt and the resulting increases in river elevations. Snow melting leads to reduced soil suction combined with the lack of buttressing support from the river elevation causing potential failures.

In their study, Sarkar and Pandit (2020) describe three rock mass classifications systems, namely, the geological strength index, the rock mass rating, and the slope mass rating. These methods are then used to determine geotechnical parameters required to perform rock slope stability analyses. The authors look at several vulnerable rock slopes in the Lesser and Higher Himalayas in Uttarakhand, India. From these slopes, it is determined that the different rock mass classification systems are interdependent. The paper also includes an example of a numerical model developed to determine the rock slope stability using the geological strength index and the rock mass rating to establish the necessary input parameters.

Mass movements in the Comba delle Foglie watershed, located in northwest Italy, following the Susa Valley wildfire were described in Vacha et al. (2020). This study attempts to identify the characteristics of the debris flows and watershed along with the process involved in the triggering of debris flows. With the use of satellite imagery and field surveys, the authors map the burn severity of the watershed, which was found to be moderately burned. Vacha et al. (2020) noted that the wildfire resulted in the generation of a discontinuous hydrophobic level, whose effects will vary with time, but were difficult to quantify through aerial images and field surveys. As a result, it is concluded that the relationship between the impacts of the wildfires and the occurrence of the debris flows were hard to establish. The determination of this relationship was further hampered by the amount of time that elapsed between these two events.

Wilopo et al. (2020) describes the work undertaken to identify sliding surfaces and crack patterns associated with soil creep were at the location a new sports hall is being constructed for the Unika Soegijapranata Campus in Indonesia. The paper describes the results from a geological surface and seismic refraction testing at the site, which was undertaken due to the formation of cracks in the building foundation during construction. These cracks were suggested to be a result of soil creep. Based on the results obtained, Wilopo et al. (2020) had several recommendations for the construction, including the need to shift the location of the sports hall and recommended that water infiltration be limited in the northeast area with drainage being directed to the southwest.

Peternel et al. (2020) aimed to provide real-time predictions of landslide dynamics for slopes threatening Koroška Bela, Slovenia. The authors instrumented and monitored two

landslides—namely, the Urbas landslide and Čikla landslide for 7 and 4.5 months, respectively. Peternel et al. (2020) found higher movement rates during the rainy period at the Urbas landslide. However, rapid displacements at the Čikla landslide occurred during rainfall in September and during the rainfall events in November. It was concluded that landslide dynamics were found to correlate with the groundwater level, morphology and size of the landslide mass.

The lack of quality spatial input data is stated to be a hindrance in the calculation of landslide risk. In de Vilder et al. (2020), the landslide hazard in the Franz Josef and Fox Glacier Valleys in New Zealand is studied, which was selected due to the region's lack of earthquake-induced landslide inventories. The authors use the inventories from three other earthquakes in the region to determine the probability that the landslide volume would exceed a given value under different levels of ground shaking. Four different sets of assessments are performed by de Vilder et al. (2020). It is found that New Zealand earthquakes primarily triggered shallow debris avalanches. This was stated to be a result of three factors including (a) the dominance of these types of landslides in previous databases, (b) the limited depth of failure as a result of the bedrock conditions and (c) fracturing of the schist rock mass in the valleys.

Kwan et al. (2020) has examined the use of remote sensing technologies for the identification and monitoring of landslide hazards, post-landslide responses and in the design of landslide prevention and mitigation measures. They found machine learning techniques can be applied to allow for the identification of geological features from aerial images; and when combined with convolutional neural networks, such applications can be used to delineate landslide boundaries with accuracies of about 80%. It is further stated that the use of satellite images may improve the results obtained. Kwan et al. (2020) also state that the identification of rock outcrops from aerial images appears to be promising. The use of unmanned aerial vehicles and handheld laser sensors in landslide-related applications is also discussed.

The study by Tanaka et al. (2020) examined the impact of vegetation on slope failures that occurred in a watershed along the Habiu River in Atsuma, Japan. These slope

failures were triggered by the 2018 Hokkaido Eastern Iwate Earthquake. Tanaka et al. (2020) also studied the impact of slope angle, rainfall, and geology on the instabilities observed. They found that the regions affected by slope instabilities were covered with Coniferous plantations, while no instabilities were observed in Hardwood natural forest. It was also stated that root resistance needs to be considered when examining slope stability.

Conclusions

While evaluating landslides for possible mitigation measures or prevention planning, detailed analysis is needed. Properties of the materials involved in the landslide process, geometry of slope and water table, are among the parameters needed for stability analysis of slopes. Moreover, numerical and physical modelling of landslides help us to evaluate the landslides and understand associated failure mechanism. There have been significant progresses in recent years regarding slope stability and deformation analysis techniques and landslide risk analysis. As such, frequent collection of such developments in books such as this volume is important to prepare the society against landslide disasters.

Acknowledgements The authors would like to thank the reviewers who provided their valuable time to review the papers submitted in this book volume, which helped the editors to make appropriate decisions regarding acceptance of those papers. Moreover, the authors appreciate authors of the papers presented in this book volume for submitting the results of their study in this book.

References

- Mikos M, Tiwari B, Yin Y, Sassa K (2017a) Advancing culture of living with landslides: volume 2, advances in landslide science, Part 1. Springer
- Mikos M, Tiwari B, Yin Y, Sassa K (2017b) Advancing culture of living with landslides: volume 2, advances in landslide science, Part 2. Springer
- Tiwari B, Sassa K, Bobrowsky P, Takara K (2020) Understanding & reducing landslide disaster risk, volume 4—testing, modeling and risk assessment. Springer

Part I
Keynote Lectures



Recent Developments in the Evaluation and Application of Residual and Fully Softened Shear Strengths for the Stability Analyses of Landslides

Binod Tiwari and Beena Ajmera

Abstract

Shear strength is an essential component of slope stability analyses and necessary for the design of landslide repair and prevention works. This paper provides an in-depth review of the shear strength of soil pertinent to landslide analysis—fully softened shear strength and the residual shear strength of soils. Methods currently used in practice to measure the fully softened and residual shear strengths are summarized along with their advantages and disadvantages. Specifically, this paper will present details regarding the methods used to measure these shearing resistances, such as direct shear, ring shear, triaxial compression and direct simple shear tests to measure the fully softened shear strength and the use of direct shear, ring shear and triaxial compression tests to obtain the residual shear strengths. Pertinent information and discussions are provided regarding the interpretation of the shear envelopes developed from these testing methods focusing on the use of linear and non-linear (or curved) failure envelopes along with the interpretation of the strengths in terms of the secant friction angles. The various forms of curved linear envelopes presented in the literature are discussed. The paper also includes details of several commonly used correlations to estimate both the fully softened and residual shear strengths. Recommendations by the authors on the use, measurement and interpretation of both the fully softened and residual shear strengths are also included.

Keywords

Residual shear strength • Fully softened shear strength • Direct shear • Simple shear ring shear • Triaxial shear • Mineralogy • Pore fluid chemistry • Shearing rate

Background

An understanding of the shear strength is essential while conducting stability analyses of slopes and design of landslide repair and prevention works. In this paper, the authors will mainly focus on the fully softened and residual shear strengths of soils as these shear strengths are more relevant to landslide analysis. The paper will provide background information regarding both of these shear strengths, details regarding the methods to measure these strengths, and an understanding of how these results should be interpreted. Also included within this paper is a summary of the factors that can influence the residual and fully softened shear strengths and a number of correlations that have been proposed in the literature that allows for the estimation of these strengths.

Shearing Behavior of Soil

Behavior and shearing resistance of soil under deformation depends on the type and nature of the soil. Figure 1 presents the behavior over-consolidated and normally consolidated soils during shearing. The peak strength is the maximum shear strength achieved in a soil mass after the nearly elastic behavior observed at the initial onset of shearing. However, as shearing continues after the soil exhibits peak resistance, stiff (or over-consolidated) soil starts softening through the increase in void ratio as it gains water from outside. As a result, shearing resistance start decreasing. The shearing resistance of the soil when soil gets fully softened is called

B. Tiwari (✉)

California State University, Fullerton, Office of Research and Sponsored Projects, 1121 N. State College Blvd., Fullerton, CA 92831, USA

e-mail: btiwari@fullerton.edu

B. Ajmera

Department of Civil and Environmental Engineering, North Dakota State University, Fargo, ND 58078, USA

e-mail: beena.ajmera@ndsu.edu

© Springer Nature Switzerland AG 2021

B. Tiwari et al. (eds.), *Understanding and Reducing Landslide Disaster Risk*, ICL Contribution to Landslide Disaster Risk Reduction,

https://doi.org/10.1007/978-3-030-60706-7_2

fully softened shear strength of soil. When the soil keeps on shearing beyond this point, the void ratio does not change due to change in moisture content; however soil particles/platelets start reorientation and shearing resistance keep on dropping until the soil platelets get their preferred orientation (in most cases clay platelets align parallel to the direction of shearing). Shearing resistance of the soil at this stage is the lowest shearing resistance and is referred to as the residual shear strength of soil. In the residual condition, polished slickenside surfaces will form when clay particles are oriented such that their long axis is parallel to the shearing direction. Skempton (1970) was the first to recognize the fully softened shear strength of soils. He noted that changes in the water content result in softening. This softening causes the strength to approach the strength at the critical state over time (Skempton 1970) at which point additional changes in shear displacements will not cause an increase or decrease in the water content. He further stated that the “the fully softened strength parameters c' and ϕ' are equal numerically to the peak strength parameters of the normally consolidated clay” (Skempton 1970). If an over-consolidated block of soil is remolded (converted to a normally consolidated soil by removing over consolidation history and diagenesis) at the moisture content close to its liquid limit and sheared at normally consolidated state, it exhibits a small peak followed by strength drop to the residual shear strength. This peak is numerically equal to the fully softened shear strength of soil (Fig. 1). Soil loses its cohesion intercept at the fully softened state as its behavior converts to that of normally consolidated soil. Residual shear strength of the soil does not change whether the soil is over-consolidated or not, as it can be observed in Fig. 1. Fully softened shear strength is achieved at the point of inflection in the shear stress versus shear displacement relationship and corresponds to a post-peak strength loss. The fully softened shear strength corresponds to the strength of the soil when it is at its critical state, i.e. the state where dilative soil gains moisture and contractive soil loses moisture during shearing to come to a critical void ratio.

Different Modes of Shearing

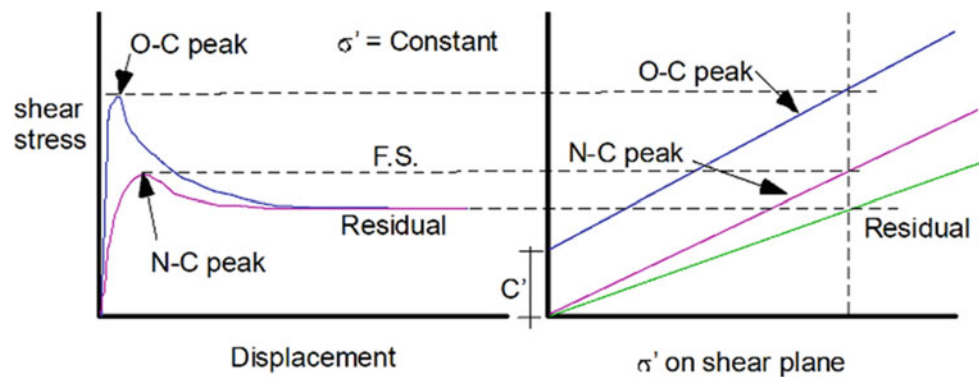
Lupini et al. (1981) identified three modes of shearing from ring shear tests conducted on bentonite-sand mixtures, showing a strong relationship of these modes with clay sized fraction and plasticity index. The turbulent or rolling mode of shearing is said to occur when the behavior of round particles and platy particles with high inter-particle friction dominates the shearing behavior. In the sliding mode, the observed behavior is dominated by the response of platy particles with low inter-particle friction. In this mode, the particles are strongly oriented. The transitional mode of shearing occurs when no particle shape dominates the shearing behavior. In this mode, both turbulent and sliding behavior is observed.

For over-consolidated (or stiff) clays, progressive failure occurs while the soil starts shearing. Progressive failure was described in Bjerrum (1967), who wrote that three conditions must be satisfied for this type of failure to occur. First, he noted that a continuous failure surface can only develop progressively if there exists a zone in which the local shear stresses are greater than the peak shear strength. Progression of the failure will continue if sufficient shear strains are induced in the shear zone to cause the material to strain beyond failure. If the material can undergo large and rapid reductions in strength after the failure strength is surpassed, differential movements will cause the stress concentration to shift to neighboring zones containing material that has not yet failed. This will lead in the advancement of the failure zone and can lead to the catastrophic failures. As such, residual shear strength is mobilized at the slope at its failure.

Appropriate Shear Strengths

Of utmost importance in landslide science is the use of the appropriate shear strengths in the stability analyses and design of prevention and repair works. Skempton (1964) established from back-analyses that the peak strength should

Fig. 1 Behavior of over-consolidated and normally consolidated soils during shearing



be used for clay deposits without joints and fissures. The residual strength should be applied to those conditions where large shear displacements have occurred to cause the clay particles to form polished slickenslided surfaces as it corresponds to the minimum strength of the soil mass. An example would be in the analysis of a reactivated landslide. However, it is almost impossible to find natural soils without fissures. As such, application of fully softened shear strength for the analysis of natural slope without any history of failure is more logical although it may be slightly conservative. More specifically, the fully softened shear strength is needed in a variety of different applications including in first-time slope failures, in excavations involving fissured clays, and in desiccated and compacted clay embankments. This strength can also be used as a way to account for strength loss with time that results from weathering, the dissipation of negative pore water pressures and stress relaxation (Duncan et al. 2011). Therefore, fully softened and residual shear strength parameters are more important for slope stability analysis pertinent to landslides and these two strengths are discussed in this paper.

Importance of Correlations

While in situ measurement of shear strength are always preferred in practice for landslide analysis, it is nearly impossible to measure mobilized in situ shear strength of soil from sliding surfaces due to various reasons such as the depth of sliding surface, inconvenience in mobilizing field testing equipment right after the sliding, etc. However, considering fully softened and residual shear strength of soil, available correlations in literature to estimate these values from index properties of sliding surface soil can be very beneficial. Moreover, although it is widely accepted that the residual shear strength should be measured in a torsional ring shear device and conducting these tests is relatively straight forward, it is not always possible due to the limited availability of such devices and conducting laboratory testing to measure the residual shear strength can be expensive. Measurement of the fully softened shear strength can also be easy. Research has shown that the resulting shear strength parameters are dependent on the different testing conditions including the devices used. There is no general consensus in the literature regarding the methods to be used. To address some of these issues, correlations become extremely important. Shear strength parameters estimated with correlation equations not only allow engineers to verify their back-analyses and laboratory test results, but they can also provide an estimate of the strength that can be used in the preliminary designs.

Fully Softened Shear Strength

Background

Gregory (1844) appears to be the first to describe a failure in a stiff-fissured clay that had been excavated for the London and Croydon railway (Castellanos 2014). The excavated slope was stated to remain stable for a period of time before the failure occurred, which Gregory (1844) attributed to be a result of wetting and drying cycles that lead to the formation of fissures through which water infiltrated weakening the slope. Castellanos (2014) stated that such failures were not described again until Terzaghi (1936). Terzaghi (1936) was the first to note that the strengths mobilized around excavations were lower than peak strengths of the clays from laboratory tests. He further suggested that these reduced strengths were a result of a reduction in the stress from the excavation process, which led to the development of fissures and the generation of negative pore water pressures. The infiltration of water to these fissures would cause the dissipation of the negative pore water pressures weakening the clayey material increasing the likelihood of the development of additional cracks. These additional cracks would then contribute to aggravating this mechanism.

Fully softened strength was first used by Skempton (1948) to describe the back-calculated strengths that was mobilized when cuts in Brown London Clay failed. This strength was determined to be lower than the strength of undisturbed samples tested in the laboratory. The softening process which reduced the strength from the laboratory measured values to the back-calculated values was stated to depend on time following a nonlinear trend. Henkel (1957) also presented a relationship describing the effective cohesion intercept as a function of the time to failure from construction. To derive this relationship, Henkel (1957) assumed that the effective friction angle remained constant. The definition of fully softened shear strength as is used today was first provided in Skempton (1970), as explained earlier.

Measurement Methods

Several different laboratory methods have been utilized to determine the fully softened shear strength of soils. Specifically, direct shear, simple shear, triaxial, ring shear and tilt table tests have been mentioned in the literature as means to obtain the fully softened shear strength parameters. Additional details regarding the use of these tests for this purpose are provided in the following subsections. For any of the tests, it is recommended at least four specimens of a sample

be tested at different consolidation or confining pressures to allow the results to capture the curvature, if any, of the shear envelope (as will be discussed in a later section of this paper).

Historically the fully softened shear strength has been measured using either direct shear or triaxial tests. (Bishop et al. 1965, Skempton 1977). The results obtained from these tests have been validated against the shear strengths obtained from back-analyses of failures. Furthermore, several researchers including Castellanos and Brandon (2013), De Mello (1946), Maccarini (1993), Moon (1984), Skempton (1964), and Thomson and Kjartanson (1985) have shown that the fully softened shear envelopes obtained from direct shear and triaxial tests are very similar. Tiwari and Ajmera (2014) have demonstrated that the fully softened shear strengths obtained from simple shear tests are similar to those obtained from the direct shear testing.

Direct Shear Tests

The use of the direct shear test to measure the fully softened shear strength possesses several advantages. Specifically, the device is widely available with a relatively easy procedure to conduct the test and interpret the data obtained. Furthermore, the post-consolidation thickness of the sample is sufficient to avoid end effects. The device also has several disadvantages including that the sample fails progressively along a horizontal shearing surface, which may not be the weakest plane. Furthermore, the cross-sectional area of the sample is not constant during the shearing process, but rather decreases with an increase in the shear displacement.

Procedures for conducting direct shear tests can be found outlined in ASTM D 3080/3080M-11. Direct shear tests are typically conducted under drained conditions (that is, volume changes are permitted during the test). The remolded or normally consolidated specimen to be tested using a direct shear test is placed in the direct shear box between two porous stones before the assembly is transferred to the direct shear device. In this device, the specimen is subjected to the desired consolidation pressure. The specimen may be consolidated in steps, in which process the consolidation pressure is gradually increased (typically doubled) until the desired consolidation pressure is achieved. The consolidation process is monitored by collecting data related to the vertical deformations until the primary consolidation is completed at which point a shearing force is applied to the box that will cause the top half of the shear box to displace at a constant rate relative to the bottom half. During the shearing phase, the applied shear force and the resulting horizontal and vertical displacements are recorded. The shearing phase should be continued until the peak shear strength is obtained. The data obtained should be used to

create plots that illustrate the changes in shear stress and vertical displacement as functions of the horizontal displacement. The process should be repeated for several different vertical pressures to allow for the determination of the shear strength parameters and to evaluate the curvature of the shear envelope (as will be discussed in a later subsection).

Tiwari and Ajmera (2011) performed direct shear tests on 36 different specimens prepared in the laboratory as mixtures of sodium montmorillonite, kaolinite and powdered quartz. They prepared their samples for testing by dry mixing the desired proportions of montmorillonite, kaolinite and quartz to achieve the desired soil mixture before adding sufficient distilled water to obtain a liquidity index of one. This step was followed by a hydration period of at least 72 h. Slurries were, then, formed by mixing in a batch mixer. Tiwari and Ajmera (2011) then used a cake decorator bag with a metal tip to even distribute the sample between the porous stones for the direct shear tests. They also measured the fully softened shear strength of a few dozens of natural samples. The sample preparation process for natural samples were similar, except that Tiwari and Ajmera (2011) started with air-dried samples rather than the dry minerals.

Castellanos and Brandon (2013), Castellanos (2014), and Stephens and Branch (2013) conducted direct shear tests on fifteen clays obtained from Texas, South Dakota, Ohio and Mississippi. For their sample preparation, they soaked the samples in distilled water for at least two days after which they washed the samples through a U.S. No. 40 sieve with an opening of 425 μm . It was noted in Castellanos (2014) that some of the samples were blenderized before they were sieved. These extremely wet samples were then allowed to air-dry in funnels and bowels with filter paper to achieve liquidity indices between 0.6 and 2.0 following which the samples were placed in the direct shear box using a spatula.

Triaxial Tests

Consolidated-drained (CD) and consolidated-undrained (CU) triaxial tests have both been used to measure the fully softened shear strength. Like the direct shear test, triaxial testing systems are also commonly available. However, it is difficult to use triaxial testing to soft samples given the difficulties associated with forming these test specimens. It is also difficult to conduct triaxial testing at low confining pressures. Furthermore, the measurement of the fully softened shear strengths in low permeability clay soils will require large amount of time when performing CD triaxial testing or will be difficult to back-pressure saturate that is necessary for CD and CU tests.

To perform these tests, a cylindrical sample with a height to diameter ratio of more than two is placed between two

porous stones and surrounded by a thin rubber membrane. The sample is confined in a cylindrical chamber filled with water, which will be pressurized to apply a cell pressure. CD triaxial tests are conducted following the procedures in ASTM D7181-20. After a sample has been mounted for a CD triaxial test, the sample is subjected to back-pressure saturation, which is verified with the use of Skempton's pore pressure coefficient (or B-value). Once a sufficiently high enough B-value is achieved (typically, 0.95, but may be lower as dedicated by the soil being tested), the cell pressure is increased to achieve the desired confining pressure. The sample is, then, allowed to consolidate under this confining pressure until the primary consolidation is complete following which the sample is sheared. The shearing phase is continued until the peak deviator stress is obtained or until the sample undergoes 20% axial strain. Data related to the cell pressure, volume change experienced by the sample, axial deformation and deviator stress are collected during the shearing phase. As with the direct shear test, the process should be repeated for at least four different confining stresses to allow for sufficient data to be collected to determine the shear strength parameters and any curvature in the shear envelope.

CU triaxial tests are conducted following the procedures in ASTM D4767-20. The procedures are similar to CD triaxial tests with the following differences: (1) In the CD triaxial test, the drainage valve is kept open during the shearing phase, but this valve is closed during the shearing phase of the CU triaxial test. (2) As the drainage valve is left open during the shearing phase in the CD triaxial test, volume change is permitted and measured. On the other hand, in the CU triaxial test, volume change is not permitted in the shearing phase. Instead, the pore pressure generated is recorded. (3) The shearing phase in CU triaxial tests is conducted at a faster rate (typically about eight times faster than CD triaxial tests).

Several researchers including Crabb and Atkinson (1991), Crawford and Eden (1966), Kamei (1987), Bahmyari (2018), Castellanos (2014), and Castellanos and Brandon (2013) have conducted CD and/or CU triaxial tests to measure the fully softened shear strength of different soils. Many of these studies (for example, Crawford and Eden 1966, and Kamei 1987) do not contain details of the sample preparation process. In other studies, only a brief description is provided. Crabb and Atkinson (1991) tested reconsolidated slurries that was prepared from intact soil samples obtained from thin-wall sampling that were oven-dried and pulverized. Bahmyari (2018) stated that Shelby tube samples were trimmed to the correct size and tested. Castellanos (2014) noted two different ways of preparing their samples for triaxial testing. In the first, whose results were also presented in Castellanos and Brandon (2013), the samples were batch consolidated, trimmed and tested. In the second, the slurry

was prepared using the same steps that were described for the direct shear testing above, and placed with a spatula in a Harvard Miniature Compaction Mold in eleven layers. The sample was then extruded out by hand and used for the triaxial tests.

Direct Simple Shear Tests

The use of the direct simple shear device to estimate the fully softened shear strength provides several advantages over the direct shear and triaxial tests. The test set-up is relatively easy like the direct shear device, but unlike direct shear tests, the sample is allowed to fail along the weakest plane and the cross-sectional area remains constant during the shearing process. As significantly smaller samples are necessary than those required for triaxial testing, simple shear tests require shorter times to complete the consolidation process, while it also provides pore water pressure information. However, this device is not widely available in commercial labs yet.

Direct simple shear tests are performed following ASTM D6528-17. Tiwari and Ajmera (2014) tested ten different soil samples using the direct simple shear testing. The sample procedures used in their study are similar to those in Tiwari and Ajmera (2011), previously described. To perform the direct simple shear tests, the samples is confined in a rubber membrane and either a stack of Telfon® rings or a wire mesh (Telfon® rings were used in Tiwari and Ajmera (2014)). The assembly is then placed in the direct simple shear box where it is consolidated and then subjected to a shear force to shear the sample. During the shearing phase, the effective normal stress, shear stress and horizontal displacement are recorded. The shearing phase is conducted in undrained conditions.

Ring Shear Tests

Although an ASTM standard (ASTM D 7608-18) exists to measure the fully softened shear strength with the use of ring shear device, there are a number of disadvantages of running these tests including the following: (1) Ring shear devices are not commonly available around the world and such tests are expensive to conduct. (2) Very thin sample remains for shearing after the completion of primary consolidation. (3) The shear displacements occurring at the inner and outer edges of the annual samples are unequal. The ring shear test has been primarily used by Stark and his colleagues (Stark and Eid 1997, Stark and Fernandez 2019, Stark et al. 2005, Stark and Hussain 2015, Eid 1996, Eid and Rabie 2016, Eid 2020) to measure the fully softened shear strength. Castellanos (2014) also performed some ring shear tests. Stark et al. (2005) noted that it was necessary to increase the fully softened friction angle obtained from a ring shear test by 2.5° as a way to account for the differences in shearing modes between in situ and ring shear tests. However, there is no scientific basis of such recommendation.

Other Tests

To obtain the fully softened shear strengths of soils at very low normal stresses, Pederson et al. (2003) conducted tilt table tests. In their study, they only tested one soil sample—kaolinite—under normally consolidated conditions. The soil was tested under normal stress ranging from 1 Pa to 2400 Pa.

Interpretation Methods

The literature contains several different interpretations of the shear envelope which defines the relationship between the shear strength and the effective normal stress for a soil specimen. Common interpretations can be divided into three major categories: (1) linear shear envelopes defined by the Mohr-Coulomb failure criteria, (2) nonlinear shear envelopes following either power, hyperbolic or parabolic functional forms, or (3) secant friction angles. Additional information about these interpretations are provided in the following subsections.

Linear Interpolation with Mohr-Coulomb Failure Envelopes

The Mohr-Coulomb failure envelope is defined by Eq. 1, where τ is shear strength, σ' is the effective normal stress, c' is the effective cohesion intercept, and ϕ' is the friction angle. Collectively, c' and ϕ' are often referred to as the shear strength parameters. It is widely accepted that linear failure envelopes are a simple and effective way to represent the shear strengths for a particular range of normal stresses. This approach was adapted by the majority of the articles in the literature when presenting test results. An example is the work conducted by the authors in Tiwari and Ajmera (2011). In that study, the authors noted that while a few samples exhibited shear envelopes that were curved in nature, the majority were linear in the range of normal stresses tested. Furthermore, they observed negligible differences between the average friction angle and the secant friction angle leading to their decision to use the average friction angle when deriving relationships to estimate the fully softened friction angles.

$$\tau = c' + \sigma' \tan \phi' \quad (1)$$

Nonlinear Failure Envelopes

Although the use of the linear shear envelope is commonly adapted in geotechnical investigations, there is significant experimental evidence dating back to the 1950s that suggests that the failure envelopes are nonlinear (or curved), especially at small normal stresses. The curvature in the failure envelopes has been attributed to the greater face-to-face orientation of clay particles that occurs during the consolidation process (Mesri and Shahien 2003). For sands and

gravels, the curvature is suggested to be a result of particle breakage combined with reductions in the tendencies for dilation to occur (Lee and Seed 1967, Marachi et al. 1972).

Some of the articles that have presented different functional forms of nonlinear failure envelopes include: Atkinson and Farrar (1985), Baker (2004), Bishop et al. (1965), Charles and Soares (1984a, b), Charles and Watts (1980), Collins et al. (1988), Crabb and Atkinson (1988), Day and Axten (1989), de Mello (1977), Duncan et al. (2011), Gamez and Stark (2014), Griffith (1924), Jiang et al. (2003), Lee and Seed (1967), Lefebvre (1981), Li (2007), Maksimović (1989a), Marachi et al. (1972), Marsal (1973), McGuire and VandenBerge (2017), Mesri and Shahien (2003), Miller et al. (2004), Noor and Hadi (2010), Penman (1953), Perry (1994), Ponce and Bell (1971), Sokolovsky (1960), Terzaghi et al. (1996), Tiwari and Ajmera (2014), VandenBerge et al. (2019), Vesic and Clough (1968), Wong and Duncan (1974), and Wright (2005). While a number of functional forms are used to describe the shear envelopes, the power function appears to be the most common in the literature. Table 1 summarizes a few of these functional forms along with definitions of the associated variables. In this table, p_a is the atmospheric pressure. Mesri and Shahien (2003) stated that m is equal to unity for a linear envelope and reduces to 0.85 when the plasticity index is 100. They state that m will remain constant at approximately 0.85 for soils with plasticity indices greater than 100.

VandenBerge et al. (2019) studied six function forms of the failure envelope using shear strength and effective normal stress results for four different soils. Specifically, they fitted a linear Mohr-Coulomb relationship, the relationships in Table 1 from Wong and Duncan (1974), Lade (2010), McGuire and VandenBerge (2017), and Jiang et al. (2003) and a modified version of the Høek-Brown relationship. They concluded that the functional form of the failure envelope had little influence in the range of normal stresses tested and a small impact on the stability of two simple slopes that they considered. However, VandenBerge et al. (2019) also concluded that the largest differences in the estimated shear strengths occurred when the relationships were extrapolated to smaller normal stresses than the range used to determine the curve fitting parameters. Stark et al. (2005) found that differences in factors of safety was not significant when using a linear or curved envelope for normal stresses greater than 2000 psf (approximately 100 kPa), but very significant at lower normal stresses (like those in shallow slides).

In this paper, the authors present the evaluation of the three functional forms for the shear envelopes using data previously published in Tiwari and Ajmera (2011, 2014), respectively. Specifically, the three functional forms considered are: (1) linear as defined by the Mohr-Coulomb failure envelope in Eq. 1, (2) the power function first proposed by Lade (2010) in Table 1, and (3) a hyperbolic

Table 1 Functional forms for several nonlinear failure envelopes presented in the literature

Functional form	Additional associated variables	Reference(s)
$\tau = \sigma' \tan\left(\phi'_o + \Delta\phi' \log\left(\frac{\sigma'}{p_a}\right)\right)$	ϕ'_o = secant friction angle at $\sigma'/p_a = 1$ $\Delta\phi'$ = change in secant friction angle over one log cycle change in stress	Wong and Duncan (1974)
$\tau = A(\sigma')^b$ $\ln(\tau) = \ln(A) + b \ln(\sigma')$	A and b = curve fitting parameters	Charles and Soares (1984a, 1984b) Atkinson and Farrar (1985) Perry (1994)
$\tau = \sigma' \tan(\phi') \left(\frac{\sigma'}{\sigma'_s}\right)^{1-m}$	m = curvature of shear envelope	Mesri and Abdel-Ghaffar (1993)
$\tau = ap_a \left(\frac{\sigma'}{p_a} + t\right)^b$	a and b = curve fitting parameters for three parameter power function t = normalized tensile intercept with the normal stress axis	Jiang et al. (2003)
$\tau = a\sigma' \left(\frac{p_a}{\sigma'}\right)^b$	a and b = curve fitting parameters	Mesri and Shahien (2003)
$\tau = \sigma' \tan(\phi'_s)^{100} \left(\frac{100}{\sigma'}\right)^{1-m}$	$(\phi'_s)^{100}$ = secant friction angle at normal stress of 100 kPa m = curvature of shear envelope	Mesri and Shahien (2003)
$\tau = A(\sigma')^b + c'$	A, b and c = curve fitting parameters for three parameter power function	Miller et al. (2004)
$\tau = ap_a \left(\frac{\sigma'}{p_a}\right)^b$	a and b = curve fitting parameters	Lade (2010) Tiwari and Ajmera (2014)
$\tau = ap_a \left(\frac{\sigma'}{p_a}\right)^b + c'$	a, b and c = curve fitting parameters for three parameter power function	Duncan et al. (2011) Gamez and Stark (2014) McGuire and VandenBerge (2017)
$\tau = A(\sigma' + T)^b + C + \sigma' \tan(W)$	A, T, b, C, and W = curve fitting parameters for five parameter power function	RocScience (2016a, b)

function, described below by Eq. 2, where α and β are curve-fitting parameters. For each of the thirty-six samples subjected to direct shear testing in Tiwari and Ajmera (2011) and twelve samples subjected to simple shear testing in Tiwari and Ajmera (2014), the curve fitting parameters for each of the three function forms were calculated. Due to space limitations, only a few results are shown here to help illustrate a few observations made by the authors.

$$\tau = \frac{\alpha\sigma' \tan \beta}{\alpha + \sigma' \tan \beta} \quad (2)$$

Shear envelopes corresponding to all three functional forms evaluated by the authors are shown in Figs. 2 and 3. Figure 2 uses the direct shear test results for a sample prepared as a mixture of 80% kaolinite with 20% quartz, whereas Fig. 3 is based on the direct shear test results for a sample prepared as a mixture of 20% montmorillonite with 80% kaolinite. As demonstrated in Figs. 2 and 3, when the effective cohesion intercept was approximately zero, the shear envelopes obtained using a power function or a hyperbolic function were nearly identical. In fact, the coefficients of determination (R2) for each of the three functional forms were greater than 0.999. On the other hand, when an effective cohesion value, with linear interpolation, is greater

than zero, as in the example in Fig. 3, the three functional forms match well in the range of the normal stresses tested (50–200 kPa), but the linear function yields higher shear strengths than the power and hyperbolic functions, which yield approximately the same values. The R2 values were 0.997, 0.998, and 0.994 for the linear, power and hyperbolic functions, respectively. The suitability of these functions to the lower normal stress ranges could not be discerned due to the lack of testing at normal stresses less than 50 kPa in Tiwari and Ajmera (2011).

Using the simple shear device, Tiwari and Ajmera (2014) were able to measure the fully softened shear strength at lower normal stresses. Through these results, it was possible to better capture the nonlinearity of the shear envelopes at low effective normal stresses. Figures 4 and 5 contain two examples of the fitted linear, power and hyperbolic functions to data obtained from direct simple shear tests conducted by Tiwari and Ajmera (2014) on mixtures of 80% kaolinite with 20% quartz and 50% montmorillonite with 50% quartz, respectively. Based on the results in Figs. 4 and 5, it can be seen that none of the three options appropriately capture the data points across the entire range of effective normal stresses tested. However, it appears from these two figures (and the others not presented in this paper), that the linear functional form works best for the data points at effective

Fig. 2 Linear, power and hyperbolic shear envelope functional forms fitted to the direct shear test data obtained for a mixture of 80% kaolinite with 20% quartz in Tiwari and Ajmera (2011)

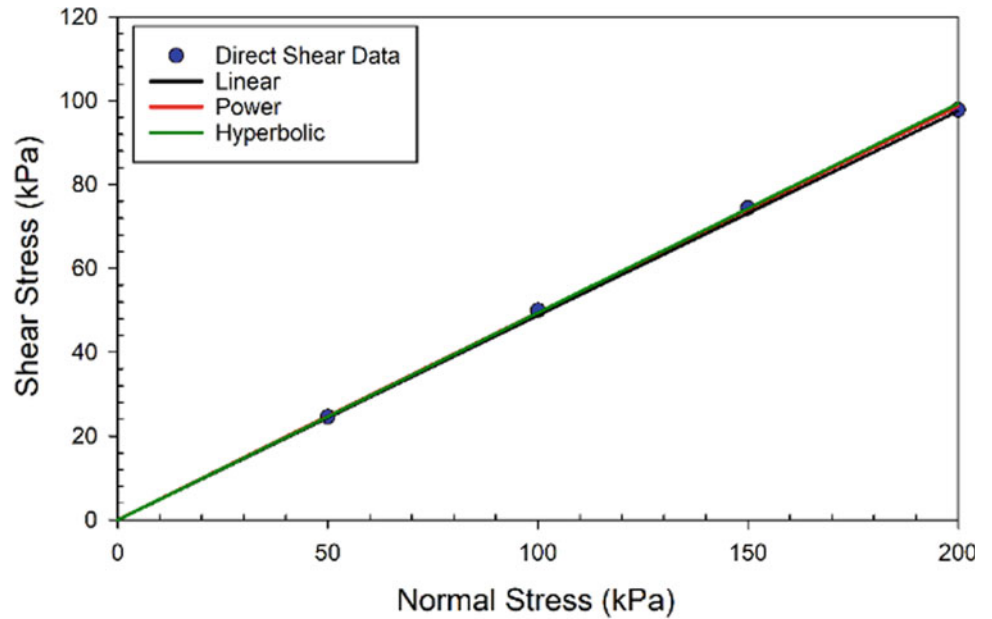


Fig. 3 Linear, power and hyperbolic shear envelope functional forms fitted to the direct shear test data obtained for a mixture of 20% montmorillonite with 80% quartz in Tiwari and Ajmera (2011)

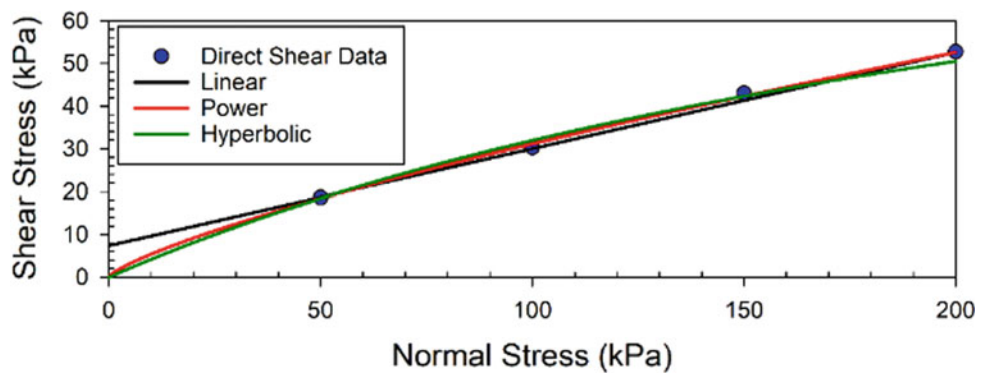


Fig. 4 Linear, power and hyperbolic shear envelope functional forms fitted to the direct simple shear data obtained for a mixture of 80% kaolinite with 20% quartz in Tiwari and Ajmera (2014)

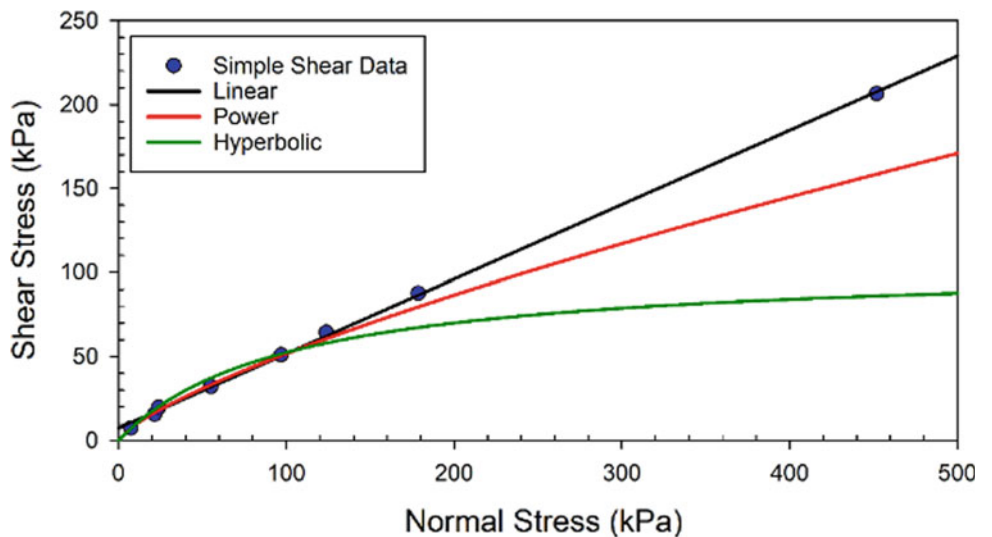
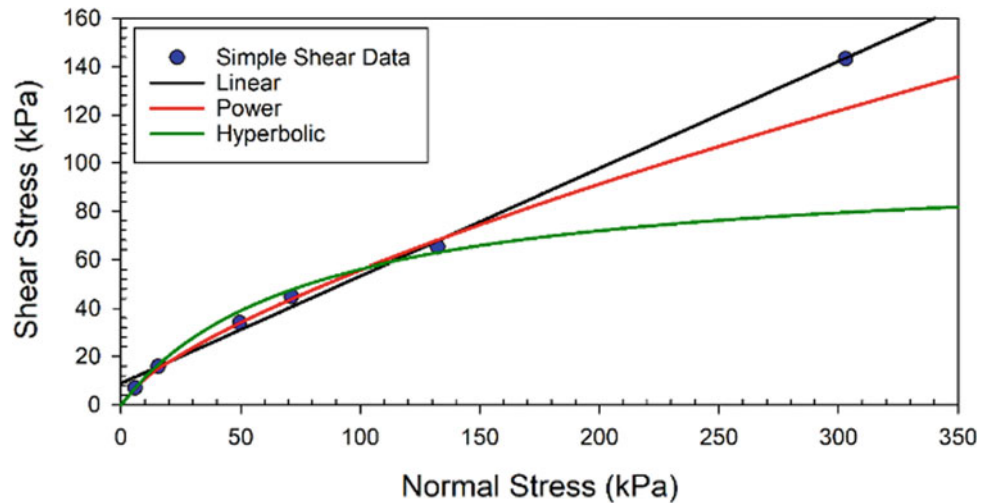


Fig. 5 Linear, power and hyperbolic shear envelope functional forms fitted to the direct simple shear data obtained for a mixture of 50% montmorillonite with 50% quartz in Tiwari and Ajmera (2014)



normal stresses greater than 50 kPa, but overestimates the shear strengths at the lower effective normal stresses. Both the power and hyperbolic functions appear to better fit through the data points at the lower effective normal stresses, but significantly underestimate the shear strength when the effective normal stress is greater than 150 kPa with larger differences observed with an increase in the effective normal stress. The hyperbolic function appears to be more significantly underestimate the strengths than the power function when the effective normal stress is greater than 150 kPa. Furthermore, as characteristic of hyperbolic functions, the shear strength reaches a plateau (upper bound) value when estimated using Eq. 2.

Secant Friction Angles

An alternate to representing the shear envelopes of soils with a linear or nonlinear function is the use of secant friction angles. The secant friction angle (ϕ'_s) is defined at each effective normal stress using Eq. 3. When the failure envelope is linear with a zero cohesion intercept, the secant friction angles will be equal to the average friction angle. However, for curved failure envelopes an increase in the effective normal stress will result in a decrease in the secant fully softened friction angle.

$$\phi'_s = \tan^{-1}\left(\frac{\tau}{\sigma'}\right) \quad (3)$$

Maksimović (1979, 1988, 1989a) suggested that this relationship between the secant fully softened friction angle and the effective normal stress followed a hyperbolic form, which he derived using a theoretical approach. This hyperbolic relationship can be expressed by Eq. 4. In Eq. 4, ϕ'_B is the basic angle of friction, $\Delta\phi'$ is the maximum angle difference and p_N is the medium angle normal stress. The

appendix in Maksimović (1989a) presents a procedure to calculate the parameters in Eq. 4 using three data points and a linearized form of Eq. 4 as shown in Eq. 5. The steps to obtain the parameters are summarized below:

- (1) Hand-draw an approximate hyperbolic curve that relates the effective normal stress to the secant fully softened friction angle.
- (2) Extrapolate the curve to obtain a value of ϕ'_o corresponding to an effective normal stress of zero.
- (3) Determine the values of effective normal stress (p'_1) and secant fully softened friction angle (ϕ'_1) that correspond to the highest effective normal stress value.
- (4) At a secant fully softened friction angle (ϕ'_2) equal to the average of ϕ'_o and ϕ'_1 , determine the value of the effective normal stress (p'_2).
- (5) Using the values obtained, calculate the parameters using Eq. 6.

$$\phi'_s = \phi'_B + \frac{\Delta\phi'}{1 + \frac{\sigma_n}{p_n}} \quad (4)$$

$$\alpha + b\sigma'_n = \frac{\sigma'_n}{\phi'_o - \phi'_s} \quad (5)$$

$$a = \alpha \quad \Delta\phi' = \frac{p'_1 - p'_2}{\frac{p'_1}{\phi'_o - \phi'_1} - \frac{p'_2}{\phi'_o - \phi'_2}}$$

$$p_n = a\Delta\phi' = \frac{p_1 p_2 \left(\frac{1}{\phi'_o - \phi'_2} - \frac{1}{\phi'_o - \phi'_1} \right)}{\frac{p'_1}{\phi'_o - \phi'_1} - \frac{p'_2}{\phi'_o - \phi'_2}} \quad (6)$$

Influencing Factors

There are a number of factors that influence the fully softened shear strength in different ways. The following subsections present a brief summary of several of these factors based on the articles published in the literature.

Weathering

Bhattacharai et al. (2006) collected soils from different depths at the Mukohidehara Landslide, Japan including from the main scrap, and from just above and just below the sliding surface. They conducted a series of simple and ring shear tests on the samples obtained. From the results obtained, they established that the fully softened shear strength increased with an increase in the depth for depths greater than 4 m until the sliding surface. They noted that the shear strength at the sliding surface was approximately the same as the residual shear strength. Bhattacharai et al. (2006) found that slaking did not alter the fully softened shear strength or the residual shear strength, but it did have an impact on the peak shear strength.

Mineralogical Composition

Tiwari and Ajmera (2011) found that the fully softened friction angle was strongly dependent on the dominant clay minerals in the soil samples. Details of the sample preparation and testing procedures used were provided earlier in this paper. From the results, Tiwari and Ajmera (2011) found that an increase in the percent of montmorillonite or kaolinite in the soil samples would result in a decrease in the slope of the shear envelope. They found that clay mineralogy had a strong influence on the fully softened friction angle even when the clay content was held constant. To illustrate this, consider two samples with the sample clay content of 50%. A sample that was composed of a mixture of kaolinite and quartz can be expected to have a fully softened friction angle that was approximately 20° higher than a mixture of montmorillonite with quartz.

Based on the results obtained from their testing, Tiwari and Ajmera (2011) provided insight into the sensitivity of the fully softened friction angle to the clay mineralogy. Specifically, they found that the fully softened friction angle was highly sensitive to the amount of montmorillonite in the soil sample when the total percentage of montmorillonite was small. In samples with kaolinite as the dominant clay mineral, the fully softened friction angle was highly sensitive to the amount of kaolinite for high quantities of kaolinite. This was clearly illustrated by a triangular correlation chart that was developed and presented in Tiwari and Ajmera (2011). A copy of this chart will be provided in the section discussing correlations.

Pore Water Chemistry

To evaluate the influence of the pore water chemistry on the fully softened shear strength, Tiwari and Ajmera (2015) performed direct shear tests on a series of samples. In their study, they tested samples from intact rocks and sliding surface materials from seven landslide areas in Japan. The intact rock samples had high concentrations of sodium chloride in the pore fluid. This sodium chloride was leached from the samples and tested again. As the samples collected from these landslide areas contained large amounts of montmorillonite and kaolinite, Tiwari and Ajmera (2015) also tested a series of laboratory prepared soil samples with distilled water and saline water (0.5 M sodium chloride solution).

Failure envelopes for the samples with saline water as the pore fluid were curved and as such, Tiwari and Ajmera (2015) presented results and correlations in terms of the average secant fully softened friction angle. A comparison of the average secant fully softened friction angles for both pore fluids tested is shown in Fig. 6. This figure illustrates that the average secant fully softened friction angle when saline water is the pore fluid is greater than or equal to those when distilled water was the pore fluid. The only exceptions in the figure were those samples with kaolinite as the dominant clay minerals or with less than 9.5% montmorillonite in the soil sample. Based on their results, Tiwari and Ajmera (2015) also presented a series of correlations to estimate the fully softened friction angle for samples with saline water as the pore fluid. These correlations will be discussed in the next section.

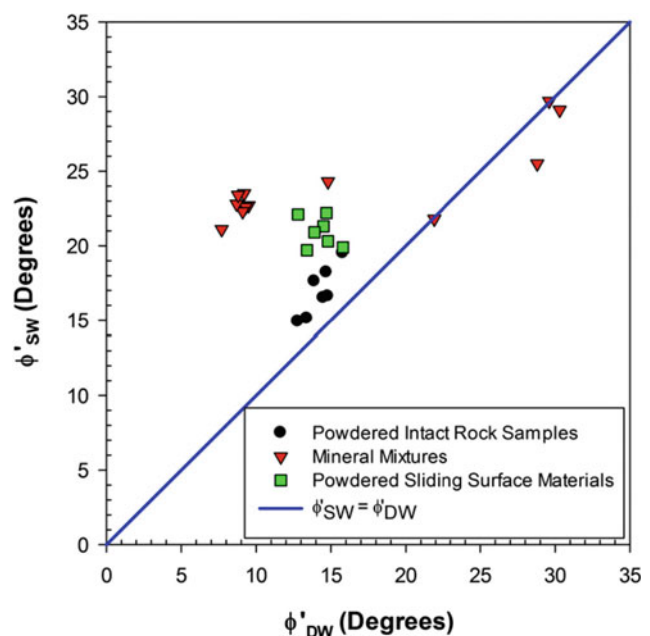


Fig. 6 Comparison of fully softened friction angles for samples with saline water and distilled water as the pore fluid (Source Tiwari and Ajmera 2015)

Available Correlations

Many articles in the literature use empirical data from the testing procedures described above to develop correlations to estimate the fully softened shear strength. A summary of these relationships is provided in Table 2. Also presented in Table 2 is information pertinent to type of testing conducted to obtain the relationships and the parameters required for its use. It is noted that the relationships that will be discussed in more detail in this section are in bold in the table.

Stark and Hussain (2015) updated the correlations by providing equations for the trend lines previously presented in Stark and Eid (1997) and Stark et al. (2005). It is noted that their relationships are based on results of ring shear testing with the measured fully softened friction angles being increased by 2.5°. The nine equations associated with the three clay fractions for three effective normal stress values, each are reproduced in Eqs. 7 to 15. Equations 7 to 9 correspond to soils with clay fractions less than 20% and only valid for liquid limits between 30 and 80. Equations 10 to 12 and 13 to 15 are for soils with clays fractions between 25% and 45% and greater than 50%, respectively. These sets of equations are valid for liquid limits between 30 and 130 and 30 to 300, respectively. Equations 7, 10, and 13 correspond to the effective normal stress values of 50 kPa. For effective normal stresses of 100 kPa, Eqs. 8, 11, and 14 should be used, whereas Eqs. 9, 12, and 15 correspond to effective normal stress of 400 kPa.

$$\phi'_{s,50\text{ kPa}} = 34.85 + 0.0709LL + 2.35 \times 10^{-4}LL^2 \quad (7)$$

$$\phi'_{s,100\text{ kPa}} = 34.39 - 0.0863LL + 2.66 \times 10^{-4}LL^2 \quad (8)$$

$$\phi'_{s,400\text{ kPa}} = 34.76 - 0.13LL + 4.71 \times 10^{-4}LL^2 \quad (9)$$

$$\phi'_{s,50\text{ kPa}} = 36.18 - 0.1143LL - 2.354 \times 10^{-4}LL^2 \quad (10)$$

$$\phi'_{s,100\text{ kPa}} = 33.11 - 0.107LL + 2.2 \times 10^{-4}LL^2 \quad (11)$$

$$\phi'_{s,400\text{ kPa}} = 30.7 - 0.1263LL + 3.442 \times 10^{-4}LL^2 \quad (12)$$

$$\phi'_{s,50\text{ kPa}} = 33.37 - 0.11LL + 2.344 \times 10^{-4}LL^2 - 2.96 \times 10^{-7}LL^3 \quad (13)$$

$$\phi'_{s,100\text{ kPa}} = 31.17 - 0.142LL + 4.678 \times 10^{-4}LL^2 - 6.762 \times 10^{-7}LL^3 \quad (14)$$

$$\phi'_{s,400\text{ kPa}} = 28.0 - 0.1533LL + 5.64 \times 10^{-4}LL^2 - 8.414 \times 10^{-7}LL^3 \quad (15)$$

The correlation presented by Eid and Rabie (2016) is based on the results of ring shear testing conducted following the procedures in ASTM D7608 for forty shale, mudstones, clays and silts. They suggested a relationship for the secant fully softened friction angle that depends on the value of the secant fully softened friction at an effective normal stress equal to the atmospheric pressure and a curve fitting parameter. Eid and Rabie (2016) presented the relationships in Eqs. 16 and 17 for these two parameters. They stated that the plasticity index in these two equations should be adjusted based on the sample preparation method used. Specifically, they stated that the plasticity index for the ball-milled samples are 70% greater than the plasticity index values associated with samples prepared using ASTM D4318.

$$\left(\phi'_f\right)_{pa} = 34.4 - 0.22PI + 0.001PI^2 - 1.77 \times 10^{-6}PI^3 \quad (16)$$

$$m_f = 0.0107 + 0.0018PI - 9 \times 10^{-6}PI^2 + 1.18 \times 10^{-8}PI^3 \quad (17)$$

Castellanos et al. (2016) provided two sets of empirical correlations for computing the fully softened shear strength using the power function form proposed by Lade (2010) and shown in Table 2. The curve-fitting parameters (a and b) for the power function could be estimated from Eqs. 18 to 19. These equations were later updated by Castellanos and Brandon (2019), who also provided a third set of correlations. The correlations for a and b presented by Castellanos and Brandon (2019) are defined by Eqs. 20 to 22 as functions of plasticity index, the product of clay fraction and plasticity index, and the product of the fines contents and plasticity index, respectively. In their correlation equations, the R² values for the equations for a and b parameters ranged from 0.67 to 0.69 and 0.45 to 0.46, respectively. Equations 20 and 21 were updates to those presented in Castellanos et al. (2016).

$$a = 4.38 \times 10^{-5}(PI)^2 - 9.00 \times 10^{-3}(PI) + 0.761$$

$$b = 1.28 \times 10^{-4}(PI)^2 - 1.27 \times 10^{-2}(PI) + 1.08 \quad (18)$$

$$a = 1.47 \times 10^{-8}(CF \times PI)^2 - 1.31 \times 10^{-4}(CF \times PI) + 0.674$$

Table 2 Summary of available correlations to estimate the fully softened shear strength

Relationship ^a	Test	Form ^b	References
Figure 57	CU, CD triaxial	$\phi' = f(PI)$	Ladd et al. (1977)
Figure 3	Direct shear, CU triaxial	$\phi' = f(PI)$	Moon (1984)
Figure 2	CU triaxial	$\phi' = f(\log PI)$	Mesri and Abdel-Ghaffar (1993)
Figure 5.1	Ring shear	$\phi'_s = f(LL, CF, \sigma'_n)$	Eid (1996)
Figure 3.1	Ring shear ^c	$\phi'_s = f(LL, \sigma'_n)$	Saleh and Wright (2005)
Equation 5.4	Ring shear ^d	$\phi'_s = 55.3 + 16.7 \log(LL) - 6 \log\left(\frac{\sigma'_n}{p_a}\right)$	Wright (2005)
Figure 5	Ring shear	$\phi'_s = f(LL, CF, \sigma'_n)$	Stark et al. (2005)
Figure 9	Direct shear	$\phi' = f(CF, M)$	Tiwari and Ajmera (2011)
Figure 10	Direct shear	$\phi' = f(LL, M)$	Tiwari and Ajmera (2011)
Figure 11	Direct shear	$\phi' = f(PI, M)$	Tiwari and Ajmera (2011)
Figure 18	Direct shear	$\phi' = f(M)$	Tiwari and Ajmera (2011)
Figure 1	Direct shear, CU triaxial	$\phi' = f(PI)$	Castellanos and Brandon (2013)
Figure 4	Ring shear	$\phi'_s = f(LL, CF, \sigma'_n)$	Stark and Hussain (2015)
Figure 7	Direct shear	$\phi' = f(LL, M)$	Tiwari and Ajmera (2015)
Figure 8	Direct shear	$\phi' = f(PI, M)$	Tiwari and Ajmera (2015)
Figure 10	Direct shear	$\frac{\phi'_{SW}}{\phi'_{DW}} = f\left(\frac{LL_{SW}}{LL_{DW}}\right)$	Tiwari and Ajmera (2015)
Figure 11	Direct shear	$\frac{\phi'_{SW}}{\phi'_{DW}} = f\left(\frac{PI_{SW}}{PI_{DW}}\right)$	Tiwari and Ajmera (2015)
Figures 6 and 8	Ring shear	$\phi'_s = \left(\phi'_s\right)_{pa} \left(\frac{\sigma'_n}{p_a}\right)^{m_f}$	Eid and Rabie (2016)
Figure 5 Figure 1	Direct shear, CU triaxial	$\tau = ap_a \left(\frac{\sigma'_n}{p_a}\right)^b$ $a = f(PI)$ $b = f(PI)$	Castellanos et al. (2016) Castellanos and Brandon (2019)
Figure 6 Figure 2	Direct shear, CU triaxial	$\tau = ap_a \left(\frac{\sigma'_n}{p_a}\right)^b$ $a = f(CF \times PI)$ $b = f(CF \times PI)$	Castellanos et al. (2016) Castellanos and Brandon (2019)
Figure 3	Direct shear, CU triaxial	$\tau = ap_a \left(\frac{\sigma'_n}{p_a}\right)^b$ $a = f(FC \times PI)$ $b = f(FC \times PI)$	Castellanos and Brandon (2019)
Figure 6	Ring shear	$\tau = ap_a \left(\frac{\sigma'_n}{p_a}\right)^b$ $a = f(LL, CF)$ $b = f(LL, CF)$	Stark and Fernandez (2019)

^aAll figure and equation numbers noted here are based on the original article cited in the reference

^b ϕ' = fully softened friction angle, ϕ'_s = secant fully softened friction angle, $(\phi'_t)_{pa}$ = secant fully softened friction angle at the effective normal stress equal to atmospheric pressure, LL = liquid limit, PI = plasticity index, σ'_n = effective normal stress, τ = fully softened shear strength, m_f = curve fitting parameter, CF = clay fraction, FC = fines content, and M represents clay mineralogy

^cThe correlation is based on the data presented by Stark and Eid (1994)

^dThe correlation is based on the data presented by Stark et al. (2005)

$$b = 1.02 \times 10^{-8}(CF \times PI)^2 - 8.57 \\ \times 10^{-5}(CF \times PI) + 0.928 \quad (19)$$

$$a = 0.664e^{-9.09 \times 10^{-3}(PI)}$$

$$b = -8.0399 \times 10^{-2} \ln(PI) + 1.0939 \quad (20)$$

$$a = 1.00 \times 10^{-8}(CF \times PI)^2 - 1.03 \\ \times 10^{-4}(CF \times PI) + 0.634$$

$$b = -5.5623 \times 10^{-2} \ln(CF \times PI) + 1.2201 \quad (21)$$

$$a = 0.652e^{-9.32 \times 10^{-5}(FC \times PI)}$$

$$b = -8.6256 \times 10^{-2} \ln(FC \times PI) + 1.4988 \quad (22)$$

Tiwari and Ajmera (2011) used the results of thirty-six laboratory prepared soil samples tested using the direct shear test. The samples were prepared as mixtures of the clay minerals, montmorillonite and kaolinite, and ground quartz. The correlation they presented between the clay content, mineralogy and the fully softened shear strength is presented in Fig. 7. Figure 8 contains the correlation that they developed between the fully softened friction angle and the liquid limit as a function of the clay mineralogy. The relationship proposed to estimate the fully softened friction angle and the plasticity index is shown in Fig. 9. They noted that unlike the relationship with liquid limit, the relationship with plasticity index could be generalized across all of the plasticity indices. Tiwari and Ajmera (2011) provided a unique perspective into the fully softened shear strength of soils by examining their results through a mineralogical point of view. They presented a triangular correlation chart, shown in Fig. 10, to estimate the fully softened friction angle in terms of the percentages of clay minerals present in the soil mass. Their correlations were validated with the results of over 80 natural soils. For these soils, they found that the estimates based on Figs. 5 and 6 were within 25% and were within 15% when estimated using the triangular correlation chart of the measured values.

The authors' previous work (Tiwari and Ajmera 2015) has examined the influence of pore fluid chemistry on the fully softened friction angle. They provided a series of unified correlations to estimate the fully softened friction angle for both soils with distilled water as the pore fluid as well as for soils with saline water (0.5 M sodium chloride) as the pore fluid. Figures 11 and 12 illustrate these relationships to estimate the fully softened friction angle using the liquid limit and plasticity index, respectively, corresponding to the appropriate pore fluid chemistry. Tiwari and Ajmera (2015) also presented the correlations in Figs. 13 and 14 that relate the ratio of the fully softened friction angle with saline water as the pore fluid to the fully softened friction angle with

distilled water as the pore fluid to the ratios of the liquid limits and plasticity indices for these pore fluids.

Residual Shear Strength

Background and Meaning

Subsequent drops in strength after the peak values have been achieved will cause soil specimens to ultimately reach the residual condition. Such drops in strength is said to be caused by dilatancy induced increases in the water and the reorientation of particles in the shear zone. At the residual condition, the shear strength of the soil is said to be at its minimum. This shear strength is referred to as the residual shear strength and is achieved after large displacements are experienced by the soil mass. Skempton (1964) referred to the residual shear strength as the ultimate strength.

Slickenside surfaces are polished surfaces formed when the plate-shaped clay particles are aligned with the direction of the sliding. Slickenside surfaces are indicative of the residual shear strength being mobilized and should be in any analyses involving this zone. Some pictures of slickenside surfaces are shown in Fig. 15.

Measurement Methods

The residual shear strength of soils is measured using one of three major test methods. Specifically, it is widely accepted to measure this strength using either the ring shear test, the direct shear test or the triaxial test. Additional details about each of these tests along with a brief discussion of their benefits and disadvantages are provided in the following subsections.

Ring Shear

As the ring shear device allows for continuous shearing of the sample in one direction, while maintaining a constant cross-sectional area (Watry and Lade 2000), it is stated to be the best way to measure the residual shear strength. In particular, Bishop et al. (1971) noted that only the torsional or ring shear test can be used to achieve truly residual conditions in the laboratory. Lupini et al. (1981) stated that the ring shear device can measure the residual shear strength with the least amount of vagueness. Hawkins and Privett (1985a) stated that the ring shear tests are more repeatable than the other tests. One potential issue with this device is the non-uniform stress distribution across the annular samples used for these tests.

The development of the ring shear device for residual strength measurements was summarized in several papers including Bromhead et al. (1999), Hvorslev (1939), and Boucek (1977). Harris and Watson (1997) noted that the

Fig. 7 Relationship between clay content, clay mineralogy and the fully softened friction angle (Source Tiwari and Ajmera 2011)

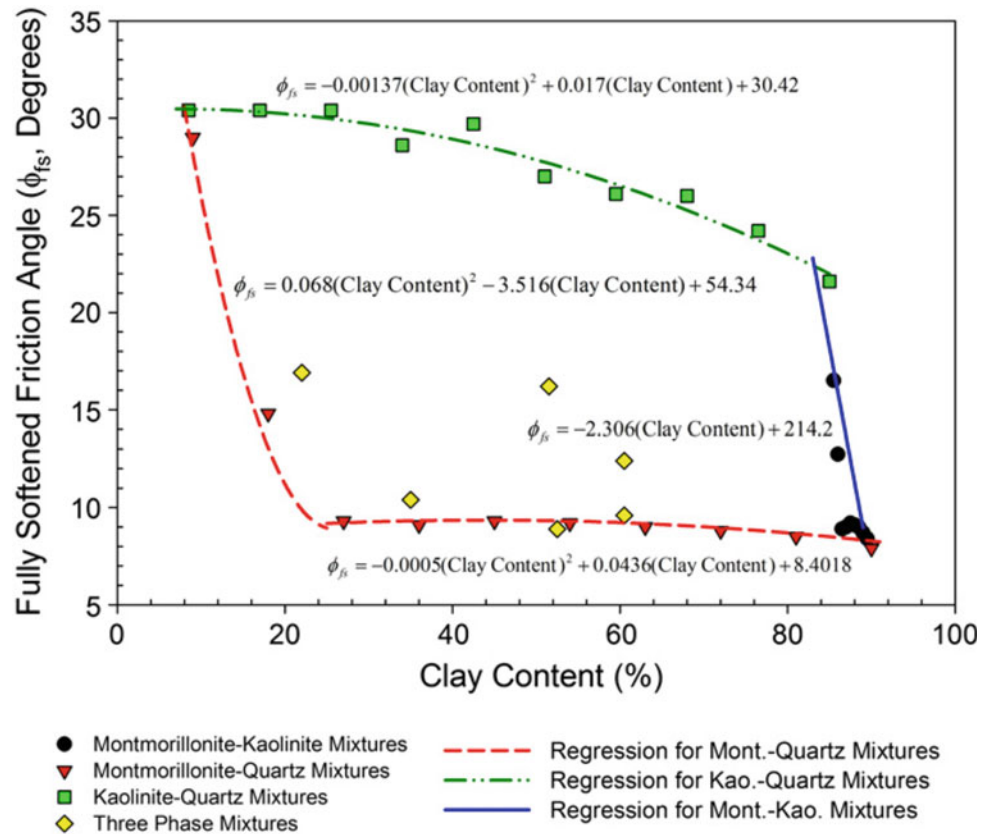


Fig. 8 Relationship between fully softened friction angle, liquid limit and clay mineralogy (Source Tiwari and Ajmera 2011)

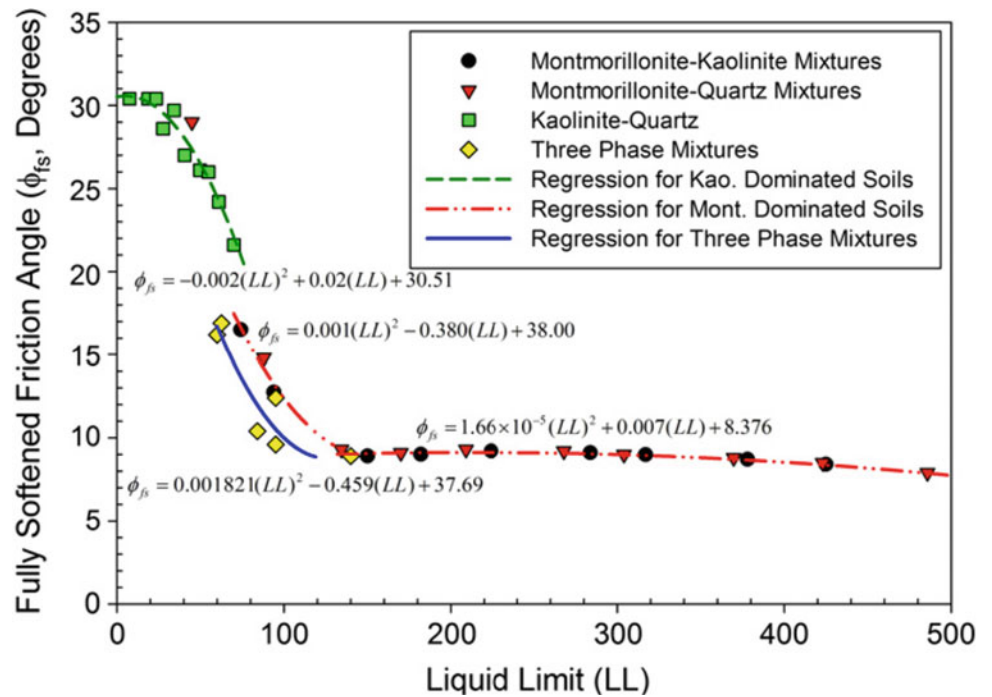


Fig. 9 Relationship between the fully softened friction angle and the plasticity index (Source Tiwari and Ajmera 2011)

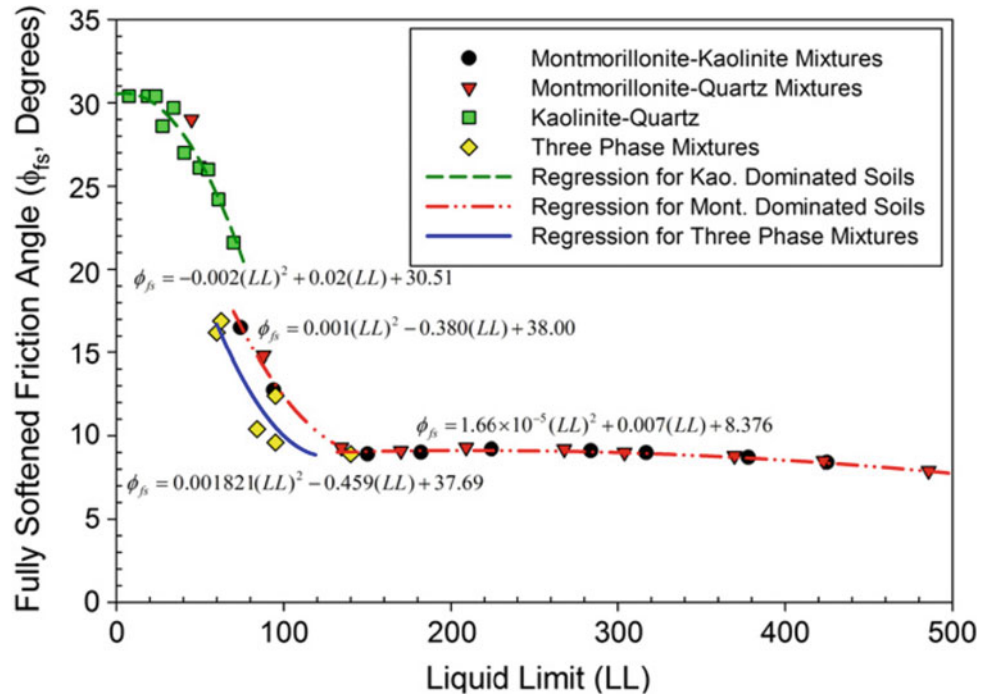


Fig. 10 Triangular correlation chart to estimate the fully softened friction angle based on clay minerals in a soil mass (Source Tiwari and Ajmera 2011)

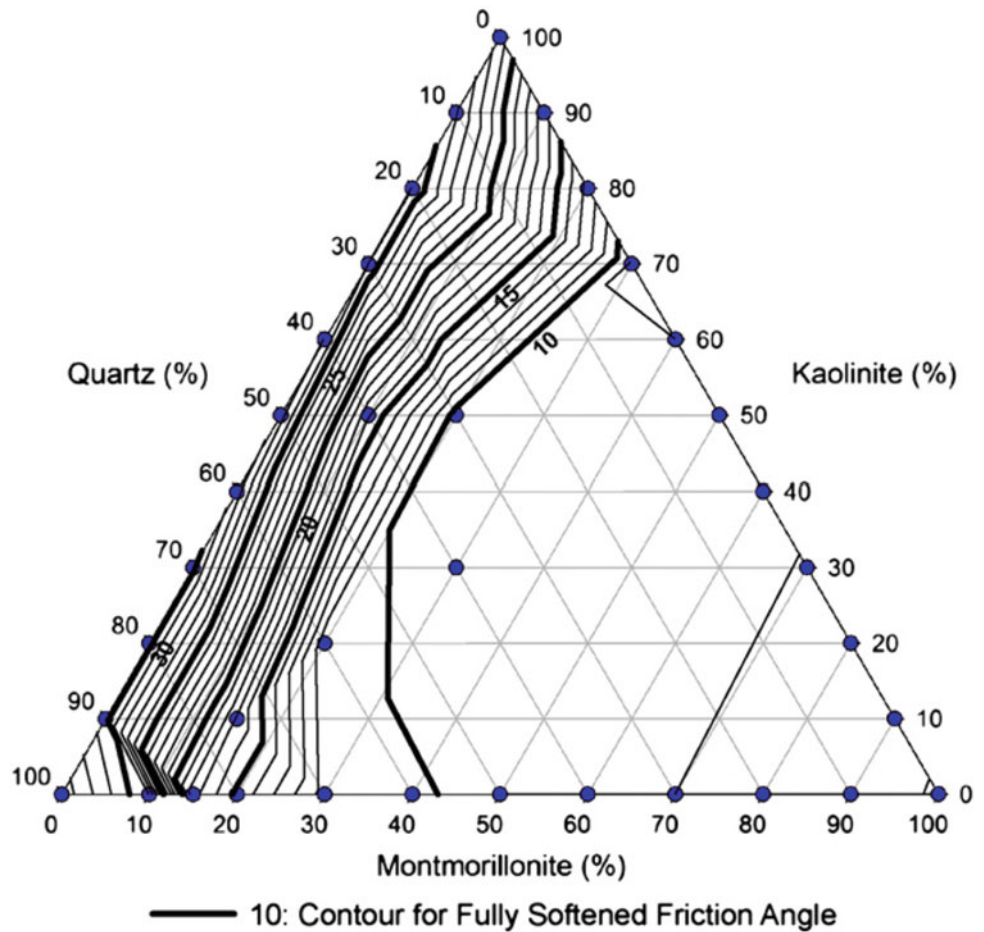


Fig. 11 Correlation to estimate fully softened shear strength for soils with distilled and saline water as the pore fluid using the corresponding liquid limits
(Source Tiwari and Ajmera 2015)

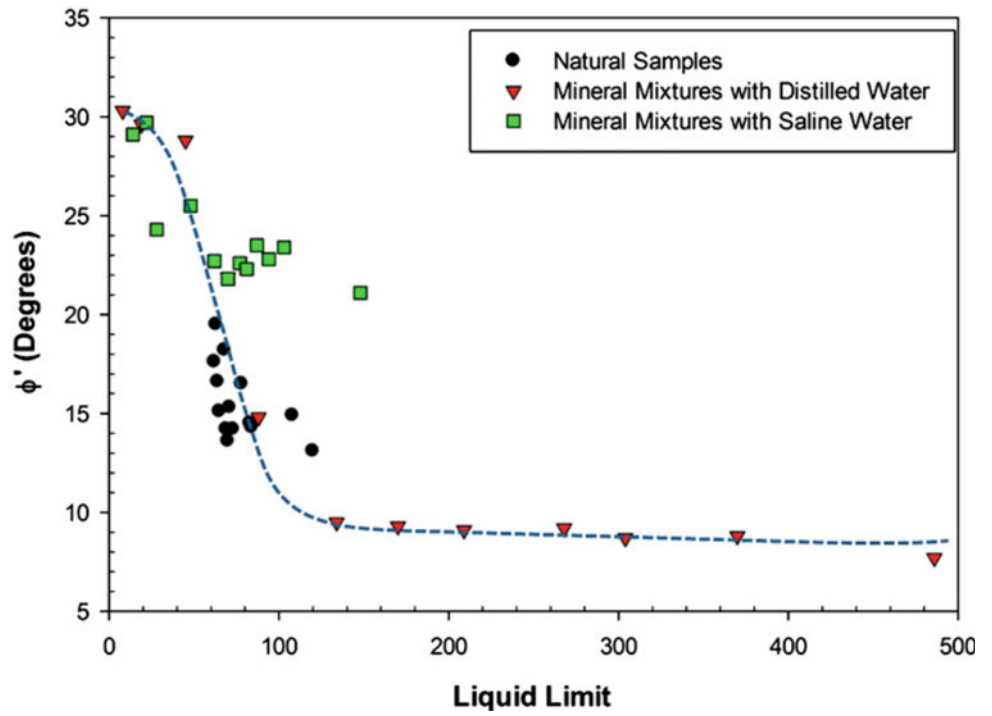


Fig. 12 Correlation to estimate fully softened shear strength for soils with distilled and saline water as the pore fluid using the corresponding plasticity indices
(Source Tiwari and Ajmera 2015)

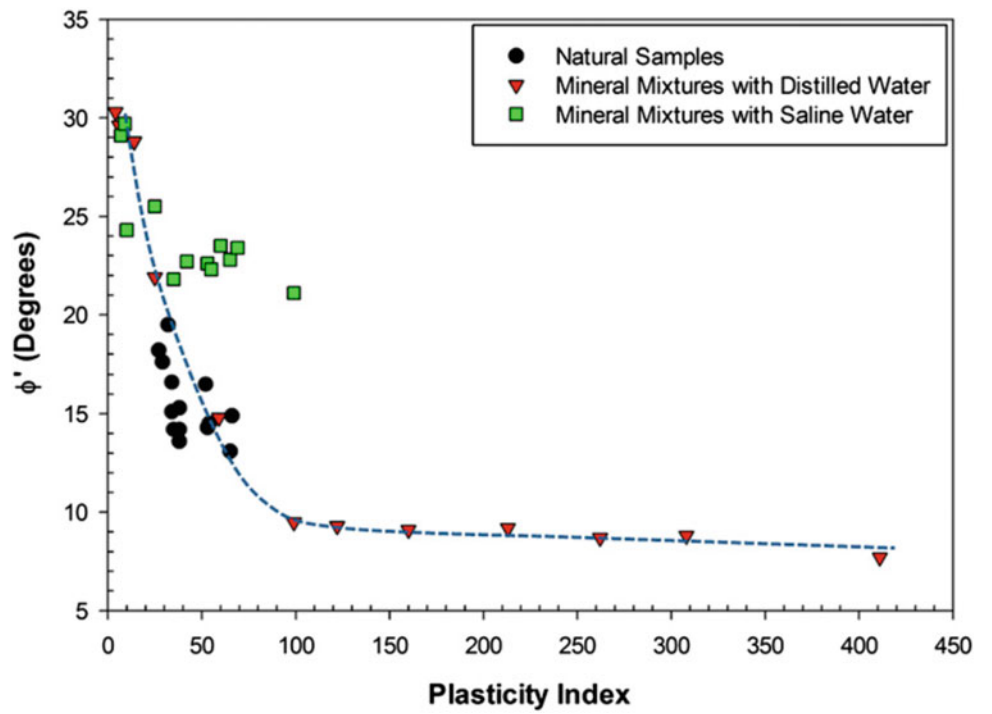


Fig. 13 Relationship between the ratio of the fully softened friction angles with saline and distilled water as the pore fluid to the ratio of the liquid limits with saline and distilled water as the pore fluids (Source Tiwari and Ajmera 2015)

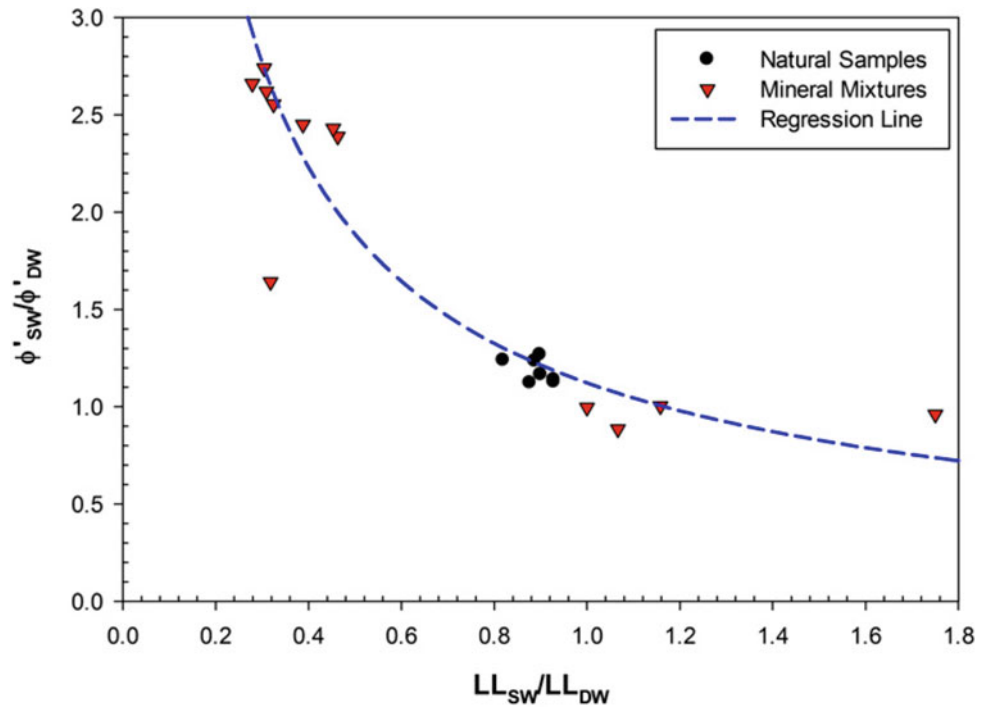


Fig. 14 Relationship between the ratio of the fully softened friction angles with saline and distilled water as the pore fluid to the ratio of the liquid limits with saline and distilled water as the pore fluids (Source Tiwari and Ajmera 2015)

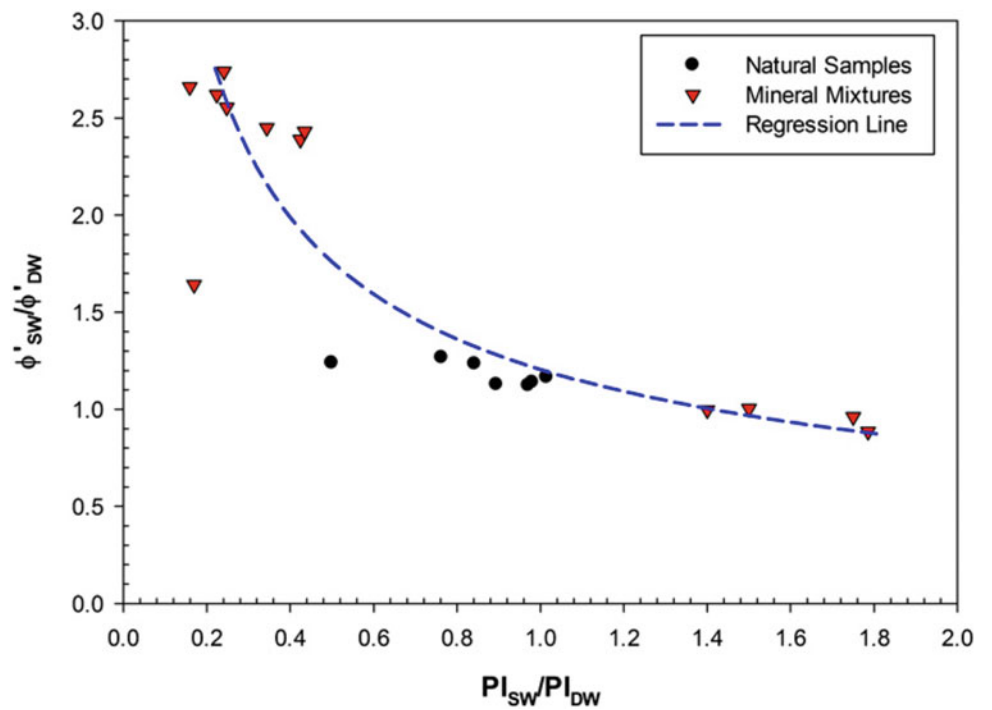


Fig. 15 Pictures of slickenslide surfaces developed during landslide motion



Arthur Casagrande first developed the ring shear test and was reported by Hvorslev (1939). One type of ring shear device was developed by Bishop et al. (1971) to measure the residual shear strength at large displacements. LaGatta (1970) and Bromhead (1979) incorporated small, thin samples to allow for quick drainage. Mechanical simplifications were then made to design which allowed sufficiently accurate measurements to be completed in a couple days. Additional modifications were proposed by Stark and Eid (1994), but Bromhead et al. (1999) noted that these modifications did not satisfy the simplicity and ease of use that was originally intended by this device. Anayi et al. (1989) also described some modifications to the Bromhead ring shear device. Specifically, they suggested the following modifications: (1) doubled sample thickness and (2) changes to the shape of the torque arm to accommodate the larger sample. Some additional modifications were proposed to the ring shear device by Steward and Cripps (1983), Hawkins and Privett (1985a), Stark and Eid (1993), and Dewhurst et al. (1996).

Due to the parallel development of different ring shear devices, each has several advantages and disadvantages. For example, the device developed by Bishop et al. (1971) allows gaps between top and bottom rings to be opened and closed. As such, this allows for the device to accept wet specimens. In this device, the sample is sheared at mid-height. In the device development primarily by Bromhead (1979) requires the use of drier samples shearing them close to the upper platen. The device requires smaller strains before the residual condition is developed.

ASTM D6467 (2013) contains the procedures for conducting ring shear tests to measure the residual shear strength of cohesive soils, specifically targeted for Bromhead type ring shear device. There are several methods for conducting these tests are different normal stresses in order to develop the failure envelope and establish the shear strength parameters. Tiwari and Marui (2004) examined three testing methods for the ring shear device—namely, separate tests for each normal stress and multistage ring shear test with

(a) increasing and (b) decreasing loads. They found that the residual friction angle was similar regardless of the testing method, but the cohesion intercept was different. Several benefits were observed and noted by Tiwari and Marui (2004) in using a multistage ring shear test instead of conducting individual tests are each normal stress. First, they stated that the use of the same sample for all of the normal stresses tested ensured more consistency, which was not possible when individual samples are used as variability may still exist even if samples were from the same location. They also noted that the required sample volume was much lower in multistage ring shear testing than for the testing of individual samples in separate ring shear tests. The benefits to multistage ring shear testing were also summarized by Bromhead (1992) and Harris and Watson (1997).

Direct Shear Testing

USACE (1986) stated that reversal direct shear tests can be used to measure the residual shear strength since ring shear is not readily available and conducting ring shear tests is also expensive. Special direct shear procedure was developed by Mesri and Cepeda-Diaz (1986). Due to the limited amount of displacement feasible during the shearing process of the direct shear, the residual shear strength is measured using a multiple reversal process. ASTM WK3822 describes the procedures for conducting such tests. Another alternative commonly used in the literature to cut the sample at the shearing height to reduce the number of reversals and amount of displacement required to obtain the residual condition. Head (1985) provided guidance on the total amount of displacement and the percent reductions in shear strength that can be used to define when the residual condition is achieved.

Anderson and Hammoud (1988) compared different testing procedures for the ring shear device. Specifically, they looked at single stage and multistage shearing finding that it multistage shearing was better in terms of test duration. They concluded that multi-stage testing might yield incorrect results when soils have large quantities of clayey

materials and recommended the use of single stage testing when more than 50% of the soil mass were clay particles. Otherwise, they suggested that multistage be used.

Meehan et al. (2010) described in great detail the procedures for preparing pre-cut polished samples for direct shear testing. In their study, samples were prepared by wire-cutting the consolidated specimens at mid-height. The two halves were then polished on different surfaces using three different methods:

- (1) Wet Polish on Frosted Glass: The halves of the sample were polished by sliding them over a wet frosted glass under moderate hand pressure. Each half was slid a distance of 30 cm for a total distance of 1.2 m in four passes.
- (2) Dry Polish on Telfon® Sheet: Each half was slid for a distance of 60 cm across a dry Telfon® sheet ten times in this method. Moderate hand pressure was applied during the polishing process.
- (3) Dry Polish on Frosted Glass: In this method, each half was subjected to 10 passes each with a distance of 60 cm on a dry frosted glass. Moderate hand pressure was applied during the polishing process.

For each of the three methods described above, the sample was slid off the side of the frosted glass or the Telfon® sheet to avoid disturbing the particles. The sliding direction was held constant and aligned to the same as the shearing direction in the direct shear test. From their experiences, Meehan et al. (2010) found that the polishing process was repeatable and unaffected by many of the different factors including the individual preparing the sample, the pressure applied and the number of passes. They found that placing the polished halves in the direct shear box required judgement and considerable experience to ensure that the surfaces were properly lined up with the shearing plane of the two halves of the direct shear box. Meehan et al. (2010) found more variability in the residual shear strength data from the direct shear tests than the ring shear tests that they conducted. They cited that this may be due to alignment issues in the shear box or variability of the soil fabric occurring during polishing process. Furthermore, they concluded that the sample preparation process affected the results obtained and recommended that these types of polishing processes not be used to determine the residual shear strength in the direct shear box.

Triaxial Testing

Bishop and Henkel (1962) first suggested the use of pre-cut samples to measure the residual shear strength using triaxial compression tests. This procedure was then used by

Chandler (1966). The most recent use of triaxial testing to measure the residual shear strength was undertaken by Meehan et al. (2011), who performed CD triaxial tests on pre-cut and polished samples. Their work builds on the efforts described in their previous study, Meehan et al. (2010) in which pre-cut polished samples were used to perform direct shear tests as described in the previous section. Meehan et al. (2011) developed a special aluminum mold to allow for the creation of polished surfaces for the tests inclined at $45 + \frac{\phi'}{2}$. The polished surfaces were formed using a variation of the wet polish on frosted glass technique described above. Specifically, each half of the sample was slid 0.3 m across the wet frosted glass to achieve a total sliding distance of 1.8 m through six passes under moderate hand pressure. Meehan et al. (2011) found that it was more challenging to prepare the samples for CD triaxial testing than for the direct shear tests in Meehan et al. (2010). Furthermore, they concluded that the residual shear strengths obtained from the triaxial tests conducted were higher than the values from the direct shear and ring shear tests despite their efforts to reduce the effects of end platen restrains and use of the appropriate membrane correction. They also concluded that additional research regarding this process was required.

Other Forms of Testing

Watry and Lade (2000) performed a couple in situ block test to measure the residual shear strength. To do so, they isolated a block of soil in a pit applying normal and shear stresses with the use of dead weights and/or hydraulic jacks. They noted that drained tests could be performed by filling this pit with water and applying shear stresses slowly enough to ensure pore pressure dissipation. Watry and Lade (2000) said that it was possible to perform multiple tests on the same block of soil. This could be done by increasing the normal stress applied once the residual strength had been obtained and re-measuring the residual shear strength at the new normal stress. Some advantages to an in situ block test include the ability to test irregular, natural samples whose behavior would not be captured in laboratory tests. However, this test also has a series of disadvantages including the cost and time required for the test set-up, insuring saturation is achieved in the in situ conditions, and ensuring sufficient displacement can be applied to achieve the residual condition. Chandler et al. (1981) developed a field shear box to measure the residual strengths in situ.

Back-analyses can be considered as a form of strength testing in the field (Chandler 1977, Hutchinson 1969). Doing so, allows for the incorporation of different aspects that would be ignored in a laboratory setting. One example of this is the side shear experienced in a landslide.

Comparison of Results from Different Tests

The literature contains several studies that examine and compare the residual shear strengths obtained from multiple different tests. Chandler et al. (1973) noted that the shear strength mobilized in the field obtained through back-analyses was higher than the values measured from the ring shear device. However, they found that back-analyzed residual shear strengths were lower than those from the direct shear tests conducted. The results from Townsend and Gilbert (1973) were also similar. Anayi et al. (1988) performed ring shear and direct shear tests. Their results showed similar values of the residual friction angle from the two tests, but noted the value from the ring shear device was slightly lower. Ring shear, direct shear and triaxial tests were conducted by Herrmann and Wolfskill (1966). Their study found that triaxial test results yield higher values for the residual shear strength than the other two tests. The results from the direct shear and ring shear tests were similar. This is in agreement with the findings from Meehan et al. (2011) presented above.

Stark and Eid (1992) used a case history to examine the residual shear strengths from different devices and sample preparation procedures. They tested remolded samples in the ring shear and direct shear devices. They also tested a remolded, but pre-cut specimen in the direct shear test. This sample was prepared following the procedures in Mesri and Cepeda-Diaz (1986). From the results obtained, Stark and Eid (1992) found that remolded specimens tested in either the ring shear or the direct shear test yield residual shear strengths that were in agreement with the field observations. The remolded, pre-cut specimens tested in the direct shear device provided unconservative, but reasonable estimates (Stark and Eid 1992). They recommended that remolded specimens be tested in the ring shear device rather than the direct shear device due to the time requirements necessary to obtain the residual shear strength.

The residual friction angles from six landslide sites in Japan were examined by Tiwari et al. (2005a). They tested both undisturbed and remolded samples obtained separately from shallow and deep locations of the same sliding surface in the ring shear device. Tiwari et al. (2005a) compared the results obtained with residual shear strengths from back-analyses performed for each of the landslide sites. The study found good agreement between all three sets of data. They also noted that higher displacements were required to achieve the residual condition in the intact samples than the remolded samples. This confirmed that healing, as described by Bishop et al. (1971), could take place on the failure plane.

Interpretation Methods

Failure envelopes presented for previous tests have been shown to be linear, curved for low normal stresses and linear

for high normal stress, and curved for the entire range of normal stresses. Townsend and Gilbert (1973) also noted that the shear envelopes were linear. Bishop et al. (1971) observed that the failure envelopes were linear for some of the soils they tested, while the failure envelope of other soils were curved. Several previous studies have indicated that the failure envelope corresponding to the residual shear strength is curved. These studies include: Garga (1970), Skempton and Petley (1967), Parry (1972), Kenney (1967), Chandler (1976), Bishop et al. (1971), Brand (1995), Bromhead and Curtis (1983), Chandler (1969), Stark and Eid (1994), Skempton (1964, 1985), Gibo (1983, 1985), Hawkins and Privett (1985a, 1985b, 1986), Gibo et al. (1987), Lupini et al. (1981), Lambe (1985), Anayi et al. (1988, 1989), and Maksimović (1989b). It has been noted that the failure envelope is curved for effective normal stresses below a certain value and linear for effective normal stresses above this value. In Hawkins and Privett (1985b), for example, curvature was observed when the normal stress was less than 200 kPa, while Anayi et al. (1988) stated that failure envelope was curved when the normal stress was lower than 150 kPa.

Hawkins and Privett (1985b) stated that a single residual friction angle should not be provided as a means to estimate the residual shear strength. Instead, they noted that if a single residual friction angle is provided, the corresponding normal stresses used to derive this value should be noted. Straight line extensions of the linear envelope developed at high normal stresses could lead to overestimates of the residual shear strength at lower normal stresses (Brand 1995). Kenney (1967) noted that higher proportions of lattice clay minerals will lead to more pronounced curvature in the failure envelope and hence, unconservative estimates of the residual shear strength at low normal stresses if a linear envelope is assumed.

Several different forms for the failure envelope have been suggested. One such form (Eq. 23) is provided by Mesri and Shahien (2003). In Eq. 23, $(\phi'_r)^{100}$ is the secant residual friction angle at effective normal stress of 100 kPa and m_r is a curve fitting parameter. Gibo and Nakamura (1999) suggested the use of two linear envelopes to define the failure envelope in the residual conditions for soils. The first envelope would apply to low normal stresses (less than 150 kPa for one of the two soils they tested and less than 200 kPa for the other soil tested), while the second would apply for the high normal stresses (greater than 150 kPa or 200 kPa, depending on which of two soils was being discussed). At high normal stresses, the cohesion intercept would be taken as zero, while at low normal stresses, the cohesion intercept was non-zero. The residual friction angle corresponding to the failure envelope for the high normal stresses was lower than that for the failure envelope for the low normal stresses. Boyce (1984) presented results in terms

of the residual friction coefficient. The residual friction coefficient was defined as the ratio of the residual shear strength to the effective normal stress or the value of the tangent of the secant residual friction angle.

$$\tau_r = \sigma'_n \tan(\phi'_r)_s \left(\frac{100}{\sigma'_n} \right)^{1-m_r} \quad (23)$$

Stark and Eid (1994) noted that the nonlinearity of failure envelopes under the residual condition was most pronounced for soils with clay-size fractions greater than 50% and liquid limits between 60 and 220. Linear envelopes were observed when the clay-size fraction was less than 45% or when the liquid limit was less than 60 and the clay fractions was greater than 50%. Soils with clay fractions greater than 50 and liquid limits less than 220 can also have linear envelopes (Stark and Eid 1994).

Influencing Factors

Several factors will influence the residual shear strength of soils. Some of these factors include the rate at which the sample is strained, the chemistry of the pore fluid, the clay content, mineralogical composition, moisture content, and healing. The impacts of these factors is summarized in the following subsections.

Strain Rate

The impact of strain rate on the residual shear strength is unclear based on the results presented in the literature. An increase in the residual shear strength with an increase in strain rate is noted by: Lupini et al. (1981), Garga (1970), Kenney (1967), LaGatta (1970), and Petley (1966) when the shearing rate was between 4×10^{-5} and 10 mm/min. Petley (1966) noted that the residual shear strength increases observed in their study could be ignored. Suzuki et al. (2001) stated that the residual shear strengths of the kaolin clay and mudstone they tested were significantly influence by shearing rate for rates between 0.02 and 2 mm/min.

No major differences were observed in residual shear strengths when the shearing rate was varied between 0.01 and 0.2 mm/min by Anayi et al. (1988). Other studies that reported no changes in the residual strength with strain rates included: Kenney (1967), Sassa (1985), Ramiah et al. (1970) for shearing rates between 0.02 and 60 mm/min, Skempton (1985) for shearing rates between 0.05 and 0.35 mm/min, Bhat et al. (2013c) with shearing rates between 0.073 and 0.586 mm/min.

Lupini et al. (1981) observed brittle behavior when the strain rate was reduced. This behavior is stated to be caused by a changes in the viscous drag forces. They noted that below a threshold value, changes in the shearing rate did not

correspond to changes in the residual shear strength. This threshold strain rate was noted by Lupini et al. (1981) to be 1 mm/min. However, they recommended that 0.048/min be used as the threshold strain rate. Tika et al. (1996) noted similar conclusions.

Pore Fluid Chemistry

Generally, most studies agree that an increase in the pore fluid salinity will correspond to an increase in the residual shear strength. Kenney (1967, 1977) stated that the residual friction angle will increase with an increase in the sodium chloride (NaCl) concentration in the pore fluid in soils. This increase was noted to be as high as three times the residual friction angle measured when the soil has distilled water as the pore fluid. The increase is expected to be more profound in clays with platy particles (Kenney 1967, 1977). Bjerrum (1954, 1955) and Bjerrum and Rosenqvist (1956) also found reductions in the pore fluid salinity corresponded to reductions in the residual shear strength.

The type of salt in the pore fluid will also have an impact on the residual shear strengths observed. Specifically, Anson and Hawkins (1998) stated that the introduction of calcium carbonate to the pore fluid at a concentration of 80 mg/L resulted in an increase in the residual shear strength in montmorillonite, but had no effect in kaolinite (Anson and Hawkins 1998). Ramiah et al. (1970) stated that the measured residual friction angles when calcium salts were present in the pore fluid would be about 4° higher than when sodium salts were present. Their work contradicts that of Kenney (1977), who found that mixtures with sodium ions in the pore fluid were stronger than those with calcium ions in the pore fluid. However, the results from Ramiah et al. (1970) are in agreement with the results presented by Moore (1991). Moore (1991) concluded that the introduction of divalent cations (such as calcium ions) in the pore fluid would result in larger increases in the residual friction angle than the introduction of monovalent cations (such as sodium ions). It was further noted that the effect was exaggerated in montmorillonite in comparison to kaolinite. Finally, Moore (1991) also stated that an increase in the concentration of the ions will correspond to an increase in the residual shear strength.

Di Maio (1996) performed a series of direct shear tests on samples that were consolidated and sheared to the residual condition. In their tests, they replaced the cell water with a sodium chloride solution and then continued to shear the sample after the residual condition was achieved. Di Maio (1996) found that this resulted in an increase in the residual shear strength. However, if the sodium chloride solution was replaced with water, the increase was reversed and the residual shear strength dropped. They noted that soils with higher activities resulting in larger changes.

Tiwari et al. (2005b) measured the residual shear strength of soils with distilled water, sea water, and the soils after leaching of sodium chloride from the pore fluid using soils from seven landslide sites in Japan. Intact rock samples along with materials from the sliding surface and the main scrap were collected and tested. From the results obtained, they concluded that there was no consistent variation in the residual shear strength when the soils were mixed with salt water. However, they found that the soils with sea water as the pore fluid had residual friction angles that were 3° – 5° higher than those with distilled water as the pore fluid. Leaching of salinity from the intact rock samples resulted in residual shear strengths that were similar in magnitude to the residual shear strengths corresponding to the sliding surface materials when they were mixed with sea water. Tiwari et al. (2005a, b) noted that when samples were mixed with sea water, the residual friction angle of the intact rock powder increased by 17–23%, by 19–25% in the case of the soil from the main scrap and by 18–29% in the materials from the sliding surface. Furthermore, leaching of the pore fluid from the intact rock powders would result in reductions in the residual shear strengths by 15–32%. Finally, they concluded that the increases varied with the dominant clay mineral with montmorillonite dominated soils seeing substantial higher increases in the residual shear strength than the kaolinite dominated soils.

Moore and Brunson (1996) found that seasonal fluctuations in the pore fluid chemistry at a landslide site contributed to the movements observed. When ion concentration in the pore fluid was high, the residual strength of the shear zone increased resulting in a stabilizing effect on the slope. However, the opposite behavior was observed when the ion concentration dropped.

Clay Content

Using multiple reversal direct shear tests, Borowicka (1965) noted that the residual friction angle decreased with an increase in the clay fraction. Their results agreed with those presented by Skempton (1964) and Kenney (1967). Kenney (1967) noted that the residual friction angle depended on both the clay content and the mineralogy.

Mineralogy

Different types of soil are expected to have different behaviors during shearing. The clay mineralogy will not only impact the residual shear strengths including the curvature of the failure envelope (Hawkins and Privett 1985a, b), but also the response of the soil to different pore fluid chemistries (Di Maio and Fenelli 1994, Kenney 1967, Müller-Vonmoos and Løken 1989, among others). Kenney (1967) noted that smaller residual strengths should be expected in soils with montmorillonite, while micaceous and massive minerals should have expected to have larger

residual strengths. He further noted that for natural soils, the residual shear strength would be strongly influenced by the mineralogical composition, but pore fluid chemistry or strain rate had small effect on the measured strengths. On the other hand, for clay minerals, ion concentration in the pore fluid was seen to have a strong impact on the residual shear strengths measured (Kenney 1967). In a later study, Kenney (1977) concluded that the residual shear strength of a soil mass depends on the percent of massive minerals in the material. It is further dependent on the salt concentration of the pore fluid. This behavior was associated with the type of matrix that forms in the mixtures with different percentages of massive minerals. Specifically, when more than 50% of the total volume is occupied by massive minerals, Kenney (1977) stated that the residual shear strength will be controlled by those massive minerals.

Di Maio and Fenelli (1994) measured the residual shear strength of kaolin and bentonite when a 1 M solution of sodium chloride was used as the pore fluid. They found that the residual shear strength of kaolin was unaffected by the pore fluid chemistry. However, they stated that bentonite experienced large changes in the residual strength as salt diffusion occurred. Müller-Vonmoos and Løken (1989) found increases in the residual shear strength of kaolinite when it was prepared with either calcium chloride, potassium chloride or sodium chloride solutions as the pore fluid. They stated that increases in the residual shear strength depended on the concentration when sodium or potassium ions were present in the pore fluid, but there was no dependence of the increases in the shear strength on the calcium concentration in the pore fluid. Similarly, Müller-Vonmoos and Løken (1989) stated that montmorillonite with a calcium sulfate solution as the pore fluid would cause an increase in the residual shear strength, but again, there was no dependence observed on the residual shear strength with increases in the concentration of the solution.

The impact of clay mineralogy on the residual shear strength was extensively studied by Tiwari and Marui (2003, 2005). They performed ring shear testing for thirty-six mixtures of kaolin, bentonite and Toyoura sand prepared in the laboratory. From the results obtained, they found that an increase in the smectite content of the mixtures corresponded to large reductions in the residual friction angle. The kaolinite content of the mixtures also had some impact on the residual friction angles, but not as high as that with smectite. Tiwari and Marui (2003, 2005) also concluded that regardless of the kaolinite content in the mixture, the value of the residual friction angle was at its minimum of 3.7° (corresponding to the residual friction angle of smectite) when less than 58% of the mixture was quartz and more than 42% was smectite. Tiwari and Marui (2005) identified six different zones to evaluate the effect of smectite content on residual friction angle when kaolinite is constant or vice versa.

Moisture Content

Chowdhury and Bertoldi (1977) found that the final moisture content in the shear zone was directly related to the residual shear strength for the two soils that they tested (Mount Ousley and Buttenshaw Drive soils). It was stated that a decrease in the residual shear strength can be expected when the final moisture content in the shear zone was increased. Initial moisture content was not found to have any influence on the residual shear strength obtained. Tiwari and Marui (2004) found that the water content after ring shear tests was similar in all of the samples. They found that this moisture content at the end of the test was close to the plastic limit of the soil.

Healing

Multi-reversal direct shear tests were used by Ramiah et al. (1973) to study the healing of soils to establish the recovery in the residual shear strength. They tested bentonite and kaolinite with a rest period of four days during which healing took place. Ramiah et al. (1973) found higher strength values after the rest period with the effects being more pronounced in bentonite than in kaolinite. In contrast, Gibo et al. (2002) stated that smectite dominated soils will not undergo recovery. However, they noted that silt and sand dominated materials will experience recovery. Stark et al. (2005) expressed the recovery of strength as a function of plasticity with higher plasticity soils corresponding to higher recovery. They noted that the recovered strength gains were lost when the soil was subjected to a small amount of displacement. Bhat et al. (2013a, b, c, 2014) and Nakamura et al. (2010) also noted that the recovery that occurred would also be lost with a small amount of displacement.

Available Correlations

As in the case of the fully softened shear strength, there are a number of correlations available in the literature to estimate the residual shear strength as a function of various parameters. Most of these relationships provide estimates for the residual friction angle based on the liquid limit, plasticity index or the clay fraction. Specifically, relationships between the residual friction angle and the liquid limit are provided in: Mesri and Cepeda-Diaz (1986), Haefeli (1951), Bishop (1971), Stark and Eid (1994), Collotta et al. (1989), Cancelli (1977), and Tiwari and Ajmera (2011). Some relationships between the residual friction angle and the plasticity index can be found in: Voight (1973), Kanji and Wolle (1977), Lupini et al. (1981), Chandler (1984), Kanji (1974), Seycek (1978), Vaughan et al. (1978), Lambe (1985), Clemente (1992), Wisley (2003), Brandon et al. (1991), Mesri and Shahien (2003), and Tiwari and Ajmera (2011). Finally,

Lupini et al. (1981), Skempton (1964, 1985), Borowicka (1965), Binnie et al. (1967), Kenney (1977), and Collotta et al. (1989) all contain relationships between the residual friction angle and the clay fraction. Some of these correlations are summarized in Table 3. In this table, those correlations that will be discussed in more detail later in this section are presented in bold.

One of the earliest correlations to estimate the residual friction angle was provided by Skempton (1964). In his study, Casagrande shear box tests were performed using multiple reversals to measure the residual friction angles of several clay samples obtained from different sites. In this study, Skempton noted that the residual friction angles were higher than those of the minerals citing that the presence of silts in the soils hindered the ability of the clay particles to completely orient themselves to reach their minimum strengths.

Hawkins and Privett (1985a, b) stated that there was little scatter in their correlations when the clay fraction was greater than 60% and/or when the plasticity index was greater than 45% as these soils will have low residual shear strengths. They further added that since soils encountered in practice typically have clay fractions between 35 and 60% and plasticity indices between 25 and 45, the correlations they proposed should not be used.

Several correlations to estimate the residual secant friction angle as a function of liquid limit, clay fraction the effective normal stress have been provided by Stark and his colleagues. The original relationship appears to be presented in Stark and Eid (1994) and is also presented in Eid (1996). This relationship was then subjected to a series of modifications and revisions in later publications. The latest publication appears to be present a series of equations in addition to a correlation chart. Specifically, Stark and Hussain (2015) provide Eqs. 24 to 39 grouped by the clay fraction to estimate the secant residual friction angle at various effective normal stresses as a function of the liquid limit. Equations 24 to 27 correspond to soils with clay fractions less than 20% and with liquid limits ranging from 30 to 80. Equations 28 to 31 correspond to soils with clay fractions between 25 and 45% with liquid limits between 30 and 130. The final set of equations (Eqs. 32 to 39) are for soils with clay fractions greater than 50%. These are subdivided based on the liquid limits with Eqs. 32 to 35 applicable to soils with liquid limits between 30 and 120 and Eqs. 36 to 39 for soils with liquid limits between 120 and 300. For material with a clay fraction between the ranges of values noted above, interpolation is suggested. Equations 24 to 39 also correspond to different effective normal stresses. Specifically, Eqs. 24, 28, 32, and 36 correspond to effective normal stress of 50 kPa, Eqs. 25, 29, 33, and 37 to 100 kPa, Eqs. 26, 30, 34, and 38 to 400 kPa and Eqs. 27, 31, 35, and 39 to 700 kPa.

Table 3 Summary of available correlations to estimate the residual shear strength

Relationship ^a	Form ^b	References
Figure 7	$\phi'_r = f(CF)$	Skempton (1964)
Figure 1	$\phi'_r = f(PI)$	Voight (1973)
Equation 1 Figure 2	$\phi'_r = \frac{46.6}{(PI)^{0.446}}$	Kanji (1974) Kanji and Wolle (1977)
Figure 6	$\phi'_r = 453.1(LL)^{-0.85}$	Cancelli (1977)
Figure 5	$\phi'_r = f(CF)$ $\frac{\tau}{\sigma'_n} = f(CF)$	Lupini et al. (1981)
Figure 6	$\phi'_r = f(PI)$ $\frac{\tau}{\sigma'_n} = f(PI)$	Lupini et al. (1981)
Figure 6	$\phi'_r = f(PI)$	Gibo (1985)
Figure 4	$\phi'_{r,s} = f(PI, \sigma'_n)$	Hawkins and Privett (1985a)
Figure 5	$\phi'_{r,s} = f(PI, \sigma'_n)$	Hawkins and Privett (1985a)
Figure 10	$\phi'_r = f(PI)$	Borden and Putrich (1986)
Figure 1	$\phi'_r = f(LL)$	Mesri and Cepeda-Diaz (1986)
Figure 2	$\phi'_r = f(CF)$	Mesri and Cepeda-Diaz (1986)
Figure 1 Figure 2	$\phi'_r = f(CF^2 \times LL \times PI \times 10^{-5}, TT)$	Collotta et al. (1989)
Figure 3 Figure 4	$\phi'_r = f(CF, TT)$	Collotta et al. (1989)
Figure 7	$\phi'_r = f(PI)$	Müller-Vonmoss and Løken (1989)
Figure 8	$\phi'_r = f(M)$	Müller-Vonmoss and Løken (1989)
Figure 4 Figure 4.3	$\phi'_r = f(LL, CF, \sigma'_n)$	Stark and Eid (1994) Eid (1996)
Figure 11	$\phi'_f - \phi'_r = f(LL)$	Stark and Eid (1997)
Figure 8	$\phi'_r = f(CF)$	Tika and Hutchinson (1999)
Figure 9	$\phi'_r = f(PI)$	Tika and Hutchinson (1999)
Figure 6	$\phi'_r = f(M)$	Tiwari and Marui (2003)
Figure 10	$\phi'_r = f(LL, M)$	Tiwari and Marui (2003)
Figure 11	$\phi'_r = f(PI, M)$	Tiwari and Marui (2003)
Figure 2	$\phi'_{r,s} = f(LL, CF, \sigma'_n)$	Stark and Hussain (2015)
Figure 17	$\phi'_r = f(PI)$	Toyota et al. (2009)
Figure 7a	$\phi'_r = f(LL, CF, \sigma'_n)$	Eid et al. (2016)
Figure 7b	$\phi'_r = f(PI, CF, \sigma'_n)$	Eid et al. (2016)
Figure 12	$\phi'_f - \phi'_r = f(LL, M)$	Tiwari and Ajmera (2011)^c
Figure 13	$\phi'_f - \phi'_r = f(PI, M)$	Tiwari and Ajmera (2011)^c
Figure 14	$\frac{\phi'_f - \phi'_s}{\phi'_r} = f(LL, M)$	Tiwari and Ajmera (2011)^c
Figure 15	$\frac{\phi'_f - \phi'_s}{\phi'_r} = f(LL, M)$	Tiwari and Ajmera (2011)^c
Figure 16	$\frac{\phi'_f - \phi'_s}{\phi'_r} = f(PI, M)$	Tiwari and Ajmera (2011)^c
Figure 17	$\frac{\phi'_f - \phi'_s}{\phi'_r} = f(PI, M)$	Tiwari and Ajmera (2011)^c

^aAll figure and equation numbers noted here are based on the original article cited in the reference

^b ϕ'_r = residual friction angle, $\phi'_{r,s}$ = secant residual friction angle, ϕ'_f = fully softened friction angle, LL = liquid limit, PI = plasticity index, σ'_n = effective normal stress, τ = residual shear strength, CF = clay fraction, M represents clay mineralogy, and TT = test type, which for Collotta et al. (1989) was either the direct shear (Figs^a. 1 and 3) or the ring shear (Figs^a. 2 and 4)

^cThe values for the residual friction angles were taken from Tiwari and Marui (2005)

$$\left(\phi'_{r,s}\right)_{50\text{kPa}} = 39.71 - 0.29LL + 6.63 \times 10^{-4}LL^2 \quad (24)$$

$$\left(\phi'_{r,s}\right)_{100\text{kPa}} = 39.41 - 0.298LL + 6.81 \times 10^{-4}LL^2 \quad (25)$$

$$\left(\phi'_{r,s}\right)_{400\text{kPa}} = 40.24 - 0.375LL + 1.36 \times 10^{-3}LL^2 \quad (26)$$

$$\left(\phi'_{r,s}\right)_{700\text{kPa}} = 40.34 - 0.412LL + 1.683 \times 10^{-3}LL^2 \quad (27)$$

$$\left(\phi'_{r,s}\right)_{50\text{kPa}} = 31.4 - 6.79 \times 10^{-3}LL - 3.616 \times 10^{-3}LL^2 + 1.864 \times 10^{-5}LL^3 \quad (28)$$

$$\left(\phi'_{r,s}\right)_{100\text{kPa}} = 29.8 - 3.627 \times 10^{-4}LL - 3.584 \times 10^{-3}LL^2 + 1.854 \times 10^{-5}LL^3 \quad (29)$$

$$\left(\phi'_{r,s}\right)_{400\text{kPa}} = 28.4 - 5.622 \times 10^{-2}LL - 2.952 \times 10^{-3}LL^2 + 1.721 \times 10^{-5}LL^3 \quad (30)$$

$$\left(\phi'_{r,s}\right)_{700\text{kPa}} = 28.05 - 0.208LL - 8.183 \times 10^{-4}LL^2 + 9.372 \times 10^{-6}LL^3 \quad (31)$$

$$\left(\phi'_{r,s}\right)_{50\text{kPa}} = 33.5 - 0.31LL + 3.9 \times 10^{-4}LL^2 + 4.4 \times 10^{-6}LL^3 \quad (32)$$

$$\left(\phi'_{r,s}\right)_{100\text{kPa}} = 30.7 - 0.2504LL - 4.2053 \times 10^{-4}LL^2 + 8.0479 \times 10^{-6}LL^3 \quad (33)$$

$$\left(\phi'_{r,s}\right)_{400\text{kPa}} = 29.42 - 0.2621LL - 4.011 \times 10^{-4}LL^2 + 8.718 \times 10^{-6}LL^3 \quad (34)$$

$$\left(\phi'_{r,s}\right)_{700\text{kPa}} = 27.7 - 0.3233LL + 2.896 \times 10^{-4}LL^2 + 7.1131 \times 10^{-6}LL^3 \quad (35)$$

$$\left(\phi'_{r,s}\right)_{50\text{kPa}} = 12.03 - 0.0215LL \quad (36)$$

$$\left(\phi'_{r,s}\right)_{100\text{kPa}} = 10.64 - 0.0183LL \quad (37)$$

$$\left(\phi'_{r,s}\right)_{400\text{kPa}} = 8.32 - 0.0114LL \quad (38)$$

$$\left(\phi'_{r,s}\right)_{700\text{kPa}} = 5.84 - 0.0049LL \quad (39)$$

Tiwari and Marui (2005) found that the correlation proposed by Stark and Eid (1994) that depended on the clay

fraction, liquid limit and effective normal stress could overestimate the residual friction angle by nearly five times. They further noted that Stark and Eid (1994) correlation could not be generalized for all types of minerals, but it only worked for a few types. To further illustrate this point, they presented Fig. 16, which correlates the residual friction angle with the clay fraction and mineralogical composition of the soil mass. It was noted that the clay fraction measured after the test should be used in Fig. 16 instead of those corresponding to before the test was conducted to ensure that the residual friction angle is not underestimated. As seen in Fig. 16, at the same clay content, the clay mineralogy can strongly influence the residual friction angle with differences over 20° in some cases. Tiwari and Marui (2005) also presented charts to estimate the residual friction angle as functions of the specific surface area, percent of smectite in the soil mass, the liquid limit (shown in Fig. 17), and the plasticity index (shown in Fig. 18). A triangular correlation chart with contours to estimate the residual friction angle in terms of the clay mineralogy was also prepared by Tiwari and Marui (2005). This has been reproduced in Fig. 19.

Correlations Between Residual and Fully Softened Friction Angles

To the authors' knowledge, only two sets of researchers have examined the relationship between the residual and fully softened friction angles. Stark et al. (2005) presented a chart that relates the difference in these two friction angles with the liquid limit. However, their correlation contained a significant amount of scatter. While Tiwari and Ajmera (2011) focused on the fully softened shear strength of soils, their work also provided several relationships between the residual and fully softened friction angles. The residual friction angles included in these relationships were taken from Tiwari and Marui (2005). Figures 20 and 21 contain the relationship that the authors proposed between the difference in the fully softened and residual friction angles in terms of the liquid limit and plasticity index, respectively. They found that their relationships had less scatter than those proposed by Stark et al. (2005) as a result of aggregating the correlations with the mineralogical composition. Tiwari and Ajmera (2011) also presented relationships between the normalized difference of the fully softened and residual friction angles. These differences were normalized by the fully softened and residual friction angles, separately. The relationships developed by Tiwari and Ajmera (2011) are provided in Figs. 22, 23, 24 and 25. These figures relate the normalizations to the liquid limit and plasticity indices of the soil samples.

Fig. 16 Relationship between the clay content and the residual friction angle as proposed by Tiwari and Marui (2005)

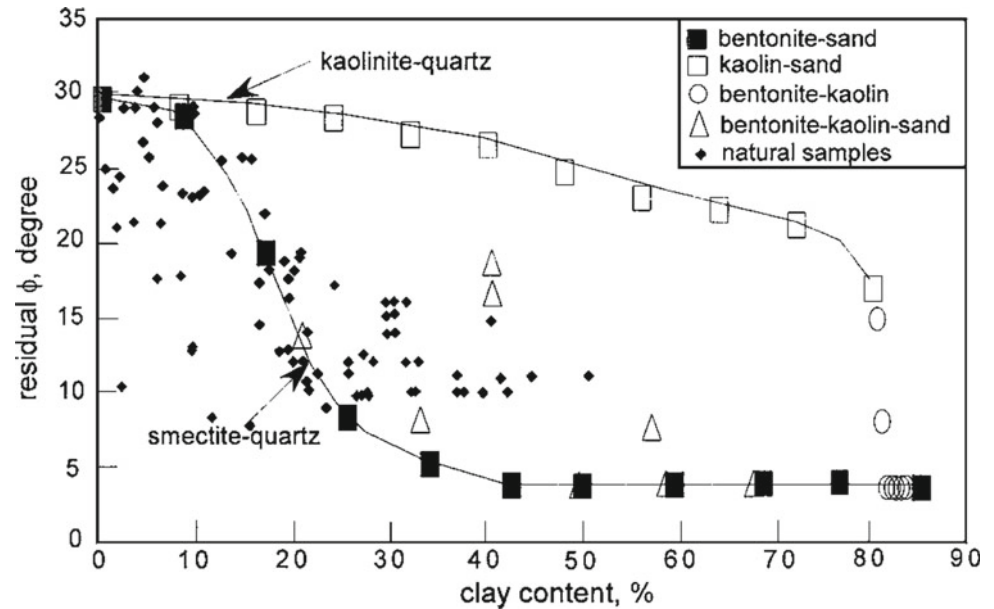
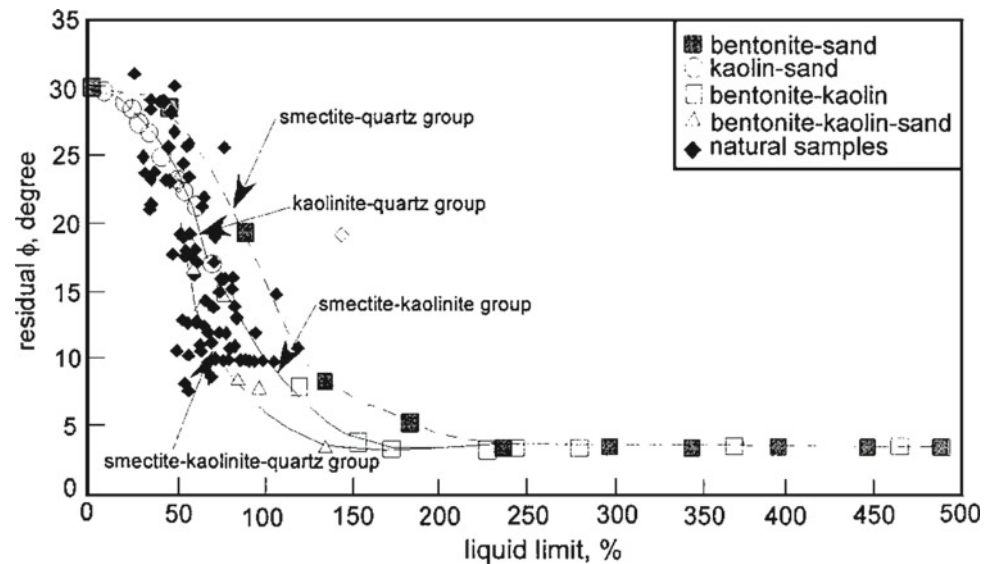


Fig. 17 Relationship between the liquid limit and the residual friction angle as proposed by Tiwari and Marui (2005)



Discussion

The fully softened shear strength can be measured using a variety of laboratory tests including the direct shear, triaxial compression, ring shear and direct simple shear. Triaxial testing to measure the fully softened shear strength of soils poses several difficulties including: (1) difficulty in preparing and handling the sample for the test and (2) long testing durations associated with saturation, consolidating and shearing specimens. The ring shear test is not able to capture the shearing mode in situ for the fully softened condition (Stark et al. 2005) and thus, requires the use of a correction factor when measuring the fully softened friction angle.

Given these issues, the authors believe that the fully softened shear strength is best measured with the use of direct shear or direct simple shear testing. Direct simple shear testing is found to be better suited for determining the fully softened shear strength at low effective normal stresses, mainly due to the machine and instrumentation sensitivity related errors in direct shear test specifically at very low normal stresses.

Measurement of the residual shear strength is fairly straightforward. It is widely accepted that the torsional ring shear test is ideal for measuring the residual shear strength. However, the authors recommend the use of an Imperial College type ring shear test over a Bromhead type device due to the many benefits it has to offer. Since there is a limited availability of ring shear devices in commercial labs,

Fig. 18 Relationship between the plasticity index and the residual friction angle as proposed by Tiwari and Marui (2005)

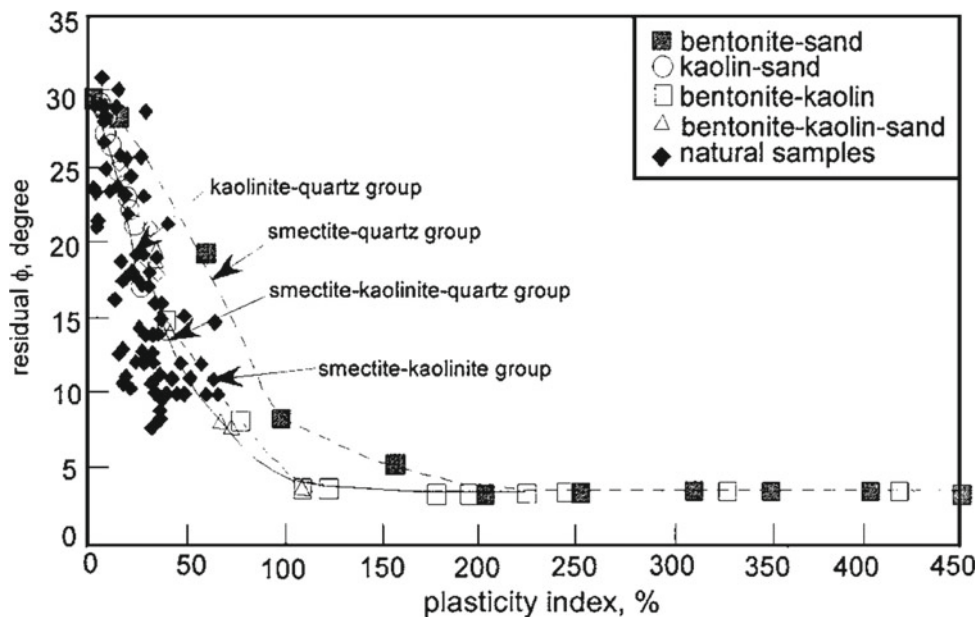
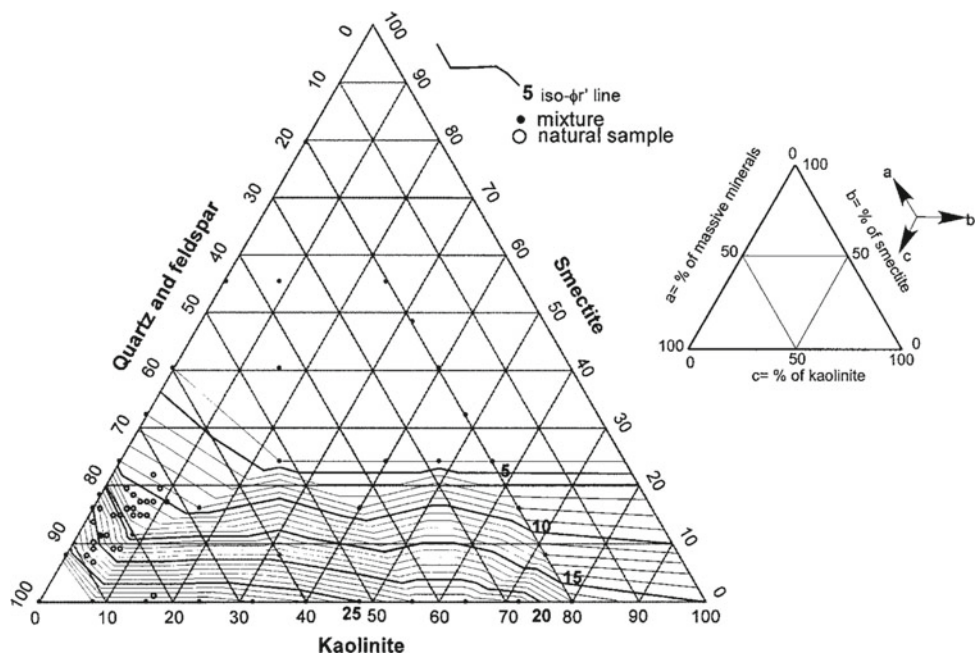


Fig. 19 Triangular correlation chart proposed by Tiwari and Marui (2005) that relates clay mineralogy to the residual friction angle



the residual shear strength can also be measured with the use of pre-cut and polished surfaces in the direct shear or triaxial compression tests. Procedures for preparing these samples are explained in detail in Meehan et al. (2010, 2011), respectively, which also note that direct shear test specimens are easier to prepare than triaxial compression test specimens.

Examination of the functional forms of the fully softened shear envelopes including linear, power and hyperbolic depictions suggested that none of those forms can accurately capture the fully softened shear strength at every effective

normal stress. Specifically, the curvature of failure envelopes at low effective normal stresses is best capture by power or hyperbolic function forms. The power function is better able to appropriately predict the shear strengths across a larger range of effective normal stresses than the hyperbolic function, which suggests a plateau in the fully softened shear strength. A linear Mohr-Coulomb failure envelope can accurately capture the behavior of soils at high normal stresses. Therefore, the ranges across which the functional form is fitted to represent the shear envelope should be noted and extrapolation beyond that the range of testing (especially

Fig. 20 Relationship between liquid limit and the difference in the fully softened and residual friction angles as proposed by Tiwari and Ajmera (2011)

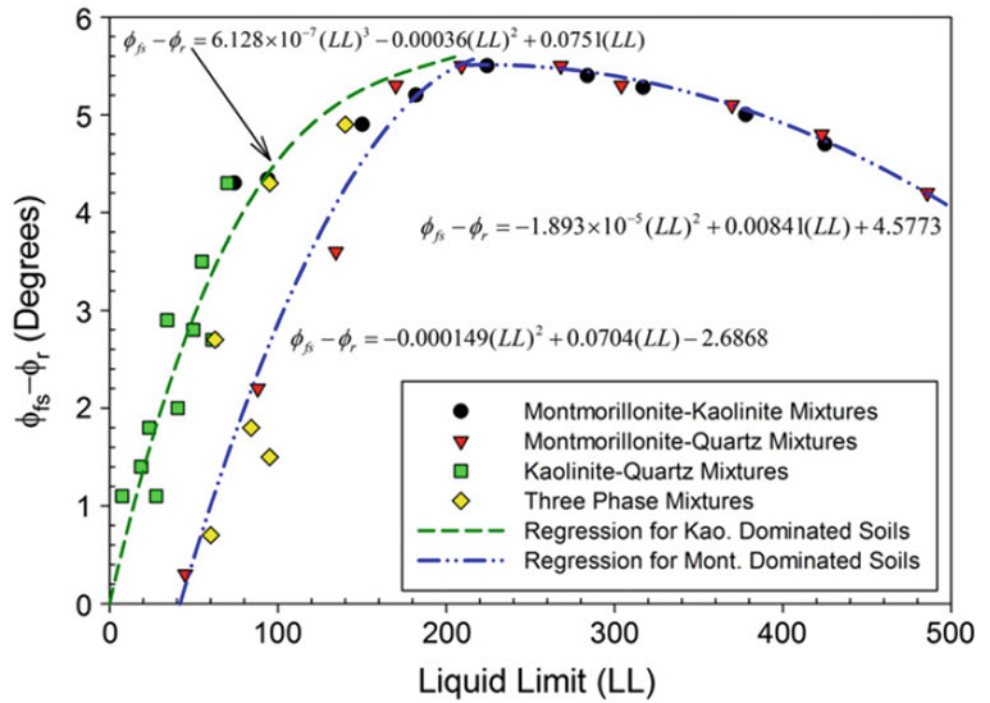


Fig. 21 Relationship between plasticity index and the difference in the fully softened and residual friction angles as proposed by Tiwari and Ajmera (2011)

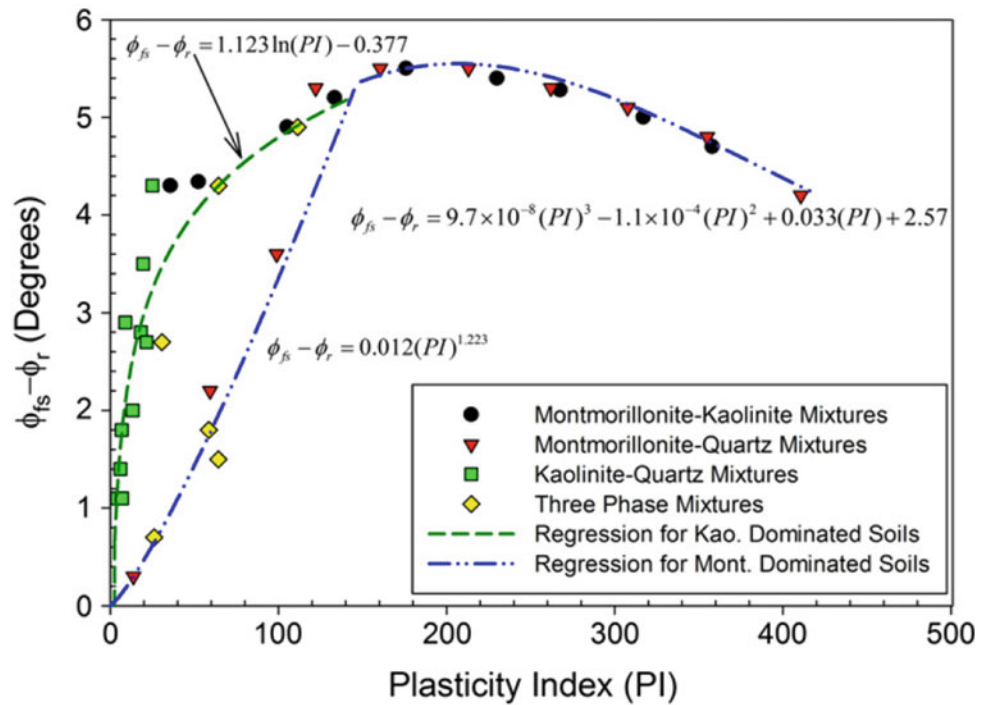


Fig. 22 Relationship between liquid limit and the ratio of the difference in the fully softened and residual friction angles with the fully softened friction angle as proposed by Tiwari and Ajmera (2011)

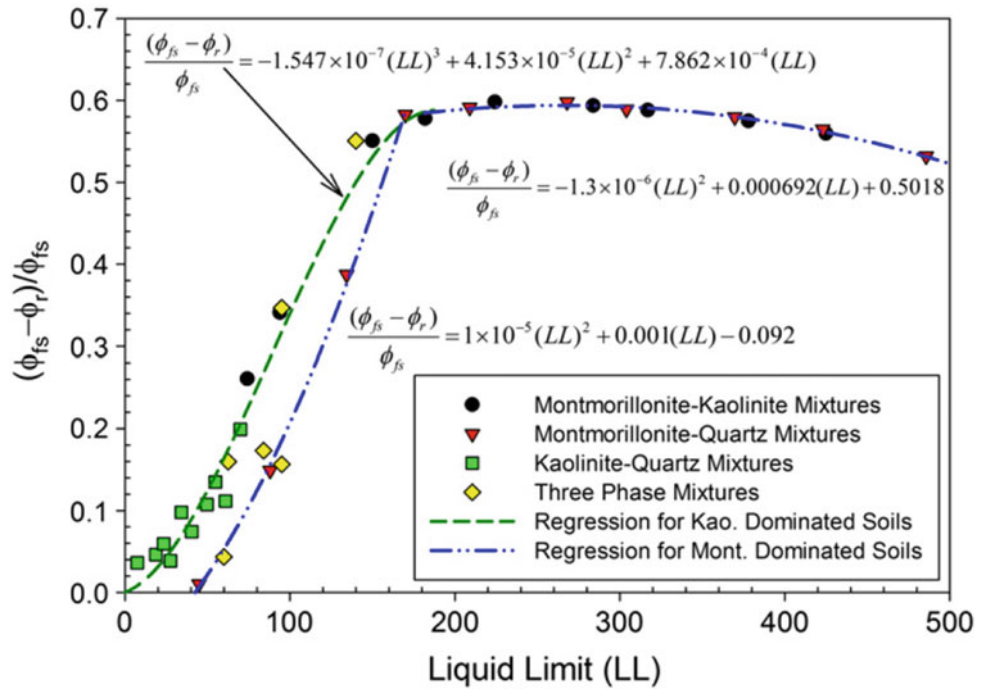


Fig. 23 Relationship between plasticity index and the ratio of the difference in the fully softened and residual friction angles with the fully softened friction angle as proposed by Tiwari and Ajmera (2011)

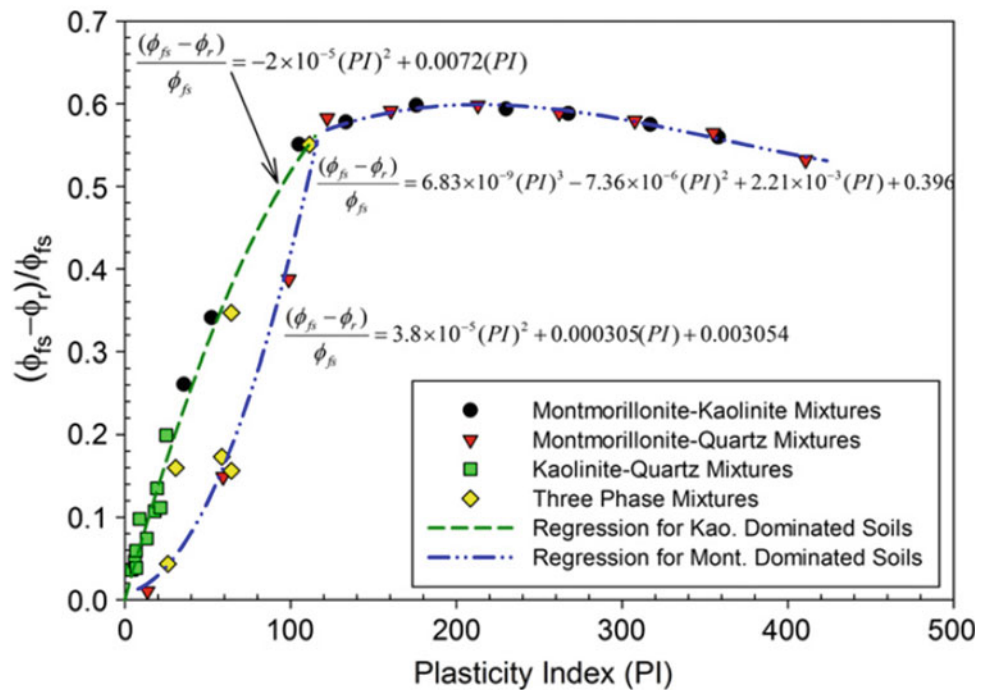


Fig. 24 Relationship between liquid limit and the ratio of the difference in the fully softened and residual friction angles with the residual friction angle as proposed by Tiwari and Ajmera (2011)

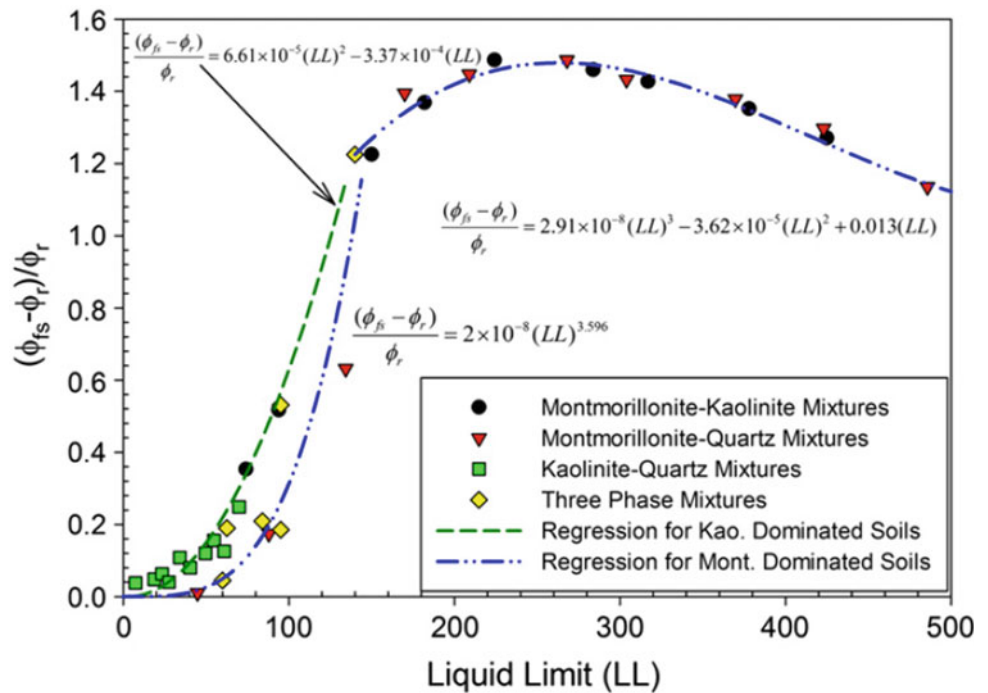
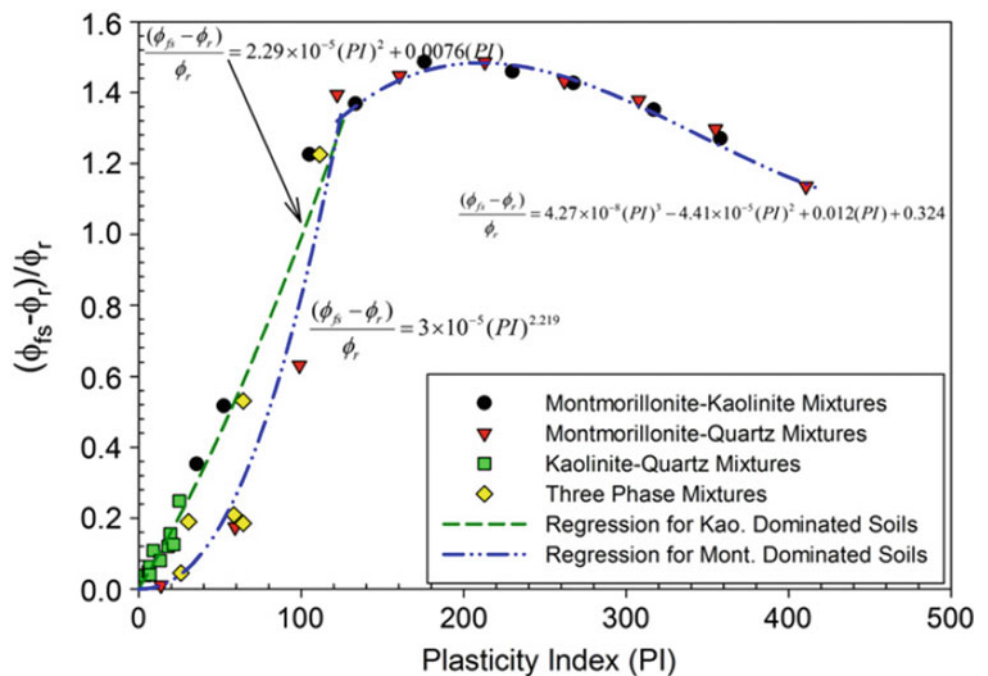


Fig. 25 Relationship between plasticity index and the ratio of the difference in the fully softened and residual friction angles with the residual friction angle as proposed by Tiwari and Ajmera (2011)



towards low effective normal stresses) should be avoided. Similar comments can also be made regarding the failure envelope for the residual failure envelope.

A number of factors were found to influence the fully softened and residual shear strengths. Some of the factors include the chemistry of the pore fluid, mineralogical composition, plasticity characteristics, strain rate, and the amount of clay within the soil mass. The shear strength uses in

analyses and design should account for these factors and potential fluctuations with seasonal changes. Additional research is necessary to better quantify both the influence of these and other factors on both the fully softened and residual shear strengths.

The literature contains many correlations to estimate both the fully softened and residual shear strengths. These correlations are extremely important in order to verify

back-calculations performed and to provide preliminary estimates for the strengths in early design calculations. However, these correlations are not perfect and will not capture all of the factors influencing the shear strength and behavior of soils globally. As such, it is still best to perform laboratory and/or field measurements of the shear strengths. Along those lines, it is also noted that soil test results from the sites should not be discarded simply because they do not agree or fit with the current correlations. Engineers should continue to use their judgement and be able to explain their choices and decisions rather than consider this or any other document as absolute. If correlations are used, it is suggested that the values obtained be reduced (or the considered factor of safety be increased) to account for uncertainties in the estimates.

The current understanding of both the fully softened and residual shear strengths can hardly be considered complete. There is still significant research that needs to be undertaken to continue to improve the state-of-practice. For example, future research avenues may explore: (1) the impacts of undrained and cyclic loading on the residual and fully softened shear strengths, (2) additional testing using triaxial compression tests to measure both the fully softened and residual shear strengths, (3) the influence of various factors including pore fluid chemistry, remolding moisture content, strain rates, mineralogy, etc., (4) development of correlations that consider these other influencing factors, and (5) the incorporation of reliability and probability. Case histories related to the fully softened and residual shear strengths should continue to be well-documented

Summary and Conclusions

In Many new developments in the understanding of the fully softened and residual shear strengths have been made in the recent years. A clear understanding of the background and meaning of both of these shear strengths has emerged along with information regarding when it is appropriate to use both the fully softened and residual shear strengths. Developments in various areas associated with both of these shear strengths are summarized below:

- **Measurement Methods:** The fully softened shear strength can be measured in the laboratory with the use of direct shear, direct simple, triaxial compression, and ring shear testing. While no consensus exists, the authors recommend the use of either the direct shear or the direct simple shear for these estimates with further research required on the use of triaxial compression tests. It is widely accepted that the torsional ring shear is best for measuring the residual shear strength. However, given its limited

availability, direct shear or triaxial testing can also be performed using pre-cut and polished specimens.

- **Interpretation Techniques:** Fully softened and residual shear envelopes have been defined using various function forms ranging from the linear Mohr-Coulomb envelope to power and hyperbolic functions. None of these forms will accurately capture the shear strengths at all effective normal stresses. Curvature is most pronounced at low effective normal stresses, for which the power or hyperbolic function is best suited for the shear envelope. The secant friction angles can also be used to capture the curvature of the failure envelopes.
- **Influencing Factors:** Many different factors including clay mineralogy, plasticity characteristics, strain rate, and pore fluid chemistry will impact the fully softened and residual shear strengths. The fully softened and residual shear strengths used in the design and analyses should account for the impact of these factors.
- **Correlations:** There are a number of correlations that exist in the literature to estimate the fully softened and residual shear strengths. These correlations are valuable to verify the back-calculated strengths and to perform preliminary design calculations. A limitation of the current correlations is the lack of those that capture the influence of the various factors that impact the shear strengths. As such, extreme caution should be applied while using one correlation method versus others.

While there is an improved understanding of both the fully softened and residual shear strengths, much work still remains. Several future research avenues have been identified in this paper.

References

- Anayi JT, Boyce JR, Rogers CD (1988) Comparison of alternative methods of measuring the residual strength of a clay. *Transp Res Rec* 1192
- Anayi JT, Boyce JR, Rogers CDF (1989) Modified Bromhead ring shear apparatus. *Geotech Test J* 12(2):171–173
- Anderson WF, Hammoud F (1988) Effect of testing procedure in ring shear tests. *Geotech Test J* 11(3):204–207
- Anson RWW, Hawkins AB (1998) The effect of calcium ions in pore water on the residual shear strength of kaolinite and sodium montmorillonite. *Géotechnique* 48(6):787–800
- ASTM D3080/3080M (2011) Standard test method for direct shear test of soils under consolidated drained conditions. ASTM International
- ASTM D4318 (2017) Standard test methods for liquid limit, plastic limit, and plasticity index of soils. ASTM International
- ASTM D4767 (2020) Standard test method for consolidated undrained triaxial compression test for cohesive soils. ASTM International
- ASTM D6467 (2013) Standard test method for torsional ring shear test to determine drained residual shear strength of cohesive soils. ASTM International

- ASTM D6528 (2017) Standard test method for consolidated undrained direct simple shear testing of fine grain soils. ASTM International
- ASTM D7181 (2020) Standard test method for consolidated drained triaxial compression test for soils. ASTM International
- ASTM D7608 (2018) Standard test method for torsional ring shear test to measured drained fully softened shear strength and stress dependent strength envelope of fine-grained soils. ASTM International
- ASTM WK3822 (2004) New test method for repeated direct shear test of soils under consolidated drained conditions. ASTM International
- Atkinson JH, Farrar DM (1985) Stress path tests to measure soil strength parameters for shallow landslips. In: Proceedings of the 11th international conference on soil mechanics and foundation engineering, pp 983–986
- Bahmyari H (2018) Shear strength characteristics and failure mechanism of slopes in overconsolidated soils of Nebraska. MS thesis, University of Nebraska – Lincoln
- Baker R (2004) Nonlinear Mohr envelopes based on triaxial data. *J Geotech Geoenviron Eng* 130(5):498–506
- Bhat DR, Bhandari NP, Yatabe R (2013a) Strength recovery from residual-state of shear on soils. *Indian Geotech J*
- Bhat DR, Bhandary NP, Yatabe R (2013b) Experimental study of strength recovery from residual strength on kaolin clay. *Int J Civ Environ Eng* 7(1):76–82
- Bhat DR, Bhandary NP, Yatabe R, Dhahal RK, Tiwari RC (2014) Strength recover from residual-state of shear on soils. *Indian Geotech J* 44(1):94–100
- Bhat DR, Yatabe R, Bhandary NP (2013c) Study of preexisting shear surfaces of reactivated landslides from a strength recovery perspective. *J Asian Earth Sci* 77:243–253
- Bhattarai P, Marui H, Tiwari B, Watanake N, Tuladhar GR, Aoyama K (2006) Influence of weather on physical and mechanical properties of mudstone. In: Disaster mitigation of debris flows, slope failures and landslides, pp 467–479
- Binnie MA, Clark, JFF, Skempton AW (1967) The effect of discontinuities in clay bedrock on the design of dams in the Mangla project. In: Proceedings of the transactions of 9th international congress of large dams, vol 1, pp 165–183
- Bishop AW (1971) Shear strength parameters for undisturbed and remolded soil specimens. In: Proceedings of the Roscoe memorial symposium, pp 3–58
- Bishop AW, Henkel DJ (1962) The measurement of soil properties. Edward Arnold Publishers Ltd.
- Bishop AW, Green GE, Garga VK, Andersen A, Brown JD (1971) A new ring shear apparatus and its application to the measurement of residual strength. *Géotechnique* 21:273–328
- Bishop AW, Webb DL, Lewin PI (1965) Undisturbed samples of London clay from the ashford common shaft: strength-effective normal stress relationship. *Géotechnique* 15(1):1–31
- Bjerrum L (1955) Stability of natural slopes in quick clay. *Géotechnique* 5:1–101
- Bjerrum L (1967) Progressive failure in slopes of overconsolidated plastic clay and clay shales. *J Soil Mech Found Div* 93(SM5):3–49
- Bjerrum L, Rosenqvist I (1956) Some experiments with artificially sedimented clays. *Géotechnique* 6(4):124–136
- Bjerrum L (1954) Geotechnical properties of Norwegian marine clays. *Géotechnique* 4:49–69
- Borden RH, Putrich SF (1986) Drained-strength parameters from direct shear tests for slope stability analyses in overconsolidated fissured residual soils. *Transp Res Rec* 1089:102–113
- Borowicka H (1965) The influence of the colloidal content on the shear strength of clay. In: Proceedings of the 6th international conference on soil mechanics, vol 1, pp 175–178
- Boucek B (1977) Ring shear tests on clay, vol 3. Publication of the Institute for Foundation Engineering, Soil Mechanics, Rock Mechanics, and Water Ways Construction, pp 7–41
- Boyce JR (1984) The residual strength of some soils in Zimbabwe. In: Proceedings of the 8th regional conference for Africa on soil mechanics and foundation engineering, pp 73–80
- Brand EW (1995) Slope stability and landslides under tropical conditions—a review. In: Proceedings of the Symposium on Hillside Development
- Brandon TL, Filz GM, Duncan JM (1991) Review of landslide investigation, phase I—part B, Olmstead locks and dams. U.S. Army Corp of Engineers Report
- Bromhead EN (1979) A simple ring shear apparatus. *Ground Eng* 12(5):40–44
- Bromhead EN (1992) Stability of slopes, 2nd edn. Surrey University Press
- Bromhead EN, Curtis RD (1983) A comparison of alternative methods of measuring the residual strength of London clay. USGS Library
- Bromhead EN, Harris AJ, Ibsen M-L (1999) Statistical variability of ring shear test results on a shear zone in London clay. In: Proceedings of the international symposium on slope stability engineering, vol 2, pp 1109–1114
- Cancelli A (1977) Residual shear strength and stability analysis of a landslide in fissured overconsolidated clays. *Bull Int Assoc Eng Geol* 16:193–197
- Castellanos BA (2014) Use and measurement of fully softened shear strength. PhD dissertation, Virginia Polytechnic Institute and State University
- Castellanos BA, Brandon T (2013) A comparison between the shear strength measured with direct shear and triaxial devices on undisturbed and remolded soils. In: Proceedings of the 18th international conference on soil mechanics and geotechnical engineering, pp 317–320
- Castellanos BA, Brandon TL (2019) Fully softened shear strength: application, measurement, and correlations. In: Geotechnical engineering in the XXI century: lessons learned and future challenges
- Castellanos BA, Brandon TL, VandenBerge DR (2016) Correlations for fully softened shear strength parameters. *Geotech Test J* 39(4):568–581
- Chandler MP (1977) Back analysis techniques for slope stabilization works: a case record. *Géotechnique* 27:479–495
- Chandler MP, Parker DC, Selby MJ (1981) The recent history and geotechnics of landslides at Gore Cliff, Isle of Wight. In: Slope stability engineering—applications and developments, pp 171–178
- Chandler RJ (1966) The measurement of residual strength in triaxial compression. *Géotechnique* 16(3):181–186
- Chandler RJ (1969) The effect of weathering on the shear strength properties of Keuper Marl. *Géotechnique* 19(3):321–334
- Chandler RJ (1976) The history and stability of two Lias clay slopes in the upper Gwash Valley, Rutland. *Philos Trans R Soc A* 283:527–556
- Chandler RJ (1984) Recent European experience of landslides in over-consolidated clays and soft rocks. In: Proceedings of the international symposium on landslides, pp 61–81
- Chandler RJ, Pachakis M, Mercer J, Wright J (1973) Four long term failures of embankments founded on landslips. *Q J Eng Geol* 6:405–422
- Charles JA, Soares MM (1984a) Stability of compacted rockfill slopes. *Géotechnique* 15(1):1–31
- Charles JA, Soares MM (1984b) The stability of slopes with nonlinear failure envelopes. *Can Geotech J* 21:397–406
- Charles JA, Watts KS (1980) The influence of confining pressure on the shear strength of compacted rockfill. *Géotechnique* 30(4):353–367

- Chowdhury RN, Bertoldi C (1977) Residual shear tests on soil from two natural slopes. *Aust Geomech J* 7:1–9
- Clemente JL (1992) Strength parameters for cut slope stability in “marine” sediments. In: Proceedings of the ASCE specialty conference on stability and performance of slopes and embankments-II, vol 1, pp 865–875
- Collins IF, Gunn CIM, Pender MJ, Wang Y (1988) Slope stability analyses for materials with a nonlinear failure envelope. *Int J Numer Anal Methods Geomech* 12(5):533–550
- Collotta T, Cantoni R, Pavesi U, Rubel E, Moretti PC (1989) A correlation between residual friction angle, gradation and the index properties of cohesive soils. *Géotechnique* 39(2):343–346
- Crabb GI, Atkinson JH (1988) Determination of soil strength parameters for the analysis of highway slope failures. In: *Slope stability engineering—developments and applications*, proceedings of the international conference on slope stability, 1991
- Crabb GI, Atkinson JH (1991) Determination of the soil strength parameters for the analysis of highway slope failures. In: *Slope stability engineering*, London, UK
- Crawford CB, Eden WJ (1966) A comparison of laboratory results with in-situ properties of Leda clay. In: Proceedings of the sixth international conference on soil mechanics and foundation engineering, vol 1, pp 31–35
- Day RW, Axten GW (1989) Surficial stability of compacted clay slopes. *J Geotech Eng* 115(4):577–580
- De Mello VFB (1946) Laboratory investigation of shearing resistance of clays. PhD dissertation, Massachusetts Institute of Technology
- De Mello VFB (1977) Reflections on design decisions of practical significance to embankment dams. *Géotechnique* 27(3):281–354
- Dewhurst DN, Clennell MB, Brown KM, Westbrook GK (1996) Fabric and hydraulic conductivity of sheared clays. *Géotechnique* 46(4):761–768
- Di Maio C (1996) The influence of pore fluid composition on the residual shear strength of some natural clayey soils. *Landslides* 1189–1193
- Di Maio D, Fenelli GB (1994) Residual strength of kaolinite and bentonite: the influence of their constituent pore fluid. *Géotechnique* 44(4):217–226
- Duncan JM, Brandon TL, VandenBerge DR (2011) Report of the workshop on shear strength for stability of slopes in highly plastic clays. Center for Geotechnical Practice and Research, CGPR Report #67, Virginia Polytechnic Institute and State University
- Eid H (2020) Fully softened and residual shear strengths of Midra shale. In: Proceedings of the international conference on civil infrastructure and construction, pp 754–758
- Eid HT (1996) Drained shear strength of stiff clays for slope stability analyses. PhD dissertation, University of Illinois at Urbana-Champaign
- Eid HT, Rabie KH (2016) Fully softened shear strength for soil slope stability analyses. *Int J Geomech* 17(1):04016023 1-10
- Eid HT, Rabie KH, Wijewickreme D (2016) Drained residual shear strength at effective normal stresses relevant to soil slope stability analyses. *Eng Geol* 204:94–107
- Gamez JA, Stark TD (2014) Fully softened shear strength at low stresses for levee and embankment design. *J Geotech Geoenviron Eng* 140(9):1–6
- Garga VK (1970) Residual shear strength under large strains and the effect of sample size on the consolidation of fissured clay. PhD thesis, University of London
- Gibo S (1983) Measure of residual strength of Shimajiri mudstone and evaluation of results—residual strength characteristics of materials in and close to the slip surface. *Trans JSIDRE* 104:61–68
- Gibo S (1985) The ring shear behavior and residual strength. In: Proceedings of the 4th international conference and field workshop on landslides, pp 283–288
- Gibo S, Nakamura S (1999) Parameters for curvilinear residual strength envelope. *Slope Stab Eng* 2:727–730
- Gibo S, Egashira K, Ohtsubo M (1987) Residual strength of smectite-dominated soils from the Kamenose landslide in Japan. *Can Geotech J* 24(3):456–462
- Gibo S, Egashira K, Ohtsubo M, Nakamura S (2002) Strength recovery from residual state in reactivated landslides. *Géotechnique* 52(9):683–686
- Gregory CH (1844) On railway cuttings and embankments: with an account of some slips in the London clay, on the line of the London and Croydon railway. *Minutes Proc* 3:135–145
- Griffith AA (1924) Theory of rupture. In: Proceedings of the 1st international congress for applied mechanics, Technische Boekhandel on Drukkerij
- Haefeli R (1951) Investigation and measurements of the shear strength of saturated cohesive soils. *Géotechnique* 2(3):186–207
- Harris AJ, Watson PDJ (1997) Optimal procedure for the ring shear test. *Ground Eng* 26–28
- Hawkins AB, Privett KD (1985a) Measurement and use of residual shear strength of cohesive soils. *Ground Eng* 22–29
- Hawkins AB, Privett KD (1985b) Measurement and use of residual shear strength reduction in Fuller’s earth clay. *Géotechnique* 42(3):453–464
- Hawkins AB, Privett KD (1986) Residual strength. Does BS5930 help or hinder? *Geol Soc Eng Geol Spec Publ* 2:279–282
- Head KH (1985) Manual of soil laboratory testing, vol 3. Pentech Press
- Henkel DJ (1957) Investigations of two long-term failures in London clay slopes at Wood Green and Northolt. In: Proceedings of the 4th international conference on soil mechanics and foundation engineering, vol 2, pp 315–320
- Herrmann HG, Wolfskill LA (1966) Engineering properties of nuclear craters: residual shear strength of weak shales. Technical Report No. 3-699, 5, U.S. Army Engineer Waterways Experiment Station
- Hutchinson JN (1969) A reconsideration of the Folkestone Warren landslides. *Géotechnique* 19(1):6–38
- Hvorslev MJ (1939) Torsion shear tests and their place in the determination of the shearing resistance of soils. *Ground Eng* 18(8):22–29
- Jiang JC, Barker R, Yamagami T (2003) The effect of strength envelope nonlinearity on slope stability computations. *Can Geotech J* 40:308–325
- Kamei T (1987) Some drained tests on normally consolidated cohesive soils. *Geology* 53–58
- Kanji MA (1974) The relationship between drained friction angles and Atterberg limits of natural soils. *Géotechnique* 24(4):671–674
- Kanji MA, Wolle CM (1977) Residual strength—new testing and microstructure. In: Proceedings of the 9th international conference on soil mechanics, vol 1, pp 153–154
- Kenney TC (1967) The influence of mineral composition on the residual strength of natural soils. In: Proceedings of the geotechnical conference, vol 1, pp 123–129
- Kenney TC (1977) Residual strength of mineral mixtures. In: Proceedings of the 9th international conference on soil mechanics, vol 1, pp 155–160
- Ladd CC, Foott K, Ishikara K, Poulos HG, Schlosser F (1977) Stress-deformation and strength characteristics. In: Proceedings of the 9th international conference on soil mechanics and foundations engineering, vol 2, pp 421–476
- Lade PV (2010) The mechanics of surficial failure in soil slopes. *Eng Geol* 114(1–2):57–64
- LaGatta DP (1970) Residual strength of clays and clay-shales by rotation shear tests. *Harv Soil Mech Ser* 86
- Lambe TW (1985) Amuay landslides. In: Proceedings of the 11th international conference on soil mechanics and foundations engineering, pp 137–158

- Lee KL, Seed HB (1967) Drained strength characteristics of sands. *J Soil Mech Found Div* 93:117–141
- Lefebvre G (1981) Strength and slope stability in Canadian soft clay deposits. *Can Geotech J* 18(3):420–442
- Li X (2007) Finite element analysis of slope stability using a nonlinear failure criterion. *Comput Geotech* 34:127–136
- Lupini JF, Skinner AE, Vaughan PR (1981) The drained residual strength of cohesive soils. *Géotechnique* 31(2):181–213
- Maccarini M (1993) A comparison of direct shear box with triaxial compression tests for a residual soil. *J Geotech Geol Eng* 11(2):69–80
- Maksimović M (1979) Limit equilibrium for nonlinear failure envelope and arbitrary slip surface. In: *Third international conference on numerical methods in geomechanics*, pp 769–777
- Maksimović M (1988) General slope stability software package for micro-computers. In: *Proceedings of the sixth international conference on numerical methods in geomechanics*, pp 2145–2150
- Maksimović M (1989a) Nonlinear failure envelope for soils. *J Geotech Eng* 115(4):581–586
- Maksimović M (1989b) On the residual shearing strength of clays. *Géotechnique* 39(2):347–351
- Marachi ND, Chan CK, Seed HB (1972) Evaluation of properties of rockfill materials. *J Soil Mech Found Div* 98(SM1):95–114
- Marsal RJ (1973) Mechanical properties of rockfill. In: *Embankment dam engineering*. Wiley, pp 109–200
- McGuire MP, VandenBerge DR (2017) Interpretation of shear strength uncertainty and reliability analyses of slopes. *Landslides* 14(6):2059–2072
- Meehan CL, Brandon TL, Duncan JM, Tiwari B (2010) Direct shear testing of polished slickensided surfaces. *Landslides* 7:157–167
- Meehan CL, Tiwari B, Brandon TL, Duncan JM (2011) Triaxial shear testing of polished slickensided surfaces. *Landslides* 8:449–458
- Mesri G, Abdel-Ghaffar MEM (1993) Cohesion intercept in effective stress-stability analysis. *J Geotech Eng* 119(8):1229–1249
- Mesri G, Cepeda-Diaz AF (1986) Residual shear strength of clays and shales. *Géotechnique* 36(2):269–274
- Mesri G, Shahien M (2003) Residual shear strength mobilized in first-time slope failures. *J Geotech Geoenviron Eng* 129(1):12–31
- Miller SM, Whyatt JK, McHugh EL (2004) Applications of the point estimation method of stochastic rock slope engineering. In: *Proceedings of 6th North America Rock Mechanics Symposium*
- Moon AT (1984) Effective shear strength parameters for stiff fissured clays. In: *Proceedings of the 4th Australia-New Zealand conference on geomechanics*, pp 107–111
- Moore R (1991) The chemical and mineralogical controls upon the residual strength of pure and natural clays. *Géotechnique* 1:35–47
- Moore R, Brunsden D (1996) Physico-chemical effects on the behaviour of a coastal mudslide. *Géotechnique* 46(2):259–278
- Müller-Vonmoss M, Løken T (1989) The shearing behavior of clays. *Appl Clay Sci* 4:125–141
- Nakamura S, Gibo S, Yasumoto J, Kimura S, Vithana S (2010) Application of recovered strength in stability analysis of reactivated landslide. Xuechengzhenm China. In: *Proceedings of GeoFlorida 2010*, pp 3149–3154
- Noor MJM, Hadi BA (2010) The role of curved-surface envelope Mohr-Coulomb model in governing shallow infiltration induced slope failure. *Electron J Geotech Eng* 15:1–21
- Parry RHG (1972) Stress-strain behaviour of soils. In: *Proceedings of the Roscoe memorial symposium at Cambridge University*
- Penman A (1953) Shear characteristics of saturated silt measured in triaxial compression. *Géotechnique* 15(1):79–93
- Perry J (1994) A technique for defining non-linear shear strength envelopes and their incorporation in a slope stability method of analysis. *Q J Eng GeolHydrogeol* 27:231–241
- Petley DJ (1966) The shear strength of soils at large strains. PhD thesis, University of London
- Ponce VM, Bell JM (1971) Shear strength of sand at extremely low pressures. *J Geotech Eng* 9(4):625–638
- Ramiah BK, Dayalu NK, Purushothamaraj O (1970) Influence of chemicals on residual strength of silty clay. *Soils Found* 10: 25–36
- Ramiah BK, Purushothamaraj P, Tavane NG (1973) Thixotropic effects on residual strength of remoulded clays. *Indian Geotech J* 3(3):189–197
- RocScience (2016a) RS2-finite element analysis for excavations and slopes, Toronto
- RocScience (2016b) Slide v7.0-2D limit equilibrium slope stability analysis, Toronto
- Saleh AA, Wright SG (2005) Shear strength correlations and remedial measure guidelines for long-term stability of slopes constructed of highly plastic clay soils. Center for Transportation Research, University of Texas at Austin
- Sassa K (1985) The mechanism of debris flow. In: *Proceedings of 11th international conference on soil mechanics and foundation engineering*, vol 3, pp 1173–1176
- Seyceck J (1978) Residual shear strength of soils. *Bull Int Assoc Eng Geol* 17:73–75
- Pederson RC, Olson RE, Rauch AF (2003) Shear and interface strength of clay at very low effective stress. *GeotechTest J* 26(1): 71–78
- Skempton AW (1948) The rate of softening in stiff fissured clays with special reference to London clay. In: *Proceedings of the 2nd international conference on soil mechanics and foundation engineering*, vol 2, pp 50–53
- Skempton AW (1964) Long-term stability of clay slopes. *Géotechnique* 14(2):77–102
- Skempton AW (1970) First-time slides in over-consolidated clays. *Géotechnique* 20(3):320–324
- Skempton AW (1977) Slope stability of cuttings in brown London clay. In: *Proceedings of the 9th international conference on soil mechanics and foundation engineering*, vol 3, pp 261–270
- Skempton AW (1985) Residual strength of clays in landslides, folded strata, and the laboratory. *Géotechnique* 35(1):3–18
- Skempton AW, Petley DJ (1967) The strength along structural discontinuities in stiff clays. In: *Proceedings of the geotechnical conference*, vol 2, pp 29–46
- Sokolovsky VV (1960) *Statics on soil media*. Butterworths Scientific Publication, London
- Stark TD, Eid HT (1992) Comparison of field and laboratory residual strengths. In: *Proceedings of the stability and performance of slopes and embankments—II geotechnical special publication*, vol 31, pp 876–889
- Stark TD, Eid HT (1993) Modified Bromhead ring shear apparatus. *Geotech Test J* 16(1):100–107
- Stark TD, Eid HT (1994) Drained residual strength of cohesive soils. *J Geotech Eng* 120(5):856–871
- Stark TD, Eid HT (1997) Slope stability analyses in stiff fissured clays. *J Geotech Geoenviron Eng* 123(4):335–343
- Stark TD, Fernandez R (2019) Fully softened shear strength measurement and correlations. *Geotech Test J*
- Stark TD, Hussain M (2015) Empirical correlations: drained shear strength for slope stability analyses. *J Geotech Geoenviron Eng* 139(6):853–862
- Stark TD, Choi H, McCone S (2005) Drained shear strength parameters for analysis of landslides. *J Geotech Geoenviron Eng* 131(5):575–588
- Stephens I, Branch AI (2013) Testing procedure for estimating fully softened shear strengths of soils using reconstituted material. U.S. Army Corps of Engineers Report No. ERDC/GSL GeoTACS TN-13-1
- Steward HE, Cripps JC (1983) Some engineering implications of chemical weathering of pyritic shale. *Q J Eng Geol* 16:281–289

- Suzuki M, Yamamoto T, Tanikawa K (2001) Variation in residual strength of clay with shearing speed. *Mem Fac Eng Yamaguchi Univ* 52(1):45–49
- Terzaghi K (1936) Stability of slopes of natural clay. In: *Proceedings of the 1st international conference on soil mechanics and foundations*, pp 161–165
- Terzaghi K, Peck RB, Mesri G (1996) *Soil mechanics in engineering practice*, 3rd edn. Wiley
- Thomson S, Kjartanson BH (1985) Study of delayed failure in a cut slope in stiff clay. *Can Geotech J* 22(2):286–297
- Tika TE, Hutchinson JN (1999) Ring shear tests on soil from the Vaiont landslide slip surface. *Géotechnique* 49(1):59–74
- Tika TE, Vaughan PR, Lemos LJ (1996) Fast shearing of pre-existing shear zones in soils. *Géotechnique* 46:197–233
- Tiwari B, Ajmera B (2011) A new correlation relating the shear strength of reconstituted soil to the proportions of clay minerals and plasticity characteristics. *Appl Clay Sci* 53(1):48–57
- Tiwari B, Ajmera B (2014) Curvature of failure envelopes for normally consolidated clays. In: *Proceedings of the third world landslide forum—landslide science for a safer Geo-environment*, vol 2, pp 117–122
- Tiwari B, Ajmera B (2015) Reduction in fully softened shear strength of natural clays with NaCl leaching and its effect on slope stability. *J Geotech Geoenviron Eng* 141(1):04014086 1-10
- Tiwari B, Marui H (2003) Estimation of residual shear strength for bentonite-kaolin-Toyouura sand mixture. *J Jpn Landslide Soc* 40(2):124–133
- Tiwari B, Marui H (2004) Objective oriented multistage ring shear test for shear strength of landslide soil. *J Geotech Geoenviron Eng* 130(2):217–222
- Tiwari B, Marui H (2005) A new method for the correlation of residual shear strength of the soil with mineralogical composition. *J Geotech Geoenviron Eng* 131(9):1139–1150
- Tiwari B, Brandon TL, Marui H, Tuladhar GR (2005a) Comparison of residual shear strengths from back analysis and ring shear tests on undisturbed and remolded specimens. *J Geotech Geoenviron Eng* 131(9):1071–1079
- Tiwari B, Tuladhar GR, Marui H (2005b) Variation in residual shear strength of the soil with the salinity of pore fluid. *J Geotech Geoenviron Eng* 131(12):1445–1456
- Townsend FC, Gilbert PA (1973) Tests to measure residual strength of some clay shales. *Géotechnique* 23:267–271
- Toyota H, Nakamura K, Sugimoto M, Sakai N (2009) Ring shear tests to evaluate strength parameters in various remoulded soils. *Géotechnique* 59(8):649–659
- USACE (1986) *Laboratory soils testing—Engineer Manual 110-2-1906*. United States Army Corps of Engineers
- VandenBerge DR, Castellanos BA, McGuire MP (2019) Comparison and use of failure envelope forms for slope stability analyses. *J Geotech Geol Eng* 37:2029–2046
- Vaughan PR, Hight DW, Sodha VG, Walbancke HJ (1978) Factors controlling the stability of clay fills in Britain. In: *Clay fills*, pp 203–217
- Vesic AS, Clough GW (1968) Behavior of granular materials under high stresses. *J Soil Mech Found Div* 94(SM3):661–668
- Voight B (1973) Correlation between Atterberg plasticity limits and residual shear strength of natural soils. *Géotechnique* 23(2):265–267
- Watry SM, Lade PV (2000) Residual shear strengths of bentonites on Palos Verdes Peninsula, California. In: *Proceedings of Geo-Denver 2000*, pp 323–342
- Wisley LD (2003) Residual shear of clays and correlations using Atterberg limits. *Géotechnique* 53(7):669–672
- Wong KS, Duncan JM (1974) Hyperbolic stress-strain parameters for nonlinear finite element analyses of stresses and movements in soil masses. University of California, Berkeley
- Wright SG (2005) Evaluation of soil shear strengths for slope and retaining wall stability analyses with emphasis on high plasticity clays. Report No. FHWA/TC-06/5-1874-01-1, Federal Highway Administration



2020 Kyoto Japan

Oso Landslide: Failure Mechanism and Runout Analyses

Timothy D. Stark and Zhengdan Xu

Abstract

This paper describes and explains the large mobility of the 2014 Oso Landslide, which caused significant fatal consequences. This landslide occurred in two phases, characterized by significantly different material behaviour, strengths, and runout. A portion of the first phase underwent significant undrained strength loss (liquefaction) and travelled over 1.7 km over a nearly horizontal valley surface and devastated a residential community. The second phase underwent brittle failure with much less strength loss and runout than the first phase. The first phase slide mass is composed of insensitive, overconsolidated glaciolacustrine silt and clay, material not traditionally recognized as susceptible to a large undrained strength loss or liquefaction. A new rheology, appropriate for liquefied overconsolidated glaciolacustrine silt and clay, is presented and used in the runout analyses. The large runout occurred in two directions, which allows various runout models to be compared. Three numerical runout models were used to investigate their applicability to similar landslide configurations and future hazard and risk assessments. These runout analyses show the importance of: (1) using a digital terrain model in the runout analysis, (2) modeling field representative shear strength properties and failure mechanisms, and (3) predicting runout distance, splash height, and duration for risk assessments and to improve public safety for this and other slopes.

Keywords

Landslide • Runout analysis • Failure mechanism • Stability analyses • Colluvium • Shear strength • Undrained strength loss • LiDAR

Landslide Overview

On 22 March 2014 a large and fast moving landslide destroyed the Steelhead Haven Community near Oso, Washington along the North Fork of the Stillaguamish River in Snohomish County. This landslide is considered the deadliest in the history of the continental U.S. with 43 fatalities (Wartman et al. 2016). The entire landslide involved approximately 8.3 million cubic meters of glacial deposits and water filled colluvium from prior landslides present along the slope toe. The colluvium-derived flowslide travelled more than 1.7 km to its distal edge on the south side of SR530 that connects Oso and Darrington, Washington. During various site visits (May 22 through 24, 2014; February 28, 2015; April 16, 2015), the first author examined various landslide features and exposed geology, obtained soil samples for laboratory testing to estimate engineering properties, reviewed aerial photographs, and conducted stability analyses to assess the impact of changes in slope geometry with time. This paper summarizes the material properties measured during the investigation, the resulting two phase failure mechanism, and accompanying runout analyses.

T. D. Stark (✉)

Dept. of Civil Engineering, University of Illinois At Urbana-Champaign, 205 N. Mathews Ave, Urbana, IL 60801, USA

e-mail: tstark@illinois.edu

Z. Xu

Hong Kong University of Science and Technology, Hong Kong, China

e-mail: zxubv@connect.ust.hk

Subsurface Conditions

The crest of the Oso landslide slope is located at an elevation of approximately 270 m on the north side of the west-trending valley of the Stillaguamish River, which is around elevation 75 m. This corresponds to a slope height of

about 200 m. The width of the Stillaguamish River Valley floor at this location varies from 2.0 km to more than 6.0 km. This slope is part of a large overconsolidated glacial terrace deposit that developed after the last advance of continental glacial ice sheets into the Puget Sound. The 2014 landslide occurred at a relatively narrow reach of the river, where it flows north and then west along the slope toe. The river erosion, especially at the eastern end, has caused a number of landslides in the lower portion of the slope including landslides in 1937, 1951, 1952, 1967, 1988, and 2006, (see 2006 landslide in Fig. 1).

Knowledge of the pre-2014 landslide subsurface conditions is important for understanding the failure mechanism, because a comparison of the initial and final locations of the various glacial soil deposits aided the understanding of landslide initiation, movement, number of phases, and run-out. Based on the exposed landslide headscarp, hand and shovel excavations during various site visits, geologic maps, borings before (Shannon and Associates 1952) and after the landslide (Badger and D'Ignazio 2015), and soil samples collected and tested herein, the subsurface profile prior to the 2014 landslide is shown in Fig. 2 and is located at the cross-section location shown in Fig. 1.

The slope subsurface profile consists of (from top to bottom):

- **Recessional Outwash:** tan to light brown unsaturated cohesionless fluvial deposits, medium dense to dense fine to coarse sands with cross-beddings. The thickness of this outwash is about 40 m from elevation 270 to 230 m. The top of this deposit is referred to locally as the Upper Plateau or Whitman Bench (see Fig. 2).
- **Glacial Till:** light grey unsaturated, stiff to very stiff, overconsolidated, and unsorted mixtures of clay, silt,

sand, and gravels with scattered cobbles and boulders. The thickness of this layer is approximately 23 m from elevation 230 to 207 m.

- **Advanced Outwash:** tan to light brown unsaturated fluvial medium dense coarse sand and sandy gravel with localized clay and silt interbeds. The Advanced Outwash thickness is approximately 30 m from elevation 207 to 177 m.
- **Advanced Glacio-Lacustrine:** light to dark grey, medium stiff to stiff, unsaturated to saturated with horizontally laminated low to high plasticity clays and silts with occasional fine sands laminae. The thickness of this layer is approximately 82 m, from elevation 177 to 95 m, and was also involved in most, if not all, of the prior low elevation landslides caused by river erosion along the slope toe. The unsaturated condition of the Advanced Glacio-Lacustrine deposit is evident in surficial exposures and in available borings.
- **Sands and Gravels:** well sorted fine to medium grained sands and gravel with possible artesian pressures.
- **Fluvial deposits/colluvium:** oxidized deposits of loose saturated sands and silts forming the river floodplain, mixed with debris from prior landslides exposed near base of slope, and is youngest deposit and not part of stratigraphic sequence.

Prior Landslide History

The 2014 landslide occurred in a slope with a history of prior landslides. Modern accounts of landslides in the lower portion of the slope date back to 1932 (Thorsen 1969). More recent high resolution topographic relief images generated by LiDAR (Light Detection and Ranging) show many large prehistoric landslides including one at the location of the 2014 landslide have occurred in this valley (see Fig. 3).

The documented history of landsliding at this site reveals two types of event: (1) large prehistoric landslides that involve the upper glacial terrace deposits, i.e., the Whitman Bench (see Figs. 2 and 3), which are similar to the 2014 landslide, and (2) smaller landslides in the lower portion of the slope between 1932 and 2014 were primarily caused by river erosion. Landslides involving the Whitman Bench exhibit significantly greater runout because of the greater elevation and potential energy of the source material than the low elevation landslides.

The occurrence of a large prehistoric landslide at the location of the 2014 landslide is important because it created the Ancient Landslide Bench shown in Fig. 3 that supported and protected the Whitman Bench from landslides primarily caused by river toe erosion and precipitation. Based on the geometry of neighboring high elevation landslides also

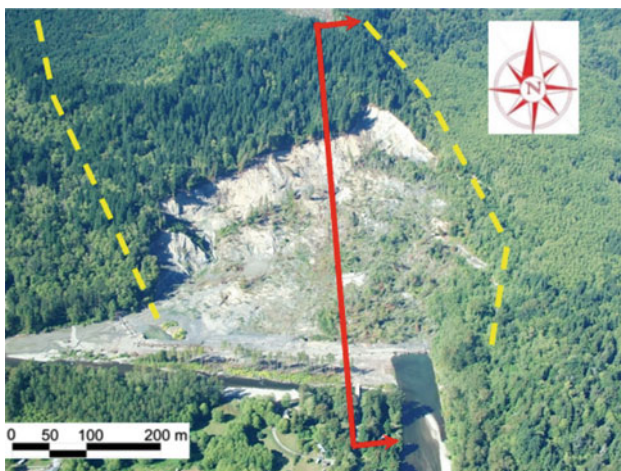


Fig. 1 Aerial view of 2006 landslide, location of cross-section in Fig. 2 (solid line), and outline of sides of 2014 landslide (dashed lines) (image courtesy of Rupert G. Tart)

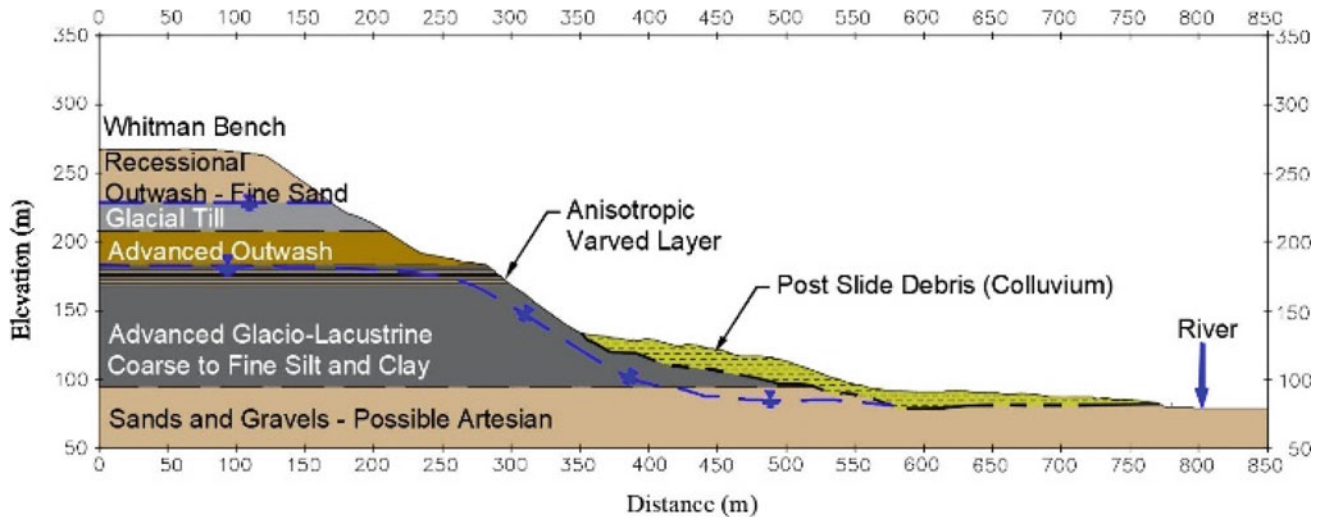


Fig. 2 Slope cross-section at location shown in Fig. 1 prior to 2014 landslide with phreatic surfaces inferred from inverse stability analyses except where observed in borings drilled from the Whitman Bench or in the slide mass

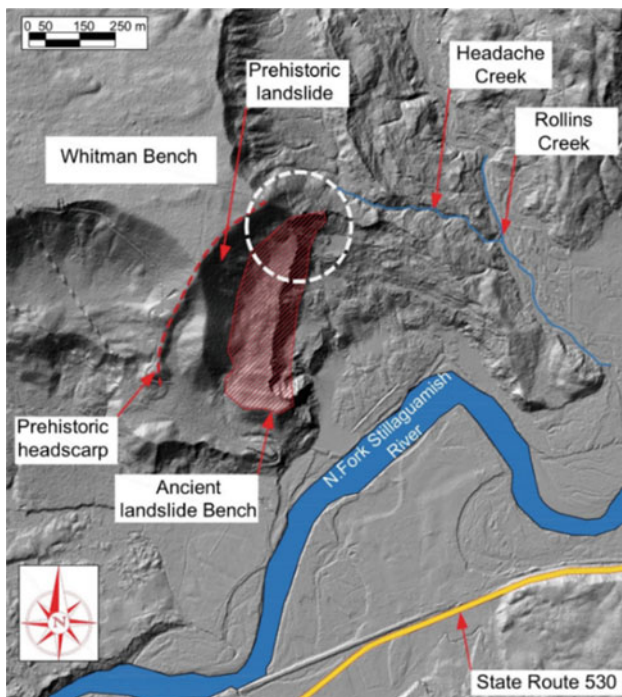


Fig. 3 2013 LiDAR-derived topography showing the Oso landslide in context with the Ancient Landslide Bench (see shaded area) (base courtesy of Puget Sound Lidar Consortium)

shown in Fig. 3, it is anticipated that the ancient landslide at this location occurred through the weak varved lacustrine layers in the upper portion of the Advanced Glacio-Lacustrine deposit and evacuated some of the overlying Whitman Bench. After this landslide, a bench or ledge was created that supported the overlying Whitman Bench slope and protected the Whitman Bench from oversteepening by landslides in the lower portion of the slope until after 2006.

The ancient slide mass travelled down the slope and across the Stillaguamish River, where it was eroded over geologic time. This is easy to visualize because the ancient slide mass consisted primarily of two unsaturated sandy outwash deposits that are quickly eroded by the river as witnessed after the 2014 landslide. During a site visit only two months after the 2014 landslide, a significant amount of these sandy outwash deposits had already been eroded by the Stillaguamish River (see Fig. 3) and exposed the underlying Advanced Glacio-Lacustrine clays. This explains the lack of a significant portion of the ancient slide mass being present on the valley floor prior to the 2006 and 2014 landslides.

Using aerial photographs of the 1937, 1951, 1952, 1967, 1988, and 2006 landslides assembled by the Seattle Times (<https://projects.seattletimes.com/2014/building-toward-disaster/>), Kim et al. (2015) and Sun et al. (2015) show only the lower portion of the slope and the Advanced Glacio-Lacustrine Clay deposits were involved. These low elevation landslides removed some of the Ancient Landslide Bench but there was still sufficient width of the bench to support the overlying Whitman Bench until after the 2006 landslide. The slide masses from these lower elevation landslides accumulated along the slope toe or advanced only 85 m in the 1947 slide, 200 m in the 1967 slide, and 250 m in the 2006 slide from the slope toe, respectively, based on aerial photographs because of their low elevation, low potential energy, and lack of significant strength loss. Nevertheless, in each of these low elevation landslides the slide mass would move the active river channel to the south away from the slope toe. The river would then start eroding the prior landslide debris to the north until it was again undermining the Advanced Glacio-Lacustrine Clays again. Based on the dates of prior landslides and aerial photographs, it

took about 35 to 40 years for the river to erode enough landslide debris/colluvium to initiate another landslide in the lower portion of the slope. Each of these landslides would remove some of the Ancient Landslide Bench especially on the eastern end where the river flowed almost north directly into the slope (see Fig. 3). This timing of 35 to 40 years is important because only eight years elapsed between the 2006 landslide and the large 2014 landslide, not 35 to 40 years, so a different failure mechanism had to be involved in the 2014 landslide.

2014 Landslide

The 2014 landslide is significantly different than the 1937, 1951, 1952, 1967, 1988, and 2006 landslides in the following four main aspects:

- (1) River erosion did not play a significant role because the river channel had been pushed significantly south of the slope toe by the 2006 landslide,
- (2) 2014 landslide occurred only eight years after the 2006 landslide not 35 to 40 years,
- (3) Slide mobility was much greater, resulting in the slide mass travelling more than 1.7 km in comparison to 85 m, 200 m, and 250 m in the 1947, 1967, and 2006 landslides, respectively.
- (4) 2014 slide mass is much larger than the 1937, 1951, 1952, 1967, 1988, and 2006 slide masses.

As a result, a different failure mechanism than river toe erosion had to initiate the 2014 landslide. The first factor considered for the 2014 landslide is precipitation. The 2014 landslide occurred during a dry sunny morning after a period of unusually intense rainfall. Nearby precipitation gauges with 86 years of data indicate that the rainfall during the twenty-one days (March 1 through 21) preceding the landslide was significantly greater than average (Keaton et al. 2014). In particular, these data show the 45-day period before the landslide was wetter than 98% of the same 45-day period in the 86-year historical record (Iverson et al. 2015). Cao et al. (2014) and Henn et al. (2015) show that the cumulative precipitation for the 21 days prior to the 22 March 2014 landslide corresponds to a return period of about 97 years making the 21 days prior to the landslide the wettest (403 mm of rainfall) on record at the Darrington, Washington rain gauge. It is anticipated that this intense rainfall, higher groundwater, and increased runoff along the eastern side of the 2014 landslide mass triggered a landslide that removed the small remaining portion of the Ancient Landslide Bench on the eastern end (see dashed circle in Fig. 3), and undermined the Whitman Bench discussed

below. This resulted in initiation of the 2014 two-phase failure mechanism described below.

Even with a record rainfall in March 2014, the Oso landslide is the only large landslide in the valley and region so this site had a unique feature, i.e., an oversteepened and/or undermined Ancient Landslide Bench on the eastern end. LiDAR images show no other ancient landslide bench in this area was oversteepened and/or undermined to the extent the eastern bench was in Fig. 3.

Phase I Slide Mass

Based on inverse 2D limit equilibrium stability analyses using the software packages SLIDE and SLOPE/W and the soil properties in Stark et al. (2017) that are reproduced in Table 1, Fig. 5 shows the probable failure surface for the initial instability that triggered the first phase (Phase I) of the 2014 two-phase failure mechanism. Table 1 shows the measured drained fully softened and residual strength envelopes for the fine-grained deposits. These strength envelopes are stress-dependent and Table 1 presents the range of effective stress friction angle from low to high normal stress.

The Phase I instability initiated in the eastern portion of the Ancient Landslide Bench slope (see Fig. 3) where the bench had been oversteepened by prior sliding in the lower portion of the slope. The failure surface in Fig. 5 is based on field observations and inverse stability analyses that yielded a factor of safety of about unity (1.0) for a variety of compound failure surfaces and piezometric levels estimated from the inverse analysis of the 2006 landslide.

Compound slip surfaces were primarily considered because of the observed internal distortion of the slide volume during each of the two phases and the differing soil types in the upper portion of the slope, i.e., outwash sands, glacial till, and varved silts and clays in the Advanced Glacio-Lacustrine deposit that contain weak horizontal layers as discussed above. Circular failure surfaces are only applicable to homogeneous soil deposits. However, a circular search also was conducted, which confirmed the critical failure surface is a compound slip surface.

Colluvial Flowslide of Phase I

The important aspect of the Phase I initial slide mass is that it quickly impacted the water filled, softened, and disturbed colluvium that had accumulated along the lower portion of the slope during prior river induced landslides. At the western end of the slope, a 0.9 to 1.2 km² sedimentation pond with a depth of about 4.6 m had been constructed in

Table 1 Input parameters for 2D limit equilibrium slope stability analyses

Description of geologic deposit	Total and saturated unit weights (kN/m ³)	Estimated peak and measured fully softened effective stress friction angles	Measured residual effective stress friction angle
Recessional outwash	20.0	28 ⁰	N/A
glacial till	20.0	35 ⁰	N/A
Advanced outwash	19.0	30 ⁰	N/A
Low plasticity advanced glacio-lacustrine	20.0	34 ⁰ to 25 ⁰	27 ⁰ to 20 ⁰
High plasticity advanced glacio-lacustrine	20.0	32 ⁰ to 21 ⁰	19 ⁰ to 12 ⁰
Sands and gravels	19.0	35 ⁰	N/A
Prior slide debris (Colluvium)	16.5	32 ⁰ to 21 ⁰	19 ⁰ to 12 ⁰

the colluvium after the 2006 landslide to reduce the amount of sediment entering the river due to precipitation, emergent stream(s) and seepage from the slope, and river flooding. Therefore, the colluvium had an abundance of water between the blocks of overconsolidated clay and within the loose matrix of disturbed colluvium filling these interstices. Many of the “intact” clay blocks were likely also at or near saturation. All of this helped produce a fluid or liquefied behavior after it was impacted by the Phase I slide mass, which is described below. The Phase I slide mass was moving rapidly downslope during its descent of about 150 m when it impacted the colluvium causing a large undrained strength loss, which allowed the colluvium to flow across the river and valley. The large undrained strength loss was evident by the runout of over 1.7 km and trees from the upper plateau still being vertical halfway across the valley.

With the large and rapid impact force from the Phase I initial slide mass, the blocky, softened, and water filled colluvium disintegrated into a fluid with the soil particles becoming suspended in a fluid matrix causing a flowslide using the classifications in Hungr et al. (2014). The fluid colluvium then flowed quickly across the valley like a flowslide ahead of the main Phase I slide mass. The rapidity of the flowslide is evident by the burial of vehicles traveling along SR530 near the middle of the valley. Without the large and rapid push of the Phase I initial slide mass, the colluvium would not have undergone this large undrained strength loss because similar colluvium was present prior to the low elevation landslides in 1937, 1951, 1952, 1967, 1988, and 2006 and these slide masses did not flow past the river and across the valley. Therefore, the large-scale and significant undrained strength loss of the colluvial mass

appears to be contingent on a sufficiently large and energetic impulse from above, which was delivered by the Phase I slide mass from the Whitman Bench in 2014 (see Fig. 5).

The fluidized material incorporated water ponded along the slope toe, about 400 mm of rainfall in the twenty-one days before the slide, and water that had infiltrated the 2006 landslide derived colluvium. This allowed the colluvial mass to lose significant strength and flow across the river and entraining further quantities of water filled colluvium and river alluvium. This is a similar mechanism proposed by Sassa (1985) for shallow landslides surcharging downslope loose granular soil so rapidly as to cause “impact liquefaction” a process which Sassa (2000) later duplicated in an undrained torsional ring shear apparatus.

Figure 6 shows rafted blocks of unsaturated outwash sands and glacial till from the Whitman Bench traveled to near the alignment of SR530. Conversely, the liquefied colluvium flowed over SR530 and continued for another 0.5 km on the west side of the hill shown in Fig. 6.

Some of the field observations that confirm the fluid nature of the colluvium are piles of rafted outwash sand and overconsolidated glacial till from the Whitman Bench near SR530 and some still upright trees that were carried on top of the rafted sand blocks from top of the slope to south of the river (see Fig. 7). The fluidized colluvium moved farther than the outwash sands from the Whitman Bench (Phase 1), which was riding or rafting along on some of the fluidized colluvium. The rheology of the disturbed colluvium (fluid like) was clearly different from the rheology of the initial Phase I slide mass, which involved unsaturated overconsolidated materials, e.g., outwash sands and glacial till, and remained frictional instead of exhibiting fluid/liquefied behavior.

Phase II Slide Mass

The mobility of the colluvium and Phase I initial slide mass caused unbuttressing of the upper slope, which initiated a retrogression into the intact material of the Whitman Bench. Based on inverse limit equilibrium stability analyses, Fig. 5 shows the probable compound failure surface for the Phase II slide mass that primarily involved the upper portion of the slope. The Phase II slide mass involves unsaturated and intact outwash sands, glacial till, and the upper portion of the Advanced Glacio-Lacustrine clay deposit. The unsaturated portions of the outwash sands and glacial till deposits exhibited frictional behavior which resulted in the formation of large landslide blocks instead of a flowslide as observed in the colluvium. As a result, the Phase II slide mass was much less mobile and is not responsible for any of the property damage or loss of life in the valley. The top of this slide mass forms the new landslide bench (see Fig. 6) that will protect the overlying Whitman Bench for many years to come because the river cannot directly erode this bench or the Upper Plateau due to the lower portion of the Phase II slide mass covering the lower portion of the slope.

Figure 7 shows an aerial photograph of the slope in July 2013, the location of the 2006 headscarp, and the extent of the Phase 1 and 2 slide masses in 2014. The Phase II slide mass primarily involves the Whitman Bench while the Phase 1 slide mass involves part of the Whitman Bench and the slope below the 2006 headscarp. The Phase II slide mass also involves the mature trees that were located on the Whitman Bench prior to the 2014 landslide and are now on the new landslide bench shown in Fig. 6.

Aerial photographs show the Whitman Bench slope remained stable for over one hundred years and LiDAR images of adjacent slopes show similar slopes have remained stable for much longer. However, landslides involving the lower portion of the slope will continue to occur as the river erodes the 2014 landslide debris and undermines portions of the new and still tree-covered landslide bench (see arrow in Fig. 6) but these lower elevation slides will not directly impact the Whitman Bench. Based on river migration and erosion rates calculated for the 1937, 1951, 1952, 1967, 1988, and 2006 landslides, it will take at least 300 years to remove enough of the Phase II slide mass and landslide bench to oversteepen and/or undermine the Whitman Bench sufficiently to cause another large landslide that moves past the river and across the valley as in 2014. This time estimate is based on aerial photographs from 1937, 1951, 1952, 1967, 1988, and 2006 that identified the location of the river at each time so the rate of migration could be estimated using the time between each photograph. As a result, studying the effect of the river on the new landslide bench using LiDAR

images, as shown in Fig. 4, is important to evaluate the landslide hazard and risk with time as discussed below.

Figure 6 shows the Phase II slide mass stretched or spread out as it moved down the slope but did not become highly mobile like the colluvial flowslide. The runout of the Phase II slide mass was limited, because it was mainly frictional and its leading edge collided with the back edge of the Phase I slide mass. On the western end, the Phase II slide mass actually over-rode the northern edge of the Phase I slide mass because some Advanced Glacio-Lacustrine Clay from the Phase II slide mass was found overlying the trees and outwash sands of the Phase I slide mass (see dashed circle in Fig. 6).

Seismic Records

The two-phase failure mechanism described above is also in agreement with nearby seismograph recordings that show two distinct ground motions separated by about two minutes. Figure 8a shows the various ground motion recording stations near the 2014 Oso Landslide. The recording stations designated as JCW, B05A, and CMW are located at distances of approximately 10, 17, and 22 km, respectively, from the 2014 landslide. Figure 8b presents the ground motions from recording station JCW (Jim Creek Wilderness Station at: 48°12'13"N 121°55'00"W). Figure 8b show two distinct ground motions with durations of 96 and 70 s separated by about two minutes.

The first ground motion recording started at 10:37.30 on 22 March 2014 and ended at 10:40.00 while the second motion started at 10:42.00 and lasted only 1.5 min. Hibert et al. (2014) conclude that these ground motions correspond to two separate landslide events (Phase I and II) with the



Fig. 4 Erosion of sandy outwash deposits by Stillaguamish River two months after landslide

Fig. 5 Two-phase failure mechanism prior to 2014 landslide with the Phase I failure surface based on field observations and inverse slope stability analyses at cross-section location shown in Fig. 1

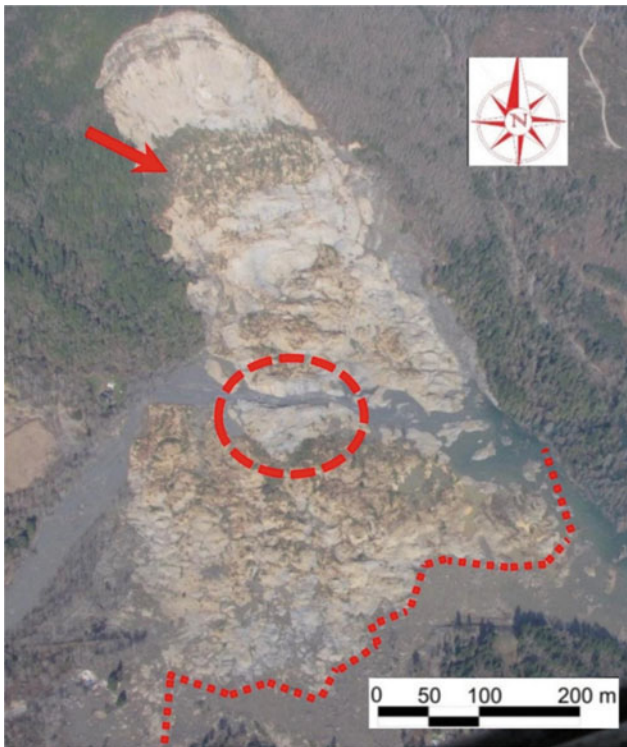
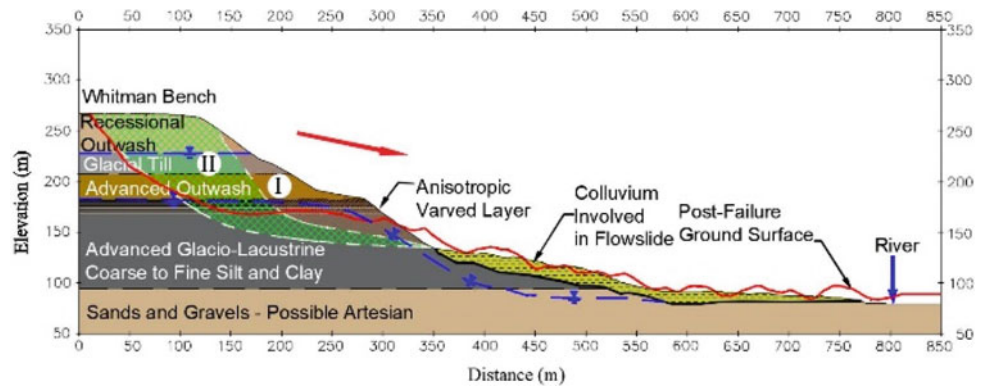


Fig. 6 Aerial view and extent of sand (dashed line) pushing and over-riding fluidized colluvium from slope toe, a new landslide bench (see arrow), and the Phase II slide mass overriding the back end of Phase I slide mass (dashed circle) (image courtesy Rupert G. Tart)

events having different characteristics and runouts. The first ground motion is indicative of a large landslide mass with a velocity and acceleration of 19.4 m/s and 1.0 m/s², respectively (Hibert et al. 2014). This first motion is larger than the second motion and caused the colluvial flowslide. The second ground motion is more impulsive and indicative of a complex breakaway sequence that merged into one landslide (Hibert et al. 2014), which is in agreement with the retrogressive nature of the Phase II slide mass. Because of the fluid nature of the colluvial flowslide, a separate ground motion was not detected for this movement.

Figure 5 illustrates the large slope movements involved in the two-phase failure mechanism, which was initially described in a 1 June 2015 Seattle Times newspaper article (Doughton 2015). The Phase I slide mass moved first with significant speed and momentum, as described by an eyewitness (described below), and impacted the water-filled colluvium that had accumulated along the lower part of the slope. The Phase I slide mass pushed some of the water filled colluvium in front of it across the river, the valley, the unexpected neighborhood, SR530 highway, and beyond. The steep valley slope then remained unsupported and some two minutes later the Phase II slide mass slid down the evacuated slope but did not move far because the materials were primarily unsaturated, dense, and frictional so it stopped at the back edge of the Phase I slide mass.

Unlike other large flow landslides, e.g., La Conchita in 2005, videos of the slide are not available so the proposed failure mechanism may not represent all aspects of the failure mechanism. For example, the geometry of the Phase I slide mass is subjective because the slide mass and scarp were removed. The Phase I slide mass geometry was estimated using results of inverse analyses of the 1967 and 2006 landslides to estimate groundwater and shear strength conditions that were used to predict the 2014 critical compound failure surface shown in Fig. 5.

Runout Analyses

The two-phase failure mechanism shown in Fig. 5. is used below to conduct runout analyses and assess the accuracy of existing runout models. This is important because the failure mechanism is the first and most important input parameter for a runout analysis. If the failure mechanism is incorrect, the runout analysis will not accurately predict the slide mass runout because the kinematics of the slide movement will not be correct.

As a result, the failure mechanism proposed by Stark et al. (2017) is used in the runout numerical models DAN3D,



(a)



(b)



(c)

Fig. 7 Photographs showing: **a** recession outwash sands and near vertical trees stopped north of SR530, **b** disturbed colluvium in foreground, blocks of outwash sand with trees in valley, and new landslide bench and scarp in background, and **c** nearly vertical tree from upper plateau in Phase I just south of override zone of Phase II

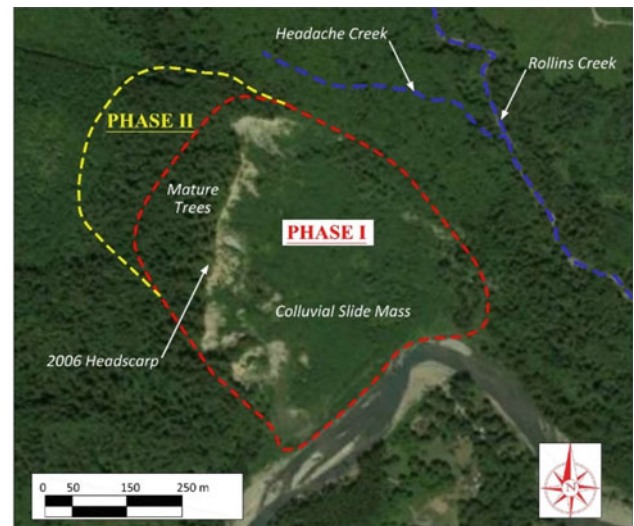
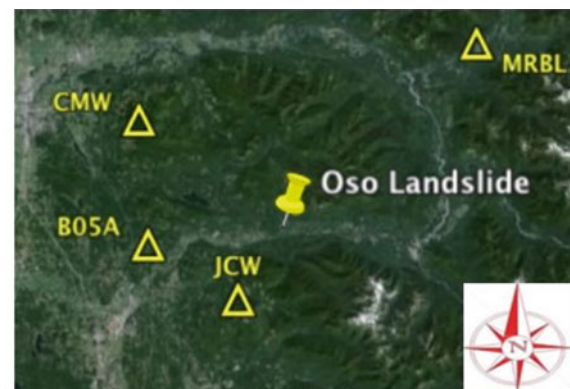
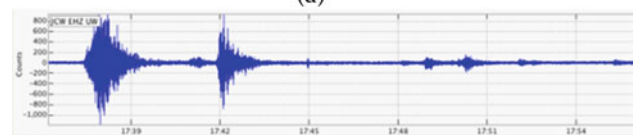


Fig. 8 Aerial view of slope in July 2013 and outline of the 2014 Phase I and II slide masses ((c) 2014 Google)



(a)



(b)

Fig. 9 **a** Aerial photograph from Google Earth showing proximity seismic recording stations to Oso Landslide and **b** ground motions from recording station JCW from Pacific Northwest Seismograph Network

Anura3D, and FLO-2D and the results are compared to field observations made between 22 and 24 May 2014, or about two months after the landslide, by the first author (see Figs. 4 and 7). In particular, the runout results are compared to field observations of the final shape, distance, splash heights, consistency, shear strength, and depth of the slide mass, post-event topography, and ground motions recorded during the two-phase landslide to assess the accuracy of the analyses.

Liquefied Shear Strength

Another important input for the runout analyses is the value of liquefied strength used to model the disturbed water-filled colluvium after being impacted by the Phase I slide mass. This section describes how the liquefied strength was estimated and the value selected for the runout analyses reported herein.

Given field observations of the flow characteristics of the water-filled colluvium (see Fig. 11), the colluvium was modeled using the empirical liquefied strength ratio correlation (Stark and Mesri 1992 and Olson and Stark 2002) developed from earthquake-induced liquefaction flow slides involving contractive granular materials. The field liquefaction case histories analyzed by Stark and Mesri (1992) have an effective overburden stress at the middle of the liquefiable layer that ranges from 0.4 to 5.4 kg/cm² with an average and standard deviation of 1.2 kg/cm² and 1.1 kg/cm². These liquefaction case histories exhibit a range of liquefied strength of 0.02 to 0.33 kg/cm² with an average of 0.11 kg/cm², which is used below for the runout analyses. The liquefied strength applied in the liquefied rheology model was estimated using the following relationship from Stark and Mesri (1992) and Olson and Stark (2002):

$$s_l = 0.033 \text{ to } 0.075 \times (\sigma_v - u) \quad (1)$$

where s_l = liquefied shear strength; σ_v = prefailure total vertical stress; and u = prefailure pore-water pressure. The liquefied strength ratio $s_l/(\sigma_v - u)$, of 0.07 was estimated using a normalized penetration resistance of six as discussed below.

Because the blow count for the heterogeneous water-filled colluvium that flowed past SR530 was not known prior to the 2014 landslide, a representative value was estimated based on field observations by the first author. This resulted in a normalized blowcount of six (6) with the blowcount normalized to an effective vertical stress of 1 kg/cm² (1 tsf) and a standard penetration test energy efficiency of 60%. This resulting value of $(N_1)_{60}$ is six (6) and was used to estimate the liquefied strength ratio of 0.07 from the empirical relationship in Eq. (3) of Olson and Stark (2002).

The liquefied strength ratio of 0.07 was selected for a trial flow analysis, which yielded good agreement with field observations and was not varied in subsequent DAN3D runout analyses even though lowering this ratio may have produced better agreement between the calculated and observed runout on the west side of the slide mass and Engineer Hill as shown below. In fact, the liquefied strength ratio could have been varied from about 0.033 to 0.075 as discussed above to improve the agreement with field observations but was not to evaluate the runout models.

The use of a liquefied strength ratio from earthquake-induced flow slides was first proposed by Oldrich Hungr for a presentation on the 2014 Oso Landslide to the Vancouver Geotechnical Society in Vancouver, British Columbia on 15 April 2015 (Hungr, 2015) with the first author. This is a creative feature of the dynamic analysis presented in Aaron et al. (2017) because this empirical method was developed by Stark and Mesri (1992) for static and seismic flow failures involving saturated, loose granular soils not overconsolidated glacial silts, clays, and till.

The basal resistance used with the liquefied rheology described above does not have an explicit dependence on shear rate, i.e., it is a constant and purely plastic strength. However, the inverse analyses performed by Olson and Stark (2002) includes flow and momentum effects on the liquefied strength. As a result, the expression in Eq. (3) indirectly includes the effects of viscosity and shear rate in the empirical relationship.

DAN3D Results

DAN3D is a depth-averaged numerical solution of the equations of motion in 2D developed by McDougall (2006) and Hungr and McDougall (2009). Depth-averaged means the governing mass and momentum balance equations are integrated and averaged with respect to the depth of predicted flow. The depth-averaged solution, when assuming shallow depth of flow, eliminates the depth-wise dimension (neglecting any shear stress in the depth direction). Thus, the 2D solution corresponds to the model that simulates the motion across a 3D terrain (McDougall 2006). The equations of motion are solved by the smooth particle hydrodynamics solution method (Monaghan 1992).

Additional details of the DAN3D analysis of the 2014 Oso Landslide are described in Aaron et al. (2017). The 2014 Oso Landslide was modeled as two separate events during the DAN3D (Hungr and McDougall 2009) simulation. These two events refer to the movement of the Phase I and Phase II slide masses, respectively, identified by Stark et al. (2017), which is shown in Fig. 5. The DAN3D results show that the Phase I slide mass traveled a long distance and was stopped by Engineer Hill near the center of the runout zone. This protruding area (see “EH” in Fig. 10) consists of slide debris from a historic landslide that initiated on the south side of the valley and moved northward over part of the valley.

The DAN3D Phase I results show good agreement with field observations on the east side of Engineer Hill (EH) but the western portion of the runout zone exhibits a shorter runout than observed. The Phase II slide mass was much less mobile due to its frictional behavior and only moved a short

distance past or south of the Stillguamish River. This runout distance is in agreement with field observations because the downslope end of the Phase II slide mass impacted with the rear of the Phase I slide mass creating an override zone just south of the river (see Fig. 6) and described below.

Figure 6 presents an aerial photograph that shows the Phase II override zone (see dashed red lines) where some of the grey glaciolacustrine silts and clays overrode the trees and recessional outwash sands from the upper plateau or Whitman Bench in Phase I. The DAN3D simulation extends a little past the override zone on the west side but is in good agreement on the east side of the Phase II slide mass. As a result, DAN3D can effectively model the two extremes of slide mass rheology, i.e., fluid flow and frictional, in the runout analysis of the 2014 Oso Landslide. However, DAN3D is not presently commercially available due to the passing of Oldrich Hungr.

ANURA3D Results

This section discusses runout analyses for the 2014 Oso Landslide performed using the Material Point Method (MPM), which is applied generally for the simulation of materials that undergo large and time-dependent deformations (Sulsky et al. 1994). The governing equations are standard mass and momentum conservations in the MPM.

The MPM uses a combination of the Lagrangian and Eulerian descriptions of continuum materials. In an MPM analysis, the materials are represented by a collection of disconnected points and a background computational mesh where the points can move throughout the mesh and carry the material properties assigned from point to point. This information is transferred to the nodes of the mesh, where

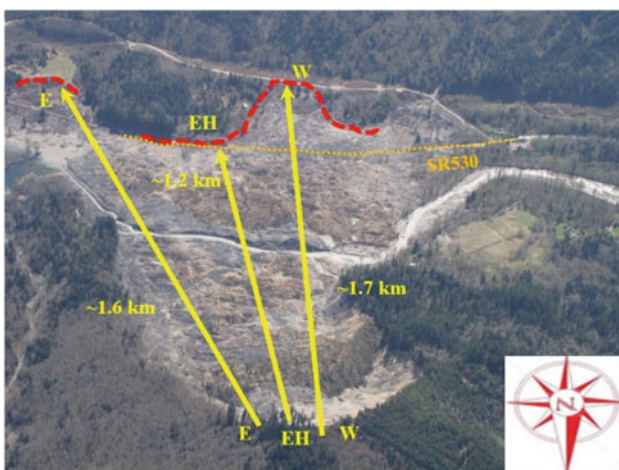


Fig. 10 Aerial view after 2014 landslide showing: observed boundaries of runout (see red dash lines) and travel distances (see yellow solid lines) on both east and west side of Engineer Hill (EH) (image courtesy of Rupert G. Tart and dated 24 March 2014; IMG_5806.jpg)



Fig. 11 Photograph showing Phase I intact grey glaciolacustrine silts and clays and recessional outwash sands behind fluidized colluvium north of SR530

the linear momentum balance equation is solved. The mesh solution then is mapped back to update the information of the material points (Bandara et al. 2016; Bardenhagen et al. 2000).

The nodes of the computational mesh do not retain any data, which means that the mesh itself remains fixed during the analysis but the material points can move to different locations in the computational mesh during the analysis. The computational mesh also facilitates the definition of the analysis boundary conditions.

The MPM is incorporated in the Anura3D software package developed by the MPM research community (Yerro et al. 2018). This software package allows the analysis of displacements along a 2D cross-section of the slope and topography adjacent to the slope consisting of one or two-phase materials. Anura3D does not allow input of a digital terrain model to generate a plan-view of the slide mass runout like DAN3D but the runout can be calculated for each cross-section and plotted on a plan-view as shown below.

The use of a two-phase material model makes it possible to simulate the phase change from solid to fluid, e.g., soil to water, in a fully saturated material. However, only the water-filled colluvium along the slope toe was considered saturated and susceptible to a phase change because the other materials involved in the 2014 landslide are unsaturated, overconsolidated, and not susceptible to a phase change. Representative soil properties were used in Anura3D for the various materials involved to assess the accuracy of the model and not properties that provided the best agreement with field observations.

The stratigraphy, material properties, and two-phase failure mechanism used in the Anura3D model are illustrated in Fig. 12 and shown in Table 1. The residual strength

properties for Slip Zones 2 and 4 were measured using torsional ring shear tests while the other shear strength parameters were estimated.

In the Anura3D analysis, the fixity of the Phase I slide mass is released to initiate the slope movement and runout processes while the Phase II slide mass is kept fixed until runout of Phase I is complete. After the Phase I slide mass stops moving, the Phase II slide mass is then allowed to move by releasing its fixity. This results in the two distinct phases or slide movements being modeled and acting separately. This allows Anura3D to calculate the duration for Phases I and II, which can be compared to the ground motions recorded during the 2014 landslide to investigate the accuracy of the Anura3D model. In addition, the calculated runout distances, slide mass depths, and splash heights are compared with field observations to assess the accuracy of the Anura3D model below.

Anura3D allows the analysis of displacements only along a 2D cross-section not over a digital terrain model. As a result, the analysis conducted herein used three cross-sections to calculate the runout distance and behavior of the slide mass east and west of Engineer Hill and across Engineer Hill (see Fig. 8). Afterwards, the results from these three cross-section are compared to the runout observed at these locations to assess the accuracy of the MPM.

Figure 13 shows the simulation results at time steps of 0, 8, 24, 28, 80, and a total of 138 s, i.e., 80 s for Phase I and 58 s for Phase II, for the western cross-section shown in Figs. 10 and 12. The results illustrate that the Phase I slide mass moved down slope and started impacting the water-filled colluvium within eight seconds of the release of the Phase I slide mass in the model. At eight seconds, the now disturbed or impacted water-filled colluvium is assigned a liquefied strength and it is pushed across the river and flows as a near liquid across most of the valley. This flow behavior continues until 80 s of total elapsed time and the unsaturated materials near the top of the Phase I slide mass are able to travel about 1.2 km in this short period of time (80 s). A distance of 1.2 km is shorter than the observed final runout of the colluvium of about 1.7 km on the west side of Engineer Hill because the unsaturated material of the

upper slope did not travel as far as the water-filled colluvium. These numerical results are consistent with field observations that the intact glacial materials of the upper part of the slope stopped just north of the SR530 at $t_1 = 80$ s. Therefore, Anura3D reasonably predicts the runout of the unsaturated glacial materials as they were transported on the water-filled colluvium across part of the valley. This is significant because it suggests that Anura3D can simulate entrainment of slide material.

The cross-section after twenty-four seconds of slide movement shows a splash of colluvium occurring on the north side of the river, which decreases in height as it continues across the river. These results also match field observations of slide debris and tree damage occurring as high as 10 m in trees just on the southside of the river near the western edge of the slide mass. The field observations show a splash height of over 12 m west of the cross-section analyzed and west of the main direction of runout. As result, it is reasonable that the splash height observed is less than that calculated by Anura3D, which shows a splash height of about 30 m just past the river at a time of 28 s (see Fig. 13).

The splash height of 30 m estimated by Anura3D is more consistent with an eyewitness account by John Reed reported in the Seattle Times that estimated the splash height in the direction of runout of about 30 m:

... When it hit the water, it shot way up, way taller than the tallest trees,” Reed said. “Then I saw this big black wall—it must have been more than 100 feet (30 m) high—rise high above the (Steelhead Drive) neighborhood. The houses, in comparison, looked minuscule. It was unbelievable.... John Reed; (Seattle Times, 3/27/14, https://old.seattletimes.com/html/localnews/2023709258_mudslideedge1.xml.html).

After 80 s of slide movement, runout of the Phase I slide mass converges and essentially stops. It takes about 58 s after the stoppage of Phase I (80 s) for the Phase II slide mass to complete runout for a total runout time of about 138 s. Figure 13 shows at the end of the simulation, the maximum calculated runout on the western cross-section is about 1.5 km, which is in good agreement with field observations of about 1.7 km on the west side of Engineer Hill.

Movement of the Phase II slide mass after 58 s also includes the downslope portion overriding the rear of the Phase I slide mass. After 58 s, the new landslide bench is visible in the upper part of the slope (see Fig. 13 at $t_2 = 58$ s). All of these runout and slide behavior characteristics are consistent with field observations.

The cross-section and surface topography for the eastern cross-section are similar to the western cross-section (see Fig. 13 at t_1 at 0 s). As a result, the east cross-section is not presented herein before discussing the results in this paragraph. In the eastern cross-section, the Phase I slide mass also reached the river after about twenty-four seconds of

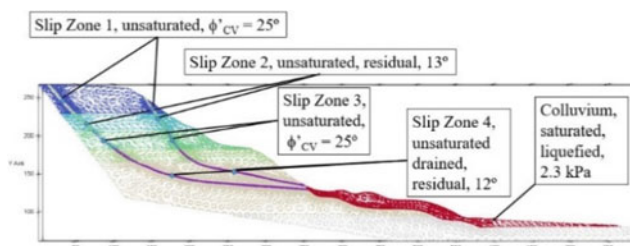


Fig. 12 Slope stratigraphy and failure surfaces for Anura3D runout model

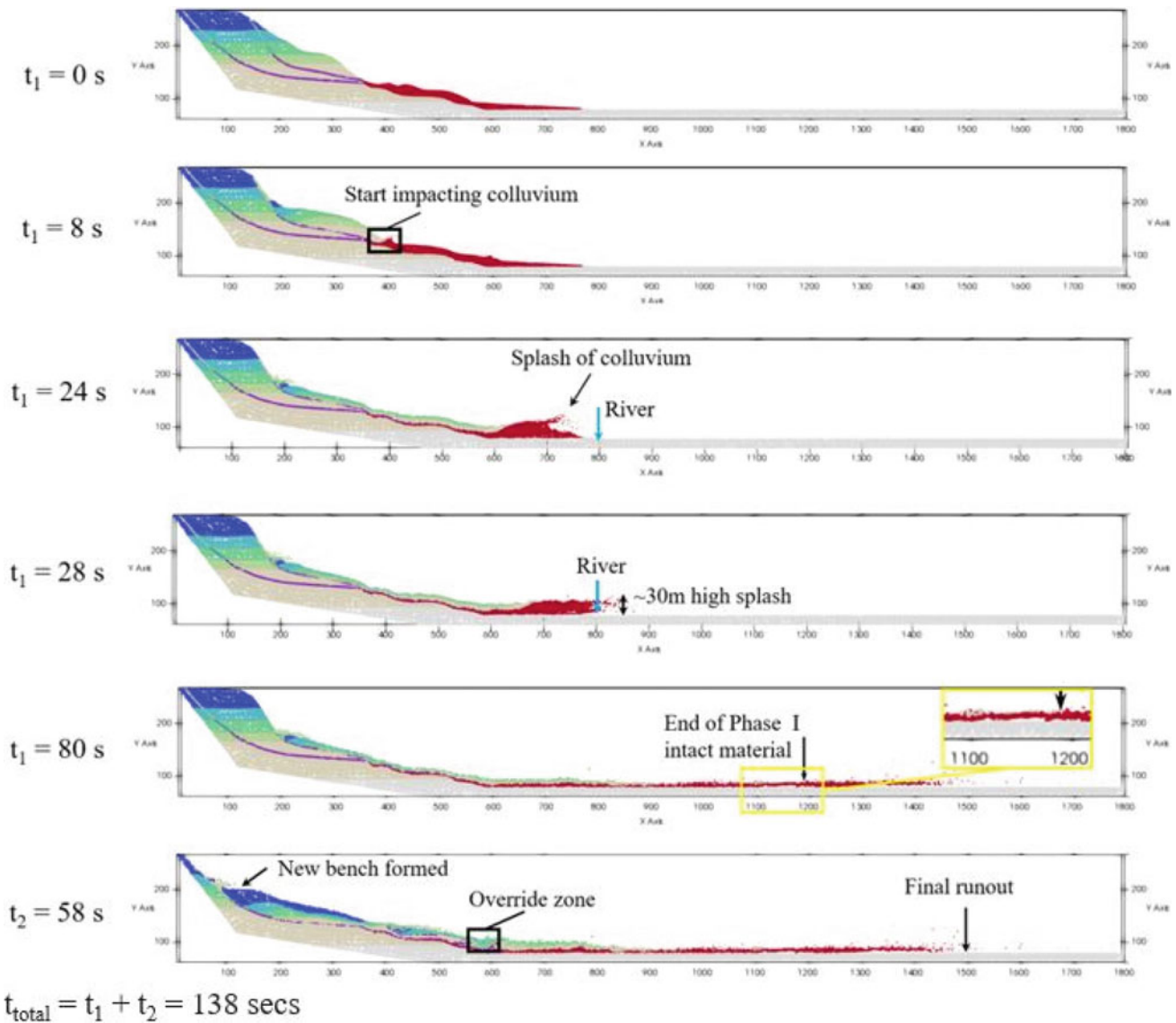


Fig. 13 Anura3D runout behaviors for west cross-section at time steps of: 0, 8, 24, 28, 80, and a total of 138 s in Phases I and II (80 + 58 s)

movement and splashes to a height of about 30 m on the east side of the slide mass. This calculated splash height of 30 m is comparable to that observed in trees along the eastern side of the slide mass given the height of the tree base above the evacuated area. The small calculated splash height of about 5 m along the eastern boundary of the slide mass near SR530 is also in agreement with field observations that show a similar splash height at this distance and a slide mass depth of only about 5 m. In summary, the Anura3D results for the eastern cross-section are in agreement with the observed splash heights and slide mass depths along the eastern cross-section.

Given the similarities between the east and west cross-sections and the topography south of the river prior to movement, the east cross-section also produced a runout of

about 1.5 km. This is also in excellent agreement with the observed runout on the east side of Engineer Hill. Coincidentally, DAN3D also provided excellent agreement with the observed runout on the east side of Engineer Hill. However, DAN3D did not provide a good runout prediction on the west side (too short) of Engineer Hill while Anura3D did provide good agreement on the west side. It is anticipated that the DAN3D analyses would have been in better agreement if the liquefied strength ratio was lowered but it was decided not to change the original ratio of 0.07 estimated by Professor Oldrich Hungr (Aaron et al. 2017). In summary, DAN3D and Anura3D provided good predictions of the observed runout with Anura3D giving better agreement on both the east and west sides and the top of Engineer Hill as discussed in the next paragraph. The results for the

cross-section that passes through Engineer Hill (see Fig. 10) are also interesting because a splash height was observed in some of the trees on top of Engineer Hill. The top of Engineer Hill is about 16 m above the SR530 pavement and there was slide debris on and damage to trees on top of Engineer Hill about 3 m above the ground surface. The force of the slide mass was evident by the presence of at least one vehicle being pushed to the top of Engineer Hill.

The Anura3D simulation results for the Engineer Hill cross-section show at a time step of 42 s the Phase I slide mass reach Engineer Hill and causes a splash of about 20 m. Given the top of Engineer Hill is about 16 m above the pavement of SR530, a total splash height of about 20 m is in agreement with observations of slide debris on and damage to trees at a height of about 3 m above pre-existing ground on top of Engineer Hill for a total splash height of about 19 m. This agreement between field observations and calculated runout reinforces the usefulness of the Anura3D analysis.

The final runout topography from Anura3D was compared with slide mass depths derived from subtracting the 2006 and 2014 LIDAR images. The two topographies compare well except for the upper portion of the slope, which indicates lower mobility of the Phase II slide mass than actually observed. Several factors may result in this Phase II difference, which include the ground motions that were recorded (see Fig. 9b) were not modeled in the Anura3D analysis, which can impact the kinematics of the flow failure, simplifications used to model the complex subsurface conditions involved in the 2014 landslide, and estimating the effective stress parameters for the outwash sand layers and glacial till at the top of the slope because these materials were not tested by Stark et al. (2017).

Another means to verify the accuracy of the Anura3D model and runout prediction is to compare the duration of the simulated Phase I and II runouts with the ground motions recorded during the 2014 landslide. For example, the ground motions recorded at station JCW during the 2014 Oso landslide on 22 March 2014 show the ground velocity time histories for the two phases of slope movement have durations of 96 and 70 s for Phases I and II, respectively, (see Fig. 8b). These two ground motions are separated by about 162 s of quiet or no significant ground motion. This quiet period cannot be modeled in Anura3D because the Phase II slide mass does not start moving until its fixity is removed by the user. The fixity can be removed after 162 s manually but it is not released by Anura3D to simulate the kinematics of the actual failure. The observed durations of slope movement of 96 and 70 s are a little greater than the Anura3D durations of 80 s for Phase I and 58 s for Phase II but these durations are in reasonable agreement.

In summary, Anura3D provided a good simulation of the runout behavior of the 2014 Oso Landslide, i.e., runout

distance, splash height, slide mass depth, and duration on the west side of Engineer Hill, using field representative input parameters. This bodes well for use of Anura3D to predict runout of other slopes along the Stillgumish River Valley.

FLO-2D Results

FLO-2D is a 2D finite difference model that simulates non-Newtonian floods and debris flows. FLO-2D was developed by O'Brien et al. (1993) and uses fluid behavior to predict runout behavior. The model adopts the continuity equation and 2D equations of motion to govern the constitutive behavior of a fluid. In a debris flow analysis, sediment-involved flows with high volumetric concentration are treated as homogeneous fluid based on Peng and Lu (2013). By inputting a digital elevation model to define the ground surface topography of the analysis area, the fluid flows along the terrain low spots and the range of runout can be predicted.

The following three factors dominate the behavior of the flowing materials in this rheology analysis: (i) yield stress, (ii) viscosity, and (iii) influence of turbulence and dispersion on flow. An expression of the total shear stress mobilized in the hyper-concentrated flow incorporating these three factors is given by the following equation from O'Brien and Julien (1988):

$$\tau = \tau_y + \eta \left(\frac{dv}{dy} \right) + C \left(\frac{dv}{dy} \right)^2 \quad (1)$$

where τ_y is the yield stress that is required to trigger the flow of the sediments, η is the viscosity of the sediment during flow, C is the inertial shear stress coefficient, and $\frac{dv}{dy}$ is the rate of shearing strain in flow. The sum of first two terms in Eq. (1) is the shear stress assumed in the Bingham plastic rheology model (Schamber and MacArthur, 1985; O'Brien, 1986), which introduces a linear stress-strain relationship. Normally Bingham fluid behavior applies to hyper-concentrated flow of clay and quartz particles in water under low shearing rates (Govier and Aziz, 1982).

The viscosity and yield stress in Eq. (7) are determined using the following empirical correlations:

$$\eta = \alpha_1 e^{\beta_1 C_v} \quad (2)$$

$$\tau_y = \alpha_2 e^{\beta_2 C_v} \quad (3)$$

where α_i and β_i are empirical coefficients and C_v is the sediment concentration by volume not mass. A rheology model that incorporates the three factors above, i.e., yield stress, viscosity, and turbulence and dispersion on flow, enables FLO-2D to simulate a variety of flooding and debris flow problems.

To be implemented in FLO-2D, the total shear stress expression in Eq. (1) is depth-integrated and rewritten in slope form as presented in O'Brien and Julien (1993). A rheology model that incorporates the three factors above, i.e., yield stress, viscosity, and turbulence and dispersion on flow, enables FLO-2D to simulate a variety of flooding and debris flow problems.

O'Brien et al. (1993) obtained empirical coefficients for several different mudflow matrices through laboratory tests, which are referred to herein for determination of the yield stress and viscosity factors to model mudflow materials. The properties of water-filled colluvium are closest to those of the Aspen Pit I mudflow materials (see O'Brien et al. 1993) based on comparison of index properties, e.g., liquid limit and clay-size fraction of 0.32 and 31%, respectively.

According to the flow properties of the Aspen Pit I mudflow summarized by O'Brien et al. (1993), $\alpha_1 = 0.036$, $\beta_1 = 22.1$, $\alpha_2 = 0.181$, and $\beta_2 = 25.7$ are used for the water-filled colluvium in the FLO-2D analysis herein. The yield stress and viscosity are also sensitive to the sediment concentration. As the volumetric sediment concentration varies from 0.1 to 0.4, the values of these two factors can be changed by three orders of magnitude (O'Brien et al. 1993). Considering a porosity of 0.61 for the water-filled colluvium based on a saturated unit weight of 16.5 kN/m^3 , the volumetric sediment concentration is taken to be 0.39. Subsequently, the yield stress and viscosity can be calculated through Eqs. (2) and (3), respectively.

An advantage of the FLO-2D software package over the Anura3D package is a digital terrain model (DTM) can be imported to initialize the FLO-2D analysis. The rupture surface for the Phase I slide mass is then added to the DTM to define the volume of the Phase I slide mass as the volume of material between the rupture and ground surfaces. The evacuation zone for the Phase I slide mass is obtained by subtracting the post-Phase I topography from the pre-event topography. On the basis of the DTM, grids with a size of 50 m by 50 m were created and elevation points were interpolated to discretize the slide mass. In the FLO-2D analysis, only the water-filled colluvium in Phase I is assumed to flow like a liquid during the simulation. Thus, flow input parameters were only assigned to grids corresponding to the initial location of water-filled colluvium.

The hydrograph at each grid, reflecting the change of flow volume with time, is assumed to be triangular-shaped (Wanielista 1990; Coroza et al. 1997; SWCB 2008; Li et al. 2010; Croke et al. 2011; Peng and Lu 2013) for simplification. Thus, the input source of flow debris linearly increases from zero to a peak and then linearly decreases to zero at each grid. These increases and decreases are occurring over each time step, which is 0.1 s for the analyses performed herein. The peak of discharge is determined by the grid area and average colluvium thickness in the

corresponding grid, and the assumed time span of 60 s is comparable to the main portion of the first recorded event duration.

The FLO2D runout (blue) is compared to the actual (orange) and DAN3D (green) runout zones in Fig. 14. In particular, Fig. 14 shows the FLO-2D analysis significantly under predicts the runout on the east side of Engineer Hill and the largest portion of the runout goes towards the west along the channel of the Stillguamish River. The runout goes primarily west along the river channel because of the decrease in elevation of the channel instead of across the river valley. This is due to FLO-2D only allowing surface topography to influence flow direction and distance instead of potential energy or kinematics of the slide mass as discussed below.

In an effort to improve the runout prediction by FLO2D, the water-filled colluvium was modeled as water in a subsequent analysis instead of a soil. Using the flow properties of water, reduces the resistance of the colluvium to flow and should yield a larger runout zone than the first analysis that utilized mudflow properties for the colluvium. It was anticipated that this analysis might give better agreement with the observed runout and is the best chance of improving the comparison between FLO-2D and field runout observations. The results of the FLO-2D runout analysis that uses water, i.e., little flow resistance, for the water-filled colluvium is shown in Fig. 14. The revised FLO-2D runout (see light blue area) is compared to the actual (orange) and DAN3D (green) runout zones in Fig. 14. This comparison still shows the largest portion of the runout going towards the west along the river channel and still does not provide a good estimate of the actual runout even assuming the colluvium has the resistance of water. As a result, it is concluded that FLO-2D

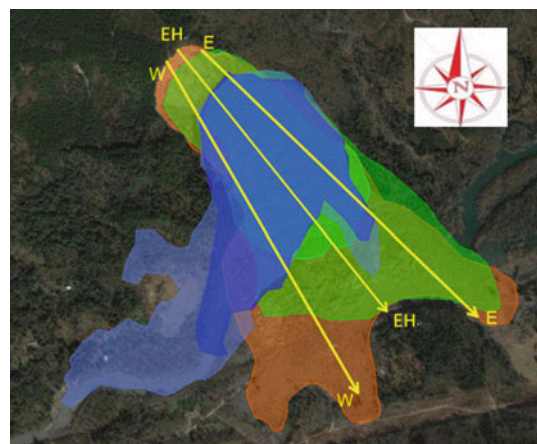


Fig. 14 Comparison of runout zones for: FLO-2D using mudflow properties (see dark blue area) and water for the colluvium (light blue area), DAN3D (green area), Anura3D (yellow lines), and observed impact zone (orange area)

is best suited for situations where only topography, not slide mass potential energy or kinematics, controls slide mass runout.

In Fig. 14 the DAN3D results include both Phases I and II with Phase I being darker green in color than Phase II, which stops just south of the river. The DAN3D results are in excellent agreement with field observations on the east side of Engineer Hill and a little short of the observed runout on the west side of Engineer Hill. The DAN3D results are also in excellent agreement with the runout reaching Engineer Hill in the middle of the debris field and causing some splashing on the top of the hill. The Anura3D runout results east and west of Engineer Hill are in good agreement with field runout observations (orange) but the results are only available for the three cross-sections analyzed.

FLO-2D does provide a better estimate of the runout zone in the westernmost portion of the landslide than DAN3D but this does not compensate for the great deviation from field observations in other portions of the slide mass. Anura3D does not provide an estimate of the influence zone if a cross-section is not drawn in the desired area so its results also have some limitations.

In summary, FLO-2D is able to provide a preliminary estimate of the runout or impact zone of a flood or fluid flowslide. However for planning and risk assessment activities, the FLO-2D results should be supplemented or replaced by another runout analysis, e.g., DAN3D and/or Anura3D, to capture the effect(s) of slope potential energy and kinematics to accurately predict runout and risk to infrastructure and public safety.

Summary

This paper summarizes the slope history, investigation, and analyses used to determine the two-phase failure mechanism of the 22 March 2014 landslide near Oso, Washington that destroyed more than 40 homes and fatally injured 43 people and the accuracy of available runout analyses to simulate the observed behavior. The key findings are:

- The 2014 landslide occurred in two phases with Phase I consisting of an initial landslide involving the Upper Plateau, i.e., Whitman Bench, that was over-steepened by the 2006 landslide. Phase II is a retrogressive landslide in the Upper Plateau caused by evacuation of the Phase I slide mass, which left the upper terrace unbuttressed.
- Rainfall in the 21 days before the 2014 landslide is the wettest on record and corresponds to a 97-year return period and contributed to initiation of the Phase I landslide on the eastern end of the ancient landslide bench.

- Slope toe erosion by the Stillguamish River did not contribute to initiation of the Phase I landslide because it had been pushed south by the 2006 landslide.
- The Phase I landslide impacted, pushed, and over-rode the water filled, disturbed, and softened colluvium along the slope toe, causing a large undrained strength loss similar to the mechanism proposed by Sassa (1985 and 2000) that enabled the colluvium to flow about two km across the valley and carry the recessional outwash sands and trees from the upper plateau across part of the valley.
- Phase II did not exhibit a large runout because the materials are overconsolidated, unsaturated, frictional, and were stopped by the back of the Phase I slide mass.
- Future LiDAR hazard mapping should identify the following two areas because they pose a high risk of a large runout across the valley floor: (1) slopes that have been oversteepened and/or undermined by prior sliding, river erosion, and/or other landslide activity, e.g., see adjacent landslides in Fig. 3, and (2) areas that are not steep over the entire slope length because of a significant accumulation of colluvium along the slope toe and do not exhibit an ancient landslide bench sufficiently wide to support the Upper Plateau, e.g., 2014 landslide. Therefore, slope height alone is not a good indicator because many other slopes along this river valley have a similar or greater height than the 2014 landslide but have a slope profile, i.e., ancient landslide bench, that is sufficient to maintain stability of the Upper Plateau or Whitman Bench.
- The runout results from DAN3D and Anura3D are in good agreement with field observations in respect to the final distance traveled, post-event topography or slide mass depth, observed splash heights, and duration of each phase of slope movement.
- It is recommended that a range of liquefied strength ratio be used for the runout analyses to bracket the range of runout and impact to infrastructure and public safety for risk assessments.
- The runout analysis performed using FLO-2D is not in agreement with field observations because the code utilizes a fluid flow model so the slide mass primarily follows the low spots in the ground surface topography and the effects of slide mass potential energy and kinematics are not incorporated. The potential energy of the Phase I slide mass caused the water-filled colluvium along the slope toe to be pushed across the Stillguamish River and undergo a large undrained strength loss, which is not modeled in FLO-2D. As a result, FLO-2D significantly under predicted the runout zone of the 2014 slide mass.

Data Availability Statement

Some or all data, models, or code generated or used during the study are available from the first author by request.

Acknowledgements The first author appreciates the financial support of the National Science Foundation (NSF Award CMMI-1562010). The contents and views in this paper are those of the individual authors and do not necessarily reflect those of the National Science Foundation or any of the represented corporations, contractors, agencies, consultants, organizations, and/or contributors mentioned or referenced in the paper.

References

- Aaron J, Hungr, O, Stark TD, Baghdady AK (2017) Oso, Washington, Landslide of March 22, 2014: dynamic analysis. *J Geotechn Geoenviron Eng* 143(9):05017001-1–05017001-13
- Badger TC, D'Ignazio M (2018) First-time landslides in vashon advance glaciolacustrine deposits, Puget Lowland, U.S.A. *Eng Geol* 243:294–307
- Bardenhagen SG, Brackbill JU, Sulsky D (2000) The material-point method for granular materials. *Comput Methods Appl Mech Eng* 187(3–4):529–541
- Bandara S, Ferrari A, Laloui L (2016) Modelling landslides in unsaturated slopes subjected to rainfall infiltration using material point method: modelling landslides in unsaturated slopes subjected to rainfall infiltration using material point method. *Int J Numer Anal Meth Geomech* 40(9):1358–1380
- Cao Q, Henn B, Lettenmaier DP (2014) Analysis of local precipitation accumulation return periods preceding the 2014 Oso mudslide. Department of Civil and Environmental Engineering, University of Washington, Seattle
- Coroza O, Evans D, Bishop I (1997) Enhancing runoff modeling with GIS. *Landscape Urban Plan* 38:13–23
- Croke BFW, Islam A, Ghosh J, Khan MA (2011) Evaluation of approaches for estimation of rainfall and the unit hydrograph. *Hydrol Res* 42(5):372–385
- Doughton S (2015). Laser map gave clue to Oso slide's ferocity. <https://www.seattletimes.com/seattle-news/science/laser-map-gave-clue-to-oso-slides-ferocity/>. June 2, 2015
- Govier GW, Aziz K (1982) The flow of complex mixtures in pipes. Krieger Publishing Co., Melbourne, Fla
- Hibert C, Stark CP, Ekstrom G (2014) Seismology of the Oso-Steelhead Landslide. *Nat. Hazards Earth Syst Sci Discuss* 2:7309–7327
- Henn B, Cao Q, Lettenmaier DP, Magirl CS, Mass C, Bower JB, St. Laurent M, Mao Y, Perica S (2015) Hydroclimatic conditions preceding the March 2014 Oso landslide. *J Hydrometeorol* 16(3):1243–1249
- Hungr O, Leroueil S, Picarelli L (2014) The Varnes classification of landslide types, an update. *J Landslides* 11(2):167–194
- Hungr O, McDougall S (2009) Two numerical models for landslide dynamic analysis. *Comput Geosci*. 35(5):978–992
- Hungr O (2015) "Non-textbook Flowslides in Fine-grained Colluvium" presentation to the Vancouver Geotechnical Society, Vancouver, British Columbia, April 15, 2015. https://hkustconnect-my.sharepoint.com/:b:/g/personal/zxubv_connect_ust_hk/EccZwLaKFGxAoFdh-IQ7TLEBm9XVv6tcGD-nSD8yr-N_kQ?e=FYJmZa
- Iverson RM, George DL, Allstadt K, Reid ME, Collins BD, Vallance JW, Bower JB (2015) Landslide mobility and hazards: implications of the 2014 Oso disaster. *Earth Planet Sci Lett* 412:197–208
- Keaton JR, Wartman J, Anderson S, Benoit J, deLaChapelle J, Gilbert RB, Montgomery DR (2014) The 22 March 2014 Oso landslide, snohomish county, Washington. Geotechnical Extreme Event Reconnaissance (GEER), National Science Foundation, Arlington, VA, p 186
- Kim JW, Lu Z, Qu F, Hu X (2015) Pre-2014 mudslides at Oso revealed by InSAR and multi-source DEM analysis. *J Geomat Nat Hazards Risk* 6(3):184–194
- Li CC, Lin A, Tsai YJ (2010) A study of the sediment problem caused by typhoon morakot—taking the watershed of tsengwen reservoir as an example. *J Taiwan Disaster Prevent Soc* 2(1):51–58
- McDougall S (2006) A new continuum dynamic model for the analysis of extremely rapid landslide motion across complex 3D terrain. Ph. D. thesis, University of British Columbia, Vancouver, BC, Canada
- Monaghan J (1992) Smoothed particle hydrodynamics. *Ann Rev Astron Astrophys* 30(1):543–574
- O'Brien JS (1986) Physical processes, rheology and modeling of mudflows. Ph.D. thesis, Colorado State University, Fort Collins, Colo
- O'Brien JS, Julien PY (1988) Laboratory analysis of mudflow properties. *J Hydraulics Eng ASCE* 114(8):877–887
- O'Brien JS, Julien PY, Fullerton WT (1993) Two-dimensional water flood and mudflow simulation. *J Hydraulic Eng* 119(2):244–261
- Olson SM, Stark TD (2002) Liquefied strength ratio from liquefaction flow failure case histories. *Can Geotech J* 39(3):629–647
- Peng SH, Lu SC (2013) FLO-2D simulation of mudflow caused by large landslide due to extremely heavy rainfall in southeastern Taiwan during typhoon morakot. *J Mt Sci* 10(2):207–218
- Sassa K (1985) The mechanism of debris flow. In: Proceedings of XI international conference on soil mechanics and foundation engineering (SMFE), vol 2, CRC Press, Taylor & Francis Group, Boca Raton, FL, pp 1173–1176
- Sassa K (2000) Mechanism of flows in granular soils. In: Proceedings of international conference of geotechnical and geological engineering, GEOENG 2000. Melbourne, vol 1, pp 1671–1702
- Schamber DR, MacArthur RC (1985) One-dimensional model for mudflows. In: Proceedings of ASCE specialty conference on hydraulics and hydrology in the small compute age, vol 2, pp 1334–1339
- Shannon WD, Associates (1952) Report on slide on north fork stillaguamish river near Hazel, Washington, unpublished report to the State of Washington Departments of Game and Fisheries, p 18
- Stark TD, Baghdady AK, Hungr O, Aaron J (2017) Case study: Oso, Washington, landslide of March 22, 2014—material properties and failure mechanism. *J Geotechn Geoenviron Eng* 143(5), 05017005-1–05017001-10
- Stark TD, Mesri G (1992) Undrained shear strength of liquefied sands for stability analysis. *J Geotechn Eng* 118(11):1727–1747
- Sulsky D, Chen Z, Schreyer HL (1994) A particle method for history-dependent materials. *Comput Methods Appl Mech Eng* 118(1–2):179–196
- Sun Q, Zhang L, Ding X, Hu J, Liang H (2015) Investigation of slow-moving landslides from ALOS/PALSAR images with TCPInSAR: a case study of Oso, USA. *J Remote Sens* 7:72–88
- SWCB (2008) Integrated watershed investigation and planning manual. Report of Soil and Water Conservation Bureau, Council of Agriculture, Chinese Taipei
- Thorsen GW (1969) Landslide of January 1967 which diverted the North Fork of the Stillaguamish River near Hazel, Memorandum dated November 28, 1969. to Marshall T. Hunting, Department of Natural Resources, Geology and Earth Resources Division, Olympia, WA
- Wanielista MP (1990) Hydrology and water quantity control. John Wiley and Sons Publishing, New York, USA, p 230

-
- Wartman J, Montgomery DR, Anderson SA, Keaton JR, Benoit J, de la Chapelle J, Gilbert RB (2016) The 22 march 2014 Oso landslide, Washington, USA. *J Geomorphol* 253:275–288
- Yerro A, Soga K, Bray J (2018) Runout evaluation of Oso landslide with the material point method. *Can Geotechn J* 1–14. <https://doi.org/10.1139/cgj-2017-0630>



Numerical Modelling for Slope Stabilizations in Modern Geotechnical Practice

Daniel Pradel

Abstract

Until recently geomechanical numerical modelling of slopes and landslides was mostly performed for academic research purposes and for the engineering design of high earth embankments. In recent years, the use of Finite Element and Finite Difference modelling packages has become commonplace, and allowed complex analyses to be performed by practicing engineers in firms of all sizes. Although these software packages have widespread use in geotechnical engineering, there are two applications that are particularly well-suited for slope stability and landslide modelling. The first one, is the analysis of slope repairs and landslide stabilizations that combine multiple structural elements (e.g., several rows of piles with tiebacks). The second is the seismic performance of slopes, e.g., designs where dynamic amplification and permanent seismic displacements are a major concern. This paper presents recent advancements for the practical design of slopes, the advantages for designers of performing geomechanical modelling, and provides guidelines for their use in modern slope engineering and landslide stabilization practice.

Keywords

Landslide • Slope stability • Geomechanical modelling • Finite element method • Finite difference method • Stabilizing piles • Tieback • Landslide stabilization • Seismic slope movement

Introduction

In large urban environments where steep topographic relief is present, hillside lots are often developed out of necessity. The added costs associated with hillside projects are generally justified by the lack of flat available undeveloped land, or because their views make hillside lots attractive developments that can be sold at a premium price. Unfortunately, landslides are a common hazard in hillside projects that practicing geotechnical engineers must confront, especially when slopes are steep and adverse underlying geologic conditions are present.

Until several decades ago, most slope stabilizations were designed using traditional limit equilibrium methods of slope stability analysis, e.g., using the method of slides. In seismic areas, these analyses were generally supplemented with simple pseudostatic limit equilibrium calculations, which were eventually replaced by simplified seismic deformation analyses based on Newmark (1965) sliding block analogy. As seismic deformations relied on more complex ground motion and soil properties, efforts grew to standardize the use of these methods and industry practice, e.g., ASCE/SCEC (2002) in California.

Compared to researchers in academic institutions who were early adopters of geomechanical modelling techniques and embraced them for landslide analyses, practicing engineers have generally lagged in implementing numerical methods for the design of slope stabilizations and evaluation landslide hazards. Nevertheless, during the last decade the use by practicing engineers of geomechanical numerical models has increased significantly. For example, it is now common in the USA for most geotechnical firms to own one or more licenses of FLAC (Itasca 2019), PLAXIS (Bentley 2019), RS2 (Rocscience 2019), and competing geotechnical numerical packages. Consequently, the high-end geomechanical modelling that was until very recently limited for multi-million-dollar projects is nowadays becoming

D. Pradel (✉)
Department of Civil, Environmental and Geodetic Engineering,
The Ohio State University, Columbus, OH 43210, USA
e-mail: pradel.1@osu.edu

increasingly available for the analysis of ordinary slope repairs and landslide stabilization projects.

In this author's experience, the use by practitioners of numerical techniques to evaluate landslide hazards and design slope stabilizations varies considerably. In the USA, this variability is largely the result of differing economic conditions (e.g., cost of land) and local engineering constraints (e.g., seismicity). In this author's opinion, there are two slope stability applications that are particularly well-suited for geomechanical modelling, are being increasingly used by practicing engineers, and should be strongly encouraged due to their potential benefits; i.e.:

- (a) Slope stabilizations using structural elements, i.e., projects where soil-structure interaction is important.
- (b) Dynamic slope stability analyses, i.e., projects where ground motion amplification and permanent seismic displacements need to be evaluated.

In this paper we will present recent advancements in geomechanical numerical modelling techniques that are important for landslide stabilizations in geotechnical practice. Its main purpose is to provide guidelines for the practical and more widespread use of numerical techniques in modern slope engineering and landslide stabilizations.

Landslide Stabilizations Using Structural Elements

Introduction

In urban environments where steep and/or adverse geologic conditions are present, deep-seated landslides often affect multiple properties. Since many homeowners on the periphery of slope failures are reluctant to allow stockpiling on their properties, and/or provide access through their land, logistically these landslides tend to be very difficult to stabilize using traditional grading techniques. Under such conditions, property lines often impose constraints that make conventional landslide stabilizations difficult, time-consuming and expensive.

To stabilize hillside properties and reduce long-term maintenance/repair costs, property owners in the USA frequently opt to mitigate landslide movements within the confines of their properties. This approach often necessitates using structural elements, such as drilled shafts, to improve the stability of a limited portion of their properties. Often, property owners request designs that only stabilizes the lot's building pad (e.g., Fig. 1).

Because of property line constraints, practicing geotechnical engineers often propose solutions to repair the slope or



Fig. 1 Photo of a failed landslide stabilization in Calabasas, California. The project used a single row of stabilizing piles (drilled shafts) near the scarp that were insufficiently deep to resist the effects of the slide

improve its stability involving alone or in combination: drilled shafts, soil nails, anchors, tiebacks, and dewatering (e.g., Fig. 2). An example of such practice in California is described in Pradel (2018).

One of the main advantages of using drilled shafts to stabilize slopes, is that they can be placed very precisely along property lines, top and toe of slopes (Fig. 4); hence, significantly restricting the area where the stabilization is performed. For developers and engineers, the ability to control the limits of the stabilization also allows partial removal and recompaction of a landslide by grading, verification and localized disruption of the landslide basal plane (e.g., using a compacted fill key or buttress), and can facilitate the total removal of a landslide (Figs. 2 and 3). For these reasons drilled shafts are widely used and considered versatile elements in slope stabilization techniques.

Traditional Techniques for the Design of Slope Stabilizations that Incorporate Structural Elements

To design landslide stabilizations with structural elements, geotechnical engineers often utilize various methods of analysis in combination (Carder and Temporal 2000). The employed design procedures and methods of analysis depend mostly on the failure mechanisms being considered, as well as their criticality. Importantly, these methods can vary significantly for the same design element. For example, different design approaches may be used to prevent the adverse consequences of soil flow between piles; some engineers may rely on arching theory (e.g., Ito and Matsui 1975, 1981), others on deformation analyses (e.g., numerical predictions), whereas some engineers may simply opt for a



Fig. 2 Photos taken during a landslide stabilization in Encino, California. The project used two rows of stabilizing piles and tiebacks which allowed the completed removal and recompaction of the landslide

narrow pile spacing considered to be adequate for a full transfer of passive pressures (e.g., the 3 shaft diameter center-to-center spacing suggested in Broms 1964).

The most commonly used methods to evaluate the global stability of a slope stabilized using structural elements can be divided into the following groups:

- (a) **Limit Equilibrium Methods:** Methods belonging to this group include Taylor’s friction circle method and methods of slices, such as the Bishop, Janbu, and Spencer methods (Duncan and Wright 2005). These methods, which were designed for the analysis soil masses were not intended for the direct determination of structural demands, such as bending moments in piles. Nevertheless, in practice the contribution from a



Fig. 3 Photos taken during construction of the drilled shafts and tiebacks shown in Fig. 2 (Top image: reinforcement of the drilled shafts with steel I-beams; Bottom image: exposed tieback anchor blocks during landslide removal)

structural element has traditionally been considered by adding a resisting force that is considered to be compatible with the expected movement of the sliding mass. In limit equilibrium methods, landslide movement is generally assumed to occur according to a



Fig. 4 Photo of a landslide mitigation in Malibu, California. Along the toe of the slope the project used piles and tiebacks to laterally support the landslide

rigid-perfectly-plastic model, with the sliding mass moving as a single rigid block in the downslope direction. Because of this assumption, displacements are often not kinematically acceptable and pressure distributions on stabilizing piles, anchored walls and buttresses cannot be defined; hence, practicing engineers must make reasonable pressure distribution assumptions to obtain the demands (e.g. bending moments) necessary for the design of stabilizing piles. Such procedure is exemplified in NAVFAC (1986) for the design of stabilizing piles by the method of slices. A more modern procedure using Taylor's friction circle method was proposed by Hassiotis et al. (1997).

- (b) **Earth Pressure Theory Method:** For simple slope stabilizations, where stabilizing piles are installed near the top of slope (Fig. 1), practicing engineers sometimes use earth pressure theories (e.g., Coulomb or Rankine theories) to design stabilizing piles. To stabilize landslides, residual strength is generally used for the calculation of the active pressure coefficient (K_a) and a triangular lateral pressure distribution is assumed to be acting on piles. Conversely, when piles are placed along the toe of slopes (Fig. 4), passive conditions prevail and soil pressures are calculated using the passive pressure coefficient (K_p). Because bending moments in stabilizing piles quickly become excessive, anchorage systems (e.g., tiebacks) are almost always required for piles along the toe of landslides (Fig. 4). Near the scarp, active pressure conditions are present, and piles can often be designed to cantilever on the order of 10 m, beyond that they generally require anchorage systems. In this author's experience, this methodology is most often used to design stabilizing

piles located near the scarp (Fig. 1) and along the sides of a building or slope, i.e., along the edge of areas needing landslide protection while allowing movement of the slope below.

- (c) **Hybrid Equilibrium/Deflection methods:** For the analysis of slopes stabilized using vertical structural elements (such as micropiles and drilled shafts), practicing engineers sometimes complement their limit equilibrium slope stability calculations with pile deflection analyses. In the USA, these analyses are often performed with the LPILE program from Ensoft (2019). In the LPILE analyses, stabilizing piles are generally subjected to the unfactored forces (or pressure distributions) predicted from limit equilibrium methods ("a") or earth pressure theories ("b"). The LPILE analyses consider the pile rigidity and often result in modifications of the original designs.
- (d) **Deflection Theory-Based Methods:** Several authors including Reese et al. (1992) and Boekmann and Loehr (2013) have proposed methods that truly combine the traditional method of slices with pile deflection theory (as opposed to the hybrid approach under "c"). These methods often incorporate the p-y method (e.g., Reese and Van Impe 2011), require numerous iterations and are relatively complex. Generally, these procedures require calculations to be repeated until the critical slip surface, the stiffness of the structural elements, the resisting forces, and pile displacements are considered compatible. Changing either pile diameter, spacing or length requires a new set of iterations since demands must be consistent with the assumed displacements of the slide mass. Adding anchorage systems (e.g., Fig. 3) increases the complexity to the procedure, and require additional iterations. In this author's experience, designers rarely use methods belonging to this group in practice.

Although many landslides have been successfully stabilized using the methods described above, in this author's experience, many designs either ignore displacements, use overly conservative forces, and/or have inconsistent resistance distribution among structural elements.

Sources of Uncertainty

In addition to uncertainties related to shear strength, groundwater and subsurface conditions, designers must find the critical failure mode that governs slope stability. When using limit equilibrium methods, engineers generally assume that increasing the number of failure plane searches will sufficiently reduce uncertainty and result in a reasonable approximation of the critical basal plane, i.e., the failure plane that is most prone to failure.

For the design of slopes, practicing engineers should also consider the following factors, as they may introduce significant uncertainty:

- (a) **Continuity of the critical failure plane:** Analysing landslide stabilization using discontinuous circular failure surfaces, Yamagami et al. (2000) showed that the placement of a row of piles in a slope results in discontinuous critical basal planes. Importantly, when a row of stabilizing piles was introduced the critical surfaces that Yamagami et al. (2000) found, did not intercept at the pile location. Since stabilizing piles are generally socketed in bedrock and through shear transmit significant forces into the stable ground below, they profoundly disrupt the continuity of interslice forces. Hence, the lack of failure plane continuity reported by Yamagami et al. (2000) is not surprising.
- (b) **Contributions from multiple structural elements:** Large landslide stabilizations often require several rows of stabilizing piles and tiebacks and are generally complex (e.g., Fig. 2). An additional complexity for designers is that traditional methods do not predict the relative contribution from different pile rows; therefore, these methods are poorly suited to evaluate the relative contributions of multiple structural systems, e.g., pile rows having various pile geometries and multiple anchorage systems.

Because of the above, it is not only hard to predict the critical failure mode for landslide stabilizations, such as the one in Fig. 2, but it is also very difficult to obtain the associated lateral pressures and structural demands acting on multiple piles and tiebacks, especially when these have diverse geometries and stiffnesses.

The critical collapse mechanism depicted in Fig. 5 was predicted by the Discontinuity Layout Optimization technique (LimitState 2020). It exemplifies how complex and far from obvious the critical failure mode can become for large landslide stabilizations. The problem with predicting the critical failure mode for large stabilizations, such as shown in Figs. 2 and 3, is described in detail in Pradel (2018).

Strength Reduction Method

Introduction

Although the Finite Element Method (FEM) began to be used for dams in the 1960s (Clough 1960; Clough and Wilson 1999), its use for the analysis of slopes and landslide stabilizations under static conditions became widespread in practice after the introduction of the Strength Reduction

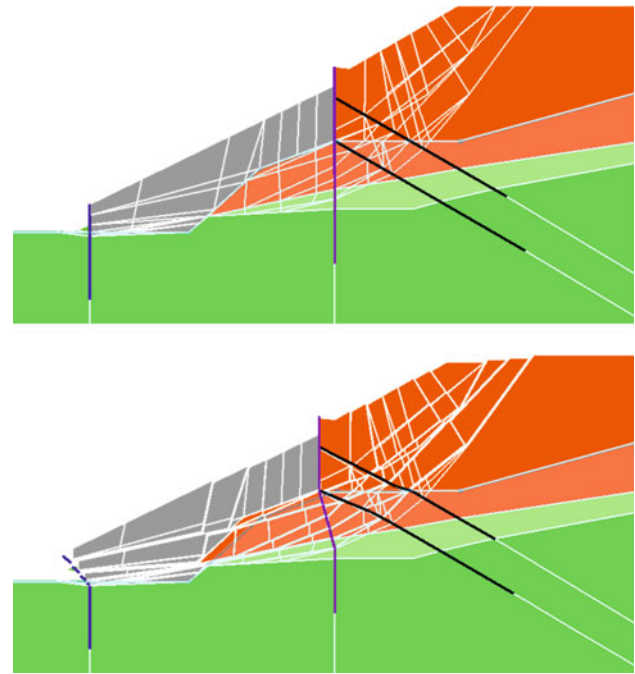


Fig. 5 Critical failure mode and kinematically acceptable displacements predicted using LimitState: Geo (LimitState 2020) for the landslide stabilization depicted in Figs. 2 and 3

Method (SRM) by Griffiths and Lane (1999). The SRM is incorporated into numerous computer programs used for the design of slopes by geotechnical engineers, including FLAC (Itasca 2019), RS2 (2020) and PLAXIS (2019). One of the main advantages of the SRM is its ability to obtain Factors of Safety, which is a building codes requirement in many jurisdictions worldwide.

The SRM involves modelling subsurface soils and rocks as elastic-perfectly-plastic materials, while simultaneously reducing their strengths, e.g., their cohesions, c , and friction angles, φ , by a strength reduction factor, R :

$$c_d = \frac{c}{R} \quad (1)$$

$$\tan(\varphi_d) = \frac{\tan(\varphi)}{R} \quad (2)$$

The reduction is repeated iteratively by a FEM or Finite Difference (FD) program, until equilibrium is no longer satisfied and the slope fails in a quasi-natural manner. The highest value of the strength reduction factor that satisfies equilibrium and is kinematically acceptable is equivalent to the Factor of Safety, FOS, of the slope:

$$FOS = R_{\max} \quad (3)$$

In engineering practice, the SRM has multiple advantages, including:

- (a) Predicted critical failure mechanisms are generally self-evident. This is especially important for stabilizations where several structural elements are combined, i.e., where the critical failure mechanism may be difficult to anticipate (e.g., Fig. 5).
- (b) No assumptions about the location and shape of the critical failure surface are required. Hence, the engineer must not characterize the shape as circular, noncircular or convex, nor be concerned about the initiation and exit points of the failure surfaces.
- (c) No restrictive hypotheses about interslice forces direction, location or magnitude are needed (e.g., similar to the constant thrust force angle hypothesis in Spencer's method).
- (d) Predictions can be easily obtained for probable, optimistic and pessimistic scenarios, by modifying slightly the FEM or FD analyses used for the SRM. With adequate field instrumentation (e.g., slope inclinometers and load cells) these scenarios may be used to assess the safety of operations, and to evaluate during construction how realistically the adopted soil properties were estimated.
- (e) The mesh used for the SRM can be modified and subjected to earthquake time-histories for assessments of seismic performance.

For safety reasons, the ability to obtain benchmarks for realistic, as well as potentially adverse scenarios, (as described under "d", above) is especially important for landslide stabilizations requiring deep cuts and slopes that may be subject to a sudden rise in groundwater pressures. A great advantage, is that benchmark predictions from numerical models may analyzed within the framework of the observational method (Peck 1969), or modified/rerun multiple times during construction operations (e.g., after alterations of the original stabilization scheme were required in the field). Similarly, when the numerical model is subject to earthquake time-histories (as in "e", above), geotechnical engineers may use the predicted accelerations, velocities and displacements to evaluate anticipated performance and increase the confidence of simpler Newmark method seismic deformation analyses (e.g., Makdisi and Seed 1978; Bray and Rathje 1998; Bray and Travararou 2007).

Implementing the SRM for soil and rock slopes without structural elements is straightforward and results in critical failure surfaces that are generally very similar to those predicted by limit equilibrium methods that consider both forces and moment equilibrium (e.g., Fig. 6).

In anchored slopes, where the failure plane is intercepted by tiebacks or soil nails, bonding failures are often the critical mode of failure; hence, implementation of the SRM

is also straightforward and the contribution from multiple anchorage systems may be easily obtained (e.g., Fig. 7).

Stabilizing Piles

The load transfer between the soil and a laterally loaded pile is governed by soil-structure interaction, and often analyzed using a p-y method (e.g., Reese and Van Impe 2011) by practicing engineers. In slopes, lateral movements depend on local rigidities, complex displacement fields, and various other factors; consequently, structural demands on stabilizing piles are hard to calculate.

In a landslide repair where a row of small diameter piles has been installed at large spacings from each other, the soil retained behind the piles will tend to flow between the deformable piles, and the piles will carry a small percentage of the total downward forces. Conversely, large diameter closely spaced piles (e.g., Figs. 2 and 3) will prevent most soil flow and result in a performance similar to that of a rigid and continuous retaining wall.

Soil-structure interaction (SSI), including the effect of pile spacing, diameter and rigidity, can be fully modelled using a three-dimensional (3D) numerical mesh. Although this approach is elegant and can solve most SSI related concerns, building a 3D mesh is time-consuming and therefore not recommended for practical applications.

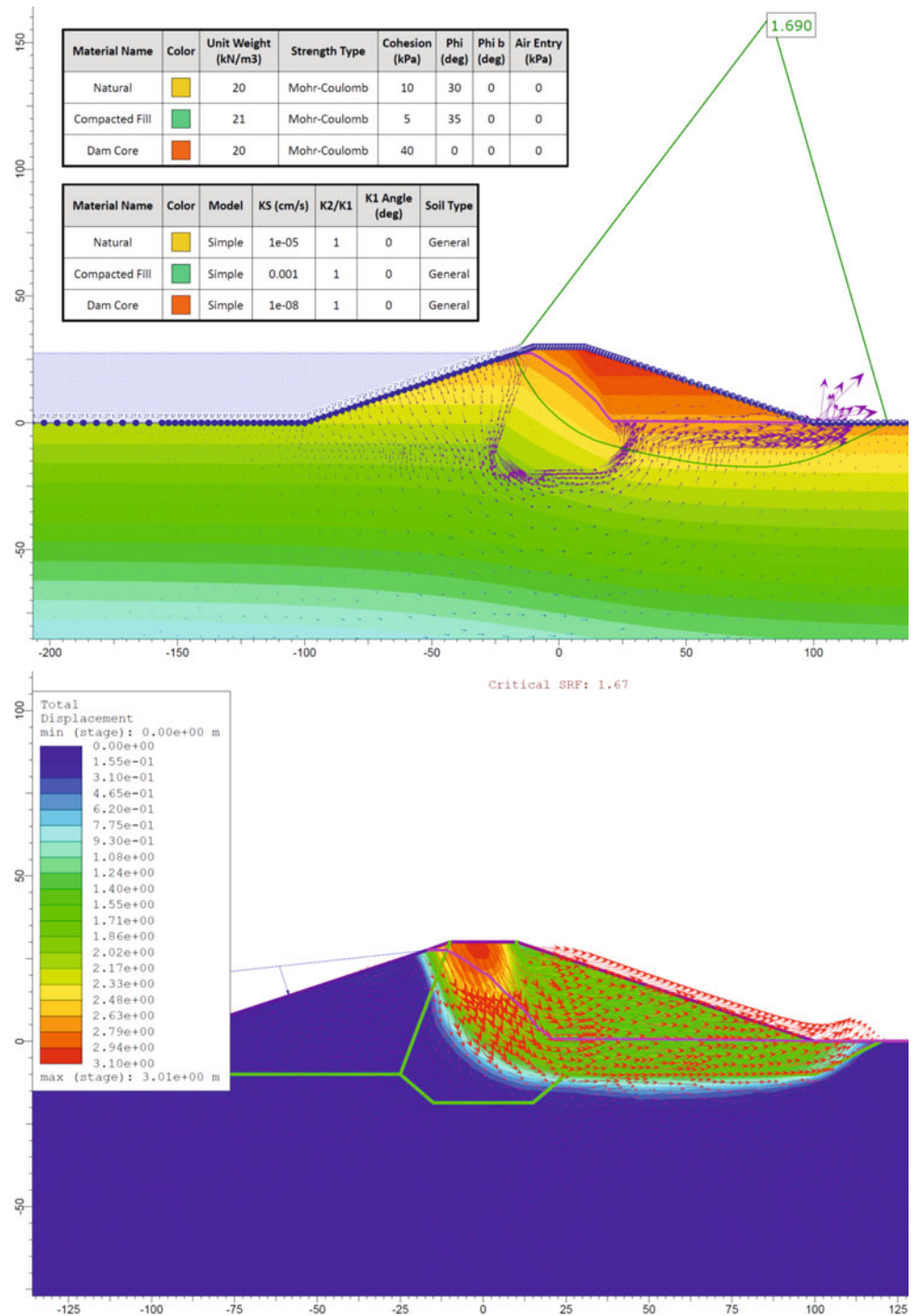
A suitable and less numerically intensive approach is the creation of equivalent two-dimensional (2D) FEM or FD models, where the structural elements are connected to the soil mesh by nonlinear springs. With an appropriate non-linear spring formulation, this approach permits large movements of the soil mesh relative to the piles, while simultaneously providing loading of the structural elements that is consistent with the p-y method.

In landslide stabilizations, allowing flow between piles while simultaneously providing a reasonable load transfer onto the piles is crucial for the determination of realistic bending moments and shear forces. In practice, two approaches are available to model this load transfer:

- (a) Using spring stiffnesses derived from published p-y curves (e.g., Reese and Van Impe 2011; Ensoft 2019).
- (b) Developing site specific p-y curves from push-over analyses. These analyses must be performed for each representative pile, and model by FEM or FD the performance of the pile pushed laterally at selected depths (Fig. 8).

Since in landslide stabilizations the predicted soil displacements tend to be very large compared to the pile

Fig. 6 Factors of safety obtained by limit equilibrium (FOS = 1.69 obtained by Spencer method) and Strength Reduction Method (FOS = 1.67 obtained by RS2 from RocScience 2019) for small dam (all dimension shown in meters)



displacements, the use of complex nonlinear p-y curves, such as the ones in LPILE (Ensoft 2019) are in the author’s opinion rarely justified for SRM analyses. Simple bilinear (elastic-perfectly-plastic) springs derived from push-over analyses are, considered sufficiently accurate to obtain reasonable structural demands for most design projects. An example of a pile push-over analysis is illustrated in Fig. 8, note that because of symmetry only half the space between stabilizing piles needs to be discretized.

Nevertheless, the analysis needs to be repeated for multiple depths (i.e., when soil properties change and as vertical stresses increase).

An example of a SRM solution where the critical failure plane was disrupted by two rows of stabilizing piles that were installed to protect a rural highway in Ohio, USA, is illustrated in Fig. 9. Note that in this project, two closely spaced rows of piles were rigidly connected at the top to create a structural moment resisting frame. Connecting piles

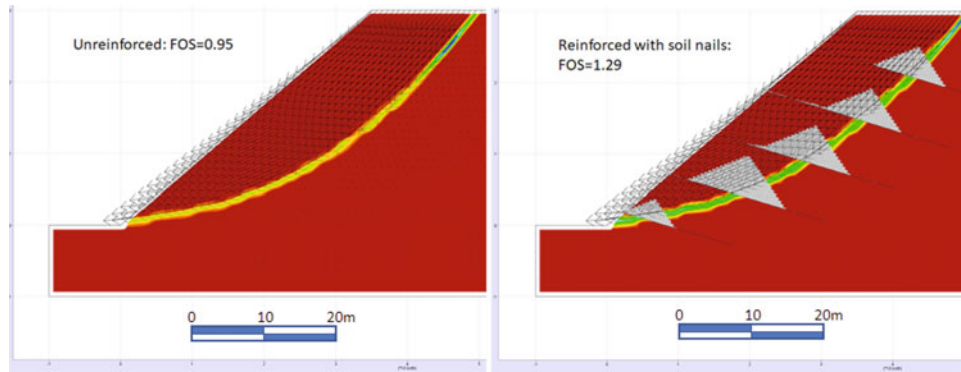


Fig. 7 Critical failure mode and soil nail forces predicted by the Strength Reduction Method (FOS obtained by FLAC from Itasca 2019) for a 30 m high slope

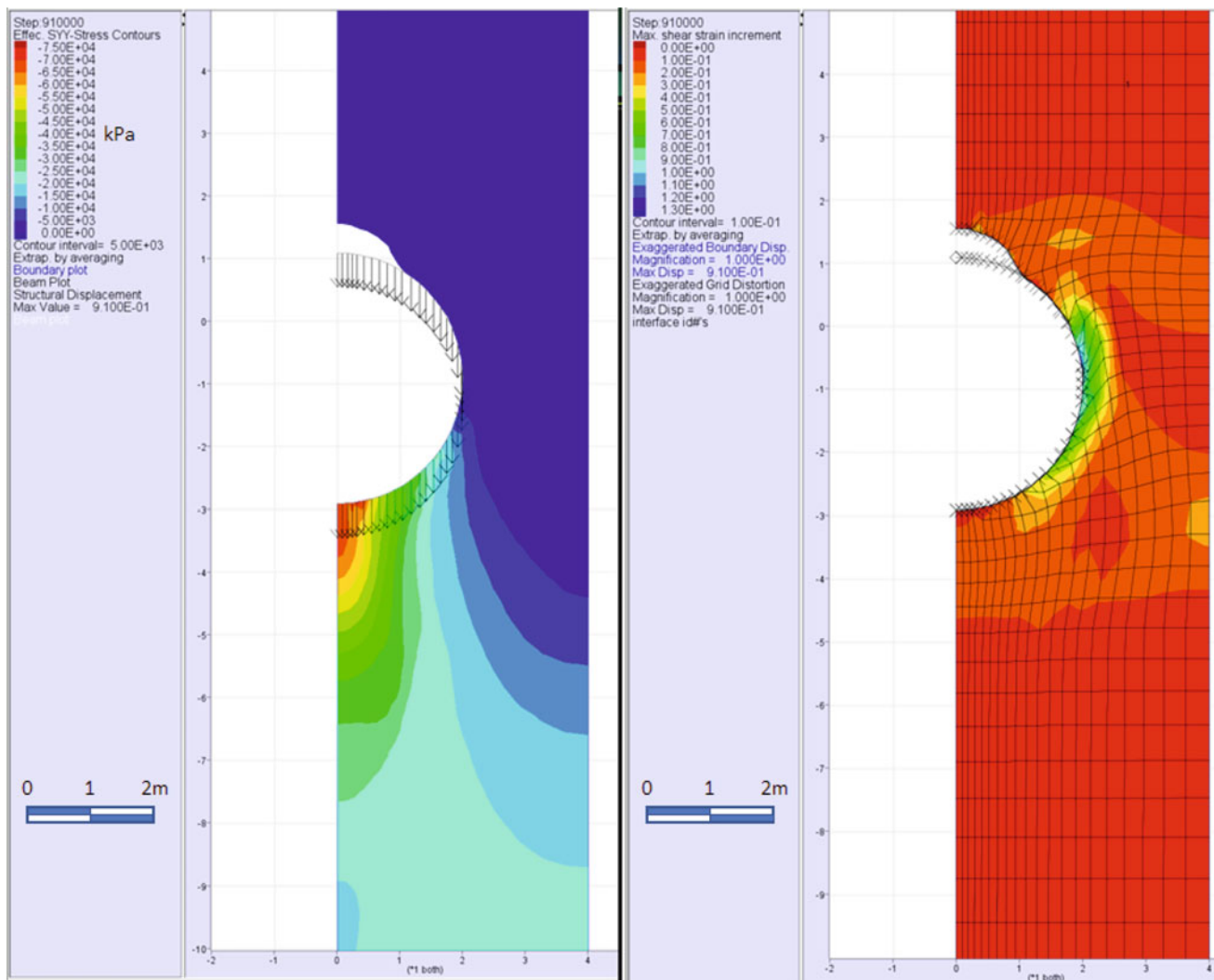


Fig. 8 Pushover analysis of 3 m diameter pile at a depth of 8 m for development of its p-y curve (note: because of symmetry, only half the spacing between piles was discretized in the horizontal direction)

Fig. 9 Deformed mesh (shown in black), maximum shear strains (blue), and pile bending moments (grey) predicted using FLAC for a landslide stabilization in Ohio, USA. To protect the road, two rows of piles (shown in yellow) were used; the piles were rigidly connected at the top to form a moment resisting frame

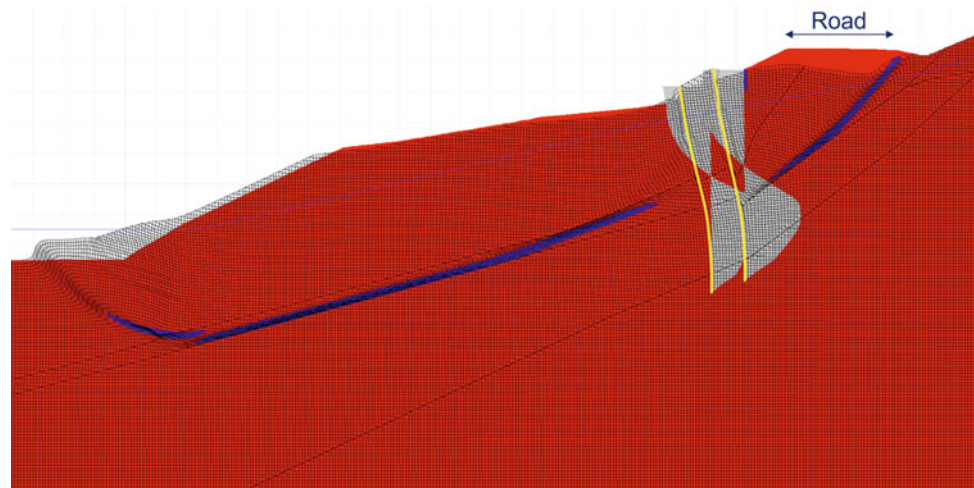


Fig. 10 Pile supported wall constructed along a highway in Ohio, to protect a road from an active landslide. A concrete cap connects two rows of steel piles, rigidly; on the right side of the cap, precast concrete panels placed between the piles' steel flanges to create a retaining wall

with grade beams, slabs and/or pile caps (e.g., Fig. 10) is advantageous, since it significantly reduces total pile displacements and maximum bending moments.

For the analyses in Fig. 9, pushover analyses were performed at 10 different depths using the procedure illustrated in Fig. 8. Note that in Fig. 9 the critical failure plane predicted by FLAC became discontinuous at the location where the piles were installed. It is clear that the piles created a disruption of the failure plane. Interestingly, the predicted critical failure mode is discontinuous, in a manner that is consistent with the findings in Yamagami et al. (2000).

Complex Stabilizations Using Piles and Anchors

Large landslide stabilizations often combine several different vertical structural elements, such as drilled shafts and

micropiles, and inclined anchorage systems, such as tiebacks, soil nails, anchors and geogrids (Fig. 3). As previously indicated, finding the critical slope stability failure mechanism is often difficult when multiple structural elements are used in a landslide stabilization. Hence, for landslide repairs such as the one shown in Fig. 2, experienced geotechnical engineers using limit equilibrium methods alone may result in missing critical failure mechanisms such as the ones in Figs. 5 and 9.

Unlike the SRM, limit equilibrium techniques require multiple trial and error attempts (i.e., involve guessing); hence, depending of the designers experience, there is always a significant probability of missing the critical failure mode. Because numerical modeling techniques such the SRM (e.g., FLAC, RS2 and PLAXIS) and theory of plasticity (LimitState 2020) do not require assuming/guessing the presumed location and shape of the failure surface, these methods are less likely to miss the critical failure mechanism. In practice, this makes the SRM a more robust technique for slope engineering, which should be encouraged, especially for the design of large/complex slope stability projects. In this author's opinion, SRM should be used in addition to traditional limit equilibrium analyses, and not be used alone; in combination, these methods vastly improve confidence in assessment of slope stability, hence, safety.

Dynamic Slope Stability

Introduction

Seismic events such as the 1994 Northridge, 2011 Tohoku and 2015 Gorkha Earthquakes have demonstrated the vulnerability of slopes to seismically induced landslides on residential developments, roads, and earth dams (Harp and Jibson 1995; Tiwari et al. 2013; Pradel et al. 2013; Tiwari et al. 2018).

For many years, practicing engineers have favoured using simple limit equilibrium methods to assess the seismic vulnerability of slopes and used the pseudostatic method routinely. In the USA, the pseudostatic method was widely used in geotechnical engineering practice until about the 1980s, with seismic coefficients on the order of 0.05–0.25 g. Starting in the 1990s, simplified dynamic deformation analyses based on Newmark's method (e.g., Makdisi and Seed 1978; Bray and Rathje 1998) slowly began to replace traditional pseudostatic analyses for the design of slopes.

As dynamic deformation analyses became increasingly complex, efforts to standardize the selection of seismic input parameters and improve the quality of predictions became necessary; one such effort in California is exemplified in ASCE/SCEC (2002). To encourage the use of dynamic deformation analyses, certain societies distributed spreadsheets during short-courses and seminars.

To assess the expected seismic performance of hillsides in California, it became standard during the 2000s to obtain shear wave velocity profiles, by SCPT (Seismic Cone Penetration Test), ReMI (Refraction Microtremor technique) or suspension logging techniques. Although the use of dynamic deformation analyses represents a significant improvement in the standard of practice, it should be recognized that Newmark based methods were not developed for the direct evaluation of slopes reinforced with piles and anchors; hence, although their use may be justified in many instances, FEM and FD techniques are, in our opinion, preferable for landslide stabilizations where dynamic SSI is important and should be modelled.

For many large engineering firms, dynamic modelling of earth dams and landslides, became feasible when the FORTRAN code of the QUAD4 computer program was published (Idriss et al. 1973). Two decades later, Hudson et al. (1994) produced a modified version of the original FEM program, known as QUAD4M, that ran on desktop computers. Like SHAKE (Schnabel et al. 1972), QUAD4 and many other programs developed at UC Berkeley during the 1970s, QUAD4M uses the equivalent linear method for the determination of soil damping, shear stresses, velocities and accelerations. Furthermore, QUAD4M was not intended to be used for SSI analyses and could not be used to directly evaluate seismic effects and structural demands in piles and tiebacks. An example of the use of QUAD4M for the analysis of landslide movement during the Northridge earthquake is described in Pradel et al. (2005).

Although designers still use QUAD4M regularly in practice, the use of programs such as PLAXIS, and FLAC, has become widespread in engineering practice during the last decade. Importantly, these programs have allowed small engineering firms to perform on desktop computers, the sophisticated numerical analyses that a couple of decades earlier would have required a mainframe computer, thus

would have been restricted to large engineering firms and researchers in universities. As a result, many small companies in the USA are capable today of advanced SSI and liquefaction analyses, which they perform routinely. These enhanced capabilities should, in this author's opinion, be encouraged as they will improve significantly the state and quality of geotechnical practice.

Examples of modern numerical modelling using the computer program FLAC (Itasca 2019) for the prediction of seismic slope movements are shown in Fig. 11 (Pradel et al. 2013) and Fig. 12 (Tiwari et al. 2018). Both examples illustrate that quality predictions of movements reported in case histories can be obtained using relatively simple soil models and widely available modelling techniques.

Recommended Practice

In hillsides where the subsurface geometry is well defined, modern dynamic analyses require the following characterization of all subsurface materials:

- (a) Densities and shear wave velocities (v_s);
- (b) Damping characteristics;
- (c) Shear strength gain/degradation.

The above properties may be obtained through a combination of field testing (e.g., SCPT and ReMI for v_s), laboratory tests, and adoption of published findings (e.g., damping and modulus reduction curves). Additionally, to use programs such as PLAXIS or FLAC for the design of a new hillside development or for a major landslide stabilization, ground motion time-histories must be available. Importantly, these time-histories must be “within ground motions” so that they can be directly applied along the base of the FEM or FD model.

Depending on the type of modeling selected by the designer and the specific computer program he/she is using, time-histories may be applied as accelerations, velocities, displacements or shear stresses.

When analyzing case histories ground motions should be as realistic as possible, but for new developments they will largely depend on how much risk is tolerable and how conservative the engineers were during the ground motions selection process. In modern practice, peak ground accelerations and response spectra obtained using probabilistic seismic hazard analyses (PSHA) methods for specified probability of exceedance (e.g., 2% in 50 years) are generally preferred. Generally, PSHA results are used to modify the scale and frequency content of existing earthquake records that designers consider appropriate for potentially damaging local fault rupture mechanisms. Design time-histories are often obtained by spectral matching or

Fig. 11 Deformed mesh and maximum shear strains of Fujinuma dam during the 2011 Tohoku earthquake

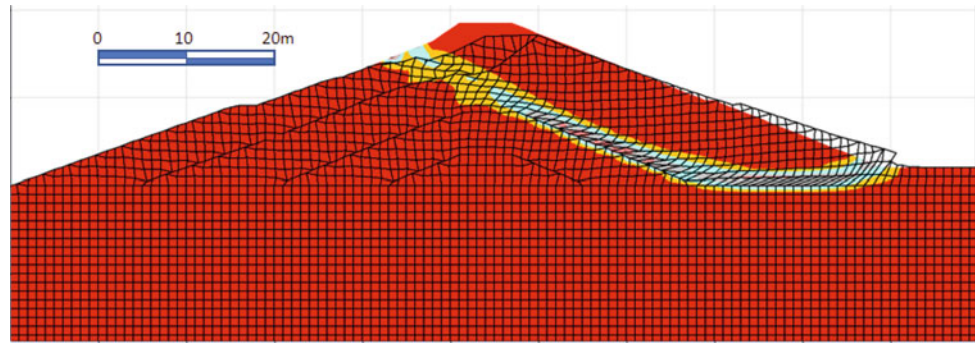
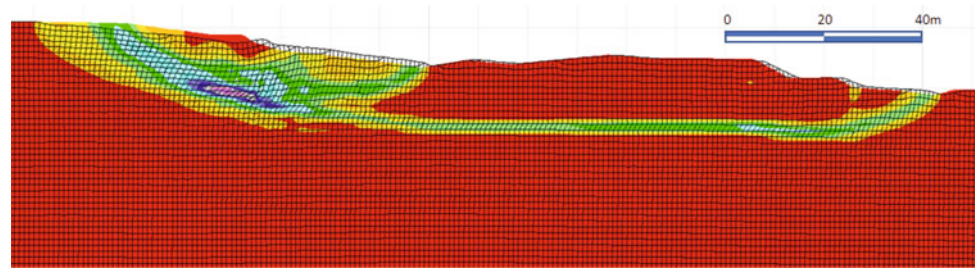


Fig. 12 Deformed mesh and maximum shear strains at Lokanthali, Nepal, during the 2015 Gorkha earthquake



similar scaling techniques and, depending on local practice and acceptable risk, 5–10 time-histories are usually selected for seismic designs.

When analyzing slopes that were adversely affected by an earthquake (i.e., case histories), nearby ground motion recordings may be few and, therefore, the total number of input time-histories for numerical modeling may be limited (e.g., Tiwari et al. 2018). For the analysis of case histories, ground motions should preferably be derived from “rock stations” (seismic station where the seismograph was installed on a bedrock outcrop) located in the vicinity of the site. In situations where only nearby “soil stations” are available, surface ground motions should be deconvoluted in order to generate depth appropriate “within motions”, i.e., time-histories at a depth equal to the base of the model and that have not been subject to near surface soft-ground amplification.

Simplified Soil Modelling

Complex soil modelling can significantly increase computational times and is rarely justified for the design of landslide stabilizations. Traditionally, dynamic FEM analyses were performed using the equivalent linear method (ELM). The main advantages of ELM are its simplicity and short computational times, and its main disadvantage is that linear properties remain constant throughout the history of shaking. As a result, soil elements are generally over-damped and too soft during quiet periods in the excitation history, and conversely, elements are under-damped and too stiff during

strong shaking. Other disadvantages resulting from the constant stiffness and damping in the ELM, include:

- ELM does not directly provide information on irreversible displacements. Hence, plastic yielding and/or landslide slippage is not predicted directly.
- The spatial variation in properties that corresponds to different levels of motion at different locations during an earthquake is not considered.
- The interference and mixing phenomena that occur between different frequency components in a nonlinear material are missing from an ELM analysis.
- The adopted stress–strain curves are always in the shape of an ellipse, a shape that cannot be modified.

Although permanent landslide displacements may be successfully estimated from the ELM stress predictions using empirical procedures that are unrelated to the method, a more robust approach is desirable.

An elegant approach to avoid over-damping during quiet periods and under-damping during strong shaking is to use hysteretic damping (Fig. 13). Using the Massing rule, this approach only requires that backbone shear moduli curves be selected for each material (e.g., Fig. 14).

As shown in Fig. 14, published and/or experimentally obtained damping and modulus degradation curves may be used to select a numerical model’s backbone hysteretic curves. Please note that at large strains, damping in published curves often deviates from what the modulus reduction curves (G/G_{\max}) ultimately predict. This discrepancy is generally the result of an overestimation of the shear strength

Fig. 13 Stress–strain loops and accumulated strains predicted with backbone curves and hysteretic damping

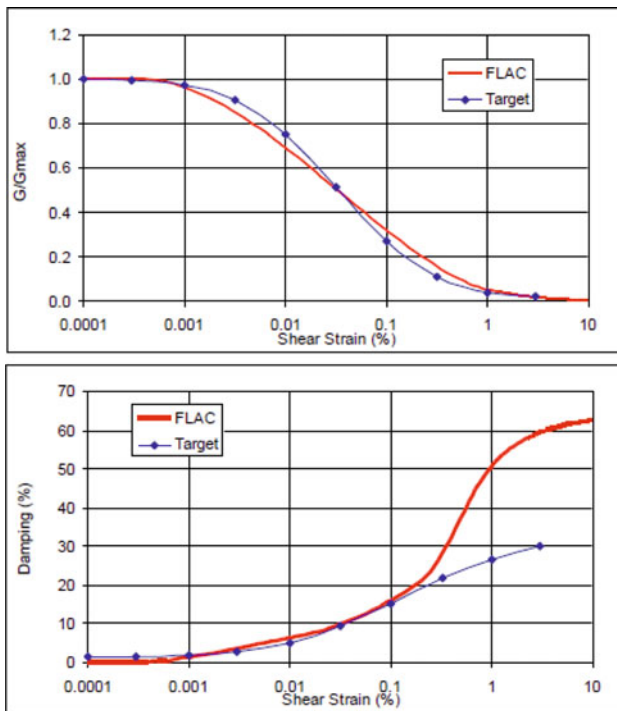
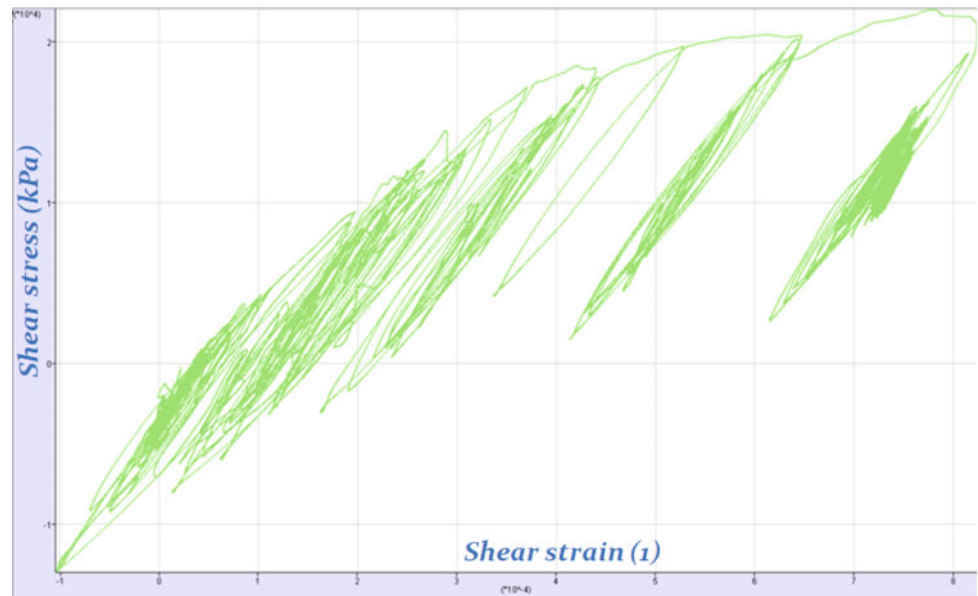


Fig. 14 Comparison of experimental (“target”) modulus reduction and damping curves, with built-in numerical model (“FLAC”) backbone hysteretic curves. These curves were used for the prediction shown in Fig. 13

inferred when creating backbone stress–strain curves from the modulus degradation curves. In projects, this discrepancy is usually a concern when shear strains exceed about 0.2% (Chiu et al. 2008).

The previously described methodology allows soil stiffness and damping to be adequately characterized at small strains (less than 0.2%) and ensures proper wave propagation modelling. For landslides, slippage along weak surfaces and plastic flow of soil between piles must be allowed. Slippage and plastic flow can be modelled by letting shear failures (i.e., slippage) develop in the soil, e.g., in accordance with a Mohr–Coulomb or similar failure criteria. Using this approach, the backbone stress–strain curves created by the hysteretic damping model cannot exceed the shear stresses predicted by the failure criteria, hence, have a clear upper bound (as shown in Fig. 13).

Model Boundaries

Trapping of energy within a model is a major concern in dynamic FEM and FD analyses. To minimize wave reflections at model boundaries, it is recommended to use a quiet viscous (i.e., absorbing) boundary along the base of models, and “free-field” boundaries along the vertical edges of the model, as shown in Fig. 15. Alternatively, the use of

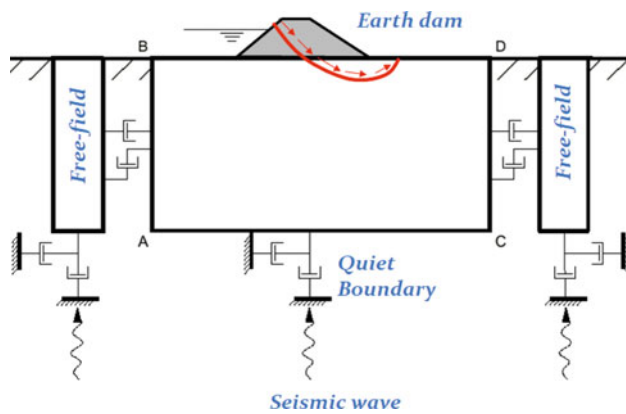


Fig. 15 Boundary conditions used for dynamic analyses to prevent trapping of energy within a model

extended boundaries to prevent boundary reflections/effects can be an option, but should be carefully assessed, especially when time histories are moderate to long duration events.

Because, FEM and FD modelling of slopes often involves vertical boundaries having different lengths and soil conditions, angled wave reflections often act on these boundaries. An elegant technique to reduce reflections is to use vertical “free-field” boundaries (Fig. 15), i.e., boundaries with properties (e.g., damping) that are continuously adjusted to closely match an independently computed one-dimensional solution.

The modeling techniques described above, are simple enough to provide reasonable seismic modeling of hillsides and landslides; therefore, they are generally recommended. Examples of dynamic modeling using the previously described techniques are exemplified in Pradel et al. (2013) for the downstream landslide at Fujinuma dam (Fig. 11), and in Tiwari et al. (2018) for the movement at Lokanthali (Fig. 12).

More complex modelling is needed when hillsides are subject to liquefaction and/or lateral spread. Analyses for such slopes require the use of a more complex constitutive models that are capable of predicting excess pore pressures, such as the Finn (Byrne 1991), Wang (Wang et al. 2006) UBC-Sand (Byrne et al. 2004) or PM4Sand (Boulanger and

Ziotopoulou 2017) models. An example of an analysis using the Finn model is exemplified in Fig. 16 for the analysis of a viaduc north of Seattle, Washington.

Conclusions

Geomechanical numerical tools are today widely available in engineering practice, and sophisticated predictions are no longer limited to researchers in academic institutions and designers in large engineering firms. The examples shown herein, illustrate that numerical modelling is extremely well suited for slope stability practice and the design of real-world landslide stabilizations.

Numerical techniques are particularly well-suited for the analysis of landslides stabilized with multiple structural elements, where their interaction often makes the critical mechanism not always obvious. Additional advantages of using geomechanical numerical modeling include: accurate modelling of soil-structure interaction, and the ability to predict benchmarks that may be used during construction operations to assess safety, and may even be analyzed within the framework of the observational method.

For seismic analyses, numerical techniques are powerful and extremely well-suited for the analysis of seismic performance of slopes and landslides. To obtain reasonable predictions, it is important to use silent and free-field boundaries, otherwise energy will become trapped within the model and excessive seismic landslide/slope movements will be predicted; additional guidelines for the use of simple models in practice are presented above. The examples presented herein, show that excellent predictions of landslide movements can be obtained using simplified models, using backbone hysteretic curves to model soil performance.

For both landslide stabilizations and seismic analyses, the examples shown above, show that numerical modelling has major advantages compared to traditional methods (e.g., limit equilibrium and deformation analyses); therefore, geomechanical numerical tools can significantly improve geotechnical engineering practice.

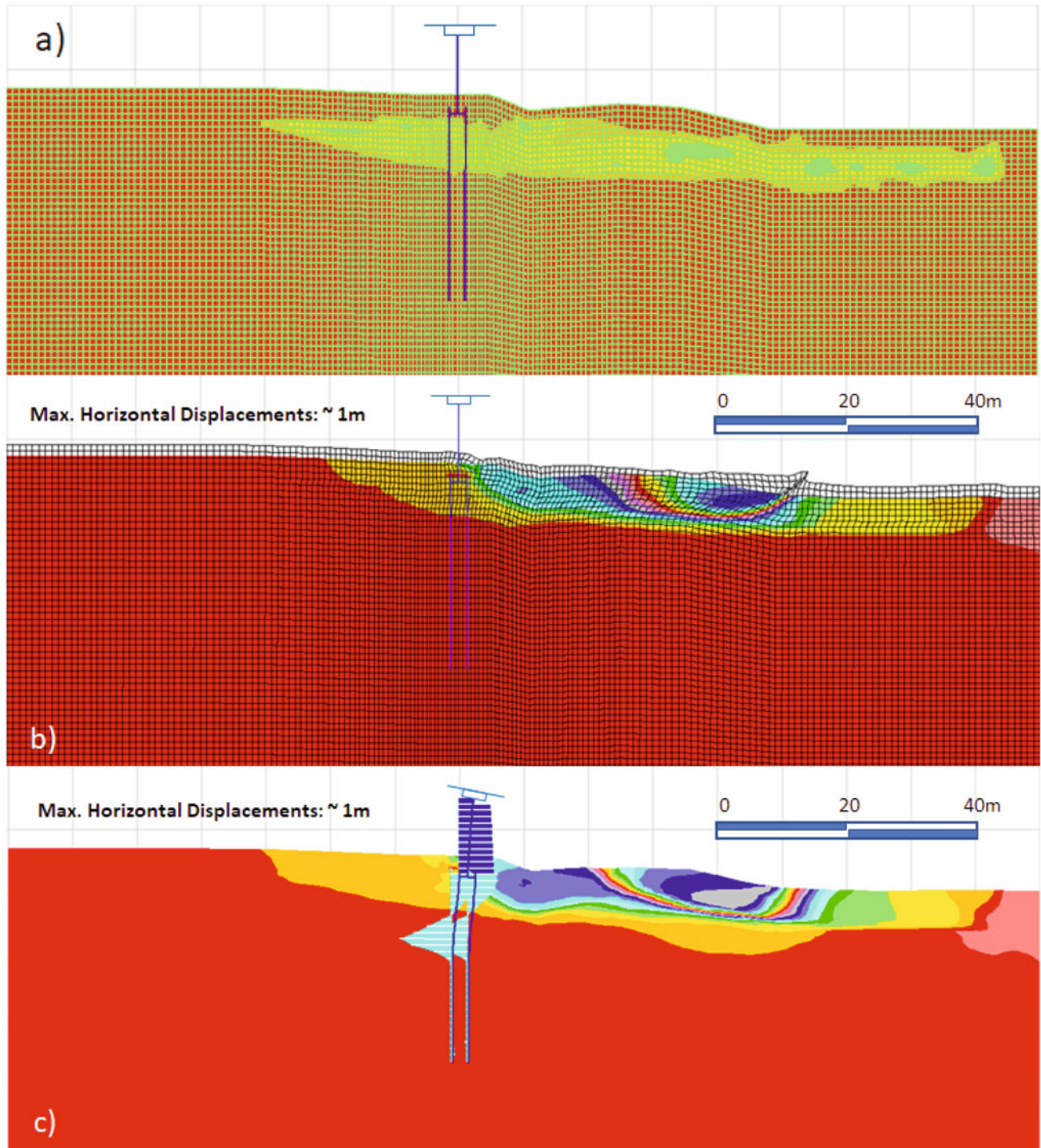


Fig. 16 Example of slope movement predicted for the design of a viaduct where liquefaction results in lateral spread. **a** Excess pore water pressures from ground liquefaction; **b** deformed mesh and contours of horizontal movement; **c** exaggerated structural displacements, axial loads on viaduct column (blue), bending moments in piles (light blue) and contours of horizontal movement

References

- ASCE/SCEC (2002) Recommended procedures for implementation of DMG special publication 117 guidelines for analyzing and mitigating landslide hazards in California. <https://sceinfo.usc.edu/resources/catalog/LandslideProceduresJune02.pdf>
- Bentley (2019) PLAXIS 2D Finite Element Program Version 20. Delft, Netherlands. www.plaxis.com
- Boekmann A, Loehr JE (2013) A procedure for predicting micropile resistance for earth slope stabilization. ASCE GeoCongress, San Diego, CA, USA, pp 2034–2037
- Boulanger RW, Ziotopoulou K (2017) PM4S and (version 3.1): a sand plasticity model for earthquake engineering applications. Report No. UCD/CGM-17/01, Center for Geotechnical Modeling, University of California, Davis
- Bray JD, Rathje EM (1998) Earthquake-induced displacements of solid-waste landfills. ASCE J Geotech Geoenviron Eng 124(3):242–253
- Bray J, Travasarou T (2007) Simplified procedure for estimating earthquake-induced deviatoric slope displacements. ASCE J Geotech Geoenviron Eng 133(4):381–392
- Broms B (1964) The lateral resistance of piles in cohesionless soils. J Soil Mech Found Div Proc ASCE 90(SM3):123–156
- Byrne PM (1991) A cyclic shear-volume coupling and pore-pressure model for sand. In: 2nd international conference on recent advances in geotechnical earthquake engineering and soil dynamics, St. Louis, MI, USA, pp 47–55
- Byrne PM, Park SS et al (2004) Numerical modeling of liquefaction and comparison with centrifuge tests. Can Geotech J 41(2):193–211
- Carder DR, Temporal J (2000) A review of the use of spaced piles to stabilize embankment and cutting slopes. TRL report 466
- Chiu P, Pradel D et al (2008) Seismic response analyses for the silicon valley rapid transit project. In: ASCE geotechnical earthquake engineering and soil dynamics IV, Sacramento, CA, USA, pp 1–10
- Clough RW (1960) The finite element method in plane stress analysis. In: 2nd ASCE conference on electronic computation, Pittsburgh, PA, USA, pp 345–378
- Clough RW, Wilson EL (1999) Early finite element research at Berkeley. In: 5th U.S. national conference on computational mechanics, Boulder, CO, USA. www.smart-fem.de/media/fe-history.pdf
- Duncan JM, Wright SG (2005) Soil strength and slope stability. Wiley, Hoboken, N.J., USA
- Ensoft (2019) Computer program LPILE Version 11, Austin, TX, USA. www.ensoftinc.com
- Griffiths DV, Lane PA (1999) Slope stability analysis by finite elements. Geotechnique 49(3):387–403
- Harp EL, Jibson RW (1995) Inventory of landslides triggered by the 1994 Northridge, California, Earthquake. USGS Open-File Report 95-213. <https://pubs.usgs.gov/of/1995/ofr-95-0213/>
- Hassiotis S, Chameau JL, Gunaratne M (1997) Design method for stabilization of slopes with piles. ASCE J Geotech Geoenviron Eng 123(4):314–323
- Hudson M, Idriss IM, Beikae M (1994) QUAD4M: a computer program to evaluate the seismic response of soil structures using finite element procedures and incorporating a compliant base. Center for Geotechnical Modeling, University of California, Davis
- Idriss IM, Lysmer J et al (1973) QUAD4: a computer program for evaluating the seismic response of soil structures by variable damping finite element procedures. EERC Report 73-16, University of California, Berkeley
- Itasca (2019) FLAC (Fast Lagrangian Analysis of Continua) Version 8.0. Minneapolis, USA. www.itascacg.com
- Ito T, Matsui T (1975) Methods to estimate lateral force acting on stabilizing piles. Soils Found 15(4):43–59
- Ito T, Matsui T, Hong WP (1981) Design method for stabilizing piles against landslide—one row of piles. Soils Found 21(1):21–37
- LimitState (2020) LimiState: geo computer program. Sheffield, UK. www.limitstate.com
- Makdisi FI, Seed HB (1978) Simplified procedure for estimating dam and embankment earthquake-induced deformations. ASCE J Geotech Eng 104(7):849–867
- NAVFAC (1986) Soil mechanics design manual 7.01. Naval Facilities Engineering Command (NAVFAC), Alexandria, VI, USA
- Newmark NM (1965) Effects of earthquakes on dams and embankments. Geotechnique 15(2):139–160
- Peck RB (1969) Advantages and limitations of the observational method in applied soil mechanics. Geotechnique 19(2):171–187
- Pradel D, Smith PM et al (2005) Case history of landslide movement during the Northridge Earthquake. ASCE J Geotech Geoenviron Eng 131(11):1360–1369
- Pradel D (2018) Case history: the Estrondo landslide stabilization in Encino, California. ASCE GeoCongress, Orlando, FL, USA, pp 232–244
- Pradel D, Wartman J, Tiwari B (2013) Failure of the Fujinuma dams during the 2011 Tohoku Earthquake. ASCE GeoCongress, San Diego, CA, USA, pp 1566–1580
- Reese LC, Van Impe WF (2011) Single piles and pile groups under lateral loading, 2nd edn. UK. Taylor & Francis Group, London
- Rocscience (2019) RS2-2019 Finite Element Program. Toronto, Canada. www.rocscience.com
- Schnabel PB, Lysmer J, Seed HB (1972) SHAKE—a computer program for earthquake analysis of horizontally layered sites. EERC Report 72-12, University of California, Berkeley
- Tiwari B, Wartman J, Pradel D (2013) Slope stability issues after Mw 9.0 Tohoku Earthquake. ASCE GeoCongress, San Diego, CA, USA, pp 1594–1601
- Tiwari B, Pradel D et al (2018) Landslide movement at Lokanthali, during the 2015 Earthquake in Gorkha, Nepal. ASCE J Geotech Geoenviron Eng 144(3), No. 05018001
- Wang FI, Makdisi Z-L, Egan J (2006) Practical applications of a nonlinear approach to analysis of earthquake-induced liquefaction and deformation of earth structures. Soil Dyn Earthq Eng 26:231–252
- Yamagami T, Jiang JC, Ueno K (2000) A limit equilibrium stability analysis of slopes with stabilizing piles. In: ASCE slope stability 2000, Denver, CO, USA, pp 343–354



2020 Kyoto Japan

Recent Advances in the Methods of Slope Stability and Deformation Analyses

Beena Ajmera and Binod Tiwari

Abstract

Landslides are among one of the most devastating natural disasters affecting millions of people, causing tens of thousands of deaths and resulting in millions to billions of dollars of damage annually. Examination of historical data suggests an increase in the number of slope failures along with an increase in the two major triggers—an increase in the number of significant earthquakes and wetter than average annual precipitations. These trends highlight the continued need to improve landslide science and understanding. This paper presents a summary of the recent advances in knowledge pertinent to the methods of slope stability and deformation analyses starting with the state of practice as detailed by Prof. J. Michael Duncan in 1996. Specifically, the paper focuses on the improvements to the computational and graphical capabilities with the widespread use and availabilities of computers, the ability to perform macro level stability analysis for regions, the advent of probabilistic slope stability analyses, developments in slope stability analyses of unsaturated slopes, and new methods to perform deformation analyses. Several case studies highlighting these advances are also included.

Keywords

Slope stability • Macro level stability analyses • Probabilistic slope stability • Unsaturated slopes • Deformation analyses • Back-analyses

B. Ajmera (✉)

Department of Civil and Environmental Engineering, North Dakota State University, CIE Building Room 201Q, Dept. 2470, 6050 Fargo, ND 58078, USA
e-mail: beena.ajmera@ndsu.edu

B. Tiwari

Department of Civil and Environmental Engineering, Office of the Research and Sponsored Projects, California State University, Fullerton, 1121 N. State College Blvd., Fullerton, CA 92831, USA
e-mail: btiwari@fullerton.edu

Background

One of the most devastating natural disasters are mass movements such as slope failures, landslides, debris flows, rockfalls, etc. Examination of the number of mass movement disasters around the world from 1903 to 2019 demonstrates an increasing trend, as illustrated in Fig. 1. The mass movements included in Fig. 1 are the number of avalanches, landslides, mudslides, rockfalls, and subsidence. Mass movements included in this figure include the cases with at least one of the following: (1) deaths of at least ten individuals, (2) at least 100 people were reported as being affected, (3) the disaster resulted in the declaration of a state of emergency and/or (4) a call for international assistance. These disasters result in thousands of deaths and billions of dollars of economic damage annually. Figure 2 summarizes the number of reported injuries and deaths around the world from 1903 to 2019, while the number of people affected during this time period is shown in Fig. 3. In Fig. 2, the large number of deaths in 1949 were a result of the Khait Landslide in the Soviet Union, which was triggered by the 1949 Khait Earthquake. The landslide buried 33 villages resulting in a very high death toll (Yablokov 2001). The large number of injuries in 1987, shown in Fig. 2, were primarily from a rainfall-induced landslide in Villatina, Columbia (Ojeda and Donnelly 2006). In Fig. 3, there are four peaks in the number of affected people. The peak in 1996 is a result of a rainfall induced landslide in Rio de Janeiro, Brazil (Jones 1973). In 1986 and 1995, peaks are a result of landslides in India. The 1986 landslide occurred in Uttar Pradesh, India, but information regarding the triggering factor for this failure is not provided (EMDAT 2020). The landslide in 1995 is attributed to a flash flood in Kullu Valley, Himachal Pradesh, India (Prasad et al. 2016). The final peak in Fig. 3 in 2010 is a result of a rainfall-induced slope failure in Guangxi, China (EMDAT 2020). Shown in Fig. 4 are estimates of the economic damage from 1951 to 2019 globally.

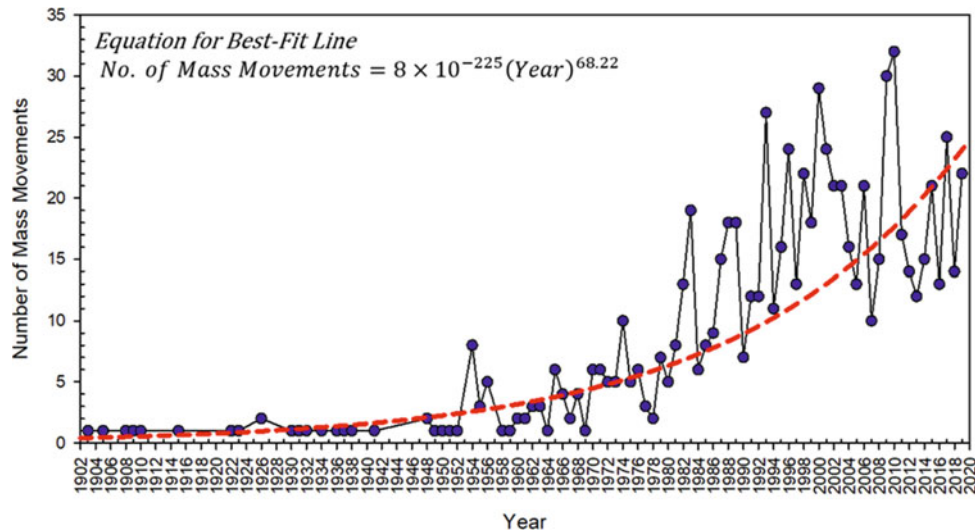


Fig. 1 Number of mass movement disasters reported from 1903 to 2019 (Data from EMDAT 2020). Mass movements included in this figure are avalanches, landslides, mudslides, rockfalls and subsidence

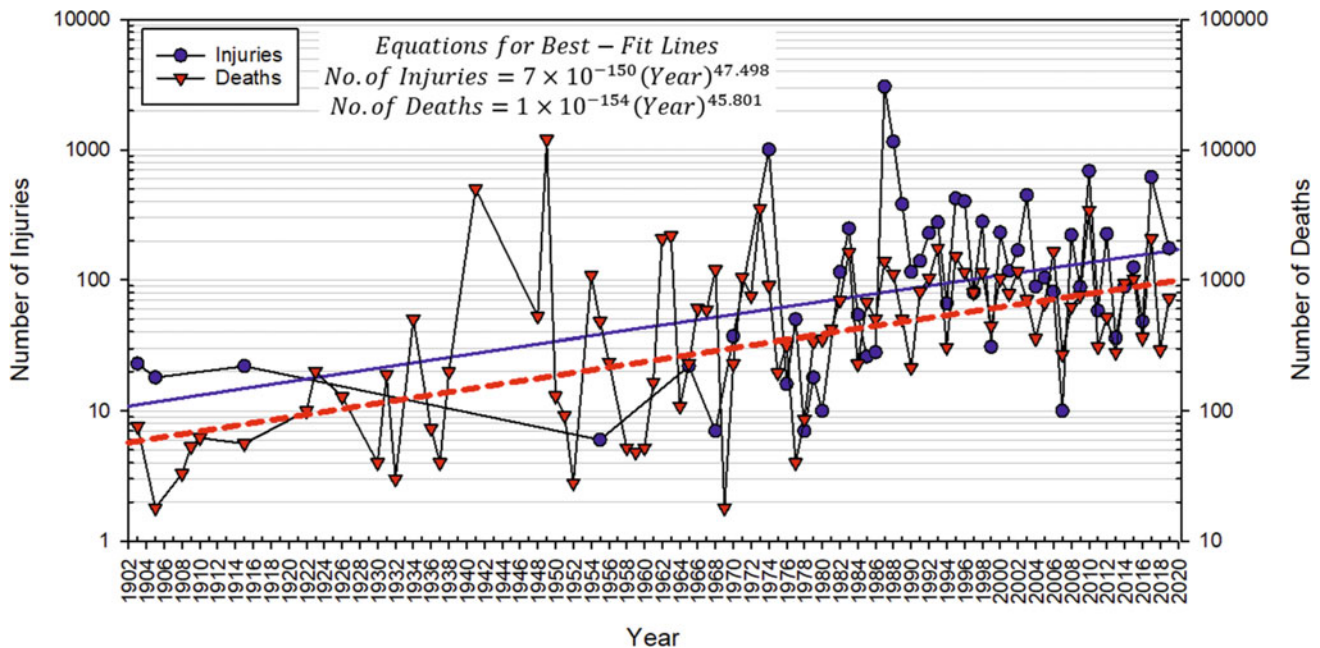


Fig. 2 Global estimates of the number of injuries and deaths from mass movement disasters from 1903 to 2019 (EMDAT 2020)

It is noted that records for the number of mass movement disasters along with resulting deaths and economic damages are more complete in the recent years than the historical records. However, the data still indicates some important trends while illustrating that much work still remains. Specifically, improvements in the understanding of the factors affecting slope stability, development of better analysis methods incorporating new knowledge and better tools combined with the increased technology allowing for slope stabilization, early warning systems, etc. is reflected in the

reductions for the number of deaths seen around the world. On the other hand, increased developments, rising costs of construction and better reporting and estimations of the losses is reflected in the increasing economic damage over the recent years.

Two of the major triggers of slope failures are earthquakes and rainfall. Shown in Fig. 5 are the number of significant earthquakes recorded from 2150 BC to 2017. Significant earthquakes are those events in which at least one of the following occurred: (1) the earthquake resulted in deaths,

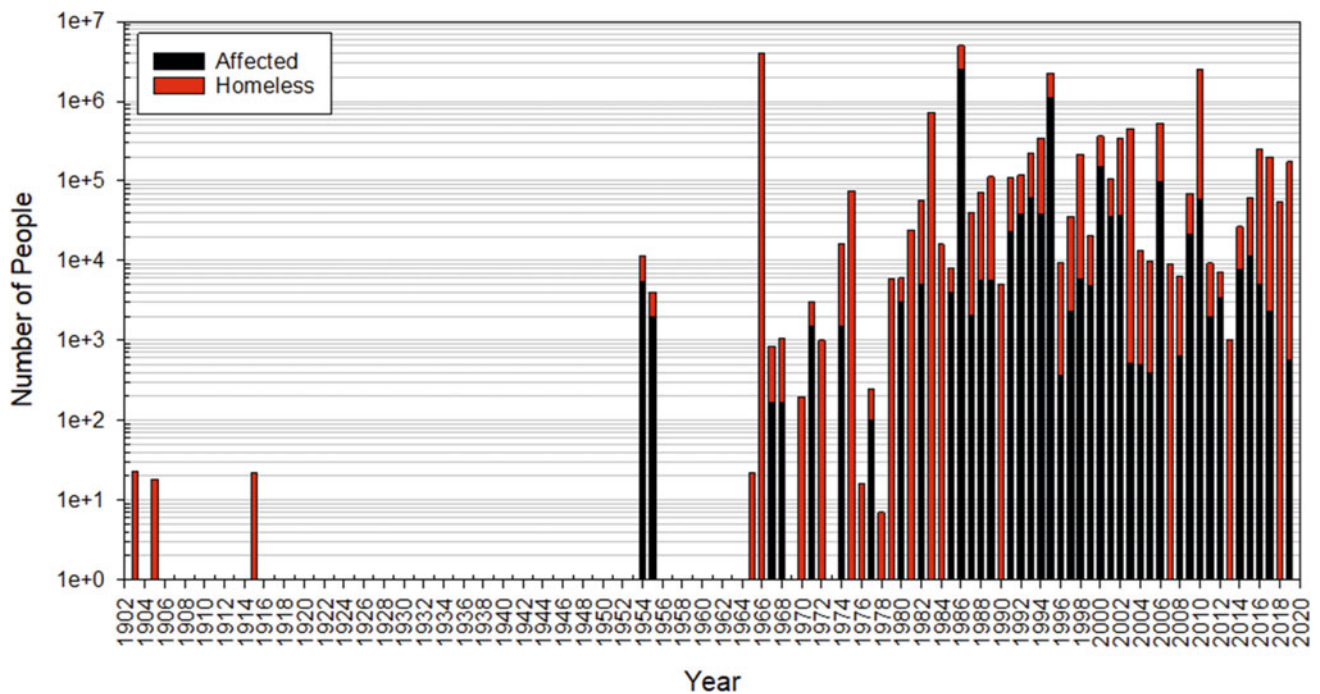


Fig. 3 Estimates of the global number of people affected by landslides by 1903–2019 (EMDAT 2020)

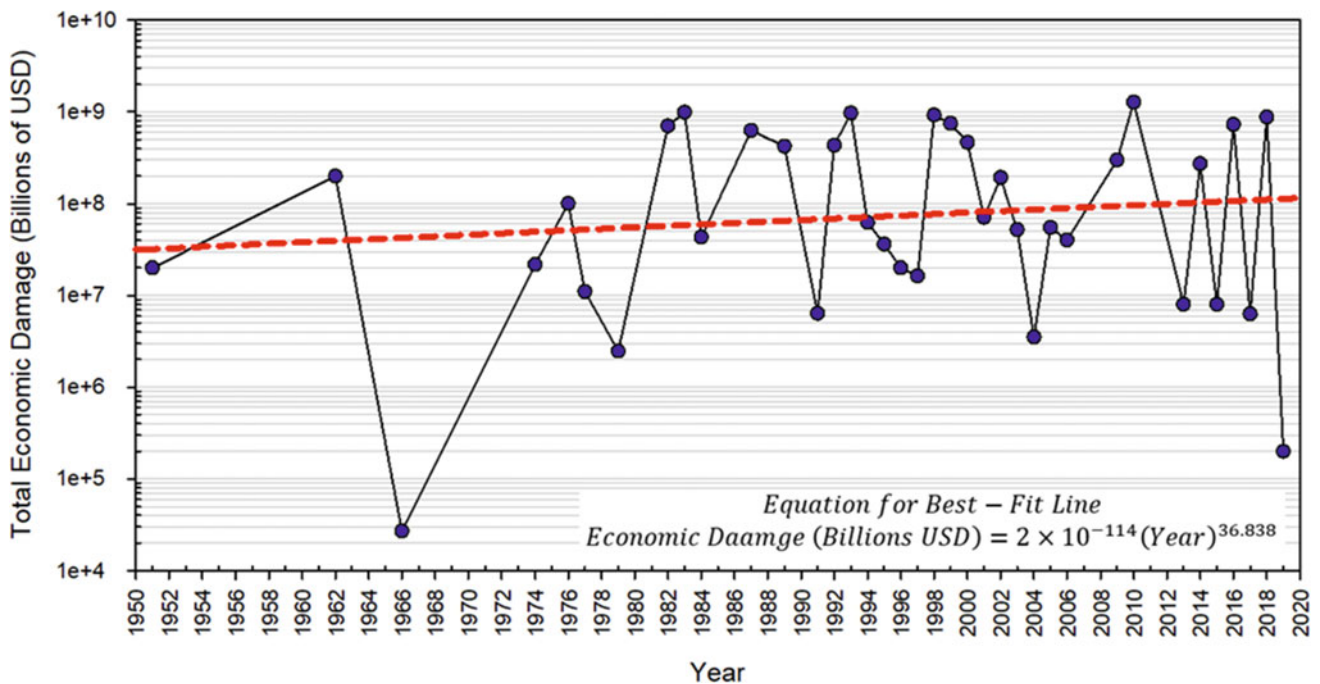


Fig. 4 Economic damage resulting from mass movement disasters in 1951–2019 (EMDAT 2020)

(2) it caused damages of at least one million dollars, (3) the magnitude of the earthquake event was at least 7.5, (4) the Modified Mercalli Intensity (MMI) was X or greater, and/or (5) a tsunami was generated as a result of the earthquake. A look at the historical trends in the number of significant

earthquakes suggest an increase in the number of earthquake events. It is, again, noted that recent records are likely more complete than the older information presented in this figure.

Annual global precipitation anomalies can be used to understand the changes in precipitation occurring each year.

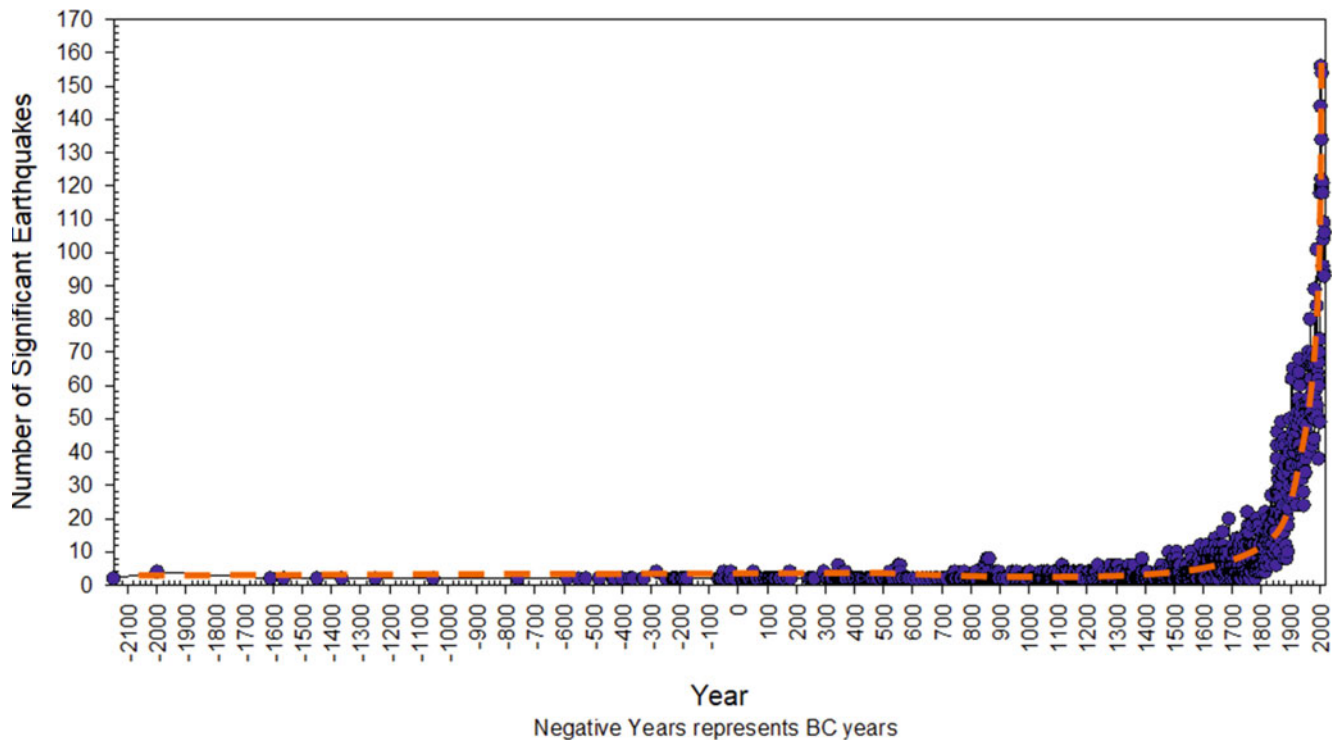


Fig. 5 Number of significant earthquakes around the globe from 2150 BC to 2017 (NOAA 2020)

The annual precipitation anomaly was the difference between the total annual precipitation at each weather station and the average precipitation at that station over the century defined from 1901 to 2000. The annual global precipitation anomaly was then computed by dividing the world into a grid. In each grid cell, the average precipitation anomaly was calculated by taking the mean of the annual precipitation anomalies from each weather station. Averaging these values across the grid yielded the annual global precipitation anomaly. Figure 6 shows the variation in the global precipitation anomaly from 1901 to 2015. Positive numbers represent that the annual precipitation during that year was greater (wetter) than the average precipitation over the 100 years from 1901 to 2000, while negative values indicate that the annual precipitation was less (drier) than the average precipitation. The figure illustrates that 30 of the past 50 years from 2015 and 11 of the last 15 years from 2015 have experienced wetter than average rainfalls. The increases in the precipitation observed in Fig. 6 may be attributed to climate change. More evaporation is expected to occur as the average temperature of the surface of the Earth increases. An increase in evaporation will translate to increases in the amount of precipitation that occurs (Bluden and Arndt 2016).

Since earthquakes and rainfall events are two of the major triggers of slope instabilities around the world, the increase in the number of significant earthquake events combined with the trends towards higher than average annual

precipitations around the world and increasing urban and infrastructure development to meet the demands of growing populations suggest that an increasing number of slope failures may be observed. The disastrous consequences including casualties, injuries and substantial economic losses highlight the continued need to improve landslide science and understanding. It is, therefore, not surprising to see the significant number of people around the world that have made great strides in landslide science. Through this paper, the authors will attempt to summarize some of the recent advances in slope stability methods and deformation analyses.

Historical Perspective of Slope Stability and Deformation Analyses

The last comprehensive summary of the state of practice of slope stability and deformation analyses was prepared by Prof. J. Michael Duncan nearly 25 years ago in 1996 (Duncan 1996). Since his summary, there have been many developments in landslide science that pertain to both topics. Before these new developments are discussed, it seems pertinent that a brief summary of the state of practice in 1996 be provided.

By 1996, the landslide community had a strong understanding of the parameters and soil properties that should be

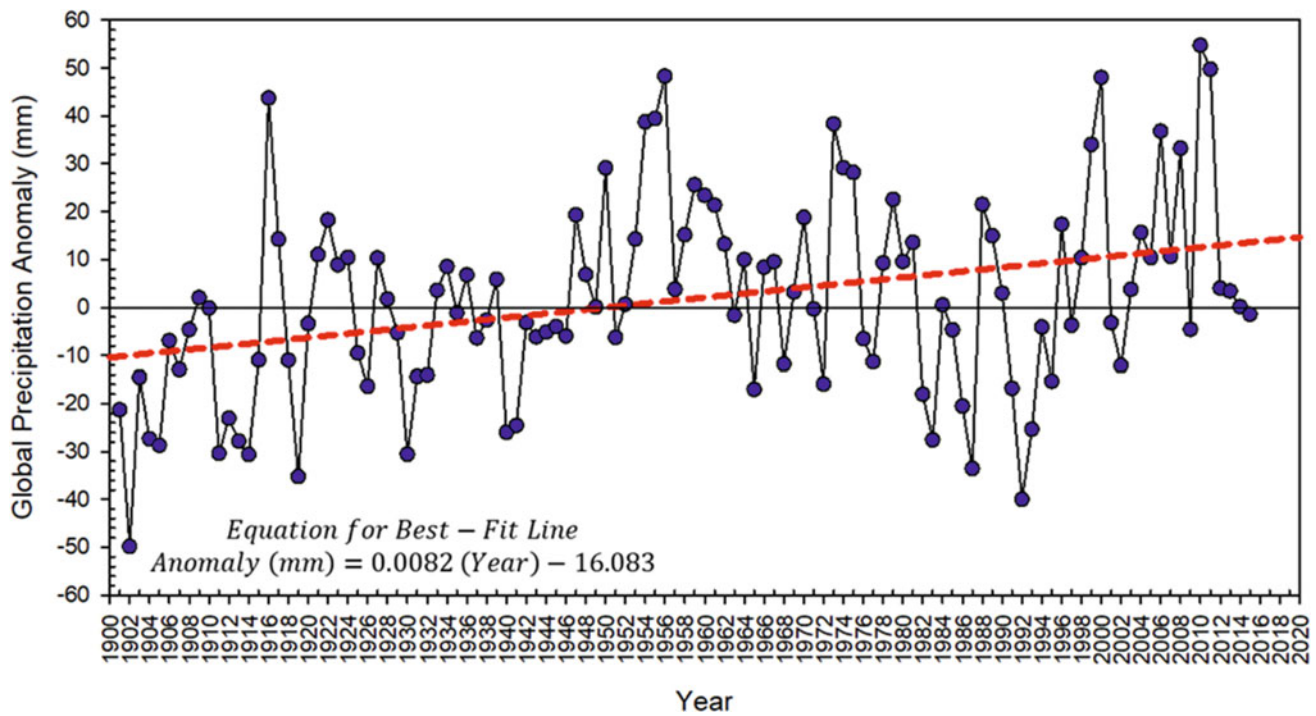


Fig. 6 Global precipitation anomaly from 1901 to 2015 (US EPA 2016)

used in evaluating the stability of slopes at the end of construction, when considering multistage loading and in the long term. Duncan (1996) summarized this information as shown in Table 1. In addition, several different methods were available to analyze the stability of slopes under plane strain (two-dimensional) simplifications. A summary of these methods and their associated assumptions were provided in Duncan (1996). Three-dimensional slope stability analyses were starting to appear in the literature with the majority of the studies focused on comparing factors of safety obtained from three-dimensional analyses to those calculated from two-dimensional methods. After closely

examining the studies in which factors of safety from the latter were less than the former, Duncan (1996) concluded that the factor of safety obtained using three-dimensional analyses should be greater than those obtained from two-dimensional methods in agreement with Cavounidis (1987).

On the topic of deformation analyses of slopes, Duncan (1996) summarized the methods developed by Poulos et al. (1972), Resendiz and Romo (1972), Clements (1984) and Walker and Duncan (1984). However, the paper focused on the use of finite-element analyses to estimate the deformations. This technique was introduced about thirty years

Table 1 Parameters and soil properties to use in slope stability analyses for different types of soils (Adapted from Duncan 1996)

Condition	Free-draining layer	Impermeable layer
End of construction	<ul style="list-style-type: none"> • Use total unit weights • Include external water pressures and internal pore pressures from steady state seepage analyses 	<ul style="list-style-type: none"> • Use total unit weights • Include external water pressures, but not internal pore pressures • Use total stress shear strength parameters
Multistage loading	<ul style="list-style-type: none"> • Use effective shear strength parameters 	<ul style="list-style-type: none"> • Use total unit weights • Include external water pressures, but not internal pore pressures • Use undrained cohesion for the shear strength
Long term		<ul style="list-style-type: none"> • Use total unit weights • Include external water pressures and internal pore pressures from steady state seepage analyses • Use effective shear strength parameters

earlier by Clough and Woodward (1967). Duncan (1996) summarized the characteristics and limitations, and provided guidance on the use of the linear elastic, multilinear elastic, hyperbolic, elastoplastic and elastoviscoplastic stress–strain relationships. Using the New Melones Dam as a case study, he concluded that finite-element deformation analyses could accurately predict the behavior of the dam and illustrated its use towards designing the instrumentation for the dam.

Developments in Slope Stability and Deformation Analyses

In the 25 years since Duncan (1996), there have been many advances in slope stability and deformation analyses. Some of the advances the landslide community has seen include: improved computational and graphical capabilities with the widespread use of computers, the ability to perform macro levels stability analyses for regions, growth in three-dimensional analyses, the advent of probabilistic slope stability analyses, developments in the stability analysis of unsaturated slopes, and new methods to perform deformation analyses. Each of these will be discussed in more detail in the following subsections.

Improvements to Computational and Graphical Capabilities

Duncan (1996) summarized a vision by Whitman and Bailey (1967) about how computers may be used in the evaluation of slope stability in the future. He commented that when he wrote that paper, the computation power available to geotechnical engineers was making a reality of their vision, but today, the personal computers with their powerful hardware and graphical capabilities that each engineer has at their fingertips far surpasses their vision. A quick search yields a list of over 50 commercial programs that can be used by geotechnical engineers to perform two-dimensional and/or three-dimensional stability analyses using a variety of methods from very simple to highly complicated. Duncan (2013) noted that some of these programs allow for the performance of computations that are so complex that it is impossible to verify the results without the use of another program. Citing the floodwall failures in New Orleans after Hurricane Katrina in 2005, he illustrates that SLIDE (RocScience, Inc. 2002), UTEXAS (Wright 2004) and SLOPE/W (GEO-SLOPE 2018) were all, at the time, ill-equipped to handle the hydraulic fracturing induced cracks in the back of the floodwalls, which without the use of multiple computer programs could have gone undetected yielding incorrect results. This issue was later resolved in all three of these programs (Duncan 2013). As a result, it is

recommended that the analyses be performed using at least two different programs to ensure that an error has not been made.

Outside of the numerous commercial programs available, spreadsheets are also a powerful and simple tool that can be used to evaluate the stability of slopes, to search for critical failure surfaces, and to perform probabilistic slope stability analyses (Duncan 2013). Ajmera and Tiwari (2018) provided detailed step-by-step procedures for the creation of Excel spreadsheets to determine the factor of safety for four commonly used slope stability methods. These are the Ordinary Method of Slices (Fellenius 1927), Bishop's Simplified Method (Bishop 1955), Simplified Janbu Method (Janbu et al. 1956; and Janbu 1973) and the Lowe and Karafiath Method (Lowe and Karafiath 1959). The use of spreadsheets to perform probabilistic slope stability analyses was described by several researchers including Low (2003), Low and Tang (2004, 2007) and Cao et al. (2017).

Case Study

A landslide located at the 62+000 km station along the Charali-Ilam Road in Ilam District in the Eastern Development Region of Nepal is used as an example to demonstrate the power of Excel spreadsheets. The landslide, which first occurred before 1984 and reactivated in 1992, covers approximately 12 hectares of land. In August 1994, due to the excessive rainfall in the region, the landslide was responsible for the collapse of 64 m of the Charali-Ilam road and caused settlements of more than 30 cm per day. Figure 7 contains an aerial view of the slope failure. A topographic map of the region from Tiwari and Douglas (2012) is shown in Fig. 8. Additional details of this landslide can be found in Tiwari and Durate (2013). A cross-section along the center of the slope failure in Block A (Fig. 9) was analyzed using Excel spreadsheets developed using the procedures outlined in Ajmera and Tiwari (2018) and compared with those obtained using RocScience Slide 6.0 (RocScience, Inc. 2002). For simplicity in the Excel spreadsheet calculations, a saturated unit weight of 18.66 kN/m³, representing the weighted average of the saturated unit weights by depth of the sliding mass was used. The cohesion and friction angle along the sliding surface were taken to be 0 kPa and 28.6°, respectively. The same parameters were also used in the RocScience Slide model for equivalent comparisons.

A summary of the factors of safety obtained from the Ordinary Method of Slices, Bishop's Simplified Method and the Lowe and Karafiath Method using the Excel Spreadsheets and from the RocScience Slide model are presented in Table 2. As seen from Table 2, the factors of safety values from the Excel Spreadsheets differed by less than 5% of those calculated using RocScience Slide 6.0, illustrating the powerful nature of spreadsheets. The authors note that although they made some simplifying assumptions to the



Fig. 7 Aerial view of the slope failure at station 62+000 km on the Charali-Ilam Road (Source Tiwari and Duarte 2013)

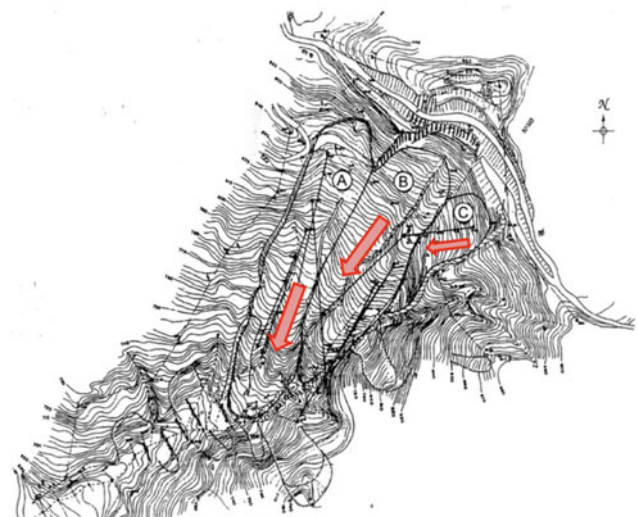


Fig. 8 Topographic map of the landslide showing block divisions (Source Tiwari and Douglas 2012)

Fig. 9 Cross section analyzed at the Center of Block A (Source Tiwari and Douglas 2012)

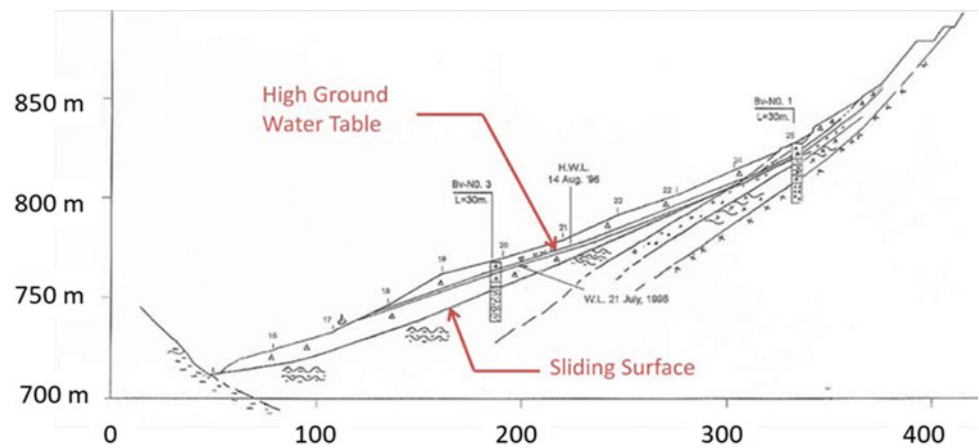


Table 2 Comparisons of factors of safety calculated using excel spreadsheets and RocScience Slide 6.0

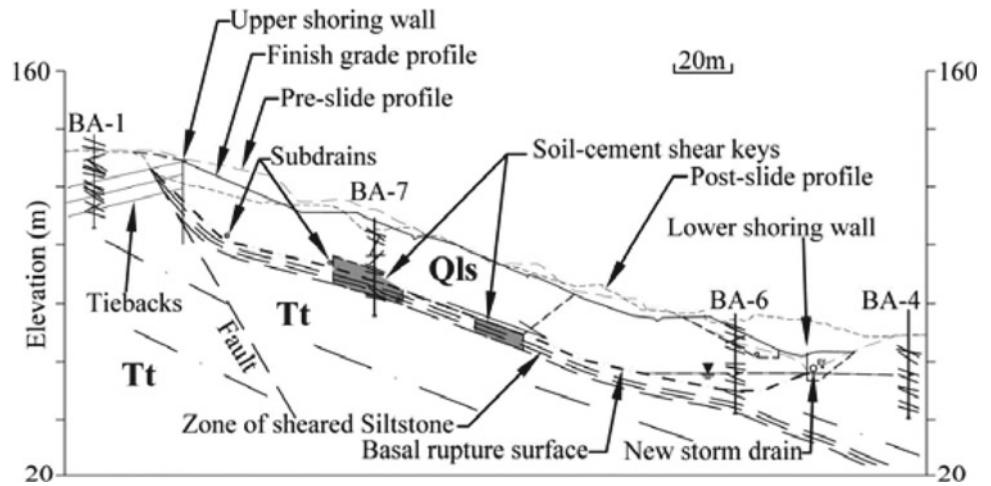
Method	Excel Spreadsheets	Rocscience Slide 6.0	Diff. (%)
Ordinary Method of Slices	1.09	1.05	3.8
Bishop’s Simplified Method	1.03	1.07	3.7
Lowe and Karafiath	1.06	1.11	4.5

models to perform these calculations, the inclusion of a few additional columns would have allowed for the inclusion of stratigraphy. Similarly, the inclusions of landslide repairs works, pseudo-static analyses and external loading conditions could also be easily built into the spreadsheets.

Case Study

Tiwari et al. (2010) performed over 140 different seismic slope stability analyses on a cross-section of the 2005 Bluebird Canyon Landslide (Richter and Trigg 2008), shown in Fig. 10, to evaluate how different two-dimensional

Fig. 10 Cross-section of the Bluebird Canyon landslide analyzed in Tiwari et al. (2010) (Source Richter and Trigg 2008)



slope stability methods will respond to the seismic excitation and variations in the ground water table. They performed each of the analyses using RocScience Slide for nine different methods, which include the Ordinary Method of Slices, Bishop Simplified, Janbu Simplified, Janbu Corrected, Spencer, Morgenstern and Price, and two Army Corp of Engineers Methods. Excel spreadsheets were also used to perform the slope stability calculations using Bishop's Simplified Method.

An example of the results obtained from Tiwari et al. (2010) is shown in Fig. 11, which presents the values of the factors of safety for each of the different methods as a function of the depth to the water table when the slope is not subjected to seismic loading. The results obtained show that the Ordinary Method of Slices yielded the most conservative values for the factor of safety. Figure 12 contains two sets of results for two different seismic coefficients of 0.1 and 0.5 for each of the different methods. While not all of the

methods are recommended for seismic slope stability analyses, pseudo-static analyses were performed using all of them (Tiwari et al. 2010). They found that it was not

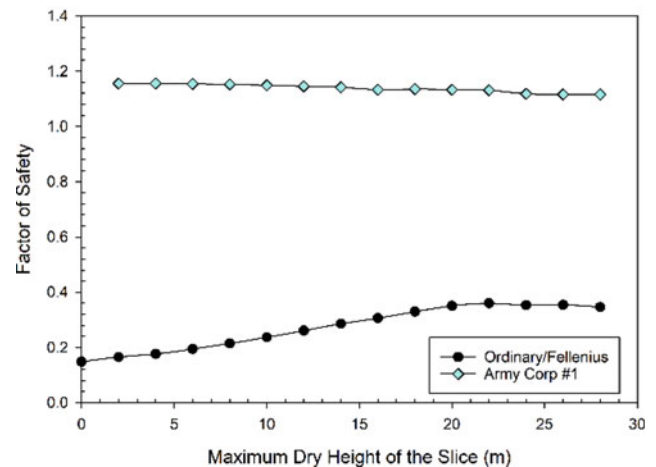
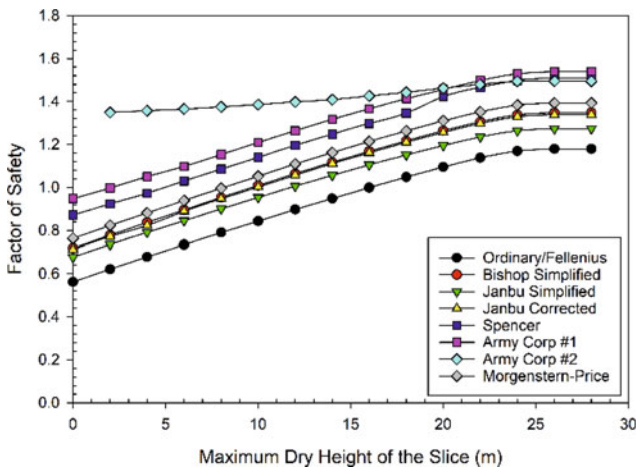
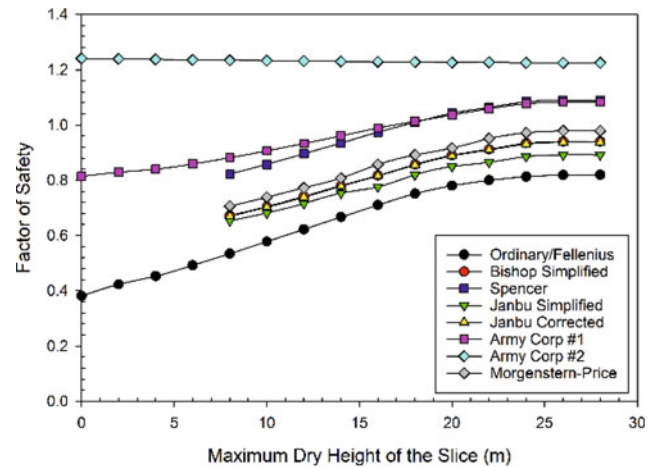


Fig. 11 Comparison of the variation in the factors of safety with depth to the water table for each of the nine methods used (Adapted from Tiwari et al. 2010)

Fig. 12 Factors of safety computed from each of the different methods evaluated for seismic coefficients of (top) 0.1 and (bottom) 0.5 (Adapted from Tiwari et al. 2010)

possible to compute the factor of safety for all of the seismic coefficients using all of the methods. In fact, only two methods could be used for all of the seismic coefficients studied. The computational tools available to engineers today allow for such parametric studies to be performed easily providing a better understanding and a comparison of the different scenarios.

Macro Level Stability Analysis for Regions

Recent advances in technology and the increasing availability of digital data has made it possible to perform macro level slope stability for regions. These macro level slope stability analyses allow geotechnical engineers to develop landslide susceptibility maps, prioritize mitigation efforts and better understand the influence of different factors on slope failures. Many approaches have been proposed to evaluate landslide hazards on a regional scale. Some of these approaches include:

- (a) Site investigations to identify and map slopes that may be susceptible to failure (Neely and Rice 1990),
- (b) Determination of patterns from slope failures to predict future instabilities (DeGraff and Canuti 1988; Wright et al. 1974; and DeGraff 1985),
- (c) Multivariate analyses of factors that will influence slope instabilities based on previous observations (Carrara et al. 1977; Pike 1988; Mark 1992; Roth 1982; Carrara 1983; and Neuland 1976),
- (d) Development of rankings of instability likelihood based on causative factors (Anbalagan 1992; Anbalagan and Singh 1996; Hollingsworth and Kovacs 1981; Brabb et al. 1972; Smith 1988; Campbell 1975; Fowler 1984; Seely and West 1990; Skirrikar et al. 1998; Dhakal et al. 1999; Pathak and Nilsen 2004; and Montgomery et al. 1991),
- (e) Probability based analyses (Hammond et al. 1992; Sidle 1992; Burroughs 1984; Bourroughs et al. 1985; and Dunne 1991), and
- (f) GIS based methods (Varnes 1984; Hansen 1984; van Westen 1994; Bonham-Carter 1994; Carrara et al. 1995; Hutchinson 1995; Soeters and van Westen 1996; van Westen et al. 1997; Aleotti and Chowdhury 1999; Guzzetti et al. 1999; Gorsevski et al. 2003; Thapa and Dhital 2000; Dhital 2000; Saha et al. 2002; Sarkar and Kanungo 2004; Bhattarai et al. 2004; Tiwari et al. 2004).

Approaches (b) and (c) has been extensively used in earthquake-induced slope failures with the creation of databases with instabilities dating back to the 1960s. Some examples of such studies include: Bonilla (1960), Plafker

et al. (1971), Morton (1971), Morton (1975), Harp et al. (1981, 1984, 2011), Rymer (1987), Rymer and White (1989), Keefer and Wilson (1989), Harp and Keefer (1990), Harp and Jibson (1996), Fukuoka et al. (1997), Keefer and Mason (1998), Bozzano et al. (1998), Okimura and Torii (1999), Esposito et al. (2000), Marzorati et al. (2002), Wang et al. (2003), Sassa et al. (1995), Keefer (2000, 2002), Sato et al. (2005, 2007), Chigira and Yagi (2006), Mahdaviifar et al. (2006), Zhang and Wang (2007), Yamagishi and Iwahashi (2007), Kamp et al. (2008), Qi et al. (2010), Gorum et al. (2011), Xu et al. (2012a, b), Alfaro et al. (2012), Collins et al. (2012), Lacroix et al. (2013), Wartman et al. (2013) and Tiwari et al. (2017).

Anbalagan (1992) and Anbalagan and Singh (1996) proposed the landslide hazard evaluation factor approach, which is a numerical rating scheme that assigns different values to causative factors based on their impact towards slope instabilities. In their method, geology, slope morphology, relative relief, land use and land cover, and groundwater conditions are considered as the causative factors. A rating value is assigned to each of these factors with higher values corresponding to greater landslide risk. Anbalagan (1992) summarizes the appropriate ratings for different categories of the causative factors. The sum of these ratings is taken as the landslide hazard evaluation factor, which can have a maximum value of ten. Higher values of the landslide hazard evaluation factor correspond to higher hazard potentials. A limitation of landslide hazard evaluation factor approach is major triggering factors such as earthquakes and rainfall events are not included in the hazard assessment.

Most of the studies that use GIS based methods do so to create maps delineating regions of landslide hazards by extending different concepts of the landslide hazard evaluation factor. They focus on demarking zones of different levels of hazards focusing on a variety of spatial data including geology, surface cover, land use, relief, slope characteristics, etc. However, GIS can be a very powerful tool that allow for detailed slope stability analyses at the micro and macro scales. Example of its use for stability analyses at the macro scale is presented here, while a subsequent section in this paper will discuss the use of GIS to perform three-dimension slope stability analyses.

Case Study

Bhattarai et al. (2004), Tiwari et al. (2008), and Tiwari and Do (2011) used ArcGIS to perform automated three-dimensional factor of safety calculations for a 200 km Krishanabhi-Kurintar sector of the Prithvi Highway in Nepal to assist local highway maintenance authorities in prioritizing roadside maintenance and bridge protection works. A picture of a slope failure observed along this sector is given in Fig. 13. Given the difficulties of predicting the

exact volume and configuration of mass movements combined with the need to have realistic modelling to ensure valuable results, Bhattarai et al. (2004) and Tiwari et al. (2008) determined equivalent depths of one-dimensional failure planes that yield equivalent factors of safety as that from a three-dimensional analysis. To do so, they used 100 three-dimensional existing slope failures to back-calculate one-dimensional depths to the sliding surface when the slopes had a factor of safety of one, as expressed by Eq. 1. In this equation, c is the cohesion, γ is the unit weight, ϕ is the friction angle, n is the number of slices in the rotational failure, z_i is the average depth to the sliding plane for the i -th slice in the rotational failure, β is the inclination of the one-dimension sliding plane and z is equivalent depth. The results were then grouped based on the geological and geomorphological conditions of the slope areas. As less than 18% variation in the equivalent one-dimensional depths to the sliding surface were found within each of the ten petrological zones in the study area, Bhattarai et al. (2004) assigned a constant sliding zone depth to each of those regions in their ArcGIS model.

$$FS_{rotational} = FS_{translational} = 1 \quad (1)$$

$$= \frac{c + (\gamma \cdot \tan\phi) \cdot \sum_{i=1}^n (z_i \cdot \cos^2\beta)}{\gamma \cdot \sum_{i=1}^n (z_i \cdot \sin\beta \cdot \cos\beta)} = \frac{c + \gamma \cdot z \cdot \cos^2\beta \cdot \tan\phi}{\gamma \cdot z \cdot \sin\beta \cdot \cos\beta}$$

The parameters needed to perform the slope stability analyses were inputted into ArcGIS. Samples from over 170 different locations were tested to establish the unit weights and shear strength parameters required. Bhattarai et al. (2004) noted that the friction angle and cohesion values with each petrological zone varied by less than 10% and therefore, assigned constant cohesion and friction angle values to

each of the ten zones within the study area based on the petrological regions. The peak (ϕ'_{peak}) and residual (ϕ'_r) friction angles used in the study for each zone are summarized in Table 3. Contours relating the unit weights to the spatial location were used to determine the density at any point. No information regarding the ground water level in the study area was available. As the ground water table will have a significant influence on the factor of safety obtained, Bhattarai et al. (2004) and Tiwari et al. (2008) developed watershed polygons using ArcHydro based on stream levels and digital elevation models (DEMs) in the region. With this information, Bhattarai et al. (2004) was able to calculate the factor of safety for each 1 m by 1 m cell in the model using the Spatial Analyst tool. Through their verification of the results with field testing, they found that 80% of the recorded slope failures in the region were in the low stability zones identified in the ArcGIS model, while the remaining 20% were in the medium stability zone.

Later, Tiwari and Do (2011) performed a parametric study to examine the influence of the ground water table as well as seismicity in the area. They developed hazard level maps for pore pressure ratios (defined as the ratio of the depth of the water above the sliding plane to the depth to the sliding plane) ranging from 0 to 1. In their analyses, they considered different seismic coefficients ranging from 0.05 to 0.5. Three examples of the hazard level maps they developed are shown in Fig. 14. Factors of safety in cells of very high hazard were less than 1.2. In high hazard cells, the factor of safety was calculated to be between 1.2 and 2. Medium, low and very low hazard cells had factors of safety between 2.0 and 3.0, 3.0 and 4.0 and greater than 4.0, respectively. Tiwari et al. (2008) noted that the concurrent occurrence of an earthquake during a rainfall event could increase the hazard potential by 2.4 times. Their results illustrated how the ground water conditions and seismicity in the region could impact the hazard potential. Combinations



Fig. 13 Picture of slope failure along the Krishanabhi-Kurintar sector of the Prithvi Highway in Nepal (Source Bhattarai et al. 2004)

Table 3 Peak and residual friction angles assigned to each petrological zone (Adapted from Bhattarai et al. 2004)

Zone no.	ϕ'_{peak} (°)	ϕ'_r (°)
1	24	22
2	32	31
3	28	26
4	28	27
5	21	20
6	35	33
7	27	26
8	28	28
9	26	24
10	26	23

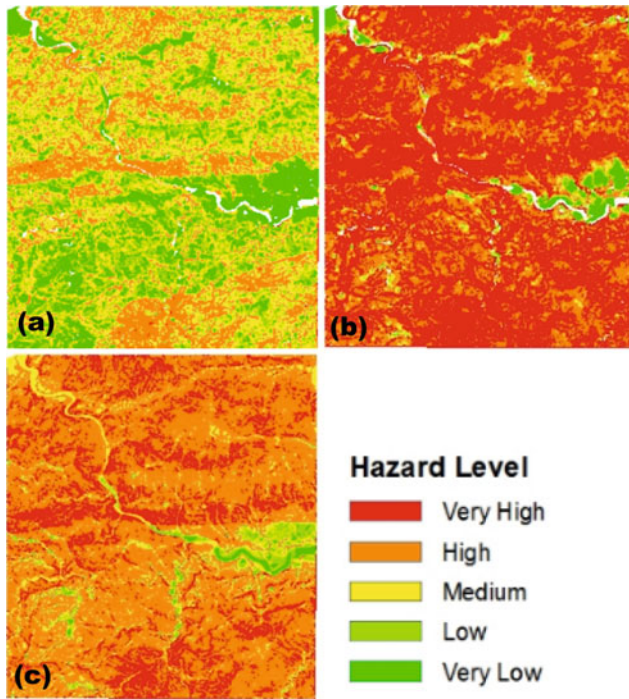


Fig. 14 Distribution of hazards for **a** dry slope with no earthquake, **b** saturated slope with no earthquake, and **c** dry slope with earthquake with seismic coefficient of 0.5 (Adapted from Tiwari and Do 2011)

of both factors could be easily studied for the entire region once the ArcGIS model was developed.

Case Study

Using the 3D Deterministic Analysis Method, Tiwari et al. (2004) and Tiwari (2007) performed a macro level study on the Higashi Kubiki County of the Niigata Prefecture, Japan utilizing ArcGIS tools. They modify the method proposed by Hovland (1977) to perform the analyses. The resolution of forces for the stability analyses is detailed in Fig. 15, which shows that the landslide area was divided into a series of vertical columns to determine the factor of safety of the slope. Following the modifications, the factor of safety can be calculated using Eqs. 2 and 3, in which ψ is the strike as described by Hovland (1977), A is the aspect of the steepest sliding surface, ψ_0 is the orientation of the displacement vector, and β is the steepest slope of the sliding surface.

$$FS = \frac{\sum_x \sum_y A + \sum_x \sum_y B}{\sum_x \sum_y C} \quad (2)$$

where,

$$A = \frac{c \cdot \sin\theta}{\cos\alpha_{xz} \cdot \cos\alpha_{yz}}$$

$$B = \left(\gamma \cdot z \cdot \cos\beta - \gamma_w \cdot h_w \left(\frac{\sin\theta}{\cos\alpha_{xz} \cdot \cos\alpha_{yz}} \right) \right) \tan\phi$$

$$C = \gamma \cdot z \cdot \sin\alpha_{yz}$$

$$\alpha_{xz} = A \cdot \tan(\cos\psi \cdot \tan\beta) \quad (3)$$

$$\theta = A \cdot \cos(\sin\alpha_{yz} \cdot \sin\alpha_{xz})$$

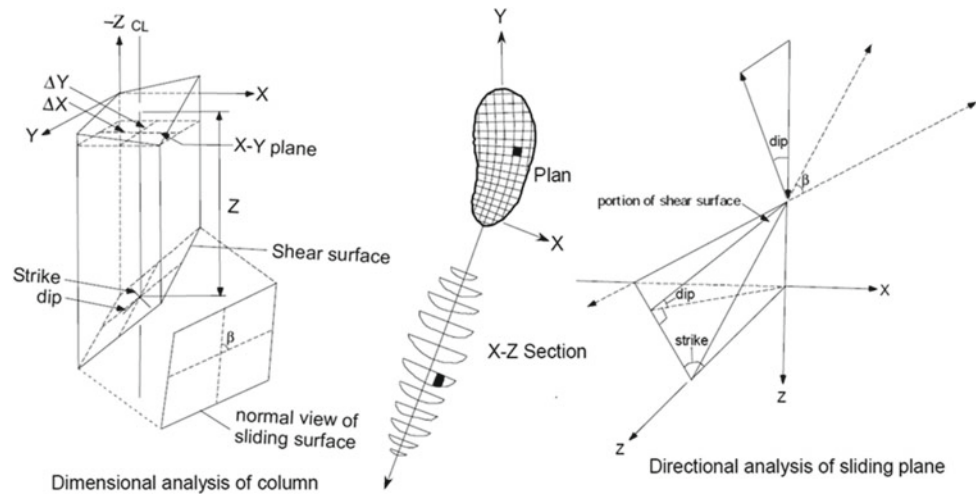
where,

$$\psi = 90 - (A - \psi_0)$$

Unit weights and shear strength parameters were assigned based on the soil/rock types using the results from a sequence of laboratory tests conducted on samples obtained from the study area. Weighted average values based on the depth of the soil/rock type were used to establish the average unit weight of the column. Using the results from Fukumoto (2004), Tiwari et al. (2004) noted that the majority of landslides in the region had width to length ratios of 0.3–0.7 and width to depth ratios between 4 and 10. Thus, they stated landslide blocks 100 m long, 50 m wide and 8 deep were representative three-dimensional blocks for the expected slope failures. Tiwari et al. (2004) further assumed that the sliding surfaces were ellipsoidal. They prepared slope units in the region with the use of reverse DEMs. Reverse DEMs are DEMs with mirrored contour fields; that is, contour fields equal to -1 times the original contour value. Slope units were established by dissecting two watershed polygons that corresponded to flow accumulations in the DEM and reverse DEM. These polygons are developed by connecting ridges to ridges and valleys to valleys in the DEM and reverse DEM, respectively, with the use of ArcGIS 3D Analyst tools. Spatial Analyst tools in ArcGIS were used to determine the parameters required to compute the factor of safety using Eqs. 2 and 3 using columns that had dimensions of 10 m by 10 m in plan. A comparison of the results obtained with the existing failures in the region showed that 83% of these failures were located in very high and high hazard zones, in which the factors of safety were computed to be less than 2 (Tiwari et al. 2004). They noted that in such macro level analyses, the hazard potential should be evaluated as opposed to the absolute value of the factor of safety due to the various uncertainties in the model.

The case histories presented here illustrate the possibilities of using ArcGIS models to perform quantitative hazard assessment as opposed to the development of hazard zonation maps. The use of ArcGIS could also be easily extend to the finite element methods using a procedure called 3D FEM GIS (Tiwari et al. 2004). Tiwari (2007) noted that additional layers should be added to the ArcGIS model such

Fig. 15 Resolution of forces for three-dimensional stability analyses using Hovland's method (Source Hovland (1997) modified by Tiwari et al. (2004))



as a map of the infrastructure in the region, using which the potential risk to a community could be ascertained. These risk calculations could include considerations for the location of the infrastructure and their associated importance along with the spatial distribution and densities of individuals. Such information could allow stakeholders to determine the vulnerability of a region to existing or potential landslide risks.

Growth of Three-Dimensional Slope Stability Analyses

Three-dimensional slope stability analysis methods have been used since 1969 with the first method proposed by Anagnosti (1969) as an extension of the Morgenstern and Price (1965) method. Since then, several three-dimensional slope stability analyses methods have been proposed. The majority of these methods are extensions of two-dimensional approaches (Kalatehjari and Ali, 2013). Duncan (1996) summarized the available three-dimensional slope stability methods at the time he wrote his paper. However, several new three-dimensional methods have been proposed by various researchers since then. Some of the methods not discussed in Duncan (1996) or proposed after are summarized here.

Extending the Azzouz and Baligh (1978) method for vertical cuts in cohesive soils, Cavounidis and Kalogeropoulos (1992) proposed a three-dimensional method for cylindrical slip surfaces with conical ends. They assumed that the axis of rotation corresponded to the crest of the vertical cut and calculated factors of safety using the moment equilibrium equation. They found that although the factor of safety from the three-dimensional method was greater than that obtained from two-dimensional calculations, the difference between the values decreased as the

length of the cylindrical central section increased when keeping the length of the conical ends constant.

A generalized three-dimensional slope stability analysis method based on variational analysis and rigorous limit equilibrium analysis was proposed by Leshchinsky and Huang (1992a). This method is an extension of a two-dimensional slope stability method proposed by Leshchinsky and Huang (1992b) and assumes that the slip surface is an extended log-spiral or a symmetrical surface. Factors of safety are calculated by solving a series of simultaneous linear equations and three nonlinear equations using an iterative process.

Extensions of the Simplified Bishop Method and the Simplified Janbu Method to three-dimensions were proposed by Hungr et al. (1989). In doing so, they neglected all of the inter-column shear forces. They assumed that all of the shear forces along the failure surface were parallel to the line of symmetry. They also assumed the failure surface was rotational. When the failure surface was non-rotational, an axis of rotation was defined following the approach from Fredlund and Krahn (1977). Hungr et al. (1989) found that the extension of Bishop's Simplified Method to three-dimensions yields factors of safety that are accurate for rotational and symmetric sliding surfaces, but the results are conservative for non-rotational and asymmetric failure surfaces. The extension of the Janbu Simplified Method to three-dimensions resulted in factors of safety that were more conservative than from Bishop's Simplified Method when the slopes had bilinear slip surface geometries.

Hungr et al. (1989) noted that extensions of the Morgenstern and Price and Sharma's Method would be developed in a few years after their publication. An extension of the Morgenstern and Price method to three-dimensions was proposed by Lam and Fredlund (1993). They assumed rotational failure surfaces, one direction of movement and proposed five different functions to represent the

inter-column forces. Through their finite-element analyses, Lam and Fredlund (1993) later ruled out three of these functions as insignificant and found that the force function had little influence on the factors of safety calculated.

All of the three-dimensional methods proposed before 1996 depended on symmetry or assumed sliding directions in order to establish the shear stresses on the failure surface. Yamagami and Jiang (1996, 1997) appear to be the first to use directions for shear stresses on the failure surface. They extended Janbu's Simplified Method to generalized slopes and slip surfaces. Inter-column forces were assumed to be related to the angle of the base of the column. The minimum factor of safety from horizontal and vertical force equilibrium equations was determined through interval calculations in which the direction of the shear stresses were altered.

The generalized Janbu (1957) method was extended to three-dimensions by Huang et al. (2002). In this method, factor of safety is calculated using two-directional force and moment equilibrium equations. Huang et al. (2002) neglected the horizontal inter-column shear forces, but calculated the vertical inter-column shear forces using an additional moment equilibrium equation. The shear forces at the base of the columns was assumed to be a unique constant and calculated using the secant method using the directional factors of safety. Two iterative procedures were required to calculate the directional factors of safety and the direction of the shear forces along the base of the column.

Extensions of the Simplified Bishop's Method, Simplified Janbu's Method and Morgenstern and Price Methods that considered the direction of shear stresses on the failure surface were proposed by Cheng and Yip (2007). For all of the methods, Cheng and Yip (2007) assumed that the slip surface was circular. For the extension of the Morgenstern and Price method, they used an arbitrary inter-column force function with mobilization factors. Factors of safety were calculated in both of the horizontal directions through an iterative process in which the mobilization factors were changed until overall moment equilibrium was satisfied and a unique factor of safety was established in both directions.

Ganjian et al. (2010) used the upper bound theorem of limit equilibrium analyses to propose a three-dimensional method to determine the factor of safety of slopes subjected to surcharge and seismic loading. They assumed rotational failure surfaces and calculated the factors of safety using the energy dissipation method. Nadukuru et al. (2011),

Michalowski and Martel (2011), and Nadukuru and Michalowski (2013) developed a series of stability charts to calculate the factor of safety of slopes subjected to seismic loading to avoid iterative processes. The charts presented by Nadukuru et al. (2011) can only be applied to those slopes with inclinations greater than 45° , while those prepared by Michalowski and Martel (2011), and Nadukuru and Michalowski (2013) are based on pseudo-static approaches for curvilinear cone sections passing through the toe of the slope.

Many computer programs commercially available today allow landslide scientists to perform three-dimensional slope stability analyses. Some programs will allow the user to export sections from a three-dimensional model to an analogous two-dimensional program to compute factors of safety at particular sections. An example of two- and three-dimensional factors of safety calculations using RocScience Slide (RocScience, Inc. 2002) and Slide3 (RocScience 2017), respectively is provided in the case study from Wang et al. (2015b).

Case Study

Using the case study from Wang et al. (2015b), RocNews (2017) presented a comparison of the factors of safety calculated using two- and three-dimensional methods. The landslide involves four soil layers and an additional weak layer along which the failure occurs. RocScience Slide and Slide3 were used to model the slope geometry, soil layers and the ground water table. The soil properties used for each of the layers are provided in Table 4, where c' and φ' are the effective cohesion and friction angle, respectively, and γ is the unit weight. Images of the models created in both programs are shown in Fig. 16. The factors of safety were calculated using Bishop's Simplified Method, Janbu's Simplified Method and Spencer's Method along with their three-dimensional extensions, as proposed by Cheng and Yip (2007). The factors of safety calculated for each of these models are summarized in Table 5, in which FS_{2D} and FS_{3D} represent the two-dimensional and three-dimensional factors of safety, respectively.

The use of ArcGIS to perform the regional level slope stability analyses was discussed earlier. However, this program also has several tools that can be used to perform three-dimensional slope stability analyses, as demonstrated

Table 4 Properties of the soil layers in the RocScience slide and Slide3 models (Adapted from RocNews 2017)

Layer	Soil 1	Soil 2	Soil 3	Soil 4	Weak layer
c' (kPa)	9.8	58.8	49.8	64	9.8
φ' ($^\circ$)	30	25	30	35	20
γ (kN/m ³)	22	24	26	27	20

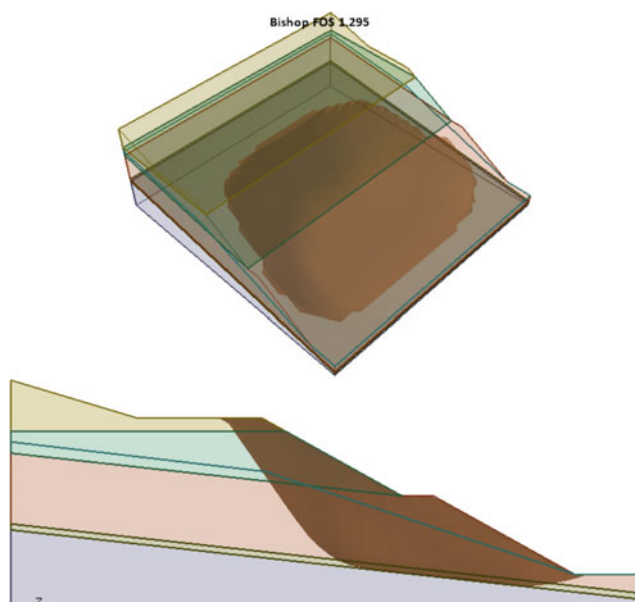


Fig. 16 Pictures of the models created in RocScience Slide3 (top) and Slide (bottom) (Source RocNews 2017)

by Tiwari and Douglas (2012), Tiwari et al. (2003), and Tiwari et al. (2004). These studies used Hovland's (1977) method to calculate the factors of safety. They also used the models created to calculate the two-dimensional factors of safety at several sections within the landslides studied. Comparing the factors of safety from the two-dimensional and three-dimensional analyses, they found that the latter factor of safety was greater than the former, in agreement with the conclusions made by Duncan (1996). All three studies noted that the cost of using ArcGIS methods was not much higher than the traditional two-dimensional analyses and while it may have been a little more time-consuming to build to the models at the start, the multi-dimensional use and ability to customize combined with the functionalities to spatial distribute prevention works and the visual and analytical analyses capabilities were well worth the time investment.

Case Study

Tiwari and Douglas (2012) preformed three-dimensional and two-dimensional slope stability analyses for the landslide located at the 62+000 km station along the Charali-Ilam

Road in Ilam District in the Eastern Development Region of Nepal, shown in Figs. 7, 8 and 9. Modifications to Hovland's (1977) method described in Fig. 8 and by Eqs. (2) and (3) were used for the calculations. Step-by-step procedures of the ArcGIS methodologies used are detailed in Douglas (2014).

Tiwari and Douglas (2012) calculated the two-dimensional factor of safety at three different sections, corresponding to the central section and sections located on the left and right side, for both of the landslide blocks. Two-dimensional factors of safety were calculated using the same tools and methodologies as for their three-dimensional factor of safety computations. However, instead of summing the A, B and C parameters in Eqs. (2) and (3) across the landslide body, the summations were limited to 1 m wide polygons. These polygons were aligned parallel to the cross section of interest.

While the study contained two different water table locations, the results, shown in Table 2, corresponded to the highest water level. As seen from Table 6, the factor of safety obtained from the two-dimensional analyses depended on the cross-section analyzed. In Table 6, $FS_{2D,left}$, $FS_{2D,mid}$, and $FS_{2D,right}$ represents the two-dimensional factors of safety at the left, central, and right, respectively, sections of each block (Fig. 8). $FS_{2D,avg}$ is computed using Eq. 4. Table 6 further shows that the midsection of the landslide blocks did not necessarily correspond to the most critical section of the landslide. Even the average of the two-dimensional factors of safety along the three sections analyzed was lower than the factor of safety obtained from the three-dimensional analyses. Orientation of the critical section, that is, the section that has lowest two-dimensional factor of safety, depends on the magnitude and orientation of the transverse slope (Tiwari et al. 2003).

$$FS_{2D,avg} = \frac{FS_{2D,left} + FS_{2D,mid} + FS_{2D,right}}{3} \quad (4)$$

Probabilistic Slope Stability Analyses and the Incorporation of Risk

In the mid-1970s, Alonso (1976), Tang et al. (1976a, b) and Harr (1977) first introduced probabilistic approaches to slope

Table 5 Factors of safety from two- and three-dimensional analyses in RocScience slide and Slide3 (Adapted from RocNews 2017)

Method	FS_{2D}	FS_{3D}	FS_{2D}/FS_{3D}
Bishop's simplified	1.076	1.295	0.831
Janbu simplified	1.026	1.259	0.815
Spencer's	1.125	1.445	0.779

Table 6 Factor of safety values obtained from ArcGIS analyses (Adapted from Tiwari and Douglas 2012)

Block	Cohesion (kPa)	FS _{3D}	FS _{2D, left}	FS _{2D, mid}	FS _{2d, right}	FS _{2D,avg/FS_{3D}}	FS _{2d,mid/FS_{3D}}
A	0	0.88	0.84	0.86	0.91	0.98	0.97
A	10	0.96	0.91	0.93	0.99	0.98	0.97
B	0	1.03	1.12	0.99	1.03	0.98	0.92
B	10	1.20	1.26	1.08	1.12	0.96	0.90

stability. Probabilistic slope stability analyses will need to incorporate several different sources of uncertainties including:

- Uncertainty in trends of the observations, as described by Neter et al. (1990), Li (1991), and Baecher (1987),
- Spatial variabilities, as summarized by Lacasse and Nadim (1996), DeGroot (1996), and Vanmarcke (1997a, b, 1983), and
- Random testing errors, as explained by Baecher (1987), Jaksa et al. (1997), and Kulhawy and Trautman (1996).

Similar to deterministic slope stability methods, probabilistic slope stability techniques also vary in terms of the assumptions made, their limitations, their ability to solve complex problems and complexity. To deal with the mathematical demands involved in probabilistic slope stability analyses, researchers often apply assumptions to simplify the methodology. One approach is the use of simple slope stability analyses methods as the basis for the incorporation of probability. For example, the method proposed in Vanmarcke (1980) uses a simple ordinary method of slice approach to perform probabilistic slope analyses on frictionless soils with circular slip surfaces. Other studies that use an ordinary method of slice approach include Honjo and Kuroda (1991), Tang et al. (1976a, b), Bergado et al. (1994), Yucemen and Tang (1975), and Harr (1977). Claes (1996) uses Janbu's stability charts while Wolff (1991), Priest and Brown (1983), and Wolff and Harr (1987) build probability into force equilibrium methods.

The methods proposed by Matsuo and Kuroda (1974), Cornell (1972), McGuffey et al. (1982) and Vanmarcke (1977b) apply only to frictionless soils. Other methods restrict the slope geometry as a way to reduce the complexity of the problem. For example, the work in Anderson et al. (1984), Yucemen and Al-Homoud (1990), Alonso (1976) and Vanmarcke (1977b) is applicable only to circular or cylindrical slip surfaces. A common assumption in several of the methods is to ignore spatial variabilities. Some examples of such methods are those proposed by Nguyen and Chowdhury (1984), Wolff and Harr (1987), Tobutt and Richards (1979), and Duncan (2000). Another common assumption is to disregard the correlations between soil properties. A few probabilistic slope stability methods that

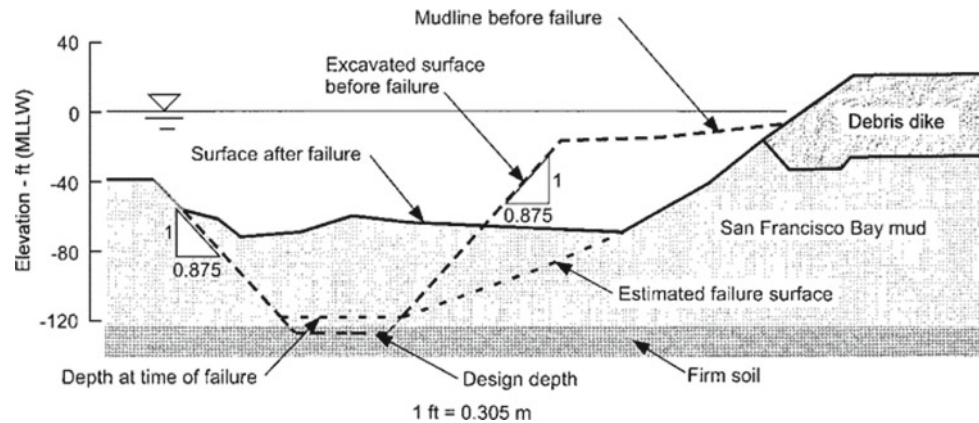
employ this assumption include Li and Lumb (1987), Christian et al. (1994), Tobutt and Richards (1979), Vanmarcke (1980), Anderson et al. (1984), and Tang et al. (1976a, b).

The use of Monte Carlo simulations in probabilistic slope stability analyses were considered uneconomical until about the 2000s. However, several researchers had proposed methods employing these simulations. To do so, they ignored either correlated random variables or spatial variability in the soil properties due to the difficulties associated with generating random values to preserve the correlations between the various parameters. Monte Carlo simulations require the use of computers due to the iterative process involved. Some methods that incorporate Monte Carlo simulations in probabilistic slope stability analyses include: Kim et al. (1978), Major et al. (1978), Tobutt (1982), Nguyen and Chowdhury (1984, 1985), Priest and Brown (1983), Kim and Sitar (2003), Griffiths et al. (2011), and Shinoda et al. (2006).

Case Study

Duncan (2000) presents an example of deterministic and probabilistic stability analyses performed for a slope that failed in August 1970 in a new Lighter Aboard Ship terminal in the Port of San Francisco. The entire failure was noted to take place in San Francisco Bay Mud, which had a liquid limit and plasticity index of approximately 50 and 20, respectively. Detailed slope stability analyses were carried out on the cross section illustrated in Fig. 17. The undrained shear strengths obtained from a series of laboratory and in-situ tests are presented in Fig. 18. Previous experience with the San Francisco Bay Mud suggested that slopes inclined at 45° would have factors of safety near 1.25. For cost reduction purposes, steeper trench slopes at approximately 49° were proposed. After significant soil testing to measure the undrained shear strength of the San Francisco Bay Mud (Fig. 18), the deterministic factor of safety for the steeper trench slope was established to be 1.17. Given the extensive soil testing and analyses, this was considered suitable and excavations at this slope commenced. After 150 m of the trench had been excavated, two slope failures occurred. The cause of the failure was studied by Duncan and Buchignani (1973). They found that creep induced strength losses in the San Francisco Bay Mud had yielded

Fig. 17 Typical cross-section analysed at the Light Abroad Ship terminal in the Port of San Francisco (Source Duncan 2000)



undrained shear strengths lower than those measured by the in-situ and laboratory testing.

In the probabilistic slope stability analyses performed by Duncan (2000), a Taylor series method was used to incorporate reliability. The results of their analyses suggested that the most likely value of the factor of safety was indeed 1.17, but it had a coefficient of variation of 0.16. The probability of failure was computed as 18%. Based on these analyses, Duncan (2000) suggested that this factor of safety may have been too low when combined with the high coefficient of variation. However, he notes that whether the design would have been changed as a result of these analyses is hard to say in retrospect.

Slope Stability for Unsaturated Slopes

The past 25 years have seen an expansion in unsaturated slope stability analyses. It is well accepted that the infiltration of rainwater will result in an increase in the pore water pressure or cause a reduction in the soil matric suction in partially saturated slopes. This reduction in the soil matric suction will cause a reduction in the shear strength of the materials along the sliding plane, which could possibly result in a failure. The infiltration of rainfall into the unsaturated pore space will also result in the flow or compression of air that is present, affecting water infiltration (Touma and Vuclin 1986; Sun et al. 2015; and Cho 2016). However, general slope stability analyses often ignore air flow because of the difficulties in measuring pore air pressure and analyzing air flow. As such, analyses are widely performed using infiltration analyses, as proposed by Richards (1931) in which only the flow of water is considered and flow of air is ignored (Sun et al. 2015). Some of the studies that have coupled hydromechanical and slope stability analyses include: Griffiths and Lu (2005), Lu and Godt (2008), Borja and White (2010), Alonso et al. (1995), Burscarnera and Whittle (2012), Lu et al. (2013), Smith (2003), Wang et al. (2015a), Hamdhan and Schweiger (2011), and Borja et al.

(2012). Several of these studies (Wang et al. 2015a; Borja and White 2010; Borja et al. 2012; Hamdhan and Schweiger 2011; and Alonso et al. 1995) ignore air flow by setting that the pore air pressure equal to atmospheric pressure by assuming that air will flow more freely than water.

The influence of air flow in the pore space has been considered in the work done by Hu et al. (2011), Zhang et al. (2009), Sun et al. (2015), Tiwari et al. (2014b, c), and Cho (2016). Hu et al. (2011) studied the factor of safety of a homogenous soil, as calculated using the Morgenstern-Price method, with a coupled three-phase model. The slope was subjected to a long, heavy rainfall event. The inclusion of air flow through the pore space was found to decrease the stability of the slope as a result of reductions in the progression of the wetting front. Using a water-air two phase flow model, Zhang et al. (2009) and Sun et al. (2015) evaluated the influence of air flow on the slope stability analyses results. Zhang et al. (2009) also found the calculated factor

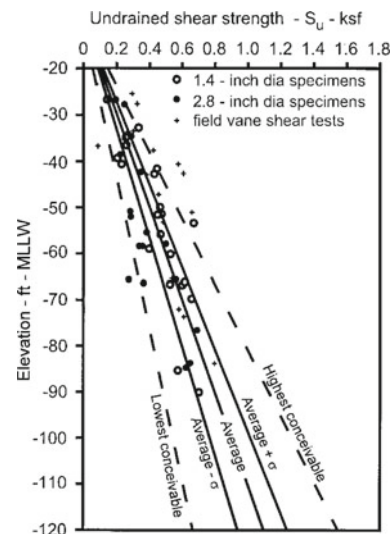


Fig. 18 Depth-wise variation of the undrained shear strength of the San Francisco Bay Mud encountered at the slope failure at the Lighter Abroad Ship terminal (Source Duncan 2000)

of safety is lower when pore air pressure in the unsaturated regions is included. They further found an increase in the impact of the pore air pressure with an increase in the distance between the sliding surface and the ground water table. Sun et al. (2015) noted that capillary pressure will result in higher factors of safety, but pore air pressures will result in less stable conditions. Tiwari et al. (2014b, c) used the air and water permeability values simultaneously to calculate the deformation of the slope and propagation of the wetting front after a rainfall event. In their study, they verified the results obtained from numerical calculation with the physical experimental model test results. Moreover, variation in suction with the duration of rainfall at different depths was also established with tensiometer data.

Lu and Godt (2008) modified the equation to calculate the factor of safety for infinite slopes to incorporate the suction stress, as defined by Lu and Likos (2004, 2006). The modified equation, as expressed by Eq. 5, reveals that the suction stress will act to increase the factor of safety above the ground water table and that the pore water pressure beneath the ground water table will act to reduce the factor of safety. In Eq. 5, ϕ' is the effective friction angle, β is the inclination of the ground surface, c' is the effective cohesion, γ is the unit weight, H_{ss} is the depth to the sliding surface from the ground surface, and σ^s is the suction stress as defined by Eq. 6, where θ , θ_r , and θ_s are the volumetric water content, residual volumetric water content and saturated volumetric water content, respectively, while S and S_r are the degree of saturation and residual degree of saturation, respectively. The pore air and water pressure are represented by u_a and u_w , respectively. Two phenomena, namely the inter-particle physico-chemical forces and the inter-particle capillary forces, are stated to be the cause of the suction stress (Lu and Godt 2008), which will reduce in magnitude as the soil approaches saturation. Lu and Godt (2008) note that sufficient long, heavy rainfall may reduce the suction stress in the upper part of a slope leading to the occurrence of shallow landslides. Iverson et al. (1997) noted that such failures may cause debris flows since the material involved is saturated or close to saturated.

$$FS = \frac{\tan\phi'}{\tan\beta} + \frac{2c'}{\gamma \cdot H_{ss} \cdot \sin(2\beta)} - \frac{\sigma^s}{\gamma \cdot H_{ss}} (\tan\beta + \cot\beta) \tan\phi' \quad (5)$$

$$\sigma^s = -\frac{\theta - \theta_r}{\theta_s - \theta_r} (u_a - u_w) = -\frac{S - S_r}{1 - S_r} (u_a - u_w) \quad (6)$$

A theoretical approach towards modeling one-dimension suction stress profiles above the ground water table is presented by Griffiths and Lu (2005) for different types of soil. They consider both infiltration and evaporation in their approach. The one-dimensional model obtained in then

substituted into two-dimensional slope stability analyses performed using finite-elements. Based on the results obtained, Griffiths and Lu (2005) note that inclusion of suction will result in higher values for the factor of safety of unsaturated slopes. The sensitivity of this factor of safety value is found to depend on the elevation of the ground water table, the types of soils involved and the infiltration conditions.

Fredlund et al. (2017) prepared a comparison between the factors of safety obtained from two-dimensional and three-dimensional analyses in unsaturated soil slopes. Their comparisons are performed using SVSLOPE (SoilVision 2019) using two simple slope geometries representing a steep and shallow slope face with varying values of the effective and unsaturated shear strength parameters. Fredlund et al. (2017) found that with an increase in either the effective cohesion, effective friction angle or unsaturated shear strength, a monotonic increase in the difference between the two- and three-dimensional factors of safety is observed. Differences on the order of 4–9% were noted in the factors of safety values of the shallow slope when the unsaturated shear strength is taken as zero. However, when the unsaturated shear strength friction angle was taken as 15°, the difference was found to be higher and between 9 and 16%. The differences in the two- and three-dimensional factors of safety were larger (between 12 and 18%) in the steep slope geometry analyzed by Fredlund et al. (2017) when the unsaturated shear strength friction angle was taken as 15°. For unsaturated slopes, Zhang et al. (2015) found very different results. They concluded that the factor of safety from three-dimensional analyses was as much as 60% larger than the factor of safety from two-dimensional analyses.

While examining the literature related to the slope stability analyses of the partially saturated slopes, the authors noted an inconsistency in the unit weights that were being used for the factor of safety computations. In several studies, including Montgomery and Dietrich (1994), D'Odorico et al. (2005) and Chiang and Chang (2009), the saturated unit weight is used in both the unsaturated and saturated zones of the slope. de Vleeschauwer and De Smedt (2002) and Acharya et al. (2006), on the other hand, used the dry unit weight in the regions that were unsaturated and the saturated unit weight in the remaining zones. Collins and Znidarcic (2004) used the effective unit weight for the saturated material and the total unit weight for the unsaturated zones in their analyses, whereas Vanacker et al. (2003) and Gabet et al. (2004) used the total unit weight in both regions. The most realistic representations for the unit weight were use of the moist unit weight in the partially saturated zones of the slope and the saturated unit weights for the materials beneath the ground water table, as adapted by Burton and Bathurst (1998) and Sidle and Ochiai (2006). Readers are cautioned

with the use of the unit weights applied to the different zones of materials when performing slope stability analyses in the unsaturated materials. The values used should be consistent with the conditions expected in the field.

Methods for Deformation Analyses

The most commonly used method for determining the deformation in slopes is probably the Newmark rigid block model proposed in Newmark (1965). The method is developed assuming that the slip surface behavior can be modeled as rigid perfectly plastic. Permanent deformations commence when inertial forces from earthquake motion exceed the yield resistance of the slip surface. They continue to accumulate until the forces applied by the earthquake drop below the yield resistance of the material along the slip surface and the velocity of the sliding block matches that of the stable underlying soil. Since 1965, several additional models for the estimations of deformations have been proposed including decoupled models that separate the soil response from the deformability (Seed and Martin 1966; Makdisi and Seed 1978; Bray and Rathje 1998; and Rathje and Bray 1999) and couple stick-slips models (Lin and Whitman 1983; Chopra and Zhang 1991; Kramer and Smith 1968; and Rathje and Bray 1999, 2001).

Seed and Martin (1966) and Makdisi and Seed (1978) proposed some of the earliest decoupled models. They presented a two-step procedure in which a preliminary dynamic analysis is first carried out to determine the equivalent acceleration that corresponds to a slippage length based on the average seismic stress history along the slip surface. This equivalent acceleration is then used in Newmark's method to determine the permanent displacement. Using a lumped mass shear beam to determine the effects of coupling and decoupling on the response observed, Lin and Whitman (1983) found that decoupled approach could lead to unconservative displacements especially when the sliding mass depth increased.

Chopra and Zhang (1991) used a generalized single degree of freedom system for their deformation calculations of earth dams. They uniformly distributed the mass and elasticity of the soil along the height of dam in their approach. From their results, Chopra and Zhang (1991) found that decoupling results in unconservative estimates of the deformation when the ratio of the yield acceleration to maximum acceleration is large. However, they found that the opposite is true when the ratio of the yield to maximum acceleration is small. Rathje and Bray (1999) expanded the work completed by Chopra and Zhang (1991) to incorporate mode shapes into the single degree of freedom system when calculating deformations. They concluded that the displacements will also depend on intensity, frequency and

duration of the seismic event. Building on their work, Rathje and Bray (2001) introduced scaling factors to modify the response from single degree of freedom system to incorporate the effects of topography.

One of the implicit assumptions made in Newmark's rigid block analysis was ignoring the influence of the downward stabilizing movements on the displacements. Stamatopoulos (1996) and Baziar et al. (2012) stated that the downward displacement of a sliding block would result in an increase in the factor of safety as it moved towards a more stable geometry. This will result in an increase in the yield acceleration and thereby, should cause a reduction in the resulting displacements of the sliding blocks. They modified the rigid block model incorporate the downward stabilizing effect. Stamatopoulos (1996) and Baziar et al. (2012) both show that the incorporation of the downward stabilizing effects will reduce the displacements measured. Baziar et al. (2012) further finds that the effects of the incorporation of the downward stabilizing movements will be greater when the sliding lengths are smaller.

Other techniques obtain the deformations of slopes with the use of finite-element analyses. In these techniques, the permanent deformation is obtained integrating by the strains induced in each element across the mesh. The permanent strains for each element are calculated from a variety of different methods. One method was proposed by Kuwano et al. (1991) in which the slope movement depends on the laboratory determined potential deformation of unrestrained soil elements. Their procedures required two sets of finite element calculations. From the first finite element calculations, the initial and dynamic shear stresses are computed. These stresses are used to perform cyclic tests to measure the strain potential. The strain potential represents the strain that develops in the soil mass when it is allowed to freely deform. These strain potentials are then inputted into a second finite element analyses, using which the expected deformations of a slope can be predicted. A three-dimension extension of this method was proposed by Orense and Towhata (1992) and is based on their previous work in Towhata et al. (1991, 1992).

Yasuda et al. (1991a, b, 1992) also proposed a method to estimate deformations requiring the performance of two static finite element analyses. Static stresses are computed in the first of these analyses. To do so, estimates of the elastic properties of the soil layers is required. During the second finite-element analyses, the stiffness of the soil is reduced to model the softening induced by an earthquake while the static stresses are kept constant. This reduction in stiffness must be appropriately determined to be able to capture the deformations induced. Yasuda et al. (1991a, b, 1992) stated the difference in the displacements between these two methods is stated to be the earthquake-induced deformations. Similar procedures were previously proposed by Lee (1974) and Serff et al. (1976).

Nonlinear inelastic soil models can also be used within the finite element analyses to compute the permanent slope deformations. For example, Finn et al. (1986) proposed a cyclic stress–strain model that can be incorporate in finite-element analyses to determine the permanent slope displacements. Advanced constitutive models were proposed by Prevost (1977), Mizuno and Chen (1982), Kawai (1985) and Daddazio et al. (1987), among others.

Case Study

Tiwari et al. (2018) analyzed deformations induced at Lokanthali, Nepal after the 2015 Gorkha Earthquake. The gentle sloping terrain in the region makes the deformations observed at this site very interesting. The average inclinations at the site were about 4°. Figure 19 contains a few pictures of the scarp-like features observed. A series of in-situ and laboratory tests were performed to determine the undrained shear strength, dynamic characteristics and strength reduction of the underlying soils. Numerical analyses were performed using FLAC (Fast Lagrangian Analysis of Continua, Itasca 2015). The FLAC analyses were performed using shear wave velocities of 200 m/s for the deconvolution and wave propagation analyses for three undrained shear strength results. Ground motions from three local stations (namely, THM, PTN and KATNP located 1.4 km, 4.3 km, and 6.3 km away, respectively) were applied. These three undrained shear strengths correspond to the lower bound shear strengths, the most likely strength estimate and the median strength. Additional details about each of these parameters can be found in Tiwari et al. (2018).

Shown in Fig. 20 are some of the deformed meshes that Tiwari et al. (2018) obtained from their FLAC analyses. Table 7 summarizes the predicted displacements from their analyses. Maximum lateral displacements around 0.5 m and vertical drops approximately 1 m were observed at the site. From the results of their numerical modeling, Tiwari et al. (2018) concluded that the predicted maximum displacements depended on undrained shear strength and seismic recording used in the analyses. Furthermore, these shear strengths



Fig. 19 Pictures of the scarp-like features observed at Lokanthali, Nepal (Source Tiwari et al. 2018)

affected the failure surfaces that were observed in the models.

Analysis to be Performed for Landslides

The design of slope stabilization works requires an estimate of the residual shear strength. This parameter can be established through a variety of methods including with the use of laboratory testing, correlations and back-analyses of failed slopes. Direct shear and rings shear tests conducted on the soil samples collected from the sliding surface can be used to measure the residual shear strength in the laboratory. If laboratory testing cannot be performed, various correlations for the residual shear strength available in the literature can provide another method of estimating the residual friction angle for the slope materials.

One of the most common methods to estimate the residual shear strength is through back-analyses of the failed slope. Different regions around the world have varying guidelines for the performing back-analyses. Tiwari et al. (2005) summarized the adapted practices in the United States and Japan. In the United States, the residual friction angle is back-calculated by setting the factor of safety to one and assuming the effective cohesion is zero. By contrast, back-calculations for the residual friction angle in Japan are performed assuming that the factor of safety is equal to 0.98 and that the effective cohesion is equal to the average depth to the sliding surface in meters. The use of these methods to back-calculate the residual friction angle was included in Tiwari et al. (2005) for six landslide sites. The results obtained are summarized in the case study below.

Tiwari and Marui (2001) proposed a different technique to estimate the residual shear strengths. In their method, a correction factor is applied to the residual friction angle and

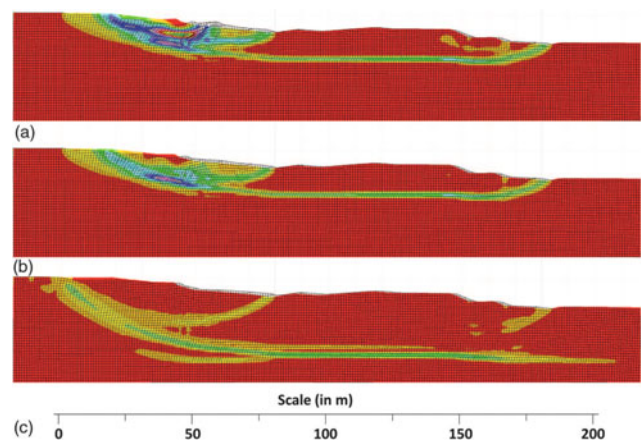


Fig. 20 Deformed meshes from FLAC analyses for **a** lower bound, **b** most likely and **c** median undrained shear strengths (Source Tiwari et al. 2018)

Table 7 Displacement predictions from each FLAC analyses for each of three ground motions applied and for each undrained shear strength considered (Adapted from Tiwari et al. 2018)

Station	THM		PTN		KATNP	
	East–West (cm)	North–South (cm)	East–West (cm)	North–South (cm)	East–West (cm)	North–South (cm)
Lower bound	224	177	77	123	240	199
Most likely	150	117	47	80	168	128
Median	139	71	33	49	95	63

the effective cohesion values after a slope stability analyses is performed using measured or estimated residual shear strengths. The correction factor is suggested to be equal to the ratio of the one and the calculated factor of safety. They note that this correction factor will account for any variations in the geometry, ground water table (and associated pore pressures) and soil shear strengths that might exist at the time of failure.

Case Study

Six landslides in the Niigata Prefecture, Japan were examined by Tiwari et al. (2005). Stabilization work at these landslide sites, which included the construction of 3 m diameter drainage galleries, allowed them to collect undrained block samples from the failure planes for each of the slopes. The samples collected from the sites were subjected to ring shear tests using a modified Imperial College and NGI-type ring shear apparatuses. Soil properties and testing conditions are summarized in Tiwari et al. (2005). The average residual friction angle from the laboratory tests were used to perform slope stability analyses using Spencer's Method. In addition, Tiwari et al. (2005) performed back-analyses for each of these sites using the procedures recommended by both the United States and Japan.

A summary of the results obtained is provided in Table 8. Tiwari et al. (2005) did not expect either of the methods to capture the residual shear strength parameters for all of the slopes. They found that the method adapted in the United States would agree well with the laboratory test results when

the effective cohesion values were close to or equal to zero. On the other hand, when the laboratory test results indicate effective cohesion values greater than zero, the method used in Japan will provide a better fit with the laboratory test results. This could have been due to the use of linearly interpolated values of cohesion and friction angles.

Discussion

Duncan (1996) noted that engineers “must have a thorough mastery of soil mechanics and soil strength, a solid understanding of the computer programs they use, and the ability and patience to test and judge the results of their analyses to avoid mistakes and misuse.” With the widespread availability of computer programs to perform slope stability analyses, these requirements are now more critical. Engineers should not only compare their results with what is believed to be the correct value, but with the improvements in in-situ sensors and better surveying tools, engineers can also validate their results with the observations in the field. The use of spreadsheets can supplement the verification of results for which slope stability charts were being used. More complicated analyses should be performed using more than one computer program to capture inaccuracies and to avoid obtaining incorrect results. Computer programs are also frequently being updated and modified based on new research. As such, engineers should note the key assumptions made and the limitations of the models used in the

Table 8 Back-calculated and measured residual shear strength parameters along with estimated factor of safety value based on laboratory test results (Adapted from Tiwari et al. 2005)

Landslide	U.S. method	Japanese method		Average laboratory results		
	ϕ_r' (°)	ϕ_r' (°)	c' (kPa)	ϕ_r' (°)	c' (kPa)	FS
Okimi	12.7	9.1	13	1.7	11.6	1.016
Yosio	14.3	9.7	5.8	4.6	12.2	1.098
Mukohidehara	19.7	15.4	11	0	19.4	0.987
Engyoji	16.2	11.2	8	8.3	7.8	0.772
Iwagami	15.1	10.4	9.6	8.1	11.9	1.038
Tsuboyama	11	6.3	7	2.7	9.9	1.057

computer programs within their reports and other documentation as older user manuals for software may become obsolete or hard to find at a later point when these analyses may be required again.

The use of GIS provides engineers with a versatile tool to not only rank the likelihood of instability based on causative factors, but also to perform more detailed analyses with the use of three-dimensional methods to calculate the factor of safety for a region. Once a model has been developed within the GIS framework, it is possible to quickly perform sensitivity studies to evaluate the impact of various triggering factors such as seismicity and seasonal fluctuations in the ground water levels. One of the major advantages of the use of GIS appears to be the visualization capabilities that it provides allowing for the development of maps that can be easily disseminated and understood by the various stakeholders.

There does not appear to be much advancement in the methods to perform three-dimensional slope stability analyses since 1996. Most, if not all, of the three-dimensional slope stability analysis methods, currently available, are extensions of two-dimensional counterparts. In doing so, the assumptions made during the derivations of the two-dimensional methods inherently translate into assumptions and limitations for the three-dimensional analyses. Furthermore, additional assumptions and constraints are placed in order to remove the indeterminacy of the problem. It is believed that additional research is required to develop better three-dimensional slope stability analyses methods. Perhaps, it is time for the profession to re-define three-dimensional slope stability analyses starting with the fundamental concepts, which may lead to methods with fewer assumptions and more realistic determinations of the factors of safety.

One of the major changes in three-dimensional slope stability analyses has been a result of the availability of computing power and visualization tools that allow engineers to more quickly and with better graphics understand and solve slope stability problems. These functionalities become apparent in the number of computer programs and GIS platforms that exist to analyze slope stability in two- and three-dimensions. Previous case histories studied using ArcGIS have illustrated the utility of this program by illustrating that:

- In addition to the use of the program to perform regional level slope stability analyses, it can be easily used to perform three-dimensional slopes stability calculations at the individual landslide scale.
- A model developed for three-dimensional analyses can be easily used to determine factors of safety along any two-dimensional section at any alignment within the

landslide body. In performing such calculations, it is possible to easily identify critical two-dimensional sections, which may not always correspond to the central section through a landslide mass.

- These analyses may be used to design landslide prevention or repair works that can be better suited for the stability issues that arise at any given site allowing for more economical and more confident designs.

Current probabilistic slope stability analyses add value to the deterministic factor of safety values that are obtained from conventional slope stability analyses. However, it appears that the methods that are available at the time this paper was written seem to make several simplifying assumptions focusing on incorporating reliability only to those parameters which are expected to have the greatest impact on the probability of failure. Engineering judgement, as with all slope stability evaluations, becomes a critical component in establishing to which factors quantified uncertainties will be included and which will be ignored. In addition to the selection of methods, caution should be employed when evaluating the values of the numerous parameters required. What may appear to be an outlier for the deterministic analyses might be an extreme value in the probability functions. On the other hand, data that is clustered may not be most representative of the variations that could be encountered, possibly having detrimental effects on the probabilistic calculations performed.

Most recent engineering graduates have likely been introduced to deterministic methods and are quite comfortable with utilizing them to evaluate slope stability. The lack of formal training on theories associated with probability and statistics with applications at many institutions may be one of the culprits as to why these techniques have not gained large popularity and widespread use in landslide science. Another cause could be misperceptions regarding the significant amount of data, time and effort that may be required to incorporate these types of analyses into routine practice. However, work by several researchers including Duncan (2000) and El-Ramy et al. (2002) has shown that small additional efforts are required.

Future work in the field of probabilistic slope stability analyses may result in methods that incorporate additional sources of uncertainty. That is, more comprehensive analyses that incorporate spatial variability and/or correlations between soil properties may become available. Work that illustrates the potential variability of various parameters including extreme values for different types of soils will be beneficial in providing the landslide community with better ideas as to the best-suited probabilistic models for those parameters.

Performance of slope stability analyses on slopes with unsaturated materials requires the incorporation of the suction stress into the existing two- and three- dimensional analyses methods. It also requires an understanding of the appropriate shear strengths as the degree of saturation varies of the material varies. The shear strengths used in the analyses should provide a gradual variation of the parameters as the condition of the soil moves from dry to saturated (or vice versa). Additionally, the seasonal fluctuations in the changes in the soil suction should be accurately captured in the analyses to ensure that the results are meaningful. Means to measure and/or estimate the soil suction values, especially for natural slopes, require further research.

Summary and Conclusions

Historical data indicates an increase in the number of landslides causing over 10,000 deaths and displacing millions of people globally each year. This increase may be partly attributed to an increase in the number of significant earthquakes and annual precipitations that exceed the average rainfall amounts observed during the century from 1901 to 2000. These trends point out the need to continue improving the understanding of landslide science and the development of methods that better simulate field conditions for analyzing slope stability and deformations. In this paper, the recent advances in these areas since the state of practice was summarized by Duncan (1996) are described. Specifically, the advances in slope stability and deformation analyses in the past 25 years can be summarized as follows:

- Improvements to computational and graphical capabilities: The availabilities of powerful personal computers with graphical capabilities has resulted in the development of over fifty commercial computer programs that can be used to compute two- and three-dimensional factors of safety. In addition, the availability of spreadsheets also presents a powerful tool for geotechnical engineers to evaluate slope stability, compute deformations and even perform probabilistic slope stability analyses.
- Macro level analysis for regions: Advances in technology and the availability of digital data has allowed for the evaluation of slope stability at a larger scale for regions prone to slope failures. This has allowed for the creation of landslide susceptibility maps and provided tools to understand how different controlling factors influence the stability of slopes at a regional level. GIS based methods, such as those proposed by Prof. Tiwari and his colleagues, extend the use of this tool to evaluate quantitative hazard potentials.
- Growth of three-dimensional slope stability analyses: While several methods for performing three-dimensional slope stability analyses existed at the time of Duncan's (1996) paper, several new methods have emerged. Most of these methods are still extensions of widely accepted two-dimension slope stability methods with some additional assumptions geared towards removing the indeterminacy of unknowns from equilibrium assumptions. Several commercial computer programs as well as GIS software can be used to perform three-dimensional slope stability calculations fairly easily.
- Probabilistic slopes stability analyses: A number of methods to perform probabilistic slope stability analyses are available in the literature. These techniques vary in terms of the assumptions, level of complexity and limitations that allow for the reduction in the number of probability distribution functions that are included in the slope stability evaluations. While methods incorporating Monte Carlo simulations existed in 1996, it is much easier and more economic to perform such simulations today. The development and use of these methods can allow landslide scientists to make more informed evaluations of the factor of safety and the probability of failure for slopes.
- Slope stability of unsaturated slopes: Significant research in the slope stability analyses of unsaturated slopes has occurred resulting in the development and use of coupled hydromechanical and slope stability analyses using existing two- and three-dimensional slope stability models. Inclusion of suction in the slope stability analyses results in an increase in the factor of safety, while considerations of the air flow through the pore space tends to cause a reduction in the factor of safety.
- Deformation analyses: While the Newmark sliding block method is still widely used to estimate the deformations of slopes, several new methods have been proposed in the literature. These methods will either decouple or couple the soil response from the deformability. Some of the newer methods have focused on incorporating other factors such as the influences of topography and downward stabilizing movements into the deformation estimates.
- Analyses to be performed for landslides: To design the repair works for landslides, an estimate of the appropriate shear strength at failure is necessary. Back-analyses with assumed effective cohesion values to calculate the residual friction angle are common and depend on the accepted practice within a country. Methods involving tested residual shear strengths and correction factors have also been proposed and may be the most appropriate to balance variations in several slope stability parameters at the time of failure and the one used for slope stability analysis.

References

- Acharya G, De Smedt F, Long NT (2006) Assessing Landslide hazard in GIS: a case study from Rasuwa, Nepal. *Bull Eng Geol Env* 65 (1):99–107
- Ajmera B, Tiwari B (2018) TXT-tool 3.001–1.4 using excel tools for slope stability analysis. *Landslide Dyn ISDR-ICL Landslide Interact Teach Tools*: 413–420
- Aleotti P, Chowdhury R (1999) Landslide hazard assessment: summary review and new perspectives. *Bull Eng Geol Env* 58(1):21–44
- Alfaro P, Delgado J, García-Tortosa FJ, Lenti L, López JA, López-Casado C, Martino S (2012) Widespread landslides induced by the Mw 5.1 earthquake of 11 May 2011 in Lorca, SE Spain. *Eng Geol* 137–138:40–52
- Alonso EE (1976) Risk Analysis of slopes and its application to slopes in Canadian sensitive clays. *Géotechnique* 26:453–472
- Alonso E, Gens A, Lloret A (1995) Effect of rain infiltration on the stability of slopes. In: *Proceedings of the first international conference on unsaturated soils*, pp. 241–249.
- Anagnosti P (1969) Three dimensional stability of fill dams. In: *Proceedings of the 7th International Conference on Soil Mechanics and Foundation Engineering*, vol. 2, pp. 275–280
- Anbalagan R (1992) Landslide Hazard evaluation and zonation mapping in mountainous Terrain. *Eng Geology* 32(4):269–277
- Anbalagan R, Singh B (1996) Landslide hazard and risk assessment mapping of mountainous terrains: a case study from Kumaun Himalaya, India. *Eng Geol* 43(4):237–246
- Anderson LR, Sharp KD, Bowles DS, Canfield RV (1984) Application of methods of probabilistic characterization of soil properties. In: *Proceedings of the ASCE symposium on probabilistics characterization of soil properties—bridge between theory and practice*, pp 90–105
- Azzouz A, Baligh M (1978) Three-dimensional stability of slopes. Final Report, Massachusetts Institute of Technology
- Baecher GB (1987) Statistical analysis of geotechnical data. Final Report to the U.S. Army Corps of Engineers
- Baziar MH, Rezaei-pour H, Jafarian Y (2012) Decoupled solution for seismic permanent displacement of Earth slopes using deformation-dependent yield acceleration. *J Earthq Eng* 16 (7):917–936
- Bergado DT, Patron BC, Youyongwatana W, Chai JC, Yudhbir. (1994) Reliability-based analysis of embankment on soft Bangkok clay. *Struct Saf* 13:247–266
- Bhattarai P, Tiwari B, Marui H, Aoyama K (2004) Quantitative slope stability mapping with ArcGIS: prioritize highway maintenance. In: *Proceedings of the ESRI's 24th annual international user's conference*, pp 1–15
- Bishop AW (1955) The use of the slip circle in the stability analysis of slopes. *Géotechnique* 5(1):7–17
- Bluden J, Arndt DS (2016) State of the climate in 2015. *Bull Am Meteorol Soc* 97(8)
- Bonham-Carter GF (1994) Geographic information systems for geoscientists: modelling with GIS. In: *Computer Methods in the Geosciences*
- Bonilla MG (1960) Landslides in the San Francisco South Quadrangle, California. U.S. Geological Survey Open-File Report
- Borja RI, White JA (2010) Continuum deformation and stability analyses of a steep hillside slope under rainfall infiltration. *Acta Geotechnica* 5:1–14
- Borja RI, White JA, Liu X, Wu W (2012) Factor of safety in a partially saturated slope inferred from hydro-mechanical continuum modeling. *Int J Numer Anal Methods Geomech* 36(2):236–248
- Bozzano F, Gambino P, Prestininzi A, Scarascia-Mugnozza G, Valentini G (1998) Ground effects induced by the Umbria-Marche earthquakes of September-October 1997, Central Italy. In: *Proceedings of the eighth international congress of the international association for engineering geology and the environment*, pp 825–830
- Brabb EE, Pampeyan EH, Bonilla MG (1972) Landslide susceptibility in San Mateo County, California, Scale 1:62,500. U.S. Geological Survey Miscellaneous Field Studies Map MF-360
- Bray JD, Rathje EM (1998) Earthquake-induced displacements of solid-waste landfills. *J Geotech Geoenvironmental Eng* 124(3):242–253
- Burroughs ER (1984) Landslide hazard rating for portions of the Oregon Coast range. In: *Proceedings of the symposium on effects of forest land use on erosion and slope stability*, pp 265–274
- Burroughs Jr ER, Hammond CJ, Booth GD (1985) Relative stability estimation for potential debris avalanche sites using field data. In: *Proceedings of the international symposium on erosion, debris flow and disaster prevention*, pp 335–339
- Burton A, Bathurst JC (1998) Physically based modeling of shallow landslide sediment yield at a catchment scale. *Environ Geol* 35(2–3):89–99
- Buscarnera G, Whittle A (2012) Constitutive modelling approach for evaluating the triggering of flow slides. *Can Geotech J* 49(5):499–511
- Campbell RH (1975) Soil slips, debris flows, and rainstorms in the Santa Monica mountains and vicinity, Southern California. U.S. Geological Survey Professional Paper, p 851
- Cao Z, Wang Y, Li D (2017) Practical reliability analysis of slope stability by advanced Monte Carlo simulations in a spreadsheet. In: *Probabilistic approaches for geotechnical site characterization and slope stability analysis*
- Carrara A (1983) Multivariate models for landslide hazard evaluation. *Math Geol* 15:403–426
- Carrara A, Cardinali M, Guzzetti F, Reichenbach P (1995) GIS technology in mapping landslide hazard. In: *Geographical information systems in assessing natural hazards*, pp 135–175
- Carrara A, Pugliese Carratelli E, Merenda L (1977) Computer-based data bank and statistical analysis of slope instability phenomena. *Geomorphology* 21:187–222
- Cavounidis S (1987) On the Ratio of factors of safety in slope stability analysis. *Géotechnique* 37(2):207–210
- Cavounidis S, Kalogeropoulos H (1992) End effects on the stability of cuts in normally consolidated Clays. *Rivista Italiana Gi Geotechnica* 2:85–93
- Cheng Y, Yip C (2007) Three-dimensional asymmetrical slope stability analysis extension of Bishop's, Janbu's and Morgenstern-Price's techniques. *J Geotech Geoenviron Eng* 133(12):1544–1555
- Chiang SH, Chang KT (2009) Application of radar data to modeling rainfall-induced landslides. *Geomorphology* 103:299–309
- Chigira M, Yagi H (2006) Geological and geomorphological characteristics of landslides triggered by the 2004 Mid Niigata Prefecture Earthquake in Japan. *Eng Geol* 82:202–221
- Cho SE (2016) Stability analysis of unsaturated soil slopes considering water-air flow caused by rainfall infiltration. *Eng Geol* 211:184–197
- Chopra AK, Zhang L (1991) Earthquake-induced base sliding of concrete gravity dams. *J Struct Eng* 117(12):3698–3719
- Christian JT, Ladd CC, Baecher GB (1994) Reliability and probability in stability analysis. *J Geotech Eng Div* 120(2):1071–1111
- Claes A (1996) Application of a probabilistic approach in slope stability analyses. In: *Proceedings of the 7th international symposium on landslides*, pp 1137–1142
- Clements RP (1984) Post-construction deformations of rockfill dams. *J Geotech Eng* 110(7):821–840
- Clough RW, Woodward RJ (1967) Analysis of embankment stresses and deformations. *J Soil Mech Found Div* 93(4):529–549
- Collins BD, Znidarcic D (2004) Stability analysis of rainfall induced landslides. *J Geotech Geoenviron Eng* 130(4):362–372

- Collins BD, Kayen R, Tanaka Y (2012) Spatial distributions of landslides triggered from the 2007 Niigata Chuetsu-Oki Japan Earthquake. *Eng Geol* 127:14–26
- Cornell CA (1972) First order uncertainty analysis of soils deformation and stability. In: *Proceedings of the 1st international on applications of statistics and probability to soil and structural engineering*, pp 129–144
- D'Odorico P, Fagherazzi S, Rigon R (2005) Potential for landsliding: dependence on hyetograph characteristics. *J Geophys Res* 110: F01007
- Daddazio RP, Eitouney MM, Sandler IS (1987) Nonlinear dynamic slope stability analysis. *J Geotech Eng* 113(4):285–298
- de Vlesschauer C, De Smedt F (2002) Modeling slope stability using GIS on a regional scale. In: *Proceedings of the 1st geological Belgica international meeting*, vol 12, pp 253–256
- DeGraff JV (1985) Using isopleth maps of landslide deposits as a tool in timber sale planning. *Bull Assoc Eng Geol* 22:445–453
- DeGraff JV, Canuti P (1988) Using isopleth mapping to evaluate landslide activity in relation to agricultural practices. *Bull Int Assoc Eng Geol* 38:61–71
- DeGroot DJ (1996) Analyzing spatial variability of in situ soil properties. *Geotech Spec Publ* 58(1):210–238
- Dhakar AS, Amada T, Aniya M (1999) Landslide mapping and the application of GIS in the Kulekhai Watershed, Nepal. *Mt Res Dev* 19(1):3–16
- Dhital MR (2000) An overview of landslide hazard mapping and rating systems in Nepal. *J Nepal Geol Soc* 22:533–538
- Douglas R (2014) Application of GIS tools for three-dimensional slope stability analysis of pre-existing landslides. Masters thesis, California State University, Fullerton
- Duncan JM (1996) State of the art: limit equilibrium and finite-element analysis of slopes. *J Geotech Eng* 122(7):577–596
- Duncan JM (2000) Factors of safety and reliability in geotechnical engineering. *J Geotech Geoenviron Eng* 126(4):307–316
- Duncan JM (2013) Slope stability then and now. *Proceedings of Geo-Congress 2013*:2191–2210
- Duncan JM, Buchignani AL (1973) Failure of underwater slope in San Francisco Bay. *J Soil Mech Found Div* 99(9):687–703
- Dunne T (1991) Stochastic aspects of the relations between climate, hydrology and landform evolution. *Trans Jpn Geomorphol Union* 12:1–24
- El-Ramly H, Morgenstern NR, Cruden DM (2002) Probabilistic slope stability analysis for practice. *Can Geotech J* 39:665–683
- EMDAT (2020) OFDA/CRED international disaster database. Université Catholique de Louvain, Brussels, Belgium, <https://www.emdat.be/>. Last Accessed 3 April 2020
- Esposito E, Porfido S, Simonelli AL, Mastrolorenzo G, Iaccarino G (2000) Landslides and other surface effects induced by the 1997 Umbria-Marche seismic sequence. *Eng Geol* 58:353–376
- Fellenius W (1927) *Erdstatische Berechnungen mit Reibung und Kohasion*. Ernst, Berlin (In German)
- Finn WDL, Yogendrakumar M, Yoshida N, Yoshida H (1986) TARA-3: a program to compute the response of 2-D embankments and soil-structure interaction systems to seismic loadings, Department of Civil Engineering, University of British Columbia
- Fowler WL (1984) Potential debris flow hazards of the Big Bend drive drainage basin, Pacifica, California. Masters thesis, Stanford University
- Fredlund DG, Krahn J (1977) Comparison of slope stability methods of analysis. *Can Geotech J* 16:121–139
- Fredlund MD, Fredlund DG, Zhang L (2017) Moving from 2D to a 3D unsaturated slope stability analysis. In: *Proceedings of the second Pan-American conference on unsaturated soils*, pp 1–10
- Fukumoto Y (2004) The substation analysis and prevention work of a landslide during movement in Niigata Prefecture. *Landslides* 41(1):65–69 ((in Japanese))
- Fukuoka H, Sassa K, Scarascia-Mugnozza G (1997) Distribution of landslides triggered by the 1995 Hyogo-ken Nanbu earthquake and long runout mechanism of the Takarazuka Golf course landslide. *J Phys Earth* 45:83–90
- Gabet EJ, Burbank DW, Putkonen JK, Pratt-Sitaula BA, Ojha T (2004) Rainfall thresholds for landsliding in the Himalayas of Nepal. *Geomorphology* 63:131–143
- Ganjian N, Askari F, Farzaneh O (2010) Influences of nonassociated flow rules on three-dimensional seismic slope stability of loaded slopes. *J CentL South Univ Technol* 17:603–611
- GEO-SLOPE International, Ltd. (2018) *Stability modeling with GeoStudio*. GEO-SLOPE International, Ltd.
- Gorsevki PV, Gessler PE, Jankowski P (2003) Integrating a fuzzy k-means classification and a Bayesian approach for spatial prediction of landslide hazard. *J Geogr Syst* 5(3):223–251
- Gorum T, Fan X, van Westen CJ, Huang RQ, Xu Q, Wang G (2011) Distribution pattern of earthquake-induced landslides triggered by the 12 May 2008 Wenchuan earthquake. *Geomorphology* 133:152–167
- Griffiths DV, Lu N (2005) Unsaturated slope stability with steady infiltration or evaporation using elasto-plastic finite-elements. *Int J Numer Anal Model Methods Geomech* 29:349–267
- Griffiths DV, Huang J, Fenton GA (2011) Probabilistic infinite slope analysis. *Comput Geosci* 38:577–584
- Guzzetti F, Carrara A, Cardinali M, Reichenbach P (1999) Landslide hazard evaluation: a review of current techniques and their application in a multi-scale study, Central Italy. *Geomorphology* 31(1–4):181–216
- Hamdhan IN, Schweiger FH (2011) Slope stability analysis of unsaturated fully coupled flow-deformation analysis. *Proc Int Assoc Math Geosci* 2011:1133–1150
- Hammond C, Hall D, Miller S, Swetik P (1992) Level 1 stability analysis (LISA) documentation for version 2.0. Geotechnical Technical Report for the U.S. Department of Agriculture
- Hansen A (1984) *Landslide hazard analysis*. In: *Slope stability*. Wiley
- Harp EL, Keefer DK (1990) Landslides triggered by the earthquake. U. S. Geological Survey Professional Paper 1487, pp 335–347
- Harp EL, Jibson RW (1996) Landslides triggered by the 1994 Northridge, California, earthquake. *Bull Seismol Soc Am* 86(1B): S319–S332
- Harp EL, Keefer DK, Sato HP, Yagi H (2011) Landslide inventories: the essential part of seismic landslide hazard analyses. *Eng Geol* 122:9–21
- Harp EL, Tanaka K, Sarmiento J, Keefer DK (1984) Landslides from the May 25–27, 1980, Mammoth Lakes, California, Earthquake Sequence. U.S. Geology Survey Miscellaneous Investigations Series Map I-1612
- Harp EL, Wilson RC, Wieczorek GF (1981) Landslides from the February 4, 1976, Guatemala Earthquake. Geological Survey Professional Paper, 1204-A
- Harr ME (1977) *Mechanics of particulate media—a probabilistic approach*. McGraw-Hill
- Hollingsworth R, Kovacs GS (1981) Soil slumps and debris flows: prediction and protection. *Bull Assoc Eng Geol* 18:17–28
- Honjo Y, Kuroda K (1991) A new look at fluctuating geotechnical data for reliability design. *Soils Found* 31(1):110–120
- Hovland H (1977) Three dimensional slope stability analysis method. *J Geotech Eng Div* 103:113–117
- Hu R, Chen YF, Zhou CB (2011) Modeling of coupled deformation, water flow and gas transport in soil slopes subjected to rain infiltration. *Sci China Technol Sci* 54(10):2561–2575

- Huang CC, Tsai CC, Chen YH (2002) Generalized method for three-dimensional slope stability analysis. *J Geotech Geoenviron Eng* 128(10):836–848
- Hungr O, Salgado F, Bryne P (1989) Evaluation of a Three-dimensional method of slope stability analysis to three dimensions. *Can Geotech J* 26:679–686
- Hutchinson JN (1995) Keynote paper: landslide hazard assessment. In: *Proceedings of the VI international symposium on landslides*, pp 1805–1841
- Itasca Consulting Group, Inc. (2015) *FLAC 8 basics: an introduction to FLAC 8 and a guide to its practical application in geotechnical engineering*. Itasca Consulting Group, Inc.
- Iverson RM, Reid ME, LaHusen RG (1997) Debris-flow mobilization from landslides. *Annu Rev Earth Planet Sci* 25:85–138
- Jaksa MB, Brooker PI, Kagawa WS (1997) Inaccuracies associated with estimating random measurement errors. *J Geotech Geoenviron Eng* 123:393–401
- Janbu N (1957) Earth pressure and bearing capacity calculations by generalized procedure of slices. In: *Proceedings of the fourth international conference on soil mechanics and foundation engineering*, pp 207–212
- Janbu N (1973) *Slope stability computations*. Embankment-Dam Engineering – Casagrande Volume, Wiley, pp 47–86
- Janbu N, Bjerrum L, Kjærnsli B (1956) *Veiledning ved Løsning av Fundamenteringsoppgaver (Soil Mechanics Applied to Some Engineering Problems)*. Norwegian Geotechnical Institute, 16, Oslo, Norway
- Jones FO (1973) Landslides of Rio de Janeiro and the Serra das Araras Escarpment, Brazil. U.S. Department of the Interior Geological Survey Professional Paper, p 697
- Kalatehjari R, Ali N (2013) A review of three-dimensional slope stability analyses based on limit equilibrium method. *Electron J Geotech Eng* 18:119–134
- Kamp U, Growley BJ, Khattak GA, Owen LA (2008) GIS-based landslide susceptibility mapping for the 2005 Kashmir earthquake region. *Geomorphology* 101:631–642
- Kawai T (1985) DIANA—dynamic interaction approach and non-linear analysis. Summary Report, Science University of Tokyo
- Keefer DK (2000) Statistical analysis of an earthquake-induced landslide distribution—the 1989 Loma Prieta California, California event. *Eng Geol* 58(3–4):231–249
- Keefer DK (2002) Investigating landslides caused by earthquakes—a historical review. *Surv Geophys* 23:473–510
- Keefer DK, Manson MW (1998) Regional distribution and characteristics of landslides generated by the earthquake. U.S. Geological Survey Professional Paper, 1551-C, pp 7–32
- Keefer DK, Wilson RC (1989) Predicting earthquake-induced landslides with emphasis on arid and semi-arid environments. *Inland Geol Surv South Calif Publ* 2(1):118–149
- Kim H-S, Major G, Ross-Brown DM (1978) Applications of Monte Carlo techniques to slope stability analyses. In: *Proceedings of the 19th US symposium on rock mechanics*, pp 28–39
- Kim J, Sitar N (2003) Importance of spatial and temporal variability in the analysis of seismically-induced slope deformations. In: *Proceedings of the 9th international conference on applications of statistics and probability in civil engineering*
- Kramer SL, Smith HB (1968) Seismic response of horizontal soil layer. *J Soil Mech Found Div* 94(SM4):1003–1029
- Kulhawy FH, Trautmann CH (1996) Estimation of in-situ test uncertainty. *Geotech Spec Publ* 58(1):269–286
- Kuwano J, Ishihara K, Haya H, Izu F (1991) Analysis of permanent deformation of embankments caused by earthquakes. *Soils Found* 31(3):97–110
- Lacasse S, Nadim F (1996) Uncertainties in characterizing soil properties. *Geotech Spec Publ* 58(1):49–75
- Lacroix P, Zavala B, Berthier E, Audin L (2013) Supervised method of landslide inventory using panchromatic SPOT5 images and application to the earthquake-triggered landslides of Pisco (Peru, 2007, Mw 8.0). *Remote Sens* 5:2590–2616
- Lam L, Fredlund D (1993) A general limit equilibrium model for three-dimensional slope stability analysis. *Can Geotech J* 30:905–919
- Lee KL (1974) Seismic permanent deformations in Earth dams. Report No. UCLA-ENG-7497, University of California, Los Angeles
- Leshchinsky D, Huang CC (1992) Generalized slope stability analysis: interpretation, modification, and comparison. *J Geotech Eng* 118(10):1559–1576
- Leshchinsky D, Huang CC (1992) Generalized three-dimensional slope stability analysis. *J Geotech Eng* 118(11):1748–1764
- Li KS (1991) Discussion: probabilistic potentiometric surface mapping. *J Geotech Eng* 117:1457–1458
- Li KS, Lumb P (1987) Probabilistic design of slopes. *Can Geotech J* 24:520–535
- Lin JS, Whitman RV (1983) Decoupling approximation to the evaluation of earthquake-induced plastic slip in Earth Dams. *Earthq Eng Struct Dyn* 11:667–678
- Low BK (2003) Practical probabilistic slope stability analysis. *Proc Soil Rock Am* 2003(2):2777–2784
- Low BK, Tang WH (2004) Reliability analysis using object-oriented constrained optimization. *Struct Saf* 26(1):69–89
- Low BK, Tang WH (2007) Efficient spreadsheet algorithm for first-order reliability methods. *J Eng Mech* 133(12):1378–1387
- Lowe J, Karafaith L (1959) Stability of earth dams upon drawdown. In: *Proceedings of the first PanAmerican conference on soil mechanics and foundation engineering*, vol 2, pp 537–552
- Lu N, Godt JW (2008) Infinite slope stability under unsaturated seepage conditions. *Water Resour Res* 44:W11404
- Lu, N., and Likos, W. J. (2004). “Unsaturated Soil Mechanics,” John Wiley.
- Lu N, Likos WJ (2006) Suction stress characteristic curve for unsaturated soil. *J Geotech Geoenviron Eng* 132(2):131–142
- Lu N, Wayllace A, Oh., S. (2013) Infiltration-induced seasonally reactivated instability of a highway embankment near the Eisenhower Tunnel, Colorado, USA. *Eng Geol* 162:22–32
- Mahdavi MR, Soleymani S, Jafari MK (2006) Landslides triggered by the Avaj, Iran earthquake of June 22, 2002. *Eng Geol* 86:166–182
- Major G, Ross-Brown DM, Kim H-S (1978) A general probabilistic analysis for three-dimensional wedge failures. In: *Proceedings of the 19th US symposium on rock mechanics*, pp 44–56
- Makdisi FI, Seed HB (1978) Simplified procedure for estimating dam and embankment earthquake-induced deformations. *J Geotech Eng* 104(GT7):849–867
- Mark RK (1992) Map of debris-flow probability, San Mateo County, California, Scale 1:62,500. U.S. Geological Survey Miscellaneous Investigations Map I-1257-M
- Marzorati S, Luzi L, De Amicis M (2002) Rock falls induced by earthquakes: a statistical approach. *Soil Dyn Earthq Eng* 22:565–577
- Matsuo M, Kuroda K (1974) Probabilistic approach to design of embankments. *Soils Found* 14(2):1–17
- McGuffey V, Grivas D, Iori J, Kyfor Z (1982) Conventional and probabilistic embankment design. *J Geotech Eng Div* 108(10):1246–1254
- Michalowski RL, Martel T (2011) Stability charts for 3D failures of steep slopes subjected to seismic excitation. *J Geotech Geoenviron Eng* 137(2):183–189
- Mizuno E, Chen WF (1982) Plasticity models for seismic analysis of slopes. Report CE-STR-82–2, Purdue University
- Montgomery DR, Dietrich WE (1994) A physically based model for the topographic control on shallow landsliding. *Water Resour Res* 30(4):1153–1171

- Montgomery DR, Wright RH, Booth T (1991) Debris flow hazard mitigation for colluvium-filled swales. *Bull Assoc Eng Geol* 28:303–323
- Morgenstern N, Price V (1965) The analysis of the stability of general slip surfaces. *Géotechnique* 15(1):79–93
- Morton DM (1971) Seismically triggered landslides in the area above the San Fernando Valley. *US Geol Surv Prof Pap* 733:99–104
- Morton DM (1975) Seismically triggered landslides in the area above the San Fernando Valley. *State Calif Div Mines Geol Bull* 196:145–154
- Nadukuru SS, Michalowski RL (2013) Three-dimensional displacement analysis of slopes subjected to seismic loads. *Can Geotech J* 50(6):650–661
- Nadukuru SS, Martel T, Michalowski RL (2011) 3D analysis of steep slopes subjected to seismic excitation. *Proc GeoFrontiers* 2011:3546–3555
- Neely MK, Rice RM (1990) Estimating risk of debris slides after timber harvest in Northwestern California. *Bull Assoc Eng Geol* 27:281–289
- Neter J, Wasserman W, Kutner MH (1990) *Applied linear statistical models*. Richard D, Irwin Inc, Boston, MA, USA
- Neuland H (1976) A prediction model of landslides. *CATENA* 3:215–230
- Newmark NM (1965) Effects of earthquakes on dams and embankments. *Géotechnique* 15:139–160
- Nguyen VU, Chowdhury RN (1984) Probabilistic study of spoil pile stability in strip coal mines—two techniques compared. *Int J Rock Mech Min Sci Geomech* 21(6):303–312
- NOAA (2020) Significant earthquake database. National Geophysical Data Center/World Data Service Center, National Oceanic and Atmospheric Administration, Colorado, USA. https://www.ngdc.noaa.gov/nndc/servlet/ShowDatasets?dataset=102557&search_look=50&display_look=50. Last Accessed 31 March 2020
- Nyugen VU, Chowdhury RN (1985) Simulation for risk analysis with correlated variables. *Géotechnique* 35(1):47–58
- Ojeda J, Donnelly L (2006) Landslides in Columbia and their impact on towns and cities. In: *The Geological Society of London*, pp 1–13
- Okimura T, Torii N (1999) A study on slope failures due to Hyogoken-Nanbu earthquake and post-earthquake rainfalls. In: *Proceedings of the Sino-Japan second workshop on seismic hazard and mitigation*, pp 62–65
- Orense R, Towhata I (1992) Prediction of liquefaction-induced permanent ground displacements: a three-dimensional approach. In: *Proceedings of the 4th Japan-U.S. workshop on earthquake resistant design of lifeline facilities and countermeasures for soil liquefaction*, NCEER-92-0019, pp 335–349
- Pathak S, Nilsen B (2004) Probabilistic rock slope stability analysis for Himalayan condition. *Bull Eng Geol Env* 63:25–32
- Pike RJ (1988) The geometric signature: quantifying landslide-terrain types from digital elevation models. *Math Geol* 20:491–511
- Plafker G, Ericksen GE, Concha JF (1971) Geological aspects of the May 31, 1970 Perú earthquake. *Bull Seismol Soc Am* 61(3):543–578
- Poulos HG, Booker JR, Ring GJ (1972) Simplified calculations of embankment deformations. *Soils Found* 12(4):1–17
- Prasad AS, Pandey BW, Leimgruberm W, Kunwar RM (2016) Mountain hazard susceptibility and livelihood security in the upper catchment area of the River Beas, Kullu Valley, Himachal Pradesh, India. *Geoenviron Disasters* 3(3):1–17
- Prevost JH (1977) Mathematical modelling of monotonic and cyclic undrained clay behavior. *Int J Numer Anal Methods Geomech* 1(2):195–216
- Priest DS, Brown ET (1983) Probabilistic stability analysis of variable rock slopes. *Trans Inst Min Metall* 92:A1–A12
- Qi S, Xu Q, Lan H, Zhang B, Liu J (2010) Spatial distribution analysis of landslides triggered by the 2008.5.12 Wenchuan Earthquake, China. *Eng Geol* 116:95–108
- Rathje EM, Bray JD (1999) An Examination of simplified earthquake-induced displacement procedures for earth structures. *Can Geotech J* 36(1):72–87
- Rathje EM, Bray JD (2001) One- and two-dimensional seismic analysis of solid-waste landfills. *Can Geotech J* 38(4):850–862
- Resendiz D, Romo MP (1972) Analysis of embankment deformations. *Proc Perform Earth Earth-Support Struct* 1:817–836
- Richards LA (1931) Capillary conduction of liquids through porous medium. *J Phys* 1:318–333
- Richter HH, Trigg KA (2008) Case history of the June 1, 2005, Bluebird Canyon Landslide in Laguna Beach, California. *Geotechnical Special Publication* 178:433–440
- RocNews (2017) Limit equilibrium, and shear strength reduction, and 3D, oh my! RocScience, Inc.
- RocScience (2017) Slide3 3D limit equilibrium analysis of slope stability. RocScience Inc.
- RocScience Inc. (2002) Slide: user's guide. RocScience Inc.
- Roth RA (1982) Landslide susceptibility in San Mateo County, California. Masters thesis, Stanford University
- Rymer MJ (1987) The San Salvador earthquake of October 10, 1986—geologic aspects. *Earthquake Spectra* 3:435–463
- Rymer MJ, White RA (1989) Hazards in El Salvador from earthquake-induced Landslides. In: *Landslides: Extent and Economic Significance*, pp 105–109
- Saha AK, Gupta RP, Arora MK (2002) GIS-based LANDSLIDE HAZARD ZONATION in the Bhagirathi (Ganga) Valley, Himalayas. *Int J Remote Sens* 70(5):617–625
- Sarkar S, Kanungo DP (2004) An integrated approach for landslide susceptibility mapping using remote sensing and GIS. *Photogrammetric Engineering and Remote Sensing* 70(5):617–625
- Sassa K, Fukuoka H, Scarascia-Mugnozza H, Irikura K, Okimura T (1995) Landslides triggered by the Hyogoken-Nanbu earthquake. *Landslide News* 9:2–5
- Sato HP, Hasegawa H, Fujiwara S, Tobita M, Koarai M, Une H, Iwahashi J (2007) Interpretation of landslide distribution triggered by the 2005 Northern Pakistan Earthquake using SPOT5 imagery. *Landslides* 4:113–122
- Sato HP, Sekiguchi T, Kojiro R, Suzuki Y, Iida M (2005) Overlaying landslides distribution of the earthquake source, geological and topographical data: the Mid Niigata Prefecture earthquake in 2004, Japan. *Landslides* 2:143–152
- Seed HB, Martin GR (1966) The seismic coefficient in Earth dam design. *J Soil Mech Found Div* 92(SM3):25–58
- Seely MW, West DO (1990) Approach to geological hazard zoning for regional planning, Inyo National Forest, California and Nevada. *Bull Assoc Eng Geol* 27:23–35
- Serff N, Seed HB, Makdisi FI, Chang C-Y (1976) Earthquake-induced deformations of Earth dams. Report EERC 76-4. University of California, Berkeley
- Shinoda M, Horii K, Yonezawa T, Tateyama M, Koseki J (2006) Reliability-based seismic deformations analysis of reinforced soil slopes. *Soils Found* 46(4):477–490
- Sidle RC (1992) A theoretical model of the effects of timber harvesting on slope stability. *Water Resour Res* 28:1897–1910
- Sidle RC, Ochiai H (2006) Landslides: processes, prediction, and land use. *Water Resour Monogr* 18
- Skirrikar SM, Rimal LN, Jäger S (1998) Landslide hazard mapping of Phewa Lake Catchment Area, Pokhara, Central West Nepal. *J Nepal Geol Soc* 18:335–345
- Smith PGC (2003) Numerical analysis of infiltration into partially saturated soil slopes. Ph.D. thesis, Imperial College of Science, Technology and Medicine
- Smith TC (1988) A method for mapping relative susceptibility to debris flows, with an example from San Mateo County. *Landslides, Floods, Mar Eff Storm* Jan 3–5, 1982

- Soeters R, van Westen CJ (1996) Slope instability recognition, analysis and zonation. *Transp Res Board Spec Rep* 47:129–177
- SoilVision Systems, Ltd. (2019) SVSLOPE: 2D/3D limit equilibrium slope stability analysis theory manual. SoilVision Systems, Ltd.
- Stamatopoulos CA (1996) Sliding system predicting large permanent co-seismic movements of slopes. *Earthq Eng Struct Dyn* 25 (10):1075–1093
- Sun DM, Zang YG, Semprich S (2015) Effects of airflow induced by rainfall infiltration on unsaturated soil slope stability. *Transp Porous Media* 107(3):821–841
- Tang WH, Yucemen MS, Ang AHS (1976a) Probability-based short term design of slopes. *Can Geotech J* 13:201–215
- Tang WH, Yucemen MS, Ang AHS (1976b) Probability-based short-term design of slopes. *Can Geotech J* 13:201–215
- Thapa PB, Dhital MR (2000) Landslide and debris flows of 1–21 July 1993 in the Agra Khola Watershed of Central Nepal. *J Nepal Geol Soc* 18:335–345
- Tiwari B (2007) GIS aided shallow sliding potential map for natural slopes. *Geotechn Spec Publ* 170:1–10
- Tiwari B, Ajmera B, Dhital S (2017) Characteristics of moderate- to large-scale landslides triggered by the Mw 7.8 2015 Gorkha earthquake and its aftershocks. *Landslides*:1–22
- Tiwari B, Do H (2011) Deterministic seismic hazard analysis of highway sector with GIS. *Geotechn Spec Publ* 211:1554–1563
- Tiwari B, Douglas R (2012) Application of GIS tools for three-dimensional slope stability analysis of pre-existing landslides. *Geotechn Spec Publ* 225:479–488
- Tiwari B, Duarte S (2013) Performance of slope stabilization works stabilized with drainage and buttress. *Geotechn Spec Publ* 231 (1):1697–1700
- Tiwari B, Marui T (2001) Concept of shear strength measurement and modification of stability analysis during countermeasure planning of landslides. *J Jpn Landslide Soc* 38(3):53–64
- Tiwari B, Bhattarai P, Garica CF (2008) GIS based quantitative risk analysis along Prithvi highway road corridor during extreme events. *Geotechn Spec Publ* 178:130–137
- Tiwari B, Brandon TL, Marui H, Tuladhar GR (2005) Comparison of residual shear strengths from back analysis and ring shear tests on undisturbed and remolded specimens. *J Geotechn Geoenviron Eng* 131(9):1071–1079
- Tiwari B, Hillman M, Ajmera K, Ajmera B (2010) Seismic slope stability of reactivated landslides—a performance based analysis. In: *Proceedings of the fifth international conference on recent advances in geotechnical earthquake engineering and soil dynamics*, 31
- Tiwari B, Caballero S, Zalzal W (2014a) Experimental modelling for the effect of rainfall and earthquake on slope stability of engineered fill. *Landslide Sci Safer Geoenviron*: 101–107
- Tiwari B, Kawai K, Viradeth P (2014b) Numerical modelling of deformation of partially saturated slopes subjected to rainfall. *Landslide Sci Safer Geoenviron*: 281–285
- Tiwari B, Kawai K, Lewis A, Viradeth P (2014c) Experimental and numerical studies on the effect of rainfall on triggering shallow landslides. *Landslide Sci Safer Geoenviron*: 123–128
- Tiwari B, Marui H, Aoyama K, Bhattarai P, Tuladhar G (2004) Preparation of geotechnical database of mountainous cities with ArcGIS. In: *Proceedings of the ESRI's 24th annual international user's conference*, pp 1–30
- Tiwari B, Marui H, Ishibashi I, Nakagawa K, Bhattarai P, Aoyama K (2003) Use of ArcMap for 3D stability analysis of preexisting landslides. In: *Proceedings of ESRI's 23rd international user's conference*, pp 1–12
- Tiwari B, Pradel D, Ajmera B, Yamashiro B, Khadka D (2018) Landslide movement at Lokanthali during the 2015 earthquake in Gorkha, Nepal. *J Geotechn Geoenviron Eng* 144(3):05018001-1–05018001-12
- Tobutt DC (1982) Monte Carlo simulation methods for slope stability. *Comput Geosci* 8(2):199–208
- Tobutt DC, Richards EA (1979) The reliability of Earth slopes. *Int J Numer Anal Meth Geomech* 3:323–354
- Touma J, Vauclin M (1986) Experimental and numerical analysis of two phase infiltration in a partially saturated soil. *Transp Porous Media* 1(1):28–55
- Towhata I, Sasaki Y, Tokida K, – I., Matsumoto, H., Tamari, Y., and Yamada, K. (1992) Prediction of permanent displacement of liquefied ground by means of minimum energy principle. *Soils Found* 32(3):97–116
- Towhata I, Tokida K, Tamari Y, Matsumoto H, Yamada K (1991) Prediction of permanent lateral displacement of liquefied ground by means of variational principle. In: *Proceedings of the 3rd Japan-U.S. workshop on earthquake resistant design of lifeline facilities and countermeasures for soil liquefaction*, NCEER-91–0001, pp 237–251
- US EPA (2016) Climate change indicators: U.S. and global precipitation. United States Environmental Protection Agency, Washington, DC, USA. <https://www.epa.gov/climate-indicators/climate-change-indicators-us-and-global-precipitation>. Last accessed 31 March 2020
- Van Westen CJ, Rengers N, Terlien MTJ, Soeters R (1997) Prediction of the occurrence of slope instability phenomena through GIS-based hazard zonation. *Geol Rundsch* 86(2):404–414
- van Westen CJ (1994) GIS in landslide hazard zonation: a review, with examples from Andes of Colombia. *Mt Environ Geogr Inf Syst*: 135–165
- Vanacker V, Vanderschaeghe M, Govers G, Willems E, Poesen J, Deckers J, De Bievre B (2003) Linking hydrological, infinite slope stability and land-use change models through GIS for assessing the impact of deforestation on slope stability in high Andean watersheds. *Geomorphology* 52(3–4):299–315
- Vanmarcke EH (1977a) Probabilistic modeling of soil profiles. *J Geotechn Eng Div* 103:1227–1246
- Vanmarcke EH (1977b) Reliability of Earth slopes. *J Geotechn Eng Div* 103:1247–1265
- Vanmarcke EH (1980) Probabilistic stability analysis of Earth slopes. *Eng Geol* 16:29–50
- Vanmarcke EH (1983) *Random fields: analysis and synthesis*. MIT Press
- Varnes DJ (1984) *Landslide hazard zonation: a review of principles and practice*. Nat Hazard 3
- Walker WL, Duncan JM (1984) Lateral bulging of Earth dams. *J Geotech Eng* 110(7):923–937
- Wang MN, Wu HL, Nakamura H, Wu SC, Ouyang S, Yu MF (2003) Mass movements caused by recent tectonic activity: the 1990 Chi-Chi earthquake in Central Taiwan on September 21, 1999. *Landslides* 38(4):318–326
- Wang LJ, Liu SH, Fu ZZ, Li Z (2015a) Coupled hydro-mechanical analyses of slope under rainfall using modified elasto-plastic model for unsaturated soils. *J CentL South Univ* 22(5):1892–1900
- Wang L, Xie M, Xu B, Esaki T (2015b) A study on locating critical slip surface of slopes. *Int J Geotech Eng* 9(3):265–278
- Wartman J, Dunham L, Tiwari B, Pradel D (2013) Landslides in eastern honshu induced by the 2011 off the Pacific Coast of Tohoku earthquake. *Bull Seismol Soc Am* 103(2B):1503–1521
- Whitman RV, Bailey WA (1967) Use of computers for slope stability analysis. *J Soil Mech Found Eng Div* 93(4):475–498
- Wolff TF (1991) Application brief—embankment reliability versus factor of safety: before and after slide repair. *Int J Numer Anal Meth Geomech* 15:41–50
- Wolff TF, Harr ME (1987) Slope design for Earth dams. In: *Proceedings of the 5th international conference on applications of statistics and probability in soil and structural engineering*, vol 2, pp 725–732

- Wright RH, Campbell RH, Nilsen TH (1974) Preparation and use of isopleth maps of landslide deposits. *Geology* 2:483–485
- Wright SG (2004) UTEXASED4: a computer program for slope stability calculations. *TexGraf4 Software*
- Xu C, Xu X, Yu G (2012) Earthquake triggered landslide hazard mapping and validation related with the 2010 Port-au-Prince, Haiti earthquake. *Disaster Adv* 5(4):1297–1304
- Xu C, Xu X, Lee YH, Tan X, Yu G, Dai F (2012) The 2010 Yushu earthquake triggered landslide hazard mapping using GIS and Weight of evidence modeling. *Environ Earth Sci* 66:1603–1616
- Yablokov A (2001) The tragedy of Khait: a natural disaster in Tajikistan. *Mt Res Dev* 21(1):91–93
- Yamagami T, Jiang JC (1996) Determination of the sliding direction in three-dimensional slope stability analysis. In: *Proceedings of the 2nd international conference on soft soil engineering, Part 1*, pp 567–572
- Yamagami T, Jiang JC (1997) A search for the critical slip surface in three-dimensional slope stability analysis. *Soils Found* 37(3):1–16
- Yamagishi H, Iwahashi J (2007) Comparison between the two triggered landslides in Mid-Niigata, Japan by July 13 heavy rainfall and October 23 intensive earthquakes in 2004. *Landslides* 4:389–397
- Yasuda S, Nagase H, Kiki H, Uchida Y (1991a) A simplified procedure for analysis of the permanent ground displacement. In: *Proceedings of the 3rd Japan-U.S. workshop on earthquake resistant design of lifeline facilities and countermeasures for soil liquefaction, NCEER-91-0001*, pp 225–236
- Yasuda S, Nagase H, Kiki H, Uchida Y (1991b) Countermeasures against the permanent ground displacement due to liquefaction. In: *Proceedings of the fifth international conference on soil dynamics and earthquake engineering V*, pp 341–350
- Yasuda S, Nagase H, Kiki H, Uchida Y (1992) The mechanism and a simplified procedure for the analysis of permanent ground displacement due to liquefaction. *Soils Found* 32(1):149–160
- Yuceman MS, Tang WH (1975) Long term stability of slopes: a reliability approach. In: *Proceedings of the 2nd international conference on applications of statistics and probability in soil and structural engineering*, pp 215–230
- Yucemen MS, Al-Homoud AS (1990) Probabilistic three-dimensional stability analysis of slopes. *Struct Saf* 9:1–20
- Zhang D, Wang G (2007) Study of the 1920 Haiyuan earthquake-induced landslides in Loess (China). *Eng Geol* 94:76–88
- Zhang L, Fredlund M, Fredlund DG, Lu H, Wilson GW (2015) The influence of the unsaturated soil zone on 2-D and 3-D slope stability analyses. *Eng Geol* 193:374–383
- Zhang XY, Zhu YM, Fang CH (2009) The role for air flow in soil slope stability analysis. *J Hydrodyn* 21(5):640–646



Engineering Risk Mitigation for Landslide Hazard Chains: The Baige Landslides on the Jinsha River in 2018

Limin M. Zhang, Jian He, and Te Xiao

Abstract

On 10 October and 3 November 2018, two large landslides occurred at Baige on the Qinghai-Tibet Plateau, and completely blocked the Jinsha River. Accordingly two landslide dams formed and breached sequentially, with the breaching of the 3 Nov. dam generating a flood larger than the 10,000-year return period flood over a river reach of approximately 400 km, endangering the serial cascade dams and towns along the river. These were two typical large-scale hazard chains originated by landslides. This paper presents a five-phase protocol to manage the risks of landslide hazard chains, which includes definitions, multi-hazard assessment, exposure assessment, multi-vulnerability assessment, and multi-risk assessment. The protocol is illustrated in the case of the Jinsha River landslide hazard chains. How the hazard chains developed in space and time are introduced. The major engineering measures for mitigating short-term and longer-term risks are described, including the use of a 15 m deep diversion channel to reduce the dam failure flow rate and flow quantity, removal of two cofferdams along the river to avoid flood amplification effects, flood regulation using six reservoirs over 630 km downstream, load relief at the crest of the instable slope to increase its stability, and removal of part of the residual landslide barrier to minimize future landslide dam risks. Finally, several scientific topics are suggested for further study.

Keywords

Hazard chain • Landslide • Landslide dam • Dam breaching • Multi-hazard risk management • Jinsha River

Managing the Risks of Landslide Hazard Chains

Some of the most challenging civil engineering projects in the world are being constructed in the eastern margin of the Qinghai-Tibet plateau, including the Sichuan-Tibet railway and many cascade large dams on the Yalung Tsangbo River, the Parlung Tsangbo River, the Nu River, the Lancang River, the Jinsha River, the Yalong River and the Dadu River. The natural environment in this area is characterized by large tectonic movements and uplift due to collision by the Indian plate, deep river incision, and diversified climate conditions. In particular the seven major rivers cut into the plateau deeply, forming valleys up to 5000 m deep. Accordingly, this area is one hotspot of natural hazards including strong earthquakes, landslides, debris flows, glacier avalanches, and flash floods. How to ensure the safety of critical infrastructures and communities in this area is a grand challenge.

When proposing any strategies to safeguard a large engineering system, four “what” questions should be answered: (1) what can go wrong? (2) what is the likelihood that it will go wrong? (3) what are the consequences if it goes wrong? and (4) what can we do to reduce the consequences? Once the first question is answered or a particular danger is clearly identified, the associated risk can be contained to a certain extent. Yet, “unexpected” hazard scenarios arising from cascading effects can lead to disastrous consequences because such hazards are not prepared for.

Cascading hazards are symbolized by a chain of events in which an initiating event causes a chain of hazardous events, the outcome of one event being the cause of one or more

L. M. Zhang (✉) · J. He · T. Xiao
Department of Civil and Environmental Engineering, The Hong Kong University of Science and Technology, Kowloon, Hong Kong, 999077, China
e-mail: cezhangl@ust.hk

T. Xiao
e-mail: xiaote@ust.hk

other events. The initiating event can be a strong earthquake, an intense rainstorm, or a glacier avalanche. For instance, the Wenchuan earthquake (lead hazard) triggered numerous landslides. Some landslides blocked rivers and formed landslide dams, which later broke and inundated much larger areas downstream the dams (e.g., Cui et al. 2009; Chen et al. 2011; Liu et al. 2013, 2016; Zhang et al. 2014). Some hanging landslide deposits on steep terrains reactivated during subsequent rainstorms, turning into deadly debris flows, jamming the rivers, aggravating the flood risk, causing significant changes in the river eco-system (Zhang et al. 2014, 2016b; Fan et al. 2019a). Significant hazard chains in the eastern margin of the Qinghai-Tibet plateau include the 1786 earthquake-landslide-damming hazard chain in Luding on the Dadu River (Dai et al. 2005), the 1933 Diexi earthquake-landslide-damming hazard chain on the Minjinag River (Liu et al. 2016), the 1988 moraine lake break-debris flow hazard chain in Midui Gully, Tibet (You and Cheng 2005), the 2000 Yigong landslide-damming-flooding hazard chain (e.g., Zhou et al. 2016), the 2018 landslide-damming-flooding hazard chain on the Jinsha River (e.g., Zhang et al. 2019) and the 2018 glacier avalanche-debris flow-damming-flooding hazard chain on the Yarlung Tsangpo River (Chen et al. 2020).

As critical infrastructures are being constructed in the hazardous environment, how a hazard chain impacts a large engineering system and how to mitigate the engineering risks emerge as challenging issues. This paper presents a systematic multi-hazard risk management protocol for future landslide hazard chains, and recaps, within the framework of the proposed protocol, the engineering measures adopted to mitigate the risks to the large cascade dams and other key infrastructures along the Jinsha River posed by the Baige landslide hazard chain in 2018.

Landslide Hazard Chains on the Jinsha River in 2018

The Landslide and Damming at Baige on 10 Oct. 2018

The Jinsha River is 2290 km long, with a basin area of approximately 340,000 km² and an elevation drop of approximately 3250 m. The annual average flow rate increases down the river, from 879 m³/s at Batang (Fig. 1) to 1700 m³/s at Panzhihua and further to about 4500 m³/s at Yibin that is the start of the Yangtze River. Given the rich hydropower resources, more than 25 large dams have been planned along the river for clean energy production (Fig. 1). As of October 2018, the Yebatan dam and the Suwalong dam were under construction, while the six dams from Liyuan to Guanyinyan in Fig. 1 have been constructed.

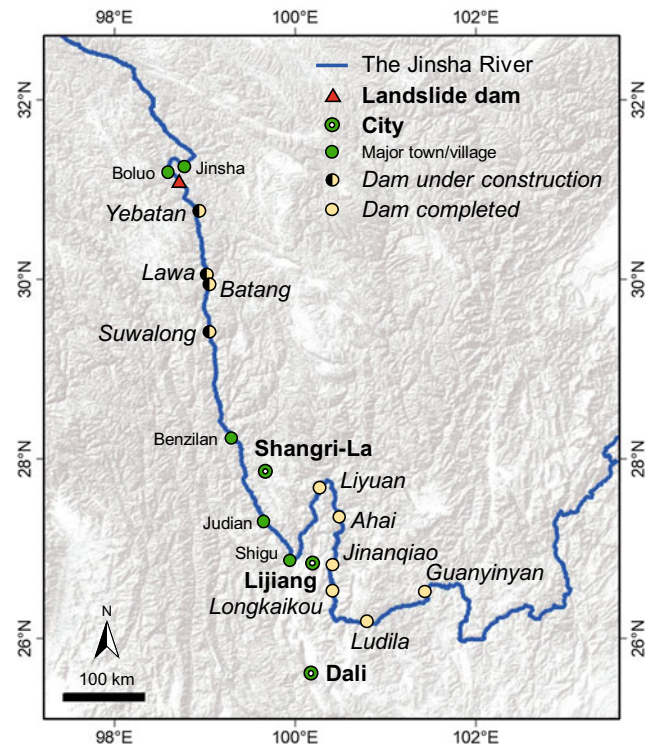


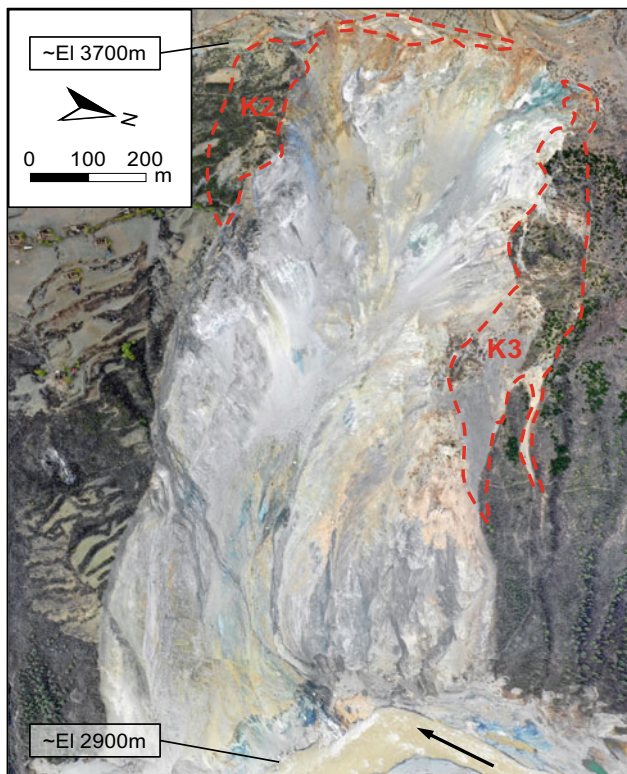
Fig. 1 Location of the Baige landslides and the cascade dams on the Jinsha River

On 10 Oct. 2018, a large landslide occurred at Baige, Jiangda County, Tibet, China on the Jinsha River (Figs. 1 and 2). The landslide scar was located at the right bank of the river at an elevation of approximately 3700 m, and the landslide front blocked the river with an internal relief of over 800 m and a travel distance of 1500 m. The total volume of the landslide was about 25×10^6 m³, the frontal part of which forming a landslide dam (Fig. 2b) with a maximum height of over 61 m and a maximum length of about 1500 m along the river. The primary bedrocks at the site are plagioclase gneiss and serpentinite. A tension zone had been observed in the shattered rock mass after experiencing a long period of downward movements. Fan et al. (2019b) and other have studied the mechanisms of the slope failure.

As the incoming flow rate that time was as large as 1680 m³/s, the lake water level rose rapidly, inundating the upstream villages (Fig. 3). When full, the landslide lake would reach elevation 2931 m, stretching 48 km upstream and having a lake volume of 249×10^6 m³.

The Landslide and Damming on 3 Nov. 2018

About three weeks after the successful disposal of the landslide dam formed on 10 October, a second slide occurred at the same site on 17:15, 3 November, with



(a)



(b)

Fig. 2 **a** The landslide (K1, K2 and K3 are tension zones that may lose stability); **b** the landslide dam that blocked the Jinsha River completely (photo credit **a** Zhang LM; **b** Ganzi Daily)

additional source and entrainment volumes of about 3×10^6 m³ and 8×10^6 m³, respectively. The landslide debris deposited on the breach formed earlier, forming a new dam 96 m in height to the lowest crest and about 1,000 m in length along the river and blocking the Jinsha River once again (Fig. 4). Typical cross sections of the new dam across and along the river are shown in Fig. 5. With an incoming flow rate of about 800 m³/s, the lake volume increased rapidly. When full, the lake volume would reach 750×10^6 m³ and the lake would extend 72 km upstream.

The magnitude of the new landslide dam formed on 3 Nov. 2018 was much larger than the first dam formed on 10

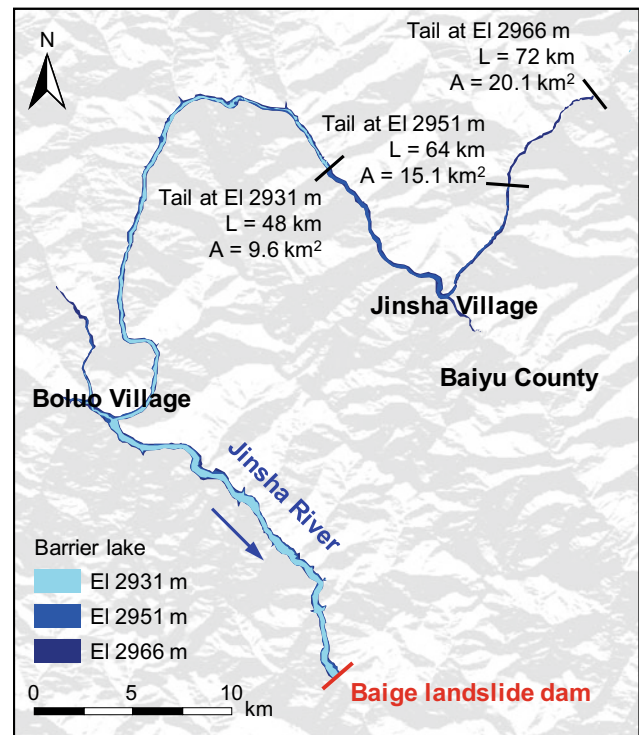


Fig. 3 Inundation areas of the barrier lakes

Oct. 2018. Hence a new strategy had to be developed to manage the risks of the new landslide dam.

Principle of Hazard-Chain Risk Management

The damming on 10 Oct. 2018 was the first record in recent history that the Yangtze River was completely blocked. Given such a significant landslide incident, the four ‘what’ questions raised earlier must be answered and a risk management plan must be made immediately and yet scientifically. Based on the experiences gained in coping with the cascading hazards associated with the Wenchuan earthquake, a protocol of multi-hazard risk assessment has been proposed to help answer these questions (Zhang et al. 2014; Chen et al. 2016; Zhang and Zhang 2017; Zhang 2019). The proposed protocol consists of five phases, including definitions, multi-hazard assessment, exposure assessment, multi-vulnerability assessment, and multi-risk assessment:

- (1) Definition of the time and space scales for hazard analysis, the risk sources, and the initiating events.
- (2) Multi-hazard assessment, which includes identifying the hazard scenarios and links among these scenarios, and quantifying their occurrence probabilities.
- (3) Assessment of interactions among the elements at risk considering possible amplification effects.

Fig. 4 The second landslide at Baige on 3 Nov. 2018 (*photo credit China News*)

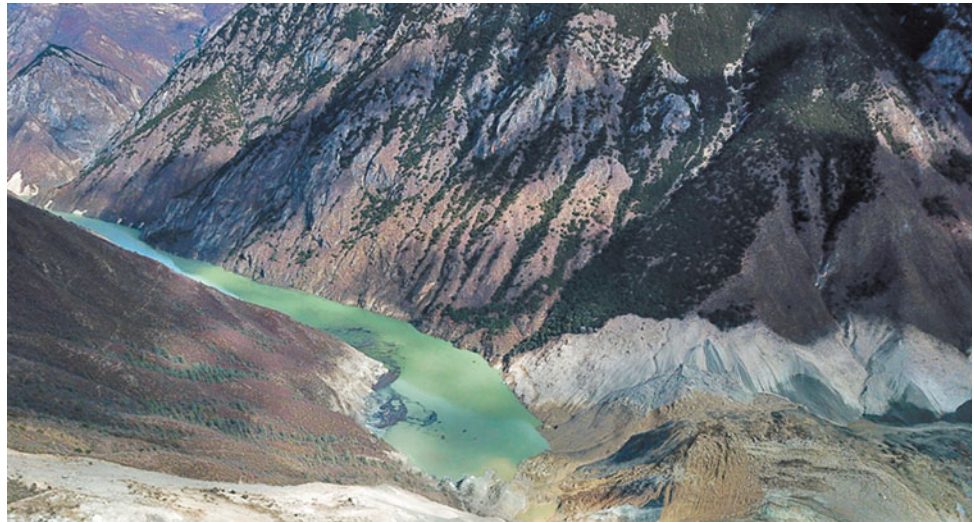
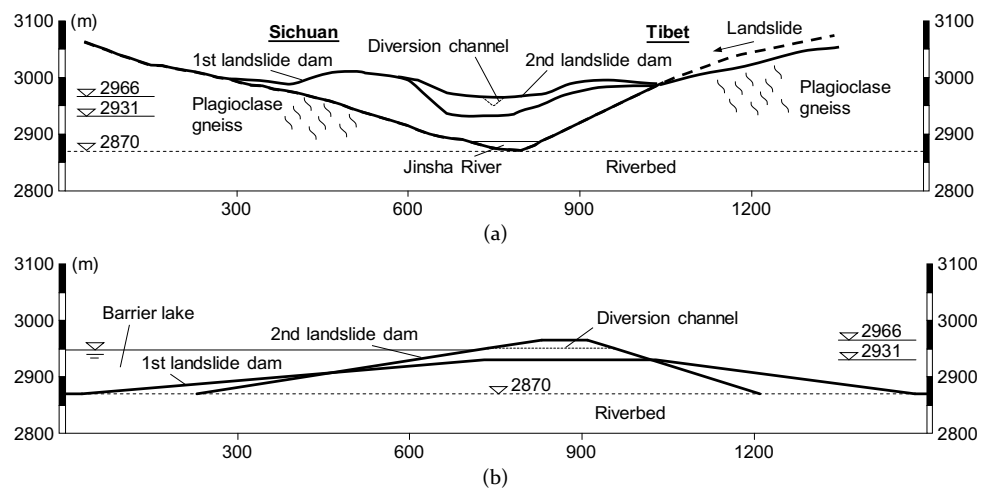


Fig. 5 Cross sections of the Baige landslide dams: **a** across the river; **b** along the river



- (4) Multi-vulnerability assessment, which quantifies the vulnerability of the elements at risk in each affected area to one or multiple hazards.
- (5) Multi-risk assessment, in which the risk of the cascading hazards is expressed as the sum of all risks posed by these hazards, as well as new hazards derived from the hazard interactions.

The protocol emphasizes hazard interactions and the lifecycle concept. How all the initial hazards (i.e., the landslides) evolve over a long period within or outside the formation catchments must first be investigated. Starting from a lead hazard, one should investigate each individual derived hazard over its entire lifecycle from the formation of the hazard to the cessation of further development, for example from the formation of a landslide dam to the breaching of the dam, from the formation of a loose soil deposit to the cessation of reactivation and erosion in the deposit, and from

sedimentation to the incision of a stream. Next, the impacts of all identified cascading hazards over their life spans need be evaluated, bearing in mind that some hazard scenarios can still be unexpected. Efforts must also be made to quantify the amplification and overlapping effects due to the interactions among two or more hazards.

The impact of a dam break covers a large area along the river from the catchment upstream of the dam to the potential flood areas downstream of the dam. In space and time scale (Fig. 6), the risk analysis for a landslide-dam hazard chain includes six steps:

- monitoring and forecasting,
- dam-break probability evaluation,
- dam breaching analysis,
- flood routing analysis,
- dam safety evaluation, and
- flood consequence assessment.

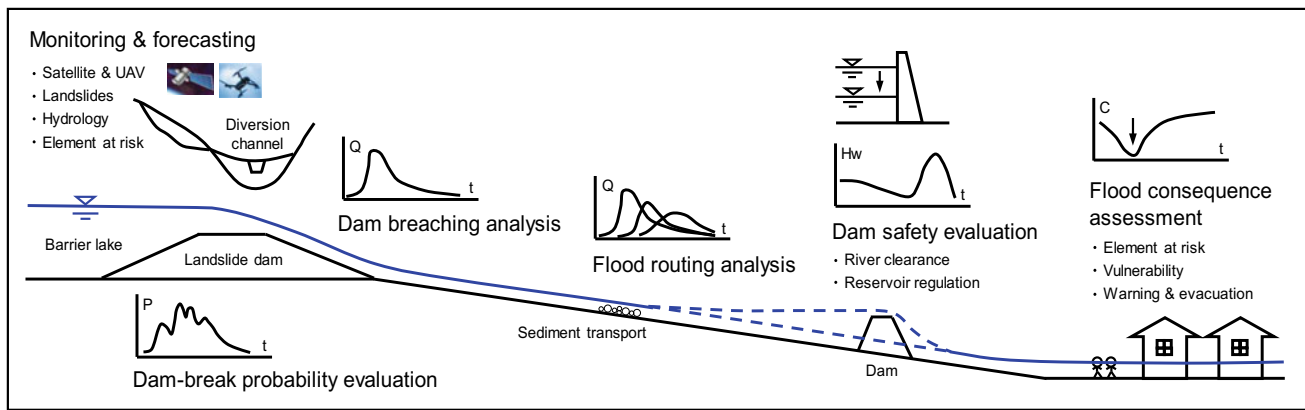


Fig. 6 Landslide dam risk management

Hydrological parameters such as lake volume, lake water level and inflow rate influence the dam safety. These parameters should be treated as stochastic processes instead of independent variables due to the correlation in time scale. The flow rate in the Jinsha River is large so that any landslide dam would fail most likely by overtopping. Overtopping occurs when the lake water level exceeds the dam crest level. The probability of dam failure is closely related to the hydrological parameters. The uncertainty is largely on the time of dam failure rather than whether the landslide dam will fail or not. The next two components are to simulate the dam breaching process and flood routing downstream of the dam. The breaching parameters significantly affect the flood consequence downstream. If there are dams downstream, then the dam safety and the feasibility of using the downstream reservoirs to regulate the flood should be evaluated.

In this study, an empirical model (Peng and Zhang 2012c) based on statistical data is used to simulate the breaching process when only geometrical parameters are available, while a physical model, DABA (Chang and Zhang 2010) is used when more soil properties (e.g., coefficient of erodibility and critical shear stress) are available. The outputs of the dam breaching simulation are peak outflow rate, breaching duration and breach size. With the breaching parameters predicted, a river analysis program, HEC-RAS developed by USACE (2016), is used to simulate the flood routing in the river downstream of the dam. Detailed simulations in a specific case can be referred to Zhang et al. (2016a,2019) and Chen et al. (2020).

This paper will focus on the practical risk management, but will not go into the mathematical aspects of multi-vulnerability assessment and multi-risk assessment.

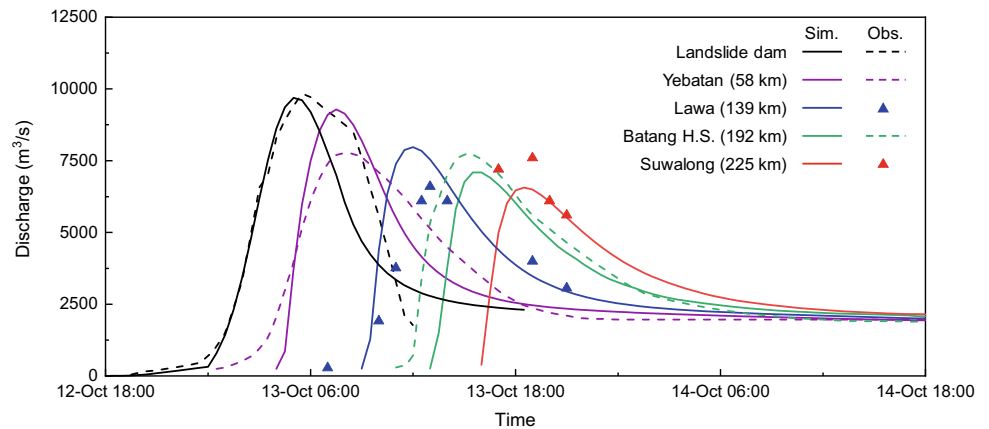
The First Test of System Coping Capability: Breaching of the Landslide Dam Formed on 10 Oct. 2018

The large dams on the Jinsha River, in the past, were designed considering floods due to rainfall but the floods from breaching of either man-made or natural dams are not considered. In this section of the Jinsha River, the 10-, 20-, 100-, 1000-, and 10,000-year return period flow rates are 5510, 6180, 7640, 9610, and 11,500 m³/s, respectively. Any floods larger than the design levels can pose a serious concern. The flood can amplify significantly if two or more dams fail.

Once the river was dammed on 10 Oct. 2018, the lake water level rose rapidly as the incoming flow rate was as large as 1680 m³/s. The landslide dam was naturally overtopped beginning 17:30, 12 October, and breached in about 21 h. The life span of the landslide dam was 2.7 days. The dam breaching flow, peaked at about 10,000 m³/s, reaching approximately the 10,000-year return period flood. The flood marched along the river, posing huge risks on the downstream hydropower projects and residents. Both empirical and numerical methods have been applied to forecast the dam-breaching hydrograph and the river flow (e.g. Zhang et al. 2019). Figure 7 shows the result of a flood routing analysis conducted at the Hong Kong University of Science and Technology.

At that time the river had not been closed at the Yebatan dam site (58 km downstream) and the Lawa dam site (139 km downstream). The first project hit by the dam-breaching flood was the Suwalong dam. The Suwalong

Fig. 7 Dam breaching flood hydrographs along the Jinsha River in Oct. 2018



dam will be a 112 m high asphalt corewall rockfill dam. It is located 225 km downstream the landslide (Fig. 1). The river closure for the dam was performed in Nov. 2017 and the cofferdams had been constructed before the landslide happened. The upstream cofferdam is 50 m high, designed for a 20-y return period flow rate, $6180 \text{ m}^3/\text{s}$. As shown in Fig. 7, the flow rate at the site reached $7600 \text{ m}^3/\text{s}$ on 13 Oct. 2018, larger than the design flow rate. All the diversion tunnels and the emptying tunnel were fully mobilized to pass the flood. The highest water level reached 2426.34 m, only 3.5 m below the design level of 2429.85 m. The cofferdam was nearly overtopped, as shown in Fig. 8.

The flood coping capability of the dams under construction is shown to have been brought to its limit in the first dam break event. Any larger floods will result in serious consequences.

Systematic River-Basin Risk Management

Likely Hazard Chain Triggered by the 3 Nov. 2018 Landslide

When a significant hazard like to 3 Nov. landslide dam is identified, the most important first step is to monitor

Fig. 8 The upstream cofferdam of the Suwalong asphalt corewall rockfill dam (*photo credit* PowerChina)



geological, hydrological and socio-economic conditions in the influence zone and answer two “what” questions “what can go wrong” and “what are the consequences if it goes wrong”. This requires a prompt assessment of the incoming river flow rate and the lake level at the landslide dam site and along the river, the influence zone of the floods, the safety of the community affected, the safety of the large dams already constructed downstream the landslide dam (Fig. 1), as well as any derived hazards due to the interactions between the flood and the natural environment and the engineering systems. Two examples of a derived hazard are the failure of one or more downstream dams due to the flood from the landslide dam break, and the collapse of some bridges leading to cutoff of the road network.

Dam Breaching and River Flood Routing Analyses

A dam-breaching analysis assuming the dam will overtop naturally has been conducted (Zhang et al. 2019), indicating that the peak flow rate at the dam site could reach $55,579 \text{ m}^3/\text{s}$ (Fig. 9). Given this hydrograph, the dam-breaching flood routing in the river reach up to 650 km downstream the landslide site is shown in Fig. 10a. The peak flow rate far

exceeds the 10,000-year return flood at the dam site ($11,500 \text{ m}^3/\text{s}$). The flow discharge attenuates along the river, but still exceeds the 10,000-year return period flood at Suwalong ($12,000 \text{ m}^3/\text{s}$) 225 km downstream, and Benzilan ($13,400 \text{ m}^3/\text{s}$) 382 km downstream. However, the flow rate at the first existing reservoir, the Liyuan reservoir 634 km downstream, will drop to $8444 \text{ m}^3/\text{s}$, smaller than the 100-year flood, $10,400 \text{ m}^3/\text{s}$.

The results of the above analysis imply that risk mitigation measures, both structural and non-structural, must be taken to reduce the risks.

Engineering Risk Mitigation Measures

Division channel. An efficient and effective way to reduce the risks of landslide dams is the use of a diversion channel as in the disposal of many landslide dams caused by the Wenchuan earthquake (e.g. Cui et al. 2012; Chen et al. 2015). The diversion channel works by reducing the lake volume and the area of inundation, and keeping the overtopping erosion in a more controllable manner. In the Baige case, a diversion channel 15 m in depth, 220 m in length, 3 m in bottom width and 42 m in top width was excavated (Fig. 11). The channel lowered the lake volume from $757 \times 10^6 \text{ m}^3$ to $494 \times 10^6 \text{ m}^3$ and the lake area from 20.1 to 15.1 km^2 (Fig. 3). Overtopped at 04:45 on 12 November, the dam experienced a 33.3-h long breach initiation phase. The outflow increased dramatically at 14:00, 13 Nov., and peaked at $33,900 \text{ m}^3/\text{s}$ at 18:20, 13 Nov. 2018.

A second round of overtopping erosion and flood routing analyses was performed. Figures 9 and 10b show the hydrographs with the diversion channel. At the dam site the peak flow rate is reduced from 56,467 to $33,900 \text{ m}^3/\text{s}$. Along the river, the peak flow rates at Suwalong, Benzilan and Shigu are significantly smaller with the help of the diversion channel (Table 1), although the flood level above Benzilan

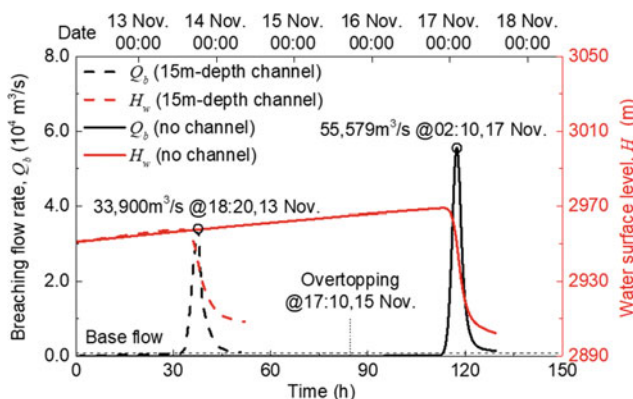


Fig. 9 Dam breaching hydrographs for the landslide dam formed on 3 Nov. 2018 (Zhang et al. 2019)

still exceeds the 10,000-year return period flood. The flood in the densely populated communities below Benzilan, however, has been lowered from a 200-year level to below the 100-year level. Hence the flood risk has been significantly reduced.

Prevention of hazard amplification effects. When handling the safety of cascade reservoirs along the Jinsha River, a key issue is to avoid the overlapping of floods from the failure of two or more dams. Shown in Fig. 8, the 50 m high Suwalong upstream cofferdam was stressed to its limit when stricken by a flood of $7600 \text{ m}^3/\text{s}$. When full, the cofferdam would retain a reservoir of approximately $126 \times 10^6 \text{ m}^3$. After the formation of the 3 Nov. landslide dam, it was apparent that the flow rate at Suwalong could be more than two times of its flood passing capacity (Table 1), hence the dam is deemed to break. A dam breaching analysis shows that (Fig. 10b), the flow rate at Suwalong would reach $19,023 \text{ m}^3/\text{s}$ even after a diversion channel had been excavated at Baige. The Suwalong reservoir would be filled quickly and the cofferdam would be overtopped. The flow rate would be more than doubled ($43,000 \text{ m}^3/\text{s}$) due to the overlap of the incoming dam-breaching flood from Baige and the flood from the break of the $126 \times 10^6 \text{ m}^3$ reservoir.

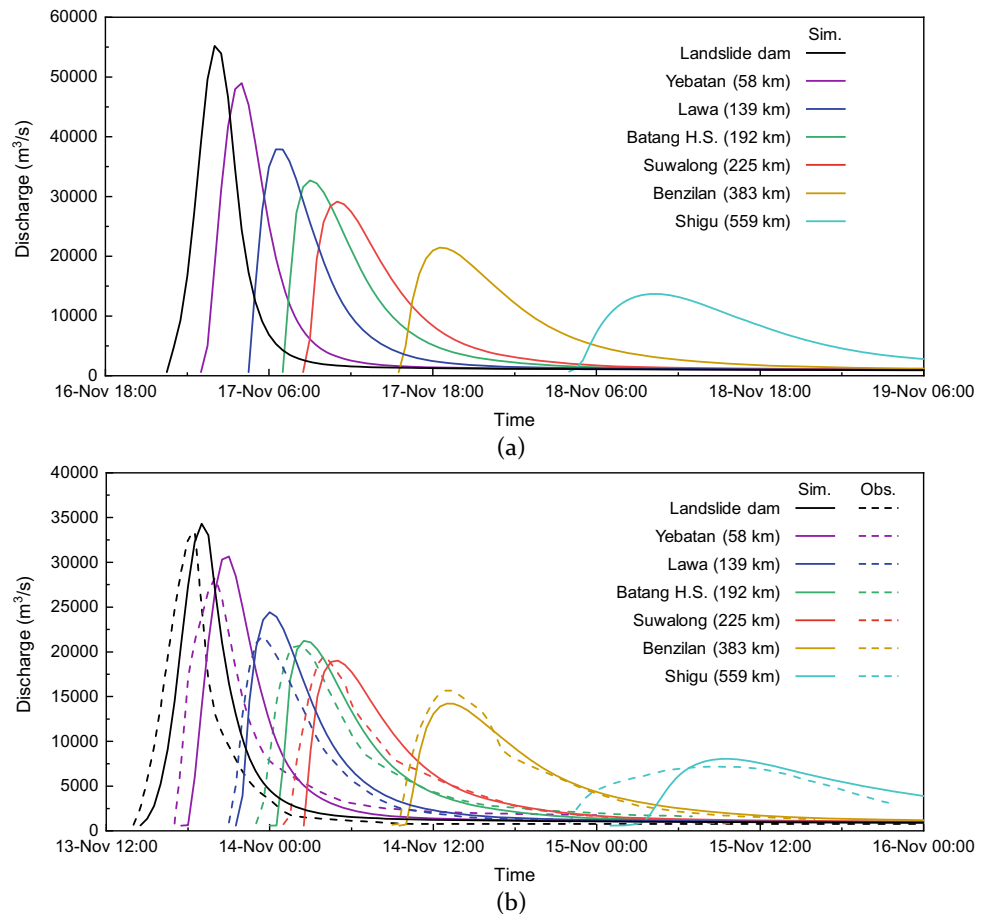
To prevent the amplification effects, it was decided to excavate a large channel through the cofferdam, 33 m in depth, 10.89 m in bottom width and 120.57 m in top width (Fig. 12). The channel was completed two days before the breaching of the Baige landslide dam. Later this was shown to be extremely effective. The entire cofferdam essentially eroded (Fig. 12b) and little flood amplification occurred (Fig. 13).

River-basin flood regulation. The landslide dam is one element of the cascade dam system on the Jinsha River (Fig. 1). Hence a system approach was applied to regulate the river flood and mitigate the flood risks during both the first dam break on 12 Oct. and the second dam break on 12 Nov. 2018.

After the first dam failure, $300 \times 10^6 \text{ m}^3$ of water was released from three reservoirs (Liyuan, Ahai and Jinanqiao, Fig. 1) before the arrival of the flood. The emptied space was larger than the landslide lake volume, $249 \times 10^6 \text{ m}^3$. In the end, $100 \times 10^6 \text{ m}^3$ of water was intercepted as of 8:00, 15 Oct. 2018.

After the second dam failure, $807 \times 10^6 \text{ m}^3$ of water was released from six reservoirs (Liyuan, Ahai, Jinanqiao, Longkaikou, Ludila and Guanyinyan, Fig. 1) before 14:00, 12 Nov. 2018. The total reservoir capacity for regulating the dam breaching flood was 1.353 billion m^3 , much larger than the landslide lake capacity, $750 \times 10^6 \text{ m}^3$. On 15 Nov., the flood entered the Liyuan reservoir at a maximum flow rate of $7410 \text{ m}^3/\text{s}$, while the releasing flow rate was only $4490 \text{ m}^3/\text{s}$

Fig. 10 Flood routing along the Jinsha River in Nov. 2018: **a** when no diversion channel is excavated; **b** when a diversion channel 15 m in depth was excavated



(Chen 2019). The large dam breaching flood then became a regular flood and came to an end. Similar dam-breaching flood water regulation through upstream and downstream reservoirs was exercised during the risk management for the Hongshiyuan landslide dam formed by the Ludian earthquake in 2014 (Shi et al. 2017).

Non-Structural Risk Mitigation Measures

The dam-breaching floods exceeded the 10,000-year return period flood above Benzilan, which was beyond the level most civil infrastructures were designed for. Hence many large bridges over the Jinsha River were destroyed by the flood (Fig. 14a). The flood was at 100–200 year levels in Judian and Shigu. Accordingly these communities were severely flooded (Fig. 14b).

In flood risk management, the most important task to save human lives is timely warning and evacuation (Peng and Zhang 2012a, b). During the Oct. 2018 flood, approximately 10,500 people were evacuated. During the Nov. 2018 flood,

approximately 67,500 people from Tibet, Sichuan and Yunnan were evacuated. No fatality was caused by the two dam-breaching floods.

Systematic Longer-Term Risk Management

Managing Residual Landslide Risks at Baige

Landslides occurred at Baige twice in 2018, caused by long-term tensile deformation of the rock masses. Deformations continue in three large areas (K1, K2 and K3 in Fig. 2a) and new landslides can occur in the future. Therefore, it is necessary to monitor the ongoing slope deformations, evaluate the possibility of the formation of new landslide dams, and assess their consequences.

To prevent the formation of a very large future landslide dam, two major actions were taken in June–July 2019 by the China Anneng Corporation. First, the barrier $2.5 \times 10^6 \text{ m}^3$ in volume above elevation 2915 m was removed, forming a 200 m wide platform (Fig. 15a) on the opposite side of the

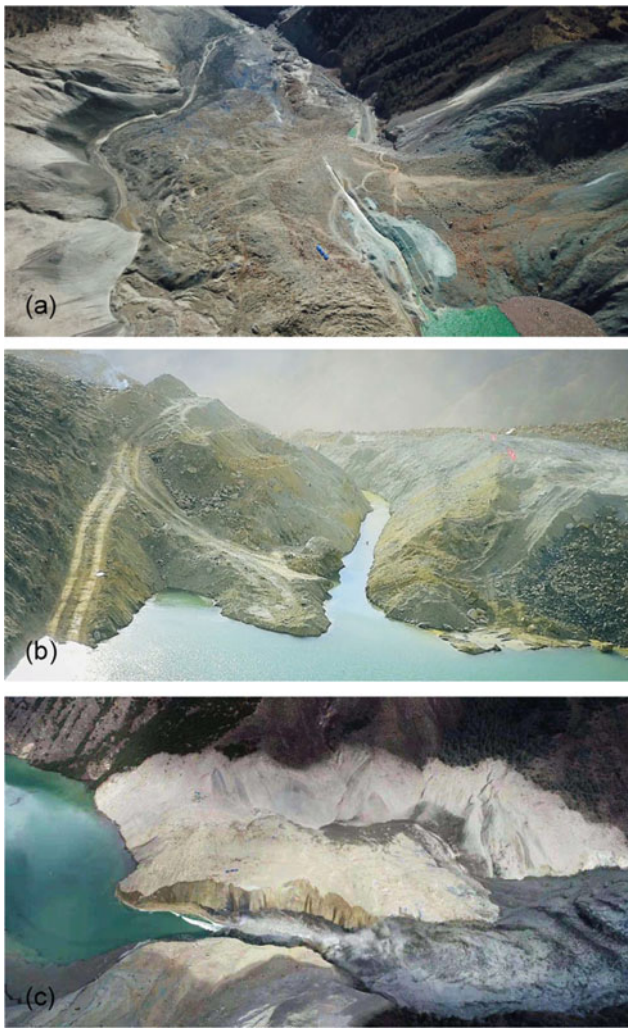


Fig. 11 Use of a 15 m deep, 220 m long diversion channel to mitigate landslide dam risk at Baige: **a** excavation; **b** water flowing through the channel; **c** breaching of the landslide dam (photo credit **a** Red Star News; **b** Xinhua Net; **c** Visual China Group)

landslide. This will provide room to accommodate the landslide debris should a large landslide occur in the future. Second, part of the slope in the K1 area, approximately $0.5 \times 10^6 \text{ m}^3$ in volume, was excavated to relief the load and enhance the stability of the slope (Fig. 15b).

Given the new configuration of the site after the barrier removal, analysis was performed using EDDA 2.0 (Shen



Fig. 12 Removal of the cofferdams at Suwalong to avoid hazard amplification: **a** removal of the upstream cofferdam; **b** after the dam-breaching flood (photo credit **a, b** PowerChina)

et al. 2018) to simulate the damming caused by the instability of K1, K2, K3, and their combinations. Assume a total volume of K1, K2 and K3 of $4.01 \times 10^6 \text{ m}^3$. When all the blocks slide at the same time, a dam can form 66.2 m in height and 46.2 m above the terrain after the breaching of the 3 Nov. 2018 landslide dam (Fig. 16). The flood risks of the dam may be comparable to that of the 10 Oct. 2018 dam. This demonstrates the importance of removing the barrier. Uncertainties should be cautioned, of course, on the scale of future landslides and barriers at the Baige site.

Table 1 Benefit of the diversion channel in mitigating the dam-breaching flood risk

Site	Distance to landslide dam (km)	Observed peak flow rate with diversion channel (m^3/s)	Peak flow rate with diversion channel (m^3/s)	Peak flow rate if no diversion channel (m^3/s)
Baige	0	33,900	34,348	55,579
Suwalong	225	19,800	19,023	29,119
Benzilan	383	15,700	14,218	21,442
Shigu	559	7,170	8,048	11,328

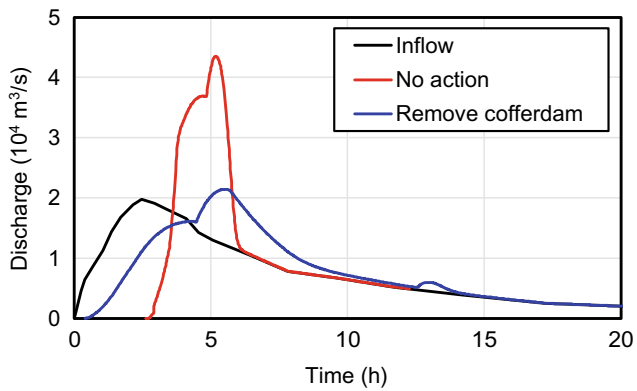


Fig. 13 Potential doubling of the flood by breaching of the upstream cofferdam at Suwalong and minimized amplification after the cofferdam has been removed



Fig. 14 Consequences caused by the dam-breaching flood: **a** damage to infrastructures; **b** flooding of densely populated communities (photo credit **a** Xinhua Net; **b** Dongfang IC)

Managing Longer-Term Landslide Risks at Baige

This study focuses on the landslide hazard chains initiated at a single site, Baige on the Jinsha River. Many other challenging hazard scenarios must be considered in the future:



Fig. 15 Actions to prevent the formation of a very large future landslide dam: **a** removal of the barrier material above 2915 m to make room for future landslide debris; **b** load removal at the slope crest at Baige (photo credit **a** SASAC; **b** Mr. Q. T. Yang)

- The risks of the dams under construction downstream the Baige landslide site should be examined. The flood-passing capacity of concrete dams and earth dams are different, with the latter subject to erosion failure. The flood-coping capacity of a dam project is also different at different stages of construction: smallest capacity shortly after river closure and increased capacity when a spillway or a flood releasing sluice is available.
- A large landslide can occur anywhere along a river, for instance at a site near a densely populated area. A comprehensive survey is necessary to identify potential landslides along the river.
- A large landslide can occur in or near the reservoir of a large dam, directly impacting the safety of the dam. Recall the case of the 1963 Vaiont dam failure in Italy (Hendron and Patton 1985).
- While the cascade reservoirs along a river can work together to regulate the flood, chances can arise when a natural dam or an engineered dam fails and endangers the entire dam system.
- The eastern margin of the Qinghai-Tibet plateau is a seismically active area. Upon a strong earthquake, numerous landslides can be triggered and a major river can be blocked at multiple places at the same time. How to cope with such extreme event is an open issue.

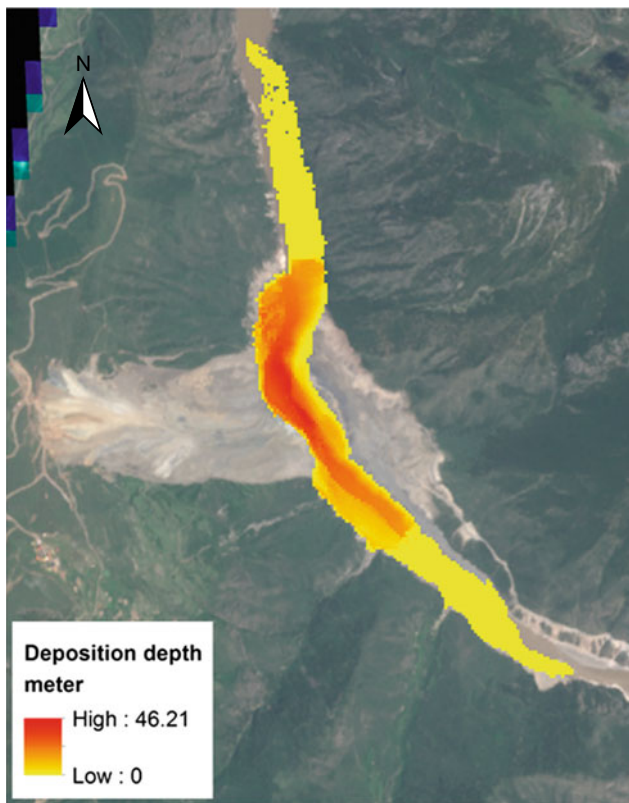


Fig. 16 Deposition depth above the residual of the 3 Nov. 2018 landslide dam

Suggested Scientific Topics for Further Research on Landslide Hazard Chain Risk Management

Management of the risks of a hazard chain is an emerging scientific challenge. In handling the Baige and other landslide hazard chains, several scientific issues are encountered and should be further studied:

- Use of remote sensing to identify intensive tension zones and potential landslides in a river catchment;
- Identification of long-range landslide hazard chains originated from glacier avalanches kilometers away (e.g. the Yalung Tsangbo landslide in Oct. 2018);
- Determination of the escalating points on a landslide hazard chain;
- Ability to expect “unknown” events on a hazard chain so that significant sources of danger are considered in engineering planning and design;
- Stress testing of landslide damming for a cascade reservoir system considering all likely triggers (Stress testing has been shown to be an effective means of managing the risks of low frequency high consequence events (e.g., Zhang et al. 2017);

- Theory for evaluating the reliability of a highly correlated engineering system (e.g. the cascade dams) subject to rare loading (e.g. dam-breaching floods of over 10,000-year return period);
- Technologies to delineate the internal structure of a large landslide barrier, so that necessary mechanical properties of the barrier can be interpreted to assist assessment of the stability and erodibility of the damming materials;
- Technologies to control the pace of the progression of the dam erosion failure process;
- Risk-based engineering risk mitigation measures for landslide dams considering various uncertainties;
- Evolution of riverbed morphology after breaching of a large landslide dam;
- Reappraisal of the risks of cascade dams and optimization of the operations of reservoir systems considering the impact of landslide hazard chains.

Summary

The paper presents a protocol to manage the risks of landslide hazard chains, and illustrates the protocol in the case of the Jinsha River landslide hazard chain in Oct. and Nov. 2018.

The proposed protocol consists of five phases, including definitions, multi-hazard assessment, exposure assessment, multi-vulnerability assessment, and multi-risk assessment. The protocol emphasizes hazard interactions and the lifecycle concept. Attention is also paid to the quantification of the amplification and overlapping effects due to the interactions among two or more hazards.

When a significant hazard like the 3 Nov. 2018 landslide dam is identified, the most important first steps are to answer two questions “what can go wrong” and “what are the consequences if it goes wrong” following the proposed five-phase multi-hazard assessment protocol. This requires a prompt assessment of the likely flood levels at the landslide dam site and along the river, the influence zone of the floods, the safety of the community affected, the safety of the large dams already constructed downstream the landslide dam, as well as any derived hazards due to the interaction between the flood and the natural environment and the engineering system. The next step is then to answer the question “what can we do to reduce the consequences?” and to implement pertinent structural and non-structural risk mitigation measures.

In the case of the Jinsha River landslide hazard chains, the structural engineering measures included the use of a 15 m deep diversion channel to reduce the dam erosion flow rate and flow quantity, removal of cofferdams along the river to avoid amplification effects, flood regulation using six

reservoirs already constructed downstream, load relief at the crest of the instable slope to increase its stability, and removal of part of residual landslide barrier to accommodate future landslides and minimize future landslide dam risks.

New technologies are yet to be developed in the future to better manage the risks of similar landslide hazard chains on the eastern margin of the Qinghai-Tibet plateau and the rest part of the world.

Acknowledgements The authors would like to thank the technical help from Dr. Ping Shen of the University of Macau and Dr. Laura C. Chen of Sichuan University. The research reported in this paper was substantially supported by the National Key Research and Development Program of the Ministry of Science and Technology of China (Project No. 2018YFC1508600), the National Natural Science Foundation of China (No. 41941017), and the Research Grants Council of the Hong Kong SAR (Nos. AoE/E-603/18 and 16206217).

References

- Chang DS, Zhang LM (2010) Simulation of the erosion process of landslide dams due to overtopping considering variations in soil erodibility along depth. *Nat Hazards Earth Syst Sci* 10:933–946
- Chen M (2019) Experiences and inspirations of reservoir regulation in urgent treatment of Baige barrier lake on Jinsha River. *Yangtze River* 50(3):10–14
- Chen Z, Ma L, Yu S, Chen S, Zhou X, Sun P, Li X (2015) Back analysis of the draining process of the Tangjiashan barrier lake. *J Hydraul Eng* 141(4):05014011
- Chen XQ, Cui P, Li Y, Zhao WY (2011) Emergency response to the Tangjiashan landslide-dammed lake resulting from the 2008 Wenchuan Earthquake, China. *Landslides* 8(1):91–98
- Chen HX, Zhang S, Peng M, Zhang LM (2016) A physically-based multi-hazard risk assessment platform for regional rainfall-induced slope failures and debris flows. *Eng Geol* 203:15–29
- Chen C, Zhang LM, Xiao T, He J (2020) Barrier lake bursting and flood routing in the Yarlung Tsangpo Grand Canyon in October 2018. *J Hydrol* 583:124603
- Cui P, Zhu YY, Han YS, Chen XQ, Zhuang JQ (2009) The 12 May Wenchuan earthquake-induced landslide lakes: distribution and preliminary risk evaluation. *Landslides* 6(3):209–223
- Cui P, Dang C, Zhuang JQ, You Y, Chen XQ, Scott KM (2012) Landslide-dammed lake at Tangjiashan, Sichuan Province, China (triggered by the Wenchuan Earthquake, May 12, 2008): risk assessment, mitigation strategy, and lessons learned. *Environ Earth Sci* 65(4):1055–1065
- Dai FC, Lee CF, Deng JH, Tham LG (2005) The 1786 earthquake-triggered landslide dam and subsequent dam-break flood on the Dadu River, southwestern China. *Geomorphology* 65(3–4):205–221
- Fan XM, Scaringi G, Korup O, West AJ, van Westen CJ, Tanyas H, Hovius N, Hales TC, Jibson RW, Allstadt KE, Zhang LM, Evans SG, Xu C, Li G, Pei X, Xu Q, Huang R (2019a) Earthquake-induced chains of geologic hazards: patterns, mechanisms, and impacts. *Rev Geophys* 57:421–503
- Fan X, Xu Q, Alonso-Rodriguez A, Subramanian SS, Li W, Zheng G, Dong X, Huang R (2019b) Successive landsliding and damming of the Jinsha River in eastern Tibet, China: prime investigation, early warning, and emergency response. *Landslides* 16(5):1003–1020
- Hendron AJ Jr, Patton FD (1985) The Vaiont slide, a geotechnical analysis based on new geologic observations of the failure surface. Final Report- 2 Vols., U.S. Army Corps of Engineers, Waterways Experiment Station, June 1985
- Liu N, Cheng ZL, Cui P, Chen NS (2013) Dammed Lake and risk management. Science Press, Beijing
- Liu N, Yang QG, Chen ZY (2016) Hazard Mitigation for Barrier Lakes. Chang Jiang Press, Wuhan
- Peng M, Zhang LM (2012a) Analysis of human risks due to dam break floods—part 1: a new model based on Bayesian networks. *Nat Hazards* 64(1):903–933
- Peng M, Zhang LM (2012b) Analysis of human risks due to dam break floods—part 2: application to Tangjiashan Landslide Dam failure. *Nat Hazards* 64(2):1899–1923
- Peng M, Zhang LM (2012c) Breaching parameters of landslide dams. *Landslides* 9(1):13–31
- Shen P, Zhang LM, Chen HX, Fan RL (2018) EDDA 2.0: integrated simulation of debris flow initiation and dynamics considering two initiation mechanisms. *Geoscientific Model Dev* 11(7):2841–2856
- Shi ZM, Xiong X, Peng M, Zhang LM, Xiong YF, Chen HX, Zhu Y (2017) Risk assessment and mitigation for the Hongshiyuan landslide dam triggered by the 2014 Ludian earthquake in Yunnan, China. *Landslides* 14(1):269–285
- United States Army Corps of Engineers (USACE) (2016) HEC-RAS, River Analysis System - Hydraulic Reference Manual (Version 5.0). Hydrologic Engineering Centre, Davis, California
- You Y, Cheng ZL (2005) Modeling experiment of debris flow in Midui Gully, Tibet. *J Mt Sci* 28(3):288–293
- Zhang LM (2019) Multi-hazard risk assessment. *Desiderata Geotechnica*, Springer Nature Switzerland AG 2019, Cham, pp 227–236
- Zhang LM, Zhang S (2017) Approaches to multi-hazard landslide risk assessment. In: Proceedings of the ASCE GeoRisk 2017, GSP No. 286. ASCE, Reston, pp 312–323
- Zhang LM, Zhang S, Huang RQ (2014) Multi-hazard scenarios and consequences in Beichuan, China: the first five years after the 2008 Wenchuan earthquake. *Eng Geol* 180:4–20
- Zhang LM, Peng M, Chang DS, Xu Y (2016a) Dam failure mechanisms and risk assessment. Wiley, Singapore
- Zhang S, Zhang LM, Nadim F, Lacasse S (2016b) Evolution of mass movement near epicenter of Wenchuan earthquake, the first eight years. *Sci Rep* 6:36154
- Zhang LM, Gao L, Zhou SY, Cheung RWM, Lacasse S (2017) Stress testing framework for managing landslide risks under extreme storms. In: Mikoš M et al (eds) Proceedings of the 4th World Landslide Forum (WLF4), Ljubljana, Slovenia, 29 May - 2 Jun 2017. Springer International Publishing AG 2017, pp 17–32
- Zhang LM, Xiao T, He J, Chen C (2019) Erosion-based analysis of breaching of Baige landslide dams on the Jinsha River, China, in 2018. *Landslides* 16:1965–1979
- Zhou J, Cui P, Hao M (2016) Comprehensive analyses of the initiation and entrainment processes of the 2000 Yigong catastrophic landslide in Tibet, China. *Landslides* 13:39–54

Part II

**Recent Development in Physical Modeling of
Landslides**



Application of Magnetic Tracking System in Laboratory-Scale Rock Avalanche Model Tests

Xiaoyu Chen and Rolando P. Orense

Abstract

Many researchers have been investigating the mechanism of rock avalanches in the laboratory using flume tests, where dry rigid blocks are released on an inclined chute and the motion of the blocks are monitored using video cameras supplemented by image-based processing technique. In this paper, a recently developed sensing technique, which consists of permanent magnets as trackers and magnetometers as receivers, is used to examine the behaviour of the blocks as they propagate downslope. For this purpose, a permanent magnet, whose density, shape and surface characteristics are adjusted to be similar to the other blocks, is incorporated into the pile of blocks at specific locations. Since a permanent magnet generates static magnetic field, its flux density is detected by the magnetometers positioned appropriately adjacent to the flume. From the readings obtained, the magnet's location and orientation at any given time is determined using an optimisation algorithm. For various combinations of pile height, block volume and surface inclination, the displacements and orientations of the permanent magnet, representing one of the blocks undergoing movement, are monitored from which kinematic quantities are captured to highlight the behaviour of the blocks as they flow down the chute. For comparison purposes, the movement of the blocks were also monitored by video camera. The results obtained using the magnetic tracking system coincide very well with those monitored using image analysis from video camera. These highlight the capability of the proposed magnetic tracking system in capturing key kinematic quantities during the downslope motion of the blocks, including translations and rotations.

Keywords

Rock avalanche • Laboratory experiment • Magnetic tracking system

Introduction

Rock avalanches are a common form of mass movement involving materials (such as dry rock) that are fragmented before or during the slope failure. They are considered a significant hazard mainly because of their prodigious capacity for destruction. Hungr et al. (2001) suggested that the term “rock avalanche” be reserved for flow-like movements of fragmented rock resulting from major, extremely rapid rock slides. Hence, a key feature which differentiates rock avalanche from other mass movement phenomena (e.g. rockfall) is that it exhibits a flow-like manner which causes the granular particles to interact with each other and move as a mass of fragments. Rock avalanches may involve the failure of entire mountain slopes, involving tens to hundreds of million m³ and long travel distances. Hence, many researchers have been investigating the process involved in rock avalanche motion for the purpose of predicting runout distance and velocity.

Small-scale laboratory experiments have been conducted by many researchers using diverse techniques to study the effects of various factors on the behaviour of the avalanche mass (e.g. Manzella and Labiouse 2008, 2009; Okura et al. 2000). These include the use of high-speed cameras where the blocks' movements are recorded through the flume's transparent sidewalls and then analysed using digital image correlation (DIC), particle image velocimetry (PIV) and other image-processing techniques. However, such image-based techniques generally require a clear light path, which results in two main disadvantages: (1) it is only possible to capture the displacements at the boundary while the behaviour inside the moving mass cannot be detected;

X. Chen · R. P. Orense (✉)
Department of Civil and Environmental Engineering, University
of Auckland, Auckland, 1142, New Zealand
e-mail: r.orense@auckland.ac.nz

X. Chen
e-mail: xche753@aucklanduni.ac.nz

and (2) the interface frictions at the transparent boundary may extensively influence the behaviour of the captured movements.

This paper introduces a novel magnetic tracking technique which can capture the kinematic qualities associated with the downslope motions of granular blocks in the laboratory scale. The sensing technique consists of a permanent magnet as tracker and magnetometers as receivers. The magnet, whose density, shape and surface characteristics are adjusted to be similar to the other blocks, is incorporated into the pile of blocks at specified locations. Since a permanent magnet generates static magnetic field, its flux density is detected by the magnetometers appropriately positioned near the flume. From the readings obtained, the magnet's location and orientation at any given time is determined using an optimisation algorithm. Hence, key kinematic quantities, including translations and rotations of the representative block during the downslope motion, can be quantified and analysed to provide insights on the behaviour of the moving blocks.

Magnetic Tracking System

Background

Magnetic tracking is a type of position sensing technique which requires a tracking target (tracker) and a reference array (receiver). A permanent magnet is used as the tracking target and incorporated as one of the blocks in the rock avalanche experiment. Note that the static magnetic field generated by the permanent magnet can be detected by the magnetometer array arranged appropriately in the vicinity of the flume. The magnetic flux density adjacent to the permanent magnet carries information about its relative locations and orientations with respect to the receiver (i.e. magnetometers). When the tracker (the block with a permanent magnet inside) moves along with other "normal" blocks, the position of that tracker block at any moment can be calculated by analysing the magnetic field it generates. Therefore, displacement is derived from the change in position over a given period of time.

Some of the advantages of the proposed magnetic tracking system in the study of mass movements in a laboratory scale are as follows: (1) non-invasive operation on trackers allows displacement sensing to be free from any disturbance; (2) the static magnetic field generated by a permanent magnet is not likely to be shielded by rock and soil due to their magnetic permeability very close to air and water; (3) because of the same reason listed above, the displacement under the surface and within the moving mass

can be investigated, which leads to a better understanding of the interaction behaviour; and (4) without battery or auxiliary circuits and devices required, permanent magnets as trackers are easy to set up and it is also possible to further reduce the size of tracker to meet the need of the laboratory tests.

Note that magnetic tracking technique has been proposed by many researchers for human medical applications. For example, Schlageter et al. (2001) developed a system capable of tracking a permanent magnet with a 2D-array of 16 cylindrical Hall sensors. Meng et al. (2004) investigated the use of magnet-based localisation in wireless capsule endoscopic technique.

Due to space limitations, detailed aspects of the tracking system, such as: (1) the mathematical model of static magnetic field produced by permanent magnet that has been used in the proposed tracking system; (2) the tracking algorithm and optimisation technique developed; and (3) calibration and verification of the tracking system using high-order polynomials for position correction, are not discussed here; readers are referred to the works of Chen and Orense (2017, 2019, 2020). Only the outline of the experimental work and some obtained results are presented in the next sections.

Algorithm to Determine Tracker Information

It is essential to develop an algorithm to calculate the location information of a tracker (or multiple trackers) from the data collected by magnetometers. Each set of data collected by a magnetometer at a specific point comprised of three-axis magnetic flux densities. The proposed algorithm can calculate the coordinate point (x, y, z) , using the magnetic flux densities.

The relationship between the magnetic flux density at a spatial point and the location of a point is given by:

$$\vec{B} = \frac{\mu_0 m}{4\pi r^3} (2\cos\theta\hat{r} + \sin\theta\hat{\theta}) \quad (1)$$

$$\vec{B} = \vec{B}_x + \vec{B}_y = 3\frac{\mu_0 m}{4\pi r^3} \sin\theta\cos\theta \cdot \hat{x} + \frac{\mu_0 m}{4\pi r^3} (3\cos^2\theta - 1) \cdot \hat{y} \quad (2)$$

where m is the magnetic moment of the dipole whose unit is $A\ m^2$; μ_0 is the permeability of a vacuum (free space), and B is measured in Tesla. The values of r and θ provide the information of the location of the magnetic tracker in polar coordinates. \hat{r} and $\hat{\theta}$ are unit vectors shown in Fig. 1. Although the above equations are easy to understand, it is difficult to develop an effective algorithm based on the above equations because during any movement, the direction of the tracker or the direction of the magnetic moment is not constant.

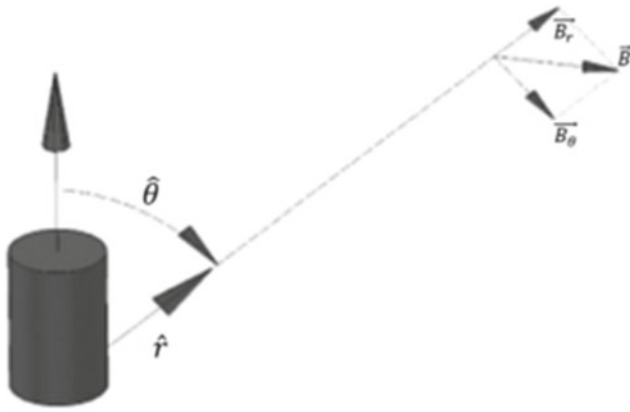


Fig. 1 Schematic of the magnetic flux density generated by a magnetic dipole

In reality, the magnetic flux density at a spatial point is not only dependent on the relative distance from the magnet, but also on the orientation of the magnet (i.e. the magnetisation direction). To solve the location (x, y, z) and the orientation (m, n, p) of a tracker, 6 independent equations are required. However, considering that the size of the tracker is much smaller than the distance between the tracker and the magnetometers and the tracker is either a disc magnet or an electromagnetic coil, spinning around the axis of the magnetisation direction will not change the spatial distributions of the magnetic flux densities. Hence, the magnetic positioning in this case is actually a 5-D positioning because, in addition to the 3 unknowns related with location, there are only 2 more unknowns required to indicate the orientation. As a result, it is more convenient to change the above equations into the following ones, including a unit vector \bar{M}_0 indicating the direction of the magnetic dipole:

$$\bar{B}_i = B_T \left(\frac{3(\bar{M}_0 \cdot \bar{R}_i) \cdot \bar{R}_i}{R_i^5} - \frac{\bar{M}_0}{R_i^3} \right) \quad (3)$$

$$R_i = \sqrt{(x_i - a)^2 + (y_i - b)^2 + (z_i - c)^2} \quad (4)$$

$$\bar{R}_i = (x_i - a, y_i - b, z_i - c) \quad (5)$$

$$\bar{M}_0 = (m, n, p) \quad (6)$$

where B_T is a constant parameter related to the magnet being used; \bar{B}_i is the magnetic flux density detected by magnetometer i , where the location of the magnetometer i is

indicated by (x_i, y_i, z_i) ; (m, n, p) denotes the magnetization direction of the magnet with $m^2 + n^2 + p^2 = 1$; and (a, b, c) is the location of interest. The schematic of the magnetic sensor system is shown in Fig. 2. In order to develop the algorithm required, Eq. (3) can be expanded as:

$$B_{xi} = B_T \left(\frac{3[m(x_i - a) + n(y_i - b) + p(z_i - c)] \cdot (x_i - a)}{R_i^5} - \frac{m}{R_i^3} \right) \quad (7)$$

$$B_{yi} = B_T \left(\frac{3[m(x_i - a) + n(y_i - b) + p(z_i - c)] \cdot (y_i - b)}{R_i^5} - \frac{n}{R_i^3} \right) \quad (8)$$

$$B_{zi} = B_T \left(\frac{3[m(x_i - a) + n(y_i - b) + p(z_i - c)] \cdot (z_i - c)}{R_i^5} - \frac{p}{R_i^3} \right) \quad (9)$$

where B_{xi} , B_{yi} and B_{zi} are the x , y and z components of \bar{B}_i respectively. An effective algorithm should be able to solve the equations for the position of the tracker (a, b, c) and the orientation (m, n, p) using the inputs of B_{xi} , B_{yi} and B_{zi} , and also with the known position of the magnetometer (x_i, y_i, z_i) . In order to solve the above high-order nonlinear equations, a Levenberg–Marquardt (L–M) algorithm (Levenberg 1944; Marquardt 1963), the Interior Point Method and a linear algorithm are used (Hu et al. 2006). Due to space limitation, the appropriate equations for these algorithms are not presented here; however, these can be coded easily in MATLAB. The nonlinear optimisation methods require initial starting point from which the iterations can begin. Hence, the linear algorithm is used to provide a set of initial guesses of the unknowns, which are then used as inputs to nonlinear optimisation algorithms.

Laboratory-Scale Rock Avalanche Experiments

Hardware and Materials Used

The permanent magnet employed in the tests used neodymium as material, which is considered the strongest available magnet material. The cylinder-shaped magnet, shown in Fig. 3a, has a diameter of 15 mm and height of 20 mm with a residual magnetism (B_r) of 1.32–1.37 T (Tesla). The receiver array consisted of 16 Freescale magnetic sensor (MAG3110, as depicted in Fig. 3b), which has a full-scale range of $\pm 1000 \mu\text{T}$ and a sensitivity of $0.10 \mu\text{T}$. The communication between sensors and computer was done through Arduino Uno by I2C interface, illustrated in Fig. 3c.

Fig. 2 Schematic of the magnetic sensor system in the global coordinate frame

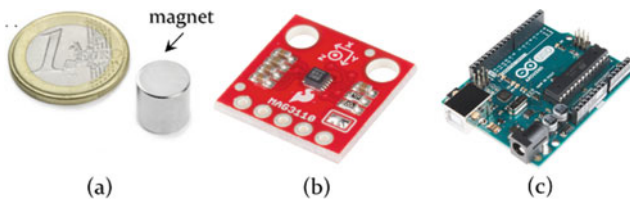
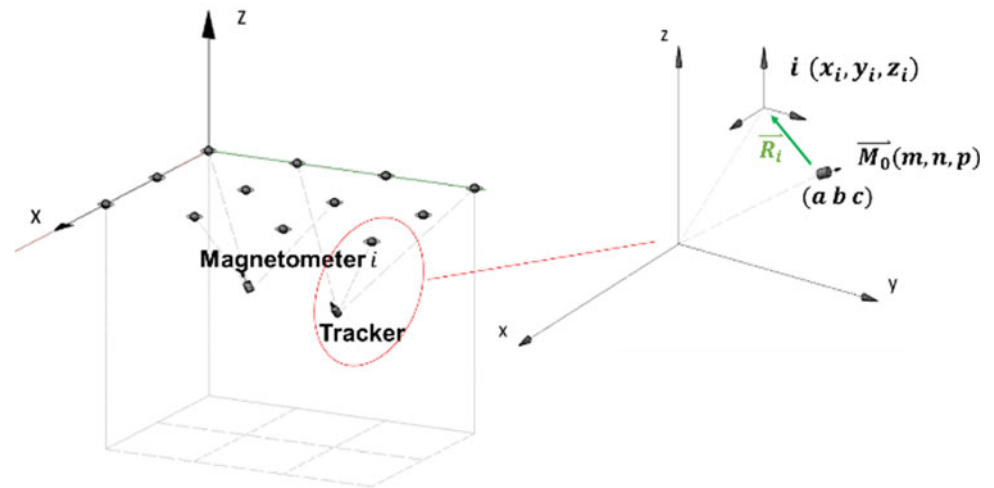


Fig. 3 Hardware used in the experiments: **a** permanent magnet; **b** magnetometer; and **c** Arduino Uno

The rigid blocks used in the experiments are 3.5 cm cubes and made of mortar, as shown in Fig. 4. The tracker block has a permanent magnet inside, with a layer of mortar as a cover material, which is the same material that makes up the normal block. The surface of the tracker block, whose density was adjusted to the same value as the normal block, i.e. 2.3 g/cm^3 is painted black and red for easy identification in subsequent image analyses. The static friction angle of the tracker block and normal block is $24\text{--}25^\circ$.

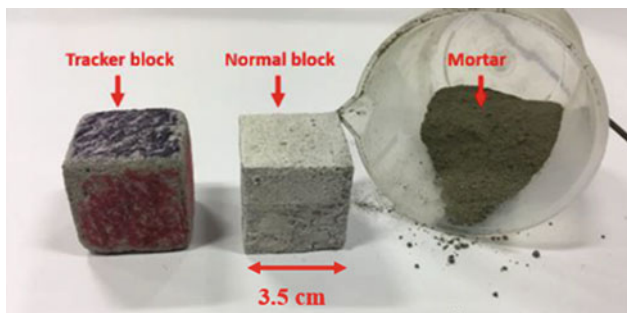


Fig. 4 Tracker block (with a permanent magnet inside) and the normal block used in the experiments

Experimental Set-Up

The laboratory tests involved releasing the pile of rigid blocks positioned in an inclined surface and ending with a horizontal depositional area. The flume used is 0.5 m wide and 1.0 m long. Detailed test configuration is shown in Fig. 5a. The tracker block is placed at a specified location within the pile mass, and indicated by the dark shade in the figure. The 16 magnetometers are arranged adjacent to flume, as indicated in Fig. 5b. The motions of the blocks are initiated by opening the trap door, as shown in Fig. 5c. Parameters such as initial volume, relative tracker location and slope inclination are changed.

Experimental Results

Validation

In order to validate and confirm that the magnetic tracking system can determine the location of the tracker, several flume tests were conducted and its locations as monitored by the magnetometers are compared with those determined by processing the images taken by the video camera at a speed of 30 frames/s. Figure 6a shows a typical results, where it is clear that there is a good agreement between the two techniques. Note that the image analysis can detect the movement only on the x - z plane. Moreover, multiple tests are conducted with the tracker released at the same location from piles having the same width, length and height; Fig. 6b shows typical results where it is observed that the tracker's movements as determined by the magnetometers are more or less similar. Note that there are minor discrepancies, partly due to the fact that movement of the tracker block is influenced by collisions that cannot be perfectly reproduced during the motion.

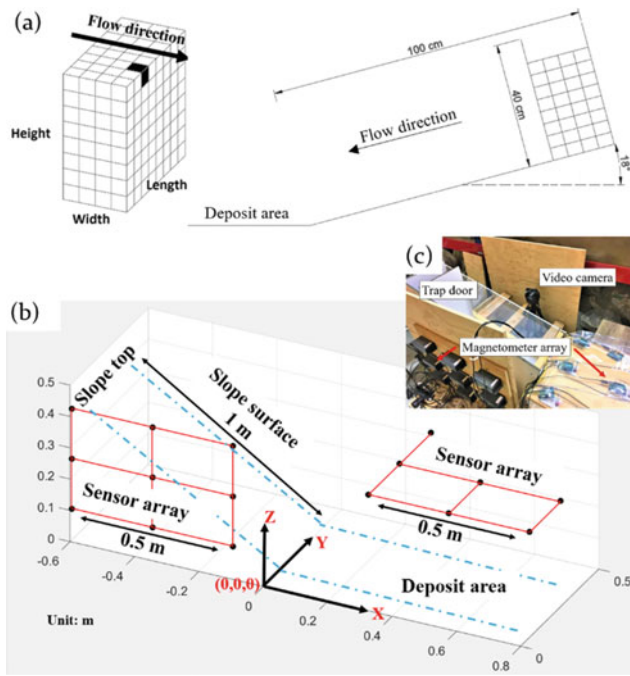


Fig. 5 Experimental set-up: **a** position of tracker block and test configuration; **b** schematic of magnetometer array along the flume and on the deposit area (note: magnetometers are placed at the vertices of the array shown, with the origin of the coordinate system located at the toe of the slope); and **c** setup of the magnetic tracking system with an additional video camera for recording motion through a transparent sidewall

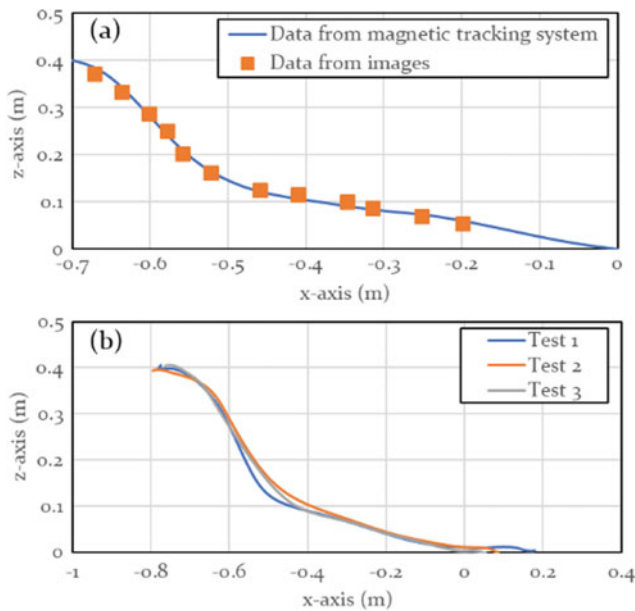


Fig. 6 Validation tests: **a** comparison between data from magnetic tracking system and from images; **b** multiple tests showing similar results

Other Kinematic Quantities

The examples above indicate that the proposed magnetic tracking system can capture the position of a tracker with acceptable accuracy. Hence, the kinematic information of tracker, including linear velocity and acceleration, can be derived by differentiating displacements with respect to time. With known orientations at consecutive timestamps, it can be expected that the average angular velocity (unit: rad/s) within that time interval can be estimated by:

$$\omega_{average} = \frac{\Delta\theta}{\Delta t} = \frac{\arccos\left(\frac{\vec{M}_{t_1} \cdot \vec{M}_{t_2}}{\|\vec{M}_{t_1}\| \cdot \|\vec{M}_{t_2}\|}\right)}{\Delta t} \quad (10)$$

where $\vec{M}_{t_1} = (m_{t_1}, n_{t_1}, p_{t_1})$, $\vec{M}_{t_2} = (m_{t_2}, n_{t_2}, p_{t_2})$, t_1 and t_2 are two consecutive timestamps with $\Delta t = 0.01$ s; $\Delta\theta$ is the angle between two consecutive orientation vectors; also, it is easy to show that $\|\vec{M}_{t_1}\| = \|\vec{M}_{t_2}\| = 1$.

Figure 7 shows the rotational motion of the tracker extracted from one of the flume tests. It shows the change in the tracker orientations and directions of angular velocity with respect to the local reference frame of the tracker (a description in Lagrangian specification). Assuming that an axis (orientation vector, \vec{M}) is attached to the tracker, the blue vectors in Fig. 7 can be regarded as the axis during the motion. Also, the local vector frame (composed of e_x , e_y and e_z) is moving with the tracker and parallel to the global coordinate system (X , Y and Z) shown in Fig. 5b. Therefore, one can imagine a camera following the tracker, with the blue vector illustrating its orientation at a given moment. For example, at $t = 0$, the orientation vector starts from \vec{M}_0 and ends at \vec{M}_5 after the whole journey. It is a way of looking at the tracker motion which the observer is always following as it moves through space and time.

Another way of looking at the rotations of the tracker is to plot the direction angles of the orientation vector (\vec{M}) with respect to time, as shown Fig. 8. As mentioned above, angular velocity is estimated using Eq. (10), and the angular acceleration is calculated by taking the time derivative of angular velocity. Results are shown in Fig. 9. From Fig. 9a, it can be inferred that after around 0.49–0.68 s, the tracker reached the inclined surface of the flume, in which the z -axis velocity (absolute value) decreased a lot significantly and the x -axis velocity also decreased because of collision; meanwhile the angular velocity also dropped, as shown in Fig. 9b.

These observations are supported by images taken at $t = 0.55$, 0.58 and 0.61 s, as shown in Fig. 10. Also, Fig. 9a

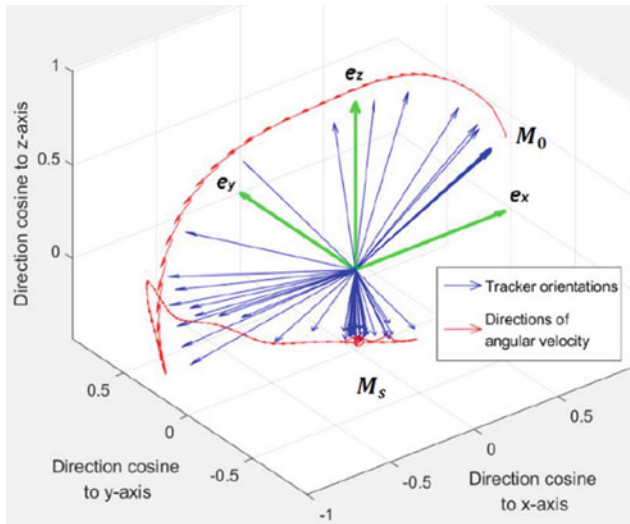


Fig. 7 Rotational motion of the tracker extracted from one of the flume tests, where e_x, e_y and e_z are the unit vectors of x, y and z axis, respectively. \bar{M}_0 and \bar{M}_s are the orientations of the tracker before and after motion

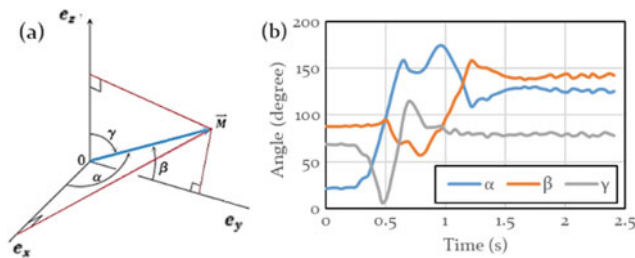


Fig. 8 **a** Definition of direction angles, where α, β and γ are the direction angles of \bar{M} to unit basis vectors of x, y and z axis, respectively; and **b** direction angles of \bar{M} with respect to time

shows that after around 1 s, the z -axis velocity decreased to ≈ 0 , and the x -axis movement started to decelerate, indicating the tracker has reached deposit area.

Chen and Orense (2020) reported some of the rock avalanche behaviour they observed by changing the volume of the moving mass, relative location of the tracker and inclination of the slope. Their results highlight the influence of the initial volume on runout distance from the analysis of the distributions of tracker’s velocity and acceleration. They note that the movement of the block is divided into two phases based on the distributions of translational kinetic energy. The result shows that the movement within the depositional area is more important in terms of its contribution to the longer runout from a larger initial volume. In addition to translational motions, rotational characteristics of a moving particle can be obtained. As highlighted by their

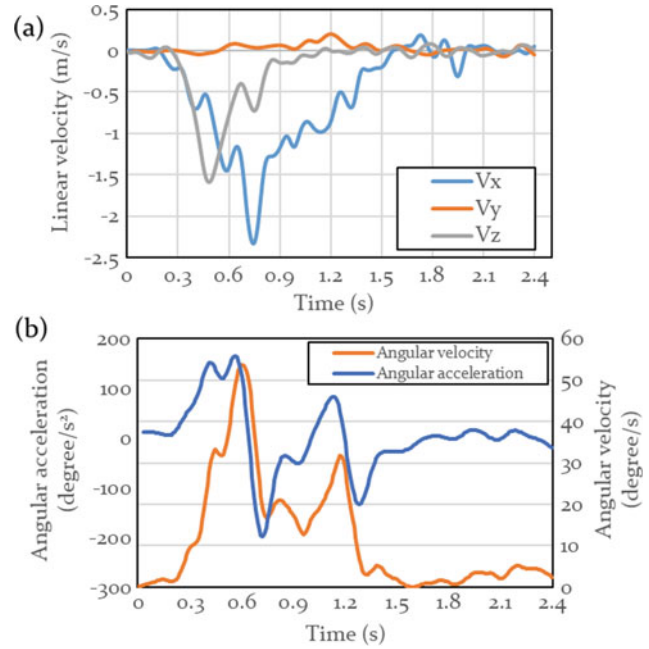


Fig. 9 **a** Linear velocity along 3 axes. Note that V_y is significantly smaller than the other velocity components since the major movement direction is along the x -axis. **b** Angular acceleration and angular velocity

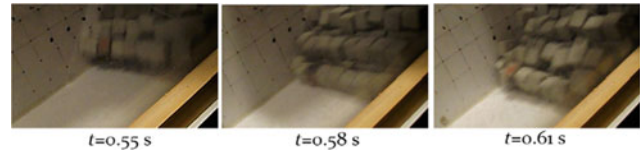


Fig. 10 Sequence of photos from the flume test

experimental results, larger volume tends to inhibit the rotations while producing propulsions to block in front.

It should be mentioned that in many rock avalanche studies, it has been suggested that the scale of the laboratory experiments should be large enough to satisfy the continuum assumption so that the mechanical behaviour of an “ideal granular avalanche” can be reproduced. In the laboratory tests conducted in this research, the depth of the moving mass was less than at least ten times the size of the rigid block, as suggested by Drake (1991). While the results presented herein pose an issue on the effectiveness of the current configuration to study granular avalanche, the experiments showed the interactions between moving particles can be observed, which actually implies a flow-like behaviour. Although extrapolating the results herein to predict the behaviour of real rock avalanche or rockfall may not be straight-forward, it is hoped that they can still indicate suggestive observations for better understanding the downslope motions of granular particles.

Concluding Remarks

In this paper, a magnetic system was developed and applied in tracking the position of a block (with a permanent magnet inside) to investigate the dynamic movement of blocks in a rock avalanche. Kinematic quantities, including displacement, linear and angular velocities and kinetic energies, can be derived. As a result, the interaction between the blocks during the dynamic movement can be investigated in detail.

While only one block of reference is used to represent the entire moving mass, the focus was on studying how the mechanism, which influences the macro behaviour (motion of entire mass), could affect the micro behaviour (one block). While only one block is tracked here, more trackers can be easily be added and supported by multi-object tracking algorithm and the dynamic behaviour of blocks at different parts within the moving mass could be studied with due consideration of the magnetic interference between the magnets.

Acknowledgements The authors would like to acknowledge the assistance of Rob Champion of the Dept. of Electrical, Computer and Software Engineering, University of Auckland, for the assembly of the magnetometers.

References

- Chen X, Orense RP (2017) Development of magnetic tracking system for monitoring ground movements. In: Proceedings of the 20th NZGS geotechnical symposium, Napier, 8 pp
- Chen X, Orense RP (2019) Development of a magnetic tracking system for monitoring soil movements induced by geohazards. In: E3S web of conferences, vol 92, p 17007
- Chen X, Orense RP (2020) Investigating the mechanisms of downslope motions of granular particles in small-scale experiments using magnetic tracking system. *Eng Geol* 265 (2020):105448, 14 pp
- Drake TG (1991) Granular flow: physical experiments and their implications for microstructural theories. *J Fluid Mech* 225:121–152
- Hu C, Meng MQ-H, Mandal M (2006) Efficient linear algorithm for magnetic localization and orientation in capsule endoscopy. In: 27th annual conference of the 2005 IEEE engineering in medicine and biology
- Hungr O, Evans SG, Hutchinson I (2001) A review of the classification of landslides of the flow type. *Environ Eng Geosci* 7(3):221–238
- Levenberg K (1944) A method for the solution of certain non-linear problems in least squares. *Q Appl Math* 2(2):164–168
- Marquardt DW (1963) An algorithm for least-squares estimation of nonlinear parameters. *J Soc Ind Appl Math* 11(2):431–441
- Manzella I, Labiouse V (2008) Qualitative analysis of rock avalanches propagation by means of physical modelling of non-constrained gravel flows. *Rock Mech Rock Eng* 41(1):133–151
- Manzella I, Labiouse V (2009) Flow experiments with gravel and blocks at small scale to investigate parameters and mechanisms involved in rock avalanches. *Eng Geol* 109(1–2):146–158
- Meng MH, Mei T, Pu J, Hu C, Wang X, Chan Y (2004) Wireless robotic capsule endoscopy: state-of-the-art and challenges. In: Fifth world congress on intelligent control and automation (IEEE Cat. No. 04EX788), vol 6, pp 5561–555a
- Okura Y, Kitahara H, Sammori T, Kawanami A (2000) The effects of rockfall volume on runout distance. *Eng Geol* 58(2):109–124
- Schlageter V, Besse PA, Popovic RS, Kucera P (2001) Tracking system with five degrees of freedom using a 2D-array of Hall sensors and a permanent magnet. *Sens Actuators A: Phys* 92(1–3):37–42



2020 Kyoto Japan

A Simple Physically-Based Distributed Translational Landslide Model

Yanto, Sumiyanto, and Arwan Apriyono

Abstract

Detailed landslide susceptibility mapping (LSM) requires a skillful landslide model. Considering that translational landslide is the most type of landslides occurred in the world, a well-behaved translational model is sought. This study presents a simple physically-based distributed translational landslide model. In this model, the incident of landslide is detected from the value of factor of safety (FoS) which is computed based on Mohr–Coulomb failure criterion. In here, FoS is calculated as the ratio of shear strength and shear stress. The lower the FoS, the higher the possibility of a landslide to occur. The model input data consists of soil cohesion c (kg/cm^2), soil specific weight γ (g/cm^3), depth of surface of rupture (m), slope of surface of rupture β (degree) and friction angle ϕ (degree). Application of the model was performed in Sirampog and Kandang Serang, two subdistricts in Western Central Java that underwent the most frequent landslides in the region. Model validation was conducted by comparing the values of FoS of unsaturated and saturated soils and identifying FoS in the sites where landslide events recorded. Several goodness of fit indices to measure the model performance are accuracy (ACC), success index (SI), average index (AI) and distance to perfect classification (D2PC). Under unsaturated condition, the result shows that the number of grids having FoS less than 1 are 0% and 0.6% for Sirampog and Kandang Serang respectively, indicating no landslide occurrence. When the soil gets saturated, 17.6% and 36% of area have FoS less than 1 for Sirampog and Kandang Serang respectively. This shows that the landslide occurred in

this region is rainfall-induced landslide. Overall, the model shows a good performance with ACC, SI, AI, D2PC values are 0.82, 0.58, 0.54, 0 and 0.64, 0.49, 0.49, 0 for Sirampog and Kandang Serang respectively.

Keywords

Translational landslide • Physical model • Factor of safety • Landslide susceptibility map

Introduction

Many parts of the world are susceptible to landslide (Allen and Voiland 2017). An accurate landslide susceptibility mapping (LSM) is therefore important for landslide hazard assessment and landslide mitigation planning (Brabb 1985). A number of approaches have been used for estimating LSM around the world such as Frequency Ratio (Choi et al. 2012; Silalahi et al. 2019), Landslide Numerical Risk Factor (Roy and Saha 2019), Analytical Hierarchical Process (Abedini and Tulabi 2018), Logistic Regression (Lombardo and Mai 2018) and many others. The most applied methods in developing LSM are statistical techniques, artificial neural network and machine learning algorithm (Chang et al. 2019; Dou et al. 2020; Segoni et al. 2020; Tien Bui et al. 2019). The physically-based model is useful in understanding the landslide physical mechanism through linking hydrology, geomorphology and geotechnical science with different degree of simplification. Nonetheless, physically-based LSM is very limited (Formetta et al. 2014, 2016; Segoni et al. 2020).

Physically, a landslide occurs if the slope stability disturbed. This happens as the maximum capacity of soil to bear load or stress (shear strength) is lower than the applied load or stress (shear stress) (Das 1994). The ratio of shear strength to shear stress is called factor of safety (FoS). Hence, suitable estimation of FoS in space is critical as it is

Yanto (✉) · Sumiyanto · A. Apriyono
Civil Engineering Department, Jenderal Soedirman University, Jl.
Mayjen Soengkonno KM 5 Blater, Purwokerto, Purbalingga,
53371, Indonesia
e-mail: yanto@unsoed.ac.id

A. Apriyono
e-mail: arwan.apriyono@unsoed.ac.id

valuable for not only an appropriate LSM but also potentially useful for the development of landslide early warning system. Accordingly, a trustful physically-based distributed landslide model is sought.

A few number of physically-based distributed model for landslide are found in literature such as GEOTop model (Formetta et al. 2014) and NewAge-JGrass hydrological model (Formetta et al. 2016). In both model, FoS is calculated from the simplification of infinite slope equation (Formetta et al. 2014). This is one of methods for modelling translational landslide, one of the most common landslide types occurred in the world (Postance et al. 2018). Translational landslide often occurs in the presence of a layer separating strong and weak soil. This layer is called surface of rupture. Therefore, trustworthy estimation of the depth of surface of rupture is critical. GEOTop and NewAge-JGrass model are dissimilar in determining this depth.

This study presents a physically-based distributed translational landslide model. The modelling framework is similar to the aforementioned model. However, we offer different approach to estimate the depth of surface of rupture. In here, we estimate this depth based on soil bearing capacity.

Model Description

The model presented here is in the first stage of development. At current form, the model is very modest. However, we show it useful in mapping landslide susceptibility zone.

The model lies on the Mohr–Coulomb failure criterion (Hackston and Rutter 2016; Labuz and Zang 2012). Following the theory, FoS in this model is defined as the ratio of shear stress and shear strength. Shear stress is resistive force per unit area in soil due to applied shear force and shear strength is ability of soil to resist external load against failure. The model is schematically presented in Fig. 1.

According to the Mohr–Coulomb theory as shown in Fig. 1, shear strength per unit volume is calculated as follow:

$$\tau_r = c + \sigma \tan \varphi \quad (1)$$

$$\sigma = \frac{Na}{L^2/\cos\beta} = \frac{\gamma L^2 H \cos\beta}{L^2/\cos\beta} \quad (2)$$

$$\tau_r = c + \gamma H \cos^2\beta \tan \varphi \quad (3)$$

In here, τ_r is shear strength (kg/cm^2), Na is normal force (kg), L is grid size (m), c is soil cohesion (kg/cm^2), γ is soil specific weight (kg/cm^3), H is depth of surface of rupture measured from ground elevation (m), β is slope of surface of rupture (degree) and φ is friction angle (degree).

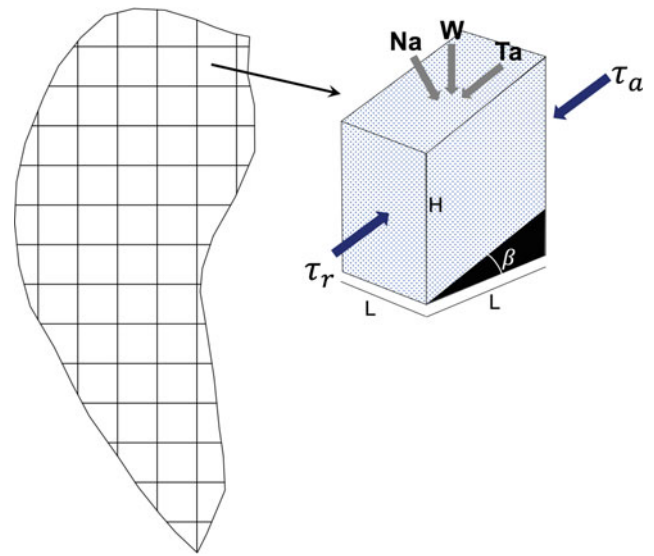


Fig. 1 Schematic representation of the model

As presented in Fig. 1, shear stress is natural force acting on the surface of rupture mainly coming from soil block above the surface. Accordingly, shear stress τ_a (kg/cm^2) is formulated as follow:

$$\tau_a = \frac{Ta}{L^2/\cos\beta} = \frac{\gamma L^2 H \sin\beta}{L^2/\cos\beta} = \gamma H \sin\beta \cos\beta \quad (4)$$

In here, Ta is shear force (kg). Based on the above-mentioned formulation, the FoS can be straightforwardly expressed as follow:

$$FoS = \frac{\tau_r}{\tau_a} = \frac{c + \gamma H \cos^2\beta \tan \varphi}{\gamma H \sin\beta \cos\beta} \quad (5)$$

According to the FoS formulation, it can be inferred that landslide will occur in the areas with FoS less than 1.

Model Configuration and Input

As shown in Fig. 1, the model is run in distributed mode. Computation of FoS is performed in each grid separately. The code is written using R programming language which can be run either in R software or through Terminal or Windows Command Prompt. The input data should be written in comma separated value (csv) file format. The output from the model is a landslide susceptibility map.

For each grid, input data required to run the model are geographic location, soil cohesion, soil specific weight, depth of surface of rupture and slope of surface of rupture. The slope of surface of rupture is deemed to be the same as the slope of land surface for simplicity. The slope along with

its corresponding geographic location is derived from the Digital Elevation Method (DEM) by Shuttle Radar Topography Mission (SRTM) at $30\text{ m} \times 30\text{ m}$ resolution. In addition, soil cohesion, soil specific weight, depth of surface of rupture are obtained from soil test using in situ Cone Penetration Test (CPT) and laboratory tests.

While slope, geographic location, cohesion and specific weight can be easily and unquestionably defined from their original sources, determination of the depth of surface of rupture is quite challenging. This is because no referenced number can be used for the specific purpose. As an alternative, we set the depth of surface of rupture for the model as the depth of soil obtained from CPT where the cone tip resistance reaches up to 250 kg/m^2 which is usually used to define the hard soil layer for designing building foundation.

Translational landslide usually takes place when the soil above surface to rupture gets saturated, partially or fully. Under saturated condition, cohesion and friction angle will variedly drop with the rate depending on the soil types, initial soil water content, etc. While soil cohesion could decrease to averagely 22%, soil friction angle could decline to about 50% (Lakmali et al. 2016; Minnesota Department of Transportation 2019). As soil parameters in this study were obtained under unsaturated condition, it is necessary to estimate their values under saturated soil using the aforementioned number.

To test the model, we run the model under unsaturated and saturated soils. It is expected that no grid will have FoS values less than 1 under unsaturated condition and some grids will possess FoS values less than 1. Hence, we can prove that the landslide occurred in this area is induced by rainfall.

Model Testing

Study Area and Data

To examine the model performance in mapping landslide susceptibility zone, we run the model on Sirampog subdistrict, Brebes, Central Java, and Kandang Serang subdistrict, Pemalang, Central Java, Indonesia as shown in Fig. 2. Sirampog and Kandang Serang have an area of 69 km^2 and 74 km^2 respectively. These places have the most frequent landslide events in the Western Central Java counting 3 events during the period of 2011–2017, (BNPB 2020).

Soil properties data to run the model were obtained from Soil Mechanics Laboratory, Civil Engineering Department, Jenderal Soedirman University. It was collected during the period of 2005–2016 with some absent data in the period of 2008–2009. The soil properties are then interpolated to the

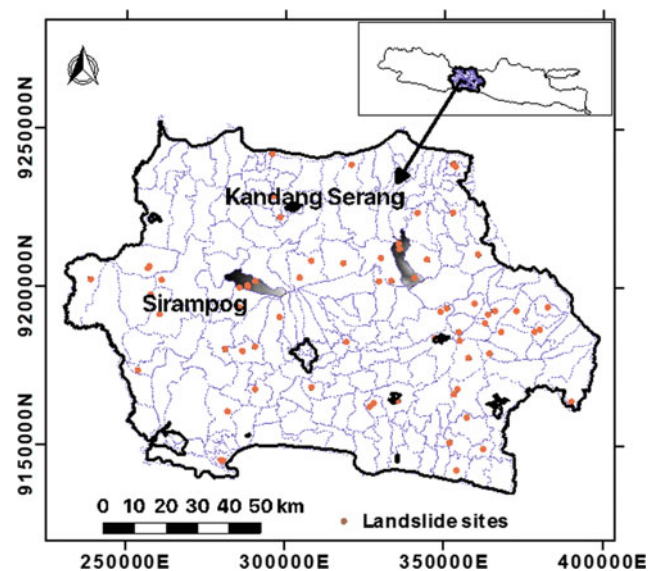


Fig. 2 Study area to test the performance of the model

$30\text{ m} \times 30\text{ m}$ SRTM DEM raster points. In here we used Inverse Distance Weighting (IDW) interpolation technique.

Model Results

To assess the goodness of fit (GOF) of the model, we calculated several GOF indices (Formetta et al. 2016) and shown in Table 1. It can be inferred that the model performance is quite good where Sirampog produces better performance than Kandang Serang.

Table 2 also presents the FoS values from the model along with the summary of model parameter values generated from IDW interpolation for the entire Sirampog and Kandang Serang area and the values for each site where landslide occurrences recorded, i.e. Site 1, Site 2 and Site 2 for both subdistrict as presented in Figs. 3 and 4. Moreover, While the values of many model parameters are similar, soil cohesion in Sirampog and Kandang Serang shows large different. In Sirampog, the dominant soil type is organic silt, while in Kandang Serang, the dominant soil is sandy clay.

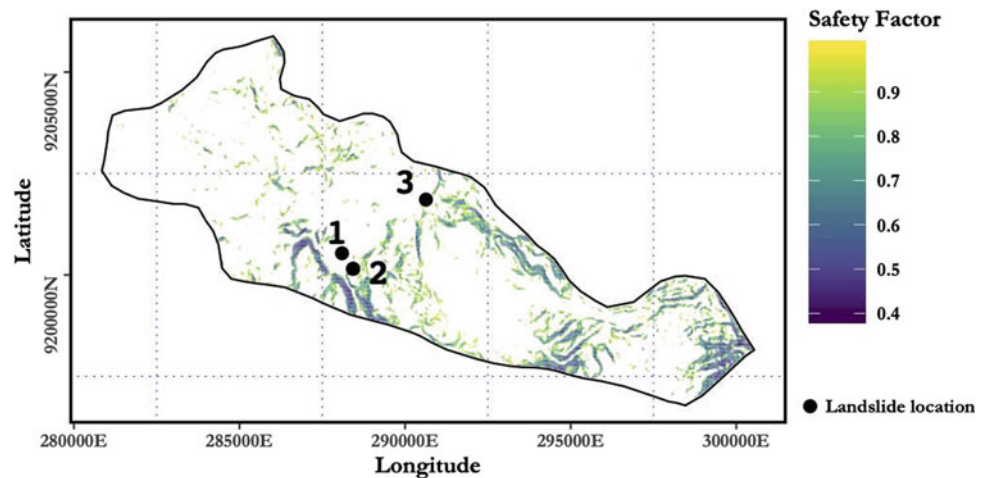
The minimum values of FoS in Sirampog and Kandang Serang are 1.27 and 0.91 respectively. The FoS values less than 1 in Kandang Serang account for 0.6% of the total area, indicating that under unsaturated condition, landslide unlikely occurs. Moreover, it can also be seen in Table 2 that the minimum FoS values of saturated soil are 0.39 and 0.27 for Sirampog and Kandang Serang respectively. The grids having FoS less than 1 under saturated condition in Sirampog and Kandang Serang are 17.6% and 36% respectively which correlated with the variability of soil cohesion in the

Table 1 Summary of GOF indices

GOF indices	Sirampog	Kendang Serang	Optimum
Accuracy (ACC)	0.82	0.64	1
Average Index (AI)	0.54	0.49	1
Success Index (SI)	0.58	0.49	1
Distance to Perfect Classification (D2PC)	0	0	0

Table 2 Summary of model parameter values

Model Parameter/Result	Sirampog			Kendang Serang				
	Range	Site 1	Site 2	Site 3	Range	Site 1	Site 2	Site 3
c (kg/cm ²)	0.08–6.15	0.49	0.51	0.57	0.06–0.31	0.30	0.29	0.31
γ (g/cm ³)	1.55–1.71	1.56	1.56	1.56	1.54–1.57	1.55	1.55	1.56
H (m)	2.77–11.53	7.17	7.15	7.08	2.57–7.63	7.31	7.22	7.41
β (°)	0–56.17	9.17	28.30	16.82	0–87	4.19	9.71	26.62
φ (°)	30.05–40.46	30.82	30.90	30.86	28.95–36.88	29.34	29.60	29.72
Unsaturated FoS	1.27–Inf	6.50	2.23	3.84	0.92–Inf	11.30	4.92	1.81
Saturated FoS	0.39–Inf	2.33	0.76	1.32	0.27–Inf	4.37	1.89	0.68

Fig. 3 Landslide susceptibility map of Sirampog along with landslide sites

two places. Accordingly, it can be inferred that the landslide events are rainfall-induced landslide.

Sirampog Subdistrict

The LSM of Sirampog overlaid with the sites of recorded landslide is presented in Fig. 3. As shown in Fig. 3, the landslide susceptible zones are more distributed to the eastward, while in the westward there exists less susceptible areas. The map is consistent with the spatial arrangement of

elevation and land surface slope (not shown due to page limitation) where elevation and slope increase eastward. Moreover, the spatial pattern of LSM is corresponding to the spatial configuration of β .

The value of FoS in Site 1, Site 2 and Site 3 is 2.33, 0.76 and 1.32 respectively showing that only 1 out of 3 sites is correctly modelled. It can be observed that these values are strongly correlated with the values of β . The β values in Site 1 and Site 3 are 9.17 and 16.82° respectively, which can be considered too low to generate a landslide. In addition, it can also be noticed that value of c decreases from 0.57 to

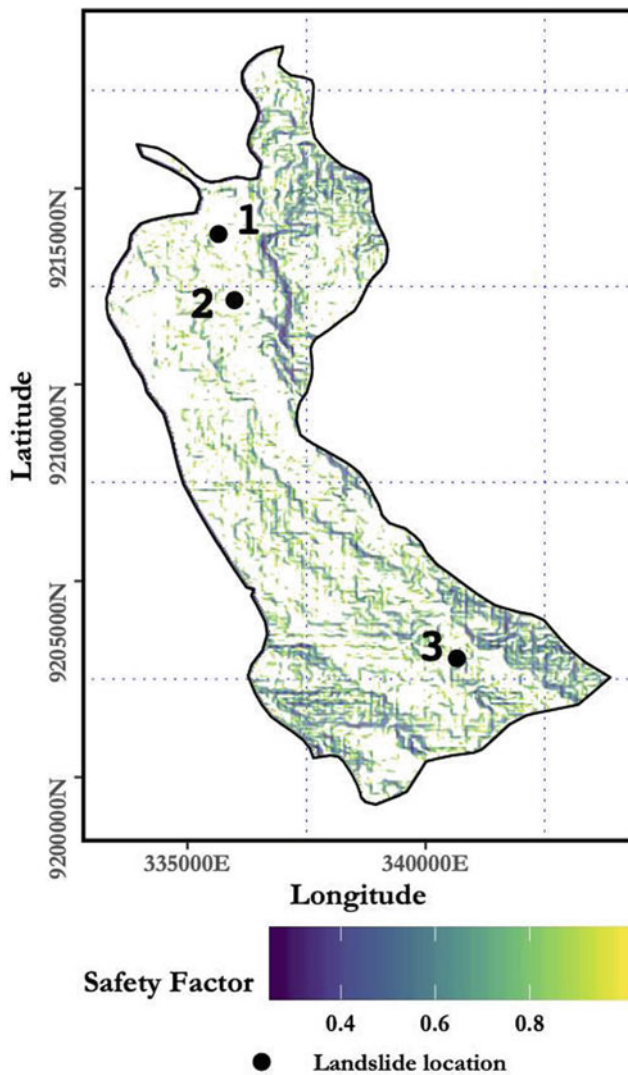


Fig. 4 Landslide susceptibility map of Kandang Serang along with landslide sites

0.51 kg/cm² as the β increases from 16.82 to 28.30°. This conforms the inference presented previously.

Based on the above analysis, it can be roughly deduced that the model is sensitive to the values of β , the slope of surface of rupture. This is in accordance with other studies showing the sensitivity of landslide model to digital terrain model (Pawluszek et al. 2018; Segoni et al. 2020). Moreover, it brings a new challenge on the model parameterization, particularly estimation of β .

Kandang Serang Subdistrict

The LSM of Kandang Serang along with the sites of landslide events is displayed in Fig. 4. As can be seen in Fig. 4, the spread of landslide susceptible zones is quite uniform.

Moreover, about 36% of Kandang Serang's area is susceptible to landslide, higher than Sirampog which is about 17.6%. This resembles the fraction of slope more than 30°. In Kandang Serang, about 11% areas have slope of more than 30°, larger than in Sirampog, which is 8%. Again, this corroborates the previous hypothesis.

In this area, there are 491 grids possessing FoS less than 1 under unsaturated condition. Theoretically, these places should be full of landslide events record, but it is not. One reason should be addressed is the model assumption to equalize slope of surface of rupture with land surface slope, which is unlikely factual for high slope values. For example, it is dubious to have soil block can rest on the surface of rupture with slope of more than 45° unless it has high soil cohesion, which is not the case of hilly topography. Another possibility is that a place with slope of more than 45° is a massive rock formation which is not subject to Mohr–Coulomb failure criterion.

To verify the above analysis, we extracted the values of β in the places where FoS less than 1 under unsaturated condition. We found that the values of β in these grids range from 49.8 to 68.6°. This finding conforms our premise.

The values of FoS in Site 1, Site 2 and Site 3 are 4.37, 1.89 and 0.68 which correspond to the values of β . The higher the β , the lower the FoS, signifying the sensitivity of the model to the value of β .

Future Model Development

Model parameterization is prerequisite for developing a skilled model (Guimaraes et al. 2003; Knowling et al. 2019; Kuriakose et al. 2009). In line with the result of model testing and to extend the use of the model, model parameterization will be directed to the estimation of β involving geological setting, valuation of c under different soil moisture to reflect the influence of rainfall on the variability of c and the connection of the model with hydrological model, such as VIC. The later enables the model to be run in a simulation mode such that it can be employed for landslide early warning.

Conclusion and Remark

A physically-based distributed translational landslide model at its very basic form is presented in this paper. Its application on two different regions shows that the model produces a good performance. However, some paucities are found and some hypothesize proposed. Nevertheless, the model is thought to be useful and it can be potentially extended for the development of a landslide early warning system.

References

- Abedini M, Tulabi S (2018) Assessing LNRF, FR, and AHP models in landslide susceptibility mapping index: a comparative study of Nojian watershed in Lorestan province, Iran. *Environ Earth Sci* 77 (11):405. <https://doi.org/10.1007/s12665-018-7524-1>
- Allen J, Voiland A (2017) A global view of landslide susceptibility. <https://earthobservatory.nasa.gov/images/89937/a-global-view-of-landslide-susceptibility>
- BNPB (2020) Results. <https://dibi.bnpb.go.id/DesInventar/results.jsp>
- Brabb EE (1985) Innovative approaches to landslide hazard and risk mapping, vol 1, pp 17–22
- Chang KT, Merghadi A, Yunus AP, Pham BT, Dou J (2019) Evaluating scale effects of topographic variables in landslide susceptibility models using GIS-based machine learning techniques. *Sci Rep* 9(1):1–21. <https://doi.org/10.1038/s41598-019-48773-2>
- Choi J, Oh HJ, Lee HJ, Lee C, Lee S (2012) Combining landslide susceptibility maps obtained from frequency ratio, logistic regression, and artificial neural network models using ASTER images and GIS. *Eng Geol* 124(1):12–23. <https://doi.org/10.1016/j.enggeo.2011.09.011>
- Das BM (1994) Principle of foundation engineering. PWS-KENT Publishing Company
- Dou J, Yunus AP, Merghadi A, Shirzadi A, Nguyen H, Hussain Y, Avtar R, Chen Y, Pham BT, Yamagishi H (2020) Different sampling strategies for predicting landslide susceptibilities are deemed less consequential with deep learning. *Sci Total Environ* 720:137320. <https://doi.org/10.1016/j.scitotenv.2020.137320>
- Formetta G, Capparelli G, Versace P (2016) Evaluating performance of simplified physically based models for shallow landslide susceptibility. *Hydrol Earth Syst Sci* 20:4585–4603. <https://doi.org/10.5194/hess-20-4585-2016>
- Formetta G, Rago V, Capparelli G, Rigon R, Muto F, Versace P (2014) Integrated physically based system for modeling landslide susceptibility. *Procedia Earth Planet Sci*. <https://doi.org/10.1016/j.proeps.2014.06.006>
- Guimaraes RF, Montgomery DR, Greenberg HM, Fernandes NF, Gomes RAT, de Carvalho Junior OA (2003) Parameterization of soil properties for a model of topographic controls on shallow landsliding: application to Rio de Janeiro. *Eng Geol* 69(1–2):99–108. [https://doi.org/10.1016/S0013-7952\(02\)00263-6](https://doi.org/10.1016/S0013-7952(02)00263-6)
- Hackston A, Rutter E (2016) The Mohr-Coulomb criterion for intact rock strength and friction—a re-evaluation and consideration of failure under polyaxial stresses. *Solid Earth* 7:493–508. <https://doi.org/10.5194/se-7-493-2016>
- Knowling MJ, White JT, Moore CR (2019) Role of model parameterization in risk-based decision support: an empirical exploration. *Adv Water Resour* 128:59–73. <https://doi.org/10.1016/j.advwatres.2019.04.010>
- Kuriakose SL, van Beek LPH, van Westen CJ (2009) Parameterizing a physically based shallow landslide model in a data poor region. *Earth Surf Process Landf* 34(6):867–881. <https://doi.org/10.1002/esp.1794>
- Labuz JF, Zang A (2012) Mohr-Coulomb failure criterion. *Rock Mech Rock Eng* 45(6):975–979. <https://doi.org/10.1007/s00603-012-0281-7>
- Lakmali ABK, Raveendra HB, Priyankara N (2016) Rain induced landslides in Sri Lanka. *Civil and Environmental Engineering Society*. https://www.researchgate.net/publication/308722373_RAIN_INDUCED_LANDSLIDES_IN_SRI_LANKA, 5 Jan 2016
- Lombardo L, Mai PM (2018) Presenting logistic regression-based landslide susceptibility results. *Eng Geol*. <https://doi.org/10.1016/j.enggeo.2018.07.019>
- Minnesota Department of Transportation (2019) Manual—MnDOT pavement design. Minnesota Department of Transportation. <https://www.dot.state.mn.us/materials/pvmt/design/manual.html>, July 2019
- Pawluszek K, Borkowski A, Tarolli P (2018) Sensitivity analysis of automatic landslide mapping: numerical experiments towards the best solution. *Landslides* 15(9):1851–1865. <https://doi.org/10.1007/s10346-018-0986-0>
- Postance B, Hillier J, Dijkstra T, Dixon N (2018) Comparing threshold definition techniques for rainfall-induced landslides: a national assessment using radar rainfall. *Earth Surf Process Landf*. <https://doi.org/10.1002/esp.4202>
- Roy J, Saha S (2019) Landslide susceptibility mapping using knowledge driven statistical models in Darjeeling District, West Bengal, India. *Geoenviron Disasters* 6(1):11. <https://doi.org/10.1186/s40677-019-0126-8>
- Segoni S, Pappafico G, Luti T, Catani F (2020) Landslide susceptibility assessment in complex geological settings: sensitivity to geological information and insights on its parameterization. *Landslides* 1–11. <https://doi.org/10.1007/s10346-019-01340-2>
- Silalahi FES, Pamela, Arifianti Y, Hidayat F (2019) Landslide susceptibility assessment using frequency ratio model in Bogor, West Java, Indonesia. *Geosci Lett* 6(1):10. <https://doi.org/10.1186/s40562-019-0140-4>
- Tien Bui D, Shirzadi A, Shahabi H, Geertsema M, Omidvar E, Clague J, Thai Pham B, Dou J, Talebpour Asl D, Bin Ahmad B, Lee S (2019) New ensemble models for shallow landslide susceptibility modeling in a semi-arid watershed. *Forests* 10 (9):743. <https://doi.org/10.3390/f10090743>



2020 Kyoto Japan

Study on the Behaviour of Slope Instability Using Physical Modelling

Mastura Azmi, Harris Ramli, Muhammad Azril Hezmi, Siti Aimi Nadia Mohd Yusoff, and Hazwan Zaki

Abstract

Rainfall has been identified as one of the main causes of slope failures in areas where high annual rainfall is experienced. The slope stability is very important consideration in management and is often being the most critical safety issue or feasibility component of many civil engineering project. An integrated analysis of rainfall-induced landslides was carried out through a laboratory test, as well as laboratory and numerical analyses. A set of laboratory-scale soil slopes was subjected to instability through different modes of rainfall intensities and slope inclination to clarify the process of failure initiation. Hydrologic responses of the model slopes to the saturation process were recorded by volumetric soil moisture sensors and tensiometer. The results of the comprehensive investigations demonstrate that landslide activity is closely related primarily to rainfall and soil properties and slope geometry. A numerical analysis was also performed to confirm the effect of these factors on landslide occurrence. In addition, the changes in the factor of safety and the volume mass of the failure surface were

compared and verified. From the results of the experiment and analyses, it is concluded that the unsaturated slope stability analysis, setting the initial conditions and boundary condition is important. If engineers use the measured porewater pressure or matric suction, the accuracy of the analysis can be enhanced. The real-time monitoring system of porewater pressure or matric suction can be used as a warning of rainfall-induced slope failure.

Keywords

Rainfall • Slope failure • Laboratory test • Volumetric soil moisture sensors • Tensiometer • Numerical analysis • Factor of safety

Introduction

Natural disasters, such as heavy snowstorms, extreme heat waves, landslides, floods, tsunamis, heavy rainfall and rising sea levels, have affected human security (Tangang et al. 2012). Landslides is the movement of mass or earth mass in the downward direction of a slope. It is also known as mass wasting, and it usually occurs on slope faces, whether natural or fabricated. The triggering factor of a slope failure can vary from among the slope morphology, groundwater movement, seepage, earthquake, etc.; however, according to Suhaila and Jemain (2012), rainfall contributed significantly to slope failure in some cases. Malaysia is situated near to equator with a tropical climate. Malaysia received wet and dry season instead of the four seasons. During the monsoon or wet season, abundant rainfall with a high intensity and prolonged period can lead to other calamities. Floods and landslides are some of the most common natural disasters in Malaysia. The monsoons in Malaysia include the Northeast Monsoon (NEM), which begins in March, and the Southwest Monsoon (SWM), which begins at the end of May, and

M. Azmi (✉) · H. Ramli · S. A. N. M. Yusoff · H. Zaki
School of Civil Engineering, Universiti Sains Malaysia,
Engineering Campus, Nibong Tebal, Seberang Perai Selatan,
14300 Pulau Pinang, Malaysia
e-mail: cemastura@usm.my

H. Ramli
e-mail: cemhr@usm.my

S. A. N. M. Yusoff
e-mail: amynadia168@gmail.com

H. Zaki
e-mail: hazwanzakihazwan@gmail.com

M. A. Hezmi
School of Civil Engineering, Universiti Teknologi Malaysia,
UTM Johor Bahru, 81310 Johor, Malaysia
e-mail: azril@utm.my

these are the wet seasons in Malaysia (Suhaila and Jemain 2012). A few studies on the projection of rainfall patterns in Malaysia indicate that the NEM would produce a higher intensity of rainfall over a shorter period (Abdul Halim et al. 2017). The increment of 200 mm rainfall annually over the past 15 years were highlighted, indicating the increase in the intensity of rainfall in Malaysia (Tang 2019). Rainfall-induced slope failure is one of the most common type of slope failure, antecedent rainfall, precedent rainfall, duration of precipitation and rainfall intensity are the governing factors causing rainfall-induced slope failure (Mukhlisin et al. 2015) according to Kristo et al. (2017), the rainfall intensity variation has a significant relationship with slope stability. The increasing trend of rainfall intensity has shown a nearly linear relationship with reductions in slope stability. In addition, the failure mechanism of the slope also varies in terms of the rainfall intensity (Tohari et al. 2007). Thus, the variation in rainfall intensity could trigger different failure mechanisms with a certain prognosis of the linear relationship between increasing rainfall intensity and the reduction in slope stability. Another characteristic that would effect the presence of the variation in rainfall intensity is groundwater flow. It was found that the accumulation of groundwater flow in a narrow period causes the groundwater table to elevate from the normal condition (Kristo et al. 2017; Zaki et al. 2020).

In this study, we performed a model slope experiment to understand the process of water seepage and slope failure caused by rainfall, and we compared and verified the result with an unsaturated slope stability analysis. In the model slope experiment, we created artificial rainfall on a slope and measured the changes in water content, which acts as a load factor during seepage, and the changes in matric suction, which acts as a resistance factor. In addition, we identified the time and shape of slope failure after rainfall seepage. An unsaturated slope stability analysis was used to calculate the change in the factor of safety due to rainfall seepage and the factor of safety was calculated from the calculated head value. We compared and verified the changes in the factor of safety, as well as the time and shape of the slope failure resulting from the rainfall with the results from the model experiment. This paper focused on the physical modelling of the slope that would be subjected to an extreme rainfall intensity. The rainfall intensity is selected from two cases of extreme precipitation in Malaysia (Zaki et al. 2020) Lastly, at the end of this paper, we should be were able to determine the extreme rainfall intensity based on a selected preceding event in Malaysia, determine the variation in saturation during the extreme intensity rainfall simulation and assess the effect of extreme rainfall on slope stability.

Materials and Method

Soil Properties

Table 1 shows the physical properties of the soil for this study. Mining sand which is retain at sieve sizes 2 mm from Kampung Kuala Trong, Taiping were used. Single size sample is used to reduce the effect of irregularity in slope failure. Figure 1 shows the particle size distribution of the soil and according to the unified soil classification system, it is designated as SP (poorly graded sand with little or no fine silty sand), with a specific gravity of 2.64 and a coefficient of uniformity of 5.26. In direct shear test carried out under the same conditions as the model slope, cohesion was 9.0 kPa and the internal friction angle was 33°. The saturated coefficient of permeability of the constant-head method was calculated to be 0.00013 ms⁻¹.

To estimate the unsaturated soil property function, the Soil Water Characteristic Curve (SWCC) was done using pressure plate apparatus.

The SWCC and the obtained parameters for this study are shown in Table 2 and Fig. 2. As shown, the air entry pressure u_b is 2 kPa, the pore size distribution parameter n is 2.4010, the residual water content θ_r is 0.11974 and the saturated volumetric water content θ_s is 0.98349.

Model Slope Experiment

The test facility and general arrangement of the slope model box are illustrated in Fig. 3. The physical model is divided into three main systems: no. 1 the model box, no. 2 water control system (groundwater level) and no. 3 rainfall simulator system, including a huge tank water equipped with a water pump.

The main element of the test is the model box. The model box has an inside dimension of 1 m × 1 m in the side view and it is 1 m deep. The sidewalls of the model box consist of 10-mm-thick acrylic windows to enable the visual observation of deformations and movement along the failure surface. The sidewalls of the model box are smooth and rigid to simulate plain strain conditions. The next element in this study is groundwater systems. Two side boxes, also known as groundwater level (GWL) boxes (1 m × 0.5 m in the side view and it is 1 m deep), were built at both sides of the rectangular flume and were equipped with a valve to observe and control the groundwater level. A big valve was placed on the sidewall adjacent to the toe of the slope at an elevation of 90 cm from bottom and was used to draw water from main box to the GWL box. In the soil container, a finite

Table 1 The physical properties of the mining sand

Properties	Unit	Mine tailing sands
Natural water content	(%)	5.474
Particle size distribution	Gravel (%)	2.41
	Sand (%)	91.31
	Fines (%)	6.286
	D ₁₀ (mm)	0.19
	D ₃₀ (mm)	0.4
	D ₆₀ (mm)	1
	Cu	5.263
	Cc	0.842
Plastic limit	(%)	NA
Liquid limit	(%)	23.5
Plasticity index		23.5
Specific gravity		2.641
USCS		SP
AASTHO		A-2-6

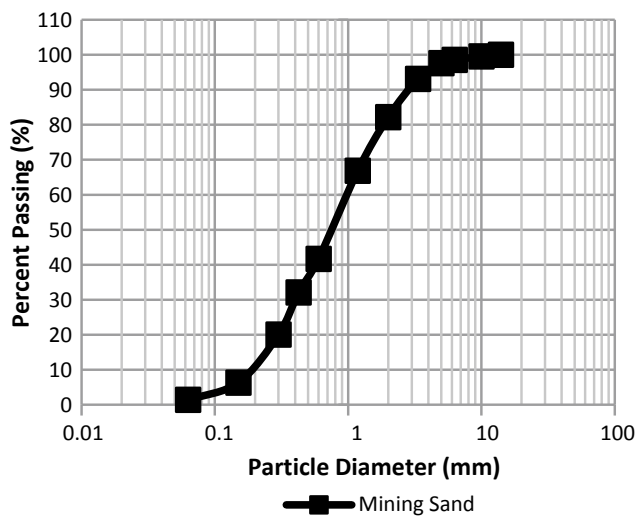


Fig. 1 Particle size distribution of mining sand

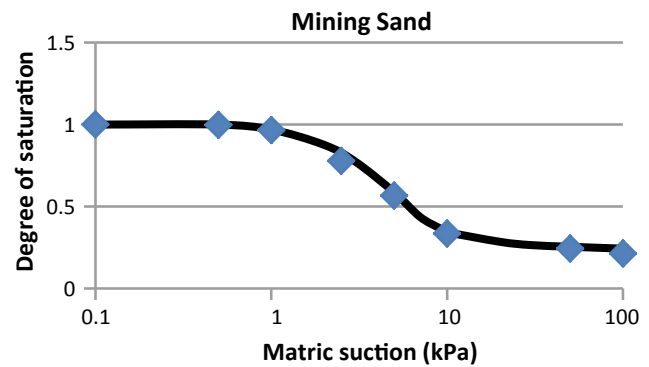


Fig. 2 Result of the SWCC of mining sand using pressure plate apparatus

Table 2 SWCC parameters from fitted SWCC experimental data using Fredlund and Xing (1994)

Soil		2 mm mining sand
Fredlund and Xing (1994)	θ_s	0.98349
	θ_r	0.11974
	a	2.9018
	m	2.4514
	n	2.4010
	R ²	0.99612

slope with height of 0.7 m. The slope was constructed uniformly, using plywood and tamper, and it was formed in three layers. Prior to the model slope experiment of 60°

inclination, the preceding experiment was performed in 40° inclination. This was done to verify the seepage behaviour of rainfall and its effect on the model slope. A water control

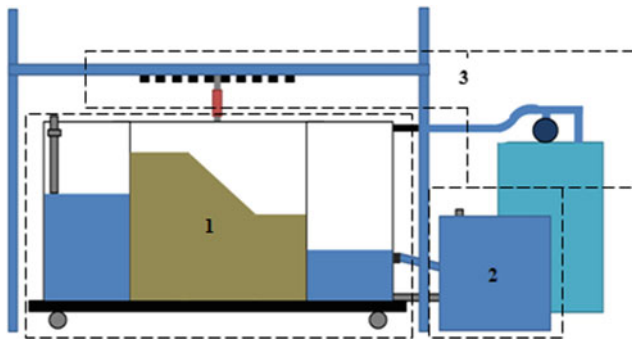


Fig. 3 General arrangement of a physical model

system was designed to regulate the rise and drawdown of water in the slope model. The water level control system consisted of a water storage tank, a valve equipped with plastic tube to draw the water from slope model boxes to the GWL boxes then to the water storage tank and a water pump inside water storage tank to pump the water from outlet to inlet. The groundwater can be elevated or lowered to any level using a water pump.

An extensive instrumentation plan was designed to assess the changes in hydrological and geo-mechanical responses of the slope during artificial events. To determine the creation process of a rainfall-induced slope failure, it is important to measure the water content, which acts as a load factor during seepage, and the matric suction, which acts as a resistance factor. Water content was measured using a time-domain reflectometer (TDR) sensor. The TDR sensor uses the association between the dielectric constant and water content (Topp et al. 1980). Electrical pulses from the TDR-measuring device go through a probe and they are then changed by the water content. After a simple correction process, we found the value for the water content. The probe for the TDR sensor was the EC-5 from Decagon Device Inc., and its dimensions are 8.9 cm \times 1.8 cm \times 1.7 cm (Bogena et al. 2007; Decagon Devices 2006). The data logger used was the GP2 from Delta -T Device measuring every 1 min. Meanwhile, matric suction was measured by using a SWT5 Tensiometer also from Delta-T Device, which consists of a sensor body and a 70-mm-long shaft fully saturated with water. A porous stone is attached at the edge of the shaft. The thickness of the shaft is 5 mm. Calibration is needed before running the test because the conduct test revealed the need for a good saturation of the sensor body and the shaft. Small bubbles will be leading to the incorrect measurement and they should be prevented from appearing inside the shaft, so it is important to proceed with the saturation of the sensor body and shaft right before calibration to ensure the preservation of the porous stone's saturation. Lastly, because contact of the porous stone with the unsaturated soil causes inevitable desaturation, calibration of the TDR and

Tensiometer takes place right before and exactly after each main test. In the model slope of 60°, the water content and matric suction sensors were installed and measured in four locations (Fig. 4). All sensors location was decided based on the location of capillary fringe. This is to ensure that the position of sensors does not influence the groundwater level. Sensor A was placed 20 cm above the slope toe and 5 cm from the top of the slope, where the rainfall seepage occurs. Sensor B was placed 15 cm from the top of the slope and sensors C and D were placed 20 cm from the top of the slope. In the model slope of 40° inclination, sensor A was placed 20 cm above the slope toe and 5 cm from the top of the slope. Meanwhile, sensor B was placed 12 cm from the top of the slope and sensors C and D were placed 18 cm and 22 cm, respectively, from the top of the slope. A digital camera was also used to monitor and investigate the deformation.

Another important element in this study is the rainfall simulator systems. The rainfall simulator was designed with the following components: drip, flow meter, water delivery system, water pump and water tank. Drips were selected

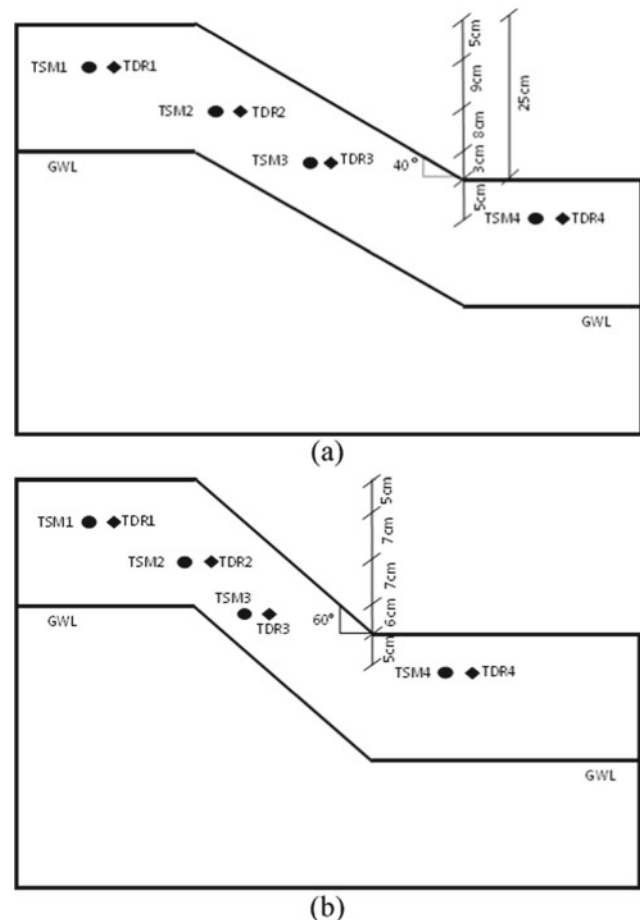


Fig. 4 a The arrangement of TSM and TDR for 40° slope. b The arrangement of TSM and TDR for 60° slope

based on an ability to distribute drops uniformly and produce drop sizes similar to natural rainfall. The flow meter was used to monitor rainfall intensity. The water delivery system was designed to provide adequate flow to the risers while maintaining a suitable operating pressure (Fig. 5). Finally, a water tank equipped with a water pump was used to pump water from the water tank to produce rain. A rainfall simulator was set approximately 1.7 m above the surface of the model slope. An intensity of artificial rainfall of 80–120 mm/h is characterised as heavy rainfall in Malaysia. In addition, saturated permeability was considered. The ponding surface may happen at toe if the rainfall intensity greater than 30 mm/h. The artificial rainfall would introduce surface erosion and the formation of gullies. The amount of water flowing into the 100 s rain drip was carefully controlled, and it was monitored using a flow meter.

Numerical and Slope Stability Analysis

Unsaturated slope stability was determined using a seepage analysis and slope stability analysis. The seepage analysis was performed under unsteady conditions, and the factor of safety was calculated using the limit equilibrium method by applying the water head value inside the slope to the slope stability analysis. For the slope stability analysis, which was done under transient unsaturated seepage conditions and the hydromechanical framework, only three additional parameters were needed. These are the residual water content θ_r , the air entry pressure u_b , and the pore size distribution parameter n . The soil water characteristic curve obtained from the pressure plate tests and fit to the Fredlund and Xing (1994)

model (Azmi et al. 2016). (Rahimi et al. 2015). The hydrological behaviour due to the infiltration of the artificial rainfall was analysed numerically using the SEEP/W module of Geostudio 2007. To analyse the unsteady state, we input the matric suction that was measured from the experimental process using the spatial function. The boundary condition applied only to the bottom of the slope, and not to the side of the slope, which replicate the same condition as in the model experiment. The inclination plane of the slope was set such that the seepage water could flow out. The results of the seepage analysis show unsteady states, so they are shown as the total stress, porewater pressure and water content with changes in time, and they were applied to the slope stability analysis. In the slope stability analysis, the limit equilibrium method was used, which the design standards have presented. It was determined by the ratio of stress and shear strength along the failure surface. The factor of safety was calculated numerically using the SLOPE/W module of Geostudio 2007. The suction stress and effective stress are incorporated into the shear strength in the SLOPE/W module, as follows:

$$\tau_f = c' + \sigma' \tan \phi' \quad (1)$$

$$\tau_f = c' + \left\{ (\sigma - u_a) + \frac{\theta - \theta_r}{\theta_s - \theta_r} (u_a - u_w) \right\} \tan \phi' \quad (2)$$

where u_a is the pore air pressure and u_w is the porewater pressure, σ' and σ are the effective stress and normal stress, $(u_a - u_w)$ is the matric suction and θ_r and θ_s are the volumetric water contents at the residual and saturated states.

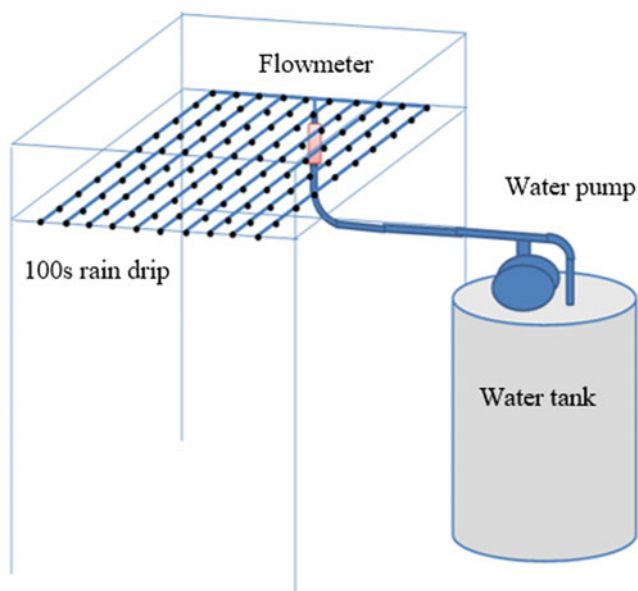


Fig. 5 Components of rain simulator

Results and Discussion

Physical Modelling

To investigate the effect of the extreme rainfall on slope stability, a physical model is used to simulate the situation. In this study, four cases were established with slope inclination angles of 40° and 60° with a rainfall intensity of 80 and 120 mm/h. Table 3 shows all the investigated cases.

The simulation was conducted by measuring the matric suction and volumetric water content, as in Figs. 6, 7, 8, 9, 10, 11, 12, and 13. This provides insight into the condition of the slope during a failure. The initial part of the simulation is meant to stabilise the reading for both TDR and TSM. Then, the rainfall simulation is done by subjecting the slope to the 80 mm/hour for 6 h followed by a 24-h stabilisation period. The positioning of the TDR and TSM are similar in each case.

The highest volume of mass wasting was during the Case 4 simulation. This indicates that the slope in Case 4 is the most vulnerable to slope failure. In Case 4, the slope angle at 60° with the intensity of 120 mm/h is the steepest angle and highest intensity of rainfall, producing the most severe combination of slope angle and rainfall intensity. All supervision is recorded and tabulated in Table 4.

For the TDR and TSM 1 & 2, the position is on the upper part of the slope, whereas for the TDR and TSM 3 & 4, it is located near the toe at lower part of the slope. For both the VMC and MS measurement in all cases, the initial trend during the rainfall simulation shows an increase in both parameter values. However, the reading in TSM 1 is unpredictable for a few cases. All readings for VMC and MS in each case drop after the rain is terminated. The difference in value and magnitude in VMC between TDR 1 & 2 and TDR 3 & 4 is due to the different position of the sensors. TDR 3 & 4 show a higher initial value and higher difference in the changes, because of the increase in saturation at that region contributes to the rising of the water table and the infiltration of the rain. During the simulation and stabilisation period, observations were made in order to detect any changes or any failure occurrence throughout the simulation. The supervision includes the total mass wasting and the time for the initial failure to occur.

Numerical Analysis

The numerical analysis of slope stability is done using the transient analysis in SEEP/W as a parent analysis, with a slope stability analysis by SLOPE/W. All the cases are modelled for a 6-h rainfall simulation. The result from the analysis for slope stability is presented in a factor of safety (FOS) value. The result is tabulated in Table 5. The initial and final values of FOS for each case are shown in Figs. 14, 15, 16, and 17.

From the results, the initial and final values of FOS in Cases 1 and 3 are similar to those in Cases 2 and 4. This similarity is caused by the same slope angle used for the cases. For Cases 1 and 3, the slope angle used in the simulation is at 40°, and for Cases 2 and 4, it is at 60°. The initial FOS value similarity is due to the same initial water table for the same slope geometry. For the final value of FOS, the similarity is due to the saturated condition that was

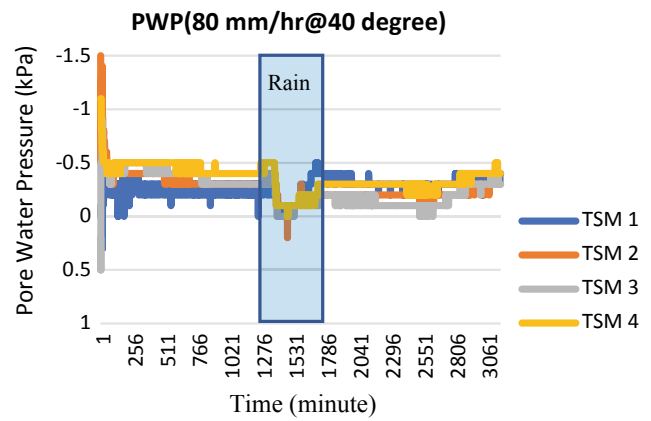


Fig. 6 Pore water pressure for cases 1

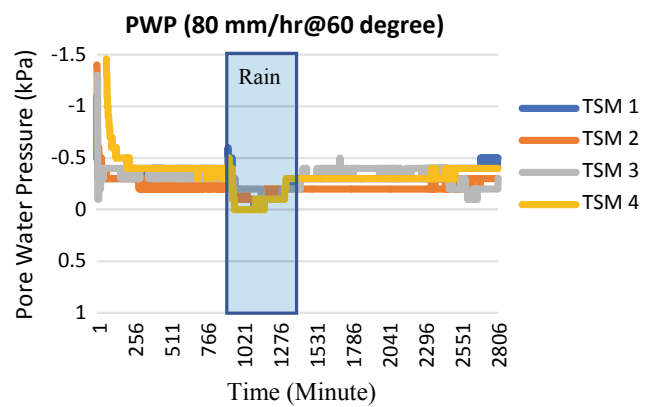


Fig. 7 Pore water pressure for cases 2

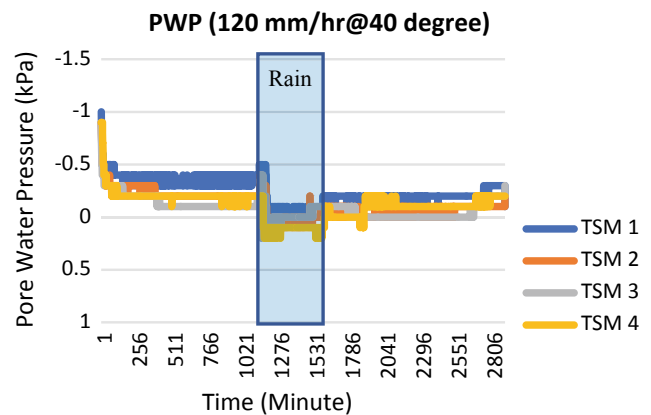


Fig. 8 Pore water pressure for cases 3

Table 3 Investigated cases

Case	Cases 1	Cases 2	Cases 3	Cases 4
Rainfall intensity (mm/h)	80	80	120	120
Slope (°)	40	60	40	60

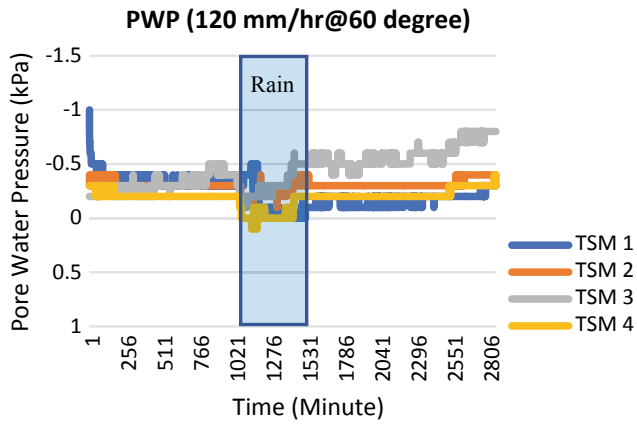


Fig. 9 Pore water pressure for cases 4

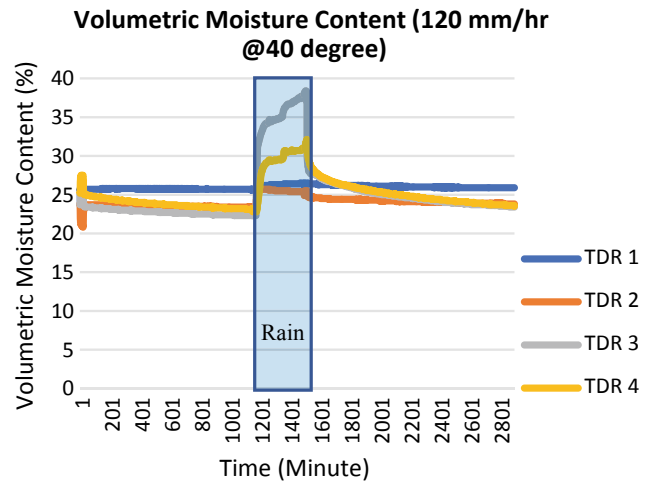


Fig. 12 Volumetric water content of cases 3

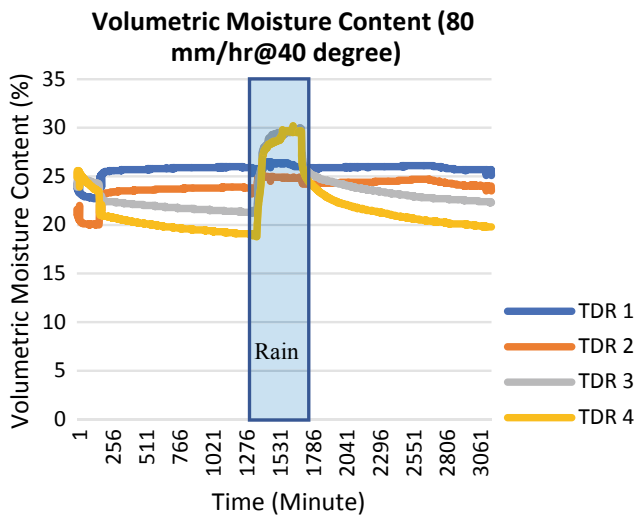


Fig. 10 Volumetric water content of cases 1

Table 4 Slope failure supervision

Case	Volume of mass wasting (cm ³)	Time of failure (hour)
Case 1	4.0	4
Case 2	7.0	3
Case 3	4.25	4
Case 4	10.0	2

Table 5 Initial and final values of FOS

Cases	Initial FOS	Final FOS
Case 1	1.985	0.885
Case 2	1.579	0.788
Case 3	1.985	0.885
Case 4	1.579	0.788

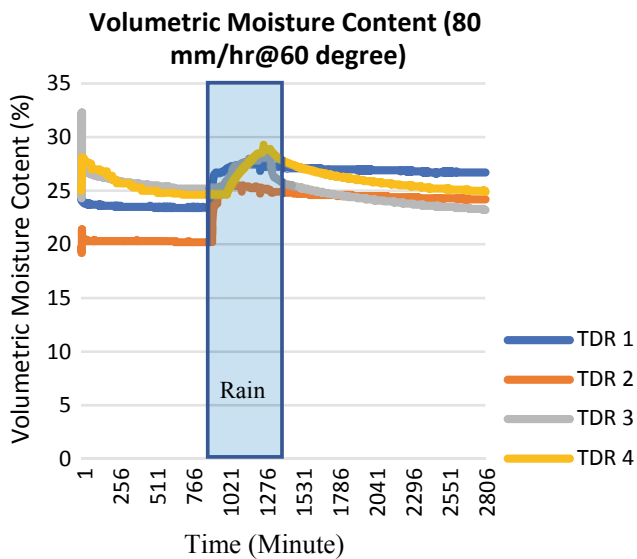


Fig. 11 Volumetric water content of cases 2

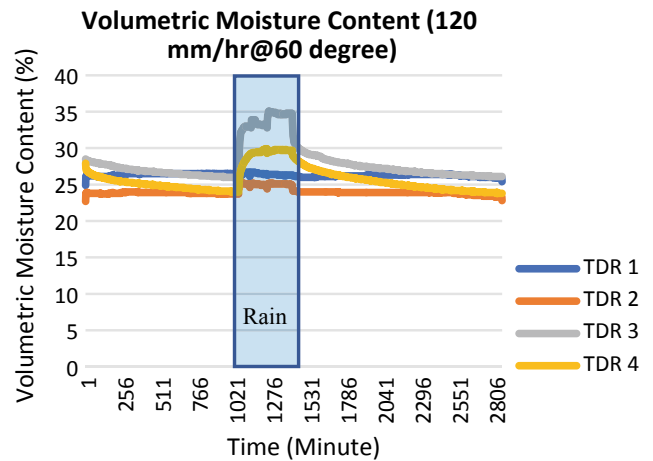


Fig. 13 Volumetric water content of cases 4

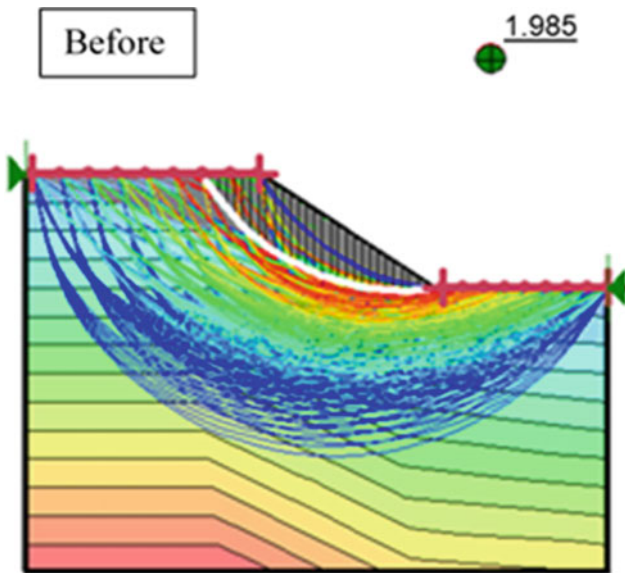


Fig. 14 Initial and final values of FOS of case 1

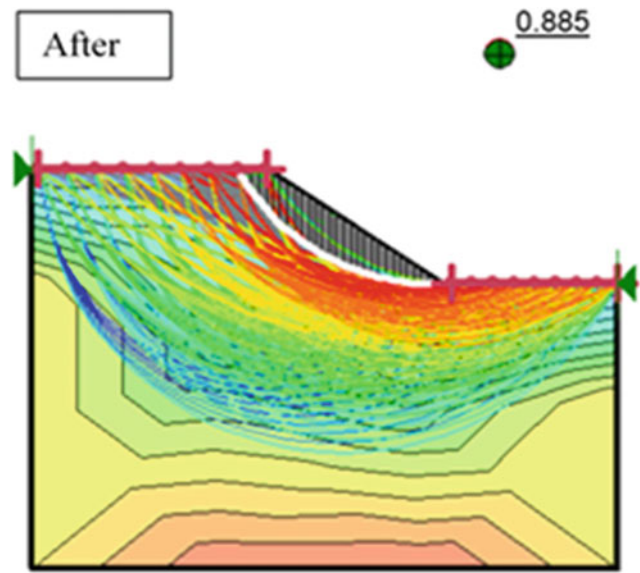


Fig. 16 Initial and final values of FOS of case 3

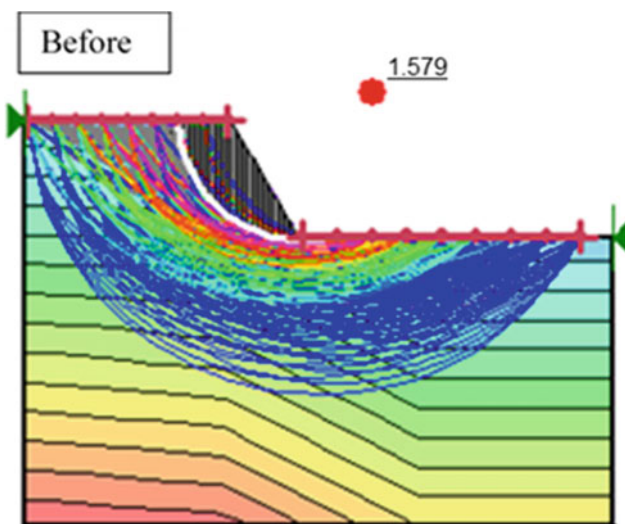


Fig. 15 Initial and final values of FOS of case 2

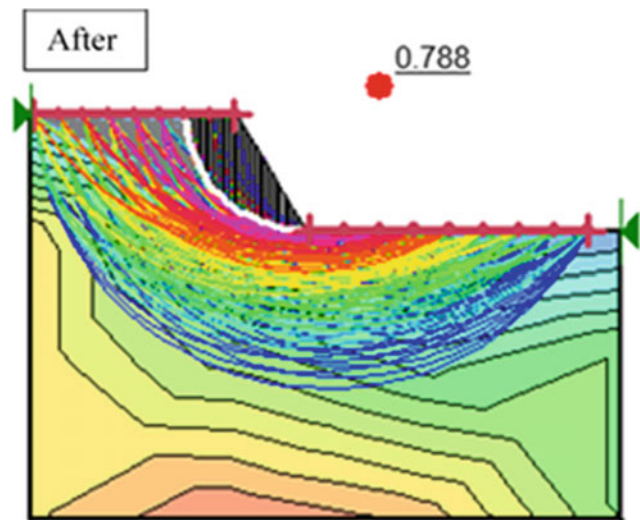


Fig. 17 Initial and final values of FOS of case 4

achieved during the simulation. The final value of FOS is assessed after the slope reaches its full saturation value.

Conclusion

From the results of the numerical analysis and the model slope experiment of 40° inclination, an increase in water contents and a decrease in matric suctions due to rainfall seepage occurred rapidly and in large amounts, but a decrease in water contents and an increase in matric suctions due to drainage occurred gradually and in small amounts.

This demonstrates a hysteresis of seepage drainage procedures in unsaturated soils. Even with similar behaviours in the model slope experiment and the numerical analysis, the difference could be considered by applying the SWCC obtained from disturbed specimens in the numerical analysis. In the model slope experiment, rainfall seepage caused the water content to increase dramatically and matric suction to decrease more gradually than water content, leading to the area around the failure surface collapsing. The model slope failure occurred when the bottom of the failure surface was unsaturated.

Acknowledgments The authors would like to thank Universiti Sains Malaysia for sponsoring this research project under research grant no. USM(RU) 1001/PAWAM/814246 and USM304/PAWAM/6050407/U107.

References

- Abdul Halim S, Abas N, Mohd Daud Z (2017) Climate projections of future extreme events in Malaysia.
- Azmi, M., Yusoff, S. A. M., Ramli, M. H., & Hezmi, M. A. (2016). Soil water characteristic curves (SWCCs) of mining sand. *Electronic Journal of Geotechnical Engineering*, 21(22), 6987–6997.
- Bogena H, Huisman J, Oberdorster C, Vereecken H (2007) Evaluation of a low-cost soil water content sensor for wireless network applications. *J Hydrol* 344:32–42
- Decagon Devices Inc. (2006) ECH₂O soil moisture sensor: operators manual for model EC-20, EC-10 and EC-5 (version 5). Decagon Devices Inc., Pullman, Wash, pp 1–20
- Kristo C, Rahardjo H, Satyanaga A (2017) Effect of variations in rainfall intensity on slope stability in Singapore. *International Soil and Water Conservation Research* 5:258–264
- Mukhlisin M, Matlan SJ, Jaykhan Ahlan M, Taha M (2015) Analysis of rainfall effect to slope stability in Ulu Klang, Malaysia
- Rahimi A, Rahardjo H, Leong EC (2015) Effects of soil-water characteristic curve and relative permeability equations on estimation of unsaturated permeability function. *Soils Found* 55(6), 1400–1411 (Japanese Geotechnical Society, November)
- Suhaila J, Jemain AA (2012) Spatial analysis of daily rainfall intensity and concentration index in Peninsular Malaysia. *Theoret Appl Climatol* 108:235–245
- Tang KHD (2019) Climate change in Malaysia: trends, contributors, impacts, mitigation and adaptations. *Sci Total Environ* 650:1858–1871
- Tangang FT, Juneng L, Salimun E, Sei KM, Le LJ, Muhammad H (2012) Climate change and variability over Malaysia: gaps in science and research information. *Sains Malaysiana* 41, 1355–1366
- Tohari A, Nishigaki M, Komatsu M (2007) Laboratory rainfall-induced slope failure with moisture content measurement
- Topp G, Davis J, Annan AP (1980) Electromagnetic determination of soil water content: measurement in coaxial transmission lines, *water Resour. Res.* 16:574–582



2020 Kyoto Japan

Centrifuge Modelling of Slope Failure Due to Groundwater During Excavation

Nobutaka Hiraoka, Naotaka Kikkawa, and Kazuya Itoh

Abstract

In order to prevent occupational accidents during slope excavation work, it is important to include slope stability in all aspects of construction design. In slope excavation work, the two major factors are the excavation height and the gradient, both of which are prescribed by some guidelines and laws. However, accidents often occur during slope excavation work, even with the required safety gradient, because existing guidelines fail to consider the effects of water. In this study, the stability of a slope with rising groundwater was examined for different excavation slopes. The results show that the slope was stable in the absence of water, but it collapsed when the groundwater rose. We also propose a method for predicting landslides using slope movement measurements. The method uses the standard deviation from past measured values to detect data abnormalities on current measurements. Predictions obtained by this method were classified under advisory, warning, or emergency warning based on the deviation rate between the moving average and standard deviation of past data. It was observed that slope failure can be reliably predicted using this method.

Keywords

Slope failure • Groundwater • Centrifuge modelling • Excavation work • Prediction of collapse

N. Hiraoka (✉) · N. Kikkawa
Construction Safety Research Group, National Institute of Occupational Safety and Health Japan, 1-4-6 Umezono Kiyose, Tokyo, 2040024, Japan
e-mail: hiraoka@s.jniosh.johas.go.jp

N. Kikkawa
e-mail: kikkawa@s.jniosh.johas.go.jp

K. Itoh
Department of Urban and Civil Engineering, Tokyo City University, 1-28-1 Tamazutsumi Setagaya, Tokyo, 1588557, Japan
e-mail: itok@tcu.ac.jp

Introduction

Every year, 10–20 workers are killed due to soil collapse during excavation work in Japan. Approximately about half of these fatal accidents occur during slope excavation work. In order to prevent labour accidents during slope excavation work, it is necessary to evaluate slope stability correctly. The stability of a slope depends on the shape of the slope, the strength of the soil or rock, and the weight of soils or rocks. Additionally, cracks, water, and ground structure involving soil layers also affect stability. Information on these factors are obtained by the ground surveys, and the excavated shape has to be determined by numerical analysis that uses them. Unfortunately, ground surveys are not sufficient for slope works in Japan where a fatal accident has occurred. The survey and/or analysis costs may not be supported by the project budget. For relatively small and common constructions, the excavation is designed according to the empirical rules of slope height and slope gradient.

The document: “The specification for road works,” which is issued by the Japan Road Association, is often used as the basis for excavation angles. Article 356 of the Occupational Safety and Health Regulations, which stipulates the slope height and angle of excavation, is also legally applicable. However, these slope heights and slope angles are provided for reference only. Slope heights and angles should ideally be designed using numerical calculations based on ground surveys. If not, the influence of geological structures, local geology, and water will not be included. In particular, water can have a significant effect on slope stability. Toyosawa et al. (2005) reported that 60% of the occupational accidents caused by landslides are due to the effects of water. Therefore, we conducted centrifugal tests using model slopes within the reference range of the Road Earth Construction Guideline and Ordinance on Industrial Safety and the Occupational Safety and Health Regulations Article No. 356 and confirmed the risks on slope stability caused by rising groundwater (Hiraoka et al. 2019). In this study, it was

verified whether slope collapse could be predicted by monitoring the slope using a strain sensor. The Non-structural measures such as monitoring is not the best policy for safety, but it is very effective.

Experimental Setup

To complement the experimental model verification, centrifugal modelling was conducted to match the stress conditions with the prototype scales.

Figure 1 shows a schematic view of the soil tank. The soil tank used for centrifugation was an aluminum container with a height of 400 mm, a length of 800 mm, and a width of 250 mm. It had a wall equipped with a groundwater control system. The water level control wall was equipped with a motor, an electrode rod, a limiter switch, and a wire displacement meter. It was possible to adjust the water level in the centrifugal field on the back and front of the slope.

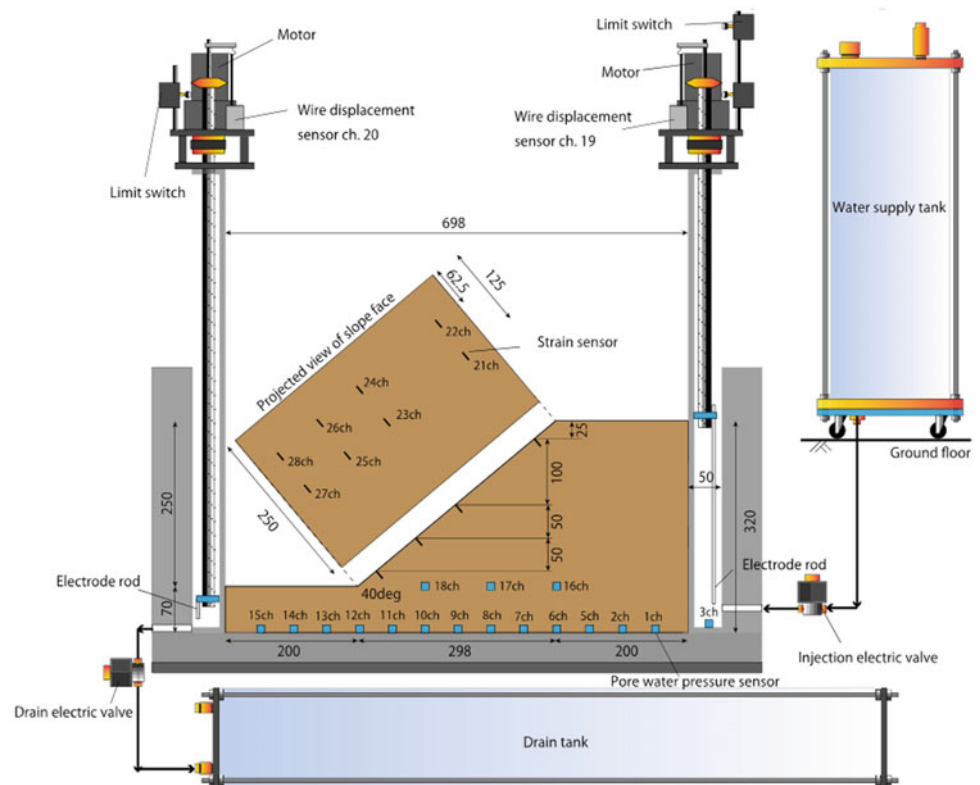
Masa soil was used which is a weathered soil composed of granite. Masa soil becomes very unstable when wet and is widely distributed in Western Japan. Soil particles having diameters of 2 mm or more were removed in this experiment. Figure 2 shows the grain size accumulation curve of Masa soil. The soil was adjusted to an optimum moisture content of 17.3% and compacted at a dry density of 1.50 g/cm^3 which degree of compaction D_c is 90%. The masa soil of this

density has a permeability $k = 5.15 \times 10^{-5} \text{ m/s}$ obtained by falling head permeameter test and the consolidated drained triaxial tests were performed to obtain a friction angle of 35.9° and a cohesion of 0.7 kN/m^2 at saturation, and a friction angle of 35.6° and a cohesion of 10.0 kN/m^2 at unsaturation ($w = 17.3\%$).

Three slope angles were tested: 40° , 60° , and 75° as shown in Figs. 1, 3 and 4. The slope angles were chosen according to “The Specification for Road Works” and “Article No. 356”. According to the former document, the excavation angle for a slope composed granite soil 5 m in height is recommended to be within 39.8° to 45° . The excavation angle of 40° was adopted. According to “Article No. 356”, the excavation gradient as “other” classified granite soil must be 75° or less for a slope 2–5 m in height, and 60° or less for heights greater than 5 m. An excavation of 5 m in height is midway between these two categories, and can thus be provided with a slope angle of either 60° or 75° . Both angles were therefore reproduced in the experiment.

In the following sentences, the scale notation is the prototype scale except for time scale. The centrifugal acceleration was set to 20 g. An area of flat ground of 1.4 m in height was created in the soil tank along with a model slope of 5 m in height (prototype scale). Using the water level control system, water was made to flow through the soil for more than 3 days at the groundwater level GL-0.4 m on both

Fig. 1 Experimental setup with the soil tank walls equipped with a groundwater control system. Case1 includes a slope angle of 40° (model scale, Unit: mm)



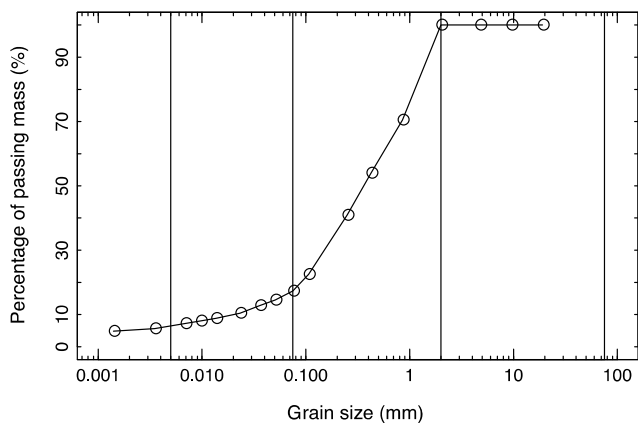


Fig. 2 Grain size accumulation curve for Masa soil

the front and drain sides of the slope. At the start of the test, the water level was fixed in front of the slope. After reaching 20 g on the backside of the slope, the water level was increased at a rate of 0.01 m/min (prototype scale).

Experimental Results

In each case, the initial value of the elapsed time was 5 min before the start of the water supply after reaching 20 g. Figure 5 shows the process of collapse for Case 1 with a slope angle of 40°. As can be seen in the sequence of photographs of the experiment, the slope tip on the left side of the slope collapsed due to the action of spring water after 1098 s. The collapse proceeded up the slope thereafter, with the

collapse progressing to a height of 1.5 m after approximately 1628 s. The collapse progressed until approximately the 1800 s mark, but stopped near a height of 1.5 m. The water supply was then cut off because the slope had become stable.

In Case 2 where the slope was 60°, the tip of the left side of the slope began to collapse at the 1151 s mark and expanded to the right and center, as shown in Fig. 6. The osmotic disintegration progressed to a height of 1.5 m at the 1370 s mark, and then to 2.5 m at the 1474 s mark. Finally, disintegration from the shoulder occurred at the 1497 s mark.

In Case 3 where the slope angle was 75°, the tip of the slope on the left side of the slope began to collapse at the 1130 s mark, and collapsed to a height of 1.5 m after 1469 s and to a height of 2.5 m after 1470 s as shown in Fig. 7. The shoulder on the left side collapsed after 1493 s, and the shoulder on the right side of the slope collapsed after 1571 s.

In both Case 2 and Case 3, the slopes were stable immediately after reaching a g-force of 20 g, and it could be seen that the slopes became independent at these angles if there was no groundwater in the slopes. In the three cases analysed in the study, the collapse began between the 1100 s and 1200 s marks and then increased with rising groundwater. According to the slope criteria adopted in this experiment, it was experimentally confirmed that the slope collapsed under the influence of groundwater.

Figures 8, 9, and 10 plot the pressure head measured by the pore water pressure gauge installed at the bottom up to 1800 s at 180 s intervals. In each case, the groundwater in

Fig. 3 Experimental setup for Case 2 with a slope angle of 60° (Unit: mm)

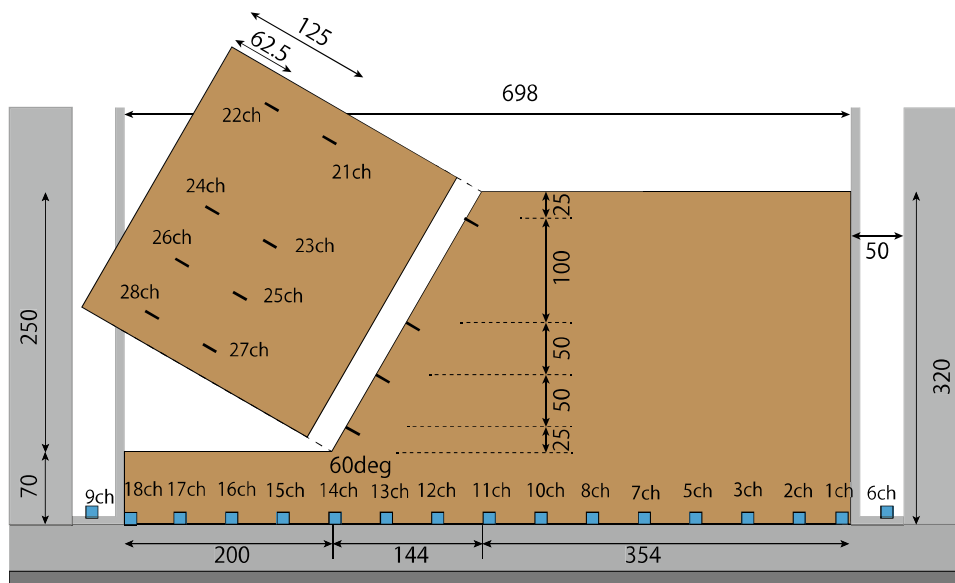
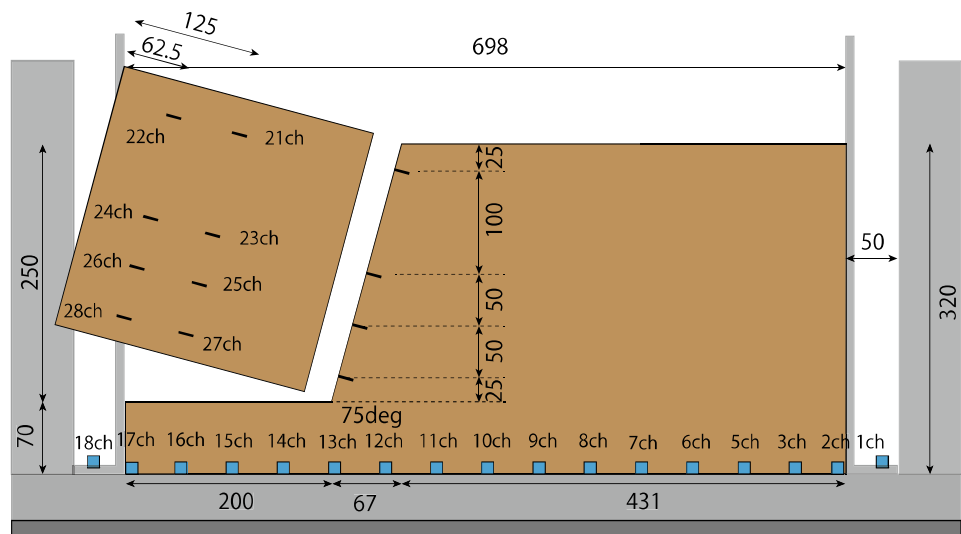


Fig. 4 Experimental setup for Case 3 with a slope angle of 75° (Unit: mm)



the slope rose in response to the rise in groundwater at the back of the slope. In Case 1 (slope angle 40°) where only a partial slope collapse occurred, the water level rose at a constant rate.

A collapse gradually progressed from the point of approach of the slope. As a result, the bearing capacity of the forehead was lost. In addition, the simultaneous rise in ground water further exacerbated the collapse progression. It

is difficult to reproduce this experimentally observed phenomenon using numerical analysis. In addition, it is expensive to fully design and engineer a slope for each excavation and situation. That is why empirical safety factors should be provided to allow the setup of gentle slope angles or the installation of appropriate drainage.

In practice, there is also a high possibility that groundwater in a slope on a particular site will rise in response to

Fig. 5 Case 1 experimental progression. The left slope collapsed to a height of 1.5 m and then became stable

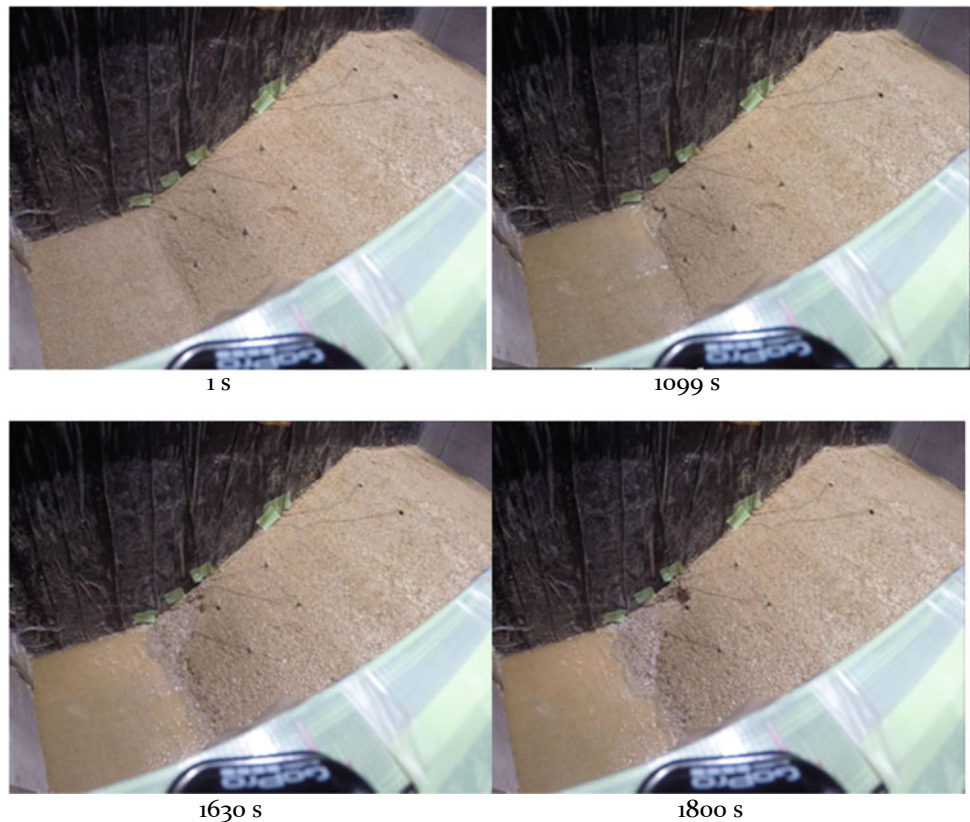
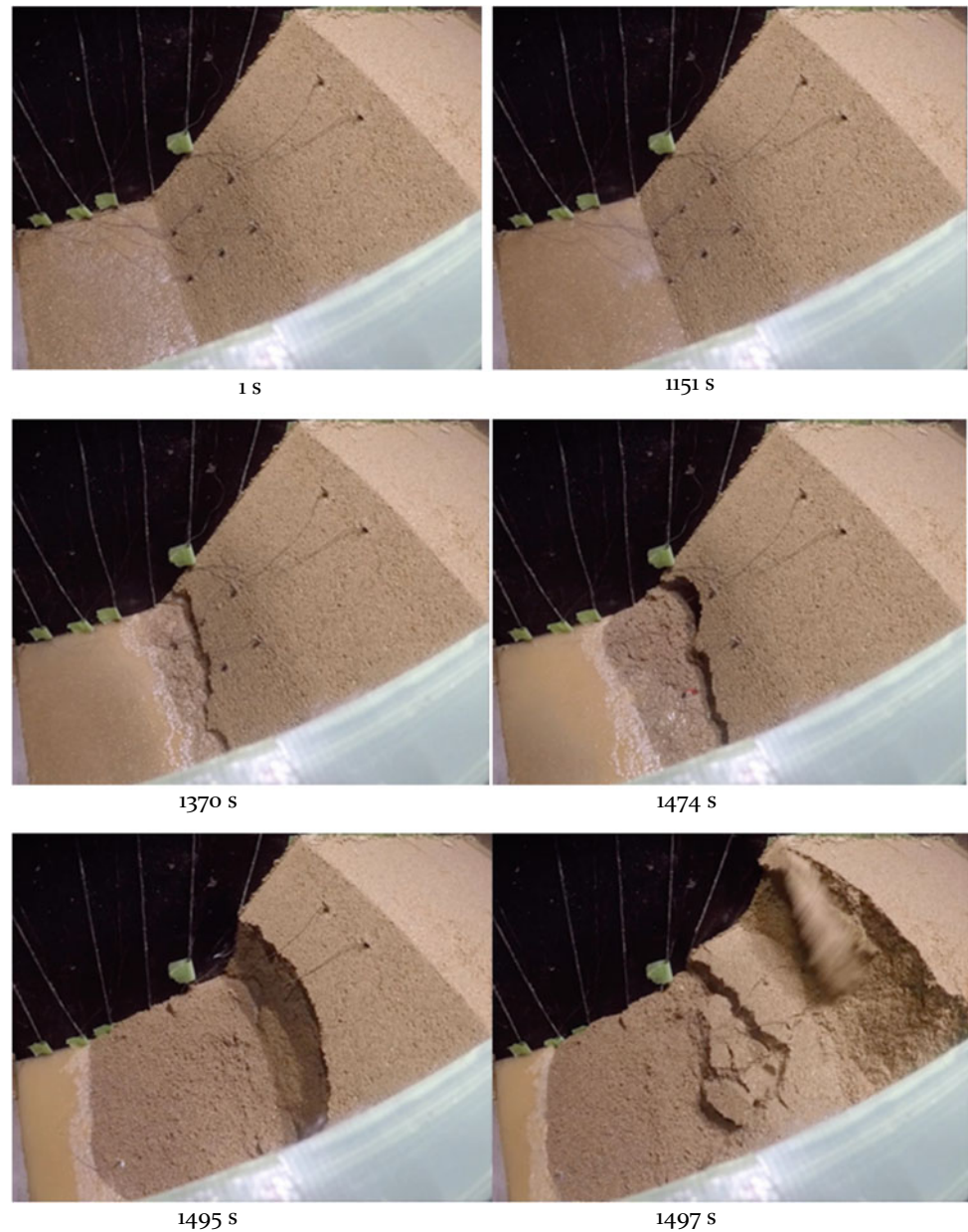


Fig. 6 Case 2 experimental progression



spring water being confined in the forehead area of the slope, which could lead to the collapse. As this presents an on-going high risk of collapse for the slope, it would be necessary to stop construction work and alter the construction plan.

Prediction of Collapse Using Slope Surface Strain

The slope surface strain sensor MPSc is set on the slope surface as shown in Fig. 1. MPSc is made of a thin iron plate (thickness: 0.1 mm) with 2 strain gauges stuck on both faces as shown in Fig. 11.

Figure 12 shows the slope surface strain obtained by MPSc during slope failure progression in Case 2. The larger the channel number, the lower the sensor is located on the slope. Odd numbers were set at the center of the slope, and even numbers were set at the left side of the slope. It can be seen that the strain values changed before the collapse near each installation position. It will be verified whether the collapse prediction can be performed using these measured values. Due to manuscript length limitations, this paper focuses on Case 2.

The authors (Hiraoka et al. 2017) proposed a method for predicting collapse by monitoring slope movement on excavated slopes. The method is applied to a slope after excavation, and is an algorithm that finds the transition point

Fig. 7 Case 3 experimental progression

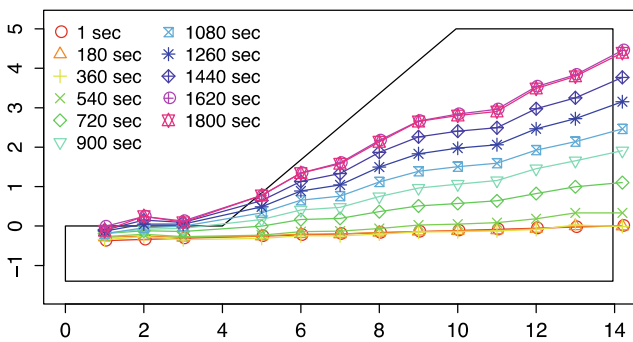
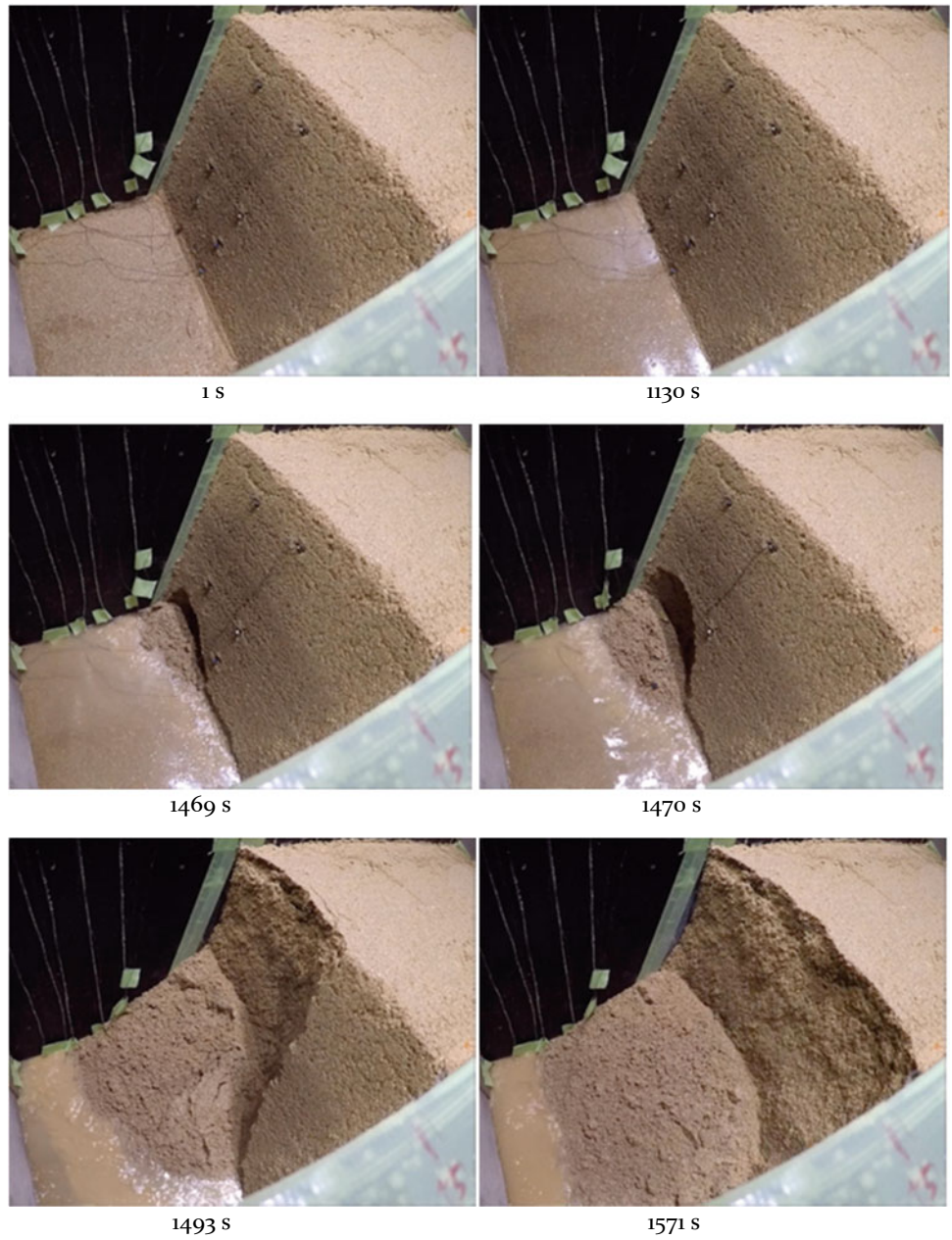


Fig. 8 The groundwater level obtained using pore water pressure sensors for Case 1

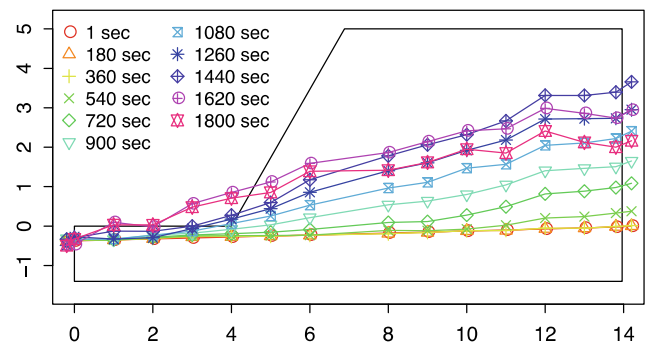


Fig. 9 The groundwater level obtained using pore water pressure sensors for Case 2

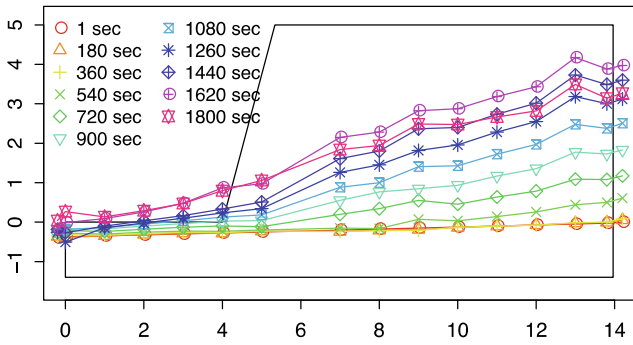


Fig. 10 The groundwater level obtained using pore water pressure sensors for Case 3

of the creep phenomenon from secondary creep to tertiary creep. In this study, the external force on the slope is changing as the water level continues to rise, and this collapse prediction method based on the creep phenomenon does not satisfy mechanical conditions. Therefore, this study used an algorithm that detects anomalies based on the amount of change in the strain value.

There are many methods for catching anomalies in time-series data. The three sigma rule (Pukelsheim 1994) which is also called as 68-95-99.7 rule is a statistical method, often used in production control and quality assessment. This rule shows the probability that, given a normal data set consisting of a normal distribution, the data will fall within two, four, and six times the width of the standard deviation from the simple moving average of the data, which are 68.27, 95.45, and 99.73%. Using this method, collapse prediction was verified using the outliers of the measured data. The measured surface strain on a non-moving slope is constant. However, some noise appears on the measured value due to mechanical noise and temperature. It is assumed that the measurement value follows a normal distribution with the amount of noise added or deleted from the true value. If the slope is not moving, the measured value should be close to the true value at the center of the normal distribution. Therefore, an abnormal value can be detected by deriving the standard deviation from past measurement values and calculating the deviation value of the present measurement value.

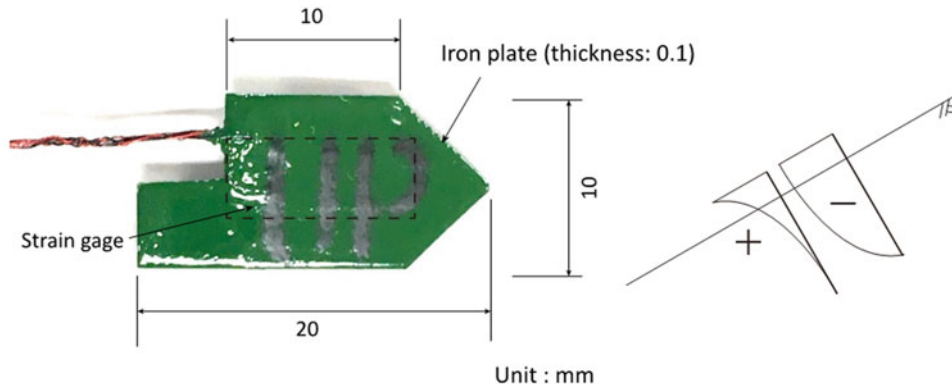


Fig. 11 Plane view of strain sensor (MPSc)

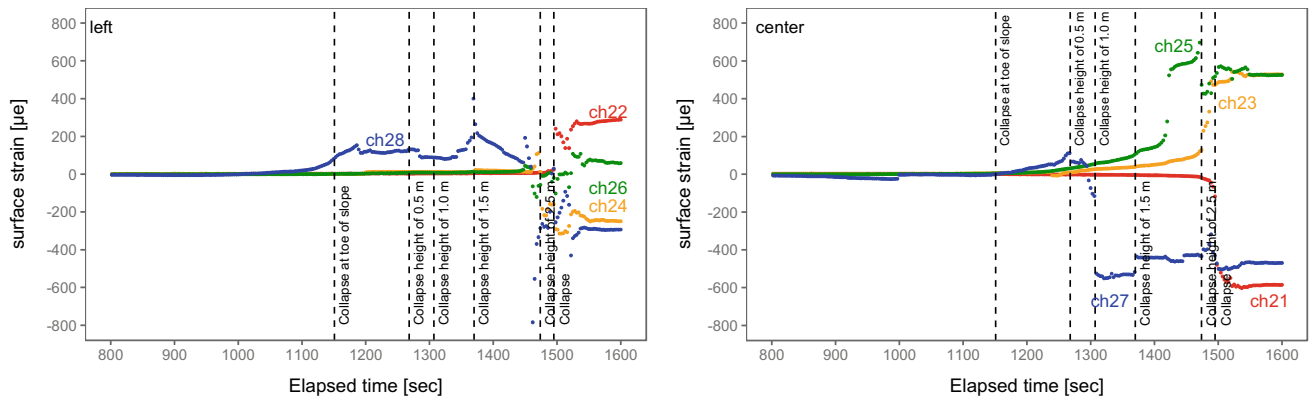


Fig. 12 The slope surface strain obtained using MPSc for Case 2

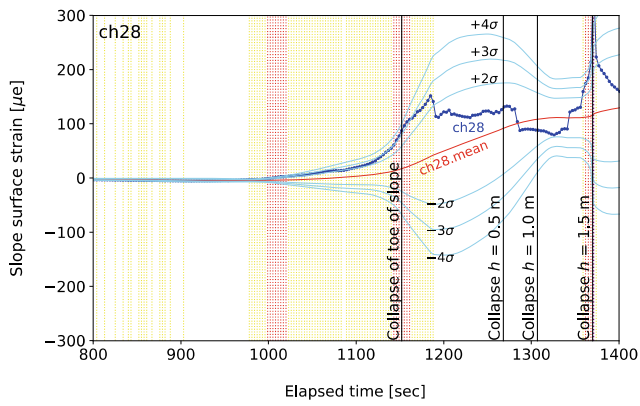


Fig. 13 The warnings (yellow lines are advisory, red lines are warning, purple lines are emergency warning) determined by the slope surface strain obtained by MPSc ch28 for Case 2

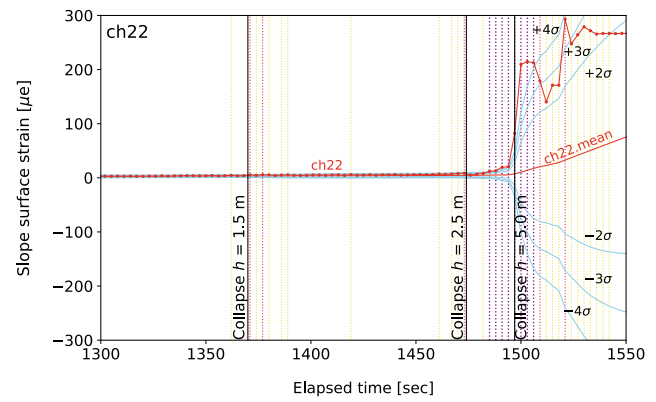


Fig. 14 The warnings (yellow lines are advisory, red lines are warning, purple lines are emergency warning) determined by the slope surface strain obtained by MPSc ch22 for Case 2

In this experiment, the strain values were recorded at 10 Hz, but were extracted from this raw data at 30 plot intervals (i.e., 0.333 Hz) without any processing in order to assume a data set in the field. According to the similarity rule, 0.333 Hz data is equivalent to 1 min in 20 g field. Assuming measurement at the construction site, a measurement interval of about 1 min is appropriate due to the battery and communication capacity of the sensor. Advisory, warning, and emergency warning were classified based on the deviation rate between the moving average and standard deviation as shown following equation.

- Advisory : $|\varepsilon| > |\bar{\varepsilon}| + 2\sigma$ (1)
- Warning : $|\varepsilon| > |\bar{\varepsilon}| + 3\sigma$ (2)
- Emergency Warning : $|\varepsilon| > |\bar{\varepsilon}| + 4\sigma$ (3)

here, ε is recent strain, $|\bar{\varepsilon}|$ is the simple moving average of strain, σ is the standard deviation.

We use 4σ (99.94% probability) instead of 3σ . In the case of 3σ , the data before the collapse is too stable, and many false alarms are detected.

The signal sensitivity depends on the sample size. As the sample size increases, the signal becomes more sensitive because the mean line changes slowly, resulting in larger deviations when the data show outliers. This means that slope deformation can be detected earlier, but the signal release time is also longer. The sample size was validated for 60, 120 and 180 plots, with 60 plots showing good results. The data preprocessing needs further validation.

Figures 13 and 14 show the advisory, the warning, and the emergency warning as determined by Chapter “On the Progression of Slope Failures Using Inverse Velocity of Surface Movements in an Undercut Slope Model” and Chapter “Preliminary Results from the SMART-SED Basin Scale Sediment Yield Model”, respectively. The yellow vertical line indicated an advisory, the red vertical line indicated a warning, and the purple vertical line indicated an emergency warning, which was indicated at the time it was issued. It can be confirmed that an advisory (red line) or an

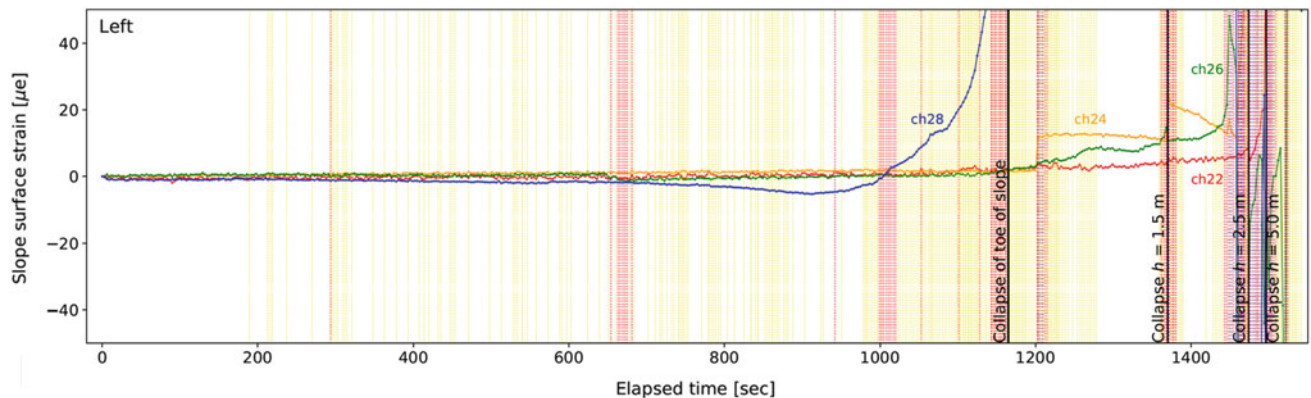


Fig. 15 All alerts (advisory, warning and emergency warning) obtained by each strain sensor for Case 2

emergency warning (purple line) is warned before the collapse near the sensor occurs, respectively.

Figure 15 shows the results of a strain gauge measuring the left side of the slope, where the collapse progressed quickly, overlaid with the resulting warnings. An alarm is effectively sounded before each collapse event by any of the sensors. Although there are still operational issues, the prediction accuracy can be improved if the information combined multiple sensor alerts. In addition, it means that occupational accidents at the excavation site can be prevented.

Conclusion

This research obtained the following key points.

- It was found in this study that slopes excavated using the slope angles recommended by the “Ordinance on Industrial Safety and Health” and “The Specification for Road Works” were stable. However, if the groundwater in the slope rose, the slope became susceptible to collapse.
 - In the case of excavation work where there is a possibility of rising groundwater, effective countermeasures include decreasing the slope angle.
- It was verified that it is possible to predict slope failure by the strain on the slope surface. Abnormal values can be detected by deriving the standard deviation from past measurement strain values and calculating the deviation value of the current measurement strain value. These results confirmed that slope failure can be predicted by time series measurement of strain.

References

- Hiraoka N, Kikkawa N, Itoh K (2019) A study on slope failure by difference of slope angle due to groundwater using centrifuge modelling. In: Asia Pacific symposium on safety 2019, pp 463–471
- Hiraoka N, Kikkawa N, Sasahara K, Itoh K, Tamate S (2017) A full-scale model test for predicting collapse time using displacement of slope surface during slope cutting work. In: The 4th world landslide forum, pp 111–121
- Toyosawa Y, Itoh K, Tamrakar SB, Horii N (2005) The characteristics of labor accidents caused by slope failure. In: The international symposium on landslide hazards in orogenic zone from the Himalaya to Island Arcs in Asia, pp 281–290
- Pukelsheim F (1994) The three sigma rule. *Am Stat* 48:88–91



2020 Kyoto Japan

Effects of Relative Density in Progressive Sliding of Tailing

Wei Hu, Xiaoyan Zhang, and Huawei Hu

Abstract

Ruptures of tailing deposits can exhibit flow-like behavior and cause major disasters. An extensive mass of tailings can be transported over large distances at high velocity and flood downstream villages, resulting in the loss of a large number of lives and huge property losses. We present a series of flume tests to observe the process of tailing slope failure when subjected to a water flow. Progressive flow slides were observed in a range of tailing deposits with varying relative densities, in which hydraulic conductivity reduced with increasing relative density. The generation of pore pressure caused a sudden collapse of the dam for very loose, loose and medium dense materials, and is also evident in seismic signals and acoustic emission signals. In dense tailing slopes, progressive failure occurred, with several successive sliding surfaces, and several seismic signals corresponding to rising acoustic emission signals. The water inflow into dense slopes is slower due lower hydraulic conductivity, resulting in successive sliding starting at the slope toe and progressing within the soil mass. The runout, internal displacement and peak flow velocity tend to be quite similar with an increase in relative density up to 0.35, and become less pronounced for denser tailings slopes. A relative density of 0.35 is a transitional density from a sudden overall failure to a progressive slope failure.

Keywords

Tailing dam • Progressive failure • Relative density • Flume test

Introduction

Tailing dams are built to store waste from mining exploitation. Tailing deposits in the impoundment ponds are a potential hazard that could lead to catastrophic failure of the tailings, as occurred at a dam in Mochikoshi gold mine, which failed after the Izu-Ohshima-Kinkai earthquake of January 15, 1978 in Japan (Ishihara 1984), and a mine tailing dam collapse caused by a small-magnitude earthquake on 5 November 2015, in Brazil. The collapse of tailing material can result in significant loss of life and property. On August 10, 2008, a failure of an iron ore tailing impoundment in Shanxi province, northwest China, caused 277 deaths (Yin et al. 2011). Recently, a mining dam collapse in southeastern Brazil on Friday 25 Jan 2019, resulted in deadly flooding that caused at least 99 deaths, while over 250 people remain missing (Schmidt and Leister 2019); the reasons for this tragic event are still under investigation.

The failure mechanisms of tailing dams have been studied by a number of authors. Caldwell and Charlebois (2010) stated that in most cases the failure of tailing dams was not triggered by a single factor, but was a consequence of a series of minor incidents. Failure can also be induced by rainfall, such as the Merriespruit Harmony Mine tailing dam failure on 22 February 1994 in South Africa, caused by a heavy rainstorm (Van Niekerk and Viljoen 2005), and the Stava tailing dam failure in Italy in 1985 (Chandler and Tosatti 1995). Apart from earthquakes or rainfall, piping, overtopping, or combination of these can also trigger failure. Agurto-Detzel et al. (2016) investigated the seismic signals recorded by the Brazilian Seismographic Network for the tailings dam failure of 5th Nov, 2015 in Brazil, and

W. Hu (✉) · X. Zhang · H. Hu
Key Laboratory of Geohazard Prevention and Geoenvironment
Protection, Chengdu University of Technology, Chengdu, 610059,
People's Republic of China
e-mail: huwei1999@126.com

X. Zhang
School of Mechanics and Civil Engineering, China University of
Mining and Technology, Beijing, 100083, People's Republic of
China

suggested nearby earthquakes should be taken into account in risk evaluation for tailing dams. Wu and Qin (2018) found that the dam breach size, flow discharge, flow velocity, and deposition volume could have an influence on the consequences of a tailings dam failure. The failure process could be simulated by numerical (Donald and Chen 1997; Cascini et al. 2016) or physical models (Ochiai et al. 2004; Olivares and Damiano 2007; Okada and Ochiai 2008; Bowman et al. 2012; Papa et al. 2012). Cuomo et al. (2014) investigated the propagation pattern of mobilized material and its velocity, thickness and runout distance, using the model 'GEO-Flow_SPH'. The variation of flow depth with velocity in small-scale flume tests suggested that grain-to-grain or grain-to-fluid collisional interactions play an important role in flowslide behavior (Spence and Guymer 1997). Using flume tests, Hu et al. (2015) studied post-earthquake huge debris flows in southwest of China due to damming and breaching. Wang and Sassa (2001) investigated the sliding distance and pore pressure generation caused by a rainfall-induced flow slide within a small flume. Despite previous research on flow-like landslides, the roles played by the relative densities of tailing materials are still unclear.

Here we present the results of flume test experiments on instrumented artificial tailing slopes, with different relative densities of tailing materials, subjected to a concentrated flow. Pore pressures, internal displacement, surface displacement, seismic signals, and acoustic emissions were monitored. The runout was measured after failure using 3D topography. Finally, we discuss the influence of the initial relative density on the mode of rupture.

Experimental Materials

The granular material used in the flume tests was collected from the iron waste deposits from a tailing pond in An-Ning, in Miyi county, about 75 km from the northeast border of Panzhihua province, China. Figure 1a shows an aerial view of the An-ning tailing pond, which consists of a main dam and a sub-dam. To obtain representative soils from the site, tailings were collected from 15 different locations at this site. They were then washed and oven-dried, prior to sieving (British standard 1377 2 1990). The grain size distributions are given in Fig. 1b. The material was found to be well graded, ranging from silt to sand, with 95% of the grains smaller than 2 mm. The maximum and minimum dry densities are 2.267 and 1.785 g/m³, respectively. The tailing samples from Md2 (Fig. 1a) were used to prepare the flume tests because of the site's accessibility.

Instrumentation of Flume Tests

The tests were carried out using an instrumented flume, 2 m in length, 0.35 m in width and 0.55 m in height, with an inclination of 20°. The floor was covered by sand grains glued to a rubber sheet to reproduce a high frictional contact to prevent the base from sliding. The side-walls of the flume were made up of transparent plexiglass sheets, to allow the sliding process to be recorded using cameras (Sony/HDR-CX210E). Details of the instrumentation are given in Fig. 1c.

Pore pressure sensors from Yom Electronic Technology were installed to monitor pore pressure. Transducers No. 1, 2, 3 and 4 were installed on the floor of the model at distances from the back of the flume of 20 cm, 30 cm, 50 cm and 70 cm, respectively. Transducers No. 5, 6 and 7 were installed 20, 40 and 60 cm from the back and 12 cm above the floor. The pore pressure transducers on the floor of the model were installed before the prepared sample was added, while the pore pressure transducers in the middle layer of the model were installed after the formation of the first layer. The internal movement was measured using a linear displacement transducer at the upper end of the flume, which was connected to a built-in styrene foam ball (2 cm in diameter and 0.1 g in weight) with a 0.5 mm thick stiff wire. A 160 g counterweight at the lower end of the flume was installed to balance the pulling resistance of the transducer and also to minimize the relative movement between the ball and the surrounding soil. A laser-point displacement transducer (ZSY/ZSDL100) was installed above the slope to measure the vertical displacements of the soil mass in the middle of the slope. A seismic accelerometer (Wilcoxon Research Company, 731A/P31) with high sensitivity (100 V/g) was positioned under the flume floor 50 cm from the back of the flume to monitor the vibrations generated by the movement of the overlying soil mass. High-frequency (100–400 khz) acoustic emissions (AEs) were measured with a high-sensitivity (40-Db amplification) wideband AE transducer (Physical acoustics, Mistral Group, inc.) on both sides of the walls. A 3D laser scanner (Pentax S-3 × 80) was installed to map the surface of the slope during and after the flume tests. Some selected tests were performed after retrogressive sliding to obtain 3D scanner data during the tests. The runout distance and the three-dimensional topographic profile of the slope could be accurately obtained using the Surfer software application. A concentrated water inflow from the rear of the slope was used to trigger sliding, and the discharge was accurately controlled by a flow meter and a flow valve.

A total of 14 tests were carried out. Seven tests were conducted with different relative tailing densities (RDs) ranging from 0.03, 0.1, 0.25, 0.35, 0.45, 0.6 to 0.75.

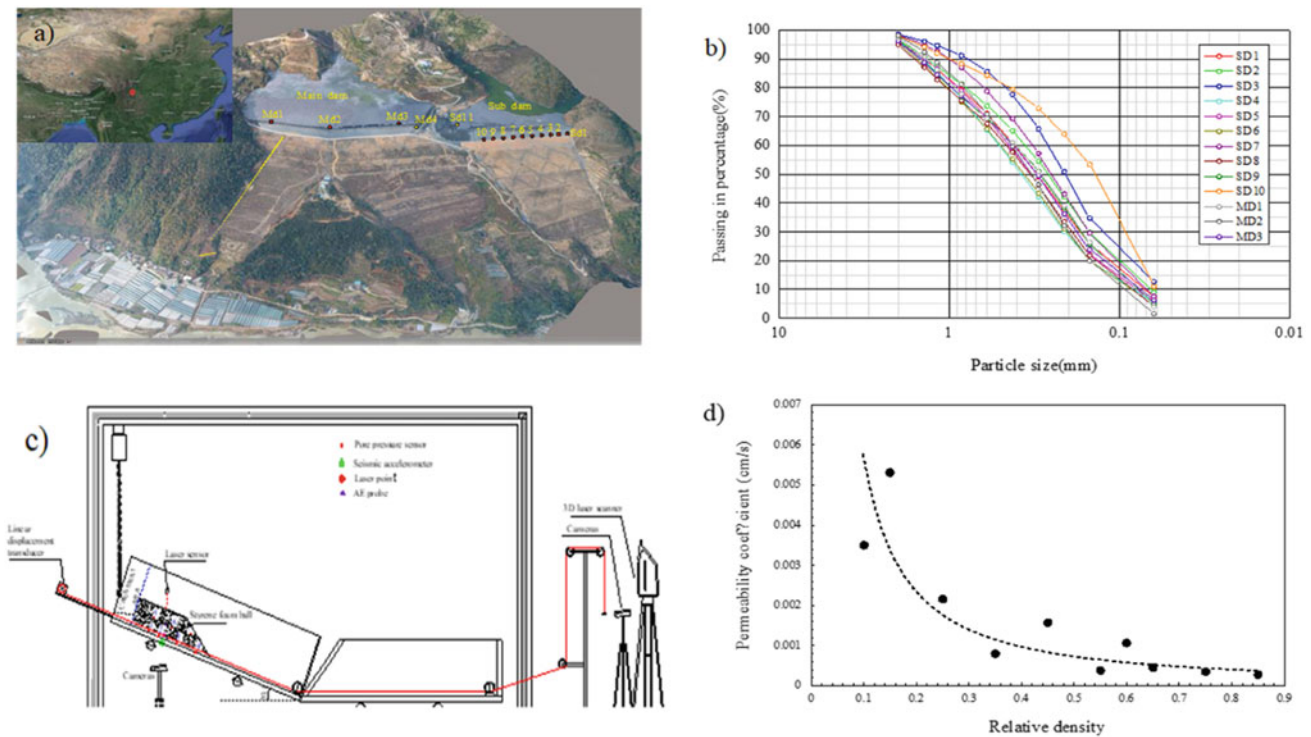


Fig. 1 a Location map of An-Ning tailing dam in Miyi county and the 3D view of An-Ning tailing dam; b particle size grading of the tailing deposits collected from different sites at the tailing dam and the one

used in experiments; c set-up of the flume apparatus; d hydraulic conductivity of the tailing deposits with relative density ranging from 0.1 to 0.95

Spence and Guymer (1997) suggested that the limits of the relative density can be defined as follows: extremely loose, <0 ; very loose, $0-0.15$; loose, $0.15-0.35$; medium dense, $0.35-0.65$; dense $0.6-0.85$; very dense, $0.85-1$. The soil with the relative density of 0.35, at the boundary of loose and medium dense, was tested three times, while the relative density of 0.25 for loose and 0.45 for medium dense was tested twice to verify the repeatability of the results. The soil was compacted layer by layer to reach the target density to prepare a homogeneous sample. The slope was prepared as a right-angled trapezoid shape with an upper length of 0.55 m and a lower length of 0.85 m and a height of 0.25 m. The thickness of the first layer was 12 cm, while the thickness of the second layer was 13 cm. An amount of water was added to the dry soil to produce the desired initial water content, which was set to be 8% for all the tests. The hydraulic conductivity k evaluated by constant-head tests decreased from 0.00531 cm/s to 0.000281 cm/s for the tests, with a relative density range from 0.1 to 0.95. It should be noted that the hydraulic conductivity decreased sharply when the relative density increased from 0.1 to 0.35 (Fig. 1d).

Results

The rupture process could be simply categorized as wetting, precursory slides and general failure. The time for water arrival of front (before sliding initiation) of different relative densities (RDs) ranges from 2614 to 3414 s, as shown in Fig. 2. The time required for the saturation and pore pressure build-up is dominated by hydraulic conductivity (Hu et al. 2017, 2018), which increased greatly with the increase in relative density, and thus affected the time from saturation to failure. With lower RDs, sudden failure occurred with a pronounced slip surface, and the time from initiation to failure just few seconds while the slope with RDs = 0.45 and 0.6 failed progressively, accompanied by fluidizing, and those tests from first collapse to general failure lasted for 6528 s and 13,454 s respectively. It slowed down the failure from sudden failure to progressive failure, and the time from saturation to general failure increased from approximately 2655–16,868 s. No major failure occurred for RD = 0.75, the test was terminated after last for 21,241 s when a small collapse occurred at the toe. Details of monitoring data at

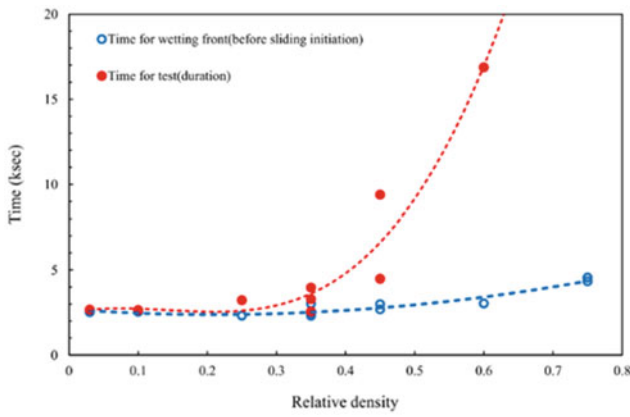


Fig. 2 The relationship between the relative density and time required for saturation and general failure

failure are given for each experiment with different relative tailing densities and therefore different hydraulic conductivities, but the same hydraulic boundary.

As the deposit became progressively saturated by a constant water head (10 cm) at the back of the slope,

densification could be observed in loose tailing slopes with RDs = 0.1 and 0.25, but not in the dense slopes. Wang and Sassa (2001) also found that, along with water infiltrating towards the base of the sample and a wetting front parallel to the base, densification could occur in loose or medium soils. The acoustic emissions were generated by particle–particle interactions such as sliding and rolling friction, and rearrangement of the particle contract network (release of contact stress and stress redistribution); thus, the detection of acoustic emission signals is an indication of material deformation (Smith et al. 2014). Acoustic emission signals were detected after approximately 500 s (Fig. 3k, l), but the seismicity signals were not detected before 2629.5 s. Densification was also evident from the surface displacement measured by a laser-point displacement transducer which started to rise after 338 s and continued to increase to 5.75 mm before general failure at 2631.25 s for the slope with RD-0.1. This densification was due to the progressive decrease of capillary cohesion with the water infiltration. With an increase of relative densities, densification become less pronounced and the acoustic emission signals before rupture decreased, as shown in Fig. 3k–m, with the cumulative acoustic emission

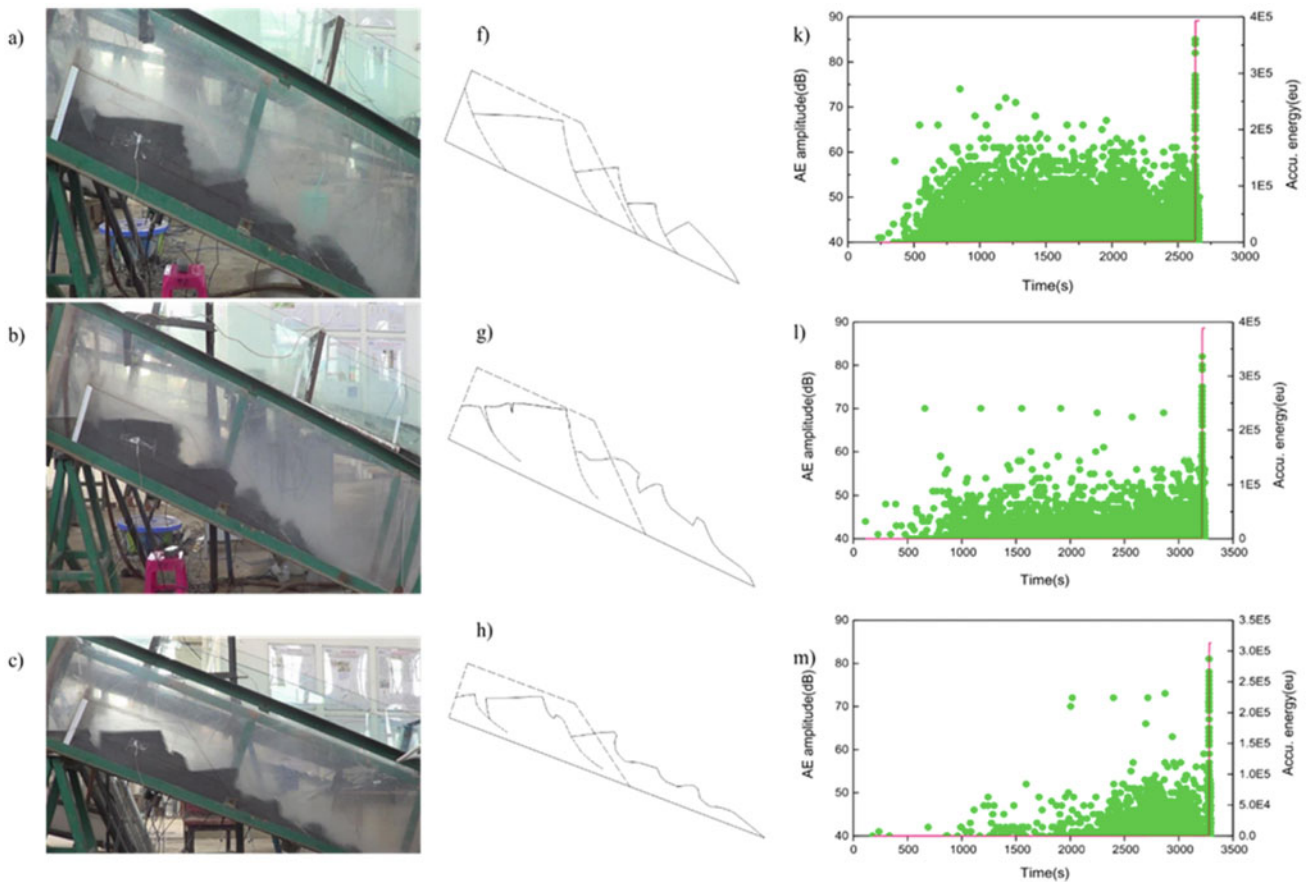


Fig. 3 Results of tests with relative tailing densities ranging from RD = 0.1 to 0.6 **a–e** The progressive failure process as observed by camera; **f–i** sketches of the progressive failure modes; **k–o** acoustic emission (AE) amplitudes and cumulative acoustic emission energy

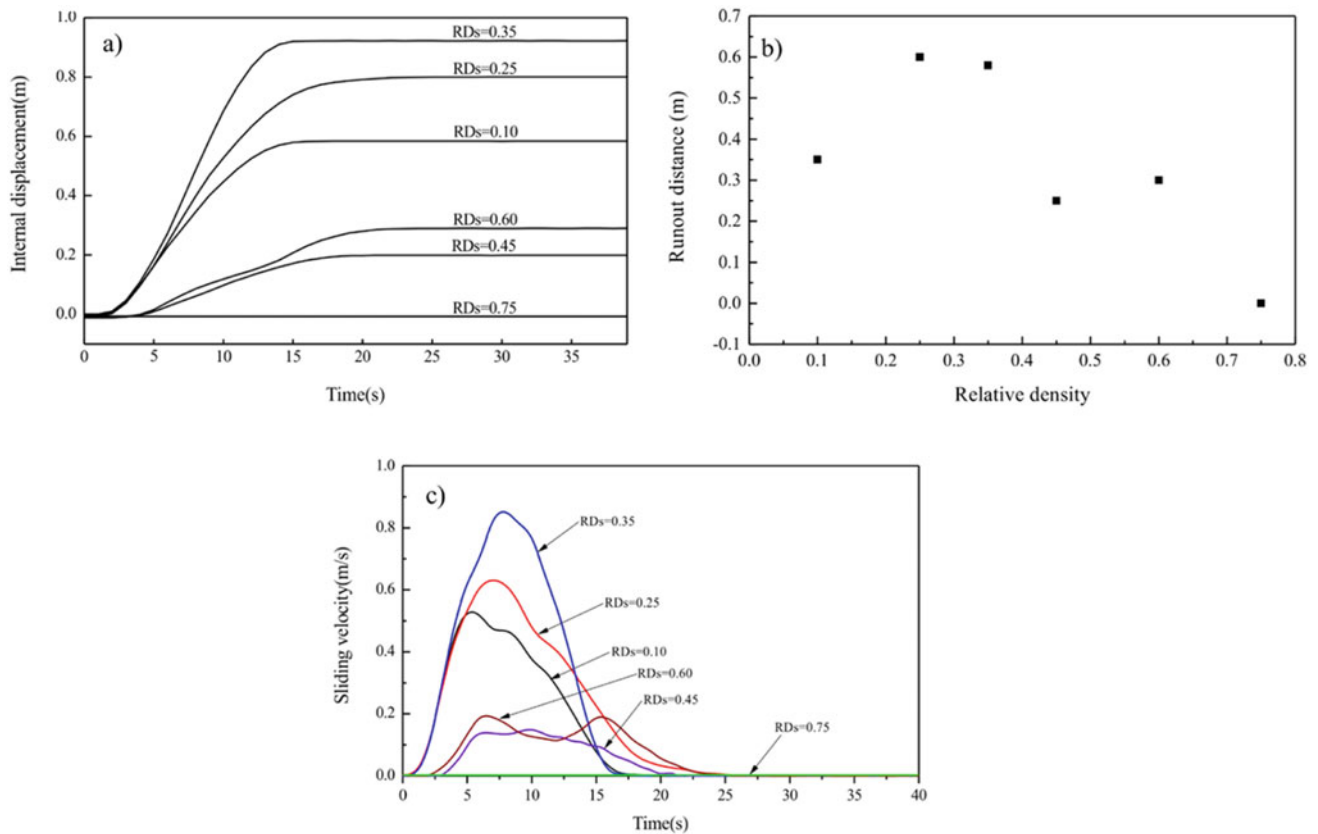


Fig. 4 Quantitative measurements for tests with different relative tailing densities (RDs) after general failure **a** internal displacement against relative density; **b** runout distance against relative density; **c** sliding velocity at the final failure

decreasing from $4E5$ eu for test tailings with $RDs = 0.1$ to approximately $3E5$ eu for test tailings with $RDs = 0.35$, and then slightly increasing for higher relative densities. Hu et al. (2018) suggested that acoustic emission signals could be more suitable than seismic signals for capturing the movement of the soil in a flume test.

The general failure modes of the slopes with different relative tailing densities is quite different. General failure of the slope with an $RD = 0.1$ happened in the form of one block sliding downward along a circle slip surface, leading to the collapse of the whole slope within an extremely short time (less than one second) (see Fig. 3a, f). The general failure induced a seismic signal with a sharp increase of amplitude, an increase in internal displacement and a sharp increase in the acoustic emission signals. Correspondingly, internal displacement occurred only during the macroscopic failure at 2631.5 s. With continuous sliding, the velocity of the internal sliding, the acoustic signal, and the amplitude of seismicity reached a peak.

The failure process of the flume tests with medium tailing densities of $RDs = 0.45$ and 0.6 , corresponding to a progressive failure, is clearly captured in six collapses, in which

several sudden rises in acoustic emission signals could be observed (Fig. 3n, m).

The internal displacement increased gradually for relative tailing densities as they increased from 0.1 to 0.35, and then gradually decreased (Fig. 4a). This tendency could be verified from the runout distance measured using three-dimensional topography after the general failure (Fig. 4b). The runout distance increased gradually with the increase of RDs to 0.35 and then gradually decreased due to the more pronounced progressive failure, resulting from the partially dissipated energy during each sliding. The slope with $RDs = 0.6$ exhibited a larger runout in comparison to the test with $RDs = 0.45$, because the soil mass and water at the rear pushed forward the previous failed soil mass during its sliding movement. Since the cumulated potential energy increasing with the increase the density from 0.03 to 0.35, the duration of the vibration signal after general failure increased, with an increase from 3 s for the test with $RDs = 0.1$ to 5 s for the tests with $RDs = 0.25$ and 0.35. It then decreased to 4 s for the tests with $RDs = 0.45$ and 0.6, due to the energy dissipation caused by the several phases of sliding that occurred before general failure. The peak

acceleration also increased from 6 mg for the test with $RD = 0.1$ to 8 mg for the tests with $RDs = 0.25$ and 0.35 , and then decreased to 4 mg for the test with $RD = 0.6$. Hu et al. (2017) suggested that gentle vibration was recorded because of the more gradual failure process and the higher viscosity of the fluidized mass.

The velocity of the movement was calculated from the internal displacement versus time during the general failure (Fig. 4c). The initiated slide experienced acceleration, deceleration and steady slow-sliding periods, where the peak velocity increased from 0.537 m/s for $RDs = 0.1$ to 0.861 m/s for $RD = 0.35$, and then decreased. This indicates that very loose and loose slopes can suffer a sudden failure in an extremely short time. Okada and Ochiai (2008) explained this could be due to the lower shear resistance caused by the excess pore pressure and an increase in cohesive resistance. Even for dense slopes, the peak velocity is greater than 0.05 m/s, which is categorized as a very rapid rupture according to the landslide velocity scale suggested by (Cruden and Varnes 1996). This could, to some extent, explain why the tailing dam failures are always very rapid.

Conclusion

We have presented experiments on artificial tailing deposits subjected to a concentrated flow, and highlighted the role of the relative density of the deposits and pore pressure generation on the progressive slope failure mechanism. The relative density controlled the hydraulic conductivity, resulting in sudden failure for very loose and loose slopes to progressive failure for medium dense slopes. This was suggested by seismic and acoustic precursory signals and by the pore pressure generation. In very loose and loose slopes, progressive saturation caused a densification of part of the soil mass, generating a crack in the middle part of the tailing dam, as well as a sudden pore pressure rise at the toe; finally, the entire slope suffered a sudden rupture. The relative density of 0.35 is a transition from loose to medium dense and the failure process showed also a transition from sudden failure to progressive failure by successive sliding, verified by three repeated tests. The failure of the dense tailing slope corresponded to successive sliding, starting at the toe and progressing inwards to the slope, until the total rupture of the slope. This succession of events led to a smaller amplitude for the seismic and acoustic emission signals and the internal displacement and runout was shorter than those of loose slopes. This, to some extent, could provide guidance to engineers by demonstrating that increasing the relative tailing densities during construction could slow down the time to failure for the same hydraulic conditions and give some warning when progressive sliding takes place before the

global destructive slope rupture. Although increasing the relative tailing densities could increase the time to failure, the slope rupture will still be able to develop if the time of saturation is long enough.

Acknowledgements This research was carried out under the National Basic Research Program of China: National fundamental scientific research grant (No. 41472273), Youth Science Foundation Project (No. 51809264), the Funds for creative research groups of China (41521002), funded by the State Key Laboratory of Geo-hazard Prevention and Geo-environmental Protection (SKLGP2018K024).

References

- Agurto-Detzel H, Bianchi M, Assumpção M, Shimmel M, Collaço B, Ciardelli C, Barbasa JR, Calhau J (2016) The tailings dam failure of 5 November 2015 in Se Brazil and its preceding seismic sequence. *Geophys Res Lett* 43(10):4929–4936
- Brand EW (1981) Some thoughts on rain-induced slope failures. In: *Proceedings of 10th international conference on soil mechanics and foundation engineering*, 15–19 June 1981, Stockholm, Swedish, vol 3, pp 373–376
- Brenner RP, Brand EW (1985) Field stress path simulation of rain-induced slope failure. In: *Proceedings of 11th international conference on soil mechanics and foundation engineering*, p 991–996
- Bowman ET, Take WA, Rait KL, Hann C (2012) Physical models of rock avalanche spreading behaviour with dynamic fragmentation. *Can Geotech J* 49(4):460–476
- Chandler RJ, Tosatti G (1995) The Stava tailings dams failure. In: *Proceedings of the institution of civil engineers-geotechnical engineering*, July 1985, Italy, vol 113, no 2, pp 67–79
- Cruden DM, Varnes DJ (1996) Landslides: investigation and mitigation. In: *Landslide types and processes*, Chapter 3. Transportation research board special report, 247
- Caldwell J, Charlebois L (2010) Tailings impoundment failures, black swans, incident avoidance, and checklists. In: *Proceedings of international conference on tailings & mine waste, tailings and mine waste*, pp 33–39
- Cuomo S, Pastor M, Cascini L, Castorino GC (2014) Interplay of rheology and entrainment in debris avalanches: a numerical study. *Can Geotech J* 51(11):1318–1330
- Cascini L, Cuomo S, Pastor M, Rendina I (2016) SPH-FDM propagation and pore water pressure modelling for debris flows in flume tests. *Eng Geol* 213:74–83
- Donald IB, Chen Z (1997) Slope stability analysis by the upper bound approach: fundamentals and methods. *Can Geotech J* 34(6):853–862
- Eckersley D (1990) Instrumented laboratory flowslides. *Geotechnique* 40(3):489–502
- Hu W, Xu Q, Rui C, Huang RQ, van Asch TWJ, Zhu X, Xu QQ (2015) An instrumented flume to investigate the initiation mechanism of the post-earthquake huge debris flow in the Southwest of China. *Bull Eng Geol Env* 74(2):393–404
- Hu W, Scaringi G, Xu Q, Pei Z, Van Asch TW, Hicher PY (2017) Sensitivity of the initiation and runout of flowslides in loose granular deposits to the content of small particles: an insight from flume tests. *Eng Geol* 231:34–44
- Hu W, Hicher PY, Scaringi G, Xu Q, Van Asch TW, Wang G (2018) Seismic Precursor to instability induced by internal erosion in loose granular slopes. *Géotechnique* 68(11):989–1001

- Ishihara K (1984) Post-earthquake failure of a tailings dam due to liquefaction of pond deposit. In: International conference on case histories in geotechnical engineering, University of Missouri, Rolla
- Orange DL, Breen NA (1992) The effects of fluid escape on accretionary wedges seepage force, slope failure, headless submarine Canyons, and Vents. *J Geophys Res Solid Earth* 97 (B6):9277–9295
- Ochiai H, Okada Y, Furuya G, Okura Y, Matsui T, Sammori T, Terajima T, Sassa K (2004) A fluidized landslide on a natural slope by artificial rainfall. *Landslides* 1(3):211–219
- Olivares L, Damiano E (2007) Postfailure mechanics of landslides: laboratory investigation of flowslides in pyroclastic soils. *J Geotech Geoenviron Eng* 133(1):51–62
- Okada Y, Ochiai H (2008) Flow characteristics of 2-phase granular mass flows from model flume tests. *Eng Geol* 97(1):1–14
- Papa MN, Medina V, Ciervo F, Bateman A (2012) Estimation of debris flow critical rainfall thresholds by a physically-based model. *Hydrol Earth Syst Sci Discuss* 9(11):12797–12824
- Spence KJ, Guymer I (1997) Small-scale laboratory flowslides. *Geotechnique* 47(5):915–932
- Smith A, Dixon D, Meldrum P, Haslam E, Chambers J (2014) Acoustic emission monitoring of a soil slope: comparisons with continuous deformation measurements. *Géotechnique Letters* 4(4):255–261
- Schmidt A, Leister E (2019) Dozens dead, hundreds still missing following Brazilian Mine dam collapse. <https://www.accuweather.com/en/weather-news/dozens-dead-hundreds-still-missing-following-brazilian-mine-dam-collapse/70007257>
- Van Niekerk HJ, Viljoen MJ (2005) Causes and consequences of the Merriespruit and other tailings-dam failures. *Land Degrad Dev* 16 (2):201–212
- Wang G, Sassa K (2001) Factors affecting rainfall-induced flowslides in laboratory flume tests. *Géotechnique* 51(7):587–599
- Wang G, Sassa K (2003) Pore-pressure generation and movement of rainfall-induced landslides: effects of grain size and fine-particle content. *Eng Geol* 69(1):109–125
- Wu T, Qin J (2018) Experimental study of a tailings impoundment dam failure due to overtopping. *Mine Water Environ* 37(2):272–280
- Yin G, Li G, Wei Z, Wan L, Shui G, Jing X (2011) Stability analysis of a copper tailings dam via laboratory model tests: a Chinese case study. *Miner Eng* 24(2):122–130



Experimental Studies on the Effect of Vegetation Density to Change Underground Seepage Rate and Stability of Slopes

Binod Tiwari

Abstract

Vegetation plays an important role in the amount of surface runoff or infiltration after a rainfall event, specifically on slopes. High infiltration or seepage reduce shearing resistance of soil through the reduction in matric suction of partially saturated slopes, ultimately causing slope instability. On the other hand, low infiltration increases surface runoff and velocity of surface flow, which ultimately causes soil erosion. In this study, three different slopes were prepared using fine sand, specifically at the same dry density and geometry, but with three different vegetation cover densities. The slopes were instrumented with tensiometers at different depths. The slopes were subjected to a rainfall event with an intensity of 30 mm/h and advancement of the wetting front of the seepage water and soil matric suction were recorded with time duration after the rainfall. The experimental result shows that up to certain threshold vegetation cover density, amount of surface flow increases causing soil erosion. For the vegetation density above that threshold, vegetation covers intercept the rainwater and the intercepted water is gradually passed to ground. Moreover, vegetation cover will ease the flow of surface runoff water. These actions, on the other hand, increase the seepage velocity. As such, less dense vegetation cover triggers more rainfall induced soil erosion and denser vegetation cover increases the instability associated with rotational or translational slides.

Keywords

Rainfall induced landslides • Vegetation cover • Soil erosion • Suction • Translational slides

Background

Rainfall is one among the major triggers of landslides. With the effect of global climate change, number of rainfall induced landslides and the loss due to such landslides have been reported more frequently all over the world. While studying the effect of rainfall on triggering landslides, it is important to consider various factors that cause rainfall induced landslides. These factors include but not limited to —(a) intensity and duration of rainfall, (b) density of soil, (c) shearing resistance of soil, (d) soil moisture content, (e) slope inclination, (f) depth of soil, and (g) vegetation cover. Effect of intensity and duration of rainfall on triggering rainfall induced landslides has been covered extensively in the literature (e.g. Piciullo et al. 2017; Xue et al. 2016). Tiwari et al. (2018, 2013) conducted extensive laboratory-based model experiments to evaluate the effect of soil density on slope stability. Most of the shallow slopes are in partially saturated condition in dry season. As such, soil mass exhibit higher shearing resistance due to apparent cohesion as a result of matric suction. Infiltration of rainwater through the soil mass will reduce this matric suction to negligible value as the wetting front proceeds into the slope. Such reduction in apparent cohesion reduces the shearing resistance of soil, mostly by reducing the effective normal stress. Tiwari and Caballero (2015), through laboratory-based experiments, has presented the effect of slope gradient on the seepage velocity and its influence on slope stability.

Rainfall has two-fold effects on slopes. A part of the rainfall converts into surface run-off, which may cause soil

B. Tiwari (✉)

Office of Research and Sponsored Projects, California State University, Fullerton, 1121 N. State College Blvd., Fullerton, CA 92831, USA
e-mail: btiwari@fullerton.edu

© Springer Nature Switzerland AG 2021

B. Tiwari et al. (eds.), *Understanding and Reducing Landslide Disaster Risk*, ICL Contribution to Landslide Disaster Risk Reduction, https://doi.org/10.1007/978-3-030-60706-7_12

erosion if the soil is prone to soil erosion problems. Other part of the rainfall infiltrates underground through soil. This will cause a reduction in soil suction and increase in pore water pressure, which ultimately reduces shearing resistance of soil. Portions of the water converting into surface run-off or infiltration depend on the vegetation cover, soil density, and type of soil. However, there are not much information available in the literature on how the density of vegetation cover affects the infiltration rate or seepage velocity of water on a slope. This study focuses on the influence of vegetation density on seepage velocity.

Experimental Methods

In this study, three different slopes were prepared in a Plexiglas container with fine sand mixed having 2% moisture. Specific gravity of the sand was 2.65 and the sand classified as SP material. Length and width of the slopes were 1.83 m and 1.22 m, respectively. Dry density of the slope was maintained to be 14.94 kN/m^3 . Thickness of the slope model was 30 cm. throughout the slope. Slope gradient for models were kept at 45° . In order to measure matric suction with time, miniature tensiometers were installed at three different locations, at the depth of 8.9 cm along the central cross-section of the slope as presented in Fig. 1. All slopes were identical in geometry and density of sand. However, these three slopes are covered with different densities of vegetation covers (ratio of area of vegetation cover to total surface area of the slope). First slope (Slope 1) was prepared without any vegetation cover, while second slope (Slope 2) was prepared with 20% vegetation cover and the third slope (Slope 3) was prepared with 90% vegetation cover. There is no specific rationale to choose these densities. Figure 2 presents the photographs of the slopes. For vegetation cover, we just used the leaves of a plant as opposed to growing those vegetations naturally.

All slopes were subjected to rainfall at the intensity of 30 mm/h using a specially designed sprinkler system, presented in Fig. 2, until the wetting front advanced to the bottom of the slope to saturate the entire soil mass. Advancement of the wetting fronts were traced with permanent ink markers on all three sides of the Plexiglas container (outside) in every 15 min in order to calculate the seepage velocity. To monitor timewise variation in suction under the ground and at mid-section of the slope and verify the seepage velocity obtained with the advancement of wetting front, miniature tensiometers were installed at three different locations along the slope (Fig. 1).

The soil sample used to prepare the slopes were mixed with different amounts of moisture and compacted in a direct shear test box at the dry unit weight exactly same as that on the experimental slopes and shearing resistance of the soil

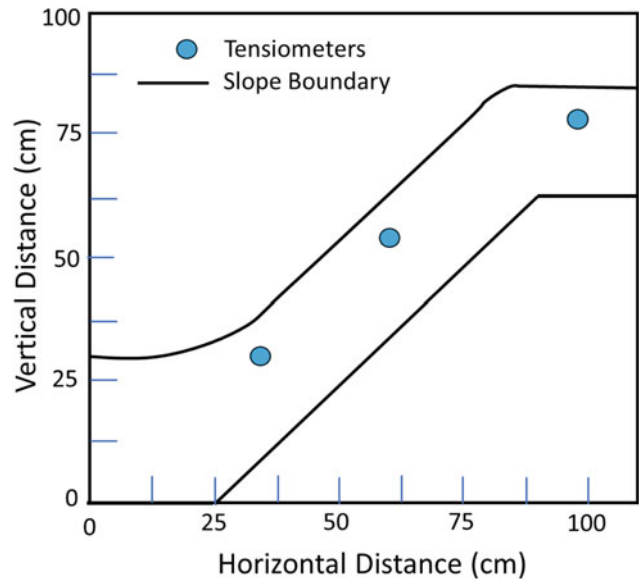


Fig. 1 Longitudinal section of the slope and location of tensiometers

samples were measured, separately, at four different normal stresses—50, 100, 150 and 200 kPa, in order to evaluate the variation in shearing resistance with moisture content (or degree of saturation). This is an indirect way of measuring total shearing resistance of the soil without measuring soil suction. Direct shear test method outlined in the ASTM D3080 was followed to measure the shearing resistances of the soil, except saturating the soil sample. The direct shear test was conducted at constant total stress and at the shearing that was calculated based on the consolidation data.

Experimental Modelling Results

Presented in Fig. 3 are the advancement of wetting front due to rainwater infiltration in every 30 min in Slope 1 (0% vegetation cover density), Slope 2 (20% vegetation cover density) and Slope 3 (90% vegetation cover density). As can be observed in Fig. 3, it took over 2.5 h for the wetting front to fully advance to the bottom of the soil layer in Slope 1 whereas it advanced in less than 2 h to the bottom of the soil layer in Slopes 2 and 3. More interestingly, as a result of higher surface runoff (although the surface runoff was not measured and the discussion here is anecdotal) due to the lack of vegetation cover, seepage velocity (velocity of advancement of the wetting front) at the top of the slope was significantly less than that along the slope and the toe in Slopes 1 and 2, while it was similar throughout the slope in Slope 3. Presented in Fig. 4 is the comparison of the advancement of wetting front in all three slopes after 1 h of the initiation of rainfall. It is evident that the seepage pattern on the top of the slope was similar in Slopes 1 and 2 until the

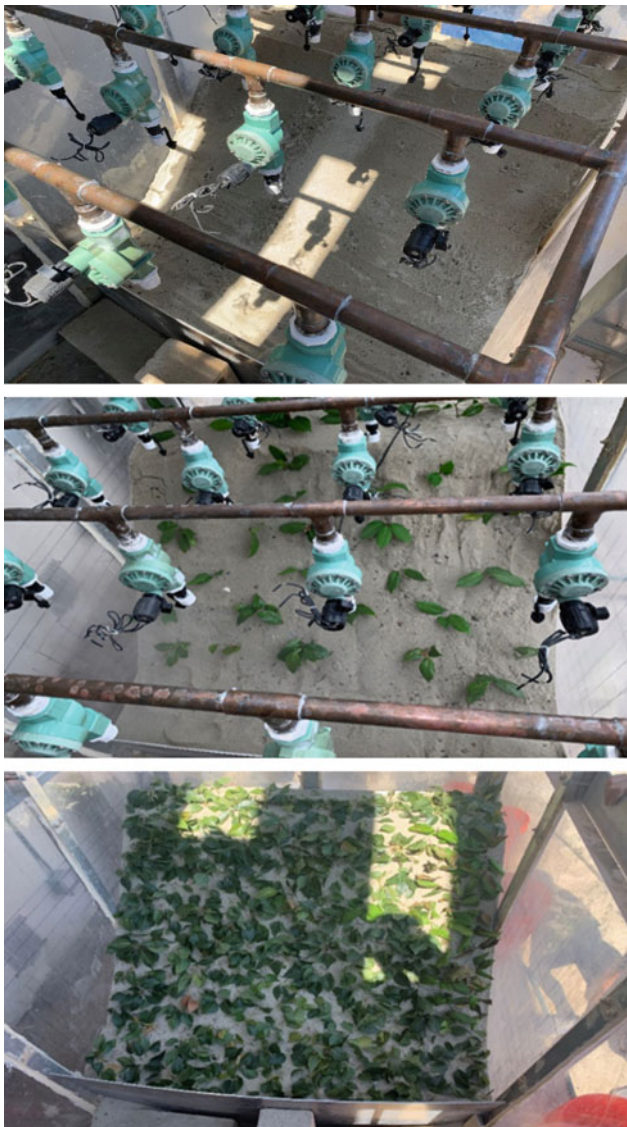


Fig. 2 Slopes prepared with three different vegetation covers—(top) 0% vegetation cover density (Slope 1), (middle) 20% vegetation cover density (Slope 2) and (bottom) 90% vegetation cover density (Slope 3)

first hour of rainfall, while there was a significant increase in seepage velocity in Slope 3 compared to the other models. However, along the sloped portion and at the toe of the slope, both Slopes 2 and 3 exhibited similar seepage pattern, demonstrating much higher seepage velocity than that in Slope 1. For this study, we performed seepage velocity analyses at the mid-way of the slope.

Advancement of wetting front with time was used to calculate the seepage velocity in the slopes having different vegetation cover densities. Suctions values measured with the tensiometers at different depths during the entire rainfall events were used to verify the information obtained with the wetting front advancement. Shown in Fig. 5 is the information pertinent to change in suction with duration of

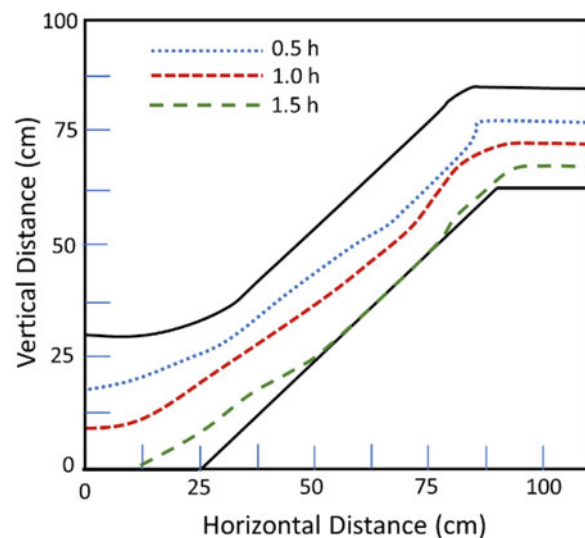
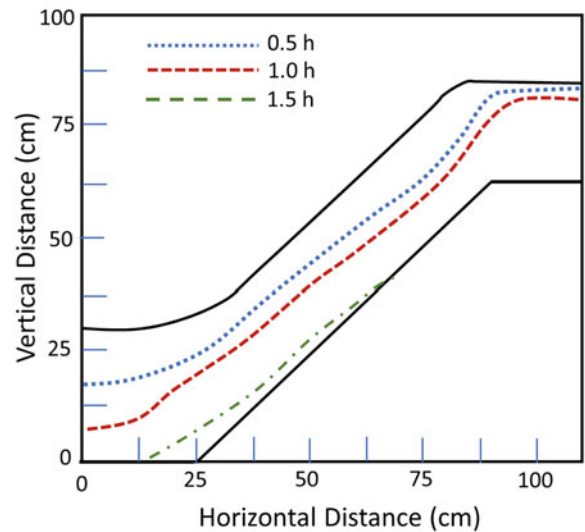
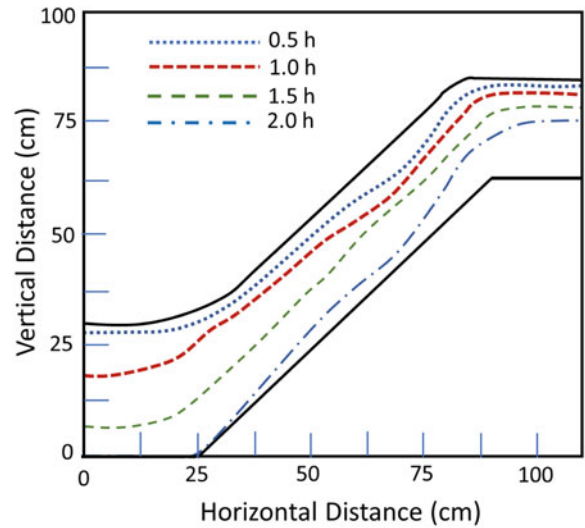


Fig. 3 Advancement of wetting front in every 30 min in slope 1 (top), Slope 2 (middle), and Slope 3 (bottom)

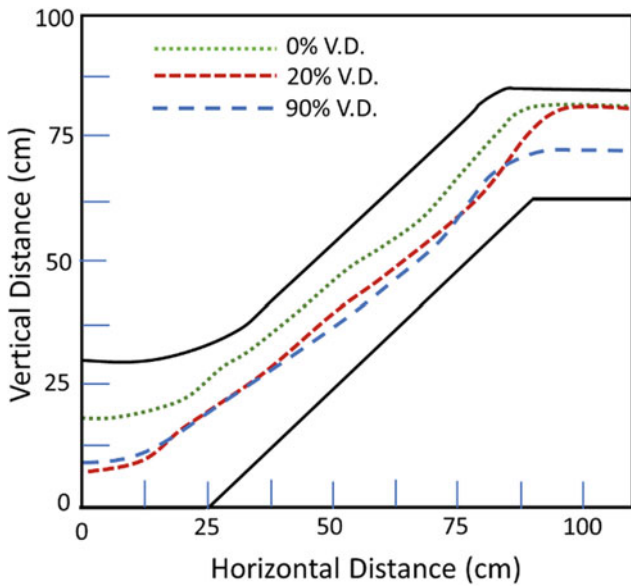


Fig. 4 Comparison of the wetting front advancement after the rainfall duration of an hour in all three slopes; V.D. refers to vegetation cover density

rainfall in Slope 3 at the tensiometer location at the middle of the slope. Other tensiometers exhibited similar results. As can be observed in Fig. 5, suction reduces suddenly from 68 kPa (suction of the compacted fill prior to rainfall) to negligible suction in 24 min. The seepage velocity calculated with this suction information and the seepage velocity calculated with the wetting front data at the tensiometer location were similar concurring the results obtained from the wetting front information.

Seepage velocity at different durations were calculated by dividing the depth of the wetting front from the surface with corresponding time. Seepage velocities at the center of the mid-section of all slopes are presented in Fig. 6. As it is evident from Fig. 6, seepage velocity decreased slightly with time for Slope 1 (0% vegetation cover density). However, there was a significant reduction in seepage velocity with time in Slopes 2 (20% vegetation cover density) and 3 (90%

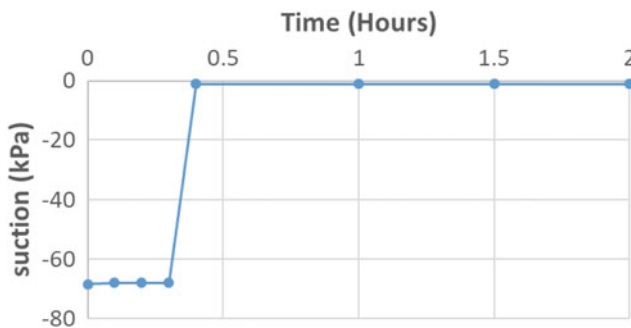


Fig. 5 Variation of suction with time at the mid-slope in Slope 3

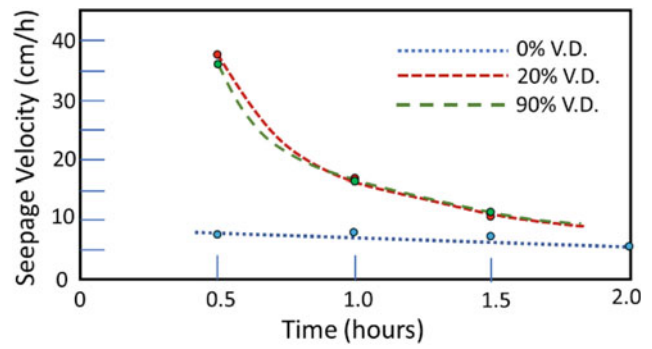


Fig. 6 Comparison of seepage velocities with time in all three slopes; V.D. refers to vegetation cover density

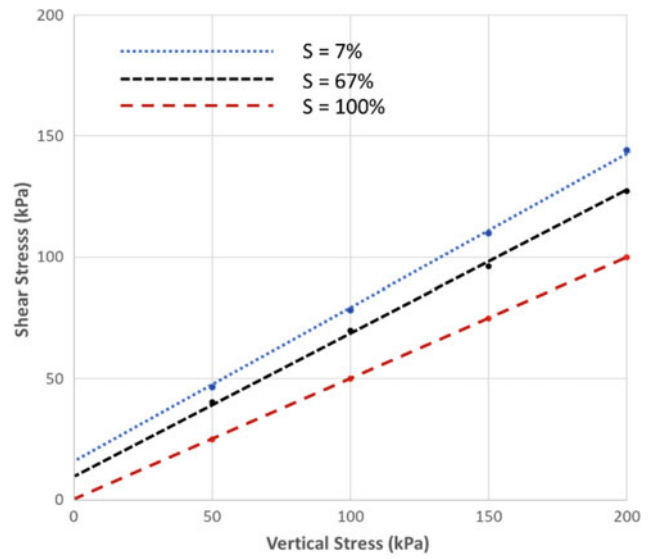


Fig. 7 Comparison of shear envelopes obtained for the soil used to prepare the model at three different degrees of saturation (S)

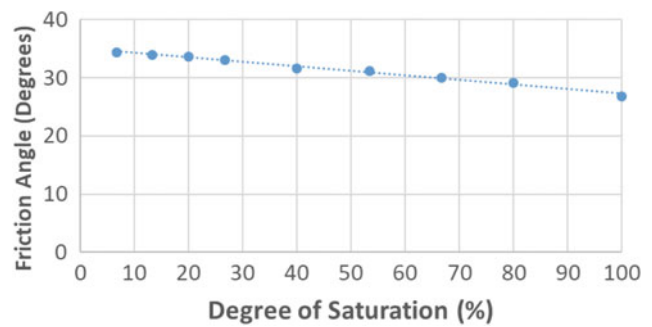


Fig. 8 Variation in internal friction angle of soil with degrees of saturation (S)

vegetation cover density). More importantly, Slopes 2 and 3 exhibited similar seepage velocities with duration of rainfall. Regression equations to estimate seepage velocity with time

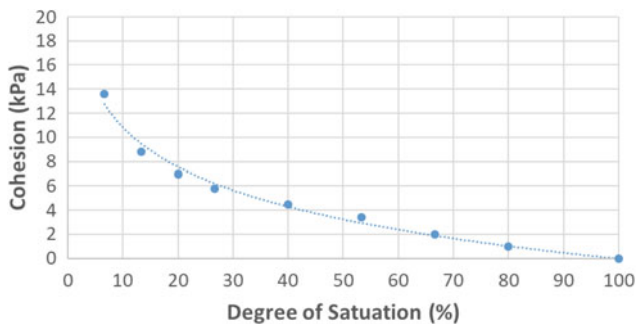


Fig. 9 Variation in apparent cohesion of soil with degrees of saturation (S)

for Slopes 1, 2, and 3 are presented in Eqs. 1, 2, and 3 respectively.

$$\text{Seepage velocity} = -1.4 \times \text{time (in hours)} + 9 \quad (1)$$

$$\text{Seepage velocity} = 16.239 \times \text{time (in hours)}^{-1.219} \quad (2)$$

$$\text{Seepage velocity} = 16.669 \times \text{time (in hours)}^{-1.089} \quad (3)$$

Soil Test Results

As mentioned earlier, soil used in the model preparation were mixed with moisture contents that provides the degrees of saturations (S) of 7% through 100%, mostly, in every 7% increment and direct shear tests were conducted to obtain the variation in shearing resistance with degrees of saturation. Presented in Fig. 7 is the shear envelopes obtained from the direct shear tests. To avoid data cluster, shear envelopes for soils compacted with only 3 different degrees of saturation have been presented in Fig. 6. As can be observed in Fig. 7, angle of internal friction did not vary significantly with an increase in the degree of saturation. However, cohesion (apparent) has significantly decreased with an increase in the degree of saturation. In order to quantify the variation in internal friction angles of the soil with the degree of saturation, friction angles were plotted against the degrees of saturation, as presented in Fig. 8. Figure 8 clearly demonstrates that friction angle of the sand gradually decreased with an increase in the degree of saturation and the relation could be fitted with a linear regression as presented in Eq. 4. Likewise, to evaluate the effect of moisture content on apparent cohesion, cohesion values were plotted against the degrees of saturation for the tested soil samples and the result is presented in Fig. 8. As can be seen in Fig. 9, there is a logarithmic reduction in the apparent cohesion with an increase in the degree of saturation, as presented in Eq. 5. These relationships are later used to analyze the stability of the slopes at different durations of rainfall.

$$f = -0.1 \times S + 36 \quad (4)$$

$$c = -4.765 \times \ln(S) + 21.835 \quad (5)$$

where, f = friction angle in degrees

S = degree of saturation in %, and

c = cohesion intercept in kPa.

Effects of the Seepage Velocity and Shear Strength of Soil on Slope Stability

In order to evaluate the effect of the increase in seepage depth (or thickness of wetting front) and reduction in shearing resistance with the duration of rainfall, the results obtained from the data recorded with tensiometer, regression equation developed for the seepage velocity, and regression equations developed for the shear strength (cohesion and friction angle) reduction with the degree of saturation were coupled in the slope stability equation developed for an infinite slope (Ajmera and Tiwari 2018). Then, variation in the factors of safety of the slope with the duration of rainfall was calculated following the developed equations. Reduction in the factor of safety of the slope with the duration of rainfall in the Slope 1, Slope 2, and Slope 3 are presented in Figs. 10, 11 and 12, respectively. As can be observed in Fig. 10, factor of safety of the Slope 1 30 min after the initiation of the rainfall was 3–4 times higher than that of Slopes 2 and 3. That can be attributed to high surface runoff as a result of the lack of vegetation cover, although we were not able to measure the surface run-off quantity. The factors of safety of the Slope 1 dropped by more than 3 times when the rainfall duration increased from 0.5 to 2 h.

As presented in Figs. 11 and 12, factors of safety of the Slopes 2 and 3 were similar throughout the rainfall period although Slope 2 exhibited slightly higher factor of safety

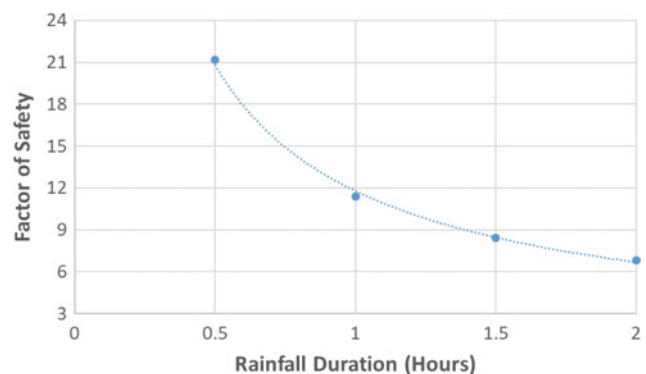


Fig. 10 Reduction in factor of safety of the slope with duration of rainfall in Slope 1

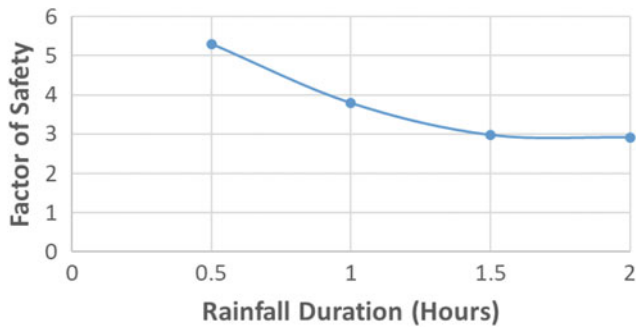


Fig. 11 Reduction in factor of safety of the slope with duration of rainfall in Slope 2

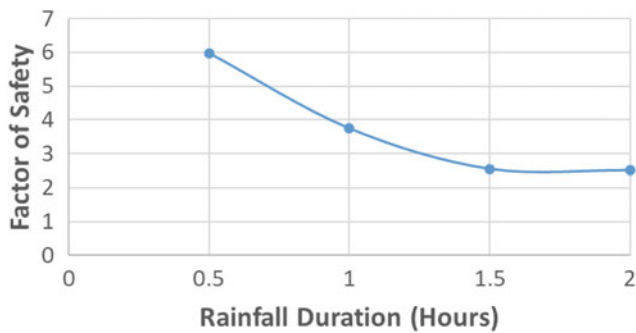


Fig. 12 Reduction in factor of safety of the slope with duration of rainfall in Slope 3

compared to Slope 3, in general. However, a significant drop in the factors of safety in Slopes 2 and 3 compared to Slope 1 can be attributed to the reduction in surface runoff quantities in Slopes 2 and 3 as a result of the vegetation cover and infiltration of intercepted rainfall underground with slight time delay. This caused an increase in seepage velocity and earlier saturation of the slopes compared to Slope 1 that did not have any vegetation cover. This caused a reduction in shearing resistance as well due to the reduction in suction. As such, factors of safety in those slopes were significantly low. We were not able to measure the run-off quantities to confirm and this discussion is anecdotal.

Figure 13 shows the reduction in factor of safety at different durations of rainfall on slopes that have vegetation densities ranging from 0 to 90%. As evident in Fig. 13, even 20% vegetation cover caused an increase in seepage velocity and reduced the safety factor significantly.

Although the factor of safety of Slope 1 was much higher than other slopes, mainly due to less amount of infiltration, Slope 1 exhibited a large surface runoff (although the quantity was not measured) and significant soil erosion. As such, such slopes without vegetation cover are vulnerable to soil erosion induced debris flow disasters.

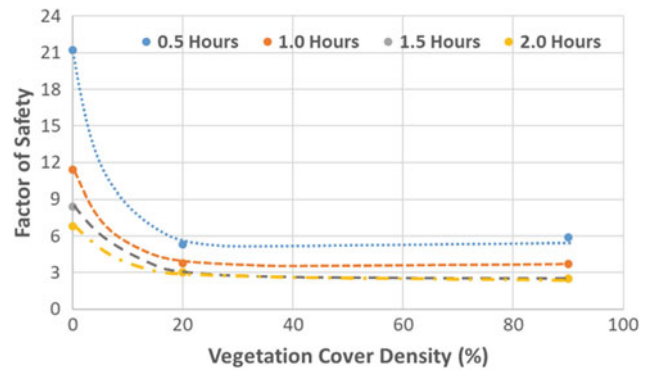


Fig. 13 Variation in factors of safety with the density of vegetation cover at different durations of rainfall

Conclusions

To evaluate the effect of vegetation cover on slope, three different slopes were prepared in the laboratory with varying vegetation cover densities. Those slopes were subjected to a rainfall of 30 mm/h for over 2 h, until the slopes were fully saturated with the rainwater infiltration. Advancement of wetting fronts and soil matric suction values were recorded with time to calculate seepage velocities at each slope. In a separate experiment, shearing resistance of the soil samples prepared at different degrees of saturation were measured using the direct shear device and variations in internal friction angle and apparent cohesion with degrees of saturation were measured. Variation of seepage velocities with time and shearing resistance with degree of saturation were augmented in the slope stability analysis equation developed for an infinite slope and variation in the factors of safety of slopes with duration of rainfall were calculated for slopes with different vegetation cover densities. Following conclusions can be made based on the experimental results and their analyses.

1. When a slope does not have vegetation cover, a major portion of the rainfall converts into runoff and it triggers soil erosion and potential debris flow problems.
2. Vegetation cover intercepts the rainfall, breaks the flow of runoff water, and slowly allows the water later to infiltrate; as such, seepage velocity of the infiltrated water increases with an increase in vegetation cover.
3. Seepage velocities on slopes do not change much with an increase in vegetation cover after a threshold vegetation cover density.
4. There is an excellent correlation between internal friction angles and apparent cohesions of fine sand with degrees of saturation. Such correlations can be directly

augmented into the slope stability analysis while analysing stability of slopes subjected to rainfall.

This study involves slopes prepared with fine sand only. More research is recommended for different types of soils, different slope gradients, and different densities of vegetation covers in order to come up with the general understanding pertinent to the effect of vegetation cover density on seepage velocity in and safety of the slopes.

Acknowledgements The author would like to thank California State University Fullerton for providing RSCA intramural funding to conduct this study. This project is a part of IPL Project No. 192. As such, the author would like to thank the International Program on Landslides for endorsing the project. The study would not have been possible without the hard work of CSUF Summer Interns from local high schools. The author appreciates the hard work of high school interns Trinity Patron, Sydney Gavela, Austin Chong, Riley Sanidad, Jeffrey Chan, and Nathan Huynh for preparing the slope models, executing the model experiments, and acquiring the experimental data.

References

- Ajmera B, Tiwari B (2018) Using excel tools for slope stability analysis. In: *Landslide dynamics: ISDR-ICL landslide interactive teaching tools*, vol 2, pp 413–420
- Piciullo L, Stefano LG, Melillo M, Brunetti MT, Peruccacci S, Guzzetti F, Calvello M (2017) Definition and performance of a threshold-based regional early warning model for rainfall-induced landslides. *Landslides* 14(3):995–1008
- Tiwari B, Ajmera B, Khalid M, Donyanavard S, Chavez R (2018) Influence of slope density on the stability and deformation of clayey slopes. *Geotech Spec Publ (ASCE)* 297:293–301
- Tiwari B, Caballero S (2015) Experimental model of rainfall induced slope failure in compacted clays. *Geotech Spec Publ (ASCE)* 256:1217–1226
- Tiwari B, Lewis A, Ferrar E (2013) Experimental simulation of rainfall and seismic effects to trigger slope failures. *Geotech Spec Publ (ASCE)* 231(1):448–451
- Xue K, Ajmera B, Tiwari B, Hu Y (2016) Effect of long duration rainstorm on stability of red-clay slopes. *Int J Geo-Environ Disasters (Springer)* 3(12):1–13



2020 Kyoto Japan

Laboratory Simulations of Submarine Landslide Failure Mechanisms

Jonathan M. Carey, Joshu J. Mountjoy, Gareth J. Crutchley, Barbara Lyndsell, and David N. Petley

Abstract

Submarine slopes are subject to a variety of failure styles, ranging from large, long runout landslides to both shallow and deep-seated landslides with limited down-slope displacements. The upper continental slope off the east coast of the North Island of New Zealand, hosts numerous landslides which vary in size, volume and runout characteristics. The region is located on an active subduction zone experiencing regular earthquakes and is close to the base of gas hydrate stability. Consequently, both seismic loading during earthquakes and overpressure in the slope from the migration of free gas may be plausible movement mechanisms for both shallow and deep landslides but their potential behaviour during earthquakes and in response to elevated pore fluid pressures remains poorly constrained. We conducted a series of experiments in a Dynamic Back Pressure Shearbox on sediments recovered from the Hikurangi subduction margin to simulate the complex stress conditions in submarine landslides and explore their potential movement mechanisms in response to elevated pore fluid pressures and seismic loading. Our experiments successfully simulated a range of landslide behaviour that advances our understanding of the variety of landslide

types observed on active continental margins. The movement behaviours observed provide credible mechanisms to explain how some submarine landslides may be subject to episodic movement without undergoing catastrophic failure as a result of overpressuring by free gas and seismic loading during earthquakes.

Keywords

Submarine landslides • Movement mechanisms • Advanced shear testing

Introduction

Although recent advances in submarine slope surveys (e.g. Huvenne et al. 2018), sub-surface investigation (e.g. Kuhlmann et al. 2017), and modelling (Urlaub et al. 2015) have allowed submarine mass movement process to be studied with unprecedented accuracy, the mechanics of submarine landslide movement remain poorly constrained.

Given that most submarine landslides fail on shallow slopes ($<2^\circ$) significantly lower than the typical friction angles of the landslide materials (e.g. Urlaub et al. 2015) high pore pressures that greatly exceed the hydrostatic pressure are a likely mechanism to promote instability. These elevated pore pressures could occur from several processes including undrained seismic loading (e.g. Sassa et al. 2012), rapid sediment burial (e.g. Stigall and Dugan 2010), focused fluid flow (e.g. Dugan and Flemings 2000; Sassa et al. 2012) or gas pressure from hydrate dissociation/gas buoyancy (e.g. Riboulot et al. 2013; Crutchley et al. 2010). However, few studies have linked these failure mechanisms to landslide movement behaviour.

The upper continental slope on the Hikurangi Subduction Margin, off the coast of Gisborne, New Zealand, hosts a variety of landslide types (Fig. 1a). These include large landslides that have run out over significant distances to

J. M. Carey (✉) · B. Lyndsell
GNS Science, 1 Fairway Drive Avalon, Lower Hutt, New Zealand
e-mail: j.carey@gns.cr.nz

B. Lyndsell
e-mail: b.lyndsell@gns.cri.nz

J. J. Mountjoy
National Institute of Water and Atmospheric Research,
Wellington, New Zealand
e-mail: Joshu.Mountjoy@niwa.co.nz

G. J. Crutchley
GEOMAR Helmholtz Centre for Ocean Research, Kiel, Germany
e-mail: gcrutchley@geomar.de

D. N. Petley
Department of Geography, University of Sheffield, Sheffield, UK
e-mail: d.n.petley@sheffield.ac.uk

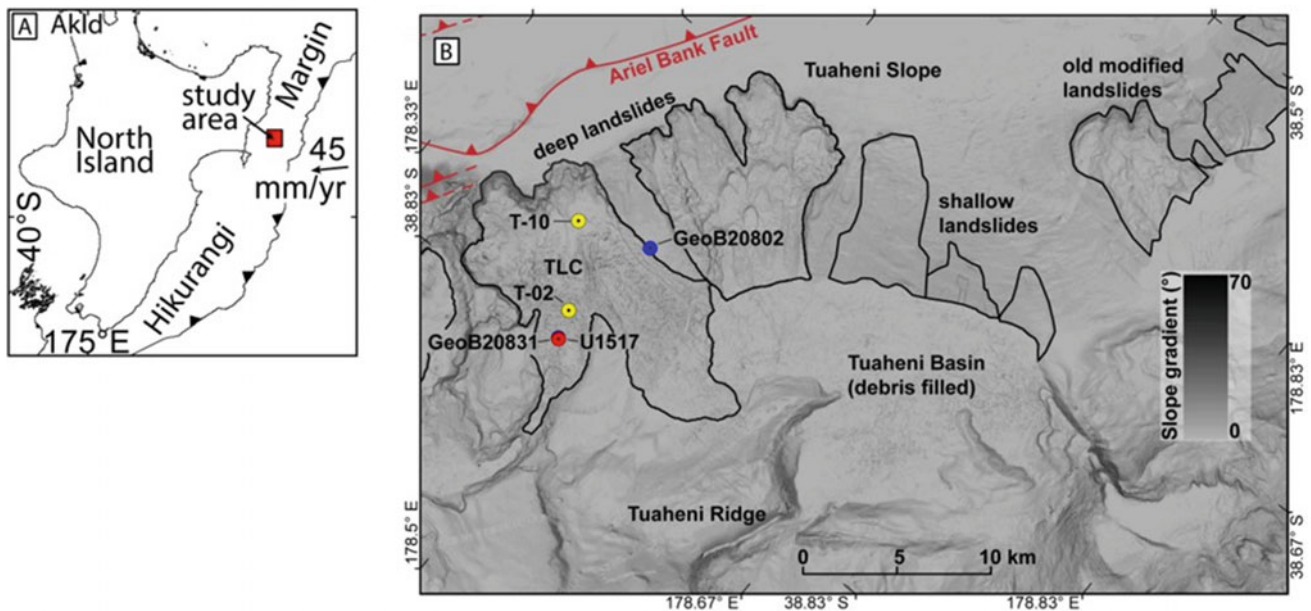


Fig. 1 Study area and sample location. **a** Location on New Zealand's Hikurangi Margin. **b** Landslides on the Tuaheni Slope including the Tuaheni Landslide Complex (TLC) where samples for this study were recovered. Sample locations are from voyages TAN1404 (yellow sites), SO247 (blue sites) and Exp372 (red site). Two of the locations (GeoB20831 and U1517) were drilled at the same location

shallow spreading failures that have moved limited distances on the slope (e.g. Micallef et al. 2016) and deep-seated active landslide complexes that could be subject to ongoing episodic reactivation.

The Tuaheni Landslide Complex (TLC) has been investigated using both shallow coring and seafloor drilling (Kuhlmann et al. 2018; Carey et al. 2019; Pecher et al. 2019) (Fig. 1b) and is composed of subaqueous sediments common across the continental slope. Shallow gravity cores down the TLC indicate the upper continental slope is dominated by mud to sand sized particles from hemipelagic drape, reworked landslide debris and airfall tephra (Kuhlmann et al. 2018). Similar materials form the shallow spreading failures observed on the upper slope of Hikurangi Margin where it is proposed that episodic movement may result from high pore fluid pressures, triggered by shallow free gas (Micallef et al. 2016).

More recently, deeper sediments from the base of the TLC have been recovered from boreholes drilled in 2016 during the Sonne Expedition SO247 (Huhn 2016; Fig. 1 GeoB20802, Geo20831) and during the IODP expedition 372 in 2017/2018 (Pecher et al. 2019; Fig. 1, U1517). Samples from U1517 show that the base of the landslide (approx. 40 m bsf) is dominated by fine-grained sandy sediments with grain size characteristics that suggest they may be susceptible to liquefaction. Although the TLC is located within an active subduction zone experiencing

regular tectonic activity (Wallace and Bevan 2010; Wallace et al. 2012), its potential response to seismic loading during earthquakes has received limited attention to date as alternative drivers for slope destabilisation have been the focus of investigations (e.g. Mountjoy et al. 2014; Micallef et al. 2016).

We conducted a series of experiments in a Dynamic Back Pressure Shearbox (DBPSB) on sediments recovered from the TLC (Fig. 1) to study the potential movement mechanisms of submarine landslides. The DBPSB can be used to undertake static and dynamic direct shear testing on sediments whilst controlling back pressure and measuring pore water pressure in the sample (Fig. 2). The DBPSB is conceptually based on a standard direct shear device, modified to allow the measurement and control of pore pressures and dynamic application of normal stress and shear stress. The apparatus uses $100 \times 100 \times 20$ mm samples and provides both static and dynamic control of: horizontal (shear) and axial (normal) force and displacement; total stress; and effective stress. The material response and pore water pressure can be monitored throughout experiments (Carey et al. 2019).

We designed a series of DBPSB experiments using different testing configurations (Fig. 2a, b and c) to explore the deformation mechanisms of (a) shallow submarine landslides in response to elevated pore fluid pressures (both water and gas) and (b) deep-seated submarine landslide complexes during seismic events.

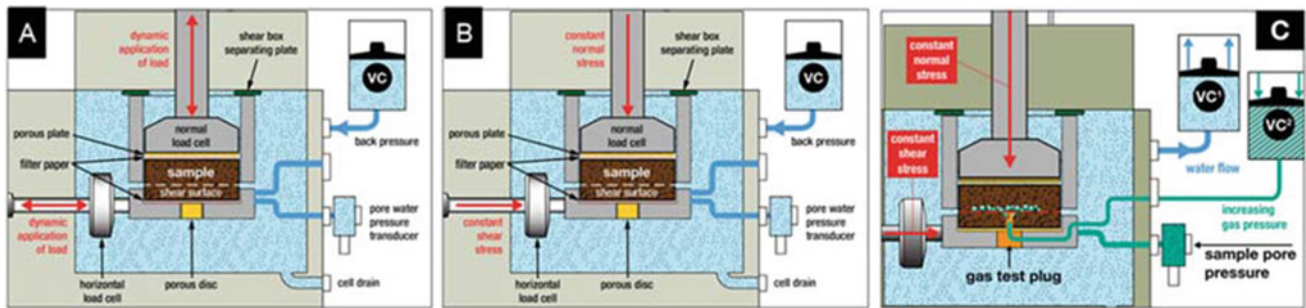


Fig. 2 The Dynamic Back Pressured Shearbox configurations (DBPSB). **a** Dynamic loading experiments. **b** Pore water pressure reinflation experiments. **c** Modified set up for Pore gas pressure experiments

Simulating Submarine Landslide Reactivation in Response to Elevated Pore Fluid Pressures

A series of specialist shear box experiments were designed to simulate the generation of excess pore-fluid pressure and associated shear displacement response in the shallow submarine landslides (Carey et al. 2019). To accurately simulate the stress conditions in the slope undisturbed samples were consolidated at a normal effective stress of 32 kPa and then slowly sheared at a constant displacement rate to avoid generating excess pore pressures whilst forming a shear zone. The drained shear strength was measured during this process. A shear-stress representing approximately 65–75% of the drained strength was then applied to each sample and both total normal and total shear stress were held at this stress state whilst the normal effective stress was reduced by linearly increasing pore pressure until the samples failed (Fig. 3a, b and c). During each experiment the shear displacement was monitored by measuring the horizontal (shear) displacement of the shear box.

Experiments were conducted using two different pore fluids: water (Fig. 3a), and water plus nitrogen gas (Fig. 3b). De-aired water was used to replicate pore-water pressure

change, representing changes to fluid movement pathways; and nitrogen was injected into the shear surface to replicate elevated pore gas pressures within the landslide shear zone as a result of gas migration from a deeper gas reservoir. Nitrogen gas was selected because it has similar physical properties to methane for the conditions of our tests (Kossel et al. 2013) but is safer to use.

The experiments successfully induced failure using both de-aired water and nitrogen gas, demonstrating that either fluid can generate similar patterns of deformation with reducing normal effective stress (Fig. 3a and b).

In both experiments, movement was initiated at low horizontal and vertical displacement rates before the conventional failure envelope was reached (Fig. 4a and b stage 1). In general, both horizontal and vertical displacement rates progressively increased once the conventional failure envelope was exceeded (Fig. 4 and b stage 2), indicating that sample failure initiated through dilation. However, the pattern of displacement was not simple, as in each case slow-episodic behaviour was observed that did not progress to rapid failure. This episodic movement was characterised initially by a rapid increase followed by a rapid decrease in horizontal and vertical displacement rates (Fig. 4 and b stage

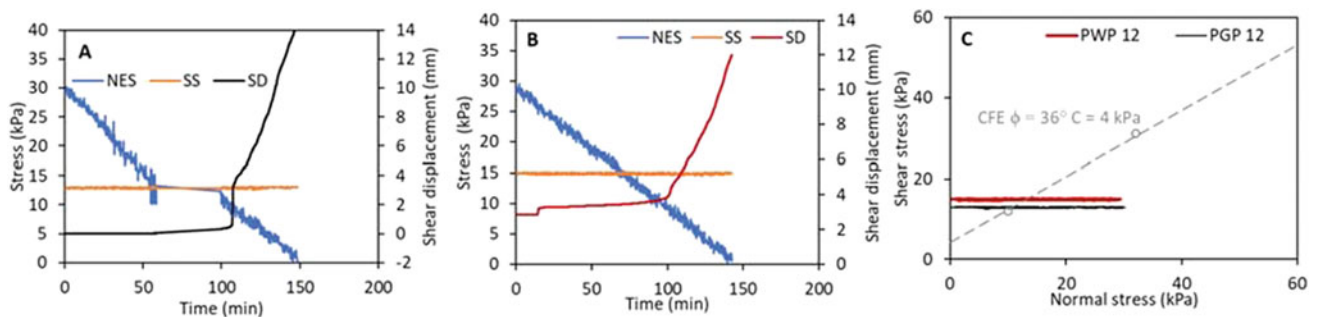
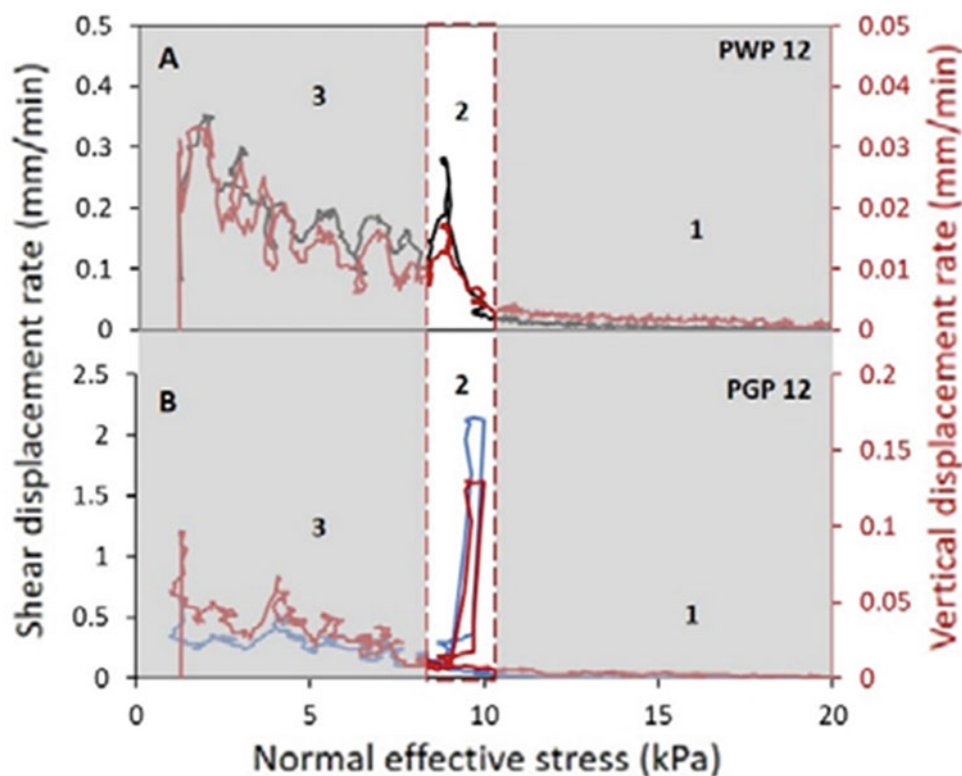


Fig. 3 Pore pressure reinflation (PPR) experiments conducted on shallow hemipelagic sediment at a pore pressure inflation rate of 12 kPa/hr (modified from Carey et al. 2019). **a** Shear displacement (SD) behaviour in response to a linear reduction in normal effective stress (NES), at constant shear stress (SS) during the pore water pressure (PWP) experiment. **b** SD behaviour in response to a linear NES, at constant SS during the pore gas pressure (PGP) experiment. **c** Pore fluid pressure stress paths for PWP and PGP experiments in relation to the conventional failure envelope (CFE) measured during standard drained shear experiments

Fig. 4 Shear and vertical displacement rate against mean effective stress illustrating the three stages of movement observed in both PWP and PGP experiments. **a** PWP experiment
b PGP experiment



3). This phase of movement developed at a similar normal effective stress (c.10 kPa) for all tests, regardless of the rate of pore-pressure increase or pore fluid type. As this episodic style behaviour was not associated with a measured change in bulk sample pore pressure, it is likely to have resulted from excess pore pressures developing rapidly along a discrete, impermeable shear zone. We hypothesized that once a critical pore-fluid pressure had been achieved the fluid migrated into areas of the sample adjoining the shear zone, thereby increasing the zone of deformation but allowing some of the excess pore-water pressure to dissipate. This in turn drove a reduction in shear displacement rate, causing the reduction in displacement rate component of the behaviour.

This process repeated itself to permit further cycles of episodic behaviour without leading to run-away displacement and catastrophic failure (Fig. 4 A and B, stage 3). We suggest that in a natural system, such phases of behaviour are likely to repeat so long as pore-fluid pressure remains high. At the point that external forcing of high pore-fluid pressure ceases, the rate of shear displacement accumulation should reduce to a background level, which in many cases will represent cessation of movement. None of the samples transitioned to run-away failure, even when the failure envelope was significantly exceeded.

Simulating Submarine Landslide Reactivation in Response to Earthquake Loading

To simulate seismic loading during earthquakes we undertook dynamic shear experiments on reconstituted fine-grained sand samples collected from base of the TLC. Each sample was initially consolidated at a normal effective stress of 150 kPa to replicate the depth of the TLC shear surface. An initial shear stress of 65 kPa was then applied to two samples to represent a marginally stable landslide shear surface (Fig. 5a and b). Both the normal stress and back pressure were then held constant and dynamic shear experiments were then conducted on each sample for a duration of 60 s and at a frequency of 2 Hz (120 dynamic cycles). A displacement -controlled dynamic shear with a shear amplitude of ± 0.5 mm was carried out on one sample (Fig. 5a) and a stress controlled dynamic shear at an amplitude of ± 25 kPa was carried out on the second sample (Fig. 5b).

In both displacement and stress-controlled experiments dynamic shear did not generate significant excess porewater pressures or rapid displacement to failure (Fig. 5a and b). Instead, permanent displacement occurred at a constant rate when the shear stress either reached or exceeded the conventional failure envelope. This suggested that movement

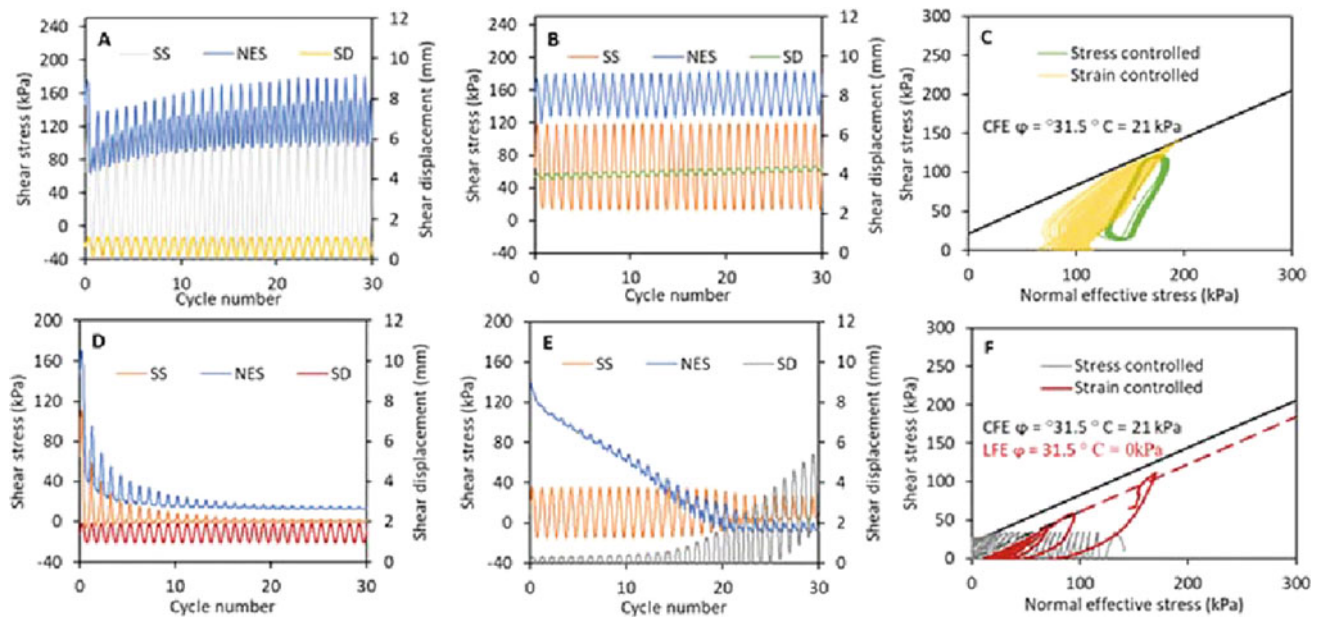


Fig. 5 Dynamic shear experiments undertaken on fine-grained sandy sediments from the Tuaheni Landslide Complex (TLC). **a** shear stress (SS) normal effective stress (NES) and shear displacement (SD) measured during dynamic displacement-controlled shear (± 0.5 mm/2 Hz). **b** SS, NES and SD measured during a dynamic stress-controlled shear (± 25 kPa/2 Hz) **c** Dynamic stress paths generated during the normal stress-controlled experiments in relation to the drained failure envelope (CFE) **d** SS, NES and SD measured during a dynamic displacement-controlled shear (± 0.5 mm/2 Hz) conducted with a constant sample volume. **e** SS, NES and SD measured during a dynamic stress-controlled shear (± 25 kPa/0.5 Hz) conducted with a constant sample volume. **f** Dynamic stress paths generated during constant volume experiments in relation to the CFE

occurred at a constant displacement rate governed by the degree to which the failure envelope was exceeded (Fig. 5c). As a result of this behaviour both samples were unable to maintain a constant volume and produced broadly similar drained stress paths (Fig. 5c).

To simulate undrained loading a testing procedure was adapted from a well-established dynamic simple shear methodology (Dyvik et al. 1987). In these experiments a constant volume is maintained during dynamic shear and the measured change in applied normal stress as the specimen height is maintained is equal to the porewater pressure that would be generated in a purely undrained experiment (Dyvik et al. 1987). In the DBPSB experiments a constant sample volume was applied by maintaining a constant sample height (axial displacement) and pore fluid volume (back volume) and the reduction in mean effective stress resulting from the reduction in applied normal stress was equal to the excess porewater pressure anticipated in undrained conditions (Fig. 5d and e).

Undrained dynamic shear experiments were undertaken on two reconstituted samples (Fig. 5d and e). An initial shear stress of 65 kPa was applied to one sample to represent the same marginally stable slope condition used in the previous dynamic shear experiments and was subjected to a dynamic displacement-controlled shear experiment (Fig. 5d). A lower initial shear stress of 10 kPa was applied to the

sample used in the other undrained loading experiment to provide a representative initial stress state analogous to the shallow angled shear surface anticipated in the TLC and was subjected to dynamic stress-controlled shear (Fig. 5e). The dynamic undrained shear experiments indicate that the fine sand forming the basal material of the TLC is susceptible to liquefaction when the initial stress state applied prior to undrained dynamic loading is close to the conventional failure envelope (Fig. 5d and e). When a lower initial stress state was applied, however, liquefaction was not observed. Instead, permanent displacement is observed when the conventional failure envelope is exceeded by either the increase in dynamic shear stress or the decrease in mean effective stress associated with the development of excess pore water pressures.

Conclusions

A DBPSB can be used to explore the complex movement mechanisms that may occur in shallow and deep submarine landslides in response to elevated pore fluid pressures and seismic loading during earthquakes. Using a variety of novel experiments, we observed a range of failure styles all of which have been hypothesised as potential failure mechanisms in subaqueous slopes.

Experiments replicating elevated pore fluid pressures in shallow landslides suggest that over-pressuring by elevated pore water or gas pressures results in slow episodic shear regulated by dilation. This movement style is a credible mechanism to support the hypothesis that over-pressuring by free gas can result in slow episodic movement that could produce submarine spreading failures observed along the Hikurangi Margin and on other continental shelves worldwide (e.g. Micallef et al. 2007; Mountjoy et al. 2009; Micallef et al. 2016). Experiments replicating undrained dynamic loading on fine-grained sand sediments collected from the base of the TLC suggest that while liquefaction could occur in marginally stable subaqueous slopes, particularly in shallow sediments on steep slopes or sediments with high initial pore fluid pressures, this is not a likely failure mechanism for deeper landslide complexes such as the TLC. Subaqueous landslides occurring along deeper, shallow angled shear zones are likely to experience episodic displacement as a result of undrained loading during large earthquakes. The observed behaviour provides another credible mechanism through which subaqueous landslides in similar materials and active tectonic settings may be subject to episodic movement without undergoing catastrophic failure.

Acknowledgements Sediment samples for the study were provided by the National Institute of Water and Atmospheric Science (NIWA) and MARUM. Financial support has been provided through the GNS Science Strategic Development Fund, Marsden Fund Contract NIW1603, GNS and NIWA Strategic Science Investment Funding and by the NERC/ESRC Increasing Resilience to Natural Hazards programme, grant NE/J01995X/1, and NERC/Newton Fund grant NE/N000315.

References

- Dugan B, Flemings PB (2000) Overpressure and fluid flow in the New Jersey continental slope: implications for slope failure and cold seeps. *Science* 289:288–291
- Dyvik R, Berre S, Lacasse S, Raadim B (1987) Comparison of truly undrained and constant volume direct simple shear tests. *Geotechnique* 37:3–10
- Carey JM, Crutchley GJ, Mountjoy JJ, Petley DN, McSaveney MJ, Lyndsell B (2019) Slow episodic movement driven by elevated pore-fluid pressures in shallow subaqueous slopes. *Geomorphology* 329:99–107
- Crutchley GJ, Geiger S, Pecher IA, Gorman AR, Zhu H, Henrys SA (2010) The potential influence of shallow gas and gas hydrates on sea floor erosion of rock garden, an uplifted ridge offshore of New Zealand. *Geo-Mar Lett* 30(3–4):283–303
- Huhn K (2016) Cruise Report/Fahrtbericht SO247—SlamZ: Slide Activity on the Hikurangi Margin, New Zealand, Wellington (NZ): 27.03.2016–Auckland (NZ): 27.04.2016. MARUM, Center for Marine Environmental Sciences, Bremen, Germany
- Huvenne VA, Robert K, Marsh L, Lo Iacono C, Le Bas T, Wynn RB (2018) ROVs and AUVs. *Submarine Geomorphology*. In Micallef A, Krastel S, Savini A (eds). Springer Geology. Springer, Cham. PP 93–108
- Kossel E, Bigalke N, Piñero E, Haeckel M (2013) The SUGAR toolbox—a library of numerical algorithms and data for modelling of gas hydrate systems and marine environments. Bremerhaven, PANGAEA
- Kuhlmann J, Asioli A, Trincardi F, Klügel A, Huhn K (2017) Landslide frequency and failure mechanisms at NE Gela Basin (Strait of Sicily). *J Geophys Res Earth Surface* 112(11):2223–2243
- Kuhlman J, Orpin A, Mountjoy JJ, Crutchley G, Henrys S, Lunenburg R, Huhn K (2018) Seismic and lithofacies characterization of a gravity core transect down the submarine Tuaheni Landslide Complex, northeastern New Zealand (SP477) Subaqueous Mass Movements and Their Consequences: Assessing Geohazards, Environmental Implications and Economic Significance of Subaqueous Landslides. In Lintern, et al. (eds). Geological Society of London Special Publications, 477: pp. 475–479
- Micallef A, Mountjoy JJ, Krastel S, Crutchley G, Koch S (2016) Shallow gas and the development of a weak layer in submarine spreading, Hikurangi Margin (New Zealand). *Submarine Mass Movements and their Consequences: 7th International Symposium, Advances in Natural and Technological Hazards Research*. Lamarche et al. (eds). New Zealand. pp. 419–426
- Mountjoy JJ, Pecher I, Henrys S, Crutchley G, Barnes PM, Plaza-Faverola A (2014) Shallow methane hydrate system controls ongoing, downslope sediment transport in a low-velocity active submarine landslide complex, Hikurangi margin, New Zealand. *Geochem Geophys Geosyst* 15:4137–4156
- Pecher IA, Barnes PM, LeVay LJ, Expedition 372A Scientists (2019) Creeping gas hydrate slides: proceedings of the international ocean discovery program, 372A. College Station, TX (International Ocean Discovery Program)
- Riboulot V, Cattaneo A, Sultan N, Garziglia S, Ker S, Imbert P, Voisset M (2013) Sea-level change and free gas occurrence influencing a submarine landslide and pockmark formation and distribution in deepwater Nigeria. *Earth Planet Sci Lett* 375:78–91
- Sassa K, He B, Miyagi T, Strasser M, Konagai K, Ostric M, Setiawan H, Takara K, Naga O, Yamashiki Y, Tutumi S (2012) A hypothesis of the Senoumi submarine megaslide in Suruga Bay in Japan—based on the undrained dynamic loading ring shear tests and computer simulation. *Landslides* 9:439–455
- Stigall J, Dugan B (2010) Overpressure and earthquake initiated slope failure in the Ursa region, northern Gulf of Mexico. *J Geophys Res* 115:B04101
- Urlaub M, Talling PJ, Masson D (2015) What causes large submarine landslides on low gradients (<2°) continental slopes with slow (~0.15 m/Kyr) sediment accumulation? *J Geophys Res Solid Earth* 120:6722–6739
- Wallace LM, Beavan J (2010) Diverse slow slip behavior at the Hikurangi subduction 390 margin, New Zealand. *J Geophys Res* 115:B007717
- Wallace LM, Beavan J, Bannister S, Williams C (2012) Simultaneous long-term and short-term slow slip events at the Hikurangi subduction margin, New Zealand: Implications for processes that control slow slip event occurrence, duration, and migration. *J Geophys Res* 112:B009489



2020 Kyoto Japan

Laboratory Tests to Simulate the Rainfall Infiltration Process of Pyroclastic Soils Subject to Instability

Gennaro Spolverino, Giovanna Capparelli, and Pasquale Versace

Abstract

Each year, rainfall events trigger a large number of landslides causing damage and victims. The study and forecast of rainfall-induced landslides is a field of great importance. Many research activities aim to understand landslide processes and to improve early warning systems. Infiltration processes and underground water circulation have an important role to define failure processes characteristics. In this work, some results from tests performed with a physical slope model are reported. Some experimental tests were conducted, using pyroclastic soil from Sarno area (Southern Italy—near the volcano Vesuvio), affected by landslide events on 5 May 1998. In these places the stratigraphy are composed from limestones covered by layers of pyroclastic deposits. These soils are the product of different eruptions of more volcanoes like Somma-Vesuvius, Flegrei fields and other volcanoes present in the Region no longer active. Generally, they are incoherent deposits with variable granulometry that range from sands, silty sands and silts (ashes) until sands with gravel (pumice) and gravels. Some tests considering both homogeneous and stratified deposits of ash and pumice were carried out. During the tests, both during evaporation and infiltration processes, suction and volumetric water content at different depth were measured by using the appropriate sensors. By comparing and analysing all the collected data it was possible to study the infiltration processes that lead to the failure and the difference between the stratified and the homogeneous deposit.

G. Spolverino (✉) · G. Capparelli · P. Versace
Dipartimento Di Ingegneria Informatica, Elettronica E
Sistemistica, Università Della Calabria, ModellisticaRende, Italy
e-mail: g.spolverino@dimes.unical.it

G. Capparelli
e-mail: giovanna.capparelli@unical.it

P. Versace
e-mail: linoversace@libero.it

Keywords

Physical slope model • Flume tests • Pyroclastic soil

Introduction

To reproduce and investigate the behavior of rainfall-induced landslides, tests can be performed in situ or laboratory analyses can be developed with physical scale models. The latter are based on the reproduction of the physical characteristics of the phenomena and the boundary conditions that control their dynamics. There are various configurations, which differ essentially in size, in the instruments installed, and in their intrinsic performance potential. Physical models have been widely used to analyze landslides (Iverson and LaHusen 1989; Eckersley 1990; Spence and Guymer 1997; Wang and Sassa 2001; Okura et al. 2002; Lacerda et al. 2003; Olivares et al. 2009). Besides having evident scientific utility, such scale models are particularly useful for all those cases which are difficult to monitor with instruments. In fact, they make it possible to observe behaviour that results in failure and the transient phases that precede it. The schemes most commonly used are those which reproduce the typical scheme of the infinite slope and, thanks to a suitable sensor system, control various measurements required to understand the phenomenon, such as suction, the degree of saturation, and small displacements. The possibility of creating and setting up large physical models enables larger soil volumes to be analyzed and more faithful reproduction of the natural phenomenon, while minimizing boundary effects. With this in mind, at the CamiLab laboratory of the University of Calabria, a large artificial channel was built, able to reproduce a rainfall-triggered landslide, analyze the correlated measurements, and observe postfailure evolution. The physical model was designed so as to lend the channel great flexibility and versatility when used. It is equipped with a sensor



Fig. 1 Physical model: **a** Side view **b** Frontal view

system to measure the main physical parameters which govern deformation and failure processes, a video recording system, lasers to measure displacements and devices to measure the velocities involved. The presence of two independent channels also makes it possible to analyze the propagation phase and allow the positioning of impact structures so as to evaluate any mitigation strategies.

The laboratory prototype partially described in (Capparelli et al. 2017) is illustrated in Fig. 1 that shows a picture of the channel. It has a rectangular section, 1 m high, 1 m width and 6 m long, and a lifting system that allows applying and reaching slope inclinations up to 50°.

Rainfall was applied by using nozzle water particle sprinkler system, which are integrated by auxiliary rain gauges in order to verify the rainfall intensity along the entire channel. The arrangement of the nozzles, in fact, was optimized so as to ensure rainfall uniformity, and minimize surface erosion.

In addition to the artificial rainfall system, further acquisition systems are installed which permit data collection with a series of sensors for a total of 48 channels from tensiometers, pressure transducer, laser sensors to detect the soil level, auxiliary sensors as slope and pressure. The system is essential for measuring and monitoring the main parameters that control the phenomenon of landslides triggered by rainfall infiltration. In addition, an equipment of small channels, connected to the sub-surface and runoff, allows to collect the drainage from the surface and each soil layers and measure the water fluxes.

Several laboratory tests have recently been developed in order to understand the dynamics underlying the instability of loose soils whose stability, also due to the high slopes and the low degree of cohesion, is strongly influenced by the dynamics in conditions of partial saturation and by vertical rain infiltration processes.

Following the research published in Capparelli et al. (2017), here are some tests that complete the first part of the study on some volcanic soils regarding, in particular, the effects produced by the highly permeable layers of pumice.

In the following paragraphs, some details of the soils and the area of origin are first indicated and then a summary of the results obtained from the experiments.

Tests With the Physical Model

Pyroclastic soils have been collected in April 2015, along the slope of Pizzo d'Alvano, close to the village of Episcopio, near Sarno, a town 30 km from Naples (Italy), about 15 km far from the volcano Vesuvius. Three pyroclastic ash samples and two pumice samples, originated by different eruptions, were collected. In May 1998, in this area, numerous and rapid mud-flows devastated the town, causing an enormous number of victims. In these places the stratigraphy are composed from limestones covered by layers of pyroclastic deposits. These soils are the product of different eruptions of more volcanoes like Somma-Vesuvius, Flegrei fields and other volcanoes present in the Region no longer active. The

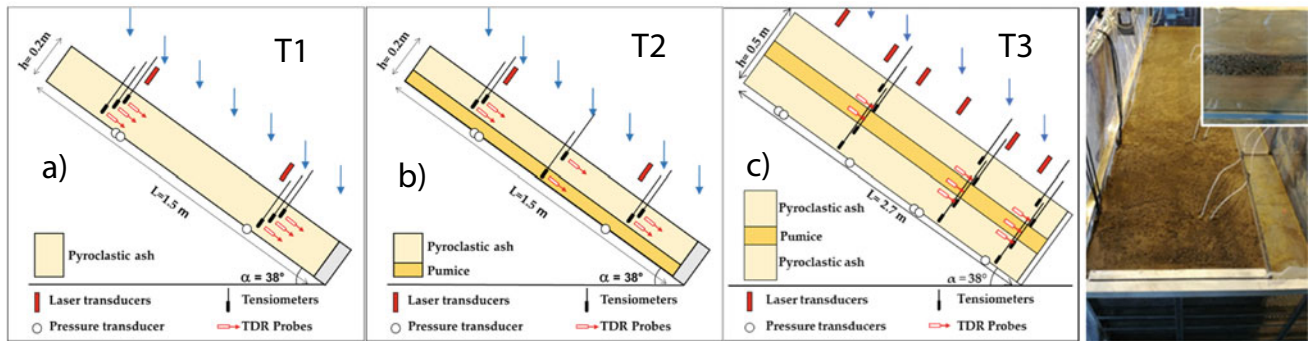


Fig. 2 Schematic representation of the tests with indication of the deposit and positioning of the sensors

ashes, coming out after the eruption and carried by the wind, travel for kilometers from the eruption zone, providing a non-uniform stratigraphy for the entire area (Del Prete et al. 1998; Del Soldato et al. 2018; Cascini et al. 2008). Generally they are incoherent deposits with variable granulometry that range from sands, silty sands and silts (ashes) until sands with gravel (pumice) and gravels.

Flume tests carried out and below discussed using these soils are (Fig. 2):

- Test **T1**: homogeneous deposit of volcanic ash;
- Test **T2**: stratified deposit layer of pumice and layer of volcanic ashes;
- Test **T3**: stratified deposit, layer of pumices interbedded between two layers of ashes.

Flume Test T1: Homogeneous Deposit

A homogeneous deposit was reconstructed inside the flume. The slope was formed by a layer of volcanic ash 20 cm thick, occupied the entire width of the flume (100 cm) and was 150 cm long (Fig. 2a). This geometry allows the deposit to be assimilated to an indefinite slope. At the base of the model there was an impervious rough bed to simulate conditions similar to those of a natural slope. At the foot of the slope a geotextile-coated drainage grid was placed. The ash in question was sieved with a 0.4 cm mesh to eliminate coarse contamination occurring during the sampling phase. The artificial slope was reconstituted inside the flume by layers, with the moisttamping technique, with volcanic ash porosity of between 68 and 76%, typical in situ conditions. The volumetric water content of the ash (θ) was about 20%. Inside the artificial slope, 6 tensiometers were installed to measure suction, and 6 TDR probes to measure volumetric water content.

The sensors were installed at depths of 5, 11 and 17 cm below ground surface, both in the upslope and downslope

zone of the deposit. Rainfall was generated with a sprinkler system placed about 100 cm above the sliding surface. The nozzles were arranged so as to ensure rainfall uniformity and avoid surface erosion. Various wetting and evaporation tests were carried out and this work reports the latest wetting test: with constant rainfall at an intensity of about 220 mm/h (this intensity was the minimum that could be applied with the first rainfall system), which lasted until slope failure (about 40 min). The suction trend during the last infiltration phase (Fig. 3) clearly shows that saturation conditions at many of the 6 tensiometers are swiftly reached. It is also possible to note the instant in which the curves for tensiometers placed downslope at 5 and 11 cm of depth change rapidly, that is when part of the slope is detached, and a small surface landslide is triggered. Trends in soil volumetric water

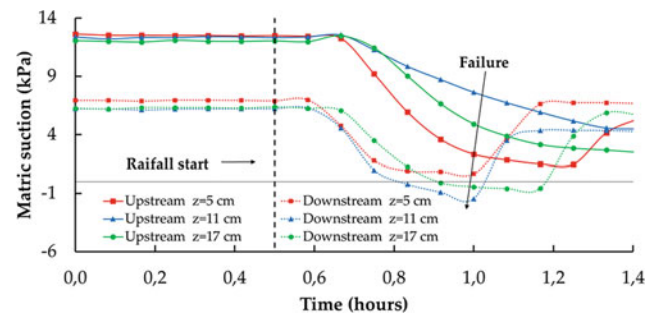


Fig. 3 Suction trend

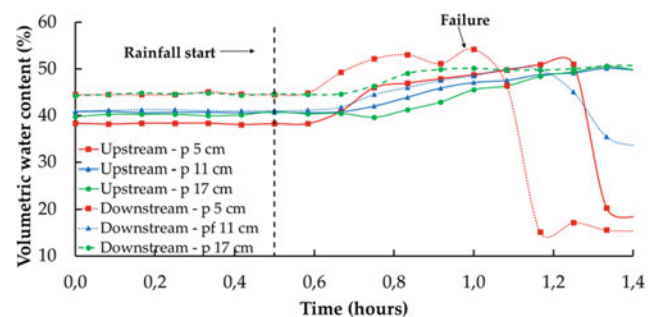


Fig. 4 Volumetric water content trend

content are reported in Fig. 4, measured with the six TDR probes.

Also in this phase, the remarkable advancement of the wetting front can be appreciated, although some differences are observed between the upslope and downslope zones where, due to the non-homogeneous distribution of the rainfall, and the sub-surface flow parallel to the slope, the increase in water content seems to be anticipated. It should also be pointed out that all the TDR probes, despite there being absolute evidence that much of the deposit reaches complete saturation conditions, detected water content values between 50 and 55%. This is doubtless to be attributed to compaction experienced by the deposit during the previous test phases, which had led to a reduction in width from the initial 20 cm to around 18 cm, corresponding to a estimated reduction in porosity of around 10%. This graph also shows the moment in which a small landslide is detached, producing an abrupt change in the steepness of the curve for the TDR positioned in the most superficial part downslope. In this case the landslide brought the TDR to the surface and from that point onward the values measured by the sensor are not representative of real water content. Slope failure, consistent with the compacted configuration assumed by the deposit during the previous test phases, did not trigger a mud-flow. It took the form of a progressive erosion of the more superficial soil layers, initially and chiefly concentrated in the downslope zone, where the intense sub-surface flow resulted in conditions of greater moisture being reached and, at the same time, encouraged soil mobilization. The first local failures began to occur about 20 min after the beginning of artificial rainfall, and only after that did they extend so far as to affect the points in which some of the tensiometers and TDR probes had been installed.

Flume Test T2: Two-Layered Deposit

We made the second test with the same geometric characteristics as the previous, but with reduced rainfall intensity (50 mm/h) and reconstructing a stratified deposit (Fig. 2b), formed by a layer of pumice (5 cm), covered with a layer of volcanic ashes (15 cm). The soil used for this test was less wet. The porosity of the deposit was the lowest ($60\% < n < 70\%$). Also in this test, there have been different wetting and evaporation phases. We report the last stage of wetting, with intensity of 50 mm/h (it was possible to apply a lower intensity because the rain system was modified). In this test, we installed 6 tensiometers for measuring suction and 6 TDR probes for measurement of the water content. The instruments were installed to depth of 5 cm, 11 cm in pyroclastic ash below the surface of the soil and a 17 cm into the pumice.

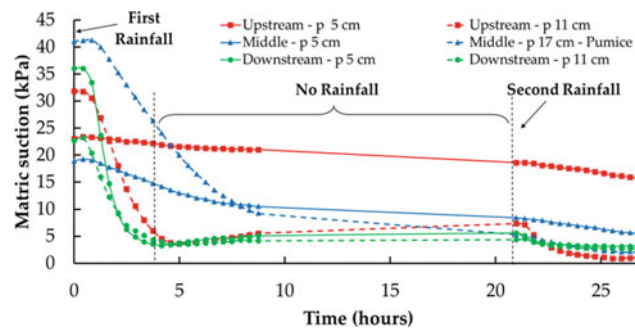


Fig. 5 Suction trend

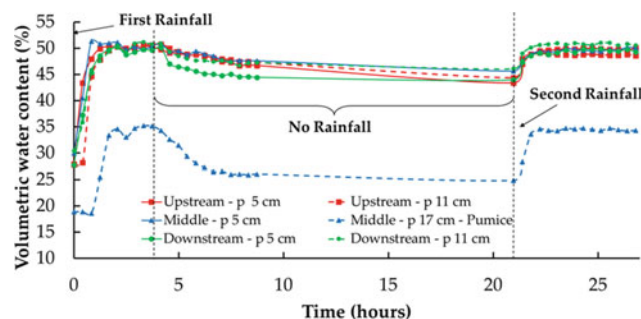


Fig. 6 Volumetric water content trend

All the last phase duration is about 25 h, of which of rainfall 16 divided in two moments: rainfall (9 h), not rainfall (9 h), rainfall (7 h). The following are the trends of the suction and the water content of the infiltration phases. Figure 5 shows the trend of suction during infiltration. The curves show a jump at the rainfall suspension. The figure shows that the suction has never become zero, and in the final part has a horizontal asymptotic behavior. The minimum recorded suction is about 3 kPa. Figure 6 shows the trends during the rainfall phases of the volumetric water content of the soil, measured with the TDR probes. Moreover, these curves show a jump in correspondence with the rainfall suspension.

Also in this case, the TDR probes have recorded a volumetric content of water (except for the pumice) of about 50%, so it is also possible to assume in this case a volumetric collapse of the deposit. Although we have simulated the rain for 16 h, the slope did not show failure.

The different behavior than the first test is probably due to the presence of pumice. It is possible that, in the range of suction in which it is carried out the test, the permeability of pumice is always higher than the permeability of the paleo-soil. This means that the pumice layer allows intense drainage, guaranteeing a water outflow greater than inflow.

With this configuration, the suction values do not reach zero value and the slope is stable.

Flume Test T3: Three-Layered Deposit

The reconstituted layered deposit was 270 cm long and 60 cm wide, and it consisted of a 10 cm thick layer of pumices interbedded between two layers of ashes. Both the upper and lower layers of ashes had a thickness of 20 cm. In Fig. 2c, the sketch of the longitudinal section of the deposit is shown, with the indication of the position of tensiometers and TDR probes. The layers were reconstituted in the flume with the moist tamping technique, so to obtain a packing of the soil particles which was similar as the one of natural covers in primary deposition conditions. Also in this test there were several wetting and evaporation cycles. During the wetting/drying cycles, the upper layer of ashes, initially very loose, experienced a volumetric strain in the order of 3%, which resulted in a mean reduction of the total thickness of the deposit of about 0.6 cm, which was detected by the laser transducers.

Aiming at detecting the effects of the layers on the infiltration process, the deposit was equipped with 10 tensiometers, located at four different depths, approximately along three alignments, orthogonal to the slope surface, near the center of the deposit, and 8 TDR probes located at three depths along the same alignments. The TDR probes, consisting of three parallel metallic rods 10 cm long and with an external interspace of 3 cm, were buried in the soil deposit with the rods parallel to the slope inclination. So, the tensiometers were placed close to the upper and lower interfaces between pumices and ashes.

Figure 7 shows the trend of pore water pressure as measured by the tensiometers installed at various depths and positions within the layered deposit, while Fig. 8 shows the

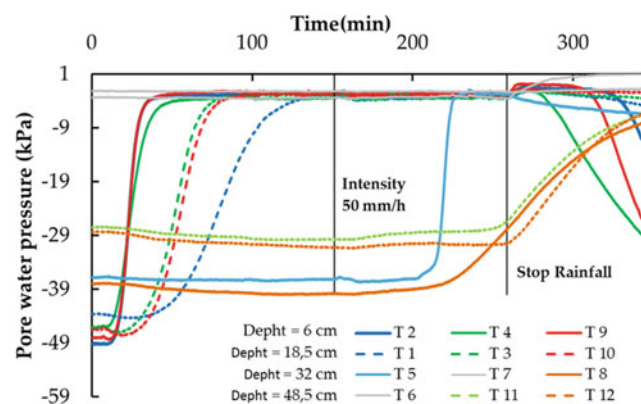


Fig. 7 Pore water pressure trend

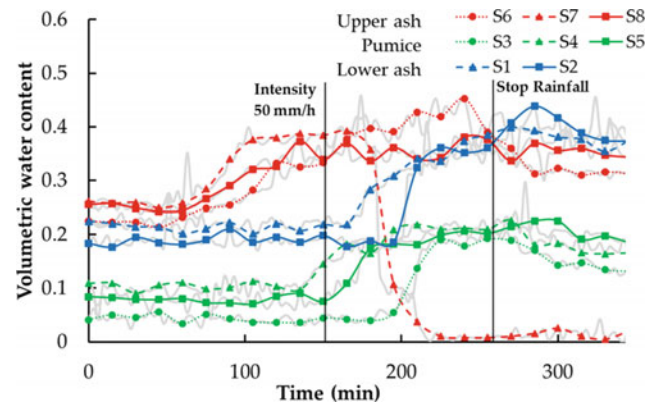


Fig. 8 Volumetric water content trend

trend of water content measured by the TDR probes. Figure 8 shows that the TDR probes placed in the layer of pumices started registering an increase of soil water content at quite different times, and in the same order as in the overlying layer of ashes.

Specifically, the wetting front was registered first in the middle alignment, after about 140 min. About 10 min later, the wetting front inside the pumice layer in the downslope section.

Finally, in the upslope alignment, a steep wetting front was formed after about 200 min from the beginning of the test. This highlights how local humidity gradients within the top ash layer strongly affects filtration in subsequent layers of dry pumice.

The time taken for the formation of such a high gradient caused a delay in infiltration and an accumulation of water inside the upper ash layer (Figs. 7 and 8).

This delay is even more evident in the graphs of Fig. 9. Specifically, Fig. 9a, b, c reports the time at which the tensiometers and TDR probes installed at the various depths recorded the arrival of the wetting front, while Fig. 9d shows trends average. The inclination of the lines plotted in the graphs gives an estimate of the propagation speed of the infiltration process (i.e. the more inclined the line is, the faster was the phenomenon), clearly showing that the phenomenon progressed more slowly through the pumices than in the ashes.

Even in this test, not mud-flow was observed but localized failures in the upper ash layer were generated.

Conclusions

With physical model, some experiments were carried out by using the pyroclastic soil of Sarno (Southern Italy), reproducing on site slope condition. Three tests were carried out:

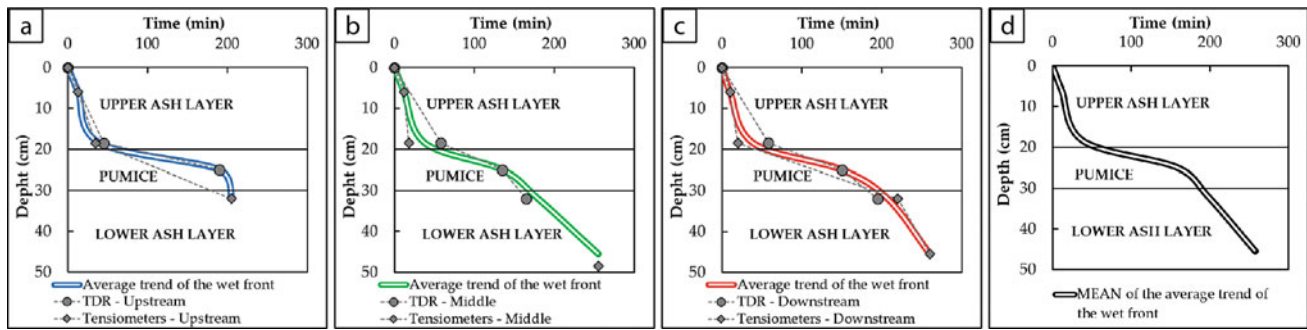


Fig. 9 Time at which the tensiometers and TDR probes recorded the arrival of the wetting front. **a** Upstream. **b** Middle. **c** Downstream. **d** Mean of the average trend of the wet front

the first, (T1) by reconstructing a homogeneous deposit of pyroclastic ash, the second (T2) with a deposit composed by a layer of ash and one of pumice, the third (T3) with a three-layer deposit.

By analysing all flume tests, the important role that pumice layers assumed on the slope stability appeared evident. The pumices in fact, depending on the initial humidity conditions, the intensity and the duration of the rain, have generated different mechanisms. During flume test T2 they have generated a draining action, avoiding a water accumulation in the upper layer and that the suction reaches values close to zero.

In the T3 test, the presence of the ashes in the layer below the pumice changes the dynamics of the water circulation inside the deposit. In addition to a subparallel outflow towards the foot of the channel, an infiltration process is generated towards the underlying layer of ash, which having a significantly lower permeability, is unable to drain the water downstream. This generates an accumulation of water and a consequent reduction in sucking levels, apparent cohesion and therefore soil strength.

The different water circulation in the deposits influenced landslides triggering mechanisms. Localized and shallow failure occurred in T1 and T3, while in T2 there was no instability.

Further tests, with more complex stratigraphy, with the control and measurement of the inflows and outflows of the deposit, the study of the volumetric deformations of the soil may add further elements to the understanding of these soils and the triggering dynamics that occur.

References

- Cascini L., Sorbino G., Cuomo S. & Ferlisi S., (2014). Seasonal effects of rainfall on the shallow pyroclastic deposits of the Campania region (southern Italy). *Landslides*.
- Capparelli G., Versace P., & Spolverino G. (2017). *Physical Modelling of the Rainfall Infiltration Processes in Pyroclastic Soil Responsible of Landslide Trigger*. Springer International Publishing AG 2017- M. Mikoš et al. (eds.), *Advancing Culture of Living with Landslides*.
- Del Soldato M, Pazzi V, Segoni S, De Vita P, Tofani V, Moretti S (2018) Spatial modeling of pyroclastic cover deposit thickness (depth to bedrock) in peri-volcanic areas of Campania (southern Italy). *Earth Surf. Process. Landforms* 43:1757–1767
- Del Prete M, Guadagno FM, Hawkins AB (1998) Preliminary report on the landslides of 5 May 1998, Campania, southern Italy. *Bull. Engineering Geology and the Environment* 57:113–129
- Eckersley JD (1990) Instrumented Laboratory Flowslides. *Géotechnique* 40(3):489–502
- Iverson RM, e LaHusen R.G., (1989) Dynamic pore pressure fluctuations in rapidly shearing granular materials. *Science* 246:796–799
- Lacerda W.A. & Avelar A.S., (2003). Flume tests on sand subjected to seepage with the influence of hidden barriers. *Proc. Int. Workshop on Occurrence and Mechanisms of Flows in Natural Slopes and Earthfills, Sorrento*.
- Okura Y., Ochiai H., Sammori T., (2002). Flow failure caused by monotonic liquefaction. *Proc. Int. Symp. Landslide Risk Mitigation and Protection of Cultural and Natural Heritage*, 21–25 January 2002, Kyoto University, Kyoto, pp. 155–172.
- Olivares L, Damiano E, Greco R, Zeni L, Picarelli L, Minardo A, Guida A, Bernini R (2009) An instrumented flume to investigate the mechanics of rainfall-induced landslides in unsaturated granular soils. *Geotechnical Testing Journal ASTM* 32(2):1–11
- Spence KJ, Guymer I (1997) Small-Scale Laboratory Flowslides. *Géotechnique* 47(5):915–932
- Wang G, Sassa K (2001) Factors affecting rainfall-induced landslides in laboratory flume tests. *Géotechnique* 51(7):587–599

Part III

**Recent Development in Numerical Modeling of
Landslides**



3D Analysis of a Fragmental Rockfall

Roger Ruiz-Carulla, Gerard Matas, Jordi Corominas,
and Nieves Lantada

Abstract

Fragmentation in a rockfall event influence the total number of fragments, the mass distribution, and the impact energies and runouts. Then, the probability of impact and hazard characterization should consider fragmentation. A fractal fragmentation model has been proposed in order to reproduce the phenomenon. The Rockfall Fractal Fragmentation Model has been implemented in a 3D rockfall propagation simulator named RockGIS. We present the analysis of a fragmental rockfall that occurred in Mallorca, Spain. Fieldworks are carried out in order to obtain the block size distribution of the rockfall deposit. A 3D terrain model is obtained using UAV surveys and digital photogrammetric techniques. The obtained 3D point cloud is cleaned of vegetation and used to create a Digital Elevation Model (DEM). The fragmentation model parameters and the propagation simulator coefficients have been calibrated to accomplish both, the resultant block size distribution and the runout distance of the blocks. The obtained results show a good reproduction of the fragmental rockfall studied. After the calibration is accomplished, older and future rockfalls in the cliff may be analyzed, considering thousands or single blocks simulations with or without fragmentation.

Keywords

Fragmentation model • Propagation model • Fragmental rockfall • Block size distribution • RockGIS • UAV

R. Ruiz-Carulla (✉)

International Centre for Numerical Methods in
Engineering CIMNE Edificio C1, Campus Norte UPC C/ Gran
Capitán S/N 08034, Barcelona, Spain
e-mail: roger.ruiz@upc.edu

G. Matas · J. Corominas · N. Lantada
Universitat Politècnica Catalunya—BarcelonaTech, C/ Jordi
Girona, 1-3 08034 Barcelona, Spain

Introduction

Fragmentation of the rock blocks during the rockfall propagation may control the number of fragments, and then, may control the impact energies, the trajectories, and the runouts as well as the whole characterization of the hazard. A single rock block impact should not be the same as hundreds of impacts against a barrier, a road or a vehicle, instead of being the same total volume. Then, the probability of impact may be adapted to the consideration of a single block that breaks creating hundreds of fragments. Finally, the risk assessment (qualitative or quantitative) may be different considering or not the fragmentation phenomenon and it should be taken into account when the hypothesis of no-fragmentation is considered on the safe side, as it is not true in some scenarios (Corominas et al. 2019).

In order to study the fragmentation phenomenon in rockfalls, we have developed a fragmentation model based on fractal theory (Rockfall Fractal Fragmentation Model, RFFM) that allow the reproduction of the block size distributions measured in inventoried rockfalls (Ruiz-Carulla et al. 2017, 2019). We also have been developed a 3D propagation simulator for rockfalls named RockGIS with the fragmentation model implemented (Matas et al. 2017), that has already been tested with real fragmentation tests (Matas et al. 2020).

The present communication shows the methodologies that we are using in order to analyze rockfall scenarios. The methodologies combine: (a) a high-quality 3D data acquisition using UAV surveys and digital photogrammetric techniques to obtain a 3D scenario model; (b) field works inventorying the event by measuring the deposited blocks; (c) the calibration of the propagation rockfall simulator including the fragmentation model, allowing to reproduce the block size distribution generated by breakage, as well as adjusting the runouts; and (d) the use of the calibrated model to study other older or future rockfall events.

We show the procedures applied in a Jurassic limestone cliff located in the north side of Mallorca, Spain. The rockfall case studied is located in the road Ma-10 between the kilometric points 102 and 103. The case can be located at <https://rockdb.upc.edu/>. This is a coastal local road with two lanes between the cliff and the sea. We have been focused on a rockfall that occurred on the 11th of September in 2019, involving around five cubic meters. The breakage of the rock blocks generates more than a hundred fragments, some of them reaching the road. After the use of this case to calibrate the model parameters, another case that has been occurred in 2015 may be reinterpreted based on some scenarios simulated.

UAV Surveys and 3D Terrain Reconstruction

The UAV (or drones) combined with digital photogrammetric techniques allow the generation of detailed 3D point clouds. A DJI Inspire 2 drone (UAV, Unmanned Aerial Vehicle) equipped with the camera X5S (17.3 × 13 mm sensor, 5280 × 3956 pixels and 15 mm of focal length) was used for photogrammetric purposes as well as for real-time observations (Fig. 1). This device mount two batteries, and can fly approximately 25 min per set of batteries, however, we always plan the automated flights of 18 min maximum for security and due to the flight plan estimation doesn't take into account possible adverse wind conditions.

The flight plan was designed before going to the field to obtain a regular acquisition of pictures to be used in a digital photogrammetry reconstruction. The flight plan was designed based on the previous LIDAR data of the zone available from the Geographic National Institute (IGN). Due to the steepness of the cliff and the whole scenario, the flight plan was designed combining zenital and obliquus pictures. The flight was programmed using the web-app service Litchi, where the drone altitude, velocity, positions coordinates, and the camera orientation and tilt were defined. We always try to maintain the same distance between the camera (drone) and the terrain to obtain a homogeneous ground pixel size (named Ground Sample Distance).



Fig. 1 Drone used: DJI Inspire 2 with the camera X5S

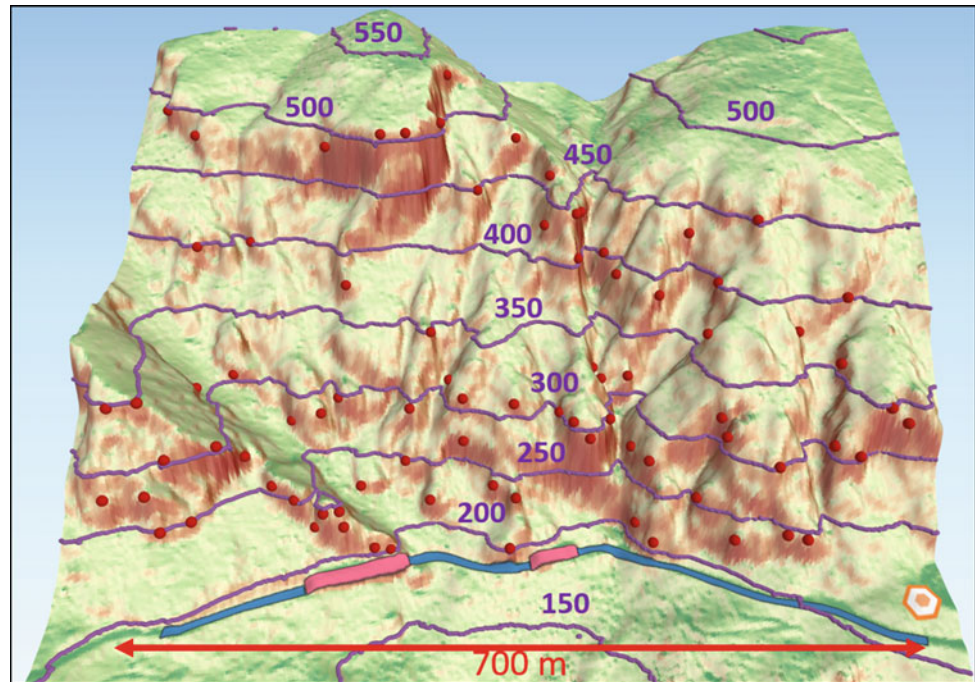
In order to decide the zone to be reconstructed, we carried out a previous analysis based on the slope and the interpretation of the pre-existing orthophotos to identify possible sources of rockfalls. Figure 2 shows the Digital Elevation Model generated based on the pre-existing airborne LIDAR, colored by the slope. The red dots (Fig. 2) are potential sources of rockfalls that we are interested in cover it with the drone flight. The blue polygon in the bottom is the road Ma-10, and the two rose tracks in the road are two protection galleries. The orange and white hexagon on the bottom right side is the point decided for the drone take-off and all the flight plans are programmed from this point. Then, the flight plan has to cover more than 700 m of road and the whole cliff from an altitude of 150 m to the top of the cliff at 550 m. We executed three programmed flight plans doing 8 tracks at different altitudes to take obliquus pictures of the cliff. A fourth flight plan was carried out taking zenital pictures for the half-lower part of the cliff, obtaining more images of the road and the galleries.

We use 542 pictures to create a point cloud with 66.3×10^6 points (Fig. 3, up) with the Agisoft Metashape software, covering an area of 0.5 km². The mean distance between the drone and the terrain was 150 m, and the GSD obtained was 3 cm/px. The point cloud was classified to filter the vegetation properly. (Fig. 3, down).

The classification of the point cloud was carried out using first the "Ground points classification" tool, and then the "Classify Points" tool, both integrated into the Agisoft Metashape software. The classification was then manually supervised and corrected in some erroneous classification. Finally, the points identified as "ground" (brown in Fig. 3, down), "road surface" (grey in Fig. 3, down) and the "buildings" referring to the protection galleries (red in Fig. 3, down), are used to create a Digital Elevation Model with 25 cm/px to be used as terrain in the RockGIS rockfall simulator. The points identified as "low points" (purple in Fig. 3, down), have not been used for the DEM generation due to refers to points with two elevations in the same planimetric coordinates. In this way, the point cloud could also be used in a propagation simulator software based on the 3D point cloud (Noël et al. 2017).

Finally, the point cloud and a 3D texturized mesh was used to characterize the fracture pattern and to identify the potentially unstable volumes for possible cleaning and monitoring purposes, as well as to check the previously potential sources of rockfalls identified (red dots in Fig. 2). On this way, the software Cloud Compare (Girardeau-Montaut 2006), and the plugins qFacets (Dewez et al. 2016) and Compass tool (Thiele et al. 2017) are very useful tools to characterize the joint pattern based on point clouds. The potentially unstable volumes can be defined based on the 3D mesh and correctly delimited using the joint sets that allow the failure based on kinematic stability

Fig. 2 Digital elevation model of the study area coloured by slope in a 3D view



analysis criteria for planar, wedge or toppling failures (Fig. 4).

Rockfall Fractal Fragmentation Model (RFFM)

Fragmentation of the rock mass is the reduction in particle size due to an external action. Despite the increasing number of studies on rockfalls, fragmentation as a consequence of the impact on the ground surface is poorly understood. The rock volume detached from a cliff consists of either an individual block or a jointed rock mass. In the latter, the intersection of joints defines individual blocks, which range of sizes is the In-situ Block Size Distribution (IBSD) (Elmouti and Poropat 2012). As a result of the impact, the rockfall fragments appear scattered along the slope and, as the rockfall volume increases, a more or less continuous debris cover is formed. The range of sizes of the rockfall fragments is the Rockfall Block Size Distribution (RBSD). Here, we use fragmentation as a generic and inclusive term, meaning the division of an initial rock block or rock mass caused by either the breakage of the rock pieces, the disaggregation of joint-determined blocks, or both (Ruiz-Carulla et al. 2017).

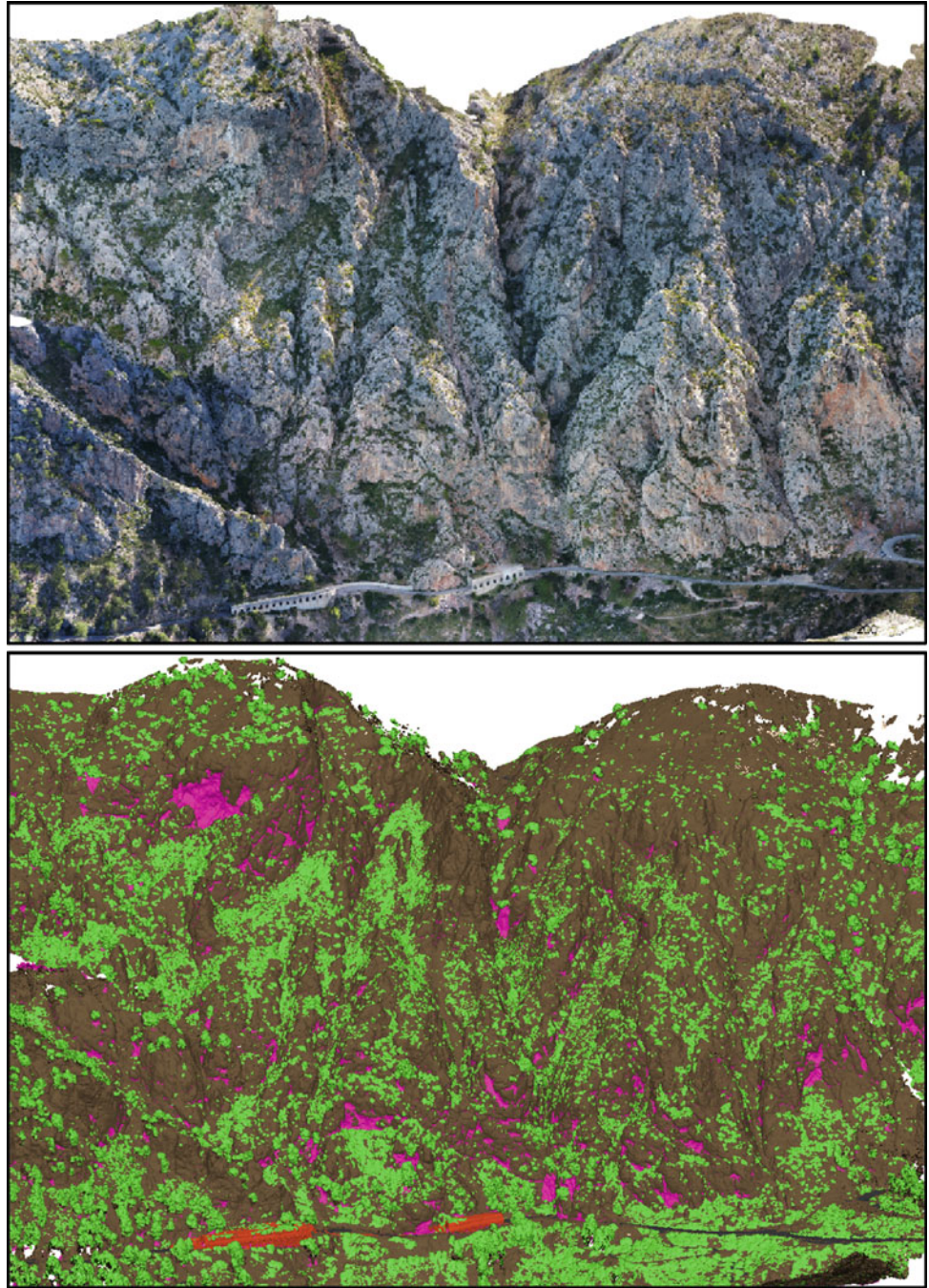
We study fragmentation in rockfalls by comparing the IBSD estimated from the detached rock volume versus the final RBSD measured in the deposit (Fig. 5).

Perfect (1997), described fragmentation as a natural phenomenon that may be characterized using fractals. The performance of the fractal fragmentation model (Ruiz-Carulla et al. 2017), simulate the processes of disaggregation and breakage in rockfalls. The model uses the scale variant equations and the cumulative number of fragments proposed by Perfect (1997) and Ruiz-Carulla et al. (2019).

The use of fractals is related to the same behavior in different scales or orders of magnitudes, also named scale-invariant behavior. This behavior can be identified plotting experimental data in terms of the cumulative number of objects versus their size in a log-log plot and observing a trend line that can be well fitted with a power-law. The exponent of the fitted power-law is also related to the fractal dimension of the system studied. However, the measurement of more than 10.000 fragments in the 7 inventoried rockfalls and real scale fragmentation tests indicate that fragments generated may follow either scale-invariant or variant behavior. The latter is characterized by a change in the proportion between the number of objects and their size. The scale variant behavior implies the modification of the fractal dimensions depending on the objects size. Then, blocks distributions cannot be fitted with a simple power law.

We adapt the equations proposed by Perfect (1997) in order to use an IBSD as a list of volumes as input and work with the initial volume of each block as initiator of a new fragment size distribution. Then, the input of the model may

Fig. 3 Point cloud obtained in real color (up) and the point cloud classified (down)



be a single block or a list of volumes. We use the Eq. 1 to generate the new fragments distribution from each initiator block:

$$V_{frag}(n) = V_o \cdot l_{max} \cdot n^{-1/D}; n = 1, 2, \dots, \infty \quad (1)$$

The V_o is the volume of each initial block. The use of the cumulative form allows the generation of the fragments one by one. The generated RBSD is obtained increasing n from 1 to infinite. The sequence of volume generation is as follows: first, the largest fragment, and then, the rest of fragments are

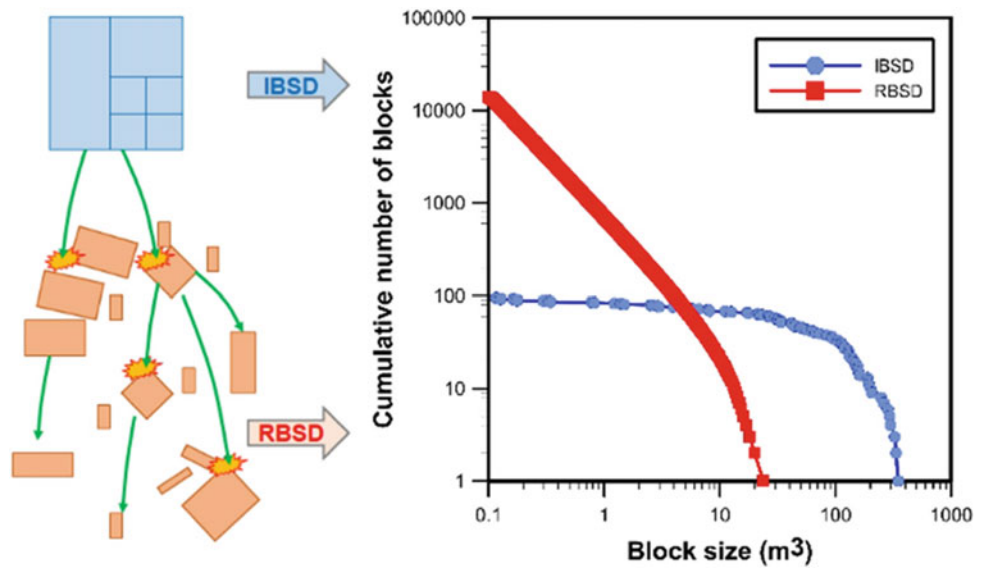
added, ordered by decreasing sizes, until either the initial block volume is completed or until the fragments become smaller than the threshold defined. The threshold value is established as the minimum volume of the fragments generated (V_{min}) that is not measured and checked in the field. The remaining mass below the threshold is computed as fine fraction.

The largest fragment generated after breakage l_{max} is defined by the Eq. 2, where q is the probability of survival of the rock block as defined by Perfect (1997). The probability

Fig. 4 Example of a potentially unstable block identified using the joint pattern characterized in the point cloud and extrapolated to cut the 3D mesh



Fig. 5 IBSD and RBSD characterizing the fragmentation process before and after a fragmental rockfall event



of survival q controls the proportion of the block that survives in combination with a geometric factor b that controls also the size relation between all the fragments generated. In scale-variant, different sizes display different patterns of fragmentation. For instance, the smaller blocks may offer greater resistance to breakage than larger blocks. The increase or decrease of the strength of the rock block as the block size diminishes is simulated with the negative or positive value of r , respectively. For $r = 0$, the scale-variant is equal to the scale-invariant case.

$$l_{max} = q(b^n)^r \tag{2}$$

Finally, the fractal dimension D is defined by Eq. 3.

$$D = 3 + \frac{\log[b^r - q(b^n)^r]}{\log[b]} \tag{3}$$

Then, the model parameters are the probability of survival q , the geometric factor b , and the scale variant factor r . From there, the largest fragment l_{max} and the fractal dimension D are calculated by Eqs. 2 and 3. The model can reproduce continuous decreasing size fragment distributions with different fractal behavior from a single block.

Trajectory simulation with RockGIS

The Rockfall Fractal Fragmentation Model is implemented in the RockGIS simulator. RockGIS is a 3D trajectory rockfall simulator developed as a GIS-tool using a Digital Elevation Model, and based on a lumped mass model (Matas et al. 2017, 2020).

In this communication, we have been focused on the reconstruction of a rockfall that occurred on the 11th of September in 2019, involving around five cubic meters single block. The breakage of the rock block generates more than a hundred fragments, some of them reaching the road. We measured the deposited blocks in the field with a tape, obtaining the RBSD (Fig. 6, red dots). The source point has been located in the cliff using pictures of the event report from the road surveys. Finally, the impact's energy controls the fragmentation parameters as proposed in Ruiz-Carulla et al. (2019). However, the relations between the impact energy and the fragmentation parameters are calibrated for this case to obtain a resultant block size distribution (Fig. 6, green dots) that fits the real measurements in the field. The fragmentation can be considered well calibrated in terms of blocks size distribution due to the well agreement with the field measurements.

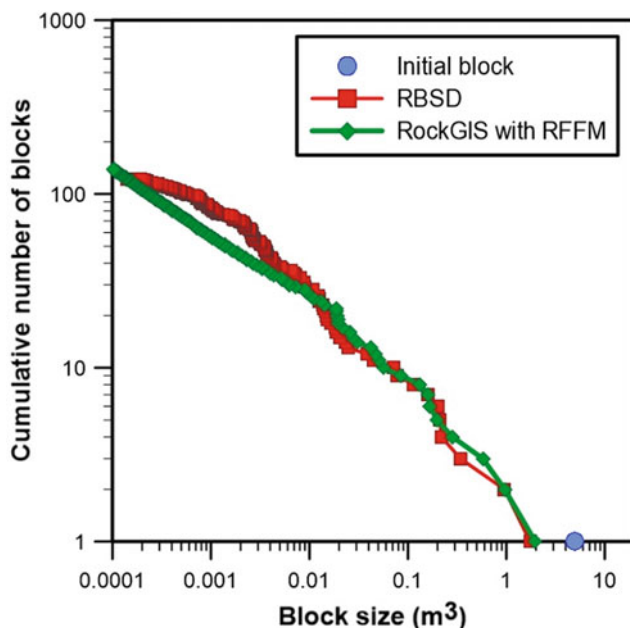


Fig. 6 Block size distribution from the deposit measurements (RBSD, red dots) and the results from the trajectory simulator reconstruction (green dots)

However, the reconstruction of the rockfall with the simulators take into account also the runouts and the stopping points. In this way, the calibration uses also the restitution coefficients to reconstruct the whole fragmental rockfall phenomenon in terms of spatial and volumetric characteristics.

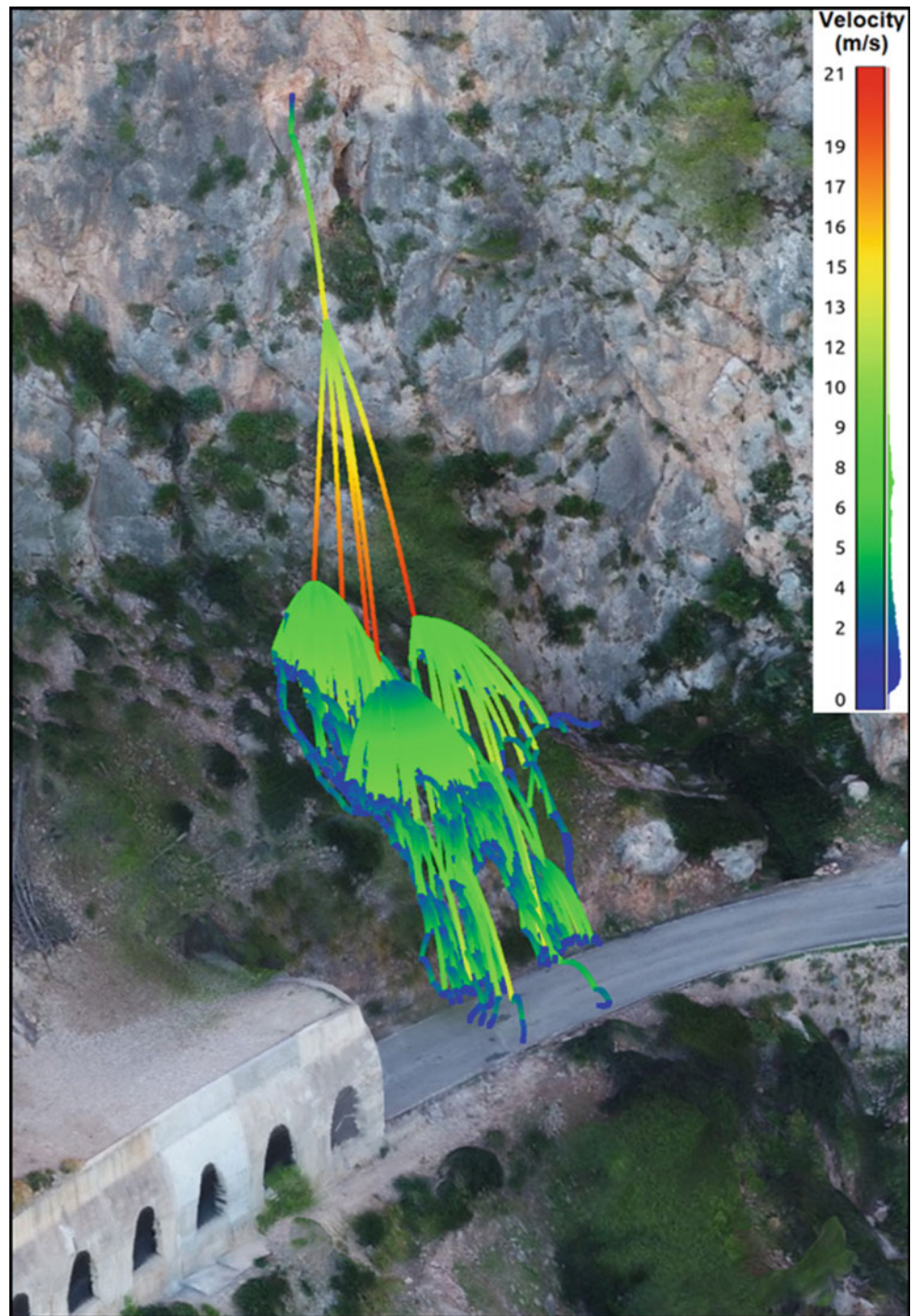
Figure 7 shows the trajectories of the fragments obtained from the calibrated simulation, colored by velocity. It can be observed that the initial block is considered as a single block that breaks generating new fragments in the first impact, and then, each independent trajectory breaks again in the second and in the following impacts depending on the impact energy. The stopping points of the fragments simulated fit with the field observations. Then, the calibration is considered well adjusted in both, block size distributions and runout distances.

Discussion

After the calibration of the model parameters for the 2019 rockfall event, the model is ready for other simulations. In 2015, another rockfall event involving 50 m^3 detached from 400 m of altitude reached a protection gallery destroying a part of it. This event is simulated considering 3 scenarios, Fig. 8a, b and c.

The scenario (a) shows a common procedure running 1000 simulations of a single block of 50 m^3 without fragmentation. Most of the trajectories simulated reach and overpass the road and the protection gallery (Fig. 8a). However, the actual rockfall event was only one of those simulations. Figure 8b shows just one simulation of a single block of 50 m^3 without fragmentation. In this case, the block impacts directly on the destroyed part of the protection gallery in 2015. Finally, Fig. 8c shows the case that better reproduces a fragmental rockfall from our point of view. The simulation shows a single block detached from the cliff of 50 m^3 considering fragmentation upon the impacts against the terrain during its propagation. Part of the fragments generated stop before the protection gallery creating small deposits along the path. The bigger fragments go further reaching the protection gallery causing a multi-impact effect. The affected area considering fragmentation increase in comparison to the single block simulation without fragmentation, as well as the probability of impact. However, Fig. 8c shows the results of only one simulation, and then, to get a probabilistic evaluation of the hazard, hundreds of simulations should be run.

Fig. 7 Results of the rockfall simulated using RockGIS, coloring the trajectories by velocity from 0 to 21 m/s



Conclusions

This communication shows a methodology to analyze fragmental rockfalls. The use of UAV and digital photogrammetry allow high-quality 3D data to characterize the potentially unstable volumes and to obtain the terrain reconstruction as input for trajectory simulators. At this

point, the correct vegetation filtering from the point cloud is necessary to create a useful Digital Elevation Model. Then, the use of our RockGIS simulator with the Rockfall Fractal Fragmentation Model implemented allows the reproduction of the fragmental rockfall behavior in terms of both, block size distributions and runouts. This is an example of fragmentation consideration to take into account working with hazards and risks associated with rockfall. Further analyses

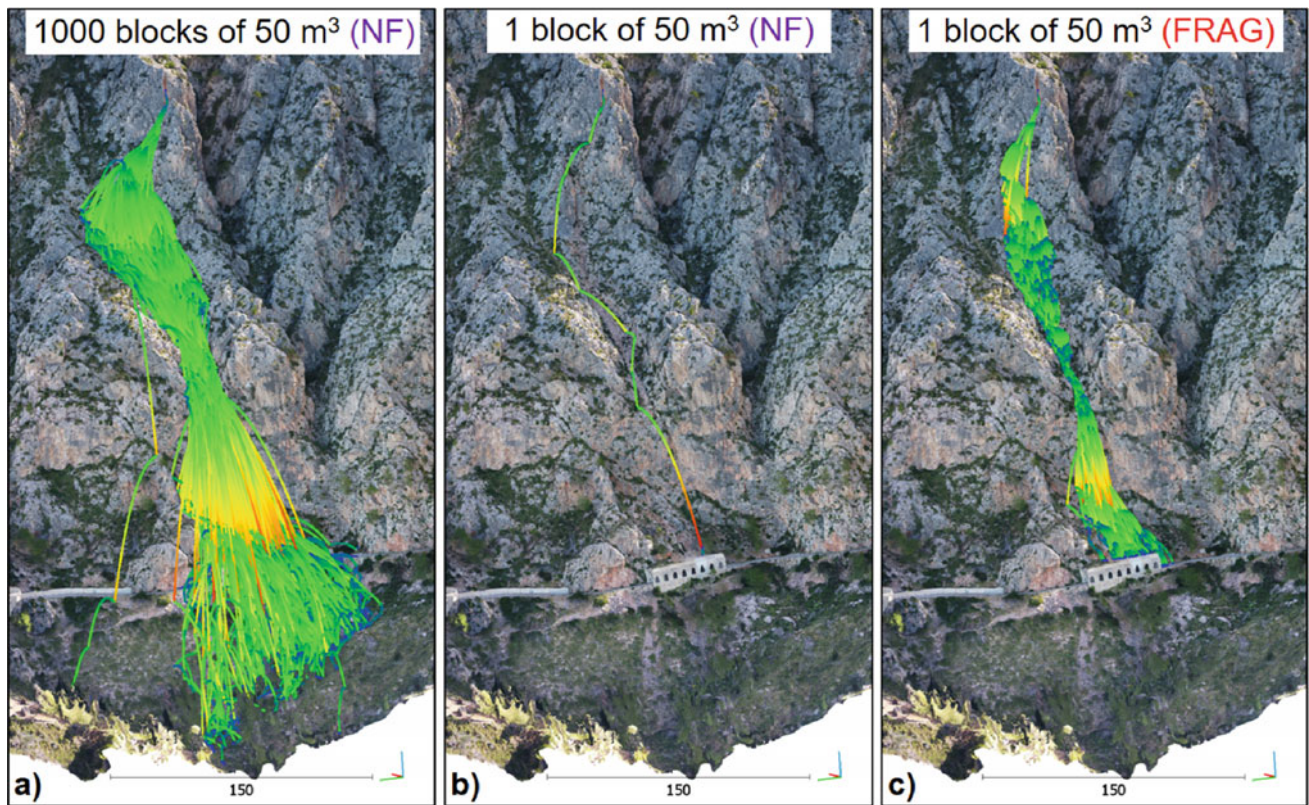


Fig. 8 RockGIS simulations result for 2015 rockfall: **a** 1000 simulations without fragmentation, **b** one simulation without fragmentation and **c** one simulation with fragmentation

and considerations are then needed to define the hazard maps taking into account the fragmentation implications, as well as the implications derived to the fragility curves for multi-impact against structures, roads, vehicles or people.

Acknowledgements This study was supported by the research project RockModels (Ref.BIA2016-75668-P, AEI/FEDER.UE) funded by the Spanish Ministry of Economy and Competitiveness. Acknowledge also, to the local government of Mallorca (Balearic Islands, Spain).

References

- Corominas J, Matas G, Ruiz-Carulla R (2019) Quantitative analysis of risk from fragmental rockfalls. *Landslides*. 16(1):5–21. <https://doi.org/10.1007/s10346-018-1087-9>
- Dewez T, Girardeau-Montaut D, Allanic C, Rohmer J (2016) Facets: A Cloud Compare plugin to extract geological planes from unstructured 3D point clouds. *International Archives of the Photogrammetry, Remote Sensing and Spatial Information Sciences*, Volume XLI-B5, 2016
- Elmouti MK, Poropat GV (2012) A method to estimate in situ block size distribution. *Rock Mech Rock Eng* 45(3):401–407
- Girardeau-Montaut D (2006) *Detection de Changement sur des Données Géométriques 3D*, PhD manuscript (french). Signal & Images Processing, Telecom Paris
- Matas G, Lantada N, Corominas J, Gili JA, Ruiz-Carulla R, Prades A (2017) RockGIS: a GIS-based model for the analysis of fragmentation in rockfalls. *Landslides* 14(5):1565–1578. <https://doi.org/DOI:10.1007/s10346-017-0818-7>
- Matas G, Lantada N, Corominas J, Ruiz-Carulla R, Prades A, Gili JA (2020) Calibration of a rockfall simulator with a fragmentation model in a real scale test. *International Symposium on Slope Stability in Open Pit Mining and Civil Engineering*. May 2020, Perth (Australia)
- Noël F, Wyser E, Jaboyedoff M, Clouthier C, Locat J (2017) Development of a 3D rockfall simulation model for point cloud topography. *EGU General Assembly Conference Abstracts*
- Perfect E (1997) Fractal models for the fragmentation of rocks and soils: a review. *Eng Geol* 48:185–198
- Ruiz-Carulla R, Corominas J (2019) Analysis of rockfalls by means of a fractal fragmentation model. *Rock Mech Rock Eng*. <https://doi.org/10.1007/s00603-019-01987-2>
- Ruiz-Carulla R, Corominas J, Mavrouli O (2017) A fractal fragmentation model for rockfalls. *Landslides*. 14(3):875–889. <https://doi.org/10.1007/s10346-016-0773-8>
- Thiele ST, Grose L, Samsu A, Micklethwaite S, Vollgger SA, Cruden AR (2017) Rapid, semi-automatic fracture and contact mapping for point clouds, images and geophysical data. *Solid Earth* 8:1241–12535



3D Landslide Models in VR

Hans-Balder Havenith

Abstract

The present paper describes the elaboration of 3D surface and geological models generated for a series of landslide sites, zones marked by large incipient slope failures, or those presenting structural characteristics of an ancient giant mass movement. For both, surface and geological models, high-resolution satellite or drone imagery was draped on the digital elevation model constructed from the same imagery or using Radar or LiDAR data. The geological models further include geophysical data, supported by differential GPS measurements, complemented by georeferenced geological and tectonic maps and related geological sections. The soft layer thickness information and borehole data are typically represented in terms of logs inside the model. For several sites also slope stability analyses were performed, either in 2D or in 3D. Inputs for those analyses were directly extracted from the 3D geomodels, outputs were again represented in the models.

Some of those models, such as the one produced for the right-bank slopes of the Rogun Dam construction site can be quite complex and we clearly could notice that an immersive analysis using VR technology helps understand their internal structure and perform a better slope stability analysis. Still these analyses have their limits, as a study in Virtual Reality is purely individual (at present time, the visiting researcher is separated from the rest of the World). Therefore, we suggest that a real advancement can only be achieved if the technological developments go along with a stronger collaboration between scientists from the various geo-domains, who could also be immersed in the same virtual model (~collaborative VR).

Keywords

Landslide dynamics • Geomodel • 3D analysis • Immersion • Collaboration

Introduction

Among all geosciences, geological-geophysical hazard research is probably the one that presents the highest challenge with respect to spatiotemporal perception requirements (Havenith et al. 2019). Geological hazards, including landslide hazards, can involve highly dynamic processes, such as rock failure, wave propagation, changing groundwater pressures, extremely slow creep, shearing, subsidence or uplift movements, or rapid collapse, which occur at micro-scale or affect wide areas, even entire mountain structures.

While exploring related hazards within a combined model is still well beyond state-of-the-art, recent technological and conceptual advances should help reach this goal in near future. At present, most single hazard components can be assessed—at least empirically—and many underlying processes can also be reliably simulated and some can be coupled, but representing them in an adequate multi-scale space–time frame is limited by existing modelling capabilities. In Havenith et al. (2019) we provide a (small) overview of what is possible today in geohazard analysis. It should be noticed that many of those tools were actually designed for other purposes related to geography-geomorphology, construction, geotechnical engineering, or mining. The geohazard scientist just adopted them for his/her applications. The most commonly applied representation basis for collected data is still the one of a 2D plane. Digital maps can be visualised and processed by using Geographic Information Systems (GIS). A series of elements can be added to these maps. A series of numerical modelling tools also handle 3D data distributions, generally with limited extent. Both the

H.-B. Havenith (✉)
Department of Geology, Georisks and Environment, Liège
University, Liège, Belgium
e-mail: HB.Havenith@uliege.be

GIS and the modelling software can also propose 3D views of the respective 2D targets, or of 3D in- and outputs if implemented in the modelling software.

From the preceding it could be understood that the main difference between GIS and numerical modelling software is the orientation of the plane on which geographic-geological elements are represented. Another difference relies in the type of analysis performed with those tools as well as in the temporal component. Usual GIS software only allows for statistical analyses applied to data which include limited discrete, if any, time information (e.g. seismic hazard maps for different return periods, multi-temporal landslide inventories or volcanic eruption maps, etc.). Numerical simulation tools can produce quasi continuous time-dependent outputs (using a time-step adapted to the type of process analysed) for sections or 3D models. However, those outputs are generally strongly limited in time and space (due to limited available computation or storage capacities and/or due to limited data availability).

A compromise is proposed by a third type of modelling techniques that can be grouped together under the general term of 3D visualisation tools or, more specifically, of 3D geomodellers. Related software can represent at the same time large maps and much smaller cross-sections or 3D numerical models representing simulation outputs. The geological modelling (or simply geomodelling) software is generally not used to create the data, but it helps represent in- and outputs in the 3D space. In addition, this software allows for some pre-processing of information needed for the numerical models and for the development of 3D volumes on the basis of points, lines or surface data distributed within a 3D space. As volumes are the core part of 3D geomodels, geomodelling tools must be able to visualise efficiently the 3D space. Therefore, their 3D visualisation capabilities generally exceed by far those of GIS or original numerical modelling tools. Geomodels also allow for 3D spatial and temporal analyses (if the required data are included in the model). Some workflows related to local geohazard studies involving also geomodels are presented in paragraph 4 (case studies) below.

Geomodels are only used by a limited number of geoscientists (typically geo-engineers), first, because geomodelling is time-consuming and, second, because the software is relative expensive for most applications, while probably all (or almost all) geoscientists, including geohazard experts, use the freely available Google Earth® (GE) software. This software provides some pseudo-3D view that is much more efficient than the one proposed by common GIS tools but it does not really exceed the basic capabilities of the latter as all elements are distributed over or above the Earth surface—just as in the GIS maps.

The preceding finally might suggest that we already possess the ‘ideal’ software system combining GIS,

numerical and geological modelling tools supplemented by GE, which covers all aspects of what is required to complete spatiotemporal geohazard analyses. But, there is still something missing, as explained in the next section.

Immersive Models

Modelling versus Visualisation

Landslide hazard assessment involves the collection of information about the possible slope destabilisation factors (e.g., presence of active faults, unstable volcanic structures, or changing groundwater pressures) for a site or a region as well as their integration within a model that can be used for simulations of dynamic geological processes. But, how to represent and visualise those elements and processes in a single digital ‘space’? Typically, input data processing and simulations are run outside the visualisation environment—as real-time processing and simulations require long computation times. Additionally, incompatibilities of data in- and outputs are often observed by changing the software; some outputs can only partly be read by the post-processing or visualisation tools.

An Integrated ‘Digital Geohazard Space’?

One of the longest lasting systematically improved systems targeting multi-dimensional dynamic geographic analysis, enhanced collaboration between geoscientists and interaction with elements to be analysed is the ‘Virtual Geographic Environment’ (VGE, see Lin et al. 2013). The VGE concept has been developed over many years in order to enhance collaboration between geoscientists using the same or similar datasets. Yet, we note that integrated collaboration is still extremely underdeveloped—especially in geohazard sciences. This way of inefficient collaboration in most geo-institutes is surprising if one considers that a few ‘collaborative virtual environments (CVEs)’ or ‘collaboratories’ have already been set up many years ago as indicated by MacEachren et al. (2006). Their approach to collaborative visualisation and analysis of geo-data combines mapping elements, cognitive aspects, interaction, cooperative work, and semiotics. They had started ‘to address the full range of space–time collaborative situations that can involve group work in the same or different places and at the same or different times.’ MacEachren et al. (2006) explain that ‘the collaboratory allows users to organize their data streams into hundreds of individualized displays—3D visual renderings and virtual reality rooms—that are then shared (both synchronously and asynchronously) with other collaborators.’ More recently Jurik et al. (2016) developed the idea of the

virtual worlds (VW) providing the ‘possibility to dynamically modify content and multi-user cooperation when solving tasks regardless to physical presence. They can be used for sharing and elaborating information via virtual images or avatars.’

Former versions of those VGEs did not specifically involve immersive visualisation. And, notwithstanding many technological advances and strongly enhanced availability of VR tools, applications in geosciences and specifically in geohazard research are still rare. Though, Kellogg et al. (2008) clearly state that ‘an immersive visualisation system is ideal for Earth scientists’ as it allows them to better approach the complex multi-scale geo-processes that often change rapidly in time and space. Their main argument in favour of an immersive geo-visualisation is that it ‘allows scientists to use their full visual capacity, helping them to identify previously unrecognized processes and interactions in complex systems. ... Reaping the full intellectual benefits of immersive VR as a tool for scientific analysis requires building on the method’s strengths, that is, using both 3D perception and interaction with observed or simulated data’.

Now, the relatively low price of VR technology (compared to the situation before the massive release of affordable mobile systems; see paragraph below) allows most geoscientists to really use the advantages of 3D perception and interaction—also in geohazard engineering. In particular, it will ‘allow users to explore inaccessible past or future environments or distant present environments, not only through their static objects but through processes that mirror their real dynamics’ (Lin et al. 2013). Garcia-Hernandez et al. (2016) further state that 3D visualisation can provide more insight in multi-variable data analysis.

Technological Aspects

The aforementioned widespread availability and affordability of VR hardware enables new applications in many fields. We developed applications to visualise fault scarps, landslide geometries, and our geohazard database for Central Asian mountain ranges. Such environments require multi-scale visualisation platforms bridging several orders of magnitude in space (and would also in time, but until now we have no full spatiotemporal model types visualised in VR).

In parallel with its improved availability, the installation and use of the VR hardware and software has also been simplified over the past decade. Although their use remains complex, their present degree of integration and documentation make this technology much more accessible than it has been in the past. This has been developed in such a way that programming skills are not required any more for certain smaller projects.

To represent the landscape in geo-models we use the (possibly textured) DEM surface. The entire geo-model also includes subsurface geological and seismotectonic information (e.g. geological cross-sections, fault structures, earthquake hypocentres), geophysical profiles (e.g. seismic or electrical tomography, various logs) that have generally been processed by adapted software. Most of those data also require georeferencing with a 3D geomodelling software before being imported in the virtual scene. The basic data for georeferencing are generally provided by geodetic measurements completed in connection with the field surveys.

Below we first present some simple surface models of landslides created from drone imagery and, second, some more complex full 3D geomodels of studied landslide sites. For representation.

Landslides and Potentially Unstable Slopes in VR

A ‘Belgian’ Landslide Model

As indicated by Havenith et al. (2019), most of our local geohazard-related studies now also include the preparation of data for visualisation in VR. This preparation follows the scheme described above, based on the creation/adaptation of a surface model (DEM), possibly textured with remote imagery, introduction of geophysical-geological profiles, logs, interpolated underground surfaces (e.g. geological layers, faults), volumes. Typically, point data, logs, surfaces and volumes are first processed in a geomodelling software. The example shown in Fig. 1 presents a landslide site along the seismically active Hockai Fault Zone (HFZ) in East Belgium. An integrated 3D geomodel made with Leapfrog® visualises the study site in terms of its surface and subsurface structures on the basis of the collected data. The inputs of this model include the DEM based on high resolution (LiDAR) surface data (possibly textured by georeferenced orthorectified remote imagery), subsurface geophysical data: microseismic ambient noise measurements (H/V—see logs in Fig. 1c), seismic refraction (P-waves) tomography and surface wave analysis results (not shown here) as well as electrical resistivity tomography (ERT, shown in Fig. 1b).

The landslide developed in a softer conglomerate unit (upper part in reddish-brownish layer shown in Fig. 1c, d) that could be outlined through its seismic resonance characteristics (H/V results). Related geophysical logs include two information: first an intermediate contact could be identified thanks to a higher frequency resonance peak (found only within the landslide zone, as highlighted by Mreyen et al. 2018) and the bottom of the log corresponds to the thickness of the entire softer conglomerate. Thus, the intermediate contact was considered to be related to the

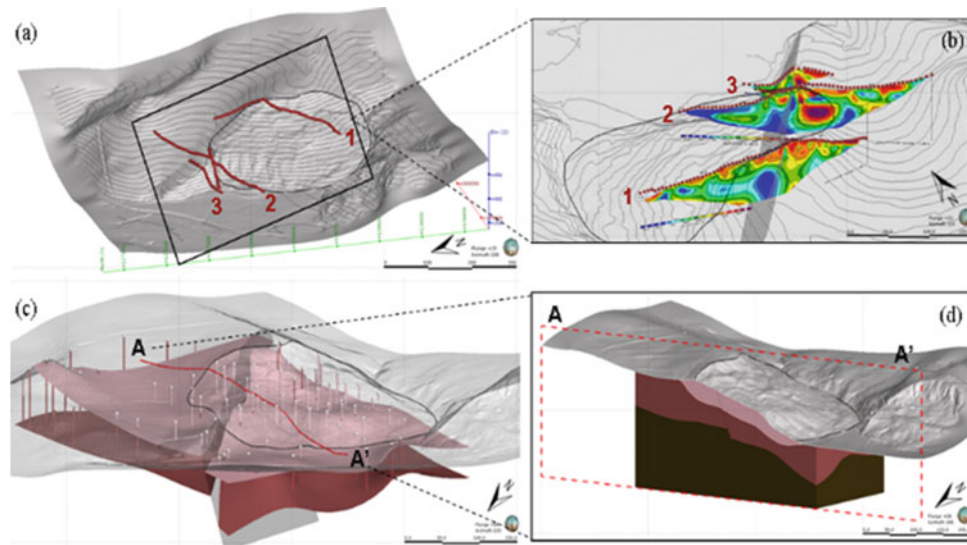


Fig. 1 3D geospatial model of a landslide (grey polygon in all figures) and fault scarp site in East Belgium (created with the Leapfrog® software) showing (a); view to the SE of the shaded LiDAR DEM with location of ERT profile lines, shown in (b); c view to SE of modelled DEM and

subsurface layers, inferred from H/V thickness estimates (colons); d view to SE of combined shaded DEM and subsurface layer volumes cut along section AA' also shown in (c)

compaction change between the weakened conglomerate within the landslide and the intact conglomerate below (seismic refraction surveys showed that this contact is related to a change of shear wave velocity from 300 m/s inside the landslide material to 600 m/s inside the intact conglomerate; the bedrock below is marked by a shear wave velocity of more than 1000 m/s. Both contacts were interpolated in the Leapfrog software to create triangulated surfaces. Between those surfaces and for the bedrock, volumes have then been formed as shown in Fig. 1d. For the interpretation of related complex inputs (high-resolution terrain and subsurface data, geophysical profiles) and outputs (modelled surfaces and volumes) we use 3D stereo visualisation using a headset system allowing for full immersion in a virtual environment.

The Koytash Landslide Case History

In spring 2017, Kyrgyzstan suffered high losses from a massive landslide activation event, during which also the largest deep-seated mass movement of the former mining area of Mailuu-Suu, landslide Koytash, was reactivated. We had started studying this and the neighbouring landslides already many years ago (in 2000), by geophysics and by using optical and radar satellite data. Thereby, we could highlight deformation zones and identify displacements prior to the collapse of Koytash landslide.

Multiple types of DEMs, including a very high-resolution DEM (0.2 m) created on the basis of drone imagery acquired in summer 2017 (after the massive failure). Figure 2 presents

an oblique view of the surface model of the landslide that can also be viewed in our VR lab. Figure 3 (from Piroton et al., subm.) shows map views of the same area with the UAV DEM included (within red polygon) in the regional TanDEM-X (11 m resolution) surface model.

The comparison of multi-temporal digital elevation models (satellite and UAV imagery-based) highlights areas of depletion and accumulation, in the scarp and near the toe, respectively. The differential synthetic aperture radar interferometry analysis identified slow displacements during the months preceding the reactivation in April 2017, indicating the long-term sliding activity of Koytash. This was confirmed by the computation of deformation time series, showing a positive velocity anomaly on the upper part of Koytash. Furthermore, the analysis of the Normalized Difference Vegetation Index, revealed land-cover changes associated to the sliding process.

The Rogun Right-Bank Slope Model

For the seismically active Tien Shan Mountains in Central Asia we had created a full GIS geohazard database (Havenith et al. 2015) that we have now transformed into a 3D geodatabase. For smaller sub-areas inside the Tien Shan region, and sites of particular interest, we also developed detailed 3D models, generally as basis for dynamic slope stability calculations or local seismic hazard analyses. Related 3D geodata visualisation examples include the results of a survey completed near the Rogun Dam

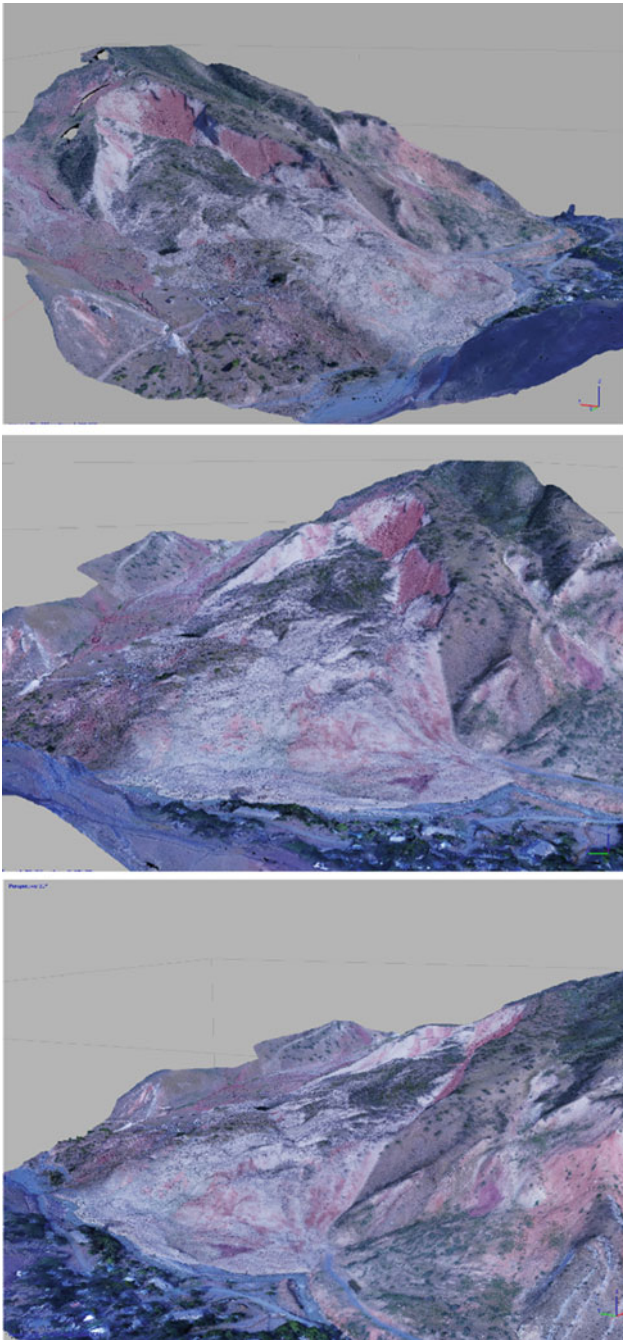


Fig. 2 Oblique views of the Koytash post-collapse (summer 2017) landslide view (UAV imagery covering the 0.2 m resolution DEM constructed from the same images) as it can be seen in VR

construction site in Tajikistan (Figs. 4 and 5, from Havenith et al. 2018). The initial pure 3D geomodel has been used to create a 2D numerical model of the slope that was analysed with UDEC (Itasca). The entire rock structure had been represented in this model on the basis of the geological sections, borehole data (shown in Fig. 4b) and geophysical tomographies (see Fig. 5) included the 3D geomodel. Rockfall simulation results were reintroduced into the model

as shown in Fig. 4d. Thus, geomodelling and numerical modelling have been completed outside the virtual environment—which until now has been used in our laboratory only for visualisation purposes. In the next paragraph we will, however, show that simulations are now also possible directly in the virtual domain.

In his Ph.D. thesis, Ondercin (2016) outlines the possibilities of physics engines belonging to the game engine model series to simulate rock fall events almost in real-time while visiting the virtual environment. Examples are shown in Figs. 6 and 7. These simulations take into account the effect of gravity, bouncing effects (according to a restitution coefficient, see impact represented in Fig. 7) and friction, considering also energy loss during interaction with other objects.

What About Uncertainties in VR?

A scientific analysis, be it in 2D or in VR, is not possible without representing the reliability of the data, and, thus, related uncertainties. Intuitively, all people know that predicting geohazards is subjected to uncertainties. Sword-Daniels et al. (2016) highlight the necessity of considering this uncertainty in connection with natural hazard assessment, considering that ‘the non-linear and dynamic nature of many complex social and environmental systems leaves uncertainty irreducible in many cases.’ Thus, any user and, in particular, any responsible scientist, engineer, or risk manager, entering a virtual world where those uncertainties do not exist would at the end mistrust what has been represented—because it has been shown as a fact (while it is not in reality!).

Total uncertainty is typically subdivided into epistemic and aleatory uncertainty, each of which can be represented in a different way. Epistemic (‘we do not really know’) uncertainties are best presented by ‘shading’ elements affected by those, or by making them partly transparent according to the degree of missing knowledge. Aleatory uncertainty (‘related to the occurrence probability’) is best visualised through the variability of possible data outputs. For graphs, such variability is shown through the standard deviation curves, maximum and minimum possible models, etc.

Comparably, in a 3D geohazard space, the variability of geohazard models (scenarios) has to be shown to represent related aleatory uncertainties. It is likely that VR technology could help visualise this variability of multiple possible ‘realities’ (through multiple parallel visualised models, changing scenarios with depth—distance models are less, front models are more likely), but according to our knowledge, presently, there are no holistic solutions to do this. Brodlie et al. (2012) stated with respect to uncertainty

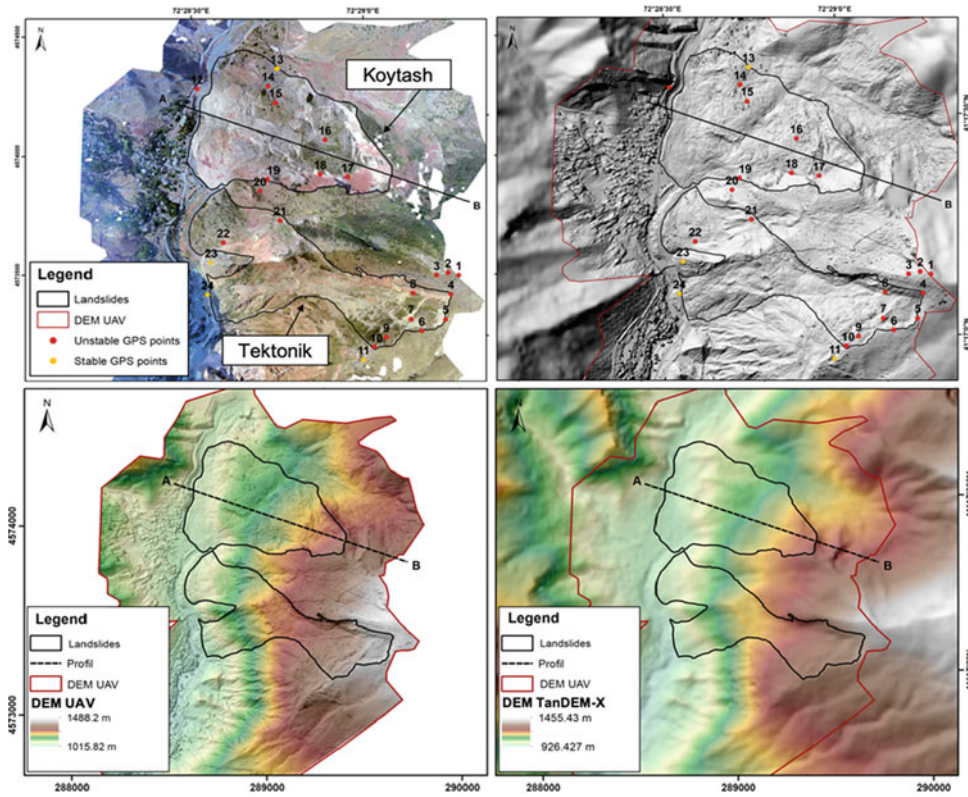


Fig. 3 Maps of Koytash landslide (upper black polygon). **a** UAV orthophoto map; **b** combined TanDEM-X (outer part) and UAV (central part) DEM hillshades; **c** 0.2 m UAV DEM of the Maily-Say area; **d** 12 m TanDEM-X DEM of the target area

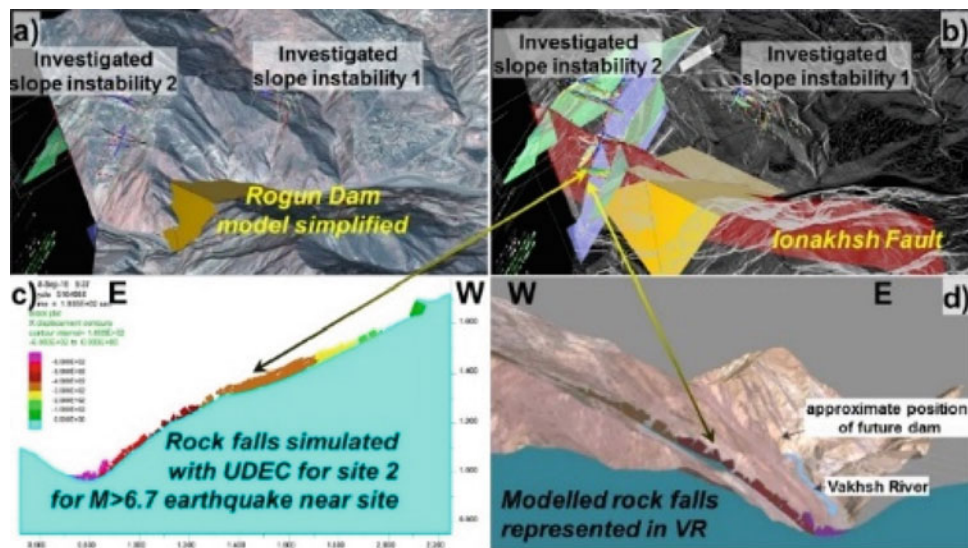


Fig. 4 3D geomodels and numerical simulation results for slopes investigated near the Rogun Dam construction site in Tajikistan with general view (a), surface representation by contour lines and subsurface

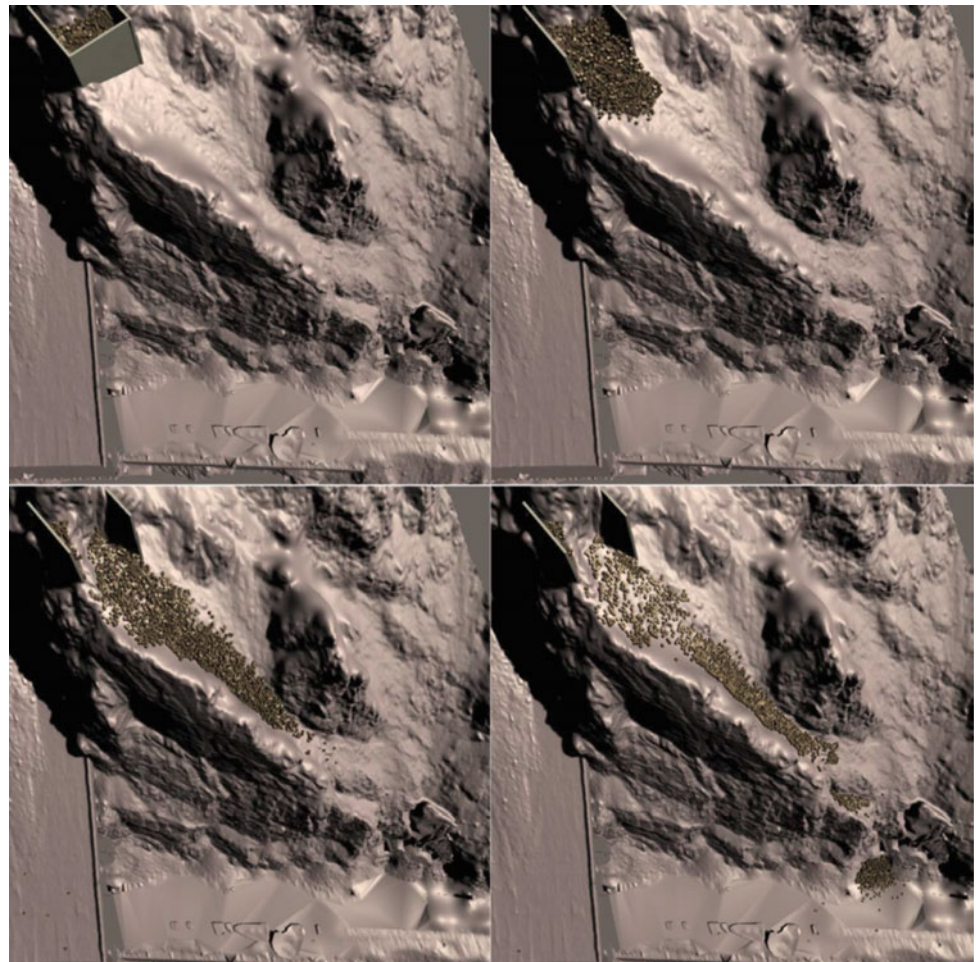
elements of 3D geomodel (b), modelling section showing rock falls simulated with UDEC for $M \sim 6.7-6.9$ scenario earthquake near site (c) and simulation results shown in virtual environment (d)



Fig. 5 Rogun site in virtual reality. **a** Researcher visiting the site in VR. **b** General semi-transparent surface view showing subsurface profiles. **c** Illuminating collected subsurface data near the Rogun site inside the virtual environment. **d** Visualisation of geophysical

(SRT) profile edited (placed at correct location) in VR. For this site also simulations of rock falls were completed in 2D with the UDEC (ITASCA) software. Final results are included as section in the virtual model (see Fig. 4d)

Fig. 6 Model showing the progression of a debris flow down the slope. First the blocks are allowed to settle and then are released. A total of 2047 blocks were used, each with a volume of 0.008 m^3 (from Ondercin 2016)



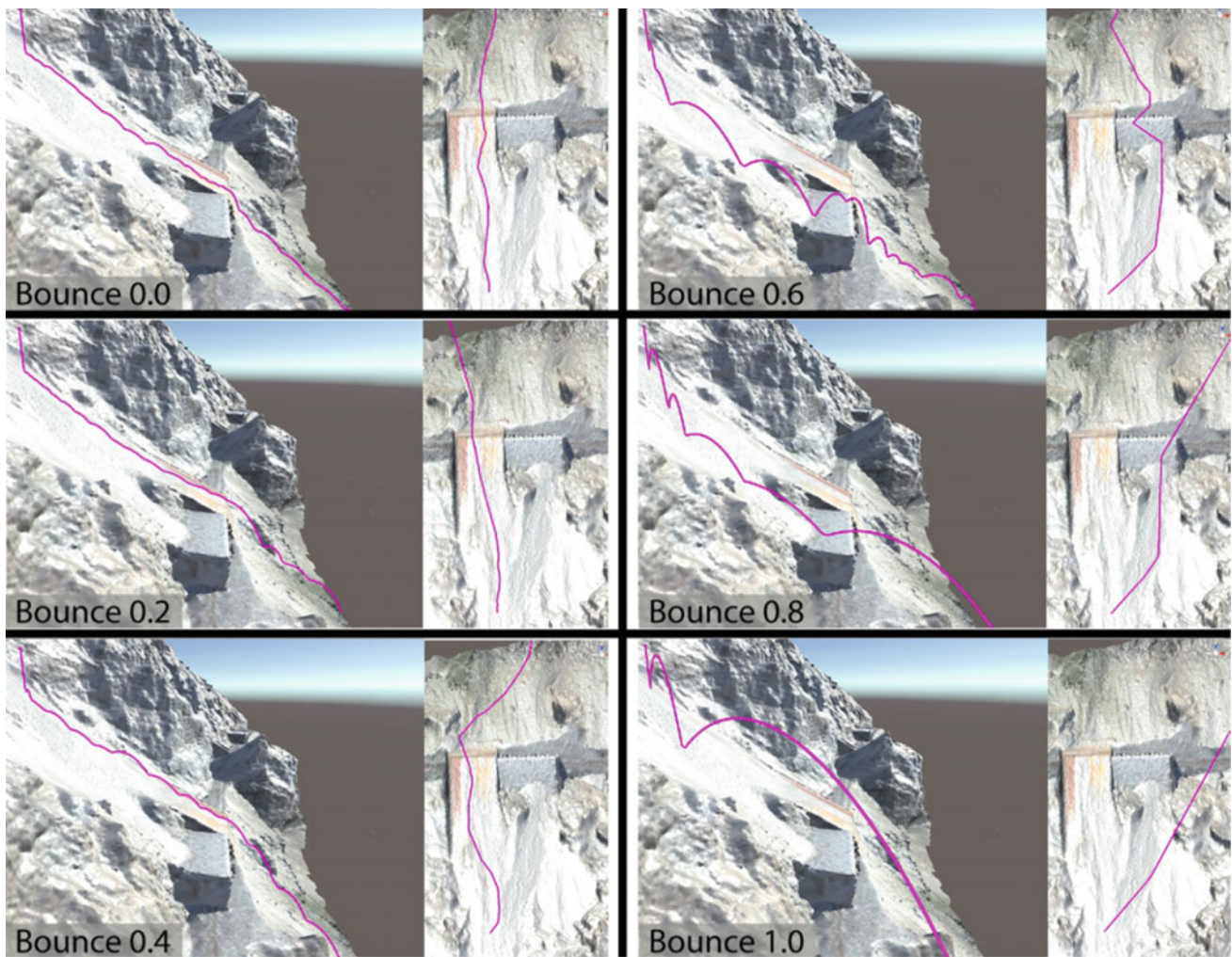


Fig. 7 A cubic rockfall occurring in the same location, changing only the bounce parameter for every test. The friction factor is set at 0.6 and a cubic shape of 1 m^3 is modelled (from Ondercin 2016)

visualisation that ‘there remain significant research challenges ahead. While incorporation of uncertainty into 1D and 2D visualisation, both as a scalar and a vector, is relatively straightforward, there are difficult perceptual issues in adding an indication of uncertainty in 3D.’

Dübel et al. (2017) provide a wide overview of possible uncertainty visualisation (see one simple example in Fig. 8), clearly stating that the author must decide if data visualisation, or related uncertainties or background conditions (e.g. hillshade of terrain) should be prioritized. If uncertainty is a major issue, then some extrinsic representation as additional symbols may be used to indicate the local data uncertainty value (as in the lower part of Fig. 8).

Finally, we can say that a digital geospace should be able to manage uncertainties affecting inputs and outputs, but at present there are no ad hoc solutions available and further

research is necessary to do so. Related studies have to accompany the development of the basic characteristics of the 4D geospace described below.

Conclusions

Havenith et al. (2019) describe six essential qualities of the digital geospace—which are not specific for landslide or any geological hazard assessment, but will certainly enhance it. They can be summarized as this: the geospace should be (1) multi-dimensional, considering that X,Y,Z must not necessarily refer to the ‘geometrical space’, multiple dimensions can also refer to multiple disciplines or multiple parameters to be represented; (2) spatiotemporal as many geoscientific disciplines, including those related to

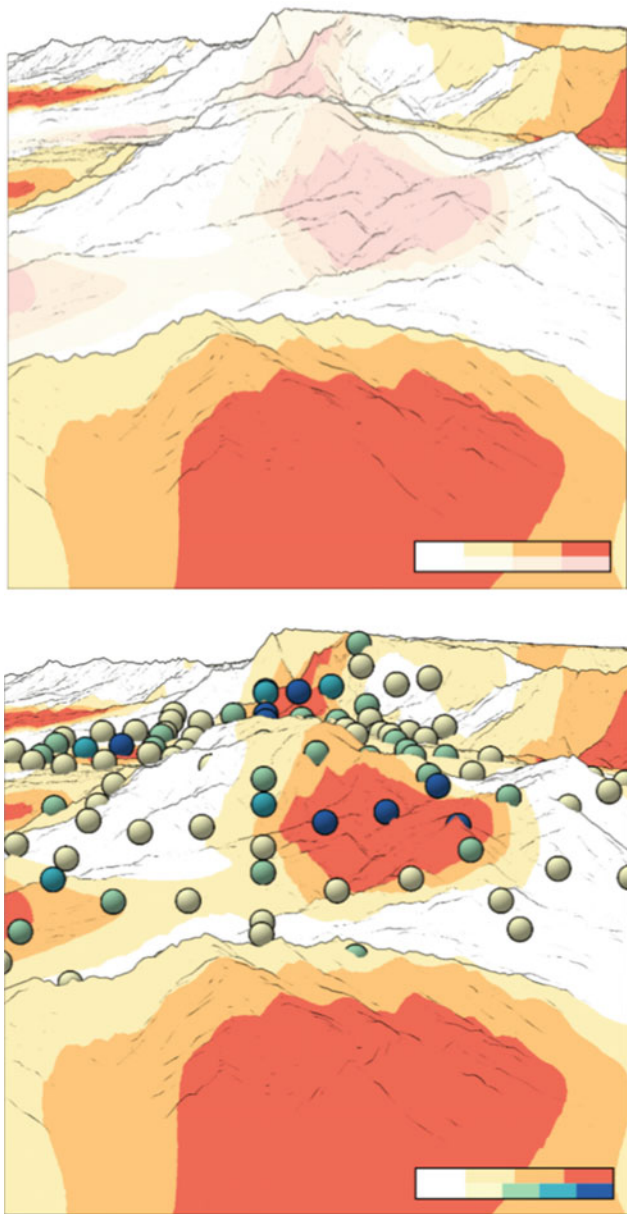


Fig. 8 Intrinsic (above) and extrinsic (below) encoding of uncertainty (here for wind prediction), respectively, by using transparency or additional coloured uncertainty symbols (white = low, blue = high values)

geohazard assessment are also ‘temporal’; (3) fully interactive, allowing for marking elements and modifying them; (4) (tele-)immersive, as it can be expected that an immersive analysis may engage the investigator, viewer, more intensively in finding solutions, than a non-immersive approach; (5) collaborative: all the preceding points essentially require technical solutions. The goal of improving those solutions is the improved collaboration between multi-disciplinary teams. So, this last quality would be an all-embracing consequence rather than an additional characteristic. For

geohazard research, achieving this goal could represent a revolution as multi-disciplinarity is essential for establishing reliable spatiotemporal models able to predict dynamic processes that may occur anytime and anywhere with a certain probability. Such models typically require inputs and re-evaluation by more than one single person!

Are there now technical solutions to create a digital geospace that could help assess geohazards better? Obstacles outlined above first include insufficient possibilities for interaction and collaboration in VR. Thus, present software developed in connection with the HMD hardware does not automatically allow for editing or collaboration in the virtual space.

To model 3D changes over time to simulate geological processes, changes in both geometry (expansion) and topology (discretisation) must be considered. Despite the progress observed in many fields, we still lack the ultimate 3D model that will allow us to integrate different representations and models from different domains.’

And even if we manage to develop fully integrated 3D geohazard models combining outputs from multiple disciplines and adapted for immersive analysis, we need to check if they really allow for an improved understanding. As Romano et al. (1998) wrote ‘an immersive virtual environment (VE) usually requires a considerable investment. Therefore it would be interesting to determine if a simple desktop VE could be used to achieve a sense of presence sufficient to provide trainees with an experience of the same cognitive value as one in the real world without the need to construct a full immersive VE with all its associated costs.’ This can be complemented by the conclusions of Westerteiger (2014) that not every problem can be efficiently solved in VR. He considers for example vector maps as type of data that are better represented in a 2D (desktop) digital environment. For this author the ‘key to the acceptance of VR methods, then, is the seamless interoperability between (existing) desktop systems and VR environments.’

Thus, the final usability of VR in any scientific research has to be analysed in a critical way, respectively, for each discipline and for multi-disciplinary approaches.

Acknowledgements Creation of most examples of models that are also visualised in our VR lab has been strongly supported by the work of our VR computer scientist, Mr. Philippe Cerfontaine.

References

- Brodlić K, Osorio RA, Lopes A (2012) A review of uncertainty in data visualization. In: Dill J, Earnshaw R, Kasik D, Vince J, Chung Wong J (eds) *Expanding the frontiers of visual analytics and visualization*. Springer, pp 81–109
- Dübel S, Röhlings M, Tominski C, Schumann H (2017) Visualizing 3D terrain, geo-spatial data, and uncertainty. *Informatics* 4(6):1–18

- Garcia-Hernandez RJ, Anthes C, Wiedemann M, Kranzlmüller D (2016) Perspectives for using virtual reality to extend visual data mining in information visualization. In: Aerospace Conference, IEEE, pp 1–11
- Havenith HB, Strom A, Torgoev I, Torgoev A, Lamair L, Ischuk A, Abdrakhmatov K (2015) Tien Shan geohazards database: earthquakes and landslides. *Geomorphology* 249:16–31
- Havenith HB, Torgoev I, Ischuk A (2018) Integrated geophysical-geological 3d model of the right-bank slope downstream from the rogun dam construction site, Tajikistan. *Int J Geophys* 1–16
- Havenith HB, Cerfontaine P, Mreyen AS (2019) How virtual reality can help visualize and assess geohazards. *Int J Digital Earth* 12 (2):173–189
- Jurik V, Herman L, Kubicek P, Stachon S, SaSinkaC (2016) Cognitive aspects of collaboration in 3d virtual environments. In: *The international archives of the photogrammetry, remote sensing & spatial information sciences XLI-B2*, pp 630–670
- Kellogg LH, Bawden GW, Bernardin T, Billen M, Cowgill E, Hamann B, Jadamec M, Kreylos O, Staadt O, Sumner D (2008). Interactive visualization to advance earthquake simulation. *Pure Appl Geophys* 165: 621–633
- Lin H, Chen M, Lu G, Zhue Q, Gong J, You X, Xu Y, Hua M (2013) Virtual geographic environments (VGEs): a new generation of geographic analysis tool. *Earth Sci Rev* 126:74–84
- MacEachren AM, Pike W, YuC BI, Gahegan M, Weaver SD, Yarnal B (2006) Building a geocollaboratory: supporting human-environment regional observatory (HERO) collaborative science activities. *Comput Environ Urban Syst* 30(2):201–225
- Mreyen AS, Demoulin A, Havenith HB (2018) Seismotectonic activity in East Belgium: relevance of a major scarp and two associated landslides in the region of Malmedy. *Geologica Belgica* 21:101–110
- Ondercin M (2016) An exploration of rockfall modelling through gam engines. Ph.D. thesis, Queen's University, Kingston, Ontario, Canada p 51
- Piroton V, Schlögel R, Barbier C, Havenith HB. Monitoring the recent activity of the Koytash landslide (Kyrgyzstan) using radar and optical remote sensing techniques. Submitted to *Geosciences*
- Romano DM, Brna P, Self JA (1998) Collaborative decision-making and presence in shared dynamic virtual environments. In: *Proceedings of the workshop on presence in shared virtual environments (Martlesham Heath: BT Labs)* pp 1–7
- Sword-Daniels V, Eriksen C, Hudson-Doyle EE, Alaniz R, Adler C, Schenk T, Vallance S (2016) Embodied uncertainty: living with complexity and natural hazards. *J Risk Res* 24:1–18
- Westerteiger R (2014) Virtual Reality Methods for Research in the Geosciences. Ph.D. thesis, Technical University Kaiserslautern



A Coupled Discrete Element and Depth-Averaged Model for Flow-Like Landslide Simulations

Xiaoli Su, Xilin Xia, and Qiuhua Liang

Abstract

Flow-like landslides commonly happen in mountainous areas and may cause economic and human life losses in the impacted areas. Computer modelling has become an effective tool for landslide risk assessment and reduction. Models based on discrete element method (DEM) have been widely used for landslide prediction; however, this method is computationally too demanding for large-scale applications. Depth-averaged models (DAMs) have been widely reported for simulating run-out and deposition of flow-like landslides over large spatial domains due to its relatively higher computational efficiency. To combine the advantages of both types of modelling approaches, this work introduces a novel landslide model developed by coupling a DEM model with DAM for simulation of flow-like landslides, in which the DEM is employed in the landslide initiation area to better simulate the failure mechanism of slope, and the DAM is adopted in the landslide runout and deposition phase, where the landslide has developed into flow-like landslide with fluid-like behaviour. Finally, the new coupled model is validated against an experimental test case. Satisfactory results have been obtained, demonstrating that the coupled model is able to accurately capture the detailed dynamics of flow-like landslides.

Keywords

Coupled model • Discrete element method • Depth-averaged model • Flow-like landslide • Granular collapse

Introduction

Landslide such as debris flow, debris avalanche and rock avalanche are common gravity driven granular flows. The granular material often moves at high velocities and travels for long distances in mountainous regions (Iverson and Ouyang 2015), bearing great damaging power that causes severe casualties and significant economic loss (Wei et al. 2019).

Deterministic numerical methods such as limit equilibrium methods (LEMs), continuum approaches and discrete element methods (DEM) have been widely and successfully used for landslide hazard assessment. LEMs are able to quantify the stability of slopes by calculating a safety factor, which is simple and practical to be applied, however, they suffer from the negligence of soil deformation behaviour and the requirement of many assumptions about inter-slice forces (Conte et al. 2014).

With the improvements of both soil constitutive models and computing efficiency, continuum numerical methods such as finite element method (FEM) have been employed in slope stability analysis to study soil deformation behaviour, but it is not well suited for dealing with large deformation and post-failure movements of soils.

To overcome these issues, some alternative numerical tools have been developed. For example, Cundall and Strack (1979) developed the discrete element method (DEM), which is capable of simulating the post-failure movements of granular assemblies, as well as providing an understanding of the mechanical behaviour of landslide materials from a particle-scale point of view (Zhao et al. 2018), thus has been widely used to simulate landslides. However, this method is computationally too demanding (Mirinavicius et al. 2010), thus frequently limited to small-scale simulation.

Observations, both in laboratory and in nature, show granular flows in the downstream are characterized by negligible velocity along the flow depth (Hutter et al. 1995), and therefore it is appropriate for depth-averaged model

X. Su · X. Xia (✉) · Q. Liang
School of Architecture, Building and Civil Engineering,
Loughborough University, Loughborough, UK
e-mail: X.Xia2@lboro.ac.uk

Q. Liang
e-mail: q.liang@lboro.ac.uk

(DAM) to describe granular flow dynamics. DAM provides a good way of assessing landslide run-out as it needs neither a precise knowledge of the mechanical behaviour within the flow nor large amount of computational resources, thus can be applied to real 3D topography (McDougall and Hungr 2004; Mangeney et al. 2000) more easily than fully 3D models. However, DAM has limitations on predicting granular flow behaviour in the region where the material has fully dimensional characteristics of flow dynamics.

Herein we propose a new coupled model to conduct landslide simulation, in which computationally expensive DEM is used only in the landslide initiation region to better simulate the soil failure mechanism, and less time-consuming DAM is adopted in the landslide runout and deposition domain in which the landslide has developed into flow-like landslide with flow characteristics. The significant advantage of the proposed coupled model is that it retains the essential flow characteristics of the granular flow with less computational complexity, which makes it possible to perform more accurate large-scale landslide simulation.

The rest of the paper is organized as follows: Sect. 2 presents the coupled landslide model; the proposed coupled model is then validated by carefully selected test cases in Sect. 3; brief conclusions is finally drawn in Sect. 4.

The Coupled Landslide Model

The coupled landslide is applicable for flow-like landslides, consisting of two main parts, i.e. DEM model and DAM. The DEM model is used in the landslide initiation region to provide spatial description of soil failure mechanics; the DAM is employed in the landslide run-out and deposition zone dominated by convective flow dynamics. During the run-out and deposition phase, the depth of landslide is often much smaller than its horizontal span. As a consequence, the changes of vertical flow velocity are negligible compared with its horizontal velocities.

Discrete Element Method (DEM) Model

For the adopted DEM model, the governing equations for translational motion and rotational motion of particles are given respectively as follows

$$m_i \frac{d\mathbf{V}_i}{dt} = m_i \mathbf{g} + \sum_{j=1}^{k_i} (\mathbf{F}_{c,ij} + \mathbf{F}_{d,ij}) \quad (1)$$

$$I_i \frac{d\boldsymbol{\omega}_i}{dt} = \sum_{j=1}^{k_i} \mathbf{T}_i + \mathbf{M}_i \quad (2)$$

where t is time; m_i is the mass; \mathbf{V}_i is the velocity; \mathbf{g} is the gravity acceleration; $\mathbf{F}_{c,ij}$ and $\mathbf{F}_{d,ij}$ are the contact force and damping force between particle i and j , and these forces are summed over the k_i particles in contact with particle i ; $\boldsymbol{\omega}_i$ is the angular velocity; I_i is the moment of inertia, given by $I_i = \frac{2}{5} m_i R_i^2$. The inter-particle forces acting at the contact point between particle i and j will also cause particle i to rotate and generate a torque \mathbf{T}_i . For a circular particle of radius R_i , \mathbf{T}_i is given by $\mathbf{T}_i = \mathbf{R}_i \times (\mathbf{F}_{ct,ij} + \mathbf{F}_{dt,ij})$, \mathbf{R}_i is a vector from the mass centre of the particle to the contact point. $\mathbf{F}_{ct,ij}$ and $\mathbf{F}_{dt,ij}$ are respectively tangential force and tangential viscous damping force between two particles. \mathbf{M}_i is the inter-particle or particle-wall rolling resistance, which is given by $\mathbf{M}_i = \mathbf{M}_i^k + \mathbf{M}_i^d$ (Ai et al. 2011), \mathbf{M}_i^k is the spring torque and \mathbf{M}_i^d is the viscous damping torque.

Depth-Averaged Model (DAM)

In the depth-averaged model, the granular material is treated as an incompressible Coulomb-type continuum. After depth integration, the fluid properties such as the viscosity and internal friction are packed into a single parameter characterising the friction between the gravel and the terrain at the landslide base (Savage and Hutter 1989).

The depth-averaged equations adopted in this work are modified by Xia and Liang (2018). The matrix form is written as

$$\frac{\partial \mathbf{q}}{\partial t} + \frac{\partial \mathbf{f}(\mathbf{q})}{\partial x} = \mathbf{S}_b + \mathbf{S}_f \quad (3)$$

where the vector terms are given by

$$\mathbf{q} = \begin{bmatrix} h \\ uh \end{bmatrix}, \mathbf{f}(\mathbf{q}) = \begin{bmatrix} u^2 h + \frac{uh}{\varphi^2} \frac{1}{2} g h^2 \end{bmatrix} \quad (4)$$

$$\mathbf{S}_b = \begin{bmatrix} 0 \\ -ah \frac{\partial b}{\partial h} + \frac{1}{2} g h^2 \frac{\partial(1/\varphi^2)}{\partial x} \end{bmatrix}, \mathbf{S}_f = \begin{bmatrix} 0 \\ -\frac{\mu a h u \varphi}{\sqrt{u^2 + (u \frac{\partial h}{\partial x})^2}} \end{bmatrix} \quad (5)$$

with $a = \frac{1}{\varphi^2} \left(g + u^2 \frac{\partial^2 b}{\partial x^2} \right)$, in which $\varphi = \left[\left(\frac{\partial b}{\partial x} \right)^2 + 1 \right]^{\frac{1}{2}}$, where h is the landslide material depth, b is the bed elevation, u is the x -direction depth-averaged velocity, μ is the friction coefficient. The factor of $\frac{1}{\varphi^2}$ describes the effects of complex topography in a Cartesian coordinate system. $u^2 \frac{\partial^2 b}{\partial x^2}$ is used for representing the effect of centrifugal force.

Boundary Conditions at the Coupling Interface

In the coupled model, the coupling takes place at the interface between the DEM model and DAM by considering conservation of mass, in which the boundary conditions of DAM such as flow discharge q and depth h are acquired from the DEM simulation results. As shown in Fig. 1, the particles may be not perfectly aligned to the interface, thus a boundary area is introduced to identify the flow variables along the interface.

The boundary conditions are written as follows

$$h^{IF}(x = x_{IF}) = h^{DEM}(x = x_{IF}) \quad (6)$$

$$q^{IF}(x = x_{IF}) = u^{IF}(x = x_{IF})h^{IF}(x = x_{IF}) \quad (7)$$

where h^{IF} and q^{IF} are the granular depth and discharge in the boundary area recognised as the boundary conditions of DAM; x_{IF} is the interface position; h^{DEM} is gained by averaging the vertical positions of the first three highest particles in the boundary area; u^{IF} is the velocity in the boundary area calculated by considering mass conservation, expressed as

$$u^{IF} = \frac{1}{N} \sum_{i=1}^N u_i^{DEM} + \frac{\Delta m}{\rho_{DAM} h^{IF}} \quad (8)$$

where N is the number of particles in the boundary area; u_i^{DEM} is the velocity of particle i ; ρ_{DAM} is the material density in the DAM, deduced as $\rho_{DAM} = \rho_{DEM}(1 - n_p)$, of which ρ_{DEM} is the density of the DEM particle material, n_p is the porosity of the material in the DAM. The term of $\frac{\Delta m}{\rho_{DAM} h^{IF}}$ is to guarantee the mass conservation, in which Δm is presented as $\Delta m = m_t^{DEM} - m_t^{DAM}$. m_t^{DEM} is the actual mass of particles feeding into the DAM region from the DEM region, denoted as $m_t^{DEM} = \sum_{i=1}^{N_0} m_i$, and m_i is the mass of the particle i , expressed as $m_i = \rho_{DEM} \pi R_i^2$, of which R_i is the radius of particle i , N_0 is the number of particles coming

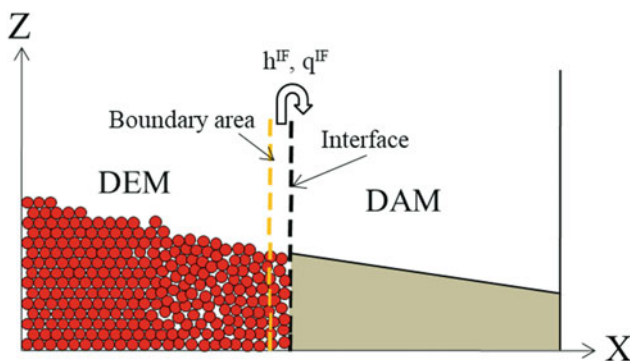


Fig. 1 Schematic of boundary conditions at the interface between the DEM and the DAM

into the DAM in the simulation time t . m_t^{DAM} is the mass of flow calculated by the interface boundary conditions, expressed as

$$m_t^{DAM} = \int_0^t \rho_{DAM} h^{IF} u^{IF} \quad (9)$$

where t is the simulation time. If $\Delta m > 0$, it means that the mass of material feeding into the DAM region is larger than the mass calculated through boundary condition in DAM, so Δm is added to m^{DAM} by increasing the velocity u^{IF} at the next time step; if $\Delta m < 0$, it means that the mass calculated by boundary conditions in DAM is larger than the actual mass coming into the DAM region, so Δm is deducted from m^{DAM} by decreasing the velocity u^{IF} at the next time step.

Model Validation and Result

In this section, and coupled model presented in the previous section are validated against an experimental test case.

Experiment of Dam-Break Granular Column Collapse

Lajeunesse et al. (2005) conducted a series of experiments on granular material collapse. In their experiments, as illustrated in Fig. 2, particles are inserted randomly into the reservoir to form a loosely packed column. The granular pile is released by quick lifting of the sliding gate, and then the granular particles spread along the horizontal plane until came to rest. The angle of response is 13.93° . The reason for choosing this experiment is that by analysing and comparing the process of granular material collapse from the experiment and different models, the added value of the coupled model for simulating granular collapse can be demonstrated.

As presented in Fig. 3, the interface between the DEM and DAM is set at the position x where $x/L_i = 2.45$. The material profiles with non-dimensionalised flow height (h/L_i) and length (x/L_i) of different models are measured at different times proportional to characteristic time τ_c . The characteristic time τ_c is expressed as $\tau_c = \sqrt{H_i/g}$, corresponding to the free-fall time of the granular material. In the measurement of granular profile in the DEM, the particles separated from the main portion of granular material are not considered.

Figure 3 shows that the simulation results of the DEM and coupled model are generally consistent with the experimental results, which highlights that both the coupled model and the DEM can provide accurate prediction of the run-out distance and run-out durations, as well as

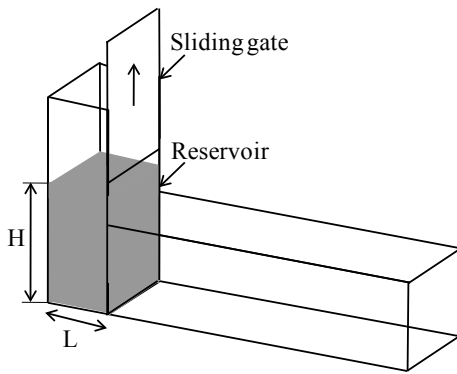


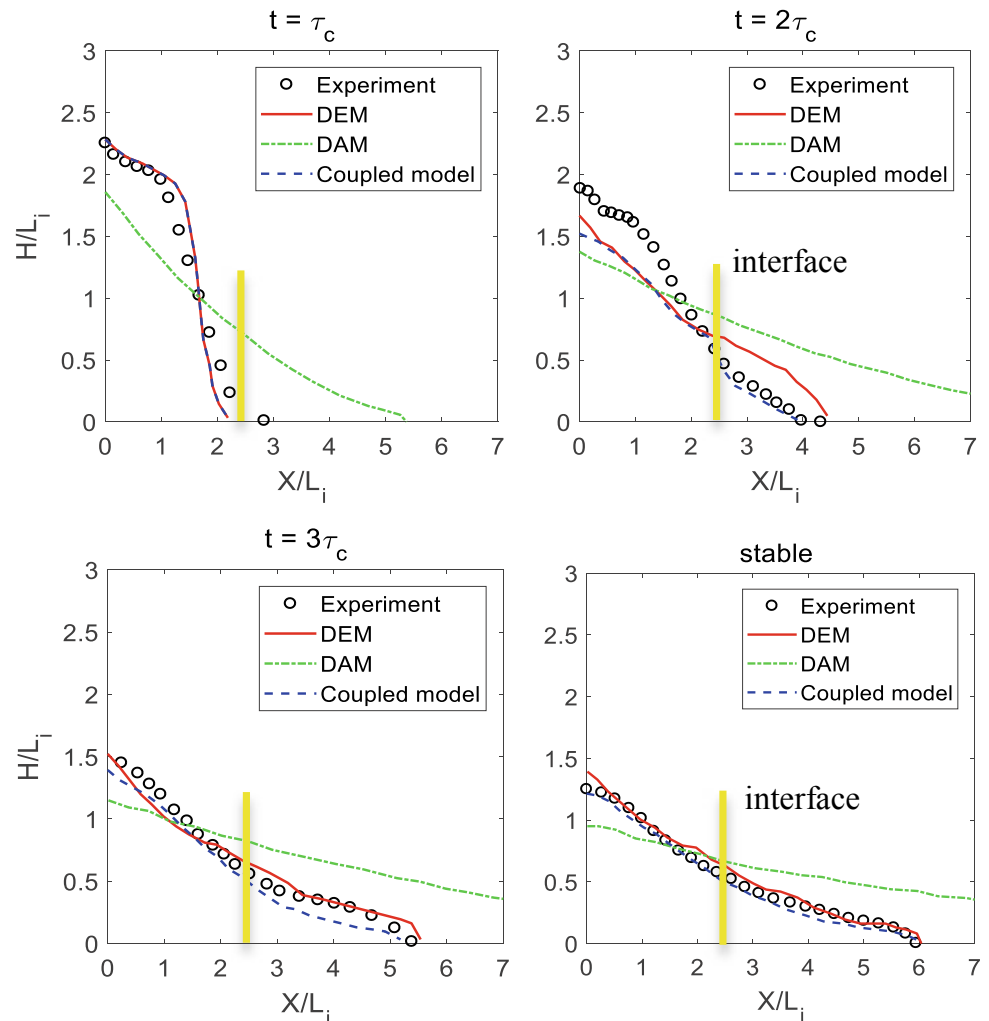
Fig. 2 Schematic of dam-break like granular material collapse

deposit morphology. In contrast, the material collapse simulated by the DAM only is not in line with the experimental results. The granular material moves more quickly and comes to rest earlier than the other two

models and the experiment. This may be because the DAM neglects the vertical momentum damping at the region of landslide initiation and thus gains bigger horizontal momentum. In addition, the whole simulation takes 200 s in the DEM model, and it is 144 s in the coupled model on the same machine. This indicates that the coupled model saves 28% computing time and is more computationally efficient compared with DEM model. The gain of efficiency is expected to be more substantial for real-world cases, where the DAM constitutes a much larger proportion of the whole domain.

There exists a general trend in Fig. 3 that the DEM results and the coupled model results converges to the experimental observation as time goes on. At the time of $t = \tau_c$ and $t = 2\tau_c$, there is a slight difference between the DEM results, coupled model results and experimental results, which may be caused by the difference in particle packing patterns in the initial settings. Although particles are randomly inserted into the reservoir to finally form a loosely packed granular

Fig. 3 Sequences of scaled profiles of granular collapse interface



column both in the experiment and DEM, the initial settings of particles are still not identical. As the granular material collapse keeps going, the effect of initial setting of particles on the granular flow dynamics diminishes. As a result, the numerical simulations converge to the experiment as the granular flow further develops.

At $t = 2\tau_c$ and $t = 3\tau_c$, the flow depth predicted by the coupled model is smaller than that by the DEM. This is mainly because in the coupled model, DAM considers flow-like granular materials as continuous matter and therefore the void ratio is minimised as like densely packed material. However, DEM discretize the material as particles and there exists additional void between particles because of collisions between particles when the granular material collapses. The additional void between particles lead to a difference on the flow depth between the DEM and coupled model. After the particle movement come into a steady state, there is little additional void between particles and the granular material profile gained from the DEM and coupled model are consistent.

Conclusion

This paper demonstrates that the newly developed landslide model is a potential alternative, with high efficiency and good predictive capabilities, to conventional methods for the simulation of large-scale landslides. The new landslide model is developed by coupling the DEM model and DAM, in which DEM analyses the failure dynamics of soils in the landslide initiation zone and also provides boundary conditions for the DAM to simulate the overall flow dynamics in the downstream area such as the landslide runout and deposition zone where the predominant advective landslide dynamics have been well developed. This longitudinal coupling strategy reduces the spatial complexity of the landslide simulation and thus significantly increases the computational efficiency.

The experiment of dam-break like granular collapse is employed to validate the coupled model. Satisfactory

solution has been obtained, which confirms the simulation capability of the coupled landslide model.

Acknowledgements The first author is sponsored by Loughborough University and the China Scholarship Council.

References

- Ai J, Chen JF, Michael Rotter J, Ooi JY (2011) Assessment of rolling resistance models in discrete element simulations. *Powder Technol* 206(3):269–282
- Conte E, Donato A, Troncone A (2014) A finite element approach for the analysis of active slow-moving landslides. *Landslides* 11(4):723–731
- Cundall PA, Strack ODL (1979) A Discrete numerical model for granular assemblies. *Geotechnique* 29(1):47–65
- Hutter K, Koch T, Pluüss C, Savage SB (1995) The Dynamics of avalanches of granular materials from initiation to runout. Part II. Experiments. *Acta Mech* 109(1–4):127–165
- Iverson RM, Ouyang C (2015) Entrainment of bed material by earth-surface mass flows: review and reformulation of depth-integrated theory. *Rev Geophys* 53:27–58
- Lajeunesse E, Monnier JB, Homsy GM (2005) Granular slumping on a horizontal surface. *Phys Fluids* 17(10)
- Mangeney A, Heinrich P, Roche R (2000) Analytical solution for testing debris avalanche numerical models. *Pure Appl Geophys* 157(6–8):1081–1096
- McDougall S, Hungr O (2004) A model for the analysis of rapid landslide motion across three-dimensional terrain. *Can Geotech J* 41(6):1084–1097
- Mirinavicius A, Markauskas D, Kacianauskas R (2010) Computational performance of contact search during dem simulation of hopper filling. In: 10th international conference modern building materials, structures and techniques, June 2014, pp 974–979
- Savage SB, Hutter K (1989) The motion of a finite mass of granular material down a rough incline. *J Fluid Mech* 199(2697):177–215
- Wei Z, lei, Qing Lü, Hong yue Sun, and Yue quan Shang. (2019) Estimating the rainfall threshold of a deep-seated landslide by integrating models for predicting the groundwater level and stability analysis of the slope. *Eng Geol* 253(March):14–26
- Xia X, Liang Q (2018) A new depth-averaged model for flow-like landslides over complex terrains with curvatures and steep slopes. *Eng Geol* 234:174–191
- Zhao S, Evans TM, Zhou X (2018) Effects of curvature-related DEM contact model on the macro- and micro-mechanical behaviours of granular soils. *Geotechnique* 68(12):1085–1098



2020 Kyoto Japan

Advanced Methods for Simulating Complex Landslides

Martin Mergili and Shiva P. Pudasaini

Abstract

Anticipation of complex cascading landslides, important to inform risk management, requires the use of advanced modelling approaches. Such approaches have become increasingly available during the last decade, and have been successfully applied for the back-calculation of well-documented test cases. These back-calculations have helped to identify the needs for further research in terms of making reliable predictive simulations possible. This paper summarizes the key challenges in doing so as well as the resulting ongoing and planned model enhancements. Thereby, the focus is put on the propagation and interaction of flow processes. The main challenges are related to the understanding of the physical processes, the numerical implementation, and model parameterization. Some important needs for enhancement are the better representation of (1) landslide-reservoir interactions and (2) entrainment, deposition, and stopping; (3) an improved numerical scheme; (4) consideration of “slow motion”; (5) interfaces to fall models; (6) guiding parameter sets; and (7) the dynamic adaptation of key parameters to flow dynamics. Further important issues, which are not the focus of this work, are landslide triggering and release as well as the communication of uncertain model results.

Keywords

Cascading landslide processes • Multi-phase mass flows • Numerical simulation • R.avaflow

Introduction

Complex—particularly cascading—landslide processes have repeatedly led to major disasters in history, particularly in glacierized high-mountain areas (Haerberli et al. 2004; Huggel et al. 2005; Evans et al. 2009a, b). Figure 1 illustrates some examples of cascading landslide processes in high-mountain areas. The anticipation of such processes is a key requirement for disaster prevention. Such an anticipation has, on the one hand, to build on detailed field and remote sensing investigations and monitoring of potentially hazardous situations. On the other hand, it has to build on computer models, whereby the triggering (e.g. by seismic activity or rainfall), the release (slope failure, dam break, etc.), the dynamic motion, and the interaction with society (exposure, vulnerability, risk) represent the most important components. In the present work, we focus on the simulation of the dynamic motion of cascading landslide processes, thereby mainly considering flow-type phenomena such as avalanches and flows of snow, ice, rock fragments, debris, water, and different types of mixtures thereof as well as process interactions. Mass flow models go back to Voellmy (1955), who has first described the dynamics of flow-like gravitational processes in mountain areas, as a response to the disastrous snow avalanches which happened in the winter of 1954 in parts of the European Alps. Thereafter, progress has been slow. Even though the Voellmy (1955) model has been refined, extended, and complemented and other, more advanced approaches, have been developed (e.g. Savage and Hutter 1989; Iverson 1997; Pitman and Le 2005), the most used software tools in debris flow risk management practice such as RAMMS (Christen et al. 2010)

M. Mergili (✉)

Cascade - Mountain Processes and Mountain Hazards, Institute of Geography and Regional Science, University of Graz, Heinrichstraße 36, 8010 Graz, Austria
e-mail: martin.mergili@uni-graz.at

Institute of Applied Geology, University of Natural Resources and Life Sciences (BOKU), Peter-Jordan-Straße 82, 1190 Vienna, Austria

S. P. Pudasaini

Geophysics Section, Institute of Geosciences, University of Bonn, Meckenheimer Allee 176, 53115 Bonn, Germany
e-mail: pudasaini@geo.uni-bonn.de

© Springer Nature Switzerland AG 2021

B. Tiwari et al. (eds.), *Understanding and Reducing Landslide Disaster Risk*, ICL Contribution to Landslide Disaster Risk Reduction, https://doi.org/10.1007/978-3-030-60706-7_18

still employ, at least in parts, Voellmy-type approaches, considering mixture flows of water and debris, instead of accounting separately for each phase. This strategy is useful for many purposes, as the models are kept as simple as possible, and the number of model parameters as low as possible. However, this type of models fails to reproduce more complex, cascading processes, where initial landslides interact with glaciers or lakes, and develop into far-reaching flow processes. Such phenomena require either model chains, where each model component is tailored exactly for the purpose it serves for (Schneider et al. 2014; Somos-Valenzuela et al. 2016), or two- or multi-phase models, considering each phase separately, making it possible to directly account for complex process interactions.

Worni et al. (2014) have raised the call for integrated models. Major progress has been made in this regard after the two-phase model of Pudasaini (2012) and the multi-phase model of Pudasaini and Mergili (2019) had been developed, and included in the open source GIS tool r.avaflow (Mergili et al. 2017; Mergili and Pudasaini 2020). This approach considers different phases (solid, fine solid, and fluid) separately, but with strong coupling, and is therefore capable to simulate complex interactions between landslides, glaciers, and lakes. It has been applied to various test cases (Mergili et al. 2018a, b, 2020a; b; Gylfadóttir et al. 2019). These case studies have helped in highlighting the huge potential of using complex multi-phase flow models, but also in identifying the major remaining challenges.

The main aim of the present work is to summarize the main challenges particularly in terms of predictive simulations, in order to build a sound basis for future improvement of the multi-phase flow model and its implementation in the tool r.avaflow. Thereby, some of the most important needs for enhancement are highlighted, most of them related to work in progress.

Methods

The main method applied for this work is the comparative analysis of the results of previous case studies performed with the tool r.avaflow, based on the Pudasaini (2012) two-phase flow model and the Pudasaini and Mergili (2019) multi-phase flow model (Mergili et al. 2018a, b, 2020a, b; Gylfadóttir et al. 2019), and the identification of challenges and needs for further development in the direction of application of this computational tool for predictive simulations in terms of risk management.

Results

Challenges

One of the key findings of several case studies is the fact that r.avaflow can be successfully applied for the

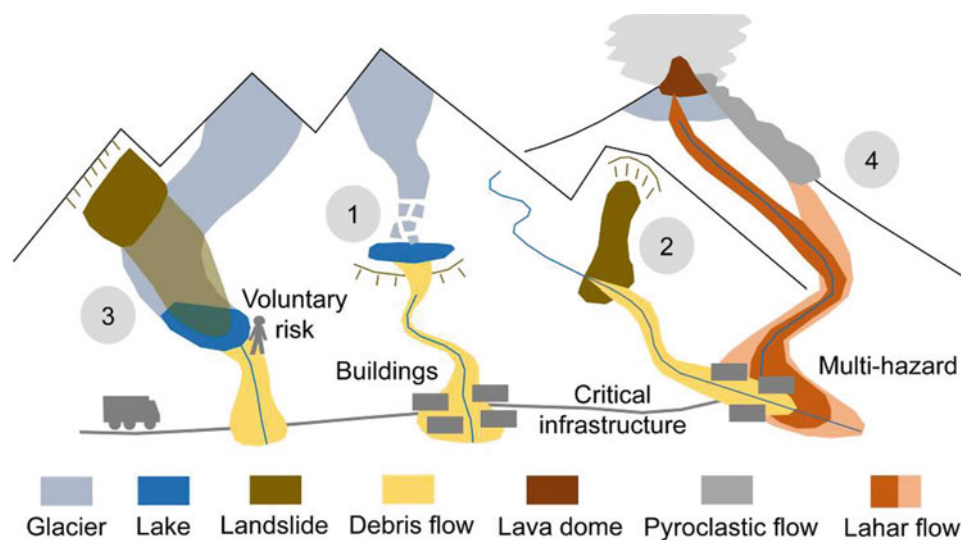


Fig. 1 Schematic illustration of selected examples of high-mountain landslide cascades. 1 = Ice avalanche impacting a lake, leading to overtopping of the moraine dam, erosion processes, and a debris flow downstream. 2 = Landslide impounding a river. Overtopping and erosion of this landslide dam results in a debris flow downstream. 3 = A landslide hits a glacier and triggers a rock-ice avalanche which impacts a proglacial lake. Again, overtopping of the dam results in

flooding or a debris flow downstream. 4 = Explosive volcanic activity with pyroclastic flow and lahar flows triggered by lava dome collapse and rapid melting of the glacier. Note that, in this example, synchronous occurrence of 2 and 4 would result in a complex multi-hazard situation. Impacts of all four cascades on society might occur directly, but also indirectly through the disruption of critical infrastructure

back-calculation of even very complex events. However, such back-calculations rely on case-specific parameter optimization efforts. The optimized parameter sets work for the event under consideration, but may fail for other events. This was most drastically shown by Mergili et al. (2018b) for the 1962 and 1970 Huascarán events, where the optimized parameter sets for either of the two landslides failed to serve for the adequate prediction of the other event. Particularly, the simulation of an important threshold effect (overtopping of a ridge) turned out as a major challenge. This means that predictive simulations—and therefore the anticipation of the dynamics of future events—remains a challenge. The reasons for such model failure are manifold, with the most important aspects summarized as follows:

- (1) Lacking physical understanding of the processes: randomly or iteratively optimizing the parameter set might lead to combinations which, by chance, lead to empirically adequate results, but are not necessarily physically correct. This phenomenon is known as equifinality, meaning that completely different parameter combinations lead to similar model results (Beven 1996).
- (2) Limitations in the numerical implementation of the physical model into the software. *r.avaflo* applies the TVD-NOC numerical scheme (Nessyahu and Tadmor 1990; Tai et al. 2002; Wang et al. 2004) which was not designed for bounded flows.
- (3) Spatial variation of the key model parameters: surface and sediment characteristics often show fine-scaled patterns which are challenging to represent in a model.

Further, *r.avaflo* is limited to rapid flow-like processes, and fails to adequately simulate slower phenomena as well as fall or slide processes.

Enhancements

Based on the challenges identified, we try to highlight seven of the most important and pressing needs for making complex mass flow models—particularly *r.avaflo*—fit for use in risk management contexts:

- (1) Better representation of landslide-reservoir interactions. Results for Lake Palcacocha in Peru (Mergili et al. 2019) have revealed that the evolution of impact waves due to landslides entering a lake is underestimated. One reason for this shortcoming can be identified in the insufficient consideration of the consequences of the relevant dynamic interactions: on the one hand, gravity has to be considered in an enhanced way whereas, on the other hand, dispersion of water in the impacted lake

has to be considered explicitly. Even though various authors have previously considered such non-hydrostatic effects (e.g. Denlinger and Iverson 2004; Castro-Orgaz et al. 2015; Yuan et al. 2018), their adequate implementation in operational simulation models still remains a challenge. Preliminary tests considering those non-hydrostatic influences on real-world case studies were promising (Fig. 2), even though their full consideration represents a challenge in terms of numerical implementation (Pudasaini 2020).

- (2) Better representation of entrainment, deposition, and stopping. Entrainment is considered following an empirical approach, where an entrainment coefficient is multiplied with the momentum or the kinetic energy of the flow at a given raster cell in order to derive the entrainment rate. Considering entrainment a threshold phenomenon, as it is done in various other models,

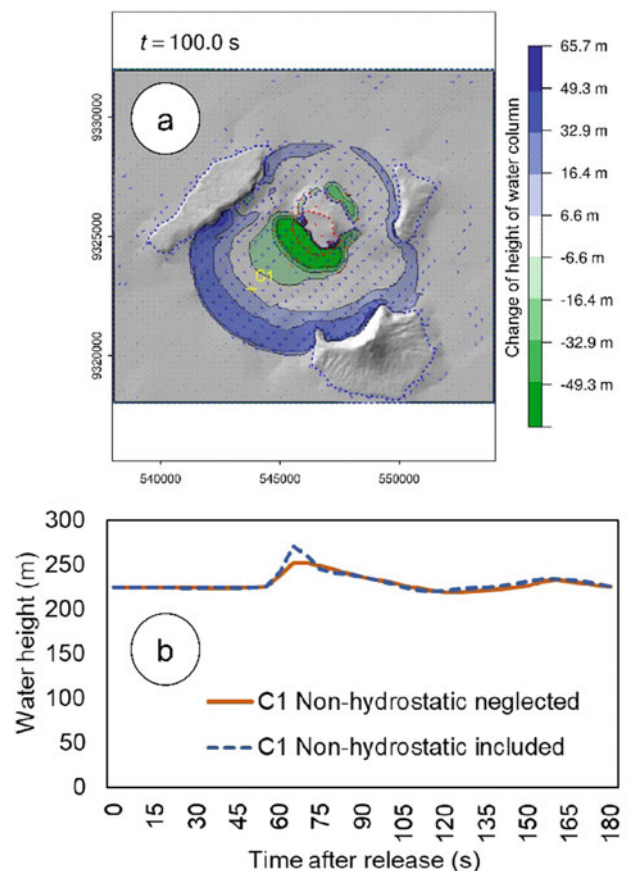


Fig. 2 Influence of non-hydrostatic effects on a preliminary, not yet evaluated simulation of the tsunami triggered by the 2018 Anak Krakatau volcanic collapse. **a** Change of height of the water column after $t = 100$ s; **b** evolution of the height of the water column at control point C1 without and with the influence of non-hydrostatic effects. It is clearly seen that the consideration of these effects result in a higher simulated tsunami peak. Data sources: GEBCO and ALOS PALSAR for the terrain; information provided in Grilli et al. (2019) for the landslide dimensions

requires threshold parameters which are often poorly known. Advanced physically-based models for entrainment do exist (Pudasaini and Fischer 2016). However, though built on a sound physical basis, this approach still has to be made ready for practical application. The Pudasaini and Fischer (2016) model also considers deposition of flow material. However, the same as said for entrainment is true here. There is still a long way from the currently used empirical and simple physically-based models for deposition and stopping to an approach which is advanced enough to account for the complexity of the processes, but simple enough to be ready for practical applications.

- (3) Improved numerical scheme. The current implementation of *r.avaflow* (Mergili and Pudasaini 2020) uses a number of complementary functions such as diffusion control (Mergili et al. 2017), which are imposed upon the NOC-TVD numerical scheme (Nessyahu and Tadmor 1990; Wang et al. 2005). Diffusion control is used to manage the dynamics at the edges of the flow, which is not handled in a completely satisfactory way by the scheme in use. The development of a new, more appropriate scheme, where all relevant issues are implicitly and directly considered, should be given high priority.
- (4) Consideration of “slow motion”. Though not directly life-threatening, the consideration of very slow movements, such as viscous earth flows or even the growth of lava domes, sometimes represents an important component in the simulation of complex process chains. Such processes are disregarded in most flow models but, in terms of their physical principle, can be simulated as soon as viscosities are considered, as it is the case in *r.avaflow* (Pudasaini and Mergili 2019). In order to avoid excessive computational times, time scaling has to be applied, for example, to viscosity. First results produced on the growth of lava domes have been promising, but further tests against real-world data are required to finally evaluate the time scaling.
- (5) Interfaces to fall models. Whereas flow models, through appropriate parameterization, can to some extent be employed to simulate processes with limited internal deformation of the moving mass (i.e. slide-like movements), they cannot be used for the simulation of fall processes, which follow completely different physical principles. Here, it is necessary to make use of model chains, by coupling models such as *r.avaflow* to fall models such as *Rockyfor3D* (Dorren and Berger 2010). For this purpose, suitable interfaces have to be created in order to ensure efficient work flows. Even more importantly, the identification of the point in space and time where to change from one process/model to the other is a key issue of coupling. Further, it is important to use suitable parameters for the definition of this critical point (Marlovits et al. 2020).
- (6) Guiding parameter sets for different process types and magnitudes. For most model parameters, it is almost impossible to determine physically “true” values which can be directly used for predictive simulations. Reasons are the fine-scaled spatial patterns of some parameters, and the impossibility to measure them at all (e.g. basal friction). Therefore, one of the key requirements is the availability of empirically derived parameter sets for processes of different types and magnitudes, which are robust enough to serve for predictive simulations. Such parameter sets have to be based on a large number of back-calculations of well-documented case studies. They should also be differentiated according to the local geomorphologic conditions. Further, parameter ranges will be more useful than values, in order to account for uncertainties, but also for the natural variability of the parameters. Such ranges can be used for building scenarios or for the computation of likelihoods such as the impact indicator index (Mergili et al. 2017). The case studies presented by Mergili et al. (2018a, b, 2020a, b; Gylfadóttir et al. 2019) will provide an important contribution to the derivation of guiding parameter values and ranges, but more studies are still required. Thereby, automated parameter optimization and sensitivity analysis tools can be useful (Kofler et al. 2019).
- (7) Dynamic adaptation of model parameters. Model parameters such as internal friction, basal friction, or fluid friction cannot necessarily be described through static values, but evolve with the dynamics of the landslide. Fluidization and lubrication effects of very rapid flows may greatly decrease the basal friction angle (Pudasaini and Krautblatter 2014). Appropriate relationships which account for such effects have to be defined, in order to more realistically simulate cascading mass flow processes, and to replace the somewhat arbitrary zonal differentiation of parameters, as applied in previous studies (Mergili et al. 2018a, b, 2020a, b; Gylfadóttir et al. 2019). Preliminary simulations using exponential relationships between the friction parameters were promising, but have to be further developed. Earlier studies have already tried to adapt friction parameters to flow dynamics, such as the work of Buser and Bartelt (2009), who employed the concept of random kinetic energy.

Discussion

The present work focuses on some of the most pressing needs for further improving our possibilities to simulate the propagation of cascading landslide processes, considering the physical model equations, their numerical implementation, and the parameterization. Thereby, we focus on the r.avaflow tool which is, to our knowledge, the most advanced and the most comprehensive open source mass flow simulation tool to date, and which is actively developed. However, most of the issues addressed in the results chapter are equally valid for any other relevant simulation tools. The issues highlighted in the present work concern only the computational side. The comprehensive anticipation of cascading landslide processes and their consequences, however, needs to consider more than just propagation, an issue that shall briefly be discussed.

On the one hand, process initiation has to be understood and simulated in an adequate way. Detailed knowledge on potentially hazardous situations, their evolution in time, and their sensitivity to different types and magnitudes of potential triggering events—obtained through field- and remote-sensing-based investigations and continuous monitoring—represents an essential basis for reliable simulations. When applying GIS-based slope stability models, it has to be considered that they usually predict a patchy pattern of the slope stability conditions which is hard to translate into discrete mass flow release areas. As a consequence, appropriate strategies for coupling are required. The most advanced approach was suggested by Bout et al. (2018), who introduced the software tool openLISEM to couple a hydraulic model with a slope stability model and a runout model.

On the other hand, the translation of model results into information useful for risk management is a tricky issue, particular in the case that the results are uncertain (as they always are). Model results are not true in a strict sense, but they can create subjective truth in the minds of stakeholders or possibly affected people. It remains a broad field of research how to tackle the multiple pitfalls emanating from the communication of uncertain model results of hazardous processes to stakeholders and to the public.

Conclusions

In the present work, we have summarized the main progress and challenges for the predictive simulation of complex, cascading landslide processes. Thereby, we have focused on mass flow propagation, and on the open source computational tool r.avaflow. The main challenges concern the physical models (landslide-reservoir, interactions,

entrainment, deposition, stopping), the numerical implementation of these models (appropriate treatment of the flow boundaries and of slow motion), and the parameterization (derivation of guiding parameter values or ranges, and adaptation of the key flow parameters to flow dynamics). Promising approaches have been found for most of these aspects, but further research is essential. However, it is not only the propagation which is important for the anticipation of the processes and the use of the results for risk management, but also the appropriate consideration of the “upper” and the “lower” parts: transferring potentially hazardous situations into the release of mass flows, and communicating uncertain results in an appropriate way.

Acknowledgements We acknowledge the financial support by the German Research Foundation (DFG) through the research project PU 386/5-1: “A novel and unified solution to multi-phase mass flows”. Also, the authors would like to thank Matthias Benedikt for technical support.

References

- Beven K (1996) Equifinality and uncertainty in geomorphological modelling. In: *The scientific nature of geomorphology: proceedings of the 27th binghamton symposium in geomorphology*, 27–29 September 1996, Wiley. pp 289–313
- Buser O, Bartelt P (2009) Production and decay of random kinetic energy in granular snow avalanches. *J Glac* 55:3–12
- Castro-Orgaz O, Hutter K, Giraldez JV, Hager WH (2015) Nonhydrostatic granular flow over 3-D terrain: New Boussinesq-type gravity waves? *J Geophys Res Earth Surf* 120:1–28
- Christen M, Kowalski J, Bartelt B (2010) RAMMS: numerical simulation of dense snow avalanches in three-dimensional terrain. *Cold Reg Sci Technol* 63:1–14
- Denlinger RP, Iverson RM (2004) Granular avalanches across irregular three-dimensional terrain: 1. Theory and computation. *J Geophys Res* 109(F1)
- Dorren L, Berger F (2010) New approaches for 3D rockfall modelling with or without the effect of forest in Rockyfor3D. *Geophys Res Abstr* 12, EGU General Assembly, Vienna, Austria, 2010, p 14811
- Evans SG, Bishop NF, Smoll LF, Murillo PV, Delaney KB, Oliver-Smith A (2009a) A re-examination of the mechanism and human impact of catastrophic mass flows originating on Nevado Huascarán, Cordillera Blanca, Peru in 1962 and 1970. *Eng Geol* 108:96–118
- Evans SG, Tutubalina OV, Drobyshev VN, Chernomorets SS, McDougall S, Petrakov DA, Hungr O (2009b) Catastrophic detachment and high-velocity long-runout flow of Kolka Glacier, Caucasus Mountains, Russia in 2002. *Geomorphology* 105:314–321
- Grilli ST, Tappin DR, Carey S, Watt SF, Ward SN, Grilli AR, Engwell SL, Zhang C, Kirkby JT, Muin M (2019) Modelling of the tsunami from the December 22, 2018 lateral collapse of Anak Krakatau volcano in the Sunda Straits, Indonesia. *Sci Rep* 9 (1):11946
- Gylfadóttir SS, Mergili M, Jóhannesson T, Helgason JK, Sæmundsson Þ, Fischer J-T, Pudasaini SP (2019) A three-phase mass flow model applied for the simulation of complex landslide–glacier–lake interactions in Iceland. *Geophys Res Abstr* 21, EGU General Assembly, Vienna, Austria, 7–12 April 2019, p 13482

- Haeberli W, Huggel C, Kääb A, Zraggen-Oswald S, Polkvoj A, Galushkin I, Zotikov I, Osokin N (2004) The Kolka-Karmadon rock/ice slide of 20 September 2002: an extraordinary event of historical dimensions in North Ossetia, Russian Caucasus. *J Glac* 50:533–546
- Huggel C, Zraggen-Oswald S, Haeberli W, Kääb A, Polkvoj A, Galushkin I, Evans SG (2005) The 2002 rock/ice avalanche at Kolka/Karmadon, Russian Caucasus: assessment of extraordinary avalanche formation and mobility, and application of QuickBird satellite imagery. *Nat Haz Earth Syst Sci* 5:173–187
- Iverson RM (1997) The physics of debris flows. *Rev Geophys* 35 (3):245–296
- Kofler A, Huber A, Fellin W, Mergili M, Oberguggenberger M, Fischer J-T (2019) Bayesian inference in snow avalanche simulation with r.avaflow. Geosciences, submitted manuscript
- Marlovits N, Mergili M, Preh A, Glade T (2020) A criteria-set for the construction of a model cascade for fall-to-flow landslide chains. *Geophys Res Abstracts* 22, EGU General Assembly, Vienna, Austria, 3–8 May 2020, p 7363
- Mergili M, Pudasaini SP (2020) r.avaflow—the open source mass flow simulation model. <https://www.avaflow.org/>. Accessed 12 March 2020
- Mergili M, Fischer JT, Krenn J, Pudasaini SP (2017) r.avaflow v1, an advanced open source computational framework for the propagation and interaction of two-phase mass flows. *Geosci Model Dev* 10:553–569
- Mergili M, Emmer A, Juřicová A, Cochachin A, Fischer J-T, Huggel C, Pudasaini SP (2018a) How well can we simulate complex hydro-geomorphic process chains? The 2012 multi-lake outburst flood in the Santa Cruz Valley (Cordillera Blanca, Perú). *Earth Surf Process Landf* 43:1373–1389
- Mergili M, Frank B, Fischer J-T, Huggel C, Pudasaini SP (2018b) Computational experiments on the 1962 and 1970 landslide events at Huascarán (Peru) with r.avaflow: lessons learned for predictive mass flow simulations. *Geomorphology* 322:15–28
- Mergili M, Jaboyedoff M, Pullarello J, Pudasaini SP (2020a) Back-calculation of the 2017 Piz Cengalo-Bondo landslide cascade with r.avaflow. *Nat Hazards Earth Syst Sci* 20:505–520
- Mergili M, Pudasaini SP, Emmer A, Fischer J-T, Cochachin A, Frey H (2020b) Reconstruction of the 1941 multi-lake outburst flood at Lake Palcacocha (Cordillera Blanca, Perú). *Hydrol Earth Syst Sci* 24:93–114
- Nessyahu H, Tadmor E (1990) Non-oscillatory central differencing for hyperbolic conservation laws. *J Comput Phys* 87:408–463
- Pitman EB, Le L (2005) A two-fluid model for avalanche and debris flows. *Philos Trans R Soc A* 363:1573–1601. <https://doi.org/10.1098/rsta.2005.1596>
- Pudasaini SP (2020) A non-hydrostatic multi-phase mass flow model. Manuscript in progress
- Pudasaini SP (2012) A general two-phase debris flow model. *J Geophys Res Earth Surf* 117:F03010
- Pudasaini SP, Fischer JT (2016) A mechanical erosion model for two-phase mass flows. [arXiv:1610.01806](https://arxiv.org/abs/1610.01806)
- Pudasaini SP, Krautblatter M (2014) A two-phase mechanical model for rock-ice avalanches. *J Geophys Res Earth Surf* 119:2272–2290
- Pudasaini SP, Mergili M (2019) A multi-phase mass flow model. *J Geophys Res Earth Surf* 124(12):2920–2942
- Savage SB, Hutter K (1989) The motion of a finite mass of granular material down a rough incline. *J Fluid Mech* 199:177–215
- Schneider D, Huggel C, Cochachin A, Guillén S, García J (2014) Mapping hazards from glacier lake outburst floods based on modelling of process cascades at Lake 513, Carhuaz, Peru. *Adv Geosci* 35:145–155
- Somos-Valenzuela MA, Chisolm RE, Rivas DS, Portocarrero C, McKinney DC (2016) Modeling a glacial lake outburst flood process chain: the case of Lake Palcacocha and Huaráz, Peru. *Hydrol Earth Syst Sci* 20:2519–2543
- Tai YC, Noelle S, Gray JMNT, Hutter K (2002) Shock-capturing and front-tracking methods for granular avalanches. *J Comput Phys* 175:269–301. <https://doi.org/10.1006/jcph.2001.6946>
- van den Bout B, Lombardo L, van Westen CJ, Jetten VG (2018) Integration of two-phase solid fluid equations in a catchment model for flashfloods, debris flows and shallow slope failures. *Environ Model Softw* 105:1–16
- Voellmy A (1955) Über die Zerstörungskraft von Lawinen. *Schweizerische Bauzeitung* 73:159–162, 212–217, 246–249, 280–285
- Wang Y, Hutter K, Pudasaini SP (2004) The Savage-Hutter theory: a system of partial differential equations for avalanche flows of snow, debris, and mud. *ZAMM. J Appl Math Mech* 84(8):507–527
- Worni R, Huggel C, Clague JJ, Schaub Y, Stoffel M (2014) Coupling glacial lake impact, dam breach, and flood processes: a modeling perspective. *Geomorphology* 224:161–176
- Yuan L, Liu W, Zhai J, Wu SF, Patra AK, Pitman EB (2018) Refinement on non-hydrostatic shallow granular flow model in a global Cartesian coordinate system. *Comput Geosci* 22:87–106



2020 Kyoto Japan

Application of Reciprocal Green's Functions on the Forecast of Submarine Landslide Tsunamis

Guan-Yu Chen, Chin-Chih Liu, and Yi-Fung Wang

Abstract

Recent submarine mass failures that generated tsunami have caused people to pay more attention because of the resultant casualties. A submarine landslide tsunami requires more computer time for the simulation because of the high spatial resolution and associated short time steps even though the computational domain is smaller than that of a seismic tsunami. To reduce the resources to forecast tsunamis, reciprocal Green's functions have been proposed and the forecast results are verified by comparing with direct numerical simulations of a tsunami model COMCOT. However, due to features different to seismic tsunamis, some precautions should be taken in applying this approach in submarine landslide tsunamis. Possible solutions to overcome difficulties using this approach are also recommended. Finally, suggestions based on reciprocal Green's functions are advanced to build a practical forecast system for submarine landslide tsunamis.

Keywords

Submarine mass failure • Reciprocal Green's function • Submarine landslide tsunami • Tsunami forecast

Application of Reciprocal Green's Functions in Submarine Landslide Tsunamis

It has long been known that landslide can generate big tsunamis. In the last few decades, some tsunami events after earthquakes were bigger than the tsunami height estimated

G.-Y. Chen (✉) · C.-C. Liu
Department of Oceanography, National Sun Yat-Sen University,
Kaohsiung, 80424, Taiwan
e-mail: guanyu@faculty.nsysu.edu.tw

Y.-F. Wang
Water Resources Agency, MOEA, Taipei, 10651, Taiwan
e-mail: fluidwang@gmail.com

with the earthquake magnitude. For the 1998 Papua New Guinea tsunami (Tappin et al. 2001), 2007 Chilean tsunami (Sepúlveda et al. 2010) and 2018 Sulawesi tsunami (Heidarzadeh et al. 2018), the submarine earthquake was not considered strong enough for a big tsunami. These events all occurred after earthquakes and are believed to be generated by submarine mass failures (SMFs) triggered by the strong co-seismic ground motion in submarine earthquakes.

Besides these recent events, some historical events are also believed to be the result of SMF. The mysterious tsunami that struck the southwest coast of Taiwan (Li et al. 2015) is an example, which will be simulated later as an example in the present study. Historical tsunami events in Grand Banks, Canada (Leonard et al. 2014), Mexico (Corona and Ramírez-Herrera 2015), Mediterranean Sea (Yalciner et al. 2014) and many other places have been considered to be the result of SMF tsunamis as well.

On top of that, submarine landslides in Nuuanu, Storegga, Currituck, Brunei and Currituck each had displacements more than one thousand km³ in volume. In these locations, very high tsunami heights have been simulated numerically and these locations are considered as possible sources for widespread megatsunamis in the future (Harbitz et al. 2013).

In fact, SMF tsunamis may be much more frequent than people expect and may have played an important role in the 2011 Tohoku tsunami, as the tsunami wave height in Iwate and neighboring prefectures was much higher than the forecast of other areas with similar earthquake intensity along the Pacific coast of Japan (Tappin et al. 2014).

Recently, a method to quickly forecast a tsunami generated by a SMF has been proposed (Chen et al. 2020). In the following, this approach based on the reciprocal Green's Function (RGF) is briefly introduced. For a deformable sea bottom with the characteristic lengths of the source area much larger than the depth, SMF tsunamis can be represented by the following shallow-water equations (SWEs)

where a new source term $-\partial d/\partial t$ is included in the continuity equation (Løvholm et al. 2015):

$$\frac{\partial}{\partial t} \begin{bmatrix} \eta \\ P \\ Q \end{bmatrix} = - \begin{bmatrix} 0 & \frac{\partial}{\partial x} & \frac{\partial}{\partial y} \\ gd \frac{\partial}{\partial x} & 0 & 0 \\ gd \frac{\partial}{\partial y} & 0 & 0 \end{bmatrix} \begin{bmatrix} \eta \\ P \\ Q \end{bmatrix} + \begin{bmatrix} -\frac{\partial d}{\partial t} \\ 0 \\ 0 \end{bmatrix} \quad (1)$$

In the SWEs, η is the free surface elevation, P and Q are volume fluxes along the x and y directions, t is time, g is gravitational acceleration, and d is the water depth. On the other hand, if the continuity equation is forced with an impulsive forcing represented by a δ -function at the source point $\vec{r}_s = (x_s, y_s)$, the SWEs will read

$$\begin{aligned} \frac{\partial}{\partial t} \vec{\eta} + \frac{\partial}{\partial x} \vec{P} + \frac{\partial}{\partial y} \vec{Q} &= \delta(t) \delta(x - x_s) \delta(y - y_s) \\ \frac{\partial}{\partial t} \vec{P} + gd \frac{\partial}{\partial x} \vec{\eta} &= 0 \\ \frac{\partial}{\partial t} \vec{Q} + gd \frac{\partial}{\partial y} \vec{\eta} &= 0 \end{aligned} \quad (2)$$

Here, $\vec{\eta}$ is the η response, \vec{P} is the response of the variable P , and \vec{Q} the response of Q to the δ -function forcing. According to Chen et al. (2020), the δ -function on the right hand side means unit elevated volume at $t = 0$. The resulting $\vec{\eta}(\vec{r}, t; \vec{r}_s)$, which is the elevation response at each receiver point $\vec{r} = (x, y)$, is called the Green's Function (GF). Both Eqs. (1) and (2) can be integrated by the Cornell Multigrid Coupled Tsunami Model (COMCOT; Wang and Power 2011).

Similarities between Eqs. (1) and (2) are obvious as the left hand sides are identical: the right hand side for the SMF tsunami is the temporal variation of the sea depth, while that for the GF is a delta function. Applying a Laplace transform, the SMF tsunami is solved as the convolution of GF and the forcing $-\partial d/\partial t$:

$$\eta = \int_0^t \iint_{\Omega_s} -\frac{\partial d}{\partial t}(\vec{r}_s, t - \tau) \vec{\eta}(\vec{r}, \tau; \vec{r}_s) d\Omega_s d\tau \quad (3)$$

Thus, the continuous contribution of the slide can be represented by a convolution.

If locations of source and receiver points are exchanged, the elevation response to an initial impulsive elevation is the desired RGF. The reciprocity between GF and RGF has been shown numerically in Chen and Liu (2009), Chen et al. (2012, 2015). Because of this reciprocity, just one RGF is required for one vulnerable city. The forecast of SMF tsunamis can be achieved by the following equation:

$$\eta = \int_0^t \iint_{\Omega_s} -\frac{\partial d}{\partial t}(\vec{r}_s, t - \tau) \vec{\eta}(\vec{r}_s, \tau; \vec{r}) d\Omega_s d\tau \quad (4)$$

Features of RGF Approaches in the Forecast of SMF Tsunamis

SMF in the 1781 Event of Taiwan

Based on echo sounder and other seismic approaches on the survey of bottom bathymetry and bottom material, a few SMF sites have been identified to the southwest of Taiwan.

In the following, the simulation and discussion of SMF tsunamis are based on a historical event to the southwest of Taiwan. These simulations extend the study of Chen et al. (2020) with more discussion and analyses added. Following Li et al. (2015), simulations at five stations are discussed. These are Anping (AP), Kaohsiung (KH), Kaoping Rivermouth (KP), Fangshan (FS) and Nanwan (NW) along the southwest coast of Taiwan, with locations indicated in Fig. 1. The historical event occurred in 1781, and has been suggested as a result of an SMF-generated tsunami that struck the southwest coast of Taiwan. According to the assumption of Li et al. (2015), the tsunami is simulated and a snapshot of the sea surface 3 min after the onset of the SMF is shown in Fig. 2.

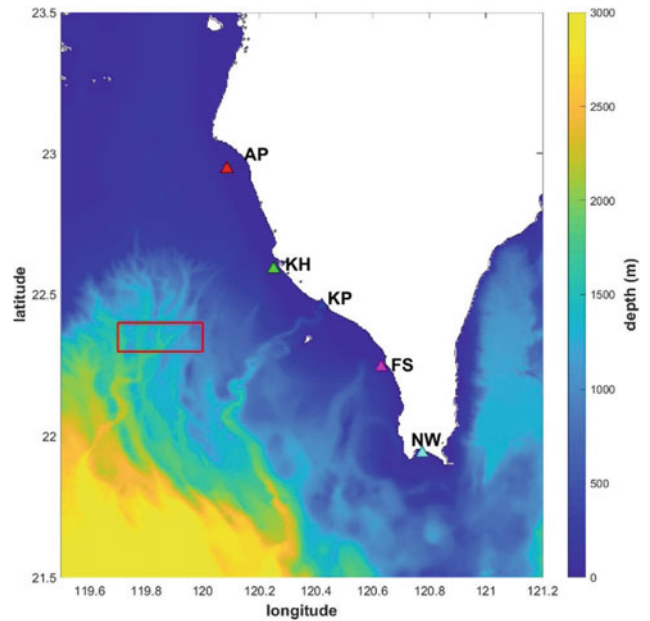


Fig. 1 Locations of five stations to the southwest of Taiwan. The area enclosed by the red rectangle to the southwest of Taiwan is a uniform Source to test the RGF approach

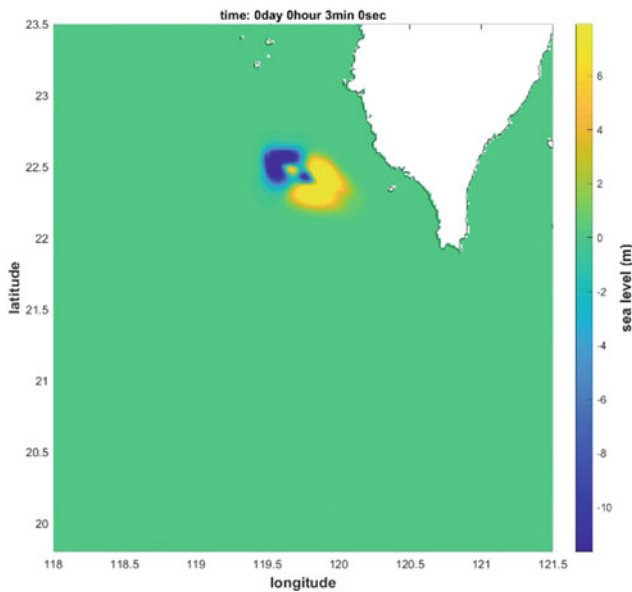


Fig. 2 The simulated water surface of the 1781 tsunami event 3 min after the onset of the SMF

Resolution Requirement

In the following, the simulation and discussion of SMF tsunamis are based on a historical event to the southwest of Taiwan. These simulations extend the study of Chen et al. (2020) with more discussion and analyses added. Following Li et al. (2015), simulations at five stations are discussed. These are Anping (AP), Kaohsiung (KH), Kaoping River-mouth (KP), Fangshan (FS) and Nanwan (NW) along the southwest coast of Taiwan, with locations indicated in Fig. 1. The historical event occurred in 1781, and has been suggested as a result of an SMF-generated tsunami that struck the southwest coast of Taiwan. According to the assumption of Li et al. (2015), the tsunami is simulated and a snapshot of the sea surface 3 min after the onset of the SMF is shown in Fig. 2.

Usually a seismic tsunami can be well-represented in a numerical simulation because the length scale of the rupture zone is large. For example, the forecast in Chen et al. (2015) uses 1 min. or even 2 min. resolution. As an SMF usually has a much smaller scale, we suspect a finer resolution is warranted and execute a convergence test. Thus, simulations with 0.3, 0.1, 0.06 and 0.03 min grid cells are employed. The maximum grid spacing, 0.3 min, is chosen because it is approximately 1/10 of the slide width of 5 km. As is shown in Fig. 3, 0.06 min. is suitable because the result is very close to that of the next finer resolution: the root mean square error divided by the maximum wave height is less than 10%.

Compared to the 1–2 min resolution used in seismic tsunamis, 0.06 min. grid spacing consumes much more computational resources. As has been mentioned previously, the fine grid spacing is closely related to the small length scale of the slide. Hence, another convergence test is executed with an SMF of larger length scales: the original 16 km long and 5 km wide SMF were changed to a 48 km long and 15 km wide SMF. Then, simulations with the same 0.3, 0.15, 0.06 and 0.03 min grid cells are executed. As shown in Fig. 4, these simulations are quite consistent with each other. With SMF three times larger in both length and width, the acceptable resolution becomes 0.15 min which is also enlarged approximately three times. We hence confirm that the slide size controls the grid spacing.

Coastal Effect

Because of the high resolution required in the simulation of SMF tsunami, coastal effects will play a more important role compared to the simulation of seismic tsunamis. As is shown in the second panel of Fig. 5, although the water level calculated by the RGF approach in KH agrees well with the direct COMCOT simulation for the first few waves, results of these two approaches diverge significantly afterwards. That is, the RGF approach cannot exactly reproduce the direct simulation which is supposed to be close to the propagation of the real tsunami.

An RGF is the response of linear SWEs to a unit concentrated forcing. Because the forcing area is small, the amplitude of an RGF is much smaller than the unit initial wave amplitude. Therefore, the RGF approach applies only when the tsunami wave height is small compared to the water depth. When the tsunami propagates directly from the deep sea to the forecast point of the vulnerable city, this linearity of the tsunami holds. As the tsunami propagates closer to the shore, the water depth becomes shallower and shallower, and the linearity assumption can be violated. Consequently, the RGF approach may result in an incorrect waveform after the tsunami wave interacts with the very shallow coastal region.

This coastal effect explains the discrepancies of the waveforms in Fig. 5. According to the arrival time of the first tsunami wave, KH is closest to the SMF site and the wave amplitude is the largest of all five stations. The tsunami wave has the highest wave height and nonlinearity. Therefore, the waveform calculated by the RGF approach cannot well represent the high nonlinearity near the shoreline. Hence, the blue line that represents the RGF results in the diagram significantly deviates from the red line that represents the direct COMCOT simulation. The KP station is the

Fig. 3 Tsunami water level at Kaohsiung simulated by various resolutions. The slide is 16 km long and 5 km wide

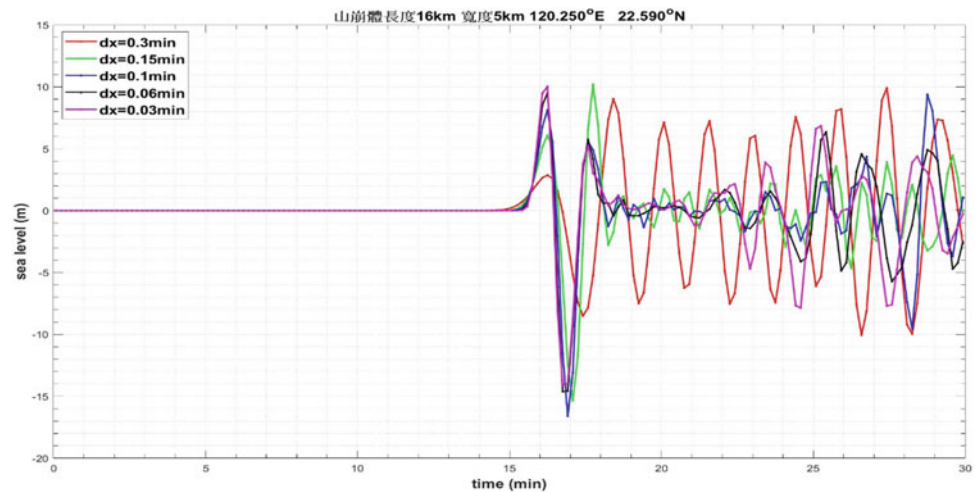
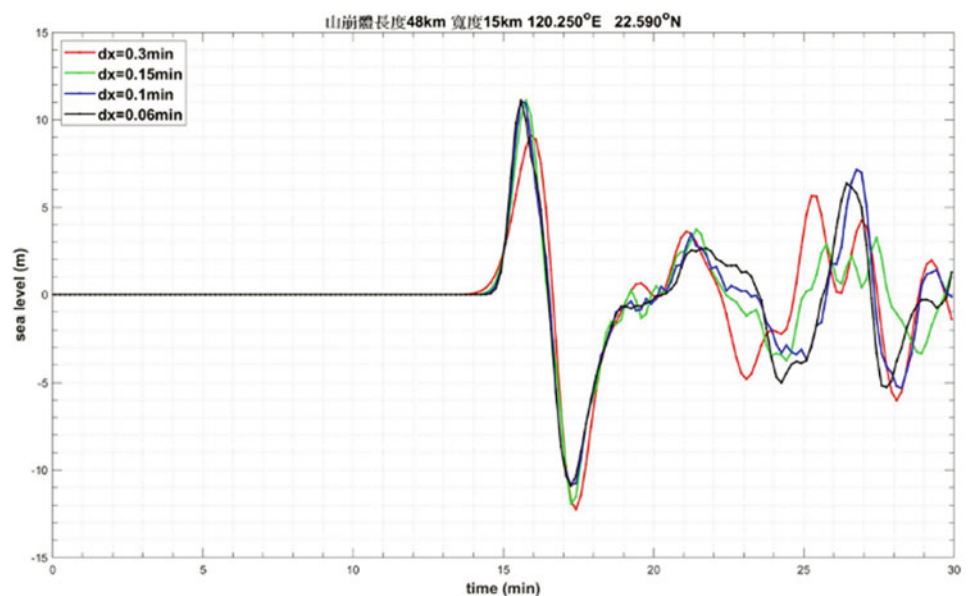


Fig. 4 Tsunami water level at Kaohsiung simulated for various resolutions. The slide is 48 km long and 15 km wide



second closest to the SMF, but the wave height is relatively small, partly due to the orientation of the slide. Some wave energy is trapped along the coastline and produces a few large humps after the first few waves. However, in the direct simulation, these trapped edge waves are less significant because trapped waves propagate along the shoreline and interact closely with the shallow water zone, as the example shown in Chen et al. (2004). The energy thus is dissipated by the local bathymetry.

Except for the wave records in AP in the top panel of Fig. 5, all other four stations show significant coastal effects after the first few waves. The agreement of RGF and direct COMCOT simulations in AP is obviously due to the small wave height. In fact, as has been exhibited in Chen et al. (2020), the discrepancy decreases if the bathymetry is arbitrarily modified by increasing the nearshore water depth to

20 m. Thus, it can be concluded that the discrepancies after the first few waves are due to nonlinear interactions with the coastal area.

On the other hand, for the first few waves at each station, the agreement between RGF and direct simulation methods is very good. In the practice of tsunami forecasting, the waveform after the first few tsunami waves is irrelevant and hence the discrepancy between the RGF and the direct COMCOT simulation can be neglected.

Computer Time Reduction

One significant benefit of the RGF approach compared to a direct SWE simulation is the reduction of computer time because an RGF can be calculated beforehand. As the

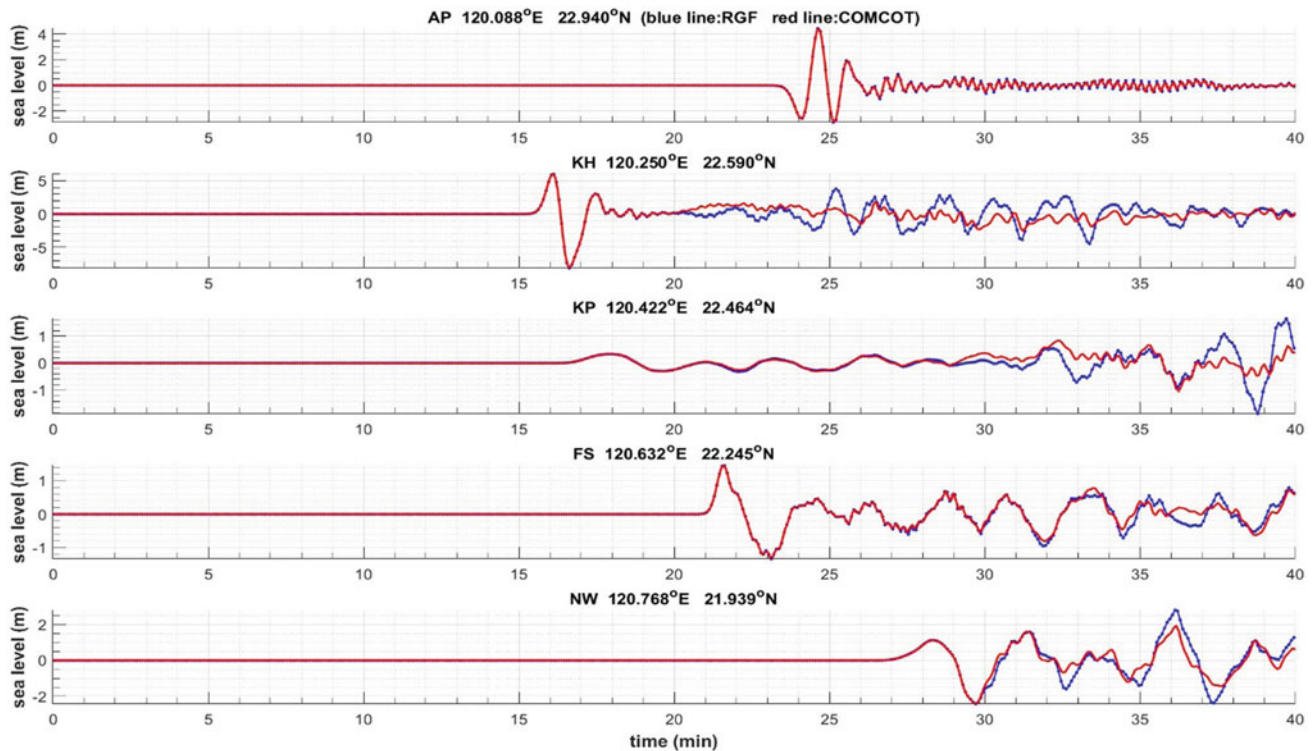


Fig. 5 Simulated tsunami water level at five stations. The slide is 16 km long and 5 km wide. The blue line represents the RGF results, while the red line represents the direct COMCOT simulation

example shown in Chen et al. (2020) with 0.06 min resolution, 0.25 s time step and 10^{-13} precision, it takes only 4.2 s for a desktop PC with 16 GB RAM and an Intel i7-9600 CPU. On the other hand, a direct COMCOT simulation takes 77 min. For a coarser 0.3 min. resolution, the benefit of computer time reduction is still significant: the RGF approach uses less than 1% of the computer time in a direct simulation. The finer the resolution of the computational domain, the more economical the RGF approach will be.

Toward a Forecast System of SMF Tsunamis

A forecast system for SMF tsunamis can be established in two ways: one depends on a reliable identification of the onset of landslide, the other counts on in-situ measurements of tsunamis. The first one is similar to a forecast system for seismic tsunamis such as the one shown in Chen et al. (2015). The tsunami is forecast after an SMF is detected. After the size and location of the SMF are determined, the tsunami can be calculated by, say, assuming an idealized truncated hyperbolic slide whose kinematics is described in Enet and Grilli (2007). However, the detection technology of SMFs is not as mature as that of earthquakes. Another

approach is to directly detect the tsunami wave. In the following, these two approaches are discussed in detail.

Detection of SMFs

One problem in constructing a forecast system for SMF tsunamis is that the detection technology for an SMF is not as mature, and the area covered is not as comprehensive as that for earthquakes. Earthquakes are serious hazards; lots of resources have been dedicated to the mitigation of related hazards and most earthquake-prone areas have been covered by seismometer networks. Earthquake information usually can be obtained promptly with very high accuracy, while there is no way to access real-time SMF information.

As tectonic faults may extend to the sea, more and more seismometers will be deployed on the ocean bottom. Previous studies on applying seismometer data in landslide detection (Caplan-Auerbach et al. 2001; Lin et al. 2014) shed light on the detection of SMFs and this trend should be appreciated by tsunami researchers. Besides, real-time information transmission to the land can be established via acoustic modems, relay buoys and satellites. Thus, it is possible to obtain real-time SMF information in the near future.

Quick Forecast of SMF Tsunami

The 1781 tsunami event had been disastrous in the southwest coast of Taiwan. But the neighboring area such as southeast China and northwest Luzon, Philippines, did not suffer significant tsunamis. By comparing 13 simulations with tsunamis generated from either earthquakes, volcanoes or SMFs, this event is suggested as the result of an SMF triggered by a submarine earthquake (Li et al. 2015).

Previous studies have shown the deformation of the slide does not significantly change the generated tsunami (Grilli et al. 2015; Løvholt et al. 2015). The SMF thus can be represented by a rigid slide body and the first order estimate of tsunami wave magnitude can be modeled with a rigid slide whose shape is assumed to be a truncated hyperbolic function represented by (Enet and Grilli 2007; Chen et al. 2020)

$$z = \frac{T}{1 - \epsilon} [\operatorname{sech}(k_b x) \operatorname{sech}(k_w y) - \epsilon],$$

where T is the maximum thickness,

$$k_b = \frac{2}{b} \operatorname{acosh}\left(\frac{1}{\epsilon}\right),$$

$$k_w = \frac{2}{w} \operatorname{acosh}\left(\frac{1}{\epsilon}\right),$$

where b and w are the longitudinal and transverse length scales of the slide, and the truncation parameter ϵ can be set as 0.717. The movement is described by semi-empirical kinematic formulas provided in Enet and Grilli (2007). For example, the slide displacement of the SMF, $s(t)$, is given as.

$$s(t) = s_0 \ln \left[\cosh \left(\frac{t}{t_0} \right) \right].$$

Here $t = 0$ is the time when the slide starts and θ is the angle between the slide motion and the horizon. The characteristic length and time of the landslide motion are

$$s_0 = \frac{u_t^2}{a_0}$$

and

$$t_0 = \frac{u_t}{a_0},$$

where u_t is the terminal speed. In this way, an SMF tsunami can be simulated in a few seconds.

Based on the in-situ investigation of the sea bottom bathymetry, including the debris of the submarine landslide (Wu 2008), three SMF sources have been chosen in Li et al. (2015). Of these three sources, the first one with $b = 16$ km, $w = 5$ km and $T = 250$ m are chosen. The location is 22.45° N and 119.7° E, as shown in Fig. 2, where the azimuth of motion is -60° East and the slope angle is 3° .

Although previous studies shed light on the detection of SMFs, available landslide information is much less accurate than the earthquake information which is used in the forecast of seismic tsunamis. Instead of forecasting seismic tsunamis based on one set of tectonic parameters, a forecast for SMF tsunamis should consider the possibility of different SMF parameters and locations. Thus, a range of tsunami heights and their arrival time, and thus an ensemble forecast, will be provided.

An RGF is pre-calculated and no equation-solving is involved; consequently the RGF approach is economical, fast and robust. According to Chen et al. (2020), with the RGF approach, the tsunami waveform can be obtained in 5 s once a submarine landslide is detected. Because of the reduced computer time in an RGF approach, a forecast for SMF tsunamis can consider the possibility of different SMF parameters and locations. This is quite different from seismic tsunamis which usually are based on just one set of fault parameters. Thus, a forecast system can be constructed using RGF. Some background information such as the density and cohesive property of the slide material, the bottom slope, the water depth and possibly the range of the slide volume can be obtained by a field survey. With all this information, a forecast system can be constructed using RGF, as the preliminary forecast system shown in Fig. 6. By combining other information such as inundation maps, quick forecasting of SMF tsunamis is possible and can be used for tsunami hazard mitigation.

After calculating all possible parameters, a range of tsunami heights and their arrival time can be broadcast as an ensemble forecast. Hence, after a submarine landslide is detected, SMF information such as the total volume, the slide location, the speed of slide movement, etc. can be estimated.

Forecast Based on In-Situ Measurement

The forecast system based on in-situ tsunami measurements can be established by deploying nearshore tsunami sensors such as accelerometers in buoys or pressure gages at the sea bottom. As the water level is measured, the tsunami waveform can be retrieved as a constantly moving average in

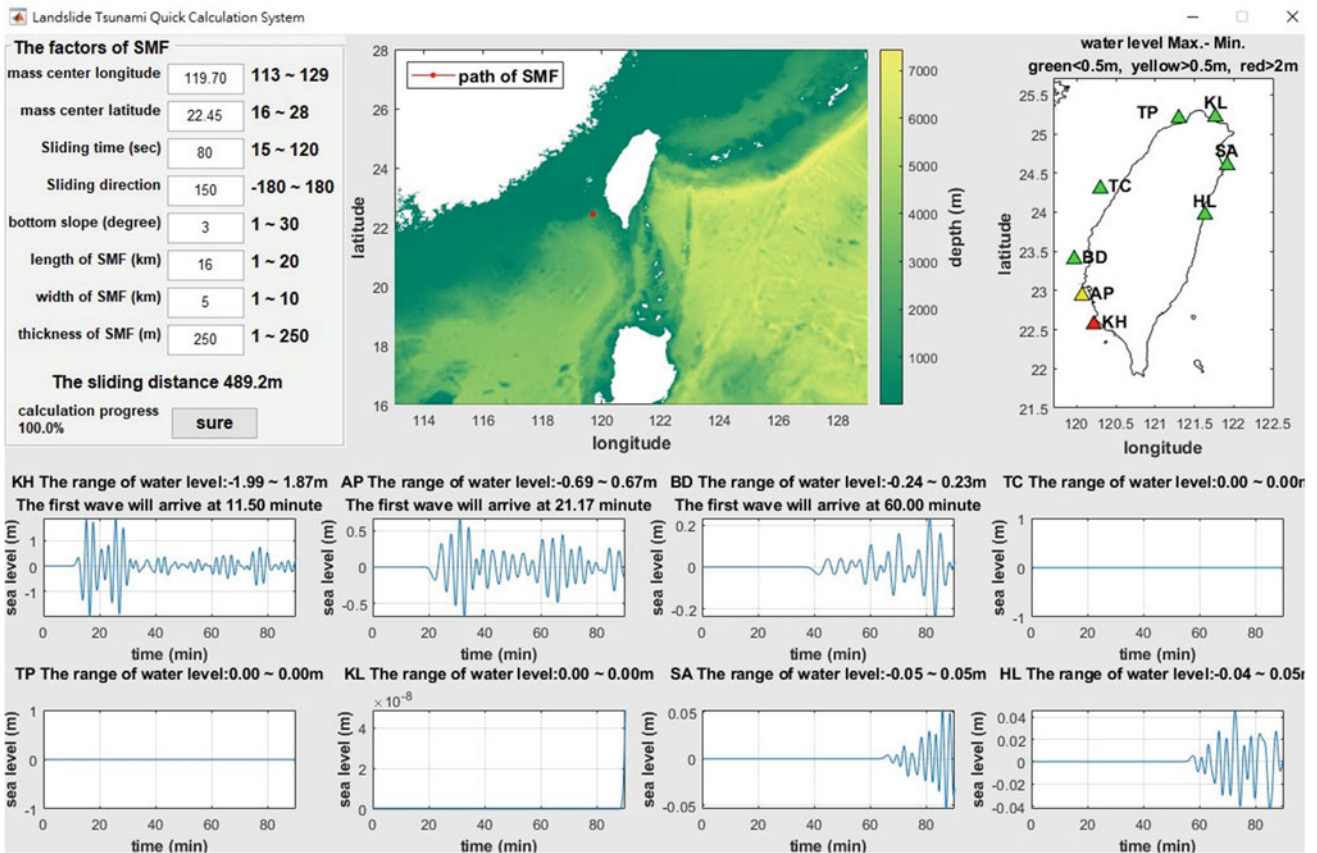


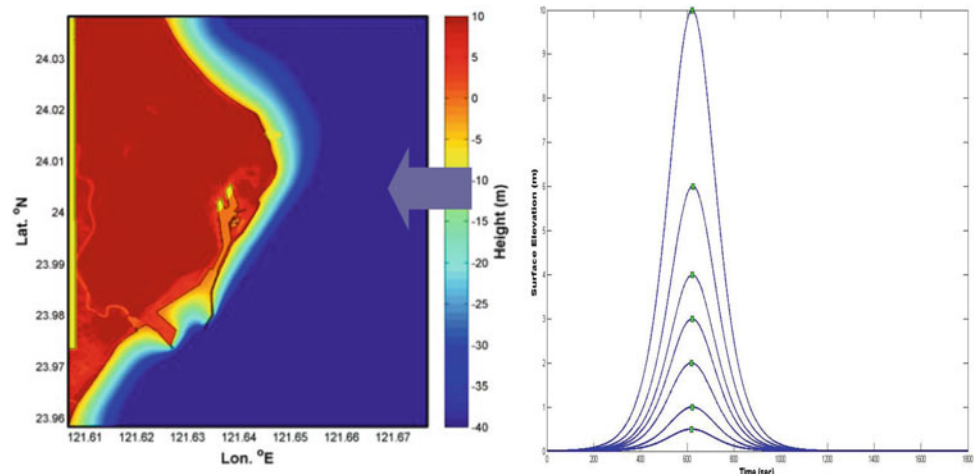
Fig. 6 A preliminary forecast system for SMF tsunamis. Water levels of eight harbors around Taiwan are calculated according to the SMF information provided by the upper left panel

time. Thus, the information on the incident tsunami has a solid basis and the result is reliable. When a tsunami is detected, there will be two ways to provide the inundation map. The simpler approach is employing the technique used in Chen et al. (2015): only the highest wave height is used and a simple bell-shaped waveform is used as the incident tsunami, as is shown in Fig. 7. Hazard maps can be

calculated beforehand because the wave height is the only variable for various tsunamis inundation scenarios. The final hazard map can be obtained by interpolating the inundation distance if the incident tsunami height is between two inundation scenarios.

A more complicated approach requires more computer time after the detection of the offshore tsunami, but the result

Fig. 7 Simulating the incidence of bell-shaped waves can generate inundation maps under eight different tsunami heights from 0.5 to 12 m



is more accurate. This method is proposed in Chen and Liu (2020) by introducing a flow RGF. The waveform can be reproduced and hence the coastal inundation is closer to the real tsunami, even when the tsunami is not incident normal to the shoreline. This approach applies well in seismic tsunamis (Chen and Liu 2020) and should work well for SMF tsunamis.

Although deploying a tsunami sensor is a useful tool in the forecast of tsunamis, the cost for manufacturing, deploying and maintaining the sensor is very high. Besides, a useful sensor should be deployed at a distance from the shoreline so that people can have time to evacuate. That means the cost of a tsunami sensor is much higher than a nearshore wave monitoring system. As tsunamis are very rare, the cost of tsunami sensors seems too high to be practical. On the other hand, both submarine earthquakes and landslides can be detected by seismometers. In the long run the detection of SMFs will be very quick, economical and reliable. Therefore, more attention should be paid to the understanding and the detection of SMFs, and RGF should be seen to be a useful tool in the forecast of SMF tsunamis.

Conclusions

Quick forecast of SMF tsunamis can be obtained in a very economical way by using RGFs. Compared to seismic tsunamis, finer spatial resolution is required in simulating RGF tsunamis because of the smaller spatial scales of an SMF. The reduced grid dimensions in the nearshore area induce coastal effects which cannot be exactly reproduced by the RGF approach. However, the first few waves of the RGF approach are exactly the same as the result of direct simulation, and the applicability in tsunami forecast is not affected.

If the SMF or the tsunami is detected, RGFs can provide SMF tsunami information in a very short time. Several scenarios can be considered before announcing the warning; hence, an ensemble forecast can be given so that countermeasures can be taken to effectively mitigate the hazard. Further integrating with the detection technologies on either SMFs or the tsunami itself shed light on the establishment of a useful forecast system for SMF tsunamis.

Acknowledgements This research was completed with grants from the Ministry of Science and Technology of Taiwan (MOST 108-2611-M-110-020).

References

Caplan-Auerbach J, Fox CG, Duennebieer FK (2001) Hydroacoustic detection of submarine landslides on Kilauea Volcano. *Geophys Res Lett* 28(9):1811–1813. [10.1029/2000GL012545](https://doi.org/10.1029/2000GL012545)

- Chen G-Y, Chien C-C, Su C-H, Tseng H-M (2004) Resonance induced by edge waves in Hua-Lien Harbor. *J Oceanogr* 60(6):1035–1043
- Chen G-Y, Lin C-H, Liu C-C (2012) Quick evaluation of runup height and inundation area for early warning of tsunami. *J Earthq Tsunami* 1250005:1–23. <https://doi.org/10.1142/S1793431112500054>
- Chen G-Y, Liu C-C (2009) Evaluating the location of tsunami sensors: methodology and application to the northeast coast of Taiwan. *Terr Atmos Ocean Sci* 20(4):563–571. [https://doi.org/10.3319/TAO.2008.08.04.01\(T\)](https://doi.org/10.3319/TAO.2008.08.04.01(T))
- Chen G-Y, Liu C-C (2020) Reciprocal elevation and flow Green's functions and the simulation of nearshore tsunami Inundation. *Ocean Eng* 210:107497. <https://doi.org/10.1016/j.oceaneng.2020.107497>
- Chen G-Y, Liu C-C, Wijetunge JJ, Wang Y-F (2020) Reciprocal Green's functions and the quick forecast of submarine landslide tsunami. *Nat Hazards Earth Syst Sci* 20:771–781. <https://doi.org/10.5194/nhess-2019-124>
- Chen G-Y, Liu C-C, Yao C-C (2015) A forecast system for offshore water surface elevation with inundation map integrated for tsunami early warning. *Ocean Eng, IEEE J.* <https://doi.org/10.1109/JOE.2013.2295948>
- Corona N, Ramírez-Herrera MT (2015) Did an underwater landslide trigger the June 22, 1932 tsunami off the Pacific coast of Mexico? *Pure Appl Geophys* 172(12):3573–3587
- Enet F, Grilli ST (2007) Experimental study of tsunami generation by three-dimensional rigid underwater landslides. *J Waterw Port Coastal Ocean Eng* 133(6):442–454
- Grilli ST, O'Reilly C, Harris JC, Bakhsh TT, Tehranirad T, Banihashemi S, Kirby JT, Baxter CDP, Eggeling T, Ma G, Shi F (2015) Modeling of SMF tsunami hazard along the upper US East Coast: detailed impact around Ocean City, MD. *Nat Hazards* 76(2):705–746. <https://doi.org/10.1007/s11069-014-1522-8>
- Harbitz CB, Løvholt F, Bungum H (2013) Submarine landslide tsunamis: how extreme and how likely? *Nat Hazards* 72:1341–1374. <https://doi.org/10.1007/s11069-013-0681-3>
- Heidarzadeh M, Muhari A, Wijanarto AB (2018) Insights on the source of the 28 September 2018 Sulawesi Tsunami, Indonesia based on spectral analyses and numerical simulations. *Pure Appl Geophys* 176:25–43. <https://doi.org/10.1007/s00024-018-2065-9>
- Leonard LJ, Rogers GC, Mazzotti S (2014) Tsunami hazard assessment of Canada. *Nat Hazards* 70:237–274. <https://doi.org/10.1007/s11069-013-0809-5>
- Li LL, Switzer AD, Wang Y, Weiss R, Qiu Q, Chan C-H, Tapponnier P (2015) What caused the mysterious 18th century tsunami that struck the southwest Taiwan coast? *Geophys Res Lett* 42(20):8498–8506. <https://doi.org/10.1002/2015GL065567>
- Lin J-H, Chen Y-F, Liu C-C, Chen G-Y (2014) Building a pre-calculated quick forecast system for tsunami runup height. *J Earthq Tsunami* 8(3):1440002. <https://doi.org/10.1142/S1793431114400028>
- Løvholt F, Pedersen G, Harbitz CB, Glimsdal S, Kim J (2015) On the characteristics of landslide tsunamis. *Phil Trans R Soc A* 373:20140376. <https://doi.org/10.1098/rsta.2014.0376>
- Sepúlveda SA, Serey A, Lara M, Pavez A, Rebolledo S (2010) Landslides induced by the April 2007 Aysén Fjord earthquake, Chilean Patagonia. *Landslides* 7:483–492. <https://doi.org/10.1007/s10346-010-0203-2>
- Tappin DR, Watts P, McMurtry GM, Lafoy Y, Matsumoto T (2001) The Sissano, Papua New Guinea tsunami of July 1998—offshore evidence on the source mechanism. *Mar Geol* 175(1–4):1–23. [https://doi.org/10.1016/S0025-3227\(01\)00131-1](https://doi.org/10.1016/S0025-3227(01)00131-1)
- Tappin DR, Grilli ST, Harris JC, Geller RJ, Masterlark T, Kirby JT, Shi F, Ma G, Thingbaijam KKS, Mai PM (2014) Did a submarine landslide contribute to the 2011 Tohoku tsunami? *Mar Geol* 357:344–361. <https://doi.org/10.1016/j.margeo.2014.09.043>

- Wang X, Power W (2011). COMCOT: a tsunami generation propagation and run-up model, GNS Science Report 2011/43, pp 129
- Wu C-Y (2008) The distribution of submarine and characteristics landslides offshore southern Taiwan (in Chinese), Master thesis, Natl. Taiwan Univ., Inst. of Oceanography, Taiwan
- Yalciner AC, Gülkan P, Dilmen DI, Aytore B, Ayca A, Insel I, Zaytsev A (2014) Evaluation of tsunami scenarios for western Peloponnese, Greece. *Bollettino di Geofisica Teorica ed Applicata*. <https://doi.org/10.4430/bgta0126>



Deformation Characteristics with Porewater Pressure Development of Shallow Landslide Triggered by Rainfall Infiltration

Kuo-Hsin Yang, Thanh Son Nguyen, Harianto Rahardjo, and Der-Guey Lin

Abstract

The identification of the slope deformation characteristics upon rainfall plays an important role in providing early warning information and implementing emergency remedial actions before landslide occurs. In this study, a coupled hydro-mechanical formulation of finite element analysis was performed to investigate the displacement behaviour of slopes triggered by rainfall infiltration. The simulation results showed in good agreement with experiment result. The model study was then carried out to investigate the hydraulic and deformation response of the shallow slope. The numerical results revealed that the developed slope displacement with time can be divided into three stages, namely constant, accelerated, and critical deformation stages, corresponding to various rates of slope movement and porewater pressure development stages. Finally, the relationships of slope displacement magnitude with the factor of safety that established from this study can be seen as a good indicator for shallow landslide hazard assessment.

Keywords

Rainfall-triggered landslides • Coupled hydro-mechanical model • Landslide movement patterns

Introduction

Rainfall-induced shallow landslides is a common natural hazard around the world, particularly for countries in tropical regions and mountainous basins, where covered by a residual or colluvium soil deposit underlain by a less permeable rock. It was observed that the failure plane is approximately parallel to the slope surface with a failure depth typically ranging from 1 to 3 m (Johnson and Sitar 1990; Bordoni et al. 2015; Zhang et al. 2017).

Numerous past studies have been conducted to investigate the hydrological response and failure mechanism of rainfall-induced shallow landslides using various approaches such as small-scale and full-scale laboratory tests (Wang and Sassa 2001, 2003; Moriwaki et al. 2004; Sasahara and Sakai 2014), field monitoring (Ng et al. 2003; Leung and Ng 2016), and numerical analyses (Casagli et al. 2005; Qi and Vanapalli 2015; Yang et al. 2017; Yubonchit et al. 2017; Ghasemi et al. 2019; Tang et al. 2019). These studies revealed that the soil water content and porewater pressure (PWP) exhibit spatiotemporal variations within the slopes when the slopes are subject to wetting and drying cycles. The failure mechanisms of rainfall-induced shallow landslides primarily involve the advancement of the wetting front, which causes the increase of PWP (loss of suction, or development of positive PWP) within soils, leading to a decrease in soil shear strength, and consequently resulting in the final failure of slopes. However, few attempts have been made to investigate the deformation characteristics (i.e., displacement–time relationship) of slopes subjected to rainfall (Alonso et al. 2003; Zhou et al. 2009; Leung and Ng

K.-H. Yang (✉)
Department of Civil Engineering, National Taiwan University
(NTU), Taipei, Taiwan
e-mail: khyang@ntu.edu.tw

T. S. Nguyen
Faculty of Bridges and Roads, National University of Civil
Engineering (NUCE), Hanoi, Vietnam
e-mail: sonnt@nuce.edu.vn

H. Rahardjo
School of Civil and Environmental Engineering, Nanyang
Technological University (NTU), Singapore, Singapore
e-mail: chrahardjo@ntu.edu.sg

D.-G. Lin
Department of Soil and Water Conservation, National
Chung-Hsing University (NCHU), Taichung, Taiwan
e-mail: dglin@dragon.nchu.edu.tw

2016; Yang et al. 2017; Tang et al. 2019) due to the complex coupled hydro-mechanical problems (Lee et al. 2011).

The improving understanding of slopes deformation characteristics upon rainfall at pre-failure process is essential and important implications for landslide risk management. Thus, a coupled hydro-mechanical formulation finite element (FE) analysis on shallow slope was conducted in this study to investigate the development of slope displacement with time triggered by rainfall infiltration. The findings can be used as further guidance for the mitigation of landslide disasters.

Numerical Simulation

Model Validation

A full-scale landslide flume test performed by Moriwaki et al. (2004) was used to validate the applicability of the proposed numerical model on predicting the slope hydraulic responses and deformation. Accordingly, the fully coupled flow-deformation analysis using finite element (FE) method framework PLAXIS 2D (Brinkgreve et al. 2019) was used to analyse the simultaneous development of deformations and PWP's within soils due to time-dependent changes of the hydraulic boundary conditions. For modeling soil mechanical response, the shear strength of an unsaturated soil was calculated by combining Bishop's effective stress concept (Bishop 1959) and extended Mohr–Coulomb failure criterion proposed by Vanapalli et al. (1996). The factor of safety (FS) of the slope was calculated using the phi/c reduction technique (Griffiths and Lane 1999).

Materials

The slope was built using loose Sakuragawa river sand, classified as a poorly graded sand (SP) according to the Unified Soil Classification System (USCS). The Hardening Soil (HS) model, an elastoplastic soil constitutive model was used to simulate the behavior of soil test. The stress-dependent modulus in the HS model is an essential feature to appropriately describe changes in the soil modulus with matric suction for modeling the unsaturated soil behavior (Yang et al. 2017).

Table 1 summaries the input soil mechanical properties used in the numerical simulation. The saturated permeability, k_s , was determined based on the best-fitted result as 3.0×10^{-4} m/s. Figure 1 presents the soil–water characteristic curve (SWCC) and hydraulic conductivity function (HCF) for the test soil using van Genuchten–Mualem's model (Mualem 1976; van Genuchten 1980). In the test, artificial rainfall with a constant intensity of $q = 100$ mm/h was applied on the entire slope surfaces. The FE mesh and boundary conditions are described in Fig. 2.

Results and comparison

Figure 3 presents the comparison of the measured and the numerically predicted location of the phreatic surface and failure surface just prior to the slope failure ($t = 9267$ s). In general, a good agreement can be observed between the measured and the predicted responses. As shown in Fig. 3, the slope failure was initialised in the upper 30° slope section for both the experimental test and numerical analysis. The

Table 1 Soil properties used in this study

Parameter	Model validation	Model study	
		soil layer	Bedrock
Material model	HS	HS	MC
Analysis type	Unsaturated drained	Unsaturated drained	Saturated undrained
γ_{unsat} [kN/m ³]	15.7	16	24
γ_{sat} [kN/m ³]	19.1	18.1	24
c' or s_u [kPa]	0.1	7	500
ϕ' [°]	34	31.5	0
ψ [°]	4	1.5	–
E_{50}^{ref} or E_u [kPa]	10,000	15,000	876×10^5
$E_{\text{oed}}^{\text{ref}}$ [kPa]	10,000	10,500	–
$E_{\text{ur}}^{\text{ref}}$ [kPa]	30,000	45,000	–
ν_{ur} or ν	0.3	0.3	0.495
m [–]	0.5	0.5	–
R_f [–]	0.9	0.9	–

Fig. 1 Hydraulic characteristic curves: **a** SWCC; **b** HCF

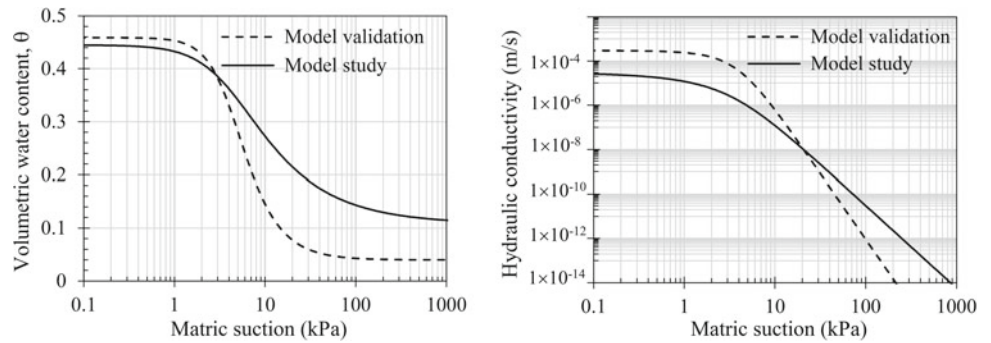


Fig. 2 Numerical model for model validation

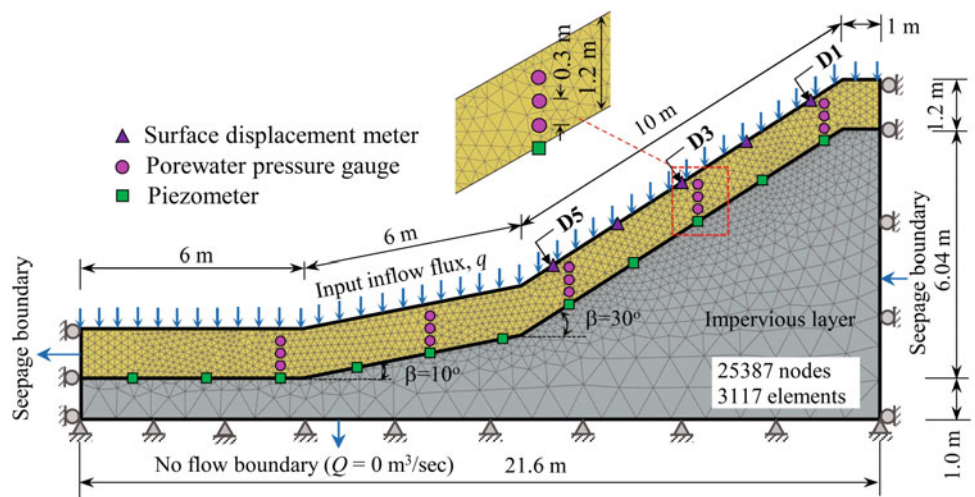
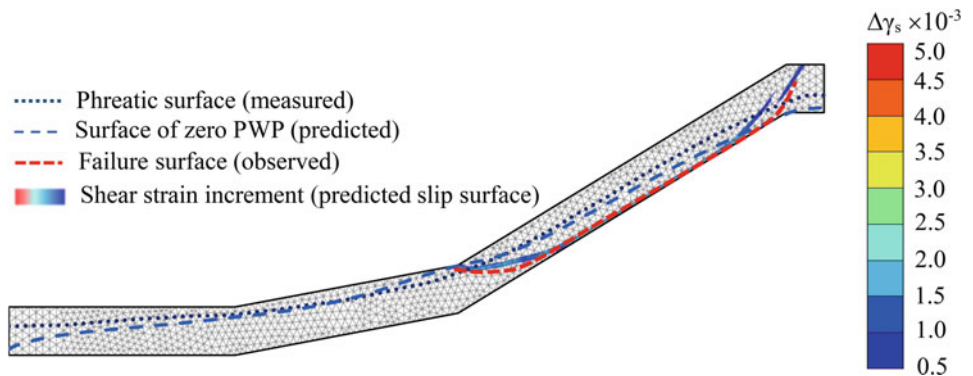


Fig. 3 Model validation by comparing the location of phreatic surface and failure surface



failure surface developed along the soil–bedrock interface at the upper slope, forming a transitional slide failure mode.

Figure 4 shows the measured and predicted surface displacement with time at three selected locations (namely D1, D3, and D5 as shown in Fig. 2) along the slope surface. The predicted displacement trends have a good match with the measured ones for all three selected locations. Both measured and predicted results show the slope started to move after $t = 6700$ s, corresponding to the timing when the

wetting front reached the bottom of the slope and positive PWP started to develop at the soil–bedrock interface. The measured and predicted slope displacement approximately reached to 51 mm at the moment of slope failure ($FS = 1$). The predicted failure timing $t = 9300$ s also matches well with the measured one $t = 9267$ s.

In summary, the location of the phreatic surface, location of failure surface, surface displacements, and failure timing predicted by FE analysis were in good agreement with the

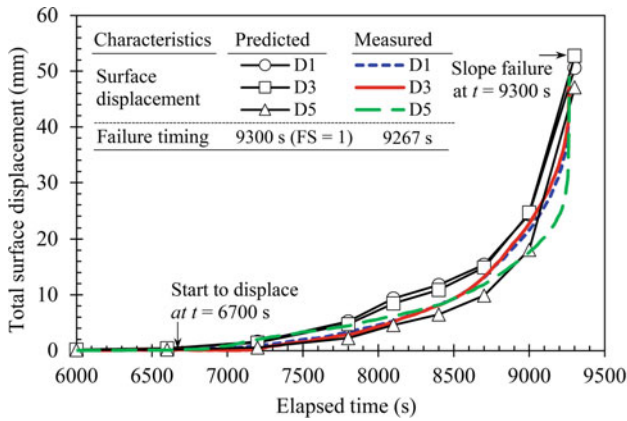


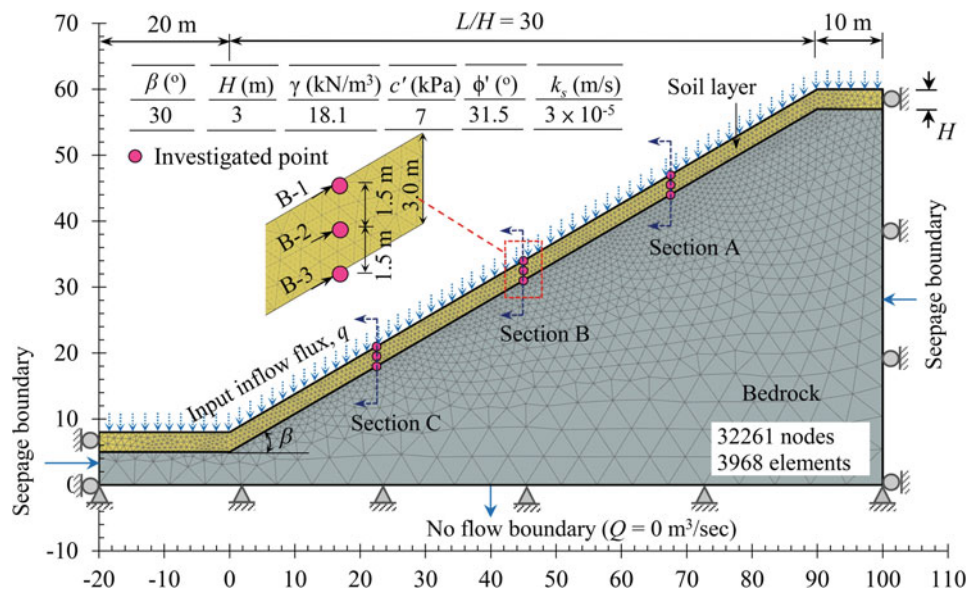
Fig. 4 Model validation by comparing the surface displacement and failure timing

observed ones from the experimentally, indicating that fully coupled hydro-mechanical model analysis based on the framework of unsaturated soil mechanics was applicable to evaluate the mechanical and hydraulic responses as well as the deformation characteristics of shallow slopes subjected to rainfall.

Model Study

In this study, a FE slope model was established to model a shallow slope that has a total length of 120 m and slope angle of 30° (Fig. 5). The slope model consists of a 3 m-thick soil layer underlain by an impermeable rock layer. The ratio of slope length to soil thickness in the slope model is $L/H = 30$, which is larger than the suggested value ($=25$) to ensure no interference from boundaries on the calculation of slope deformation (Milledge et al. 2012). The FE mesh

Fig. 5 Shallow slope model used in this study



with 15-noded triangular elements consists of 32,261 nodes and 3968 elements in total (Fig. 5). The numerical simulation was performed in two steps: initial suction of 10 kPa was first generated and then a rainfall intensity of $q = 16.25$ mm/h was prescribed on the top surface of the slope until the failure of shallow slopes is occurrence. The value of rainfall intensity used herein were referenced from the Taiwan Soil and Water Conservation Bureau for 263 mass movement caused by rainfall events (Chen et al. 2015), in which reported that mean rainfall intensity ranged from 8.9 to 64.8 mm/h.

The characterizing residual soil slopes were statistically determined from a large database of soil properties soils compiled from 35 landslide case studies in the literature. The datasets cover a wide range of soil types including both residual weathered soils and transported colluvium deposits all over the world. The mean values of soil properties are provided in Table 1. The bedrock was modeled using the Mohr–Coulomb model with a very high Young’s modulus to ensure the deformation of the bedrock is negligible in the analysis (Camera et al. 2014). The hydraulic properties of soil model study (i.e., SWCC and HCF) is also described in Fig. 1.

Results and Discussion

PWP and Volumetric Water Content (VWC) Response

Figure 6 presents the variation of PWP and volumetric water content (VWC) with time. The results are presented for three depths below the slope surface (denoted as Depth-1, -2, and -3 in Fig. 5) for each selected location (Sections A, B, and C).

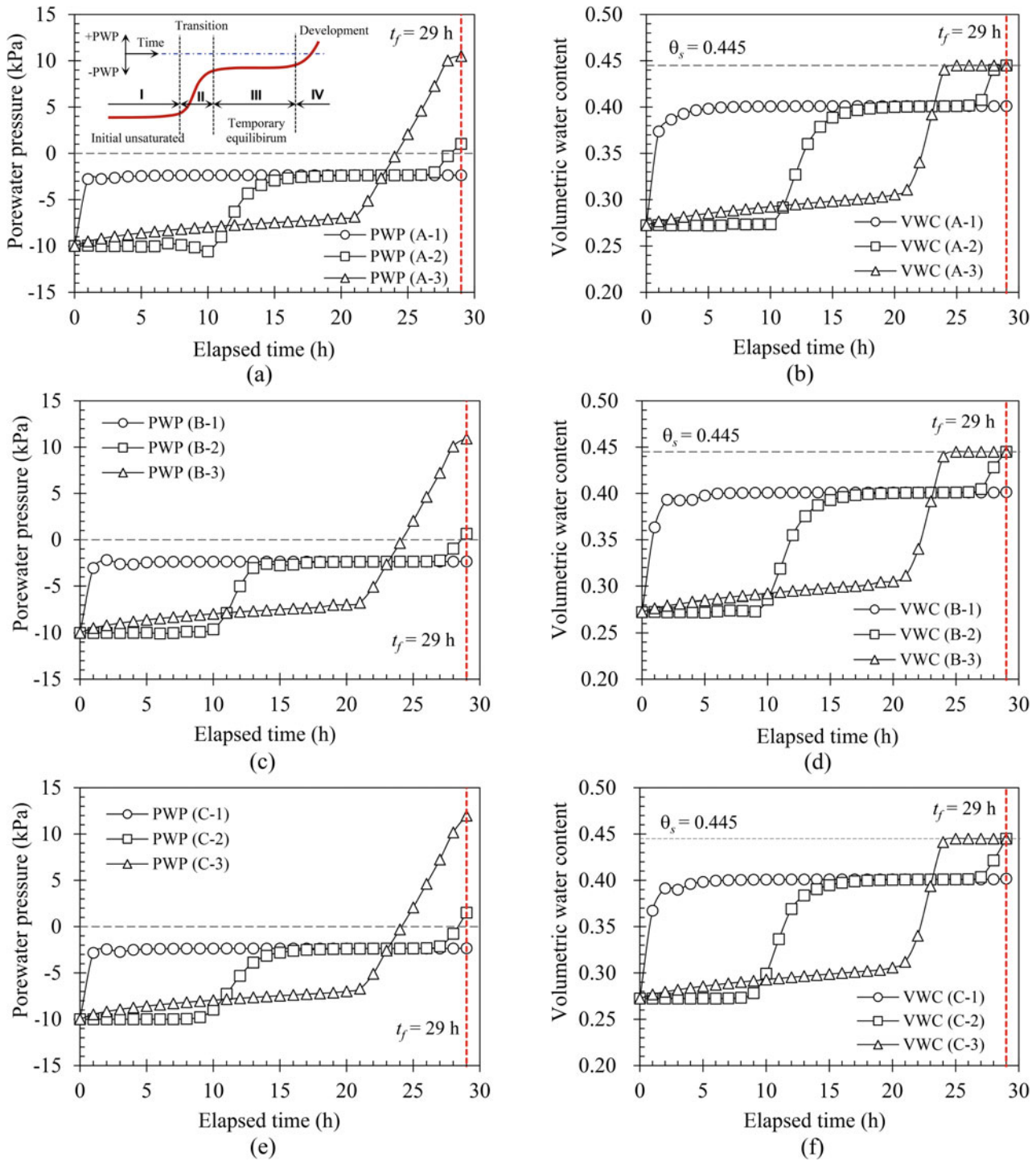


Fig. 6 Variation of PWP and VWC at: **a, b** Section A; **c, d** Section B; **e, f** Section C, with various depth below the ground surface

The numerical results show that the development of PWP with time generally can be divided into four stages: initial unsaturated stage, transition stage, temporary equilibrium stage, and development stage (inserted figure in Fig. 6). The soil was unsaturated originally in the initial unsaturated stage. The increase of PWP at the transition stage was due to

the loss of matric suction caused by the advancement of the wetting front. As the wetting front past, the inflow and outflow flux reached a balance and PWP remained equilibrium at the temporary equilibrium stage. Upon rainfall infiltration reached the base of the soil (approximately at $t = 21$ h), rainwater accumulated and then positive PWP

began to develop at the soil–bedrock interface (at $t = 24$ h) because the permeability of the bedrock was much lower than that of the soil. At this stage (the development stage, $t > 24$ h), the PWP exhibited a rapid increase trend as rainfall proceeded. The rapid increase of PWP happened later for the soil located higher from the soil–bedrock interface because it took some time for the accumulation of PWP to reach a higher location. Notably, slope failure occurred at $t_f = 29$ h when PWP at the base of the soil reached a critical threshold (≈ 11 kPa), corresponding to the PWP ratio (PWP divided by total overburden pressure, $u/\gamma H$) $r_u = 0.2$.

The variation of VWC over time (Fig. 6b, d, and f) shows similar trends with those in the PWP (Fig. 6a, c, and e). An increase in VWC was associated with an increase in PWP in the transition stage. The VWC reached temporary equilibrium at $\theta = 0.39$, corresponding to $S = 88\%$. The temporary equilibrium of VWC is also known as the initial quasi-saturated VWC, reported by Tohari et al. (2007) and Ling and Ling (2012), as an indicator to identify the onset of the slope movement. After rainfall infiltration reached the base of the soil ($t > 21$ h), the VWC of the soil at the base increased rapidly and becomes fully saturated ($\theta_s = 0.445$) at $t = 24$ h. It is worth highlighting that, in contrast to the trend of continuous development of positive PWP in the development stage, the VWC remained a constant value after soil was saturated.

The Development of Slope Displacement with Time

Figure 7 shows the slope total displacement (s – t curve) and the variation of FS with time. It was observed that the development of slope displacement is divided into three stages (constant, accelerated, and critical deformation stage) according to the rate of slope movement as suggested by Xu et al. (2011). Table 2 summarizes the slope displacement stage and the corresponding PWP development.

The slope deformation was not significantly developed at $t < 21$ h before the rainfall infiltration reached the base of the soil. The slope gradually moved with a low displacement rate ($v < 1$ mm/h) in the constant deformation stage

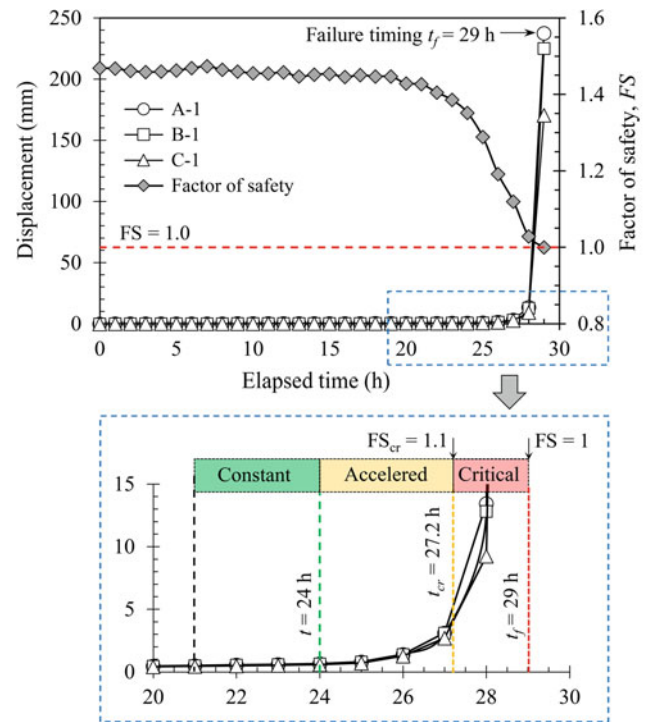


Fig. 7 FS versus time and slope displacement curve (s – t curve)

($21 \text{ h} < t < 24 \text{ h}$), where v is defined, $v = (u_{t_2} - u_{t_1}) / (t_2 - t_1)$, where u_{t_1} and u_{t_2} are the displacement corresponding to the interval time t_1 to t_2 , respectively. In this deformation stage, the PWP steadily increased but still remained a negative value, corresponding to the first three stages in the PWP development. Evident slope deformation developed with a displacement rate ranging from $v = 1$ – 3 mm/h in the accelerated deformation stage ($24 \text{ h} < t < 27.2 \text{ h}$). The development of evident slope deformation was triggered by the full saturation of soil and accumulation of positive PWP at the base of the soil starting from $t = 24$ h, corresponding to the early PWP development stage (refer to Fig. 6). The slope displacement increased rapidly with a large displacement rate ($v > 3$ mm/h) in the critical deformation stage ($t > 27.2$ h). This deformation stage corresponds to the late PWP development stage when the accumulation of positive PWP was larger than 7 kPa ($r_u = 0.15$). The corresponding

Table 2 Slope deformation stage and PWP development

Slope deformation stage	Timing	Displacement rate	Factor of Safety	PWP development stage	PWP value	PWP ratio
	t (h)	v (mm/h)	FS		(kPa)	r_u
Constant	21–24	<1	1.43–1.35	Initial unsaturated, transition, and temporary equilibrium	<0	<0
Accelerated	24–27.2	1–3	1.35–1.10	Early development	0–7	0–0.15
Critical	27.2–29	>3	<1.1	Late development	7–11	0.15–0.2

factor of safety at the beginning of the critical deformation stage is $FS_{cr} = 1.1$. The final slope failure ($FS = 1$) occurred at $t_f = 29$ h. The maximum slope displacement occurred at the upper slope (Sections A and B) reached 240 mm at the moment of failure (Fig. 7).

Conclusion

A fully coupled hydro-mechanical analysis was carried out to investigate the hydraulic and deformation response of the slopes subjected to rainfall infiltration. The following conclusions can be drawn:

- The results confirmed that fully coupled hydro-mechanical analysis was capable of accurately predicting the mechanical and hydraulic responses as well as the deformation characteristics of shallow slopes subjected to rainfall.
- The slope deformation was highly correlated with the development of PWP as rainfall proceeded. The slope failure was triggered by the full saturation of the soil and the accumulation of positive PWP at the soil–bedrock interface. The failure surface was developed along the soil–bedrock interface and was determined as a transitional slide failure.
- The development of slope displacement with time can be divided into three stages. In the constant deformation stage, the slope gradually moved with a low displacement rate ($v < 1$ mm/h) and PWP still remained negative. In the accelerated deformation stage, evident slope deformation developed with a displacement rate ranging from $v = 1$ –3 mm/h and the PWP become positive at the base of the soil. In the critical deformation stage, the displacement increased rapidly with a large displacement rate ($v > 3$ mm/h) when the accumulation of PWP reached a critical threshold.

References

- Alonso EE, Gens A, Delahaye CH (2003) Influence of rainfall on the deformation and stability of a slope in overconsolidated clays: a case study. *Hydrogeol J* 11(1):174–192
- Bishop AW (1959) The principle of effective stress. *Teknisk Ukeblad*. 106(39):859–863
- Bordoni M, Meisina C, Valentino R, Lu N, Bittelli M, Chersich S (2015) Hydrological factors affecting rainfall-induced shallow landslides: from the field monitoring to a simplified slope stability analysis. *Eng Geol* 193:19–37
- Brinkgreve RBJ, Kumarswamy S, Swolfs WM (2019) PLAXIS 2019 manual. PLAXIS bv, Delft, Netherlands
- Camera CAS, Apuani T, Masetti M (2014) Mechanisms of failure on terraced slopes: the Valtellina case (northern Italy). *Landslides* 11(1):43–54
- Casagli N, Dapporto S, Ibsen ML, Tofani V, Vannocci P (2005) Analysis of the landslide triggering mechanism during the storm of 20th–21st November 2000 Northern Tuscany. *Landslides* 3(1):13–21
- Chen CW, Saito H, Oguchi T (2015) Rainfall intensity–duration conditions for mass movements in Taiwan. *Prog Earth Planet Sci* 2(1):14
- Ghasemi P, Cuomo S, Di Perna A, Martinelli M, Calvello M (2019) MPM-analysis of landslide propagation observed in flume test. In: *Proceeding of 2nd international conference on the material point method for modelling soil-water-structure interaction*. Cambridge, UK
- Griffiths DV, Lane PA (1999) Slope stability analysis by finite elements. *Geotechnique* 49(3):387–403
- Johnson KA, Sitar N (1990) Hydrologic conditions leading to debris-flow initiation. *Can Geotech J* 27(6):789–801
- Lee LM, Kassim A, Gofar N (2011) Performances of two instrumented laboratory models for the study of rainfall infiltration into unsaturated soils. *Eng Geol* 117(1–2):78–89
- Leung AK, Ng CWW (2016) Field investigation of deformation characteristics and stress mobilisation of a soil slope. *Landslides* 13(2):229–240
- Ling H, Ling HI (2012) Centrifuge model simulations of rainfall-induced slope instability. *J Geotech Geoenviron Eng* 138(9):1151–1157
- Milledge DG, Griffiths DV, Lane SN, Warburton J (2012) Limits on the validity of infinite length assumptions for modelling shallow landslides. *Earth Surf Proc Land* 37(11):1158–1166
- Moriwaki H, Inokuchi T, Hattajji T, Sassa K, Ochiai H, Wang G (2004) Failure processes in a full-scale landslide experiment using a rainfall simulator. *Landslides*. 1(4):277–288
- Mualem Y (1976) A new model for predicting the hydraulic conductivity of unsaturated porous media. *Water Resour Res* 12(3):513–522
- Ng CWW, Zhan LT, Bao CG, Fredlund DG, Gong BW (2003) Performance of an unsaturated expansive soil slope subjected to artificial rainfall infiltration. *Geotechnique* 53(2):143–157
- Qi SC, Vanapalli SK (2015) Hydro-mechanical coupling effect on surficial layer stability of unsaturated expansive soil slopes. *Comput Geotech* 70:68–82
- Sasahara K, Sakai N (2014) Development of shear deformation due to the increase of pore pressure in a sandy model slope during rainfall. *Eng Geol* 170:43–51
- Tang Y, Wu W, Yin KL, Wang S, Lei G (2019) A hydro-mechanical coupled analysis of rainfall induced landslide using a hypoplastic constitutive model. *Comput Geotech* 112:284–292
- Tohari A, Nishigaki M, Komatsu M (2007) Laboratory rainfall-induced slope failure with moisture content measurement. *J Geotech Geoenviron Eng* 133(5):575–587
- van Genuchten MT (1980) A closed-form equation for predicting the hydraulic conductivity of unsaturated soils. *Soil Sci Soc Am J* 44(5):892–898
- Vanapalli SK, Fredlund DG, Pufahl DE, Clifton AW (1996) Model for the prediction of shear strength with respect to soil suction. *Can Geotech J* 33(3):379–392
- Wang G, Sassa K (2001) Factors affecting rainfall-induced flowslides in laboratory flume tests. *Geotechnique* 51(7):587–599
- Wang GH, Sassa K (2003) Pore-pressure generation and movement of rainfall-induced landslides: effects of grain size and fine-particle content. *Eng Geol* 69(1–2):109–125

- Xu Q, Yuan Y, Zeng YP, Hack R (2011) Some new pre-warning criteria for creep slope failure. *SCI China Technol Sci* 54(1):210–220
- Yang KH, Uzuoka R, Thuo JN, Lin GL, Nakai Y (2017) Coupled hydro-mechanical analysis of two unstable unsaturated slopes subject to rainfall infiltration. *Eng Geol* 216:13–30
- Yubonchit S, Chinkulkijniwat A, Horpibulsuk S, Jothityangkoon C, Arulrajah A, Suddeepong A (2017) Influence factors involving rainfall-induced shallow slope failure: Numerical study. *Int J Geomech* 17(7):04016158
- Zhang S, Xu Q, Zhang Q (2017) Failure characteristics of gently inclined shallow landslides in Nanjiang, southwest of China. *Eng Geol* 217:1–11
- Zhou YD, Cheuk CY, Tham LG (2009) Deformation and crack development of a nailed loose fill slope subjected to water infiltration. *Landslides* 6(4):299–308



2020 Kyoto Japan

Debris Flow Simulations Due to Landslide Dam Outburst and Considering Effective Countermeasures

Kana Nakatani, Ken'ichirou Kosugi, and Yoshifumi Satofuka

Abstract

Recently, deep-seated landslides, DSLs, have become more frequent due to heavy rain events. Due to DSLs, there have been some cases of landslide dam formations in mountainous regions. When landslide dam outburst occurs, large scale debris flow might devastate the downstream area. Therefore, debris flow scenarios, arising from landslide outbursts, are studied to predict and prevent the damages in the downstream regions. In this study for the purpose of simulation, we applied the Hyper KANAKO system with the digital elevation model, DEM, taken before and after the landslide dam formation. First, we simulated the landslide dam outburst scenario by comparing it with the downstream deposition. When the sediment diameter and the fluid phase density were set to 0.2 m and 1,000 kg/m³, respectively, the results were satisfactory. Then, we considered an effective countermeasure installation in the torrent by setting one closed type sabo dam with an effective height of 15 m. We found that setting the sabo dam in the downstream side of the torrent prevented the sediments from moving downstream; this setup effectively prevented the damage. Therefore, simulations are useful for landslide dam outburst hazard mapping and for effective countermeasure implementation.

Keywords

Debris flow • Simulation • Landslide dam • Hazard mapping • Countermeasure

Introduction

Recently, deep-seated landslides, DSLs, have become more frequent due to heavy rain events. Due to DSLs, there have been some cases of landslide dam formations in mountainous regions. When landslide dam outburst occurs, large scale debris flow might devastate the downstream area. Therefore, debris flow scenarios, arising from landslide outbursts, are studied to predict and prevent the damages in the downstream regions. Debris flow simulation is an effective tool for investigating the landslide dam outbursts that occur due to overtopping and debris flow flooding, as well as for investigating the downstream depositions due to the outbursts. For debris flow simulation, several models and systems have been proposed and applied. However, the Takahashi model is widely applied, and it demonstrates good results not only in the experimental cases but also in the real debris flow disaster cases (Takahashi 2007). Some studies have considered the DSLs, large landslide dam formations, and outbursts. However, most of the studies have focused on the debris flow peak discharges due to outbursts. In 2018, Braun et al. had conducted simulation studies on the formation and the stability of landslide dams in China using SPH analysis. However, only a few studies were aimed at understanding the downstream side of landform changes, such as the deposition distributions in Japan.

In this study, we focused on a landslide dam formed in the Akatani area, Nara Prefecture, Japan, due to typhoon No. 12 in 2011, which had occurred in the Kii peninsula. A landslide dam was formed due to a DSL, an outburst occurred due to overtopping, and a debris flow moved downstream. Detailed data was observed and collected through surveys. We applied debris flow simulations to achieve our goals. Therefore, first we did a back analysis of the simulation settings that could describe the observed landslide dam outburst situation. Then, we simulated the effective countermeasure implementations in the downstream region of the landslide dam. In this study, we aimed

K. Nakatani (✉) · K. Kosugi
Graduate School of Agriculture, Kyoto University, Oiwake-cho,
Kitashirakawa, Sakyo-ku, Kyoto, 6068502, Japan
e-mail: kana2151@kais.kyoto-u.ac.jp

Y. Satofuka
Department of Civil Engineering, Ritsumeikan University,
Noji-higashi 1-1-1, Kusatu, 5258577, Japan
e-mail: satofuka@se.ritsumeik.ac.jp

© Springer Nature Switzerland AG 2021

B. Tiwari et al. (eds.), *Understanding and Reducing Landslide Disaster Risk*,
ICL Contribution to Landslide Disaster Risk Reduction,
https://doi.org/10.1007/978-3-030-60706-7_21

to show that debris flow simulations could be useful for landslide dam outburst hazard mapping and for effective countermeasure implementation.

Simulation Target and Methods

Akatani Landslide Dam Formation in 2011 Nara Prefecture, Japan

The simulation target was the landslide disaster that occurred in the Kii peninsula, Japan due to typhoon No. 12 in 2011 (Matsumura et al. 2012; Kinoshita et al. 2018). In this study, the target region was in the Akatani area, Nara Prefecture, Japan. Due to the long-duration and the high intensity of the rain, a DSL occurred with a sediment volume of approximately 9 million m³. Due to the DSL, a landslide dam with approximately 85 m height was formed in the Akatani river, which is a tributary of the Kawarabi river. Figure 1, which has been taken from the Ministry of Land, Infrastructure, Transport and Tourism in Japan, MLIT, shows the landslide dam that was formed in 2011 due to a DSL, and Fig. 2, which has been edited to Kinoshita et al. (2018) shows the elevation difference before and after the disaster.

Many researchers had conducted countermeasure works in the Kii peninsula, including the Akatani area, after the DSL and the subsequent formation of landslide dams. However, structural countermeasures, especially for DSLs, are expensive and time consuming. Thus, we also needed to consider non-structural countermeasures, such as simulating hazard mappings. Therefore, we first aimed to consider the debris flow scenario due to the landslide dam outburst that occurred in 2011.

Simulations for Debris Flow Due to the Landslide Dam Outburst in the Akatani Area 2011

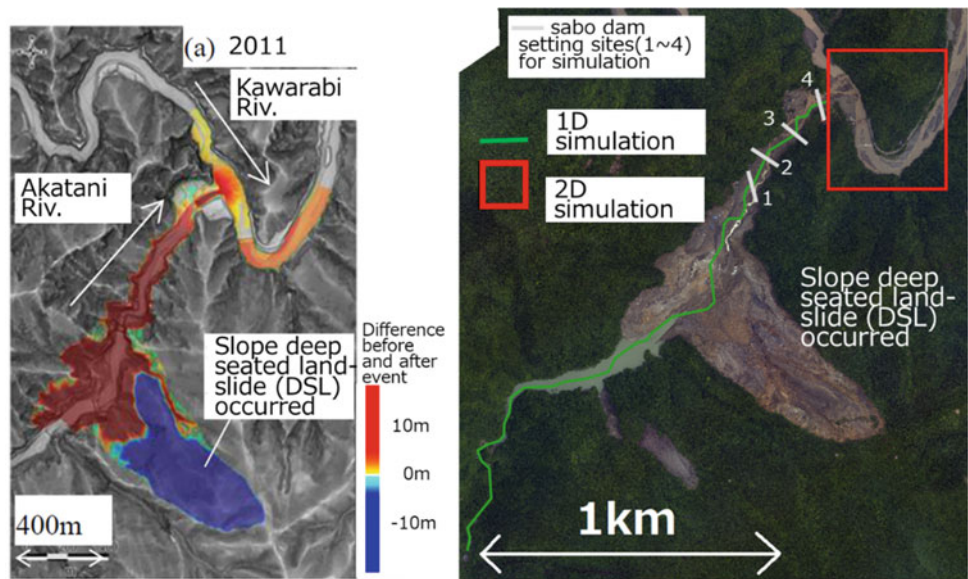
The authors used a debris flow simulation system, which was based on geographic information system, GIS, called the Hyper KANAKO system (Nakatani et al. 2012). In the Hyper KANAKO system, the numerical simulation of the debris flow takes into account the erosion/deposition due to the equilibrium concentration that is based on the model presented by Takahashi et al. (2001) and Takahashi (2007). The Hyper KANAKO system includes equations for momentum, continuation, riverbed deformation, erosion/deposition, and riverbed shearing stress. Moreover, an integrated model (Wada et al. 2008) was developed and implemented, incorporating the influences not only on the 1D simulation areas, such as the steep mountainous valley area but also on the 2D simulation areas, such as the alluvial fans. The effects of the sabo dams or the check dams on the 1D areas were simulated based on the model developed by Satofuka and Mizuyama (2005).

We set the Akatani River area, where the landslide dam had formed, as the 1D simulation area. Typically, 2D simulation areas are set at the valley exit where there are alluvial fans and residential areas that help in analyzing the high-risk area. However, in this study, we set the 2D simulation area from the confluence to the Kawarabi River, as shown in the right portion of Fig. 2. The right portion of Fig. 2 shows the orthophoto taken by MLIT after the disaster. We considered the deposition distribution in the Kawarabi River as a debris flow hazard, because a change in the riverbed, especially large deposition, might reduce the discharge capacity of the main river and cause flooding/deposition around the main river.

Fig. 1 DSL and landslide dam after the 2011 disaster (taken from MLIT)



Fig. 2 DSL and landslide dam after the 2011 landslide disaster (left: edited to Kinoshita et al. 2018; right: the simulation area with the orthophoto taken from MLIT after the 2011 landslide disaster)

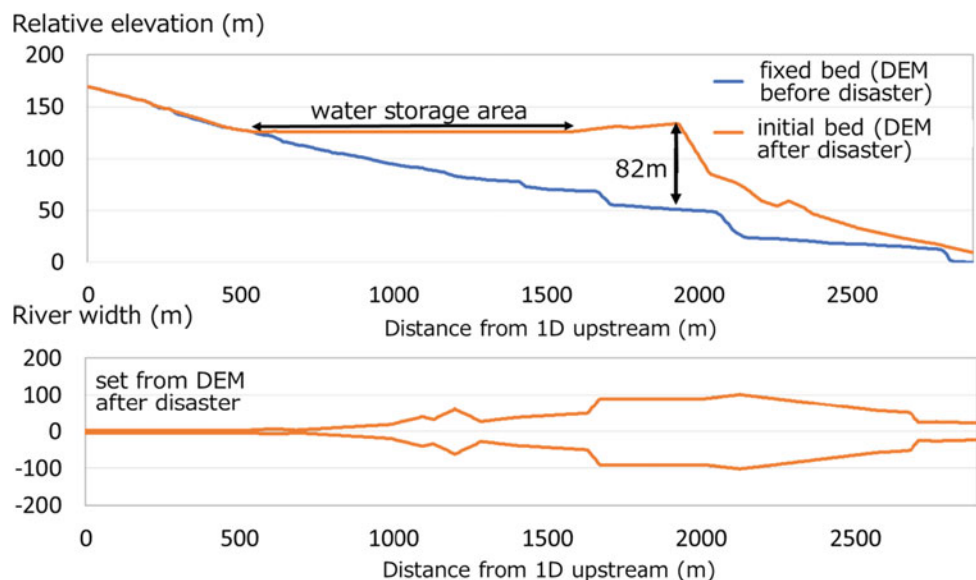


The top portion of Fig. 3, shows the longitudinal figure in the 1D area. Fixed bed was set from the digital elevation model, DEM, taken before the disaster, and the initial bed was set from the DEM taken after the disaster. The DEM was obtained by MLIT through the airborne laser scanning method with a 1 m mesh resolution. The difference between the initial bed and the fixed bed is a movable bed layer, and the landslide dam showed a maximum height of 82 m at 1,825 m downstream from the 1D upstream end. The bottom portion of Fig. 3, shows that the river width was set from the DEM that was taken after the disaster. To consider the risk factor of the landslide dam outburst due to overtopping, we assumed that the overtopping and the erosion occurred in the entire width of the river.

Figure 4 shows that for the debris flow simulation, we supplied water from the upstream end. Initially, we supplied water at the rate of 1,000 m³/s from the upstream end of the landslide dam. From 40 s before the overtopping occurred, we supplied water at the rate of 300 m³/s until the simulation ended.

For simulating a debris flow, it is important to set the parameters in relation to the constituent materials of the debris flow. There are two parameters which are as follows: (a) the representative grain diameter '*d*', whose unit is m, is for sediments behaving as a solid phase, and (b) fluid phase density '*ρ*', whose unit is kg/m³, is for finer materials behaving as a fluid phase. We referred to the disaster reports and also conducted field surveys in the Akatani and

Fig. 3 Longitudinal figure (top) and river width (bottom) in the 1D simulation area, set from DEM taken from MLIT



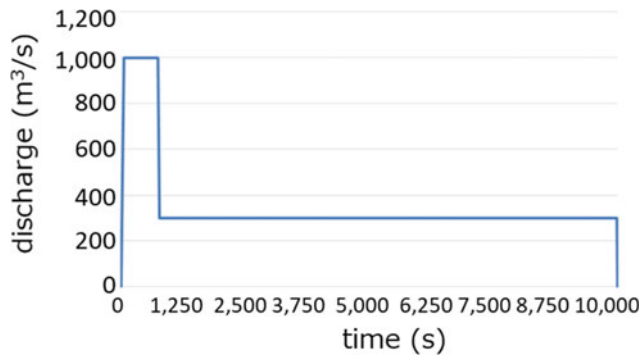


Fig. 4 Water supply from upstream

Table 1 Simulation cases

Case	Representative grain-diameter (m)	Fluid phase density (kg/m ³)
1	0.2	1,000
2	0.2	1,400
3	1.0	1,000
4	1.0	1,400

considered 0.2 m and 1.0 m as the values for ‘ d ’. Furthermore, for ‘ ρ ’, we considered the values 1,000 kg/m³ in the usual situation of stony debris flow, and 1,400 kg/m³ in the scenario when most of the fine sediments behaved as fluid phase indicated by recent studies (e.g., Nakatani et al. 2018; Takahashi 2007). We considered the four cases that are listed in Table 1. Other parameters used in the simulation are listed in Table 2.

Table 2 Simulation parameters

Parameter	Value	Unit
Simulation time	10,000	s
Time step	0.01	s
Mass density of sediment	2650	kg/m ³
Concentration of movable bed	0.65	
Erosion velocity coefficients	0.007	
Deposition velocity coefficient	0.05	
Manning’s coefficient	0.03	s/m ^{1/3}
1D simulation points interval	5	m
Number of 1D points	5	
2D simulation mesh size	10 × 10	m × m
Number of 2D meshes	51 × 62	

Simulation Results and Effective Countermeasures

Simulation Results

Figure 5 shows the simulation results of the deposition thickness for the 2D area that have been compared with the actual situations reported by Kinoshita et al. (2018). The area bordered by the purple line indicates a deposition of more than 300 cm. In the east section (right portion of the figure) of the Kawarabi River, the purple dotted line shows the downstream end of the deposition that is more than 1 cm. By comparing the simulation cases, we concluded that Case 1 with ‘ d ’ and ‘ ρ ’ whose values are 0.2 m and 1,000 kg/m³ were in good agreement to the observed situations of the deposition distributions.

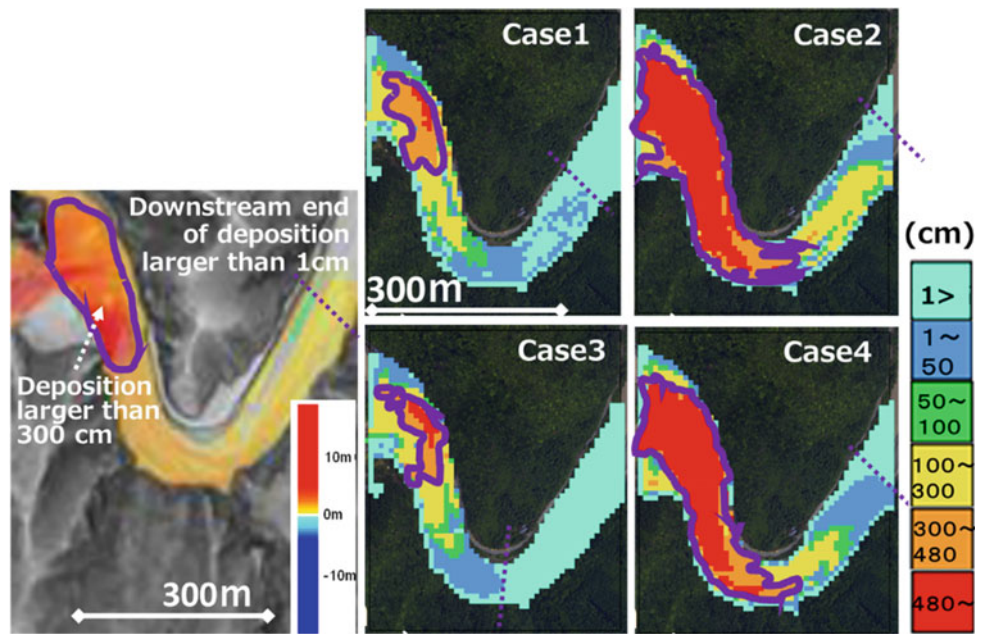
Simulations Considering the Effective Structural Countermeasures

Using debris flow simulations, we can estimate the distribution of numerical values such as the deposition thickness, flow depth, and velocity, and can also estimate the hazard zoning of the target area. In this paper, we found that Case 1 showed a good agreement with the observed deposition. Typically, removing the sediments of the landslide dam and the DSL as well as draining the upstream water of the landslide dam are conducted for disaster mitigation planning.

However, in this study, we considered a simple disaster mitigation planning to set a single sabo dam at the downstream side of the landslide dam using debris flow simulation. This method illustrated how we could apply simulations for considering effective countermeasures. We applied the debris flow scenario due to the landslide dam outburst, as described in Case 1. We considered to set a single closed type sabo dam with effective height of 15 m in the four installation sites, whose distances from the upstream end were set as 2,372.5 m, 2,517.5 m, 2,682.5 m and 2,767.5 m, respectively. We selected the four sites from the trial simulations which had relatively smaller slopes and better effective sediment capturing characteristics compared to the surrounded sites. The locations are shown in Fig. 2. Other settings such as the supplied discharge and the parameters were kept the same.

Figure 6 shows the simulation results of the deposition thickness in the 2D area. We also considered the sedimentation volumes, which were moved to the 2D area from the simulated 1D Akatani River area, with and without the installed sabo dam, as listed in Table 3. From the deposition distribution shown in Fig. 6 and the numerical values listed in Table 3, it is evident that setting a sabo dam at the

Fig. 5 Simulation results of the deposition thickness for the 2D area (right) and the observed deposition (left) as reported by Kinoshita et al. (2018)



downstream side was more effective than setting it up at the upstream side. Setting a dam at 2,767.5 m from the upstream end (dam 4), decreased the sediment movement to the Kawarabi River by 4% compared to when there was no sabo dam. When the sabo dam was set on the downstream side, the distance from the downstream of the landslide dam to the

upstream of the sabo dam increased. Furthermore, by comparing the four installation sites it was observed that the slope of the installation site decreased when the dam was set on the downstream side. Therefore, the capacity of the sabo dam to store sediments increased when the sabo dam was set on the downstream side.

Fig. 6 Simulation results for the deposition thickness in the 2D area by taking the sabo dam setting into consideration as described in Case 1

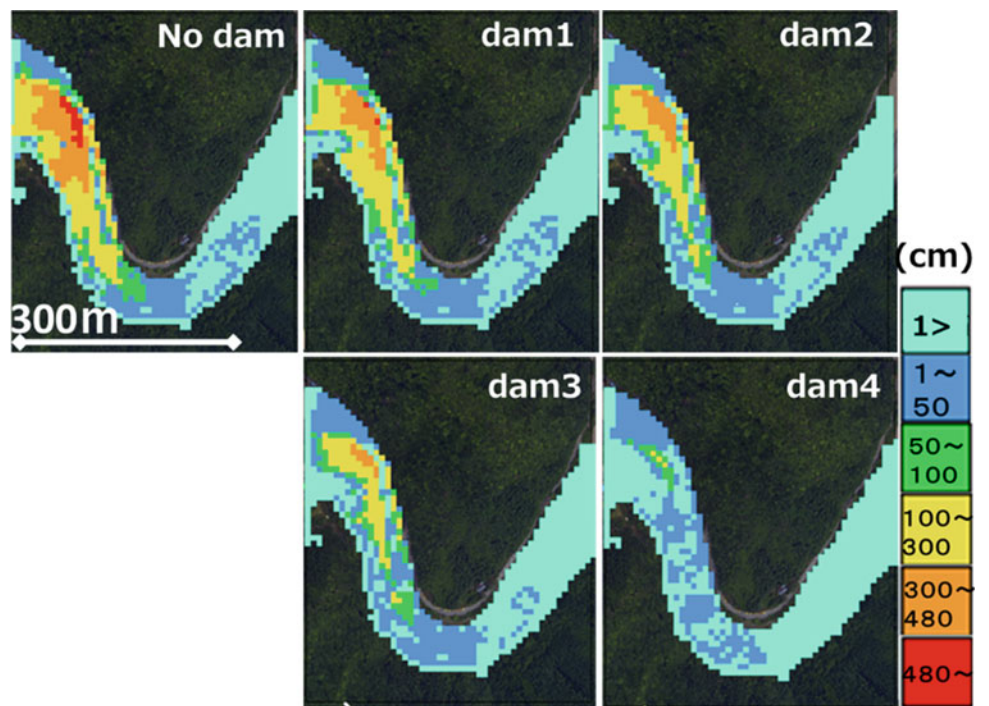


Table 3 Sabo dam installation conditions and the sediment movement to the 2D area described in Case 1

Sabo dam installation	Sediment moved to 2D area
No dam (NO)	83,344 m ³
2372.5 m from upstream end (dam1)	62,584 m ³ (75% comparing with NO)
2517.5 m from upstream end (dam2)	41,260 m ³ (50% comparing with NO)
2682.5 m from upstream end (dam3)	28,100 m ³ (34% comparing with NO)
2767.5 m from upstream end (dam4)	3,462 m ³ (4% comparing with NO)

Conclusions and Future Works

In this study, we focused on a large debris flow that occurred due to the landslide dam outburst in the Akatani area, Nara Prefecture, Japan, due to typhoon No. 12 in 2011, that had occurred in the Kii peninsula. For the purpose of simulation, we applied the Hyper KANAKO system with the DEM landform data, taken before and after the landslide disaster, respectively. First, we considered the simulation settings that described the actual landslide dam outburst situation and compared it with the deposition distribution. It was observed that a sediment diameter of 0.2 m and a fluid phase density of 1,000 kg/m³ showed satisfactory results. Then, we considered the effective countermeasure implementation in the torrent by setting a single closed type sabo dam with an effective height of 15 m. We found that setting the sabo dam in the downstream of the torrent was effective in preventing sediments from moving downstream to the Kawarabi River and thereby preventing the damage around the river. Therefore, simulations can be useful for landslide dam outburst hazard mapping and for considering effective countermeasures.

However, we considered only one landslide dam outburst event and only one sabo dam installation in the Akatani area. Since 2011, large volume of sediments weathered away from the DSLs and there have been several sediment runoffs from the landslide dams. Some countermeasure works, such as removing sediments and setting up of water passes, have also been conducted on the landslide dams.

In our future works, we will focus on other events, countermeasures, and effective use of numerical simulations in preventing disasters.

Acknowledgments We would like to give great thanks to the Ministry of Land, Infrastructure and Transport and Tourism, Japan, Kinki

Regional Development Bureau, Kii Mountain District Sabo Office, for providing LP data before and after the disaster.

References

- Braun A, Cuomo S, Petrosino S, Wang X, Zhang L (2018) Numerical SPH analysis of debris flow run-out and related river damming scenarios for a local case study in SW China. *Landslides* 15:535–550
- Kinoshita A, Tanaka K, Sakurai W, Uchida T, other 4 authors (2018) Focusing on riverbed variation at confluence, the impact by the sediment discharge from Akadani river basin on Kawarabi river. In: *Proceeding of annual meeting on Japan Society of Erosion Control Engineering*, JSECE publication 83, ISSN 2433-0477, pp 495–496 (in Japanese)
- Matsumura K, Fujita M, Yamada T, Yutaka G, other 17 authors (2012) Sediment disasters due to typhoon No. 12 at 2011, occurred in Kii peninsula. *J Japan Soc Eros Control Eng* 64(5):43–53 (in Japanese)
- Nakatani K, Furuya T, Hasegawa Y, Kosugi K and Satofuka Y (2018) Study on fine sediment phase change factors and influence on debris flow behaviour. *J Japan Soc Erosion Control Eng* 70(6):3–11 (in Japanese with English abstract)
- Nakatani K, Iwanami E, Horiuchi S, Satofuka Y, Mizuyama T (2012) Development of “Hyper KANAKO”, a debris flow simulation system based on Laser Profiler data. In: *Proceedings of INTER-PRAEVENT 2012*, April 2012, Grenoble, France, vol 1, pp 269–280
- Satofuka Y, Mizuyama T (2005) Numerical simulation of a debris flow in a mountainous river with a sabo dam. *J Jpn Soc Eros Control Eng* 58(1):14–19
- Takahashi T, Nakagawa H, Satofuka Y, Kawaike K (2001) Flood and sediment disasters triggered by 1999 rainfall in Venezuela: a river restoration plan for an alluvial fan. *J Nat Disaster Sci* 23(2):65–82
- Takahashi T (2007) *Debris flow: mechanics, prediction and countermeasures*. Taylor & Francis, Leiden, CRC Press, London, UK. (ISBN _978-0-415-43552-9), 448 p
- Wada T, Satofuka Y, Mizuyama T (2008) Integration of 1- and 2-dimensional models for debris flow simulation. *J Jpn Soc Eros Control Eng* 61(2):36–40 (in Japanese with English abstract)



2020 Kyoto Japan

Preliminary Results from the SMART-SED Basin Scale Sediment Yield Model

Federico Gatti, Luca Bonaventura, Alessandra Menafoglio, Monica Papini, and Laura Longoni

Abstract

In this work we describe a first version of the simulation tool developed within the SMART-SED project. The two main components of the SMART-SED model consist in a data preprocessing tool and in a robust numerical solver, which does not require a priori identification of river beds and other surface run-off areas, thus being especially useful to provide accurate input data to more localized landslide and debris-flow models. Furthermore, a geostatistical tool is available to downscale SoilGrids particle size fractions (psf) data to a given resolution. The psf data is employed also within the SCS-CN method, used to model the infiltration process. The results of a complete numerical simulation are reported and possible future developments of the model are discussed.

Keywords

Sediment yield modelling • Geostatistical kriging • Semi-implicit finite volume method • 2D shallow water equations

Introduction

Hydrogeological instability is a major concern for inhabited areas, due to its negative consequences as a natural hazard for people and infrastructures. Appropriate tools to identify areas prone to instabilities should include available information in flexible and easy-to-use databases, which are presently not fully exploited, as one can also deduce simply by the fact that this point is among the objectives of the present call.

The SMART-SED project (Sustainable Management of sediment transpoRT in responSE to climate change conDi-tions) stems out from the above considerations. Part of this project consists in the development of a tool able to simulate sediment transport resulting from slope erosion. The project is regarded as a reaction to demands of local territorial management institutions and professionals which lack the proper decision-making support tools regarding hydro-geological natural hazards (Brambilla, D., Papini, M., Ivanov, Vladislav Ivov, Bonaventura, L., Abbate A, Longoni, n.d.).

In this paper, we describe a first version of the simulation tool developed in the SMART-SED project. While not directly useful for modelling and prediction of landslide evolution, this kind of model can help to highlight the regions of greatest sediment yield and mobility, thus identifying critical areas where more specific landslide and debris-flow models can be applied.

Conceptual Scheme of the Model

The simulation tool is divided in two modules. A first module is able to downscale, via geostatistical methods, digital soil maps, while a second module solves the model equations with a finite volume—finite difference numerical scheme. In the first module, digital soil maps for the prediction and stochastic simulation of terrain-related quantities are used to estimate the input parameters of the second module.

F. Gatti (✉) · L. Bonaventura · A. Menafoglio · M. Papini · L. Longoni
MOX-Department of Mathematics, Politecnico Di Milano, Piazza Leonardo da Vinci, 32, 20133 Milano, Italy
e-mail: federico.gatti@polimi.it

L. Bonaventura
e-mail: luca.bonaventura@polimi.it

A. Menafoglio
e-mail: alessandra.menafoglio@polimi.it

M. Papini
e-mail: monica.papini@polimi.it

L. Longoni
e-mail: laura.longoni@polimi.it

Input data consist in rasters of digital soil maps taken from the SoilGrids repository, see (Hengl et al. 2017) and DTMs, as well as meteorological data in an ASCII file format. In the following, we first present the model equations and their numerical discretization, and later the geostatistical downscaling module.

Model Equations

The model solves the 2D shallow water equations for the surface runoff, coupled with transport equations for the sediment concentration and water content in the soil. These equations are coupled by source terms that represent the precipitation, infiltration and evaporation processes. The ground elevation is given on a spatial domain Ω by a Digital Terrain Model (DTM), which is based on a Cartesian uniform mesh. A basin subdomain Ω_b is then identified a priori by geometric considerations, which includes a drainage subdomain Ω_d that varies in time. We denote with H, η the depth of the surface runoff water layer and the water free surface from zero orography height, respectively, and with $u \in \mathbb{R}^2$ the surface water velocity. In the drainage subdomain, the following conservation laws are assumed:

$$\partial_t H + \nabla \cdot (Hu) = (1 - \mu)p - f \quad (1)$$

$$\partial_t u + g \nabla \eta + u \cdot \nabla u + \gamma(u)u = 0 \quad (2)$$

Here, p is the rainfall rate, f is the infiltration rate, g the gravity field, μ an indicator function which is equal to one in regions with snowfall and γ a friction coefficient defined according to (Rickenmann 1994).

Furthermore, if we denote with h_g the water depth in the gravitational layer, with h_{sd} the sediment layer depth and with h_{sn} the depth of the snow layer, the following conservation laws hold in the basin subdomain:

$$\partial_t h_g + \nabla \cdot f_g = f - ev + s, \quad (3)$$

$$\partial_t h_{sd} + \nabla \cdot f_{sd} = w \quad (4)$$

$$\partial_t h_{sn} = \mu p - s, \quad (5)$$

where ev is the evapotranspiration computed via Hargreaves model (Hargreaves and Allen 2003), s the snow melting rate computed with the Degree-Day approach (Day 2006), and w the sediment source term defined according to the Gavrilovic approach (Gavrilovic 1988). The dynamic of infiltration is modeled via the classical SCS-CN model, see e.g. (Ponce and Hawkins 1995) and the improvements proposed in (Michel et al. 2005):

$$F = \frac{SP}{P + S}, \quad (6)$$

where F is the cumulated infiltrated water, P is the cumulated total rainfall and S is the potential maximum soil moisture retention function of the Curve Number, which is a function of the soil texture. The gravitational flux f_g is modelled as:

$$f_g = h_g u_g, \quad (7)$$

where u_g represents the water velocity vertically averaged over the layer. This velocity is modeled as $u_g = \beta_g n$, where β_g is a function of the soil characteristics and of the water level in the layer, while n is the unit vector determined by the terrain slope b :

$$n = \frac{\nabla b}{|\nabla b|}. \quad (8)$$

The solid flux is defined via dimensional analysis considerations following (Zhang et al., 2009), (Papini, M., Ivanov, V., Brambilla, D., Arosio, D., Longoni, 2017) as:

$$f_{sd} = a \nabla b^b q, \quad (9)$$

where $a, b \in \mathbb{R}$ and $q = h_{sd} u$.

Numerical Discretization

To solve these equations numerically, we adopt for the surface runoff equations a first order semi-implicit Eulerian–Lagrangian discretization. This choice ensures good numerical stability also in case of Courant numbers greater than one, see (Casulli 1990) and (Casulli and Cheng 1992). Given input data rasters with a resolution $\Delta x \Delta y$, this results in a discrete surface layer depth equation is given for each cell by:

$$\begin{aligned} & \left[1 + g \frac{\Delta t^2}{\Delta x^2} \left(\alpha_{i+\frac{1}{2},j} H_{i+\frac{1}{2},j}^n + \alpha_{i-\frac{1}{2},j} H_{i-\frac{1}{2},j}^n \right) \right. \\ & \left. + g \frac{(\Delta t^2)}{(\Delta y^2)} \left(\alpha_{(i,j+\frac{1}{2})} H_{(i,j+\frac{1}{2})}^n + \alpha_{(i,j-\frac{1}{2})} H_{(i,j-\frac{1}{2})}^n \right) \right]_{(i,j)}^{(n+1)} \\ & - g \frac{\Delta t^2}{\Delta x^2} \alpha_{i+\frac{1}{2},j} H_{i+\frac{1}{2},j}^n \eta_{i+1,j}^{n+1} \\ & - g \frac{\Delta t^2}{\Delta x^2} \alpha_{i-\frac{1}{2},j} H_{i-\frac{1}{2},j}^n \eta_{i-1,j}^{n+1} \\ & - g \frac{\Delta t^2}{\Delta y^2} \alpha_{i,j+\frac{1}{2}} H_{i,j+\frac{1}{2}}^n \eta_{i,j+1}^{n+1} \\ & - g \frac{\Delta t^2}{\Delta y^2} \alpha_{i,j-\frac{1}{2}} H_{i,j-\frac{1}{2}}^n \eta_{i,j-1}^{n+1} = G_{i,j}^n, \end{aligned} \quad (10)$$

$$\begin{aligned}
 \mathcal{G}_{i,j}^n &= \eta_{i,j}^n + \Delta t(1 - \mu)p_{i,j}^n - \Delta t f_{i,j}^n \\
 &- \frac{\Delta t}{\Delta x} \left(\alpha_{i+\frac{1}{2},j} H_{i+\frac{1}{2},j}^n \mathcal{F}u_{i+\frac{1}{2},j}^n - \alpha_{i-\frac{1}{2},j} H_{i-\frac{1}{2},j}^n \mathcal{F}u_{i-\frac{1}{2},j}^n \right) \\
 &- \frac{\Delta t}{\Delta y} \left(\alpha_{i,j+\frac{1}{2}} H_{i,j+\frac{1}{2}}^n \mathcal{F}v_{i,j+\frac{1}{2}}^n - \alpha_{i,j-\frac{1}{2}} H_{i,j-\frac{1}{2}}^n \mathcal{F}v_{i,j-\frac{1}{2}}^n \right), \\
 \alpha_{i\pm\frac{1}{2},j} &= \frac{1}{1 + \Delta t \gamma_{i\pm\frac{1}{2},j}^n}, \alpha_{i,j\pm\frac{1}{2}} = \frac{1}{1 + \Delta t \gamma_{i,j\pm\frac{1}{2}}^n}
 \end{aligned}$$

Note that this set of equations defines a linear system to be solved at each time step, whose matrix is symmetric and positive definite. Here $\mathcal{F}u_{i\pm\frac{1}{2},j}^n$ and $\mathcal{F}v_{i,j\pm\frac{1}{2}}^n$ denote the semi-Lagrangian discretization of the convective term of the surface runoff momentum equations. For the other conservation laws, a first order explicit time upwind finite volume scheme (LeVeque 1992) is employed. While well known since a long time, the outlined method has not yet been applied to basin scale simulations. Its distinctive advantages consist in its numerical robustness and efficiency, which allows to use time steps that are only limited by accuracy, rather than by stability considerations, and in the fact that no a priori identification of river beds and other run-off areas is necessary. This enables a much more realistic description of the actual run-off during long range simulations.

Geostatistical Downscaling

The potential maximum soil moisture retention is a function of soil texture. Soil texture can be determined from particle-size fractions (psf), i.e. the relative percentages, in terms of soil composition, of clay, silt and sand, the three categories in which grains of fine earth are divided depending on their size (Soil texture, 2014). The psf data are compositional, i.e. vectors of positive components with a unit-sum constraint:

$$\sum_{1 \leq i \leq 3} z_i = 1 \quad (11)$$

where $z_i, i = 1, 2, 3$ are the fractions of clay, silt and sand, respectively. To avoid spurious correlations among ratios, (Kim 1999), the standard approach to the statistical analysis of compositional data is that proposed in (Aitchison, 1982). In this setting, the data are transformed through appropriate isomorphisms e.g. via an Isometric Log Ratio transform, (Martin-Fernandez et al., 2012), to operate within the Aitchison geometry without modifying the classical statistical techniques based on the Euclidean metric. The Soil-Grids data are then downscaled to match the desired

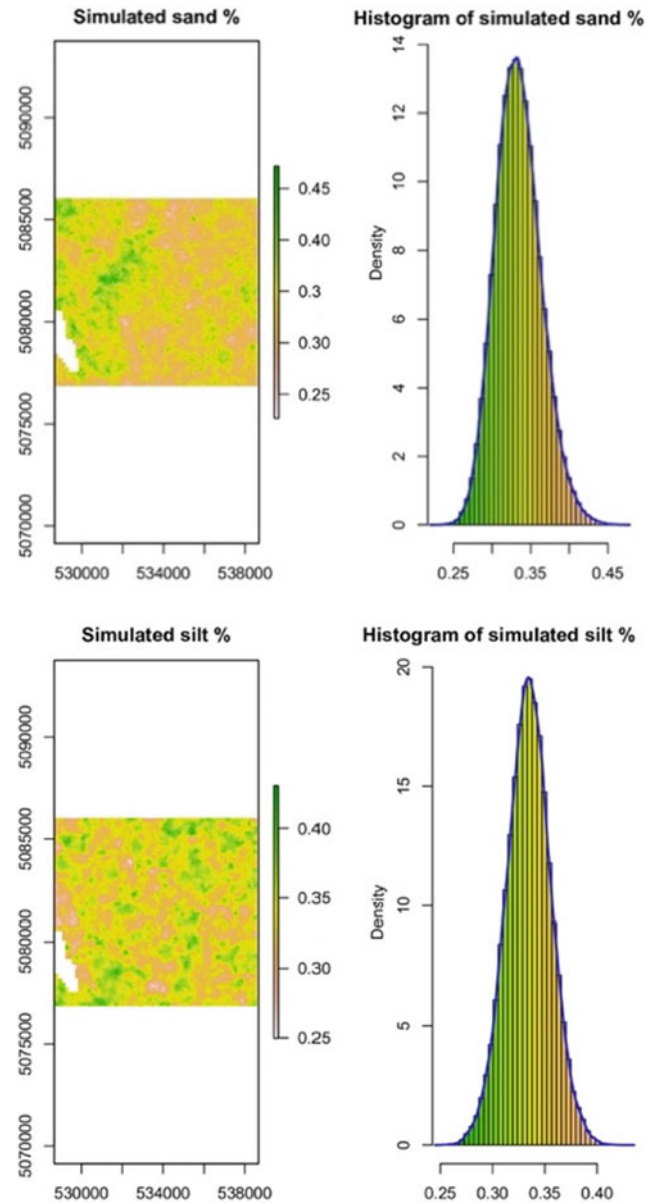


Fig. 1 Raster objects with an isotropic resolution of 20 m that represent sand (top) and silt (bottom) percentages of the topsoil of a real scenario (Caldone catchment (Ivanov et al. 2020)). These are results from Conditional Simulation based on the Compositional Area to Point Kriging

resolution a Compositional Area To Point Regression Kriging method (Togni 2019). Finally, we perform a geo-statistical Conditional Simulation to analyze, in a Monte Carlo setting, how the uncertainty propagates to the output of a numerical simulation (Soares 2001). In Fig. 1, we present an example of realization of the downscaled field, for a

raster resolution of $\Delta x = \Delta y = 20$ m starting from SoilGrids data with a resolution $\Delta x = \Delta y = 250$ m. Generation of multiple maps enables to estimate the uncertainty affecting psf data in the study area.

We want to remark here the importance of using SoilGrids data in our model. Indeed, at such length-scales, most of the time psf data are very difficult or impossible to be determined.

Numerical Results

We report here some results for the case of raster resolution of $\Delta x = \Delta y = 20$ m on a realistic scenario concerning the Caldane catchment, (Ivanov et al. 2020), see Fig. 2. The axis of the Caldane valley is oriented to the north-east and all the plots in Figs. 2, 3, 4, 5, and 6 are oriented to the north. The input data include a potential maximum soil moisture retention given by Fig. 3 and a rainfall rate $p = 1$ mm/h constant on the whole basin domain. 5 simulated days were considered with 100 time steps per hour. Initial fields are set to zero and the threshold under which surface run-off is set to zero is 1 mm. In Fig. 4 we have the final time height of the snow h_{sn} , in Fig. 5 and Fig. 6, top line, are shown final simulation time results of velocity and surface runoff height

fields u, H , finally in Fig. 6, bottom line, we show the final time water content in the gravitational layer h_g and sediment height h_{sd} .

From these results we can see that the river bed is determined automatically by numerical model during the simulation, see Fig. 5. No flattening of the non-convex regions has been necessary, in contrast to what is required by most numerical models of this kind. Finally, areas of high sediment yield are highlighted. This ability to describe fine details of the surface run-off processes without unrealistic a priori assumptions on the flow path makes of this modelling framework a very useful tool to provide input parameters and boundary conditions for more localized landslide and debris-flow models.

Conclusions and Future Developments

Future developments consist in the addition of the exfiltration process that occurs once the gravitational layer reaches its maximum capacity water content $h_{g,max}$. To account for this phenomenon, the equations have to be modified as:

$$\partial_t H + \nabla \cdot (Hu) = (1 - \mu)p - f + e, \quad (12)$$

Fig. 2 Isolines of the DTM height (in meters) used with raster size $20 \text{ m} \times 20 \text{ m}$

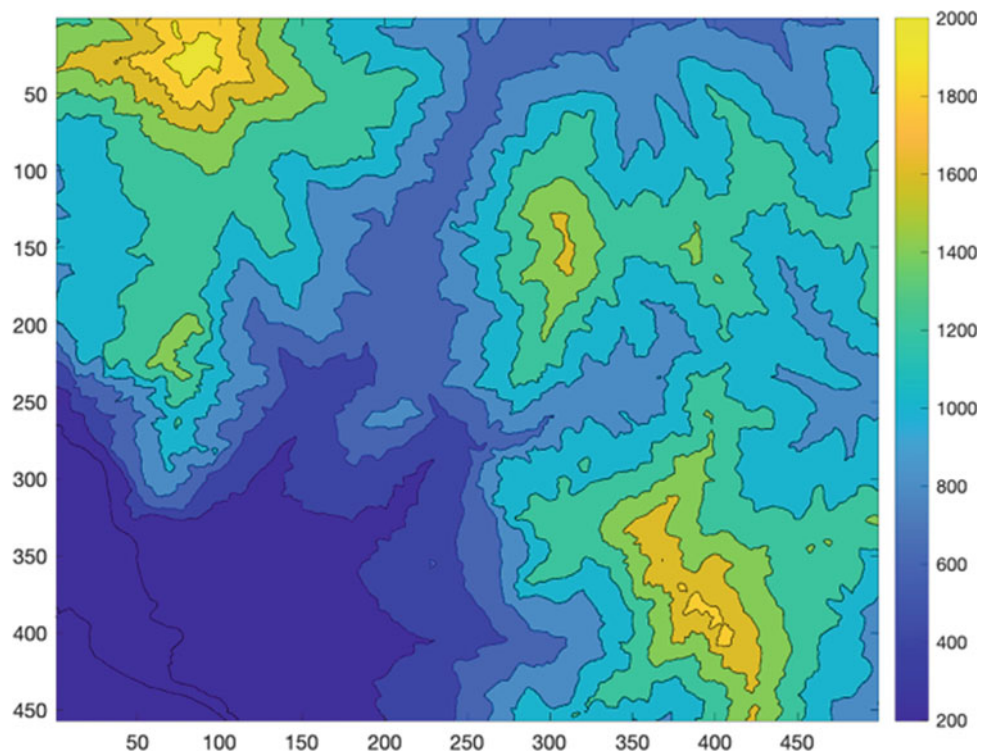


Fig. 3 Maximum potential soil moisture retention map, in meters, computed with the psf given by results shown in Fig. 2. Note that here are only shown values related to the basin zone

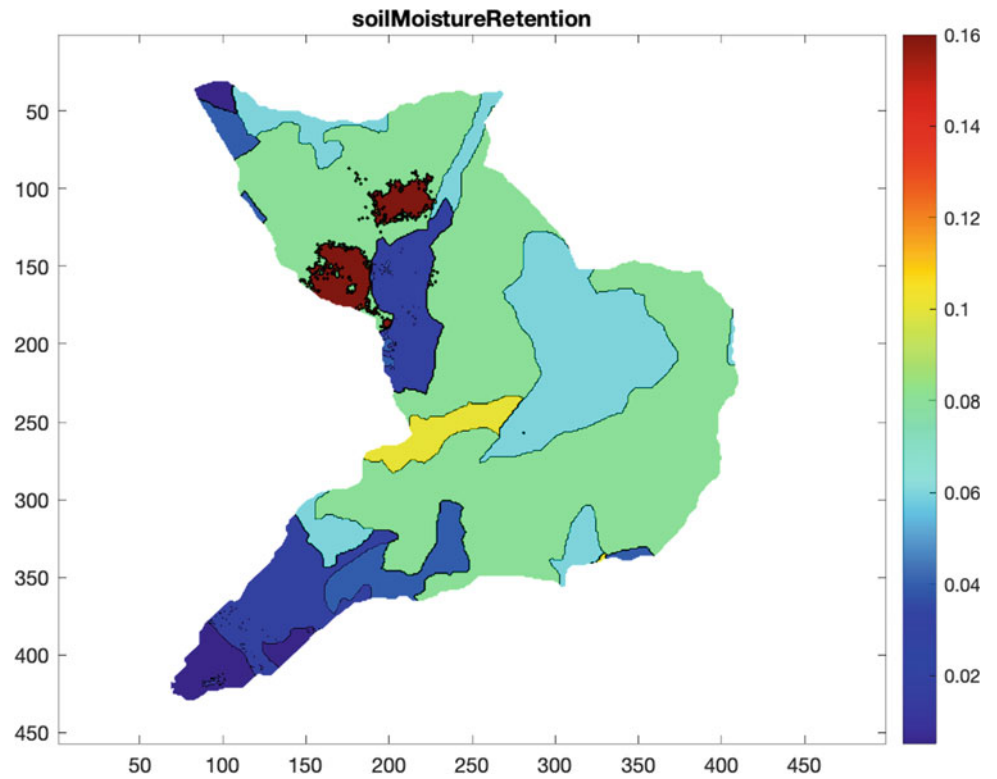


Fig. 4 Height of the final time snow in meters

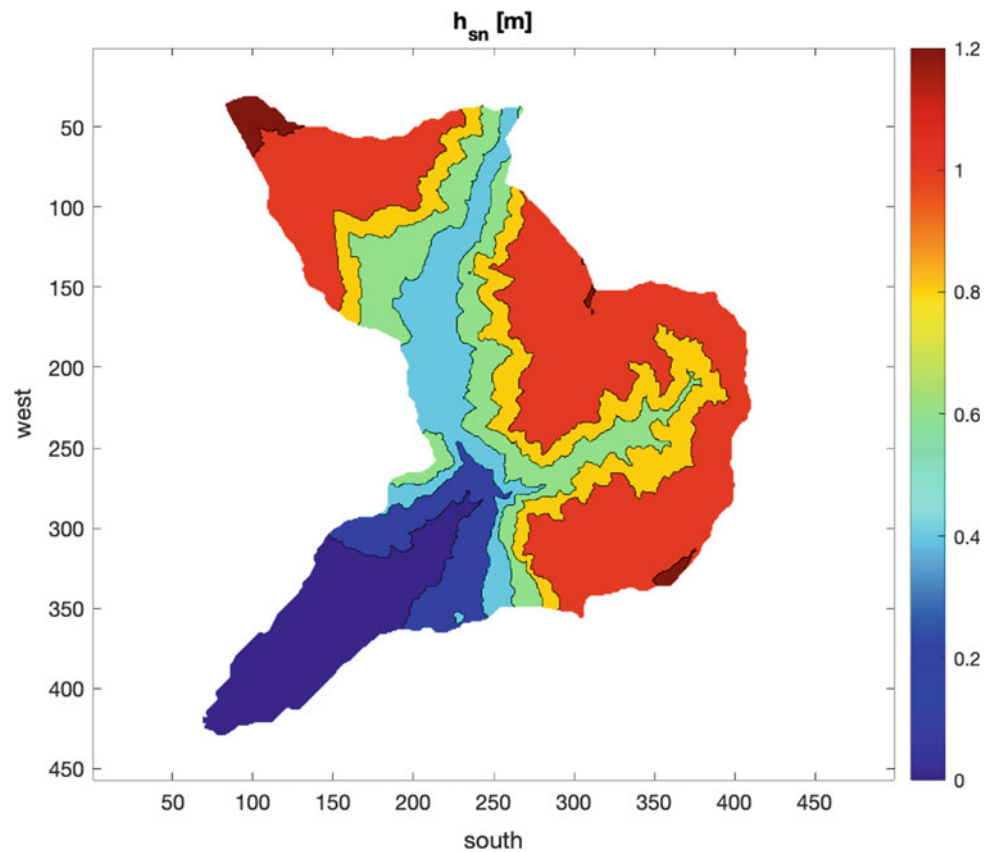
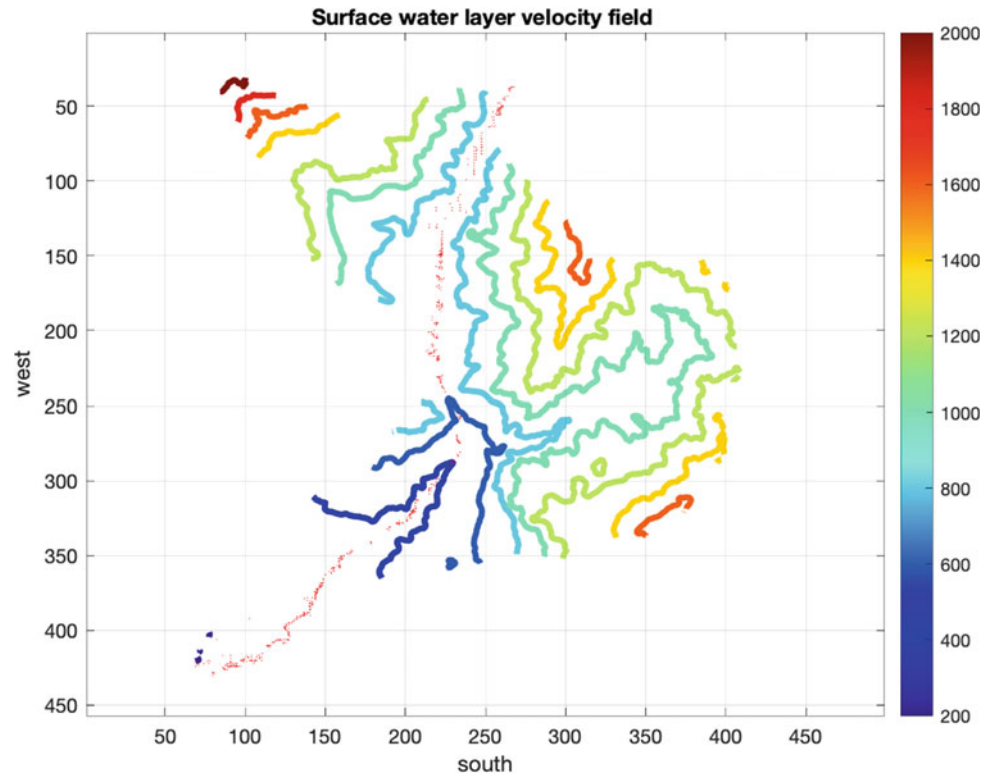


Fig. 5 Orography contour map, in meters, superimposed with the final simulation time velocity field (red arrows)



$$\partial_t h_g + \nabla \cdot f_g = f - ev + s - e, \quad (13)$$

incorporation of the treatment of subgrid scale orographic features proposed in (Casulli, 2019) would allow for even finer resolution runs at a reduced computational cost.

where e denotes the exfiltration rate. A full validation of the proposed model and a parallel implementation of its second module are other possible updates, as well as its coupling to localized models of landslides and debris flow. Finally, the

Acknowledgments The authors gratefully acknowledge the financial support of Fondazione Cariplo, grant number 2017-0722. We thank an anonymous reviewer for several suggestions which helped in improving the quality of the paper.

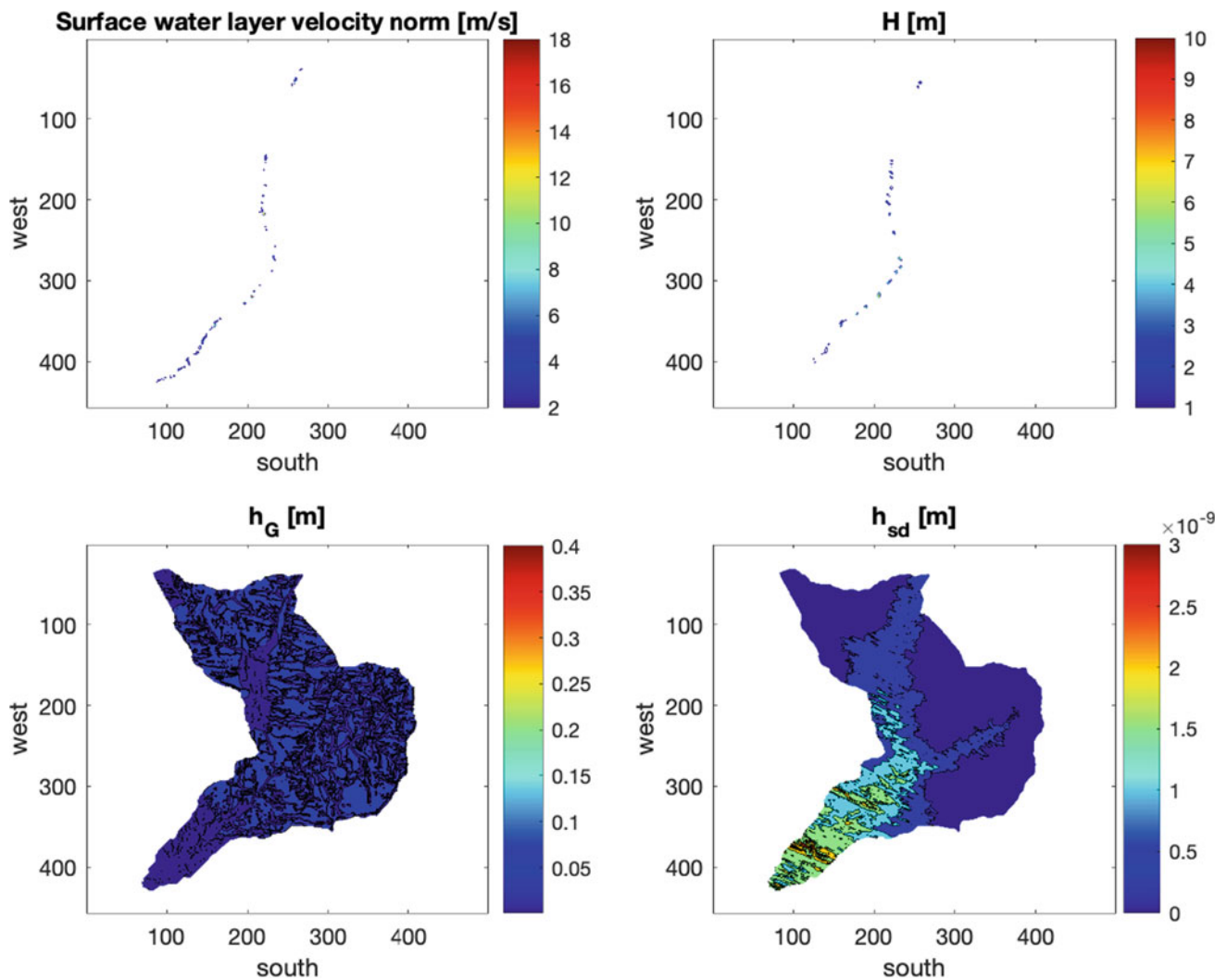


Fig. 6 On the upper-left: isolines of magnitude surface velocity runoff. On the upper-right: isolines of the height of superficial water. Both are final simulation time and the values are in meters. On the lower-left:

isolines of water content in the gravitational layer at the final time. On the lower-right: isolines of the height of sediment at the final time. Both values are in meters

References

- Aitchison J (1982) The Statistical Analysis of Compositional Data. *J Roy Stat Soc B* 44:139–160
- Brambilla, D., Papini, M., Ivanov, Vladislav Ivov, Bonaventura, L., Abbate A, Longoni, L. (n.d.). Sediment yield in mountain basins, analysis and management: the SMART-SED project. In (*In press*) *Sediment yield in mountain basins, analysis and management: the SMART-SED project*. In *Applied Geology: Approaches to future resource management*. De Maio, M & Tiwari, A. K. (eds).
- Casulli V (1990) Semi-implicit finite difference methods for the two-dimensional shallow water equations. *J Comput Phys* 86:56–74
- Casulli V, Cheng RT (1992) Semi-implicit finite difference methods for three-dimensional shallow water flow. *International Journal of Numerical Methods in Fluids* 15:629–648
- Casulli V (2019) Computational grid, subgrid, and pixels. *Int J Numer Meth Fluids* 90:140–155
- Day, T (2006) Degree-days: theory and application. *Tm41, CIBSE*.
- Gavrilovic Z (1988) Use of an empirical method (erosion potential method) for calculating sediment production and transportation in unstudied or torrential streams. In: International conference on River Regime. Hydraulics Research Limited, Wallingford, pp 411–422
- Hargreaves GH, Allen RG (2003) History and evaluation of Hargreaves evapotranspiration equation. *Journal of Irrigation and Drainage Engineering*. 129:53–63
- Hengl T, De Jesus JM, Heuvelink GBM, Gonzalez MR, Kilibarda M, Blagotić A, Shangguan W, Wright MN, Geng X, Bauer-Marschallinger B, Guevara MA, Vargas R, MacMillan RA, Batjes NH, Leenaars JGB, Ribeiro E, Wheeler I, Mantel S, Kempen B (2017) SoilGrids250m: Global gridded soil information based on machine learning. *PLoS ONE* 12:e0169748
- Ivanov V, Radice A, Papini M, Longoni L (2020) Event-scale pebble mobility observed by RFID tracking in a pre-Alpine stream: a field laboratory. *Earth Surf Proc Land* 45:535–547
- Kim JH (1999) Spurious correlation between ratios with a common divisor. *Statistics and Probability Letters*. 44:383–386

- LeVeque RJ (1992) *Numerical Methods for Conservation Laws*. Springer
- Martín-Fernández JA, Hron K, Templ M, Filzmoser P, Palarea-Albaladejo J (2012) Model-based replacement of rounded zeros in compositional data: classical and robust approaches. *Comput Stat Data Anal* 56:2688–2704
- Matthews JA (2014) Soil texture. In: *Encyclopedia of environmental change*
- Michel C, Andréassian V, Perrin C (2005) Soil Conservation Service Curve Number method: How to mend a wrong soil moisture accounting procedure? *Water Resour Res* W02011
- Papini M, Ivanov V, Brambilla D, Arosio D, Longoni L (2017) Monitoring bedload sediment transport in a pre-Alpine river: an experimental method. *Rendiconti Online Societa Geologica Italiana* 43:57–63
- Ponce VM, Hawkins RH (1995) Runoff curve number: Has it reached maturity? *Journal of Hydrological Engineering* 1:11–19
- Rickenmann D (1994) Alternative equation for the mean velocity in gravel-bed rivers and mountain torrents. *Hydraulic Engineering* 94:672–676
- Soares A (2001) Direct sequential simulation and cosimulation. *Math Geol* 33:911–926
- Togni N (2019) Geostatistical analysis for uncertainty quantification in the SMART-SED model: a downscaling approach based on Digital Soil Mapping data. Master Thesis in Mathematical Engineering, Politecnico di Milano
- Zhang GH, Liu YM, Han YF, Zhang XC (2009) Sediment transport and soil detachment on steep slopes: i. transport capacity estimation. *Soil Sci Soc Am J* 73:1291–1297



2020 Kyoto Japan

Hazard Assessment of a Rainfall-Induced Deep-Seated Landslide in Hakha City, Myanmar

Khang Dang, Doan Huy Loi, Kyoji Sassa, Do Minh Duc, and Nguyen Duc Ha

Abstract

One of the most disastrous landslide events happened in Myanmar was Chin state landslides due to abnormal heavy rainfall in July 2015. The landslides destroyed and damaged nearly 3,000 buildings and killed 5 people. In particular, a deep-seated landslide occurred at Mt. Rung, Hakha city on 27 July 2015 was a serious event in the history of the Chin state with about 500 m wide and 1,000 m long. On the day of the landslide occurrence, an intense rainfall of 180 mm fell within a short time span in the Hakha area. This research aims to assess the potential rainfall-induced landslides of the remained body on the slope of July 2015 landslide based on assumed pore pressure ratio (r_u), soil parameters from the ring-shear tests and computer simulation. In the simulation, pore pressure ratio r_u was gradually increased from 0 (no groundwater) to 0.5 (groundwater table at ground surface) to simulate two potential cases of rainfall-induced landslides with the depths of 30 and 60 m. The landslides started when pore pressure ratio reached 0.35 and 0.39 which are corresponding to the groundwater level height equal to 71 and 80% of the total thickness of the sliding layers. The volumes and velocities as well as the affected areas of the landslides were also calculated. The method would provide an assessment of landslide hazard

triggered by rainfall and the result would be of great help for the authorities in the management of slope disasters.

Keywords

2015 hakha landslides • Rainfall-induced landslide • Ring-shear apparatus • LS-RAPID • Landslide risk assessment

Introduction

Myanmar is one of the Asian countries has been experienced many geological hazards including earthquakes and landslides. In the country's mountainous regions, such as Chin State, Shan State, landslides recently have been a major natural disaster. A Report from the UN Office for the Coordination of Humanitarian Affairs (2015) stated that, in 2015, Myanmar experienced heavy monsoon rains, and cyclone Komen triggered landslides and the most widespread flooding in decades, leaving 125 dead and 1,676,086 temporarily displaced. Particularly, the most devastating landslide event on record in Myanmar occurred in July 2015 and completely destroyed 1,162 buildings, damaged 1,825 buildings and caused 5 fatalities (Mon et al. 2018). The western part of Myanmar was severely hit by rain flood due to the impact of cyclone Komen and caused hundreds of landslides which severely blocked all roads and even swept away several houses in Hakha, the capital of the Chin State. Due to the massive damage and persisting landslide risk, settlements in the city were resettled in a new location.

In 2017, a group of researchers from the International Consortium on Landslides (ICL) in cooperation with the Department of Geology Survey and Mineral Exploration (DGSE) carried out a detailed field survey on a large-scale landslide occurred at Mt. Rung in Hakha city (Fig. 1). According to the research from Kyi et al. (2019), before the

K. Dang (✉) · D. H. Loi · K. Sassa
International Consortium on Landslides, Kyoto, Japan
e-mail: khangdq@gmail.com

K. Dang · D. M. Duc
VNU University of Science, Vietnam National University, Hanoi, Vietnam
e-mail: ducdm@vnu.edu.vn

N. D. Ha
Vietnam Institute of Geosciences and Mineral Resources (VIGMR), MONRE, Hanoi, Vietnam
e-mail: nh14vn@gmail.com

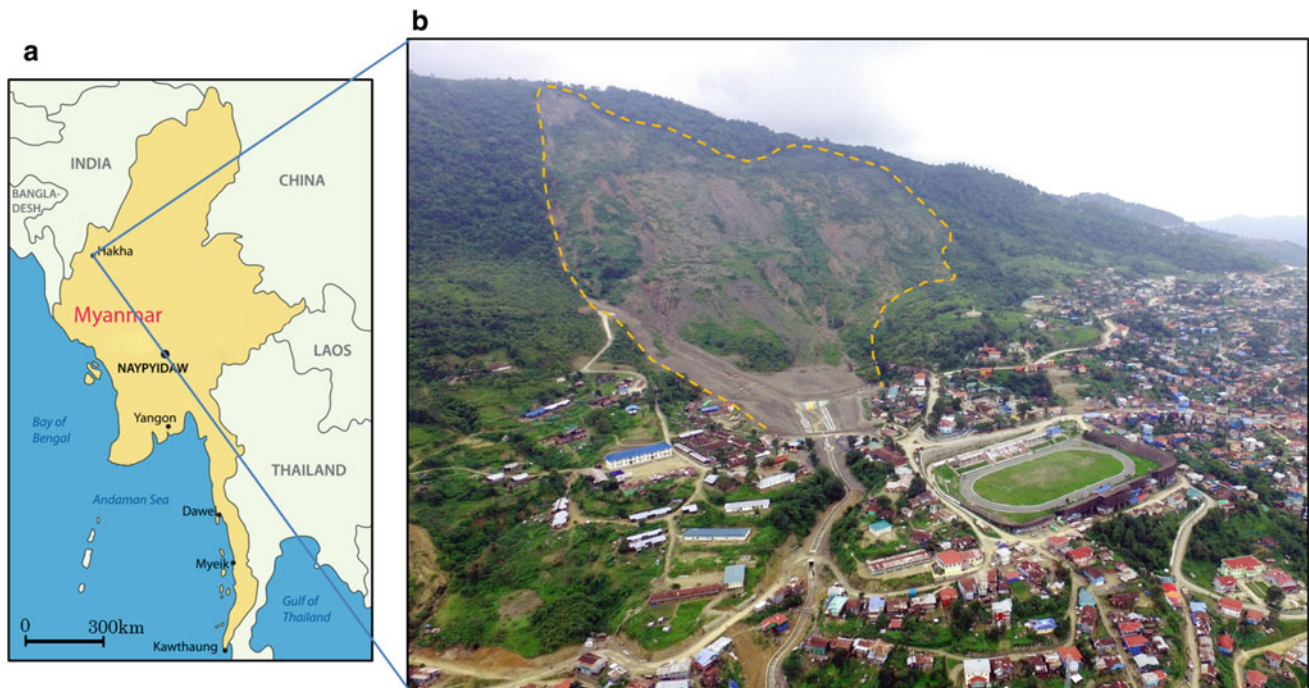


Fig. 1 Overview of the 2015 Mt. Rung landslide. **a** Location of the landslide in Hakha city, Chin state, Myanmar, **b** Aerial photo of the landslide (view from the town, the yellow dot line shows the estimated border of the landslide)

Mt. Rung landslide, the local people were noticed by warning signs of the initial cracks on the slope, the increase of water level on the roads, and the deterioration of houses. Therefore, they were evacuated to safe locations and no one faced to death in this event, but a school and 540 houses located under the slope could continue to living in the dangerous area. During the investigation, an Unmanned Aerial Vehicle (UAV) was employed to take aerial photos of the whole landslide and its surrounding areas. A soil sample was also taken from a valley wall of the displaced landslide block for laboratory tests. Then the Digital Surface Models (DSM) was created by Agisoft PhotoScan software. Landslide dynamics parameters will be measured from the ring-shear tests using a new ring-shear apparatus ICL-2 at the UNITWIN laboratory in Kyoto University, Japan. These parameters and DSM then will be used to analyse the further landslides which may occur in this slope by LS-RAPID software.

The LS-RAPID model has been developed and improved from 1988 (Sassa 1988; Sassa et al. 2004, 2010, 2012, 2014a, b; Dang et al. 2016). The ICL-2 is a new type of undrained dynamic-loading ring-shear apparatus (UDRA) which was developed based on a series of developments of ring-shear apparatus from DPRI-1, 2, 3, 4, 5, 6, and DRPR-7 (Sassa et al. 2004). The first UDRA is a compact and transportable one ICL-1 with maximum loading capacity and undrained capacity of 1000 kPa. The second one is ICL-2

which is a high-stress UDRA with maximum loading capacity and undrained capacity of 3000 kPa. The new ring-shear apparatus and the landslide simulation model LS-RAPID have many successful applications in analyzing mechanism of landslide initiation and motion, estimating potential landslide volume, landslide velocity as well as assessing the landslide hazard zonation. They were applied to simulate earthquake-induced landslides (Sassa et al. 2010, 2012; Tsuchiya et al. 2013; Setiawan et al. 2016), rainfall-induced landslides (Gradiški et al. 2013; Igwe et al. 2014; Loi et al. 2017; Cuomo et al. 2017; Tien et al. 2018; Arbanas et al. 2017; Lam et al. 2018; Sodnik et al. 2018; Dang et al. 2019; Setiawan et al. 2019) or combination of earthquake and rainfall-induced landslides (Sassa et al. 2014a, b; Dang et al. 2016).

In this study, we do not attempt to reveal the mechanism of initiation and motion of the 2015 Mt. Rung landslide in Hakha city but, in order to reduce the landslide risk, examine the probability of the other landslide occurrence in the future from the remaining blocks when heavy rainfall occurs. As rainfall infiltrates a hill, the water content increases in the soil and results in the pore water pressure rising which will cause landslide. This study allows future displacement scenarios to be predicted from expected pore water pressure ratio scenarios. The landslide hazard area will be estimated by the LS-RAPID then it may be referred to the landslide disaster mitigation planning. The economical early warning

is the prediction of large cumulative rainfalls which are similar to the landslides in 2015. The measures for landslide mitigation are also briefly discussed because the potential landslide is estimated as a deep-seated with a very large volume.

Study Area and Field Investigation

Geological and Climate Settings

Hakha city is the capital of Chin State, Myanmar, located in the Northwest of the country, about 1,870 m a.s.l. The city is situated at the foot of Mt. Rung with its peak of about 2,280 m a.s.l. As shown in Fig. 2, the area is mainly covered by sedimentary and metasedimentary rocks of the Falam Mudstone-Micrite Formation. The Formation is composed of grey to black mudstone, silty mudstone, and sandstone turbidites. In which, sandstones are mostly fine-grained and some are calcareous and carbonaceous (Mon et al. 2018). According to Kyi et al. (2019), heavily jointed nature and numerous local folds are observed in this area due to tectonic process of the Indo-Burma plate.

The climate in the study area is characterized by a very seasonal variation of the Southwest monsoon belt with pronounced rainfall occurring in the months of May to October.

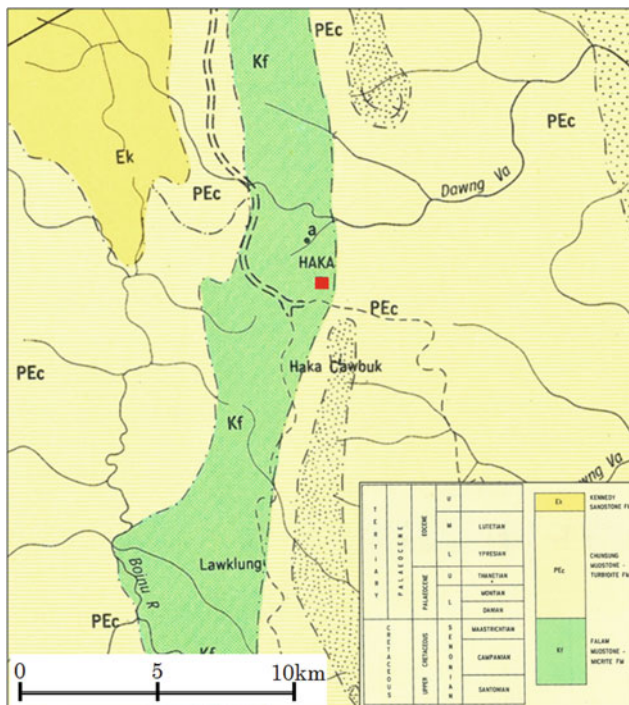


Fig. 2 Geological map of the Hakha and its environs (from Mon et al. 2018)

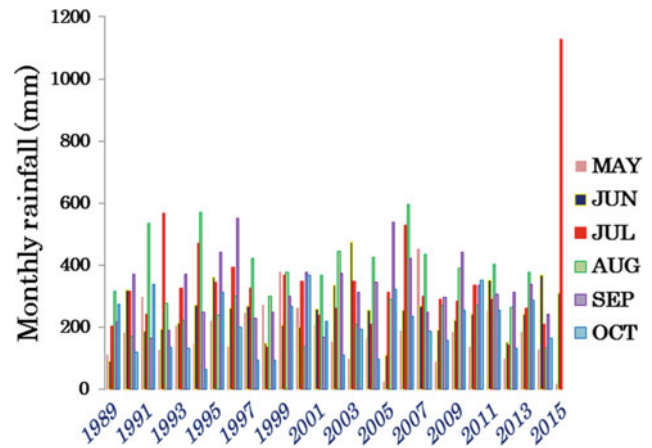


Fig. 3 Monthly precipitation in Hakha city in rainy season for period of 1989–2015 (from Mon et al. 2018)

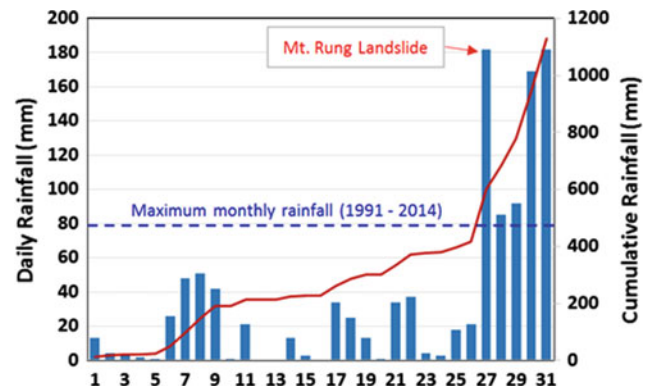


Fig. 4 Daily and cumulative precipitation for HaKha in July 2015 (from the Government of the Union of Myanmar 2015)

The dry season is from November to April with a small value of rainfall (Htun et al. 2019). The monthly rainfall of the Hakha area in rainy season of the period from 1989 to 2015 is presented in Fig. 3 with the average monthly rainfall of about 250 mm. The rainfall intensity of July 2015 was more than two times higher than other months of the previous year which would be equal to a 1-in-1,000-year rainfall. In particular, as stated in the report of the Government of the Union of Myanmar (2015), rainfall of the last seven days of July 2015 fell more 30% than that of any other month over the past 25 years (Fig. 4).

Field Investigation

An investigation on the Mt. Rung landslide was conducted by the ICL group in cooperation with the Department of Geology Survey and Mineral Exploration (DGSE) of Myanmar on 19 June 2017, around 2 years after the event.

A quadcopter UAV (DJI Phantom 4) was employed to acquire aerial photography of the landslide. Recently, there has been a significant improvement in the spatial resolution of remote sensing technology for landslide monitoring in particular with the introduction of unmanned aerial vehicles (UAVs) which is a flexible and cost-effective method (Lucieer et al. 2014). 424 digital images of the entire landslide area were captured then used to generate digital surface model (DSM) and ortho-photographs by Agisoft PhotoScan software based on photogrammetric processing achieving geometric accuracies of 0.3 to 0.5 m. Figure 5a shows an aerial photograph (orthomosaic) of the Mt. Rung slope acquired by UAV photographs and Agisoft PhotoScan software. Longitudinal sections of the slope were also estimated based on the DSM (Fig. 5b). The whole landslide and surrounding residential area are clearly visible. Locations of the affected houses were presented on the figure based on comparison with Google Earth images taken on 17 December 2013 (before landslide event) and on 17 January 2016 (after the landslide event). The head scarp of the landslide is located at the elevation of 2,270 m a.s.l with a maximum width of around 600 m and a longitudinal length of 1,000 m. Figure 6 shows soil sampling at a valley wall of the displaced landslide block for laboratory tests. The valley wall provides the exposed soil layers to avoid surface soils. Sampling location is presented in Fig. 5a.

Ring-Shear Testing and Computer Simulation

Ring-Shear Tests

The high-stress dynamic-loading undrained ring-shear apparatus ICL-2 developed since 2012 (Sassa et al. 2014a) is the most improved and advanced type in ring-shear apparatus series so far. The apparatus can reproduce the processes from the initial stage, stresses changes due to pore water pressure increasing or seismic loading, to the formation of a sliding surface and the post-failure motion. The detailed and updated description of the ICL-2 as well as its applications are presented in Sassa and Dang (2018).

In this study, two potential landslides are estimated based on the current topography and longitudinal section of the Mt. Rung slope (Fig. 5b). The first one is shallower with its sliding surface located at around 30 m depth and the second one is deeper with its sliding surface at around 60 m depth. Then, two undrained monotonic shear stress control tests on the Hakha sample were conducted to measure the soil parameters under normal stresses of 500 kPa and 1,000 kPa corresponding to the sliding surfaces of 30 m and 60 m depths, respectively (Fig. 5b). For each test, the sample was

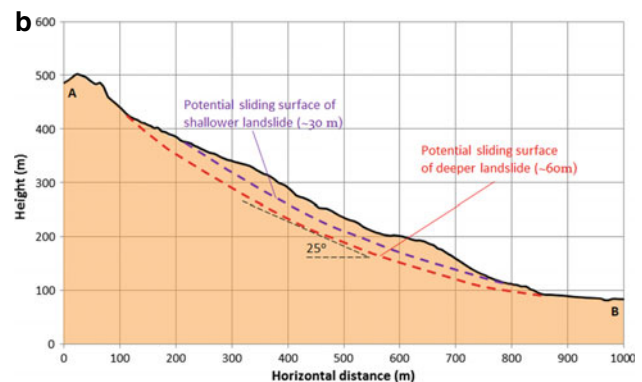
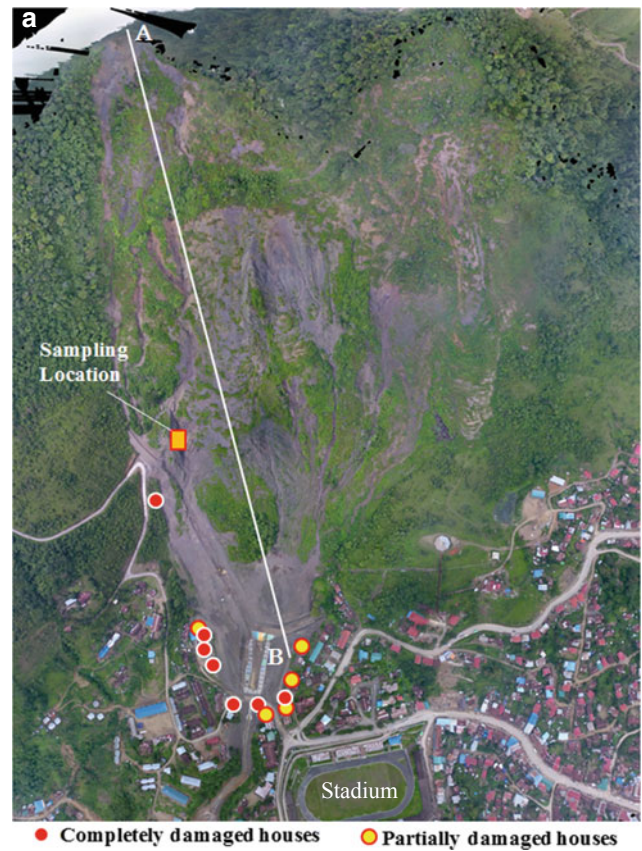


Fig. 5 Orthophoto mosaic of the Mt. Rung landslide acquired by UAV on 19 June 2017 (a) and longitudinal section of the Mt. Rung slope with potential sliding surfaces (b)

saturated with de-aired water and placed in a vacuum tank at least 24 h before testing (Fig. 7b). Then, the saturated sample was placed into the ring-shear box (Fig. 7a) which was already percolated by CO_2 and filled with de-aired water. Therefore, fully saturated sample was successfully prepared which was confirmed by BD value of more than 0.95 (Sassa et al. 2014a). After that, the sample was consolidated to the planned normal stress of 500 and 1,000 kPa

Fig. 6 Photos of soil sampling at a valley wall of the displaced landslide block. **a** Photo of sampling location from the top of gully, **b** Photo of sampling, **c** Sieving of sample



in the drained condition. The shear box was then changed to the undrained condition, and shear stress was loaded gradually at a rate of 1 kPa/s. When shear stresses became high enough, effective stress path reached the failure line, failure occurred and the lower half of the shear box started to move in a clockwise direction. Mobilized shear resistance, pore water pressure, shear displacement during the tests are monitored by load cells and displacement sensors. In the case of undrained shearing on saturated soil, pore water pressure was generated in progress with shear displacement due to volume reduction when soil particles were crushed. Shearing was continued in each test until the shear displacement reached 10 m. Figure 7c shows the sample after shearing and the upper shear box was taken out.

The testing results are shown in Fig. 8 and Table 1. During the shear displacement, the pore pressure generated was not well monitored by the pore pressure sensor due to permeability of the sample decrease. It should also be mentioned that grain crushing of sand and/or particle

orientation of clay lead the structural changes in the shear zone which will consequently result in a slower dissipation rate for generated excess pore pressure.

Landslide Susceptibility Assessment Using LS-RAPID Model

Soil parameters derived from the ring-shear tests (Table 1) together with slope geometry, estimated sliding surface position were used as input parameters to LS-RAPID model for analysing the Mt. Rung landslide susceptibility. The concept of the simulation method and its application are presented in Sassa and Dang (2018). We analyse the possibility of the two potential landslides with the depths of 30 and 60 m due to the influence of the pore water pressure acting on the sliding surfaces caused by rainfalls, which was the triggering factor of the 2015 Mt. Rung landslide.

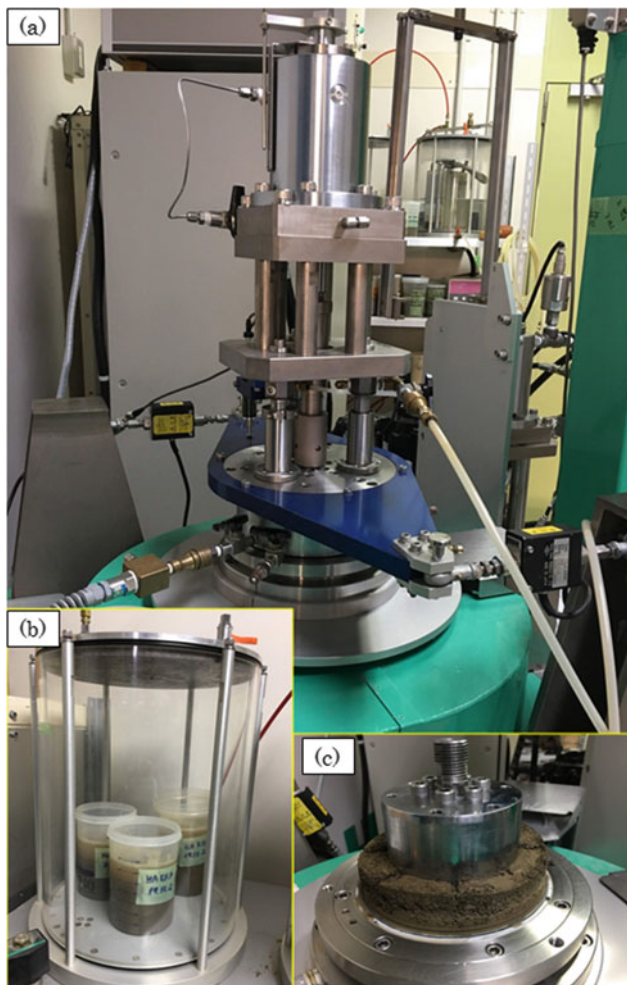


Fig. 7 a Photo of ring-shear box after setting, b Samples in vacuum tank for saturation, c Sample after shearing

Pore pressure ratio r_u was gradually increased from 0 (represents no groundwater) to 0.5 (represents groundwater table at ground surface) in consideration of ground water rising due to rainfalls. The pore pressure ratio $r_u = 0.5$ is the worst scenario when the slope is fully saturated. The stability analyses of the two cases conducted in LS-RAPID are shown step by step in Fig. 9 in which the influence of pore pressure ratio r_u is clearly presented at every moments of the slope failure. The depths of moving mass are depicted from orange to red colours. In the shallower landslide case, when pore pressure ratio reached 0.39, local failure occurred in the middle part of the slope (Fig. 9a). When pore pressure ratio reached 0.5, the main landslide body is formed and moving downward with the maximum velocity of 15.2 m/s (Fig. 9b). The landslide stopped after 89 s with calculated volume of around $1.4 \times 10^6 \text{ m}^3$ (Fig. 9c). While, in the deeper

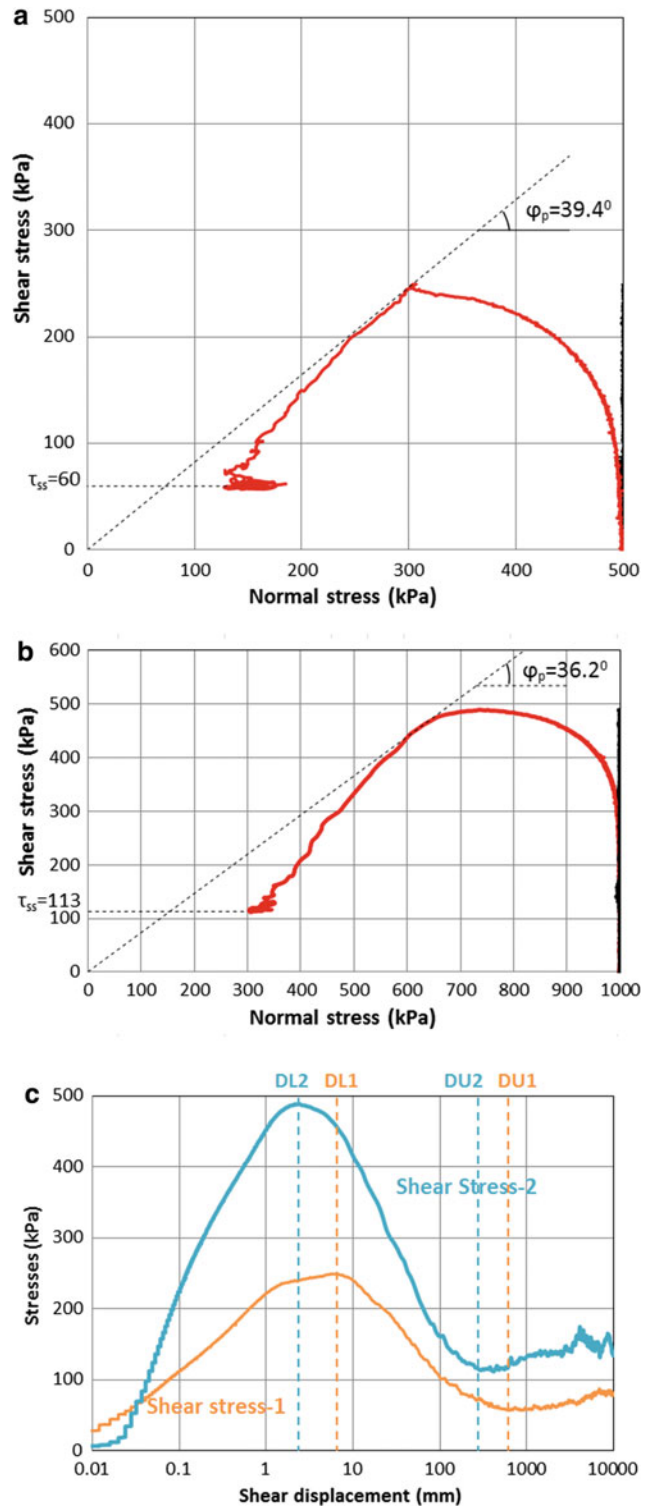


Fig. 8 Results of undrained monotonic shear stress control tests on Hakha sample with normal stress of 500 kPa (a) 1,000 kPa (b) and combined graph of shear strength reduction in progress of shear displacement (c)

Table 1 Values of soil parameters from ring-shear tests and parameters used in LS-RAPID model

Parameters	Shallower landslide (30 m depth)	Deeper landslide (60 m depth)
φ_p , degree	39.4	36.2
φ_m , degree	39.4	36.2
τ_{ss} , kPa	60	113
D_L , mm	6	2
D_U , mm	550	250
$k = \sigma_H/\sigma_v$	0.4	0.4
B_{ss}	0.8	0.8
c_p , kPa	100	150
γ , kN/m ³	20	20

φ_p —friction angle at peak; φ_m —friction angle during motion; τ_{ss} —steady state shear resistance at sliding surface; D_L —shear displacement at the start of strength reduction; D_U —shear displacement at the start of steady state; k —lateral pressure ratio; B_{ss} —pore pressure generation rate; c_p —peak cohesion at sliding surface; γ —unit weight of soil mass

landslide case, failure starts when r_u reached 0.35 (Fig. 9d), the main body is formed and moving downward when r_u reached 0.5 with maximum velocity of 15.2 m/s (Fig. 9e). The landslide stopped after 86 s with its volume of around $4.5 \times 10^6 \text{ m}^3$ (Fig. 9f).

Conclusions

This study presents the application of LS-RAPID model in the landslide hazard assessment based on the field investigation data and soil parameters derived from the ring-shear testing. The simulation model is used for the small area that is assumed as the homogeneous slope. Pore water pressure/groundwater level increase caused by rainfalls is used as the triggering factor of the future landslide on the Mt. Rung slope in Hakha city, Chin state, Myanmar. It is determined from the current topography and longitudinal section that the potential sliding surfaces are located at the depth of around 30 and 60 m with the slope angle of 25° .

The potential landslides occur when the pore water pressure ratio r_u reaches 0.35 and 0.39 in the cases of deeper landslide and shallower landslide, respectively. In the former case, groundwater level is equivalent to around 71% of the depth of the 60 m-sliding surface (or around 17.16 m from the ground surface) while it is around 80% of the depth of

the 30 m-sliding surface (or 6.13 m from the ground surface) in the latter one. These results indicate that the deeper landslide is easier to occur when groundwater rises. In both cases, the whole landslide masses are formed and move down to the city area when r_u reached 0.5 corresponding to the groundwater level is at the same level of the ground surface.

For mitigating the landslide risk, it is feasible to establish a real-time slope failure warning system that is based on pore-water pressure and groundwater level monitoring system installed on the Mt. Rung slope. When the pore pressure ratio is close to 0.35 or groundwater level is around 17.16 m from the ground surface, evacuation is recommended for the people living under the slope between its toe and the city stadium (as shown in Figs. 5a and 9).

Acknowledgements The authors would like to acknowledge Dr. Lwin Soe, Mr. Win Phyoo and other researchers of the Department of Geology Survey and Mineral Exploration (DGSE), Myanmar for their guidance and support during the landslide field investigation. We also like to thank Dr. Yasukuni Okubo (Chair, the IUGS Task Group for Geohazards), Prof. Hiroshi Fukuoka (Director, Research Institute for Natural Hazards and Disaster Recovery, Niigata University, Japan), Dr. Hasi Bateer (Senior Engineer, Asia Air Survey Co. Ltd., Japan), Damodar Lamsal (Engineer, Asia Air Survey, Co. Ltd., Japan), and Dr. Stefano Morelli (Researcher, Earth Sciences Department of Florence University, Italy) for their cooperation in implementation of the Myanmar-Japan joint landslide investigation for possible mitigation of landslide disasters in Myanmar.

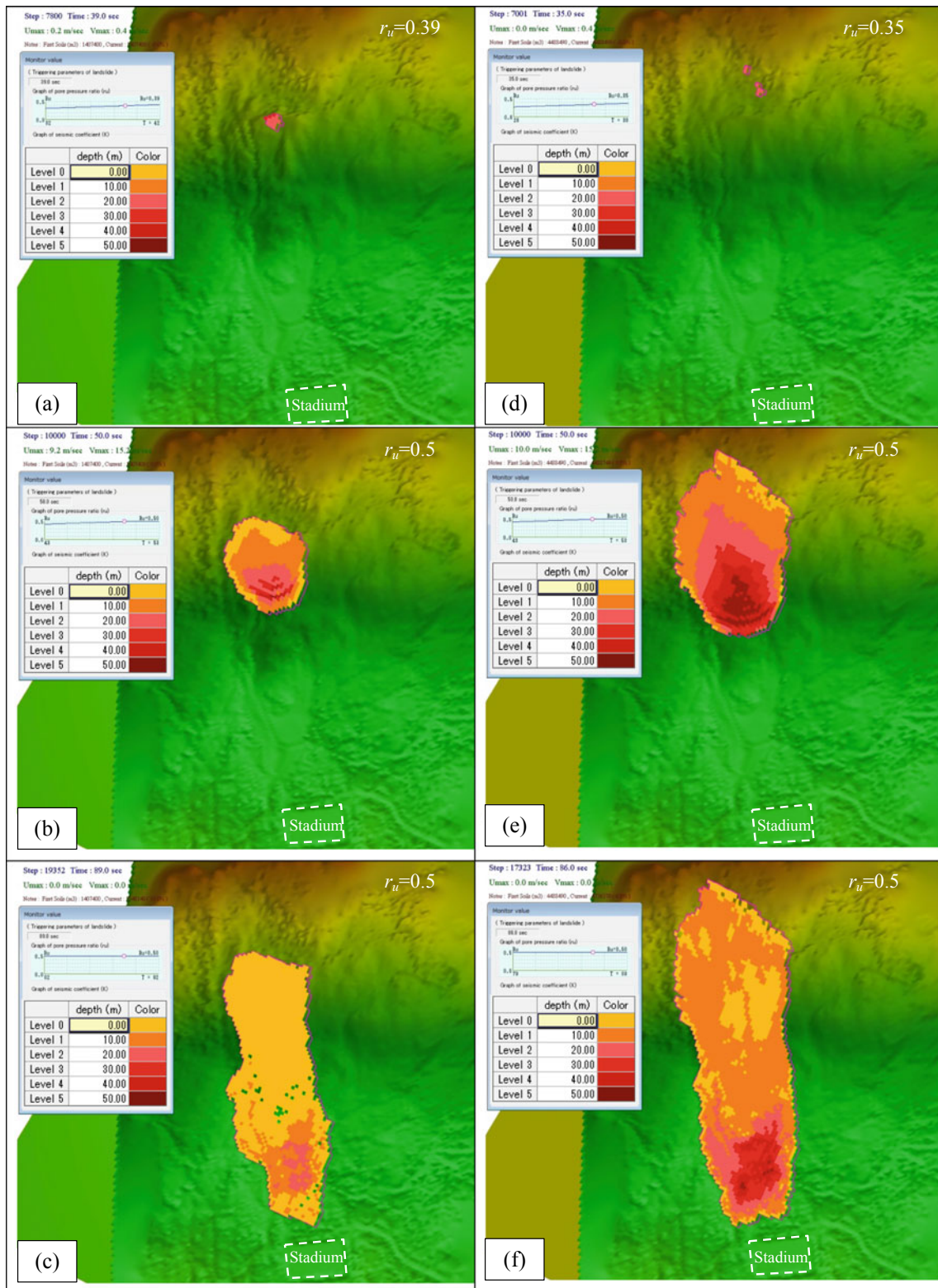


Fig. 9 Simulation results on the two potential Mt. Rung landslides with the depths of 30 m (a–c) and 60 m (d–f)

References

- Arbanas Ž, Mihalić Arbanas S, Vivoda Prodan M, Peranić J, Sečanji M, Bernat Gazibara S, Krkač M (2017) Preliminary Investigations and Numerical Simulations of a Landslide Reactivation. In: Mikoš, M., Tiwari, B., Yin, Y., Sassa, K (eds) *Advancing culture of living with landslides*, vol 2. *Advances in Landslide Science*, pp 649–657
- Cuomo S, De Chiara V, Dugonjić Jovančević S, Vivoda Prodan M and Arbanas Ž (2017) Insights from LS-Rapid Modeling of Montaguto Earthflow (Italy). In: Mikoš, M., Tiwari, B., Yin, Y., Sassa, K. (eds) *Advancing culture of living with landslides*, vol 2. *Advances in Landslide Science*, pp 611–619
- Dang K, Sassa K, Fukuoka H, Sakai N, Sato Y, Takara T, Quang LH, Loi DH, Tien PV, Ha ND (2016) Mechanism of two rapid and long-runout landslides in the 16 April 2016 Kumamoto earthquake using a ring-shear apparatus and computer simulation (LS-RAPID). *Landslides* 13(6):1525–1534
- Dang K, Sassa K, Konagai K, Karunawardena A, Bandara RMS, Hirota K, Tan Q, Nguyen DH (2019) Recent rainfall-induced rapid and long-traveling landslide on 17 May 2016 in Aranayaka, Kagelle District Sri Lanka. *Landslides* 16(1):155–164
- Government of the Union of Myanmar (2015) Myanmar—Post-disaster needs assessment of floods and landslides: July–September 2015
- Gradiški K, Sassa K, He B, Arbanas Ž, Mihalić Arbanas S, Krkač M, Kvasnička P, Oštrič M (2013) Application of integrated landslide simulation model ls-rapid to the Kostanjek Landslide, Zagreb, Croatia. In: *Proceedings of the 1st Regional Symposium on Landslides in the Adriatic-Balkan Region*, Zagreb
- Igwe O, Mode W, Nnebedum O, Okonkwo I, Oha I (2014) The analysis of rainfall-induced slope failures at Iva Valley area in Enugu State Nigeria. *Environmental Earth Sciences* 71:2465–2480
- Htun K, Oo CT, Zaw TN, Aung DW (2019) Landslide Hazard in Chin State: a case study in hakka and its environs. In: James H (ed) *Population, development, and the environment*. Palgrave Macmillan, Singapore
- Kyi SS, Htun K, Myint W, Zan M, Thein ZZ (2019) The analysis of engineering properties of soils facilitating the mechanism of landslides in Hakha Area, Chin State, Myanmar. *J Myanmar Acad Arts Sci* XVII(5):299–310
- Lam HQ, Doan HL, Sassa K, Takara K, Ochiai H, Dang K, Abe S, Asano S, Do NH (2018) Susceptibility assessment of the precursor stage of a landslide threatening Haivan Railway Station Vietnam. *Landslides* 15(2):309–325
- Loi DH, Quang LH, Sassa K, Takara K, Dang K, Thanh NK, Tien PV (2017) The 28 July 2015 rapid landslide at Ha Long City Quang Ninh, Vietnam. *Landslides* 14(3):1207–1215
- Lucieer A, Jong SM, Turner D (2014) Mapping landslide displacements using structure from motion (SfM) and image correlation of multi-temporal UAV photography. *Prog Phys Geogr* 38(1):97–116
- Mon MM, Naing T, Numada M, Khin Than Yu, Meguro K, Latt KZ (2018) Analysis of disaster response during landslide disaster in Hakha, Chin State of Myanmar. *J Disaster Res* 13(1):99–115
- Sassa K (1988) Geotechnical model for the motion of landslides. In: *Proceedings 5th international symposium on Landslides, “Landslides”*, vol 1. Balkema, Rotterdam, pp 37–56
- Sassa K, Fukuoka H, Wang G, Ishikawa N (2004) Undrained dynamic-loading ring-shear apparatus and its application to landslide dynamics. *Landslides* 1(1):7–19
- Sassa K, Nagai O, Solidum R, Yamazaki Y, Ohta H (2010) An integrated model simulating the initiation and motion of earthquake and rain induced rapid landslides and its application to the 2006 Leyte landslide. *Landslides* 7(3):219–236
- Sassa K, He B, Miyagi T, Strasser M, Konagai K, Ostric M, Setiawan H, Takara K, Nagai O, Yamashiki Y, Tutumi S (2012) A hypothesis of the Senoumi submarine megaslide in Suruga Bay in Japan—based on the undrained dynamic-loading ring shear tests and computer simulation. *Landslide* 9:439–455
- Sassa K, He B, Dang K Q, Nagai O (2014a) Progress in landslide dynamics. *Landslide science for a safer geoenvironment*. In: *Proceedings of the third world landslide forum*, vol 1. Springer, pp 37–67
- Sassa K, Dang K, He B, Takara K, Inoue K, Nagai O (2014b) A new high-stress undrained ring-shear apparatus and its application to the 1792 Unzen–Mayuyama megaslide in Japan. *Landslides* 11(5):827–842
- Sassa K and Dang K (2018) TXT-tool 0.081-1.1: landslide dynamics for risk assessment. In: Kyoji, S., Fausto, G., Hiromitsu, Y., Zeljko, A., Nicola C., Mauri M., Khang, D (eds) *Landslide dynamics: ISDR-ICL landslide interactive teaching tools*, Springer, vol 1. *Fundamental, Mapping and Monitoring*, pp 1–79
- Setiawan H, Sassa K, Takara K, Miyagi T, Fukuoka H (2016) Initial pore pressure ratio in the earthquake triggered large-scale landslide near Arotazawa Dam in Miyagi prefecture Japan. *Procedia Earth Planet Sci* 16:61–70
- Setiawan H, Wilopo W, Wiyoso T et al. (2019) Investigation and numerical simulation of the 22 February 2018 landslide-triggered long-traveling debris flow at Pasir Panjang Village, Brebes Regency of Central Java, Indonesia. *Landslides* 16:2219–2232
- Sodnik J, Maček M, Mikoš M (2018) Estimating landslide volumes using LS-rapid model-The 2000 Stože Landslide in NW Slovenia. In: *Proceedings of the symposium in large scale sediment disasters in orogenic zones and countermeasures INTERPRAEVENT*. pp 32–41
- Tien PV, Sassa K, Takara K, Fukuoka H, Dang K, Shibasaki T, Nguyen DH, Setiawan H, Doan HL (2018) Formation process of two massive dams following rainfall-induced deep-seated rapid landslide failures in the Kii Peninsula of Japan. *Landslides* 15(9):1761–1778
- Tsuchiya S, Sassa K, Nagai O (2013) Simulation of the largest landslide caused by the 2008 Wenchuan earthquake by rapid-landslide-movement simulation. In: Ugai K, Yagi H, Wakai A (eds) *Earthquake-induced landslides*. Springer, Berlin, Heidelberg, pp 575–582



2020 Kyoto Japan

Landslide Hazard Zoning Based on the Integrated Simulation Model (LS-Rapid)

Doan Huy Loi, Kyoji Sassa, Khang Dang, and Hong Le Luong

Abstract

Urbanization has been related to natural disasters such as landslides and debris flows that can cause fatality, destruction of infrastructure and environmental impacts. From 19 to 20 August, 2014, heavy rainfall occurred in Hiroshima city causing many landslides and debris flows. This disaster killed 74 people, 255 houses damaged and a total of 4,576 houses were affected reported by the Ministry of Land, Infrastructure, Transport, and Tourism of Japan (MLIT). The cumulative rainfall from 8:30 PM of August 19 until 04:30 AM of August 20 reached 248 mm at Miiri rain gauge station in Hiroshima. This is the main reason caused the Hiroshima disasters. Although intense rainfall in the short time was the trigger, urbanization into the foot of steep mountain slope lead to increase the loss of life. This paper presents the adverse effects of urbanization on basis of site investigation and multi-temporal satellite images and estimate hazard zoning causing by a potential landslide using the ring shear tests and integrated simulation model.

Keywords

Hiroshima disaster • Urbanization • Ring shear test • Integrated simulation model • Land-use change

Introduction

Urbanization is the process by which people migrate from the countryside to urban areas (Goryakin et al. 2017) and land-use change from agricultural to non-agricultural (Li et al. 2017). Urban area have higher population densities and greater concentration of facilities which can lead to huge economic losses and casualties when landslide occurs (Moore and McInnes 2016; Luo et al. 2019). For example, catastrophic event occurred in May 2014 in Afghanistan. This mudslide killed 2,700 people, destroyed 300 houses and affected over 14,000 houses (Wikipedia). On 17 May 2016, a rainfall-induced landslide occurred in Aranayaka, Kagelle District, Sri Lanka. The landslide mass travelled over an approximately 2-km distance and resulted in 127 deaths and destroying 75 houses (Dang et al. 2019). On 9 January 2018, the terrible mudflow ravaged Montecito, California triggered by heavy rainfall leading to 23 deaths, at least 167 injuries and 408 damaged houses (Kean et al. 2019; Luo et al. 2019). More recently, disastrous rainfall-induced landslides in the Hiroshima, Japan in July 2018 caused extensive damage including 107 fatalities.

LS-RAPID is an integrated computer model that can simulate the initiation and motion of a landslide using soil parameters obtained from the ring-shear apparatus. This simulation model LS-RAPID was developed from the geotechnical model for the motion of landslides (Sassa et al. 2010). The LS-Rapid model has been widely applied all the world for rainfall induced landslide (Dugonjić Jovančević

D. H. Loi (✉) · K. Sassa · K. Dang
International Consortium on Landslides, 138-1, Tanaka
Asukaicho, Sakyo-ku, Kyoto, 606-8226, Japan
e-mail: doanhuyloi@gmail.com

K. Sassa
e-mail: sassa@iclhq.org

K. Dang
e-mail: khangdq@gmail.com

K. Dang
VNU University of Science, Vietnam National University, Thanh
Xuan, 334 Nguyen Trai, Hanoi, Vietnam

H. Le Luong
Institute of Transport Science and Technology, Hanoi, Vietnam
e-mail: lehongluong@gmail.com

Fig. 1 Study area in Hiroshima city (Google earth)



et al. 2013; Gradiski et al. 2013; Vivoda et al. 2013; Dugonjić Jovančević and Arbanas 2017; Senthilkumar et al. 2017; Cuomo et al. 2017; Quang et al. 2018; Loi et al. 2017, 2018; Sodnik et al. 2018; Tien et al. 2018; Dang et al. 2019; Setiawan et al. 2019).

Hiroshima city is the biggest city in Chugoku region with population of about 1.17 million (Sakatani 2014). Many debris flows and landslides took place in Hiroshima city in the early morning of August 20, 2014 (Fig. 1). The deconstruction results are 74 deaths, 255 homes destroyed and 4562 houses were affected according to MLIT report. The objectives of this paper are to briefly assess the urbanizations and their consequences and conduct hazard assessment of rainfall induced

landslide in Yagi and Midori, Hiroshima. The 2014.8.20 landslide disasters in Hiroshima, Japan was selected as the case study to examine the adverse of urbanization.

Process of Urbanization in Yagi and Midorii

After the war, the population of Hiroshima city growth fasts from 137,000 in 1945 to 1.17 million in 2015. It became a major urban center as Japan's tenth by population. Settlement areas had expanded into hill slope especially along the torrents which pose major economic and social risks. The establishment of settlements in unstable areas is often due to

Fig. 2 Urbanization in Midorii-8 and Yagi-3 (Modify from Fukuoka et al. 2014)

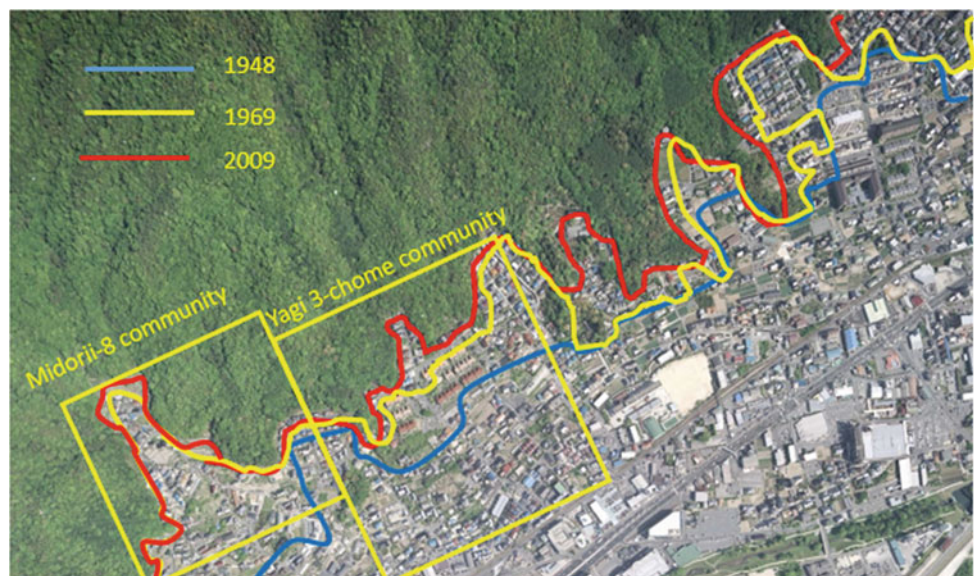
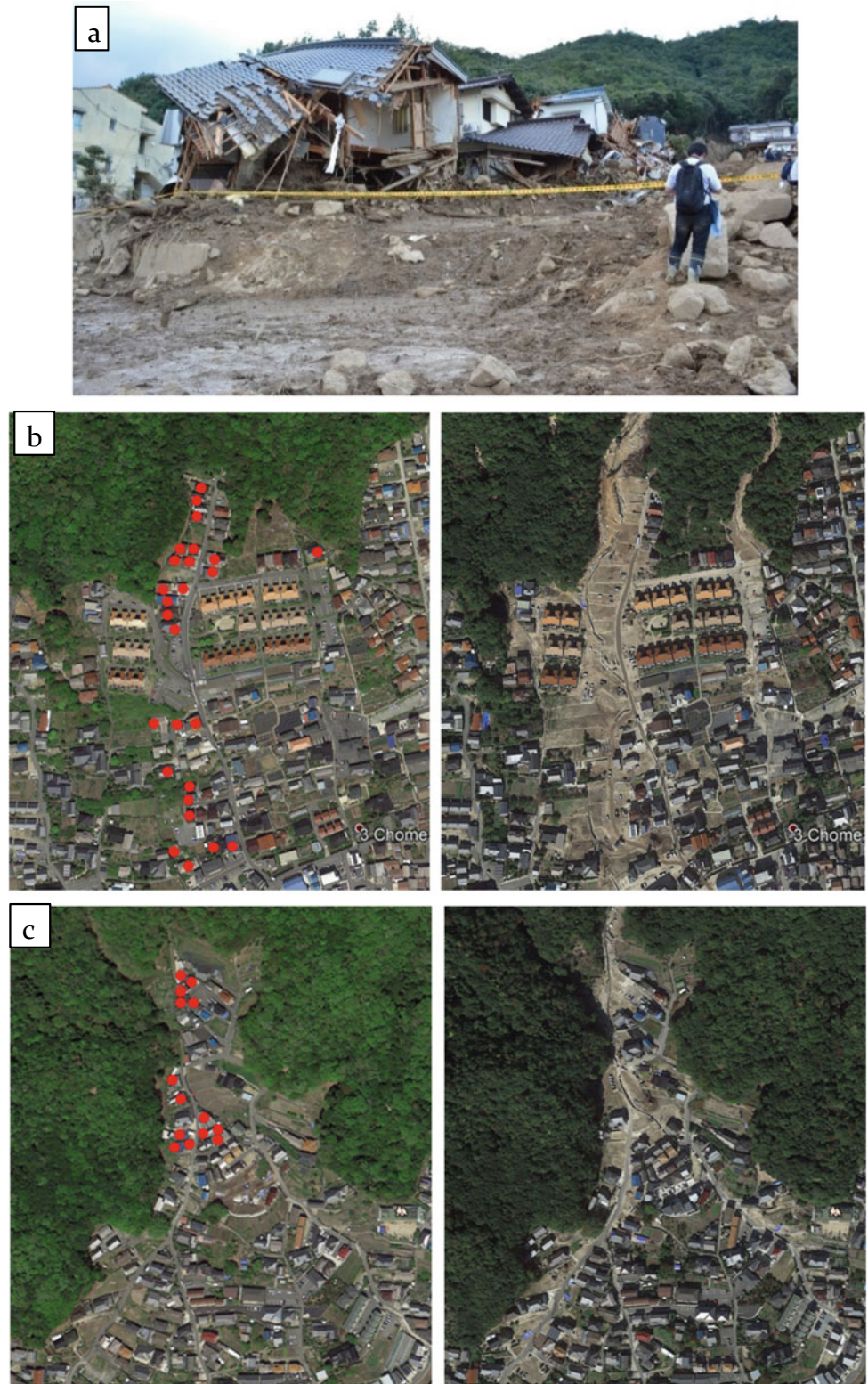


Fig. 3 Damaged houses in Yagi-3 (Fukuoka et al. 2014) (a) and Google earth photos comparison of pre- and post-disaster in Yagi-3 (b) and Midori-8 (c)



a lack of landslide information and complacency related to the potential landslide hazard. The border of residences expanded to hill slope and toward the exit torrents year by year which is illustrated in Fig. 2. The border of residences rapidly expands from 1948 to 1969 and slowly from 1969 to 2009. Due to many settlement areas located close to the mountainous areas, Hiroshima has more high-risk areas for sediment disasters than other Prefectures.

Characteristics of the Debris Slide—Debris Flow Disasters in Hiroshima

A lot of countermeasures and preparedness against sediment-related disasters has been implemented in Hiroshima Prefecture after landslides and debris flows on 29 June 1999. However, urban development leads to increasing risk for residents in the mountainous area.

Fig. 4 **a** The hyetograph of daily rainfall from 1990 to 2014 at Miiri station **b** Disaster alert and issue of evacuation

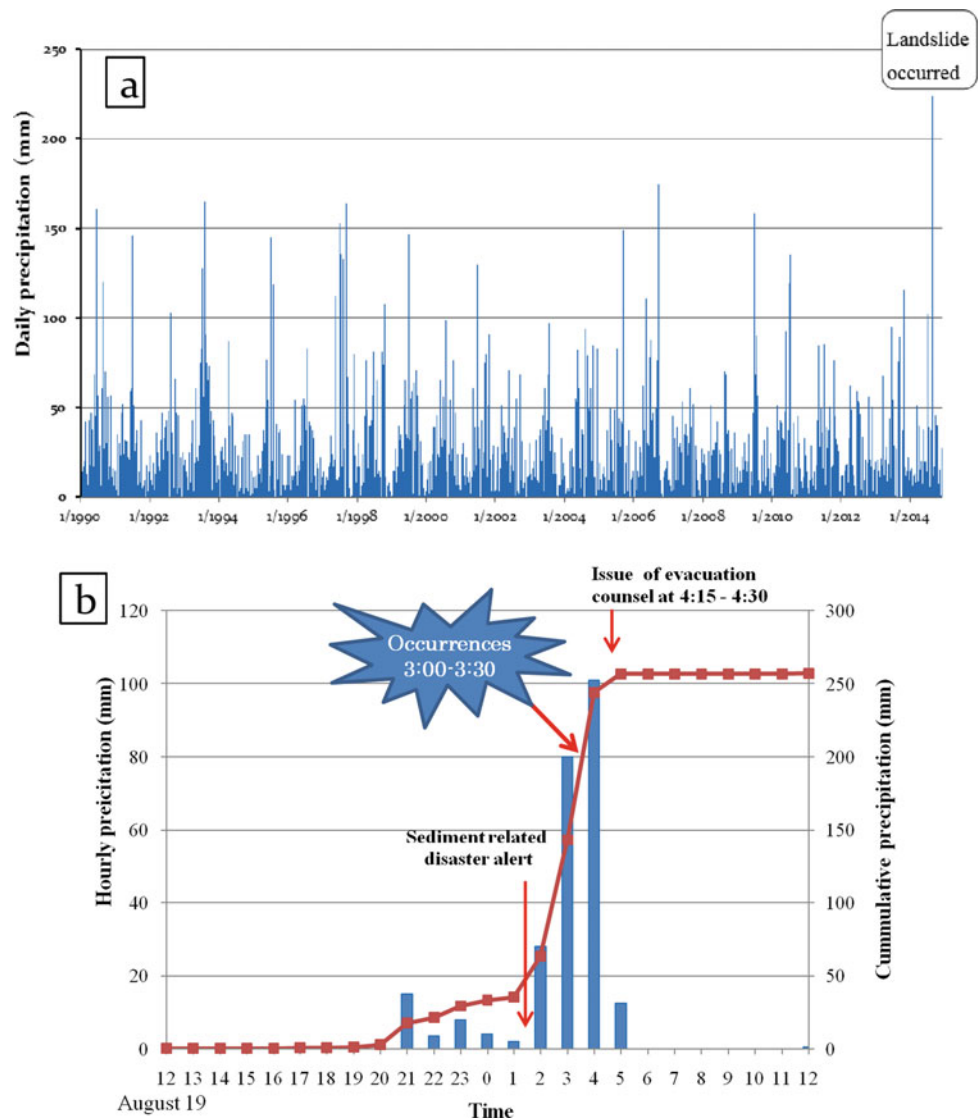


Table 1 Previous landslide disaster by heavy rainfall in Hiroshima prefecture (Hiroshima Crisis-Management Department Crisis-Management Division 2014)

No	Date	Disaster name	Death toll
1	01/07/1967	Heavy rain disaster	149
2	01/07/1972	Heavy rain disaster	35
3	21/07/1988	Heavy rain disaster	14
4	29/06/1999	Hiroshima earth and sand disaster	31
5	11/07/2012	July heavy rain disaster	5

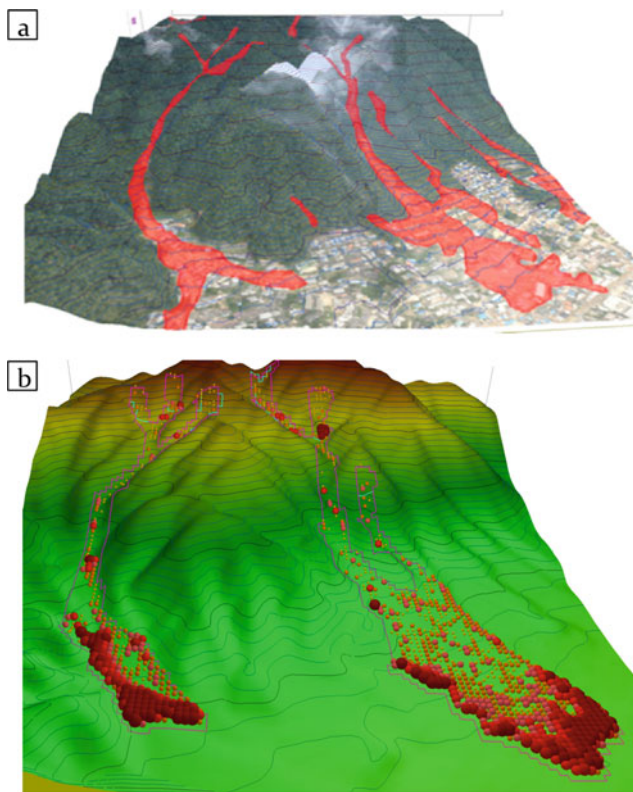


Fig. 5 3D view comparison of landslide deposits by Air photo interpretation by GSI (a) and LS-RAPID (b)

The 1999 event occurred in the area of sparse population, while the 2014 event occurred in the area of dense population. Thus, 2014 disaster became the extensive damage even with a relatively narrow range. The most catastrophic landslides and debris flows occurred in Midorii and Yagi areas of Hiroshima city which were studied in detail in this research. Like the 1999 disasters, the 2014 landslides took place in heavily weathered granitic sand “masa” on sliding surface, resulting in landslide-induced debris flows (Fukuoka et al. 2014). Most of them were shallow (0.5–2.0 m deep). Figure 3a presents severely damaged houses in Yagi-3 where debris flows claimed 41 casualties. The comparison of google earth photos of the most devastated area pre- (left) and post-disaster (right) was shown in the Fig. 3b, which enables to assess the affected buildings. Red circles show the 26 and 14 completely damaged houses in Yagi-3 and Midorri-8, respectively.

Triggering Factor

The rainfall data (daily rainfall from 1990 to 2014) was collected from the Japan Meteorological Agency at Miiri station. The hyetograph of daily rainfall from 1990 to 2014 is shown in Fig. 4.

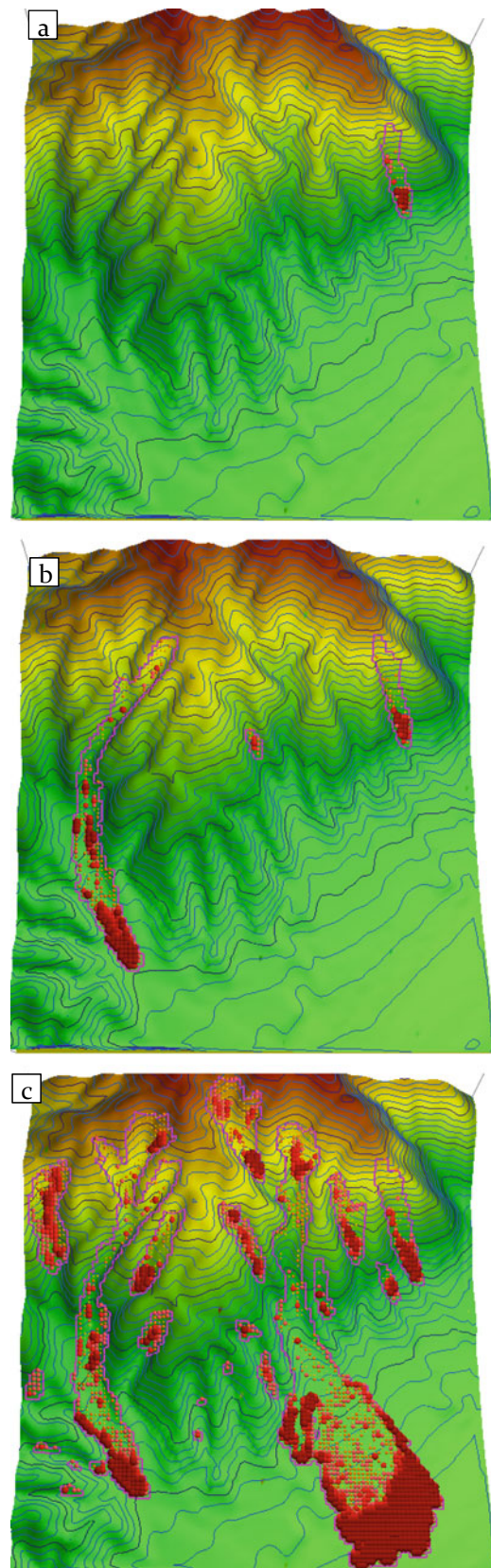


Fig. 6 Final simulation results with different depths of unstable slope (a 0.9 m; b 1 m and c 1.5 m)

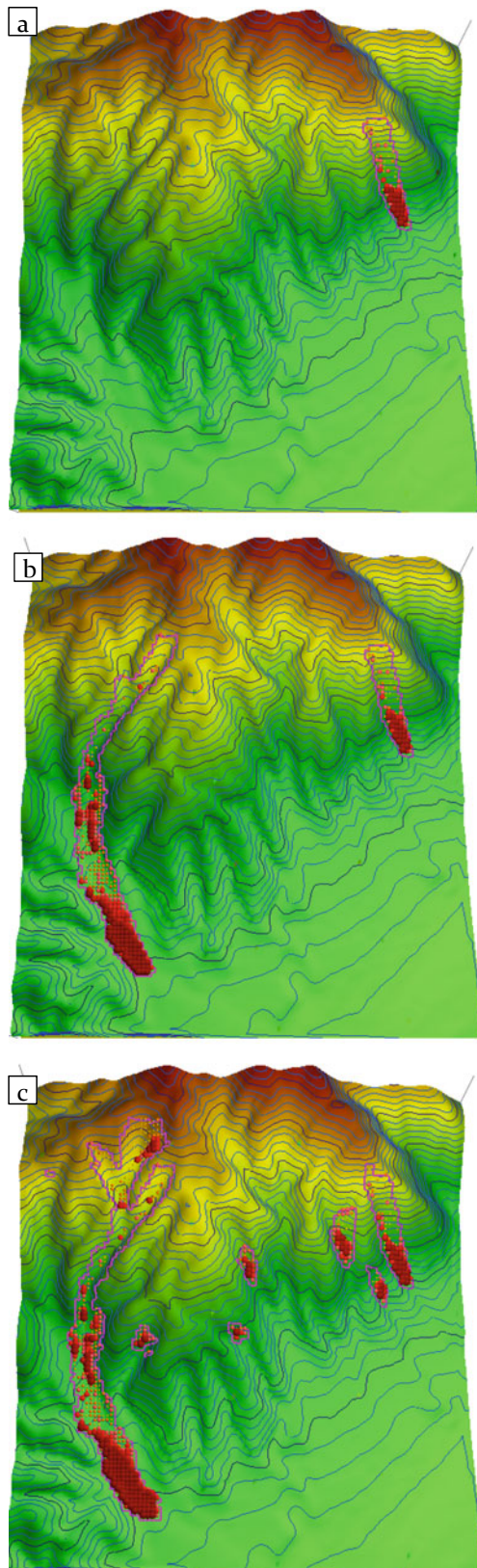


Fig. 7 Final simulation results with different pore water pressure ratios (a 0.2; b 0.3 and c 0.4)

From Fig. 4a, daily precipitation at Miiri station is less than 200 mm, except on 20 August 2014. In the 2014 Hiroshima landslide disasters, Hiroshima meteorological observatory of JMA announced this disaster at 1:15 a.m. on August 20. After two hours, debris flows and landslides occurred and the Hiroshima government issued the evacuation counsel at 4:15 am. It indicates landslide disaster alert is not directly related to evacuation counsel. This is one of the reasons that many people were killed in 2014 landslide disasters. The cumulative rainfall from 20:00 PM of 19 August until 04:00 AM of 20 August reached 248 mm at Miiri rain gauge station in Hiroshima. This is main reason caused the Hiroshima disasters.

Table 1 presents the previous landslide disaster by heavy rainfall in Hiroshima prefecture. It indicates that Hiroshima has experienced with disasters especially the Hiroshima disaster in 1999. This disaster claimed 31 dead and very similar to the 2014 Hiroshima disaster. After the 1999 Hiroshima debris flow disaster, the Landslide disaster reduction law which intends to promote the designation of landslide potential risk zones was adopted in 2000. However, some areas in which landslides occurred in 2014 have not been designated as special caution areas under the law. It means urbanization is too rapid for land-use management and measures to reduce natural disasters.

Hazard Mapping Using LS-RAPID

LS-RAPID is a 3D landslide simulation model that can be simulated the initiation and motion of a landslide triggered by rainfall and earthquake. The main soil parameters for LS-RAPID were obtained from ring shear apparatus. The detail of LS-RAPID is described in Sassa et al. 2010. The LS-RAPID and ring shear apparatus were used to estimate hazard area and time of occurrence in the 2014 Hiroshima disaster (Loi et al. 2018). The estimated hazard area is similar to the actual landslide moving area reported by the Geospatial Information Authority of Japan (GSI) (Fig. 5). In addition, the time of landslide occurrence is closed with actual occurrence that was reported by Hiroshima city office.

The purpose of this study was to apply the LS-RAPID to estimate a potential landslides triggered by heavy rainfall in the future. For the landslide dynamic parameters using in this paper see Loi et al. (2018) Table 1 page 163.

Based on the field investigation, soil depths (potential unstable mass) from 0.5 m to 1.5 m were used in the model. The LS-RAPID model uses pore water pressure ratio r_u as a triggering factor. The pore-water pressure is:

$$r_u = \frac{u}{\sigma} = \frac{Z_w \cdot \gamma_w}{Z_s \cdot \gamma_s}$$

Table 2 Landslide volume with different landslide depths and pore water pressure ratios

Depth (m)	r_u (maximum)	r_u (at initial failure)	Volume (m ³)
0.5–0.8	0.53	No landslide	0
0.9	0.53	0.50	1526
1.0	0.53	0.40	11,751
1.5	0.53	0.18	60,058
1.5	0.2	0.18	2,651
1.5	0.3	0.18	11,625
1.5	0.4	0.18	18,777

Here, Z_w is vertical depth of ground water flow, γ_w is unit weight of water, γ_s unit weight of soil, Z_s is vertical landslide depth.

When the soil full saturation $Z_w = Z_s$, $r_u = 9.8/18.5 = 0.53$ that is the worst case scenario. In the case of 2014 Hiroshima disaster, landslides took place when pore-water pressure ratio reached 0.27.

For analysis of influence of the depth of potential unstable slope, we selected maximum value $r_u = 0.53$ (r_u increasing from 0 to 0.53) and changed value of depth from 0.5 to 1.5 m. With the value Z_s changing from 0.5 to 0.8 m, there was no unstable slope. On Fig. 6a we can see that small unstable slope can be found when $Z_s = 0.9$ m was given at each mesh. Figure 6b shows the landslide simulation for landslide depth of 1 m at each mesh. Three landslides were found but only the left landslide reached residential area. The central landslide was a local slope failure. Many landslide were found in Fig. 6c ($Z_s = 1.5$ m). The biggest landslide moved to Yagi community. It was the serious scenarios. The pore water pressure ratio $r_u = 0.53$ represents full saturation which is a very low probability scenario. Therefore, in order to examine a realistic scenario, the authors fixed value $Z_s = 1.5$ m and used different values of $r_u = 0.2$; 0.3 and 0.4 (water table at 75% layer height). On Fig. 7a, we can see that only one unstable slope moved and spread as the same in Fig. 6a while the volume was approximately 1.7 times the volume of the model with $r_u = 0.53$ and $Z_s = 0.9$ m. Model with $r_u = 0.3$ shows that the final deposit (Fig. 7b) and the landslide volume (Table 2) were similar to those with $r_u = 0.53$ and $Z_s = 1.0$ m. Model with $r_u = 0.4$ (Fig. 7c) shows that landslide mass can move a long distance and attack the Midori community. This landslide volume was about 18,777 m³. The large differences in the modelled landslide volumes were found in Table 2 for different scenarios.

Discussions

Landslides and debris flows present fatal hazard in Hiroshima in the past. The hazard assessment of rainfall induced landslide should be well conducted in the process of

development land use planning in Hiroshima prefecture. The LS-Rapid model using parameter from ring shear apparatus is of wide applied by landslide researchers. The results of hazard assessment of rainfall induced landslide in Midori and Yagi area may give effective information for the local government authorities in Hiroshima city. Research on rainfall induced landslide is need to investigate reliable pore water pressure at each mesh. However, the main limitation of the model is that only one pore water pressure was given for all mesh as the triggering factor. Future research should consider the potential effects of rainfall more carefully, for example, improved LS-Rapid model with linking to a hydrological model. In addition, different pore water pressure in each mesh should be used in the improved model.

References

- Cuomo S, De Chiara V, Dugonjić Jovančević S, Vivoda Prodan M, Arbanas Ž (2017) Insights from LS-rapid modeling of Montaguto Earthflow (Italy). In: Mikoš M, Tiwari B, Yin Y, Sassa K (eds) Advancing culture of living with landslides, vol 2. Advances in Landslide Science, pp 611–619
- Dang K, Sassa K, Konagai K et al (2019) Recent rainfall-induced rapid and long-traveling landslide on 17 May 2016 in Aranayaka, Kagelle District, Sri Lanka. *Landslides* 16(1): 155–164
- Dugonjić Jovančević S, Nagai O, Sassa K, Arbanas Ž (2013) Deterministic landslide susceptibility analyses using LS-Rapid software. In: Proceeding of the 1st regional symposium on landslides in the Adriatic-Balkan region: landslide and flood hazard assessment. Croatian Landslide Group, Zagreb, pp 73–77
- Dugonjić Jovančević S, Arbanas Ž (2017) Influence of the runoff potential on landslide-susceptible areas along the flysch–karst contact in Istria, Croatia. *Nat Hazards* 85:1347–1362
- Fukuoka H, Mizuno M, Yasuda H (2014) Field investigation of the 20 August 2014 Hiroshima debris flow disaster. In: Proceeding of international forum of “urbanization and landslide disaster”, Kyoto, October, 2014
- Goryakin Y, Rocco L, Suhrcke M (2017) The contribution of urbanization to non-communicable diseases: evidence from 173 countries from 1980 to 2008. *Econ Hum Biol* 26:151–163
- Gradiski K, Sassa K, He B, Arbanas Z, Arbanas S, Krkac M, Kvasnicka P, Ostric M (2013) Application of integrated landslide simulation model LS-Rapid to the Kostanjek landslide, Zagreb, Croatia. Proceedings of the 1st regional symposium on landslides in the Adriatic Balkan Region, pp 11–16

- Kean JW, Staley DM, Lancaster JT, Rengers FK, Swanson BJ, Coe JA, Hernandez JL, Sigman AJ, Allstadt KE, Lindsay DN (2019) Inundation, flow dynamics, and damage in the 9 January 2018 Montecito debris-flow event, California, USA: Opportunities and challenges for post-wildfire risk assessment. *Geosphere* 15(4):1140–1163
- Li GR, Lei YL, Yao HJ, Wu SM, Ge JP (2017) The influence of land urbanization on landslides: an empirical estimation based on Chinese provincial panel data. *Sci Total Environ* 595:681–690
- Loi DH, Quang HL, Sassa K, Takara K, Dang K, Nguyen KT, Pham VT (2017) The 28 July 2015 rapid landslide at Ha Long city, Quang Ninh, Vietnam. *Landslides* 14(3):1207–1215
- Loi DH, Sassa K, Fukuoka H, Sato Y, Takara K, Setiawan H, Pham T, Dang K (2018) Initiation mechanism of rapid and long runout landslide and simulation of hiroshima landslide disasters using the integrated simulation model (LS-RAPID). In: Sassa K, Tiwari B, Liu KF, McSaveney M, Strom A, Setiawan H (eds) *Landslide dynamics: ISDR-ICL landslide interactive teaching tools*. Springer, Cham, pp 149–168
- Luo HY, Shen P, Zhang LM (2019) How does a cluster of buildings affect landslide mobility: a case study of the Shenzhen landslide. *Landslides* 16(12):2421–2431
- Moore R, McInnes RG (2016) Ground Instability and landslide management: raising awareness and increasing capacity for change within affected societies. In: Aversa et al (eds) *Landslides and engineered slopes*, vol 3. Experience, Theory and Practice, pp 1469–1476
- Quang LH, Loi DH, Sassa K, Takara K, Ochiai H, Dang K, Abe S, Asano S, Ha DN (2018) Susceptibility assessment of the precursor stage of a landslide threatening Haivan Railway Station Vietnam. *Landslides* 15(2):309–325
- Sakatani Y. (2014). Measures against the Hiroshima debris flow disaster on August.20, 2014. In: *Proceeding of international forum of “urbanization and landslide disaster”*, Kyoto, October, 2014
- Sassa K, Nagai O, Solidum R, Yamazaki Y, Ohta H (2010) An integrated model simulating the initiation and motion of earthquake and rain induced rapid landslides and its application to the 2006 Leyte landslide. *Landslides* 7(3):219–236
- Senthilkumar V, Chandrasekaran S, Maji V (2017) Geotechnical characterization and analysis of rainfall—induced 2009 landslide at Marappalam area of Nilgiris district, Tamil Nadu state, India. *Landslides* 14(5):1803–1814
- Setiawan H, Wilopo W, Wiyoso T et al (2019) Investigation and numerical simulation of the 22 February 2018 landslide-triggered long-traveling debris flow at Pasir Panjang Village, Brebes Regency of Central Java, Indonesia. *Landslides* 16(12):2219–2232
- Sodnik J, MačekMatej M, Matjaž M (2018) Estimating landslide volumes using LS-Rapid model—The 2000 Stože landslide in NW Slovenia. *INTERPRAEVENT 2018 in the Pacific Rim—Symposium Proceedings*, pp 32–48
- Tien PV, Sassa K, Takara K, Fukuoka H, Dang K, Shibasaki T, Ha ND, Setiawan H, Loi DH (2018) Formation process of two massive dams following rainfall-induced deep-seated rapid landslide failures in the Kii Peninsula of Japan. *Landslides* 15(9):1761–1778
- Vivoda M, Dugonjić Jovančević S, Arbanas Ž (2013) Landslide occurrence prediction in the Rječina River Valley as a base for an early warning system. In: *Proceeding of the 1st regional symposium on landslides in the Adriatic-Balkan region: landslide and flood hazard assessment*. Croatian Landslide Group, Zagreb, pp 85–90
https://en.wikipedia.org/wiki/2014_Badakhshan_mudslides. Last accessed 15 Aug 2019



Numerical Models of Debris Flows with Entrainment Analysis-Case Studies from the Republic of Serbia

Jelka Krušić, Biljana Abolmasov, and Miloš Marjanović

Abstract

The results of material entrainment analysis in RAMMS debris flow software, as well as numerical models of final flow heights for two case studies from the Republic of Serbia are presented. Both cases were triggered after extreme rainfall period in May 2014. These debris flow processes started with initial sliding of huge volume block, prolonging to behave as flowing process. They are situated in different regions of country and quite different in sense of geology, gravel size, geometry etc. Results of the analysis showed that entrainment material affects final results of transportation model, runout distance, deposition area and volume of debris flow. In both cases entrainment volume is very huge, but it is much less than initial volume (about 11% of total volume in both case studies). Final results are validated with pre- and post-event DEMs (Digital Elevation Models and analysis of ERT geophysical results).

Keywords

Debris flow • Entrainment • RAMMS • Validation

Introduction

The entrainment of material is important part of flow-type processes, which consider change in volume and momentum during transfer of material procedure of incorporating the

eroded sediment into the debris flow. Therefore it is important part of runout modelling. There are different approaches for modelling entrainment from empirical methods that require the input of user-prescribed volume growth rates (Takahashi 1991; Hungr et al. 2005; Iverson 2012) to process based methods that simulate entrainment as a function of basal shear stress conditions (Iverson 2012). Many observations of entrainment are made in different parts of the world (Hungr et al. 2005; Iverson et al. 2011; Frank et al. 2015). RAMMS debris flow software, based on Voellmy (1955) rheology, was specially designed for snow avalanches (Bartelt et al. 2013; Christen et al. 2007; 2010a; b). Nevertheless, it is also suitable for modelling of other processes such as rock avalanches and debris flows (Schraml et al. 2015; Sosio et al. 2008).

One of the observation tests of entrainment was made by Frank et al. (2016) in Swiss Alps and used for improvement in RAMMS debris flow software. After continuous monitoring and measurement on debris flows and avalanches in two catchments, it was resulted in defining specific erosion rate as a default. Beside three main inputs (Digital Elevation Model, source area, rheology parameters) it is necessary to define entrainment zones. Zones were registered by field observations and comparison of pre- and post-event topography.

In this paper will be presented two case studies from Serbia, already tested in RAMMS. In both cases entrainment volume is very huge, but it is much less than initial volume (about 11% of total volume in both cases). Final results were validated comparing two epoch DEM and ERT field investigation.

Case Studies

The Selanac Debris Flow

The Selanac debris flow was triggered in May 2014 as a consequence of cyclone Tamara (Ivette) event. In wider region over 100 mm of rain has fallen during the 14–15 May

J. Krušić · B. Abolmasov (✉) · M. Marjanović
Faculty of Mining and Geology, University of Belgrade,
Đušina 7, 11000 Belgrade, Serbia
e-mail: biljana.abolmasov@rgf.bg.ac.rs

J. Krušić
e-mail: jelka.krusic@rgf.bg.ac.rs

M. Marjanović
e-mail: milos.marjanovic@rgf.bg.ac.rs

2014 (more than 200 mm for 72 h). That resulted in that huge block of material started to flow through two old gullies. Estimated initial block has volume of about 450,000 m³. Dimensions of debris flow are 1.2 km long and about 350 m wide in widest part which is in source area (Fig. 2).

The oldest geological formation is Palaeozoic- “Drina” formation. It is a complex of Lower (¹C_{1,2}) and Middle Carboniferous age (²C_{1,2}) phyllite, metasandstone, clay and graphitic schists, limestone, diabase, tuff and tuffite. In the “Jadar formation” Pz is developed as a complex of sandstone, argillophyllite and black limestone. Both formations are transgressively overlain by sandstone, shale and limestone of the Permian, which pass into the block bituminous limestone of the Upper Permian (P₃). Lower Triassic (T₁) and Middle Triassic (T₂) consist of dolomite, dolomitic limestone, sandstone, limestone, and andesite with pyroclastics. The Jurassic (J_{1,2}) consist of oolitic to nodular, limonitized to siliceous limestones, sandstone, shale, conglomerate, chert, spilite, amphibolite, gabbro and serpentinite. The Jurassic (J_{1,2}) weathered ophiolitic melange is the main formation involved in debris flow process.

Deposited material is from matrix of fine gravel to very huge boulders of ophiolites over 1.5 m in diameter. Some amount was transported further with Selanačka river, so in all results actually is shown total runout including transport in river valley after the deposition zone. All results in simulations were compared with deposited material measures.

The Leva Reka Debris Flow

The Leva reka debris flow was occurred near city of Kraljevo during the same event in 2014. Huge block started firstly as slide and prolonged as a flow. Travel distance is not so huge in comparison to length of source area and deposition area, so this is very possible flow-slide type of movement. As a previous case, the material made natural dam, making small lake on river in the bottom of valley. Also material destroyed a road across the river valley, and on that way made a problem in transportation in some parts of municipality for few days. Similar material was transported through river even further, but in these cases that amount was not as huge as in Selanac debris flow. Total travel distance from source to deposition area was about 300–400 m, and it is 100 m wide in deposition zone. Deepest part in source area is 15 m. The geographical position of both case studies is presented on Fig. 1.

From geological part, debris flow occurred in the thick weathered core of flysch (Cretaceous period—K13+4), predominantly sandstone, clay schist, claystone and marl, and



Fig. 1 Position of case studies on the map of Serbia

secondary conglomerates and marly-sand limestone. Wider area is also made of the flysch formation.

RAMMS (Rapid Mass Movement Software)

RAMMS DBF software is FVM (Finite Volume Method) software for modelling of debris flows, based on well used rheological Voellmy (1955) model. It is one-phase model which assumes the initiation mass starts to move as a plug defining shear stress in different points of transportation path.

The mass balance equation incorporates the field variables flow height $H(x, y, t)$ and flow velocity $U(x, y, t)$ and is given by:

$$Q(x, y, t) = \partial_t H + \partial_x (H U_x) + \partial_y (H U_y) \quad (1)$$

where $Q(x, y, t)$ describes the mass production source term, and U_x and U_y represent the depth-averaged velocities in horizontal directions x and y (Christen et al. 2010a; Frank et al. 2016). The depth-averaged momentum balance equations account for the conservation of momentum in two directions x and y

$$Sgx - Sfx = \partial t(HUx) + \partial x(cxHUx^2 + g_z k_p \frac{H^2}{2}) + \partial y(HUxUy) \tag{2}$$

$$Sgy - Sfy = \partial t(HUy) + \partial x(HUxUy) + \partial y(c_y HUy^2 + g_z k_p \frac{H^2}{2}) \tag{3}$$

where the earth pressure coefficient $k_a = p$ is normally set to 1 when running the standard Voellmy–Salm friction approach, c_x and c_y represent topographical coefficients determined from the digital elevation model, S_g is the effective gravitational acceleration, and S_f is the frictional deceleration in directions x and y (Christen et al. 2010b).

The frictional deceleration S_f of the flow is determined using the Voellmy friction relation and specifies the dry-Coulomb term (friction coefficient μ) scaling with the normal stress and the viscous or turbulent friction (coefficient ξ depending on the flow velocity U) (Christen et al. 2010a; Bartelt et al. 2013):

$$S_f = \mu \rho g H \cos \varphi + \frac{\rho g u^2}{\xi} \tag{4}$$

where ρ is the mass density, g is the gravitational acceleration, φ is the slope angle, and $H \cos \varphi$ is the normal stress on the overflowed surface. The tangent of the effective internal friction angle of the flow material can be defined for the resistance of the solid phase (the term containing μ which extensively controls deceleration behaviour of a more slowly moving flow. The resistance of the viscous or

turbulent fluid phase (the term including ξ prevails for a more quickly moving flow (Bartelt et al. 2013).

Entrainment Model

The erosion algorithm in the RAMMS model, is defined using the maximum potential erosion depth e_m and a specific erosion rate. The erosion algorithm predicts the maximum potential depth of erosion e_m as a function of the computed basal shear stress in each grid cell:

$$e_m = 0 \text{ for } \tau < \tau_c \tag{5}$$

$$e_m = dz/dt(\tau - \tau_c) \text{ for } \tau \geq \tau_c \tag{6}$$

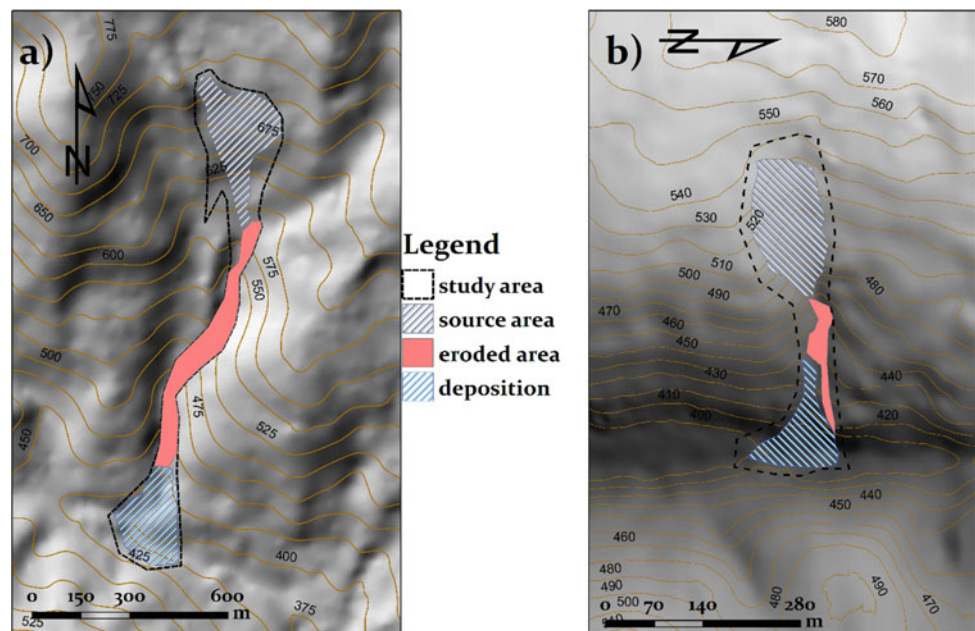
and the shear stress τ is approximated using the depth–slope product:

$$\tau = \rho g h S \tag{7}$$

The potential erosion depth (per kPa) dz/dt controls the rate of vertical erosion (in the z -direction) as a linear function of channel-bed shear stress.

When the critical shear stress τ_c is exceeded, sediment can be entrained from the channel. Entrainment stops when the actual erosion depth e_t reaches the maximum potential erosion depth e_m (Eq. 6). Normally, the specific erosion rate is implemented using the default value $dz/dt = -0.025 \text{ m}^{-1}$. Detailed position of source, deposited and potential eroded area for both cases are shown on Fig. 2.

Fig. 2 Main geometrical parameters for Selanac (a); and Leva reka (b)



Results and Discussion

For entrainment testing of the Selanac debris flow was used estimated eroded depth of 12 m. Comparison of two epoch DEM data were used for defining differences in deposition, erosion and source area. Hence, the most precise is depth of source area, since there is eroded material and deposited material in transport zone. As critical shear stress we used default value of 1 kPa, and rate proportionality factor $dz/dt = 0.1 \text{ m/kPa}$. Greater values of proportionality factor over predict erosion volume. Results of volume and

transportation of material with/without entrainment were compared. Considering entrainment of material deposition heights are little bit larger, but total volume is quite greater. Entrainment influenced in outflow in Selanačka river (Fig. 3).

For Leva reka, the same parameters were used as default, with estimated maximum eroded depth of 6 m. Final model show greater and more real height in deposition zone than model without entrainment included (Fig. 4). Also, some other options were tested for greater potential erosion depth (0.2 m/kPa), which resulted in over prediction of erosion depth (almost 20 m).

Fig. 3 Entrainment model for Selanac (a); Final deposition model (b)

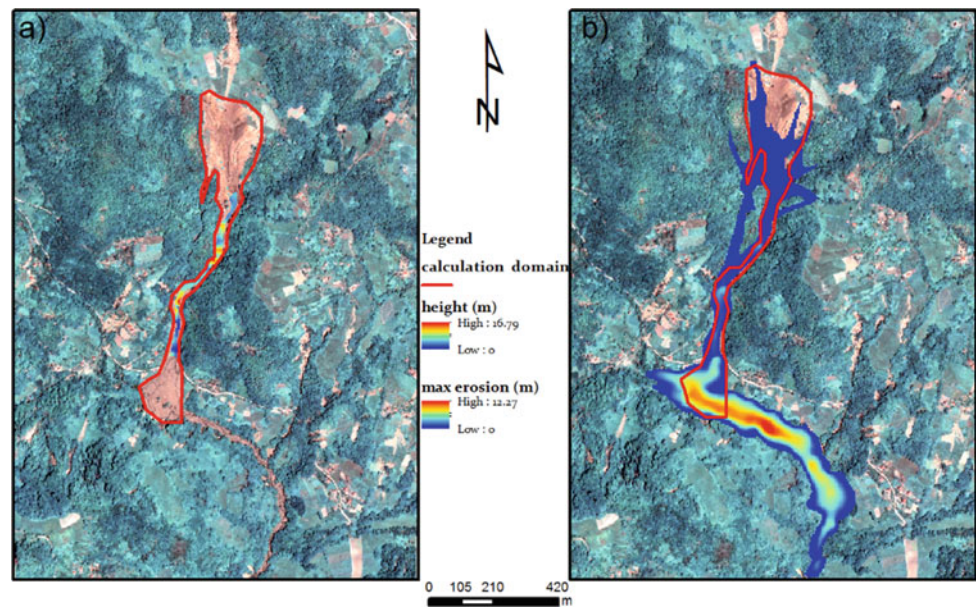


Fig. 4 Entrainment model for Leva reka (a); Final deposition model (b)

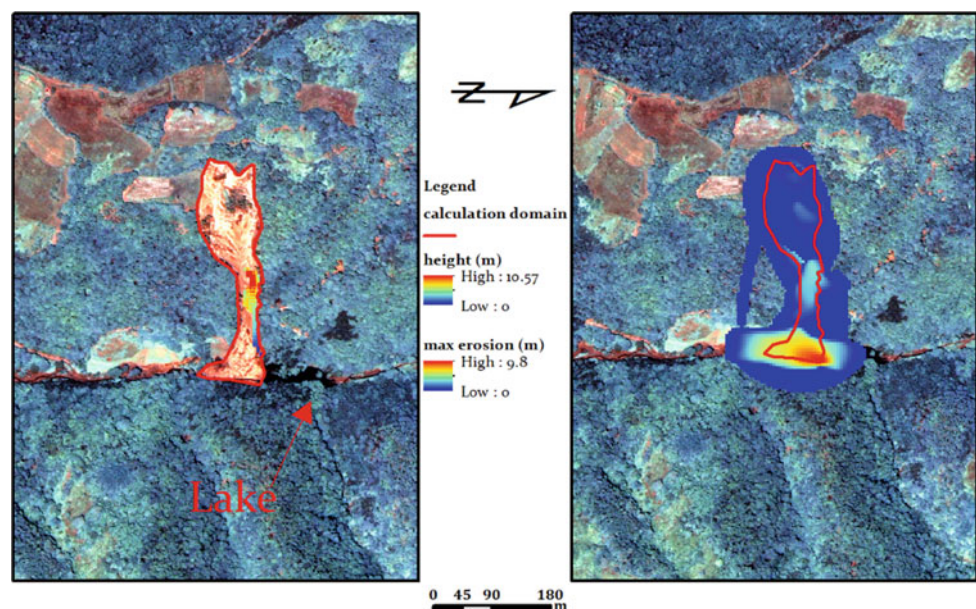


Table 1 Input and output parameters

Debris flow case study	Rheology (Voellmy) $\mu, \xi(\text{ms}^{-2})$	Initial block volume (m^3)	Eroded volume (m^3)	VG index
Selanac	0.11, 500	453061.58	41023.35	1.09
Leva reka	0.35, 1000	68663.15	6584.44	1.1

Table 2 Comparison of estimated and calculated results

Debris flow case study	Maximum deposition height (m)		Deposition volume (m^3)		Maximum erosion depth (m)	
	Estimated	Calculated	Estimated	Calculated	Estimated	Calculated
Selanac	20	16.79	≈121.000	≈118.000	12	12.27
Leva reka	12	10.57	≈28.000	≈23.000	6	9.8

In both cases percentage of eroded material is small comparing total volume of debris flow. Regarding to VG index (Frank et al. 2016) that percent is very small (Table 1) calculated with equation:

$$VG = V_{final}/V_{ini} = (V_{ini} + V_{ero})/V_{ini} \quad (8)$$

where V_{ini} is *initial volume*, and V_{ero} —*eroded volume*.

This small values are real regarding to very huge initial volume and depths in main block (Selanac 30 m maximum, Leva reka 17 m maximum) and could be concluded that is connected with large occasions and deep source areas.

For best fitted parameters were used 0.11 for μ and 500 ms^{-2} for ξ for Selanac and 0,35 for μ and 1000 ms^{-2} for ξ for Leva reka. Results of analysis and modelling without entrainment influence are presented in (Krušić et al. 2019). For the second case study, some preliminary results were published in Krušić et al. (2018), but since that was first testing, it should be emphasized that in further investigation with more precise topography more precise model is made which is shown here.

Validation

Main comparison was made with analysis of pre vent and post event DEM, and ERT investigation. Comparison of two epochs DEM helped in better defining source area and precise eroded zone. Estimated deposition volumes, heights and erosion depths are given in Table 2

Conclusion

Entrainment has a very important role in modelling of debris flows. However, this methods are new and still improving in runout numerical models. Most of them are made regarding

to voluminous monitoring on the field. Algorithm implemented in RAMMS is a result of continuous field investigation in Swiss Alps. Better validation of entrainment needs better observation of event on the field. Here we compared with experienced prognosis on the field and potential depth regarding to DEMs and ERT investigation. Comparing previous models without erosion effect, main difference is in deposition heights and generally deposition volume and runout distance, which are more precise using it.

Acknowledgements The research results will be not possible without Project BEWARE (BEYond landslide aWAREness) funded by the People of Japan and the UNDP Office in Serbia (grant No 00094641). The project was implemented by the State Geological Survey of Serbia, and the University of Belgrade Faculty of Mining and Geology. All activities are supported by the Ministry for Energy and Mining and the Ministry for Education, Science and Technological Development of the Republic of Serbia Project No TR36009, too.

References

- Bartelt P, Buehler Y, Christen M, Deubelbeiss Y, Graf C, McArdell BW (2013) RAMMS—rapid mass movement simulation, A modeling system for debris flows in research and practice, user manual v1.5, debris flow. Institute for Snow and Avalanche Research SLF
- Christen M, Bartelt P, Kowalski J, Stoffel L (2007) Calculation of dense snow avalanches in three-dimensional terrain with the numerical simulation program RAMMS. In: Proceedings of the differential equations, pp 709–716
- Christen M, Kowalski J, Bartelt P (2010a) RAMMS: numerical simulation of dense snow avalanches in three-dimensional terrain. Cold Regions Sci Technol 63(2010):1–14
- Christen M, Bartelt P, Kowalski J (2010b) Back calculation of the In den Arelen avalanche with RAMMS: Interpretation of model results. Ann Glaciol
- Frank F, McArdell BW, Huggel C, Vieli A (2015) The importance of entrainment and bulking on debris flow runout modeling: examples from the Swiss Alps. Nat Hazards Earth Syst Sci 15:2569–2583. <https://doi.org/10.5194/nhess-15->

- Frank F, McArdell BW, Oggier N, Baer P, Christen M, Vieli A (2016) Debris flow modeling at Meretschibach and Bondasca catchment, Switzerland: sensitivity testing of field data-based erosion model. *Nat Hazards Earth Syst Sci Discuss*
- Hungr O, McDougall S, Bovis M (2005) Entrainment of material by debris flows. In: Jakob M, Hungr O (eds) *Debris-flow hazards and related Phenomena*. Springer, New York, pp 135–158
- Iverson RM (2012) Elementary theory of bed-sediment entrainment by debris flows and avalanches. *J Geophys Res* 117:F03006. <https://doi.org/10.1029/2011JF002189>
- Iverson RM, Reid ME, Logan M, LaHusen RG, Godt JW, Griswold JG (2011) Positive feedback and momentum growth during debris-flow entrainment of wet bed sediment. *Nat Geosci* 4:116–121. <https://doi.org/10.1038/NGEO1040>
- Krušić J, Abolmasov B, Samardžić Petrović M (2019) Influence of DEM resolution on numerical modelling of debris flows in RAMMS—Selanac case study. In: *Proceedings of the 4th Regional symposium on in the adriatic—balkan region 23–25 October 2019*. Sarajevo, Bosnia and Herzegovina, pp 163–169. https://doi.org/10.35123/ReSyLAB_2019
- Krušić J, Samardžić PM, Marjanović M, Abolmasov B, Miljković S (2018) Preliminary results of numerical modelling of debris flow—case study Leva reka. *Serbia* 2:707–712. <https://doi.org/10.1002/cepa.753>
- Schraml K, Thomschitz B, McArdell BW, Graf C, Kaitna R (2015) Modeling debris-flow runout patterns on two alpine fans with different dynamic simulation models. *Nat Hazards Earth Syst Sci* 15(7):1483–1492
- Sosio R, Crosta GB, Hungr O (2008) Complete dynamic modeling calibration for the Thurwieser rock avalanche (Italian Central Alps). *Eng Geol* 100(1–2):11–26
- Takahashi T (1991) *Debris flow*. IAHR-AIRH Monograph series. A. A. Balkema
- Voellmy A (1955) Über die Zerstörungskraft von Lawinen. *Schweizerische Bauzeitung* 73:212–285



Numerical Simulation of a Creeping Landslide Case in Japan

Akihiko Wakai, Deepak Raj Bhat, Kenta Kotani, and Soichiro Osawa

Abstract

Creeping landslides are one of the major natural disasters in mountainous regions. Therefore, study of the creeping behavior of a landslide and associated Geotechnical issues are important. This study has addressed and evaluated the creeping behaviour of a the Tomuro landslide Gunma, Japan induced by snow melt water using the 2D-FEM based elasto-viscoplastic constitutive model as a case study. Two new control constitutive parameters were incorporated in the numerical model for the first time to better understand the creeping behaviour of a landslide. Such control constitutive parameters were estimated based on the relation between the total factor of safety, calculated by the various Limit Equilibrium Methods such as Ordinary Method of Slice (Fellenius 1936) (case I), Bishop's Method (1955) (case II), Janbu's Simplified Method (1973) (case III), and Finite Element Method (case IV), and the field monitoring displacement rate of the Tomuro landslide. In addition, the snowfall precipitation was also considered during the calculation of total factor of safety using both limit equilibrium methods and finite element method. Others required material parameters for landslide simulation were calculated based on the field investigation and laboratory tests of the collected blocked samples. First, the predicted and measured time histories of horizontal displacement of the Tomuro landslide was compared for the validity of the proposed numerical model and found in good agreements with each other. Then, the simulation results of deformation pattern and shear strain pattern were presented and discussed. Finally, the possible failure mechanism along

the slip surface of a landslide induced by snow melt water was discussed.

Keywords

Numerical simulation • Snow melt water • Creeping behaviour • Tomuro landslide

Introduction

Terzaghi (1950) was most likely the first to consider the relationship between soil creep and landslides. Ter-Stepanian (1963) has introduced the threshold approach to explain soil creep in simple natural slopes by considering the zone of creep and its rate as being dependent on the groundwater level. Calvello et al. (2008) have presented an extensive study using a numerical model that focuses on active landslides controlled by rainfall-induced pore pressure fluctuations with movements concentrated within a relatively narrow shear zone above which the sliding mass moves essentially as a rigid body. Fernández-Merodo et al. (2014) have proposed a 2D-viscoplastic finite element model for slow-moving landslides and also applied this model to the Portalet landslide of Spain as a case study. Bhat and Yatabe (2016) have proposed a new regression model to understand the creeping behavior of clayey soils along the sliding surface at the residual-state of shear based on the residual-state creep test results of clayey soils (Bhat et al. 2011, 2012, 2013).

Previous studies (e.g., Conte et al. 2014; Picarelli et al. 2004; Ter-Stepanian 1963) have highlighted that creeping landslides are controlled by the groundwater fluctuations therefore; groundwater fluctuations should be incorporated in the numerical simulation of such landslides. However, most of previous numerical approach (e.g., Picarelli et al. 2004; Patton 1984; Ter-Stepanian 1963) of soil creep and associated problems are focused on the laboratory creep tests

A. Wakai (✉) · K. Kotani · S. Osawa
Gunma University, Tenjin-cho 1-5-1, Kiryu, 376-8515, Japan
e-mail: wakai@gunma-u.ac.jp

D. R. Bhat
Okuyama Boring Co. Ltd., Yokote, Akita, 013-0046, Japan
e-mail: deepakbhat@okuyama.co.jp

(i.e., consolidation/oedometer test and triaxial test), which could not address the fluctuation of groundwater level. Based on the theoretical, experimental, and numerical models, a few researches (e.g., Bhat and Yatabe 2016; Bhat et al. 2014a, b; Huvaj and Maghsoudloo 2013; Picarelli et al. 2004; Patton 1984; Ter-Stepanian 1963) have tried to address these issues till 1950 to until now; but they are not fully understood, especially in relation to the displacement behavior of a creeping landslide. Huvaj and Maghsoudloo (2013) have simulated the fluctuation of groundwater level in different phases to understand of displacement behavior of a slow-moving landslide, but the exact value of the deformation at any required point (location) couldn't be captured perfectly. Recently, a few researchers (e. g., Savage and Chleborad 1982; Ishii et al. 2012; Conte et al. 2014; Fernández-Merodo et al. 2014, etc.) have proposed a 2D-Elasto-viscoplastic constitutive model using finite element method based on the field instrumentation and monitoring results, but they are only considered the single control constitutive parameter based on the trial and error method, which could not control the displacement rate of the landslide, and also far to address the realistic field problem of creeping behavior of a landslide induced by snow melt water. Therefore, the main objective of this study is to address the above-mentioned problems by the help of FEM based numerical simulation and analysis of a landslide induced by snow melt water.

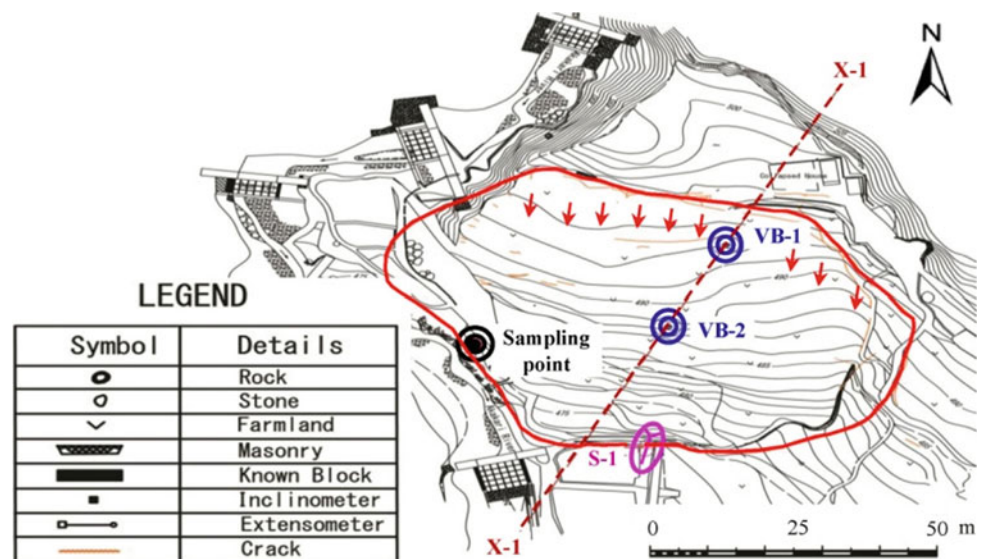
Study Area

The Tomuro landslide of Gunma prefecture of Japan has been considered in this study (Wakai et al. 2019, Bhat et al. 2019; Bhat and Wakai 2019). Figure 1 shows the simplified

topographical map of Tomuro landslide, showing the location of Sampling point, Piezometers and Extensometer. The size of Tomuro landslide has been measured approximately 135 m × 110 m. Figure 2 shows the variation of the rainfall and snowfall precipitation. The snow has accumulated at a thickness of 2 to 73 cm on the surface of landslide body during the period of 2014/2/8 to 2014/2/25. The maximum snowfall was recorded up to 73 cm on 2014/2/15. After the 2014/2/25, the deposited snow was starting to melt, and the groundwater level was also starting to rise. The Piezometers were installed at the location of BV-1 and VB-2 for monitoring the groundwater level of the landslide body. The results of the groundwater fluctuations at the boreholes (BV-1, and BV-2) are presented in Fig. 3. In this study, the results of groundwater fluctuations during the period of 2014/1/14 to 2015/7/6 are considered (Fig. 3).

The extensometer was installed at S-1 to measure the horizontal displacement of the landslide mass. The variation of the displacement rate during the period of 2014/1/14 to 2015/7/6 is presented in Fig. 4. The maximum displacement rate of 9.9 mm/day was recorded on 2014/3/4, where the groundwater level was also recorded maximum at the VB-1 and VB-2. From the comparative study of groundwater level and displacement rate with various time periods, it is understood that the displacement rate depends upon the fluctuation of the groundwater level. When the groundwater level is rising, the displacement rate is also increased and vice versa. The creep displacement of the landslide is directly related to the groundwater condition (Patton 1984). Eberhardt et al. (2007) have also agreed with Ter-Stepanian (1963) and Patton (1984). The fluctuation of groundwater should be considered to better understand the creeping behavior of a landslide (Bhat et al. 2017a, b). In this study, the groundwater fluctuation is considered for the stability

Fig. 1 The simplified topographical map of Tomuro landslide, showing the location of Sampling point, Piezometers and Extensometer



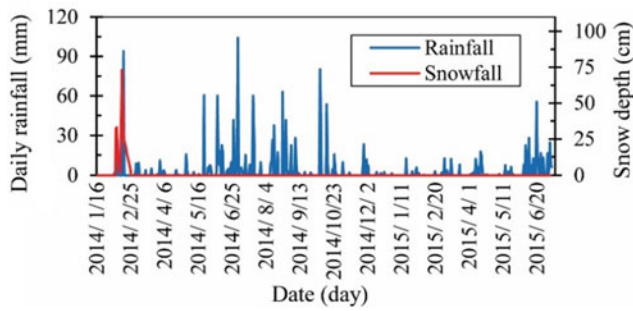


Fig. 2 Variation of the rainfall and snowfall precipitation

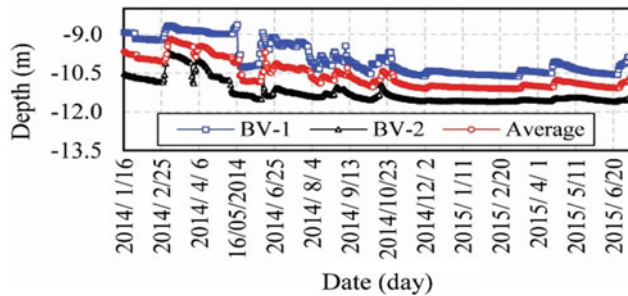


Fig. 3 Groundwater fluctuation in boreholes (BV-1, BV-2)

analysis using the various limit equilibrium methods and finite element method, as well as the numerical simulation of the Tomuro landslide.

Numerical Simulation

Most of the previous 2D-Elasto-viscoplastic constitutive model (e.g., Conte et al. 2014; Fernández-Merodo et al. 2014; Ishii et al. 2012), one parameter was considered, which was calculated based on trial and error method after calculating the results of displacement rate. This means that the displacement rate couldn't directly control in the previous two-dimensional Elasto-viscoplastic constitutive models. Moreover, such usual previous approaches are time consuming, tedious and difficult for estimating the appropriate parameters for the better simulation. However, the newly proposed numerical model has incorporated two new control constitutive parameters ($\dot{\alpha}$, n) for the first time for directly controlling the displacement rate and factor of safety of the landslide. Moreover, the newly proposed method is capable to easily estimate the exact control constitutive parameters for the better numerical simulation of the creeping behavior of the landslide, which may help for investigating the realistic field problem of a creeping landslide in the future. The basic concept of the proposed relation between the displacement rate and local factor of safety with

new control constitutive parameters ($\dot{\alpha}$, n) is shown in Eq. 1. Such Eq. 1 has been incorporated in the 2D- Elasto-viscoplastic constitutive model for the first time.

$$\dot{\gamma}_{\max} \leq \frac{\dot{\alpha}}{F_{s,\text{local}}^n} \tag{1}$$

where, $\dot{\gamma}_{\max}$ is displacement rate, $F_{s,\text{local}}$ is local factor of safety, and $\dot{\alpha}$, n are new control constitutive parameters, which can directly control the displacement rate and local factor of safety of the sliding block/mass. The detail of the newly proposed model has discussed by Wakai et al. (2019), Bhat et al. (2017a, b, 2018, 2019), and Bhat and Wakai (2019).

The proposed numerical model is applied to analysis the creeping behavior of Tomuro landslide of Gunma, Japan. Figure 5 shows the 2D-finite element mesh used for the analysis, which is prepared based on the geological cross-section of the slope of such landslide site. The base of the model is assumed to be fully impervious and fixed, and the lateral side (left and right) is constrained by hinged. The hydraulic head is imposed at the lateral boundaries based on the field monitoring results of groundwater fluctuation. The variations of the groundwater level fluctuations of 8.63–10.62 m and 9.7–11.61 m below the ground surface were recorded for VB-1 and VB-2 respectively from 2014/1/14 to 2015/7/6 (Fig. 3). S-1 shows the location of point (i.e., node 199 or element 278) of extensometer which was considered in this study. The main cause of using the S-1 only is that S-1 is the nearest to the cross-section x-1-x-1, and also shows the maximum displacement rate of the landslide body compared to other three installed extensometers reading during 2014/1/14 to 2015/7/6 (Figs. 1 and 4).

The two new unknown control constitutive parameters ($\dot{\alpha}$, n) are estimated based on the relation between the total factor of safety and displacement rate based on the Eq. 1. Initially, the total factor of safety (F_s) is calculated using the

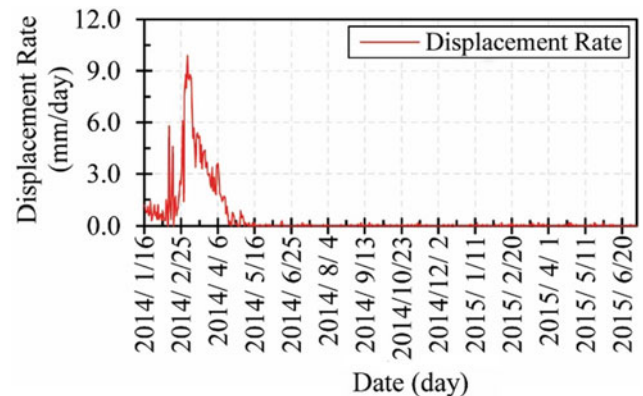


Fig. 4 Time variation of displacement rate at S-1

Fig. 5 Finite element model of Tomuro landslide

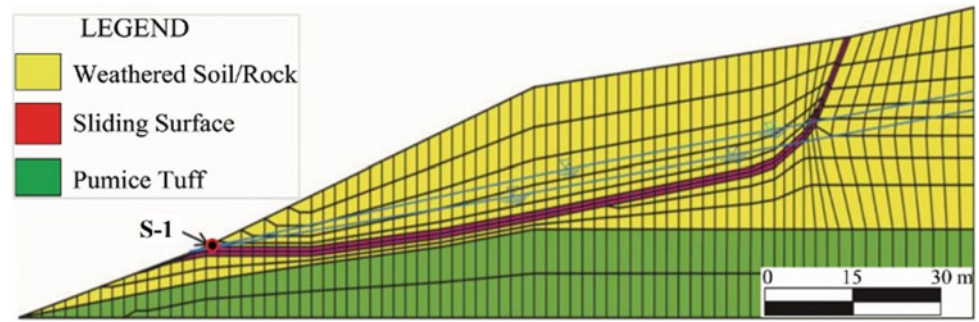


Table 1 Material parameters for landslide simulation

Materials parameters	Weathered soil/rock	Sliding surface				Pumice tuff
		Case I	Case II	Case III	Case IV	
Young's modulus, E (kN/m ²)	5000	1000				50,000
Poisson's ratio, ν	0.40	0.30				0.45
Cohesion, c' (kN/m ²)	50	0				5000
Internal friction angle, ϕ' (°)	35	15.2				30
Dilatancy angle, ψ (°)	0	0				0
$\dot{\alpha}$ (day ⁻¹)	–	0.00089	0.000489	0.00023	0.0011	–
n	–	53.398	46.4900	55.833	67.233	–
Unit weight, γ (kN/m ³)	24	20				26

various Limit Equilibrium Methods (LEM) based on the slices and Finite Element Method (FEM). In LEM Methods, three frequently used methods are used to calculate F_s of Tomuro Landslide of Gunma, Japan. At first, the ordinary method of Slices (Swedish Method of Slices or Fellenius 1936) is used, which is referred as Case I. Bishop's method (1955) has used to address the limitation of the ordinary method of slices, which is referred as Case II. Again, Janbu's Simplified method (1973) is also used to incorporate the drawback of the Bishop's method (1955), which is referred as Case III. Finally, the FEM Method is also used to address the drawback of the LEM, which is named as Case IV. In FEM method, Shear Strength Reduction Method (SSRM) is used to estimate the F_s of Tomuro Landslide of Gunma, Japan.

Matsuura et al. (2017) have highlighted the influences of snow cover on landslide displacement in winter period in Japan. Matsuura et al. (2003) have also reported that snow melt water and/or rainwater are closely related to groundwater level and landslide displacement. Therefore, the snowfall precipitation (Fig. 2) is also considered during the calculation F_s of the landslide body. After the calculation of F_s , the relations between $\dot{\gamma}_{\max}$ and F_s have been established for the cases I–IV. After that, the general equations are obtained based on the well fitted curve between $\dot{\gamma}_{\max}$ and F_s . Then, the unknown two new control constitutive parameters

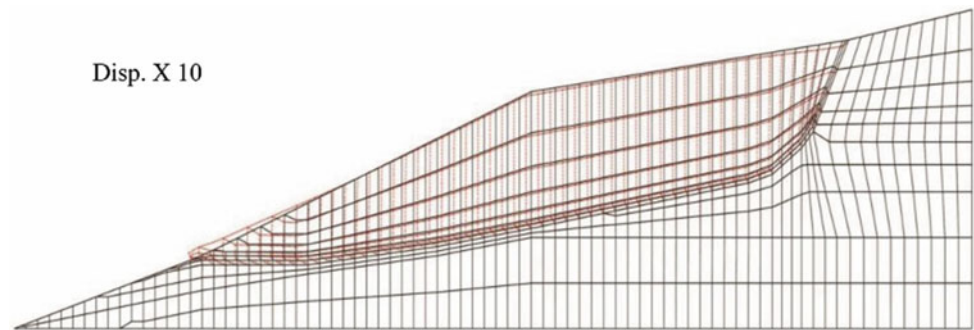
($\dot{\alpha}$, n) were estimated by solving of these general equations for each case. The method of estimating the new control constitutive parameters ($\dot{\alpha}$, n) has presented by Wakai et al. (2019), Bhat et al. (2017a, b, 2018, 2019) and Bhat and Wakai (2019) in details. The other required materials parameters for the landslide simulation (Table 1) are estimated based on field and laboratory test results. The summary of the material parameters for landslide simulation is tabulated in Table 1.

Results and Discussion

Results of Deformation Pattern and Shear Strain Pattern

Figure 6 shows the results numerical analysis of deformation pattern at the end (i.e., 2015/7/6) in the case IV ($\dot{\alpha} = 0.00089$, $n = 53.398$). The red dot line shows the result of a maximum deformation pattern of each node at the end of the numerical simulation with compare to without the deformation (i.e., initial condition). The maximum deformation of 0.26921 m was obtained at node 199 (i.e., S-1) on 2015/7/6 (i.e., at the end) from the analysis results of deformation pattern of numerical simulation for the case IV ($\dot{\alpha} = 0.00089$, $n = 53.398$) (Fig. 6). Similarly, the

Fig. 6 Results of deformation pattern (Case IV)



maximum deformation of 0.26921, 0.26735 and 0.26683 m were obtained at the same node 199 (i.e., S-1) on 2015/7/6 (i.e., at the ends) based on the numerical analysis results of deformation pattern for the case I ($\dot{\alpha} = 0.000489$, $n = 46.49$), case II ($\dot{\alpha} = 0.00023$, $n = 55.833$) and case III ($\dot{\alpha} = 0.00111$, $n = 67.233$) respectively. From the comparative analysis of the simulation results of deformation pattern in the cases I–IV, it was found that the value of the deformation at node 199 is almost the same. Moreover, the maximum deformation was occurring at the same node 199, where the maximum displacement of the landslide body was recorded during field monitoring. Hence, any one case (method) among these four representative cases (i.e. I–IV) can be used to understand the deformation pattern of a creeping landslide induced by snow melt water in the future.

Similarly, Fig. 7 show the results of the shear strain pattern of numerical simulation at the end (i.e., 2015/7/6) in the case IV ($\dot{\alpha} = 0.00089$, $n = 53.398$). The value of the maximum shear strain of 0.93865 was obtained at S-1 (i.e., element 278) on 2015/7/6 (i.e., at the end) from the numerical analysis results in the case IV ($\dot{\alpha} = 0.00089$, $n = 53.398$) (Fig. 7). Similarly, the value of maximum shear strain of 0.92647, 0.91059 and 0.90419 were found at the same location point S-1 (i.e., element 278) on 2015/7/6 (i.e., at the end) based on the numerical simulation results of deformation pattern for the case I ($\dot{\alpha} = 0.000489$, $n = 46.49$), case II ($\dot{\alpha} = 0.00023$, $n = 55.833$) and case III ($\dot{\alpha} = 0.00111$, $n = 67.233$) respectively. Based on the comparative study of the simulation analysis results of shear

strain pattern in the cases I–IV, it was found that the maximum shear strain has exhibited on the sliding surface soils. Moreover, the results of overall shear strain trends of each case were found almost same. The maximum shear strain value is also almost same and occurred at the same element 278 (i.e., S1), where the maximum displacement rate of the landslide body was recorded during the field monitoring. Therefore, any one case (method) among the four representative cases (i.e., I–IV) can be apply to study the shear strain pattern of a slow-moving landslide induced by snow melt water in the future.

Results of Time Histories

Figure 8 shows the comparison of predicted time histories of displacement in model and measured displacement in the field. Here, the predicted time histories of displacement were measured at the same point S-1 (i.e., node 199), where the displacement was measured in the field. Moreover, the horizontal component of displacement was considered for predicting time histories of displacement in the model. In field monitoring, the measured time histories of horizontal displacement at S-1 has slightly increased from 2014/1/14 to 2014/2/14. After that, it was rapidly increased until 2014/4/29. Then, it has almost constant from 2014/4/29 to 2015/7/6. Similarly, the predicted time histories of horizontal displacement at S-1 has slightly increased from 2014/1/14 to 2014/2/17. After that, it has also rapidly

Fig. 7 Results of shear strain pattern (Case IV)

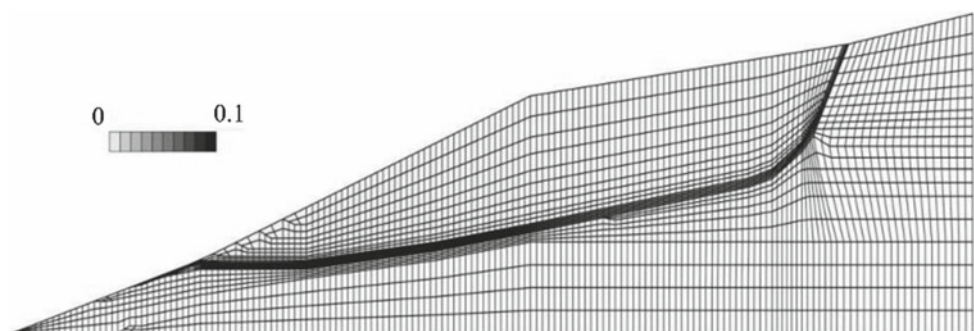
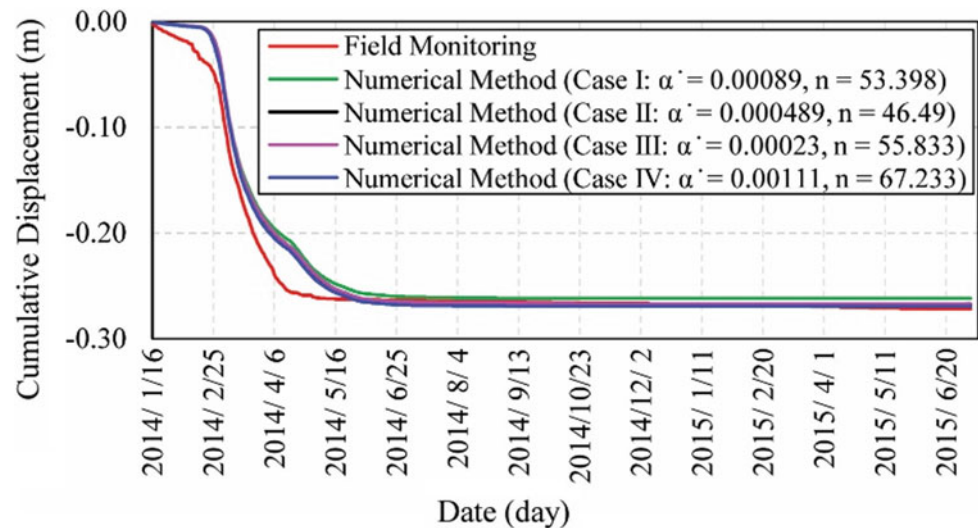


Fig. 8 Comparison of predicted and measured time histories of horizontal displacement at S-1



increased from 2014/2/18 to 2014/5/14. Then, it has also almost constant until 2015/7/6. The maximum horizontal displacement of 0.2717 m was recorded at the end of the field monitoring. Similarly, the maximum displacement of 0.2617, 0.2673, 0.2668, and 0.2692 m was obtained by the numerical method in the cases I–IV respectively. In numerical method, the results of maximum horizontal displacement at the same point (i.e., S-1) is almost same and they are also following the similar trends with respect to time. Therefore, any one case (method) among the four representative methods (i.e., cases I–IV) can be used to predict the horizontal displacement of a landslide body in the future.

Failure Mechanisms

The distribution of local factor of safety ($F_{s,local}$) in various location points along the slip surface during the maximum and the minimum displacement rate were checked for better understanding of the failure mechanisms along the slip surface. Figure 9 shows the location of different points (i.e., 1–12) where the distribution of local factor of safety ($F_{s,local}$) was observed during the maximum and minimum

displacement rate. The maximum displacement rate of 8.9586, 10.2385, 10.1426, and 9.4537 mm/day were noted at the S-1 on 2014/3/5 in the cases I–IV respectively, where the maximum raised in ground water level was also recorded on that day (Figs. 3 and 8).

Figure 10 shows the results of variation of the $F_{s,local}$ with different location points during maximum displacement rate in the cases I–IV. Similarly, the minimum displacement rate was found at the S-1 on 2014/3/5 in the cases I–IV, where the minimum raised in ground water level was also recorded on that day. The distribution of $F_{s,local}$ with different location points along the slip surface during the minimum displacement rate in the cases I–IV is presented in Fig. 11. It can thus be suggested that the change in mobilized shear stress along the slip surface due to ground water fluctuation has a major role in landslide displacement. In addition, when the mobilized shear stress along the slip surface is increased, the $F_{s,local}$ will be decreased and vice versa (Figs. 9 and 10). In the other word, the failure mechanism of a creeping landslide is strongly dependent on shear stress mobilized along the slip surface due to the change in ground water level. The previous researchers (e.g., Ter-Stepanian 1963; Patton 1984; Picarelli et al. 2004; Eberhardt et al. 2007, etc.) have also agreed on it.

Fig. 9 Location of the observed point for measuring $F_{s,local}$



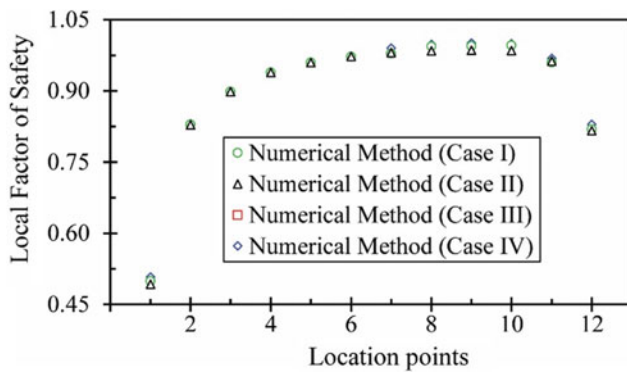


Fig. 10 Distribution of $F_{s,local}$ along the slip surface during the maximum displacement rate

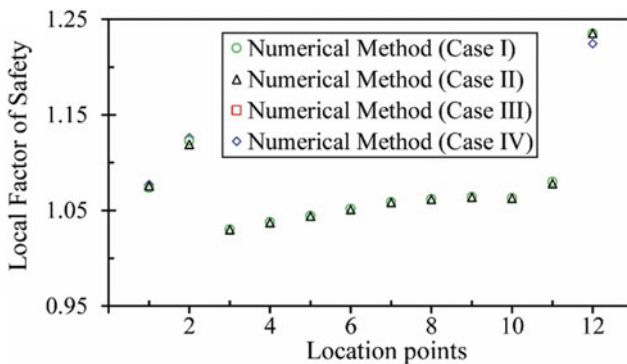


Fig. 11 Distribution of $F_{s,local}$ along the slip surface during the minimum displacement rate

Conclusions

The creeping behaviour of Tomuro landslide induced by snow melt water has been studied using the 2D-Elastoviscoplastic constitutive model. The numerical simulation results of deformation pattern and shear strain pattern have been presented to evaluate the creeping behaviour of clayey soils along the sliding surface of Tomuro landslide owing to groundwater level fluctuations by snow melt water. The results of predicted and measured time histories of horizontal displacement at S-1 has been compared and found in good agreements with each other. It is understood that the mobilized shear stress along the slip surface due to the change in groundwater level fluctuations has played a major role for movement of a creeping landslide. It is believed that this study will be useful to understand the creeping behaviour of a landslide induced by snow melt water in the future and at the same time, long-term monitoring and management of such landslide induced by the snow melt water will be much easier.

Acknowledgements This work has been supported by JSPS KAKENHI Grant Number 16F16354. The authors would like to acknowledge Mr. Yoshihiko EGUCHI and Mr. Haruo SEKI, Nihon Survey Co. Ltd., and Yuuichi UENO, Nittoc Construction Co. Ltd. for providing the field investigation data and supports during the field visit. The authors are also grateful to Nakanajo Public Works Office and Sediment Control Division of Gunma Prefectural Government for their support and cooperation.

References

- Bhat DR, Bhandary NP, Yatabe R, Tiwari RC (2011) Residual-state creep test in modified torsional ring shear machine: methods and implications. *Int J Geotech Const Mater Environ* 1(1):39–43
- Bhat DR, Bhandary NP, Yatabe R, Tiwari RC (2012) A new concept of residual-state creep test to understand the creeping behavior of Claye soils. *Geotech Spec Publ* 225:683–692
- Bhat DR, Bhandary NP, Yatabe R (2013) Residual-state creep behavior of typical clayey soils. *Nat Hazards* 69(3):2161–2178
- Bhat DR, Bhandary NP, Yatabe R (2014a) Creeping displacement behavior of clayey soil in a new creep test apparatus. *Geotech Spec Publ* 236:275–285
- Bhat DR, Bhandary NP, Yatabe R (2014b) Residual-state creep behavior of clayey soils and its implication in landslide displacement prediction. In: *Proceedings of the international symposium geohazards: science, engineering and management, Nepal*, pp 212–223
- Bhat DR, Yatabe R (2016) A regression model for residual state creep failure. In: *Proceedings of the 18th international conference on soil mechanics and geotechnical engineering, USA*, pp 707–711
- Bhat DR, Wakai A, Kotani K (2017a) A finite element approach to understand the creeping behaviour of large-scale landslides. In: *Proceedings of the 19th international summer symposium, Japan*, pp 9–10
- Bhat DR, Wakai A, Kotani K (2017b) New numerical approach to understand the creeping behavior of landslides and its implication. In: *Proceedings of the 14th Japan Kanto chapter conference on Japanese geotechnical society, Japan*, pp 234–237
- Bhat DR, Wakai A, Kotani K (2018) A comparative study of two newly developed numerical models to understand the creeping behaviour of landslides. In: *Proceedings of the 20th international summer symposium, Japan*, pp 101–102
- Bhat D, Wakai A (2019) Numerical simulation of a creeping landslide induced by a snow melt water. *Tech J* 1(1):71–78
- Bhat DR, Wakai A, Kotani K (2019) Numerical modelling of a creeping landslide using the finite element method: a case study. *Geotech Spec Publ* 1(6):Act3-005
- Calvello M, Cascini L, Sorbino G (2008) A numerical procedure for predicting rainfall-induced movements of active landslides along pre-existing slip surfaces. *Int J Numer Anal Meth Geomech* 32:327–351
- Conte E, Donato A, Troncone A (2014) A finite element approach for the analysis of active slow-moving landslides. *Landslides* 11(4):723–731
- Eberhardt E, Bonzanigo L, Loew S (2007) Long-term investigation of a deep-seated creeping landslide in crystalline rock. Part II. Mitigation measures and numerical modelling of deep drainage at Campo Vallemaggia. *Can Geotech J* 44(10):1181–1199
- Fernández-Merodo JA, García-Davalillo JC, Herrera G, Mira P, Pastor M (2014) 2D viscoplastic finite element modelling of slow landslides: the Portalet case study (Spain). *Landslides* 11(1):29–42

- Huvaj N, Maghsoudloo A (2013) Finite element modeling of displacement behavior of a slow-moving landslide. *Geo-Congress 2013*:670–679
- Ishii Y, Ota K, Kuraoka S, Tsunaki R (2012) Evaluation of slope stability by finite element method using observed displacement of landslide. *Landslides* 9(3):335–348
- Matsuura S, Okamoto T, Asano S, Osawa H, Tatsuya ST (2017) Influences of the snow cover on landslide displacement in winter period: a case study in a heavy snowfall area of Japan. *Environ Earth Sci* 76(10):1–10
- Matsuura S, Asano S, Okamoto T, Matsuyama K, Takeuchi Y (2003) Characteristics of the displacement of a landslide with shallow sliding surface in a heavy snow district of Japan. *Eng Geol* 69:15–35
- Patton FD (1984) Groundwater pressure and stability analyses of landslides. In: *Proceedings of the 4th international symposium on landslides, Canada*, pp 43–60
- Picarelli L, Urciuoli G, Russo C (2004) Effect of groundwater regime on the behaviour of clayey slopes. *Can Geotech J* 41(3):467–484
- Savage WZ, Chleborad AF (1982) A model for creeping flow in landslides. *Bull Assoc Eng Geol* 19(4):333–338
- Ter-Stepanian G (1963) On the long-term stability of slopes. *Nor Geotech Inst* 52:1–14
- Terzaghi K (1950) Mechanism of landslide. In: *Application of geology to engineering practice. Berkeley Volume*, Geological Society of America, pp 83–123
- Wakai A, Bhat DR, Kotani K, Osawa S (2019) Finite element modelling of a creeping landslide induced by snowmelt groundwater. In: *Proceedings of the of the 4th regional symposium on landslides, Bosnia and Herzegovina*, pp 53–57



Numerical Simulation of Debris Flows After Ash Fall at Mt. Fuji

Takashi Kitazume, Takahiro Abe, and Satoshi Goto

Abstract

Mt. Fuji is the largest polygenetic volcano in the Japanese archipelago. Its last eruption was Hoei in 1707. Since it has been dormant for over 300 years, not only people live near Mt. Fuji, but the area supports many economic activities in Japan. Because volcanic eruptions are accompanied by sediment movements, debris flow occurs due to heavy rainfall after ash fall, snow-melting volcanic mud flow, etc. Debris flow occurs frequently and intensively when ash has accumulated. Herein we simulate debris flows caused by rainfall after an eruption with ash fall using a method that combines Cellular Automaton (CA) and Multi Agent (MA) Systems. The CA/MA method can realize high-speed calculations because large-scale simultaneous equations do not need to be solved and the results can be easily imaged. Although local rules must be set experimentally and calibrated, the CA/MA method can easily reflect knowledge and experiences of experts such as geologists, geomorphologists, and geotechnical engineers.

Keywords

Mt. Fuji • Debris flow • Numerical simulation • Cellular automaton • Multi agent system

Introduction

Mt. Fuji is the largest polygenetic volcano in the Japanese archipelago. Its last eruption was Hoei in 1707. Since it has been dormant for over 300 years, not only people live near Mt. Fuji, but the area supports many economic activities in Japan.

Against this background, the “Emergency mitigation measures sabo plan for volcanic eruption of Mt. Fuji” was issued in March 2018 to respond to various disasters associated with the eruption of Mt. Fuji. This plan assumes hazards based on the deformation of ground and terrain during and after the eruption of Mt. Fuji. Hazards include pyroclastic flows, lava flows, debris flows after ash fall, and snow-melting volcanic mudflows.

Because debris flow occurs frequently and intensively when volcanic ash is deposited, herein we simulate debris flows caused by rainfall after volcanic eruptions with ash fall.

Numerical Analysis Method

For debris flow simulation after ash fall, a lightweight and high-speed simulation tool based on the Cellular Automaton (CA) and Multi Agent (MA) systems were used (Kitazume et al. 2018; Nishimura et al. 2018; Abe et al. 2019). In CA, the analysis region is divided into regularly arranged spatial grids (cells), where each cell has an arbitrary environment or state in step s . The state quantity of step $s + 1$ is sequentially determined by considering the interaction with the state

T. Kitazume (✉)
Civil Engineering Division, Tokyo Electric Power Services Co.,
Ltd., 9F KDX Toyosu Grandsquare 1-7-12, Shinonome, Koto-ku,
Tokyo 135-0062, Japan
e-mail: dkita@tepsc.co.jp

T. Abe
UNIC Co., Ltd., Numerical Analysis Division, 3-5-18, Komaba,
Meguro-ku, Tokyo 153-0041, Japan
e-mail: abe@unic-co.co.jp

S. Goto
Department of Civil Engineering, University of Yamanashi,
Takeda 4-3-11, Kofu, Yamanashi 400-8511, Japan
e-mail: goto@yamanashi.ac.jp

quantity of the adjacent cell (also referred to as a local rule). The changes in the environment and the entire analysis area are expressed because all cells change synchronously. Cells are represented as a digital elevation model generated from LiDAR data, etc., and debris flow simulation methods using this model have been widely used (Scheidl and Rickenmann 2011; Han et al. 2017). On the other hand, the MA system arranges multiple elements called “agents” that recognize and act on the environment or state. Agents perform actions that affect each other. The environment and state are expressed as the sum of complex phenomena.

In this study, the simulations use the following local rules:

- (1) The cell is a square, and the state change in the attention cell (i, j) is determined from the relationship between the state of the cell and eight neighbor cells (Fig. 1). Each cell contains elevation information for the base surface.
- (2) Agents are water and sediment (ash fall).
- (3) For each agent, the minimum gradient at which the flow starts is given as a parameter. Agents move to a neighbor cell when the gradient between the cell of interest and the neighbor cell exceeds the minimum flow gradient.
- (4) The minimum flow gradient of the sediment agent decreases as the water agent amount in the same cell increases.
- (5) The distribution amount of the flow destination to each adjacent cell is determined by the ratio of the gradient between the cells.
- (6) The debris flow may cross a ridge at the momentum of the flow. Then the amount corresponding to the kinetic energy is introduced to express its straightness (inertia).

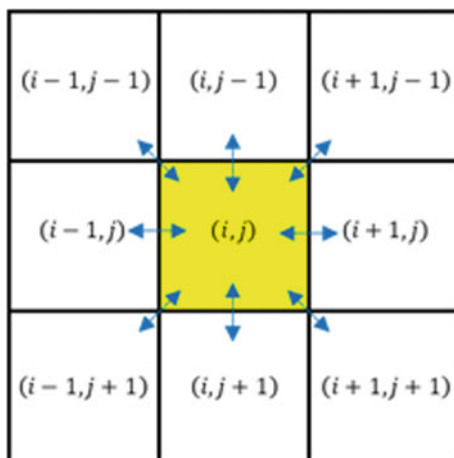


Fig. 1 Attention cell and neighbor cells in the CA method

- (7) The analysis ends when the movement of each agent disappears in all cells. It is also possible to end at the specified step.

The calculation results based on this method are verified by comparing the actual sediment flow caused by heavy rainfall in Aso-Saishigahana region (Fig. 2, Seki et al. 2020 publication decision).

Analysis Model and Analysis Conditions

Analysis Model

The analysis area is about 45 km in the east–west direction and about 55 km in the north–south direction of Mt. Fuji (Fig. 3). A digital elevation model (10-m mesh) was downloaded from the Geographical Survey Institute’s basic map information site (accessed: 2019.08.13).

Figure 4 shows the analysis model. It consists of 990,000 square cells measuring 50 m \times 50 m (900 in the east–west direction and 1,100 in the north–south direction).

Analysis Conditions

Table 1 shows the list of cases considered as well as their conditions and parameters. Cases 1–4 consider a summit eruption with different levels of rainfall and minimum flow gradients. Cases A–D consider four hillside eruptions.

Figures 3 and 5 show the ash fall and deposition conditions. Two patterns are assumed. One is a summit eruption and the other considers a hillside eruption. The basement is set as the initial surface thickness where outflow may occur.

- (1) For the summit eruptions, a concentric surface thickness distribution with a depth of 1.5 m at the summit and a depth of 0.0 m at an elevation of 2,200 m, is assumed. The total sediment volume is approximately 17.2 million m^3 .
- (2) For the hillside eruptions, the concentric surface thickness distribution has a depth of 0.5 m at the center of each crater and a depth of 0.0 m at a radius of 3.0 km. The total sediment volume is about 4.7 million m^3 .

The simulations considered two rain conditions (total rainfall 500 mm and total rainfall 1,000 mm) and three minimum flow gradient of sediment (ash fall) (30° , 40° , and 50°).

Figure 6 shows the flow characteristics of the agents defined by the volume ratio of water to sediment. The behaviours of sediment and water agents are modeled as the following three categories.

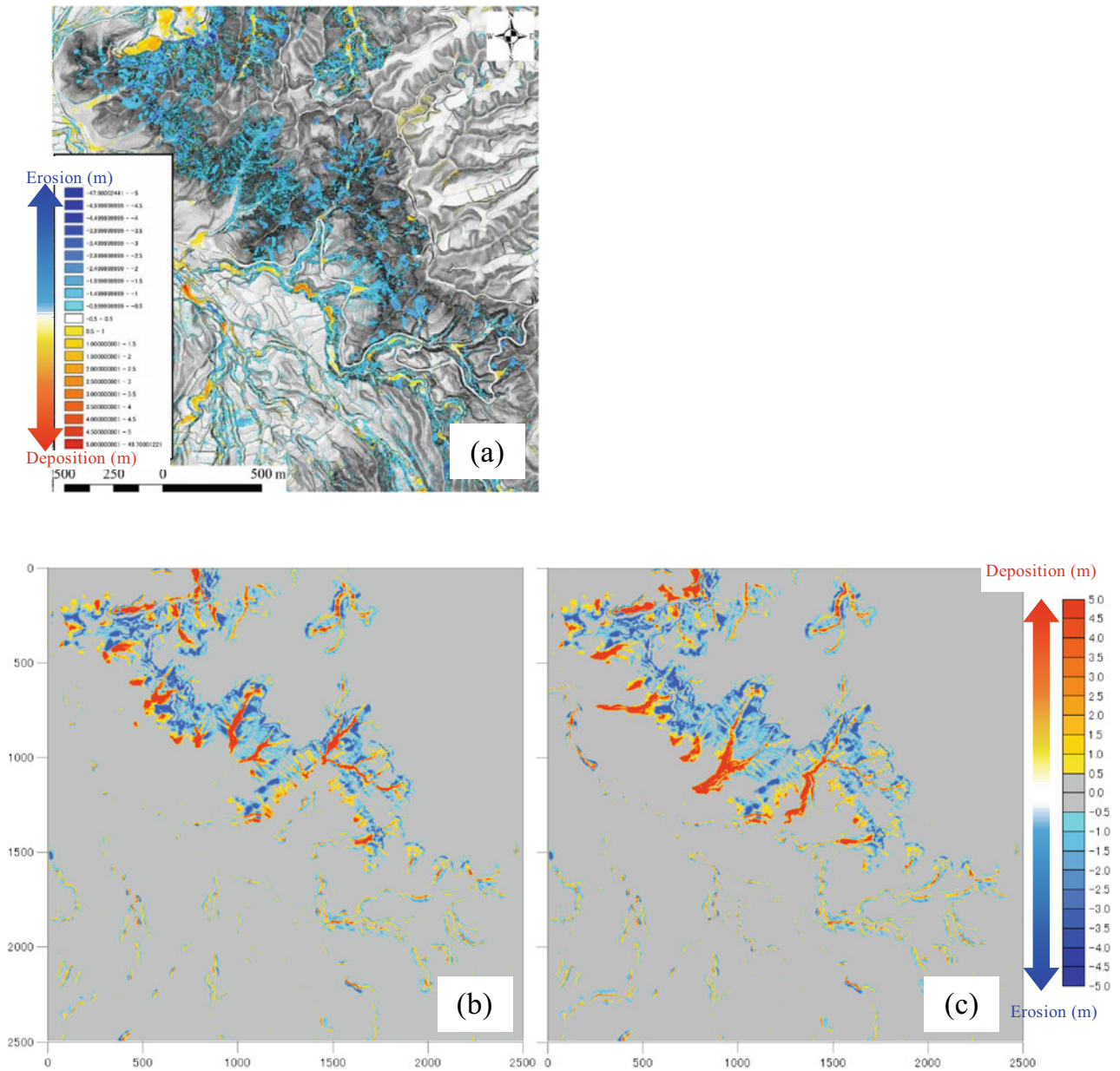


Fig. 2 Comparison of observed deposition/erosion areas and calculated deposition/erosion areas (Seki et al. 2020 publication decision). Aso-Saishigahana where the sediment flow occurred due to heavy rainfall, July 2012. **a** Observed deposition/erosion areas. Elevation

difference value obtained by LiDAR-DEM acquired in 2010 and 2013. **b** Calculated deposition/erosion areas at 50 steps when the rain ended. **c** Calculated deposition/erosion areas at 350 steps where sediment flow stopped

- (1) When V_r is 0 to V_{rlim} , sediment and water agents flow according to the same minimum flow gradient θ_{s0} .
- (2) When V_r is from V_{rlim} to V_{r2} , each agent flows according to its minimum flow gradient.
- (3) When V_r is larger than V_{r2} , each agent flows according to θ_{wmin} .

All cases are analysed for 1000 steps.

Analysis Results

The flow conditions shown in each figure span a range with a sediment thickness of 10 cm or more.

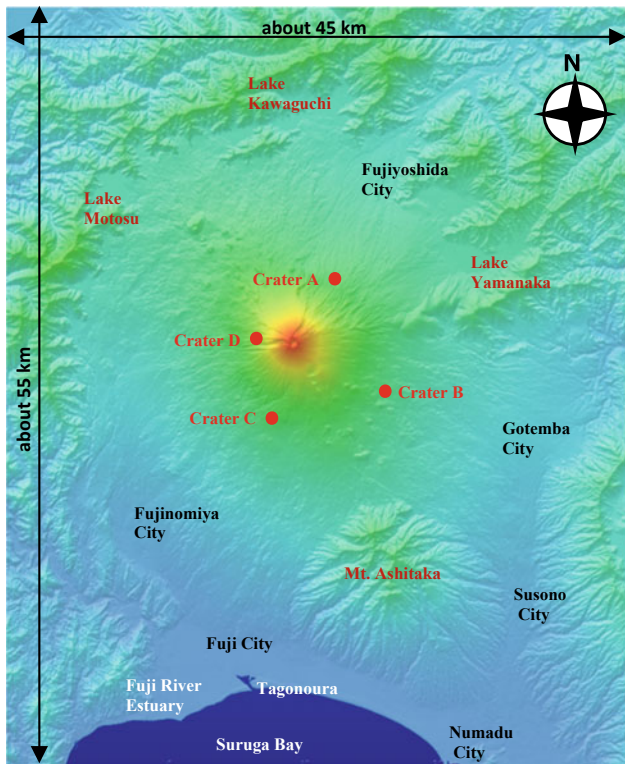
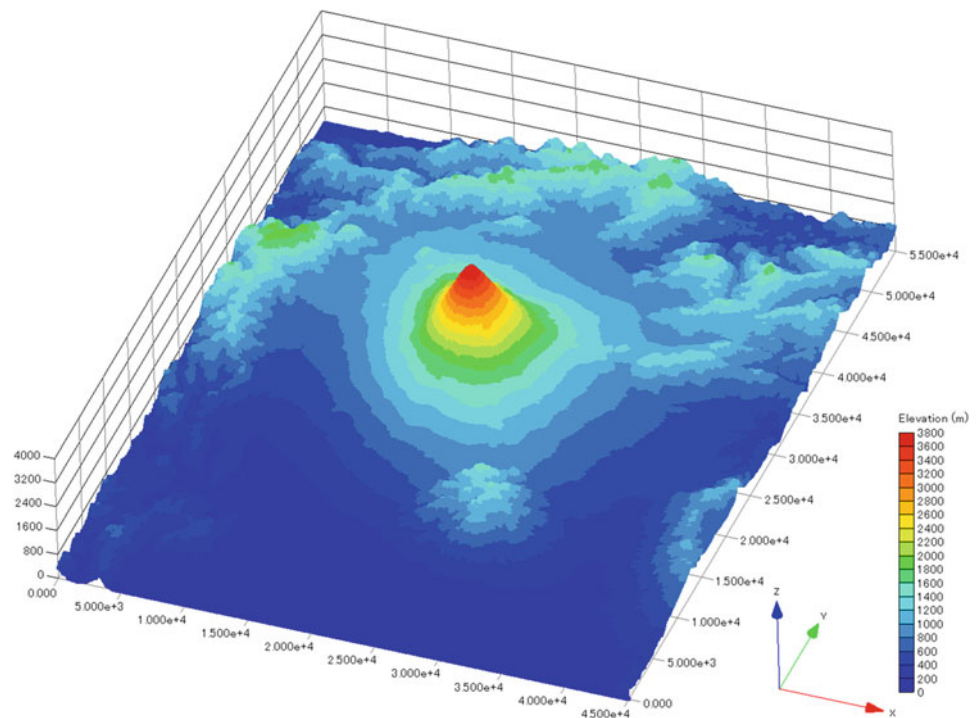


Fig. 3 Analysis area. Add the place name and assuming four craters to the display by Geographical Survey Institute Geographic Map Viewer

Fig. 4 Three-dimensional display of the analysis model. Elevation display is by 50 m × 50 m cell



Summit Eruption

Case 1: In the simulation, part of the ash fall accumulated on the summit flows out (Fig. 7). Sediment more than 10-cm thick reaches all areas except for Lake Motosu and Mt. Ashitaka, which are located on the northwest and southeast side of the summit, respectively. The sediment reaches Fujiyoshida City, Gotemba City → Susono City → Numadu City, Fujinomiya City → Fuji City.

Case 2: Most of the ash fall accumulated on the summit flows out (Fig. 8). During the flow process, more than 1.5 m of sediment is re-deposited on the hillside, especially on Osawa River and Tempo Crater. Sediment more than 10-cm thick reaches all areas except Lake Motosu and Mt. Ashitaka, which are located on the northwest and southeast side of the summit, respectively. Sediment reaches Fujiyoshida City, Gotemba City → Susono City → Numadu City, Fujinomiya City → Fuji City.

Case 3: The rate of ash fall deposited on the summit increases (Fig. 9). Because the amount of sediment deposited on the mountainside during the flow process is small, the amount of sediment that reaches urban areas does not change much.

Case 4: Because the rainfall increases compared to Case 1, most of the ash fall that accumulates on the summit flows out (Fig. 10). Although the reach is similar

Table 1 Analysis case

Case no	Assumed crater	Total rainfall (mm)	Minimum flow gradient (°)
1	Summit	500	40
2	Summit	500	30
3	Summit	500	50
4	Summit	1000	40
A–D	Hillside A, B, C, and D	1000	40

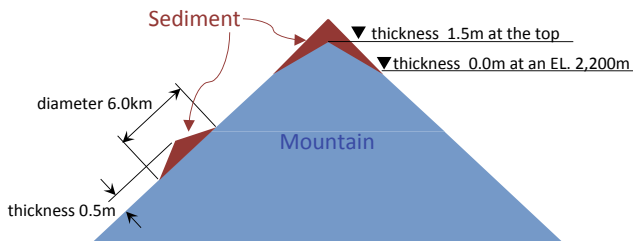


Fig. 5 Initial surface thickness of sediment with the potential for outflow

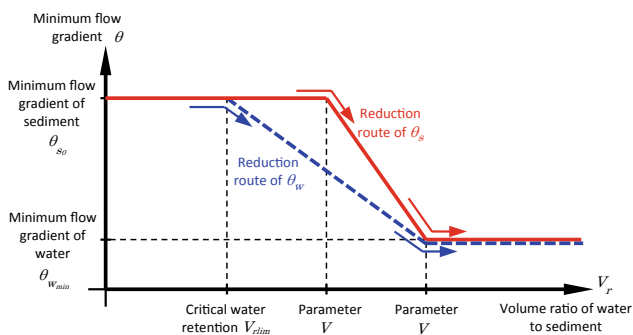


Fig. 6 Flow characteristics of the agents

to Case 1, the amount of sediment flowing into each urban area increases.

Four Hillside Eruptions

Crater A: The sediment flows into Fujiyoshida City and Lake Yamanaka (Fig. 11).

Crater B: Sediment flow reaches to Gotemba City and eventually Susono City and Numadu City. However, sediment flow to Lake Yamanaka does not occur because the ridge on the northeast side of the crater cannot be passed (Fig. 12).

Crater C: Sediment flow reaches Fujinomiya City, Fuji City, and Tagonoura, and eventually flows out to Suruga Bay (Fig. 13). Sediment does not flow east due to the mountain. Inflow to the Fuji River is very limited.

Crater D: Sediment flow reaches Fujinomiya City, Fuji City, and Tagonoura. It eventually flows out to Suruga Bay (Fig. 14). The amount of sediment flowing into the Fuji River is relatively large.

The CA/MA method can provide high-speed calculations because large-scale simultaneous equations do not need to be solved. Hence, the analysis results can be easily visualized. Although local rules must be set experimentally and calibrated, experiences of experts such as geologists, geomorphologists, and geotechnical engineers can be easily reflected.

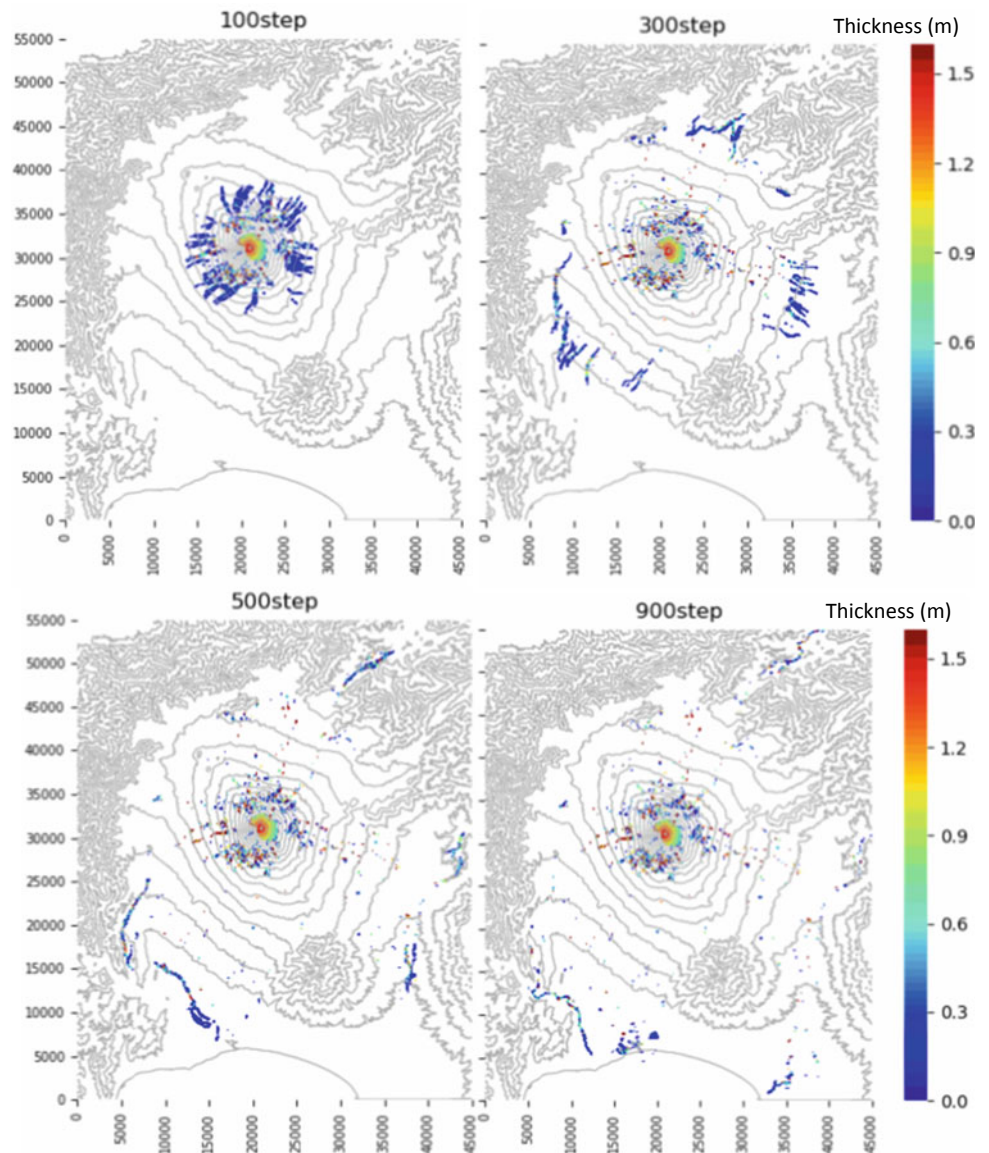
Furthermore, an animation can reveal the change of a complicated situation. For example, at locations where sediment is deposited, the flow temporarily stops, but resumes due to continuous rainfall.

Tasks and Future Plans

The above results are based on specific assumptions such as the location of craters, amount of ash (sediment) that erupts, amount of rainfall, and local rules governing sediment flow. Therefore, the simulations may differ from the actual situation of sediment flow. By performing simulations under highly accurate eruption scenarios that reflect expert knowledge such as volcanology, the reliability of analysis and evaluation will increase.

The CA/MA simulation tool used in this report is applied to a pre-analysis-type hazard map arrangement according to different eruption scenarios. In this analysis, a computer with OS: Windows Server 2016 Standard, CPU: Intel Xeon Gold 6143 CPU @ 2.80 GHz, Memory: 1.13 TB was used. The calculation time to solve a model with 990,000 cells in 1,000 steps was about 50 min per case. In addition, about an hour was required to combine the movie output.

Fig. 7 Sediment flow in Case1 (steps 100, 300, 500 and 900)



The calculation time depends on the number of cells and number of steps. However, to more precisely grasp the state of the sediment flow, the cell size must be reduced while increasing the number of cells. This will increase the calculation time. On the other hand, the CA/MA method does not require matrix calculations because it is an explicit method. Hence, parallel processing is easy, which will significantly reduce the calculation time.

In the future, it will be possible to refine the parameter settings in the CA/MA method to reduce the calculation time by accumulating survey and analysis examples (teacher data) of actual sediment transport phenomena and machine learning. Hence, utilizing this high-speed analysis method, we aim to calculate and evaluate the movement of debris in real time during a heavy rain forecast using a preset model and parameters for each cell.

Fig. 8 Sediment flow in Case2 (steps 100, 300, 500 and 900)

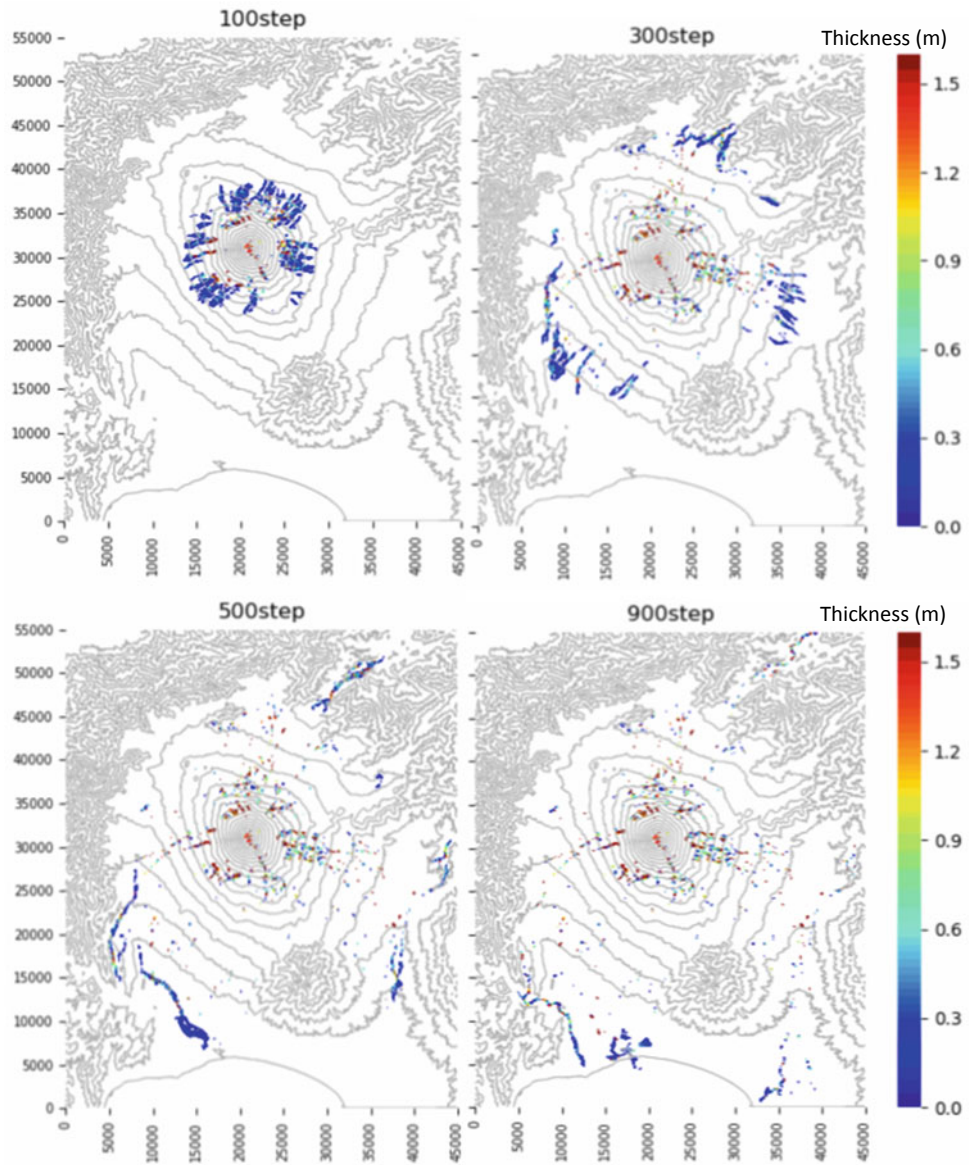


Fig. 9 Sediment flow in Case3 (steps 100, 300, 500 and 900)

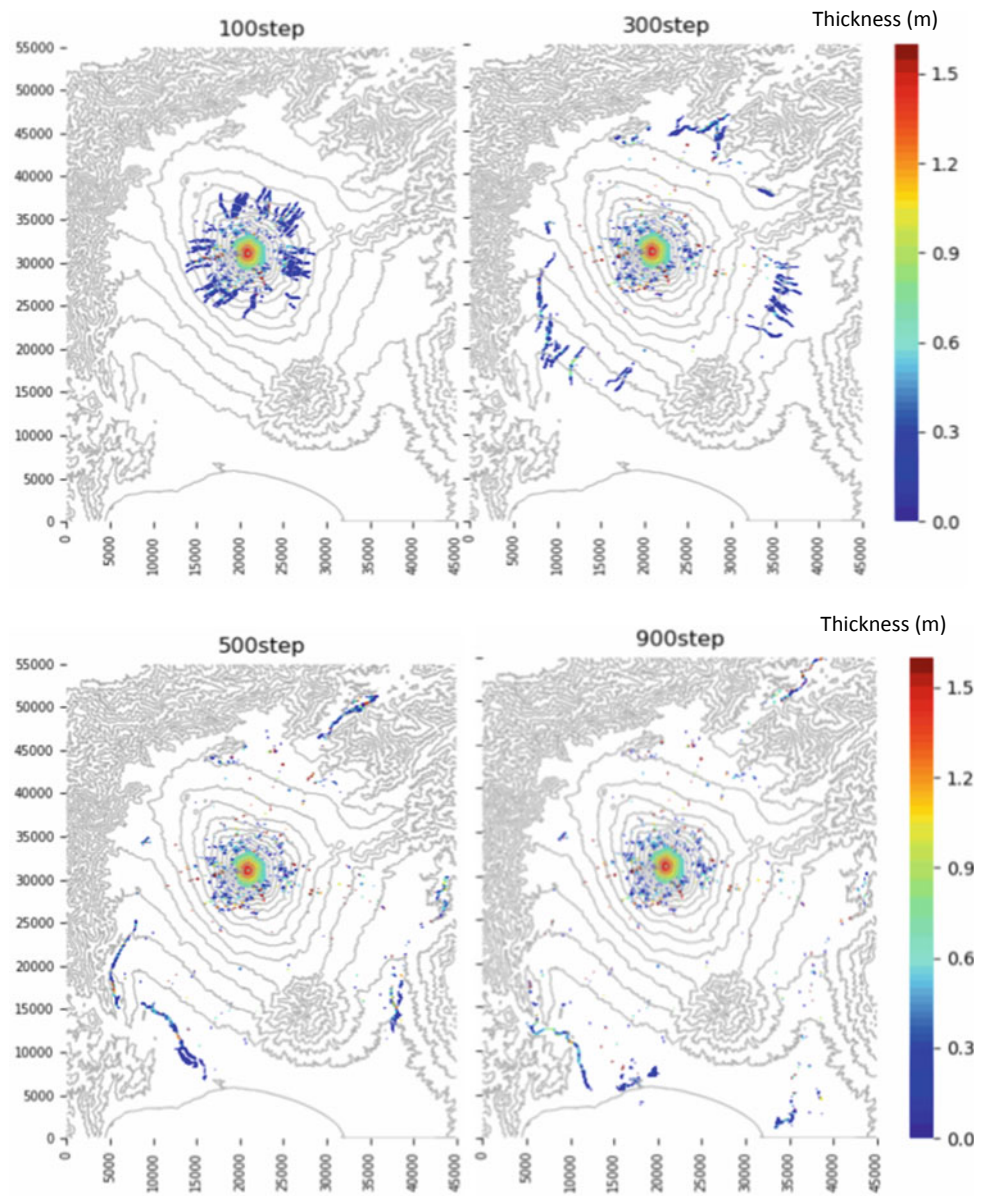


Fig. 10 Sediment flow in Case4 (steps 100, 300, 500 and 900)

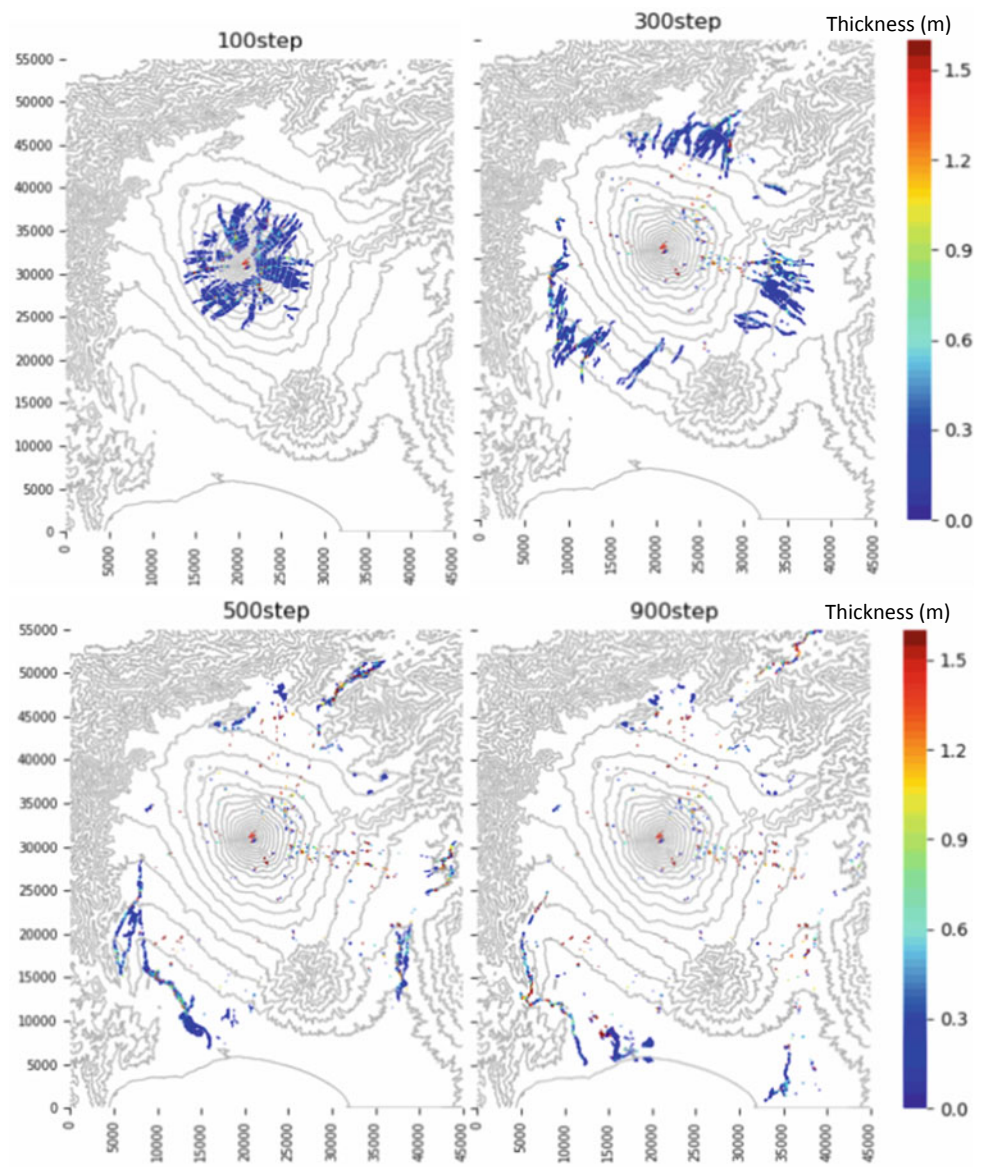


Fig. 11 Sediment flow in Case-A (steps 50 and 450)

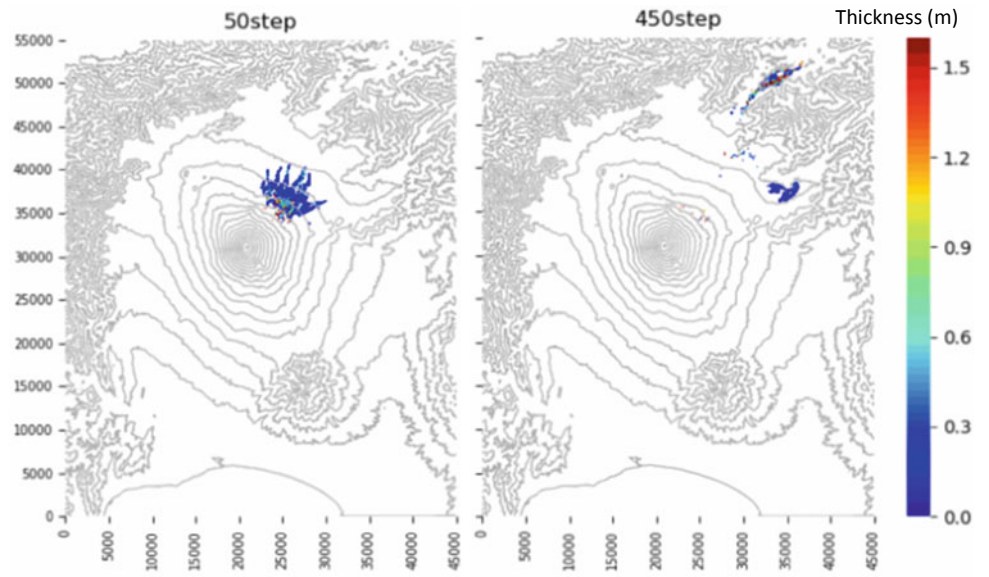


Fig. 12 Sediment flow in Case-B (steps 50 and 450)

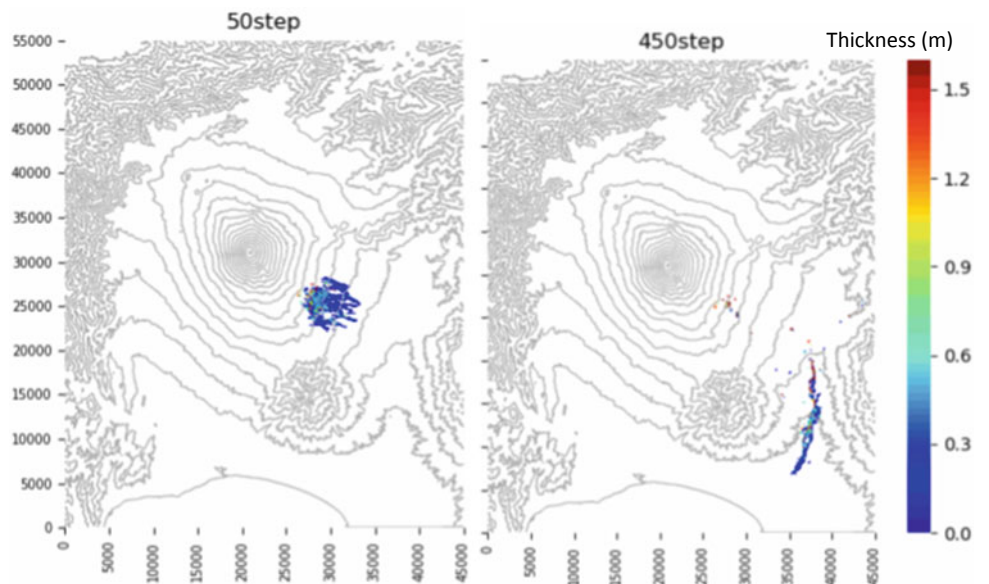


Fig. 13 Sediment flow in Case-C (steps 50 and 450)

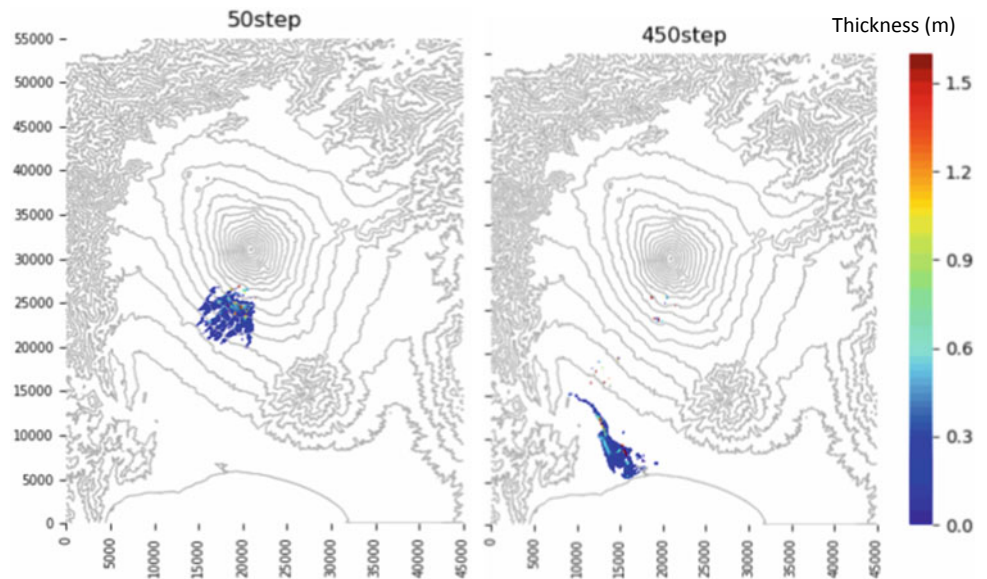
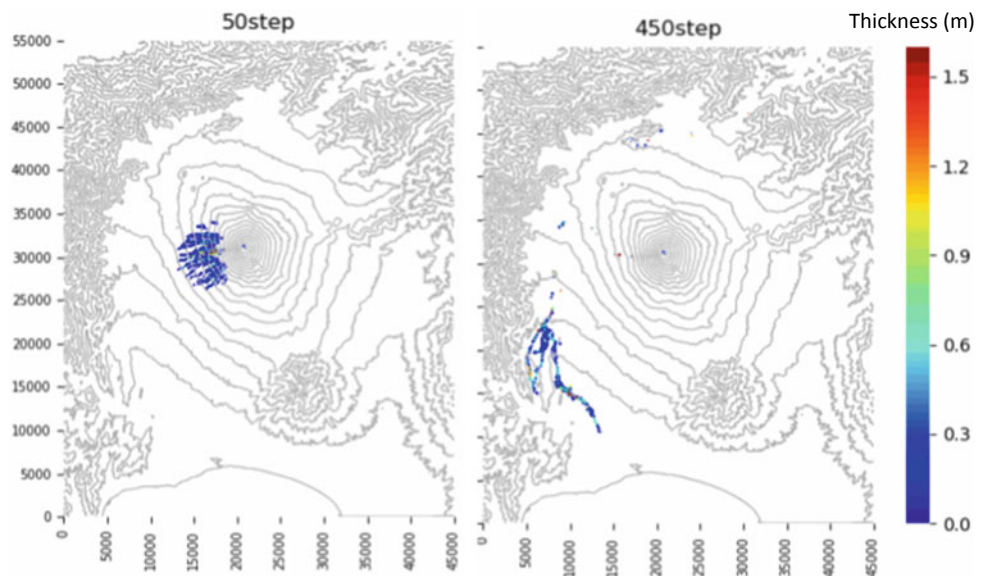


Fig. 14 Sediment flow in Case-D (steps 50 and 450)



Acknowledgements This study was partly supported by JSPS KAKENHI (Grant Number JP17H03303). We would like to express our acknowledgments to the members concerned. The authors also extend gratitude to anonymous reviewers for providing insightful comments.

References

- Abe T, Nishimura S, Kitazume T, Sato K, Endo S, Goto S (2019) Extension of debris flow simulation tool by MA/CA method (No. 1). In: Proceedings of 74th Japan society of civil engineers symposium, pp 3–470 (in Japanese)
- Geographical Survey Institute's basic map information site. <https://fgd.gsi.go.jp/download/menu.php>. Last accessed 13 Aug 2019
- Han Z, Li Y, Huang J, Chen G, Linrong Xu, Tang C, Zhang H, Shang Y (2017) Numerical simulation for run-out extent of debris flows using an improved cellular automaton model. *Bull Eng Geol Environ* 76:961–974
- Kitazume T, Nishimura S, Abe T, Sato K, Goto S (2018) Development of tool for debris flow simulation (No. 1). In: Proceedings of 57th the Japan landslide society symposium, pp 69–70 (in Japanese)
- Ministry of Land, Infrastructure, Transport and Tourism Chubu Regional Development Bureau Fuji Sabo Office, Yamanashi Prefectural Maintenance Department Sabo Section, Shizuoka Prefectural Transportation Infrastructure Department Sabo Section (2018) Emergency mitigation measures sabo plan for volcanic eruption of Mt. Fuji (in Japanese)

- Nishimura S, Abe T, Kitazume T, Sato K, Goto S (2018) Development of tool for debris flow simulation (No. 2). In: Proceedings of 57th the Japan landslide society symposium, pp 71–72 (in Japanese)
- Scheidl C, Rickenmann D (2011) TopFlowDF—a simple gis based model to simulate debris-flow runout on the fan. *Ital J Eng Geol Environ* 030:253–261
- Seki Y, Endo S, Sato K, Kitazume T, Abe T, Nishimura S, Goto S (2020 publication decision) Numerical simulation of sediment flow due to rainfall using CA/MA method. In: Proceedings of 55th Japanese geotechnical society symposium (in Japanese)



2020 Kyoto Japan

On the Progression of Slope Failures Using Inverse Velocity of Surface Movements in an Undercut Slope Model

Thirapong Pipatpongsa, Krit Aroonwattanaskul, and Kun Fang

Abstract

The undercutting method applied together with the cut-and-fill technique has been realized through open-pit coal mining. To predict the time of slope failure, a method of forecasting slope failure time by the inverse velocity of slope surface proposed by Fukuzono (1985 in A new method for predicting the failure time of a slope. Japan Landslide Society, Japan, pp. 145–150) is employed in practice. However, the characteristics of slope movements in undercut slopes are different from those of typical slopes due to arch action across the pit; therefore, more investigations are required to examine whether this method can be effectively used to predict the failure time for an undercut slope. In this study, the undercut slope failure prediction technique following this approach was examined via geotechnical centrifuge modelling. The movement distributions of the slope surface were recorded by a high-speed VDO camera and analysed by the image processing software. This study confirms that the inverse of the average surface velocity is qualitatively valid for a centrifuge model of undercut slope.

Keywords

Physical model • Monitoring • Undercut slope

Introduction

Slope instabilities involve excessive surface movements caused by several factors, e.g. gravity, geological activity, hydrological influence and sequence of excavation. These factors affect different movement configurations and modes of failure. To predict the time of slope failure, a method of forecasting slope failure time by the inverse velocity of slope surface proposed by Fukuzono (1985) is practically employed.

Fukuzono (1985) proposed the monitoring method for predicting the onset of slope failure using straight line or curves drawn by the inverse of the surface velocity crossing the axis of time. The monitoring of the changes of surface displacement in large-scale rainfall-induced slope failure has been carried out in various base conditions including flat and convex. Based on the experimental results, the relation of acceleration and velocity of surface displacement was built. With the transformation of the equation, the relation between inverse number of velocity ($1/v$) and time (t) were demonstrated.

In fact, Fukuzono's method was based on Saito and Uezawa (1961)'s assumption proposing that the increment of the logarithm of creep rupture is proportional to the logarithm of strain rate. Herein, the method proposed by Fukuzono is related to tertiary creep stage since slope failure occurs at the final stage of tertiary creep in the process of time to failure.

Consequently, the inverse numbers of the velocity of surface displacement with respect to time are appeared in linear line or convex/concave curve. The failure time of slope can be estimated by the point at which the tangential line of the curve/line crosses the axis of time.

Fukuzono's original work still has many unclear points such as type of physical model, triggering mode, measurement procedures, and mode of failure. Moreover, Fukuzono's approach had been developed based on typical slopes using observation points in downward movement, not

T. Pipatpongsa (✉)

Department of Urban Management, Kyoto University, C1-2-236, Katsura Campus, Kyoto, 15-8540, Japan
e-mail: pipatpongsa.thirapong.4s@kyoto-u.ac.jp

K. Aroonwattanaskul

Penta-Ocean Construction Co., Ltd., 2-2-8, Koraku, Bunkyo-ku, 112-8576, Tokyo, Japan
e-mail: aroonwattanaskul.krit@gmail.com

K. Fang

Faculty of Engineering, China University of Geosciences, No. 388 Lumo Road, Wuhan, 430074, China
e-mail: 331758475@qq.com

undercut slopes using observation areas with surface movement in various directions. The characteristics of slope movements in undercut slopes are different from those of typical slopes due to arch action across the pit; therefore, more investigations are required to examine whether this method can be used to predict the onset of failure.

The undercutting method together with the cut-and-fill technique has been realized through open-pit coal mining (Pipatpongsa et al. 2013). Previous researchers have carried out some studies on deformation of undercut slope model and presented by displacement vectors (Khosravi et al. 2011). This measurement might not be effective enough to track the onset of slope failure because displacement vectors show only accumulative movements at each time interval of snap shot before the failure. The undercut slope failure prediction technique following Fukuzono’s approach has been examined by using 1G physical model (Minamide et al. 2019). Comparisons between undercut slope models with and without shear pin reinforcement confirmed that the inverse velocity approach is effective for forecasting the time of undercut slope failure under the suitable conditions of resolution setting.

However, the inverse velocity approach for predicting the time of slope failure time of an undercut slope using geotechnical centrifuge modelling has not been adequately reported. Hence, this study (Aroonwattanaskul et al. 2019) performed at Geotechnical Centrifuge Centre of Disaster Prevention Research Institute (DPRI), Kyoto University aims to examine the reliability of the failure time prediction for centrifuge model of an undercut slope.

moist Edosaki sand and a Teflon sheet by fitting a piece of the Teflon sheet in the lower part of the shear box.

Three specimens were prepared with a diameter and height of 50 and 100 mm to conduct the unconfined compression test. The average of these three values is selected as the unconfined compressive strength (σ_c) of moist Edosaki sand in the slope model. The model was divided into two parts as shown in Fig. 1, the basal support, and slope part; each of which was compacted to the bulk unit weight $\gamma = 15.3 \text{ kN/m}^3$. Basal support was placed on a rigid plane covered by sandpaper while the slope part was inclined by the angle 40° on a rigid plane covered by a Teflon sheet for simulating the low friction interface plane.

After the preparation of basal support and slope part, the trapezoidal trench was excavated through the basal support as shown in Fig. 2. Finally, the marking lines were drawn on the surface every 5 cm from bottom of the slope part for clear observations. A high-speed VDO camera was installed above the model to observe the movements of an undercut slope as shown in Fig. 3.

Justification on Low-Frictional Interface

A case study of the Mae Moh open-pit coal mine in Thailand is considered in this study. The presence of some weak and thin clay seams in the under burden of coal seams and claystone layers becomes a significant problem because of their extremely low strength causing some slope instability in Mae Moh open-pit mine. These clay seams have the

Materials and Methods

Materials Properties

The physical models were made of Edosaki sand. Basic properties of Edosaki sand are shown in Table 1. The internal friction angle of the compacted sand was tested by a direct shear apparatus. Also, the direct shear apparatus was used to measure the interface friction angle and the apparent adhesion between

Table 1 Basic properties of Edosaki sand

Parameter	Value
Water content (w)	10%
Bulk unit weight (γ)	15.3 kN/m^3
Unconfined compressive strength (σ_c)	14.7 kN/m^2
Interface friction angle (ϕ_i)	17.5°
Apparent adhesion (c_i)	0 kN/m^2
Internal friction angle (ϕ)	40.9°

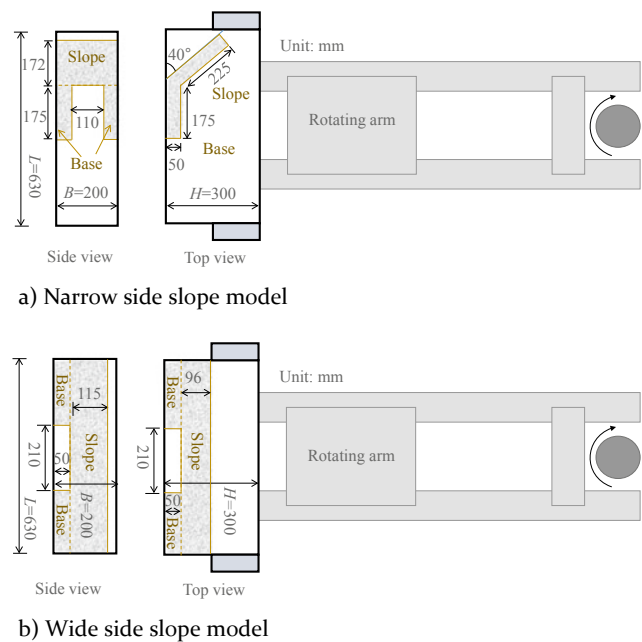


Fig. 1 Slope model configuration and dimensions

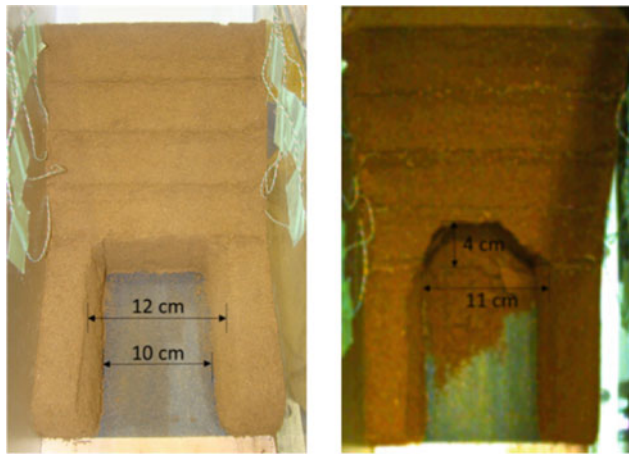


Fig. 2 Physical model of undercut slope (left) and mode of failure (right)

potential to slip when the toe of the slope is excavated while the portion of slope above the excavated pit has the potential to fail if the excavated span reaches its maximum span because of sufficient basal supports.

Due to the aforementioned problem, the potential sliding surface is made of a Teflon sheet so that a low-frictional interface can be simulated in the physical model. The interface friction between sand and a Teflon sheet ($\phi_i = 17.5^\circ$) is much less than the internal friction of sand ($\phi = 40.9^\circ$); therefore, this interface can be considered as a thin weak layer of clay seams underlying a sliding layer.

Experimental Setup

The physical models of an undercut slope, narrow side slope model, and wide side slope model, were conducted. The schematic illustrations of the model slopes are shown in Fig. 1a as a narrow side slope model and Fig. 1b as a wide side slope model. Dimensions of the physical models are listed in Table 2. During the test, the centrifugal acceleration was gradually increased until 50 g while monitoring the initial collapse of the model. The movement distributions of the slope surface were recorded through a high-speed VDO camera and analysed by using the image processing software “Flow Expert 2D”. This software shows the result in the form of velocity vectors of instantaneous velocity. However, the limitation of this software is only a 2D analysis. Therefore, the deformation along the depth direction and the displacement of soil mass inside the surface cannot be observed. Figure 3 shows the schematic of a high-speed

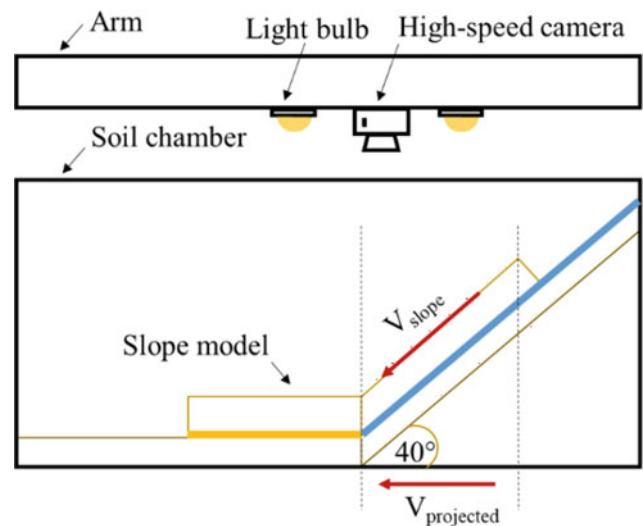


Fig. 3 Schematic of a high-speed VDO camera installation

Table 2 Dimensions of the physical model

Dimensions of model	Narrow side slope	Wide side slope
Slope width (cm)	20	63
Slope length (cm)	22.5	15
Slope thickness (cm)	5	5
Slope angle (°)	40	40
Pillar width (cm)	5	21.5
Pillar length (cm)	17.5	5
Pillar thickness (cm)	5	5
Top trench width (cm)	12	22
Base trench width (cm)	10	20
Average undercut width (cm)	11	21

VDO camera installation and lighting system for an undercut slope model.

A high-speed VDO camera fixed to the arm of the centrifuge and not perpendicular to the slope surface in a narrow side slope model. Therefore, the dimension of the slope surface needs to adjust in the calibration process of image processing software by substituting 76.6 mm as a projected length instead of 100 mm as a real length. The results were primarily in the form of instantaneous projected velocity $V_{projected}$ and were converted to the instantaneous slope surface velocity $V_{slope} = V_{projected} / \cos 40^\circ$. For a wide side slope model, using a similar procedure with a different

Table 3 Summary of various parameter setting

Parameter	Value
FPS (frame per second)	500
1/FPS (second per frame)	0.002
Frame interval (frame)	60
Grid interval-x direction (mm)	10
Grid interval-y direction (mm)	10

corrected value in the calibration process. The procedure of velocity acquisition and the different methods to find the suitable setting parameters in velocity analysis are described in details by Fang (2019). Brief setting parameters are listed in Table 3. The resolution used in the image processing was 512×512 pixels.

Results

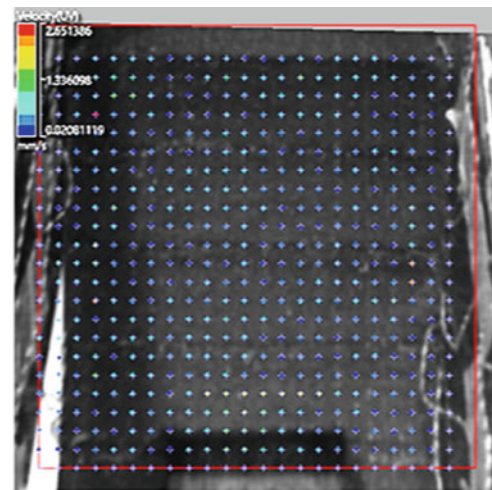
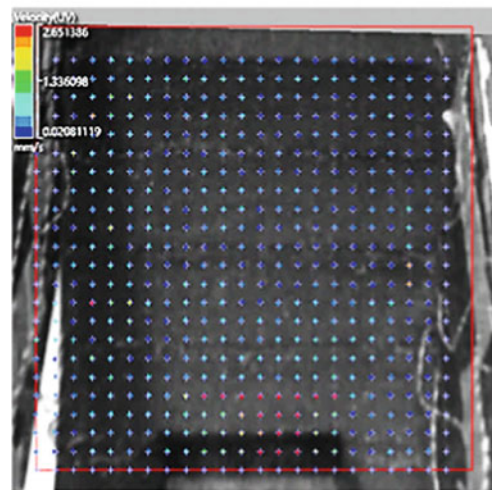
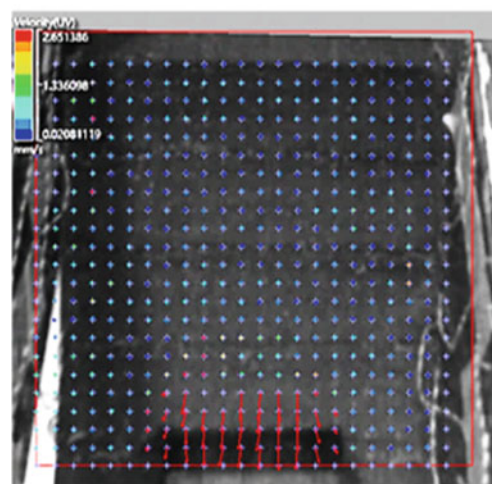
Characteristics of Velocity Vectors

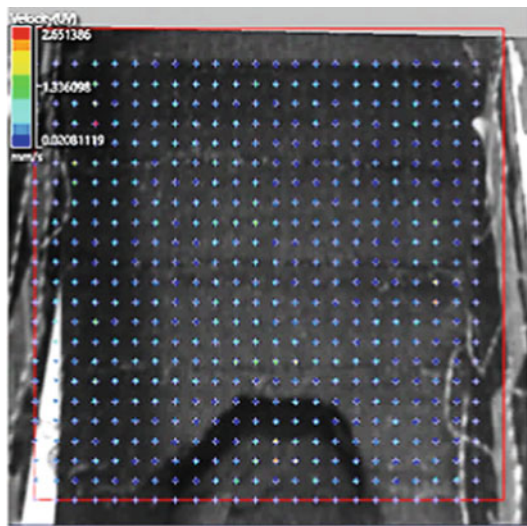
In the process of velocity acquisition, the displacement vector of each grid point in the selected monitoring area, the interrogation window can be searched at different times. Searching for the correlation coefficient is operated by shifting sub-domain in the search window for every 1 pixel and the highest correlation coefficient can be found, which represents the position of the grid point. Therefore, the velocity of each grid point can be calculated from the obtained displacement and the time frame interval using the check area and the exploration area.

Results of image processing software in the narrow side slope model are shown in Fig. 4 from the initial movement until the slope failure occurred. Confining supports restrict the model from lateral movements, resulting in a symmetrically downward movement. The increasing velocity vectors started from the central part of the slope above the excavated area of basal support (Fig. 4a, b) and spread to the adjacent part until reaching the excavated width (Fig. 4c). After 0.39 s, the arch-formed crack completely detached from the stable scarp (Fig. 4d).

The stability of the scarp could be explained by arch action. The arching failure in undercut slope involves progressive failure of stacks of arch. The velocity vectors at the central part are straight downward with similar magnitude as rigid body motion. However, the magnitude of velocity vectors near the corner of the pillars is a little lower than the central part of the slope due to the load transfer to the basal supports.

The characteristics of displacement vectors which show the accumulative movements of the slope part is different

(a) Velocity vectors before failure ($t=t_0$)(b) Velocity vectors before failure ($t=t_0+0.05$ s)(c) Velocity vectors before failure ($t=t_0+0.09$ s)**Fig. 4** Velocity vectors in a narrow side slope model



(d) Velocity vectors after failure ($t=t_0+0.39$ s)

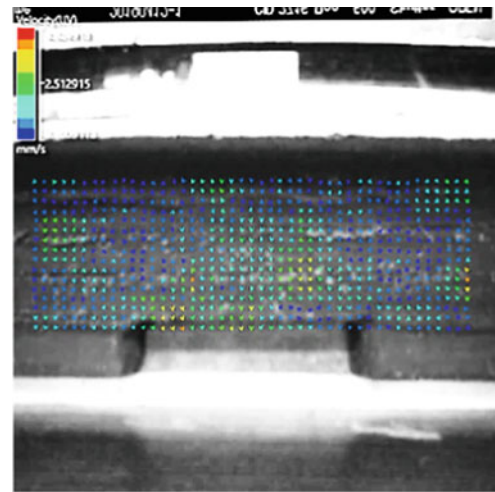
Fig. 4 (continued)

from the velocity vectors by showing the maximum displacement at the centre of the slope. Herein, lateral displacement vectors moved to approach to the centre as reported in Khosravi et al. (2011). Velocity vectors in a wide side slope model with an average undercut width 21 cm and reproduced test showed a similar movement characteristic as illustrated in Figs. 5a–d and 6a–d, respectively.

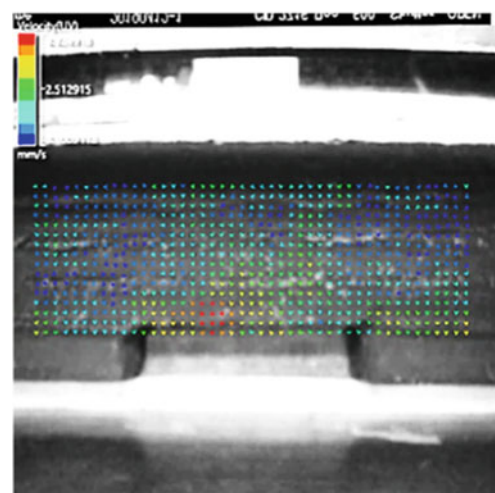
Predicted Failure Time of Undercut Slope Model

The inverse of the average surface velocity in the narrow side slope model is plotted with time as shown in Fig. 7. The fluctuation of inverse of the average surface velocity is uneven; however, there is a portion where the downward sloping straight line can be observed and nearly reduced to zero when the slope failure occurred. The red dotted line shows the slope of inverse velocity curve while the black dotted line shows the experimental failure time of a slope at which the detached part moved from the remaining part with the clearly visible crack width around 2–3 mm observed by the naked eye. Due to the limitation in observation, the actual failure can occur earlier than this observed time.

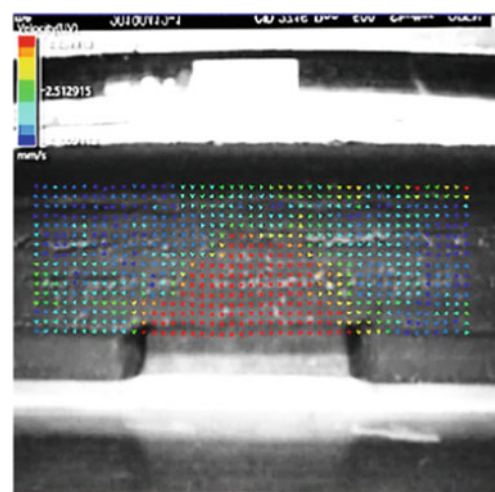
The predicted failure time is determined by drawing an extended straight-line correlating with the gradient of inverse velocity crossing the axis of time. The result revealed that the predicted failure time in this experiment was far from actual failure time. The predicted failure time under the narrow side slope (11 cm in model), the first wide side slope (21 cm in model) and the second wide slope are listed in Table 4. The difference in prediction appeared in a narrow



(a) Velocity vectors before failure ($t=t_0$)

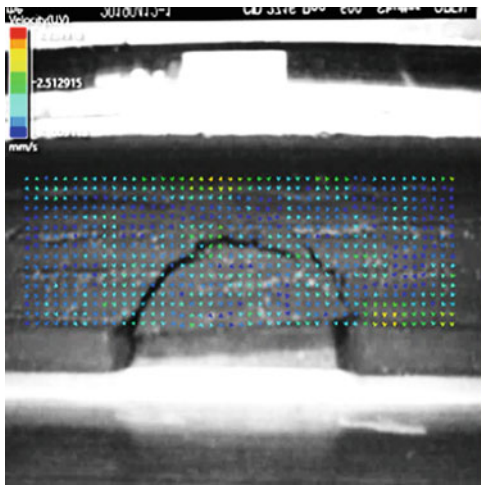


(b) Velocity vectors before failure ($t=t_0+0.01$ s)



(c) Velocity vectors before failure ($t=t_0+0.03$ s)

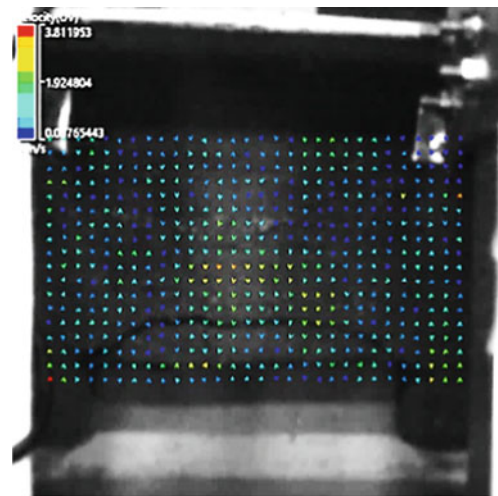
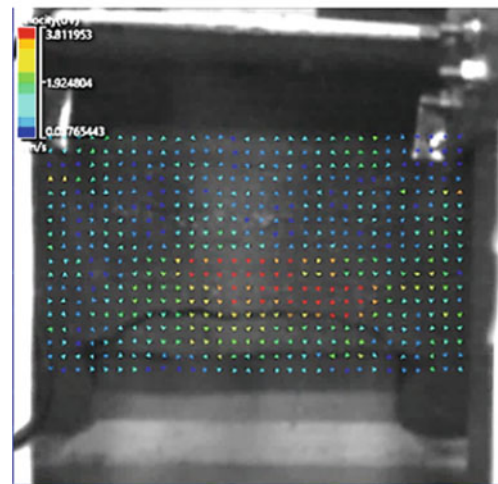
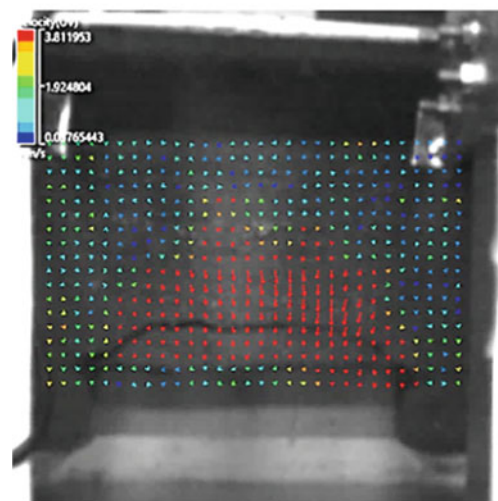
Fig. 5 Velocity vectors in a wide side slope model

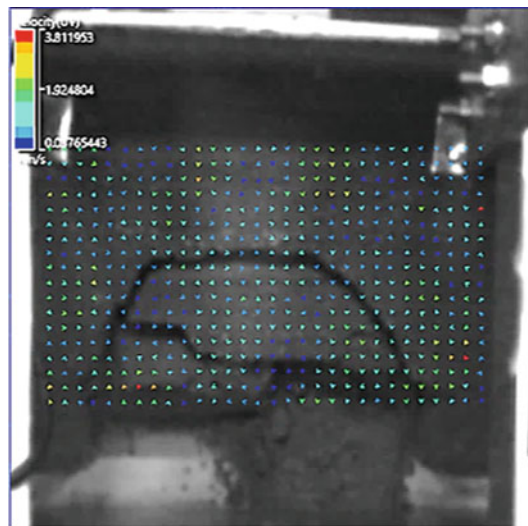
(d) Velocity vectors after failure ($t=t_0+0.25$ s)**Fig. 5** (continued)

range between 0.11 ± 0.01 s (model) or 3.45 ± 0.31 s (prototype) indicates the sufficiently precise prediction. If the initiation of cracks can be determined by more accurate method such as particular image processing technique, the predicted failure time would be relatively close to the experimental failure time. Therefore, Fukuzono's method could be effectively used to predict the failure time of an undercut slope in the centrifuge model test.

Monitoring Regions

The monitoring region is important for predicting failure time in an undercut slope. Four different regions were selected to compare the predicted failure time as shown in Fig. 8a–d. The sizes of the monitoring regions are listed in Table 5 for both model and prototype scales using the similitude. A scaling (model/prototype) law $1/N$ is applied to a length where $N = 31.4$ represents the centrifugal acceleration relative to the gravitational acceleration at failure. Hence, the area in prototype is $N^2 = 986$ times that of the model. As a similitude velocity scale ratio is 1, the centrifugal acceleration does not affect the inverse velocity but crack widths 2–3 mm (model) representing 62–94 mm (prototype) might enlarge the discrepancy in prediction. The predicted failure time shown in Fig. 9 indicated that the inverse of the average surface velocity for predicting the failure times determined for all types of monitoring region were comparatively parallel to one near the onset of failure; thus, they are all good for prediction. But that of the total area was higher; thus its offset predicts the time closer to the actual failure time at 0.48 s (model) or 15.1 s (prototype) judged by the definition of failure initiation used in this study.

(a) Velocity vectors before failure ($t=t_0$)(b) Velocity vectors before failure ($t=t_0+0.02$ s)(c) Velocity vectors before failure ($t=t_0+0.04$ s)**Fig. 6** Velocity vectors of the reproduced test in a wide side slope model



(d) Velocity vectors after failure ($t=t_o+0.42$ s)

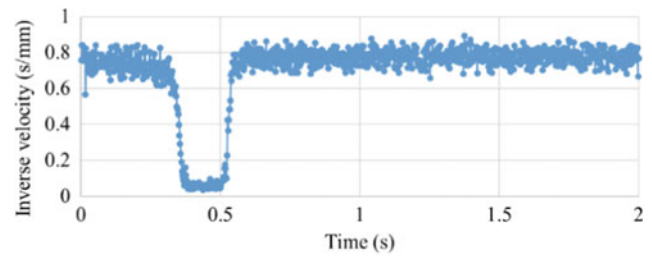
Fig. 6 (continued)

Table 4 Comparisons between the predicted time of failure and the experimental failure time

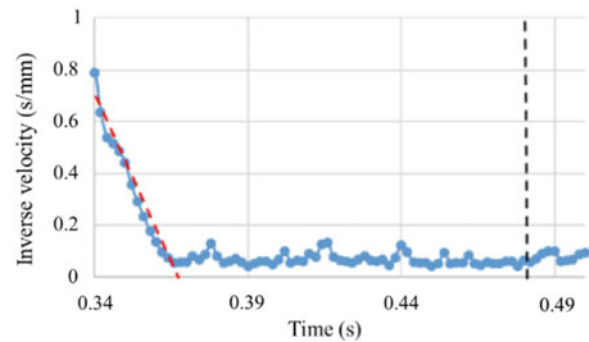
Type	Narrow side slope	Wide side slope	Wide side slope
Prediction (s)	0.37	0.40	0.74
Experiment (s)	0.48	0.52	0.84
Difference (s)	0.11	0.12	0.10
Average	Model scale: 0.11 ± 0.01 s Prototype scale: 3.45 ± 0.31 s (at 31.4 g)		

Discussion

The judgement indicating that the total area was the best monitoring region is depended on definition of the actual failure; thus, the conclusion would be different if the



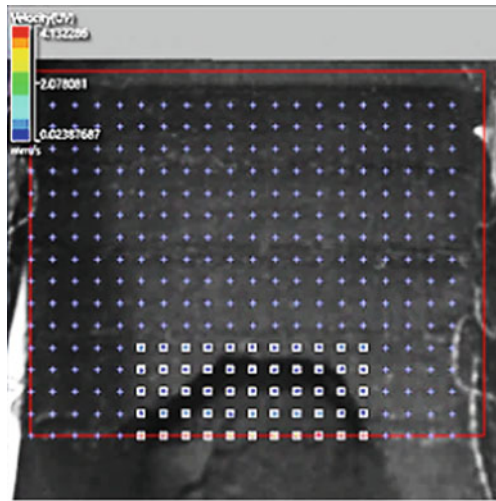
(a) Inverse of the average surface velocity



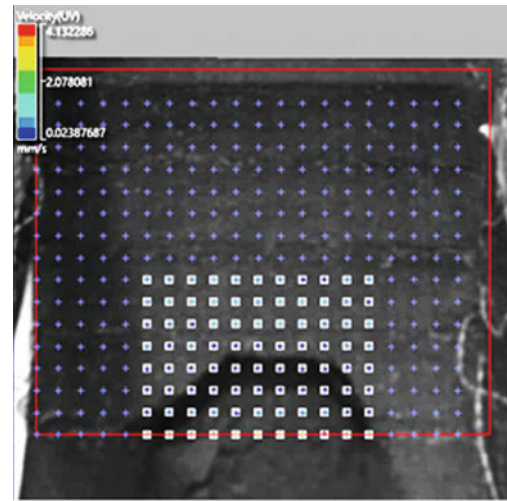
(b) The predicted time of failure

Fig. 7 Portion of inverse of the average surface velocity

definition of failure was changed by including local failure initiation or the failure observation technique was improved. In practical application, the primary instrument for monitoring longitudinal deformations is the inclinometer. So, the velocity can be determined by the relationship between slope displacement and time, following the method of failure time prediction from the inverse of the velocity. But, it is difficult to cover the total area of slope for monitoring slope movement in the actual site. After conducted many undercut slope experiments, the failures were found to be normally occurred only above the excavated part until reaching the undercut width. Therefore, the monitoring region at the site can be focused on this area.



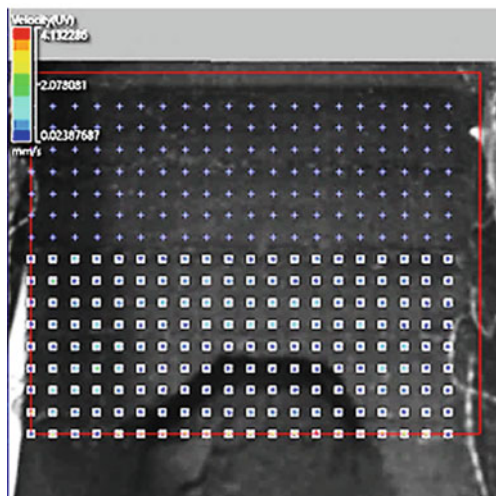
(a) Failure area



(d) Area over the pit



(b) Total area



(c) Half area

Fig. 8 (continued)

Table 5 Sizes and areas of monitoring regions in the model scale and the prototype scale using the scaling law determined by a scale factor $N = 31.4$

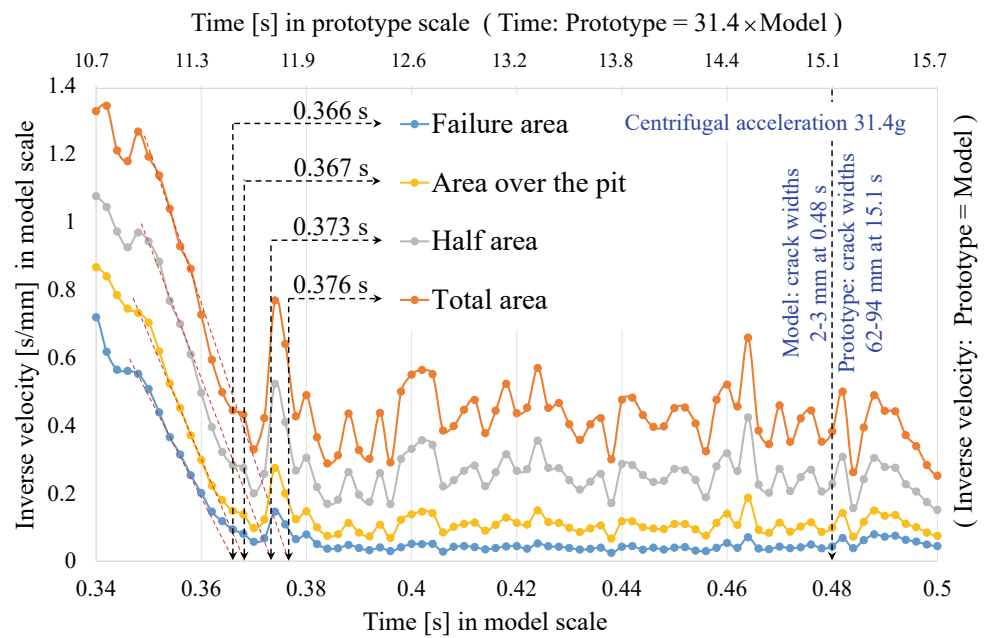
Monitoring regions	Model scale (width × length)	Prototype scale (failed at 31.4 g) (m ²)
Failure area	11 cm × 5 cm	5.42
Total area	20 cm × 22.5 cm	44.37
Half area	20 cm × 10 cm	19.72
Area over the pit	11 cm × 10 cm	10.84

Conclusion

The movements of the slope surface were recorded and analysed by the image processing software. The velocity vectors start to move downward with the same magnitude from the centre and expand to the adjacent part until reaching the excavated width. Although the velocity vectors were partially different in amounts and directions from the displacement vectors, both measurements show a similar tendency by which the onset of failure can be interpreted. In spite of inconsistency in the predicted results to the actual failure time, three centrifuge models can confirm that the inverse of the average surface velocity is qualitatively valid for an undercut slope model.

Fig. 8 Monitoring regions

Fig. 9 Comparison of suitable monitoring regions



Acknowledgements This work was financially supported by Electricity Generating Authority of Thailand (EGAT).

References

- Aroonwattanaskul K, Pipatpongsa T, Kitaoka T, Ohtsu H (2019) Surface movements of an undercut slope studied by centrifuge model. In: Proceedings of the 21st international summer symposium, JSCE, 3–4 Sept 2019. Japan Society of Civil Engineers, Japan, pp 41–42
- Fang K (2019) Progression and onset of undercut slope failure observed by surcharge velocity in physical models subjected to arch action. Doctoral thesis, Kyoto University, Japan
- Fukuzono T (1985) A new method for predicting the failure time of a slope. In: Proceedings of IV international conference and field workshop on landslides, 23–31 Aug 1985. Japan Landslide Society, Japan, pp 145–150
- Khosravi MH, Pipatpongsa T, Takahashi A, Takemura J (2011) Arch action over an excavated pit in a stable scarp investigated by physical model tests. *Soils Found* 51(4):723–735
- Minamide K, Kun F, Pipatpongsa T, Kitaoka T, Ohtsu H (2019) On the failure mechanisms of slope due to undercutting and reinforcement effects of slope stabilizing piles. *Jpn Geotech J* 14(1):31–41 (in Japanese)
- Pipatpongsa T, Khosravi MH, Takemura J (2013) Physical modeling of arch action in undercut slopes with actual engineering practice to Mae Moh open-pit mine of Thailand. In: Proceedings of the 18th international conference on soil mechanics and geotechnical engineering, vol 2, 2–5 Sept 2013. International Society for Soil Mechanics and Geotechnical Engineering, France, pp 943–946
- Saito M, Uezawa H (1961) Failure of soil due to creep. In: Proceedings of the 5th international conference on soil mechanics and foundation engineering, 17–22 July 1961. International Society for Soil Mechanics and Geotechnical Engineering, France, pp 315–318



2020 Kyoto Japan

Rainfall Boundary Condition in a Multiphase Material Point Method

Mario Martinelli, Wei-Lin Lee, Chjeng-Lun Shieh, and Sabatino Cuomo

Abstract

The Material Point Method (MPM) is an emerging computational tool to simulate the complex dynamic process of rainfall-induced landslide. In this field, hydraulic boundary conditions play an important role. In recent researches, the average relative velocity of pore water with respect to the solid skeleton is considered as Darcy's velocity usually. Hence, rainfall intensity (mm/h) can be assigned to the node of the mesh as a velocity boundary directly. However, the evolution of true velocities of liquid and solid phases has missed so far in the investigation of the landslide process. In order to keep the information of true velocities in the simulation, this paper provided a new solution to estimate the true velocity of the liquid phase at the node of the boundary layer and has been implemented a coupled hydro-mechanical model using MPM. The validation of such implementation was achieved by simulating a 1D infiltration problem and comparing with the MPM results with those obtained through the commercial software PLAXIS. With the help of this newly implemented boundary condition, rainfall-induced landslides can be better investigated using MPM.

Keywords

Material point method • Boundary condition • Rainfall • Landslide

Introduction

The Material Point Method (MPM) is a mesh-free method particularly suitable for simulating large deformation processes of history-dependent materials.

The original formulation of MPM was initially developed by Harlow (1964) for fluid mechanics and, then, it was applied to solid mechanics (Sulsky et al. 1994) and dry granular materials (Wieckowski et al. 1999; Wieckowski 2003). Later, the method was extended to handle saturated soils (Jassim et al. 2013) using the acceleration of both solid and liquid as primary unknowns (a_s - a_l formulation). MPM has been used to successfully simulate several geotechnical problems, such as cone penetration tests (Beuth and Vermeer 2013; Ceccato 2015; Ghasemi et al. 2019), close-ended and open-ended pile installation (Phuong et al. 2016; Galavi et al. 2019), collapse of dams (Alonso and Zabala 2011) and riverbanks (Bandara and Soga 2015). MPM is also particularly suitable for studying slope instability and rainfall-induced landslides (Cuomo et al. 2019a, b).

Rainfall-induced landslide is a complex physical dynamics process, which has to consider the hydro-mechanical response, such as the interactions of soil, pore water, and pore air. In this field, Yerro et al. (2015) proposed a three-phases dynamic formulation of MPM (soil, liquid, and air) using single layer of material point (1-point), where the total velocities of soil, liquid, and air are the primary unknowns. This formulation can capture evolution of gas pressures and it is particularly accurate in case of high suction, low degree of saturations and high derivative of the degree of saturation (Ceccato et al. 2019).

M. Martinelli
Deltares, P.O. Box 177 2600 MH Delft, The Netherlands
e-mail: mario.Martinelli@deltares.nl

W.-L. Lee · C.-L. Shieh
Department of Hydraulic and Ocean Engineering, National Cheng Kung University, n.1, University Road, Tainan City, 701, Taiwan
e-mail: glaciallife@gmail.com

C.-L. Shieh
e-mail: shieh@dprc.ncku.edu.tw

S. Cuomo (✉)
Department of Civil Engineering, University of Salerno,
84084 Fisciano, Italy
e-mail: scuomo@unisa.it

In many landslide applications, the gas can be assumed to flow freely in the soil matrix and the influence of gas pressure can be neglected (Touma and Vauclin, 1986). Under this hypothesis, Bandara et al. (2016) and Wang et al. (2016) proposed a simplified approach where the momentum balance of gas is neglected, and the gas pressure is assumed constant.

In Bandara et al. (2016) the primary unknowns are the absolute acceleration of the solid skeleton and the seepage velocity of the fluid in the solid matrix ($\mathbf{a}-\mathbf{w}$ formulation), whereas the relative acceleration of the liquid with respect to the solid skeleton is neglected. This framework is particularly suitable for boundary conditions written in terms of water pressures and in terms of seepage flow (or rainfall intensity).

Wang et al. (2016) propose a generalization of the original two-phase dynamic formulation of Jassim et al. (2013), which allows simulating the behaviour of partially saturated soils. However, this framework was only used when boundary conditions are expressed in terms of pore pressure (e.g. ponding condition), and not in terms of seepage flow (e.g. rainfall intensity). An application of this formulation for a landslide failure is shown in Lee et al. (2019).

The ideal case of “ponding” boundary condition can result in an extreme infiltration rate, which in some cases may be higher than the saturated soil permeability, and it may lead to over-conservative failure predictions, and in some cases different failure modes. Previous literature investigated the case of excessive amount of rainwater compared to soil infiltration capability resulting in ponding condition at ground surface and water runoff (Cuomo and Della Sala 2013). In order to properly simulate the effect of rainfall on the slope stability and the following run-out distances, a proper infiltration boundary condition must be used.

Using the formulation of Wang et al. (2016) as framework, this paper describes a generalized algorithm used to incorporate the rainfall boundary condition. The numerical scheme is then validated in the simple case of 1D condition, against a well-established commercial code (PLAXIS) used as benchmark.

MPM Formulation for Partially-Saturated Soils

Model Equations

In the simplified two-phase formulation (Wang et al. 2016), the governing equations for gas phase are neglected. The mass exchange of air and water between liquid and gas phase are also neglected and the air pressure is set to zero.

The media is divided in two phases (solid, liquid) and the corresponding phases (ph) are denoted by the subscripts of s and l , respectively. The subscript of m indicates the mixture.

The dynamic behaviour of the partially-saturated porous medium is described under the following general assumptions:

- isothermal condition,
- no mass exchange between solid and liquid,
- solid grains are incompressible,
- smooth distribution of porosity in the soil,
- small spatial variations of water mass.

The motion of the partially-saturated media is described by the system of two momentum balance equations (liquid phase and solid phase), using separate velocity fields, \mathbf{v}_l and \mathbf{v}_s for liquid and solid phase respectively:

$$\rho_l \mathbf{a}_l = \nabla p_l + \rho_l \mathbf{b} - \frac{n S_l \mu_l}{k_{rel} k_l} (\mathbf{v}_l - \mathbf{v}_s) \quad (1)$$

$$(1-n)\rho_s \mathbf{a}_s = \nabla \cdot (\boldsymbol{\sigma} - n S_l p_l \mathbf{I}) + (\rho_m - n S_l \rho_l) \mathbf{b} + \frac{n S_l \mu_l}{k_{rel} k_l} n S_l (\mathbf{v}_l - \mathbf{v}_s) \quad (2)$$

The vectors \mathbf{a}_l and \mathbf{a}_s are the acceleration of the liquid and solid phases, respectively; p_l is the liquid pressure, $\boldsymbol{\sigma}$ is the total stress tensor of the mixture and \mathbf{I} is unit stress tensor, μ_l is the dynamic viscosity of the liquid; k_l is the intrinsic permeability of the solid skeleton, and \mathbf{b} is the body force vector. The term k_{rel} is given by a relationship between the soil permeability and saturation, which is equal to 1 for a fully saturated soil and it decreases with the degree of saturation. However, in this study k_{rel} is set constant to 1.

The total volume (V) is summation of the volume of the solid phase (V_s) and the volume of the voids (V_{void}). The porosity is n and defines as V_{void}/V . The degree of saturation is S_l , whereas the volume of liquid (V_l) fills the volume of voids. According to Eq. (2), the seepage velocity (or Darcy's velocity) (\mathbf{w}) can be defined as $n S_l (\mathbf{v}_l - \mathbf{v}_s)$.

The mass balance equation for solid phase results as

$$\frac{\partial n}{\partial t} = (1-n) \nabla \cdot \mathbf{v}_s \quad (3)$$

Under the assumption of a barotropic liquid phase, the time derivative of the liquid density is only function of time derivative of the pore water pressure. For the partially saturated soil, the suction (s) is equal to $p_a - p_l$, where p_a is the air pressure which is set to zero.

The mass balance equation for liquid can be derived as follows:

$$\frac{\partial p_l}{\partial t} = \frac{K_l}{\left(1 - \frac{K_l}{S_l} \frac{\partial S_l}{\partial s}\right)} \left[\frac{(1-n)}{n} \nabla \cdot \mathbf{v}_s + \nabla \cdot \mathbf{v}_l \right] \quad (4)$$

where K_l is the bulk modulus of liquid, and s is the suction equal to $p_a - p_l$, where p_a is the air pressure which is set to zero.

The concept of Bishop effective stress is used here to include the effect of the partial saturation in the soil behaviour, and the effective stress ($\boldsymbol{\sigma}'$) is equal to $\boldsymbol{\sigma} - S_l p_l \mathbf{I}$. The general form of material stress–strain relationship can be presented incrementally as $d\boldsymbol{\sigma}' = \mathbf{D}d\boldsymbol{\varepsilon}$, where \mathbf{D} is the tangent matrix, $d\boldsymbol{\varepsilon}$ is the strain increment vector. In case of large deformation, the Jaumann stress rate is adopted which writes the material time derivative of the Cauchy stress tensor as follows $d\boldsymbol{\sigma}' = \mathbf{D}d\boldsymbol{\varepsilon} + \boldsymbol{\sigma}'\mathbf{W}^T - \mathbf{W}\boldsymbol{\sigma}'$. The first term is the rate of change due to the material response; the other two terms represent the change of stress due to rotation and the term \mathbf{W} is the skew part of the velocity gradient tensor.

A linearised relation between the degree of saturation and suction is used, which is written as:

$$S_l = 1 - a_v s \quad (5)$$

where a_v is a constant value. The effect of the saturation on the relative permeability is not considered in this study, and the hydraulic conductivity is kept equal to the saturated one.

Discretization and Algorithm of Material Point Method

The discretized form of Eqs. (1) and (2), both written per unit volume of mixture, is shown as follows:

$$\mathbf{M}_l \mathbf{a}_l = \mathbf{f}_l^{ext} + \mathbf{f}_l^{grav} - \mathbf{f}_l^{int} - \mathbf{f}^{drag} \quad (6)$$

$$\mathbf{M}_s \mathbf{a}_s = \mathbf{f}_s^{ext} + \mathbf{f}_s^{grav} - \mathbf{f}_s^{int} + \mathbf{f}^{drag} \quad (7)$$

where \mathbf{f}^{ext} is the vector of nodal external forces, \mathbf{f}^{grav} is the vector of body forces, \mathbf{f}^{int} is the vector of nodal internal forces, \mathbf{M} is the nodal mass matrix and \mathbf{f}^{drag} is the vector of drag forces.

In MPM, the continuum body is represented by a cloud of points, called material points (MPs). They carry all information of the continuum body, such as density, velocity, strain, stress, material parameters and external loads (Al-Kafaji 2013). They are not physical particles, like for example single solid grains described in Discrete Element Method, but they represent a portion of continuum body. A schematic representation of MPM and the background mesh is shown in Fig. 1.

A single computational cycle is described as follows.

- (a) The nodal forces are computed based on the information stored at the material points by means of the shape functions.

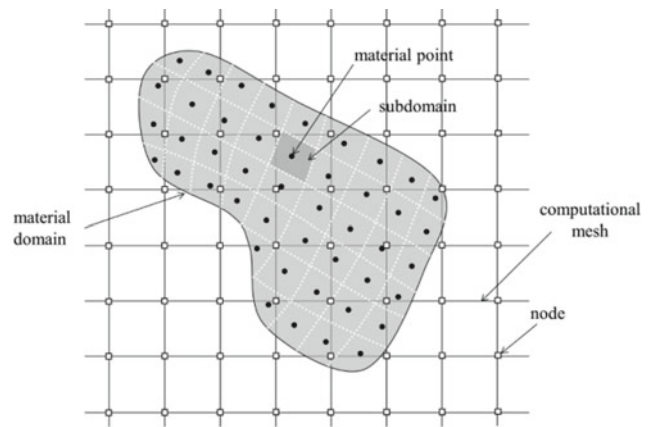


Fig. 1 Spatial discretization in MPM (Yerro et al. 2015)

- (b) The nodal acceleration \mathbf{a}_l is determined by Eq. (6).
- (c) The nodal acceleration \mathbf{a}_s is determined by Eq. (7).
- (d) If rainfall boundary condition is specified, the nodal accelerations are adjusted in order to comply with the rainfall. This point is described in detail in the next paragraph.
- (e) The material point velocities are computed from the nodal accelerations, and the nodal velocities are finally computed as the ratio between nodal momentum and nodal mass.
- (f) Strain increments are then computed at the location of each material point.
- (g) The increments of pore water pressure and effective stress are computed using Eq. (4) and Bishop effective stress equations, respectively.
- (h) Displacement and position of each material point are finally updated.

The explicit integration scheme, such as the one presented above, is conditionally stable. The size of the time step for stable solution depends on the properties of the materials: it decreases with stiffness and with low permeability (Mieremet et al. 2015).

Rainfall Boundary Condition

The vectors \mathbf{f}^{ext} in Eqs. (6) and (7) are computed using loads stored at the material points, which are derived from distributed loads acting at the surface boundary of the continuum body. In case of “ponding” condition, the external load is set to zero ($\mathbf{f}^{ext} = 0$) and step (d) of the computational cycle is not performed. The resulting seepage flow in the soil is not controlled, as it is directly determined by the gradient of pressures and soil permeability (Eq. 1).

In case of rainfall specification, the following steps are defined.

Step 1 definition of the free-surface nodes, i.e. nodes shared between active (with at least 1 MP) and non-active elements (see Fig. 2), and calculation of the outer normal \mathbf{n} at node i as:

$$\mathbf{n}_i = \frac{\sum_{MP} m_{MP} \nabla N_i}{|\sum_{MP} m_{MP} \nabla N_i|} \quad (8)$$

where m_{MP} is the mass of each material point and ∇N_i is the gradient of the shape function at node i .

Step 2 the liquid and solid accelerations at *free-surface nodes* are computed assuming the “ponding” condition, i.e. $f^{ext} = 0$.

Step 3 the liquid and solid velocity are computed as

$$\mathbf{v}_{l,t+1}^* = \mathbf{v}_{l,t} + \mathbf{a}_l \Delta t \quad (9)$$

$$\mathbf{v}_{s,t+1}^* = \mathbf{v}_{s,t} + \mathbf{a}_s \Delta t \quad (10)$$

where Δt is the increment of time in the calculation.

Step 4 The rainfall boundary condition is imposed at the free-surface nodes if the seepage flow is higher than the rainfall intensity, which reads as follows:

$$\left[n S_l (\mathbf{v}_{l,t+1}^* - \mathbf{v}_{s,t+1}^*) - \underline{\mathbf{w}} \right] \cdot \mathbf{n} \leq 0 \quad (11)$$

If this condition is met, correction to the velocity field of both liquid ($\Delta v_{l,n}$) and solid ($\Delta v_{s,n}$) phase along the normal direction is applied such that:

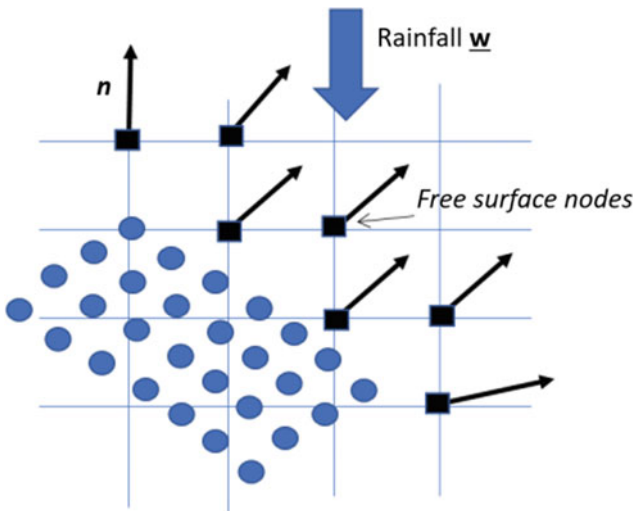


Fig. 2 Definition of *free-surface* nodes and outer normal

$$n S_l (\mathbf{v}_{l,t+1}^* + \Delta v_{l,n} \mathbf{n} - \mathbf{v}_{s,t+1}^* - \Delta v_{s,n} \mathbf{n}) \cdot \mathbf{n} = \underline{w}_n \quad (12)$$

where \underline{w}_n is the component of the rainfall velocity normal to the surface.

Equation (12) can be rewritten as follows:

$$\Delta v_{l,n} - \Delta v_{s,n} = - \frac{\left[n S_l (\mathbf{v}_{l,t+1}^* - \mathbf{v}_{s,t+1}^*) - \underline{\mathbf{w}} \right] \cdot \mathbf{n}}{n S_l} \quad (13)$$

The velocity correction in both phases should fulfill the condition that momentum of the mixture is conserved, i.e.:

$$m_l \Delta v_{l,n} + m_s \Delta v_{s,n} = 0 \quad (14)$$

where m_l and m_s are the liquid and solid nodal masses.

It follows, that:

$$\Delta v_{s,n} = - \frac{m_l \Delta v_{l,n}}{m_s} \quad (15)$$

$$\Delta v_{l,n} = - \frac{\left[n S_l (\mathbf{v}_{l,t+1}^* - \mathbf{v}_{s,t+1}^*) - \underline{\mathbf{w}} \right] \cdot \mathbf{n}}{n S_l \left(1 + \frac{m_l}{m_s} \right)} \quad (16)$$

The final velocities and the acceleration field are then computed:

$$\mathbf{v}_{l,t+1} = \mathbf{v}_{l,t+1}^* + \Delta v_{l,n} \mathbf{n} \quad (17)$$

$$\mathbf{v}_{s,t+1} = \mathbf{v}_{s,t+1}^* + \Delta v_{s,n} \mathbf{n} \quad (18)$$

$$\mathbf{a}_l = \frac{\mathbf{v}_{l,t+1} - \mathbf{v}_{l,t}}{\Delta t} \quad (19)$$

$$\mathbf{a}_s = \frac{\mathbf{v}_{s,t+1} - \mathbf{v}_{s,t}}{\Delta t} \quad (20)$$

Validation Case: 1D Infiltration Problem

Geometry, Material and Boundary Conditions

The proposed implementation is validated considering a 1D infiltration problem, for both “ponding” and rainfall boundary condition.

A 1D soil column is considered for this study, with an initial height of 1.05 m and with a uniform grid size of 0.025 m. Six material points are assigned initially in each triangular element of the mesh.

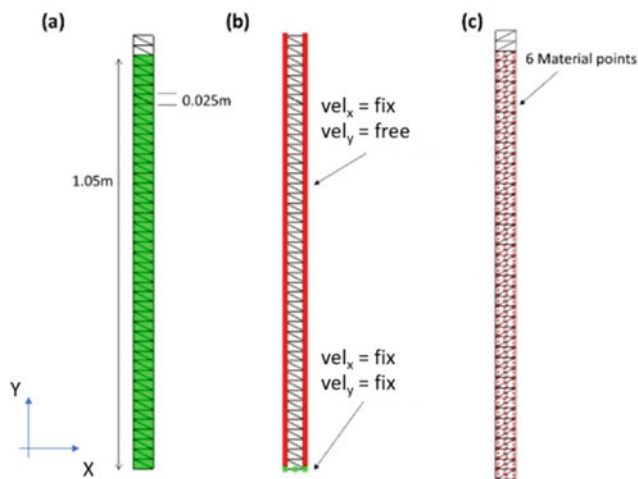


Fig. 3 **a** The geometry and the computational mesh; **b** the boundary conditions for the soil and liquid phase; **c** the distribution of the material points

The computational mesh and the material point distribution is shown in Fig. 3. The boundary conditions are set for both liquid and solid phase. The velocities are fully fixed in both directions at the bottom boundary, whereas on the vertical boundaries they are fixed only in the X direction.

The initial stress state in the soil column is initialized assuming a geostatic condition, with a k_0 coefficient set to 0.5. The water table is defined at the bottom of the column and a linear suction profile is consequently initialized, which is zero at the bottom and approximately 10.2 kPa at surface.

The material is considered as elastic body and relative parameters are listed in Table 1. It is worth noticing that the saturated soil permeability is 0.2 mm/s.

Two rainfall conditions are considered, set constant for the entire calculation: “ponding” condition, by applying an extremely large rainfall velocity \underline{w} (which is equivalent to setting only zero pore pressure at *free-surface* as Eq. (11) is

never met), and a rainfall of 0.5 mm/s, which is still larger than the saturated permeability.

The results of the proposed MPM implementation are discussed in the next paragraph where they are also compared against the well-established commercial code PLAXIS, used as benchmark.

Model Results

The infiltration process is simulated for approximately 60 s, long enough to get the soil fully saturated.

The ponding boundary condition is defined applying zero external load at surface throughout the entire simulation. In this case, the water is free to flow vertically and thus the pore water pressure at the free surface remains zero.

The results are shown in Fig. 4 as profile of pore water pressure at different time instants. The results of PLAXIS are plotted with a red dashed line and the result of MPM with black dots at several depths (0.1, 0.3, 0.5, 0.7, 0.9 m) and at surface.

In this case, very large gradients of pore pressure are induced in the soil body, especially close to the free surface where the ponding condition is applied, and the seepage flow can be larger than the saturated permeability. Overall, the entire soil column needs approximately 40 s to be fully saturated, and about 50 s to reach the final hydrostatic configuration.

If the rainfall boundary condition is specified, the seepage flow at surface cannot be greater than the maximum rainfall, specified by the user. In this case the results are shown in Fig. 5. Although the specified rainfall intensity (0.5 mm/s) is still larger than the saturated permeability, after 30 s, almost the entire column still presents positive pore pressures (suction) which identifies the condition of partly-saturation of the soil body. As before, tensile tensions are assumed

Table 1 List of material parameters in MPM

Parameter	Value	Unit
Young's modulus	5000	kPa
Poisson's ratio	0.0	–
Density of solid grains	2700	kg/m ³
Density of water	1000	kg/m ³
Porosity	0.33	–
Bulk modulus of water	200,000	kPa
Dynamic viscosity of water	10 ⁻⁶	kPa s
Intrinsic permeability	2 × 10 ⁻¹¹	m ²
Linear model parameter (a_v)	0.01	–

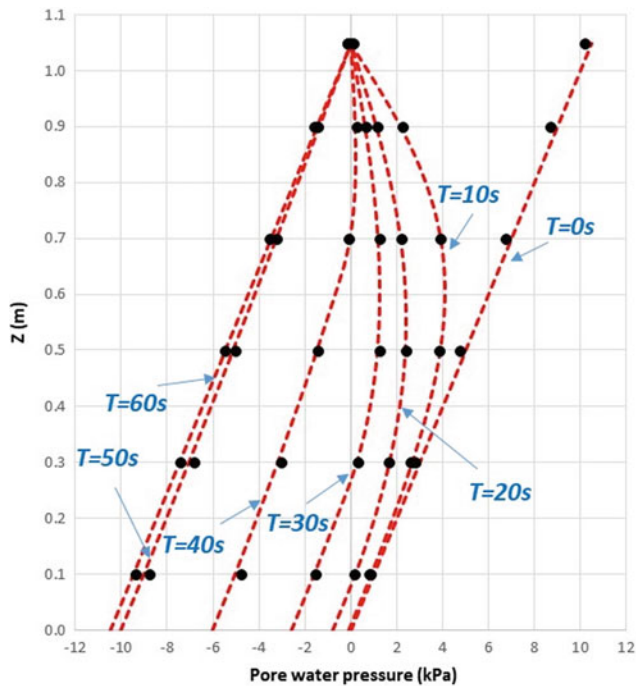


Fig. 4 Ponding condition: profile of pore water pressure at different time instants. PLAXIS (red dashed lines) and MPM (black dots)

positive. After 40 s, only the bottom third of the soil column is saturated. In this case, the final hydrostatic conditions are only met after 60 s.

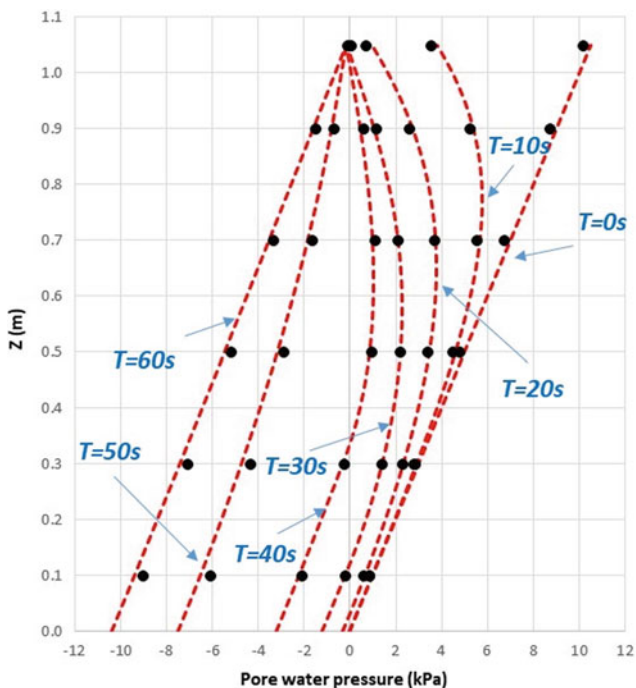


Fig. 5 Rainfall condition: profile of pore water pressure at different time instants. PLAXIS (red dashed lines) and MPM (black dots)

Overall, a good agreement is observed between MPM solution and PLAXIS.

Conclusions

This study presents and validates an algorithm which allows including the infiltration boundary condition in a multiphase dynamic MPM model. The algorithm is written using both liquid and solid true velocities fields instead of the Darcy's seepage velocity, used in other implementations.

This allows expanding the capabilities of the dynamic a_s - a_l formulation (Zienkiewicz et al. 1999), already widely used in several MPM simulations (e.g. www.anura3d.com), in the field of rainfall-induced landslides focusing on both the triggering and runoff.

It is worth mentioning that the proposed algorithm is validated only for small deformations. Validation in case of extremely large deformations, where material points cross elements of the background mesh, will be part of future work.

References

- Al-Kafaji IKA (2013) Formulation of a dynamic material point method (MPM) for geomechanical problems. PhD thesis, Universität Stuttgart
- Alonso EE, Zabala F (2011) Progressive failure of Aznalcóllar dam using the material point method. *Géotechnique* 61(9):795–808
- Bandara S, Soga K (2015) Coupling of soil deformation and pore fluid flow using material point method. *Comput Geotech* 63:199–214
- Bandara S, Ferrari A, Laloui L (2016) Modelling landslides in unsaturated slopes subjected to rainfall infiltration using material point method. *Int J Numer Anal Meth Geomech* 40(9):1358–1380
- Beuth L, Vermeer PA (2013) Large deformation analysis of cone penetration testing in undrained clay. In *Proc. Installation Effects in Geotechnical Engineering – Hicks et al. (eds) 2013 Taylor & Francis Group, London, ISBN 978-1-138-00041-4*
- Ceccato F (2015) Study of large deformation geomechanical problems with the material point method. PhD thesis, University of Padua
- Ceccato F, Girardi V, Yerro A, Simonini P (2019) Evaluation of dynamic explicit MPM formulations for unsaturated soils. In: Oñate E, Bischoff M, Owen DRJ, Wriggers P, Zohdi T (Eds) VI International Conference on Particle-based Methods – Fundamentals and Applications Particles 2019
- Cuomo S, Della SM (2013) Rainfall-induced infiltration, runoff and failure in steep unsaturated shallow soil deposits. *Eng Geol* 162:118–127
- Cuomo S, Di Perna A, Ghasemi P, Martinelli M, Calvello M (2019a) Combined LEM and MPM analyses for the simulation of a fast moving landslide in Hong Kong. In: II international conference on the material point method for modelling soil–water–structure interaction, Cambridge, pp 103–108. ISBN 978-7-5210-0316-1
- Cuomo S, Ghasemi P, Martinelli M, Calvello M (2019b) Simulation of liquefaction and retrogressive slope failure in loose coarse-grained material. *Int J Geomech* 19(10):04019116. <https://doi.org/10.1007/s1006>
- Galavi V, Martinelli M, Elkadi A, Ghasemi P, Thijssen R (2019) Numerical simulation of impact driven offshore monopiles using the

- material point method. In: The XVII European conference on soil mechanics and geotechnical engineering, Reykjavik, 1–6 Sept 2019
- Ghasemi P, Calvello M, Martinelli M, Galavi V, Cuomo S (2019) MPM simulation of CPT and model calibration by inverse analysis. In: Proc. Cone Penetration Testing, pp 295–301
- Harlow FH (1964) The Particle-in-Cell computing method for fluid dynamics. *Methods Comput Phys* 3:319–343
- Jassim I, Stolle D, Vermeer P (2013) Two-phase dynamic analysis by material point method. *Int J Numer Anal Meth Geomech* 37:2502–2522
- Lee WL, Martinelli M, Shieh CL (2019) Modelling rainfall-induced landslides with the material point method: the Fei Tsui Road case. In: XVII European conference on soil mechanics and geotechnical engineering, Iceland
- Mieremet M, Stolle DFF, Ceccato F, Vuik C (2015) Numerical stability for modelling of dynamic two-phase interaction. *Int J Numer Anal Meth Geomech* 40
- Phuong NTV, van Tol AF, Elkadi ASK, Rohe A (2016) Numerical investigation of pile installation effects in sand using material point method. *Comput Geotech* 73:58–71
- Sulsky D, Chen Z, Schreyer HL (1994) A particle method for history-dependent materials. *Comput Methods Appl Mech Eng* 118 (1–2):179–196
- Touma J, Vauclin M (1986) Experimental and numerical analysis of two-phase infiltration in a partially saturated soil. *Transp Porous Media* 1(1):27–55
- Wang B, Vardon PJ, Hicks MA (2016) Preliminary analysis of rainfall-induced slope failures using the material point method. In: Landslides and engineered slopes, experience, theory and practice: proceedings of the 12th international symposium on landslides, Naples, pp 2037–2042
- Wieckowski Z (2003) Modelling of silo discharge and filling problems by the material point method. *Task Q* 4:701–721
- Wieckowski Z, Youn S-K, Yeon J-H (1999) A particle-in-cell solution to the silo discharging problem. *Int J Numer Meth Eng* 45:1203–1225
- Yerro A, Alonso EE, Pinyol NM (2015) The material point method for unsaturated soils. *Géotechnique* 65(3):201–217
- Zienkiewicz OC, Chan AHC, Pastor M, Schrefler BA, Shiomi T (1999) *Computational geomechanics with special reference to earthquake engineering*. Wiley



2020 Kyoto Japan

Response of Slopes to Earthquakes and Rainfall

Jiawei Xu, Ryosuke Uzuoka, and Kyohei Ueda

Abstract

Earthquakes can cause landslides on many scales in mountainous areas and pose danger to the residential area at the bottom of mountains. In some areas where the earthquake intensity is not high enough to cause large soil movement, the shaking effect on the stability of slopes during the following rainfall is not significant. However, in certain areas, shaking-caused large cracks on the slope surface play an important role in the stability of slopes subject to the following rainfall. The effect of pre-shaking on the slope stability when the slope is subject to rainfall is still not fully studied. In this study, centrifuge model tests on slopes subject to earthquakes and rainfall were carried out and due to insufficient shaking intensities and soil suction in the unsaturated slope, cracks were not seen on the surfaces of the slopes after shaking and only small displacement was induced, which made it difficult to specify the influence of earthquakes on the stability of slope subject to the following rainfall. The soil displacement and mobilization patterns of two slopes in this study were similar and the negative contribution of shaking to the slopes were not thoroughly investigated. However, the intensity and duration were the main factors that affected the occurrence and mode of the slide caused by rainfall; a uniform rainfall distribution is also necessary to validate the triggering mechanism of slide in the model tests.

Keywords

Slope • Earthquake • Rainfall • Landslide • Centrifuge model test

Introduction

Earthquakes and rainfall are two common natural disasters causing slopes failure such as landslides and large soil movement in mountainous areas. In the past several earthquakes such as 1995 Kobe Earthquake (Tomita et al. 1996), 1999 Chichi Earthquake (Hotta et al. 2005), 2008 Sichuan Earthquake (Tang et al. 2011), 2011 Tohoku Earthquake (Usui et al. 2012), and 2016 Kumamoto Earthquake (Geospatial Information Authority of Japan 2016), a lot of slopes didn't display failure or slide, but only cracks were left on the surfaces and the slopes still remained stable. It was known that water infiltration into soil in slopes will cause the increase in pore water pressure or reduction in soil suction (especially in unsaturated soil slopes), the continual drop of the shear strength of soil contribute mostly to the failure of slopes that are pre-shaken by earthquakes. Numerical analyses were carried out by researchers on the slope stability during rain infiltration (Cho and Lee 2001; Qi and Vanapalli 2015; Cai and Ugai 2004; Sharma and Nakagawa 2010; Tian et al. 2017) and the decrease in soil shear strength caused by suction losses and raised water tables were regarded as two main reasons why slopes failed during rainfall events. Physical model experiments such as large/small-scale model experiments at 1 g (Wang and Sassa 2001; Montrasio and Valentino 2004; Sharma and Nakagawa 2010), field tests (Ng et al. 2003; Springman et al. 2013; Rahardjo et al. 2005; Chen et al. 2018), and centrifuge model tests (Take et al. 2004; Tamate et al. 2012; Bhattacharjee and Viswanadham 2018) were also conducted to investigate the behavior of slopes and mechanisms of slope failure during rainfall. Studies on the seismic response of

J. Xu (✉)

Department of Civil and Earth Resources Engineering, Kyoto University, Gokasho, Uji, Kyoto, 611-0011, Japan
e-mail: xu.jiawei.38z@st.kyoto-u.ac.jp

R. Uzuoka · K. Ueda

Disaster Prevention Research Institute, Kyoto University, Kyoto, 611-0011, Japan
e-mail: uzuoka.ryosuke.6z@kyoto-u.ac.jp

K. Ueda

e-mail: ueda.kyohei.2v@kyoto-u.ac.jp

© Springer Nature Switzerland AG 2021

B. Tiwari et al. (eds.), *Understanding and Reducing Landslide Disaster Risk*, ICL Contribution to Landslide Disaster Risk Reduction, https://doi.org/10.1007/978-3-030-60706-7_30

slopes or embankments to earthquakes were also carried out by different researchers using various methods including centrifuges model tests (Matsuo et al. 2000a, b; Liang and Knappett 2017), numerical modelling (Xiong et al. 2014), and shaking tables tests (Koga and Matsuo 1990; Matsumaru et al. 2012). However, the impact of rainfall on the stability of slopes after earthquakes was not fully studied in previous research.

In this study, two centrifuge model tests were performed: one was on an unsaturated slope subject to shaking and then rainfall and the other was on an unsaturated slope subject to only rainfall. An inflight rainfall simulator was designed and applied to the tests where rainfall-caused slide was replicated and its triggering mechanism was also analyzed.

Methodology

Small scale centrifuge models were used to simulate the prototype behavior of unsaturated infinite slopes in a centrifugal acceleration field of 50 g. An inflight rainfall simulator was designed and used to model rainfall in the centrifuge models.

Test Program

Two centrifuge model tests were carried out in the Kyoto University centrifuge and the test program is summarized in Table 1.

Centrifuge Modelling Scales

Since soil is highly stress dependent and the geotechnical centrifuge can provide an accelerated field of N times Earth's gravity for a model scaled down by $1/N$, results from the tests can be extrapolated to a prototype situation. This is the basic scaling law of centrifuge modelling, that stress similarity is achieved at homologous points by accelerating a model of scale N to N times Earth's gravity. Centrifuge scaling factors of common parameters are given in Table 2.

Experimental Setup

The centrifuge model tests were carried out on the shaking table in Kyoto University centrifuge. The centrifuge has an

effective radius of 2.5 m and a maximum capacity of 24 g-ton. The shaking table is integrated with the swing basket of the centrifuge and has maximum accelerations of 50 g for dynamic tests and maximum displacement amplitudes of ± 5.0 mm in the model scale. Both slopes were made of unsaturated soil with the same degree of compaction and the rainfall intensities were also the same. The centrifuge model test geometry and instruments are shown in Fig. 1.

Markers were put between soil and the transparent wall, and a high-speed camera fixed in front was used to view and photograph the testing.

Inflight Rainfall Simulator

Rainfall simulator (in Fig. 2), which was made with 18 nozzles, was mounted on top of the container. A rain droplet in the centrifuge should have a size of 50 times smaller than that in the prototype. Air pneumatic nozzles were used to model small rain droplets with average size of 20–40 μm in the tests. A water tank providing water supply was on connected with the container and an air cylinder was placed on the centrifuge arm to provide air supply. Nozzles were also carefully arranged to produce as uniform rainfall as possible. A remote control was used to control the solenoids valves so that starting and ending of rainfall could be realized inflight. In this study, the lower part of the slopes in tests got more uniform rainfall rather than the upper part, and this was because the distance of the nozzles above the upper part of the slopes were much smaller due the height limitation of the container and slope base. But the rainfall patterns above the lower parts of slopes were quite uniform so analyses of displacement caused by rainfall were mainly conducted in the lower parts.

Since the rainfall intensity is defined as the ratio of the amount of rain in a given period of time and the amount of rain is usually represented by the water head, according to the centrifuge modelling scales for length and time, the rainfall intensity in the model scale should be N times larger than that in the prototype scale. In this test, the model rainfall intensity was selected as 250 mm/h, which corresponded to 5 mm/h in the prototype scale.

Soil Material

Masado, which is usually silty sand or sand with silt and commonly found in West Japan, was used. The soil was

Table 1 Test program

Test	Description
A	Slope subject to shaking and then rainfall
B	Slope subject to only rainfall

Table 2 Centrifuge scaling factors

Parameter	Prototype-model ratio
Length	N
Density	1
Time (dynamic)	N
Time (diffusion)	N^2
Frequency	$1/N$
Stress	1

Fig. 1 Centrifuge model test geometry and instrument

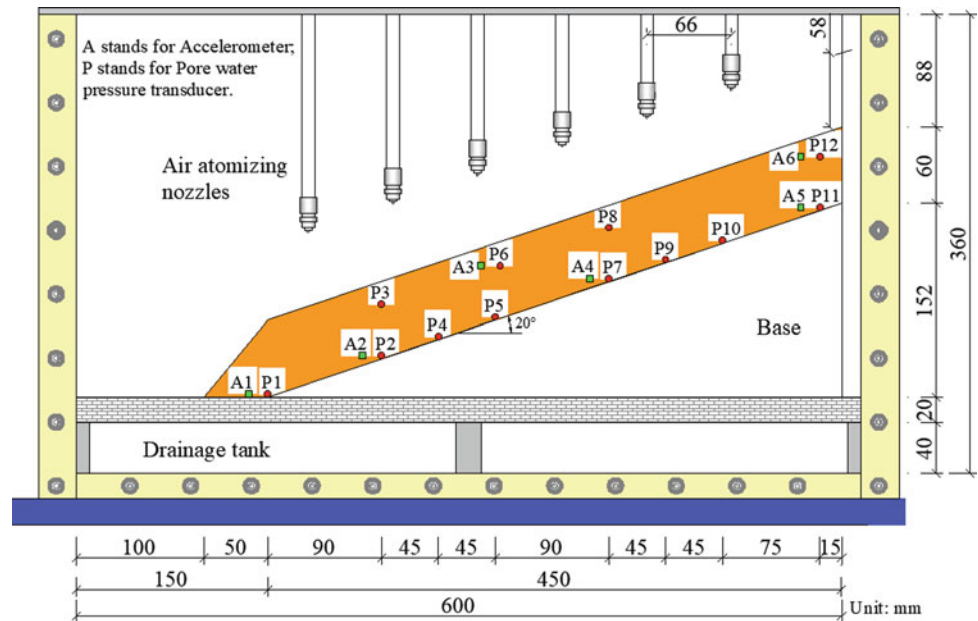


Fig. 2 Rainfall simulator

named Well-graded sand with silt (SW-SM) using the ASTM classification system. Masado has a uniformity coefficient C_u of 7.46, curvature coefficient C_c of 1.01, maximum dry density of 1.77 g/cm^3 , and optimum water content of 13%. Since Masado sand used in the tests has a fines content of around 10%, it's not considered appropriate to adopt relative density as a density index. Instead, the degree of compaction, defined as the ratio of soil dry density to its maximum dry density, is used as a density index. The

degree of compaction of the soil here was 87% with a dry density of 1.55 g/cm^3 . The initial degree of saturation in the slope was about 37.7%. The slope rests on a wood base with an angle of 20° , which is normal compared with natural infinite slopes and the interface between soil and base was covered by sand paper. The reason why water was used instead of other heavy fluid to mix the slope and model rainfall was because high suction existed in the slope and it was unlikely to cause liquefaction in the slope during shaking. Since there is practically no seepage flow or diffusion of water, the dynamic time scaling factor of 1: N should apply. Subsequent to the earthquake, any dissipation of excess pore pressures would be modelled using a time scaling factor of 1: N^2 .

Test Results and Discussion

Test A: Slope Subject to Shaking and Rainfall

In Test A, shaking (Fig. 3) was excited once the centrifugal acceleration reached 50 g. Rainfall with a model intensity of

250 mm/h was introduced after shaking was completed. The displacement vectors (Fig. 4) of the slope during shaking and rainfall were obtained through image analyses and progressive failure of the slope was shown in Fig. 5.

The slope didn't show large displacement during shaking. The largest displacement occurred around the toe of the slope which was 3.67 mm in the prototype scale and the direction was about 28.6°. However, rainfall caused displacement developed very fast and flow slide initiated 50 s after the rainfall started and presented a final shape shown in Fig. 4b.

The slope initially had a fast increase in displacement and sudden slide occurred, which was about 0.1 s in the model scale after the rain started. The soil above the sliding soil kept moving and secondary slide in the upper part took again soon (in Fig. 5d–f). Displacement in various sections of the infinite slope were examined. Different sections of the infinite slope were chosen and designated as A-A, B-B, C-C, D-D, and E-E (in Fig. 6) and displacement of three points (10, 30, 50 cm below the initial slope surface) in each section (in Fig. 6) were selected for discussion.

Surface soil displayed the largest displacement and traveling speed in all sections. First slide started from the beginning of rainfall and ended 50 s afterwards and the soil slightly below the slope surface traveled at an increasing rate till it suddenly collapsed. A1 had a displacement of 9.1 mm in the model scale while B1 only showed only 2.3 mm. Then, surface soil in the upper part away from A-A section was mobilized and moved at high speed which could be seen in the displacement of B1. After the first slide concentrating below A-A completed, new slide above A-A started to develop and extended to the upper part farther.

Though A1 showed the largest final displacement of 19.8 mm and B1 19.3 mm, most of B1 displacement developed during the second slide rather than the first slide.

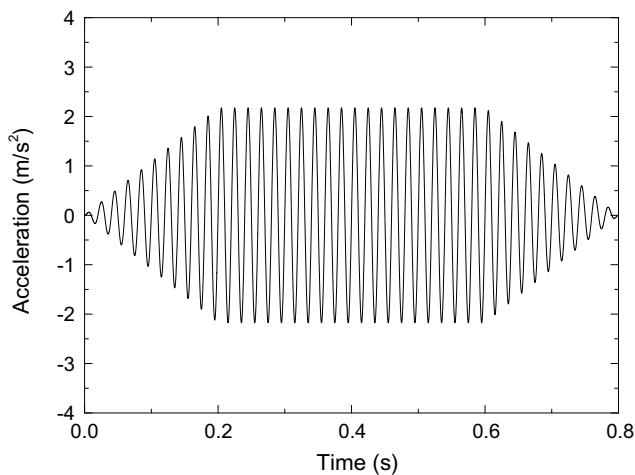


Fig. 3 Input motions during shaking in test A

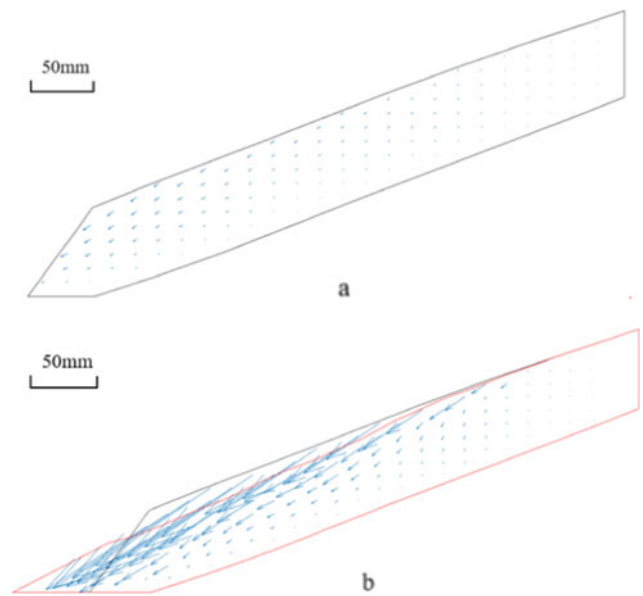


Fig. 4 Soil displacement of the slope caused by shaking (a) and rainfall (b) in test A

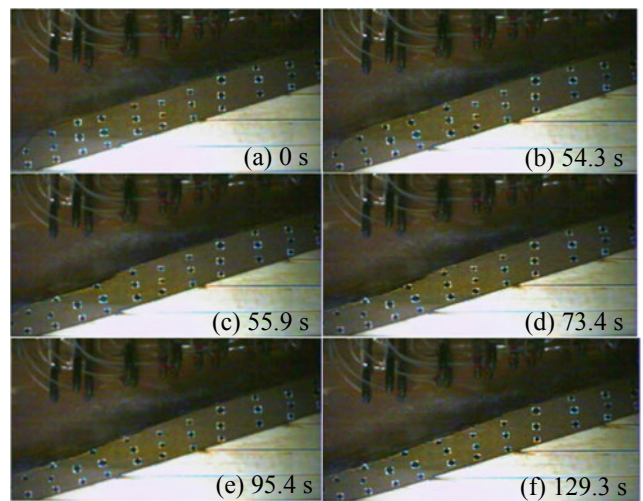


Fig. 5 Progressive failure process of the slope during rainfall in test A (time in the model scale)

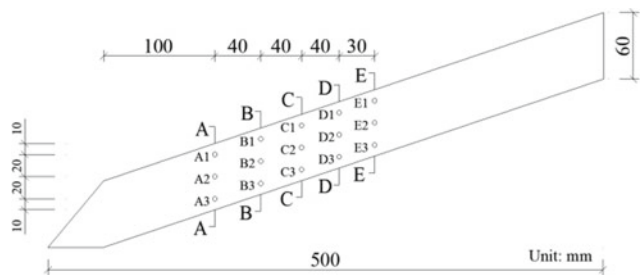
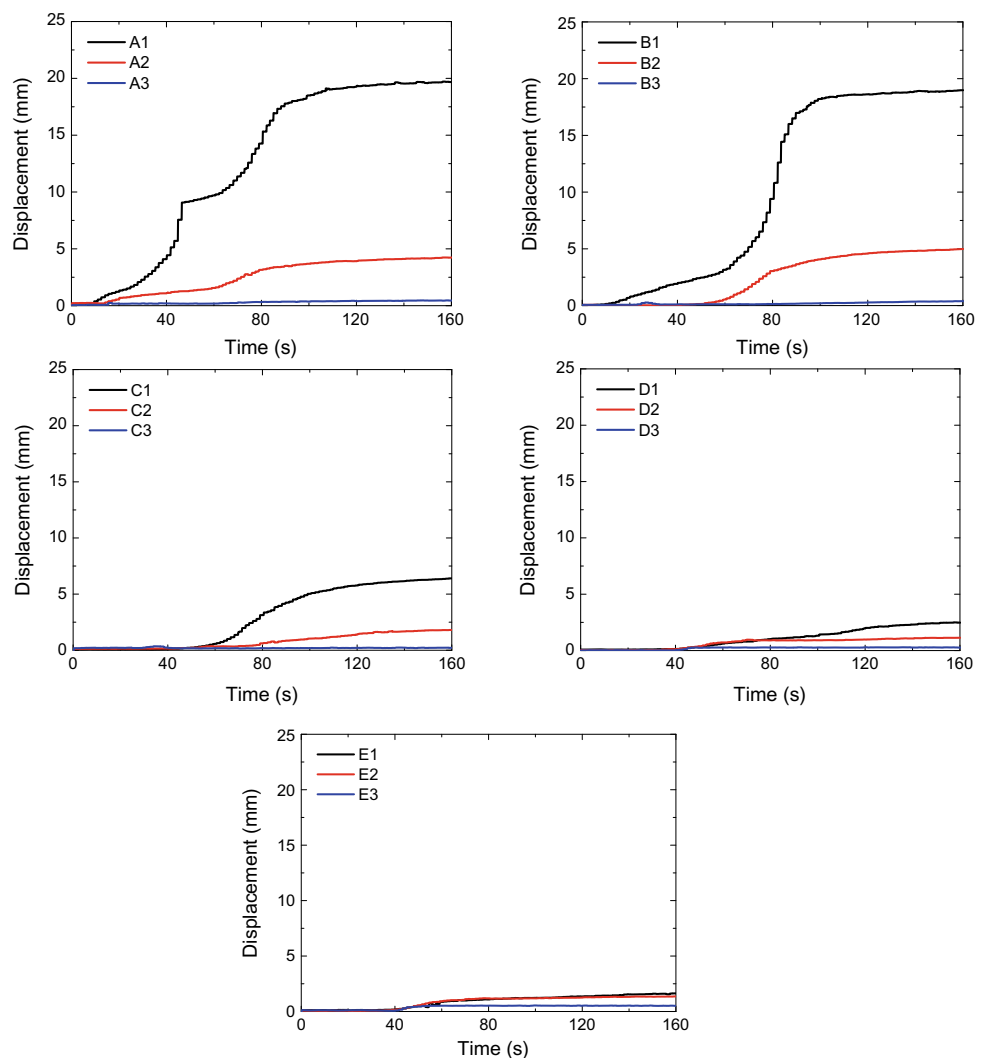


Fig. 6 Slope sections for displacement analyses

In C-C, D-D, and E-E sections, the displacement was not mainly induced by the first slide but the second slide. The maximum traveling velocities of soil in B-B section were 18.6 and 18.2 mm/s in the model scale. The second slide had an impact range as far as E-E section where displacement was negligible.

Rainfall-caused slide was along a plane 2 cm at most below the slope surface, while the highest water table was about 2.6 cm below the slope surface according to pore water pressures in Fig. 8, which meant the surface failure took place above the phreatic line. PWP near the base foundation (P2, P4, P5, P7, P9, and P10) kept increasing and ceased at considerably large values when the steady state flow was achieved. PWP near the slope surface, however, showed quite small growth. The uppermost part of the slope (where P11 and P12 were located) didn't get enough rainfall on account of nozzles being too close to the surface and soil near this area were more stable than the lower part. This was the main reason why D-D and E-E sections in Fig. 7 showed little displacement.

Fig. 7 Displacement in various sections in the slope in test A (in the model scale)



Test B: Slope Subject to Only Rainfall

The final slope profile in test B (Fig. 9) had the similar pattern to that in test A; the effect of pre-shaking on the stability of the slope during rainfall was not obvious. It could be seen from the soil displacement (Fig. 10) and PWP (Fig. 11) in the slope in test B where only rainfall with the same intensity and duration as those in test A was applied that.

The slope failure was characterized by two flow slide as well, and the first flow slide lasted for 44.7 s (A1 displacement Fig. 10). As rainfall continued, soil below the slide plane didn't mobilize, instead, soil above A-A section including soil between B-B section and E-E section started moving and the second surface failure occurred and ended at 87 s. Displacement in A1 displayed the largest values both in the first and second slide, which were 15.3 and 12.3 mm. In the first slide, the maximum traveling velocities of soil in A-A section were 34.7 and 20.6 mm/s in the model scale. Though B1 in the first slide developed more displacement (5.2 mm)

Fig. 8 PWP in the slope during rainfall in test A

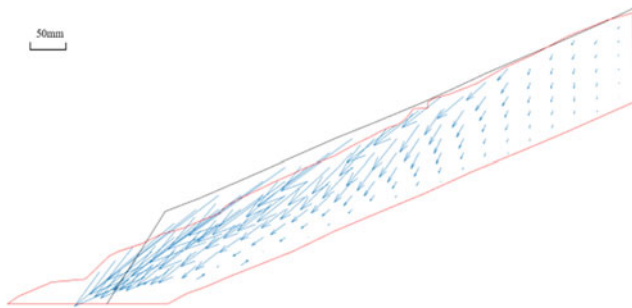
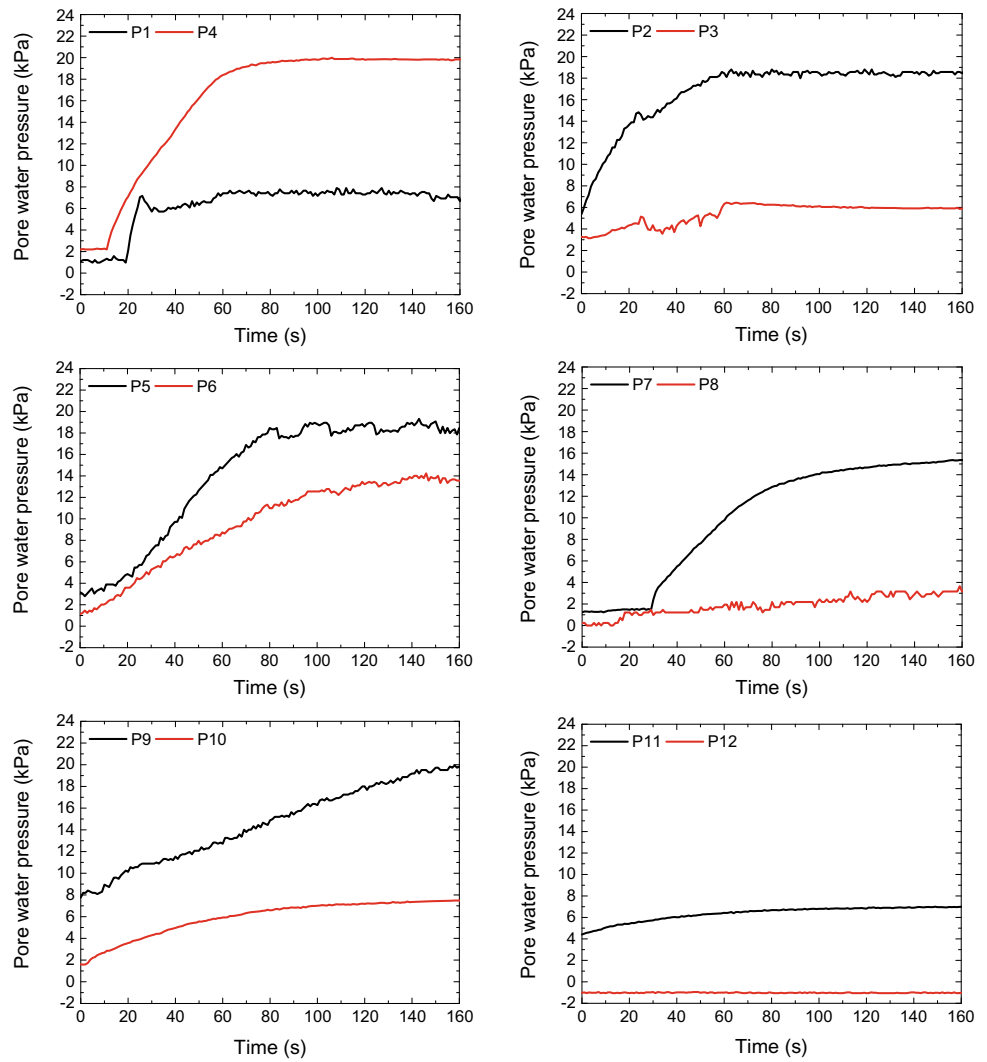


Fig. 9 Soil displacement caused by rainfall in test B

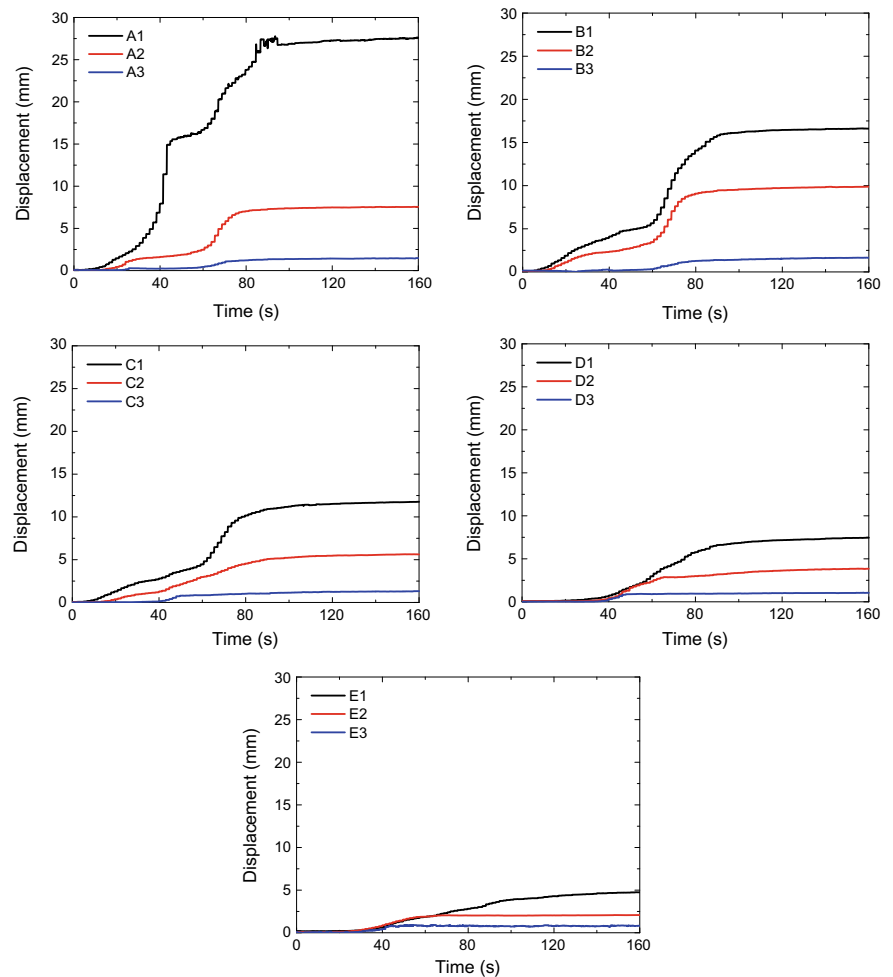
than that in test A, the second slide induced displacement (11.4 mm) and the total displacement (16.6 mm) were less than the those in test A. But B2 had more displacement during both slide: 2.7 mm in the first slide and 7.1 mm in the second slide. Soil displacement in C-C, D-D, and E-E sections, was slightly larger than their counterparts in test A.

PWP near the base showed basically the same changing trend as those in Fig. 8. As shown in Fig. 10, considerably large displacement was mainly in the lower part of the slope where rainfall was evenly distributed to the slope surface and PWP increased to high levels when the steady state flow was achieved. PWP near the slope surface, showed quite small growth.

Conclusions

Two centrifuge model tests on infinite slopes subject to (1) shaking and then rainfall and (2) rainfall were carried in this study. Since the shaking intensity of the pre-shaking event was not large enough and the slopes were made up with unsaturated soil, slope failure patterns in both tests were similar and displacement displayed in the tests was not significantly different.

Fig. 10 Soil displacement in various sections in test B

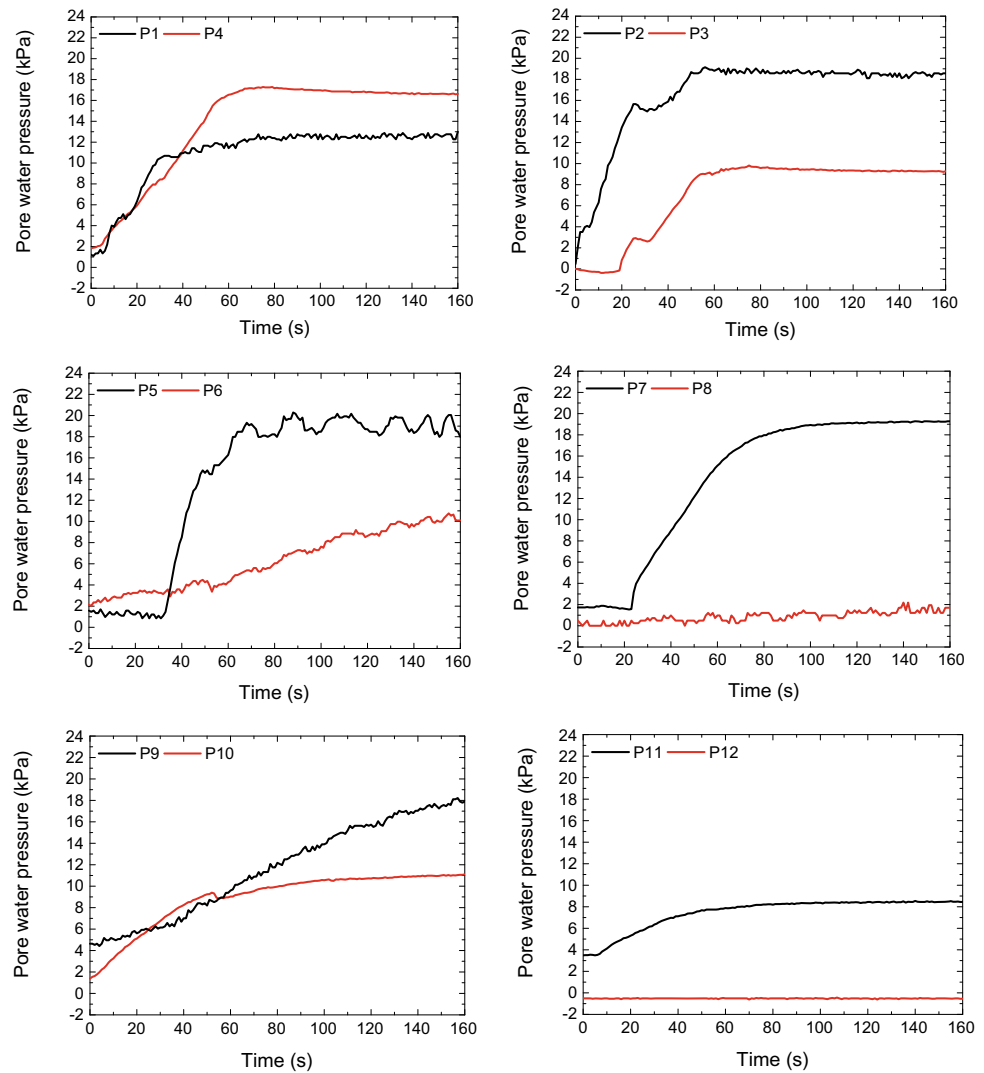


Slope stability depends on the rainfall intensity and rainfall distribution, since the intensity of the rainfall in this study was quite low (5 mm/h in the prototype scale), to cause large landslides, a more intense rainfall is needed. Also, a uniform rainfall is necessary to validate the slide triggering mechanism. The upper part of each slope didn't get as much uniform rainfall as the lower part though the rainfall intensity is equal in each area. The slope failure took place during the transient flow state when pore water pressures within the soil were still increasing. Surface failure

occurred above the phreatic line and the slide was mobilized along a plane 2 cm at most below the slope surface. The first slide was initiated at the lower part of the slopes and travelled at fast speed, resulting in a following second slide away from the collapsed soil. After the steady flow state was reached, further displacement was induced and the phreatic remained stable below the slope surface.

In the future study, shaking with a much higher intensity is needed to cause cracks on the slope surface and the effect of rainfall infiltration into cracks could be clearly investigated.

Fig. 11 PWP in the slope during rainfall in test B



Acknowledgements This study was supported by the Core-to-Core Collaborative research program of the Earthquake Research Institute, The University of Tokyo and the Disaster Prevention Research Institute, Kyoto University.

References

- Bhattacharjee D, Viswanadham BVS (2018) Design and performance of an in-flight rainfall simulator in a geotechnical centrifuge. *Geotech Test J* 41(1):72–91
- Cai F, Ugai K (2004) Numerical analysis of rainfall effects on slope stability. *Int J Geomech* 4(2):69–78
- Chen G, Meng X, Qiao L, Zhang Y, Wang S (2018) Response of a loess landslide to rainfall: observations from a field artificial rainfall experiment in Bailong River Basin, China. *Landslides* 15(5):895–911
- Cho SE, Lee SR (2001) Instability of unsaturated soil slopes due to infiltration. *Comput Geotech* 28:185–208
- Geospatial Information Authority of Japan. (2016). 2016 Kumamoto earthquake. <https://www.gsi.go.jp/BOUSAI/H27-kumamoto-earthquake-index.html>
- Hotta N, Kan YH, Wei TH et al (2005) Relationship between slope failures and precipitation before and after the Chi-chi earthquake investigated using long-term repair records of forestry roads in the National Taiwan University Forest. *J Jpn Soc Eros Control Eng* 58 (1):3–13
- Koga Y, Matsuo O (1990) Shaking table tests of embankments resting on liquefiable sandy ground. *Soils Found* 30(4):162–174
- Liang L, Knappett JA (2017) Centrifuge modelling of the influence of slope height on the seismic performance of rooted slopes. *Geotechnique* 67(10):855–869
- Matsumaru T, Suga M, Uzuoka R (2012) Shaking table test of embankment on inclined ground affected by rainfall. In: *Proceedings of international symposium on earthquake-induced landslides, Kiryu, 7–9 Nov 2012*, pp 437–444
- Matsuo O, Saito Y, Sasaki T, Kondoh K, Sato T (2000a) Earthquake-induced flow slides of fills and infinite slopes. *Soils Found* 42(1):89–104
- Matsuo O, Shimazu T, Uzuoka R, Mihara R, Nishi K (2000b) Numerical analysis of seismic behavior of embankments founded on liquefiable soils. *Soils Found* 40(2):21–39
- Montrasio L, Valentino R (2004) Experimental analysis and modelling of shallow landslides. *Landslides* 4(3):291–296

- Ng CWW, Zhan LT, Bao CG, Fredlund DG, Gong BW (2003) Performance of an unsaturated expansive soil slope subjected to artificial rainfall infiltration. *Geotechnique* 53(2):143–157
- Pilgrim NK (1998) Earthquake-related deformation beneath gently inclined ground. *Geotechnique* 48(2):187–199
- Qi S, Vanapalli SK (2015) Hydro-mechanical coupling effect on surficial layer stability of unsaturated expansive soil slopes. *Comput Geotech* 70:68–82
- Rahardjo H, Lee TT, Leong EC, Rezaur RB (2005) Response of a residual soil slope to rainfall. *Can Geotech J* 42(2):340–351
- Sharma RH, Nakagawa H (2010) Numerical model and flume experiments of single- and two-layered hillslope flow related to slope failure. *Landslides* 7(4):425–432
- Springman SM, Thielen A, Kienzler P, Friedel S (2013) A long-term field study for the investigation of rainfall-induced landslides. *Geotechnique* 63(14):1177–1193
- Take WA, Bolton MD, Wong PC, Yeung FJ (2004) Evaluation of landslide triggering mechanism in model fill slopes. *Landslides* 1(3):173–184
- Tamate S, Suemasa N, Katada T (2012) Simulation of precipitation on centrifuge models of slopes. *Int J Phys Model Geotech* 12(3):89–101
- Tang C, Zhu J, Qi X, Ding J (2011) Landslides induced by the Wenchuan earthquake and the subsequent strong rainfall event: a case study in the Beichuan area of China. *Eng Geol* 122:22–33
- Tian D, Zhen H, Liu D (2017) A 2D integrated FEM model for surface water–groundwater flow of slopes under rainfall condition. *Landslides* 14(2):577–593
- Tomita Y, Sukurai W, Naka N (1996) Study on the extension of collapse caused by rainfall after the earthquake in Rokko Mountain Range. *J Jpn Soc Eros Control Eng* 48(6):15–21
- Usui Y, Shimada H, Innami H, Amao H, Higashi K, Kawabata H (2012) Case study on heavy rainfall-induced reactivation of seismically disturbed slope caused by the 2011 off the Pacific Coast of Tohoku earthquake. In: *Proceedings of the international symposium on earthquake-induced landslides, Kiryu, 7–9 Nov 2012*, pp 323–329
- Wang G, Sassa K (2001) Factors affecting rainfall-induced flowslides in laboratory flume tests. *Geotechnique* 51(7):587–599
- Xiong Y, Bao X, Ye B, Zhang F (2014) Soil-water-air fully coupling finite element analysis of slope failure in unsaturated ground. *Soils Found* 54(3):377–395



2020 Kyoto Japan

Reproduction of Sedimentation State During Rock Slope Failure Using the Simplified DEM Model

Hitoshi Nakase and Yukio Nakata

Abstract

Safety estimations of nuclear facilities must assess the risk of earthquakes stronger than that assumed in the original design. We propose a simple model using the discrete element method to evaluate the traveling distance of a collapsed rock mass when slope collapse occurs. We introduce a new parameter, rotational friction, to evaluate the reach distance and the accumulation state of collapsed soil. We also present the range value of rotational friction and its evaluation method.

Keywords

Rotational friction • Repose angle • Numerical simulation • Validation

Introduction

We have proposed a simple model (Nakase et al. 2015), which employs the discrete element method (DEM, Cundall (1971)) to calculate the traveling distance of collapsed rock. In our model, the shapes of all rock masses are simplified as spheres, and the apparent restitution coefficients are expressed by boundary roughness. The estimated traveling distance of a rock mass is not based on individual rocks but on the distribution of all dropped rocks.

In this study, we introduce a new model parameter to evaluate the reach distance and accumulation state of

collapsed soil called rotational friction. To determine the range of appropriate values for the rotational friction, numerical simulations are conducted to reproduce laboratory experiments for finding the repose angle (RA) of various sands. Next, a parametric study is performed on the actual damage within the rotational friction range. Finally, we confirm whether the RA of the actual damage is within the range of the RA given by the simulation results.

Overview of the DEM Simple Model

DEM Simple Model

In our simple model, the rock mass is modeled by one sphere instead of its exact shape. The roughness of the rock shape is expressed by the ball spacing with the same radius on the slope or the floor in equal intervals (Fig. 1).

When a ball is dropped onto another fixed ball, it generally rebounds with a rotation in a direction other than vertical except when it falls exactly to the top of the fixed ball. The apparent restitution coefficient indicates the ratio of the vertical component in the rebound velocity to the contact velocity. The restitution coefficient is maximized when a ball is dropped directly above the top of a fixed ball. Hence, if the rock mass modeled by a ball drops to the floor arranged of fixed balls, the restitution coefficient is called the maximum restitution coefficient. However, if a realistic rock mass drops to the floor, the restitution coefficient is called the apparent restitution coefficient. In a simple sphere model, changing the spacing distance of the fixed balls on the slope or floor alters the average apparent restitution coefficient. By specifying the appropriate intervals for the fixed balls, the simulation shown in Nakase et al. (2015) well reproduces the apparent restitution coefficient for a realistic rock bounce problem.

Figure 2 compares the simulation using the simple model with a ball size of 6 cm to the experiment performed by

H. Nakase (✉)

Tokyo Electric Power Services Co. Ltd, Gland Square KDX
Toyosu (9f), Shinonome 1-7-12, Koto-ku, 135-0062, Tokyo,
Japan
e-mail: nakase@tepsc.co.jp

Y. Nakata

Yamaguchi University, Tokiwadai 2-16-1, Ube City, 755-8611,
Yamaguchi, Japan
e-mail: nakata@yamaguchi-u.ac.jp

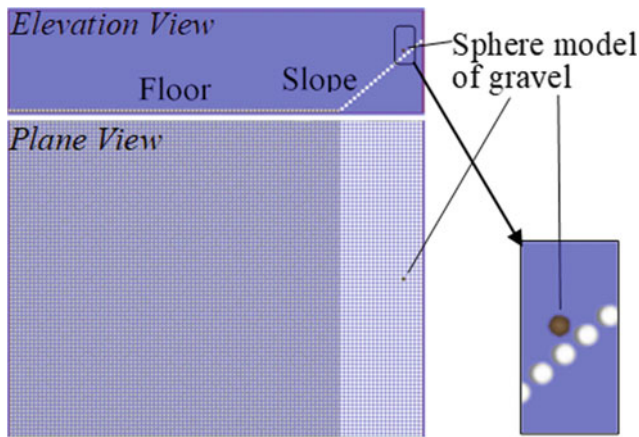


Fig. 1 Example of our simple model

Tochigi et al. (2009). The number of simulations is 177, which is equivalent to that in the experiment. The maximum restitution coefficient between the balls that is equivalent to the rock mass is 0.48.

Figure 3 depicts the simple model in the simulation. To restrict the initial movement without resistance, the surface where the sample balls is initially presented is modeled by tightly spacing the balls with a friction coefficient of 0. The slope and floor are modeled by spacing balls with the same diameter at intervals equal to the diameter in the vertical view.

Figure 4 plots the cumulative distribution probability of the arrival distance compared to the experiment. The simulation reproduces the experimental results well.

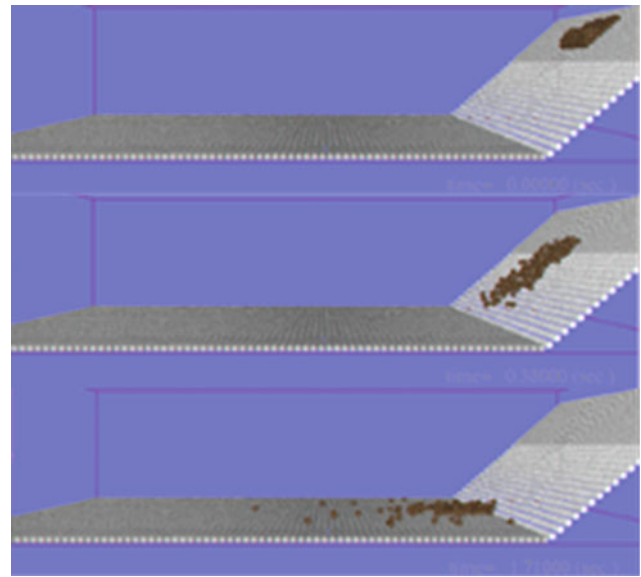


Fig. 3 Simulation of the simple model

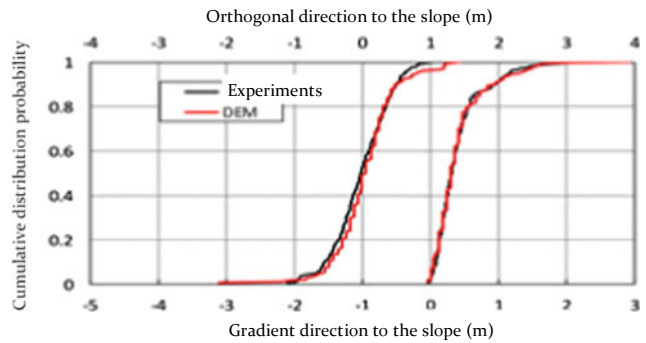


Fig. 4 Comparison of the cumulative distribution probability

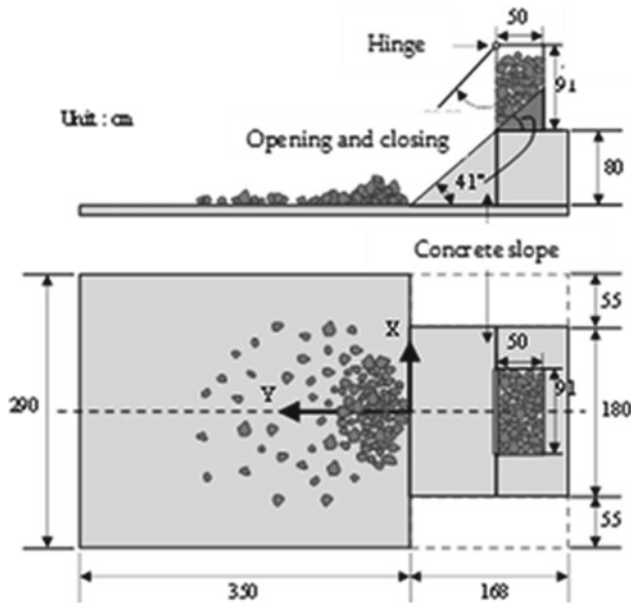


Fig. 2 Description of the experiment by Tochigi

Rotational Friction

When a slope collapses, the debris from the collapse accumulates at a relatively large RA by interlocking due to the unevenness of the individual rocks (Fig. 5). On the other hand, if the shape is a sphere such as a DEM element, the RA should be very small. We introduce rotational friction (Sakaguchi et al. 1993) to analytically represent a large RA using a DEM element with a spherical shape. The rotational friction μ_r is described in reference to Fig. 6.

As shown in Fig. 6, the elements are assumed to make contact with each other by surfaces and not points. A resistance F^* is generated at the end of the surface with respect to the rotational moment M acting on this element, thereby generating rotational resistance M_r . The rotational friction μ_r is a parameter that defines size δ of the surface, which is obtained by multiplying element radius R .

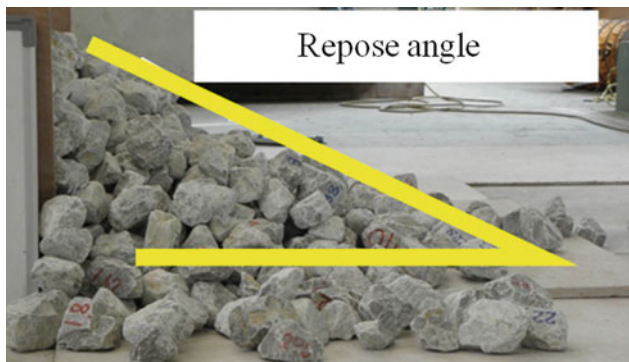


Fig. 5 Rock lumps deposited with a certain RA

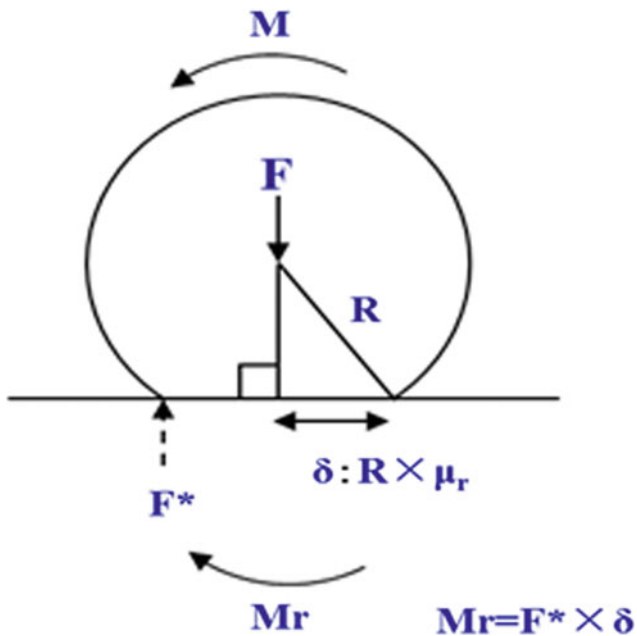


Fig. 6 Conceptual diagram of the rotational friction

Laboratory Experiments to Determine the RA of Various Particles and Reproduction Analysis by DEM

Experimental Device

Figure 7 shows a conceptual diagram of the experimental laboratory device used to determine the RA of various particles. The lower left is an enlarged view of the container portion for filling particles. After filling the particles, gradually lifting the back of the table causes the particles to spill from the edge of the cylinder, forming a conical peak. The angle of the slope of this peak is the RA. The middle photo shows the experimental results using glass beads as the particles.

Experimental Results

Figure 8 shows the experimental results for various sand and glass bead samples. The glass beads have a spherical shape, and their RA is as small as 25°. The RA of the sand is larger than that of the glass beads. The RA varies between 32° and 45°, depending on the grain shape.

Simulation Results

We performed a reproduction analysis of the experiment in Fig. 7 using rotational friction as a parameter. The particle size was 1 cm. Particles in contact with the cylinder and those spilled out are shown in yellow-green. The remaining particles are shown in brown. Figure 9 shows the simulation results by DEM assuming a rotational friction of 0, 0.05, 0.1, and 0.2. As the rotational friction increases, the RA increases. It is 49° at 0.2, which is a much larger RA than those of the five types of sand materials. Figure 8 shows a RA of 30° for a rotational friction of 0 and a RA of 49° for the rotational friction of 0.2 by the orange lines together with the experimental results. In the future, for reproduction analysis on the accumulation of granular materials, the maximum rotational friction is about 0.2.

Reproduction Analysis of Actual Damage

Figure 10 shows a scene of bedrock collapse occurring in Shono, Erimo-cho in 2004. Figure 11a shows the numerical elevation model with 0.5-m intervals for after slope collapse. A 1-m diameter sphere was placed at the grid coordinates, where each color represents a 10-m interval over a 14-m elevation (white). The lower part of the slope shows fan-shaped deposits of collapsed sediment containing rock mass.

Figure 11b shows the numerical elevation model constructed by removing the sediment containing rock mass as well as the collapsed rock shed by referencing aerial photographs and topographic maps obtained prior to the collapse.

Table 1 shows the DEM analysis parameters used to construct the granular model of collapsed sediment containing rock mass in the simulation.

The collapsed slope is steep, and the entry angle of the slope to the roadbed is close to vertical. Assuming that the behavior of a relatively large diameter of rock mass is predominant, we adjusted the relationship between the spring and damping coefficients to produce a restitution coefficient of 0.1.

We examined the values of the rotational friction in the range of 0–0.2 parametrically with reference to the

Fig. 7 Conceptual diagram of the experimental laboratory to determine the RA of various particles

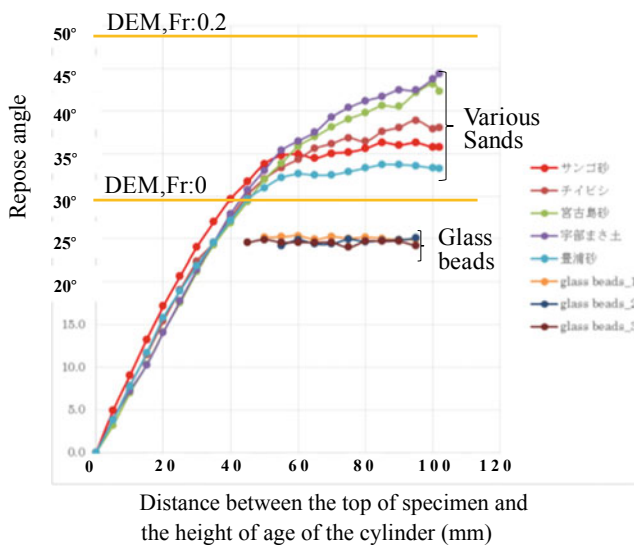
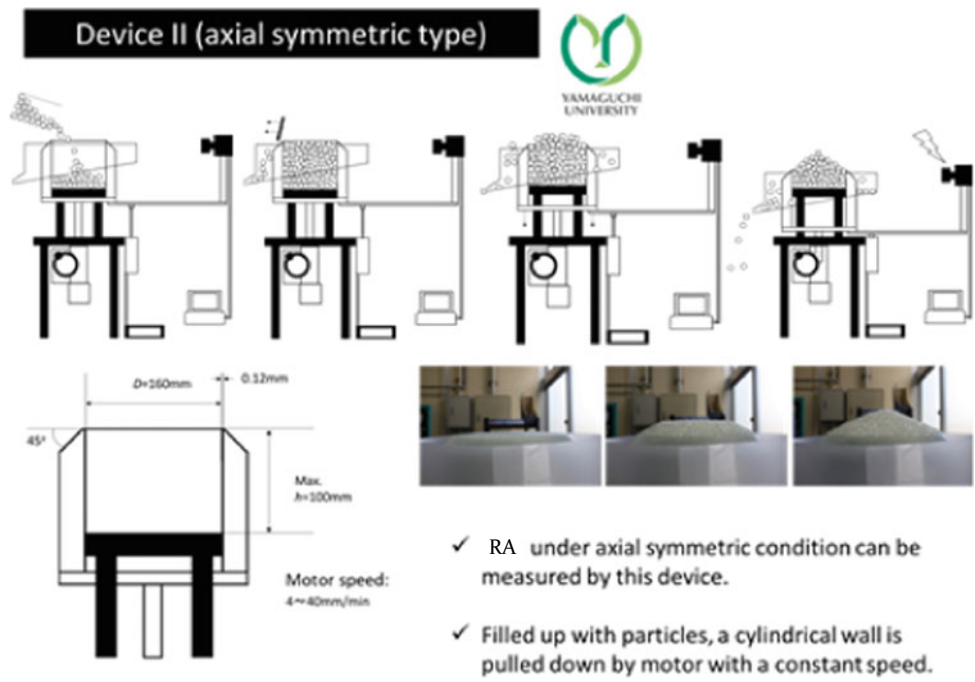


Fig. 8 Experimental results

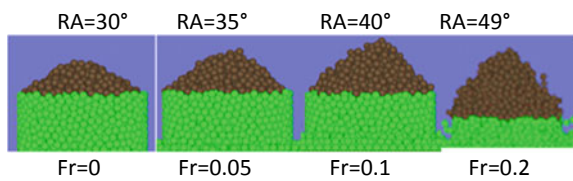


Fig. 9 Simulation results



Fig. 10 Bedrock collapse of Shono, Erimo-cho in 2004

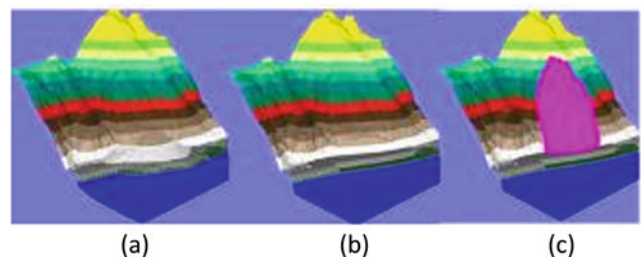


Fig. 11 Numerical elevation model after slope collapse and analysis models based on the model. **a** Numerical elevation model after slope collapse. **b** Numerical elevation model after removing collapsed soil, sand, and rock shed. **c** Numerical elevation model of the original slope

Table 1 DEM analysis parameters

Parameters	Value
Particle diameter (m)	2.0
Density (km/m ³)	2600
Spring coefficient (N/m)	2×10^6
Damping coefficient (N s/m)	1.74×10^5
Friction coefficient (°)	30
Rotational friction	Variable

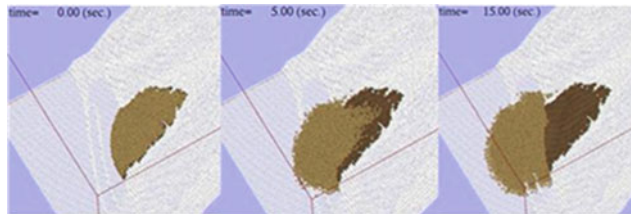


Fig. 12 Initial and collapse states in the simulation

Table 2 RA by survey line

Rotational friction	0	0.1	0.15	0.2	Actual survey
Line 1	0.22	0.38	0.47	0.53	0.43
Line 2	0.36	0.34	0.53	0.57	0.51
Line 3	0.40	0.37	0.54	0.66	0.53
Line 4	0.38	0.42	0.60	0.69	0.60
Average	0.34	0.37	0.53	0.61	0.52

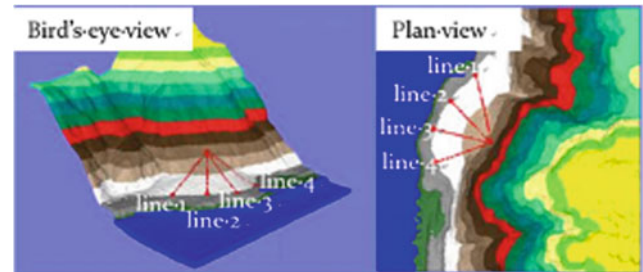


Fig. 14 Survey lines to derive the RA

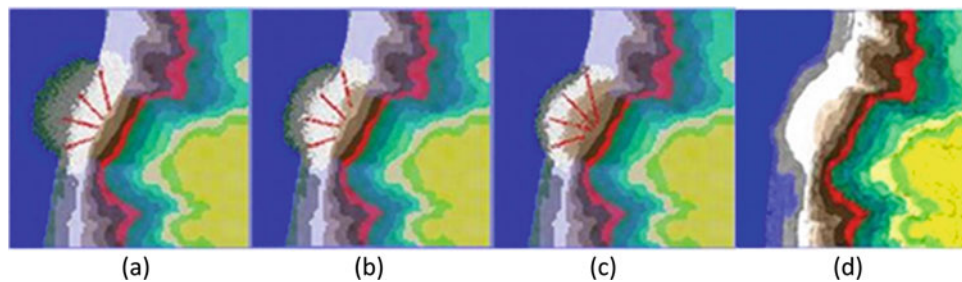


Fig. 13 Results of the parametric study. Rotational friction of **a** 0, **b** 1.0, **c** 2.0 and **d** actual damage

examination in the previous section. A simple model allocated and set sphere elements of 2-m diameter on the slope and the bottom area of non-collapsed area using the same grid coordinates at 2-m intervals as the collapsed soil and sand model. The grid coordinates for the collapsed surface were in 1.0-m intervals, and the friction was set to 0. The slope collapsed by its own weight. Figure 12 shows the initial, analyzed, and reconstructed states in the simulation. Figure 13 shows the partial results of the parametric study related to rotational friction.

We evaluated the simulation results using the RA for the sediment of collapsed soil and sand as an index. To derive the RA for the sediment on a collapsed slope, we used four survey lines (Fig. 14, line 1 to line 4).

Table 2 compares the RA derived from these survey lines and those from the simulations corresponding to the survey lines. The RA increases with rotational friction. For a rotational friction of 0.2, the RA exceeds that of the actual

damage. In contrast, the simulation result with a rotational friction of 0.15 fits the actual slope collapse.

Figure 15 shows the simulation result with a rotational friction as 0.15 and the survey lines. Figure 16 compares the elevation-longitudinal distance relationship between the actual slope collapse and simulation result by each survey line. They agree well.

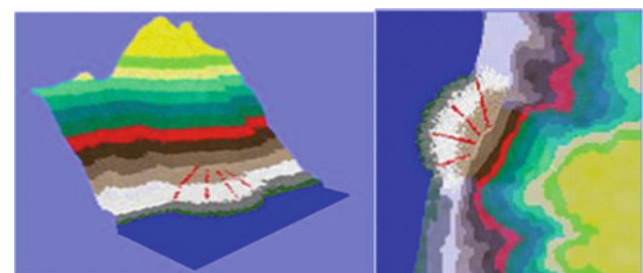
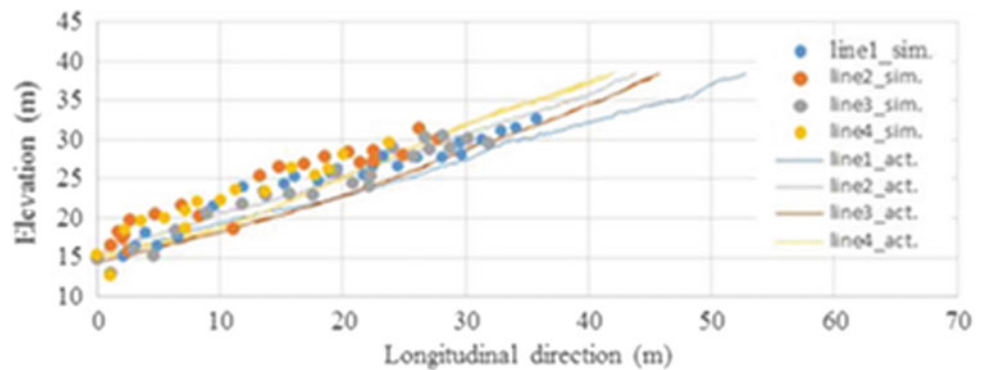


Fig. 15 Simulation results with a rotational friction of 0.15

Fig. 16 Comparison of the elevation-longitudinal distance relationship between the actual slope collapse and simulation result by survey line



Conclusion

To determine the range of practical values of the rotational friction, reproduction analysis using DEM for laboratory experiments was performed to determine the RA of various particles. For the five types of sand particles, an upper limit for the rotational friction range is 0.2.

A parametric study for a bedrock slope collapse of 42,000 m³ was investigated for a rotational friction between 0 and 0.2. The RA after collapse is reasonably reconstructed using a restitution coefficient of 0.1 and a rolling friction of 0.15. This result can be referenced to validate the values of slope collapse simulations for similar bedrock slopes.

Acknowledgements We received tremendous support from the Incorporated Administrative Agency Public Works Research Institute, Civil Engineering Research Institute for Cold Region. In particular, we recognize Dr. Katsuhito Agui.

References

- Cundall PA (1971) A computer model for simulating progressive large scale movement in blocky rocksystem. In: Symposium ISRM, Nancy, Proceedings, vol 2, pp 129–136
- Nakase H, Cao G, Tabei K, Tochigi H, Matsushima T (2015) A method to assess collision hazard of falling rock due to slope collapse application of DEM on modeling of earthquake triggered slope failure. *J Jpn Soc Civ Eng Ser A1 (Struct Eng Earthq Eng (SE/EE))* 71(4):I_476–I_492 (in Japanese)
- Sakaguchi H, Ozaki E, Igarashi T (1993) Plugging of the flow of granular materials during the discharge from a silo. *Int J Mod Phys B* 7:1949–1963
- Tochigi H, Ootori Y, Kawai T, Nakajima M, Ishimaru M (2009) Investigation of influence factor concerned with traveling distance-development of influence area prediction method by shaking table test of slope failure and two dimensional distinct element analysis. Civil Engineering Research Laboratory Rep. No. N08084 (in Japanese)

Part IV

**Recent Development in Soil and Rock Testing
Techniques, Application and Analysis Methods**



2020 Kyoto Japan

Analysis of Shear Strength Variability of Ash-Fall Pyroclastic Soils Involved in Flow-Like Landslides

Rita Tufano, Luigi Annunziata, Enrico Di Clemente, Giovanni Falgiano, Francesco Fusco, and Pantaleone De Vita

Abstract

Rainfall-induced shallow landslides of flow-like type are very common in ash-fall pyroclastic soils originated from explosive activity of the Somma-Vesuvius volcano (southern Italy). Over the last few centuries, these phenomena have frequently affected pyroclastic soil-mantled slopes of mountain ranges that surround the volcano causing hundreds of casualties. Many researches have been focused on this topic, especially after the occurrence of the deadly debris flow events of May 1998, which hit Sarno Mountains causing 160 victims. Among the various aspects studied, aimed at the assessment and mapping of hazard to landslide initiation and propagation, the estimation of shear strength of ash-fall pyroclastic soils still deserves to be advanced. This is especially due to the relevant spatial variability of geotechnical properties which are controlled by complex stratigraphic settings. According to such a research focus, the present paper deals with physical and shear strength laboratory characterizations of ash-fall pyroclastic soils and the estimation of the inherent variability. A total number of 97 direct shear tests, supported by grain size and Atterberg's limits analyses, were carried out. The

high number of tests allowed to perform a statistical analysis based on quantile regression approach and aimed at considering the uncertainty related to the high variability of Mohr–Coulomb's shear strength parameters. The results obtained show values, especially for the drained friction angle (ϕ'), generally higher than those considered in literature. Outcomes of the study and the approach proposed can be conceived as a benchmark for further analyses aimed at the assessment of hazard to initiation of this type of landslides or related physically-based rainfall thresholds.

Keywords

Ash-fall pyroclastic soils • Shear strength parameters • Variability • Quantile regression analysis

Introduction

Shallow landslides triggered by rainfall events occur worldwide and involve different soil types covering bedrock. The hazard related to the occurrence of such phenomena is generally very high, inducing a high risk condition in areas characterized by an extensive urbanization (Sidle and Ochiai 2006). Significant and world-wide known examples are flow-like mass movements that periodically involve the ash-fall pyroclastic soil mantled slopes of peri-Vesuvian carbonate mountains, such as Sarno-Avella-Salerno and Lattari in Campania Region (southern Italy). As a matter of fact, ash-fall pyroclastic soils mantling these mountain slopes are highly susceptible to landslide onset under prolonged rainfall followed by intense rainstorms (Fiorillo and Wilson 2004; Napolitano et al. 2016).

Different consecutive evolutionary stages characterize these flow-like movements: (1) initial debris slide (soil slip) (Campbell 1974), involving a few tens of cubic meters of ash-fall pyroclastic soils; (2) debris avalanche (Hungr et al.

R. Tufano (✉) · E. Di Clemente · F. Fusco · P. De Vita
Department of Earth, Environmental and Resources Sciences (DiSTAR), University of Naples "Federico II", Naples, Italy
e-mail: rita.tufano@unina.it

E. Di Clemente
e-mail: enrico.diclemente@unina.it

F. Fusco
e-mail: francesco.fusco@unina.it

P. De Vita
e-mail: padevita@unina.it

L. Annunziata · G. Falgiano
External Collaborator, Naples, Italy
e-mail: gigiannu93@gmail.com

G. Falgiano
e-mail: giannifal1610@gmail.com

2014) that widens the depleted mass and volume along the slope; (3) debris flow (Revellino et al. 2004; Hungr et al. 2014), when the flow-like landslide channelizes into the hydrographic network. The initial debris slide is always present and may evolve directly into a debris flow or into a debris avalanche only.

The most recent and deadly events occurred in May 1998 along slopes of Sarno Mountains caused 159 casualties and damaged severely four towns (Bracigliano, Quindici, Sarno and Siano) located at the footslope of Mount Pizzo d'Alvano (Bilotta et al. 2005).

Several factors related to local surficial geology, geomorphology, hydrology and topography have been considered as fundamental in controlling hazard to the initiation this type of mass movements. Among these factors, also geotechnical properties of ash-fall pyroclastic soils were recognized as very relevant. Therefore, several studies tackled with this topic trying to manage complex stratigraphic settings and spatial variability of geotechnical properties (Cascini et al. 2005; De Vita et al. 2013).

In such a scientific framework, the present study is focused on the assessment of shear strength of ash-fall pyroclastic soils covering Sarno Mountains by a high number of laboratory tests to consider statistically the inherent variability. In fact, due to the high grain size heterogeneity as well the low stress condition, related to the shallow depth, the estimation of shear strength in these soils is often challenging as well as unclear the interpretations of results of laboratory tests. To consider the uncertainty related to results of direct shear tests, a quantile regression analysis was carried out for the shallower soil horizon, which is the most involved in the initial failure. The proposed approach and the results obtained advance the characterization of shear strength of ash-fall pyroclastic soils, representing potentially a benchmark for the setting of distributed landslide hazard and stability models or physically-based rainfall thresholds.

Geological Setting

Sarno, together with Lattari, Avella and Salerno Mountains, belong to the westernmost sector of the Apennines Chain and face at a short distance (10–20 km) the Somma-Vesuvius volcano. These mountain ranges are formed by Mesozoic carbonate platform series which were thrust during the Miocene compressive tectonic events over the external palaeogeographical units. Subsequently they were faulted during the Quaternary by extensional tectonic phases (Vitale and Ciarcia 2018). During Quaternary, ash-fall pyroclastic deposits derived by the explosive volcanic activity of Somma-Vesuvius and Phlegrean Fields volcanoes covered discontinuously these mountain ranges

(Rolandi et al. 1998, 2000). The older volcanic deposits, mainly represented by ash-flow deposits of Ignimbrite, pumices and ashes, erupted by the Phlegrean Field volcanoes (39 k-years), form the “Ancient Pyroclastic Complex” (APC), while the younger products, mainly associated to Somma-Vesuvius explosive activity, form the “Recent Pyroclastic Complex” (RPC) (Rolandi et al. 2000).

The most important eruptions associated with RPC are: Codola eruption, 25 k-years B.P. (Rolandi et al. 2000); Sarno eruption, 17 k-years B.P. (Rolandi et al. 2000); Ottaviano eruption, 8.0 k-years B.P. (Rolandi et al. 1993a); Avellino eruption, 3.6 k-years (Rolandi et al. 1993b); Pompei eruption, A.D. 79 (Lirer et al. 1973); A.D. 472 (Rolandi et al. 1998) and A.D. 1631 eruption (Rosi et al. 1993). Along slopes, complete volcanoclastic series were observed in the most conservative area only, which are characterized by slope angle values lower than 30°, while elsewhere they appear incomplete due to the action of the denudational processes. Due to this phenomenon, thicknesses of the ash-fall pyroclastic soil mantle range from maximum values, varying from 7 to 4 m in the slope angle range lower than 30°, to zero for slope angle values greater than 50° (De Vita et al. 2006a, 2013).

Volcanoclastic series along slopes have a greater complexity due to the alternation of unweathered ash-fall soil and pedogenized horizons (paleosols). In particular, considering the principal pedogenetic soil horizons (USDA 2014), lithostratigraphic features and USCS soil classification system, a typical stratigraphic setting can be recognized (De Vita et al. 2006b) as formed by: (1) A soil horizon, consisting of abundant humus (Pt); (2) B soil horizon, mainly characterised by pumiceous clasts highly subjected to pedogenetic processes (SM); (3) C soil horizon, formed by pumiceous pyroclasts, weakly weathered (GW or GP); (4) B_b horizon, corresponding to a B horizon buried by a successive depositional event and thus considerable as a paleosol (SM); (5) C_b soil horizon, representative of a buried C horizon (GW or GP); (6) B_b_{basal} soil horizon, corresponding to a residual pyroclastic deposit, highly weathered by pedogenesis (SM); (7) R horizon, consisting of fractured carbonate bedrock with open joints filled by the overlying paleosol, for the first few meters and below by air.

Data and Methods

Undisturbed and disturbed soil samples were taken at different depths in exploratory trenches, dug at the top of main scarps of four landslides (F1, F2, F3 and F4) triggered on May 1998 (Fig. 1). In particular, two sets of samples were collected for geotechnical characterizations at different depth ranges: 17 samples were taken from 1.10 to 1.30 m (B soil horizon); 18 samples were collected from 2.00 to 2.50 m

(C–Bb soil horizons). Undisturbed sampling was carried out by pushing into the soil surface cubical steel boxes (12 cm side) with an open face and a basal cutting edge. Stratigraphic setting observed in the exploratory trenches (Fig. 1) confirmed the existence of a volcanoclastic series corresponding to that described in previous studies (De Vita et al. 2006b, 2013).

Geotechnical index properties were determined by means of standard laboratory procedures: specific gravity of solid particles (G_s) (ASTM D854), grain size analysis by means of both sieving and sedimentation methods (ASTM D421 and ASTM D422), Atterberg's limits (w_L and w_P) and Plasticity Index ($PI = w_L - w_P$) (ASTM D4318). Porosity (n) and void ratio (e) were also estimated. 97 standard direct shear tests (ASTM D3080) were carried out to estimate the drained Mohr–Coulomb's shear strength parameters, c' and ϕ' . All shear tests were performed on standard specimens with dimensions of $60 \times 60 \times 24$ mm. Values of drained normal stress (σ') were set around that estimated at the depth of sampling and considering variations corresponding to depth steps of 0.20 m. Due to grain size heterogeneity affecting the same soil horizon, and specifically for the occurrence of a small fraction of lapilli found both in the B and Bb soil horizons, tangential stress (τ) values at the failure resulted significantly variable for the same σ' interval. Dilatancy effects and crushing of coarse lapilli pyroclasts were recognized as mainly controlling this variability and therefore values of drained friction angle (ϕ') and intercept drained cohesion (c').

To consider uncertainty related to high spatial variability of shear strength and generalize results derived by sampling in different areas, results of laboratory tests were aggregated

for the same soil horizon and analysed by a quantile regression approach.

Finally, a comparison of results obtained with those proposed in literature by various authors (Crosta and Dal Negro 2003; Bilotta et al. 2005; Cascini et al. 2005; De Vita et al. 2013) for ash-fall pyroclastic of Sarno Mountains was carried out.

Results

Results of grain size analysis, by wet sieving standard procedures of American Society for Testing and Materials and consistency limits are shown in Fig. 2. The grain size curves present a significant variability for each soil horizon due to heterogeneity of the analysed samples, even if belonging to the same soil horizon. In general, considering all samples, the gravel fraction ranges from 8.8 to 79.6%, sand fraction from 20.4 to 69.4%, silt fraction from 0.0 to 32.2% and clay fraction from 0.0% to 3.0%. These results confirmed the negligible presence of clay fraction which, accounting also for results of consistency limits (Fig. 2), allowed to consider these soils as non-plastic. Moreover, by USCS—Unified Soil Classification System (Stevens 1982), sampled soils were classified as Silty Sand (SM), for B and Bb soil horizons, and as Gravel with Sand, from well graded (GW) to poor graded (GP), for lapilli C soil horizons.

Considering field recognitions about the prevailing involvement of B soil horizon in the development of the landslide surface of rupture, as well as the feasibility of undisturbed sampling, the most part of samples were collected for B and Bb soil horizons. While only disturbed

Fig. 1 Study area: location of landslides F1, F2, F3 and F4 and photographs of exploratory trenches

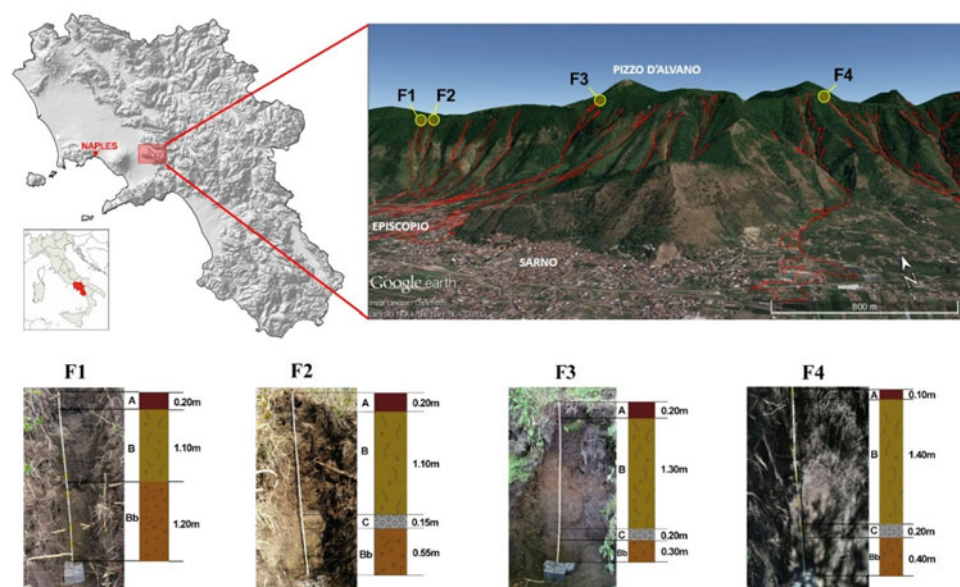
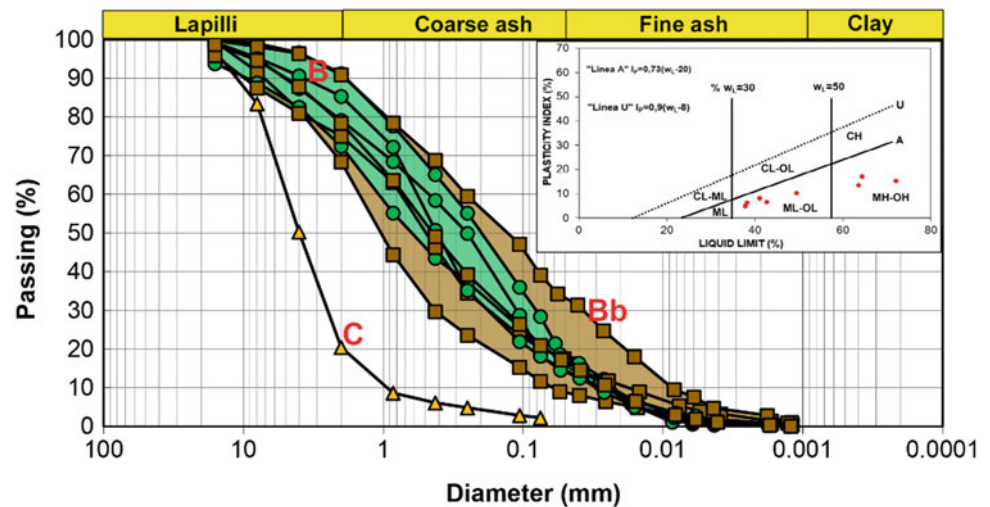


Fig. 2 Grain size and consistency limits of volcaniclastic soil horizons (B, C and Bb horizon) sampled at landslides F1, F2, F3 and F4



samples were collected for lapilli C horizon. Consequently, τ - σ' plots to estimate Mohr–Coulomb envelopes, for B and Bb soil horizons, were based on a high number of data, much greater than three, as it is recommended at least by standard procedure. Result values of σ' and τ data obtained for each soil horizons of each landslide were aggregated to perform different linear regression analyses, thus allowing to assess variability of c' and ϕ' (Table 1). Due to extreme cohesionless of lapilli soil horizon, direct shear tests were carried out on disturbed samples only, which were reconstituted in laboratory at the same value of void ratio as estimated in the other experimental field and laboratory determinations (De Vita et al. 2013).

The results obtained show values of ϕ' ranging from 38.5° to 53.6° , for B horizon, and from 31.0° to 61.2° for Bb soil horizon. In some cases, results appear very high due to the presence of coarse lapilli pumiceous pyroclasts, which caused crushing and dilatancy phenomena. To confirm such a finding, a consistent linear empirical relationship ($R^2 = 0.7511$) was found between drained friction angle (ϕ') and the sum of gravel and sand grain size fractions, which showed a control of grain size on shear strength. A unique

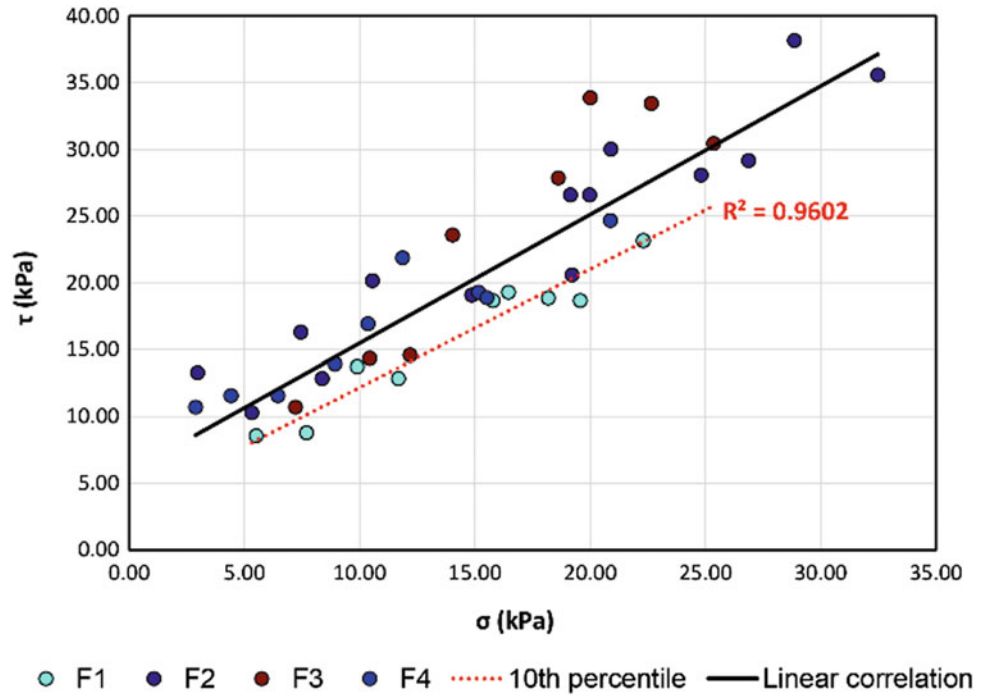
value of 70.1° was estimated for reconstituted samples of lapilli C soil horizon. This very high value was interpreted as being related to dilatancy effect due to both coarse grain sizes and low stress levels considered in testing.

Drained cohesion (c') was found ranging from 1.47 to 8.14 kPa for B soil horizon, and from 5.39 to 9.61 kPa for Bb soil horizon. Due to the general cohesionless behaviour of these soil horizons, the not negligible values of c' were attributed to both reinforcement of root apparatuses and effect of crushing of lapilli pumiceous pyroclasts. Instead, a very high value of 32.75 kPa was found for the drained cohesion (c') of the lapilli C soil horizon. This result, apparently very anomalous for a typical cohesionless soil, was understood as due to the effect of intercept (apparent) cohesion, caused by the crushing of lapilli pumiceous pyroclasts and favoured by the interlocking and angular shape of grains (Mitchell and Soga 2005). Due to the limited number of direct shear tests carried out on C soil horizon as well as the effect of scale factor related to the limited dimensions of the shear box in comparison to grain sizes, results obtained were considered with a lower reliability and not useful for any slope stability calculations.

Table 1 Values of Mohr–Coulomb's shear strength parameters obtained by unique regression analyses carried out on results obtained by N tests for samples taken in landslide crowns of four landslides (F1, F2, F3 and F4) and different soil horizons (B, C and Bb). The sample ID is made by joining the landslide and soil horizon identifications. Depth of sampling is also shown

ID	Depth (m)	N	c' (kPa)	ϕ' ($^\circ$)
F ₁ -B	1.30	9	3.63	40.70
F ₂ -B	1.20	14	8.14	41.18
F ₃ -B	1.30	10	1.47	53.61
F ₄ -B	1.10	11	8.04	38.49
F ₂ -C	1.30	9	32.75	70.12
F ₁ -B _b	2.50	12	6.67	61.23
F ₂ -B _b	2.00	11	5.39	56.30
F ₃ -B _b	2.00	9	8.43	31.02
F ₄ -B _b	2.10	12	9.61	49.02

Fig. 3 Results of direct shear tests carried out on B horizon for F1, F2, F3 and F4 landslides. The continuous black line indicates the unique linear correlation related to all data, while the dotted red line shows quantile regression analysis (10th percentiles)



However, due to the wide range of variability of shear strength parameters, a quantile regression analysis was attempted to elaborate results of 44 direct shear tests obtained for B soil horizon. The latter is the most involved in initial landslides phenomena and therefore is considered as the most representative in this study.

In particular, a quantile regression analysis was carried out considering the 10th percentile (Fig. 3). Such a low percentile value was conceived as representative of lower values of shear strength occurring in zones with finer grain sizes, thus to take into account spatial variability of shear strength by a conservative approach. The results obtained show values of drained friction angle $\phi'_{10th} = 41.5^\circ$ and drained cohesion $c'_{10th} = 3.24$ kPa.

Finally, a comparison with results of Mohr–Coulomb’s shear strength parameters known in literature (Crosta and Dal Negro 2003; Bilotta et al. 2005; Cascini et al. 2005; De Vita et al. 2013) was performed (Table 2). Values of drained friction angle (ϕ') related to B, C and Bb soil horizons, resulted always the highest, except for the case of Crosta and Dal Negro (2003) and particularly for the soil horizon that Authors identified as characterized by clay accumulation (B_t) and with little or no apparent illuvial accumulation of materials (B_w). In these cases, Crosta and Dal Negro (2003) indicated a range of drained friction angle (ϕ') that in both cases includes the experimental values obtained in this research for the B soil horizon by quantile regression analysis at the 10th percentiles. Differently, drained cohesion (c')

Table 2 Comparison between Mohr–Coulomb’s shear strength parameters estimated in this study (for B horizon—quantile regression at the 10th percentile) and literature data. De Vita et al. (2013) considered c'_{10th} and ϕ'_{50th} . Class “A” in Bilotta et al. (2005) and Cascini et al. (2005) means ashy soils with a finer grain size distribution, while class “B” ashy soils with higher porosity values and lower specific gravity. In Crosta and Dal Negro (2003), B_b stands for buried horizons, B_t for clay accumulation and B_w for little or no apparent illuvial accumulation of materials

	Horizon	c' (kPa)	ϕ' ($^\circ$)
This research	$B_{10th\ perc}$	3.33	41.5
	C	32.75	70.1
	Bb	7.65	49.4
De Vita et al. (2013)	B	5.00	32.0
	C	0.00	37.0
	Bb	3.43	34.0
Bilotta et al. (2005)	Class “A”	<2.94	30.0–35.0
	Class “B”	<2.94	36.0–41.0
Cascini et al. (2005)	Class “A”	4.90–15.00	32.0–35.0
	Class “B”	0.00–4.90	36.0–41.0
Crosta and Dal Negro (2003)	B_b	34.02	38.5
	B_t	0.00–15.00	37.8–44.9
	B_w	10.00–18.34	35.5–45.9

values resulted by this research match better with values known in literature (Table 2).

Conclusion

Physical and shear strength characterizations of ash-fall soils involved in rainfall-triggered shallow landslides represent a crucial aspect for advancing the assessment of hazard to slope instability initiation. Several attempts were made in literature to estimate reference values for Mohr–Coulomb’s shear strength parameters even if results obtained up to now appear affected by a high variability due soil heterogeneity and difficult sampling. According to such a focus, this research is aimed at advancing the characterization of shear strength for these soils also considering the inherent variability related to grain size heterogeneity of the same soil horizon. Preliminary results of direct shear tests have highlighted a relevant variability, confirming the complex behaviour of these soils. In this research a quantile regression analysis is proposed as a possible approach to manage variability of shear strength by a conservative approach. The obtained results can be considered consistent due to the high number of data and potentially advancing the assessment of hazard to landslide initiation by slope stability distributed modelling or the assessment of physically-based rainfall thresholds.

References

- Bilotta E, Cascini L, Foresta V, Sorbino G (2005) Geotechnical characterisation of pyroclastic soils involved in huge flowslides. *Geotech Geol Eng* 23(4):365–402
- Campbell R (1974) Soil slips, debris flows and rainstorms in the Santa Monica Mountains and vicinity, Southern California. In: USGS professional paper, vol 851. U.S. Geological Survey, Washington, p 51
- Cascini L, Cuomo S, Sorbino G (2005) Flow-like mass movements in pyroclastic soils: remarks on the modelling of triggering mechanisms. *Riv Ital Geotec* 4:11–31 (in Italian)
- Crosta GB, Dal Negro P (2003) Observations and modelling of soil slip-debris flow initiation processes in pyroclastic deposits: the Sarno 1998 event
- De Vita P, Agrello D, Ambrosino F (2006a) Landslide susceptibility assessment in ash-fall pyroclastic deposits surrounding Mount Somma-Vesuvius: application of geophysical surveys for soil thickness mapping. *J Appl Geophys* 59:126–139
- De Vita P, Celico P, Siniscalchi M, Panza R (2006b) Distribution, hydrogeological features and landslide hazard of pyroclastic soils on carbonate slopes in the area surrounding Mount Somma-Vesuvius (Italy). *Ital J Eng Geol Environ* 1:1–24
- De Vita P, Napolitano E, Godt JW, Baum RL (2013) Deterministic estimation of hydrological thresholds for shallow landslide initiation and slope stability models: case study from the Somma-Vesuvius area of southern Italy. *Landslides* 10(6):713–728
- Fiorillo F, Wilson RC (2004) Rainfall induced debris flows in pyroclastic deposits, Campania (southern Italy). *Eng Geol* 75(3–4):263–289
- Hungr O, Leroueil S, Picarelli L (2014) The Varnes classification of landslide types, an updated. *Landslides* 11:167–194
- Lirer L, Pescatore TS, Booth B, Walker JPL (1973) Two plinian pumice-fall deposits from Somma-Vesuvius. *Geol Soc Am Bull* 84:759–772
- Mitchell JK, Soga K (2005) *Fundamentals of soil behavior*, 3rd edn. Wiley, 592 p
- Napolitano E, Fusco F, Baum RL, Godt JW, De Vita P (2016) Effect of antecedent-hydrological conditions on rainfall triggering of debris flows in ash-fall pyroclastic mantled slopes of Campania (southern Italy). *Landslides* 13(5):967–983
- Revellino P, Hungr O, Guadagno FM, Evans SG (2004) Velocity and runout simulation of destructive debris flows and debris avalanches in pyroclastic deposits, Campania region, Italy. *Environ Geol* 45(3):295–311
- Rolandi G, Mastrolorenzo G, Barrella AM, Borrelli A (1993a) The Avellino plinian eruption of Somma-Vesuvius (3760 y.B.P.): the progressive evolution from magmatic to hydromagmatic style. *J Volcanol Geotherm Res* 58:67–88
- Rolandi G, Maraffi S, Petrosino P, Lirer L (1993b) The Ottaviano eruption of Somma-Vesuvio (8000 y B.P.): a magmatic alternating fall and flow forming eruption. *J Volcanol Geotherm Res* 58:43–65
- Rolandi G, Petrosino P, McGeehin J (1998) The interplinian activity at Somma-Vesuvius in the last 3500 years. *J Volcanol Geotherm Res* 82:19–52
- Rolandi G, Bartolini F, Cozzolino G, Esposito N, Sannino D (2000) Sull’origine delle coltri piroclastiche presenti sul versante occidentale del Pizzo d’Alvano. *Quad Geol Appl* 7–1:213–235
- Rosi M, Principe C, Vecchi R (1993) The 1631 Vesuvius eruption. A reconstruction based on historical and stratigraphical data. *J Volcanol Geotherm Res* 58:151–182
- Sidle RC, Ochiai H (2006) *Landslides: processes, prediction, and land use*, vol 18. American Geophysical Union
- Stevens J (1982) Unified soil classification system. *Civ Eng ASCE* 52(12):61–62
- USDA (2014) *Keys to soil taxonomy*, 12th edn. United States Department of Agriculture Natural Resources Conservation Service, 372 pp
- Vitale S, Ciarcia S (2018) Tectono-stratigraphic setting of the Campania region (southern Italy). *J Maps* 14(2):9–21



Comparison of Soil Parameters and Soil Moduli E_{50} and E_{70} of Residual Soils Used in Stability Analysis

L. K. N. S. Kulathilake, E. H. N. Premasiri, and A. A. Virajh Dias

Abstract

Soil moduli E depends on soil skeleton, particle shape and size, void ratio, moisture content, dry density and stress history. Residual soil contains more silica with inorganic clay compounds and soil structure depends on its parent rock and weathering state. Undisturbed soil samples were collected from two different rainfall precipitation zones of 2500 mm and above 5000 mm subjected to frequent cycles of wetting and drying. Our study explored the numerical relationships between standard soil physical properties such as void ratio, dry density and the elastic parameters such as Young's moduli, E and secant moduli E_{50} and E_{70} of residual soil. We found that void ratio and dry density are fully dependent on formation characteristics of their parent materials and strongly impact on soil Young's moduli, E and secant moduli, E_{50} and E_{70} . The soil moduli of residual soil with void ratio and dry density relationships were derived. However, soil dry density had less influence than the void ratio. The study indicates

residual soil is subjected to different precipitation and can have the same dry density but different soil skeleton, like loose or dense, and thus have different moduli. This may help in the evaluation of complex forms of slope instability.

Keywords

Residual soil • Elastic behaviour • Secant moduli • Void ratio • Consolidated undrained strength

Introduction

Landslide are a major hazard in hill slopes and occur frequently in slopes of less than 36° and above 17° (Bhandari et al. 1992) in Sri Lanka. Frequent slope failure along the road cut is significant if the cut slope angle exceeds 45° (Herath et al. 2014). Stability models used to investigate cut slope performance commonly require five major parameters. These are: E and ν (Poisson's ratio of soil) for linear elastic behaviour; c and ϕ for yield function, and ψ as dilation angle for plastic deformation behaviour (Phien-wej et al. 2012). The variation of soil module E for residual soils in areas with different rainfall characteristics is a research project registered as an IPL 155 of the International Programme of Landslides, during 2012. Failures of residual earth cutting along the road networks are increasing (Herath et al. 2014) and, in some areas their height exceed 15 m (Fig. 1) making their failure a significant risk to road users. Therefore, determining accurate elastic deformity parameters of soil with different soil density, void ratio and strength characteristics are considered essential to better understand their potential stability.

A A Virajh Dias, former AGM NRMS&LS, Central Engineering Consultancy Bureau (CECB), No 500, T B Jaya Mawatha, Colombo 10, Sri Lanka.

L. K. N. S. Kulathilake (✉) · E. H. N. Premasiri
Natural Resources Management & Laboratory Services
(NRM&LS), Central Engineering Consultancy Bureau (CECB),
No. 11, Jawatta Road, Colombo, 05, Sri Lanka
e-mail: nimanikulathilake@gmail.com

E. H. N. Premasiri
e-mail: ephnavoda@yahoo.com

A. A. Virajh Dias
Integrated Watershed and Water Resources Management Project
(IWWMP), Ministry of Mahaweli, Agriculture, Irrigation and
Rural Development, No 500, T B Jaya Mawatha, Colombo, 10, Sri
Lanka
e-mail: aavirajhd@yahoo.com



Fig. 1 Roadside residual soil overlaying with completely weathered rock (soil height is almost 18 m high)

Parameters and Residual Soil Origins

Rainfall and Slope Failure Records

Rainfall in Sri Lanka is influenced by two monsoons, resulting in two distinct monsoon seasons and two inter-monsoonal seasons. The monsoonal, rain from the South-West typically falls between May and September, and North-East monsoonal rain falls from December to February. The inter monsoonal periods are usually occur between March and April and between October and November. These periods are characterised by light, variable winds and evening thundershowers. During late 1980s, when limited records are available, the landslide triggering threshold was estimated at 200 mm of rainfall in a 72-h period, provided rain in the area continued (Bhandari et al. 1992). However, with improved rainfall data the conditional probability of landslide occurrences as a ratio of rainfall intensity of the month of the landslide event and average monthly rainfall of the place against average monthly rainfall intensity (Bhandari and Dias 1996) criterion worked only partially, in cases of reactivation of recent, seasonally active landslides (Mallawarachchi et al. 2014). A relationship of rainfall records of a very large number of landslides conveys that 24 h rainfall associated with a landslide event was generally 2–23 times higher than average daily rainfall (Bhandari and Dias 1996).

Elastic Behaviours of Residual Soil

One of the most important recent advances in geotechnical engineering is the realisation and acceptance of the fact that the stress strain behaviour of almost all soils is non-linear (Fahey 1999). Therefore, evaluation and comparison of non-linear stress–strain response in the soil has been

accepted for evaluation of slope stability. Such factors provide a valuable contribution to numerical simulations of slope stability. Infiltration of rainwater into a residual soil slope may also influence slope stability by modifying the pore-water pressure in the soil (Rahardjo et al. 2005). Usually unsaturated residual soils experience high matric suction (i.e., negative pore-water pressure) during dry periods, which results in an indirect increase in soil strength. Therefore, the elastic moduli of a residual soil may have a very high value during dry periods which may reduce rapidly during rainstorms. The Young's modulus of the soil appears to increase with increasing net normal stresses and increasing matric suctions (Rahardjo et al. 2011).

However, at low strain levels, these soils behave like cemented soils as the stiffness of the skeleton is mainly controlled by the presence of weak bonds between particles caused by the presence of oxides and sesquioxides, and matric suction (Francisca and Bogoda 2019). Deformities of soil are indicated with propagation of “riedel shears” and field observations of exceedance of elastic strain (Figs. 2 and 3).

Riedel shears show systematic variation of the stress–strain boundary of a failure and exceedance of elastic strain of soil indicates by propagation of riedel shear marks at the stress boundary of a failure as an evidence at the field.

Methodology

The stress–strain characteristics of a soil is essential for the estimation of its response to external overloading. The stress–strain curve obtained from laboratory tests is the basis to determine soil parameters that characterize soil stiffness: the elastic modulus corresponding, in a sense, with Young's modulus E , as in the case of soil the stress–strain

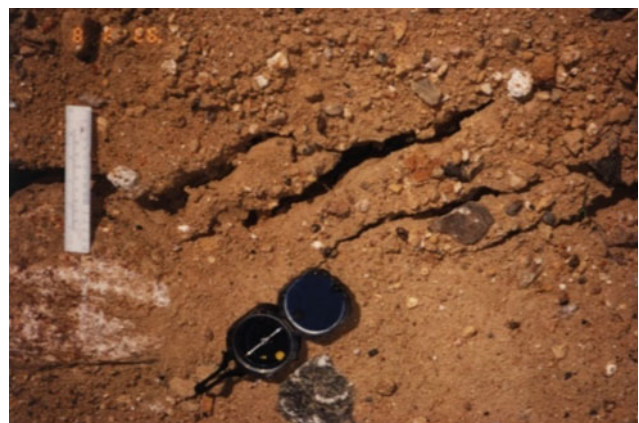


Fig. 2 Observations of exceedance of soil elastic strain at site and initiation of “Riedel shear marks” in a landslide before catastrophic failure event

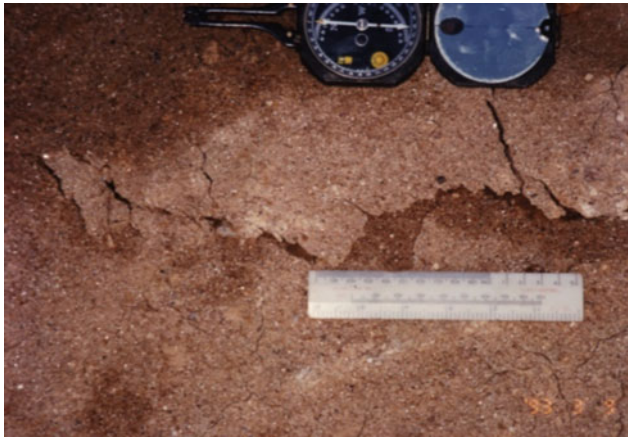


Fig. 3 Exceedance of elastic stain of soil at site boundary of a first time occurrence of landslide and before failure

relationships are not linear and the deformation is of elasto-plastic character. Numerical interpretation of the determination of E_{50} is shown in Fig. 4.

The Young's secant undrained modulus E_{50} is determined from the stress–strain curve of the consolidated undrained shearing tests, according to the relationship,

$$E_{50} = \frac{\partial \sigma}{\partial \epsilon_{50}} \quad (1)$$

where, $\delta \sigma$ is the change of vertical stress and $\delta \epsilon_{50}$ is the corresponding strain at stress equal 50% of peak strength value. Similarly, E_{70} is calculated in corresponding to the

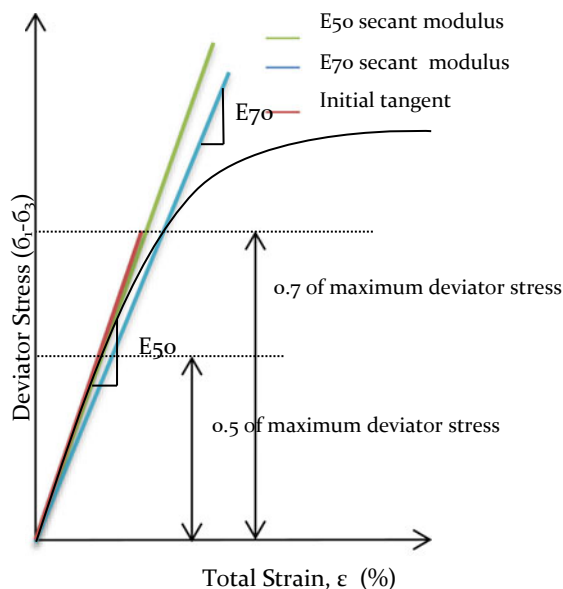


Fig. 4 Interpretation of moduli, E_{50} , E_{70} and E in a standard stress–strain plot in CU triaxial test

70% of the peak strength value and the initial tangent is the gradient of the line drawn to the initial part of the stress–strain curve.

Results and Discussion

Residual Soil Strength Parameters, C' , ϕ'

In residual soils, grain size distribution has a significant influence on internal friction and percentage of clay, silts and sand particles which could drastically change the properties exhibited by the sample. Drained or undrained triaxial shear and drained direct shear test are generally considered as the most appropriate laboratory tests to determine shear strength characteristics of soils. The preliminary finding of the study as shown in Table 1 (Mallawarachchi et al. 2014) indicates that the mechanical behavior of residual soils at high strain levels is mainly controlled by the degree of weathering, the initial void ratio and the effective stress (Francisca and Bogoda 2019).

Interpretation of E_{50} , E_{70} of Residual Soils

The study determined E_{50} (secant moduli) and E_{70} as an experiment setup to understand the behaviour of residual soils under changing stress conditions at site. Twenty-nine silty clay or sandy clay residual soil samples were collected from study sites of Watawala, Koslanda, Nuwara Eliya Landslide areas (>5000 mm) and Colombo and Sub regions (>2500) and used in a series of triaxial experiments. The number of soil samples collected from study sites are shown in Table 2.

The measurements of E , E_{70} , E_{50} (secant moduli), void ratio (e_0), dry density and frictional parameters (cohesion and friction angle) were determined according to the BS 1377 and corresponding results are shown in Figs. 5, 6, 7, 8, 9 and 10.

At the initial stage of the stress–strain curve is nearly linear dependence, but elastic strain of soils is a very small due to overall value of the strain. Therefore, initial tangent moduli is not frequently used in numerical model studies in many soils compared to secant moduli of E_{50} and E_{70} .

The secant moduli of E_{50} and E_{70} is widely used in many numerical analysis and those are showing reasonable relationship with dry density and the void ratio. Void ratio, which is directly related to packing characteristics of geo-materials, has a strong impact on soil Young's moduli, E_{50} . It is also noted that the influence of void ratio can be taken into account by using an empirical void ratio function considering the values of E_{50} and E_{70} both. The study made

Table 1 Some of the recorded parameters of residual slope failures in different precipitation regions

Rainfall precipitation zone (ave annual)	Cohesion C'	Friction ϕ'	E ₅₀ (at EC 100 kPa–120 kPa) kN/m ²	e _o (void ratio)
Balangoda to Bandarawela >2500 <4000 mm	25	31	39,290	0.84
Koslanda landslide >4000 mm	16	31	41,960	0.81
Gampola to Nuwara Eliya >4000 mm	13	33	35,180	0.94
Watawala landslide >5000 mm	9	32	10,710	1.15
Colombo sub region earth cuts, deep excavation pits >2000 and <3000 mm	17	35	56,900	0.79
	5	31	25,720	0.64
	7	34	11,910	1.35

Table 2 Number of samples collected from study sites

Precipitation zone	Study sites	No of samples tested
Zone 1 (Avg. annual rainfall >5000 mm)	Watawala	06
	Koslanda	05
	Nuwara Eliya	05
Zone 2 (Avg. annual rainfall >2500 mm and <3000 mm) -Colombo and sub regions	Akuregoda	06
	Kadawatha	03
	Mirigama	04

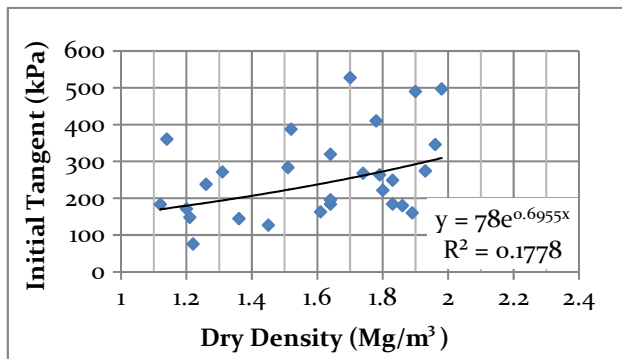


Fig. 5 Exponential relationship of dry density versus initial tangent

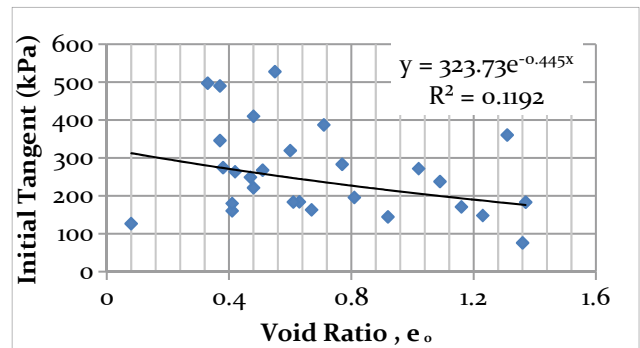


Fig. 6 Exponential relationship of initial void ratio, e_o versus initial tangent

an attempt to define a comparison between the void ratio and the elastic parameters as shown in Figs. 6, 8 and 10.

Recent findings indicate that residual soil samples can have the same dry density but different soil skeleton such as loose or dense, and thus have different moduli (Francisca and Bogoda 2019). If the soil has been subjected to stress in the past, it will impact the modulus. An over-consolidated soil will generally have a higher modulus than the same normally-consolidated soil (Briaud 2001).

Water content also impacts moduli. At low water content levels, the water binds the particles, increases the stress and suction between the particles and leads to a high soil

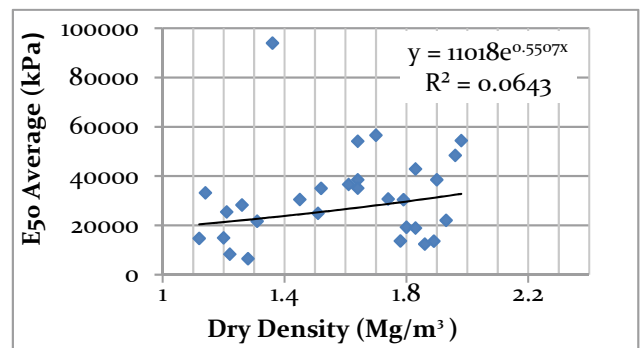


Fig. 7 Exponential relationship of dry density versus average E₅₀

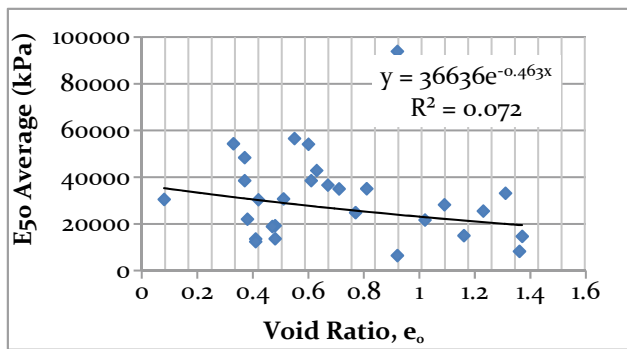


Fig. 8 Exponential relationship of initial void ratio e_0 versus average E_{50}

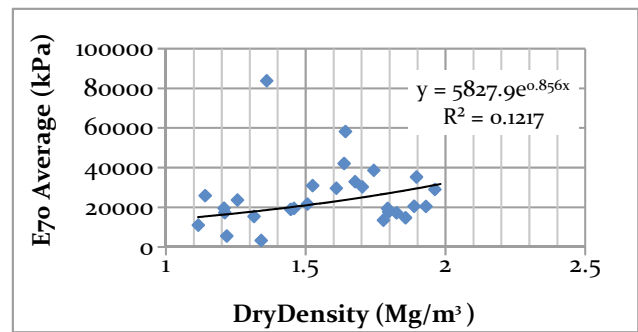


Fig. 9 Exponential relationship of dry density versus average E_{70}

modulus. The effective confining pressure increases E_{50} also significantly as in Fig. 11.

Visual characteristics of samples differ significantly from each other and an attempt have been made to group or classify the samples of residual soils, but most of them are classified as a Silty Sand (SM) or Inorganic Silts (silty or clayey fine sand with slight plasticity, ML) according to the Unified Soil Classification System.

In addition, composition of clay mineralogy and texture were visually assessed using standard method (BS standards 1377, 1990) which provides a basis for dividing residual soils into many groups that can be expected to have fairly similar engineering properties.

Collected residual soil samples usually has a yellow to brown or brown to red in colour due to mineralogical weathering of feldspar, and other parent rock formations. Soil also contains Mica (silicate minerals), known as sheet silicates because they form in distinct layers. Micaceous particles are fairly light and relatively soft, and the sheets and flakes of mica are flexible and give relatively low strength during testing.

Residual soil has coarse grain soil structure and, if water content rises too much during rainfall, the particles may get pushed apart and generate excess porewater pressures in the

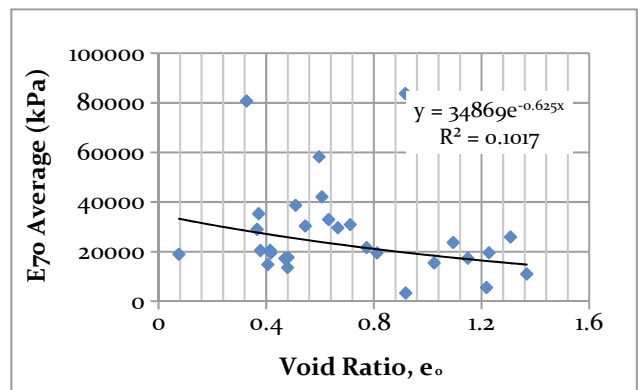
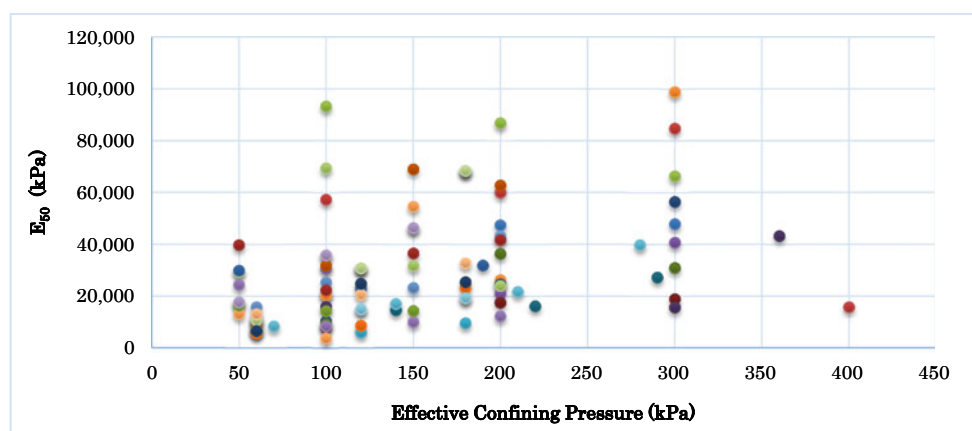


Fig. 10 Exponential relationship of initial void ratio, e_0 versus average E_{70}

soil thus reducing the effective stress and the modulus (Rahardjo et al. 2005) and also making the slope more susceptible to failure. However, angle of internal friction will increase due to coarse fraction of soil skeleton and its integrity and increase stability in the other way. Samples also contain more sand and silt fraction compared to inorganic forms of low activity clays. Therefore, structural integrity of the soil skeleton significantly influences both from absorbed water due to lacy mineralogy and mica.

Fig. 11 Interpretation of E_{50} under different effective confining pressure in residual form of soils. Each colour represent a specific site location of residual soil sample



It was difficult to replicate the soil stress and strain history during the experiments. Stress history is created mainly due to soil deposition, rainfall precipitations, movement of soils, unloading effects and re-loading effect caused by erosion etc. The stresses in the past due to various deformities, loading and unloading, will impact the modulus.

Conclusions and Recommendations

In this study, the relative relationship between soil physical properties (void ratio, e_0 , degree of saturation, and confining pressure), and the soil elastic moduli E , E_{50} and E_{70} has been considered for a variety of residual soils samples collected from two different precipitation zones of Sri Lanka.

The study focused on two major categories of residual soils, quartz silt (silty sand, SM) and inorganic clayey silts (silty or clayey fine sand with slight plasticity, ML). According to the results presented, it can be observed that each void ratio function can only be applied for a certain type of residual soil (minimum to be satisfied with soil structure, moisture content, dry density gradation and plasticity properties). The results do have a strong interdependence of e_0 and secant moduli of E_{50} and E_{70} and not with the shear strength parameters. It is noted that void ratio and dry density are fully dependent on formation characteristics of geo-materials and has a strong impact on soil Young's moduli, E , E_{50} and E_{70} . However, dependence of dry density shows relatively low consistence compared to the void ratio. Residual soils are subjected to different precipitation may have the same dry density but different soil skeleton, like loose or dense, and thus have different moduli. In practice, soils may have undergone various complex stress history which has not been taken in to account during this study. Therefore, further study on such issues has been recommended with different state of stress and fully saturated soils. However, findings of moduli E_{50} and E_{70c} will account for evaluation of complex forms of slope stability problems in residual soil.

Acknowledgements This paper forms an integral part of the IPL-155 registered research on "Determination of Soil Parameters of Subsurface to be used in Slope Stability Analysis in Two Different Precipitation Zones of Sri Lanka" being implemented by the Centre for Research & Development, Natural Resources Management & Laboratory Services,

Central Engineering Consultancy Bureau (CECB) of the Ministry of Mahaweli, Agriculture, Irrigation and Rural Development. It is published with their permissions. The views expressed in the paper are however those of the authors only. Our grateful thanks are due to Eng. U S Karunarathna, Chairman, Eng. T D Wickramaratna, General Manager Central Engineering Consultancy Bureau for the permission. Eng Aravinda Kalugaldeniya, Addl. General Manager, Natural Resources Management & Laboratory Services is appreciated for his continuous encouragement and guidance towards many advanced soil research works and publications.

References

- Briaud JL (2001) Introduction to soil moduli. Geotechnical News, June 2001. BiTech Publishers Ltd, Richmond, B.C. Canada (geotwchnicalnews@bitech.ca)
- Bhandari RK, Dias AAV (1996) Rain triggered slope movement as indicators of landslide dynamics. In: Proceedings of 7th international symposium on landslides, 17–21 June 1996 Trondheim, Norway, Balkema, pp 1515–1520
- Bhandari RK, Jeyatharan K, Raviskanthan A (1992) Dynamics of rockfalls in Sri Lanka and landslide hazards. In: Proceeding of the international conference on case histories in geotechnical engineering, St Louis, May 1992
- Francisca FM, Bogoda GO (2019) Weathering effect on the small strains elastic properties of a residual soil. https://www.researchgate.net/publication/332382671_Weathering_effect_on_the_small_strains_elastic_properties_of_a_residual_soil (15/12/2019)
- Fahey M (1999) Determining the parameters of a non-linear elastic model for prediction of ground deformation. Aust Geomech, 34 (1):39–59
- Herath HM, Janaki MK, Kodagoda SSI, Dias AAV (2014) Shallow modes of slope failure in road earth cuttings in Sri Lanka. In: Landslide science for a safer geoenvironment, vol 2, pp 51–58. Springer, Berlin
- Mallawarachchi MASN, Ekanayake EMTM, Kodagoda SSI, Dias AAV (2014) Comparison of soil modulus E_{50} of residual soil slope failures in two different rainfall zones. In: World landslide forum3 (WLF3), vol 1, pp 135–141. Springer, Berlin
- Rahardjo H, Lee TT, Leong EC, Rezaur RB (2005) Response of a residual soil slope to rainfall. Can Geotech J 42:340–351
- Rahardjo H, Melinda F, Leong EC, Rezaur RB (2011) Stiffness of a compacted residual soil. Eng Geol 120(1):60–67
- Phien-wej N, Humza M, Zaw Aye Z (2012) Numerical modeling of diaphragm wall behavior in Bangkok soil using hardening soil model. In: Viggiani G (ed) Geotechnical aspects of underground construction in soft ground, Taylor & Francis Group, London. ISBN 978-0-415-68367-8. <https://www.issmge.org/publications/online-library>



Influence of Plant Root Asperities and Architectural Traits on Soil Shear Resistance

Qi Liu, Lijun Su, and Jun Zhang

Abstract

To investigate the friction characteristic of root-soil interface and to quantitatively evaluate the contribution of shrub roots on soil shear strength, a new aspect of generalized equivalent confining pressure (GECP) was considered in the terms of the function of plant roots in reinforced soil was equivalent to confining pressure. *Indigofera amblyantha* was selected as the test plant of which the roots were sliced and the root surface roughness were calculated. In order to evaluate the influence of root diameters and soil moisture content no friction characteristics of root-soil interface, and different root distribution patterns were launched to analyze the influences on the shear strength of soil-root composites. Pull-out friction tests and triaxial shear tests were conducted on the soil-root composites prepared by sieving and remolding. The results showed that there was no significant difference in surface roughness of *Indigofera amblyantha* roots with the gradual increase of root diameter. The pull-out shear stress of roots in soil-root composites presented a downward trend with the increase of soil moisture content, which concentrated in 15–25 kPa. Under the CU condition, GECP of complex roots (CR) is 1–2 times that of vertical roots (VR) and 2–5 times that of horizontal roots (HR). GECP of plant roots augmented by 20–50%, when confining pressure increased from 50 to 150 kPa. The research results are great guiding significance to use shrubs plants to improve

the stability of slope soil structure and prevent soil erosion and other geological disasters.

Keywords

Indigofera amblyantha • Soil-root composite • Friction characteristic • Shear strength index • Generalized equivalent confining pressure • Root architectural

Introduction

Plant roots play an important role in improving the overall stability of slope superficial soil and increasing the safety coefficient of the slope (Watson et al. 1999; Marie et al. 2010). The main reason that roots can improve slope stability is that soil-root composite is a composite system of which plant roots with a high deformation modulus but soil weak. When soil-root composites are destroyed under external load, dislocation between soil and roots occurs due to the tremendous difference in deformation modulus. The dislocation is constrained by frictional resistance and interlocking force between soil particles and plant roots. Ulteriorly, root tensile strength and soil compressive strength are effectively combined by the friction of soil-root interface, thus soil shear strength is improved (Waldron 1977; Waldron and Dakessian 1981; Wu et al. 1988; Wu and Watson 1998).

The friction characteristics of root-soil interface is the key to study the root reinforcement mechanism. The interface friction characteristics between the roots of tree and soil were studied that the friction coefficient decreases with the increase of soil moisture content (Song et al. 2006; Xing 2009), and the maximum friction force at the root-soil interface is positively correlated with root diameter (Liu et al. 2012). The oblique traction effect of lateral roots of *Pinus yunnanensis* on soil was researched by the methods of calculation model and field direct measurement, and

Q. Liu · L. Su (✉) · J. Zhang
Institute of Mountain Hazards and Environment, Chinese Academy of Sciences, Chengdu, 610041, China
e-mail: sulijun1976@163.com

L. Su
CAS Center for Excellence in Tibetan Plateau Earth Sciences, Chinese Academy of Sciences, Beijing, 100101, China

L. Su
University of Chinese Academy of Sciences, Beijing, 100049, China

concluded that lateral roots can effectively improve the oblique tensile strength of vegetated soil and the incremental value of traction effect has a positive correlation with root biomass (Zhou et al. 1999; Zhang et al. 2002).

The effect of root reinforcement on slope stability can be evaluated directly in terms of the additional shear strength provided by plant roots in reinforced soil. To analyze the effect of plant roots on slope stability, many in-situ and laboratory tests were carried out on the vegetated soil (Wu and Watson 1998; Operstein and Frydman 2000), and the corresponding analytical models for soil-root composites have also been developed (Waldron 1977; Waldron and Dakessian 1981; Wu et al. 1988). However, some researchers have reached the consensus that the Wu-Waldron model is potentially a significant overestimate of actual cohesion of soil-root composites (Waldron 1981; Operstein and Frydman 2000; Pollen and Simon 2005).

At present, there are many researches on the root-soil interface frictional characteristics of tree roots, but the existing research results cannot be fully applied to herbs and shrubs in slope protection due to the different bio-mechanical characteristics of different roots. Based on the fact that the differences in depth, soil moisture content and root characteristics may result in a substantial change in soil shear strength. Expression of generalized equivalent confining pressure (GECF) was derived to investigate the influence of confining pressure and root distribution patterns on the shear strength of reinforced soil. To explore the effects of soil moisture content and root diameter on the frictional characteristics of root-soil interface. As a result, the quantitative evaluation method of GECF used to give an intuitively understanding on the reinforcing effect of roots.

Material and Experimental Methods

Generalized Equivalent Confining Pressure (GECF)

Roots exert a constraint to limit the lateral deformation of soil when soil-root composites are destroyed, the effect of roots in reinforced soil is understood as an additional confining pressure to the soil. Namely, the shear strength of reinforced soil under the confining pressure of σ_3 is the same as the un-reinforced soil under the confining pressure of $(\sigma_3 + \Delta\sigma_3)$ (Fig. 1), and GECF is the deviator of confining pressure between reinforced and un-reinforced soil at the same shear strength.

Huang et al. (2007) proposed GECF of reinforced soil depending on the fact that the Mohr–Coulomb strength theory is also obeyed. The limited balance equation of un-reinforced soil:

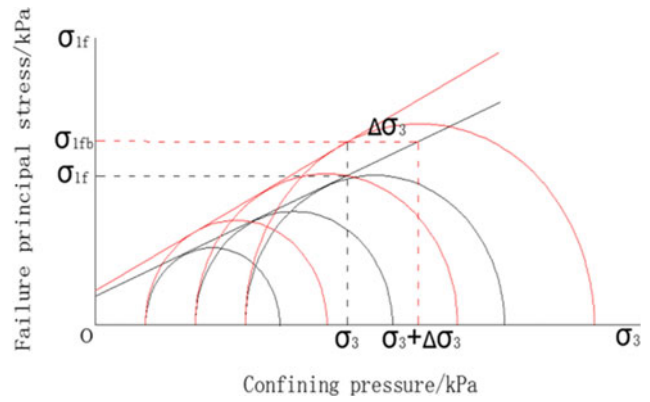


Fig. 1 The relationship of σ_1 and σ_3 of reinforced and un-reinforced soil

$$\sigma_{1f} = \sigma_3 K_p + 2c\sqrt{K_p} \quad (1)$$

where, σ_{1f} —the failure principal stress of un-reinforced soil; σ_3 —the confining pressure; K_p —the passive earth pressure coefficient of cohesive soil, $K_p = \tan^2(45^\circ + \frac{\varphi}{2})$; c and φ represent respectively shear strength indexes.

The limited balance equation of reinforced soil in terms of un-reinforced according to the deviator of confining pressures between reinforced and un-reinforced soil specimens at the same shear strength:

$$\sigma_{1fb} = (\sigma_3 + \Delta\sigma_3)K_p + 2c\sqrt{K_p} = \sigma_{1f} + \Delta\sigma_3 K_p. \quad (2)$$

In Eq. (2), $\Delta\sigma_3$ represents GECF.

Expression of GECF:

$$\Delta\sigma_3 = \sigma_3 \frac{\Delta\sigma_{1f}}{\sigma_{1f} - 2c\sqrt{K_p}}. \quad (3)$$

Expression (3) indicates that GECF of soil-root composite depends on the deviator of failure principal stresses of reinforced and un-reinforced soil, the failure principal stress of un-reinforced soil and the shear strength indexes of un-reinforced soil.

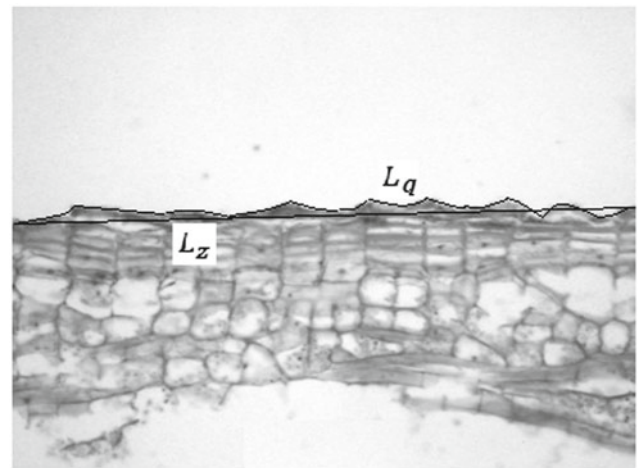
Experimental Materials

In this paper, silty clay was taken from cutting slope on the first phase urban expressway in Xiazhou avenue in Yichang, China. Test soil was chosen below the surface of 0.3 m, and impurities in the soil were removed. The soil was air-dried, crushed and sieved through a 2.0 mm sieve. After that, soil particle distribution and several basic physical properties were measured (Table 1) (Jiang et al. 2009; Wang and Liang 2009).

Table 1 The basic physical properties of experimental soil

Bulk density (g cm ⁻³)	Natural moisture content	Air dried soil moisture content	pH value	Percentage of soil less than a certain size (%)						
				2.0 mm	1.5 mm	1.0 mm	0.5 mm	0.25 mm	0.10 mm	0.075 mm
1.80	14.37%	2.78	6.2	100	82.32	60.57	36.13	17.04	10.13	4.62

Indigofera amblyantha, the most common soil–water conservation plant in tropical and subtropical regions, which of roots was selected as the reinforcing material. *Indigofera amblyantha* is a perennial deciduous shrub, and possesses excellent ability for drought resistance and barren resistance (Xu et al. 2017; Xia et al. 2018). The *Indigofera amblyantha* with a growing age of a year and the same growth situation were excavated by the whole excavated method. Normal and straight taproots were cut by scissors based on the length of 70 mm. An electronic caliper with an accuracy of 0.001 mm was used to measure the average diameter of the roots. The average diameter ranged from 0.35 to 3.48 mm. The roots of *Indigofera amblyantha* in the diameter range of 0.5–3.0 mm were classified according to the range of 0.5 mm root diameter. In addition, the roots which the average diameter of 1.4–1.6 mm were chosen and cut based on the length of 30 and 60 mm, tensile strength of the roots were measured (Table 2).

**Fig.2** Analysis of root concave-convex surface

$$T = \frac{L_q - L_z}{L_z} \times 100\% \quad (4)$$

Experimental Methods

Root Surface Roughness

To slice the roots and measure the surface roughness, the roots in the diameter range of 0.5–3.0 mm was selected. The roots were sliced along the axis, the clear and visible slices of concave-convex surface were photoed under the electron microscope with a magnification of 200 times, and five slices in the magnified state were obtained along the root surface.

MAPGIS software was used to process the graph and the basic characteristics of the root surface roughness were analyzed. A curve and a straight line were drawn along the root concave-convex surface, and the length of each line was calculated (Fig. 2).

Five curves and straight lines of each slice were added respectively, and the root surface roughness was calculated according to Eq. (4) (Xing 2009):

where, T —root surface roughness; L_q —total length of concave-convex curve of root slice, mm; L_z —total length of straight line on the surface of root slice, mm.

Based on the previously described procedures, the root slices in each diameter range were processed. Five roots were chosen from each diameter range, and 2 slices were taken from each root. The averaged surface roughness of 10 slices as the surface roughness in each diameter range. T value and F value of root roughness in each diameter range were obtained based on the SPSS software.

Single Root Pull-Out Friction Test

In the test, soil moisture contents were set at 12.00, 14.37 and 16.00% according to the natural moisture content of test soil is 14.37% (Lu and Li 2005; Zhong et al. 2015). The soil

Table 2 Tensile strength indexes of *Indigofera amblyantha* roots

Average diameter (mm)	Average tensile resistance (N)	Average tensile strength (Mpa)	Standard deviation of tensile strength	Significance test of difference
1.49	62.10	35.86	1.17	1.73

density was set according to the actual situation of test soil taken from cutting slope (Bulk density is 1.80 g cm^{-3}). Soil-root composites were remolded in a circular vessel with 61.8 mm in diameter and height of 40 mm. Single root was buried vertically in the soil and the method of three-layer compaction was adopted to remold soil-root composites in the circular loading box according to the methods of soil mechanics test standardization and specimen preparation (Xia et al. 2015). AHP-50 Edberg digital display push-pull meter was applied to conduct the pull-out friction tests, and the loading rate was controlled at 10 mm/min. The single root pull-out tests were carried out three times of each diameter range (Song et al. 2006; Xing 2009).

There are two assumptions in the calculation model of the single root pull-out friction test: (1) the frictional stress distribution at the root-soil interface is uniform during the process of single root drawing; (2) the uniformly distributed pull-out shear stress and drawing force at root-soil interface meet the static equilibrium (Zhao 2006), and then

$$\tau \cdot d \cdot l - F = 0 \quad (5)$$

where, τ —pull-out shear stress at the root-soil interface, kPa; d —the average diameter of root, mm; l —root length in soil, mm; F —the drawing force when root is pulled, N.

Triaxial Shear Test

The soil moisture content and bulk density designed in triaxial shear tests are the same as that in the single root pull-out friction test. Root contents (Quality percentage: the ratio of the root mass to soil mass in the specimens) was set at 0.5%.

Soil-root composites were remolded in a circular vessel with 39.1 mm in diameter and height of 80 mm, and the size of circular vessel is matched with the specimen of the TSZ-1 strain-controlled triaxial apparatus. The preparation processes

of root-soil composite were consistent with the above, and specimens of un-reinforced soil were also prepared, except that no roots were present in the specimens.

Root distribution pattern was divided into three forms, as shown in Fig. 3. The first form is vertical root (VR), root length is 60 mm; the second form is horizontal root (HR), and the root length is 30 mm; and then the third form is complex root (CR), the content of horizontal and vertical roots account for 1/2, respectively. Plant roots were organized in the center of soil-root composites in three forms.

A prepared specimen was put into the pressure room on which 20 kPa confining pressure was forced. According to the test plan in Table 3, the shear strengths of soil-root composites and un-reinforced soil were measured by the triaxial tests on 15% of axial strain (Zhang et al. 2010).

Results and Discussions

Surface Roughness of *Indigofera Amblyantha* Roots

Figure 4 is slice pictures of the *Indigofera amblyantha* roots at each diameter range.

Table 4 shows that the surface roughness is the largest in the diameter range of 1.0–2.5 mm, varying from 6.50 to 7.50%. The root surface roughness in the diameter range of 0.5–1.0 and 2.5–3.0 mm were relatively small, which were 4.05 and 5.17%, respectively. ANOVA is adopted to achieve the difference analysis of 5 sets of root diameter, there was no significant difference ($\alpha = 0.134$) in root surface roughness of *Indigofera amblyantha* with the gradual increasing of root diameter. Therefore, the phenomenon that a large root diameter leads to a great friction effect of root-soil interface was not observed. When the diameter range of *Indigofera amblyantha* roots within 1.0–2.5 mm, the cracking resistant of roots on soil will be strong.

Fig. 3 Root distribution patterns in the triaxial test

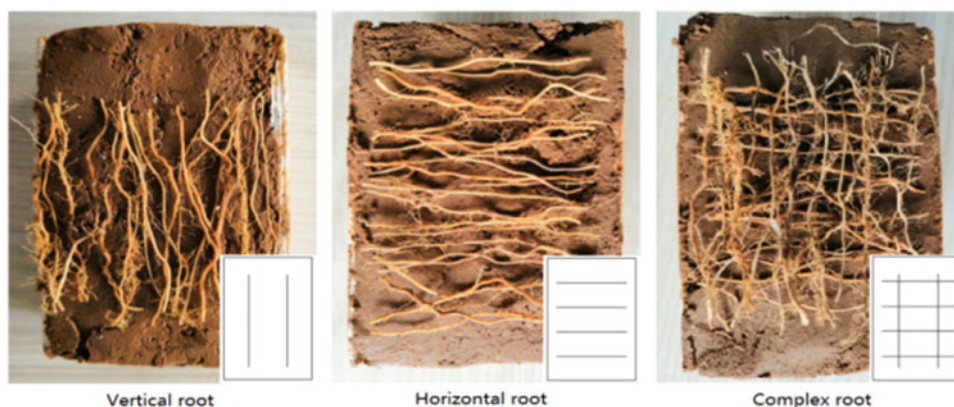


Table 3 Triaxial test program of soil-root composites

Control condition	Experimental method
	Consolidates undrained (CU)
Sample type	Un-reinforced, Reinforced
Root distribution pattern	Horizontal, vertical, complex
Confining pressure1 (kPa)	50
Confining pressure2 (kPa)	100
Confining pressure3 (kPa)	150
Shearing rate (mm/min)	0.12

Fig.4 Slices of *Indigofera amblyantha* roots

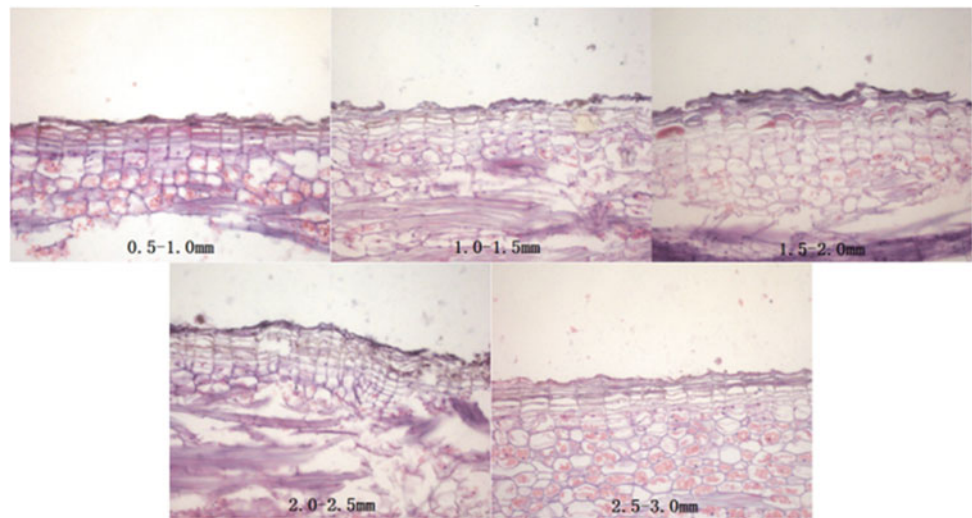


Table 4 Surface roughness and difference analysis of *Indigofera amblyantha* roots

Diameter (mm)	Averaged roughness (%)	Standard deviation	Testing significance of difference	F values between diameters	Significant difference between diameters
0.5-1.0	4.05	1.81	2.36	1.913	0.134
1.0-1.5	7.36	3.76	1.64		
1.5-2.0	6.88	3.97	1.35		
2.0-2.5	7.17	3.63	1.73		
2.5-3.0	5.17	1.04	2.75		

Effect of Soil Moisture Content and Root Diameter on Pull-Out Shear Stress

Figure 5 shows the effect of soil moisture content and root diameter on the pull-out shear stress of *Indigofera amblyantha* roots. When soil moisture content are 12.00 and 14.37%, the pull-out shear stress of roots were characterized by a decrease followed by an increase with the advance of root diameter in root-soil composites, which is positively correlated with the change in root surface roughness. When

the soil moisture content is 16.00%, the pull-out shear stress of roots decreases with root diameter increases. Stated thus, soil moisture content can significantly affect the role of root morphology in the frictional properties of root-soil interface.

In root-soil composites, the concave-convex structure on root surface is interlaced with soil particles, and the soil particles at root-soil interface will move and rearrange in the process of single root drawing and shearing, until root-soil interface tends to be smooth. The bite force is produced due to soil particles are closely contacted with roots in a low soil

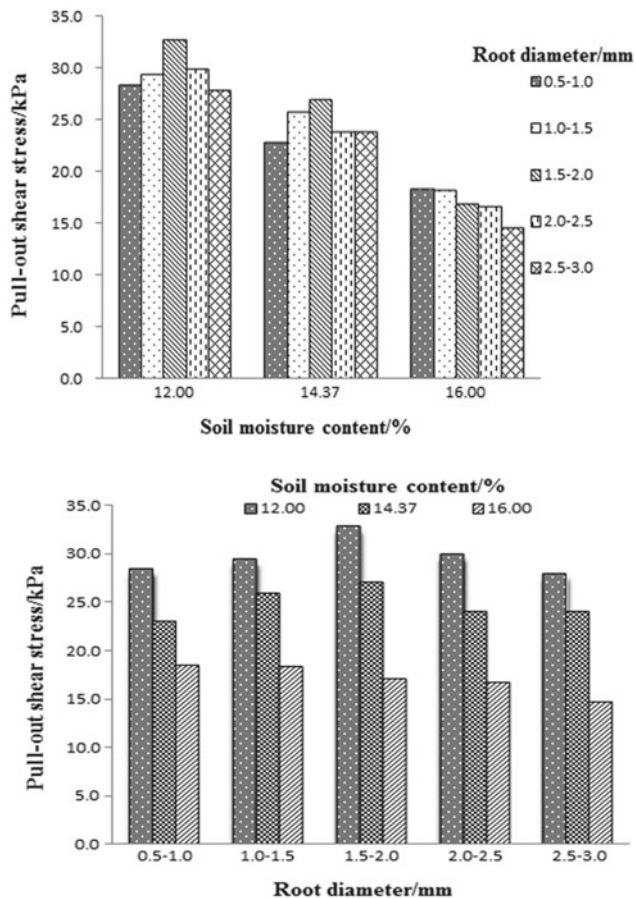


Fig. 5 Influence of soil moisture content and root diameter on pull-out shear stress of roots

moisture content, and the friction characteristics of root-soil interface are positively correlated with root surface roughness. When soil moisture content increases gradually, the concentration of electrolyte in aqueous solution reduces, and the spaces of soil particles increase. The thicken water film at root-soil interface result in a weak strength junction between the soil particles and the root concave-convex structure, and the root surface morphology on friction effect of root-soil interface is not demonstrated. On the other hand, the contact specific surface area between root and soil is reduced due to root diameter increases, so the pull-out shear stress of root falls.

Effect of Root Characteristics and Confining Pressure on GECP in Reinforced Soil

Figure 6 showed the relationship between GECP of plant roots in soil-root composites and confining pressure under different root distribution patterns. Among the three root distribution types (HR, VR and CR), CR is the best to enhance soil shear strength. Under the confining pressure of

150 kPa, when root distribution pattern is CR, GECP of the plant roots in soil-root composites is 1.2–1.5 times that of VR and more than 3 times that of HR. Take CR as an example, when soil-root composites are forced by 150 kPa confining pressure, GECP of plant roots in soil-root composites is 40.10 kPa (Table 5). Namely, the shear strength of soil-root composites in the condition is equivalent to the strength of un-reinforced soil that subjected to the confining pressure of 190.10 kPa.

HR doesn't work as a "reinforcement" on soil when root content is less, owing to soil integrity is destroyed and there is less contact area between soil particles and root system. However, when the root system is decussately placed in specimens, root system bears partly horizontal shear force that limits soil lateral deformation, because of the interaction between soil particles and root system. Meanwhile, the rigid modulus of soil-root composites is notably improved, which mainly reflected in the compression modulus of specimens increase, and soil deformation is effectively restrained (Lewis 1956).

The variation trend of GECP resulted from the change of confining pressure is observed in Fig. 6. From three root distribution patterns perspectives, GECP shows the same phenomenon with the advance of confining pressure and an extremely significant positive correlation ($\text{Sig} < 0.05$) was observed. GECP of plant roots augmented by 20–50% when confining pressure increased from 50 to 150 kPa.

The values of GECP are positive showed that the existence of plant roots in reinforced soil plays a positive role in shear strength. The density of soil-root composites increased as confining pressure augments, resulting in an increase in soil quality of per unit volume. Soil particles gap decreased is more conducive to making plant roots joint with soil, which limits the lateral deformation of specimens. On the other hand, the density increases of specimens aggrandized

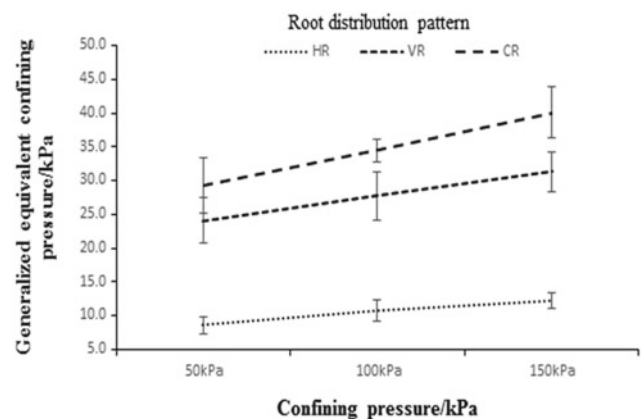


Fig 6 The relationship between GECP of *Indigofera amblyantha* roots in the reinforced soil and confining pressure under different root distribution patterns

Table 5 GECP of plant roots in the reinforced soil

Root type	Confining pressure (kPa)	CU		
		HR	VR	CR
<i>Indigofera amblyantha</i>	50	8.56	24.03	29.26
	100	10.69	27.71	34.50
	150	12.34	31.30	40.10

the number of soil particles contacted with root surface, resulting in a larger contact area and presumably to a higher cohesion of soil-root composites (De Baets et al. 2008; Abernethy and Rutherford 2010).

Conclusion

There was no significant difference in surface roughness of *Indigofera amblyantha* roots with the gradual increase of root diameter. The pull-out shear stress of roots presented a downward trend with the advance of soil moisture content and root diameter, the pull-out shear stress was concentrated in 17.36–32.76 kPa. The change of root surface asperities have a significant effect on the pull-out shear stress of roots when soil moisture content is small.

The significant relationships are found between reinforcing effect and root architectural. The reinforcing effect of root distribution patterns in soil-root composites is very low under HR, intermediate for VR and highest for CR. The shear strength of soil-root composites is improved when confining pressure increase, however, the reinforcing effect of plant roots diminishes as confining pressure augment. GECP as an indicator to quantitatively evaluate the reinforcing effect of plant roots on soil is intuitionistic and credible, it greatly enriches the mechanism of plant roots' soil-reinforcement.

Acknowledgements This study was financially supported by the National Natural Science Foundation of China (Grant no. 41790432; 41761144077). Great appreciation also goes to the editorial board and the reviewers of this paper.

References

- Abernethy B, Rutherford ID (2010) The distribution and strength of riparian tree roots in relation to riverbank reinforcement. *Hydrol Process* 15(1):63–79
- De Baets S, Poesen J, Reubens B et al (2008) Root tensile strength and root distribution of typical Mediterranean plant species and their contribution to soil shear strength. *Plant Soil* 305:207–226
- Huang Y, Fu BC et al (2007) Generalized equivalent confining pressure and limited balance conditions of reinforced laterite. *Rock Soil Mech* 28(3):533–539
- Jiang HH, Dong XB, Wang HB (2009) Effects of slope soil water content on soil shear strength of different vegetation. *Forest Eng* 25(3):77–80
- Lewis J G (1956) Shear strength of rockfill. In: Proceedings of the 2nd Australia-New Zealand conference on soil mechanics and foundation engineering, pp 181–202
- Li WP, Shi HB, Hu M (2012) The effect of root diameter of *Sabinavulugaris* on the shear strength in root-soil composites. *Chin J Soil Sci* 43(4):934–937
- Liu XG, Zhao HH, Ji XD et al (2012) Friction characteristics of root-soil interface of *Pinus Tabulaeformis* and *Larix Gmelinii*. *Tribol* 32(6):550–556
- Lu HY, Li P (2005) Effects of surface temperature and soil particle composition on shear strength. *J Inner Mongolia Agric Univ* 26(1):75–78
- Marie G, Alexia S, Thierry F et al (2010) The influence of plant diversity on slope stability in a moist evergreen deciduous forest. *Ecol Eng* 36(3):265–275
- Operstein V, Frydman S (2000) The influence of vegetation on soil strength. *Proc Inst Civil Eng Ground Improv* 4(2):81–89
- Pollen N, Simon A (2005) Estimating the mechanical effects of riparian vegetation on stream bank stability using a fiber bundle model. *Water Resour Res* 41(7):1–11
- Song WF, Chen LH, Liu XP (2006) Experiment on characteristic of interface between root system and soil. *Sci Soil Water Conserv* 4(2):62–65
- Waldron LJ (1977) The shear resistance of root-permeated homogeneous and stratified soil. *Soil Sci Soc Am J* 41(5):843–849
- Waldron LJ, Dakessian S (1981) Soil reinforcement by roots: calculation of increased soil shear resistance from root properties. *Soil Sci* 132(6):425–435
- Wang L, Liang H (2009) The influence of the water ratio on the shearing strength of silty clay. *J Inner Mongolia Agric Univ* 30(1):170–175
- Watson A, Phillips C, Marden M (1999) Root strength, growth, and rates of decay: root reinforcement changes of two tree species and their contribution to slope stability. *Plant Soil* 217:39–47
- Wu TH, McOmber RM, Erb RT et al (1988) Study of soil-root interaction. *J Geotech Eng* 114(12):1351–1375
- Wu TH, Watson A (1998) In situ shear tests of soil blocks with roots. *Can Geotech J* 35(4):579–590
- Xia ZY, Guan SF et al (2015) Experimental study on pull-out resistive properties of *Ophiopogon japonicas* and *Indigofera amblyantha* roots. *Bull Soil Water Conserv* 37(08):110–113
- Xia ZY, Liu Q, Xu WX et al (2018) Characteristics of interface friction between *Indigofera amblyantha* root system and soil. *J Soil Water Conserv* 32(01):128–134
- Xing HW (2009) Test studies on the surface friction characteristics of 4 kinds of plant roots-soil. *Inner Mongolia Agric Univ*
- Xu WN, Xia D, Zhao BQ et al (2017) Technical research of vegetation restoration in disturbance area of hydropower project. Science Press, Beijing

- Zhang CB, Chen LH, Liu XP et al (2010) Triaxial compression test of soil-root composites to evaluate influence of roots on soil shear strength. *Ecol Eng* 36(1):19–26
- Zhang YW, Liu YM, Zhou Y (2002) Study for the destroy principle and model of the *Yunnan pines* lateral root-soil friction bond. *J Mt Sci* 20(5):628–631
- Zhao YN (2006) Study on rapid cultivation seedlings and anti-tensile strength of the rhizomes of *Phragmites communis*. Northeast Normal University, Changchun
- Zhong SQ, Liu B, Wei CF et al (2015) The rock fragments (<2mm) and their action mechanism on the shear strength of purple mudstone-developed Soils. *Sci Agric Sinica* 48(23):4846–4858
- Zhou Y, Xu Q, Luo HS et al (1999) Traction effect of lateral roots of trees (I principle and calculation). *J Mt Sci* 17(1):4–9



2020 Kyoto Japan

Modelling of Creep Behavior of Claystone in Mae Moh Open-Pit Mine Using the Soft Soil Creep Model

Pongsakorn Wongchana, Peerapong Jitsangiam,
Suriyah Thongmune, and Tawatchai Tanchaisawat

Abstract

Mae Moh lignite mine is the largest open-pit mine in Thailand. The current mine operation is with over 250 m depth. The mine has been operated for over 50 years and would have a plan for the further operation of the next 20 years approximately. With a much deeper mine operation, this open-pit mine would be unavoidably to deal with more stress condition complexity of slope stability analysis, in particular for the long-term (time-dependent) stability. The long-term slope stability generally relates to the material “creep behavior” of which the time-dependent effect of a small deformation scale continually takes place under the constant stress condition. The main component of the Mae Moh open-cut slope is “claystone” which can be classified as the soft rock. It has properties in between soil and rock, causing difficulties in setting an appropriate test facility and determining a constitutive model to investigate its creep behavior. This study aimed to investigate the use of the soft soil creep (SSC) model to describe the creep behavior of the Mae Moh claystone based on a series of test results obtained creep tests from an own customized triaxial creep test facility designed to suit with the soft rock-like material. Plaxis 3D, the powerful commercial finite element program, was also used to simulate such creep behavior using the SSC model, one of its build-in constitutive material models. The Mohr-Coulomb

(MC) model was also used as a benchmark in the finite element simulation. Results showed the SSC model could better simulate the time-dependent deformation of the Mae Moh claystone than using the MC model. It could be noticed that the SSC model would be an option to describe the creep behavior of the soft rock, using derived inputs based on the soft rock properties as it can be seen from a good agreement between test results and simulation of the slope of this study.

Keywords

Creep behavior • Triaxial creep test • Soft soil creep model • Claystone

Introduction

Over the past 50 years, Mae Moh open-pit mine has been operated and excavated with over 250 m depth. The main structural component of its open-cut slope is “claystone” which could be classified as the soft rock, having properties of between soil and rock. Thus, its complexity behaviour can be expected. Mae Moh open-pit mine has a continue plan to further operate for more than 20 years approximately, by which its operation depth would be up to 500 m at the final operational stage. Therefore, Mae Moh claystone is strongly required to be better understood under the conditions of more geological complexity and much higher applied stress. Furthermore, up to the around 500 m operational depth, the long-term stability in relation to the time-dependent movement of the slope would be more crucial to determine. “Creep” which is the time-dependent behaviour of a material under the constant stress condition would be investigated for the Mae Moh claystone. This study aiming to model the creep behaviour using the soft soil creep (SSC) model in Plaxis 3D is one of a series of creep studies on the creep behaviour of Mae Moh claystone.

P. Wongchana (✉) · P. Jitsangiam · S. Thongmune ·
T. Tanchaisawat
Department of Civil Engineering, Chiang Mai University, Chiang
Mai, 50200, Thailand
e-mail: egco.pongsakorn@gmail.com

P. Jitsangiam
e-mail: peerapong@eng.cmu.ac.th

S. Thongmune
e-mail: suriyah@eng.cmu.ac.th

T. Tanchaisawat
e-mail: tawatchai@eng.cmu.ac.th

As known, creep is one of the most essential mechanical properties of a rock material and can deliberate an important basis for interpreting and analyzing the circumstance of geological tectonic movement, as well as predicting long-term stability for rock engineering (Tsai et al. 2008; Zhang 2012). Furthermore, time-related stability for geotechnical engineering is even more essential nowadays as the collapse of geotechnical engineering structures for a period after the construction, appeared in many projects (Yang et al. 1999). Loss of stability for geotechnical engineering structures as the result of deformation, that did not happen immediately, but the deformation occurs continuously and deforms for some time. (Boukharov et al. 1995; Damjanac, Fairhurst, & Engineering 2010). For instance, deformation of dam and collapse of underground tunnel occurred after decades of construction (Fan 1993; Gudmundsson et al. 2010). Consequently, Studies on creep behavior of rock in relation to geotechnical engineering structures are imperative.

In soil and rock mechanics, creep refers to the continuing deformation of a material under constant effective stress (Mitchell and Soga 2005). Creep behavior of the slope is a behavior that describes the movement down due to the influence of gravity, in the long term. The movement may be slow, cannot find abnormalities of surface soil, but can be observed from the steep inclines of the tree, the tilting of the mast and including subsidence of buildings or roads (Goodman 1993).

Creep slopes occur long-term effects of weathering and gravity may gradually deform leading to geological structures, for example, bending, bucking, fracturing, or even progressive failure. (Chang et al. 2015) Measurement of creep deformation, a little movement in each year. The motion estimation surface of the rock slope. 4–30 mm/year during the past 10,000 years, and 80 mm/year, a higher rate of the last 50 years. The creep behavior is related to time and gravity. The stress causes the accumulation and reduces the hardness of the material, leading to the erosion at the end (Mufundirwa et al. 2010). Characteristics of rock behavior are usually considered in the form of elastic-plastic. However, rock behavior does not have the function of time. Rock has creep behavior or viscosity that influence time function (Bhoi 2012). Creep behavior study has been wells studied in many countries. Laboratory of creep is a uniaxial test and triaxial test, nevertheless, the triaxial test can provide confining pressure (Yang et al. 1999).

The major constitutive of this research material is “claystone”, which is a one of sedimentary rock and its forms from clay-size (between 1/256 and 1/16 mm in diameter) of weathering debris. By that, the inherent characteristics of claystone of which properties line in between rock and soil. On the one hand, claystone on dry condition seems like a rock behavior that hardness of strength. on the other, when

the moisture content increased, the claystone would be lost strength as a soil behavior. Whereupon, creep behavior of claystone should be necessarily investigated using a suitable test facility of which the soil-and-rock material can be specially tested. Such test facility must able to test rock and soil and it also can measure a small strain of creep behavior. The triaxial compression test is a spacious test for determining strength parameters. Therefore, this study used the triaxial compression test concept to make an own customized high pressure triaxial test facility to accommodate all test requirements of the creep test for Mae Moh claystone. This was called “triaxial creep tests”.

Methodology

Creep Behavior

One of important properties of soil is a creep property of which the soil layer deform continuously when stress condition has remained. the accumulation of deformation maybe happen over a decade; therefore, the creep behavior involves time-dependent. A slope may have experienced numerous episodes of sliding or deformation over the decades. Whether slopes were under rains or earthquakes, stress keeps on changing on any slopes (Mitchell and Soga 2005).

Creep refers to the time-dependent deformation of soil or rock. Deformation causes loss of strength due to the surface accumulates resistance to constant shear in response to shear stress caused by loading or unloading. Creep behavior modeling has been applied to the solution of various engineering fields, such as the closure of and loads on tunnels, chambers, and pillars.

Conceptual creep behavior is shown in Fig. 1 which can ideally describe the creep behavior of rock and soil. From Fig. 1, creep behavior would explicit in 3 stages which are the primary stage, the secondary stage and the tertiary stage (failure point). Creep behavior stages are more explained as follows.

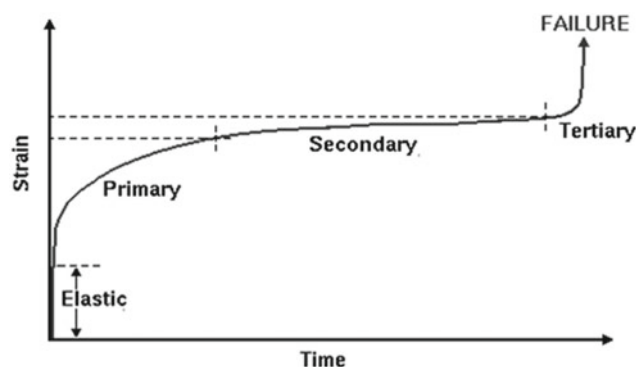
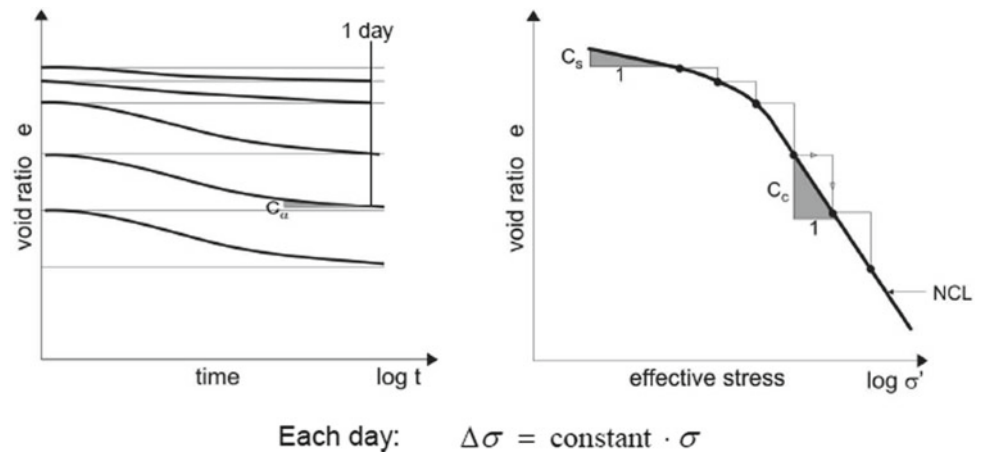


Fig. 1 Idealized creep behavior for rock materials and cohesive soils

Fig. 2 Primary and Secondary Consolidation behavior



- “*Primary*”: Stress decreases due to material resistance.
- “*Secondary*”: Strain rate increased slightly (reaches a steady-state) creep behavior.
- “*Tertiary*”: Failure because the material is less resistant.

Referring to the secondary stage of strain in Fig. 1, Plaxis 3D which is the powerful commercialized finite element program has a soft soil creep model that can simulate creep behavior of soft soil with the parameters as shown in Fig. 2 based on secondary subsidence. The secondary settlement generally occurs for a relatively long time. However, testing would take much a shorter time to observe the trend of the movement graph.

Figure 2 shows the slope of settlements in the stages of the primary and secondary consolidation. For the primary consolidation stage, Settlement parameters of C_s (swelling index) and C_c (Compressive index) can be obtained from the Oedometer test. The primary consolidation is defined by the relationship graph between the void ratio (e) and stress (\log -stress). For the secondary consolidation, the tests of

(1) creep tests and (2) constant rate of strain tests should be followed. However, both of which do not have the standard tests to follow. The parameter of the creep indication is C_α (creep index). The creep index is defined by the relationship graph between the void ratio (e) and time (\log -time).

Laboratory

The so-called triaxial creep tests of this study were based on the own customized triaxial test facility to address the soil-and-rock like materials as mentioned. For this triaxial test facility, the triaxial compression tests in accordance with ASTM D2664 can be conducted. This triaxial compression tests can comprehensively determine the strength of the sample of a cylindrical stone core in an undrained condition under triaxial compression loading. To determine the strength of claystone, therefore, such own customized triaxial test facility must provide an applied force of up to 25 kN with a confining pressure up to at least 5.0 MPa. For the accessories of such test facility to record test data, the 50 kN load-cells with the handheld data logger to collect loading data and the digital dial gauges to measure vertical deformation the loading rate of 1 mm/min were used. The own customized triaxial test set is shown in Fig. 3. For small scale deformations of creep movements of a test sample, the strain gauges with its sensitivity of the micro-strain level were attached on a test sample to measure a sample deformation during the constant compression creep tests (see Fig. 3).

In this study, claystone samples were collected from the Mae Moh mine and samples at the depths of 50, 100 and 150 m (see Fig. 4) to be used for the triaxial compression tests and triaxial creep tests with the confining pressure levels of 0.5 MPa, 1.0 MPa, and 1.5 MPa, respectively.

For the tests, the triaxial compression tests were firstly conducted to determine the maximum compressive strength



Fig. 3 Testing and installation equipment



Fig. 4 Claystone samples collected

of claystone corresponding to a given confining pressure. Based on the triaxial compression test results, the shear strength (Mohr-Coulomb, MC) parameters of cohesion (c) and internal friction angle (ϕ) were determined in conjunction with establishment of the Mohr-Coulomb (MC) failure criterion in the shear-normal stress space. Then, triaxial creep tests under the multi-stage loading regimes (40%, 60%, and 80% Strength) corresponding to a series of confining pressure levels (0.5 MPa, 1.0 MPa, and 1.5 MPa) were carried out by applying constant deviatoric stress for one day (24 h.) on each loading step. Figure 5 shows an example of these creep test results

Based on the required parameters for the SSC model, in this study, the creep test results were used to determine the creep index (C_c). For the compression index (C_c) and swelling index (C_s) of claystone, they were estimated from the back-calculate method from the Plaxis 3D using its lab test function (the simulation triaxial compression test).

The defined the SSC model parameters were shown in Table 1. The MC parameters are C' (Cohesion) of 1.2 MPa and ϕ' (Friction angle) of 30.96° derived from the triaxial compression test results. C_c , C_s and C_α are 0.07, 0.0001 and 0.01, respectively. It should be noted that C_c and C_s from the back calculation process of this study show good agreement with recommended values (C_c of mudstone 0.02–0.07 and C_s of mudstone 0.001–0.01) (Zhang 2012).

Model Comparison

Plaxis 3D was used to simulate the triaxial creep tests (see Fig. 6) based on the SSC model and the MC model. The creep triaxial test result was a benchmark to compare with the simulation results.

Figure 7 shows the comparison trends. It is clearly seen that based on the SSC model, the good agreement between the simulation and the test results can be seen. For the simulation based on the MC model, the strain increment with an increase of stress and time cannot be captured. At this stage, based on the triaxial creep test, the SSC model can be used to explain the creep behaviour of claystone with a good validation.

Determination Exercise of the Creep Movement on a Slope

The slope of 120 m in width by 120 m in length by 120 m in height was modelled using Plaxis 3D (see Fig. 8a) based on the open-cut slope configurations of Mae Moh mine. The assumption of only one type of the materials of claystone with the homogeneous manner was applied to this determination exercise. The SSC model and The MC model were used as the claystone material model with all input parameters and their values utilized in the model comparison (validation) process. The creep movements were determined corresponding to time.

Figure 8b illustrates the shade of various colors for a 25-year time. The red zone represents the maximum horizontal deformation toward the slope, and the blue zone exhibits where no movement occurs. The maximum movements value at a certain node were selected to represent the movement trend against the time as shown in Fig. 9 of which the graph deformation (m, y-axis) and time (years, x-axis) is illustrated.

From Fig. 9, the deformation of Mohr-coulomb (red-line) has moved only 0.1 m in less than 1 year after the construction stage. On the other hand, the result of the SCC model occurs 1.3 m of deformation, for 5 years. Next, after the first 5 years, the slope deformed continuously 20 mm/year. It could be said that based on the SCC model,

Fig. 5 (1) Strain and Time under confining pressure of 0.5 MPa.
 (2) Strain and Time under confining pressure of 1.0 MPa.
 (3) Strain and Time under confining pressure of 1.5 MPa

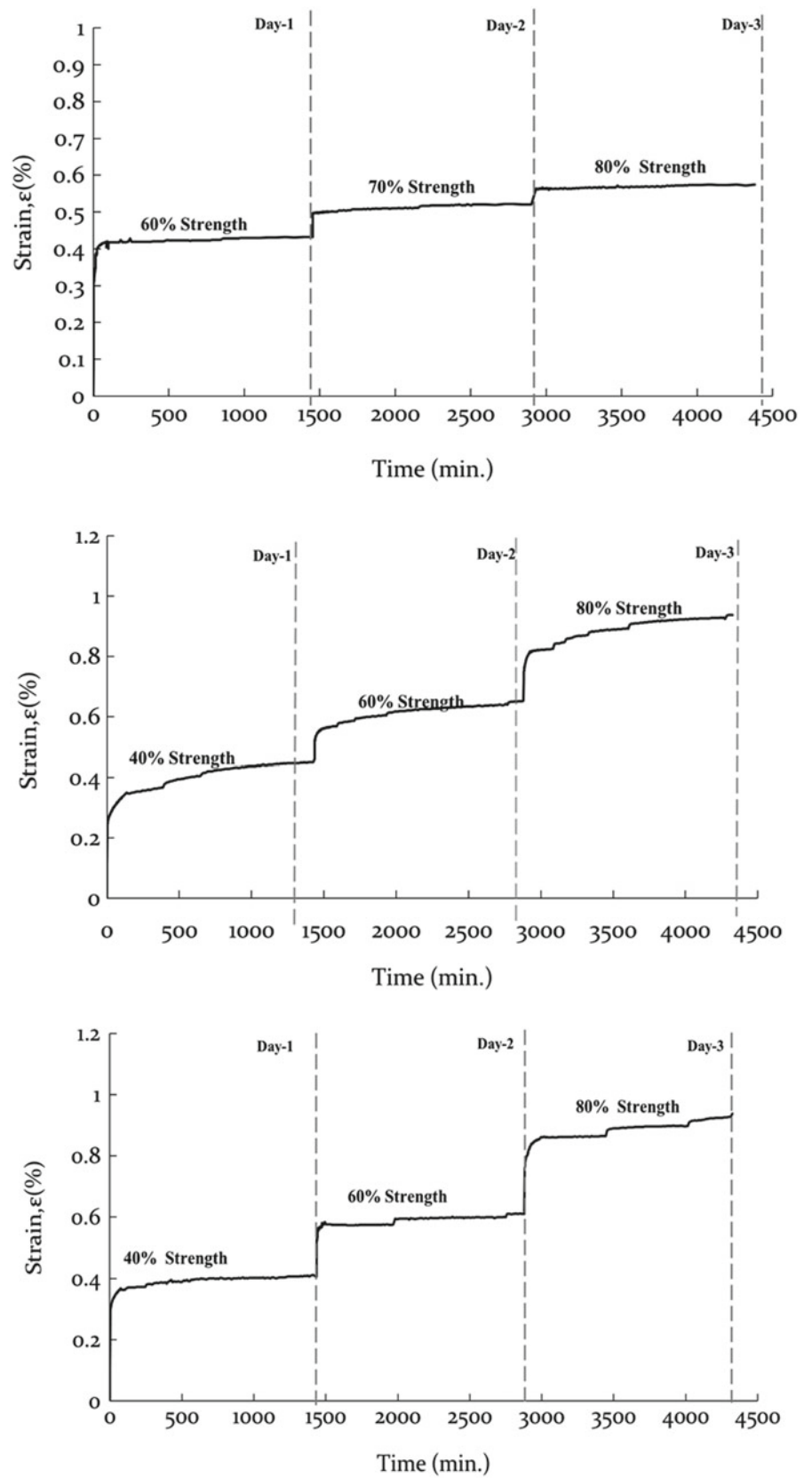


Table 1 Parameters for the MC model and the SSC model

Model	Mohr-Coulomb	Soft soil creep	Source	Unit
Drainage type	undrained(A)	undrained(A)		
γ_{unsat}	20.4	20.4	Field lab test	kN/m ³
γ_{sat}	25.3	25.3	Field lab test	kN/m ³
E	309,572	–	Triaxial compression test	kN/m ²
ν	0.15	0.15	Recommend	–
C'	1200	1200	Triaxial compression test	kN/m ²
ϕ'	30.96	30.96	Triaxial compression test	°
C _c	–	0.07	Back calculation	–
C _s	–	0.001	Back calculation	–
C _{α}	–	0.004	Triaxial creep test	–

*Back calculation from Lab test by the Plaxis 3D Program

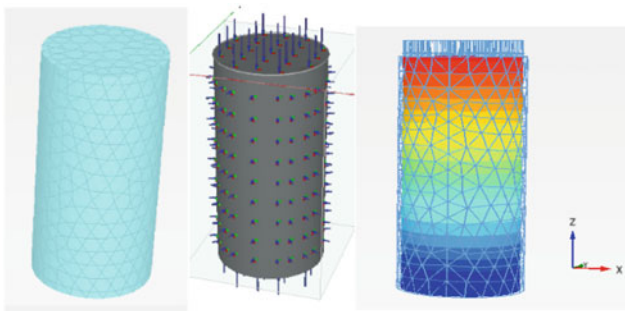


Fig. 6 Triaxial creep test simulation on Plaxis 3D

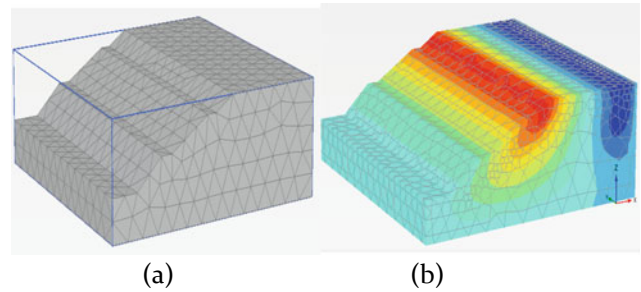


Fig. 8 Model simulation by PLAXIS3D version 2017. **a** Model before analyze, **b** Model after analysis, show horizontal deformation

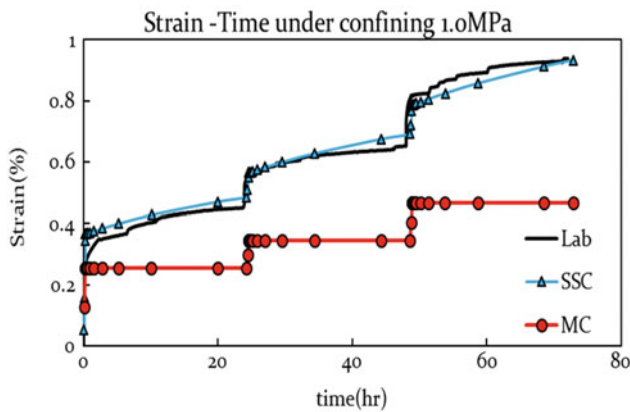


Fig. 7 Comparison between simulation results and test results

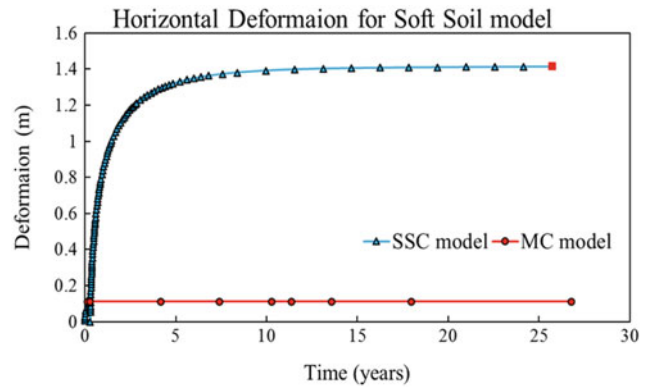


Fig. 9 Creep characteristics of the claystone slope

the movement characteristics of the claystone slope can be well explained in accordance with the theory of the creep of the geomaterial. The primary stage was observed in the first five years and the secondary stage could be defined after that with the movement rate of approximately 20 mm/year. However, based on this simulation, the tertiary stage or failure is still not able to recognize.

Conclusions

The concluding remarks of this study can be summarized as follows;

- (1) the creep behavior of Mae Moh claystone can be successfully explained using the own customized triaxial

test facility to conduct the test of the triaxial compression tests and the triaxial creep tests. Triaxial compression tests was performed to determine the maximum compressive strength under three confining pressure levels of 0.5, 1.0 and 1.5 MPa. Triaxial creep tests in relation to a multi-stage loading method of 40, 60 and 80% maximum compressive strength with one day of constantly remaining load for each loading increment were performed to capture the creep characteristics of Mae Moh claystone subjected to such designed loading conditions.

- (2) Test results from the triaxial creep tests can be used to define the creep index ($C\alpha$) of Mae Moh claystone, by which its secondary deformation under a certain pressure could be detectable.
- (3) The primary consolidation parameters (the compression index (C_c) and swelling index (C_s)) of Mae Moh claystone can be determined using the back calculation process based on a data set of the triaxial creep test results and Lab test function results of Plaxis 3D program.
- (4) The SSC model can be successfully used to simulate the creep behavior of Mae Moh claystone with a good agreement with the triaxial creep test results. The MC model cannot be used to capture such creep behavior.
- (5) The creep characteristic of the claystone slope was demonstrated through the Plaxis 3D simulation using all input parameters and their values as the validation process. The creep movement based on the SSC model after five years of the primary deformation was in the rate of 20 mm/year.
- (6) The SSC model which is one of material model options in Plaxis 3D was promising to use to simulate the creep characteristics of the soft rock (like claystone).

financial support (Grant ID 61-G201000-11-IO.SS03G3) to the project. Special thanks are extended the Faculty of Engineering, University of Phayao for assisting in the Plaxis 3D analysis. The first author would like to sincerely thank and acknowledge the Graduate School and Faculty of Engineering, Chiang Mai University for providing the full post-graduate scholarship throughout the study of 2017–2018.

References

- Bhoi MR (2012) *Creep behavior of rock*
- Boukharov G, Chanda M, Boukharov N (1995) *The three processes of brittle crystalline rock creep*. Paper presented at the International Journal of rock mechanics and mining sciences & geomechanics abstracts
- Chang KT, Ge L, Lin HHJE. e. s (2015) Slope creep behavior: observations and simulations 73(1):275–287
- Damjanac B, Fairhurst CJRM., Engineering R (2010) Evidence for a long-term strength threshold in crystalline rock 43(5):513–531
- Fan GJCCIPH (1993) *Rheological mechanics of geotechnical engineering*, Beijing
- Goodman RJI (1993) *Engineering geology: Rock in Engineering Construction*. John Wiley & Sons, New York
- Gudmundsson A, Simmons TH, Larsen B, Philipp SLJJ. o. S. G (2010) Effects of the internal structure and local stresses on fracture propagation, deflection, and arrest in fault zones 32(11):1643–1655
- Mitchell JK, Soga K(2005) *Fundamentals of soil behavior* (vol 3), John Wiley & Sons, New York
- Mufundirwa A, Fujii Y, Kodama JJJ. o. R. M, Sciences M (2010) A new practical method for prediction of geomechanical failure-time 47(7):1079–1090
- Tsai L, Hsieh Y, Weng M, Huang T, Jeng FJJ. o. R. M., Sciences M (2008) Time-dependent deformation behaviors of weak sandstones 45(2):144–154
- Yang C, Daemen J, Yin JHJJ. o. R M, Sciences M (1999) Experimental investigation of the creep behavior of salt rock 36(2):233–242
- Zhang Y(2012) *Experimental investigation on rheological mechanics of dam foundation deflection zone cataclastic rock and its study of constitutive model*. Ph. D. dissertation. Hohai University, Nanjing (in Chinese)

Acknowledgements The authors would like to express their deep gratitude to Electricity Generating Authority of Thailand (Egat) for the



2020 Kyoto Japan

Monotonic and Cyclic Behaviour of Tephra Layer Landslide at Takanodai from the 2016 Kumamoto Earthquake

Satoshi Goto and Kento Okada

Abstract

The 2016 Kumamoto earthquakes, Japan, caused a large numbers of slope failures, especially a large—scale flow—type landslide was induced in the area near the Aso Volcanological Laboratory of Kyoto University in Takanodai, Minamiaso Village Kumamoto, Japan. From the field observation, sliding surface was the tephra layer of Kusenrigahama fallen pumice (Kpfa) which was deposited by the volcanic activity (around 30,000 years ago, Miyabuchi et al. in VSJ 48(2):195–214, 2003). This tephra layer (Kpfa) was a key soil to understand the mechanism of this large-scale flow-type landslide, then some soils from this tephra layer were retrieved from the sliding surface in the field. This study is focused on the physical properties, monotonic and cyclic direct shear behaviour for the tephra layer (Kpfa) to understand the mechanism of this landslide during earthquake. Constant vertical stress and constant volume cyclic direct shear tests were performed to study the cyclic behaviour of the tephra layer (Kpfa). From the constant vertical stress test, strain hardening behaviour was observed. From the constant vertical stress test, shear displacement increased largely during cyclic loading, despite the tephra layer being in an unsaturated state, which were similar to the behaviour of saturated sand during liquefaction. In the future, this research will be developed considering the study of particle breakage on Kpfa.

Keywords

Monotonic and cyclic shear behaviour • Tephra layer landslide • Kumamoto earthquake • Shear strength

Introduction

On April 14th, 2016, an earthquake occurred in Kumamoto with a magnitude of 6.5 Richter scale. Two days later, another earthquake occurred with a magnitude of 7.3 Richter scale. Main shock of these seismic activities caused a large numbers of slope failures. Among them, a large-scale flow-type landslide with the gentle sloping angle of about 12–15° were induced in the area near the Aso Volcanological Laboratory of Kyoto University in Takanodai, Minamiaso Village, Kumamoto, Japan as shown in Fig. 1. This large-scale flow-type landslide was about 100 m in width, 5–10 m in depth, and 300–600 m in length which killed five people and destroyed at least seven houses (Dang et al. 2016; Mukunoki et al. 2016; Chiaro et al. 2017). Precipitation before earthquake had little effect on this landslide (Japan Meteorological Agency 2016).

Field observation suggested that the sliding surface was located at orange-colored Kusenrigahama fallen pumice (Kpfa) layer which was deposited by the volcanic activity (around 30,000 years ago, Miyabuchi et al. 2003) with depth of 7–8 m from ground surface (Fig. 2a and b). This landslide is called a large—scale flow—type “tephra layer landslide” in this study (Goto and Kimura 2019). This tephra layer (Kpfa) was important key soil to understand the mechanism of this landslide.

A series of monotonic and cyclic direct shear tests (box shear tests) under various conditions were performed to evaluate strength properties and seismic behavior. This study is focused on the physical properties, monotonic and cyclic direct shear behaviour for the tephra layer (Kpfa) to understand the mechanism of this tephra layer landslide during earthquake.

S. Goto (✉)

Department of Civil and Environmental Engineering, University of Yamanashi, Takeda 4-3-11, Kofu, Yamanashi 400-8511, Japan
e-mail: goto@yamanashi.ac.jp

K. Okada

Graduate School of Civil and Environmental Engineering, University of Yamanashi, Takeda 4-3-11, Kofu, Yamanashi 400-8511, Japan
e-mail: g20tc002@yamanashi.ac.jp

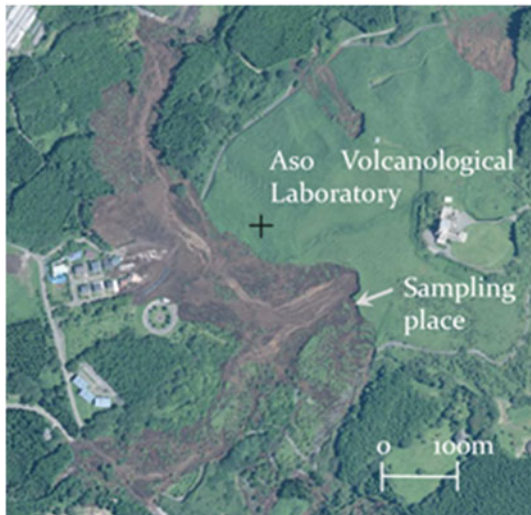


Fig. 1 Tephra layer landslide at Takanodai (GSI 2016)

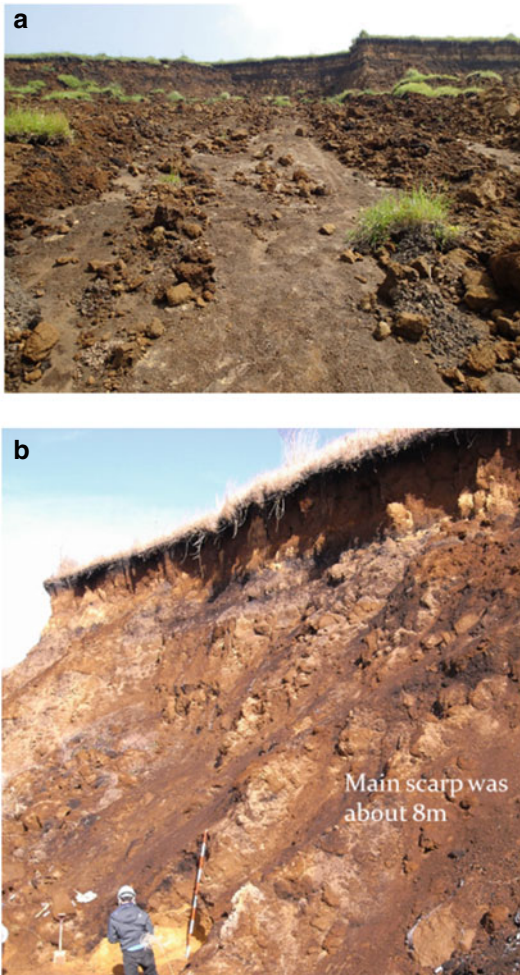


Fig. 2 a Tephra layer landslide at Takanodai, b Place of the main scarp and sampling place

Chigira and Suzuki (2016) summarized the earthquake-induced landslides of pyroclastic fall deposits in Japan and Indonesia, which occurred on gentle slopes and were highly mobile with long runout distance. Cyclic behaviours of the tephra layer (Kpfa) were obtained by ring-shear tests (Dang et al. 2016), by torsional shear tests (Chiaro et al. 2018; Umar et al. 2018) and by box shear tests (Kasama et al. 2018).

Shallow landslides repeatedly occurred on the slopes of Aso volcano during heavy rainfall in 1990, 2001 and 2012 (Paudel et al. 2007; Matsushi et al. 2013; Sato et al. 2017; Higaki et al. 2019; Kimura et al. 2019; Sato et al. 2019).

Field Observation and Physical Properties of Kpfa

Field Observation

Figure 3a shows the stratigraphy and thickness of the tephra layer (Kpfa), Boundary layer and Dark brown layer for the main scarp in the research area. The sliding surface was located at the Kpfa layer at lower part-b. This research was focused on this lower part-b of the Kpfa layer near the sliding surface (Fig. 3a).

Figure 3b shows the Kpfa layer penetrated by boundary layer (white layer) which may demonstrate that the pore water pressure of boundary layer was increased during earthquake. Figure 3c shows undisturbed sample of boundary layer between Kpfa lower part—b and Dark brown layer for direct shear tests (diameter of cutter ring is 6.0 cm).

Physical Properties of Kpfa

Table 1 shows physical properties of the tephra layer (Kpfa) and Dark brown layer for the undisturbed samples. The dry density (ρ_d) for each soils are around 0.5 g/cm^3 . The degrees of saturation (S_r) for the tephra layer (Kpfa) are around 70.0–75.0%, and the degrees of saturation for the Dark brown layer are around 97.6%. The degrees of saturation had quite large values even though there was little rainfall before earthquake.

Figure 4 shows the particle size distribution for the Kpfa lower part-a and b and Dark brown layer. Particle size distribution tests were performed to observe the relation between particle size (mm) and mass percentage passing (%) (JIS A1204, 2009 cited in JGS 2015). It is shown in Fig. 4 that the fine contents for natural Kpfa lower part-a and b are smaller than that for Kpfa lower part-a* and b* crushed by wooden hammer.

Figure 5a shows natural condition of the Kpfa lower part-b sampled near sliding surface, and Fig. 5b shows Kpfa

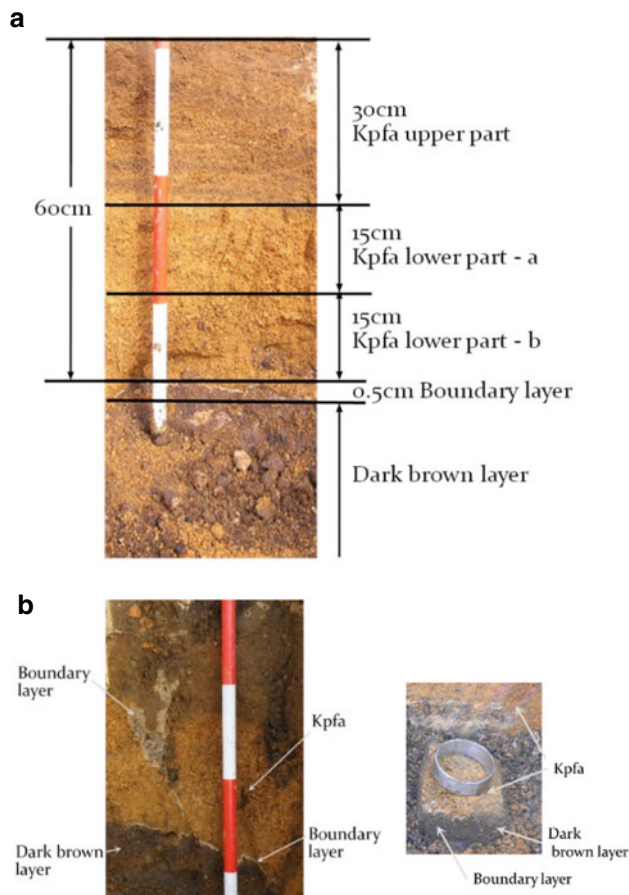


Fig. 3 a Stratigraphy and thickness, b Kpfa layer penetrated by boundary layer (left), c Undisturbed sample of boundary layer between Kpfa lower part -b and Dark brown layer for direct shear tests (diameter of cutter ring is 60mm) (right)

lower part-b crushed by wooden hammer. It is recognized that Kusasenrigahama fallen pumice (Kpfa) layer has a high particle crushability property.

Figure 6 shows saturated permeability of Kpfa lower part-a and b and Dark brown layer. It is shown that saturated permeability for each soils are increasing with the increase of void ratio and that saturated permeability for Kpfa lower part-a and b show similar values. Saturated permeability for Kpfa lower part-a and b is larger than that for Dark brown layer.

Testing Method of Monotonic Direct Shear Tests

On the monotonic direct shear test, a conventional monotonic direct shear box testing machine was used. Undisturbed and reconstituted samples were 60 mm in diameter and 20 mm in height. The shear displacement rate in the

constant vertical stress monotonic direct shear test was set at 0.2 mm/min.

Undisturbed samples (Kpfa lower part-b, Boundary layer, Dark brown layer) tested with vertical stress of 10–50 kN/m² were conducted. The reconstituted samples (Kpfa lower part-b) were tested at 80 kN/m² and 100 kN/m² in addition to 10–50 kN/m².

Moreover, cyclic direct shear tests were conducted with a shear displacement rate of 1.55 mm/min. Both the constant vertical stress and the constant volume for cyclic direct shear test was performed. The vertical loading was measured on the load cell and the clearance between the upper and lower parts of the shear box was set to 0.25 mm. The initial vertical stress in both tests was at 100kN/m² with the reconstituted samples being 60 mm in diameter and 20 mm in height. Cyclic direct shear tests were performed to know the dynamic behaviour of tephra layer (Kpfa) by the “method for consolidated constant volume direct box shear tests on soils” (JGS 0560–2009) and by the “method for consolidated constant pressure direct box shear tests on soils” (JGS 0561–2009).

Constant Vertical Stress Monotonic Direct Shear Tests

Figure 7 shows the results of the constant vertical stress monotonic direct shear test. Reconstituted samples are the similar condition as the lower part-b of Kpfa in the field. The dry density, water content of the samples, and the strength parameters obtained from the tests are shown respectively in Tables 2 and 3. Two approximate lines in Fig. 7 are shown with only a slight deviation, hence the strength parameters c (adhesive cohesion) and ϕ (angle of shear resistance) in Table 3 are similar. Therefore, it can be said that shear strength of reconstituted samples is the same as that of undisturbed samples.

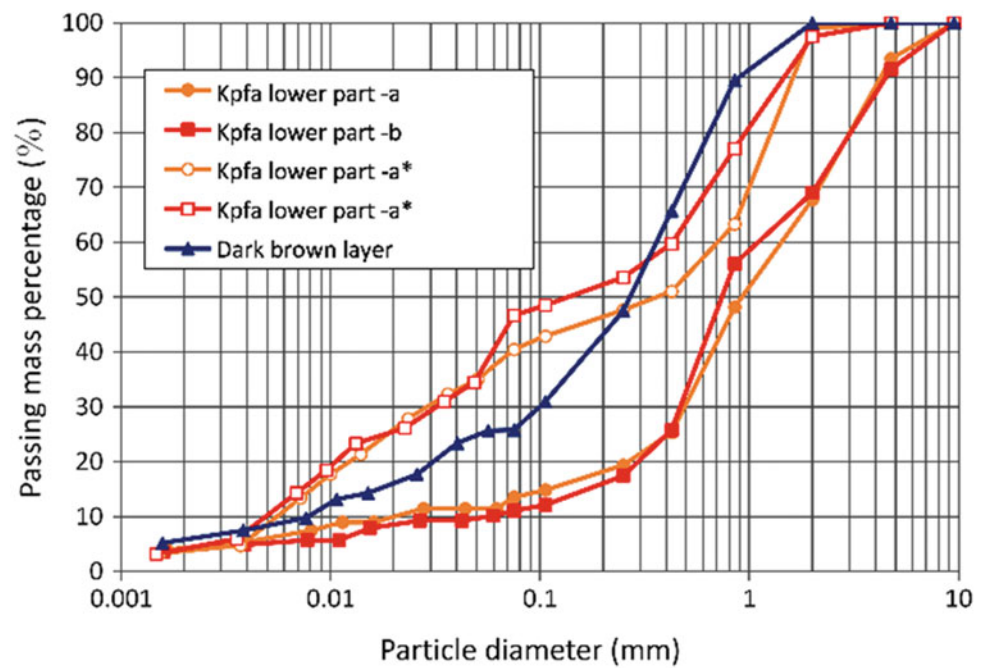
Figure 8 shows the result of constant vertical stress monotonic direct shear tests for Kpfa lower part-a and b, Boundary layer and Dark brown layer which all samples are undisturbed. It is shown that the relation between maximum shear stress and vertical stress for Kpfa lower part-a and b are almost similar although samples are scattered. However, the maximum shear stress and vertical stress relation for Dark brown layer shows different behaviour from that for Kpfa lower part-a and b. Shear strength properties for Dark brown layer around 100 kN/m² may be larger than that for the tephra layer (Kpfa).

Figure 8 also shows the relation between maximum shear stress and vertical stress for Boundary layer between the tephra layer (Kpfa) and Dark brown layer. It was recognized that it was quite difficult to obtain the valuable data for

Table 1 Physical properties of Kpfa and Dark brown layer for the undisturbed samples

	sample	wet density ρ_t [g/m ³]	dry density ρ_d [g/m ³]	water content w [%]	void ratio e	Degree of saturation S_r [%]	density of soil particle ρ_s [g/m ³]
Kpfa lower part -a	1	1.103	0.505	110.1	3.622	73.7	2.425
	2	1.097	0.528	107.8	3.593	72.8	
	3	1.093	0.525	108.2	3.621	72.5	
	4	1.164	0.532	118.9	3.563	81.0	
	Average	1.114	0.522	111.3	3.600	75.0	
Kpfa lower part -b	1	1.092	0.537	103.5	3.734	70.5	2.541
	2	1.083	0.540	100.4	3.702	68.9	
	3	1.074	0.568	89.3	3.476	65.2	
	4	1.159	0.570	103.2	3.456	75.9	
	Average	1.102	0.554	99.1	3.592	70.1	
Dark brown layer	1	1.303	0.557	133.9	3.293	97.2	2.713
	2	1.315	0.569	131.2	3.203	97.9	
	3	1.345	0.588	128.6	3.063	100.3	
	4	1.271	0.536	137.3	3.462	94.8	
	Average	1.309	0.563	132.8	3.255	97.6	

Fig. 4 Particle size distribution of Kpfa and Dark brown layer



Boundary layer from the undisturbed samples by using direct shear box tests.

The water content and dry density of the samples for direct shear tests of Kpfa, Boundary layer, Dark brown layer and reconstituted samples as shown in Table 3 have similar physical properties in Table 2. Table 3 shows Strength

parameters of Kpfa, Boundary layer, Dark brown layer and reconstituted samples. It is shown in Table 3 that strength parameters for undisturbed Kpfa lower part-a and b are similar to those for reconstituted Kpfa lower part-b and that strength parameters for Dark brown layer are larger than those for Kpfa lower part-a and b.

Fig. 5 **a** Natural condition of the Kpfa lower part-b (left), **b** Kpfa lower part-b crushed by wooden hammer (right) (sampled near sliding surface)

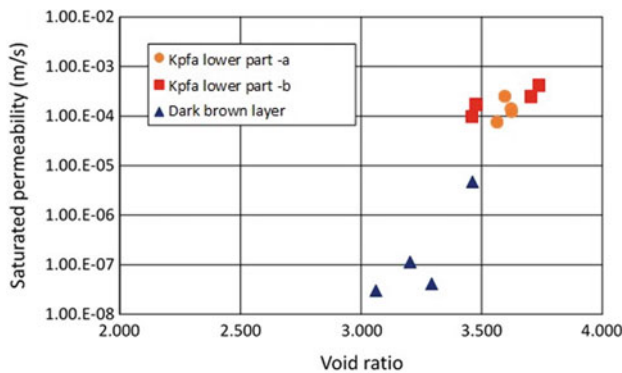


Fig. 6 Saturated permeability of Kpfa and Dark brown layer

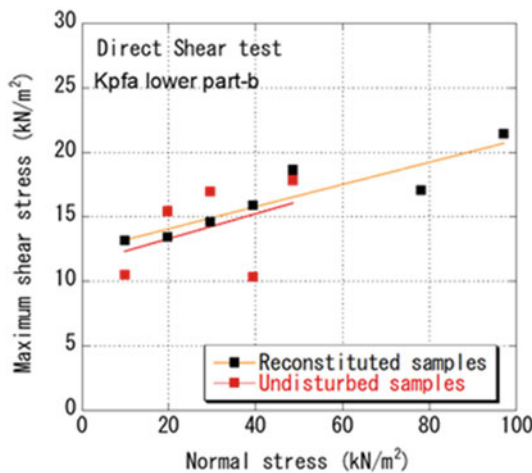


Fig. 7 Result of constant vertical stress monotonic direct shear test for reconstituted and undisturbed samples

Testing Method of Cyclic Direct Shear Tests

Cyclic direct shear tests for constant vertical stress and constant volume were performed to know the cyclic behaviour of tephra layer (Kpfa) during earthquake. The speed of shear displacement was controlled, and the shear direction was reversed when the shear stress reached $+60 \text{ kN/m}^2$ or

-60 kN/m^2 . The number of cycles were ten times for constant vertical stress test and three times for constant volume test.

The measurement range of the shear displacement transducer was from $+10$ to -10 mm. Therefore, if the shear displacement exceeds $+10$ mm or -10 mm during cyclic loading, the direction of the shear displacement is reversed at $+10$ mm or -10 mm of the shear displacement.

Constant Vertical Stress Cyclic Direct Shear Test

Figure 9a shows the relationship between shear stress/vertical stress and shear displacement. The shear displacement reaches about 1.7–1.8 mm at first cyclic loading, and shear displacements are gradually reducing by the next cyclic loadings.

Figure 9b shows the relationship between shear stress/vertical stress and vertical displacement. This sample is gradually being contracted by the cyclic loadings, and the vertical displacement is converged around 2.5 mm. Strain hardening occurs showing that shear displacement gradually reduces by cyclic loadings.

Constant Volume Cyclic Direct Shear Test

Figure 10a shows the relationship between shear stress and shear displacement. The shear displacement is gradually increased by the cyclic loading. At the 2nd loading, the shear displacement reached $+ \geq 10$ mm or $- \leq 10$ mm. The shear displacement increases as the number of cycles increase. The shear displacement for constant volume test is larger than that of the constant vertical stress test.

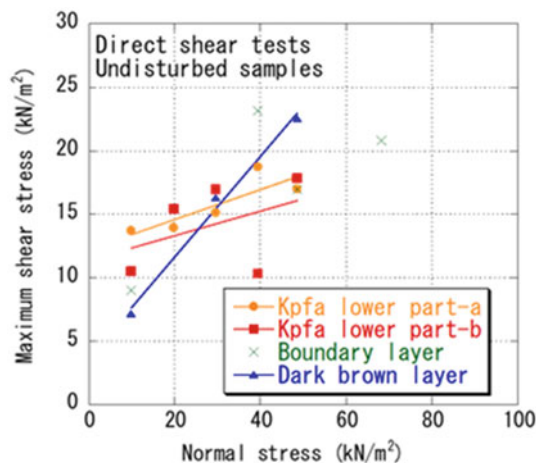
Figure 10b shows the relationship between vertical stress and shear stress. The vertical stress is decreasing to zero value of vertical stress by the first loading. It can be said that this behavior may be similar to the phenomena of cyclic mobility for saturated sand during an earthquake.

Table 2 The water content and dry density of the samples for direct shear tests of Kpfa, Boundary layer, Dark brown layer and reconstituted samples

Vertical stress (kN/m ²)	Kpfa lower part -a		Kpfa lower part -b		Boundary layer		Dark brown layer		Reconstituted sample	
	ρ_d (g/cm ³)	w (%)	ρ_d (g/cm ³)	w (%)	ρ_d (g/cm ³)	w (%)	ρ_d (g/cm ³)	w (%)	ρ_d (g/cm ³)	w (%)
9.86	0.504	124.09	0.511	98.65	0.521	111.07	0.596	123.99	0.580	82.8
19.72	0.471	114.00	0.550	99.26					0.555	95.9
29.53	0.502	110.88	0.535	96.11			0.592	122.45	0.595	78.8
39.39	0.476	116.50	0.547	109.90	0.637	107.51			0.570	83.5
48.54	0.432	117.87	0.576	96.59	0.590	105.84	0.606	121.73	0.590	88.1
68.21					0.642	102.95				
78.07									0.625	78.3
97.08									0.619	75.9
Average	0.477	116.67	0.544	100.10	0.598	106.84	0.598	122.72	0.591	83.3

Table 3 Strength parameters of Kpfa, Boundary layer, Dark brown layer and reconstituted samples

	c (kN/m ²)	ϕ (°)
Kpfa lower part -a	12.2	6.72
Kpfa lower part -b	11.4	5.56
Boundary layer	–	–
Dark brown layer	3.7	21.66
Reconstituted sample (Kpfa lower part -b)	12.4	4.97

**Fig. 8** Result of constant vertical stress monotonic direct shear test for Kpfa lower part-a and b, Boundary layer and Dark brown layer which samples are undisturbed

Soil Strengths by Yamanaka-Type Soil Penetrometer

Table 4 shows soil strengths by using Yamanaka-type soil penetrometer in the field. It can be shown that the strength for Kpfa lower part—a is similar to that for Kpfa lower part

—b and that strengths for Boundary layer and Dark brown layer are smaller than that for Kpfa lower part—a and b. These results by Yamanaka-type soil penetrometer are similar to the results for direct shear tests by using undisturbed samples at low normal stress as shown in Fig. 8.

Conclusions

The following conclusions can be derived from this study:

1. The monotonic direct shear strengths of the undisturbed and reconstituted samples of the tephra layer (Kpfa) have similar results.
2. From the constant vertical stress cyclic direct shear test, strain hardening occurs showing that shear displacement gradually reduces by cyclic loadings.
3. From the constant volume cyclic direct shear test, despite being at an unsaturated state, Kpfa behaves in a way similar to the liquefaction of saturated sand during earthquake. Shear displacement for constant volume test is considerably larger than that for constant vertical stress test.
4. This study will be developed considering the Kpfa particle breakage.

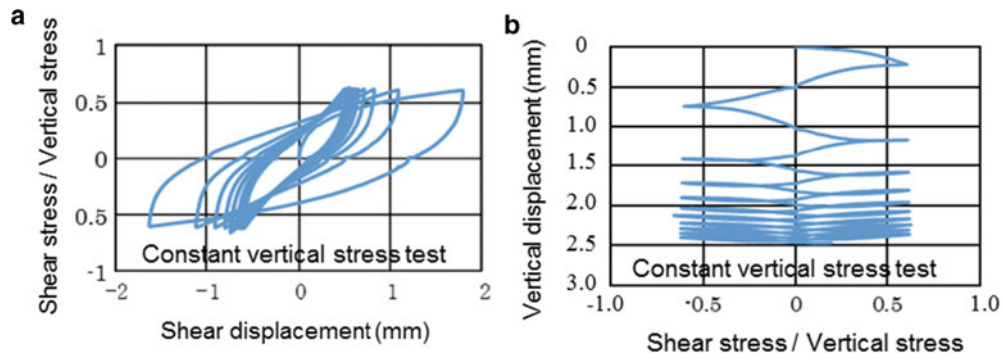


Fig. 9 **a** Relationship between shear stress/vertical stress and shear displacement for constant vertical stress, **b** Relationship between shear stress/vertical stress and shear displacement for constant vertical stress

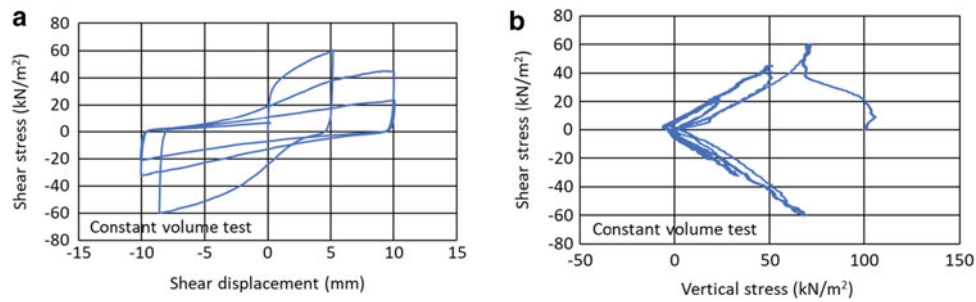


Fig. 10 **a** Relationship between shear stress and shear displacement for constant volume, **b** Relationship between vertical stress and shear stress (stress path) for constant volume

Table 4 Results of soil strengths by Yamanaka-type soil penetrometer in the field

Tephra layers	1	2	3	4	5	6	Average	Average
Kpfa lower part -a	23.0	23.0	23.5	24.5	24.0	23.0	23.5	23.5
	23.5	23.0	23.5	23.0	24.5	23.0	23.4	
	23.0	22.5	23.0	23.5	24.5	24.5	23.5	
Kpfa lower part -b	24.0	24.0	25.0	23.5	26.5	25.5	24.8	24.1
	23.0	24.5	24.5	23.0	25.0	24.5	24.1	
	22.0	24.0	25.0	23.5	22.0	24.0	23.4	
Boundary layer	24.0	22.0	20.0	25.0	21.0	19.0	21.8	21.8
Dark brown layer	21.0	19.5	20.0	21.0	22.0	20.5	20.7	21.5
	21.0	23.5	21.0	22.0	20.5	20.0	21.3	
	23.5	23.5	23.5	22.5	20.0	21.5	22.4	

Acknowledgements Prof. Toshitaka Kamai. and Prof. Gonghui Wang of DPRI of Kyoto University are acknowledged for their discussion on Takanodai landslide. Sincere appreciation is also dedicated to many

students, particularly Ms Mega Lia Istiyanti, Mr. Shuto Akashi and Mr. Naoya Ozawa. A part of this study was carried out by JSPS KAKENHI Grant Number JP17H03303.

References

- Chiaro G, Alexander G, Brabbaharan P, Massey C, Koseki J, Yamada S, Aoyagi Y (2017) Reconnaissance report on geotechnical and geological aspects of the 14–16 April 2016 Kumamoto earthquakes, Japan. *Bull New Zealand Soc Earthquake Eng* 50(3):1–29
- Chiaro G, Umar M, Kiyota T, Massey C (2018) The Takanodai landslide, Kumamoto, Japan: insights from post-earthquake field observations, laboratory tests, and numerical analyses. *Geotech Earthquake Eng Soil Dyn* 98–111
- Chigira M, Suzuki T (2016) Prediction of earthquake-induced landslides of pyroclastic fall deposits. *Landslides and Engineered Slopes. Experience, Theory and Practice*. In: Aversa S, Cascini L, Picarelli L, Scavia C (Eds.), CRC Press. 93–100
- Dang K, Sassa K, Fukuoka H, Sakai N, Sato Y, Akara K, Quang LH, Loi DH, Tien PV, Ha ND (2016) Mechanism of two rapid and long-runout landslides in the 16 April Kumamoto earthquake using a ring-shear apparatus and computer simulation (LS-RAPID). *Landslides* 13:1525–1534
- Geographical Survey Institute Map (2016) Around the Kyoto University Volcano Research Center in the Takanodai area of Minamiaso village. URL: <https://www.gsi.go.jp/BOUSAI/H27-kumamoto-earthquake-index.html> (Last accessed 30 Aug 2019)
- Goto S, Kimura T (2019) Introduction of the special issue on “Toward the prediction of shallow landslides induced by heavy rainfalls on tephra-covered slopes. *J Japan Landslide Soc* 56:211–217 (in Japanese)
- Higaki D, Li X, Hayashi I, Tsou C, Kimura T, Hayashi S, Sato G, Goto S (2019) Geomorphological setting of shallow landslides by heavy rainfall on tephra-covered slopes of Aso Volcano, southwest Japan. *J Japan Landslide Soc* 56:218–226 (in Japanese with English abstract)
- Japanese Geotechnical Society (2015) Japanese geotechnical society standards, laboratory testing standards of geomaterials. 1
- Japan Meteorological Agency (2016) Information related to the 2016 Kumamoto earthquake. URL: https://www.jma.go.jp/jma/menu/h28_kumamoto_jishin_menu.html (Last Accessed: 30 Aug 2019)
- Kasama K, Yamagata S, Tanaka K, Furukawa Z, Yasufuku N (2018) Seismic stability evaluation of volcanic soil at Takanodai, Minamiaso village, Kumamoto. *Geotech J* 13(3):171–181 (in Japanese with English abstract)
- Kimura T, Goto S, Sato G, Wakai A, Hayashi S, Higaki D (2019) Evaluation of landslide susceptibility by slope stability analysis using an estimated distribution of tephra deposits—A case study in the northeastern part of Aso caldera—. *J Japan Landslide Soc* 56:240–249 (in Japanese with English abstract)
- Matsushi Y, Saito H, Fukuoka H, Furuya G, (2013) Landslides of tephra deposits on hillslope of the Aso caldera wall and volcanic central cones by the North-Kyushu heavy rainfall at July 2012. URL: <http://repository.kulib.kyoto-u.ac.jp/dspace/bitstream/2433/181543/1/a56b0p28.pdf> [Last accessed: 19 Mar 2020]
- Miyabuchi Y, Hoshizumi H, Takada H, Watanabe K, Xu S (2003) Pumice-fall Deposits from Aso Volcano during the Past 90,000 Years, Southwestern Japan. *Volcanological Soc Japan* 48(2):195–214 (in Japanese with English abstract)
- Mukunoki T, Kasama K, Murakami S, Ikemi H, Ishikura R, Fujikawa T, Yasufuku N, Kitazono Y (2016) Reconnaissance report on geotechnical damage caused by an earthquake with JMA seismic intensity 7 twice in 28 h, Kumamoto, Japan. *Soils Found* 56(6):947–964
- Paudel PP, Omura H, Kubota T, Inoue T (2007) Spatio-temporal patterns of historical shallow landslides in a volcanic area, Mt. Aso, Japan. *Geomorphology* 88:21–33
- Sato G, Goto S, Kimura T, Hayashi S, Istiyanti ML, Komori J (2017) Gravitational deformation as a precursor of shallow landslide within tephra-covered slope deposits in the Aso caldera, Japan. *J Japan Landslide Soc* 54(5):199–204 (in Japanese with English abstract)
- Sato G, Wakai A, Goto S, Kimura T (2019) Strength characteristics of gravitationally deformed slope deposits of tephra and kuroboku soils in the Aso caldera, Japan—Application of revised vane-shear-cone test for estimating shear strength—. *J Japan Landslide Soc* 56:250–253 (in Japanese with English abstract)
- Umar M, Chiaro G, Kiyota T, Miyamoto H (2018) Monotonic and cyclic undrained behavior of Kumamoto-Aso pumice soil by triaxial and torsional shear tests. 16th European Conference on Earthquake Engineering. 1–11



2020 Kyoto Japan

Shearing Rate Effect on Residual Strength of Typical Clay Soils in Ring Shear Test

Deepak Raj Bhat

Abstract

This paper presents the effect of shear rates on residual strength of four typical clay soils having high to low plasticity in its soil natures. The shear rates were fixed in a range of 0.073–0.586 mm/min. A series of tests were performed by means of ring shear apparatus. The effect of shear rates on residual strength of the high plasticity soils, medium plasticity soils and low plasticity soils were compared. The results showed that hardly increases in the strength from the residual-state of shear after the shear rate of 0.233 mm/min.

Keywords

Residual strength • Rate effect • Clay soils • Ring shear test

Introduction

The residual strength of clay soils is defined as the minimum constant value attained after large shear displacements in low shear rates. A ring shear apparatus is being widely used to measure the residual shear strength of a clay soils in these days. The main advantage of the ring shear apparatus is that it can shear the specimen continuously in one direction to obtain the large displacement, and this allows clay particles to be oriented parallel to the direction of shear to develop the true residual shear strength condition (Bishop et al. 1971; Tika 1999; Bhat et al. 2013c). Another advantage of the ring shear apparatus is that no change occurs in the shear plane area during shear (Tiwari and Marui 2004; Vithana et al. 2012, Bhat et al. 2014). For the precise measurement of

residual strength, the large deformation is applied to a soil sample so that clay particles are oriented along the shear surface in the direction of shear to the maximum possible extent (Skempton 1985; Sassa et al. 2004; Bhat et al. 2013a and 2013b).

The residual strength of soils is the most important parameter in the stability analysis of ancient landslide and reactivation potential evaluation. For the stability analysis and design of countermeasures works against the reactivation of landslides, the shear strength parameters such as residual frictional angle and the cohesion of soil are necessary. If there is a slight change in the residual strength parameters, the net results of the stability assessment of landslides might also be affected. Hence, the exact value of the shear strength parameters should be considered for the slope stability design and countermeasure works of landslides. Therefore, study of shear rate effect of residual strength seems important for estimating the exact design parameters with high accuracy and reliability.

The residual shear strength changes with clay content of the cohesive soil in ring shear test (Lupini et al. 1981). The effect of shear rate between 0.002–0.1 mm/min on residual strength was negligible in clay soils (Skempton 1985). Yatabe et al. (1991) reported that the residual strength of clays in fractured-zone landslide areas hardly increase with increase in the shear rates. Tika et al. (1996) stated that some soils show greater shear strength than the residual strength (positive rate effect) in high shear rates, while some soils exhibit a lower strength (negative rate effect) or a constant shear strength (neutral rate effect) with varying in shear rates. Suzuki et al. (2001) reported that the shear rate in a range of 0.02–2.0 mm/min significantly influenced the residual strength of clay soils and mud stone. Bhat et al. (2013c and Bhat and Yatabe 2015) reported that the hardly increase in the strength from the residual-state of shear on kaolin clay in slow shear displacement rates. The shear strength of natural clays was increased in ring shear test when the shear rate decreased (Gratchev and Sassa 2015).

D. R. Bhat (✉)
Engineering Department, Okuyama Boring Co. Ltd,
Yokote, Akita 013-0046, Japan
e-mail: deepakbhat@okuyama.co.jp

In summary, the previous studies have been recognized the three types of variation of residual strength of clay soils with variation of shear rates, which are named as positive, neutral, and negative rate effect. In the positive shear rate effect, the residual shear strength increases with variation of shear rates under a given normal stress. Similarly, when the residual shear strength does not change with variation of shear rates for the same given normal stress, it is called neutral rate effect. On the other hand, if the residual shear strength of clay soil may decrease with variation of shear rates, it is named as negative rate effect. Therefore, there is still confusion that various of sharing rates affect the residual strength of a clay soil or not. This study addresses such issues by the help of ring shear test on four typical clay soils having high plasticity to low plasticity in their soil's nature with varying the shear rates of 0.073 mm/min–0.586 mm/min.

Materials and Method

In this study, four typical clayey soils were chosen for the ring shear tests. One of them is commercially available kaolin clay, name as “Clay soil-I” and the other three were collected from the landslide sites in Japan and Nepal. The second sample from Nepal (from Krishnabhir landslide area) was confirmed to have a comparatively high amount of mica, which is referred to as “Clay soil-II.” Similarly, the clay sample from a landslide site in Shikoku area of Japan was confirmed to have a comparatively high amount of chlorite, which is referred to as “Clay soil-III,” and the clay sample from a landslide site in Kobe area of Japan was confirmed to have a comparatively high amount of smectite, which is referred to as “Clay soil-IV.”

The physical properties of the tested samples are presented in Table 1. The plasticity index of the Clay soil-I was the highest and followed by the Clay soil-IV, the Clay soil-III, and then the Clay soil-II respectively. The clay particle size (i.e. <2 μm) of the Clay soil-I was also the

highest, and the lowest for the Clay soil-III (Table 1). Similarly, the grain size distribution curve of the typical clay soils is shown in Fig. 1.

In ring shear apparatus, the lower half of the apparatus below the plane of failure is made to rotate while the upper part is fixed. During the running of the apparatus; resistance develops in the upper part and such value is measured by load measuring device (e.g. force transducer or a load cell), which measured the shearing force due to rotation of the lower part transmitted to the upper through the sheared soil specimen. During the soil test, the rotation is continuous until the resistance value will be constant, and such constant value is called residual state of shear. Bishop et al. (1971) type of ring shear apparatus was used in this study. In this ring shear apparatus, the specimen container has inner and outer diameters of approximately 8.0 centimetres and 12.0 centimetres, respectively, and an average thickness of 3.2 centimetres. The specimen is sheared through a level of 0.7 centimetres above the base of the lower plate. The ratio of the outer to inner ring diameters is 1.5.

There are three basic major steps/stages in the ring shear test: (a) Sample preparation: First, sample preparation was carried out. For this, about 200 grams of finer than 425 μm dry sample was mixed with distilled water until it turned into a thick liquid (i.e. viscous liquid). The fully mixed thick liquid sample was then de-aired in a vacuum chamber to make it fully saturated. The de-aired sample was then poured into a specimen mold and pre-consolidated under desired loads for about 24 h. Then, the specimen was carefully transferred from the specimen mold to the specimen container of the ring shear apparatus for further consolidation and shearing. (b) Consolidation stage: Next, the specimen was consolidated further before shearing was begun. In the consolidation stage, at first an effective normal stress of 196.2 kN/m^2 was applied, and after the end of the consolidation stage, the effective normal stress was reduced to 98.1 kN/m^2 so as to achieve an over consolidation ration (OCR) of 2. This was done for the purpose of obtaining a distinct difference in peak and residual strength because in most cases of normally consolidated clayey samples

Table 1 Physical properties of the tested samples

Sample name	Solid density, Gs (g/cm^3)	Liquid limit, LL (%)	Plastic limit, PL (%)	Plasticity index, PI (%)	Soil classification (%)		
					Clay	Silt	Sand
Clay soil-I	2.72	52	22	30	74	26	0
Clay soil-II	2.74	34.1	20.7	13.4	21	59.7	19.3
Clay soil-III	2.75	47.5	31.2	16.3	20	68.1	11.9
Clay soil-IV	2.65	96.5	59.0	37.5	24	18.0	58.0

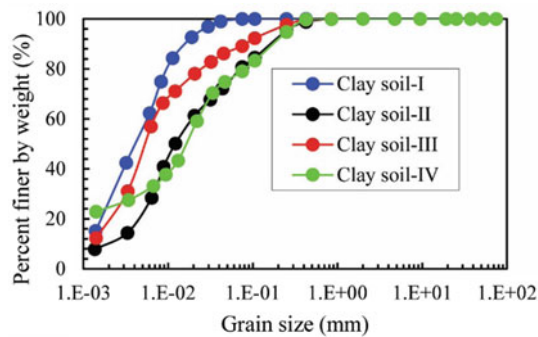


Fig. 1 Grain size distribution curves

in the ring shear machine, the amount of drop from the peak to residual strength is insignificant. So, all shear tests were conducted under an effective normal stress of 98.1 kN/m^2 . (c) Finally, the over consolidated sample were sheared at different rates of shear. The shearing rates were varied from 0.073 mm/min to 0.586 mm/min (as 0.073 mm/min , 0.162 mm/min , 0.233 mm/min , 0.313 mm/min , 0.398 mm/min , and 0.586 mm/min) and the shearing was continued until a specimen reached its residual state.

Results and Discussion

As the representative results, the results of the various shear rates of the Clay soil-IV is presented in terms of variation of shear stress and volumetric strain to shear displacement in Fig. 2. The overall ring shear test results indicated that the peak strength and the residual shear strength of the Clay soil-I was the highest, and followed by the Clay soil-II, the Clay soil-III, and the Clay soil-IV. For example, at the shear rate of 0.073 mm/min , the peak strength and the residual strength of the Clay soil-I were noted 53.45 kN/m^2 and 48.13 kN/m^2 respectively. Similarly, the peak strength and the residual strength of the Clay soil-II, the Clay soil-III, and the Clay soil-IV were recorded 51.10 kN/m^2 and 44.87 kN/m^2 , 43.70 kN/m^2 and 24.88 kN/m^2 , and then 40.55 kN/m^2 and 8.88 kN/m^2 respectively. However, the difference between the peak strength and the residual strength of the Clay soil-IV was the highest (i.e. 31.67 kN/m^2), followed by the Clay soil-III (i.e. 18.82 kN/m^2), the Clay soil-II (i.e. 6.23 kN/m^2), and then the Clay soil-I (i.e. 5.32 kN/m^2) respectively. In case of the shear rates of 0.162 mm/min to 0.586 mm/min , the test results of the shear stress versus the shear displacement and the volumetric strain versus the shear displacement of the Clay soil-I followed the similar pattern as the results obtained at a shear rate of 0.073 mm/min . Similarly, the similar patterns of the stress-strain curves were observed in the shear rate of 0.162 mm/min to 0.586 mm/min in case of the Clay soil-II, the Clay soil-III, and the Clay soil-IV respectively. It was observed that the

Clay soil-I was the strongest and the Clay soil-IV was the weakest. The Clay soil-IV showed the high plasticity in its soil's nature and the Clay soil-III, and the clay soil-II showed the medium plasticity in their soil's nature. Similarly, the Clay soil-I showed the low plasticity in its soil nature. Summary of the various shear rate tests of the Clay soil-I, the Clay soil-II, the Clay soil-III, and the Clay soil-IV are presented in the Table 2.

The residual shear strengths of the Clay soil-I were found to vary from 48.13 kN/m^2 to 49.24 kN/m^2 with the shear rates of 0.073 – 0.586 mm/min (Table 2). The residual shear strengths of the Clay soil-II, the Clay soil-III, and the Clay soil-IV were found to vary in a range of 44.87 – 46.0 kN/m^2 , 24.88 – 26.94 kN/m^2 , and 8.88 – 11.85 kN/m^2 for shear rates of 0.073 – 0.586 mm/min (Table 2). In case of the Clay soil-I, the same values of the residual strength (i.e. 48.1 kN/m^2) were recorded for the shear rates of 0.073 and 0.0162 mm/min . The same value of the volumetric strain (i.e. 1.4%) was also obtained with that shear rate of 0.073 mm/min and 0.162 mm/min . Similarly, the same value of the residual shear strength and the volumetric strain were found in the shear rates of 0.073 and 0.0162 mm/min in case of the Clay soil-II, the Clay soil-III, and the Clay soil-IV. In this study, the residual shear strengths for all tested samples were found to remain almost the same for the shear rates range from 0.073 mm/min to 0.162 mm/min (i.e. neutral rate effect). This may lead to understand that a clay material exhibits only negligible effect of slower shear rate (up to 0.162 mm/min) on the residual shear resistance. The

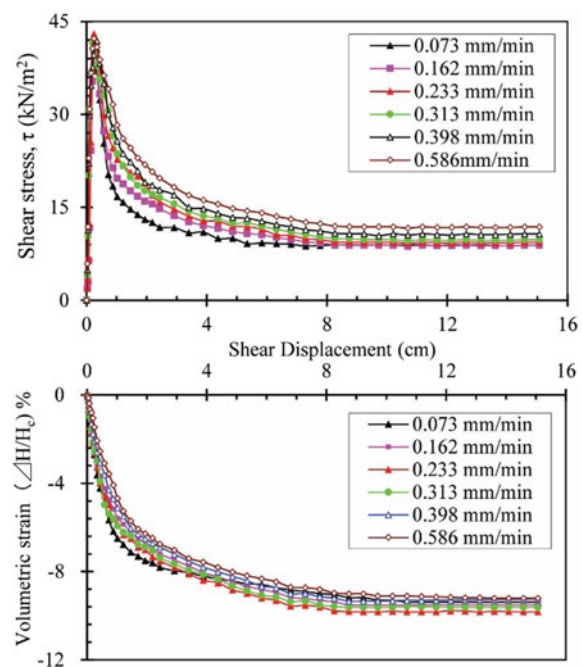


Fig. 2 Typical results of shear rate tests (Clay soil-IV)

Table 2 Summary of shear rate tests of the clay soils

Test no.	Shear rate (mm/min)	Residual strength of clay soils, τ_r (kN/m ²)			
		I	II	III	IV
1	0.073	48.13	44.87	24.88	8.88
2	0.162	48.19	44.86	24.89	8.87
3	0.233	48.56	44.95	24.96	9.35
4	0.313	48.94	45.25	25.3	9.78
5	0.398	49.05	45.65	26.05	10.71
6	0.586	49.24	46.05	26.94	11.85

findings in this study has been confirmed the conclusions made by the Skempton's (1985). Moreover, the finding of this study is also agreed with the finding of Yatabe et al. (1991) and Bhat et al. (2013c, 2014 and Bhat and Yatabe 2015).

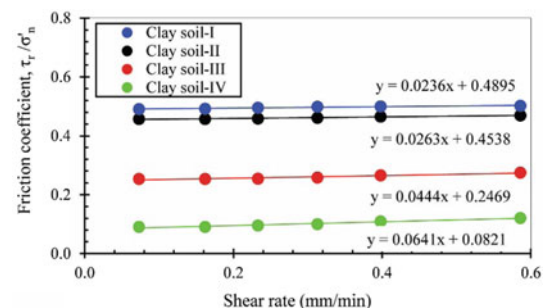
Lemos et al. (1985) reported that residual strength of high plasticity soils increases and decreases for low plasticity soils with increase in shear rate. Non plastic soils show the negative rate effect and plastic soils show the positive rate effect (Parathiras 1994). In this study, the plastic index of Clay soil-IV is the highest (i.e. 37.5%) to compared with the other tested landslides involved clay soils. Therefore, the Clay soil-IV shows the high plasticity in its soil nature. Similarly, the plasticity index of 16.3% and 13.4% were found for the Clay soil-III and Clay soil-II (Table 1), which represent the medium plasticity soil and low plasticity soil respectively. From overall analysis of the test results, the maximum value of the increased in shear strength of 2.97 kN/m² from its residual state of shear was observed in case of Clay soil-IV (high plasticity soil), followed by the Clay soil-III (medium plasticity soil) and Clay soil-II (low plasticity soil) with the value of maximum increase in shear strength value of 2.06 and 1.18 kN/m² respectively. Hence, it can be concluded that the effect of the shear rates on the residual strength are noticeable for the high plasticity soils with compare to the low plasticity soils. From this, it understood that the effect of shear rates on residual strength will be slightly greater in higher plastic soils than in less plastic soils. These results are agreed with the conclusion made by Skempton (1985), Lemos et al. (1985), and Parathiras (1994).

The relation between residual friction coefficient and shear rate of the tested clay soils are presented in Fig. 3. In case of the Clay soil-I, the same residual friction coefficient (i.e. 0.491) were found with the shear rates of 0.073 mm/min and 0.162 mm/min. Similarly, the value of the residual friction coefficient of the Clay soil-II, the Clay soil-III, the Clay soil-IV were observed 0.457, 0.254, and 0.091 for the shear rates of 0.073 mm/min and 0.162 mm/min respectively (Fig. 3). Based on those results, it was understood that the residual friction coefficient of clay soils has not affected

by the shear rate up to 0.162 mm/min. When the shear rates were varied in a range of 0.162–0.586 mm/min, the residual friction coefficients of the tested clay soils were found to be affected. The residual friction coefficients of the Clay soil-I, the Clay soil-II, the Clay soil-III, and the Clay soil-IV were found to vary in a range of 0.491 to 0.502, 0.457 to 0.469, 0.254 to 0.275, and 0.091 to 0.121 with variation of shear rates from 0.162 mm/min to 0.586 mm/min respectively. The value of increased in residual friction coefficient for the Clay soil-I, the Clay soil-II, the Clay soil-III, and the Clay soil-IV were found 0.011, 0.012, 0.021, and 0.030 respectively. Therefore, the residual friction coefficient of clay soil is a slight increase when the shear rate is also increased. Lupini et al. (1981) reported that the residual friction coefficient increased continuously increased in the slow the shear rates in the ring shear tests. The results thus obtained in this study are also in close agreements with the finding of Lupini et al. (1981) and Gratchev and Sassa (2015).

Conclusions

This paper presents the shearing rate effect on residual strength of four typical clay soils having high to low plasticity. Three clay samples were collected from the landslide sites in Japan and Nepal, while another sample was commercially available kaolin clay. The shear tests were carried out using Bishop et al. (1971) type of ring shear apparatus.

**Fig. 3** Relation between residual friction coefficient and shear rate

The shear rate was varied in a range from 0.073 mm/min to 0.586 mm/min (as 0.073, 0.162, 0.233, 0.313, 0.398 and 0.586 mm/min) and the shearing was continued until a specimen reached its residual-state of shear. From the analysis of test results, it was understood that the negligible effect on the residual strength of clay soils was observed in the shear rates of 0.073–0.162 mm/min in case of the Clay soil-II, Clay soil-III, and Clay soil-IV (i.e. neutral rate effect). A slight increase in strength from its residual-state of shear was observed after a shear rate of 0.233 mm/min for all tested clay soils (i.e. positive rate effect). Moreover, the increase in shear strength from its residual state with increase in shear rate were slightly higher in high plasticity soils than in low plasticity soils in a shear rate range from 0.233 mm/min to 0.586 mm/min.

Acknowledgements The author would like to acknowledge Dr. Ryuichi Yatabe (Emeritus Professor, Ehime University, Japan) and Dr. N. P. Bhandary (Professor, Ehime University, Japan) for giving a series of advices and suggestions during the laboratory test of this work in Ehime University, Japan.

References

- Bhat DR, Yatabe R (2015) Effect of shearing rate on residual strength of landslide soils. *Eng Geol Soc Territory* 2:1211–1215
- Bhat DR, Yatabe R, Bhandary NP (2014) Slow shearing rates' effect on residual strength of landslide soils. *Geotech Spec Publ* 236:293–303
- Bhat DR, Bhandary NP, Yatabe R (2013a) Study of preexisting shear surfaces of reactivated landslides from a strength recovery perspective. *J Asian Earth Sci* 77:243–253
- Bhat DR, Bhandary NP, Yatabe R (2013b) Residual-state creep behavior of typical clayey soils. *Nat Hazards* 69(3):2161–2178
- Bhat DR, Bhandary N, Yatabe R (2013c) Effect of shearing rate on residual strength of kaolin clay. *Electron J Geotech Eng* 18 (G):1387–1396
- Bishop AW, Green E, Garge VK et al (1971) A new ring shear apparatus and its application to the measurement of residual strength. *Geotechnique* 21(4):273–328
- Gratchev I, Sassa K (2015) Shear strength of clay at different shear rates. *J Geotech Environ Eng* 141(5):06015002–6015011
- Lemos LJJ, Skempton AW, Vaughan PR (1985) Earthquake loading of shear surfaces in slopes. *Proc 11th ICSFE, San Francisco, USA*, 4:1955–1958
- Skempton AW (1985) Residual strength of clays in landslides, folded strata, and the laboratory. *Geotechnique* 35(1):3–18
- Tiwari B, Marui H (2004) Objective oriented multistage ring shear test for shear strength of landslide soil. *J Geotech Geoenviron Eng* 130 (2):217–222
- Lupini JF, Skinner AE, Vaughan PR (1981) The drained residual strength of cohesive soils. *Geotechnique* 31(2):181–213
- Parathiras AN (1994) Displacement rate effects on the residual strength of soils. Ph.D. Thesis, University of London. (Imperial College of Science, Technology and Medicine)
- Sassa K, Fukuoka H, Wang G, Ishikawa N (2004) Undrained dynamic-loading ring-shear apparatus and its application to landslide dynamics. *Landslides* 1:7–19
- Suzuki M, Yamamoto T, Tanikawa K (2001) Variation in residual strength of clay with shearing speed. Research Report, Yamaguchi University 52(1):45–49
- Tika TE (1999) Ring shear tests on a carbonate sandy soil. *Geotech Test J* 22(4):342–355
- Tika TE, Vaughan PR, Lemos LJ (1996) Fast shearing of pre-existing shear zones in soil. *Geotechnique* 46(2):197–233
- Vithana SB, Nakamura S, Kimura S, Gibo S (2012) Effects of overconsolidation ratios on the shear strength of remoulded slip surface soils in ring shear. *Eng Geol* 131–132:29–36
- Yatabe R, Yagi N, Enoki M et al (1991) Strength characteristics of landslide clay. *J Japan Landslide Soc* 28(1):9–16. (Japanese)



2020 Kyoto Japan

Simple Shear Tests for Unsaturated Soils

Mariagiovanna Moscariello and Sabatino Cuomo

Abstract

Rainfall-induced landslides in Southern Italy often affect the pyroclastic soils produced by the past explosive activity of Vesuvius volcano. Along hilly zones these soils are mostly unsaturated and characterized by a metastable structure, which can experience static liquefaction upon shearing. Several authors studied the mechanical behaviour and the wetting-induced collapse through triaxial tests and direct shear tests. Here, a new series of tests is performed—on remolded specimens—through the Suction Controlled Simple Shear apparatus, which is particularly suitable to reproduce the in-situ stress–strain hillslope conditions and the strain/stress paths induced by rainfall during the failure and post-failure mechanisms. The results are discussed in terms of shear strain, axial strain and saturation degree.

Keywords

Suction • Failure • Deformation • Wetting • Mechanisms

Introduction

Shallow landslides are frequently triggered by rainfall in several geo-environmental contexts, and typical examples are those in pyroclastic soil deposits of Southern Italy, where loose unsaturated soils experience static liquefaction and collapse upon shearing. The stress–strain behaviour and soil strength parameters have been investigated through triaxial

tests and direct shear tests in saturated and unsaturated conditions, as reported by Bilotta et al. (2005) and Cuomo et al. (2015, 2017). Particularly, suction produces a significant increase in shear strength of both undisturbed and remoulded soils, more evident for remoulded specimens, probably due their different internal structure.

However, triaxial and direct shear apparatus cannot properly reproduce the rotation of the original directions of the principal stress axes, which is a mechanism often occurring at failure for slopes covered by shallow deposits (Cuomo et al. 2017; Sorbino et al. 2011). Moreover, the effect of shear stress and shear deformation on soil hydraulic response is not yet fully understood because the soil water retention was usually investigated through volume extractor, Richard's plate and oedometric apparatus where shearing is prevented. In the same way, the collapse of pyroclastic soils in the literature was mostly investigated through wetting tests using standard or suction-controlled oedometer and suction-controlled triaxial tests, i.e. using devices that do not completely reproduce the in-situ conditions of deposits along steep slopes.

This paper aims to go beyond the state of the art on this topic, so that the hydro-mechanical behaviour is here analysed through simple shear tests and wetting tests in simple shear condition.

Materials and Methods

Testing Device

The Suction Controlled Simple Shear (SCSS) device allows applying a vertical load to a soil specimen, and a “shearing mode” through the application of a controlled (i) horizontal force or (ii) horizontal displacement. For this reason, the SCSS is suitable to reproduce the in-situ conditions of a slope and the strain and stress paths induced by rainfall during the failure and post-failure mechanisms. The equipment used for the tests was described in detail by Cuomo

M. Moscariello · S. Cuomo (✉)
Department of Civil Engineering, University of Salerno, 84084
Fisciano, Italy
e-mail: scuomo@unisa.it

M. Moscariello
e-mail: mamoscariello@unisa.it

et al. (2017) and Moscariello (2017). Hereafter, the main characteristics are briefly reported.

The axis translation technique is used to measure or apply the matric suction (s), i.e. the difference of pore-air pressure (u_a) and pore-water pressure (u_w) in the soil specimen, from 0 to 1000 kPa with 0.1 kPa resolution. Pore-air pressure is equal to chamber pressure (p_c), as the air freely move from specimen to chamber and vice-versa through a sintered steel ring in the top cap. The u_w value can be applied either at top, bottom or both of the specimen.

The peculiarity of SCSS is related to the shearing box, which is cylindrical with diameter equals to 51 and 22 mm high. The zero lateral strain conditions is ensured through a stack of twelve hollow disks. The specimen is sheared due to synchronized movement of two external double pendulum, fixed on bottom and top disks. Each of 12 disks is displaced along the shear direction using a small pivot (machined on the upper side of each disk), which can move only inside a linear fluting groove (machined on the lower side of each disk).

The improvements achievable through the SCSS consist in the: (i) control of matric suction or water content upon simple shearing, (ii) specimen volume variations prevented or allowed (as for the tests herein reported) under stress- or strain- control, (iii) smooth and continuous transition from partially-to fully-saturated condition upon wetting, (iv) monitoring of hydro-mechanical response upon wetting, with both simple shearing and void ratio variations allowed.

Soil Tested and Experimental Programme

The experimental programme was carried out on remoulded specimens of pyroclastic soil produced by the explosive activity of Vesuvius volcano (Southern Italy) and involved in catastrophic landslides of the flow-type. The pyroclastic soils due to their nature are characterized by material heterogeneity, complex microstructure and complex unsaturated hydro-mechanical behaviour. Here, the specimens

were prepared from the finer ashy soil present in the Campania region, namely ashy soil “A” (Bilotta et al. 2005), which is typically found at the bedrock contact of the pyroclastic deposits. The grain size distribution consists in 43.6 ÷ 51.9% Sand, 43.9 ÷ 54.03% Silt, and 1.4 ÷ 4.7% Clay.

This pyroclastic soil is very loose soil ($n = 65\%$) with metastable structure whether along steep slopes (Sorbino et al. 2011). On the contrary, remoulded specimens exhibit lower porosity ($n = 60\text{--}66\%$). The soil specific gravity (G_s) is 2.45; the saturation degree (S_r) is comprised between 79.6% and 99.3% (data from Migliaro 2008); the dry unit weight (γ_d) is 8.41 and 8.85 kN/m³. The average water content (w) is 51.9%, while the liquid limit (w_L) is 53.8% and the plastic limit (w_p) is 49.3%.

Some SCSS tests on remoulded specimens with mean initial porosity of 0.66 are discussed (Table 1). The mechanical behaviour was analysed at different suction, at constant vertical load or constant soil volume. Soil Water Retention Curves were evaluated through two tests not associated to soil failure or significant shear and vertical strain upon wetting. The transition from unsaturated to saturated condition was analysed through wetting simple shear tests (Table 2) performed zeroing suction at different rates.

Shear Strength

The tests were interpreted in terms of shear stress and vertical effective stress as defined by Bishop (1959), referring to the “effective saturation degree” (S_{re}) as follows:

$$\sigma'_{ij} = \sigma_{ij} - u_a \cdot \delta_{ij} + S_{re} \cdot (u_a - u_w) \cdot \delta_{ij} \quad (1)$$

where σ_{ij} is the total stress tensor, u_a is the pore air pressure, u_w is the pore water pressure, $u_a - u_w$ is the matric suction (s), and δ_{ij} is the Kronecker delta.

Table 1 Shear strength tests

#	Test	e (-)	S_r (-)	s (kPa)	σ' (kPa)	$\sigma - u_a$ (kPa)
SSRPSF03a ^a	CV	1.6	0.7	40	120	95
SSRPSF03b ^a	CV	1.6	0.9	53	139	95
SSRPSG23	CL	1.6	0.9	25	72	50
SSRPSG24	CL	1.6	0.9	26	119	100
SSP0115 ^b	CL	1.9	1.0	0	100	100
SSP0215 ^b	CV	1.9	1.0	0	69	69
SSP0315 ^b	CL	1.9	1.0	0	74	74

CL = Constant vertical Load, CV = constant Volume, WCL = wetting at constant vertical Load;

^amultistage test ^bfrom Cuomo et al. (2016); e : void ratio; S_r : degree of saturation; s : suction; σ' vertical Bishop effective stress; $\sigma - u_a$ net vertical stress

Table 2 Wetting tests

	e (-)	S_r (-)	s_b (kPa)	σ' (kPa)	τ (kPa)	$\Delta s/\Delta t$ (kPa/h)
						After suction equalization
SSRPSG03	1.76	0.85	50.17	87.72	51	-0.5 ^a
SSRPSG04	1.79	0.84	50.26	68.37	43	-0.5 ^a
SSRPSG06	1.8	0.84	50.1	64.85	27	-0.5 ^a
SSRPSG09	1.62	0.88	49.52	71.87	34	-0.5 ^a
SSRPSG14	1.65	0.81	29.03	51.25	34	-0.5 ^b
SSRPSG15	1.65	0.89	29.23	79.14	34	-1.0 ^b
SSRPSG20	1.42	0.82	38.55	50.75	34	-1.0 ^c
SSRPSG21	1.66	0.9	30.03	55.95	34	s(t) ^d

s_b is the suction values at the bottom of the specimen after equalization; ^asuction is decreased at the bottom of specimen, with an upwards inflow to the specimen; ^bsuction is decreased at the top of specimen, with a downwards inflow to the specimen; ^cas previous group (^b), but performed at constant volume; ^das previous group (^b), but with a specific function s(t) taken from Cascini et al. (2010) i.e. $-0.06 < s(t) < -1.15$

Effective saturation degree is evaluated as follows:

$$S_{re} = \frac{S_r - S_{r0}}{1 - S_{r0}} \quad (2)$$

where S_{r0} is the residual saturation degree here assumed equal to 0.31.

Two simple shear tests (SSRPSG23 and SSRPSG24) were performed at constant net vertical stress of 50 and 100 kPa and suction 25 kPa. The results were then compared to the previous tests on saturated specimens reported by Cuomo et al. (2015).

The new tests performed in unsaturated condition show a slight hardening (Fig. 1a), associated to dilative behaviour (Fig. 1b), while saturated specimen upon shearing exhibited a soil hardening behaviour associated to contractive behaviour. The evolution of volumetric water volume upon shearing was also evaluated in the $\theta - s$ plane and compared with the behaviours (Fig. 2): (i) hardening for SSRPSF03b, while (ii) the SSRPSF03a reached the maximum shear stress (80.77 kPa) at shear strain 0.07; the Soil Water Retention Curve (SWRC) was obtained through wetting tests in simple shear condition shown later.

Both paths are inside the zone of the predicted SWRC (Fig. 1c). Three more tests were performed at constant volume and different suction (Table 1). The tests on unsaturated specimens exhibited two different behaviours (Fig. 2): i) hardening for SSRPSF03b, while ii) the SSRPSF03a reached the maximum shear stress (80.77 kPa) at shear strain 0.07; the shear stress was then constant for shear strain reaching 0.2, and τ decreased to 72.44 kPa at $\gamma = 0.66$. The test at constant volume on saturated specimen exhibited an hardening behaviour associated to an initial high decrease (20 kPa) of the vertical effective stress at low shear strain (Fig. 2b) followed by an almost constant trend of σ' at larger shear strain ($\gamma > 0.12$). In Fig. 2 the evolution of volumetric

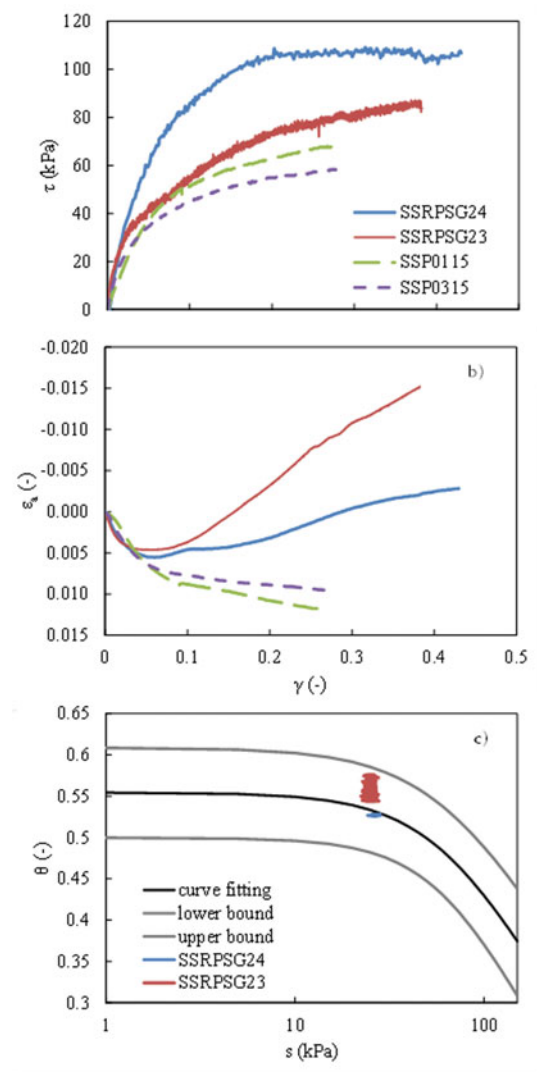


Fig. 1 Constant load simple shear tests performed on saturated (dashed lines) and unsaturated specimens

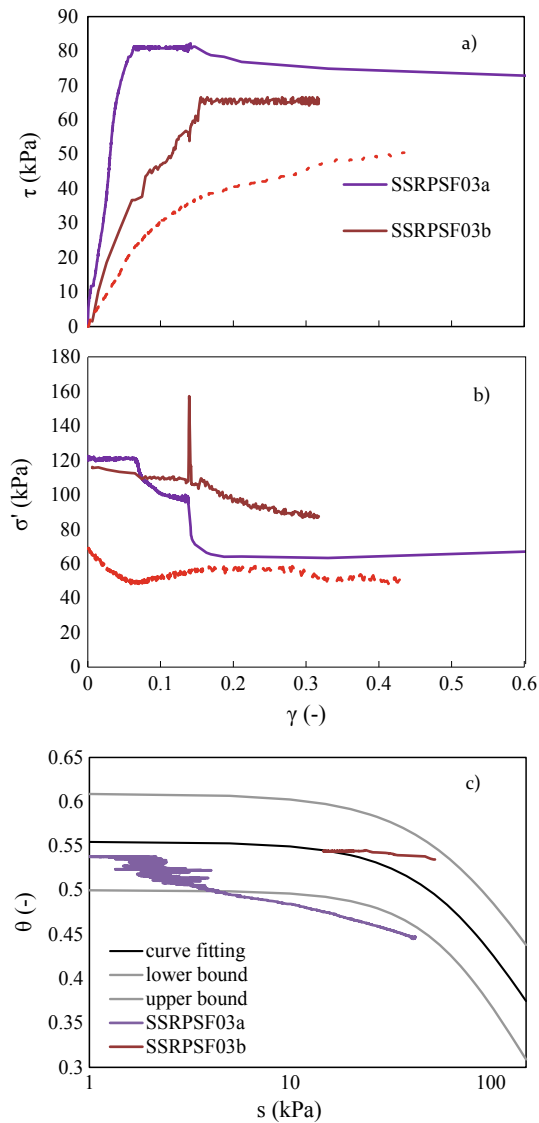


Fig. 2 Constant volume simple shear tests for saturated (dashed lines) and unsaturated specimens

water content is shown. The suction was not constant for both tests and decreased upon shearing, while volumetric water content exhibited relevant variation only in SSRPSF03a. The $\theta - s$ path of SSRPSF03a specimen was not completely included in the predicted bounds. Moreover, the shear strength envelope was obtained for the shear stress values corresponding to the maximum horizontal displacement reached during all the tests. The shear strength parameters were compared to those in the literature (Bilotta et al. 2005 and 2008; Moscariello et al. 2018) and showed in Fig. 3, where the failure shear envelopes obtained through Simple Shear, Direct Shear and Triaxial tests on saturated and unsaturated specimens are plotted. Five shear strength envelopes specified for different testing conditions were obtained through a curve fitting with no cohesion and the

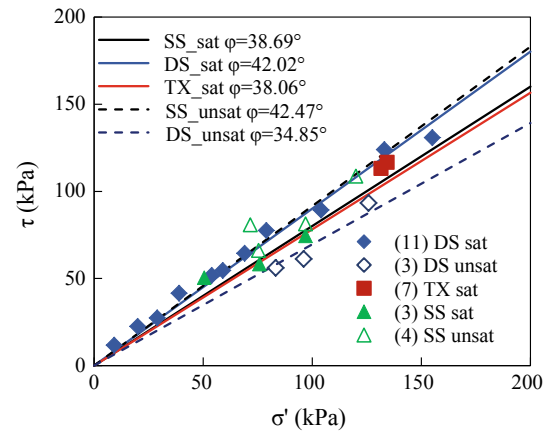


Fig. 3 Shear strength envelopes achieved through simple shear tests (SS), direct shear tests (DS) and triaxial tests (TX) on saturated and unsaturated specimens (SS, TX and DS data is taken from Bilotta et al. 2005, 2008; Moscariello et al. 2018). The numbers in the brackets are the number of tests

friction angle was evaluated. Figure 3 illustrates the variability of the friction angle under different testing conditions (Moscariello et al. 2020).

Soil Water Retention

A complete description of soil mechanical and hydraulic behaviour in partially saturated conditions required the identification of a suitable retention model.

Previous studies (Moscariello 2017; Cuomo et al. 2017) showed satisfactory correspondence between experimental data obtained through both conventional equipment (Richard's plate, volumetric extractor) and simple shear device (Moscariello et al. 2020) with van Genuchten model (1980):

$$\theta(s) = \theta_r + \frac{(\theta_s - \theta_r)}{[1 + (\alpha s)^n]^m} \quad (3)$$

where α , m and n are model parameters, while θ_s and θ_r represent the saturated and residual water content, respectively and s is the matric suction. Specifically, drying and wetting path performed through Richard's plate, volumetric extractor were well interpreted through both Van Genuchten (1980) model ($R^2 = 0.95 \div 0.99$), with parameters: $\alpha = 0.01 \div 0.50$, $n = 1.24 \div 1.23$, and $m = 1 - 1/n = 0.19 \div 0.19$. Van Genuchten (1980) model was also used to describe the results of two wetting tests performed in simple shear condition. The tests were performed keeping constant the vertical stress and the shear stress, while the suction was zeroing with a fixed rate of 0.1 kPa/h. The experimental data considered to evaluate the parameters of Van Genuchten

(1980) model were extracted from the wetting tests considering only the part at constant and low shear strain ($\gamma = 0.05$). The parameters α , n , and m were evaluated fitting simultaneously the results of both tests on the $\theta - (u_w - u_a)$ plane: α equal to 0.01, $n = 1.58$, and $m = 0.36$. Upper and lower bounds of the water retention curve were estimated using a confidence interval associated with the available data equals to 95%.

Wetting Tests Under Different Shear Stresses

The wetting tests in simple shear conditions allowed studying the soil mechanical behaviour in terms of hydraulic response (SWRC), shear strain (γ) and axial strain (ϵ_a), in relation to the current value of shear stress (τ) and soil suction (s), during the whole wetting process.

In the tests performed at constant load, the soil exhibited a similar strain behaviour during the shear stage, while having four different strain behaviour during the wetting: (i) contractive behaviour connected to negligible shear strains (SSRPSG03); (ii) tendency to move from contractive

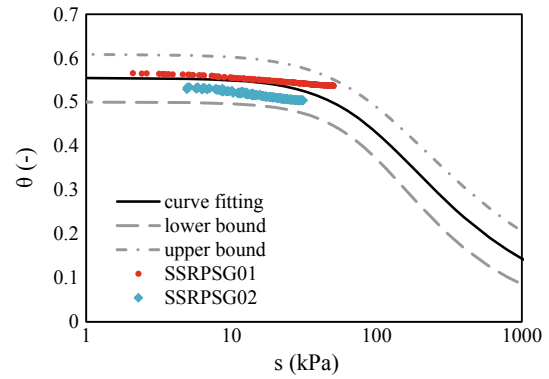


Fig. 4 SWRCs obtained through wetting tests in simple shear condition and interpolated using the van Genuchten model (1980). Dashed lines are the prediction bounds with 95% confidence level, and the table lists the values of the fitting coefficients with $\theta_r = 0.0002$ (Moscariello et al. 2020)

to dilative behaviour connected to moderate shear strains and failure occurrence at low suction (SSRPSG06); (iii) failure coupled with dilative behaviour connected to large shear strain (SSRPSG09, SSRPSG14, SSRPSG21).

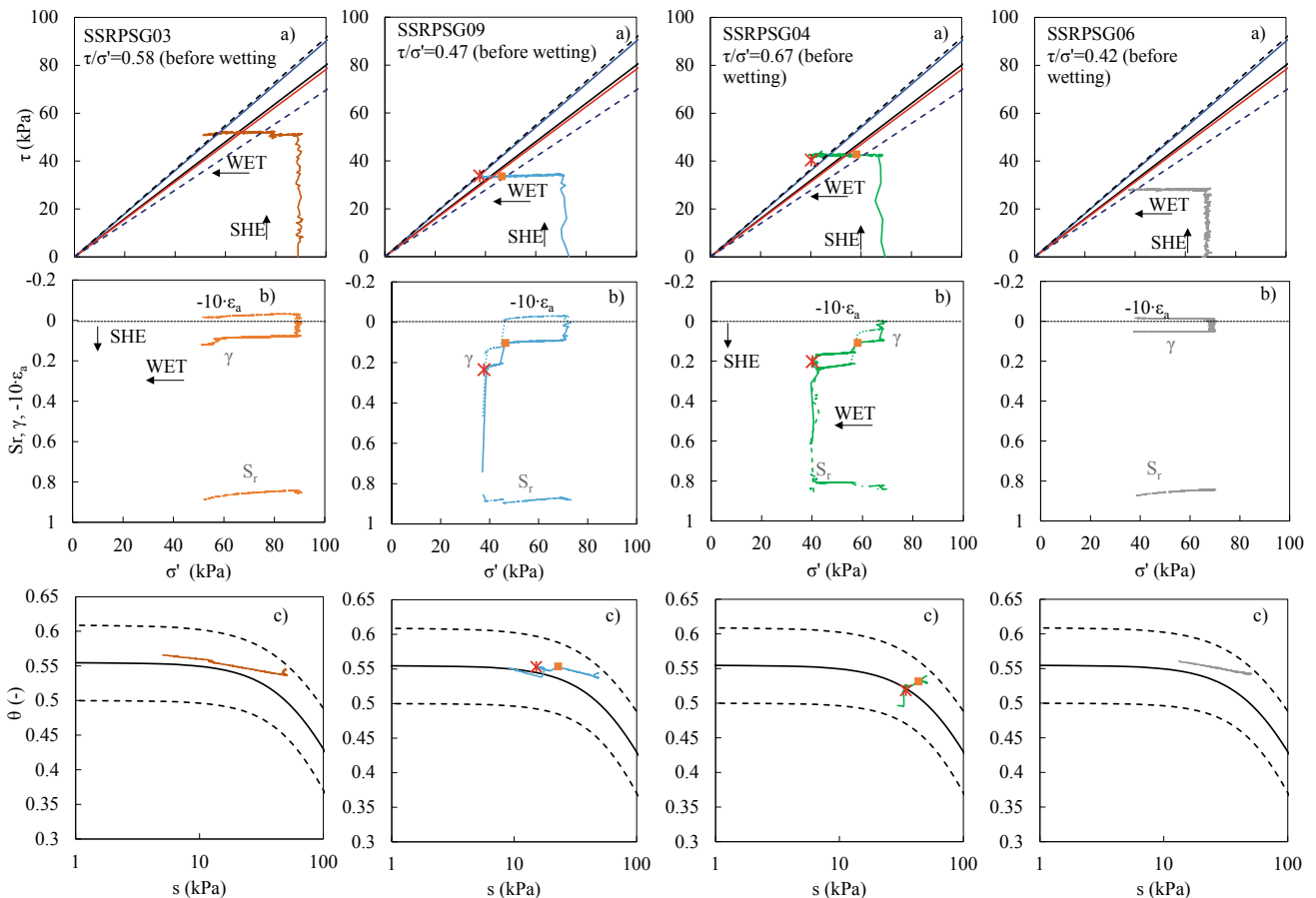


Fig. 5 Experimental results of wetting tests under different shear stresses evaluated through effective vertical stress (σ'), shear stress (τ), axial (ϵ_a) and shear (γ) strain, degree of saturation (S_r) and volumetric water content (θ)

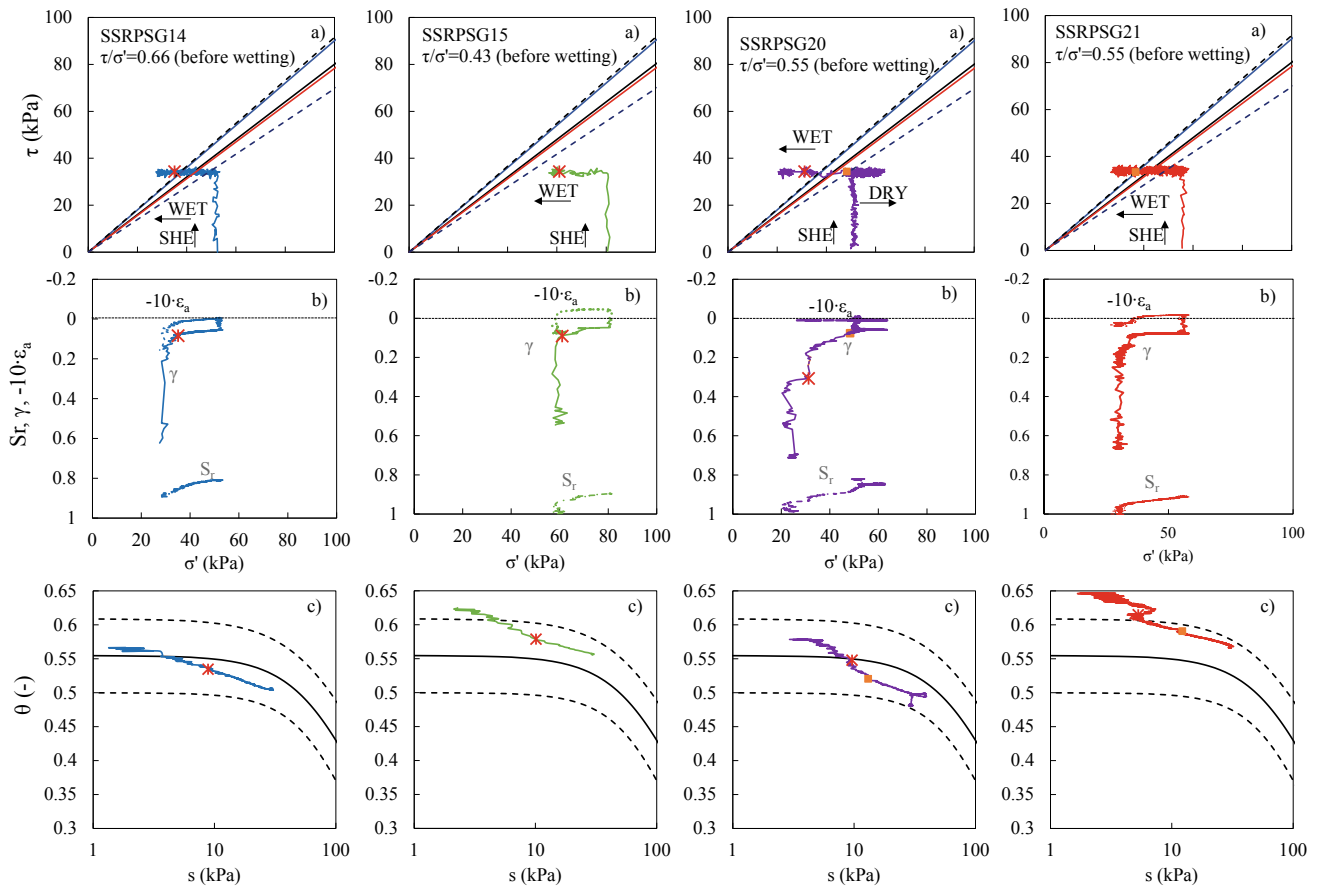


Fig. 5 (continued)

Some differences were observed between tests performed at the same suction rate, but carried out zeroing the suction from different side: the shear strain and axial strain rates were higher in the tests with suction reduction applied from the bottom. All tests exhibited some sudden increase of γ and ϵ_a before failure coupled with the increase of the suction measured rate. Comparing the stress path of each wetting test with the shear strength fuse identified in previous section, it was noticed that the sudden increase of γ and ϵ_a before failure occurred inside the shear strength fused, often close to the lower limit (SSRPSG09, SSRPSG04 and SSRPSG20). The failure occurred close to the upper limit of shear strength fused in SSRPSG09, SSRPSG04, SSRPSG14, SSRPSG20 and SSRPSG21 tests. The evolution of volumetric water content was analysed in $\theta - s$ plane and compared with the SWRC showed in Fig. 4. The water content evolution was not always included in the prediction bounds (dashed lines in Fig. 5c).

The stress ratio (i.e. shear stress divided by effective vertical stress at failure) versus the suction measured at failure were showed in Fig. 6. The tests wetted using the saturation ratio equal to 0.1 kPa/h exhibited a stress ratio at

failure between 0.80 and 1.10, even if the failure was reached at different measured suction values. The SSRPSG21 specimen exhibited a lower stress ratio, this behaviour could be attributed to the saturation rate adopted upon wetting ($\Delta s/\Delta t = 1$ kPa/h). The highest stress ratio was

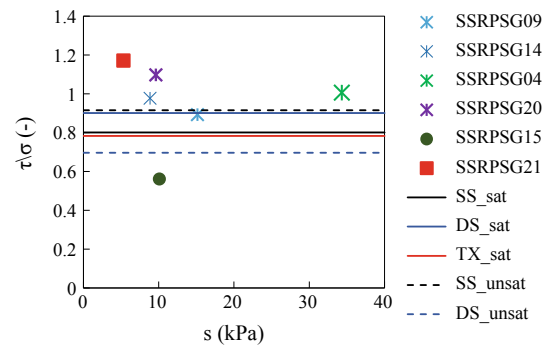


Fig. 6 Stress ratio versus suction at failure. Markers: stars represent the failure at $s(t) = 0.5$ kPa/h, circle represents the failure at $s(t) = 1$ kPa/h and square represents the failure at $-0.06 < s(t) < -1.15$. Continuous and dashed lines are the failure envelopes of Fig. 3

exhibited by SSRPSG21 specimen, which was wetted at a specific function $s(t)$ taken from Cascini et al. (2010).

Concluding Remarks

Simple Shear (SS) tests were performed to investigate the mechanical behaviour of a remoulded pyroclastic soil. The saturated shear strength parameters were evaluated and compared with those formerly achieved through Direct Shear (DS) and Triaxial (TX) tests. A range of variation of friction angle and failure envelope was identified. The soil water retention response was also evaluated in simple shear condition. The wetting tests in simple shear conditions performed at several saturation rates and applying the suction from the bottom or from the top of the specimens were shown and discussed. The suction rate influenced the stress ratio at which failure occurred and high suction rate (i.e. 1 kPa/h) induced the failure before approaching the shear strength.

References

- Bilotta E, Cascini L, Foresta V, Sorbino G (2005) Geotechnical characterisation of pyroclastic soils involved in huge flowslides. *Geot Geo Eng* 23(4):365–402
- Bilotta E, Foresta V, Migliaro G (2008) The influence of suction on stiffness, viscosity and collapse of some volcanic ashy soils. In: Toll et al. (eds) *Unsaturated soils: advances in geo-engineering*, pp 349–354
- Bishop AW (1959) The principle of effective stress. *Teknisk Ukeblad* 39:859–863
- Cascini L, Cuomo S, Pastor M, Sorbino G (2010) Modelling of rainfall-induced shallow landslides of the flow-type. *ASCE's J Geotech Geoenviron Eng* 1:85–98
- Cuomo S, Moscariello M, Foresta V (24–25 September, 2015) Shear strength of a Vesuvian pyroclastic soil measured in different testing devices. In: *Proceedings of Workshop on Volcanic Rocks and Soils, Ischia (Italy)*, pp 231–236
- Cuomo S, Moscariello M, Foresta V (2017) Wetting tests of partially saturated soils under simple shear conditions. *Géotec Lett* 7(2):197–203
- Moscariello M (2017) Multi-scale laboratory testing and constitutive modelling of unsaturated pyroclastic soils. PhD thesis, University of Salerno, p 233
- Moscariello M, Chen Y, Cuomo S, Buscarnera G (2020) Modelling of simple shear tests on volcanic unsaturated sands, *Conf. E-UNSAT2020* (accepted)
- Moscariello M, Cuomo S, Foresta V (2018) Validating new simple shear tests on a partially saturated pyroclastic soil. In: *Proceedings of the 7th International Conference on Unsaturated Soils, Hong Kong, 3–5 August 2018, ISBN: 978-988-78037-3-7, vol 1*, pp 257–262
- Migliaro G (2008) Il legame costitutivo dei terreni piroclastici per la modellazione di scavi in ambiente urbanizzato ed influenza della parziale saturazione. Diss. PhD Thesis, Università degli studi di Salerno (Italy), pp 305
- Sorbino G, Migliaro G, Foresta V (2011) Laboratory investigations on static liquefaction potential of pyroclastic soils involved in rainfall-induced landslides of the flow-type. In: *Unsaturated Soils, Alonso and Gens (eds) Proceedings of the 5th International Conference on Unsaturated Soils, London, vol 1*, pp 375–380
- Van Genuchten MT (1980) A close form equation predicting the hydraulic conductivity of unsaturated soil. *Soil Sci Soc Am J* 44:892–898



2020 Kyoto Japan

Simplest Methods of Determining Dynamic Soil Properties for Use in Co-seismic Hazard Analysis

Beena Ajmera and Binod Tiwari

Abstract

The loss of shear strength in a soil subjected to cyclic loading resulting from a reduction in the effective stress is known as cyclic mobility. Although the occurrence of cyclic mobility can have disastrous consequences including the loss of lives due to landslides and structural failure as well as substantial damages, quantitative evaluation of strength loss as a result of cyclic loading is not well described in the literature. In this study, eighteen laboratory prepared mineral mixtures composed of powdered montmorillonite and kaolinite clay minerals mixed with ground quartz are used to perform static and cyclic simple shear tests to establish the degradation in undrained shear strength that results from cyclic loading. The results are used to establish a relationship between the normalized undrained strength ratio and the post-cyclic effective stress ratio. This relationship is then used to examine the expected reduction in undrained shear strength and corresponding factor of safety against landslide at a post-earthquake landslide site in the Lokanthali region of Nepal after the 2015 Gorkha earthquake. The estimates from the proposed relationship are within 10% of the measured values.

Keywords

Seismic slope stability analysis • Dynamic soil properties • Earthquake induced landslides

Background

Cyclic mobility is the loss of shear strength from a reduction in effective normal stress in a soil subjected to cyclic loading. It can result in reductions in the bearing capacity of the soil such as after the 1999 Chi-Chi Earthquake (Chu et al. 2008), slope instabilities including the cases after the 1964 Alaska Earthquake (Stark and Contreras 1998; Boulanger and Idriss 2004), the 2015 Gorkha Earthquake (Tiwari and Pradel 2017; Tiwari et al. 2018), and the 2018 Anchorage Earthquake (Franke et al. 2019), or lateral spreading and settlements similar to those observed after the 1989 Loma Prieta Earthquake (Boulanger et al. 1998). Such occurrences result in fatalities along with significant damages.

To evaluate the stability of a slope during and after cyclic loading, it is necessary to perform seismic slope stability analyses or deformation analyses using dynamic soil properties. In performing seismic slope stability analyses, it is necessary to understand the stresses acting on a slope as a result of the cyclic loading as well as how those stresses will impact the strength and deformation behavior of the slope materials. To address the impact of variation in the stresses from cyclic loading, these analyses are usually performed using a pseudostatic approach, which was first explicitly expressed by Terzaghi (1950). In this approach, inertial forces acting at the centroid of the failure mass in both the horizontal and vertical directions are used to represent the effects of the cyclic loads. Considering these two additional forces into the limit equilibrium procedure, Eq. 1 can be used to find the factor of safety using the Ordinary Method of Slices. In Eq. 1, FS is the factor of safety, c and ϕ are the cohesion and friction angle on the failure plane, L_n , W_n , F_h , F_v and α_n are the length, weight, horizontal and vertical inertial forces from the cyclic loading, and the inclination, respectively, of the failure surface of the n th slice, and p is the total number of vertical slices. F_h and F_v are typically computed as the product of the horizontal and vertical pseudostatic accelerations and the mass of the slice. Extra

B. Ajmera (✉)

Department of Civil and Environmental Engineering,
North Dakota State University, CIE Building Room 201Q,
NDSU Dept. 2470, PO Box 6050 Fargo, ND 58108, USA
e-mail: beena.ajmera@ndsu.edu

B. Tiwari

Office of Research and Sponsored Projects, California State
University, Fullerton, 1121 N. State College Blvd.,
Fullerton, CA 92831, USA
e-mail: btiwari@fullerton.edu

attention should be paid to use appropriate values of c and φ for seismic slope stability analysis as they will be different from the peak or residual shear strength.

The impact of the stresses induced from the cyclic loading on the strength and deformation of the soils is more difficult to quantify. The impact on the strength is the focus of this study. The changes in the strength of the slope materials can span the entire gamut from experiencing negligible variations to experiencing significant reductions that can compromise the stability of the slope. Since the focus of this study is on fine-grained soils, complete loss of shear strength or liquefaction will not be discussed as part of this paper.

$$FS = \frac{\text{Shear Strength}}{\text{Shear Stresses}} = \frac{\sum_{n=1}^{n=p} (c\Delta L_n + ((W_n - F_v)\cos\alpha_n - F_h\sin\alpha_n)\tan\phi)}{\sum_{n=1}^{n=p} ((W_n - F_v)\sin\alpha_n + F_h\cos\alpha_n)} \quad (1)$$

Post-Cyclic Shear Strength Recommendations in the Literature

There are several potential values that can be used to estimate the post-cyclic shear strength. These are the peak drained shear strength, the peak undrained shear strength, the residual shear strength or some other intermediate undrained shear strength values. While the literature contains several different recommendations for the appropriate value to use when performing seismic slope stability analyses, a consensus has not been reached. Using the results from a conventional static slope stability analyses performed using the conditions at the end of the cyclic loading, Marcuson et al. (1990) suggested that residual shear strengths be assigned to those points along the failure surface where the factor of safety was less than unity. At the remaining points, they stated that the shear strength corresponding to the post-cyclic effective stresses (that is, effective stresses accounting for the pore pressures developed during the cyclic loading) should be assigned. Matsui et al. (1999) provided a relationship, as shown in Eq. 2, to estimate the degradation ratio (δ) in strength as a function of the cyclic axial strain (ε_c) and the plasticity index (PI) of the material. The degradation ratio is defined as the ratio of the post-cyclic shear strength to the static shear strength of the material.

$$\delta = -0.23\varepsilon_c + k$$

where,

$$k = \begin{cases} 0.022PI + 0.30 & PI < 25 \\ 0.003PI + 0.77 & PI > 25 \end{cases} \quad (2)$$

Outside the work of Marcuson et al. (1990) and Matsui et al. (1999), the only other recommendations for the post-cyclic shear strength to be used in stability analysis are available in MSHA (2009). MSHA (2009) provides two sets of lower bound post-cyclic shear strengths. In the first, the manual states that the 80% of the peak undrained shear strength should be used for soft clays, while the residual shear strength should be used in stiff clays. These recommendations are given arbitrarily. The manual also recommends shear strengths based on the liquidity index of the material. The second set of recommendations are based on Baziar and Dobry (1995), Yoshimine et al. (1999) and Olson and Stark (2002). Specifically, MSHA (2009) states that if the liquidity index is less than or equal to one or if the material is non-plastic, the post-cyclic shear strength should be based on an undrained strength ratio (undrained shear strength normalized by effective normal stress) of 0.04. For materials with liquidity indices greater than one, it is suggested that the lower bound post-cyclic shear strength be equal to approximately 1 kPa with an upper bound value based on an undrained strength ratio of 0.04. These values appear to be unreasonably low especially since Mitchell and Soga (2005) stated that a remoulded soil at a liquidity index of one will have an undrained shear strength of 3 kPa, which is approximately three times higher than the strengths suggested in MSHA (2009).

Materials and Methods

In this study, an experimental program was undertaken to provide relationships that would allow for the estimation of the appropriate shear strength to use in seismic slope stability analyses. Eighteen laboratory prepared fine-grained soil mixtures and nine natural samples were tested to determine the static shear strength using the simple shear apparatus and the post-cyclic shear strength using a cyclic simple shear apparatus presented in Fig. 1. The laboratory prepared soil mixtures were developed from powdered montmorillonite, kaolinite and quartz to obtain a wide range of plasticity characteristics. The clay fraction (percentage of particles finer than 2 μm) was 70% in the kaolinite used. It had a maximum particle size of 0.02 mm. Montmorillonite had a clay fraction of 80% and a maximum particle size of 0.075 mm. The clay fraction in ground quartz was approximately 10%. The maximum particle size was approximately

0.09 mm. The samples tested in this study ranged from non-plastic materials to soils with plasticity indices of 431 and liquid limits of 486. The natural samples were collected from a landslide site at a housing development project in Mission Viejo, CA, from the montmorillonite seam underlying the Portuguese Bend Landslide in Rancho Palos Verdes, CA, and from a site along the Araniko Highway in Nepal where a landslide was observed after the 2015 Gorkha Earthquake. For both the static and cyclic simple shear tests, the samples were mixed with sufficient distilled water to have an initial moisture content equal to the liquid limit of the sample. These slurries were then hydrated in an airtight container for at least 24 h before they were used to conduct any testing.

Both the static and cyclic simple shear apparatus used in this study are fully automated, computer controlled NGI-type devices. The hydrated soil slurries are placed in a membrane confined by a stack of Teflon-coated rings. The sample is, then, step-consolidated to a vertical stress of 100 kPa. All of the samples tested as part of this work were normally consolidated. When primary consolidation at this stress is complete, in the static simple shear apparatus, the sample is sheared at a rate of 5% per hour (ASTM 2007) until either the peak shear strength is observed or the sample experiences 25% shear strain. In the cyclic simple shear test, following the consolidation, the sample was subjected stress-controlled constant volume undrained cyclic loading. Cyclic loading consists of a sinusoidal wave with a frequency of 0.5 Hz whose amplitude is governed by the cyclic stress ratio. In this study, the cyclic stress ratio is defined as the ratio of the amplitude of the cyclic shear stress to the consolidation pressure. Cyclic loading was applied until either the sample experienced 10% double amplitude shear strain or 500 cycles were applied, whichever occurred first. The post-cyclic undrained shear strength of the sample was

measured immediately following the end of the cyclic loading using the shearing procedures as those described previously for the static simple shear tests. It is noted that although all of the tests in this study were conducted at a single consolidation pressure of 100 kPa, the results are presented in terms of the cyclic stress ratio. By doing so, it is generally accepted that the results will be applicable to any consolidation pressure.

Results

The variations in the undrained and the post-cyclic undrained strength ratios with the plasticity index are shown in Fig. 2. The post-cyclic undrained strength ratio is defined as the ratio of the post-cyclic undrained shear strength to the consolidation pressure. The results in Fig. 2 indicate that both undrained and the post-cyclic undrained strength ratios increase with an increase in the plasticity index. The undrained strength ratio appears to reduce as the plasticity index increases above 60, while the post-cyclic undrained strength ratio begins to reduce when the plasticity index increases beyond 40. Figure 2 also illustrates the degradation in undrained shear strength that occurs as a result of the cyclic loading. The degradations in undrained shear strength are greater in soils with lower plasticity indices, while negligible reductions were observed in soils with plasticity indices greater than 80.

Figure 3 shows the relationship between the degradation ratio (δ or the ratio of the post-cyclic undrained shear strength to the baseline undrained shear strength) and the plasticity index. The post-cyclic undrained shear strength is between 55 and 100% of the static undrained shear strength. Furthermore, the undrained shear strength is not observed to experience degradations as a result of cyclic loading in soils with plasticity indices greater than 80. For comparison, the relationship shown in Eq. 2 provided by Matsui et al. (1999) is also included in Fig. 3. The relationship from Matsui et al. (1999) appears to significantly overestimate the strength reduction (underestimate the post-cyclic undrained shear strength) in soils with plasticity indices less than 20. On the other hand, for soils with plasticity indices greater than 80, the relationship appears to overestimate the post-cyclic undrained shear strength suggesting that is even higher than the static undrained shear strength for soils having higher plasticity indices.

Since cyclic mobility is the loss of shear strength as a result of the reduction in the effective vertical stress from pore pressures generated during the cyclic loading, the degradation in undrained shear strength is related to the excess pore pressures generated during cyclic loading, as presented in Fig. 4. The normalized undrained strength ratio (Norm. USR) and the post-cyclic effective stress ratio



Fig. 1 Cyclic simple shear device used for this study

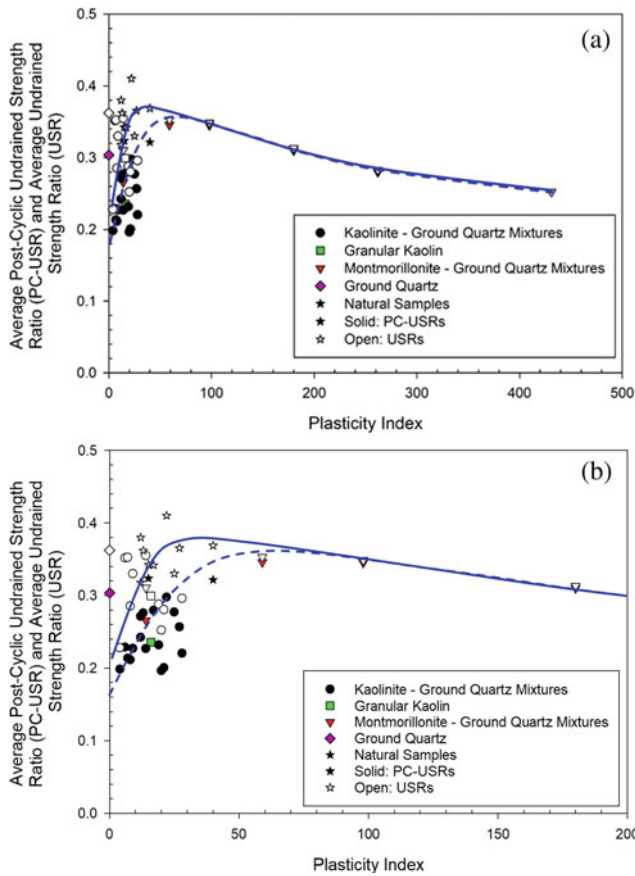


Fig. 2 Variation in the undrained strength ratio and the post-cyclic undrained strength ratio with plasticity index for **a** all of the soils tested and **b** soils with plasticity indices less than 200

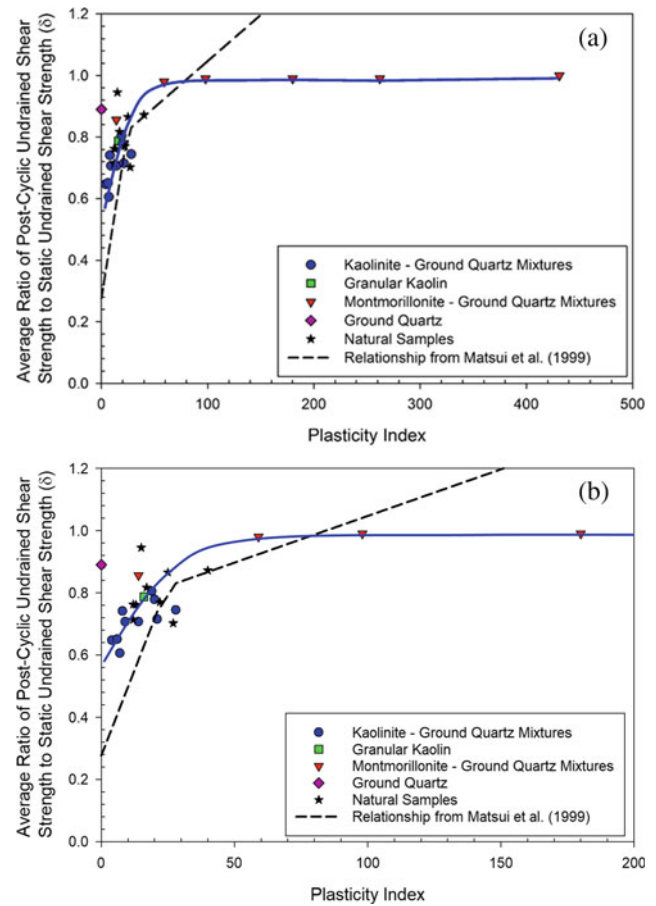


Fig. 3 Variation in the degradation ratio as a function of the plasticity index for **a** all of the soils tested and **b** soils with plasticity indices less than 200

(PC-ESR) are defined as shown in Eqs. 3 and 4, respectively (Ajmera et al. 2019), where, $s_{u,pc}$ is the post-cyclic undrained shear strength, s_u is the static undrained shear strength, σ'_{pc} is the effective normal stress at the end of the cyclic loading, σ'_c is the consolidation pressure, and r_u is the pore pressure ratio, or the ratio of the excess pore water pressure immediately after cyclic loading to the consolidation pressure.

$$Norm.USR = \frac{s_{u,pc}/\sigma'_{pc}}{s_u/\sigma'_c} = \delta \times (PC - ESR) \quad (3)$$

$$PC - ESR = \frac{\sigma'_c}{\sigma'_{pc}} = \frac{1}{1 - r_u} \quad (4)$$

A linear relationship is observed in Fig. 4 between the logarithm of normalized undrained strength ratio and the logarithm of post-cyclic effective stress ratio. The relationship shown was established ignoring the results of the ground quartz specimens. The results corresponding to the ground quartz samples are merely used to provide a reference point for the parameters studied. Specifically, at a post-cyclic effective stress ratio of one, the normalized

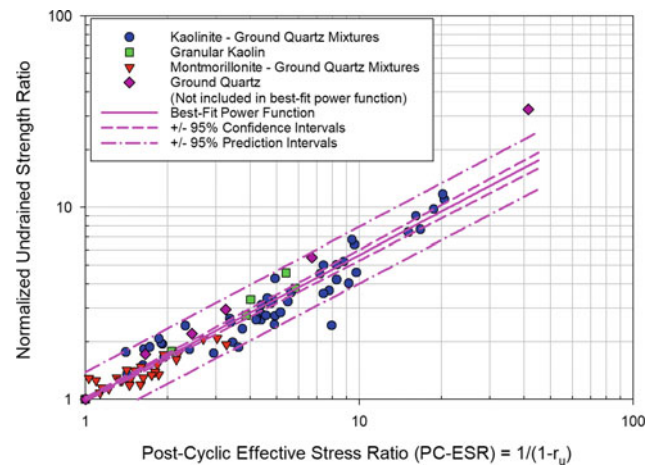


Fig. 4 Relationship between the normalized undrained strength ratio and the post-cyclic effective stress ratio

undrained strength ratio is also equal to one. This confirms that there is no degradation in the post-cyclic undrained strength when no excess pore pressures are generated during

the cyclic loading. As the post-cyclic effective stress ratio increases, that is, as the excess pore pressures are generated during the cyclic loading, the normalized undrained strength ratio increases suggesting that the post-cyclic undrained shear strength reduces. The best-fit power function shown in Fig. 4 is described by Eq. 5 and has a coefficient of determination (R^2) value of 0.93. Figure 4 also contains two sets of lines representing the $\pm 95\%$ confidence intervals and $\pm 95\%$ prediction intervals. The confidence interval delineates the potential variation in the best-fit line representing the boundaries within which the best-fit line will lie with 95% confidence. The prediction interval depicts the range within which 95% of the predictions using the best-fit line should lie.

$$\text{Norm.USR} = (\text{PC} - \text{ESR})^{0.753} \quad (5)$$

The natural samples, whose results have been included in Figs. 2 and 3, are used to validate the relationships established in this paper. As seen from these figures, the results from the natural samples are in good agreement with the relationships proposed. Figure 5 shows how the experimental results of the natural samples compare to the estimates from Eq. 5. In Fig. 5, only four of the results from the natural samples are outside of the 95% prediction interval. The relationships are further validated with the use of a case study.

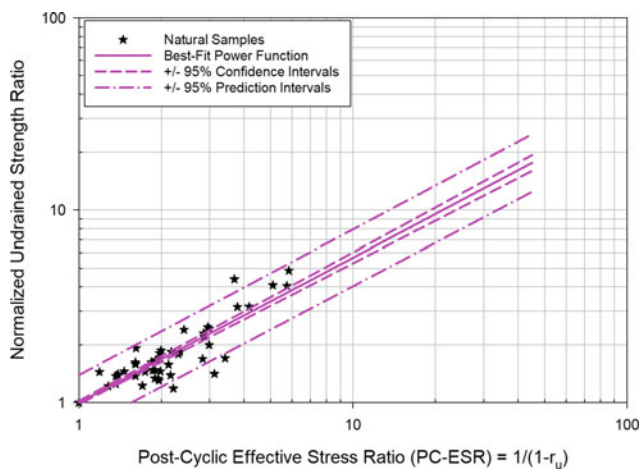


Fig. 5 Comparison of experimental results from the natural samples to best-fit function established in Fig. 4



Fig. 6 Seismically induced ground failure site at Lokanthali, Kathmandu after the 2015 Gorkha Earthquake, Nepal

Case Study—Ground Failure at Lokanthali, Nepal

Ground failure was observed in the Lokanthali area of Kathmandu, Nepal during the 2015 Gorkha earthquake. Located about 1 km east of the Tribhuvan International Airport, this site has a very gentle inclination with an average slope of approximately 4° (Fig. 6). At this site, Hashash et al. (2015) reported vertical and horizontal displacements of approximately 1 m and 0.5 m, respectively. Additional details regarding the ground failure and the impact on the surrounding area can be found in Tiwari et al. (2018). Per Tiwari et al. (2018), the soils collected from the site had liquid limits between 32 and 46% and plasticity indices between 12 and 27%.

Pore pressure ratios at the end of cyclic loading for the samples collected from this site were on the order of 0.32–0.69 with an average of 0.54. The static undrained strength ratio was reported to be between 0.28 and 0.40 (Tiwari et al. 2018). The degradation ratio from an experimental laboratory program undertaken by Tiwari et al. (2018) was found to be between 0.71 and 0.82 with an average of 0.75. From Eq. 4, the post-cyclic effective stress ratio will range from 1.47 to 3.22 with an average of 2.17. These values can be used to estimate the normalized undrained strength ratio from Eq. 5 yielding normalized undrained strength ratios between 1.33 and 2.42 with an average 1.79. Using Eq. 3, the degradation ratio is estimated to range from 0.75 to 0.90 with an average of 0.82. As seen from this simple example, the estimated values for the degradation ratio are within 10% of the measured values. When undrained shear strength of

the soil without strength degradation was used for seismic slope stability analysis, the slope yielded a factor of safety over 1.1, which is not justifiable as the slope already failed. However, when degraded strength obtained from the laboratory tests was used, the factor of safety dropped slightly below 1.0. As such, it is recommended to use the reduced shear strength of soil (due to cyclic loading) for post-earthquake seismic slope stability analysis.

Conclusions

Given the potential substantial consequences of cyclic mobility and the lack of techniques in the literature to estimate the reductions in shear strength to be expected in soils subjected to cyclic loading, eighteen laboratory prepared soil mixtures were used to determine relationships between the plasticity characteristics, mineralogical composition and the post-cyclic shear strength or degradation ratio. The results showed that the static undrained strength ratio increases with an increase in the plasticity index when the plasticity index is less than 60 beyond which the undrained strength ratio decreases with an increase in the plasticity index. The post-cyclic undrained strength ratio exhibited similar trends reaching maximum values when the plasticity index was approximately 40. Cyclic loading was found to cause a reduction in the undrained shear strength when the soil had a plasticity index less than 80 with greater reductions observed in soils with lower plasticity indices. For soils with plasticity indices greater than 80, the post-cyclic undrained shear strength was approximately equal to the static undrained shear strength. A linear relationship (Eq. 5) was proposed between the logarithm of the post-cyclic effective stress ratio and the logarithm of the normalized undrained strength ratio. Using this relationship, the degradation in undrained shear strength at Lokanthali, Nepal at the location of ground failure during the 2015 Gorkha earthquake was estimated. The estimated degradation ratios were found to be within 10% of the measured values suggesting that the proposed relationship can be used to determine the reduction in undrained shear strength to be expected in soils after cyclic loading. Use of the reduced undrained strength (due to cyclic loading) for the seismic slope stability analysis provided reasonable factor of safety of the failed slope at Lokanthali.

Acknowledgements The authors would like to thank California State University, Fullerton for providing intramural funding to conduct soil

tests from Lokanthali landslide area. The authors also thank CSU Fullerton graduate students Brian Yamashiro and Quoc-Hung (Bob) Phan for conducting soil tests on the natural samples.

References

- Ajmera B, Brandon T, Tiwari B (2019) Characterization of the reduction in undrained shear strength in fine-grained soils due to cyclic loading. *J Geotech Geoenviron Eng ASCE* 145(5):04019017
- Baziar MH, Dobry R (1995) Residual strength and large-deformation potential of loose silty sands. *J Geotech Eng* 121(12):896–906
- Boulanger RW, Meyers MW, Mejia LH, Idriss IM (1998) Behavior of a fine-grained soils during the Loma Prieta earthquake. *Can Geotech J* 35(1):146–158
- Boulanger RW, Idriss IM (2004) Evaluating the potential for liquefaction or cyclic failure of silts and clays. Report No. UCD/CGM-04/01. University of California, Davis
- Chu DB, Stewart JP, Boulanger RW, Lin PS (2008) Cyclic softening of low-plasticity clay and its effect on seismic foundation performance. *J Geotech Geoenviron Eng* 134(11):1595–1608
- Franke KW, Koehler R, Beyzaei CZ, Cabas A, Christie S, Dickenson S, Pierce I, Stuedlein A, Yang A, Dow S, Freeman M, Lee K, Pierce G (2019) Geotechnical engineering reconnaissance of the 30 November 2018 Mw 7.1 Anchorage, Alaska Earthquake. GEER Report
- Hashash YMA, Tiwari B, Moss RES, Asimaki D, Clahan KB, Kieffer DS, Dreger DS, Macdonald A, Madugo CM, Mason HB, Pehlivan M, Rayamajhi D, Acharya I, Adhikari B (2015) Geotechnical Field Reconnaissance: Gorkha (Nepal) earthquake of April 25, 2015 and related shaking sequence. GEER Association Report No. GEER-040
- Marcuson WF III, Hynes NE, Franklin AG (1990) Evaluation and use of residual strength in seismic safety analysis of Embankments. *Earthquake Spectra* 6(3):529–572
- Matsui T, Nabeshima Y, El Mesmary MA (1999) Degradation in cyclic shear behavior and soil properties of saturated clays. In: *Proceedings of the ninth international offshore and polar engineering conference*, vol 1, pp 536–541
- Mitchell JK, Soga K (2005) *Fundamentals of soil behavior*, 3rd edn. Wiley Inc.
- MSHA (2009) *Engineering and design manual for coal refuse disposal facilities*. Mine Safety and Hazard Administration
- Olson SM, Stark TD (2002) Liquefied strength ratio from liquefaction flow failure case histories. *Can Geotech J* 39:629–647
- Stark TD, Contreras IA (1998) Fourth Avenue landslide during 1964 Alaskan earthquake. *J Geotech Geoenviron Eng* 124(2):99–109
- Terzaghi K (1950) Mechanisms of landslides. *Engineering Geology*
- Tiwari B, Pradel D (2017) Ground deformation at Lokanthali, Kathmandu due to Mw 7.8 2015 Gorkha earthquake. *Geotech Spec Pub* 278(1):333–342
- Tiwari B, Pradel D, Ajmera B, Yamashiro B, Diwakar K (2018) Landslide movement at Lokanthali during the 2015 earthquake in Gorkha, Nepal. *J Geotech Geoenviron Eng* 144(3):05018001 1–12
- Yoshimine M, Robertson PK, Wride CE (1999) Undrained shear strength of clean sands to trigger flow liquefaction. *Can Geotech J* 36:891–906



2020 Kyoto Japan

The Acoustic Emission Characteristics and Shear Behaviour During Granular Shearing

Yao Jiang and Gonghui Wang

Abstract

Rapid landsliding phenomena demonstrate that their constituent grains can flow with extremely low friction along their runout paths. Over the past several decades, many studies have been motivated to reveal such kind of unusual physical process; however, the progressive maturation of these events is still lack of enough scientific evidence. Modern insight into the granular dynamics indicates that the force fluctuations may be in behaviour of abrupt perturbations of internal forces and release of strain energy. Remarkably, such energy release events are manifested in the generation of elastic waves, termed acoustic emissions (AE), which deliver invaluable information concerning the granular deformations. We thus employed a high frequency range of AE sensor to capture the elastic waves and examined the relationships between characteristics of AE and fluctuations of shear resistance. Our results suggested that there was a strong correlation between shear resistance drops and AE events; the characteristics and occurrence rates of generated AE events were influenced not only by shear velocity but also by particle size. The drops of shear resistance and the amplitude of AE waveforms were greater with increase of

particle size, and the AE rates increase with increase of shear velocity.

Keywords

Acoustic emission • Stress fluctuation • Granular materials • Particle size • Shear velocity • Rapid landslides

Introduction

Understanding the behaviour of granular materials have been continuously attracted considerable interest in the context of various geophysical applications ranging from earthquakes to landslides (Scholz 2002; Clague and Stead 2012). Field observations support that the progressive maturation of these events may undergo different styles of movement, such as slow, stable creep, periodicity of stick–slip or accelerative sliding; laboratory experiments also manifest that the granular frictional properties are strongly dependent on the sliding rate- and state- variables, showing diverse frictional properties such as strengthening or weakening (Wang et al. 2010; Di Toro et al. 2011; Schulz and Wang 2014). Over the past few years, insight into these granular frictional processes has been provided by new evidence that instabilities may be in behaviour of abrupt perturbations of internal forces and release of strain energy (Davies et al. 2012). Remarkably, such energy release events are manifested in the generation of high-frequency (kHz–MHz) elastic waves, termed acoustic emissions (AE), which deliver invaluable information concerning the physical processes and also raise the possibility that investigations of granular failure could conceivably be made (Goren et al. 2011).

A significant, though still inconclusive, body of research has involved underlying mechanisms giving rise to abrupt release of acoustic emission occurring in intact rocks (Lockner 1993; Yabe et al. 2003) and along existing

Y. Jiang (✉)

Key Laboratory of Mountain Hazards and Earth Surface Process/Institute of Mountain Hazards and Environment, Chinese Academy of Sciences (CAS), No. 9, Block 4, South Renmin Road, Chengdu, 610041, China
e-mail: yjiang@imde.ac.cn

Y. Jiang

CAS Center for Excellence in Tibetan Plateau Earth Sciences, Chinese Academy of Sciences (CAS), Beijing, 100101, China

Y. Jiang

University of Chinese Academy of Sciences, No. 19 (A) Yuquan Road, Shijingshan District Beijing, 100049, China

G. Wang

Research Center on Landslides, Disaster Prevention Research Institute, Kyoto University, Gokasho, Uji, 611-0011, Kyoto, Japan
e-mail: wanggh@landslide.dpri.kyoto-u.ac.jp

© Springer Nature Switzerland AG 2021

B. Tiwari et al. (eds.), *Understanding and Reducing Landslide Disaster Risk*, ICL Contribution to Landslide Disaster Risk Reduction, https://doi.org/10.1007/978-3-030-60706-7_40

discontinuities (Mair et al. 2007; Jiang et al. 2017). Michlmayr et al. (2012) reviewed several mechanisms for the generation of AEs in granular geologic material during progressive failure as well, and their observations demonstrated that there were strong correlations between the measured stress fluctuations and generated acoustic waveforms, suggesting that these signals might be sourced from the failure of buckling force chains and frictional slip between grain-to-grain interactions. Moreover, by simulating a granular layer of fault gouge, Mair et al. (2007) found that the occurrence rate of AEs showed a systematic dependence on shearing velocity, which indicated that the frictional contact junction area was reduced at increasing shear velocity. Although the fact that these existing benchmark studies do effectively providing evidence of AE activities and deformation processes during granular shearing, there are still many unanswered questions about the linkages among granular material properties, mechanical conditions and characteristics of generated AEs, respectively.

Generally, it is still a scientific challenge to better understand the role of AEs during micro-slip instabilities nucleation, propagation and failure among sheared granular assemblies to date. For instance, the unexpected weakness of some faults and sturzstroms has been attributed to the emergence of acoustic waves that promote failure by reducing the overburden pressure through a mechanism known as acoustic fluidization (Melosh 1996; Collins and Melosh 2003). The acoustic fluidization has also proposed to explain the remote triggering earthquake (Johnson et al. 2008). Indeed, these results clarify that the acoustic wave is potentially crucial for understanding the rupture processes of earthquake. However, it is unclear whether these failures are triggered by internal or (and) external acoustic vibrations. Herewith, we sought to evaluate the characteristics of acoustic emissions and slip instability for locally sheared granular materials. In the present study, we designed specific laboratory experiments aiming at arguing the central questions concerning this intriguing topic: whether the AE events are dependent on particle size and shear velocity.

Experimental Method

We performed a series of tests by employing a servo-hydraulic controlled ring shear apparatus (Fig. 1). The geometry has two independent servo-controlled load feedback firmware to maintain constant normal stress and shear stress (or shear velocity), respectively. The rotating (lower) part of the chamber is forced by a servo-controlled ram at different constant displacement rate, while the stationary (upper) opposes shearing through two arms with integrated force sensors. Such fixed shear plane results in the formation of a horizontal shear zone near where the upper- and

lower-cylinder parts meet. Sample thickness changes are continuously monitored by using a displacement transducer. A set of rubber gaskets between the upper- and lower-cylinder pairs is designed to prevent leakage of sample and pore fluid. Extension work has been done to investigate the shear behaviours for landslide materials using this assembly (Sassa et al. 2004; Wang and Sassa 2009; Wang et al. 2010; Schulz and Wang 2014; Xing et al. 2015) and additional details concerning this intelligent device are reported by Sassa et al. (2003, 2004).

We conducted a series of laboratory experiments on granular analogues composed of spherical glass beads in a ring shear configuration under conditions of room temperature and atmospheric humidity (Fig. 2). We used spherical glass beads as an ideal analogy material for exploring the role of particle size and ruling out the large uncertainty associated with the particle shape effects (Yang and Wei 2012; Jiang et al. 2016). Experiments with three kinds of uniform particle sizes (i.e., 1.0–1.4, 2.0–2.5 and 4.7–5.3 mm) were conducted under shear velocity sequence from 0.005 to 1.0 mm/s and constant vertical stress of 200 kPa. All dry spherical samples were sheared under room temperature and humidity (about $\sim 20^\circ\text{C}$ and $\sim 50\text{--}70\%$, respectively) in order to exclude the possible influence of hydrothermal and physicochemical processes on grain-scale frictional contact (Anthony and Marone 2005; Mair et al. 2007). Annular specimens were constructed at 3 cm wide (within an inner diameter of 12 cm and outer diameter of 18 cm) and about 5 cm high. Additionally, we installed a broadband frequency AE transducer (100–1000 kHz) near

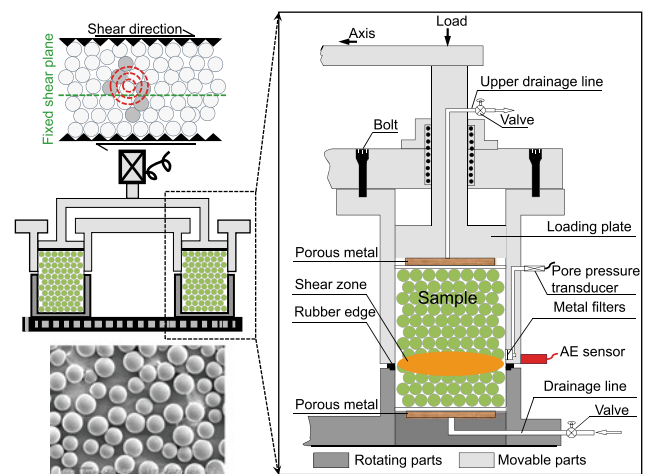


Fig. 1 Schematic diagram of the ring shear apparatus. Right figure shows that sample is assembled in the ring-shear box. One high-frequency AE sensor was installed near the shear plane. Left figure (top) indicates the possible mechanism for the generation of AEs during shearing. Left figure (middle) shows cross section of the entire specimen configuration. Normal stress is applied vertically, and shear velocity is controlled by rotating the lower part. Left figure (bottom) shows the SEM image of glass beads before shearing

the shear plane to capture the generated elastic waves during tests. Data of AEs, sample thickness and shear resistances were simultaneously recorded with a sampling rate of 1 MHz.

Results

Time Series of Shear Resistance and AE Characteristics

Figure 2a presents a selected section of data from an experiment to reveal the recorded shear resistance as a function of time. Figure 2b–c shows the monitored AEs and sample thicknesses (vertical displacement), respectively. Our observed results exhibit significant variations and scatter. The general form of the shear resistance–time curve is characterized by sawtooth-shaped fluctuations, or stress drops (instabilities), that varies in magnitude and recurrence

time with progression of granular shearing. In response to the shape of one cycle of instability, several characteristic observations can be made. Single stress decrease event is gradually preceded by initially elastic deformation, indicated by a linear buildup shear resistance.

With continually shearing, plastic deformation becomes dominant, leading to decrease of steepness of curve. During these processes, sample dilations are often observed suggesting the particle arrangements in structuring of force network. Finally, the stress buildup ends by an abrupt drop that reflects a major failure of granular assemblies, where we captured the abrupt energy release and sample compaction (Fig. 2b–c). Comparing the duration periods between stress buildup and jump for each instability, the latter is often less than one second.

It is noted that our observed dynamic instabilities are also shear-velocity-dependent as shown in Fig. 2a. During a series of multiple instability events, AE activity and sample thickness show a strong correlation along with the observed stress drops and shear velocity (Fig. 2a–c). In Fig. 2d, we enlarge one instability event to illustrate the characteristics of stress drop associated with acoustic waveforms which are characterized by shorter-duration, higher-frequency signals with more impulsive onsets. As also demonstrated in Fig. 3, the magnitude of stress drops and the characteristics (i.e., magnitude and shape) of AEs qualitatively show a nontrivial correlations with shear velocity and particle size. Figure 3a reveals the stress drops decrease and the shape of acoustic waveforms are also varied with increasing shear velocities. Results also present a significant influence on particle size (Fig. 3b): Large (4.7–5.3 mm) glass beads generally produce high stress jumps relative to the intermediate (2.0–2.5 mm) and small (1.0–1.4 mm) glass beads, following the same tendency of magnitude and shape for measured AEs.

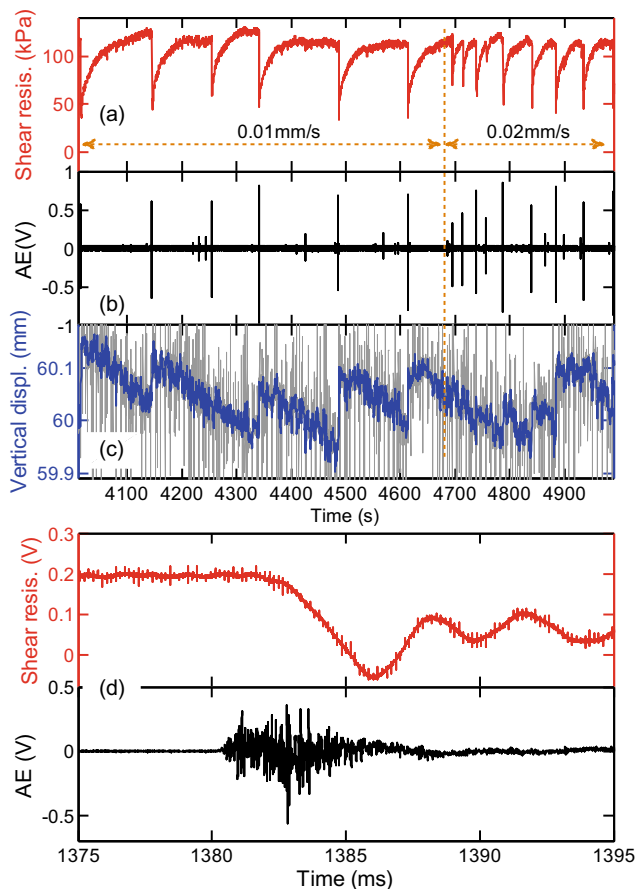


Fig. 2 One selected result of correlations among **a** observed shear resistance; **b** monitored acoustic emission; **c** recorded vertical displacement at different shear velocities. It is noted that the sample dilations occur during stress buildups and compactions occur upon the dynamic failures and stress drops; **d** detail information of recorded shear resistance and acoustic signals for one granular instability event

Average Occurrence Rate of AE Events

The foregoing results suggest that stress drops associated with the imposed shearing directly result in acoustic signals, which are systematically influenced by shear velocity and particle size. We analysed acoustic activity data from different tests to identify the average occurrence rate during granular shearing. Each acoustic waveform was identified by involving a threshold value (i.e., 0.01 V), and all data are reported the mean value and statistical variability, with error bars calculated by using a standard error of the mean method. The mean number of AE per sec (time-domain) for different particle sizes are plotted against shear velocity in Fig. 4a. For all particle sizes, an increasing in shear velocity promotes an immediate and sustained increase in AE per sec. Such positive dependence on shear velocity can be explained that more shear displacement is involved per unit

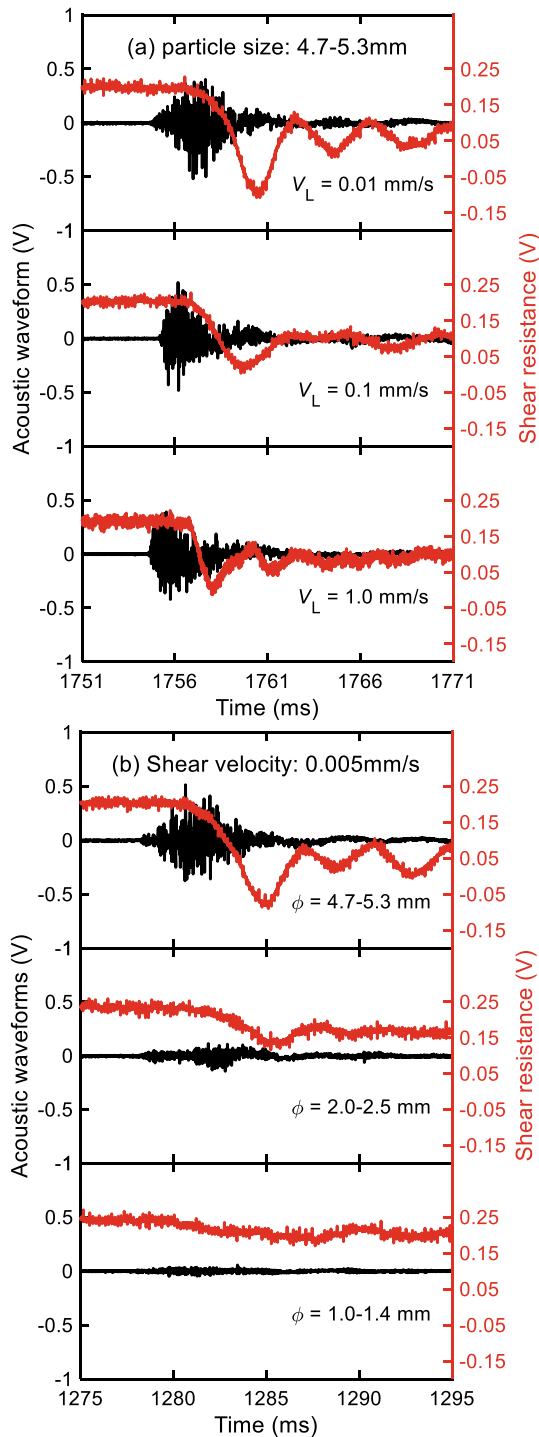


Fig. 3 The measured shear resistance (red color) and the generated AEs (black color) among granular materials. Note that all shear resistances and acoustic signals for different conditions are shown in the same scale to depict the difference. **a**: different shear velocities with the same particle size. From top to bottom, the shear velocities are 0.01 mm/s, 0.1 mm/s and 1.0 mm/s, respectively; **b**: different particle sizes with the same shear velocity. From top to bottom, the particle sizes are 4.7–5.3 mm, 2.0–2.5 mm and 1.0–1.4 mm/s, respectively

time during shearing at higher velocities. In order to further explore the influence of shear velocity on AE rate, these data (mean number of AE per second) are also used to normalize the mean number of AE by unit shear displacement (per millimeter), and the AE rates in displacement-domain are depicted in Fig. 4b.

Dissimilarly, it is clearly noted that the AE rate exhibits a systematic decrease with increasing shear velocity for small (1.0–1.4 mm) glass beads, indicating that AE is not rate independent on per unit displacement. The deficit of AE activity in displacement domain consists with previous observations, and also can be understood by considering the reduction of grain-scale contacts at increasing shear velocity (e.g., Yabe et al. 2003; Mair et al. 2007). However, it is also supported by our results that the AE activity (AE per unit

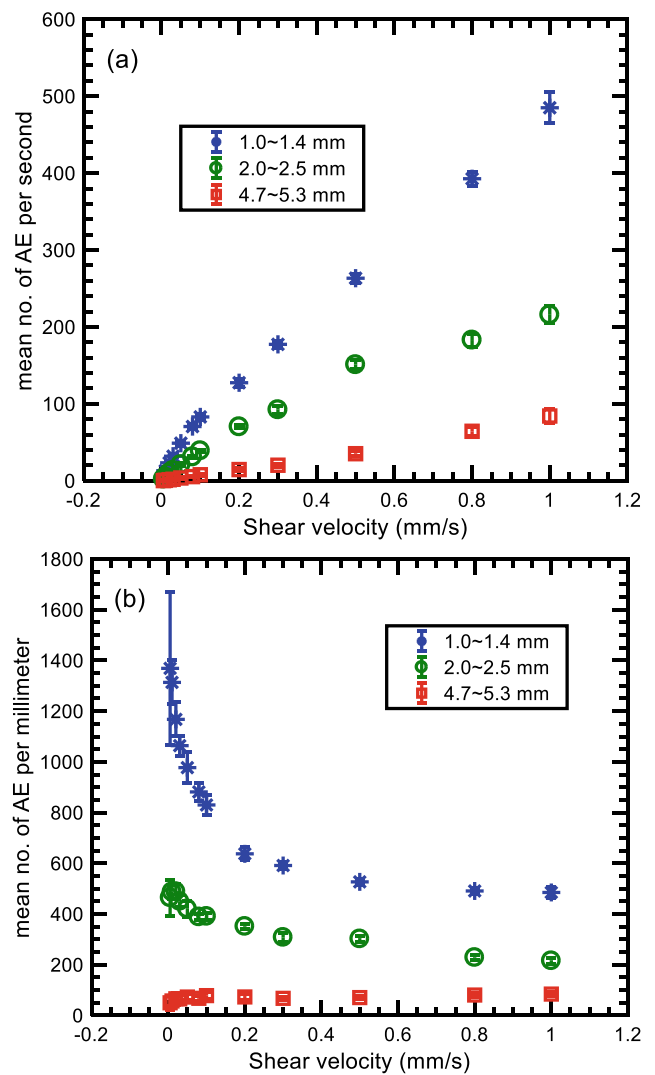


Fig. 4 The occurrence rate of AE events as a function of shear velocity for different particle sizes: **a** mean number of AEs per second; **b** mean number of AEs per millimeter. It is noted that AE rates increase in time-domain and decrease in displacement-domain at certain range of shear velocities

displacement) appears to be rate independent for some cases (e.g., small and intermediate particles sheared beyond the shear velocity of ~ 0.3 mm/s; the large particles sheared at our tested range of shear velocity.) To account for this, we suggest that the AE rate is not only sensitive to the preceding velocity conditions but also particle sizes, and both parameters can highly dominate the evolution of grain-scale contacts. Given our assumptions, it is perceivable that small particles would have larger contact junction area and hence enhanced AE relative to large particles due to the amount of particles under the same volume. Therefore, for all particle sizes under a given shear velocity, the smallest particle size deliver the highest AE rates no matter whether in time-domain or in displacement-domain (Fig. 4).

Discussions

Our current investigation for sheared granular materials notably extends the recent work where AEs and stress drops were monitored between bare rock surfaces and rock discontinues (Yabe et al. 2003; Mair et al. 2007). It is considered that many degrees of freedom and complicated evolutions of grain contact in granular system give rise to different interpretations for the physical process. The asperity model has been proposed to examine the source mechanisms on bare surfaces, and the stress drop associated with AE event is caused by coherent rupture of many asperities (Lockner 1993; Yabe et al. 2003). When considering the deformation processes in sheared granular materials, however, it has been documented that the external load is preferentially carried by a system of grain bridges or force chains (Mair et al. 2002; Anthony and Marone 2005; Scuderi et al. 2014). These force chains are transient features and highly sensitive to particle characteristics and mechanical conditions. With progression of granular shearing, the force chains can constantly form, stress, fail and reform, but the failure of individual force chain is meaningless or not sufficient to induce the global failure. Therefore, it is plausible that the single stress drop event recorded in sheared granular materials require the coherent rupture of many grain contacts or cluster of force chains where the stored elastic energy can be abruptly released. According to our results, such rapid release of elastic energy is short duration and priors to the stress drop ~ 2 ms. The observed ultrasonic precursor indicates that the implosive signals may be sourced from the major restructuring of grain force network which takes place before the rupture of stressed contact junctions.

Although we did not directly observe the evolution of force chains and measure the population of contact area during granular shearing, we can gain some possible insights

from the recorded AE activity. On one hand, in time-domain, mean number of AE shows a positive systematic dependence on the shear velocity. This type of relationship can be applied to assess the stability of slopes and obtain velocity profiles for sliding events. Previous studies have been devoting linkages to field applications and real-time monitoring systems (Dixon et al. 2015). On the other hand, the normalized AE activity in displacement-domain clearly depicts a nonlinear reduction tendency. At low shearing velocity, grain-scale contacts have time to grow and therefore would be expected to have larger total contact area leading to more AE activity during deforming. At higher shear velocity, grain-scale contacts are less mature, have little time to develop, and therefore have smaller total contact areas resulting in less AE activity. However, such changes are constrained for large particles. According to the numerical simulations of Morgan (1999), large-grained assemblages would cause a reduction of coordination number (i.e., the number of other grains contacting each particle), which result in the decrease of total contact area at grain junctions. Perhaps this is the reason why we can observe high AE rate for small-grained assemblages under constant volume. The independence of AE rate (per unit displacement) in our experiments indicate that the critical coordination number might exist during quasi-static deformations of granular materials.

Conclusions

Our results highlight the links among granular material properties, mechanical conditions and characteristics of generated AEs, and provide some preliminary issues regarding the extrapolation of physical approximations to real landslide motions. The frictional properties of granular materials are entwined with the particle properties and mechanical conditions, and the generated AEs also exhibit different characteristics. Our results reveal the strong correlations between stress fluctuations and AE activity during granular shearing. The magnitude and average occurrence rate for recorded AEs are not only dependent on shear velocity but also on particle size. However, we have not been able to establish a clear relationship between the magnitudes of stress drops and frequency-size distributions of AE events for different granular materials. Herewith, as future directions, we will concentrate on analysing the characteristics of AE events, and endeavour to provide a new insight into the physical processes and better understand the fundamental mechanisms for such kind of catastrophic phenomena in rapid landslides, if similar mechanisms likely operate in nature.

Acknowledgements Financial support for this study was partially provided by the NSFC of China (no. 41807278) and the MEXT of Japan (no. 25560181). Yao Jiang acknowledges support from the CAS Pioneer Hundred Talents Program.

References

- Anthony JL, Marone C (2005) Influence of particle characteristics on granular friction. *J Geophys Res: Solid Earth* 110:B08409
- Clague JJ, Stead D (2012) *Landslides: types mechanisms and modelling*. Cambridge University Press, New York
- Collins GS, Melosh HJ (2003) Acoustic fluidization and the extraordinary mobility of sturzstroms. *J Geophys Res: Solid Earth* 108 (B10):2473
- Davies TRH, McSaveney MJ, Boulton CJ (2012) Elastic strain energy release from fragmenting grains: effects on fault rupture. *J Struct Geol* 38:265–277
- Di Toro G, Han R, Hirose T, De Paola N, Nielsen S, Mizoguchi K, Ferri F, Cocco M, Shimamoto T (2011) Fault lubrication during earthquakes. *Nature* 471(7339):494–498
- Dixon N, Spriggs M, Smith A, Meldrum P, Haslam E (2015) Quantification of reactivated landslide behaviour using acoustic emission monitoring. *Landslides* 12(3):549–560
- Goren L, Aharonov E, Sparks D, Toussaint R (2011) The mechanical coupling of fluid-filled granular material under shear. *Pure Appl Geophys* 168(12):2289–2323
- Jiang Y, Wang G, H, Kamai T, McSaveney M J, (2016) Effect of particle size and shear speed on frictional instability in sheared granular materials during large shear displacement. *Eng Geol* 210:93–102
- Jiang Y, Wang G, H, Kamai T, (2017) Acoustic emission signature of mechanical failure: Insights from ring-shear friction experiments on granular materials. *Geophys Res Lett* 44(6):2782–2791
- Johnson PA, Savage H, Knuth M, Gombert J, Marone C (2008) Effects of acoustic waves on stick-slip in granular media and implications for earthquakes. *Nature* 451(7174):57–60
- Lockner D (1993) The role of acoustic emission in the study of rock fracture. *Int J Rock Mech Mining Sci Geomech Abs* 30(7):883–899
- Mair K, Frye KM, Marone C (2002) Influence of grain characteristics on the friction of granular shear zones. *J Geophys Res: Solid Earth* 107(B10):2219
- Mair K, Marone C, Young RP (2007) Rate dependence of acoustic emissions generated during shear of simulated fault gouge. *Bull Seismol Soc Am* 97(6):1841–1849
- Melosh HJ (1996) Dynamical weakening of faults by acoustic fluidization. *Nature* 379(6566):601–606
- Michlmayr G, Cohen D, Or D (2012) Sources and characteristics of acoustic emissions from mechanically stressed geologic granular media — a review. *Earth Sci Rev* 112(3–4):97–114
- Morgan JK (1999) Numerical simulations of granular shear zones using the distinct element method: 2. Effects of particle size distribution and interparticle friction on mechanical behavior. *J Geophys Res: Solid Earth* 104(B2):2721–2732
- Sassa K, Wang GH, Fukuoka H (2003) Performing undrained shear tests on saturated sands in a new intelligent type of ring shear apparatus. *Geotech Test J* 26(3):257–265
- Sassa K, Fukuoka H, Wang GH, Ishikawa N (2004) Undrained dynamic-loading ring-shear apparatus and its application to landslide dynamics. *Landslides* 1(1):7–19
- Scholz CH (2002) *The Mechanics of earthquakes and faulting*, 2nd edn. Cambridge Univ. Press, New York
- Schulz WH, Wang GH (2014) Residual shear strength variability as a primary control on movement of landslides reactivated by earthquake induced ground motion: implications for coastal Oregon, U. S. *J Geophys Res: Earth Sur* 119(7):1617–1635
- Scuderi MM, Carpenter BM, Marone C (2014) Physicochemical processes of frictional healing: Effects of water on stick-slip stress drop and friction of granular fault gouge. *J Geophys Res: Solid Earth* 119(5):4090–4105
- Wang GH, Sassa K (2009) Seismic loading impacts on excess pore-water pressure maintain landslide triggered flowslides. *Earth Surf Proc Land* 34(2):232–241
- Wang GH, Suemine A, Schulz WH (2010) Shear-rate-dependent strength control on the dynamics of rainfall-triggered landslides, Tokushima Prefecture Japan. *Earth Surf Proc Land* 35(4):407–416
- Xing AG, Wang GH, Li B, Jiang Y, Feng Z, Kamai T (2015) Long-runout mechanism and landsliding behaviour of large catastrophic landslide triggered by heavy rainfall in Guanling, Guizhou China. *Canadian Geotech J* 52(7):971–981
- Yabe Y, Kato N, Yamamoto K, Hirasawa T (2003) Effect of sliding rate on the activity of acoustic emission during stable sliding. *Pure Appl Geophys* 160(7):1163–1189
- Yang J, Wei LM (2012) Collapse of loose sand with the addition of fines: The role of particle shape. *Géotechnique* 62(12):1111–1125

Part V

**Recent Advancements in the Methods of Slope
Stability and Deformation Analyses**



Prediction of Deformation of Caisson Type Piles in Open cut Works and Countermeasures Employing Early Closure Method

Masahiro Katayama, Tsuyoshi Nakade, Tetsuji Yamaguchi, and Masafumi Okawara

Abstract

In open cut works in landslide areas, caisson type piles suffer much more severe deformation than predicted. The site was studied based upon additional geological surveys. From ground measurement results and back analysis, measures were considered necessary to prevent loosening associated with excavation at an early stage. In this project, as part of open cut works, the early closure method that has been proven to be effective in controlling deformation in mountain tunnels was used. In order to replicate the 3D restraint effect of natural ground, an appropriate construction method was planned from 3D FEM analysis. As a result, not only the rebound of the excavated bottom was suppressed, but also displacement of the pile and increase in rebar stress could be restricted. We believe that this method proved to be an effective construction method and established a prediction study method, and that this construction method can be used as a reference for similar construction.

Keywords

Hayama group • Landslide • Deformation • Early closure method

M. Katayama (✉) · T. Nakade · T. Yamaguchi
KUMAGAIGUMI Co., Ltd., Tsukudocho, Shinjuku, 162-8557,
Tokyo, Japan
e-mail: makataya@ku.kumagaigumi.co.jp

T. Nakade
e-mail: tnakade@ku.kumagaigumi.co.jp

T. Yamaguchi
e-mail: teyamagu@ku.kumagaigumi.co.jp

M. Okawara
Department of System Innovation Engineering, Faculty of Science
and Engineering, Iwate University, Ueda, Morioka City, Iwate
Prefecture, 020-8551, Japan
e-mail: okawara@iwate-u.ac.jp

Introduction

The Hayama Group distributed around the central area of the Miura Peninsula, Kanagawa Prefecture is known as a landslide prone area. In addition, since the hilly area where the Hayama Group is distributed is an area that has undergone rapid urbanization, ground deformation caused by new development activities may inflict significant damage on the surrounding area, thus requiring detailed consideration in design and construction (Nakayama 1999, Miyamoto et al. 2004).

For this project, when a semi-underground road was constructed by open earth cutting in a landslide area adjacent to a residential area, we faced a difficult problem that excessive stress was generated in the reinforcement of caisson type piles (hereinafter referred to as piles), producing excessive earth pressure and landslide force. The cause of this was thought to be the loosening of the ground during excavation and the generation of earth pressure that was higher than expected. From this result, if the construction was carried out as planned, there was a concern that the restraining effect of the piles would be impaired during construction, and that landslide movement would be intensified along with the loosening. The authors, facing the problem of open cutting excavation work at such a precarious landslide site, applied the early closure method which has in the past been tested in sites of mountain tunnel construction with large deformation, and was able to complete the construction safely. This paper describes the design method and predictive analysis method that have been established in order to implement these countermeasures.

Geological Overview

The construction site is located near the south eastern Hayama Group distribution area almost in the center of the Miura Peninsula. In Kanagawa Prefecture, the landslide

prevention area in the Hayama Group includes 12 of the 16 landslide prevention construction locations. Therefore, it can be said that the Hayama Group distribution area should be studied minutely in terms of landslides. Figure 1 is the landslide distribution map of the construction site. The scale of landslide is about length (L) = 95 m, width (W) = 50 m, depth (D) = 10–12 m. As shown in the cross-sectional view of Fig. 2, this geology consists of Hayama Group mudstone, which, from the ground surface, forms the topsoil and bed-rock. The mudstone is classified into highly weathered mudstone (W1), moderately weathered mudstone (W2) and slightly weathered mudstone (W3) according to the degree of weathering. The landslide that must be controlled is a ship-bottom type weathered rock landslide where landslides are assumed to have occurred near the boundary between highly weathered mudstone and moderately weathered mudstone, with a raised terrain at the toe of landslides. The groundwater level is located near the boundary with topsoil and highly weathered mudstone.

Construction Overview and Deformation of the Piles

Construction Overview

This project is designed to construct, through open excavation, a semi-underground type road with the following dimensions: excavation depth (H) = 7–16 m, excavation width (W) = 22–24 m, length (L) = 200 m, while preventing landslides by piles in the urban landslide distribution area. In this design, No. 6–No. 9, No. 27–No. 31 of the piles

are of a self-supporting structure and No. 10–No. 26 piles are designed to suppress earth pressure such as landslides as a beam structure connecting the upper and lower piles with a beam at the top and a floor slab (Figs. 1 and 2). After excavating and constructing the piles (diameter 3 m) on both the upper and lower sides, initial excavation (H = 5–9 m) was conducted for the placement of a beam. After the construction of the beam, excavation reaching to the bottom rock was conducted to the depth of (H) = 7 m (Fig. 2). During excavation, the equipment for measuring structure behavior—inclinometers (in ground and piles) and rebar stress meters (in piles) were installed as shown in Fig. 1.

Deformation of Piles

Immediately after the initial excavation was completed and the main excavation proceeded from the terminal side to the starting side, the stress from the rebar stress meter (bottom excavation) which was installed in the lower pile at No. 24 in Fig. 3 began to increase with time, and still grew even after the excavation was stopped, exceeding the allowable value (180 N/mm^2) of the tensile stress of the reinforcement. Then, countermeasures were taken, and the stress reached 216 N/mm^2 finally. Figure 3 compared the real behavior and the behavior of piles on the upper side and lower side of the No. 24, which is assumed in the original design. Initially, it was assumed that the load from the upper ground is transferred to the lower pile through the beam, and the lower pile inclines to the back. However, when the initial excavation started, both the upper and lower piles were temporarily displaced to the excavation side (center), and when excavating in front of the piles, the ground protruded from the foundation bottom in the excavation release direction. At this point, there was no sign of inducing a landslide from the observation of dynamic behavior on the back of the upper pile.

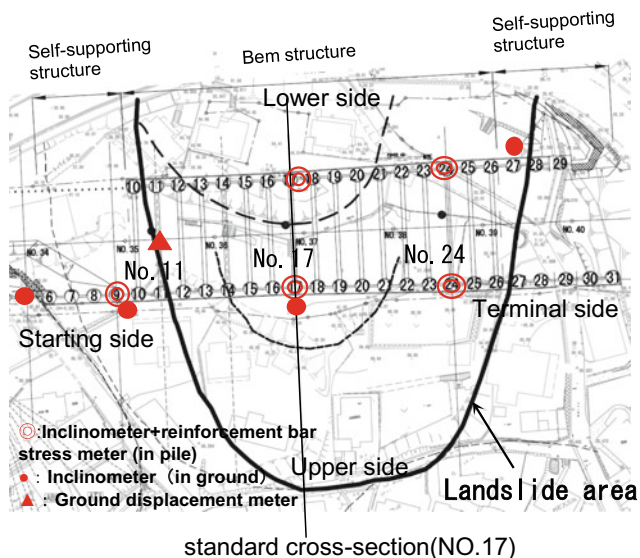


Fig. 1 Plan of construction points, layout of landslide locations and dynamic behavior observation points

Cause of Deformation

Decrease in Strength Due to Ground Deterioration After Excavation

In order to investigate the cause of the behavior of deformed piles, it was considered necessary to grasp the ground conditions during excavation, and we conducted additional boring-based geological surveys by using boring results. Strength and deformation characteristics were determined.

As a result, the depths shallower than GL-6.0 m (Fig. 4) from the bottom are significantly loosened. The deformation coefficient E was $1,200\text{--}6,900 \text{ (kN/m}^2\text{)}$, with a deviation of about $1/4\text{--}1/20$ from the original design. In addition, the internal friction angle was about $10\text{--}20^\circ$ close to the original design, and the adhesive strength was about $3\text{--}15 \text{ (kN/m}^2\text{)}$, about $1/3\text{--}1/10$ of the original design value.

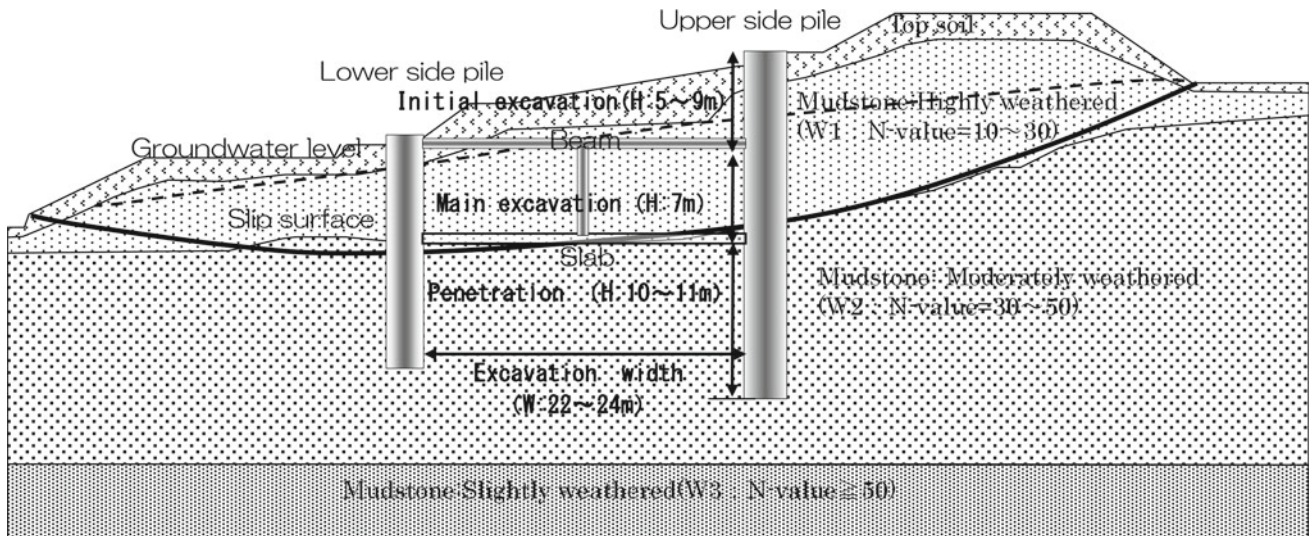


Fig. 2 Standard cross-section (No. 17)

Horizontal Force Generated by Stress Release After Excavation

In order to reproduce the behavior of the piles as shown in Fig. 3, reproduction analysis was performed using a structural analysis model shown in Fig. 4 using the physical property values in a deteriorated state. As a result, in addition to the earth pressure calculated with the earth pressure coefficient $K = 0.35$, it was confirmed that horizontal force

greater than expected was working on the lower pile. The cause of this horizontal force is considered to be the following.

1. Stress release due to post-excitation rebound induced a decrease in strength.
2. It is known that the uplift area at the toe of the ship-bottom type landslide where the lower pile is located is in a compression zone (Watari and Kohasi (1987), and it was assumed that the region near the lower pile would have a large compressive stress (initial ground pressure) compared with the upper ground.
3. Since mudstone contains a large amount of smectite, it was assumed that there was also the effect of time-delayed expansion pressure resulting from ground swelling due to clay minerals.

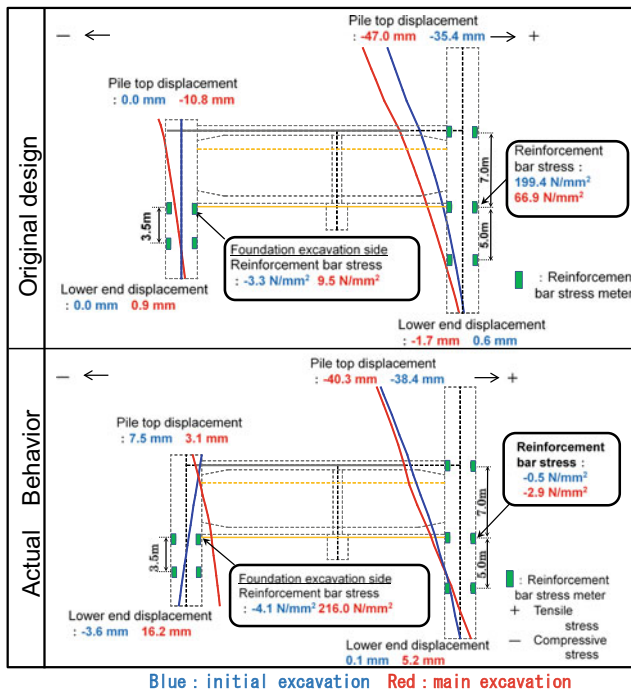


Fig. 3 Behavior of the piles during excavation (No. 24)

In addition, the pile was short in length in the loosened region, helping further generate horizontal forces associated with excavation release stress. A part of the behavior and

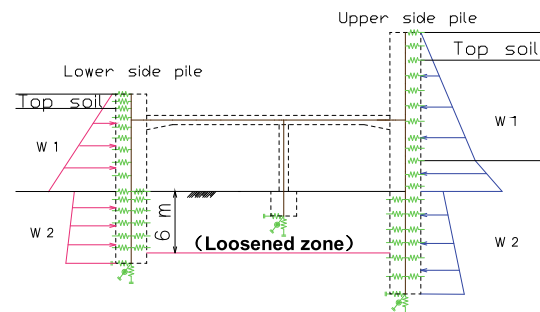


Fig. 4 Structural analysis model

cause of the deformation has already been reported (Katayama et al. (2019)).

Examination of Countermeasures

Concept of Countermeasures

In this construction, it was found that the deformation and strength characteristics suddenly decreased during excavation, and that the horizontal force at work exceeded the expected level. Loosening due to deterioration of such ground near the bottom had the potential of exercising an adverse effect on the stability of piles and of inducing landslides. It was judged that it was necessary to secure stability by integrating the bottom with the piles at an early stage. In addition, it was considered necessary to use reinforcing material that resists horizontal force at the bottom. From this point of view, considering that it was necessary to suppress loosening at an early stage by controlling the loosened amount of excavation and to take preventive steps for reinforcement, we examined the use of the early closure method (Japan Society of Civil Engineers (2013), the effectiveness of which has been proven especially effective against deformations in mountain tunnels (NATM).

Overview of Countermeasures

Figure 5 shows a conceptual diagram of the countermeasures and the construction procedure. Construction was determined to start from the construction starting side where no boring had been conducted. Bench-cut excavation was used to shorten the downward boring length in order to reduce the excavation release force and release time – factors related to excavation release and ground deterioration. The bottom was closed with invert struts at an early stage. In general, the early closure method is more effective when the distance between the bench release surface and the invert strut is shorter. In this construction, if the bench was shortened, it would be difficult to obtain work space, with safety problems associated with work in confined spaces. Therefore, for this project, by referring to the NATM early closure method, we decided to restrict the deformation of the ground taking the following measures suitable for the site conditions (Fig. 5).

1. The excavation was divided into bench cuts with a shift length of 10 m depth, while continuing with the excavation of the central portion of the cross-section.
2. Preliminary temporary concrete ($t = 70$ cm) was placed to form a cover on the ground surface which was expected to function as an inverse strut reaction body.

3. Side bench in front of the pile was excavated.
4. Invert struts (H500) were quickly installed, and the piles on both sides were integrated into one unit through preloading.

Prediction and Examination of Countermeasures

Predictive Analysis

The release distance in front of the piles, the most important element to be considered before the installation of the inverts, was set at 10 m due to construction restrictions. In order to quantitatively evaluate the relevance of this release distance and the effectiveness of countermeasures, prediction analysis after the final excavation was performed using the analysis model in Fig. 4, following the analysis steps in Fig. 8 here, the stress release rates before and after installation of the invert struts were set separately, and the three-dimensional ground-restraining effect from split excavation and the effect of early closure by the invert struts were reflected in the analysis.

Setting of the Stress Release Rate

FEM excavation analysis of full step excavation and split excavation was performed using a three-dimensional model that simply simulated the site conditions as shown in Fig. 6. The rate of progress of the displacement of the pile by split excavation was compared with the case of release by full step

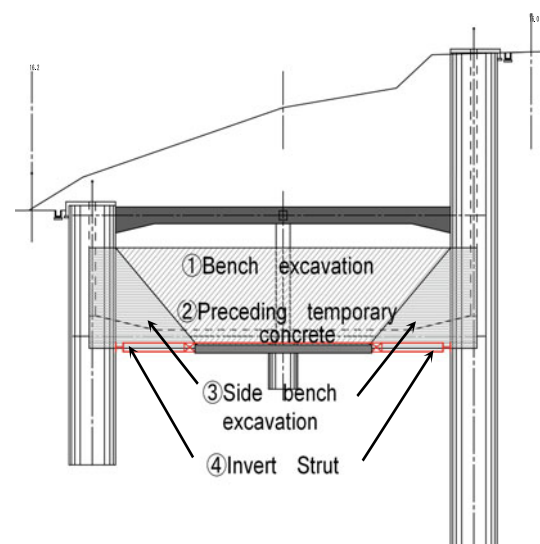


Fig. 5 Concept of countermeasures

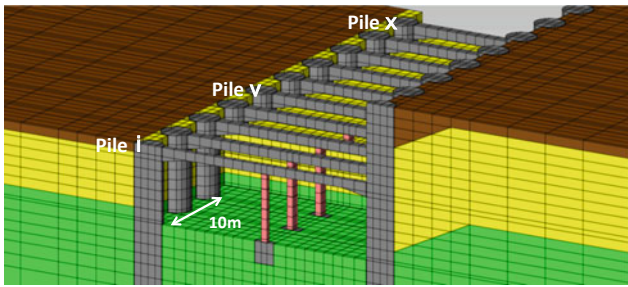


Fig. 6 3D FEM analysis model of excavation

excavation. Figure 7 shows the progress of split excavation at the foundation level (pile position) and the rate of change in pile displacement. The three-dimensional ground suppression effect is that in the case of split excavation, the displacement (release width 10 m) when the excavation reaches the target pile remains 63% compared to full step excavation (100%). Based on this result, in the analysis, the stress release rate, after being replaced by earth pressure, was evaluated. 70% of the total earth pressure during the main excavation was applied before installation of the struts, and the remaining 30% was applied after installation of the struts (Fig. 8).

Predictive Analysis Results

As a result of prediction analysis, Table 1 shows the stress level in No. 11 and No. 17 piles. When no countermeasures were taken, it was estimated that a stress level exceeding the allowable value would occur at the time of final excavation (No. 11), and that when a landslide occurs, the allowable stress level could not be satisfied for both compression and tension (No. 11, No. 17). On the other hand, by taking countermeasures, the stress level during excavation could be reduced to approximately 60% of the allowable value, and

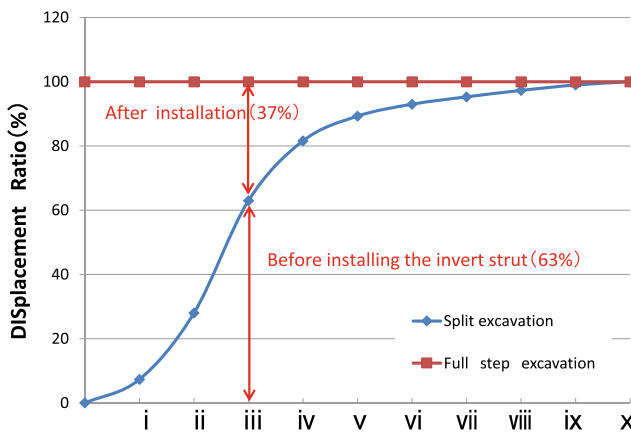


Fig. 7 Relationship between excavation positions and pile displacement

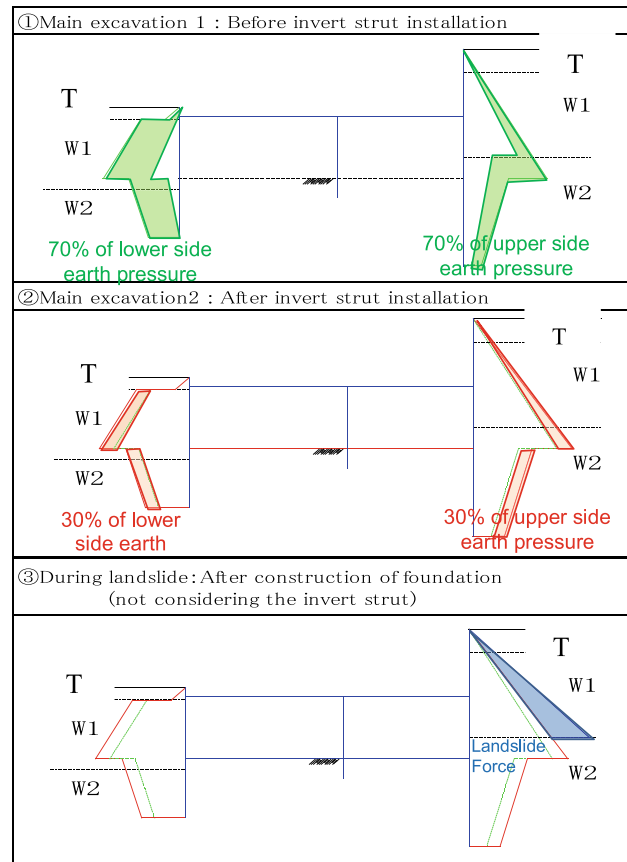


Fig. 8 Predictive analysis procedure

the results satisfying the allowable value were obtained even for potential landslides. It was judged that the construction could proceed while ensuring the integrity of the structure.

Effect of Countermeasures

Figure 9 compares the measured values before and after countermeasures for the relative horizontal displacement from the head of pile No. 17. The horizontal displacement measurement is almost the same as the analytical value, and the amount of displacement is about half that of the No. 24 pile where deformation occurred, demonstrating significant restraining effect. In addition, as for the reinforcement stress near the foundation bottom, it was confirmed that all the measurement values were lower than predicted. From these results, we were able to confirm that the countermeasures were extremely effective and the relevancy of the prediction analysis method applied to this construction method.

Furthermore, with the aim of grasping the behavior of natural ground during this excavation, the ground swelling was measured with an underground displacement meter on

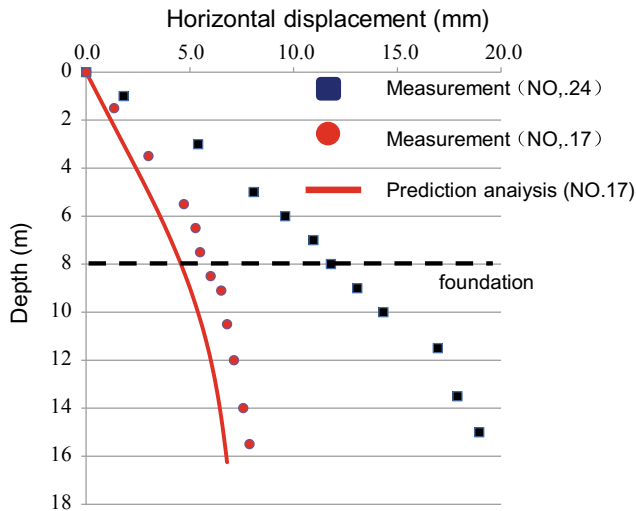


Fig. 9 Horizontal displacement of piles

the starting side (No. 11) where there is no loosening effect (Figs. 10 and 11). As a result, from the start of this excavation, a ground upheaval occurred from the start of this excavation around G.L. -1.0 m directly below the foundation bottom, and a rebound of about 16 mm was confirmed by the time of the preceding temporary concrete pouring in the central section. After construction of the preceding temporary concrete, the rebound was able to be suppressed. These results prove that the early closure method is an effective method in suppressing loosening and displacement.

Conclusion

The authors describe the main findings obtained through this study below.

1. During excavation in the Hayama Group, the surrounding mountain loosened greatly, leading to stress relief from the compressive region at the rebound of the foundation bottom and the toe of the ship-bottom type

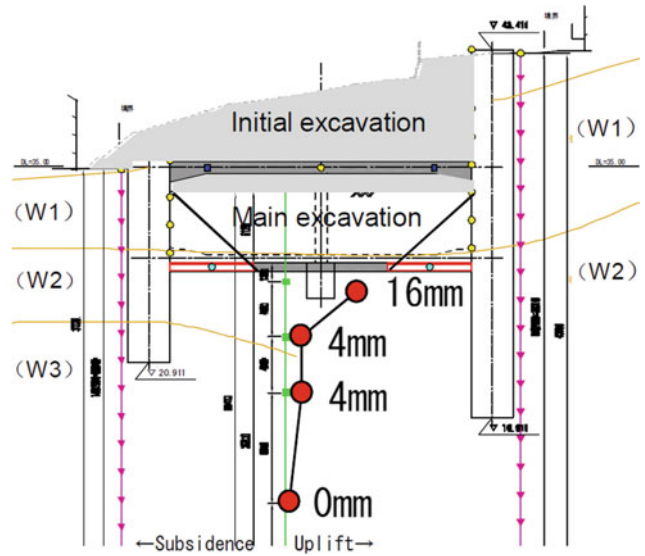


Fig. 10 Measurements of in-ground displacement (No.11)

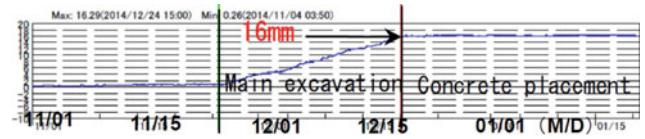


Fig. 11 Rebound amount over time (G.L.-1.0 m)

landslide. The expansion pressure associated with the swelling clay minerals caused a higher than expected horizontal force.

2. The three-dimensional restraining effect of the mountain was able to be reflected in the design for deformation of the piles due to the loosening of excavation, and a rational construction plan was able to be established.
3. Although the shift length was determined from construction conditions, we were able to establish the evaluation and prediction method for such countermeasures by using a 3D FEM analysis.
4. By applying the NATM-based early closure method, the rebound of the foundation bottom was able to be

Table 1 Results of prediction analysis

		No countermeasures		With countermeasures	
		Main excavation	During landslide	Main excavation	During landslide
No. 11	σ_c	5.5	7.4	3.7	5.7
	σ_s	183.1	245.6	114.6	176.9
No. 17	σ_c	5.0	7.1	3.3	5.5
	σ_s	156.1	223.7	89.7	157.0
Tolerance: Compressive $\sigma_c = 7.2$					
Tensile $\sigma_s = 180.0$ (N/mm ²)					

suppressed, controlling the increase of displacement in piles and of stress in reinforcement.

During road construction by open cutting of ground through the Hayama Group, unexpected deformation occurred, but we were able to determine the cause by the reproduction analysis through additional investigation and measurement. In addition, with these results, we were able to create an early closure method according to the NATM, verify the effect of the method, and establish a prediction and study method.

Katayama M, Nakade T, Yamaguchi T, Okawara M (2019) A study on the deformation of the caisson type pile retaining wall in semi-underground type excavation work in the distribution area of Hayama group. *J JSCE (F1)* 75(1):107–115

Miyamoto K, Hayakawa T, Ueno S, Endo K (2004) Topographic geological features and stability evaluation of landslides in the Hayama formation, Miura peninsula. In: Abstracts of the 43rd Annual Meeting of the Japan Landslide Society, pp 347–350

Nakayama Y (1999) Prevention areas of steep slope failure and landslide in the central Miura Peninsula. *J Japan Land-Slide Soc* 36 (1):43–48

Watari M, Kohasi S (1987) Prediction and counter measures for landslides and slope failures. Sankaido (ISBN4381–00764–6), pp 38–39

Reference

Japan Society of Civil Engineers (2013) Tunnel Library 25 Invert for Mountain Tunnels. pp 34–39



2020 Kyoto Japan

Slope Stability Assessment of Weak and Weathered Rocks with BQ System

Timur Ersöz, Merve Özköse, and Tamer Topal

Abstract

Rock slopes can be affected by weathering and human activities. Depending on the type of the rock, the impact of weathering and excavation can change. This leads some strength reductions and consequently some stability problems. Limit equilibrium analyses are widely used to assess slope stability but empirical methods are also very useful and quick. Basic quality (BQ) system is very popular method which is developed in China to assess slope stability of the rock slopes. Generally it leans on strength and rock soundness/GSI to determine slope stability. In this study, rock slope stabilities were assessed with limit equilibrium method and BQ system. 55 cut slopes located in Western Black Sea Region of Turkey were used to evaluate the stability conditions. 39 of the cut slopes are located in flysch deposits consisting mudstones and sandstone/limestone alternations. Other rock types are granite, basalt, andesite, granodiorite, serpentinite and tuff. According to the field observations, degree of weathering of most of the cut slopes are moderate (38), and the rest are slightly (10) and highly (7). Uniaxial compressive strength, point load strength index and Schmidt hammer tests were applied to find strength values. According to the tests, most of the rocks are in the category of weak and medium strong (5–50 MPa) throughout the study area. The field observations revealed that all cut slopes are stable except surficial failures due to weathering and excavation. According to limit equilibrium analyses, all cut slopes are stable, but

only surficial failures were observed due to degradation which is completely coherent with the field observations. However, BQ System revealed that most of the results are not coherent with the field observations and limit equilibrium results. It is concluded that rocks stronger than 50 MPa can be assessed properly by BQ System in the study area.

Keywords

BQ system • Excavation • Flysch • Rock strength • Slope stability • Weathering

Introduction

Rock slopes can be affected by weathering agents as freeze and thaw, rainfall and wind, and human activities like excavation or blasting. Due to these activities and disturbances properties of the rocks change and the slope loses stability condition in time. Depending on the type of the rock, the impact of weathering and excavation can change. This can lead to differential weathering and consequently some stability problems.

There are many ways to investigate slope stability. Maybe the most popular one is limit equilibrium analyses but empirical methods are also very useful and quick. Slope Mass Rating (SMR) (Romana 1985), Slope Stability Probability Classification (SSPC) (Hack 1998), Falling Rock Hazard Index (FRHI) (Singh 2004), Rockslope Deterioration Assessment (RDA) (Nicholson and Hencher 1997) and QSlope (Barton and Bar 2015) are only some of the most popular ones. They are very advantageous to use providing quick solutions with limited data gathered from the field.

Basic Quality (BQ) system (The National Standards compilation group of People's Republic of China 1994) is also a very popular method which is developed in China to assess slope stability of the rock slopes. In general, it leans

T. Ersöz (✉) · T. Topal
Department of Geological Engineering, Middle East Technical University, 06800 Ankara, Turkey
e-mail: tersoz@metu.edu.tr

T. Topal
e-mail: topal@metu.edu.tr

M. Özköse
Koza Gold Corporation, 06370 Ankara, Turkey
e-mail: merveozkose@gmail.com

on strength and rock soundness in order to determine the stability of a slope. It is very advantageous that there are only two parameters should be used to assess whole slope. This presents a very quick and simple data collection to evaluate rock slope stability. Determining the strength of a material is relatively more widespread and easier than soundness of the rock mass. Therefore, BQ system is developed by the users to estimate rock soundness by considering Geological Strength Index (GSI) value of the rock mass into the equation. This improvement made it possible to determine BQ ratings by using Geological Strength Index values in the equation without any rock soundness test results.

In this study, rock slope stabilities were assessed by both limit equilibrium method and BQ system. 55 cut slopes located in Western Black Sea Region of Turkey were used to evaluate the stability conditions. Selected rock slopes contain many different rock types namely flysch, granite, basalt, andesite, granodiorite, serpentinite and tuff. Field performances, limit equilibrium analyses results and BQ system rating solutions were compared and discussed in this paper. In addition, undisturbed and disturbed zones of the cut slopes were assessed separately in order to evaluate the real field conditions.

Study Area

Location of the study area is chosen as Western Black Sea Region of Turkey, including Zonguldak, Karabük, Bolu, Düzce, Kastamonu, Çankırı and Northern parts of Ankara (Fig. 1). In these regions, heavy rainfalls are very famous. In the study area, generally flysch type of deposits are dominant, but also igneous and metamorphic rocks can be observed. Among 55 cut slopes, 39 of them contain flysch deposits and the rest are igneous and metamorphic rocks. The study area is located around North Anatolian Fault Zone (NAFZ) which disturbed whole region in years. Due to these active tectonic activities, most of the cut slopes are highly jointed. Flysch deposits are extremely affected by differential weathering. Undercutting actions can be observed on these kinds of rocks throughout the study area contributing surficial failures like rock falls and raveling.

In the study area, 55 cut slopes were investigated having different properties. 39 of the cut slopes are located in flysch deposits consisting mudstones and sandstone/limestone alternations. Other rock types are also abundant in the study area namely granite, basalt, andesite, granodiorite, serpentinite and tuff. Slope angle and height of the slopes are in the range of 30–80° and 6–60 m, respectively (Fig. 2).

Weathering degrees of the cut slopes were determined according to field observations and assigned according to BS5930 (1981). As many flysch deposits consist of

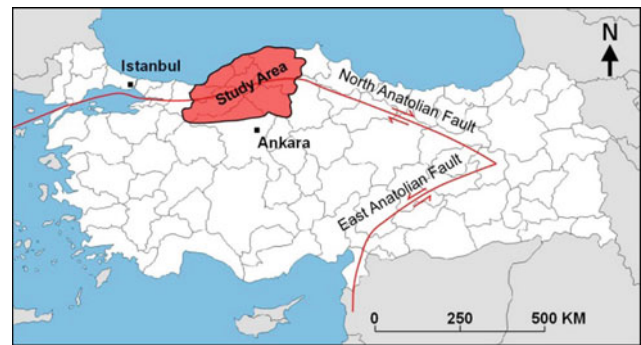


Fig. 1 Location map of the study area

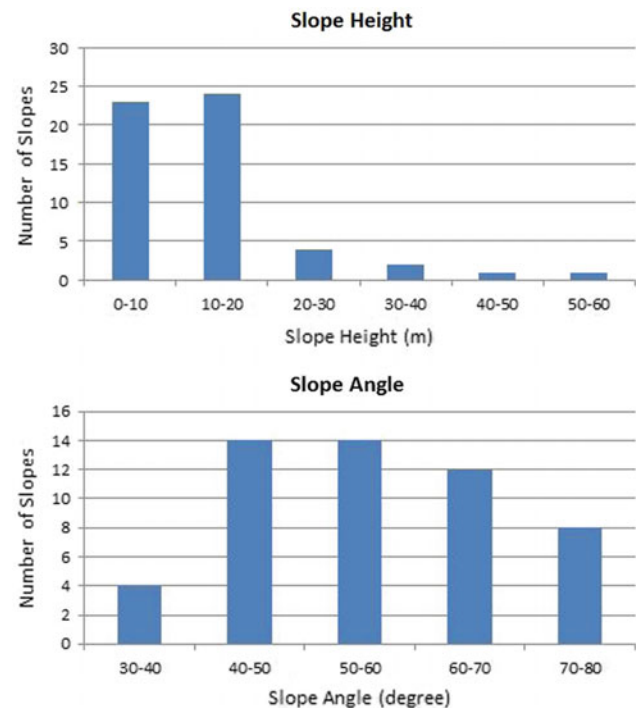


Fig. 2 Slope height and slope angle distributions the in study area

alternating rock types, weighted average method (Marinos and Hoek 2001) was used to assign weathering degree of the cut slope. According to the field observations, it is determined that among 55 cut slopes most of them are moderately (38), and the rest are slightly (10) and highly (7) weathered. Excavation types of the cut slopes were also determined in the field in addition to personal communications with General Directorate of Highways (KGM Turkey). According to this, excavation type is determined as mechanical except only one cut slope which is by smooth blasting.

Detailed study was made for strength determination of the cut slopes. It is known that, due to weathering and excavation a certain thickness on the surface of a cut slope can be affected. In order to investigate this, samples were gathered

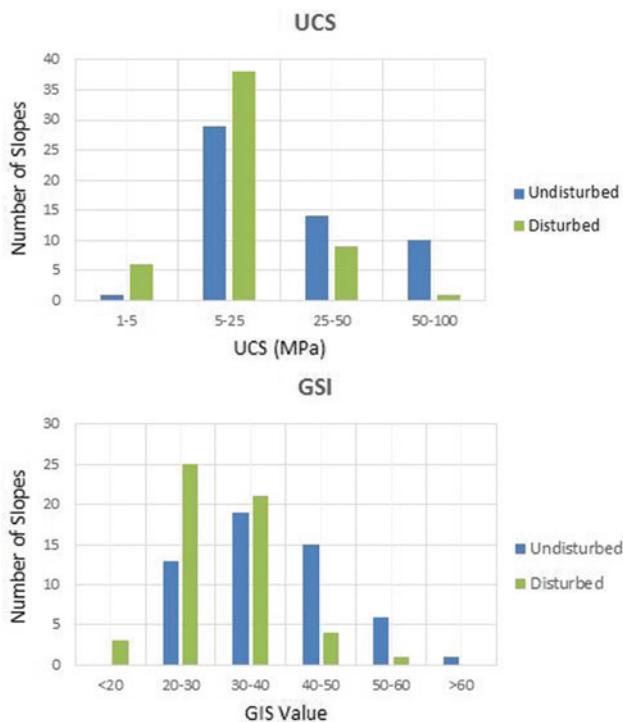


Fig. 3 Disturbed and undisturbed UCS and GIS value distributions in the study area

from both disturbed and undisturbed zones. It is important to mention that, the disturbed zone at the surface was determined according to visual estimations on weathering degrees and Schmidt hammer measurements. The mean rebound values of Schmidt measurements were gathered from the surface of the cut slope with at least ten measurements. Afterwards, other measurements were taken from the visually decided depths from the surface. This way, the strength differences were supported with visual estimations considering the rock disturbances.

Detailed investigation was made to assign strength values to alternating rocks of flysch units by using weighted average method (Marinos and Hoek 2001). Oriented samples were taken from the disturbed and undisturbed zones of the cut slopes in order to apply uniaxial compressive strength (UCS) ($5 \times 5 \times 5$ cm cubic) and point load index (irregular samples) tests. According to the test results, undisturbed and disturbed zone strength values were calculated separately (Fig. 3). Based on the results, it is clear that most of the rocks are in the category of weak and medium strong (5–50 MPa) throughout the study area.

In addition to this, GSI values were also assigned differently to the disturbed and undisturbed zones. Due to stress relief, excavation and weathering, the GSI values should be different than the relatively fresh parts. Because of these impacts, additional apertures and fractures were identified on the surfaces of the road cuts. Therefore, two different GSI

values were assigned to each road cut, namely for the disturbed and undisturbed zones (Fig. 3).

Methodology

BQ System is a national standard in China (The National Standards compilation group of People's Republic of China, 1994) which is widely used in China to assess rock slopes. There are two quantitative indices which are UCS and K_v (rock integrity index). UCS can be obtained from point load strength index or uniaxial compressive strength test. K_v , on the other hand, can be obtained from P-wave velocity of rock mass and intact rock. In years, a new formula is developed (Rui-Xin and Yan-Jun 2015) in order to replace K_v with GSI values. Other parameters used in BQ System are related to groundwater conditions (K_4) and key discontinuity attitude (K_5). In addition to them, a correction factor for key discontinuity types and extensibility (λ) is also introduced to obtain more reliable results. The basic BQ value can be obtained by the equation (Eq. 1) given as follows:

$$BQ = 100 + 3UCS + 250K_v \quad (1)$$

where K_v can be replaced by KGSI in an equation (Eq. 2) given below:

$$K_{GSI} = 1 / (1 + \exp(60 - GSI) / 12) \quad (2)$$

Finally, the ultimate [BQ] value can be obtained by using the basic BQ value and other correction factors (Eq. 3) (Song et al 2019).

$$[BQ] = BQ - 100 (K_4 + \lambda K_5) \quad (3)$$

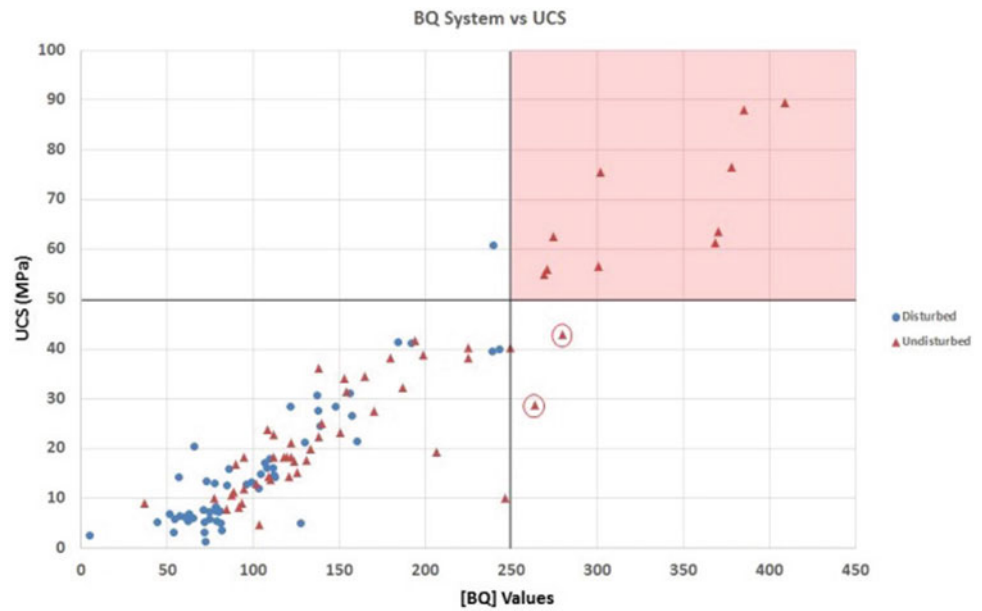
According to this formula, [BQ] values can give solutions related to the stability of the rock slopes.

Throughout the study area, cut slopes were analysed by using limit equilibrium methods. Cut slopes were investigated considering discontinuity controlled failures and mass failures.

Results and Discussion

In this study, 55 cut slopes were investigated according to BQ System (Fig. 4). In this regard, both undisturbed and disturbed zones of the cut slopes were assessed. According to the results, most of the slopes-independent of being undisturbed or disturbed zone- are in the range of below 250 [BQ] value which means that they are complete unstable. Other values larger than 250 indicating partially or completely stable are only obtained from the undisturbed zones' of the cut slopes.

Fig. 4 [BQ] results in relation with UCS (MPa)



The field observations revealed that all cut slopes are stable except surficial failures due to weathering agents and excavation activities. Limit equilibrium analyses were done considering these disturbed zones which have certain depths changing at each cut slope (Fig. 5). According to the limit equilibrium analyses, all cut slopes are found to be stable, but only surficial failures were obtained due to surficial degradation. Minimum factor of safety of the undisturbed zones was determined as 1.3 (static) and 1.1 (dynamic) which are considerably stable. On the contrary, factor of safety results of the disturbed zones were calculated below 1 throughout the study area (Ersöz and Topal 2018a, b; Özköse 2019). Therefore, it is concluded that these results are coherent with the field observations.

Limit equilibrium analyses were done by assigning strength, unit weight, GSI, weathering and disturbance factor to proper zones (disturbed and undisturbed) in order to reflect the real field conditions. As indicated in the limit equilibrium analyses section, all results are matching with the field observations which prove the accuracy of the related parameters.

BQ system uses discontinuity features in addition to strength and GSI to analyse stability of the cut slopes. Figure 4 shows that most of the values are clustered below 250 [BQ] in accordance with strength values. It is observed that values below 250 [BQ] are not only from disturbed zones (unstable zones) but also undisturbed zones (stable zones). Values larger than 250 [BQ] are only obtained from undisturbed zones (stable zones) which are coherent with the field observation. However, according to BQ System, many stable (undisturbed) cut slopes are below 250 [BQ] which shows unstable conditions. This relation is not coherent with the field observations and limit equilibrium results.

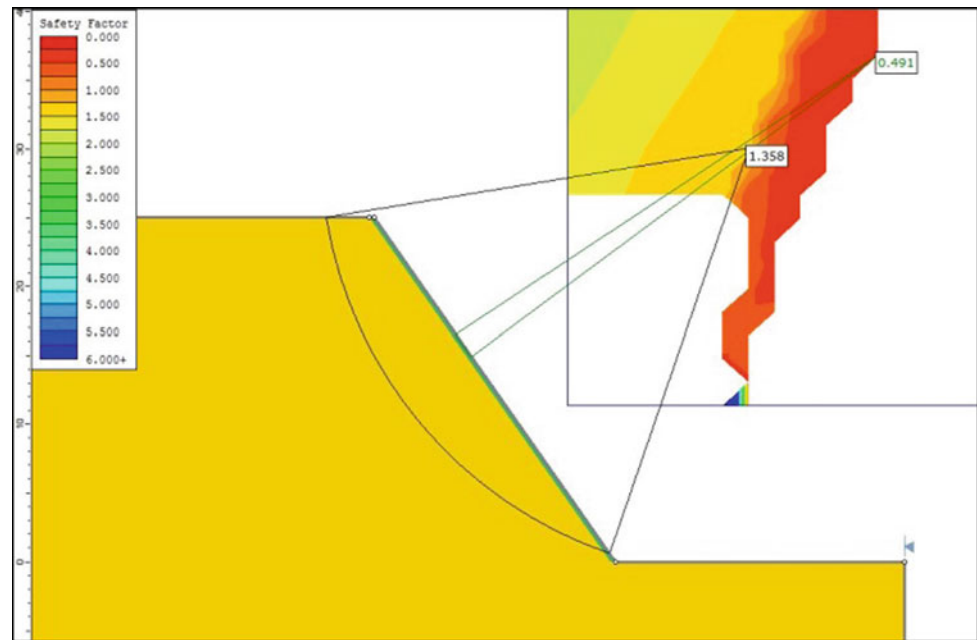
BQ values larger than 250 showing partially or completely stable conditions can be also observed from Fig. 4. In general, these values are clustered over 50 MPa indicating the category of strong rock. Two exceptions are observed below 50 MPa having higher values than 250 [BQ] (encircled with red). In detail, it is observed that these two cut slopes have GSI values larger than 50.

Results show that BQ System mainly relies on UCS and GSI values more than discontinuity features. This comes with a solution that it can be very useful for the rocks having strength more than 50 MPa (strong rock). Medium strong, weak and very weak rocks (lower than 50 MPa) are observed to be not suitable for BQ System according to the analyses.

Conclusions

There are many ways to analyse rock slopes either with limit equilibrium or empirical methods. BQ System is a very popular method especially in China to assess stability of rock slopes in a quick and easy way by using limited data. In this study, 55 cut slopes from Western Black Sea Region of Turkey were investigated with limit equilibrium methods and BQ System. In this research, cut slopes were assessed based on their undisturbed and disturbed zones. Differentiation of these zones was done by Schmidt hammer measurements, strength and unit weight differences in the laboratory and field observations in the field. Thickness of the disturbed zones was determined for each cut slope throughout the study area. Limit equilibrium methods and BQ System were used by considering these features. According to the field observations, it is observed that all cut

Fig. 5 Limit equilibrium analysis showing different factor of safety results on disturbed and undisturbed zones of a cut slope in the study area



slopes are stable except surficial failures at the disturbed zones on the slope surface due to weathering and excavation effects. Limit equilibrium analyses were done considering these zones and coherent results were obtained. According to BQ System, the rocks having strength more than 50 MPa (strong rock) show coherent results with field observations. Moreover, many stable cut slopes appeared at unstable zone of BQ System which is not coherent with the field observations and limit equilibrium analyses. It can be concluded that BQ System show very good results over 50 MPa (strong rock). On the other hand, it shows incompatible results with field observations for many slopes having strength lower than 50 MPa (medium strong, weak and very weak rocks).

References

- Assessing the potential for deterioration of engineered rock slopes. In: Proceedings of the IAEG symposium, pp 911–917. Athens
- Barton N, Bar N (7–10 October, 2015) Introducing the Q-slope method and its intended use within civil and mining engineering projects. In: Schubert W, Klunckner A (eds) Future development of rock mechanics; Proceedings of the ISRM regional symposium, Eurock 2015 and 64th Geomechanics colloquium, pp 157–162. Salzburg
- BS5930 (1981) Code of practice for ground investigations. British Standards Institute London
- Ersöz T, Topal T (2018a) Weathering and excavation effects on the stability of various cut slopes in flysch-like deposits. *Geotech Geol Eng.* <https://doi.org/10.1007/s10706-018-0566-z>
- Ersöz T, Topal T (2018b) Assessment of rock slope stability with the effects of weathering and excavation by comparing deterministic methods and slope stability probability classification (SSPC). *Environ Earth Sci* 77:547. <https://doi.org/10.1007/s12665-018-7728-4>
- Hack R (1998) Slope stability probability classification; SSPC; 2nd version. University of Technology Delft; International Institute for Aerospace Survey and Earth Sciences; ITC, Delft, Enschede, The Netherlands
- Marinos P, Hoek E (2001) Estimating the geotechnical properties of heterogeneous rock masses such as Flysch. *Bull Eng Geol Env* 60:85–92
- Nicholson DT, Hencher S (1997) Assessing the potential for deterioration of engineered rock slopes. In: Proceedings of the IAEG symposium, pp 911–917. Athens
- Özköse M (2019) Assessment of cut slope stability in Western Black Sea Region (Turkey). Master Thesis, Middle East Technical University, Ankara, Turkey
- Romana M (1985) New adjustment rating for application of the Bieniawski classification to slopes. Proceeding of international symposium on rock mechanics, mining civil works. ISRM. Zacatecas, Mexico, pp 59–63
- Rui-Xin Y, Yan-Jun S (2015) Correlation of revised BQ system in china and the international rock mass classification systems. *J Civil Eng Res* 5(2):33–38
- Singh A (2004) FRHI—a system to evaluate and mitigate rockfall hazard in stable rock excavations. *J Instit Eng (India): Civil Eng Div* 85: 62–75
- Song Y, Xue H, Meng X (2019) Evaluation method of slope stability based on the Qslope system and BQ method. *Bull Eng Geol Env.* <https://doi.org/10.1007/s10064-019-01459-5>
- The National Standards compilation group of People's Republic of China (1994) GB 50218–94 Standard for engineering classification of rock masses, pp 1–22. China Planning Press, Beijing (In Chinese)



2020 Kyoto Japan

Soil Databases to Assist Slope Stability Assessments in the Eastern Caribbean

Paul J. Vardanega[✉], Elizabeth A. Holcombe[✉], Myrto Savva, Casey J. Shephard[✉], Rose Hen-Jones[✉], and Flavia De Luca[✉]

Abstract

Rainfall-triggered landslides are an ‘everyday risk’ to Small Island States, such as Saint Lucia in the Caribbean, and have the potential to destroy or damage buildings and disrupt lifelines such as roads and pipelines. To better evaluate these landslide hazards, efforts have been made to develop decision-support tools linking rainfall scenarios to stability for different types of road cut slope. Many thousands of stochastic simulations can be performed using a combined hydrology and slope stability model (CHASM) which requires inputs of slope cross-sectional geometry, soil and hydrological parameters which allows representative rainfall-triggered landslide scenarios to be produced. To use CHASM for this purpose the statistical variation of the relevant geotechnical properties such as friction angle needs to be assessed. This paper presents the analysis of an updated database for Saint Lucian soils that has been compiled using data supplied by the Government of Saint Lucia Ministry of Infrastructure, Port Services and Transport. The Coefficient of Variation values of the key soil mechanics parameters are reported and previously developed transformation models for estimating effective friction angle are updated. The Weibull statistical distribution is shown to be the best fit to the friction angle data.

Keywords

Coefficient of variation • Soil database • Soil variability • Transformation models • Statistical distributions • Tropical soils

Introduction

Landslides in the humid tropics are typically rainfall triggered (e.g. Lumb 1975; Toll 2001). Considerable research has focused on modelling rainfall triggered landslides in the Eastern Caribbean (Anderson and Kemp 1991; Holcombe et al. 2016; Shephard et al. 2018a). As a developing country, Saint Lucia is more vulnerable to the effects of natural disasters than other nations (c.f. Alcantara-Ayala 2002) with socio-economically vulnerable communities and lifeline infrastructure (Fig. 1) particularly affected (Bull-Kamanga et al. 2003; Larsen and Parks 1997).

Methods to better assess geotechnical variability are needed to enhance geotechnical design (e.g. Lumb 1966, 1970). Geotechnical databases are needed to enable measures of geotechnical variability of a soil parameter to be determined, such as the coefficient of variation (COV); or the best-fit probability density functions; or to develop transformation models allowing a more complex soil parameter to be estimated from basic ones (e.g. Kulhawy and Mayne 1990; Phoon and Kulhawy 1999a, b; Phoon 2017).

Recent efforts to develop a geotechnical database for Saint Lucia have been reported by Vardanega et al. (2018) and Shephard et al. (2018b, 2019). In Shephard et al. (2019), the first 91 entries in the database were reported and analysed. In this paper the database is expanded using data collected during a 2018 research visit. This database was then expanded and further analysed in the thesis of Savva (2019).

Such geotechnical data are necessary for mechanistic slope stability analyses such as those performed using

P. J. Vardanega · E. A. Holcombe (✉) · R. Hen-Jones · F. De Luca

Department of Civil Engineering, University of Bristol, Queen’s Building, University Walk, Bristol, BS8 1TR, UK
e-mail: liz.holcombe@bristol.ac.uk

M. Savva

Formerly affiliated to Department of Civil Engineering, University of Bristol, Queen’s Building, University Walk, Bristol, BS8 1TR, UK

C. J. Shephard

Department of Engineering, University of Cambridge, Trumpington Street, Cambridge, CB2 1PZ, UK



Fig. 1 Road cut slope, Saint Lucia primary road network, after landslide debris cleared (Photo: E A Holcombe)

CHASM (e.g. Wilkinson et al. 2002), and more recently by placing such models within a stochastic high-performance computing framework (e.g. Almeida et al. 2017). Potential decision-support outputs include synthetic rainfall thresholds for landslide triggering (cf. Larsen and Simon's 1993, empirical-statistical thresholds for Puerto Rico). These can be used to assess whether a region will experience landslides for a given storm event (this topic is discussed further in Holcombe et al. 2021).

Soil Classification Parameters

The use of basic soil classification parameters (e.g. plasticity index) to develop transformation models is the subject of many studies (e.g. Kulhawy and Mayne 1990). In this paper the COV of the liquid limit (w_L), plastic limit (w_P), plasticity index (I_P), the silt–clay fraction (SCF) (which is defined in this work as the percentage passing the 0.075 mm sieve) and field water content (w) are studied along with the soil effective peak friction angle (ϕ'_p or ϕ'_{peak}) and apparent cohesion (c').

Soil Friction Angle

The effective friction angle has been studied for soils from various Caribbean islands e.g. Dominica (Rao 1996; Reading 1991; Rouse et al. 1986; Rouse 1990) and Trinidad (Roopnarine et al. 2012). To ensure long-term stability of slopes the critical state friction angle (Take and Bolton 2011) or the fully softened or residual friction angle (e.g. Eid and Rabie 2017; Hayden et al. 2018) would be preferred.

However, in Saint Lucia only the ϕ'_p is typically available from hand-powered direct shear tests in the government materials laboratory. Shepherd et al. (2019) describe the details of the testing process in which the stress increment is believed to have been constant for all the tests in the database (37.2–112.4 kPa). Field samples are placed directly into the shear box without sieving, but with inevitable disturbance and change in moisture content due to sample extraction, transporting and testing (Shepherd et al. 2019). Further verification of the shear box testing procedure would be required if individual test data were intended for site-specific analysis and design rather than for stochastic modelling and diagnosis of general slope behaviour thresholds (see Almeida et al. 2017).

Soil friction angle is related to changes in the Atterberg limits (e.g. Brooker and Ireland 1965; Sorensen and Okkels 2013; Stark and Eid 1997; Stark and Hussain 2013; Wesley 1977, 2003) and clay fraction (Skempton 1985).

Building the Saint Lucia Soils Database

In 2016 a field trip was undertaken by the first two authors to Saint Lucia where data was obtained from the digitised records from the Saint Lucia Ministry of Infrastructure, Port Services and Transport. This data along with other information from past projects undertaken by the second author was used to produce the database with 91 data entries presented in detail in Shepherd et al. (2019) and analysed in Shepherd (2017), Vardanega et al. (2018), Shepherd et al. (2018b).

In 2018, a follow-up visit was undertaken by another research team from the University of Bristol (again the first two authors were involved). In this visit, further data was collected by scanning past data reports. This new data was processed, added to the database and the statistical analysis methodology presented in Shepherd et al. (2019) was re-run. Preliminary results of this new analysis are presented in Savva (2019). In the analysis that follows the number of data-points (n) on each chart can vary, as for each entry in the expanded database not all the parameters of interest were available.

Statistical Analysis

Computation of COV can be used to assess relative variability of different soil parameters (Phoon and Kulhawy 1999a, b). Phoon (2017) gives the COV values for many transformation models from the literature. Table 1 shows the relevant summary statistics for the updated Saint Lucia database. A range of soil types are present on the island of

Saint Lucia (see Shepherd et al. 2019). Figure 2 shows the soils from the expanded database plotted on the Casagrande chart: a range of plasticity levels is shown with both silts and clays present in the database. Figure 3 shows the pairs of ϕ'_p and c' with a high degree of scatter shown (the COV for c' is about 2.7 times that of ϕ'_p ; see Table 1).

Regression Analysis

Past transformation models have been developed for early versions of the Saint Lucia database. I_p is often used to estimate ϕ'_p (e.g. Brooker and Ireland 1965; Sorensen and Okkels 2013). The coefficient of determination (R^2) and the number of data-points used to generate the regression (n) are quoted for each transformation model presented along with the p value. For the Saint Lucia soils (data from the 2016 field work) the following transformation model was developed (Shepherd et al. 2018b, 2019):

$$\phi'_p = 26.4 - 0.22(I_p) \quad [R^2 = 0.15, n = 55, p = 0.004] \quad (1)$$

However, for the Saint Lucia soils Shepherd et al. (2018b) also showed a superior correlation using w :

$$\phi'_p = 30.7 - 0.32(w) \quad [R^2 = 0.36, n = 52, p < 0.001] \quad (2)$$

Vardanega et al. (2018) showed further improvement in R^2 when ϕ'_p was regressed against liquidity index (I_L):

$$\phi'_p = 20.8 - 10.2(I_L) \quad [R^2 = 0.43, n = 48, p < 0.001] \quad (3)$$

Equations 1–3 are compared with updated transformation models in the following section.

Updated Regressions

Figure 4 shows ϕ'_p plotted against w_L for the expanded database (the number of available data-points for the new

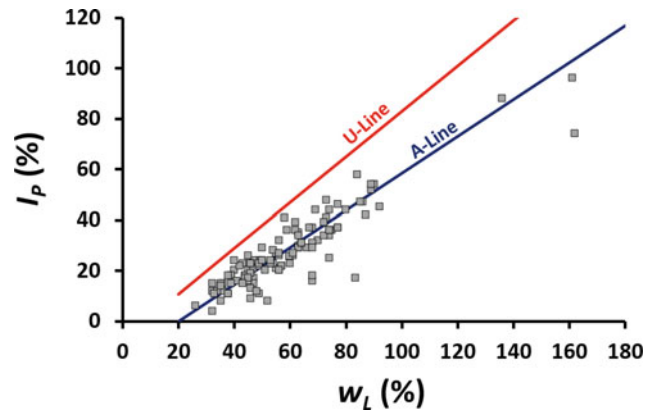


Fig. 2 Expanded Saint Lucia Database ($n = 114$) plotted on the Casagrande-style classification chart

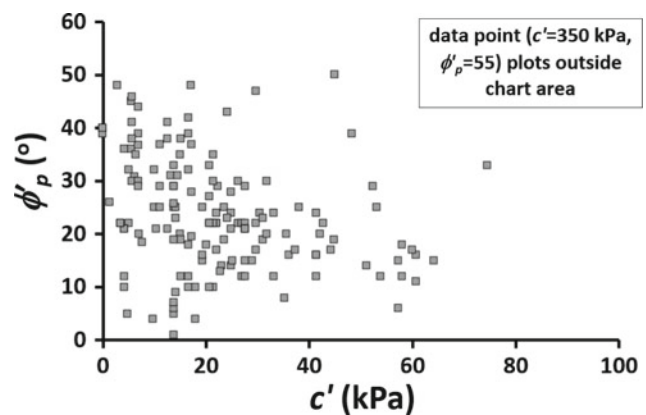


Fig. 3 ϕ'_p plotted against c' (kPa) (expanded database)

regressions is about double that from the previous studies). An exponential model was found to be the best fit to the ϕ'_p versus w_L data:

$$\phi'_p = 37.2e^{-0.011(w_L)} \quad [R^2 = 0.23, n = 102, p < 0.001] \quad (4)$$

Figure 5 shows ϕ'_p plotted against w_p for the expanded database with an exponential relationship:

$$\phi'_p = 31.0e^{-0.015(w_p)} \quad [R^2 = 0.088, n = 101, p < 0.01] \quad (5)$$

Table 1 Summary statistics for the updated Saint Lucia soils database (all soil types) (SD = standard deviation)

	c' (kPa)	ϕ'_p ($^\circ$)	w_L (%)	w_p (%)	I_p (%)	w (%)	SCF (%)
n	153	152	115	115	120	132	119
Max	350	55	162	88	96	117	96
Average	25	24	59	31	27	32	40
Min	0	1	26	16	3	8	3
SD	31	11	22	10	15	16	24
COV (%)	125	46	38	32	58	49	59

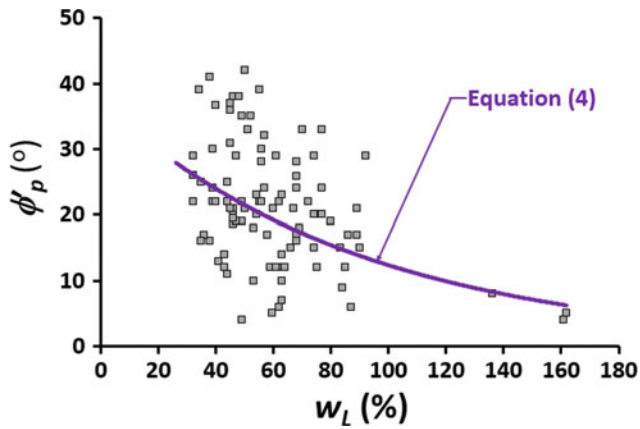


Fig. 4 ϕ'_p plotted against w_L (%) (expanded database)

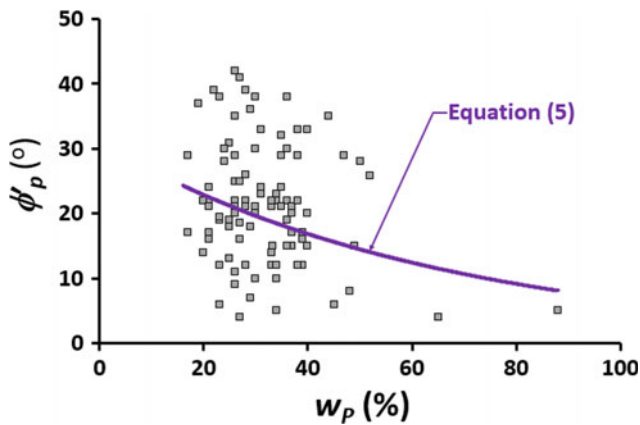


Fig. 5 ϕ'_p plotted against w_P (%) (expanded database)

Figure 6 shows ϕ'_p plotted against I_p compared with Eq. 1 and the following exponential relationship developed for the updated database (reasonable agreement between Eqs. 1 and 6 is shown):

$$\phi'_p = 29.6e^{-0.016(I_p)} \quad [R^2 = 0.23, n = 104, p < 0.001] \quad (6)$$

Figure 7 shows ϕ'_p plotted against w compared with Eq. 2 and with the following exponential relationship developed for the updated database (reasonable agreement between Eqs. 2 and 7 is shown):

$$\phi'_p = 39.0e^{-0.020(w)} \quad [R^2 = 0.39, n = 114, p < 0.001] \quad (7)$$

Figure 8 shows ϕ'_p plotted against SCF for the expanded database with the following exponential relationship:

$$\phi'_p = 26.6e^{-0.0079(SCF)} \quad [R^2 = 0.14, n = 101, p < 0.001] \quad (8)$$

Figure 9 shows ϕ'_p plotted against I_L compared with Eq. 3 and the following linear relationship developed for the updated database:

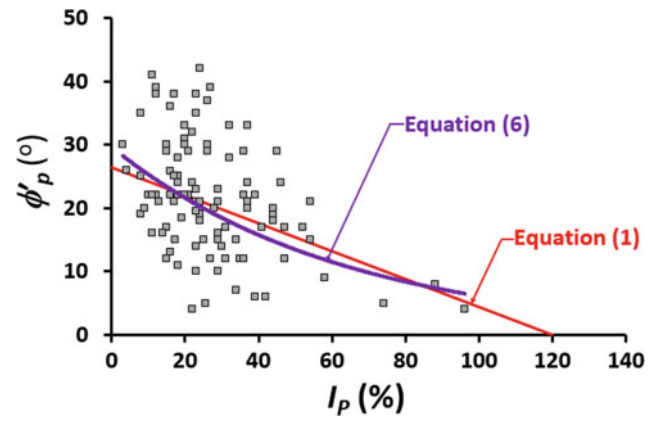


Fig. 6 ϕ'_p plotted against I_p (%) (expanded database)

$$\phi'_p = 21.4 - 6.6(I_L) \quad [R^2 = 0.21, n = 94, p < 0.001] \quad (9)$$

The slope of Eq. 9 is smaller than Eq. 3 and the R^2 is considerably lower. Of the studied correlations Eq. 7 has the highest R^2 and is higher than for the correlation with I_L (Eq. 9). Figure 10 shows the predicted measured plot for Eq. 7 with $\pm 50\%$ bounds shown.

Multiple Linear Regression (MLR) Analysis

MLR studies of the early database were reported in Shephard (2017) and Shephard et al. (2018b). The following correlation was found (Shephard et al. 2018b):

$$\phi'_p = 19.8 - 0.14(w_L) + 0.77(w_P) - 0.46(w) \quad [R^2 = 0.56, n = 47, p < 0.001] \quad (10)$$

The same analysis was re-run for the expanded database:

$$\phi'_p = 23.6 - 0.078(w_L) + 0.42(w_P) - 0.31(w) \quad [R^2 = 0.28, n = 84, p < 0.001] \quad (11)$$

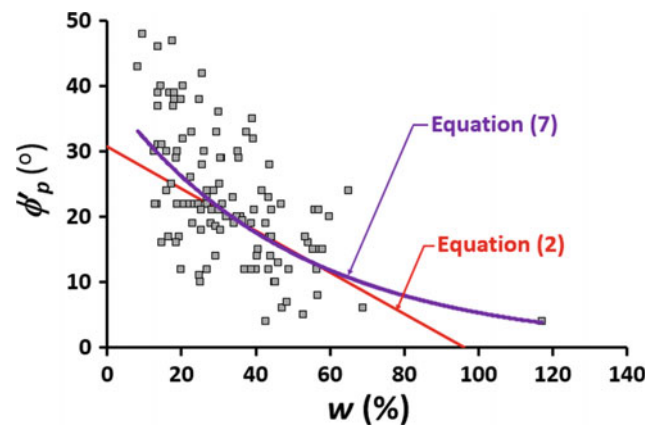


Fig. 7 ϕ'_p plotted against w (%) (expanded database)

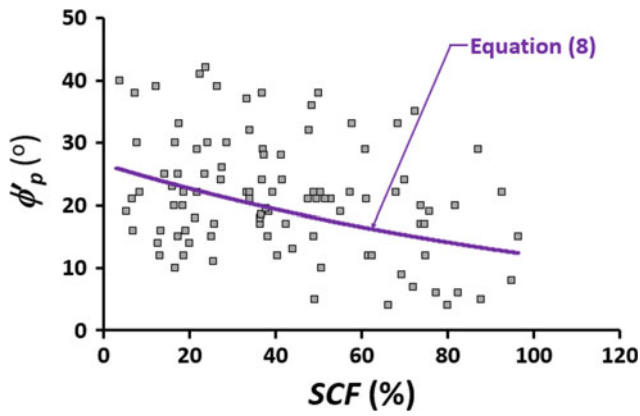


Fig. 8 ϕ'_p plotted against SCF (%) (expanded database)

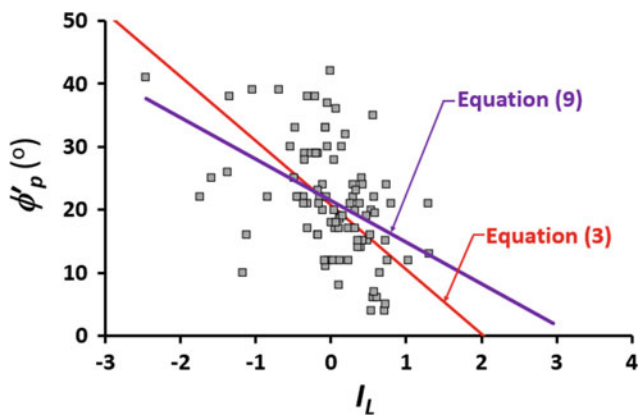


Fig. 9 ϕ'_p plotted against I_L (expanded database)

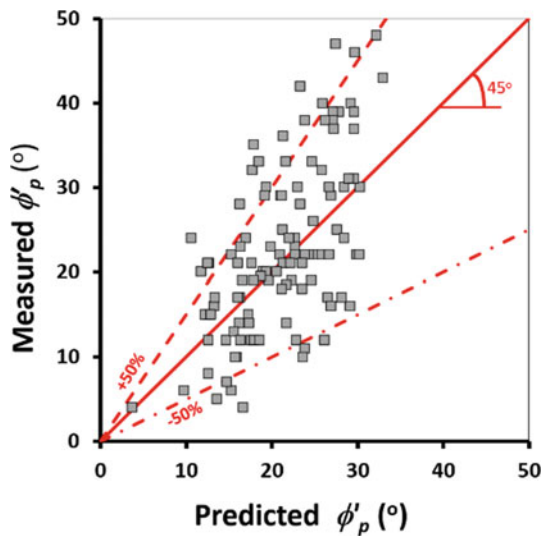


Fig. 10 Predicted versus measured plot for Eq. 7

Statistical Models

Distributions of soil parameters are needed for stochastic slope stability analysis. Fits of statistical distributions to the early database were presented in Shephard et al. (2019) in which it was found that the Weibull distribution was the best fit. With the ϕ'_p data in the extended database ($n = 152$), the Weibull distribution is again shown to be the most appropriate (Fig. 11, Table 2). Table 2 provides a summary of the Akaike Information Criteria (AIC) (Akaike 1974) and Anderson Darling (AD) (Anderson and Darling 1954) test statistics confirming the suitability of Weibull distribution over the others. For the AIC also the Generalised Extreme Value (GEV) fit was tested giving a value of 1278 (still higher than the 1153 obtained using the Weibull fit).

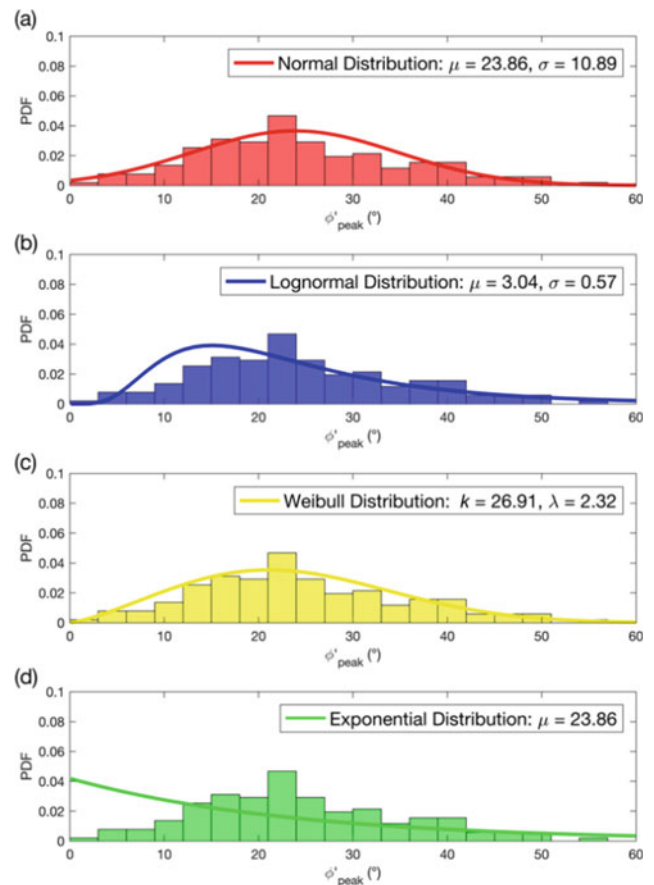


Fig. 11 Normal a Lognormal b Weibull c and Exponential d probability density functions fitted to ϕ'_p data from the extended database (fitting parameters for each distribution shown on the figure)

Table 2 AIC and AD statistics for the distributions fitted to the Saint Lucia ϕ'_p data from the extended database (best fit shown in bold)

	Normal	Lognormal	Weibull	Exponential
AIC	1160	1190	1153	1270
AD	1.0154	2.4775	0.4210	19.9490

Summary and Conclusions

This paper has presented preliminary analysis of an expanded geotechnical database for Saint Lucia. The new database has approximately double the number of data-points available to develop transformation models to predict ϕ'_p . Future work will analyse classes of soils within the database. Interestingly, the relative strength of the previous correlations with I_p and w has remained consistent with slightly higher computed R^2 values for the correlations developed using the expanded dataset. However, the models developed using I_L and a combination of w_L , w_p and w have reduced R^2 values compared with those for the earlier version of the database. The best predictor of ϕ'_p appears to be w , and with Weibull as the best statistical distribution.

Acknowledgements Funding for soil database development came from: 'Landslide risk assessment of lifeline roads for public asset management and rainfall based index insurance' (part of EP/P510920/1) and 'PRISM: Platform for Road and Infrastructure Slope Management (GCRF pump-priming project)' (part of EP/R512771/1). The authors acknowledge the contributions of Dr Mair Beesley and Ms Charlotte Gilder during the field work in 2018. We thank the Government of Saint Lucia Ministry of Infrastructure, Port Services and Transport for providing access to their soil data. **Data Availability Statement:** This research has not generated new experimental data.

References

- Akaike H (1974) A new look at the statistical model identification. *IEEE T Automat Contr* 19(6):716–723
- Alcantara-Ayala I (2002) Geomorphology, natural hazards, vulnerability and prevention of natural disasters in developing countries. *Geomorphology* 47(2–4):107–124
- Almeida S, Holcombe EA, Pianosi F, Wagener T (2017) Dealing with deep uncertainties in landslide modelling for disaster risk reduction under climate change. *Nat Haz Earth Sys* 17:225–241
- Anderson TW, Darling DA (1954) A test of goodness of fit. *J Am Stat Assoc* 49(268):765–769
- Anderson MG, Kemp MJ (1991) Towards an improved specification of slope hydrology in the analysis of slope instability problems in the tropics. *Prog Phys Geog* 15(1):29–52
- Brooker EW, Ireland HO (1965) Earth pressure at rest related to stress history. *Can Geotech J* 2(1):1–15
- Bull-Kamanga L, Diagne K, Lavell A, Leon E, Lerise F, MacGregor M et al (2003) From everyday hazards to disasters: the accumulation of risk in urban areas. *Environ Urban* 15(1):193–204
- Eid HT, Rabie KH (2017) Fully softened shear strength for soil slope stability analysis. *Int J Geomech* 17(1):04016023
- Hayden CP, Purchase-Sanborn K, Dewoolkar M (2018) Comparison of site-specific and empirical correlations for drained residual shear strength. *Géotechnique* 68(12):1099–1108
- Holcombe EA, Beesley MEW, Vardanega PJ, Sorbie R (2016) Urbanisation and landslides: hazards drivers and better practices. *P I Civ Eng Civ Eng* 169(3):137–144
- Holcombe EA, Hen-Jones R, Vardanega PJ, Beesley MEW, Gilder CEL, Bozzolan E (2021) Co-producing data and decision support tools to reduce landslide risk in the humid tropics. In: Sassa K et al. (eds) *Understanding and reducing landslide disaster risk, ICL contribution to landslide disaster risk reduction* (in press). https://doi.org/10.1007/978-3-030-60196-6_49
- Kulhawy FH, Mayne PW (1990) *Manual on estimating soil properties for foundation design*. Electric Power Research Institute, Palo Alto, CA, Report EL-6800
- Larsen MC, Parks JE (1997) How wide is a road? The association of roads and mass-wasting in a forested montane environment. *Earth Surf Proc Land* 22(9):835–848
- Larsen MC, Simon A (1993) A rainfall intensity-duration threshold for landslides in a humid-tropical environment, Puerto Rico. *Geogr Ann A* 75(1–2):13–23
- Lumb P (1966) The variability of natural soils. *Can Geotech J* 3(2):74–97
- Lumb P (1970) Safety factors and the probability distribution of soil strength. *Can Geotech J* 7(3):225–242
- Lumb P (1975) Slope failures in Hong Kong. *Q J Eng Geol* 8(1):31–65
- Phoon K-K (2017) Role of reliability calculations in geotechnical design. *Georisk* 11(1):4–21
- Phoon K-K, Kulhawy F H (1999a) Characterization of geotechnical variability. *Can Geotech J* 36(4):612–624
- Phoon K-K, Kulhawy F H (1999b) Evaluation of geotechnical property variability. *Can Geotech J* 36(4):625–639
- Rao SM (1996) Role of apparent cohesion in the stability of Dominican allophane soil slopes. *Eng Geol* 43(4):265–279
- Reading AJ (1991) Stability of tropical residual soils from Dominica, West Indies. *Eng Geol* 31(1):27–44
- Roopnarine R, Eudoixe G, Gay D (2012) Soil physical properties as predictors of soil strength indices: Trinidad case study. *Geomaterials* 2(1):1–9
- Rouse C (1990) The mechanics of small tropical flowslides in Dominica, West Indies. *Eng Geol* 29(3):227–239
- Rouse WC, Reading AJ, Walsh RPD (1986) Volcanic soil properties in Dominica, West Indies. *Eng Geol* 23(1):1–28
- Savva M (2019) A geo-database of tropical soil data for the island of Saint Lucia in pursuit of quantifying geotechnical uncertainty. MSc thesis, University of Bristol, Bristol, UK
- Shepherd CJ (2017) Prediction of the angle of friction for fine grained plastic soils: a St Lucia case study. Undergraduate Research Report no. 1617RP007m. Department Civil Engineering, University of Bristol, Bristol, UK
- Shepherd CJ, Vardanega PJ, Holcombe EA, Michaelides K (2018a) Analysis of design choices for a slope stability scenario in the humid tropics. *P I Civ Eng Eng Su* 171(1):37–52
- Shepherd CJ, Vardanega PJ, Holcombe EA, Hen-Jones R, De Luca F (2018b) On the variability of the effective friction angle of Saint Lucian soils: investigations through a laboratory database. *ce/papers* 2(2–3):779–784

- Shepherd CJ, Vardanega PJ, Holcombe EA, Hen-Jones R, De Luca F (2019) Minding the geotechnical data gap: appraisal of the variability of key soil parameters for slope stability modelling in Saint Lucia. *B Eng Geol Environ* 78(7):4851–4864
- Skempton AW (1985) Residual strength of clays in landslides, folded strata and the laboratory. *Géotechnique* 35(1):3–18
- Sorensen KK, Okkels N (2013) Correlation between drained shear strength and plasticity index of undisturbed overconsolidated clays. In: *Proceedings of the 18th ICSMGE, Paris, France*, pp 423–428
- Stark TD, Eid HT (1997) Slope stability analysis in stiff fissured clays. *J Geotech Geoenviron* 123(4):335–343
- Stark TD, Hussain M (2013) Empirical Correlations: Drained Shear Strength for Slope Stability Analyses. *J Geotech Geoenviron* 139(6):853–862
- Take WA, Bolton MD (2011) Seasonal ratcheting and softening in clay slopes, leading to first time failure. *Géotechnique* 61(9):757–769
- Toll DG (2001) Rainfall-induced landslides in Singapore. *P I Civ Eng Geotech* 149(4):211–216
- Vardanega PJ, Crispin JJ, Gilder CEL, Voyagaki E, Shepherd CJ, Holcombe EA (2018) Geodatabases to improve geotechnical design and modelling. *ce/papers* 2(2–3):401–406
- Wesley LD (1977) Shear strength properties of halloysite and allophane clays in Java, Indonesia. *Géotechnique* 27(2):125–136
- Wesley LD (2003) Residual strength of clays and correlations using Atterberg limits. *Géotechnique* 53(7):669–672
- Wilkinson PL, Anderson MG, Lloyd DM (2002) An integrated hydrological model for rain-induced landslide prediction. *Earth Surf Proc Land* 27(12):1285–1297



2020 Kyoto Japan

The Mt Gamalama Instability Level in Generating Landslide-Induced Tsunami in Ternate Island, Indonesia

Saaduddin, Jurgen Neuberg, Mark E. Thomas, and Jon Hill

Abstract

Mt Gamalama is a volcanic island which has a history of tsunamigenic volcanic eruptions with known events in 1608, 1840, and 1871, where tsunami generation is suspected due to landslides or sector collapse of the steep flanks entering the Molucca Sea threatening the coastal population and infrastructure. The potential landslides were investigated by applying a limit equilibrium method and the generalized Hoek–Brown failure criteria. This resulted in a so-called factor of safety (FoS) which describes the Mt Gamalama slope stability level. The critical FoS values ranging from 1.945 to 3.361 have been obtained for the four sections of the Mt Gamalama edifice—the north, south, west, and east sides and are considered in a relatively stable condition. These values hold for a static condition only under gravity and in the absence of any volcanic activity. The application of so-called seismic loads k_h of 0.103, and 0.155, 0.457, and 0.685, and magma pressures of 2–17 MPa due to vertical and tilted dyke intrusion decreases FoS values ($FoS < 1.000$) in all sections. We show that these additional factors destabilize the Mt Gamalama slopes and even lead to failure.

Keywords

Mt gamalama • Instability • Landslides • Tsunami

Introduction

Active volcanoes are dynamically evolving structures which are continuously deforming in both vertical and horizontal directions; this leads to potential edifice instabilities. Furthermore, these instabilities can cause tsunami generation, so-called volcanic tsunamis, especially for volcanoes in marine settings: volcanic islands, submarine volcanoes, and coastal volcanoes. The eruption of Anak Krakatau (the child of Krakatoa) caused a tsunami which took place in Lampung and Banten on 22nd December 2018. PVMBG (2018) reported that Anak Krakatau lost two third of the height of its edifice from 338 m high to 110 m.

Mt Gamalama is another volcano in Indonesia which has a history of tsunami generation in 1604, 1840 and 1871 (Hamzah et al. 2000; Paris et al. 2014). This volcano is a volcanic island due to the subduction of the Molucca sea plate and Halmahera thrust as depicted in Fig. 1. As a very active stratovolcano, its activities lead to an inherently unstable condition. The formation of two maars, Tolire in the west and Laguna in the south edifice, denoted an instability are the result of Mt Gamalama activities (Bronto et al. 1982).

The causes of instability depend on the nature of the slope including the composition of an edifice related to the strength or permeability boundaries and the related orientation of bedding planes, joints, and faults to the slope geometry (Del Potro et al. 2013). Furthermore, McGuire (1996) classified the factors destabilizing the volcanic edifice into internal (e.g., steep slopes, magma intrusion, and volcanic seismicity) and external (e.g., sea level change, tectonic seismicity and fault activity).

This paper is a novel project investigating the instability level of Mt Gamalama which shows the possible occurrence

Saaduddin (✉) · J. Neuberg · M. E. Thomas
School of Erath and Environment, University of Leeds, Leeds,
LS2 9JT, UK
e-mail: eessa@leeds.ac.uk; ; saad@sci.unhas.ac.id

J. Neuberg
e-mail: j.neuberg@leeds.ac.uk

M. E. Thomas
e-mail: m.e.thomas@leeds.ac.uk

Saaduddin
Department of Geophysics, Faculty of Mathematics and Natural
Sciences, Hasanuddin University, Makassar, 90245, Indonesia

J. Hill
Department of Environment and Geography, University of York,
Heslington, York, YO10 5NG, UK
e-mail: jon.hill@york.ac.uk

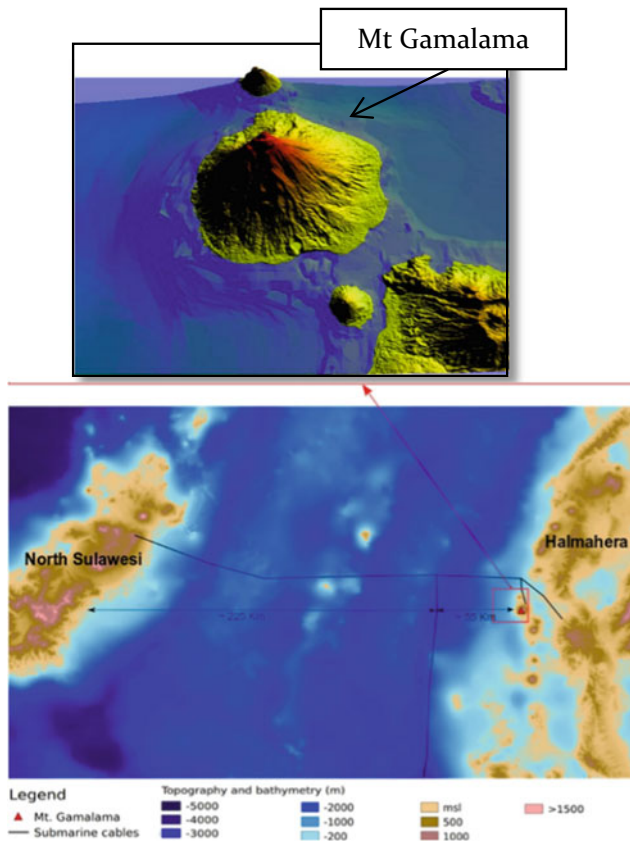


Fig. 1 Mt Gamalama is located between North Sulawesi and Halmahera island

of landslides using the limit equilibrium method. In addition, although Mt Gamalama has currently a stable edifice, this study attempts to assess the factors that can destabilize the edifice leading to landslides that can generate tsunamis.

Geotechnical Properties of Mt Gamalama

Geological Unit Classification

The geological formation processes result in heterogeneous deposits making up the Mt Gamalama edifice. Bronto et al. (1982) categorised the Mt Gamalama deposits into 32 materials which were mapped based on lava flows and related rocks, pyroclastic, maar, lahar, and surficial deposits. This map is used as a data source throughout this project, since this project does not include a fieldwork component. In addition, a report of vertical electric surveys in Mt Gamalama is used to gain information regarding the mass distribution in the subsurface (Achmad 2016). These two sources comprise a diverse range of rock masses observed at Mt Gamalama, which are used to classify the geotechnical units.

In order to classify the Mt Gamalama deposits, this study considers both geological and morphological data including the appearance and the general performance of deposits (Apuani et al. 2005a; Moon et al. 2005; Rodriguez-Losada et al. 2007). Based on this consideration, the deposits are classified into six geological units; andesites, basaltic andesites, breccia, pyroclastic deposits, lahar deposits, and volcanic ocean crust which describes materials below sea level.

The deposits are selected for four sections as depicted in Fig. 4: section AO in the west, section OB in the east, section CO in the south, and section OD in the north. The selection of these sections is based on the difference of bathymetry depth and the hazards related to these directions (Fig. 1).

Generalized Hoek Brown Failure Criteria

The flank instability study of a volcano ideally combines both geomechanical surveys identifying weak zones and geotechnical analysis determining the rock strength using numerical methods. Due to the lack of geomechanical survey data, the Mt Gamalama instabilities were investigated using a geotechnical analysis. Since the objective of this project is to predict the strength of volcanic flanks, we utilized the Generalized Hoek–Brown failure criterion. This criterion relies on the strength of the intact material, and the interaction and the conditions of contact surfaces between each rock mass (Dong-ping et al. 2016).

The Generalized Hoek–Brown criterion is a non-linear strength calculation based on empirical data and is expressed as:

$$\sigma_1 = \sigma_3 + \sigma_{ci} \left(m_b \frac{\sigma_3}{\sigma_{ci}} + s \right)^a \quad (1)$$

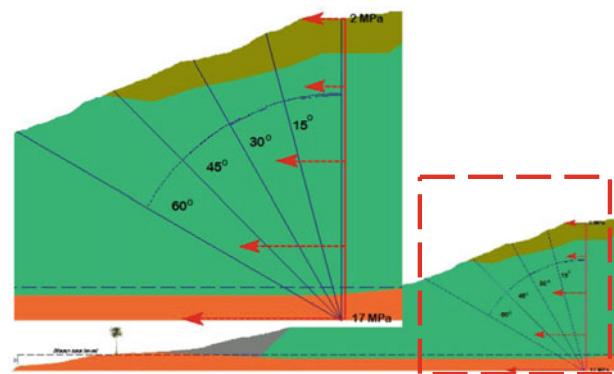


Fig. 2 Tilted dykes following a pressure point source model (Poppe et al., 2019)

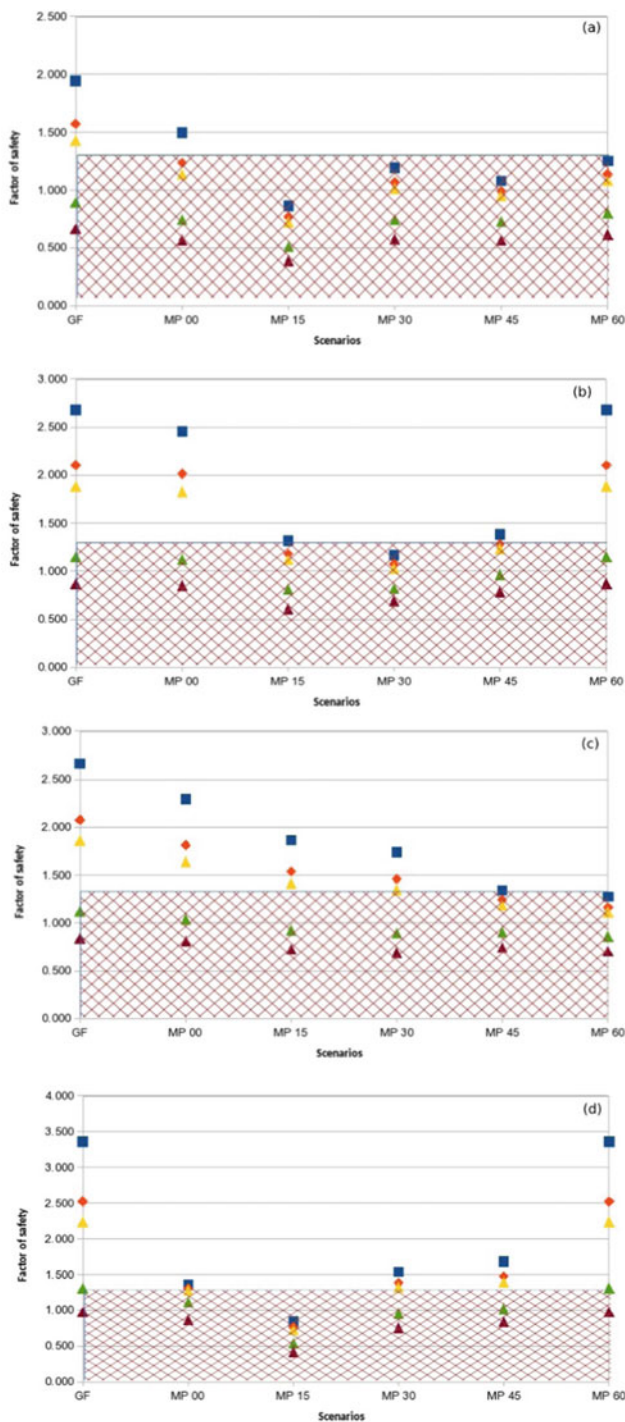


Fig. 3 The FoS values in the Mt Gamalama edifice. **a** section OB in the east, **b** section AO in the west, **c** section OD in the north, and **d** section CO in the south. Red crossed area represents the unstable critical FoS. The horizontal axis shows scenarios of gravity force (GF) and magma pressure (MP) with different angles of intrusion. The implementation of seismic coefficient is denoted by color differences: blue (without seismic coefficient), orange ($k_h = 0.103$), yellow ($k_h = 0.155$), green ($k_h = 0.457$), and red ($k_h = 0.685$)

where σ_{ci} is the uniaxial compressive strength of the intact rock strength which represents the relationship between the principal stresses, σ_1 and σ_3 , at failure. Variables of m_b, s , and a are rock mass constants which depend on material constant m_i , the geological strength index (GSI) and the disturbance factor D (Hoek et al. 2002).

Regarding this failure criterion, there are several parameters which must be determined for all geotechnical units. The parameters are unit weight γ (kN/m^3), intact uniaxial compressive strength σ_{ci} (MPa), material constant m_i , GSI (MPa), and D . Property values of the geotechnical units are taken from the relevant literature and listed in Table 1.

Rock Mass Properties

Geotechnical properties of deposits at Mt Gamalama are still unknown due to a lack of specific surveys, hence data from similar volcanoes were used. Selected key properties from reviewed literature are shown in Table 1. In this project, we determine D as zero or minimal disturbance (Hoek 2007).

The units and the properties above are used in the calculation of the factor of safety (FoS) describing the instability level of Mt Gamalama.

The Instability Level of Mt Gamalama

Slope Stability Calculation

In the field of geotechnical engineering the stability of slopes is routinely assessed by what is known as a factor of safety (FoS), a numerical approach in determining the slope stability. It has recently found more application in volcanology. The FoS is the ratio between the capacity or the resisting force $F_{resisting}$ and the demand or driving force $F_{driving}$ (Abdalla et al. 2015; Hoek 2007). This can be defined as:

$$FoS = \frac{F_{resisting}}{F_{driving}} = \frac{\text{shearstrength}}{\text{shearstress}} \quad (2)$$

For stable slopes the shear strength is greater than the shear stress. Conversely, the slopes destabilise because the resisting force is lower than the driving force. The slope assessment declares stable condition when FoS is greater than 1.5, failure when FoS less than 1.0, and potentially unstable conditions when FoS is between these two values (Hoek 2007; Schaefer et al. 2013). Furthermore, if FoS is 1, a state of just-stable limiting equilibrium is reached (Duncan et al. 2014).

This project utilizes *Slide 2018* from Rocscience to calculate the FoS. This tool is a 2D (two-dimensional)

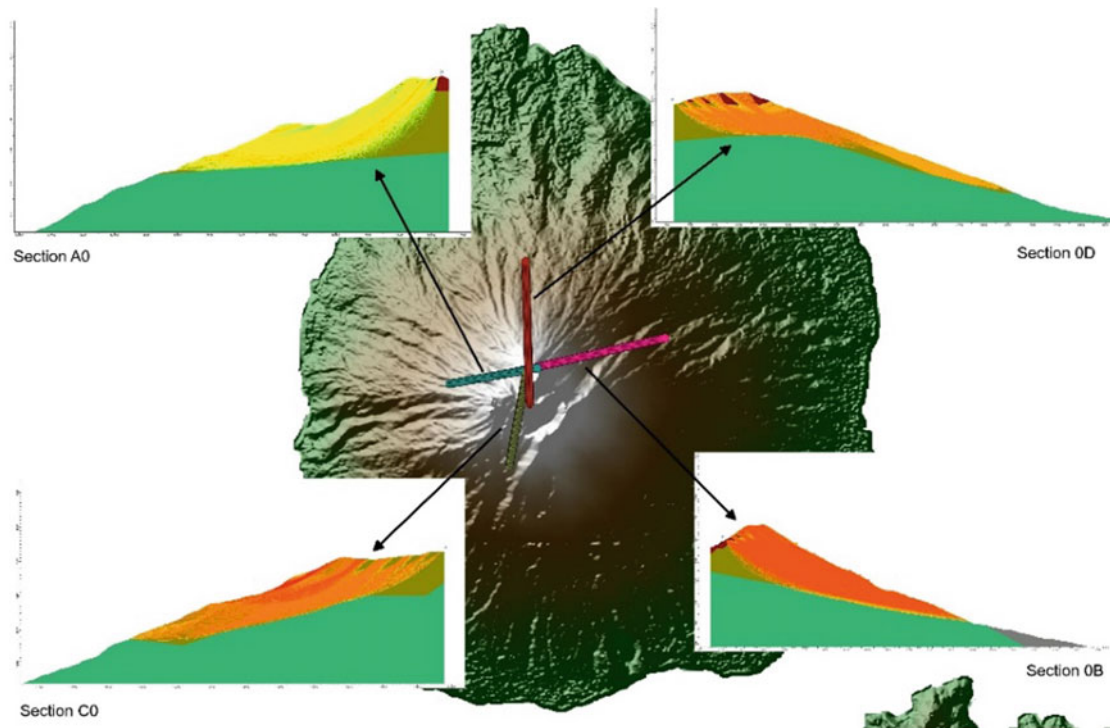


Fig. 4 Slip surfaces describing the most unstable FoS in section AO, OD, OB, and CO of the Mt Gamalama edifice

modelling software of the slope stability; showing slip surfaces which exhibit weak zones that can lead to potential landslides in a volcanic edifice.

For the calculation of slip surfaces in this project we adopted the Bishop Simplified method. This method is based on circular surfaces (Reid and Brien 2006). In addition, this method tends to be conservative and results in tolerably small errors despite being a simple analysis process (Hungur et al. 1989; Saade et al. 2016).

Scenarios Applied in Calculations

The FoS calculation for Mt Gamalama applied several factors, both internal and external, i.e., gravity force, seismic

coefficient, magma pressure, and angle of dyke intrusion. Gravity force will show the instability level of Mt Gamalama under a static condition without any volcanic activity. By applying the other factors, the conditions destabilizing Mt Gamalama can be detected.

The seismic coefficient k_h was the most likely factor applied in the Mt Gamalama stability analysis as this volcano is in an earthquake prone area, close to a doubled-subduction zone. This parameter was utilized corresponding to ground acceleration particularly in lateral direction. Zulkifli et al. (2017) discovered the peak ground acceleration PGA of 0.31–1.37 g in Ternate Island. Melo and Sharma (2004) define the relationship between seismic coefficient k_h and PGA as $k_h = 1/3$ to $1/2$ PGA. Therefore,

Table 1 Selected values of geotechnical properties as input parameters in analysing the Mt Gamalama instabilities based on the Generalized Hoek–Brown failure criterion

Geotechnical units	Geotechnical properties					References
	γ (kN/m ³)	σ_{ci} (MPa)	GSI (MPa)	m_i	D	
Basaltic andesite	22.40	24.14	50	25	0	1, 6, 8
Pyroclastic deposit	13.20	10.40	50	13	0	4, 8
Andesite	24.70	184.00	68	25	0	7, 8
Breccia	14.71	52.00	50	18	0	2, 8
Lahar deposit	22.53	82.52	40	25	0	5, 8
Volcanic ocean crust	18.44	150.00	42	13	0	3, 5, 8, 9

¹Achmad 2016; ²Apuani et al. 2005b; ³Brown 1981; ⁴del Potro and Hürlimann 2008; ⁵Diñçer et al. 2004; ⁶Koca and Kınca 2016; ⁷Moon et al. 2005; ⁸Rocscience 2018; ⁹Thomas et al. 2004)

Table 2 Parameters weakening the Mt Gamalama slopes with the most unstable conditions

Sections	Angle of dyke intrusion	Seismic coefficient	FoS
OB	15°	0.685	0.385
AO	30°	0.685	0.805
OD	0° (vertical)	0.685	0.687
CO	15°	0.685	0.417

we used k_h of 0.103, 0.157, 0.457, and 0.685 which are derived from both PGA values.

In addition, magma pressure with various angles of dyke intrusion plays a role as an internal destabilizing factor. Schaefer et al. (2013) applied magma pressure of 2–17 MPa; the value reaches a maximum point in the bottom of the edifice and a minimum point in the top. This value can be applied to Mt Gamalama and becomes a trigger for the destabilizing condition.

Furthermore, we vary the magma pressure and the angles of dyke intrusion rather than only a vertical one. As a stratovolcano, the direction of the intrusion follows the model of a pressure point source (Poppe et al. 2019). This model has been adopted in Agung and Cotopaxi volcano (Morales Rivera et al. 2017; Albino et al. 2019). The angles used are 15°, 30°, 45°, and 60° as depicted in Fig. 2.

In this project we keep the geotechnical units and properties constant and vary the scenarios. In total we applied 30 trials for each section. The modelling began from a static condition only under gravity force and the continued application of seismic loads with different coefficients and the magma pressure with different angles of dyke intrusion. The application of the scenarios yielded different FoS values. Therefore, we were able to determine a condition that can destabilize the Mt Gamalama edifice and generate a failure.

The Mt Gamalama Factor of Safety

The slopes of Mt Gamalama which is under the static condition are stable (FoS > 1.5) for all sections. Gradually, the critical FoS values decreased because of the variation of the seismic coefficient and magma pressure. The result of FoS calculation for all sections is depicted in Fig. 3.

Decreasing the critical FoS does not mean that the geometry of weakening areas will enlarge. Therefore, based on Hoek's classification regarding instability level which refers to FoS (Hoek 2007), we decided to display slip surfaces with FoS below 1.30 as unstable areas leading to failure in the Mt Gamalama edifice. Further, we selected the largest surfaces in all sections. The selection resulted in FoS of 0.385 in section OB, 0.687 in section AO, 0.805 in section OD, and 0.417 in section CO. The geometry referring to these values is depicted in Fig. 4.

Discussion and Conclusion

The destabilization that takes place on the Mt Gamalama slopes was due to the effect of seismic loads and magma pressure as depicted in Fig. 3. Although the volcano has high FoS values (FoS > 1.90) in all sections under the static condition, we need to consider the additional potential factors that can generate landslides due to its location in a double subduction zone and its potential volcanic activity. The most likely conditions which weaken the Mt Gamalama edifice are summarised in Table 2.

The geometry of slip surfaces as depicted in Fig. 4 shows that the unstable areas in Mt Gamalama can reach half of the edifice. These will generate massive landslides. Furthermore, as the location is close to the Molucca Sea, landslides can enter the sea and generate tsunamis. This assumption will be the next step of this project.

Acknowledgements This work was supported by Scholarship Program in Marine and Maritime from Newton Fund in collaboration with the Ministry of Education and Culture, The Republic of Indonesia.

References

- Abdalla JA, Attom MF, Hawileh R (2015) 'Prediction of minimum factor of safety against slope failure in clayey soils using artificial neural network. *Environ Earth Sci*. Springer Berlin Heidelberg, 73 (9):5463–5477. <https://doi.org/10.1007/s12665-014-3800-x>
- Achmad R (2016) *Kajian Hdrogeologi Pulau Ternate*. Universitas Gadjah Mada
- Albino F, Biggs J, Syahbana DK (2019) Dyke intrusion between neighbouring arc volcanoes responsible for 2017 pre-eruptive seismic swarm at Agung. *Nature Commun*. Springer US, 10(1). <https://doi.org/10.1038/s41467-019-08564-9>
- Apuani T, Corazzato C et al (2005a) 'Physical and mechanical properties of rock masses at Stromboli: a dataset for volcano instability evaluation. *Bull Eng Geol Environ* 64:419–431. <https://doi.org/10.1007/s10064-005-0007-0>
- Apuani T, Corazzato C et al. (2005b) Stability of a collapsing volcano (Stromboli, Italy): Limit equilibrium analysis and numerical modelling. *J Volcanology Geotherm Res* 191–210. <https://doi.org/10.1016/j.jvolgeores.2004.11.028>
- Bronto S, Hadisantoro RD, Lockwood JP (1982) *Geological map of Gamalama Vulcano*. Ternate, North Maluku
- Brown ET (1981) *Rock characterization testing and monitoring*. Pergamon press

- Dinger I, Acar A, Çobanoğlu I, Uras Y (2004) Correlation between Schmidt hardness, uniaxial compressive strength and Young's modulus for andesites, basalts and tuffs. *Bull Eng Geol Env* 63 (2):141–148
- Dong-ping D, Liang L, Jian-feng W, Lian-heng Z (2016) Limit equilibrium method for rock slope stability analysis by using the Generalized Hoek-Brown criterion. *Int J Rock Mech Min Sci* 89:176–184
- Duncan JM, Wright SG, Brandon TL (2014) Soil strength and slope stability. John Wiley & Sons
- Hamzah L, Puspito NT, Imamura F (2000) Tsunami catalog and zones in Indonesia. *J Nat Disaster Sci* 22(1):25–43
- Hoek E (2007) Practical rock engineering. Online. ed. Rocscience
- Hoek E, Carranza C, Corkum B (2002) Hoek-brown failure criterion—2002 edition. In: NARMS-TAC conference, pp 267–273. [https://doi.org/10.1016/0148-9062\(74\)91782-3](https://doi.org/10.1016/0148-9062(74)91782-3)
- Hungr O, Salgado FM, Byrne PM (1989) Evaluation of a three-dimensional method of slope stability analysis. *Can Geotech J* 26 (4):679–686. <https://doi.org/10.1139/t89-079>
- Koca MY, Kincal C (2016) The relationships between the rock material properties and weathering grades of andesitic rocks around İzmir, Turkey. *Bull Eng Geol Environ*. Springer Verlag, 75(2):709–734. <https://doi.org/10.1007/s10064-015-0813-y>
- McGuire WJ (1996) Volcano instability: a review of contemporary themes. In *Volcano instability on the earth and other planets*. Geol Soc London, Special Publication, pp 1–23. <https://doi.org/10.1144/GSL.SP.1996.110.01.01>
- Melo C, Sharma S (2004) Seismic coefficients for pseudostatic slope analysis. In: 13 th world conference on earthquake engineering, Vancouver, Canada
- Moon V, Bradshaw J, Smith R, de Lange W (2005) Geotechnical characterisation of stratocone crater wall sequences, White Island Volcano, New Zealand. *Eng Geol* 81(2):146–178
- Morales Rivera AM, Amelung F, Mothes P, Hong SH, Nocquet JM, Jarrin P (2017) Ground deformation before the 2015 eruptions of Cotopaxi volcano detected by InSAR. *Geophys Res Lett* 44 (13):6607–6615
- Paris R, Switzer AD, Belousova M, Belousov A, Ontowirjo B, Whelley PL, Ulvrova M (2014) Volcanic tsunamis: a review of source mechanisms, past events and hazards in Southeast Asia (Indonesia, Philippines, Papua New Guinea). *Nat Hazards* 70 (1):447–470
- Poppe S, Holohan EP, Galland O, Buls N, Van Gompel G, Keelson B, Kervyn M (2019) An inside perspective on magma intrusion: quantifying 3D displacement and strain in laboratory experiments by dynamic X-ray computed tomography. *Front Earth Sci* 7, 62
- Del Potro R, Hürlimann M (2008) Geotechnical classification and characterisation of materials for stability analyses of large volcanic slopes. *Eng Geol* 98:1–17. <https://doi.org/10.1016/j.enggeo.2007.11.007>
- Del Potro R, Hürlimann M, Pinkerton H (2013) Modelling flank instabilities on stratovolcanoes: Parameter sensitivity and stability analyses of Teide, Tenerife. *J Volcanol Geotherm Res*. Elsevier B. V., 256, pp 50–60. <https://doi.org/10.1016/j.jvolgeores.2013.02.003>
- PVMBG (2018) Pers rilis aktivitas Gunung Anak Krakatau, 28 Desember 2018. Available at: <https://www.vsi.esdm.go.id/index.php/gunungapi/aktivitas-gunungapi/2572-pers-rilis-aktivitas-gunung-anak-krakatau-28-desember-2018>
- Reid ME, Brien DL (2006) Assessing massive flank collapse at stratovolcanoes using 3-D slope stability analysis. In: *Landslides from massive rock slope failure*, pp. 445–458. Springer, Dordrecht.
- Rocscience (2018) Slide 2018: 2D limit equilibrium analysis of slope stability. Tutorial 01: Quick Start Tutorial
- Rodriguez-Losada JA, Hernández-Gutiérrez LE, Olalla C, Perucho A, Serrano A, del Potro R (2007) The volcanic rocks of the Canary Islands. Geotechnical properties
- Saade A, Abou-Jaoude G, Wartman J (2016) Regional-scale co-seismic landslide assessment using limit equilibrium analysis. *Eng Geol*. Elsevier B.V., 204, pp 53–64. <https://doi.org/10.1016/j.enggeo.2016.02.004>
- Schaefer LN, Oommen T, Corazzato C, Tibaldi A, Escobar-Wolf R, Rose WI (2013) An integrated field-numerical approach to assess slope stability hazards at volcanoes: the example of Pacaya, Guatemala. *Bull Volcanol* 75(6):720
- Thomas ME, Petford N, Bromhead EN (2004) Volcanic rock-mass properties from Snowdonia and Tenerife: implications for volcano edifice strength. *J Geol Soc* 161(6):939–946. <https://doi.org/10.1144/0016-764903-166>
- Zulkifli M, Rudyanto A, Sakti AP (2017) The view of seismic hazard in the Halmahera region. In: AIP conference proceedings. AIP Publishing LLC

Part VI

Recent Development in Disaster Risk Assessment



2020 Kyoto Japan

Effect of Pore Pressure Dynamics on Progressive Failure in a Clayey Glaciolacustrine Landslide

Kelvin Sattler, David Elwood, Michael T. Hendry, David Huntley, Jessica Holmes, and Paul B. Wilkinson

Abstract

The cyclic fluctuations of matric suction and its influence on unsaturated soil mechanics in the active zone is largely disregarded in many slope stability calculations. However, the depth of the unsaturated zone can be significant, especially in semi-arid to arid climates where large portions of the slope are not governed by saturated soil mechanics. Additional tools are used to characterize historical climate and compare several factors that have resulted in changing landslide movement rates and magnitude. Infiltration of precipitation and snowmelt directly contributes to matric suction losses in the head scarp and is exacerbated by the presence of tension cracks. While groundwater levels are primarily correlated to changing movement rates in the Thompson River valley, seasonal changes in matric suction can influence the degree to which movement rates change. Climatic events and trends over the past few years alter the long-term soil water accumulation in the valley. By accounting for the additional strength or potentially rapid losses in strength due to increasing water content, it may be possible to develop a more complete understanding of the climate change mechanisms driving changing movement rates in the translational, metastable earthen slides that dominate the Thompson River valley.

Keywords

Variable matric suction • Infiltration • Soil moisture deficit • Retrogressive landslides

Introduction

Periodic changes in movement rates and magnitude for translational, compound landslides in the Thompson River valley are often hard to anticipate due to the complex interaction of multiple contributing factors. Near the base of these slides, factors include elevated pore pressures trapped in low hydraulic conductivity layers due to changing hydraulic gradients; loss of landslide toe buttressing due to falling river elevation; and erosion and scour removing material from the slide's toe (Clague and Evans 2003; Eshraghian et al. 2007, 2008; Hendry et al. 2015). The upper reaches of a slide mass may experience an increasing water content in the vadose zone due to infiltration through tension cracks or the slide mass itself by means of any single factor, or a combination of irrigation; precipitation; snowmelt; or near surface ground thawing, and the release of frozen pore water (Stanton 1898; Bishop 2008). The movement of water, both vadose and phreatic, is a universal theme causing landslide instability throughout the valley.

The present study investigates the use of soil moisture deficit (SMD) trends and weather patterns compared to field measurements of matric suction, water content, and resistivity over a span of several years to determine their contribution to changes in landslide movement rates. SMD and long-term weather data may be used to identify multi-year trends resulting in vadose zone water content changes. Increased water content can lead to deeper infiltration due to increased hydraulic conductivity (Fredlund et al. 1994; Leong and Rahardjo 1997). These variations in water content, and corresponding matric suction, have the potential to

K. Sattler (✉) · D. Elwood
University of Saskatchewan, Saskatoon, SK, Canada
e-mail: kelvin.sattler@usask.ca

M. T. Hendry
University of Alberta, Edmonton, AB, Canada

D. Huntley
Geological Survey of Canada, Vancouver, Canada

J. Holmes
Queen's University Belfast & British Geological Survey,
Belfast, UK

P. B. Wilkinson
British Geological Survey, Keyworth, Nottingham, UK

reactivate dormant slides or cause movement magnitudes to vary from year to year.

Background

The Thompson River Valley

A high concentration of metastable, translational, and retrogressive landslides occurs in the arid climatic region south of Ashcroft, British Columbia, Canada affecting the right of way for both Canadian Pacific (CP) and Canadian National (CN) railways (Fig. 1). This corridor is a vital route for all goods travelling between the Port of Vancouver and the rest of Canada. Because of its importance, the rail corridor is one of North America's busiest sectors. Over the last several years, the Thompson River corridor has seen dramatic increases in rail traffic and increases in rail car numbers with some trains reaching up to 2 km in length (Bunce 2008). Closure of the corridor due to landslide activity would result in millions of dollars in lost revenue for the rail operators and have a direct impact on Canada's economy.

The Ripley Landslide Extents and Instrumentation

The Thompson River rail corridor has been problematic since the railway's construction in the late 1800s (Stanton 1898; Bishop 2008). The research at this landslide was named as an International Programme on Landslides (#202) in 2016. The Ripley Landslide has been heavily instrumented with, but not limited to, Shape Accel Array (SAA) inclinometers, matric suction sensors (Macciotta et al. 2016), vibrating wire piezometers (Hendry et al. 2018), water content sensors, and electrical resistivity tomography (ERT) (Fig. 2). A weather station was installed and became operational in July 2016. Wildlife cameras installed at each end of the ERT transects to monitor animal activity confirm weather patterns documented by the weather station and in-ground sensors.

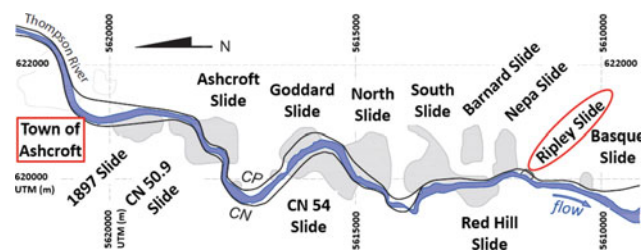


Fig. 1 High landslide concentration south of Ashcroft, British Columbia, Canada (after Eshraghian et al. 2007; Macciotta et al. 2014; Hendry et al. 2015; Journault et al. 2017)

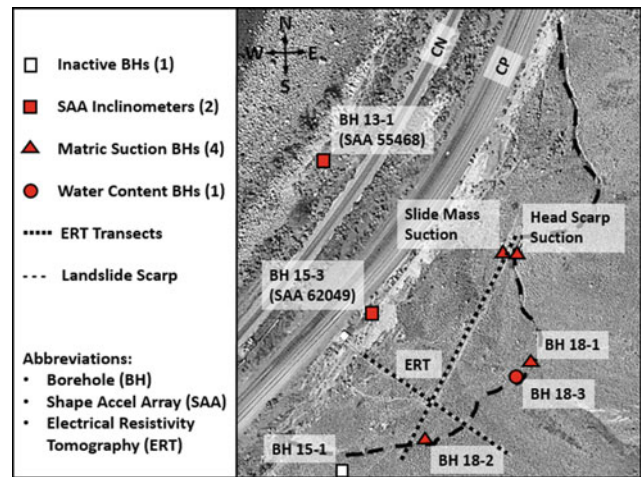


Fig. 2 Plan layout for the Ripley Landslide showing pertinent instrumentation used during the current study

Regional and Local Geology

The Thompson River valley around the Ripley Landslide has been subjected to at least three glaciations, leading to complex stratigraphic sequences of glaciolacustrine deposits, till, and glaciofluvial outwash (Ryder et al. 1991; Clague and Evans 2003). Post-glacial river incision through weaker stratigraphic sequences has been proposed as the initial triggering factor for landslide movement (Clague and Evans 2003; Eshraghian et al. 2007, 2008). The failure planes in the Thompson River valley landslides are commonly focused in weak non-swelling clay layers of the glaciolacustrine stratigraphy (Eshraghian et al. 2007).

The river stages create seasonal changes in the direction of hydraulic gradients within the ground. During the winter months when the river level is at its lowest, an upward gradient acts on the base of the rupture surface within a sub-till glaciolacustrine clay layer. During the spring freshet, the high river stage exceeds the deeper groundwater pressures, and this results in a reversal of the groundwater flow regime and increases slope stability. The upward gradient and the corresponding pore pressures contribute to reactivation or increasing movement rates (Eshraghian et al. 2007).

Investigation Methods

Soil Moisture Deficit (SMD)

Soil moisture deficit summarizes a combination of climatic conditions for a given site. Climatic highs and lows over the observation period help identify multiyear patterns of wet

and dry cycles. Soil moisture deficit is the difference between reference evapotranspiration and precipitation over a set period. The reference evapotranspiration is determined using the following formula developed by the Food and Agriculture Organization (FAO) for native prairie grassland and is based on the Penman–Monteith equation (Allen et al. 1998).

$$ET_0 = \frac{0.408\Delta(R_n - G) + \gamma \frac{900}{T+273} u_2 (e_s - e_a)}{\Delta + \gamma(1 + 0.34u_2)} \times d \quad (1)$$

where,

- Δ the slope of the vapour pressure curve [kPa °C⁻¹];
- R_n is net radiation at the crop surface [MJ m² day⁻¹];
- G is soil heat flux density [MJ m² day⁻¹];
- γ is the psychrometric constant [kPa °C⁻¹];
- T is the mean daily air temperature at 2 m height [°C];
- u_2 is wind speed at 2 m above ground surface [m s⁻¹]; and
- $e_s - e_a$ is the saturation vapour pressure deficit [kPa].

The soil moisture deficit over the past decade has been determined for the Ashcroft area based on historical records of wind speed, relative humidity, air temperature, atmospheric pressure, and precipitation. Representative data for these factors was collected from Environment Canada and the on-site weather station. Shortwave solar radiation on inclined surfaces was documented by Hay (1979) for various aspects and slope angles at Summerland, British Columbia and applied to the evapotranspiration calculation.

Matric Potential (Suction) Monitoring

Measurement of the in-situ potential has historically proven difficult due to method limitations, and a wide range of possible values for suction (Guan 1996; Ridley and Wray 1996; Rahardjo and Leong 2006; Tarantino et al. 2008). However, advancements have resulted in more efficient and reliable monitoring due to improved manufacturing, and increased sensitivity in sensors for both in-situ water content and matric water potential (suction). The contribution of matric suction can be a factor for stability in slopes with extensive vadose zones and should be considered in many geotechnical applications (Leroueil 1999; Blight 2003; Siemens 2018).

The matric suction sensors used in this study measure water potential indirectly through a printed circuit board placed between two manufactured porous stones. The sensor body also contains an internal thermistor. Dielectric

permittivity for the porous ceramic stones is directly correlated to water content based on known values of dielectric permittivity for air, the ceramic stone, and water which are 1, 5, and 80, respectively (Meter Group 2019). Dielectric permittivity depends on the amount of water that occupies pore spaces in the ceramic stone. As a result, a unique relationship directly relates the porous stone's dielectric permittivity to its water content. The manufacturer has determined the soil water characteristic curve (SWCC) for the ceramic porous stone using mercury porosimetry. The SWCC relationship allows for computation of water potential based on the porous stone water content. Accurate measurement of water potential ($\pm 10\%$ accuracy from -9 to -100 kPa) requires intimate contact with the surrounding soil over the entire ceramic surface to maintain water potential equilibrium (Meter Group 2019).

Matric suction sensors were installed at several locations across the Ripley Landslide. The depth of the sensors was limited by hand auger refusal on cobbles found throughout the investigated stratigraphy. Sensors were installed at a minimum depth of 0.3 m and a maximum depth of 2.7 m below the ground surface (Sattler et al. 2018). Vertical spacing between sensors was consistently 0.3 m in order to achieve enough vertical stratigraphic resolution in the water content and matric suction datasets. The borehole locations were established with the intent of demonstrating how matric suction varies within the active zone, both spatially and temporally.

Proactive Infrastructure Monitoring and Evaluation (PRIME)

The PRIME system uses an in-place or fixed ERT array, which was developed by the British Geological Survey (BGS). Ongoing surveys of the soil resistivity have been conducted at the Ripley Landslide since the fall of 2017. By conducting periodic measurements of the apparent resistivity between various electrodes in the ERT array, it is possible to identify patterns of changing resistivity related to changes in the sub-surface volumetric water content (Gunn et al. 2015). Once the SWCC is known, the volumetric water content can be related to matric suction for stability calculation considerations.

The ERT network at the Ripley Landslide consists of two perpendicular intersecting rows of ERT electrodes installed in 20 cm deep trenches as detailed by Huntley et al. (2019). An initial survey of electrical resistivity detailed coarse-grained (high resistivity) and fine-grained (low resistivity) materials in the subsurface directly below the ERT electrodes. Subsequent surveys have analyzed changes in the resistivity from the initial background survey. These changes are directly correlated to temporal changes in soil

water content and temperature (Bobrowsky et al. 2017; Holmes et al. 2018; Huntley et al. 2019).

The ERT provides a valuable method of observation to study the infiltration of water. The electrode array extends across the slide mass, intersecting various tension cracks along its length. As precipitation, snowmelt or ground thawing occur, corresponding changes in electrical resistivity are documented and visually represented in a tomograph. The method is particularly advantageous in the tension crack regions where it is possible to observe the depth and extent of surface water penetration. Currently, the ERT only provides relative changes and the actual in-situ water contents are not known. As a result, ground truthing and determination of matric suctions are still required.

Results and Discussion

Meteorology and Soil Suction Influence on Landslide Movement Trends

The soil moisture deficit provides one meteorological trend indicator that helps to identify wet/dry cycles in climatic data. A plot of the soil moisture deficit over several years demonstrates which years were wet or dry in comparison to other years (Fig. 3). If the soil moisture deficit drops below zero, the soil demonstrates a surplus of water. However, the region around Ashcroft, British Columbia is known for its semi-arid to arid climate. As such, the region experiences a soil moisture surplus infrequently and is typically confined to the winter months as shown in Fig. 3.

Displacement data can be compared to soil moisture deficit trends to indicate potential correlations to landslide movement involving atmospheric interactions. A significant downslope movement occurred in February 2017. The soil moisture deficit had dropped by more than 50 mm from its 2015 peak during the summer of 2016. Figure 3 demonstrates the landslide's susceptibility to increased movement

rates following a wetter year with a lower soil moisture deficit.

Previous authors have shown that increased movement rates are more prominent when the river elevation is at its lowest (Eshraghian et al. 2007, 2008; Hendry et al. 2015). At the peak river elevation, the landslide movement rate decreases significantly as the slide mass is partially buttressed by the river and the hydrogeologic regime changes from an upward to a downward gradient. Movement rates increased in winter 2017, following a wet year in 2016. The rates stabilized over the following dry year (Fig. 3). It follows that the river elevation peaked around 268.3 masl in summer 2016 and 270.3 masl in summer 2017. The minimum river elevation dropped to 263.4 masl in winter 2017 and 263.1 masl in the winter 2018. Rates of movement increased in winter 2017 but did not increase to the same degree when the river elevation dropped to an even lower level in winter 2018. From this information, it is evident that river elevation and changing hydraulic gradients are not the sole cause of total displacement and changing movement rates for the Ripley Landslide.

Matric suction has been monitored at the Ripley Landslide since late 2017. Sensors installed in the head scarp and slide mass have continuous records showing ongoing changes in matric suction up to 2.7 m below ground (BG). Comparing the matric suction to the monthly soil moisture deficit demonstrates some correlation between the variables. As expected, the matric suction in the head scarp and the slide mass drops when the soil moisture deficit is lower (pore pressures are less negative). There is a clear delay between a decrease in soil moisture deficit and falling matric suction in the intact slide mass as shown in Fig. 4. The delay is related to the infiltration rate, hydraulic conductivity, and depth of soil above individual sensors.

Total precipitation and the precipitation rate can be expected to affect matric suction as water content changes, moving up the wetting curve of the SWCC. During gaps in precipitation, it is expected that evapotranspiration occurs, and the soil moves down the SWCC drying curve. The soil

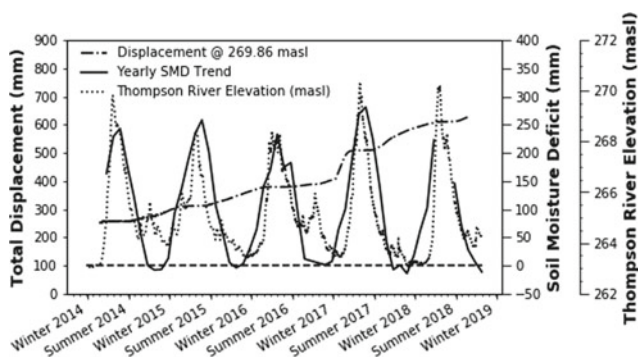


Fig. 3 Mid slide displacement at the slip surface combined with soil moisture deficit and river elevation over the same period

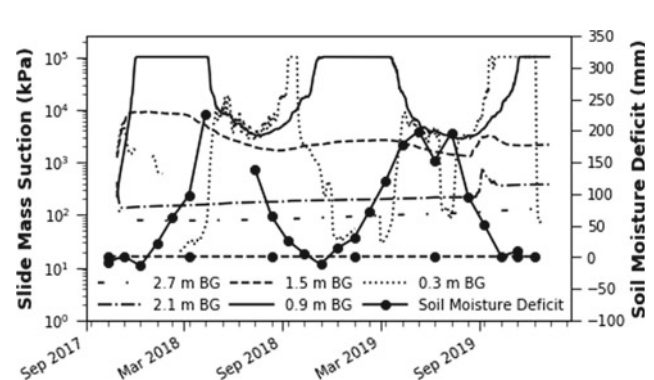


Fig. 4 Slide mass suction association to soil moisture deficit

constantly undergoes hysteretic behaviour as the soil dries out and wets through successive series of meteorological events. A prolonged period of high-intensity precipitation can bring the soil in the vadose zone closer to saturation.

Temperature affects the soil's matric suction in climatic regions where the soil tends to freeze, and winter snowpack develops. While saturation is indicated by matric suction approaching a value of 0 kPa, frozen water registers infinite matric suction as the surrounding liquid turns into a solid. During this time, suction increases in the freezing zone as the amount of liquid water reduces, generating higher levels of suction. A suction gradient develops, drawing more water into the freezing zone (Fredlund et al. 2012). While the ground is frozen and snowpack exists, water is unable to infiltrate from the surface and evaporation ceases.

Ground thaw and snowpack melting in the spring releases a potentially large reserve of water. The water influx increases the soil's hydraulic conductivity at a time when air temperatures are lower (less evaporation) and vegetation is inactive, resulting in deeper infiltration. Deeper infiltration is evident in the sensors located at or above 1.5 m BG (Fig. 5). The rapid loss in matric suction occurs when the Thompson River elevation is at its lowest in early spring.

If the snow melts rapidly, it will take time for the watershed to funnel resulting runoff into the Thompson River. Furthermore, the snowpack in the mountains melts slowly and is delayed compared to lower elevation snowpack melting. As a result, the river stage does not increase at the same time as the snow is melting within the river valley. The response is delayed, creating a potentially dangerous situation where the matric suction in the landslide can be dropping while the buttressing effect from the Thompson River is at a minimum. River elevation reaches a minimum around the same time as SMD (Fig. 3). The seasonal minimum for shallow soil suction can occur around the same time, depending on the current weather trends (Fig. 4).

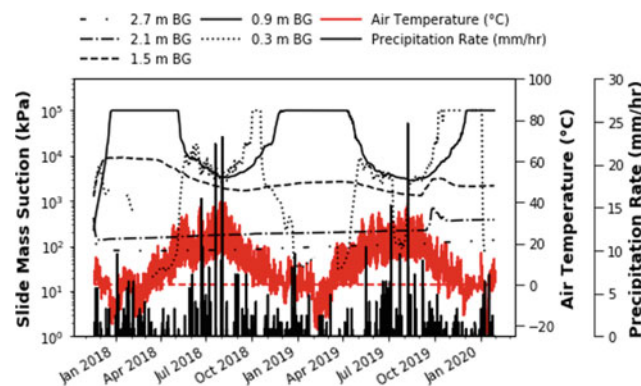


Fig. 5 Temporal record of temperature and precipitation rate related to slide mass matric suction

The lower level of matric suction reaches a minimum later in the summer. During the summer, infiltration is reduced as air temperatures are elevated (more evaporation) and vegetation takes up more of the precipitation. At this time, the Thompson River has reached its maximum elevation and the potential for movement has decreased. After reaching a minimum matric suction, the soil experiences a slight increase in matric suction as the days get shorter and vegetation reduces activity. In the late fall, suction near the surface becomes unreliable. As the freezing front progresses from the ground surface through the active zone, the sensors become unable to register suction in the soil due to the subsequent liquid–solid phase transition and loss of pressure equilibrium between the ceramic stone and the soil pore water. Suction data was removed when sensor temperatures were less than zero degrees Celsius.

Net infiltration Observations

The PRIME system using ERT has been operational since December 2017 providing weekly visual representation of changes in soil resistivity (water content). The initial resistivity survey was conducted in December 2017 and provides a base to which all future measurements are compared. The subsurface and surface features are described in the figure indicating the slide mass extent and potential infiltration zones including the slide tension cracks. Subsequent surveys during the spring of 2018 depict changes in resistivity due to changes in soil water content caused by snowmelt and ground thawing (Fig. 6a–d). Timestamps attached to each tomograph provide reference to the temporal record of temperature and precipitation (Fig. 6e). Positive changes in resistivity (decreasing water content) are shown by hotter colours while negative changes in resistivity (increasing water content) are indicated by cooler colours.

The progression of snowmelt and ground thawing is evident in the tomography, particularly in the tension cracks. Near surface soil indicates lower resistivity as the snow melts and ground thaws, increasing water content. In the tension cracks, water starts to infiltrate deeper as indicated by a blue crescent shading in the tomograph extending into the deeper high resistivity red shading. The wildlife cameras help document snowmelt progression for comparison to ERT resistivity.

Extended periods of precipitation are well understood to have the potential to contribute to deeper infiltration. This pattern of reduced runoff and increased infiltration are clearly indicated by the ERT data and confirmed with onsite precipitation data. Temperatures start to rise above freezing concurrently with increasing cumulative precipitation. If the snowpack is melting, the ground is thawing, and precipitation is maintained over the span of several days, the soil is

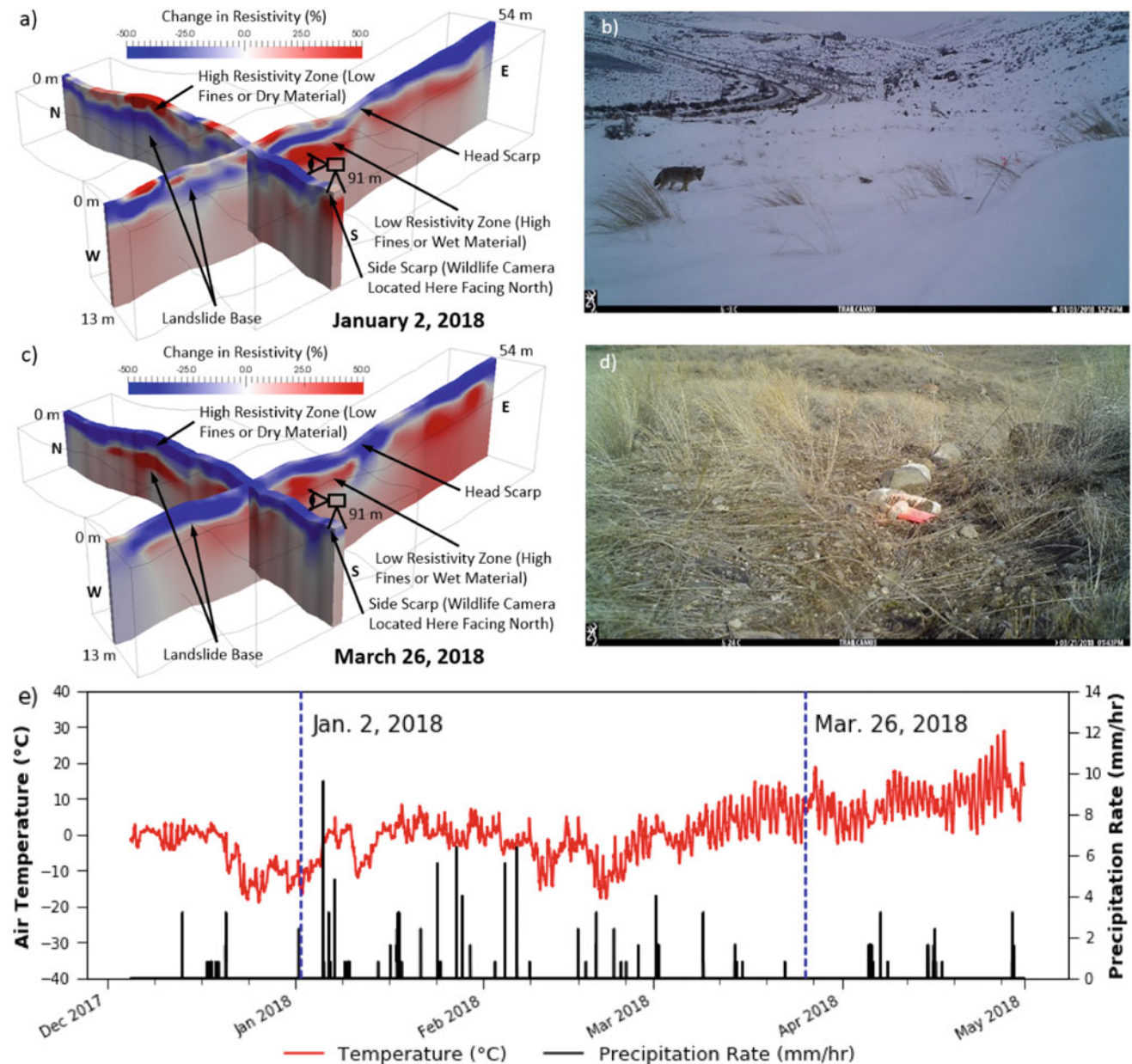


Fig. 6 Changes in resistivity across ERT transects: **a** Resistivity change from Dec. 5, 2017 to Jan. 2, 2018 **b** Field image from Jan. 3, 2018. **c** Resistivity change from Dec. 5, 2017 to Mar. 26, 2018. **d** Field

image from Mar. 21, 2018. **e** Temperature and precipitation over the survey period (after Holmes et al. 2018; Huntley et al. 2019)

subject to increasing hydraulic conductivity (up to the saturated hydraulic conductivity) due to an increasing water content. The increasing water content starts at the ground surface and progressively makes its way downward through the vadose zone as infiltration and percolation occurs. The saturated hydraulic conductivity represents the maximum possible hydraulic conductivity and is achieved approximately when the water content is equal to the AEV. Increased water content reduces the amount of suction generated by the soil, effectively reducing the soil's strength and ultimately, the landslide stability.

Summary

Methods of visualizing and interpreting changing water content in the vadose zone have been explored for a slow-moving, retrogressive landslide in the Thompson River valley south of Ashcroft, British Columbia, Canada. The landslide impacts both national rail operators, restricting the flow of goods between the west coast and interior Canada. Several studies have examined similar landslides in the Thompson River valley and identified fluctuating river

elevation/pore pressures, riverbank erosion, artesian pressures, and irrigation as possible contributing factors to ongoing landslide movement. The current study analyzes climatic factors in terms of short to long term changes in vadose water content.

Changing water content has a direct impact on the matric suction that can be generated near the head scarp. Further work is required to relate changes in electrical resistivity from the ERT to changes in soil water content. Long-term study of meteorology combined with several other stability factors provides a method of understanding why movements change or occur when they do. By considering more factors involved in changing landslide movement rates, it may be possible to more accurately determine when movement rates may be set to increase. With advanced warning, railway and other transportation infrastructure authorities can properly allocate funding and resources to prepare for potentially costly maintenance seasons.

Acknowledgements Installation and monitoring would not be possible without continued access to the research site and ongoing support from CP and CN. Productive collaboration and data sharing with the Geological Survey of Canada (Peter Bobrowsky), the British Geological Survey (Jonathan Chambers and Philip Meldrum), as well as Shane Donohue (University College Dublin), have been greatly appreciated as we work towards the common goal of protecting railway infrastructure. The authors would like to thank Canada (TC), the (Canadian) Railway Ground Hazard Research Program (RGHRP), and the Canadian Rail Research Laboratory (CaRRL) for continued financial support and resources. These entities are supported by the Natural Sciences and Engineering Research Council of Canada (NSERC), CP, and CN. Holmes and Wilkinson publish with permission of the Executive Director of the BGS (UKRI).

References

- Allen RG, Pereira LS, Raes D, Smith M (1998) Crop evapotranspiration—guidelines for computing crop water requirements—FAO irrigation and drainage paper 56. Food and Agriculture Organization, Rome, Italy
- Bishop NF (2008) Geotechnics and hydrology of landslides in Thompson River Valley, near Ashcroft, British Columbia. MSc thesis, University of Waterloo, Waterloo, Canada
- Blight GE (2003) The vadose zone soil-water balance and transpiration rates of vegetation. *Géotechnique* 53(1):55–64
- Bobrowsky P, Huntley D, Neelands P, MacLeod R, Mariampillai D, Hendry MT, Macciotta R, Reeves H, Chambers J (2017) Ripley landslide—Canada’s premier landslide field laboratory. In: Proceedings volume of the geological society of America annual meeting, Seattle, USA, p 1
- Bunce CM (2008) Risk estimation for trains exposed to landslides. PhD thesis, University of Alberta, Edmonton, Canada
- Clague JJ, Evans SG (2003) Geological framework of large historic landslides in Thompson River Valley, British Columbia. *Environ Eng Geosci* 9(3):201–212
- Eshraghian A, Martin CD, Cruden DM (2007) Complex earth slides in the Thompson River Valley, Ashcroft, British Columbia. *Environ Eng Geosci* 13(2):161–181
- Eshraghian A, Martin CD, Morgenstern NR (2008) Movement triggers and mechanisms of two earth slides in the Thompson River Valley, Ashcroft, British Columbia, Canada. *Canadian Geotech J* 45(9):1189–1209
- Fredlund DG, Xing A, Huang S (1994) Predicting the permeability function for unsaturated soils using the soil-water characteristic curve. *Can Geotech J* 31(4):533–546
- Fredlund DG, Rahardjo H, Fredlund MD (2012) *Unsaturated soil mechanics in engineering practice*. John Wiley & Sons, Hoboken, USA
- Guan Y (1996) The measurement of soil suction. PhD thesis, University of Saskatchewan, Saskatoon, Canada
- Gunn D, Chambers J, Uhlemann S, Wilkinson P, Meldrum P, Dijkstra T, Haslam E, Kirkham M, Wragg J, Holyoake S, Hughes P, Hen-Jones R, Glendinning S (2015) Moisture monitoring in clay embankments using electrical resistivity tomography. *Construct Build Mater* 92:82–94
- Hay JE (1979) An analysis of solar radiation data for British Columbia. Province of British Columbia Ministry of Environment RAB Bulletin 14 131 p
- Hendry MT, Macciotta R, Martin CD, Reich B (2015) Effect of Thompson River elevation on velocity and instability of Ripley Slide. *Can Geotech J* 52(3):257–267
- Hendry MT, Smith LA, Hendry MJ (2018) Analysis of the measured pore pressure response to atmospheric pressure changes to evaluate small strain moduli: Methodology and case studies. *Can Geotech J* 55(9):1248–1256
- Holmes J, Chambers J, Donohue S, Huntley D, Bobrowsky P, Meldrum P, Uhlemann S, Wilkinson P, Swift R (2018) The use of near surface geophysical methods for assessing the condition of transport infrastructure. Civil engineering research association, Special issue on structural integrity of civil engineering infrastructure, *J Struct Integrity Maintenance* 6
- Huntley D, Bobrowsky P, Hendry MT, Macciotta R, Elwood D, Sattler K, Best M, Chambers J, Meldrum P (2019) Application of multi-dimensional electrical resistivity tomography datasets to investigate a very slow-moving landslide near Ashcroft, British Columbia, Canada. *Landslides* 16(5):1033–1042
- Journault J, Macciotta R, Hendry MT, Charbonneau F, Huntley D, Bobrowsky P (2017) Measuring the activity of the Thompson River Valley landslides, south of Ashcroft, BC, Canada, using satellite InSAR. *Landslides* 15(4):621–636
- Leong E, Rahardjo H (1997) Permeability functions for unsaturated soils. *J Geotech Geoenviron Eng* 123(12):1118–1126
- Leroueil S (1999) Natural slopes and cuts: movement and failure mechanisms. *Géotechnique* 51(3):197–243
- Macciotta R, Hendry MT, Martin CD, Elwood D, Lan H, Huntley D, Bobrowsky P, Sladen W, Bunce C, Choi E, Edwards T (2014) Monitoring of the Ripley Landslide in the Thompson River Valley, BC. In: Proceedings and abstracts volume Geohazards 6 symposium, Kingston, Canada, p 1
- Macciotta R, Hendry MT, Martin CD (2016) Developing an early warning system for a very slow landslide based on displacement monitoring. *Nat Hazards* 81(2):887–907
- Meter Group (2019) Teros 21 manual. URL: https://publications.metergroup.com/Manuals/20428_TEROS21_Manual_Web.pdf. Last accessed 15 Jan 2020
- Rahardjo H, Leong EC (2006) Suction measurements. In Miller GA, Zapata CE, Houston SL, Fredlund DG (eds) Proceedings of 4th international conference on unsaturated soils, Carefree, USA. *Unsaturated Soils. Geotechnical Special Publication* 147. ASCE, 1:81–104
- Ryder JM, Fulton RJ, Clague JJ (1991) The Cordilleran ice sheet and the glacial geomorphology of southern and central British Columbia. *Géographie Physique Et Quaternaire* 45(3):365–377

- Sattler K, Elwood D, Hendry MT, Macciotta R, Huntley D, Bobrowsky PT, Meldrum PI (2018) Real-time monitoring of soil water content and suction within a slow moving landslide. In: Proceedings of 71st Canadian geotechnical conference, Edmonton, Canada, p 8
- Siemens G (2018) Thirty-ninth Canadian geotechnical colloquium: unsaturated soil mechanics—bridging the gap between research and practice. *Can Geotech J* 55(7):909–927
- Stanton RB (1898) The great land-slides on the Canadian pacific railway in British Columbia. In: Proceedings of the institution of civil engineers, Session 1897–1898, Part II, Section 1, pp 1–46
- Tarantino A, Ridley AM, Toll DG (2008) Field measurement of suction, water content, and water permeability. *Geotech Geol Eng* 26:751–782



2020 Kyoto Japan

Engineering Geological Investigation and Slope Stability Analysis for Landslide Hazard Assessment in Indian Himalayas

Shantanu Sarkar and Koushik Pandit

Abstract

The Indian Himalaya is very prone to landslides due to its complex geology and tectonic set-up along with high intensity rainfall and aggravated slope conditions as a result of anthropogenic activities. Landslide hazard assessment is very essential before any hill development construction activity begins. Engineering geological investigation forms the primary basis for any slope stability assessment leading to plan for any construction so that landslide occurrences are minimized. Engineering geological data for rock slope stability assessment can be very easily collected from the field. These data can be used for rock mass characterization and classification such as Geological Strength Index (GSI), Rock Mass Rating (RMR) and Slope Mass Rating (SMR). The paper describes these rock mass classification techniques and presents some field examples. The paper also presents application of these techniques to derive some relevant geotechnical parameters for numerical analysis to determine the stability of slopes in terms of factor of safety.

Keywords

Engineering geology • Landslide • Slope stability • Rock mass classification

Introduction

Landslide occurrences are very common in hilly regions all over the world. Though these phenomenon is not so spectacular as compared to the other natural hazards such as earthquake, floods, tsunami etc. but due to its frequent occurrences the losses resulted from landslides are quite large. Landslides happenings are always of major concern in the Indian Himalayas where these are quite frequent largely because of its complex geology, tectonic instability, continuous erosion by rivers and streams, and high-intensity rainfall substantiated by upcoming hill development activities (Sarkar et al. 2018). There were several landslide disasters that occurred in the recent past in the NW part of the Himalayas which caused loss of many lives and enormous property.

Besides these, there have been slope failures along the highways which are under construction (Fig. 1). It is worth mentioning that as a result of increasing urbanization, hill slopes are being disturbed due to various construction activities particularly the road and building construction (Sarkar et al. 2008). To assess the slope stability particularly for rock slopes, engineering geological data defining the rock mass strength are necessary. These data are mostly from geological discontinuities/rock joints. It is well known that the rock mass characterization is largely governed by the properties rock mass discontinuities and based on which several rock mass classification techniques were proposed. Presently there are many rock mass classification methods. The most frequently used are Rock Quality Designation (RQD), Geological Strength Index (GSI), Rock Mass Rating (RMR) system and Slope Mass Rating (SMR). These rock mass classification techniques are greatly used to describe the quality of rocks and slope stability assessment. It has been observed that roads in the hilly regions are often constructed without having much knowledge on the strength of rocks and stability of slopes. The present paper discusses the

S. Sarkar (✉) · K. Pandit
Geotechnical Engineering Group, CSIR—Central Building
Research Institute, Roorkee, 247667, Uttarakhand, India
e-mail: shantanu_cbri@yahoo.co.in

K. Pandit
e-mail: koushik@cbri.res.in



Fig. 1 Completely unstable debris slide due to road excavation in the Lesser Himalayas

Fig. 2 Rock slopes showing various engineering geological parameters for rock mass characterisation

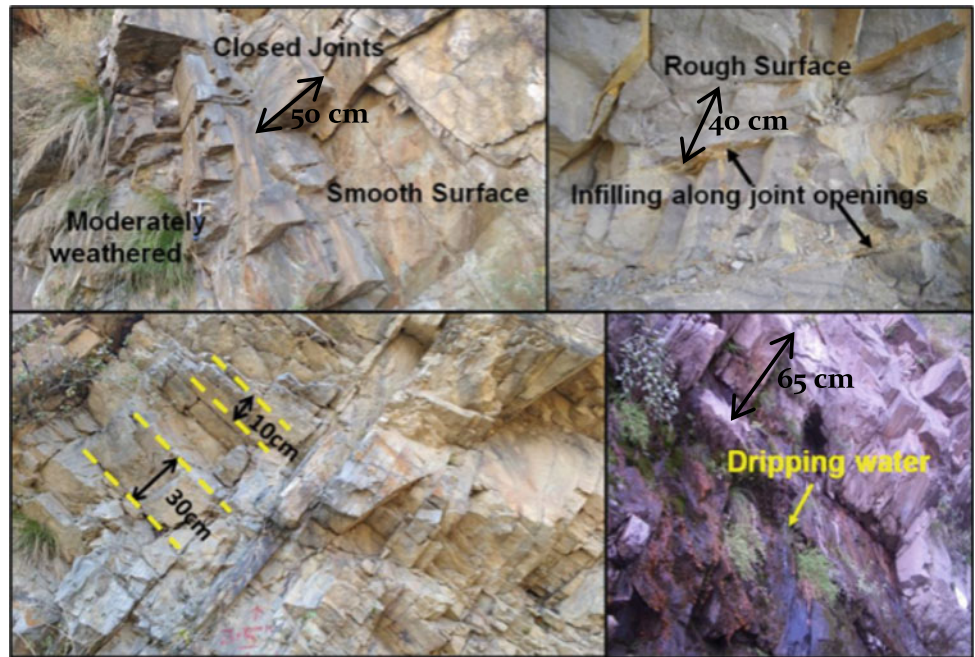
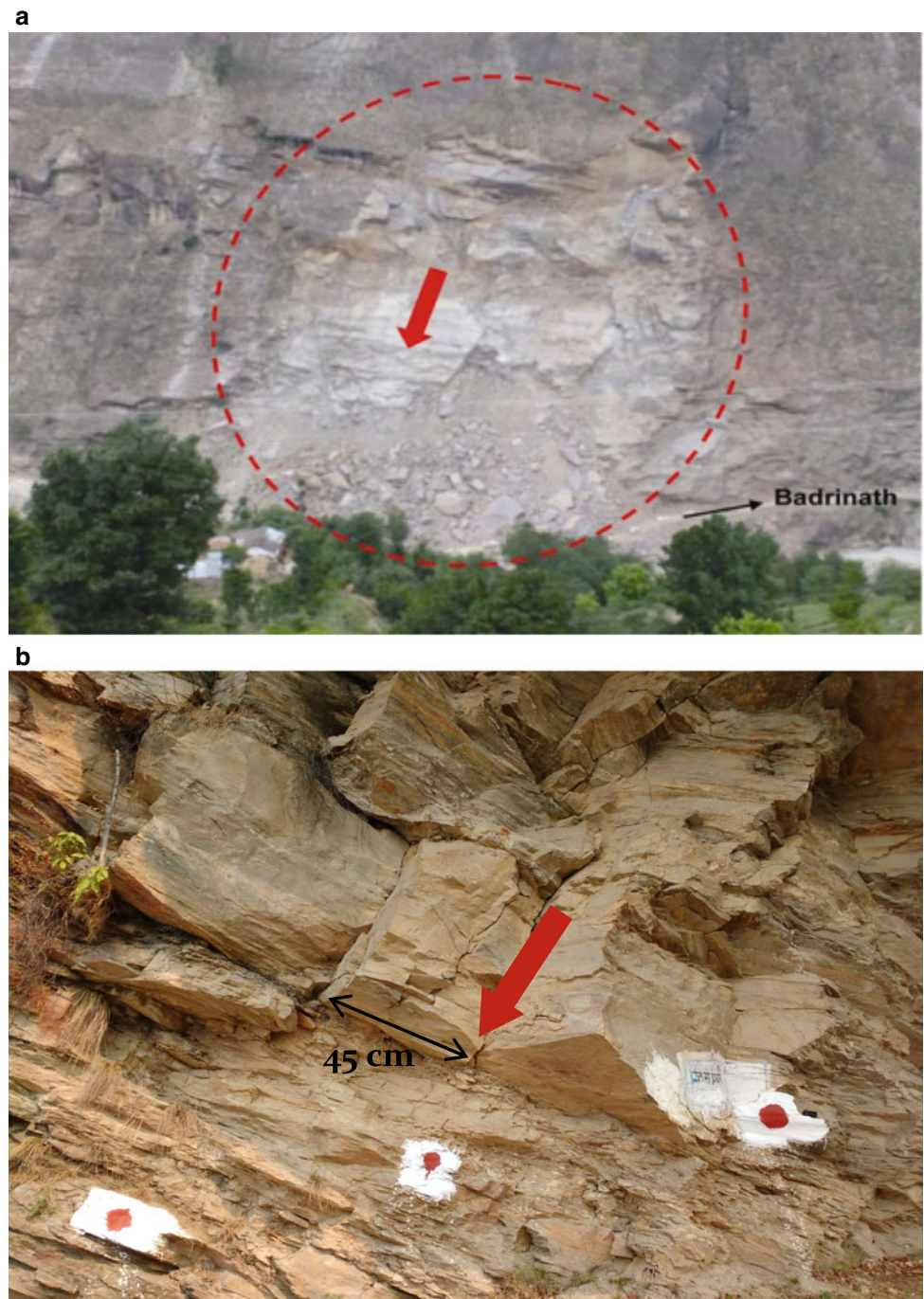


Table 1 Description of SMR classes (Romana 1985)

Class No.	V	IV	III	II	I
SMR	0–20	21–40	41–60	61–80	81–100
Description	Very bad	Bad	Normal	Good	Very good
Stability	Completely unstable	Unstable	Partially stable	Stable	Completely stable
Failures	Big planar or soil like	Planar or big wedges	Some joints or many wedges	Some blocks	None

Fig. 3 Rock slide due to **a** planar failure & **b** wedge failure (Sarkar et al. 2018)



importance of engineering geological data and application of these techniques for rock slope stability assessment.

Engineering Geological Parameters

The engineering geology dealing with rock mass strength and rock joint properties forms the most critical base for rock slope stability assessment. This involves an in-depth knowledge of rock mass strength, rock mass structure, joint spacing, joint condition, RQD, hydrological condition, joint-slope orientation and method of slope excavation.

RQD defines degree of jointing and fracturing and can be obtained from drilled cores. Since it is not always possible to have the drilled cores, RQD is most commonly estimated from $RQD = 110 - 2.5 J_v$, where J_v is the volumetric joint count which is total number of joints in a unit cubic meter rock mass (Palmstrom 2005). The next important parameter is the Uniaxial Compressive Strength (UCS) of rock, which can be determined in the laboratory by testing the core in uniaxial testing machine. More often point load strength index (I) is determined by testing the rock lumps (collected from the field) in a point load testing machine and the UCS of the rock sample is estimated from

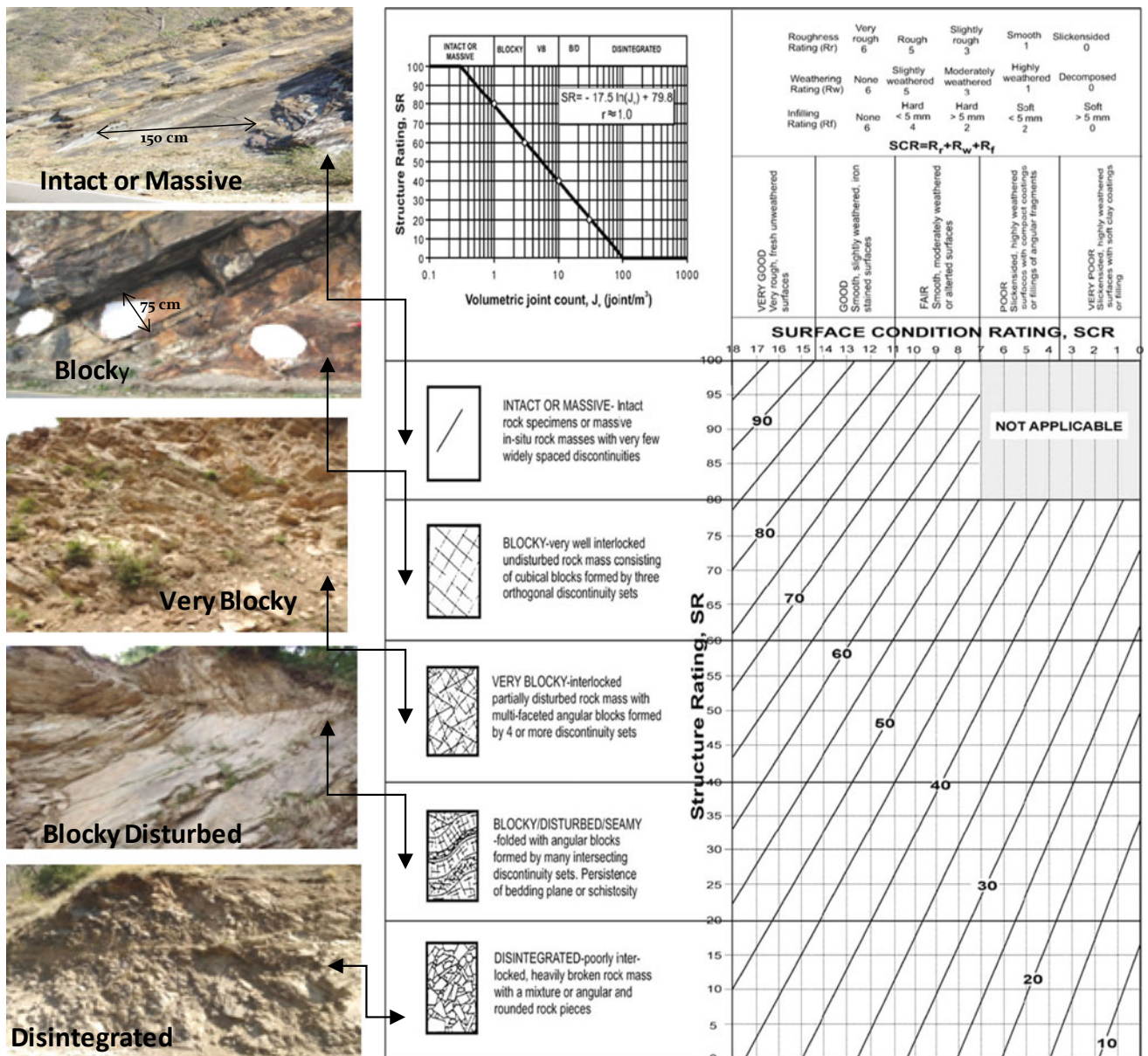


Fig.4 The modified quantitative GSI System (Sonmez and Ulusay 2002) and different rock mass structure

$UCS = 15 * I$. The UCS of rock mass can also be determined by using the rebound hammer on rock joint surface at the site itself. The other parameters like rock mass structure which depends upon the blockiness, joint spacing, joint condition, hydrological condition and joint-slope orientation are determined at the site only. Hydrological condition is assessed based on the water saturation and seepage and is described as completely dry, damp, wet, dripping and flowing. Some of these parameters are pictorially explained in Fig. 2.

Rock Mass Classifications

The rock mass classification schemes most commonly used for rock mass characterisation and slope stability assessment are GSI, RMR and SMR. A brief about these are described below.

Rock Mass Rating (RMR)

The Rock Mass Rating (RMR) system was developed by Bieniawski (1973) and has been modified over the years (Bieniawski 1979, 1989). The RMR include five input parameters to obtain basic RMR value (RMR_{basic}). These are (i) Uniaxial Compressive Strength (UCS) of rock mass, (ii) Rock Quality Designation (RQD), (iii) Spacing of discontinuities, (iv) Condition of discontinuities and (v) Groundwater condition.

The rating tables for these five parameters and the rock mass classes are given by Bieniawski (1989). The ratings for these five parameters are summed to yield the RMR_{basic} ranging between 0 and 100. RMR has a wide application in engineering geology and hill slope stability.

Slope Mass Rating (SMR)

Slope Mass Rating technique was developed by Romana (1985) for stability assessment of the rock slopes. This is primarily based on the application of RMR_{basic} and the orientation of discontinuities and slope. This technique is applicable for preliminary assessment of rock slope stability.

SMR can be determined by following relation:

$$SMR = RMR_{basic} + (F_1 \cdot F_2 \cdot F_3) + F_4 \quad (1)$$

where are, F_1 (ranges from 0.15 for very favourable to 1.00 for very unfavourable) depends on parallelism between the slope face and the joint plane or the line of intersection between two joint planes; F_2 (ranges from 0.15 for very favourable to 1.00 for very unfavourable) depends on the dip of the joint plane or the plunge of the line of intersection between two joint planes; and F_3 (ranges from 0.0 for very favourable to -60.0 for very unfavourable) depends on the relation between the dip of the slope face and dip of the joint plane or plunge of the line of intersection of two joint planes and F_4 (ranges from $+15$ for natural slopes to -8 for deficient blasting) is adjustment rating for excavation method.

Fig. 5 Kinematic analysis of two slopes having planar and wedge failures

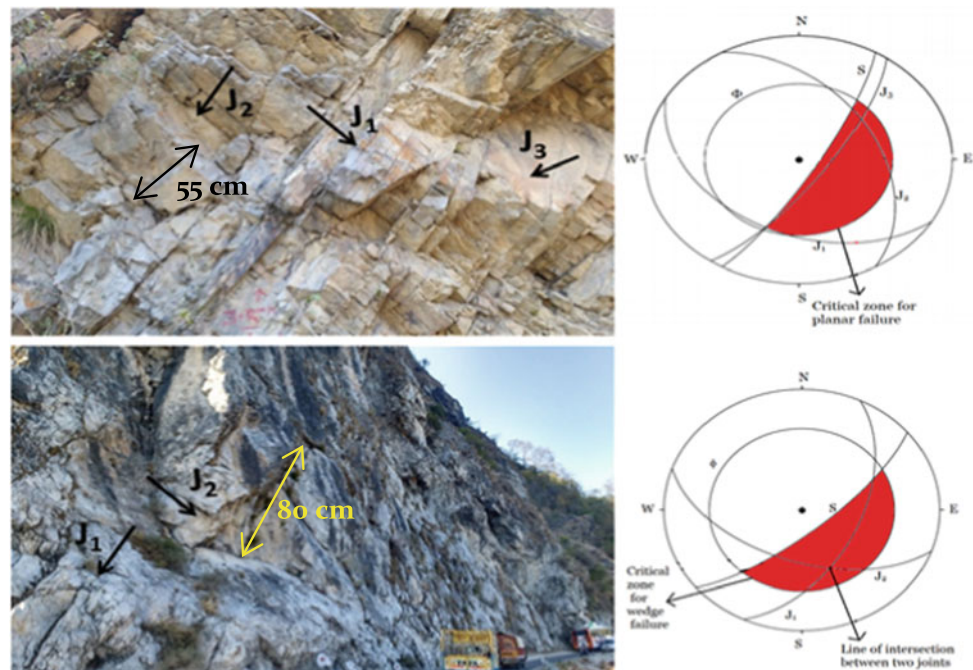


Table 2 GSI, RMR, SMR and stability grades of studied slopes

Region	Slope	GSI	RMR	SMR	Stability grade
Lesser Himalaya	1	53	64	24	U
	2	49	64	56	PS
	3	43	55	47.5	PS
	4	42	53	13	CU
	5	27	38	13	CU
	6	52	59	9	CU
	7	53	54	64	S
	8	38	45	20	CU
	9	44	63	65.5	S
	10	43	51	44.5	PS
	11	42	55	23	U
	12	41	53	13	CU
	13	50	62	47	PS
	14	48	62	54	PS
	15	38	48	15.5	CU
	16	37	45	4	CU
	17	38	48	39	U
	18	39	43	15.3	CU
	19	37	38	4	CU
	20	44	58	18	CU
	21	52	62	37	U
	22	53	64	31	U
	23	47	60	26	U
	24	23	30	18	CU
	25	48	58	58	PS
Higher Himalaya	26	42	53	18	CU
	27	44	59	17	CU
	28	42	53	2	CU
	29	44	63	59	PS
	30	48	59	57	PS
	31	42	52	48.4	PS
	32	38	63	42.6	PS
	33	38	64	29	U
	34	36	61	31.6	U
	35	52	79	75.4	S
	36	39	56	48.35	PS
	37	42	74	53.6	PS
	38	38	62	45.2	PS

Where are, *S* = stable, *PS* = partially stable, *U* = unstable, *CU* = completely unstable

The SMR values range from 0 to 100 which has been classified into five different stability classes (Table 1).

The SMR can be calculated for probable failure mechanisms such as plane, wedge and toppling failures involving unfavourably oriented discontinuity planes. A planar failure

occurs when a discontinuity plane dips in the same direction (within 20°) as the slope face, at an angle gentler than the slope angle but greater than the friction angle along the failure plane (Fig. 3). A wedge failure occurs when the line of intersection of two discontinuities, forming the wedge

plunges in the same direction as the slope face and the plunge angle is lower than the slope angle but greater than the friction angle along the planes of failure. Further to know the probable failure modes, geological discontinuities and slope are plotted in a stereonet for kinematic analysis. Depending on the joint slope relation it may be possible that the slope may fail by planar and wedge both. In that case the lowest SMR value is considered to define the stability of the slope.

Geological Strength Index (GSI)

The rock mass classification known as Geological Strength Index (GSI) was proposed by Hoek and Brown (1997) which is an engineering geological assessment of the rock mass. The GSI is essentially based on the blockiness of the rock mass and the surface conditions of discontinuities. A chart was proposed by Hoek and Brown (1997) which classifies the rock mass structure into four classes. Since then GSI has been modified several times by different authors (Hoek et al. 1998; Marinos and Hoek 2000). Sonmez and Ulusay (2002) later suggested a quantitative approach to estimate more precise values of GSI. This modified quantitative rock mass classification is based on the structure rating (SR) and surface condition rating (SCR). SR depends on volumetric joint count (J_v) while SCR depends on roughness, weathering and infilling in joints. The rating for SR can be obtained from the relationship of J_v and SR given in the chart. The modified chart represents five rock mass categories ranging between 5 and 100 (Fig. 4). Cai et al. (2004) also suggested a quantitative measure for the GSI based on the concept of block size considering a prismatic block resulted from three discontinuity sets and surface conditions.

Rock Mass Characterization and Slope Stability Assessment

Slope stability assessment of a few vulnerable rock slopes along the National Highway in the Lesser and Higher Himalayas of Uttarakhand state of India has been carried out in the recent past and the study is still continuing to achieve more findings. Some of the findings are already reported by the authors (Sarkar et al. 2012; Neeraj et al. 2018). In these studies GSI and RMR are primarily used for rock mass characterization and SMR is used for slope stability assessment. RMR and GSI are the two very basic rock mass classification systems which describe the rock mass in terms of blockiness, joint condition, rock mass strength and hydrological condition. To know the potential failure surface, kinematic analysis was carried out (Fig. 5). The study has shown that SMR can be very well used for a rapid

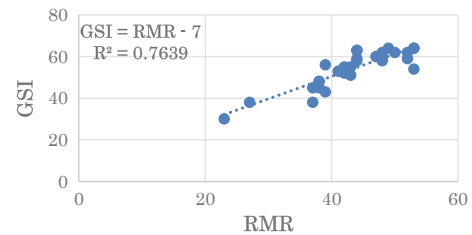


Fig. 6 Relation between GSI and RMR

assessment of slope stability particularly for road cut and excavated rock slopes. The values of GSI, RMR and SMR obtained for the studied slopes are given in Table 2.

The values of GSI and RMR as shown in Table 2 show that RMR value is always little higher than the GSI value. The relation between GSI and RMR given by Hoek and Brown (1997) is $GSI = RMR - 5$ and Sarkar et al (2012) while studying some road cut slopes in Garhwal Himalayas found that $GSI = RMR - 9$. The slopes reported here show $GSI = RMR - 7$ which is very close to the earlier findings (Fig. 6).

The values of GSI, RMR and SMR are plotted to evaluate the relation amongst each other (Fig. 7). It can be inferred from Table 2 to Fig. 7 that SMR values in general follows the trend of RMR as it describes the rock mass characters. However, some slopes are showing very low values of SMR even though the RMR is considerably on higher side which can be explained by the adverse joint orientation with respect to the slope.

Application of Rock Mass Classification for Numerical Analysis

Computational methods like the traditional limit equilibrium methods (LEM) and finite element method (FEM) combined with shear strength reduction (SSR) technique are popular practices in the assessment of a slope's stability. The finite element methods takes into account inputs of engineering

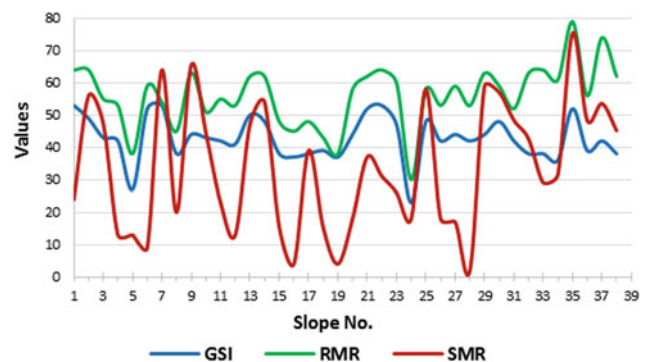


Fig. 7 Relationship among GSI, RMR and SMR

Fig. 8 Field photograph of the illustrated partially stable rock slope in the Higher Himalayas



Table 3 Empirical correlations for estimating deformation modulus of rock mass, E_d (GSI & RMR)

Researchers	Correlation	Remarks
Bieniawski (1978)	$E_d = 2 \text{ RMR} - 100$ (GPa)	$\sigma_{ci} > 100$ MPa and RMR > 50
Serafim and Pereira (1983)	$E_d = 10^{(RMR - 10)/40}$ (GPa)	$\sigma_{ci} \geq 100$ MPa & RMR < 50
Hoek and Brown (1997)	$E_d = (\sigma_{ci}/100)^{0.5} * 10^{(GSI - 10)/40}$ (GPa)	For $\sigma_{ci} < 100$ MPa
Ramamurthy (2004)	$E_d/E_i = \exp[(RMR - 100)/17.4]$	
Hoek and Diederichs (2006)	$E_d = E_i [0.02 + (1 - D/2)/(1 + \exp(60 + 15D - GSI)/11)]$	

Where are, E_i = elastic modulus and σ_{ci} = unconfined compressive strength of intact rock, E_d = deformation modulus of the rock mass, D = disturbance factor

Table 4 Derivation of Hoek—Brown parameters with respect to GSI (Hoek et al. 2002)

Parameter	Expression	Remarks
m_b	$m_b = m_i \exp[(GSI - 100)/(28 - 14D)]$	m_b and m_i (from tri-axial tests) are strength parameters for rock mass and intact rock respectively
s	$s = \exp[(GSI - 100)/(9 - 3D)]$	s ($s = 1$ for intact rock) is a material constant
a	$a = 0.5 + (1/6) * [\exp(-GSI/15) - \exp(-20/3)]$	a is the curve fitting co-efficient
D	$D = 0, 0.7$ & 1.0 for undisturbed slope, good & poor blasting respectively	D = disturbance factor due to slope excavation method

Table 5 Empirical relations based on rock mass classification for estimating UCS of rock masses

Researchers (year)	Correlation
Yudhbir and Prinzl (1983)	$\sigma_{cm}/\sigma_{ci} = \exp [7.65(RMR - 100)/100]$
Kalamaras and Bieniawski (1993)	$\sigma_{cm}/\sigma_{ci} = \exp [(RMR - 100)/24]$
Ramamurthy (1996)	$\sigma_{cm}/\sigma_{ci} = \exp [(RMR - 100)/18.75]$
Hoek et al. (2002)	$\sigma_{cm}/\sigma_{ci} = s^a$ (s and a can be computed from Table 4)

Where are, σ_{cm} is the equivalent unconfined compressive strength of rock mass, determined from the above correlations

properties of slope mass such as elastic modulus, Poisson’s ratio, shear strength parameters, dilation angle, unconfined compressive strength etc. and capable using appropriate constitutive model or failure strength criterion (e.g. Mohr–Coulomb, Generalized Hoek and Brown model etc.). Many times, it is a difficult task to determine all these parameters by laboratory or field based tests. As an alternative, rock mass classification methods can be utilized to provide a viable solution since many of the classification methods have well-established correlations with many of the above engineering properties.

For example, one typical rock slope (Fig. 8) having GSI value of 42 and RMR of 53 has been analysed for which the engineering properties required as inputs to the finite element code have been estimated from the established correlations with rock mass classification systems e.g. GSI and RMR as given in Tables 3, 4 and 5. In the next step, the rock slope is modelled as an equivalent continuum slope mass to simulate the behaviour of a jointed rock mass. The safety factors of the slope have been computed for different loading conditions (gravity/static and pseudo-static) and explained with displacement contours in Figs.9 and 10.

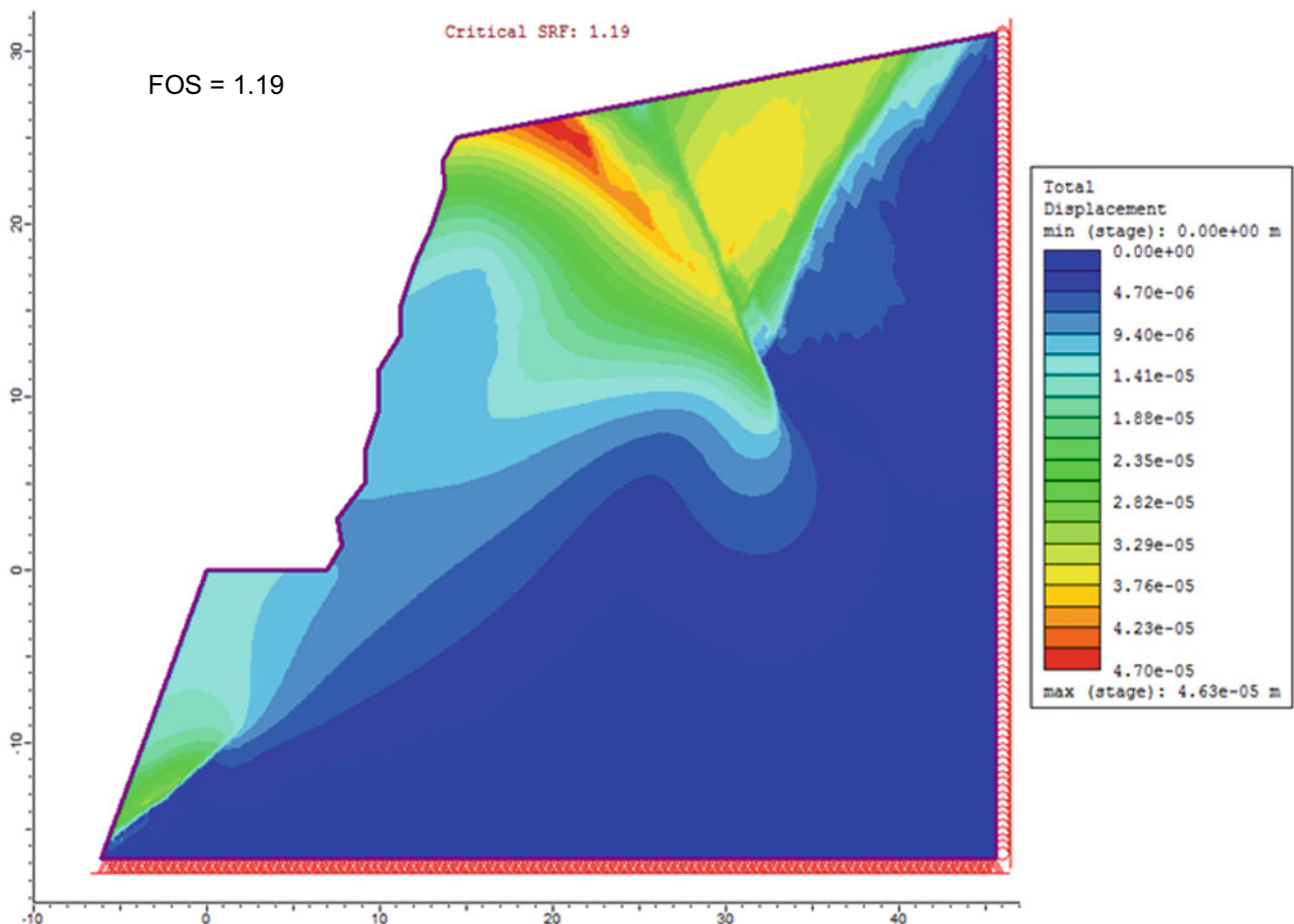


Fig. 9 Total displacement contours with computed FoS of the illustrated slope under static condition

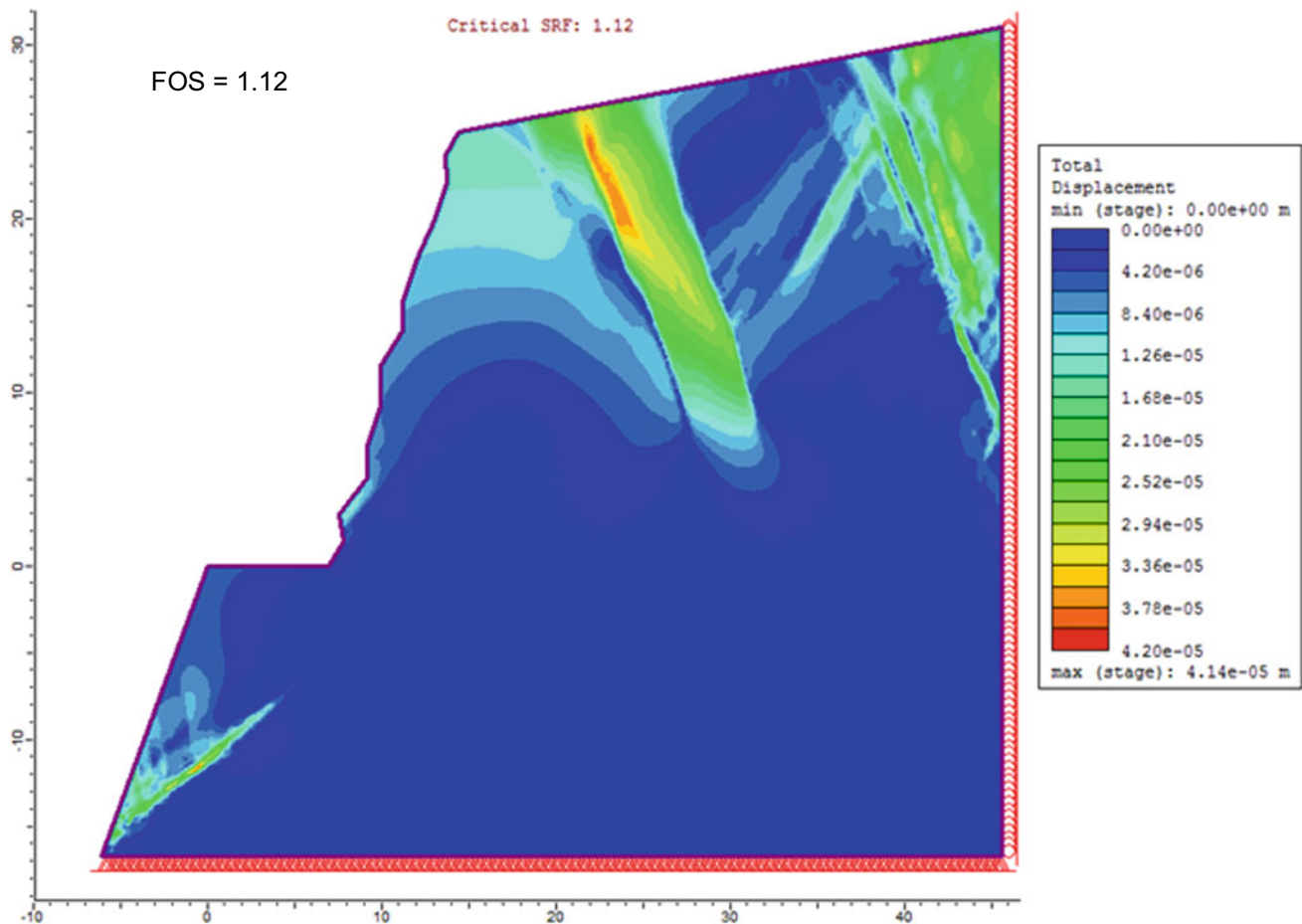


Fig. 10 Total displacement contours with computed FoS of the illustrated slope under pseudo-static condition

Conclusions

Rock slope stability assessment is one of the important aspects of landslide disaster mitigation/hazard assessment particularly for hill roads. The highways in Indian Himalayas are very prone to landslides due to lack of proper investigation and adequate measures. The rock mass classification techniques by collecting the engineering geological data helps in assessing the rock slope stability. The paper described the most commonly used techniques and their application. The study of few rock slopes has shown the interdependency of the rock mass classification systems. The paper also explained about the estimation of some engineering properties of rocks essential for carrying out numerical modelling of slopes to determine the safety factor.

Acknowledgements The authors would like to acknowledge the Director, CSIR—CBRI, Roorkee for his kind permission to publish this paper.

References

- Bieniawski ZT (1973) Engineering classification of jointed rock masses. *Trans S Afr Inst Civ Eng* 15:335–344
- Bieniawski ZT (1978) Determining rock mass deformability: experience from case histories. *Int J Rock Mech Min Sci Geomech Abstr* 15(5):237–247
- Bieniawski ZT (1979) The geomechanical classification in rock engineering applications. In: *Proceedings of the 4th international congress rock mechanics*, vol 2, Montreux, Balkema, Rotterdam, pp 41–48
- Bieniawski ZT (1989) *Engineering rock mass classifications*. Wiley-Interscience, New York, p 251. (ISBN 0-471-60172-1)
- Cai M, Kaiser PK, Uno H, Tasaka Y, Minami M (2004) Estimation of rock mass deformation modulus and strength of jointed hard rock masses using the GSI System. *Int J Rock Mech Min Sci* 41(1):3–19
- Hoek E, Brown ET (1997) Practical estimation of rock mass strength. *Int J Rock Mech Min Sci* 34(8):1165–1186
- Hoek E, Marinos P, Benissi M (1998) Applicability of the geological strength index (GSI) classification for very weak and sheared rock masses. The case of the Athens Schist formation. *Bull Eng Geol Env* 57(2):151–160

- Hoek E, Carranza-Torres C, Corkum B (2002) Hoek-Brown failure criterion e 2002 edition. In: Proceedings of the 5th North American Rock Mechanics Symposium & the 17th Tunneling Association of Canada Conference (NARMS-TAC 2002). Mining Innovation and Tech., Toronto, Canada, pp 267–273
- Hoek E, Diederichs MS (2006) Empirical estimation of rock mass modulus. *Int J Rock Mech Min Sci* 43(2):203–215
- Kalamaras GS, Bieniawski ZT (1993) A rock mass strength concept for coal seams. In: Proceedings of the 12th conference on ground control in mining, Morgantown, pp 274–83
- Marinos P, Hoek E (2000) A geologically friendly tool for rock mass strength estimation. In: Proceedings of international conference on geotechnical and geological engineering (GeoEng2000), pp 1422–1440
- Neeraj, Pandit K, Sarkar S (2018) Stability assessment of cut slopes along Shivpuri – Kaudiyala road (NH-58), Uttarakhand Himalayas. Indian Geotechnical Conference, IISC, Bangalore, December 2018.
- Palmstrom A (2005) Measurements of and correlations between block size and rock quality designation (RQD). *Tunnels Underground Space Technol* 20:362–377
- Ramamurthy T (1996) Stability of rock mass. *Indian Geotech J* 16:1–73
- Ramamurthy T (2004) A geo-engineering classification for rocks and rock masses. *Int J RockMech Min Sci* 41:89–101
- Romana M (1985) New adjustment ratings for application of Bieniawski classification to slopes. In: Proceedings of international symposium on “the role of rock mechanics”, Zacatecas, pp 49–53
- Sarkar S, Kanungo DP, Patra AK, Kumar P (2008) GIS based spatial data analysis for landslide susceptibility mapping. *J Mountain Sci* 85(5):52–62
- Sarkar S, Pandit K, Sharma M, Pippal A (2018) Risk assessment and stability analysis of a recent landslide at Vishnuprayag on the Rishikesh-Badrinath highway, Uttarakhand, India. *Curr Sci* 114 (7):1527–1533
- Sarkar S, Kanungo DP, Kumar S (2012) Rock mass classification and slope stability assessment of road cut slopes in Garhwal Himalaya. *Geotech Geol Eng* 30(4):827–840
- Serafim JL, Pereira JP. (1983) Consideration of the geomechanical classification of Bieniawski. In: Proceedings of international symposium on engineering geology and underground construction, vol 1. A.A. Balkema, Rotterdam. II: 3–44
- Sonmez H, Ulusay R (2002) A discussion on the Hoek-Brown failure criterion and suggested modification to the criterion verified by slope stability case studies. *Yerbilimleri (Earth Sciences)* 26:77–79
- Yudhbir WL, Prinzl F (1983) An empirical failure criterion for rock masses. In: Proceedings of the 5th international congress on rock mechanics, vol 1, Melbourne, B1–8



2020 Kyoto Japan

First Consideration About Post 2017 Wildfire Erosion Response and Debris Flow in Susa Valley (NW Italy)

Damiano Vacha, Giuseppe Mandrone, Matteo Garbarino, and Donato Morresi

Abstract

This paper contains the first results of an ongoing research dealing with post-fire mass movements in Italy. Although the attention of the scientific community is increasing worldwide, very few geo-hydrological processes occurring in burned areas are reported for Italy. As the probability of occurrence and magnitude of wildfires is expected to increase in the future because of climate change, more efforts should be made to deepen knowledge on interacting disturbances. Here, we present a case study regarding the erosional response after fire recurrence in a watershed located in NW Italy, where multiple flow processes occurred after six months since the last wildfire, as a consequence of different rainstorms. It contains a description of the geological and geomorphological background, the burn severity assessment together with the analysis of the triggering rainfalls and the outline of the main geomorphic effects that affected people and lifelines.

Keywords

Wildfire • Debris flow • Erosion • Fire severity • Susa Valley - N-W Italy

Preface

Every year wildfires occur worldwide, resulting in remarkable damage, leading to a severe modification in natural ecosystems, causing economic losses and increasing risks for

D. Vacha (✉) · G. Mandrone
Earth Sciences Department, University of Turin, Via Valperga
Caluso 35, 10135 Turin, Italy
e-mail: damiano.vacha@unito.it

M. Garbarino · D. Morresi
Department of Agricultural, Forest and Food Sciences (DISAFA),
University of Turin, Largo Paolo Braccini 2, 10095 Grugliasco
(TO), Italy

people. They affect the hydrologic response of watersheds by changing the infiltration rates and erodibility of the soil. This effect is due to litter and vegetation removal, ash deposition, soil physical alteration and generation or destruction of water repellent soils (Parise and Cannon 2012).

Rainstorms are commonly recognized as one of the most frequent triggering factors of post-wildfire gravitative phenomena (Moody et al. 2013). Unfortunately, strong statistics on this matter are usually lacking but cases where wildfires could have played a major role in favouring landslides are many. Climate crisis causing an increase in extreme events (both for temperature and rainfalls) and land use changes (especially in rural areas) request a special attention on these items (IPCC 2014).

While several post-fire high-magnitude debris flows are reported for Canada, USA, and Australia, few examples are reported in Europe, and even less in Italy (Esposito et al. 2017, 2019; Carabella and Paglia 2019). For this reason, a group of Italian multidisciplinary researchers is developing a program of studies included in the ICL project No. 4938, started in 2019 (Mandrone et al. 2019).

Introduction

Debris flow susceptibility and erosion rates in burned areas can increase substantially with respect to the unburned situation (Moody and Martin 2001; Parise and Cannon 2008, 2012; Staley et al. 2017).

Different processes for the initiation of post-fire debris flows have been identified: a) runoff-dominated erosion by surface overland flow, b) infiltration triggered failure and c) mobilization of a discrete landslide mass and increased runoff by water cascading on easily erodible material. a) is most frequent immediately after the fire. It is the result of rainsplash, sheetflow and rill erosion. Surface runoff may concentrate in hollows and in low order channels, eroding sediments until enough material has been accumulated to

generate debris flow (Meyer and Wells 1997; Shakesby and Doerr 2006; Parise and Cannon 2012). Failure of shallow discrete landslide masses b), has also been documented in burned watershed (Cannon and Gartner 2005; Parise and Cannon 2012). The increase in soil moisture and the reduction of soil cohesion due to tree mortality and deterioration of anchoring roots play a major role in this case (Cannon et al. 2001). c), described as the “firehose” effect in unburned areas, can erode material owing to the increased kinetic energy of the flow, and involve a major area down valley (Calcaterra et al. 2000; Larsen et al. 2006).

In dry conditions, the availability of material to be mobilized by a flow might also increase, due to the transport of sediments by gravity and accumulation at the bottom of the valley. This process, called “dry ravel” is intensified in absence of vegetation (Florsheim et al. 2016).

Methodologies

A complete description of a post-wildfire response needs to include the analysis of multiple aspects: local geology and geomorphology, soil characteristics, fire intensity and recurrence, severity and regimes, precipitation regime, modification of the soil hydraulic and geotechnical properties, soil erosional processes, event magnitude and effects. All of these issues are under investigation using field observations, in situ measurements, geophysical surveys, remote sensing, laboratory test and modelling.

As a starting point, the multiple flows (debris flow and debris floods) occurred on April and May 2018 in Bussoleno (Susa Valley, one of the Turin 2006 Olympic valleys—Piedmont, NW Italy), are described. The aim is to report the phenomena, to highlight their main characteristics, to identify the processes responsible for the triggering, and lastly to improve knowledge about post-fire watershed behaviour in alpine regions.

The Susa Valley Case Study

The Susa Valley Wildfire, October 2017

During October 2017, nine large wildfires (>150 ha) occurred in Piedmont, burning a total area of 10,000 hectares of which 7000 were forests. By comparison, the average forest area burned for the entire region, between 2005 and 2013, was 600 ha/year (regional Fire Management Plan 2015–2019).

Dry conditions (−40% of rainfall with respect to 1958–2016 average from Jan to Oct), high temperatures (+2.1 °C in Turin compared to 1981–2010 average for October) and hot and dry winds (Föhn from NW) favoured fire spread. The largest and severe fire was in the Susa Valley, were nearly 4,000 ha burned, involving 14 basins, placed on the left of the Dora Riparia River. The same area experienced another wildfire in 2003, which burned approximately 480 ha (moderate and high burn severity, Ascoli et al. 2011) but not producing instability phenomena.

Satellite imagery and field surveys were used to map burn severity at the landscape-scale, by employing a methodology based on US FIREMON framework (Key and Benson 2005). The analysis of spectral changes caused by 2017 wildfires was carried out using multispectral images acquired by Sentinel-2 A/B satellites (European Space Agency) during August 2017 (pre-fire) and August 2018 (post-fire). Normalized Burn Ratio (NBR) index was calculated at 20 m spatial resolution using surface reflectance in the near infrared (NIR) and in the shortwave infrared (SWIR2), as expressed in Eq. 1.

$$NBR = (NIR - SWIR) / (NIR + SWIR) \quad (1)$$

The Relative delta Normalized Burn Ratio (RdNBR) index (Miller and Thode 2007) was chosen to infer burn severity from remote sensing as it provides relative changes using pre-fire NBR.

$$RdNBR = \frac{(prefireNBR - postfireNBR)}{\sqrt{|prefireNBR/1000|}} \quad (2)$$

For the 2003 wildfire, the same methodology was applied to Landsat 5 pre (Aug 2003) and post-fire (Sept 2003) 30 m resolution images (Fig. 1c).

The CBI (Composite Burn Index) field protocol was used to define RdNBR thresholds of unburned/low, moderate and high severity classes and to validate 2017 burn severity maps (Miller and Thode 2007; Miller et al. 2009).

The study focuses on The Comba delle Foglie watershed, where debris flows occurred. It was characterized by moderate burn severity due to the low amount of pre-fire forest cover (due to previous wildfires), mostly dominated by young trees of *Populus tremula* and *Salix caprea* (Fig. 1d).

Geological and Geomorphological Setting

The Comba delle Foglie (CdF) watershed is one of the 14 basins affected by the Susa Valley wildfire. It's a steep basin, ranging between 490 and 1790 m a.s.l., with an average slope of 32° and an area of approximately 1.37 Km² (Fig. 1b).

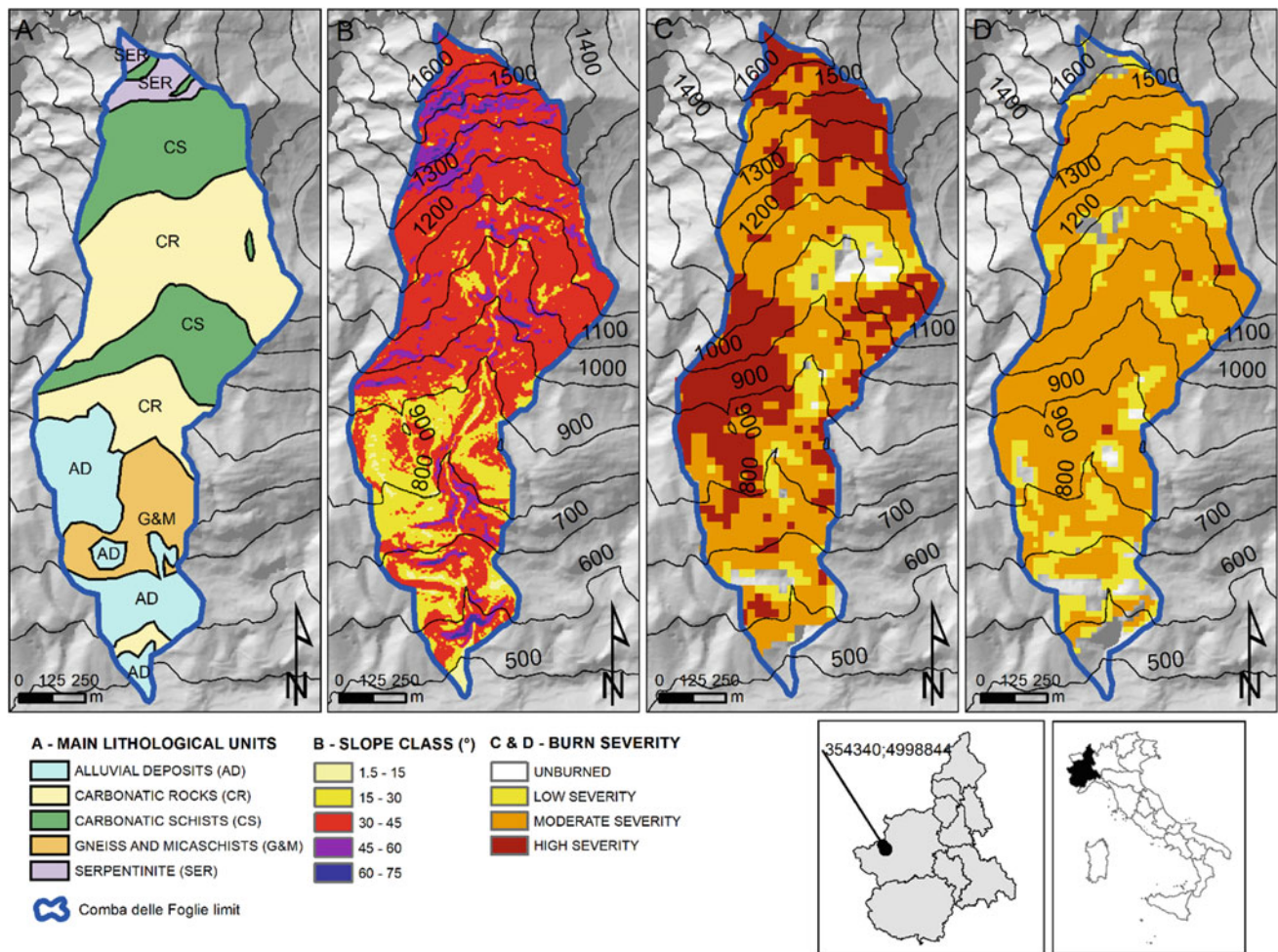


Fig. 1 a Geological setting, b geomorphological setting and c, d burn severity map of the Comba delle Foglie watershed (2003, 2017). In the small boxes the geographic location of the study area is provided.

The East–West mountain ridge is mainly formed by rock belonging to two tectonic elements: the Upper Unit of the Dora Maira Massif (DM) and the Lower Piedmont Zone (PZ). DM is one of the nappes of the inner Penninic Domain, characterized a pre-Triassic basement (DMb) and its Mesozoic cover (DMc); the PZ, represents the remnant of the Tethys ocean, which over-thrust the DM units with different structural elements (Gasco et al. 2011). Micaschists and gneiss of the DMb, calcschists, marbles and dolomitic marbles belonging to DMc, calcschists, serpentinites, serpentinoschists and chloritoschist belonging to PZ outcrop in the lower part of the catchment (Carraro et al. 2002) (Fig. 1a). The stream has an average slope of 28.9° which drops in the fan at about 8.8°. The talweg, poorly incised, is barely visible on the fan, because of the high urbanization. The streamflow does not reach the main valley river (Dora Riparia), but it flows into a network of irrigation channels.

Post Fire Response

Debris Flow

In the spring of 2018, precipitation in the Piedmont area far exceeded the annual averages, leading to many instability phenomena. In detail:

- April 29, 2018: a debris flow hit the northern portion of Bussoleno Municipality, coming from Comba delle Foglie watershed, affecting the fan in several positions and causing damages to roads. Traces of enhanced erosion in the stream path were found, while debris, finer material and floated burn residuals were deposited at the upper portion of the fan.
- Minor debris flow and floods events were recorded on May 2, 9 and 13, 2018.

- June 7, 2018: a major debris flow, which caused severe damage to roads, buildings and infrastructures were registered. Up to two meters of mud and debris were deposited at the fan outlet. The event caused the complete destruction of two houses, the compromising of two others, structural damage to other 12 buildings. Gas, water and electrical energy supply were interrupted, and 150 people were evacuated.

Rainfall Data

Rainfall series from rain gages (Arpa Piemonte Network) and radar rainfall intensities were collected. Four meteorological stations are located at about 8.7 km, 7 km, 7.8 km and 5.4 km respectively from the study area. The rainfall intensity estimated by radar for the June 7 event showed peaks between 60 and 100 mm/h at 12: 00 UTC. Then between 12:00 and 12:10 about 10 mm fell with an intensity of 60 mm/h. The cumulated rainfall on the ground relative to the interval 11: 55–12: 25 was about 15 mm. These quantities correspond to a return period of 5 years (Fig. 2).

Processes Description

Field surveys and tests led to the characterization of the main processes occurring in the watershed, and to the discovery of some peculiar feature. Consecutive flows events occurred in the Comba delle Foglie six months after the wildfire.

The upper part of the basin was characterized by very sparse vegetation constituted of shrubs and grass associated with few trees. In this area the bedrock outcrops discontinuously, and the soil coverage is very shallow (up to some centimetres).

The fire effects resulted in a patched distribution in which bare soil was exposed near spots where the new grass was re-growing on black charred soil. The results of the surveys conducted in June are shown below.

High on the hillslope, traces of overland flow coalescing into rills and then into the main drainage line at the watershed bottom were found. Zero-order drainage showed evidence of increased erosion and sediment transport, since the very beginning close to the divide of the catchment (Fig. 3 a). On open slopes, in condition of exposed soil, the dominant erosional process was found to be the sheetflow erosion, occasionally associated with rill dominated sectors where the tree vegetation was denser (Fig. 3b).

The lower part of the basin revealed generally a higher percentage of vegetation cover, which was dominated by shrubs and trees. In these sectors rill and little gullies were detected. Also, some pathway showed signs of erosional processes due to overland flow.

In the main channel the erosion, increasing proceeding downstream, was marked by channel incision with steep banks and frequently exposed bedrock. At 1000 m a.s.l., where two second-order drainages converge, localized debris-flow levees were found in flat areas and behind obstacles: these well sorted deposits were constituted by cobbles and boulders up to 500 mm in a poor silt and sandy matrix. Other deposits were found between 1000 m a.s.l. and 900 m a.s.l., alternated with erosion dominated sectors.

Down the channel, the sorting of the deposit decreased while the amount of matrix increased. At 900 m a.s.l., where the slope is flattened due to a road crossing, a bigger deposition area was found: cobble and small boulders, in a chaotic disposition, supported by a gravelly-sandy matrix were found.

Below the road cut, the erosion level increased again. At 650 m a.s.l. two small lobes, made of cobbles mixed with abundant sandy-silty matrix and floated materials (wood, char...) were found in a flat area above a road cut.

After this point, the channel is again very incised and reaches a steep jump just above the fan (570 m a.s.l.). A survey conducted on June 5, two days before the main debris-flow occurrence, revealed a massive amount of debris and material accumulated in the channel, especially at the bottom of the last cliff overhanging the fan apex. After the debris flow occurrence, this sector showed a marked erosion, up to 3 m (Fig. 3c). Below this point the signs of the flow path were clearly visible: the bedrock was exposed and polished, and the flow splash signs could be found some meters above the valley bottom on the trees. At 500 m a.s.l., the gorge ends and reaches the fan apex. Where the main deposition zone, made of gravels and cobbles were mixed in an abundant sandy silty matrix, was found. The original channel incision, covered by a road pavement, was exhumated (Fig. 3d).

The maximum deposit thickness (reconstructed via photogrammetric modelling) was approximatively 2 m, giving a maximum estimated volume of 20,000 m². The coarser fraction was concentrated in the central part of the deposit and was approx. 600 m in length, while the fluid fraction had propagated for a longer distance (900 m from the apex) (Fig. 4).

Discussion

Studying the post-wildfire response usually includes a series of uncertainties. Among these, it is worth highlighting the following items.

The cause-effect relationship is hard to establish, since the longer the time between the fire and the flows triggering, the higher the probability that other factors could have influenced the phenomenon occurrence.

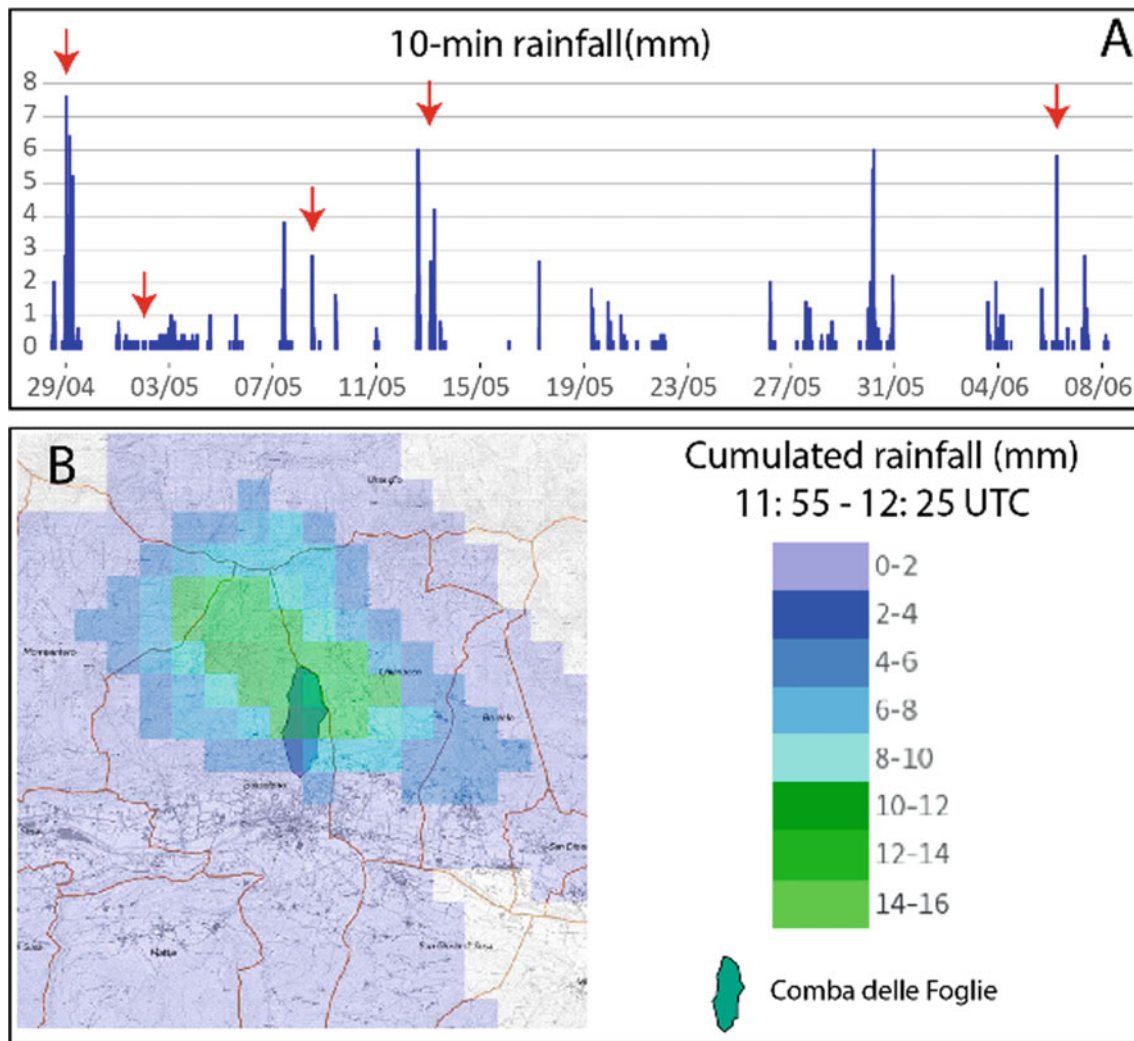


Fig. 2 10-min rainfall at the nearest rain gauge **a** and radar cumulated rainfall (June 7, 11: 55–12: 25 UTC) **b**

The evolution of the slope is usually very rapid: in a short time there is a re-mobilization of the combustion products (ashes, char, ...), and the vegetative regrowth of herbaceous species is usually very rapid, especially in conditions of low or moderate fire severity. In addition, although the fire may have been extensive and continuous, the effects on the sub-soil are usually very uneven and depend mostly on the type and amount of fuel, the type of soil, the style and residence time of the fire and the water content of the soil.

Therefore, the transformations induced by the fire in the first centimetres of soil are very variable, thus hard to be sampled properly. Locally there is the generation of a discontinuous hydrophobic level, and where the root anchoring function decay the soil cohesion decreases abruptly. The availability of abundant material produced by the wildfire

combustion modifies the particle size distribution of the erodible material, significantly increasing the finer fraction, the organic substance and the overall volume of the rainfall-triggered debris flow and floods.

Moreover, is hard to establish a direct correlation between burn severity and landslide susceptibility because this parameter comes from aerial images and field surveys but it is always correlated to the impact of the fire on vegetation: soil and subsoil modification is not included in this evaluation and they can vary a lot in space and depth due to time lasting and fuel availability.

The general aim of this study is to standardize these observations in an ad hoc database so data will be available to scientist to elaborate correlation and modelling effects of fire on soils.

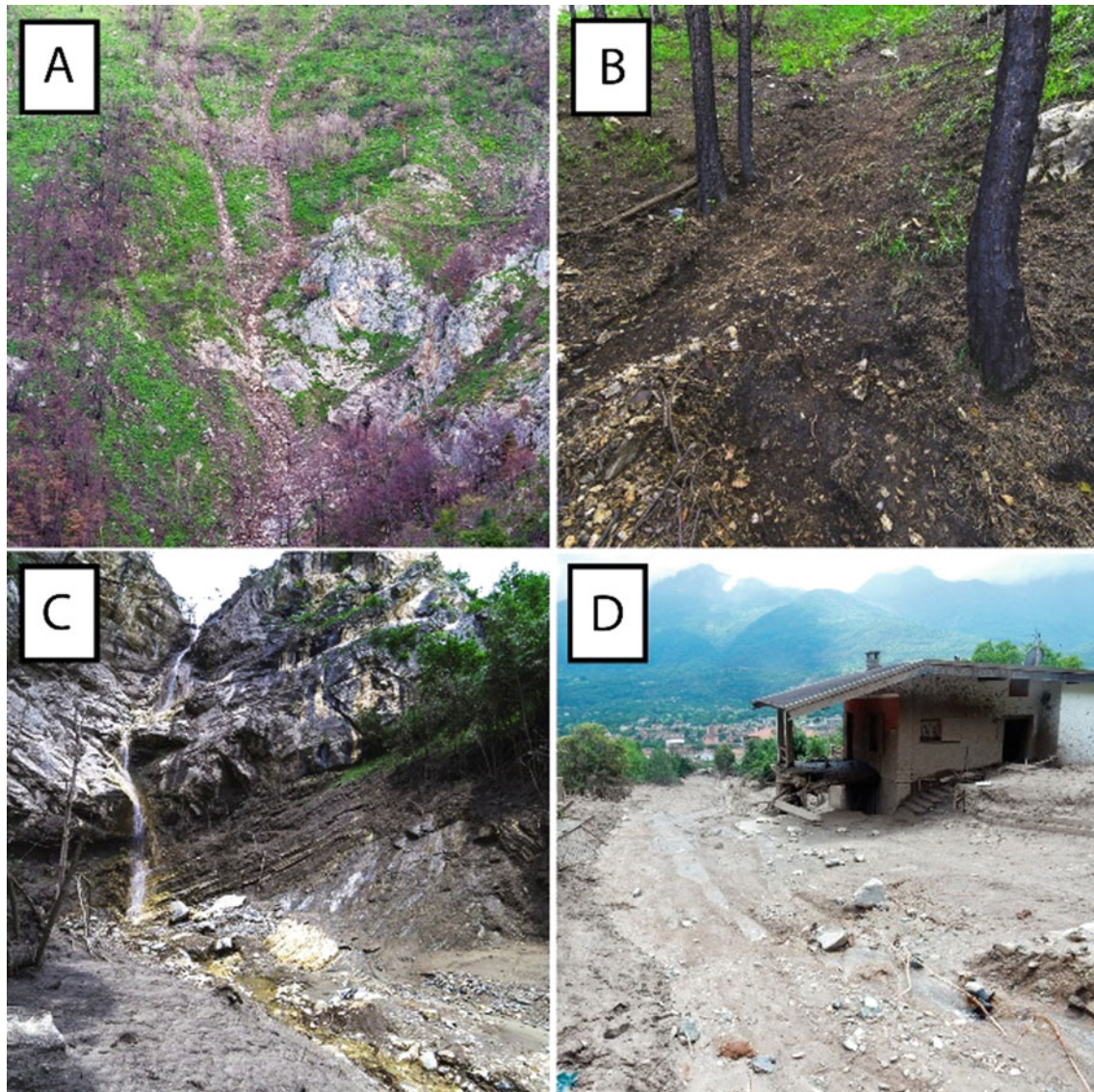


Fig. 3 Erosional features on low order drainage **a**, and open slopes **b**, bottom of the channel **c**. Deposition area and one of the evacuated houses **d**

Conclusions

This study describes post-fire erosion response of the Comba delle Foglie watershed after the 2017 Susa Valley wildfire. Due to a series of short-duration rainfall events, at least 5 flows and flooding processes were registered. The last one (June 7, 2018) was the higher in magnitude and involved the village causing severe damages.

Field survey and data analysis allowed to identify the main process involved in the flows triggering: both signs of runoff-dominated erosion by surface overland flow and increased runoff by water cascading on easily erodible material were detected in the field. The first process is evident in the upper portion of the watershed and caused the

entrainment of material (loose material, charred wood and ash) in the low order and in the main channel. The second one played a major role in correspondence of the last cliff overhanging the fan apex; here at least tree meters of loose deposits, burn residuals and wood were eroded and enhanced the last debris-flow final volume.

Since no significant rainfall event have been recorded between the end of the wildfire (Oct 2017) and the first flow events (Apr 29, 2018), also the dry ravel process could have played a role in increasing the sediment availability in the channels. Doubts remain about the role of previous wildfire and the role of burn severity, but this debris flow can be clearly identified as wildfire induced. In other word, wildfire effects on soil and sub-soil are for sure a predisposing factor while rainstorms triggered several debris flows.

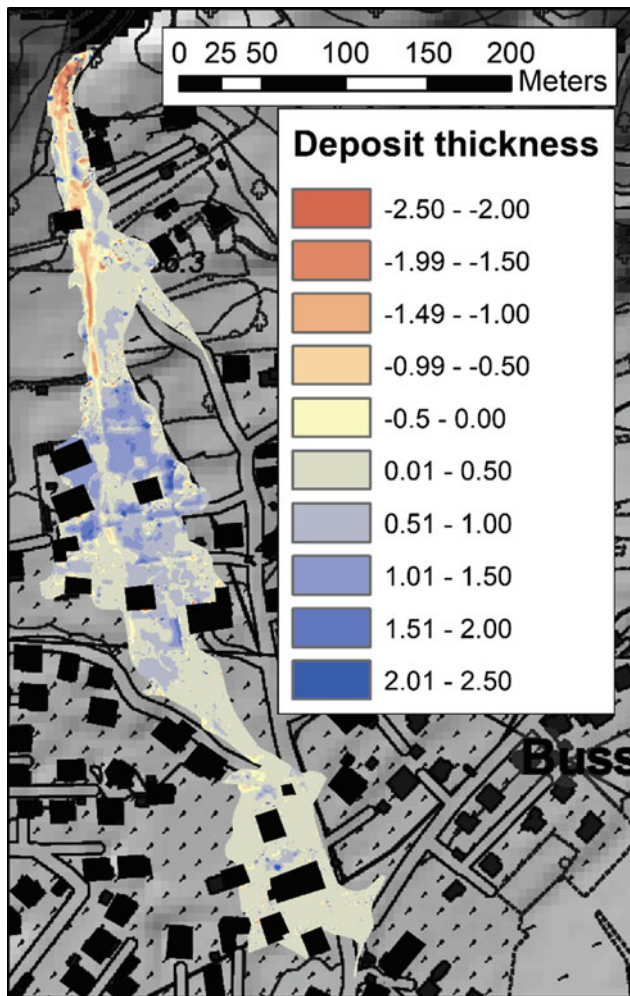


Fig. 4 Deposition area and deposit thickness reconstructed by photogrammetric modelling

Acknowledgements Many thanks to Arpa Piemonte for rainfall data and to the Provincial Command of the Turin Fire Brigade UAV for images of the landslide. Field survey were conducted in the framework of the Institutional Technical Table of the Piedmont Region.

References

Ascoli D, Valsecchi C, Conedera M, Bovio G (2011). Wildfires and beech forests of Southern Alps during the summer 2003 climate anomaly: fire effects and post-fire management. In The 5th international Wildland fire conference, AfriFireNet pp 1–10

Calcaterra D, Parise M, Palma B, Pelella L (2000) Multiple debris flows in volcanoclastic materials mantling carbonate slopes. In: Wiczorek GF, Naeser ND (eds) Proceedings of 2nd international Nat Hazards (2012) 61:217–227 225 123 conference “Debris-flow

hazards mitigation: mechanics, prediction, and assessment”, Taiwan, pp 99–107

Cannon SH, Gartner JE (2005) Wildfire-related debris flow from a hazards perspective. In: Jakob M, Hungr O (eds) Debris-flow hazards and related phenomena. Praxis, pp 363–385

Cannon SH, Kirkham RM, Parise M (2001) Wildfire-related debris-flow initiation processes, Storm King Mountain, Colorado. *Geomorphology* 39:171–188

Carabella C, Miccadei E, Paglia G, Sciarra (2019) Post-Wildfire landslide hazard assessment: the case of the 2017 Montagna Del Morrone Fire (Central Apennines, Italy). *Geosciences* 9:175

Carraro F, Cadoppi P, Baggio P et al (2002) Foglio 154 – Susa – Carta Geologica d’Italia, scala 1:50.000. Carta Geol - Serv Geol D’Italia Coord CARRARO F 126

Esposito G, Matano F, Molisso F et al (2017) Post-fire erosion response in a watershed mantled by volcanoclastic deposits, Sarno Mountains, Southern Italy. *CATENA* 152:227–241

Esposito G, Parodi A, Lagasio M, et al (2019) Characterizing Consecutive Flooding Events after the 2017 Mt. Salto Wildfires (Southern Italy): Hazard and Emergency Management Implications. *Water* 11:2663.

Florsheim JL, Chin A, O’Hirok LS, Storesund R (2016) Short-term post-wildfire dry-ravel processes in a chaparral fluvial system. *Geomorphology* 252:32–39

Gasco I, Gattiglio M, Borghi A (2011) Lithostratigraphic setting and P-T metamorphic evolution for the Dora Maira Massif along the Piedmont Zone boundary (middle Susa Valley, NW Alps). *Int J Earth Sci* 100:1065–1085

IPCC (2014) Climate change 2014: synthesis report. In: Core Writing Team, Pachauri RK, Meyer RK (eds) Contribution of working groups I, II and III to the fifth assessment report of the intergovernmental panel on climate change, IPCC, Geneva, Switzerland, p151

Key CH, Benson NC (2005) Landscape Assessment (LA). Sampling and analysis methods. USDA Serv Gen Tech Rep RMRS-GTR-164-CD 1–55

Larsen IJ, Pederson JL, Schmidt JC (2006) Geologic versus wildfire controls on hillslope processes and debris flow initiation in the Green River canyons of Dinosaur National Monument. *Geomorphology* 81:114–127

Mandrone G, Parise M, Vacha D et al (2019) Wildfire induced landslides: state of the art and future developments also with reference to climate changes. *Geol. Dell’Ambiente* (In press)

Meyer GA, Wells SG (1997) Fire-related sedimentation events on alluvial fans, Yellowstone National Park, U.S.A. *SEPM J Sediment Res*, Vol 67

Miller JD, Knapp EE, Key CH et al (2009) Calibration and validation of the relative differenced Normalized Burn Ratio (RdNBR) to three measures of fire severity in the Sierra Nevada and Klamath Mountains, California, USA. *Remote Sens Environ* 113:645–656

Miller JD, Thode AE (2007) Quantifying burn severity in a heterogeneous landscape with a relative version of the delta Normalized Burn Ratio (dNBR). *Remote Sens Environ* 109:66–80

Moody JA, Martin DA (2001) Hydrologic and sedimentologic response of two burned watersheds in Colorado. U.S. Geological Survey, DENVER WATER DEPARTMENT and the U. S. FOREST SERVICE

Moody JA, Shakesby RA, Robichaud PR et al (2013) Current research issues related to post-wildfire runoff and erosion processes. *Earth-Sci Rev* 122:10–37

- Parise M, Cannon SH (2012) Wildfire impacts on the processes that generate debris flows in burned watersheds. *Nat Hazards* 61:217–227
- Parise M, Cannon SH (2008) The effects of wildfires on erosion and debris-flow generation in Mediterranean climatic areas: a first database. In: *Proceedings of 1st World Landslide Forum, Tokyo, Japan*, pp 465–468
- Shakesby R, Doerr S (2006) Wildfire as a hydrological and geomorphological agent. *Earth-Sci Rev* 74:269–307
- Staley DM, Negri JA, Kean JW et al (2017) Prediction of spatially explicit rainfall intensity–duration thresholds for post-fire debris-flow generation in the western United States. *Geomorphology* 278:149–162



Identification of Sliding Surface and Crack Pattern in the Soil Creep, Case Study: Unika Soegijapranata Campus, Semarang, Central Java, Indonesia

Wahyu Wilopo, Hendy Setiawan, Doni Prakasa Eka Putra,
and Teuku Faisal Fathani

Abstract

The development of a sports hall in the Unika Soegijapranata Campus in Central Java is constrained by geological conditions. At the time of land preparation, a crack appears on the fence of the sports hall foundation that was predicted as a sign that they have a soil creep. This condition has threatened the implementation of such development. Therefore, it is necessary to know the subsurface conditions, especially the sliding surface location and pattern of the existing cracks in the ground. This information is beneficial to avoid soil creep risk. In order to support the information, both the geological survey and seismic refraction were conducted in this location. According to the survey, it is found that the sliding surface was identified as volcanic breccia with the depth from 5 m up to 20 m. There are many faults found based on the seismic data, and many cracks appear on the surface, which suspected as the creep crown. Some areas of the sports hall are located in the soil creep crown. According to the drilling data and geo-electrical survey, the sliding surface location of the soil creep was identified within volcanic breccia layers. It is recommended to shift the planned location of the sports hall in order to avoid or minimize the soil creep risk.

W. Wilopo (✉) · H. Setiawan · D. P. E. Putra · T. F. Fathani
Department of Geological Engineering, Faculty of Engineering,
Universitas Gadjah Mada, Kampus UGM, Jl. Grafika No. 2,
Yogyakarta, 55281, Indonesia
e-mail: wilopo_w@ugm.ac.id

H. Setiawan
e-mail: hendy.setiawan@ugm.ac.id

D. P. E. Putra
e-mail: putra_dpe@ugm.ac.id

T. F. Fathani
e-mail: tfathani@ugm.ac.id

W. Wilopo
Center for Disaster Mitigation and Technological Innovation
(GAMA-InaTEK), Universitas Gadjah Mada, Yogyakarta,
Indonesia

Keywords

Seismic refraction · Geological survey · Crack structure and pattern · Soil creep

Introduction

In order to develop the University of Soegijapranata (UNIKA) Campus in Semarang, Central Java, the administrators planned to construct a sports hall building in the northwest of the existing buildings. In practice, the construction of this sports hall has a problem with the many occurring cracks in the south-western part of the foundation. Based on the results of field reconnaissance of existing conditions, there is much evidence of a soil movement, which is supported by the presence of many cracks that occur in the vicinity of the UNIKA Campus up to the downslope in Garang River. This condition is certainly not favorable for the development of the campus area. It is necessary to know the geological engineering conditions at the location where the sports hall building would be built. Engineering geological research is focused on the method of surface mapping and the application of seismic refraction to explain the subsurface conditions.

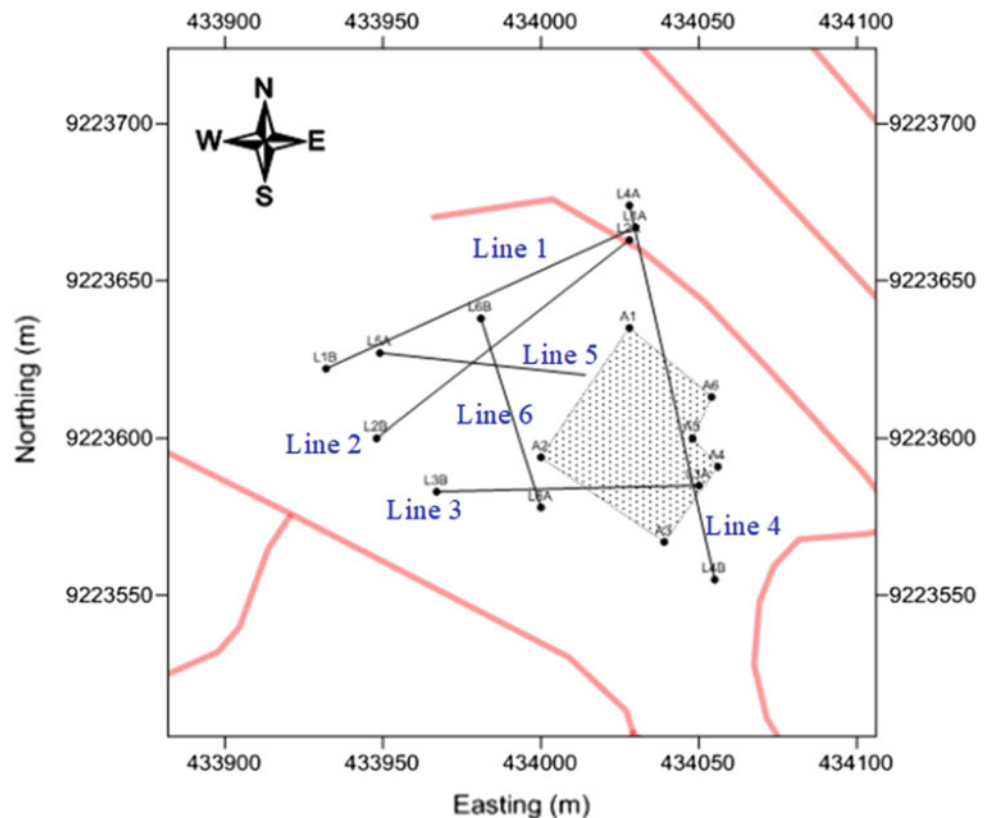
Expected results of geological engineering studies will provide an image surface and subsurface conditions of soil and rocks, including the geological structure of the rock, rock bedding, cracks or fractures, faults, unconformity that affect to the movement of soil at the sites. Engineering geological information will be much needed by civil engineers to solve the problems in the construction of a sports hall building. One of the methods to identify subsurface conditions is by using the geophysical method. One of the geophysical methods is seismic, which can be divided into seismic reflection and seismic refraction (Kearey et al. 2002). The seismic refraction has been proved to identify the

layer of soil/rock (Anomohanran 2013) and geological structure (Alhassan et al. 2010).

Methodology

The research was conducted by field investigation and seismic refraction surveys. It consists of collecting geomorphology data, lithology data, and geological structure by using a geological hammer, compass, and magnifying glass. The seismic survey was conducted using PASItm seismic data logger, geophone equipment, and GPS. Seismic refraction measurements at UNIKA campus, Gunungpati, Semarang Regency, Central Java were carried out with a whole line of 600 m long, which is divided into six measurement channels/lines, as shown in Fig. 1. In the seismic refraction, measurements used many geophones, which configured in one straight line with an interval of 5 m. Determination of seismic refraction measurement lines direction based on the geological conditions found in the location with considering the regional geologic conditions of the UNIKA campus area. It aims to obtain data correlation between the results of engineering geological investigations with seismic refraction data presented to determine the subsurface conditions at the project site.

Fig. 1 Seismic lines at UNIKA Campus (a shading area is planned sports hall building)



Result and Discussion

The location of the UNIKA campus is located on the slope of the hill. In general, morphology around this area is hilly and has an elevation between 18 and 120 m above sea level. The general direction of the spreading of hills is northwest-southeast.

In the regional geology, the UNIKA campus is located in the Damar formation (Thaden et al. 1975). It is composed of tuffaceous sandstones, conglomerate, volcanic breccia, and tuff, with a total thickness of 50–150 m (Fig. 2). According to the observation of the physical characteristics in the field, the rock in the Unika campus can be separated into four lithologies from the oldest to the youngest are mudstone, volcanic breccia, colluviums, and alluvium units. The rock unit on the surface has been primarily weathered to form the cover layer of soil to sand-clay sized.

The soil movement was recognized after the development of the highway Semarang-Jakarta in the upper area of the UNIKA Campus. The movement of soil is ranging between 0.02 and 1.57 m/year, where the highest movement occurs during the rainy season.

Detailed observations of the crack structures in the area where the Sports Hall building will be constructed show that many cracks appear with the general orientation of N160°E

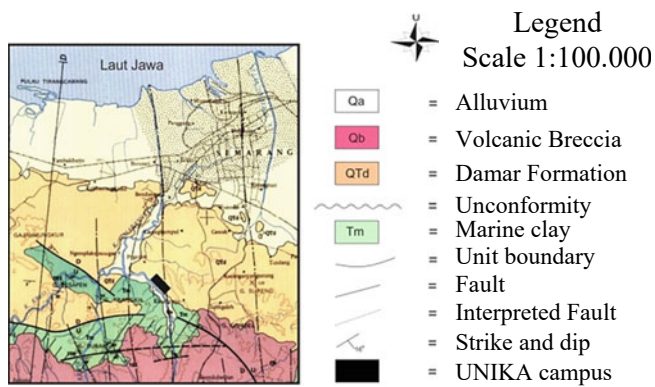


Fig. 2 Regional geological map of Unika campus (Thaden et al. 1975)

on the cliffs along the highway. The crack has high ranged from 3 to 5 m and can be larger, while the width of the fracture can reach up to 3–6 cm thick. In each 10 m distance, it can be found around 2 until 5 pieces of crack. The frequency of occurrence of these cracks will be higher in the direction close to the valley. The minor faults can also be found in the direction of N40°E.

Besides the closed cracks as described above, other cracks formed by an open force or gravity load also can be found in the area of the UNIKA campus. The cracks are generally not open to have a regular pattern and directed according to the

morphological control but also can be growing from stout open-fracture trending fracture of N160°E. The distribution of the cracks at the study site is shown in Fig. 3.

Seismic refraction measurements conducted at the project site resulted in curve data in the form of time travel versus distance that can be used to interpret a subsurface condition. Those curves then converted into trajectories vertical cross-section. It can be observed that different layers exist based on the different patterns of the speed of the travel time, which indicated by blue, green, and yellow color gradation (Fig. 4). The value of the travel time and drilling data can be used to interpret lithological types and fault structures.

Based on the value of travel time of seismic refraction measurements, field observations, reports of the previous study on geological engineering conditions of UNIKA campus (Department of Geological Engineering 1995) and geo-electric survey on the project site sports hall (PT. Seli-mut Bumi Adhi Cipta 2011) the lithology at the site of the project can be interpreted as follows (Fig. 5):

- (a) Lithologic units with travel time >900 m/s, interpreted as the bedrock and is obtained at a depth that varies between 5 and 20 m from ground level. The bedrock is a volcanic breccia unit with low weathering rates—fresh.

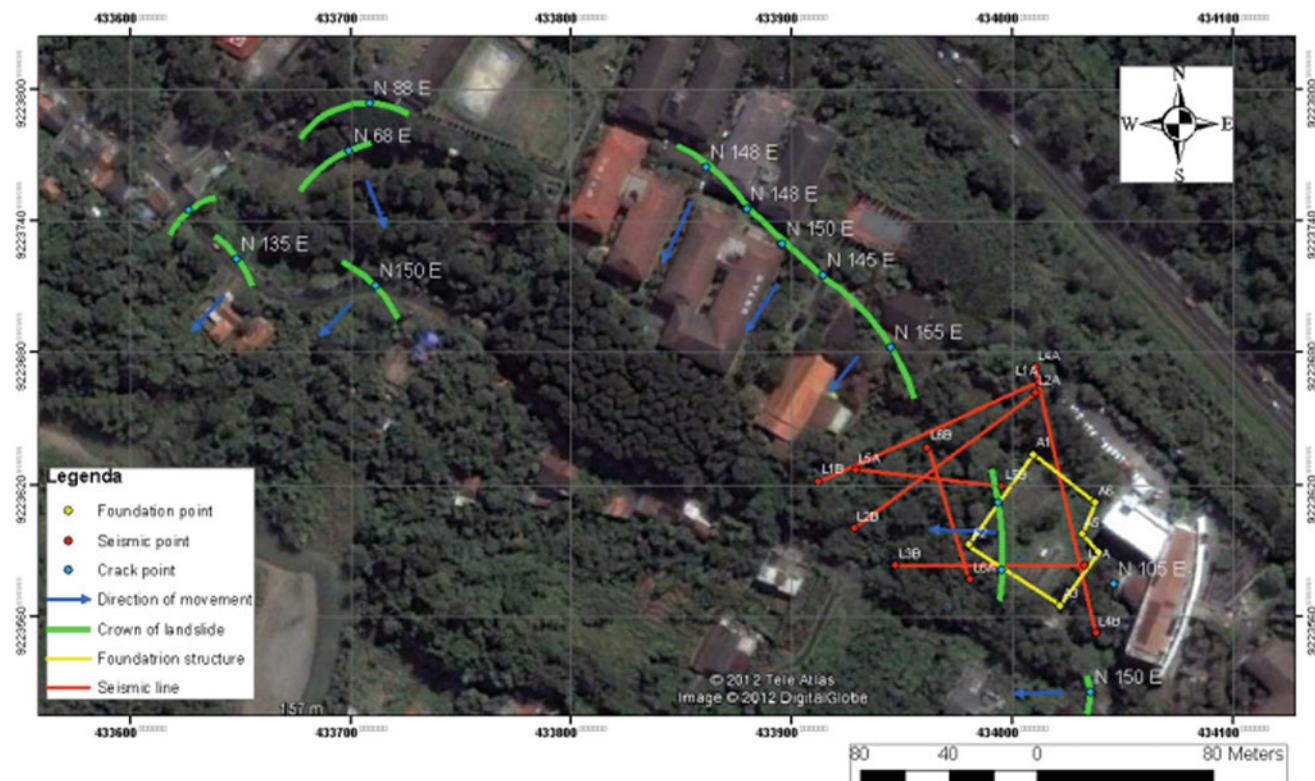


Fig. 3 Distribution of cracks in the UNIKA campus (blue line is the direction of creep movement, a green line connecting the blue dots which are the cracks, red lines are seismic survey lines)

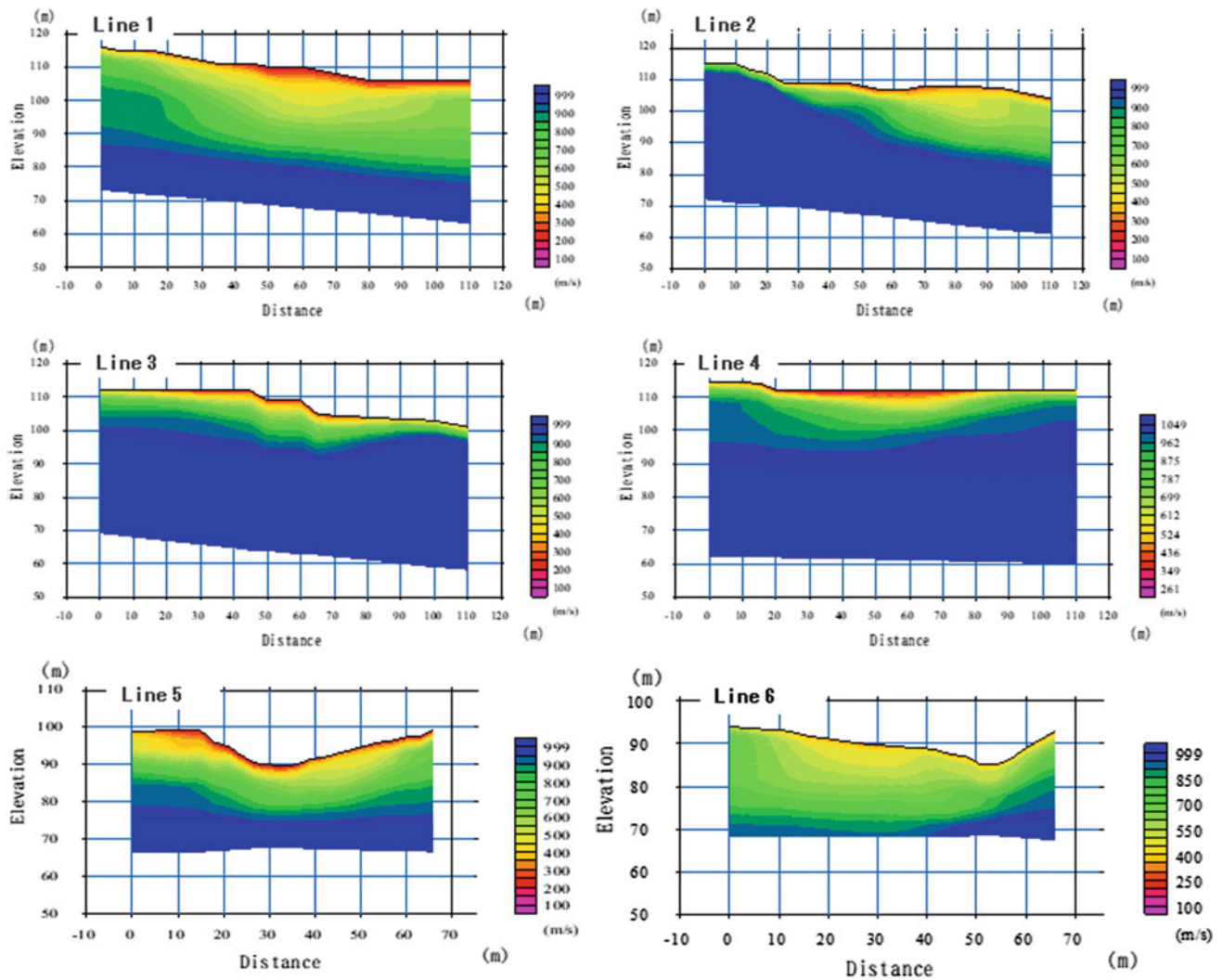


Fig. 4 Travel time of soil/rock layer based on a seismic survey in all six channels

- (b) Lithologic units with travel time 600–900 m/s, interpreted as sandy clay-clayey sand units, a result of weathering of the volcanic breccia unit. This layer located above the bedrock and has a thickness varies from 2 to 15 m, with an average thickness of 10 m.
- (c) Material units with travel time 300–600 m/s; this lithology was started at a depth of 1.5–2 m, with an average thickness of 5 m, estimated consists of clay-silt size materials.
- (d) Material units with travel time <300 m/s, interpreted as a layer of fill material at the project site location, with an average thickness of 1.5–2 m.

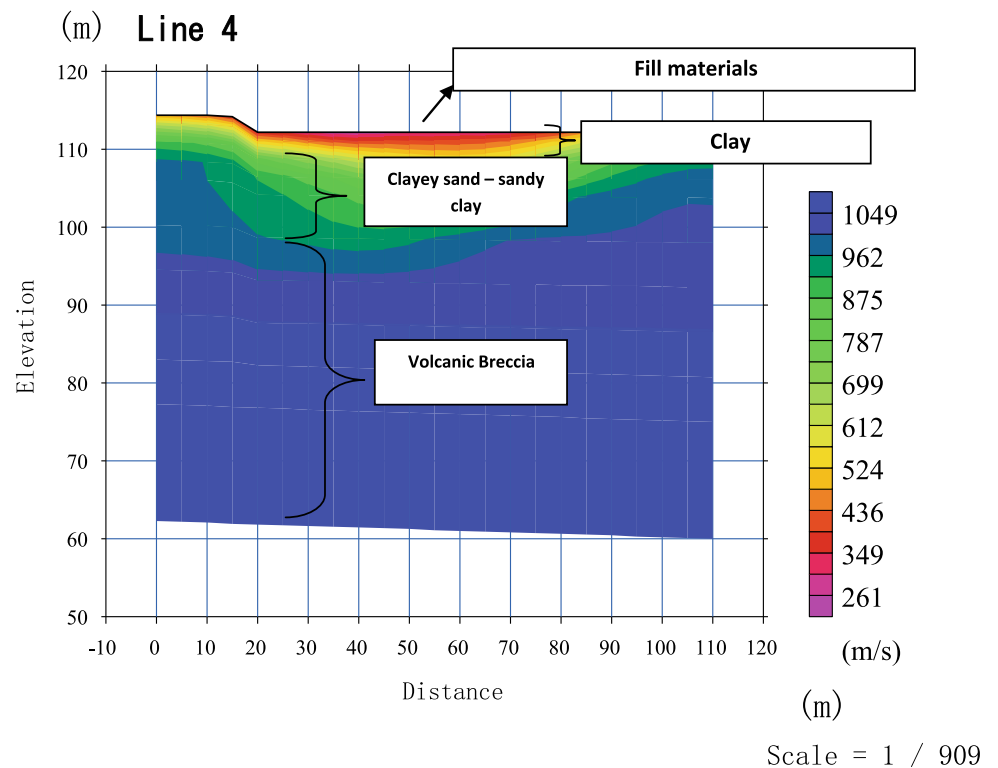
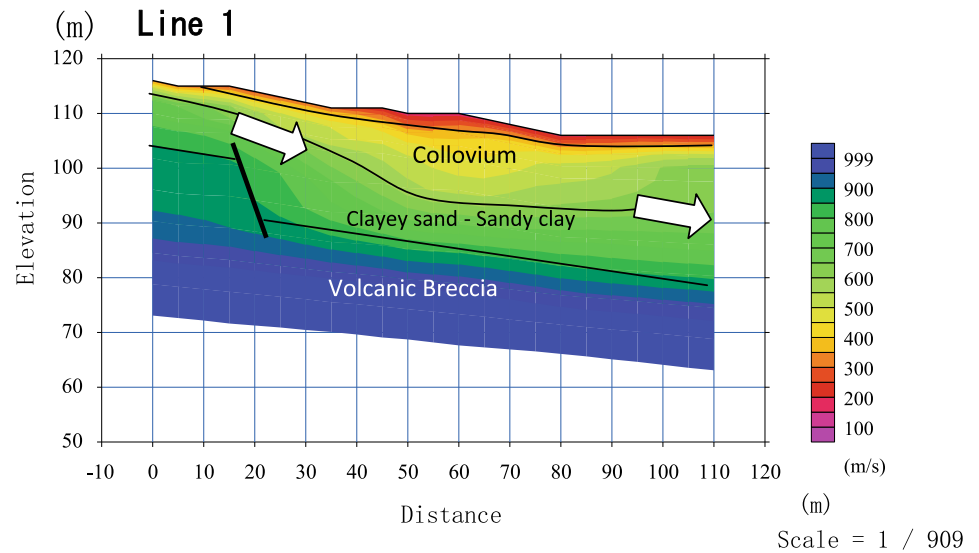
Interpretation of the presence of faults in the subsurface can be made based on seismic refraction data. Faults are interpreted from the discontinuity layer of travel time or a sudden change travel time layer from seismic measurements.

There are only 3 lines from 6 lines that indicated the presence of fault beneath the surface, as shown in Fig. 6.

Fault below the surface is interpreted at a distance of approximately 20 m from the measurement point Line 1, characterized by a sudden elevation difference in travel time on the same layer (greyish-green). The fault is estimated to be at a depth of 15–20 m from the ground with a length field of less than 15 m. At least two faults across the sports hall at a distance of approximately 50 and 65 m are identified based on the line measurement of seismic at the point L3. While the measurement of seismic line L5 indicates a fault in the subsurface encountered at shallow depths of 0–5 m from the surface and 15–20 m from the ground level. This interpretation is matching with the existing direction of cracks in the foundation of a sports hall project site (Fig. 7).

The sliding surface of the movement was indicated based on lithology and their characteristics. Volcanic breccia is

Fig. 5 Interpretation of lithology on Line 1 and Line 4 based on the travel time value

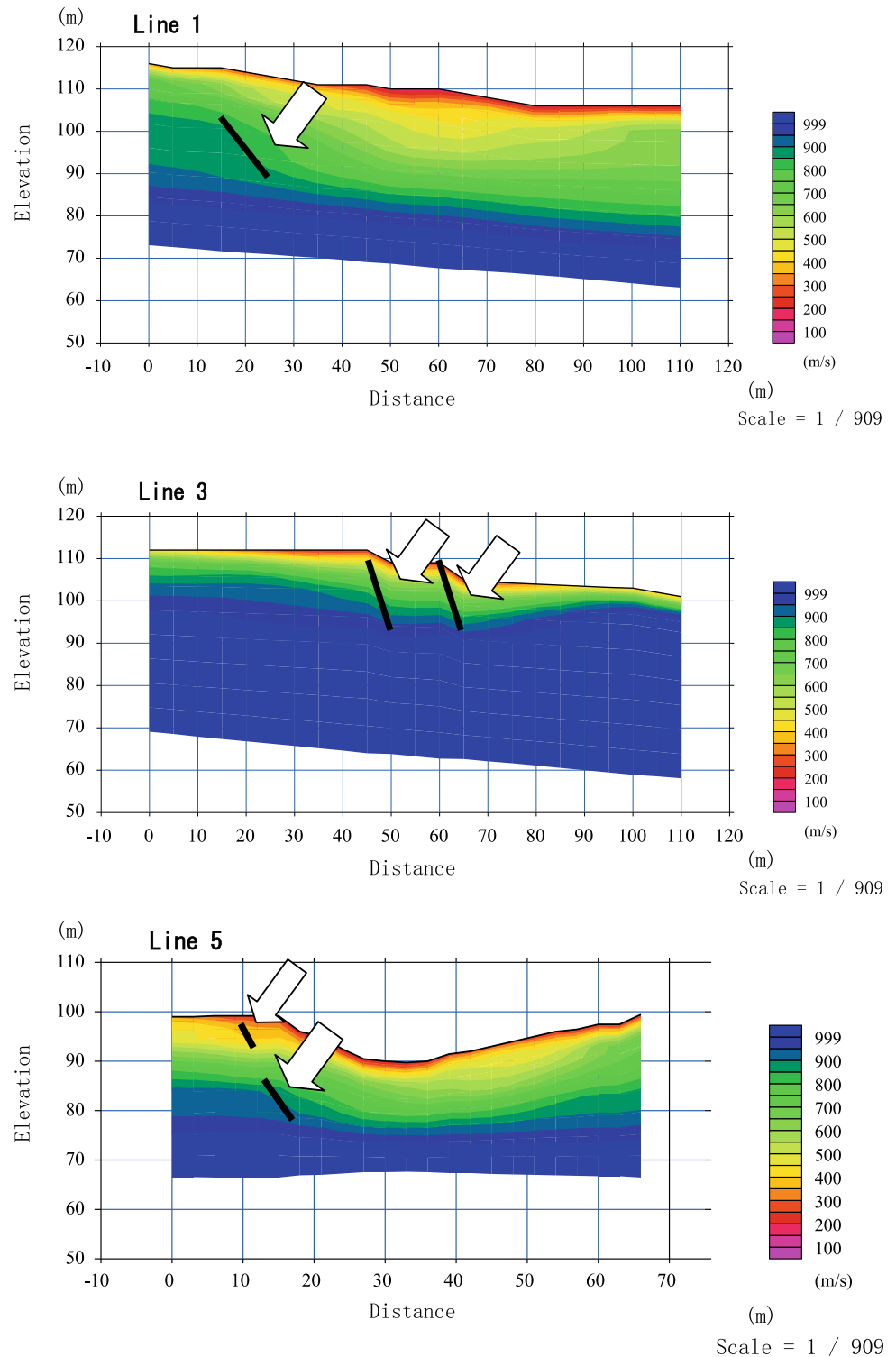


interpreted as a sliding surface due to impermeable materials. This layer has depth with high variation from 5 m up to 25 m depending on the location. The result is in line with previous research that mentions the sliding surface in Gunungpati area based on the geoelectrical survey have a depth 11–14 m (Wakhidah and Khumaedi 2014) and 12–26 m based on the drilling log data (Nugroho et al. 2012).

Conclusion

Soil movement at Sports Hall UNIKA Soegijapranata Campus has a thick around 5–25 m. It is controlled by the presence of large fractures of the crown complex of landslide with a sliding surface of the volcanic breccia. Based on the field

Fig. 6 Interpretation of fault/crack (black line) based on the travel time at Lines 1, 3 and 5



observation, the landslide is active and moves slowly. Therefore, the landmass movement will continue to move to follow the main landslide, which has been developed. The movement of the soil at the project site will be more progressive because (1) the increasing burden due to construction activities even when the building was finished, and

(2) the increased load due to the accumulation of a mass influx of groundwater in fragile lands such moves. One aspect that triggers the progressive movement is the increased volume of soil into the groundwater of the landmass.

The results of seismic refraction measurements show the crack of the landslide has a catchment area in the northeast

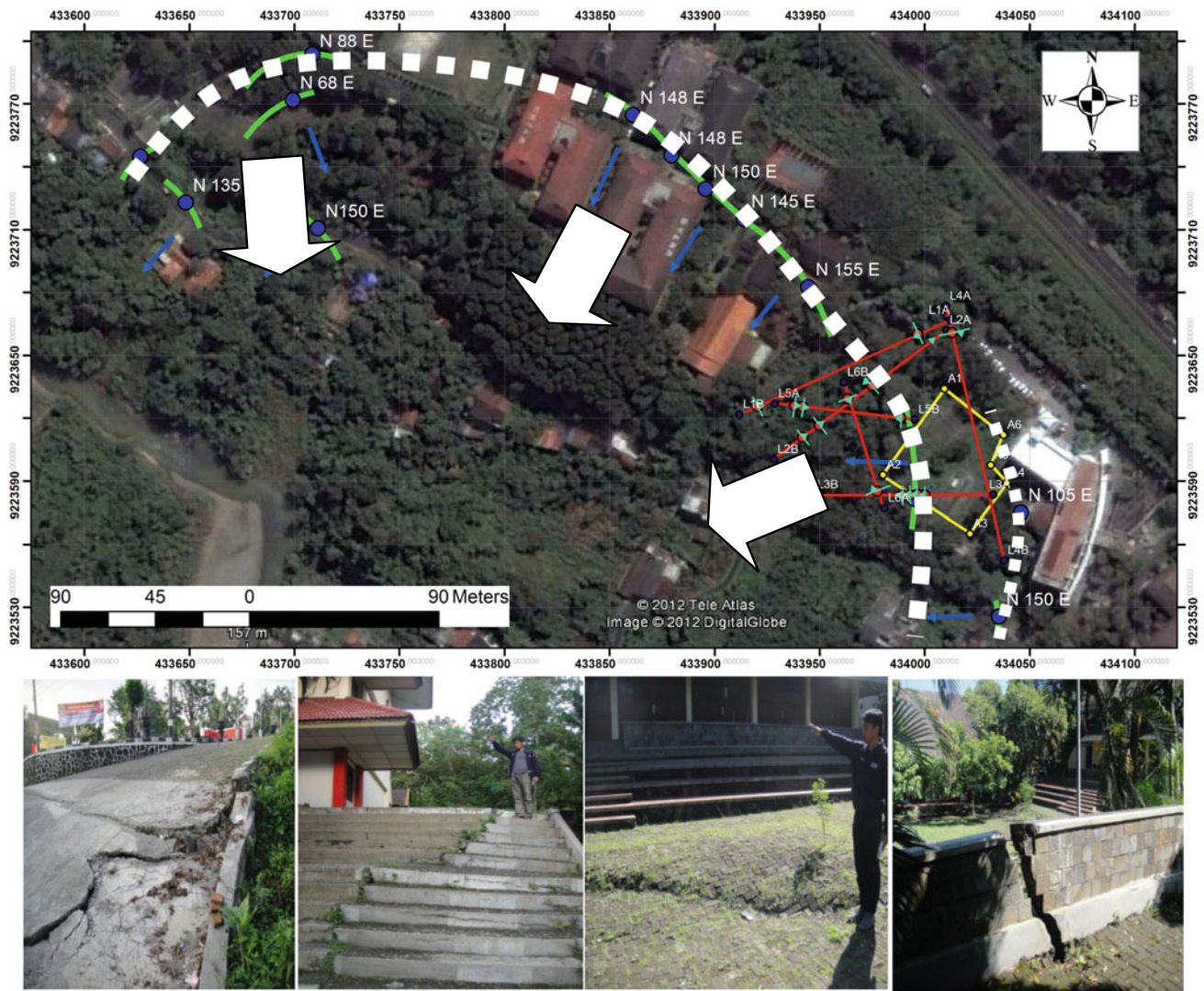


Fig. 7 Sports hall area inside the campus and existing cracks (white dashed line is the connecting crack spots which form a crown, big white arrows are the susceptible movement directions)

(highway Semarang-Jakarta), where the unit clayey sand exposed at the surface. Therefore, the water will be easier to seep into the soil and trigger the movement. It should be arranged to minimize the infiltrated water in the northeast area, and drainage is directed to the southwest.

Acknowledgements We acknowledge the help and assistance of our colleague Dr. Wiwit Suryanto and his team from Geophysics of UGM. The UNIKA Soegijapranata financially supports this research.

References

Alhassan DU, Dangana LM, Salako KA, Jonah SA, Ofor NP (2010) Seismic refraction investigation of the subsurface structure at the southern part of Niger State College of Education, Minna, Nigeria. *Bayero J Pure Appl Sci* 3(2):56–61

Anomohanran O (2013) Seismic refraction method: a technique for determining the thickness of stratified substratum. *Am J Appl Sci* 10(8):857–862

Department of Geological Engineering (1995) Research report on engineering geology for new building locations in Kampus Unika Soegijapranata area. Department of Geological Engineering UGM, Yogyakarta (in Indonesian language)

Kearey P, Brooks M, Hill I (2002) An introduction to geophysical exploration, 3rd edn. Blackwell, UK

Nugroho U, Cahyo HT, Purnomo M (2012) Mechanim of landslide in the road section Sekaran-Gunungpati Semarang. *J Teknik Sipil Perencanaan* 1(14):71–80 ((in Indonesian language))

PT. Selimut Bumi Adhi Cipta (2011) Geoelectrical Report of Sport Hall Universitas Soegijapranata, Semarang (in Indonesian language)

Thaden RE, Sumadirdja H, Richard PW (1975) Geologic map of Magelang and Semarang, Java. Directorate Geology of Bandung

Wakhidah N, Khumaedi DP (2014) Identification of soil movement using the Wenner-Schlumberger configuration method in Deliksari Gunungpati, Semarang. *Unnes Phys J* 3(1):1–6 ((in Indonesian language))



2020 Kyoto Japan

Preliminary Result of Real-Time Landslide Monitoring in the Case of the Hinterland of Koroška Bela, NW Slovenia

Tina Peternel, Ela Šegina, Matija Zupan, Mateja Jemec Auflič, and Jernej Jež

Abstract

Landslides are a common and widespread phenomenon in Slovenia, as they are in most European countries. Because we cannot avoid the risk of landslides and must live with it, it is important to understand and predict landslide dynamics. Research on landslide dynamics forms the basis of landslide hazard prevention and serves as a basic requirement for the development of prediction models and for defining prevention and mitigation measures. The principal aim of this study is to form a basis to predict real-time dynamics of landslides that have been posing a direct threat to settlement Koroška Bela (with approximately 2200 inhabitants) for centuries. Prediction modelling is based on monitoring and recognition of displacement triggering mechanisms and their interactions. The study area is located above the settlement of Koroška Bela (NW Slovenia, Karavanke) which exhibits a number of deep-seated landslides (the Urbas and Čikla landslides) in weathered siltstone and claystone.

Keywords

Real-time monitoring • Landslide • Koroška Bela • Slovenia

Introduction

Hillslope morphology, unfavourable geological and tectonic conditions as well as climatic diversity all contribute significantly to the high rate of exposure to landslides in Slovenia, as in most European countries (Haque et al. 2016; Herrera et al. 2018). Landslides in Europe are mostly concentrated in the mountainous areas and coastal cliffs, but many of them are strongly controlled by unfavourable geological conditions consisting of clay layers with weak geomechanical properties and the local hydrological setting (Crosta 1998; Herrera et al. 2018).

In recent years, landslide prediction modelling has become increasingly popular, and the topic is addressed by number of authors (Sassa et al. 2010; Federico et al. 2012; Li et al. 2012; Chae et al. 2017; Huang et al. 2017; Li et al. 2018; Gao et al. 2020). However, the reliable temporal prediction of landslide occurrence still remains a big challenge (Gao et al. 2020). To improve prediction models related practices in various parts of the world show that a good understanding of landslide dynamics can be achieved with the establishment of flexible and reliable monitoring systems (Stumpf 2013; Intrieri et al. 2013; Mihalič et al. 2015). This kind of systems is used to implement periodic and continuous measurements for monitoring displacement through time and space. It can be monitored using various surveying techniques (Michoud et al. 2012; Stumpf 2013; Peternel et al. 2017a, b; Peternel et al. 2018). Acquisition of systematic data on real-time displacement enables researchers to gain a better understanding, produce better interpretations of landslide dynamics and established correlation with their triggering mechanisms.

Landslide triggering mechanisms largely depend on hydro-meteorological data, which is very complex and changes in time and space. Consequently, reliable temporal prediction of landslide dynamics still remains a challenge. The ability to simulate this process using real-time monitoring data (displacement velocity, ground water level and

T. Peternel (✉) · E. Šegina · M. Zupan · M. J. Auflič · J. Jež
Geological Survey of Slovenia, Dimičeva ulica 14,
1000 Ljubljana, Slovenia
e-mail: Tina.Peternel@geo-zs.si

E. Šegina
e-mail: Ela.Segina@geo-zs.si

M. Zupan
e-mail: Matija.Zupan@geo-zs.si

M. J. Auflič
e-mail: Mateja.Jemec-Auffic@geo-zs.si

J. Jež
e-mail: Jernej.Jez@geo-zs.si

precipitation) can significantly improve the reliability of landslide prediction (Intrieri et al. 2013; Krkač et al. 2017; Devoli et al. 2018).

This paper presents preliminary results of observation of landslides above the settlement of Koroška Bela (NW Slovenia) using real-time monitoring data. Previous investigations showed that the hinterland of Koroška Bela settlement has number of source areas that have the potential to mobilize the material there into debris flow.

Data and Methods

Study Case

The hinterland of Koroška Bela is located in the outskirts of town Jesenice in the Karavanke mountain ridge in north-western Slovenia.

Historical sources describe the broader area of Koroška Bela as known to have experienced several debris-flow events in the recent geological past. The most recent of these events occurred back in the eighteenth century and caused the partial or total destruction of more than 40 buildings and cultivated areas in a Koroška Bela village located in the area of the debris fan deposits (Lavtižar 1897; Zupan 1937).

Presently, some 2200 inhabitants live in the area of the alluvial fan of past debris flows. With this risk potential in mind, monitoring the sliding mass and assessing the displaced material volumes is crucial, and more important than the purely scientific value of any assessment efforts (Peternel et al. 2017b). In this regard, the Koroška Bela hinterland was investigated using a combination of detailed engineering geological mapping, together with geotechnical, hydrogeological, geophysical and geodetic methods (Jež et al. 2008; Komac et al. 2014; Peternel 2017; Peternel et al. 2017a, 2017b, 2018; Janža et al. 2018). Previous research found out: (1) that Koroška Bela settlement lies on sequence of diamicton layers and related subaeric sediments that had been deposited by several debris flow events in the past (Jež et al. 2008) and that landslide in the hinterland of Koroška Bela mechanisms are related to: (1) geological and tectonic conditions affecting rocks that are heavily deformed, and, consequently, very prone to fast and deep weathering, (2) surface and underground water circulation and infiltration in the wider landslides area and precipitation (Peternel et al. 2018; Janža et al. 2018).

The hinterland of Koroška Bela has complex geological and tectonic conditions (Fig. 1). Geological units of this area are mainly represented by Upper Carboniferous and Permian sedimentary clastic rocks, Permian carbonates and Triassic to

Lower Jurassic carbonate rocks (Jež et al. 2008). The main slope instabilities are related to tectonic contacts between the Upper Carboniferous to Permian clastic rocks (claystone, siltstone, sandstone and conglomerate) and different Permian and Triassic carbonate and clastic rocks (Fig. 1).

In terms of tectonics, the area is part of the Košuta fault zone and is dissected by numerous NW–SE faults linking two major fault zones (the Sava and Periadriatic fault zones) (Jež et al. 2008). Due to active tectonics the Upper Carboniferous and Permian clastic rocks are heavily deformed, and, consequently, very prone to fast and deep weathering.

Due to its lithological and structural conditions and precipitation rates, the area of the Koroška Bela hinterland is highly prone to landslides. The upper part of the Urbas landslide at the main scarp and the part below are dominated by rockslides and runoff of the scree material. The main body of both landslides is formed by heavily deformed and weathered clastic rocks and is presumed to be a rotational deep-seated slow-motion slide that has accelerated predominantly with the percolation of surface and ground water (Jež et al. 2008; Komac et al. 2012; Peternel et al. 2018).

Landslides activity can be evidenced by hummocky terrain comprised of protrusions and depressions, curved pine trees, longitudinal tension cracks, erosion slumps and ponds on the surface, as well as the common deformation of local roads.

The monitoring sites have been established at the Urbas and Čikla landslides which are considered to be the most active parts of the Bela stream hinterland based on previous investigations and field observations (Jež et al. 2008; Peternel 2017; Peternel et al. 2017a; 2018).

The Urbas landslide is 420 m in length and 320 m in width, its estimated volume is 895,000 m³ and the main sliding direction is SW direction. The Čikla landslide has a length of 130 m, a length of 105 m and estimated volume of 140,000 m³.

The Urbas landslide is crossed by the Bela stream, meanwhile, the Čikla landslide is crossed by Čikla torrent which is a tributary of the Bela stream. Both landslides have a gully-type morphology. The sliding mass is composed of tectonically deformed and weathered Upper Carboniferous and Permian clastic rocks covered with a large amount of talus material, which is prone to slope instability (Peternel et al. 2018; Jež et al. 2019).

Recently, in April 2017, a part of Čikla landslide body collapsed and mobilized into mass flow with a huge amount of talus material and vegetation. The sliding material slide few hundred meters along the Čikla torrent. In the future this kind of event or larger could pose a direct risk to the underlying settlement Koroška Bela.

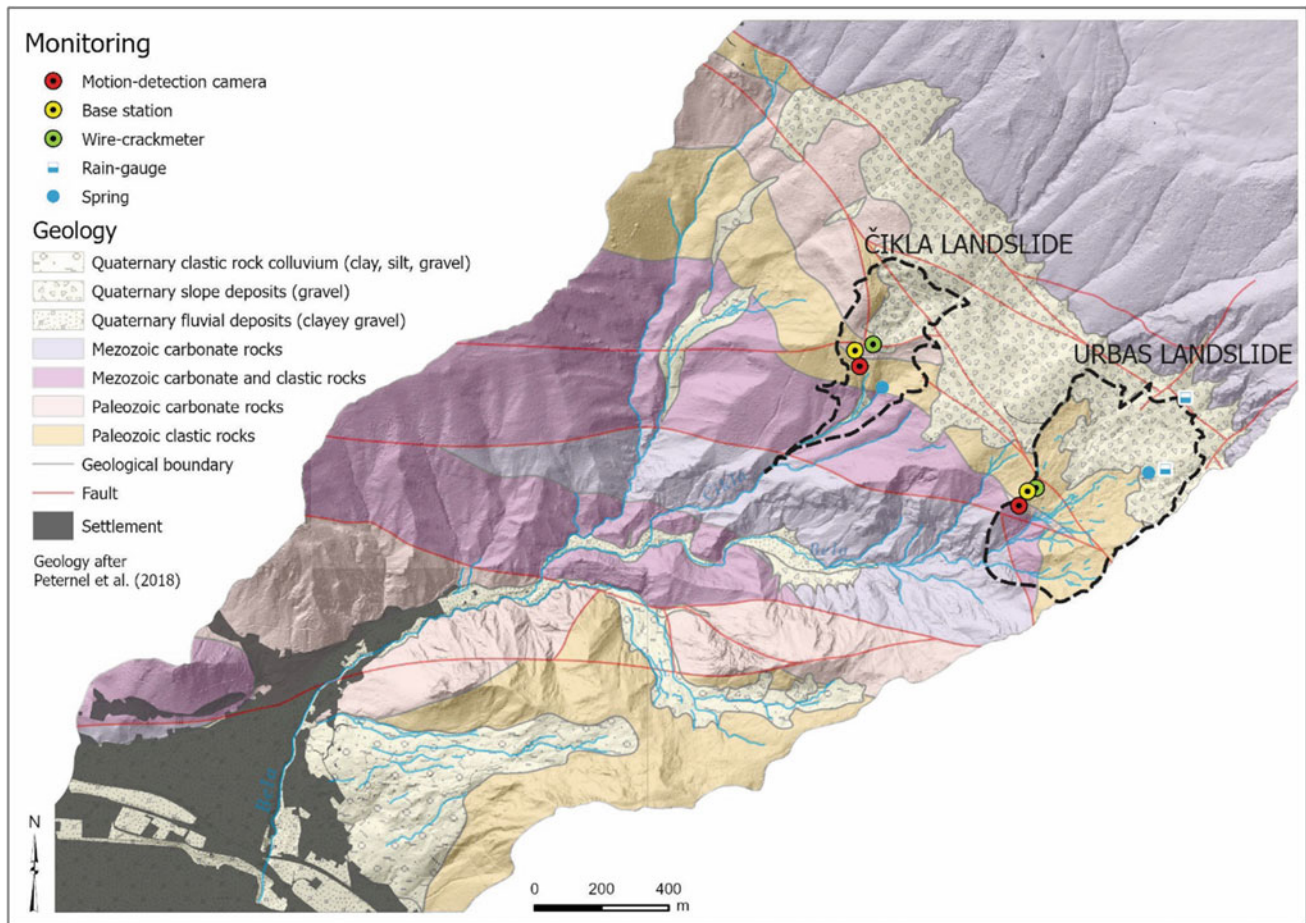


Fig. 1 Geological map of the hinterland of Koroška Bela with the spatial distribution of applied monitoring equipment

Real-Time Monitoring System

In order to assess the landslides dynamics it was crucial to implement a flexible and reliable real-time monitoring system. The Urbas and Čikla monitoring systems were established in the frame of the project “Establishment of real-time monitoring system for Urbas and Čikla landslide” founded by Municipality Jesenice in order to provide real-time data on displacements and to monitor the kinematics of the landslides. To achieve this, different (low-cost) geotechnical sensors were set up at specific sites on the Urbas and Čikla landslides. Each established monitoring site consist of (Fig. 2):

1. wire crackmeter allows to monitor the changes in the distance between two anchor points;
2. motion detection camera automatically transmits an image of observed area when motion is detected;
3. geotechnical sensors are wired and powered through base station which also serves as in-situ data storage.

Precipitation data (mm) for the whole area of the hinterland of Koroška Bela is gathered by one rain-gauge which is located atop of Urbas landslide.

The monitoring sites are located at the lower parts of Urbas and Čikla landslides which are considered to be the most active. The sliding mass of both landslides is composed of tectonically deformed and weathered Upper Carboniferous and Permian clastic rocks covered with a large amount of limestone talus material. Additionally, the Bela stream and its Čikla tributary cause significant erosion and increase the possibility of the sliding mass mobilizing downstream. The active parts of the Urbas and Čikla landslides are characterized by bare ground with fallen trees, rugged surfaces, strong gully erosion and flank ridges (Peternel et al. 2018; Jež et al. 2019).

The observation period for landslide Urbas started in June 2019, meanwhile landslide Čikla has been monitored since 12 August 2019.

The selection of the most suitable monitoring techniques and location largely depended on the geological and

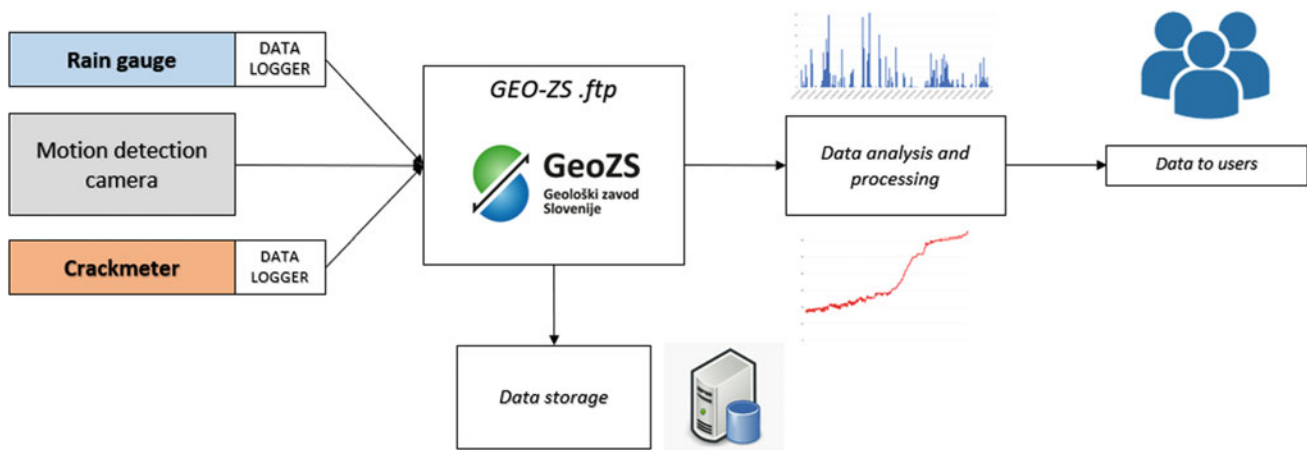


Fig. 2 A schematic presentation of sensor network and data management scheme in landslide monitoring system to monitor landslide Urbas and Čikla

morphological conditions (size and extent of study site, surface material, etc.).

Figure 2 shows a schematic presentation of sensor network and data management scheme that has been implemented at the Urbas and Čikla landslide in order to monitor their dynamics.

Results and Discussion

A prediction modelling at the monitoring sites (lower parts of landslides Urbas and Čikla) was carried by analysing data series gathered by continuous monitoring of landslide displacements and rainfall data.

Table 1 shows the initial and final state of crackmeter for 2 monitoring periods. At landslide Urbas monitoring using crackmeter started on 1st of June, meanwhile at landslide Čikla began on August 12th due to installation issues. In this paper we used data until December 31st, 2019. Both crackmeters have been collecting hourly data (with minor interruptions).

Table 2 and graph in Fig. 3 represents the monitoring result for the monitoring periods. In graph hourly displacements are represented by dots (Urbas: red and Čikla:

orange), sometimes seen as short vertical lines—daily fluctuation.

Rainfall is represented by daily and monthly cumulative values.

As shown in Fig. 3 two types of displacements can be observed:

- (1) Steady displacements,
- (2) Episodic rapid displacements.

During the entire monitoring period (7 months) the toe of Urbas landslide moved for app. 42 mm. Based on Urbas crackmeter data, landslide Urbas has experienced steady displacements. Higher displacement rate (app. 16.5 mm) was calculated during the November rainy period. The rough estimate of the displacement rate during this period amounts to app. 18.8 mm per month and appears rather steady.

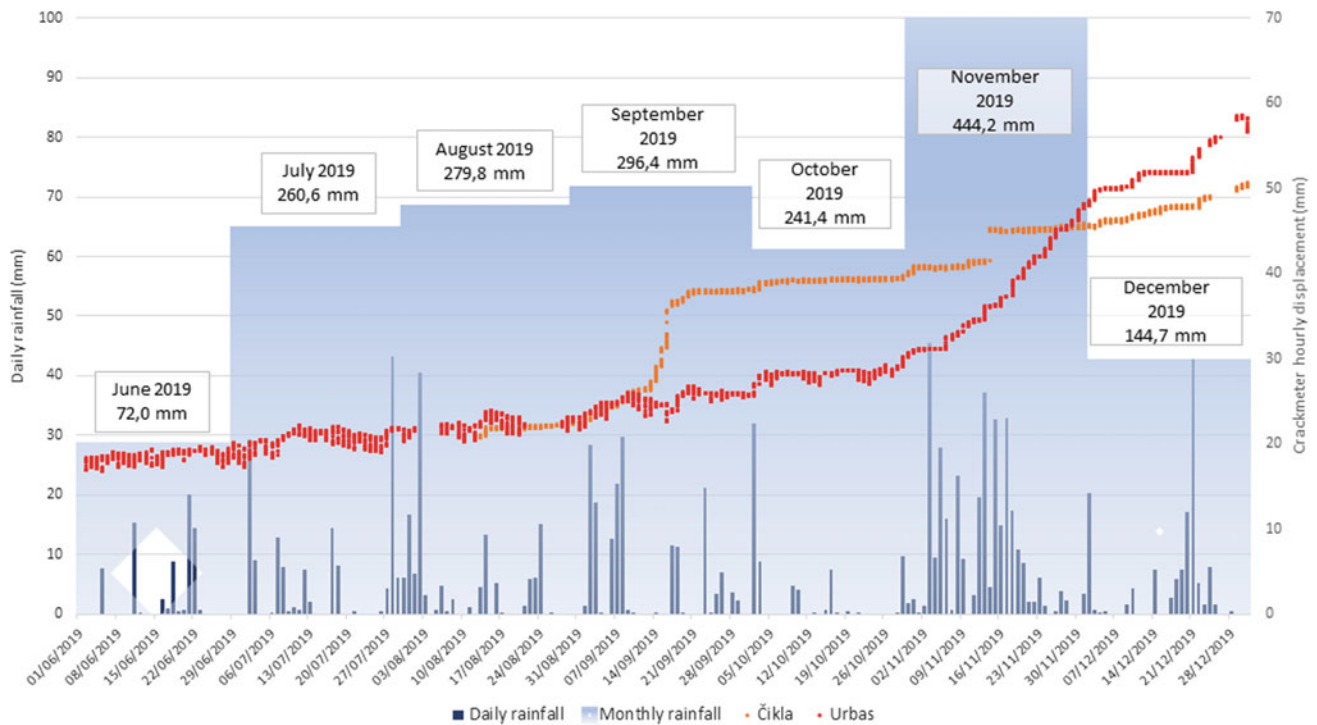
Čikla landslide has shorter observation period. During the observation period (4.5 months), the toe of Čikla landslide moved for app. 30.0 mm. It has experienced two episodic rapid displacements. The first one could be related to September rainfall event with displacement rate of 15.6 mm, meanwhile the second one (6.0 mm) is considered to be related to November rainy period as in the case of landslide Urbas.

Table 1 Initial and final state of crackmeter

Landslide	Monitoring period	Period length (month)	Initial state of crackmeter (mm)	Final state of crackmeter (mm)	Δ (mm)
Urbas	(1/6/2019–31/12/2019)	7	16.8	58.6	41.8/7 mth
Čikla	(12/8/2019–31/12/2019)	4.5	20.7	50.6	30.0/4.5 mth

Table 2 Monthly amount of rainfall (mm) and cumulative monthly displacements (mm) for Urbas and Čikla landslides

	Jun 2019	Jul 2019	Aug 2019	Sept 2019	Oct 2019	Nov 2019	Dec 2019
Monthly amount of rainfall (mm)	72.0 mm	260.6 mm	279.8 mm	296.4 mm	241.4 mm	444.2 mm	144.7 mm
Urbas cum. displ. (mm/mth)	3.2	2.1	1.7	2.9	4.2	16.5	11.1
Čikla cum. Dipl (mm/mth)	/	/	2.0	15.6	2.6	6.0	3.8

**Fig. 3** Monitoring result for the period from 1 June 2019 until 31 December 2019. Graph shows cumulative daily rainfall, cumulative monthly rainfall and hourly displacement rate measured at Čikla and Urbas landslides

Compared to Urbas landslide, Čikla landslide has more unregular dynamics. The apparently steady displacement rate occurred outside the periods 15.9.–16.9.2019 and on 14.11.2019 when considerable displacements have been recorded. For this reason, the continuous slow displacement rate is hard to determine.

Episodic rapid displacements that have been detected in the toe of Čikla landslide were short in time but were characterized by high intensity and consider to be related to prolonged or intense precipitation. It is apparent that both landslides exhibit rather different internal dynamics, which is, among the others, most probably correlated to the groundwater level and also to morphology of the terrain and the size of the landslide masses.

Conclusions

The preliminary results of real-time landslide monitoring suggest that the movement pattern represents a combination of steadily sliding mass behaviour as well as episodic rapid displacements corresponding to increased rainfall. In the both cases (Urbas and Čikla landslides) sliding material is moving downslope towards the bottom of the landslide toe where the material is being fed into the stream. It is essential to point out that surge events of larger dimensions could dam the Bela torrent, which could pose a hydrological hazard for the village downstream.

In order to estimate the real effect of meteorological and hydrogeological conditions on landslide dynamics, the model should consider also groundwater levels related to precipitation, landslide displacements, geotechnical properties in correlation with groundwater levels.

In the future steps we are looking to develop prediction model depend on the definition of threshold values that will be calculated based on a time series of data on landslide displacements, groundwater levels and precipitation. Data will be gathered from a monitoring system that include inclinometers, piezometers, rain-gauges and geotechnical sensors (wire crack meter, tiltmeter, etc.).

Acknowledgements The results of this study are part of the projects “Establishment of real-time monitoring system for Urbas and Čikla landslide” founded by Municipality Jesenice; J1-8153 “Studying Landslide Movements from Source Areas to Zone of Deposition using a Deterministic Approach” that is financed by the Slovenian Research Agency (ARRS). Moreover, part of investigations has been also financially supported by the Ministry of the Environment and Spatial Planning and Municipality Jesenice.

References

- Chae BG, Park HJ, Catani F, Simoni A, Berti M (2017) Landslide prediction, monitoring and early warning: a concise review of state-of-the-art. *Geosci J* 21(6):1033–1070
- Crosta G (1998) Rationalization of rainfall threshold: an aid to landslide hazard evaluation. *Environ Geol* 35:131–145
- Devoli G, Tiranti D, Cremonini R, Sund M, Boje S (2018) Comparison of landslide forecasting services in Piedmont (Italy) and Norway, illustrated by events in late spring 2013. *Nat Hazards Earth Syst Sci* 18:1351–1372
- Federico A, Popescu M, Elia G, Fidelibus C, Internò G, Murianni A (2012) Prediction of time to slope failure: a general framework. *Environ Earth Sci* 66:245–256
- Gao W, Dai S, Chen X (2020) Landslide prediction based on a combination intelligent method using the GM and ENN: two cases of landslides in the Three Gorges Reservoir, China. *Landslides* 17:111–126
- Haque U, Blum P, da Silva PF, Andersen et al (2016) Fatal landslides in Europe. *Landslides* 13:1545–1554
- Herrera G, Mateos RM, Garcia-Davalillo JC, Grandjean G, Poyiadji E, Maftai R, Filipciuc TM, Jemec Auflič M, Jež J, Podolszki L, Trigila A, Iadanza C, Raetzo H, Kociu A, Przyłucka M, Kułak M, Sheehy M, Pellicer XM, McKeown C, Ryan G, Kopačková V, Frei M, Kuhn D, Hermanns RL, Koulermou N, Smith CA, Engdahl M, Buxó P, Gonzalez M, Dashwood C, Reeves H, Cigna F, Liščák P, Pauditš P, Mikulénas V, Demir V, Raha M, Quental L, Sandić C, Fusi B, Jensen OA (2018) Landslide databases in the Geological Surveys of Europe. *Landslides* 15:359–379
- Huang F, Huang J, Jiang S, Zhou C (2017) Landslide displacement prediction based on multivariate chaotic model and extreme learning machine. *Eng Geol* 218:173–186
- Intrieri E, Gigli G, Casagli N, Nadim F (2013) Landslide early warning system: toolbox and general concepts. *Nat Hazards Earth Syst Sci* 13:85–90
- Janža M, Serianz L, Šram D, Klasinc M (2018) Hydrogeological investigation of landslides Urbas and Čikla above the settlement of Koroška Bela (NW Slovenia). *Geologija* 61(2):191–203
- Jež J, Mikoš M, Trajanova M, Kumelj Š, Budkovič T, Bavec M (2008) Vršaj Koroška Bela – Rezultat katastrofičnih pobočnih dogodkov. *Geologija* 51(2):219–227
- Jež J, Peternel T, Milanič B, Markelj A, Novak M, Celarc B, Janža M, Jemec Auflič M (2019) Čikla landslide in Karavanke Mts (NW Slovenia). In: Uljarevič M et al (eds) Proceedings of the 4th regional symposium on landslides in the Adriatic—Balkan Region. Geotechnical Society of Bosnia and Herzegovina, Sarajevo
- Komac M, Holly R, Mahapatra P, Van der Marel H, Bavec M (2014) Coupling of GPS/GNSS and radar interferometric data for a 3D surface displacement monitoring of landslides. *Landslides* 12(2):241–257
- Krkač M, Špoljarič D, Bernat S, Mihalič Arbanas S (2017) Method for prediction of landslide movements based on random forests. *Landslides* 14:947–960
- Lavtižar J (1897) Zgodovina župnij in zvonovi v dekaniji Radolica. Self-published, Ljubljana
- Li X, Kong J, Wang Z (2012) Landslide displacement prediction based on combining method with optimal weight. *Nat Hazards* 61(2):635–646
- Li H, Xu Q, He Y, Deng J (2018) Prediction of landslide displacement with an ensemble-based extreme learning machine and copula models. *Landslides* 15:2047–2059
- Michoud C, Abellan A, Derron MH, Jaboyedoff M (2012) Review of techniques for landslide detection, fast characterization, rapid mapping and long-term monitoring. SafeLand deliverable 41 (7th Framework Programme). Université de Lausanne
- Mihalič Arbanas S, Arbanas Ž (2015) Landslides: a guide to researching landslide phenomena and processes. In: Gaurina-Međimurac N (ed) Handbook of research on advancements in environmental engineering. Hershey, Pennsylvania, pp 474–510
- Peternel T (2017) Dinamika pobočnih masnih premikov na območju Potoške planine z uporabo rezultatov daljinskih in terestričnih geodetskih opazovanj ter in-situ meritev. Dissertation, Univerza v Ljubljani
- Peternel T, Kumelj Š, Oštir K, Komac M (2017) Monitoring the Potoška planina landslide (NW Slovenia) using UAV photogrammetry and tachymetric measurements. *Landslides* 14(1):395–406
- Peternel T, Jež J, Milanič B, Markelj A, Jemec Auflič M, Kumelj Š, Celarc B, Novak M, Janža M, Šram D, Serianz L, Bole Z, Demšar M, Klasinc M, Sodnik J (2017b) Izvedba najnujnejših inženirskogeoloških, hidrogeoloških, geofizikalnih in geomehanskih ter geodetskih raziskav za ugotovitev objektivne stopnje tveganja za prebivalstvo zaradi masnih premikov na območju Potoške planine in izdelava strokovnih podlag s predlogi zaščitnih ukrepov: izdelava celovitih geoloških strokovnih podlag in izdelava modela monitoringa za oceno ogroženosti naselja Koroška Bela s pojavi pobočnega masnega premikanja. Geološki zavod Slovenije, Ljubljana
- Peternel T, Jež J, Milanič B, Markelj A, Jemec Auflič M (2018) Engineering-geological conditions of landslides above the settlement of Koroška Bela (NW Slovenia). *Geologija* 61(2):177–189
- Sassa K, Osamu N, Solidum R, Yamazaki Y, Ohta H (2010) An integrated model simulating the initiation and motion of earthquake and rain induced rapid landslides and its application to the 2006 Leyte landslide. *Landslides* 7:219–236
- Stumpf A (2013) Landslide recognition and monitoring with remotely sensed data from passive optical sensors. Dissertation, University of Strasbourg
- Zupan G (1937) Krajevni leksikon Dravske banovine. Uprava Krajevnega leksikona dravske banovine, Ljubljana



2020 Kyoto Japan

Quantitative Risk Analysis of Earthquake-Induced Landslides

Saskia de Vilder, Chris Massey, Tony Taig, Biljana Lukovic, Garth Archibald, and Regine Morgenstern

Abstract

Quantitative risk analysis is a valuable tool in risk management, yet the calculation of risk is often hampered by a lack of quality spatial input data, particularly landslide event inventories. These event inventories provide information to determine the number, size and spatial location of landslides triggered by discrete events such as rainfall or earthquakes. This paper presents an approach whereby we use historical New Zealand earthquake-induced landslide inventories to estimate the landslide hazard for the Franz Josef and Fox glacier valleys, West Coast, South Island, New Zealand, as no pre-existing complete earthquake-induced landslide inventories exist for this area of New Zealand. We outline a methodology for the calculation of earthquake-induced landslide magnitude-frequency relationships from the 2016 Mw 7.8 Kaikōura earthquake, the 1968 Mw 7.1 Inangahua earthquake, and the 1929 Mw 7.8 Murchison earthquake to determine the probability of a given volume of landslide occurring for different levels of ground shaking.

Keywords

Earthquake-induced landslides • Magnitude—frequency analysis • Quantitative risk analysis

Introduction

Quantitative risk analysis (QRA) is an important tool for assessing, managing and communicating the risk from landslide hazards (Corominas et al. 2014). However, QRA can often be difficult to undertake due to the lack of relevant input spatial data (Westen and Soeters 2006; van Westen et al. 2008). This is particularly true for landslides triggered by discrete events, such as earthquakes and rainfall (Westen and Soeters 2006), where a particular location may not have a record of landslides generated by such an event. A landslide inventory provides information critical to understand landslide susceptibility, magnitude and frequency, and therefore landslide hazard (Guzzetti et al. 2012). In tectonically active areas, the lack of magnitude-frequency and susceptibility information for landslides generated by earthquakes represents a limitation in an accurate and complete calculation of risk for all landslide hazards. Numerous New Zealand landslide event inventories exist for earthquake-induced landslides (e.g. Hancox et al. 2002; Rosser et al. 2017; Massey et al. 2018). However, no complete landslide event inventories exist for an Alpine Fault earthquake, which represents a major contributor to the seismic hazard in New Zealand (Stirling et al. 2012). To address this gap in information we use landslide event inventory data from the other historical earthquake-induced landslide inventories, which share similar geological, geomorphological and climatic characteristics with the West Coast of New Zealand. Relationships derived from this data are used to estimate the landslide hazard from earthquakes for two case-study areas: the Franz Josef and Fox glacier valleys, West Coast, South Island, New Zealand (Fig. 1).

S. de Vilder (✉) · C. Massey · B. Lukovic · G. Archibald · R. Morgenstern
GNS Science, 1 Fairway Drive, Avalon, Lower Hutt, 5010, New Zealand
e-mail: s.devilder@gns.cri.nz

C. Massey
e-mail: c.massey@gns.cri.nz

B. Lukovic
e-mail: b.lukovic@gns.cri.nz

G. Archibald
e-mail: g.archibald@gns.cri.nz

R. Morgenstern
e-mail: r.morgenstern@gns.cri.nz

T. Taig
TTAC Ltd., 10 The Avenue, Marston, CW9 6EU, Cheshire, UK
e-mail: tony.taig@ttac.co.uk

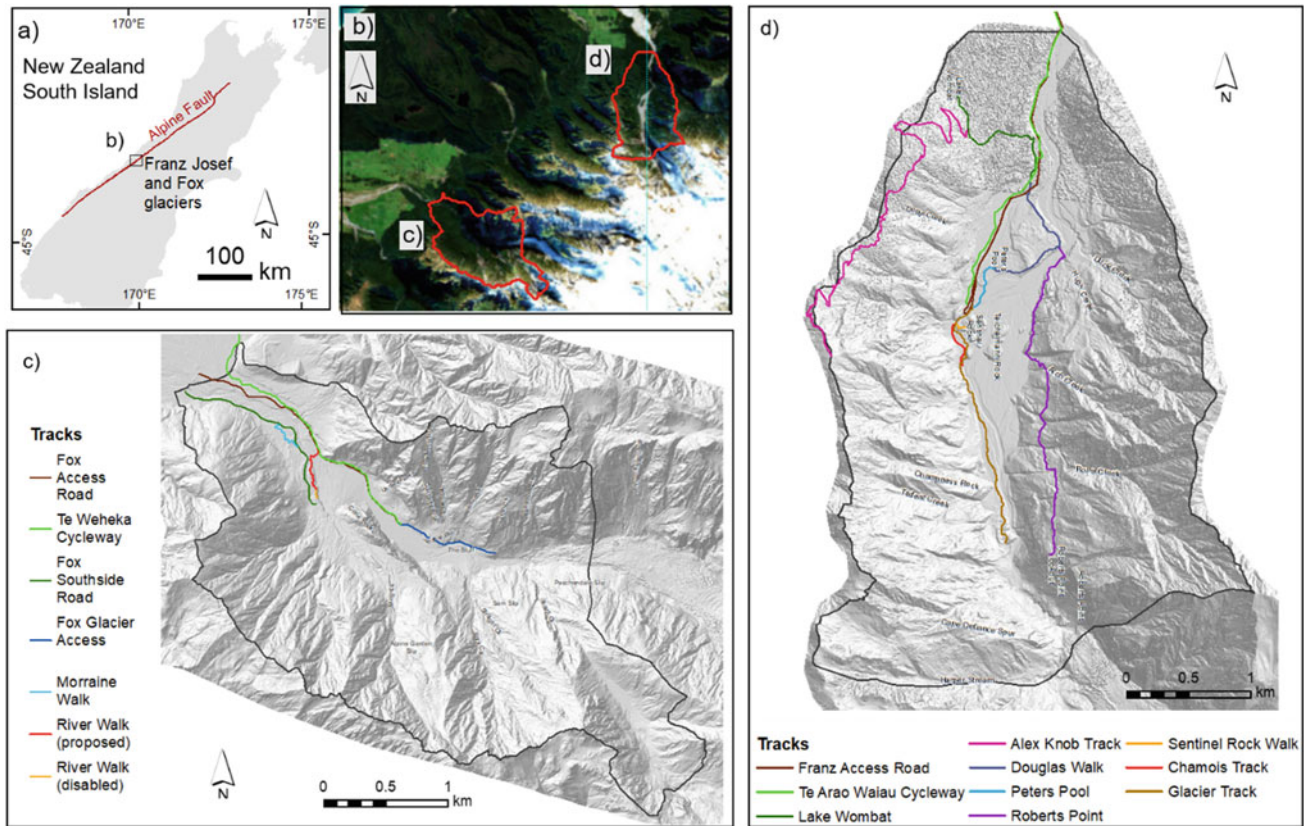


Fig. 1 Location of the Franz Josef and Fox Glacier Valley on the West coast of the South Island (a, b). c Fox Glacier Valley, including roads and tracks within it. d Franz Josef Glacier valley, including the roads and tracks within it

Case Study: Franz Josef and Fox Glacier Valleys

Franz Josef and Fox glacier valleys are important tourist destinations, which contain a series of tracks and walks that allow visitors to easily access and experience a glacial environment. Evidence of landsliding is present within each valley, including documented instances of landslides debris reaching the tracks, cycleways and roads in both valleys. Earthquakes are a potential triggering mechanisms, with the valleys located proximal, within ~ 2 km, to the Alpine Fault (Fig. 1a) The valleys are dominated by ice-free slopes comprised of Alpine Schist, with the quality of the fractured rock mass highly variable within both valleys, changing with proximity and location relative to persistent faults throughout the valleys (Cox and Barrell 2007).

Risk Analysis Approach

To undertake a complete landslide QRA, we use information from historical New Zealand earthquake inventories to forecast the generation of earthquake-induced landslides. We

use the landslide inventories from the 2016 Mw 7.8 Kaikōura earthquake (Massey et al. 2018), the 1968 Mw 7.1 Inangahua earthquake (Hancox et al. 2014), and the 1929 Mw 7.8 Murchison earthquake (Hancox et al. 2015). We selected these three landslide inventories as they represent the most complete New Zealand inventories for earthquake triggered landslides that occurred in fractured hard rock (such as greywacke) similar to that of schist. The three landslide inventories also occurred in mountainous and hilly terrain. Within this paper, we specifically detail the method we undertook to derive landslide magnitude-frequency relationships for different levels of ground shaking to understand the number and size of landslides that could be generated in earthquake events. We carried out this magnitude–frequency assessment in four stages, by:

1. Estimating the landslide frequency and source area scaling relationship
2. Estimating the landslide source area to volume scaling relationship
3. Investigating the relationship between landslide occurrence and peak ground acceleration (PGA), slope angle and lithology using the Kaikōura, Inangahua, and Murchison inventories; and

- Combining the estimates of the annual frequency of the representative event PGA from the Probabilistic Seismic Hazard Model (PSHM) (Stirling et al. 2012) for New Zealand with the relationship between landslide occurrence, slope area and PGA as determined in step 3.

We determine the spatial susceptibility to earthquake-induced landsliding by applying the logistic regression model of Massey et al. (2018) to each of the glacier valleys. We use both the magnitude-frequency relationships, and the susceptibility model to estimate the spatial and temporal earthquake-induced landslide hazard and associated risk within each valley.

Methodology

Landslide Frequency to Source Area Scaling

We derived a relationship between landslide frequency and landslide source area to determine how many landslides of a particular size are likely to occur for a given earthquake event. Many studies have documented an inverse power-law relationship for landslide frequency–area distributions (FAD), whereby smaller landslides occur more frequently than larger landslides (cf. Tanyaş et al. 2018). The power law exponents for Kaikōura, Inangahua and Murchison are 1.88, 2.71, and 2.62, respectively. Differences in landslide size, type, distribution and trigger mechanism do not appear to affect this relationship (Malamud et al. 2004).

Landslide Source Area to Volume Scaling

We convert landslide area (A) to landslide volume (V), using the following power-law relationship:

$$V = \alpha A^{\gamma}$$

Many studies document a power law relationship between landslide volume and landslide area (e.g. Guzzetti et al. 2009; Larsen et al. 2010). These power-law relationships have been produced for the landslide inventories of Inangahua and Murchison from field measurements of landslide depth to calculate volume (Hancox et al. 2014, 2015), and change models derived from digital surface models (DSMs) from the Kaikōura earthquake (Massey et al. 2020). The exponents for each of the three inventories are outlined in Table 1. We take the mean of the exponents to create a mean power law relationship.

Development of Magnitude—Frequency Relationships

We determined the number of landslides that occurred at different levels of peak ground acceleration (PGA) for each earthquake event. We used PGA as it displays a strong correlation with landslide occurrence (e.g. Hancox et al. 2002; Meunier et al. 2007; Massey et al. 2018). For Inangahua and Murchison earthquakes, the PGA values were derived from a PGA isoseismal grid generated for each earthquake. For the Kaikōura earthquake, PGA values were derived from ShakeMap NZ (GeoNet 2016). The PGA values were grouped into 5 PGA bands:

- Band 1: <0.2 g
- Band 2: 0.2–0.35 g
- Band 3: 0.35–0.65 g
- Band 4: 0.65–1.2 g
- Band 5: >1.2 g.

We determined the cumulative number of landslides for different landslide source area categories within each PGA band. For the landslide source area bins, we adopted bin widths that increased with increasing landslide source area, so that bin widths were equal in logarithmic space. For each PGA band, we divided the number of landslides by the total slope area which experienced that PGA, and had a slope angle of greater than 30°, as we assumed that any slope with an angle greater than 30° could generate landslides. We converted the landslide source areas into volumes using our mean exponent values (see Table 1). We then determined the relationships between cumulative number of landslides greater than a given volume occurring per km² and landslide volume (see Fig. 1). We fitted power law relationships by defining a minimum landslide volume bin of 10,000 m³ for bands 3 and 4, and a minimum landslide volume bin of 17,800 m³ for Band 5, as the data less than these landslide volumes deviates from the linear log-log power law relationship and displays the “roll-over” effect. We use these power laws to forecast the cumulative number of landslides greater than a give volume class per km² for each PGA band. The power law scaling exponents were varied for each PGA band based on the power law fits to the data (Table 2).

No landslides were mapped by Hancox et al. (2014, 2015) or Massey et al., (2018) in PGA band 1, indicating that 0.2 g is the likely threshold above which landslides tend to occur. Only a few small landslides were mapped by Massey et al. (2018) in the PGA band 2, indicating that

Table 1 Magnitude—Frequency Exponents for the three New Zealand earthquake-induced landslide inventories of Kaikōura (Massey et al. 2020), Inangahua (Hancox et al. 2014) and Murchison (Hancox et al. 2015)

Earthquake Inventory	Log α	γ
Kaikōura	0	1.076
Inangahua	0	1.125
Murchison	−0.05	1.165
Mean	−0.017	1.122

Table 2 Magnitude–frequency exponents of the number landslides generated of a given volume for different levels of ground shaking

Earthquake inventory	Log α	γ
Band 2 ^a	6.59	−1.88
Band 3	6.76	−1.76
Band 4	7.33	−1.67
Band 5	7.64	−1.62

^aInterpolated power law relationship from bands 3 to bands 5

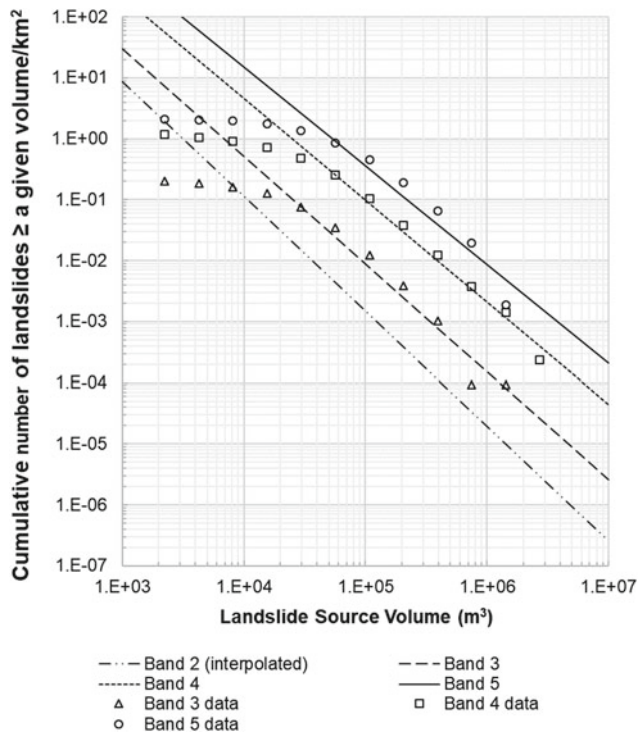


Fig. 2 The cumulative number of landslides greater than a given volume per km² for each PGA band as determined from the three earthquake-induced landslide inventories of Kaikōura, Inangahua and Murchison. The trend lines for Bands 3–5 represent power laws fitted to this data (shown as points). Trend lines for Band 2 are interpolated from the power laws derived for bands 3–5

although landslides occur at these lower PGA values, they tend to be small in volume and few in number. Given the lack of data to generate a meaningful relationship for Band 2 landslides, the number of landslides in each volume bin for PGA band 2 was interpolated from the power laws derived for PGA bands 3–5 (Table 2; Fig. 2).

Application to Franz Josef and Fox Glacier Valleys

We use these power law relationships to forecast the number of landslides that could occur for different levels of ground shaking in both Franz Josef and Fox glacier valleys. We calculated the number of landslides for a series of 8 volume bins:

1. 1000–5000 m³
2. 5000–10,000 m³
3. 10,000–50,000 m³
4. 50,000–100,000 m³
5. 100,000–500,000 m³
6. 500,000–1,000,000 m³
7. 1,000,000–5,000,000 m³
8. >5,000,000 m³.

We did not include volume classes less than 1000 m³ as the three earthquake-induced landslide inventories are incomplete for these landslide volumes, and the numbers of smaller landslides generated in earthquakes cannot be represented by the power law trends (Fig. 1). We adopted the landslide volume bins to represent the full volume range of landslide distributions recorded in the glacier valleys; those documented in the literature that have occurred in the Southern Alps (Whitehouse and Griffiths 1983; Cox and Allen 2009; e.g. Allen et al. 2011), and those contained in the Kaikōura, Inangahua and Murchison landslide inventories. We calculated the number of landslides per volume bins by fitting histograms to the data in Fig. 1, following the method of Moon et al. (2005), where the width of each landslide volume bin was used to estimate the number of

landslides that could be generated within the given volume bin per km² of slopes with angles greater than 30°. The number of landslides in each volume class were scaled to each glacier valley by multiplying them by the total area of slopes greater than 30° in each valley (Table 3).

Annual Frequency of Earthquakes

We obtained the annual frequency of the different levels of ground shaking from the New Zealand National Seismic Hazard Model (NSHM: Stirling et al. 2012). We de-aggregated the NSHM to understand the fault sources which contribute to the shaking hazards for the glacier valleys. The main contributor of seismic hazard is the Mw 8.1 Alpine Fault event. The second largest hazard comes from moderate magnitude (Mw 5–Mw 6). Although the Alpine fault is the main seismic source in the area, the section of fault that could rupture might be located some distance away from the glacier valleys. We therefore estimate the landslide severity for different bands of PGA.

Discussion

The application of the Kaikōura, Inangahua and Murchison datasets is based on the assumption that the landslides generated during these earthquakes are representative for the potential earthquake-induced landslides on the West Coast. To assess their applicability we compared the exponents of the Kaikōura, Inangahua and Murchison FAD's with those of global landslide inventories (cf. Tanyaş et al. 2018). Globally, the power law exponent can range from 1.82 to 3.76, with an average of 2.55, and standard deviation of 0.37 (cf. Tanyaş et al. 2018). The Kaikōura power law scaling exponent (1.88) falls within the range of observed landslide inventories but is greater than a standard deviation difference

from the global mean value, while both Inangahua (2.71) and Murchison (2.62) exponents are within the standard deviation of the mean. For Kaikōura, the exponents may differ from the global mean due to the complex nature of the Kaikōura earthquake, which included the rupture of more than 20 faults to the ground surface (Massey et al. 2018). Differences in mapping methodology, quality and resolution of imagery may also result in a variation in the value of the exponent (Tanyaş et al. 2018). Use of the Kaikōura earthquake-induced inventory by itself may underestimate landslide hazard, highlighting the need for assessing the three landslide datasets.

Massey et al. (2020) compares the exponents in Table 1 with global power law scaling relationships to understand their applicability for determining landslide volume. Small variations in the values of the exponents may result in substantial over or under estimates of landslide volume (Larsen et al. 2010). For all three New Zealand landslide inventories the γ exponent values are lower than global averages. This suggests that the majority of landslides for the New Zealand earthquakes were shallower debris avalanches, with such failure types potentially being the dominant earthquake-induced landslide type (Keefer 2002). Massey et al. (in review) suggests that this may be due to the fractured nature of the predominant greywacke bedrock limiting the depth of failures. The schist rock mass of the glacier valleys is also fractured with persistent faulting in each valley (Cox and Barrell 2007), and therefore we assume that shallow debris avalanches may be dominant failure mechanisms during an earthquake event. This assumption needs further verification and analysis, particularly with regards to the structural controls and anisotropy of schist in controlling failure depth (Clarke and Burbank 2010).

The reoccurrence intervals of ground shaking derived from the NSHM are time-independent (Stirling et al. 2012) and therefore do not consider time-elapsd since the last Alpine Fault earthquake in 1717. As such, we may

Table 3 Number of landslides generated within each glacier valley for each band of PGA and landslide volume

Landslide volume (m ³)	Fox				Franz Josef			
	Band 2	Band 3	Band 4	Band 5	Band 2	Band 3	Band 4	Band 5
1000	190	650	4621	13,530	194	662	4706	13,778
5000	181	612	4306	12,527	184	623	4385	12,757
10,000	7	27	216	676	7	27	220	688
50,000	2.4	10.5	92.2	303	2.4	10.7	93.9	308
100,000	0.09	0.46	4.6	16.34	0.09	0.47	4.7	16.64
500,000	0.031	0.18	2.0	7.32	0.031	0.19	2.0	7.45
1,000,000	0.0011	0.008	0.10	0.40	0.0012	0.008	0.10	0.40
5,000,000	0.00040	0.003	0.04	0.18	0.00041	0.003	0.04	0.18
>5,000,000	0.000015	0.0001	0.002	0.01	0.000015	0.0001	0.002	0.01

underestimate the landslide hazard. These assumptions in the analysis and quantification of risk are important to document and understand. Further sensitivity analysis may allow us to understand the effect of the assumptions outlined above on the eventual estimated risk levels (Fell et al. 2005). We suggest our outlined method for estimating landslide magnitude—frequency relationships for earthquake events provides a pragmatic first pass approach.

Conclusions

For areas with a high seismic hazard but lack of historical records of landslide activity triggered by earthquakes, we suggest the use of landslide inventories from similar geological and geomorphological environments. We detail a method where we estimate the number and size of landslides that can be generated for different levels of ground shaking. We use the earthquake-induced landslide inventories of the 2016 Mw 7.8 Kaikōura earthquake, the 1968 Mw 7.1 Inangahua earthquake, and the 1929 Mw 7.8 Murchison earthquake, and apply the resulting magnitude-frequency relationships to the glacier valleys of Franz Josef and Fox, New Zealand. We suggest that this represents a pragmatic approach for the estimation of earthquake-induced landslide hazard and risk.

Acknowledgements Funding and support for this project was provided by the Department of Conservation (DOC), New Zealand. We would like to thank Wayne Costello, Owen Kilgour, Tony Hart and Don Bogie (DOC) for their help and support of the project. We would also like to thank Marc-Andre Brideau for comments and feedback on this paper.

References

- Allen SK, Cox ISC, Owens IIF (2011) Rock avalanches and other landslides in the central Southern Alps of New Zealand: a regional study considering possible climate change impacts, pp 33–48
- Clarke BA, Burbank DW (2010) Bedrock fracturing, threshold hillslopes, and limits to the magnitude of bedrock landslides. *Earth Planet Sci Lett* 297:577–586
- Corominas J, van Westen C, Frattini P et al (2014) Recommendations for the quantitative analysis of landslide risk. *Bull Eng Geol Environ* 73:209–263
- Cox S, Allen SK (2009) Vampire rock avalanches of January 2008 and 2003, Southern Alps, New Zealand. *Landslides* 6:161–166
- Cox SC, Barrell DJA (2007) Geology of the Aoraki area: institute of geological and nuclear sciences 1:250,000 geological map. Lower Hutt, New Zealand
- Fell R, Ho KK, Lacasse S, Leroi E (2005) A framework for landslide risk assessment and management
- Guzzetti F, Ardizzone F, Cardinali M et al (2009) Landslide volumes and landslide mobilization rates in Umbria, central Italy. *Earth Planet Sci Lett* 279:222–229
- Guzzetti F, Cesare A, Cardinali M et al (2012) Landslide inventory maps: new tools for an old problem. *Earth Sci Rev* 112:42–66
- Hancox GT, Perrin N, Dellow G (2002) Recent studies of historical earthquake-induced landsliding, ground damage, and MM intensity in New Zealand
- Hancox GT, Ries W, Lukovic B, Parker RN (2014) Landslides and ground damage caused by the Mw 7.1 Inangahua earthquake of 24 May 1968 in northwest South Island, New Zealand. *GNS Sci Rep* 2014(06):89
- Hancox GT, Ries W, Parker RN, Rosser B (2015) Landslides caused by the MS 7.8 Murchison earthquake of 17 June 1929 in northwest South Island, New Zealand. *GNS Sci Rep* 2015/42:105
- Keefer DK (2002) Investigating landslides caused by earthquakes—a historical review. *Surv Geophys* 23:473–510
- Larsen IJ, Montgomery DR, Korup O (2010) Landslide erosion controlled by hillslope material. *Nat Geosci* 3:247–251
- Malamud BD, Turcotte DL, Guzzetti F, Reichenbach P (2004) Landslide inventories and their statistical properties. *Earth Surf Process Land* 29:687–711
- Massey C, Townsend D, Rathje E et al (2018) Landslides triggered by the 14 November 2016 Mw 7.8 Kaikōura earthquake, New Zealand. *Bull Seismol Soc Am* 108:1630–1648
- Massey CI, Townsend D, Jones K et al (2020) Volume characteristics of landslides triggered by the Mw 7.8 2016 Kaikōura earthquake, New Zealand, derived from digital surface difference modelling. *J Geophys Res* 125
- Meunier P, Hovius N, Haines AJ (2007) Regional patterns of earthquake-triggered landslides and their relation to ground motion 34:1–5
- Moon A, Wilson R, Flentje P (2005) Developing and using landslide size frequency models. *Fac Eng* 384
- Rosser BJ, Carey JM, Jane B et al (2017) Comparison of landslide inventories from the 1994 Mw 6.8 Arthurs Pass and 2015 Mw 6.0 Wilberforce earthquakes, Canterbury, New Zealand. *Landslides* 14:1171–1180
- Stirling M, McVerry G, Gerstenberger M et al (2012) National seismic hazard model for New Zealand: 2010 update. *Bull Seismol Soc Am* 102:1514–1542
- Tanyaş H, van Westen CJ, Allstadt KE, Jibson RW (2018) Factors controlling landslide frequency-area distributions. *Earth Surf Process Land* 1
- van Westen CJ, Castellanos E, Kuriakose SL (2008) Spatial data for landslide susceptibility, hazard, and vulnerability assessment: an overview. *Eng Geol* 102:112–131
- Van Westen CJ, Soeters R (2006) Landslide hazard and risk zonation—why is it still so difficult? 167–184
- Whitehouse I, Griffiths G (1983) Frequency and hazard of large rock avalanches in the central Southern Alps, New Zealand. *Geology* 11:331–334



Role of Remote Sensing Technology in Landslide Risk Management of Hong Kong

Julian S. H. Kwan, W. K. Leung, and Clarence E. Choi

Abstract

Natural terrain covers over 60% of the land area of Hong Kong. With the close proximity of developments to hillsides and high annual rainfall, Hong Kong is under a constant threat from natural terrain landslides. Over the past years, the Geotechnical Engineering Office (GEO) of the Civil Engineering and Development Department of the Hong Kong Special Administrative Region Government has applied state-of-the-art remote sensing techniques, for example, laser scanning, photogrammetry and interferometric synthetic aperture radar, in landslide risk management. These include landslide hazard identification and monitoring, post-landslide responses and residual risk management, design of landslide prevention and mitigation measures etc. This paper discusses the advantages of remote sensing technology and their applications to enhance the slope safety of Hong Kong. Pilot studies applying machine learning on identification of geological features from aerial imageries and further studies being/to be conducted are also covered.

Keywords

Remote sensing • Natural terrain • Slope safety management • Machine learning

Introduction

Natural terrain covers over 60% of the land area of Hong Kong. With high annual rainfall (about 2400 mm) and the close proximity of developments to hillsides, landslide risk management is of vital importance to secure the lives and properties of citizens. The Geotechnical Engineering Office (GEO) has been devoted to ensure slope safety in Hong Kong since its establishment in 1977.

Field instrumentation was adopted to obtain ground movement information in the past. However, with more focus being placed on natural terrain hazards and the advancement in technology, the GEO has applied state-of-the-art remote sensing techniques and conducted relevant studies in recent years.

Advantages and Applications of Remote Sensing Technology

Remote sensing technology has been commonly adopted for the advantages over traditional ground instrumentation. It can cover a large area and give geographically continuous movement data while ground survey only provides point-based information. It is less labour intensive and can be applied to inaccessible areas. Some remote sensing techniques are weather-permitting, allowing data collection and analysis under adverse weather conditions. Moreover, the resolution, both spatial and temporal, of remote sensing data is very high nowadays.

The above advantages, together with the increased computer processing power, explain the extensive use of remote sensing techniques, especially at management of natural terrain landslide risk, in recent years.

Remote sensing technology can be applied to the following aspects of landslide risk management:

J. S. H. Kwan · W. K. Leung (✉)
Geotechnical Engineering Office, Civil Engineering
and Development Department, Hong Kong SAR, China
e-mail: waikinleung@cedd.gov.hk

J. S. H. Kwan
e-mail: juliankwan@cedd.gov.hk

C. E. Choi
Department of Civil Engineering, The University of Hong Kong,
Hong Kong SAR, China
e-mail: cechoi@hku.hk

1. Landslide hazard identification and monitoring
2. Post-landslide responses and residual risk management
3. Design of landslide prevention and mitigation measures.

Landslide Hazard Identification and Monitoring

A thorough understanding of the geomorphological features of the natural terrain in Hong Kong is essential to landslide identification, landslide susceptibility assessment and natural terrain hazard study. The GEO conducted territory-wide airborne light detection and ranging (LiDAR) surveys in Hong Kong in 2011 (by fixed-wing aircraft) and in 2020 (by helicopter). With the multi-return nature of the laser pulses, virtual deforestation can be achieved revealing the ground profile underneath the dense vegetation. Point density of 16 points/m², vertical accuracy of 0.1 m and horizontal accuracy of 0.3 m can be achieved providing accurate topographic information of the whole Hong Kong. The topographic information can help identify areas of past failures (Fig. 1) and major tension cracks, to generate slope angle map (Fig. 2) and to facilitate landslide debris mobility modelling for quantitative risk analysis.

Besides, the GEO has established an Enhanced Natural Terrain Landslide Inventory (ENTLI) through review of all aerial photographs taken since 1924 (MFJV 2007). About 110,000 natural terrain landslides have been identified in

Hong Kong up to 2016 (GEO 2016). The ENTLI database provide indispensable information for identifying the vulnerable catchments which warrant landslip prevention and mitigation works. Currently, regular updating of the ENTLI is conducted by manual inspection and interpretation of aerial photographs. With about 10,000 new aerial photographs taken in Hong Kong each year, this process is both time consuming and labour intensive, requiring notable experienced professional input. With the advancement in digital image processing techniques and machine learning technology, computerised algorithm is being developed to facilitate an automatic landslide identification process from digital aerial photography (Kwan et al. 2019). A convolutional neural network (CNN) has been trained using training datasets that show boundaries of natural terrain landslides delineated manually on aerial photographs. Trials have been conducted over five study areas in Hong Kong. The accuracy is in general above 80% (Fig. 3) (Arup & Shi 2019). The use of AI technique shortens the turnaround time for the updating of the ENTLI database and the ranking of the vulnerable catchments. Apart from the landslide boundaries, other landslide attributes, for example, slope angle of landslides and landslide area can be generated automatically on a geographic information system platform.

Despite the promising landslide extraction results using aerial imageries, the GEO is planning to explore the use of satellite imageries for landslide extraction. With the more spectral bands than aerial imageries (up to 8 bands for Worldview-3 images versus 4 bands for aerial imageries),

Fig. 1 Reveal of landslide scars from the digital terrain model generated by airborne LiDAR survey

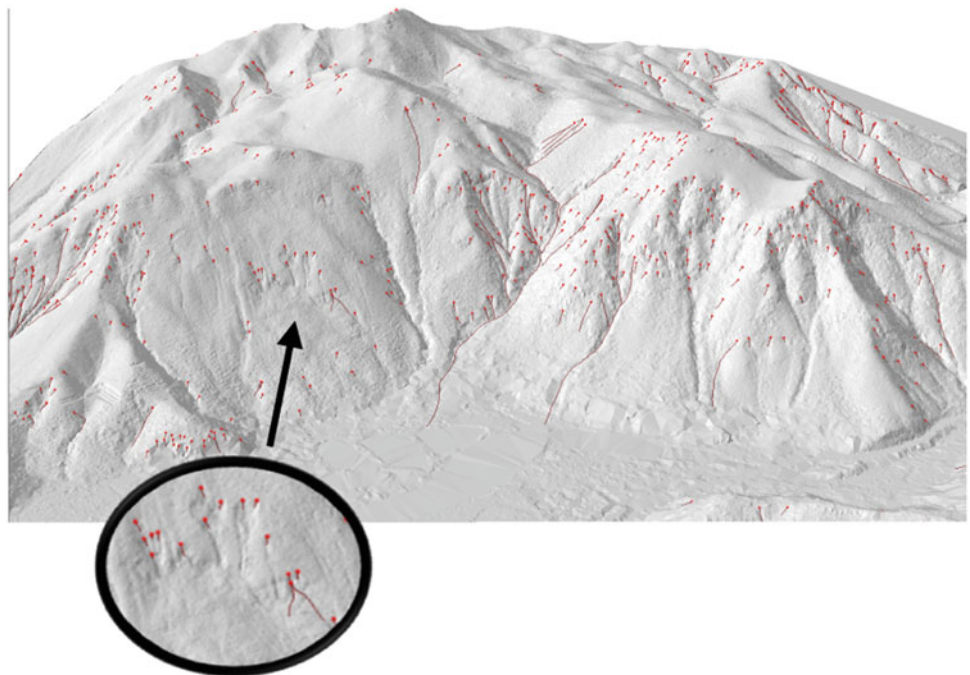


Fig. 2 Generation of slope angle maps for natural terrain hazard study and digital elevation models for debris mobility modelling

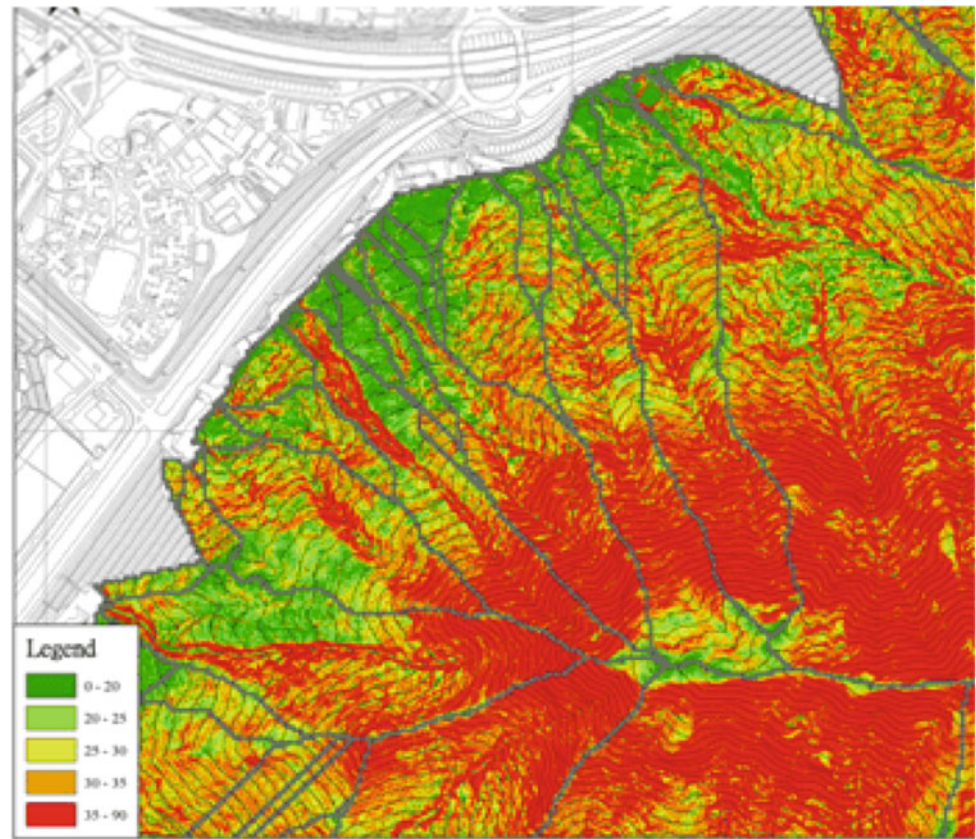


Fig. 3 Automatic identification of recent natural terrain landslides from aerial imageries



and the high spatial and temporal resolution of satellite images, it is expected that the use of satellite imageries would result in better extraction results.

Another pilot study has been conducted to automatically extract rock outcrop from aerial imageries (Fig. 4), which helps improve the landslide susceptibility of the natural

terrain in Hong Kong. In developing territory-wide landslide frequency map, information including rainfall, topographic, geology and materials on ground surface are needed. The map production requires differentiation of soil slopes and rock outcrops, since the landslide frequency model is pertinent to soil slope only. In view of the large extent of natural

terrain in Hong Kong, a method to automatically generate the rock outcrop distribution is required. 12,000 sample images were extracted from the ortho-rectified aerial photographs of Hong Kong and classified into five different types, viz. rock outcrops, grassland, woodland, badland and urban area (Wong 2018) to train the CNN. The extent of rock outcrop extracted by the CNN was compared with that delineated by engineering geologists through aerial photograph interpretation at selected areas. Promising extraction results have been obtained.

The GEO is currently conducting study to investigate the applicability of interferometric synthetic aperture radar (InSAR) in monitoring the ground movement of natural terrain. With the higher temporal resolution of InSAR satellites and the advanced algorithms for data interpretation, there could be improvement in the accuracy despite the known limitations of InSAR applications at steep and densely vegetated natural terrain.

Post-landslide Responses and Residual Risk Management

After the occurrence of natural terrain landslides that may affect facilities, the GEO has to promptly identify the extents of landslide source and trail, to assess the stability of the failed masses and whether further failures are likely to occur. Traceable records of the landslide morphology and volume

is also essential for understanding the cause of landslide, for forensic investigation purpose. All these analyses can be facilitated with the aid of remote sensing techniques.

Unmanned aerial vehicles (UAV) are promptly deployed after the report of landslides, especially for remoted natural terrain landslides where the access is difficult. Photographs taken by UAV can provide a quick overview of the distribution, extent, type and volume of natural terrain landslides, and to identify whether major tension cracks and/or loose detached soil masses are present that may result in further landslides (Fig. 5). This provides valuable information for the assessment of residual landslide risk.

Besides, UAV photogrammetry can generate post-landslide digital surface model (Fig. 6). This, when compared with the terrain model generated before landslide, for example, by territory-wide airborne LiDAR survey, provides accurate volume of the landslides. The digital surface model also provides detailed morphological information of the landslides.

Apart from photogrammetry, if needed, UAV equipped with LiDAR apparatus are employed to provide post-landslide topographic information with point density much higher than that collected by fixed-wing aircraft and helicopter.

The GEO has also applied handheld laser scanner (HLS) for surveying landslides. HLS is a portable system comprising a lightweight laser scanner and a data logger (Fig. 7). Landslide survey by HLS is adopted when UAV

Fig. 4 Extract of the rock outcrop map generated by the CNN

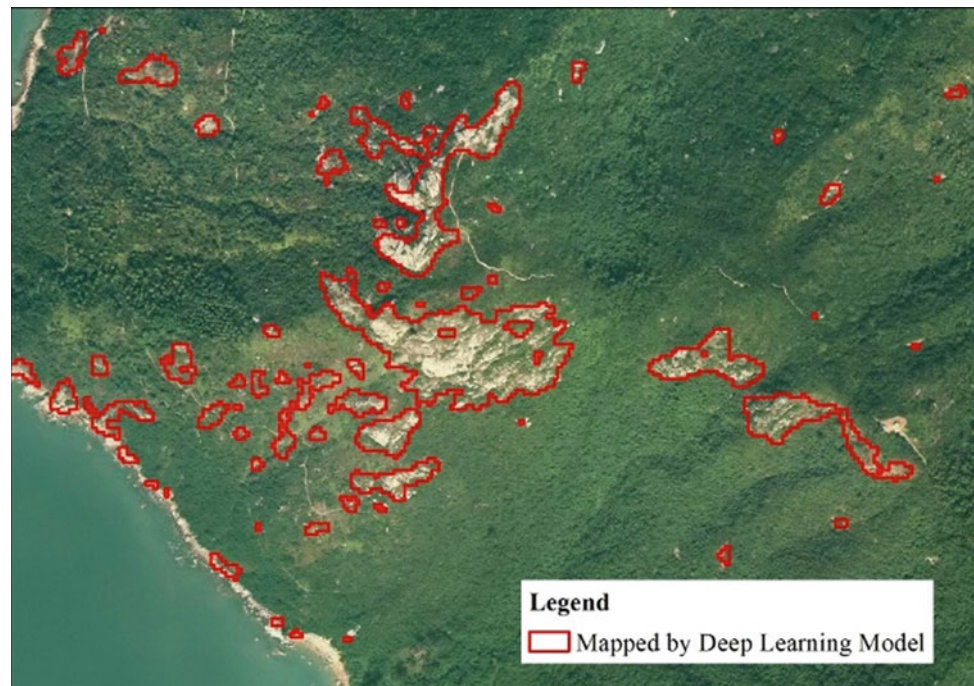


Fig. 5 Photograph taken by UAV few hours after the occurrence of natural terrain landslides above Fan Kam Road, Hong Kong in August 2018



flight is not feasible due to adverse weather or obstructions like vegetation. The HLS can be operated manually without the need of a stable platform with a maximum detection range of 100 m. This technology is capable of providing

rapid, high resolution topographic information for landform mapping and slope investigation in difficult site settings (e.g. remote landslide site, bouldery stream, etc.). Owing to its handy, mobile, speedy and robust nature, HLS is able to provide high quality topographic data of landslides soon after the occurrence of landslides (Fig. 8). The functions are further enhanced by the recent advancements in HLS, which allow real-time review of acquisition results and user-friendly data processing. A study on the applicability and accuracy of HLS has been carried out, which demonstrates that the accuracy of HLS is about 3 cm, which is robust enough for landslide mapping and volume estimation. HLS can be used at night since the transmission of laser pulses is independent to the brightness level of the environment. GEO's experience shows that the performance under rainy condition is satisfactory.

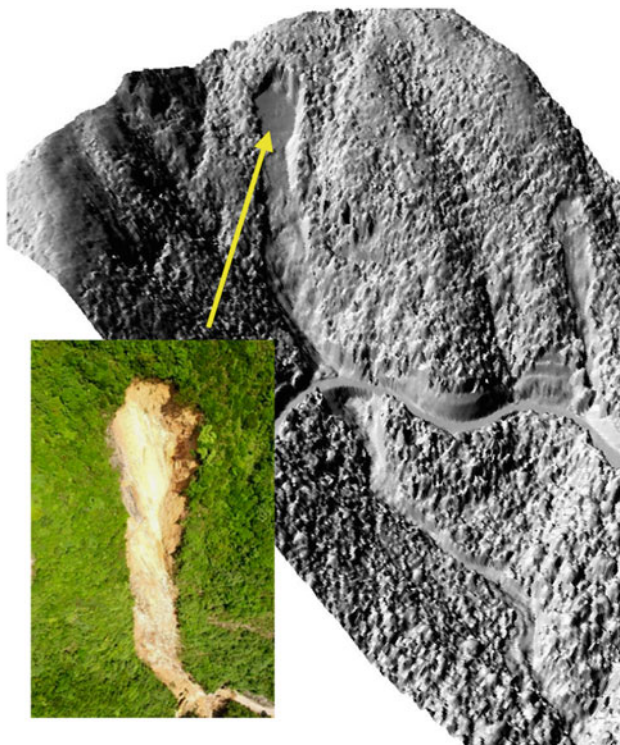


Fig. 6 Generation of digital surface model of landslide scar using UAV photogrammetry



Fig. 7 Handheld laser scanner

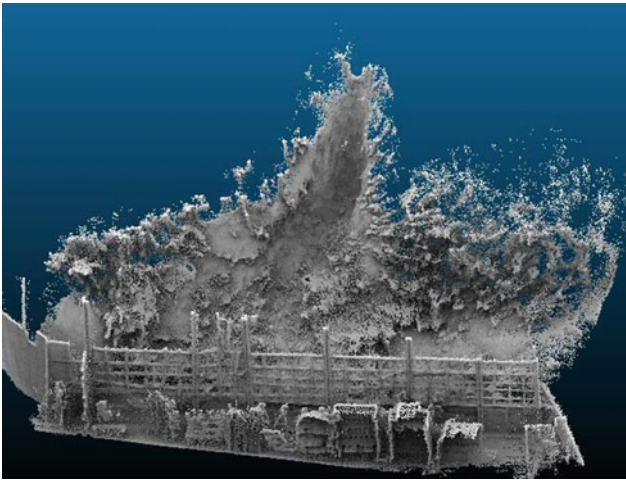


Fig. 8 Point cloud of landslide collected by HLS

Design of Landslide Prevention and Mitigation Measures

Remote sensing technology can facilitate the design of landslide prevention and mitigation measures, for example, rock mass discontinuity mapping. Conventionally, rock mass discontinuity mapping is carried out on site by geologists/engineers using a geological compass to measure the dip angle and dip direction of rock mass discontinuities and to record other discontinuity properties such as, persistence, aperture, nature of infilling, unevenness etc. This process is time-consuming and can be conducted at accessible discontinuities only. With the advancement in remote sensing technology and computer processing power, there are potential benefits/advantages for adopting remote sensing technology to supplement conventional rock mass discontinuity mapping. Handheld laser scanning or terrestrial laser scanning can be conducted to collect the point cloud data of the rock slope. Mesh can be generated using geo-referenced point cloud (Fig. 9) by software.

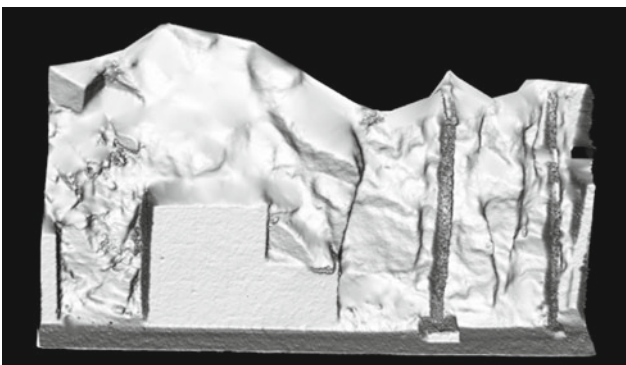


Fig. 9 Surface model generated from geo-referenced point cloud data

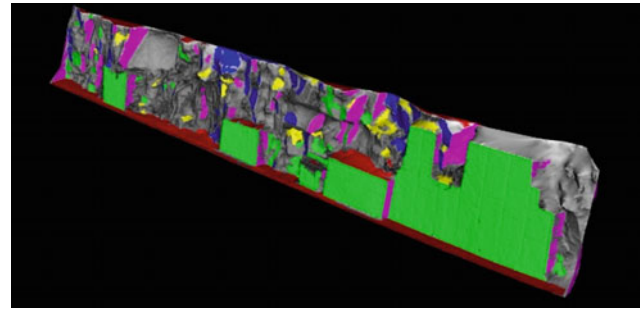


Fig. 10 Example of rock joint surfaces identified. The extensive green surfaces are butresses

Discontinuities can then be detected (Fig. 10) according to parameters input by the users, like search radius for combining individual meshes to form a single plane, minimum area of planes and the overall surface orientation variability etc. (Voge et al. 2013). Cost and time saving can be achieved by digital rock mass discontinuity mapping especially for inaccessible sites such as high rock slopes or slopes at remote areas, since erection of scaffoldings is not necessary. Under the technological advancement initiative promulgated by the GEO, local practitioners in Hong Kong has adopted the UAV and remote sensing technologies to carry out rock joint mapping for slope stability analysis. Figure 11 shows some preliminary rock joint data of a 40 m high rock slope acquired in a project. When the digital data is supplemented by suitable field inspection in which information of such as rock joint infilling, aperture, unevenness etc. is obtained, preliminary design of rock slope upgrading works can be produced.

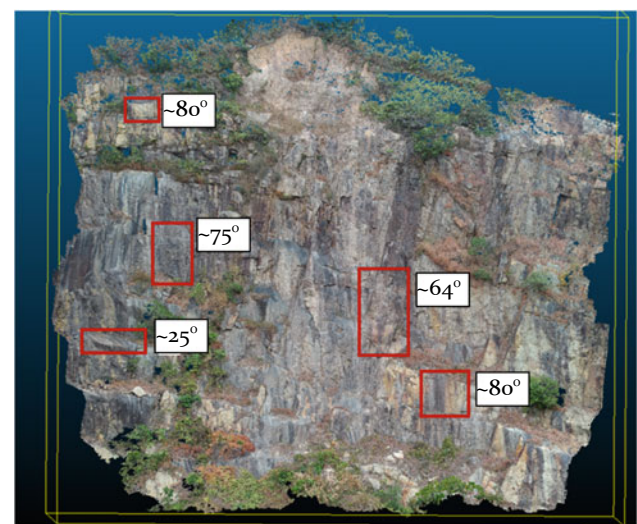


Fig. 11 Rock joint dip angle of a 40 m high slope determined using UAV and remote sensing technologies

Besides, topographic information collected by remote sensing techniques, for example, airborne LiDAR or HLS, can be used to optimize the design configurations of landslide debris-resisting barriers and slope works ensuring that there would be minimum excavation and that the measures are located at the most suitable locations where an optimal balance of cut and fill can be achieved.

UAV, either UAV photogrammetry or coupled with LiDAR equipment, can be used for routine inspection of slopes and mitigation measures, for example, to inspect whether barriers have been impacted by landslides.

Conclusion

Remote sensing technology has been commonly applied to and can facilitate different aspects of landslide risk management, from identification of landslide hazards, residual risk management to the design of landslide prevention and mitigation works. With the advancement in technology, further applications, especially in combination with machine learning, are being explored and are expected to enhance the accuracy and applicability. The role of remote sensing in landslide risk management of Hong Kong is irreplaceable.

Acknowledgements This paper is published with the permission of the Director of Civil Engineering and Development and the Head of the Geotechnical Engineering Office of the Hong Kong Special Administrative Region of China.

References

- Arup, Shi JWZ (2019) Automatic identification of recent natural terrain landslides from aerial photographs—interim report. Agreement No. CE49/2017 (GE). Geotechnical Engineering Office, Hong Kong
- GEO (2016) Management of natural terrain landslide risk—information note 6/2016. Geotechnical Engineering Office, Hong Kong
- Kwan JSH, Leung WK, Lo FLC, Millis S, Shi JWZ, Wong MS, Kwok CYT (2019) Territory-wide identification of geological features on aerial photographs using machine learning for slope safety management. Proceedings of the 3rd international conference (ICITG), Guimaraes, Portugal—Information Technology in Geo-Engineering, 29 Sept–2 Oct 2019, pp 527–539
- MFJV (Maunsell Fugro Joint Venture) (2007). Final report on compilation of the enhanced natural terrain landslide inventory (ENTLI). Agreement No. CE15/2005 (GE). Geotechnical Engineering Office, Hong Kong
- Voge M, Lato MJ, Diederichs MS (2013) Automated rockmass discontinuity mapping from 3-dimensional surface data. *Eng Geol* 164:155–162
- Wong CMS (2018) Service for identification of rock outcrops using remote sensing techniques—final report. Geotechnical Engineering Office, Hong Kong



2020 Kyoto Japan

The Characteristics of the Vegetation Distribution Related to the Slope Failure Caused by the Earthquake

Yoshikazu Tanaka, Kyohei Ueda, and Ryosuke Uzuoka

Abstract

The Hokkaido Eastern Iburi earthquake was occurred at 3:07 on 6th September 2018, the southern part of Hokkaido, Japan. At the same time, many mountain areas have slope failures in Atsuma. It is necessary to assess the mechanisms of the landslide from geological and topographic factors, rainfall, seismic motion, vegetation. The objective of our study investigates the relationship between slope failure and vegetation of the slope in Atsuma. This study compares the slope failure data with vegetation distribution data and DEM data. The whole analysis area is located in the watershed along the Habu river. The vegetation distribution is investigated in the whole analysis area within the collapsing slope using spatial analysis of GIS. As a result, vegetation on the slope of the whole analysis area mainly distributed with Hardwood's natural forest and Coniferous plantation, Weed. We do not fully clarify the classification of the vegetation distribution on the collapsing slope of the whole analysis area. Then, we focus on some small watershed to consider the classification of the vegetation distribution on the collapsing slope. The collapsing slope area in the study area is mainly covered with Coniferous plantations. The no collapsing area in the study area is mainly covered with Hardwood's natural forest. Therefore, it is a possibility that the collapsing slopes of the Atsuma region are affected by the vegetation on each slope.

Keywords

Earthquake • Slope failure • Vegetation • GIS

Introduction

Mountain area occupies 70% of the national land use in Japan. Disasters happen whenever heavy rain and an earthquake is occurring. Japanese climate is classified at the Cfa in Köppen climate classification, which is constructed the high humidity and heavy rain trough the annual. Earthquakes cause severe damage to the building and the road, the slope, the agricultural field.

The Hokkaido Eastern Iburi earthquake occurred at 3:07 on 6th September 2018, the southern part of Hokkaido, Japan. Due to the earthquake, many mountain areas have slope failures in Atsuma. Such a huge area of the landslide has never occurred in Japan. The huge amount of damages occurred, including the lifeline such as water supply and electricity, houses. In general, slope disasters are mainly caused by topographic features and geological features, vegetation, heavy rain, a strong wind of typhoon, an earthquake. The main causes of the Hokkaido Eastern Iburi earthquake are geological factors (Chigira et al. 2019; Wang et al. 2019), topographic effects (Kasai and Yamada 2019), rainfall (Zhang et al. 2019), and huge earthquake motion (Wang et al. 2019). One of the mechanisms is the volcanic deposits behaved as a sliding layer during the landslides (Kameda et al. 2019). It is also necessary to study the mechanism of slope failure in terms of vegetation.

Tree root plays an important role in the soil as the resistance for slope stability. For instance, the root distribution and penetrations affected the slope stability in Thailand (Nilaweera and Nutalaya 1999). Plant density with the root system influences the reinforcement of the soil (Loades et al. 2010). Root pull-out forces are important for slope stability based on the test results (Schwarz et al. 2011).

Y. Tanaka (✉) · K. Ueda · R. Uzuoka
Kyoto University, Disaster Prevention Research Institute,
Gokasho, Uji, Kyoto 611-0011, Japan
e-mail: tanaka.yoshikazu.5m@kyoto-u.ac.jp

K. Ueda
e-mail: ueda.kyohei.2v@kyoto-u.ac.jp

R. Uzuoka
e-mail: uzuoka.ryosuke.6z@kyoto-u.ac.jp

Root-soil mechanical interactions depend on the root bundle (Schwarz et al. 2010). Therefore, it is necessary to investigate the effects of tree root on the slope failure in the damaged area. However, it is not enough to study the vegetation on slope failures in the Hokkaido Eastern Iburi earthquake.

The objective of this study investigates the relationship between slope failure and vegetation of the slope in Atsuma. Spatial analysis is useful for simply assessing slope failure. Topology, geology, vegetation, and distribution of slope data are analyzed using GIS.

Study Area

Geological and Topographic Features

The study area is located in the watershed along with the Habu river around the red line as shown in Fig. 1. The slope of the study area is composed of volcanic ash soil. The tephra layers consisted of the many types of volcanic ashes from the Eniwa and Tarumae volcanoes (Nakagawa et al. 2018). Slip surface is defined as the Ta-d layer from the Tarumae volcano 9,000 years ago and En-a layer from the Eniwa volcano about 200,000 years ago (Chigira et al.

2019). These characteristics are commonly configured in the Atsuma region, eastern Iburi Hokkaido.

The whole analysis area (surrounded by a red line) is located about 15 km from the epicenter. The total of the whole analysis area is about 23.2 km², and the total of collapsing area is about 4.0 km². The slope angle of the whole analysis area is mainly composed of 26–35 degrees as shown in Fig. 2a. Four small watersheds are selected in Fig. 1 to investigate the classifications of vegetation distribution on collapsing and no collapsing slopes. Four small watersheds consist of two collapsing slope areas and two no collapsing areas. Collapsing slope area is presented by square symbols with a brown and light brown in Fig. 1. The total of collapsing slope area 1 is about 1.2 km², and the total of collapsing slope area 2 is about 0.40 km². The slope angle of collapsing slope area 1 is mainly distributed from 26 to 30 degrees, and the slope angle of collapsing slope area 2 is distributed from 31 to 35 degrees as shown in Fig. 2b. No collapsing area is presented by circle symbols with black and gray in Fig. 1. The total of no collapsing area 1 is about 0.53 km², and the total of no collapsing area 2 is about 0.51 km². The slope angle of no collapsing area 1 is distributed from 16 to 20 degrees, and the slope angle of no collapsing area 2 is distributed from 21 to 30 degrees as shown in Fig. 2c.

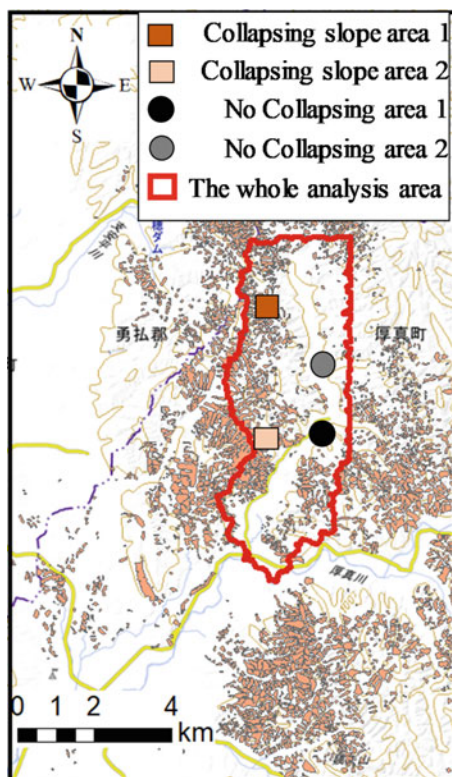


Fig. 1 Typical the collapsing slope in the Atsuma region (Aerial image refers to Geospatial Information Authority of Japan)

Rainfall

Rainfall is observed at several points of AMeDAS site, JMA. Atsuma observation site is located near the slope failure area. Figure 3 shows the daily rainfall and 30-years (1981–2010) average rainfall through six days before the earthquake. Rainfall event of the day before the earthquake is recorded at four days.

Methodology

First, vegetation distribution of the whole analysis area calculates the area based on the vegetation data and DEM data, the slope failure area data. The flowchart of methodology for the whole analysis area is shown in Fig. 4. Vegetation distribution of collapsing slope calculates the area by combining the vegetation data and DEM data. The classification of vegetation compares the whole analysis area with collapsing slope.

Second, vegetation distribution of four small watersheds calculates the area based on the vegetation data and DEM data. The flowchart of methodology for four small watersheds is shown in Fig. 5. We select four small watersheds in the whole analysis area to clear the classification of the vegetation related to the slope failure. Vegetation

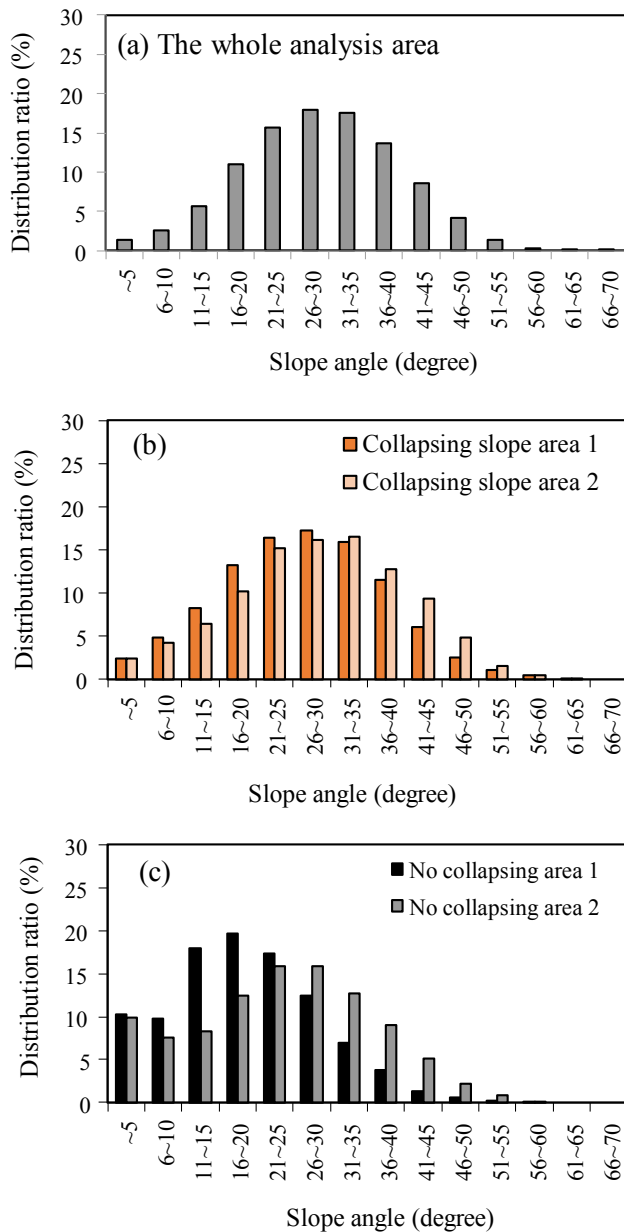


Fig. 2 Distribution ratio of slope angle: **a** The whole analysis area, **b** Collapsing slope area, **c** No collapsing area

distribution of four small watersheds calculates the area by combining the vegetation data and DEM data. The classification of vegetation compares the collapsing slope area with the no collapsing area.

The spatial analysis and mapping tool use Arc GIS Desktop ver. 10.6. 1. The GIS data of vegetation distribution refer to 1/25000 vegetation distribution map 2012 of Atsuma, Horonai, and Kamihoronai presented by the Ministry of Environment. DEM data composes of 5 m mesh on Atsuma, Horonai, and Kamihoronai presented by Geospatial Information Authority of Japan. The slope failure

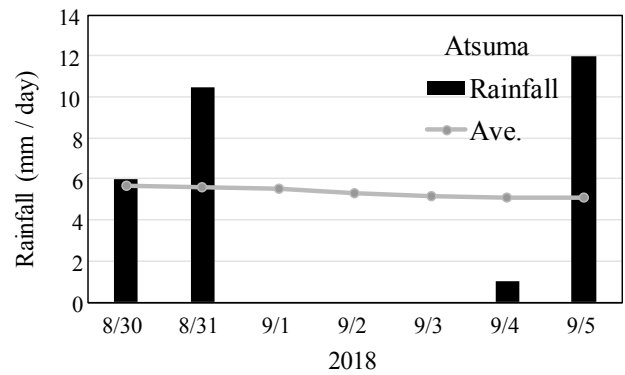


Fig. 3 The daily rainfall and 30-years average rainfall (1981–2010) through six days before the earthquake

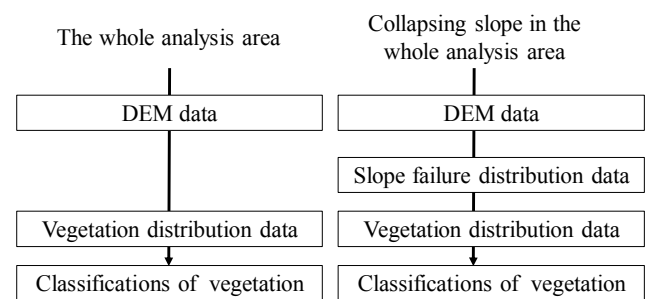
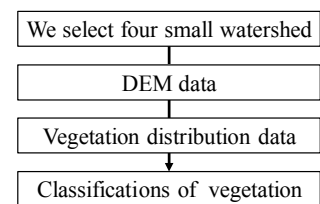


Fig. 4 The flowchart of methodology for the whole analysis area

Fig. 5 The flowchart of methodology for four small watersheds



distribution map refers to the GIS data traced from the orthographic images of the 2018 Hokkaido Eastern Iburi Earthquake presented by the Geospatial Information Authority of Japan (Kita 2018).

Results Overview in the Whole Analysis Area

The vegetation distribution on the whole analysis area and collapsing slope as shown in Fig. 6. The whole analysis area defines the red mark area (Fig. 1). The vegetation distribution of the whole analysis area is composed of the Hardwood's natural trees 48%, Hardwood's plantation 1.9%, Coniferous plantation 33.4%, Logging site 1.7%, Bamboo 0.6%, Weed 13.8%, other(houses and open water area) 0.5%. Hardwood's natural trees and Coniferous plantation are mainly distributed in the analysis area. On the other

hand, the vegetation distribution of collapsing area is composed of the Hardwood's natural tree 10.5%, Hardwood's plantation 0.1%, Coniferous plantation 6.2%, Logging site 0.4%, Bamboo grass 0.2%, Weed 0.1%. Hardwood's natural trees and Coniferous plantation are also mainly distributed in the collapsing area. The investigation of the vegetation in the whole analysis area shows the trend of the distribution, whereas the classifications of the vegetation in the collapsing slope are not clear. The features of the vegetation may have disappeared in the collapsing slope. It is difficult to find the vegetation distribution classifications peculiar to the slope failure.

Then, this study focuses on the small watershed to investigate the characteristic of vegetation distribution. The small watershed is selected along the Habiu river to compare the area including slope failure with the area where little collapse has occurred. The slope collapsing area is selected for the two sites. The almost no collapsing area are also selected the two sites.

Results of the Selected Area

Figure 7 shows the distribution of vegetation on the collapsing slope area 1 and 2. The collapsing slope area 1 is composed of Hardwood's natural forest 29.9%, Coniferous plantation 69.4%, Logging site 0.4%, Weed 0.3%. Coniferous plantations are distributed about 2.3 times wider than Hardwood's natural forests. The collapsing slope area 2 is composed of Hardwood's natural forest 11.5%, Coniferous plantation 88.5%. Coniferous plantations are distributed about 7.7 times wider than Hardwood's natural forests. The collapsing slope area 1 and 2 are mainly distributed with Coniferous plantation.

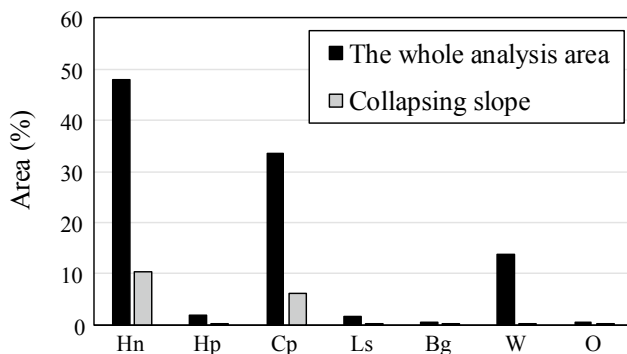


Fig. 6 The vegetation distribution on the whole analysis area and collapsing slope (Hn: Hardwood's natural forest, Hp: Hardwood's plantation, Cp: Coniferous plantation, Ls: Logging site, Bg: Bamboo grass, W: Weed, O: Other such as houses, pond). The whole analysis area shows the ratio of all vegetation species areas to each species. Collapsing slope shows the ratio of the vegetation species to each species on the slope

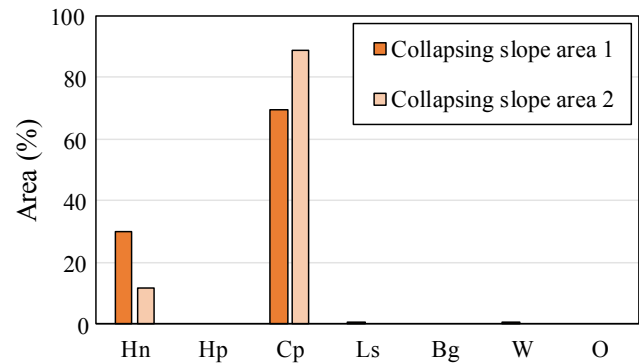


Fig. 7 The vegetation distribution on the collapsing slope area in the two sites

Figure 8 shows the distribution of vegetation on the no collapsing area 1 and 2. No collapsing slope area 1 is composed of Hardwood's natural forest 90.5%, Bamboo grass 1.2%, Weed 8.2%. It is mainly distributed with Hardwood's natural forests. No collapsing slope area 2 is composed of Hardwood's natural forest 53.2%, Coniferous plantation 42.8%, Weed 3.8%, Other 0.2%. Hardwood's natural forest is distributed about 1.2 times wider than Conifer's plantation. Hardwood's natural forest is widely distributed on the no collapsing area.

Discussion

The classification of the vegetation distribution is different between the collapsing slope area and the no collapsing area in the selected areas. Coniferous plantation distributed wider than Hardwood's natural forests in the collapsing slope area. In the no collapsing area, Hardwood's natural forests distributed wider than Coniferous plantation. Coniferous plantations are involved in the slope failure during the earthquakes.

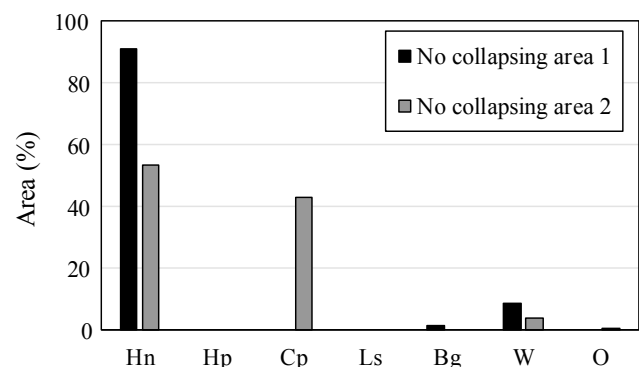


Fig. 8 The vegetation distribution on the no collapsing area in the two sites

Trees fallen by storm cases have been reported at the site of the coniferous plantation slope area (Inagaki 1999). Root resistance depends on the root system in the soil and is related to slope failure. Then we need to investigate the seismic behavior of trees considering root resistance related to slope failure.

Moreover, the vegetation distribution data do not include the growing condition of the tree. The height of the tree and root resistance depends on the growing condition of the tree. We need to investigate tree height and tree diameter as the growing condition data. In the investigations of slope failure, Unmanned Aerial Vehicles (UAV) are an effective tool in landslide hazard management (Brook and Merkle 2019). Aerial images are effective to obtain detailed vegetation and damage data.

Conclusions

The objective of this study investigates the relationship between slope failure and vegetation of the slope in Atsuma using GIS. The new finding is the classifications of the vegetation on the collapsing and no collapsing slopes. The vegetation of the collapsing slope area mainly distributes with Coniferous plantation. The vegetation of the no collapsing slope area mainly distributes with Hardwood's natural forest. Distribution of Coniferous plantation is related to the slope failure. In future work, we need to investigate the seismic behavior of trees considering root resistance related to slope failure.

Acknowledgements This paper was supported by The Kyoto University Foundation, DPRI Research grant support(2019H-02), and Association for Disaster Prevention research grant support.

References

Brook MS, Merkle J (2019) Monitoring active landslides in the Auckland region utilizing UAV/structure-from-motion photogrammetry. *Japan Geotech Soc Spec Publ* 6(2):1–6

- Chigira M, Tajika J, Ishimaru S (2019) Landslides of pyroclastic fall deposits induced by the 2018 eastern iburi earthquake with special reference to the weathering of pyroclastics. *DPRI Annuals*, No. 62 B, pp 348–356 [in Japanese]
- Geospatial Information Authority of Japan. DEM data. URL: <https://fgd.gsi.go.jp/download/mapGis.php?tab=dem> [Last accessed: 19th, March, 2020]
- Inagaki H (1999) An occurrence of trees fallen by storm due to the difference of the vegetation and the following slope failures. *J Japan Soc Eng Geol* 40(4):196–206 [in Japanese]
- Kameda J, Kamiya H, Masumoto H, Morisaki T, Hiratsuka T, Inaoi C (2019) Fluidized landslides triggered by the liquefaction of subsurface volcanic deposits during the 2018 Iburi-Tobu earthquake, Hokkaido. *Sci Rep* 9:13119
- Kasai M, Yamada T (2019) Topographic effects on the frequency-size distribution of landslides triggered by the Hokkaido Eastern Iburi Earthquake in 2018. *Earth, Planets and Space* 71(89):1–12
- Kita K (2018) 2018 Hokkaido Eastern Iburi earthquake orthographic image traced map. URL: https://github.com/koukita/2018_09_06_atumatyou [Last accessed: 12th, March 2020]
- Loades KW, Bengough AG, Bransby MF, Hallett PD (2010) Planting density influence on fibrous root reinforcement of soils. *Ecol Eng* 36:276–284
- Ministry of Environment. The vegetation map. URL:http://gis.biodic.go.jp/webgis/?_ga=2.221667608.1666951614.1551252547-657782141.1551252547 [Last accessed: 4th, March 2020]
- Nakagawa M, Miyasaka M, Miura D, Uesawa S (2018) Tephrostratigraphy in Ishikari Lowland, Southwestern Hokkaido: Eruption history of the Shikotsu-Toya volcanic field. *J Geol Soc Japan* 124 (7):473–489 [in Japanese]
- Nilaweera NS, Nutalaya P (1999) Role of tree roots in slope stabilization. *Bull Eng Geol Environ* 57:337–342
- Schwarz M, Cohen D, Or D (2010) Root-soil mechanical interactions during pullout and failure of root bundles. *J Geophys Res* 115: F04035
- Schwarz M, Cohen D, Or D (2011) Pullout tests of root analogs and natural root bundles in soil: experiments and modeling. *J Geophys Res* 116:F02007
- Wang F, Fan X, Yunus AP, Subramanian SS, Rodriguez AA, Dai L, Xu Q, Huang R (2019a) Coseismic landslides triggered by the 2018 Hokkaido, Japan (M_w 6.6), earthquake: spatial distribution, controlling factors, and possible failure mechanism. *Landslides* 16:1551–1566
- Wang G, Furuya G, Watanabe N, Doi I, Ma N (2019) On the features of landslides triggered by the 2018 Hokkaido Eastern Iburi Earthquake. *DPRI Annuals*, No. 62 A, 48–56 [in Japanese]
- Zhang S, Li R, Wang F, Iio A (2019) Characteristics of landslides triggered by the 2018 Hokkaido Eastern Iburi earthquake, Northern Japan. *Landslides* 16:1691–1708



Cutting-Edge Technologies Aiming for Better Outcomes of Landslide Disaster Mitigation

Kazuo Konagai

The International Consortium on Landslides (ICL) and The Global Promotion Committee of the International Programme on Landslides (GPC/IPL) have been responsible for organizing the World Landslide Forums (WLFs) every three years since 2008. Ever since the 1st WLF, the forums have long been the arena for landslide researchers and practitioners to exchange up-to-date information of recent devastations caused by landslides, cutting-edge technologies for landslide disaster mitigations and early warnings etc. to establish synergies among all participants worldwide.

Though the upcoming WLF5 has officially been postponed by one year to 2–6 November 2021 due to the global disruption caused by the coronavirus pandemic, the WLF5 will be all the more important with the Kyoto Landslide Commitment 2020 (KLC2020) to be launched as planned in the final online signatory meeting on 5 November 2020; the KLC 2020 is intended to be our action goals as the further advanced successor of the ‘Sendai Landslide Partnerships 2015–2025 for Global Promotion of Understanding and Reducing Landslide Disaster Risk’ in line with some of 17 Sustainable Development Goals (SDGs), particularly SDG 11, “Make cities and human settlements inclusive, safe, resilient and sustainable,” of the United Nations.

For these important goals, the ICL has been inviting sponsorship from industries, businesses, and government agencies; all leading players in landslide science and technologies. They have been supporting a variety of the

ICL/IPL activities such as publishing the International full-color journal “Landslides (Journal of the International Consortium on Landslides), full-color books for WLFs, exhibiting their cutting-edge technologies in WLFs, etc. Here follow short introductions of their activities with their names, addresses and contact information:

Marui & Co. Ltd

1-9-17 Goryo, Daito City, Osaka 574-0064, Japan

URL: <http://marui-group.co.jp/en/index.html>

Contact: hp-mail@marui-group.co.jp

Marui & Co. Ltd. celebrates its 100th anniversary in 2020. Marui, as one of the leading manufacturers of testing apparatuses in Japan, has been constantly striving to further improve its service since its foundation in 1920, thus contributing to the sustainable development of our nation and society. Our main products cover a wide variety of destructive and non-destructive testing apparatuses in the fields of geotechnical engineering, concrete engineering (mortar, aggregates, etc.), and ceramic engineering. Of special note is that Marui has been helping manufacture ring-shear apparatuses half-century long based on the leading-edge idea of Dr. Kyoji Sassa, Professor Emeritus at the Kyoto University. Marui has delivered total seven ring-shear apparatuses to the Disaster Prevention Research Institute, Kyoto University, and 2 to the International Consortium on Landslides. Also the apparatuses were exported to the United States of America, China, Croatia and Vietnam.

Marui & Co. Ltd. takes great pleasure in developing, manufacturing, and providing new products of high value sharing the delight of achievement with our customers, and thus contributing to the social development. The whole staff of Marui & Co. Ltd. are determined to devote ceaseless effort to keep its organization optimized for its speedy and high-quality services, by the motto “Creativity and

K. Konagai (✉)
Organizing Committee of the Fifth World Landslide Forum,
International Consortium on Landslides, Kyoto, 606-8226, Japan
e-mail: konagai@iclhq.org

Revolution”, and strive hard to take a step further, as a leading manufacturer of testing apparatuses, to answer our customer’s expectations for the twenty-second century to come.

Nippon Koei Co. Ltd

5-4 Kojimachi, Chiyoda-ku, Tokyo 102-8539, Japan

URL: <https://www.n-koei.co.jp/english/>

Contact: <https://www.n-koei.co.jp/english/contact/input>

Nippon Koei Co. Ltd. and its group companies conduct many projects to support the growth of developing countries in Asia, Africa, the Middle and Near East, Latin America and other regions. Examples of their efforts include environmental measures to combat global warming, development of regional transportation infrastructure to support the rapid growth of emerging economies, and reconstruction assistance for regions affected by conflict and/or natural disasters.

OSASI Technos, Inc

65-3 Hongu-cho, Kochi City, Kochi 780-0945, Japan

URL: <http://www.osasi.co.jp/en/>

Contact: cs@osasi.co.jp

OSASI Technos, Inc. has been making its best efforts to develop its cutting-edge technologies for landslide early warning. Its unique compact and lightweight sensors making up the Landslide Early Warning System enable long-term monitoring of unstable landslide mass movements, precipitations, porewater pressure buildups, etc. in a remote mountainous area where commercial power is often unavailable. OSASI Technos, Inc. is also proud of its advanced technology to transfer observed data even in areas with poor telecom environments as proven in the successful implementations in South Asia.

All staff members of OSASI Technos work together for mitigation of landslide disasters worldwide.

Godai Corporation

1-35 Kuroda, Kanazawa, Iihikawa 921-8051, Japan

URL: [https://soft.godai.co.jp/En/Soft/Product/](https://soft.godai.co.jp/En/Soft/Product/Products/LS-RAPID/)

Products/LS-RAPID/

Contact: pp-sales@godai.co.jp

Ever since its foundation in 1965, Godai Kaihatsu Co. Ltd., a civil engineering consulting firm, has long been providing

a variety of software and measures particularly for natural disaster mitigation. With its rich expertise in both civil engineering and information technology (IT), the company has its primary goal to address real world needs of disaster mitigation. All the staff of Godai Kaihatsu Co. Ltd. feel it more than happy that their cutting-edge technologies help mitigate natural disasters.

Japan Conservation Engineers & Co. Ltd

3-18-5 Toranomon, Minato-ku, Tokyo 1050001, Japan

URL: <https://www.jce.co.jp/en/>

Contact: go_info@jce.jp

Japan Conservation Engineers & Co. Ltd. (JCE) is a general consulting firm working on landslide prevention research and consulting. JCE provides various disaster prevention technologies for debris flows, landslides, slope failures, rockfalls, etc. In addition, JCE is proud of its expertise having been conducting surveys and consulting works on coastal erosions and tsunami countermeasures for about 20 years. JCE contributes to the world through its activities in the realm of both structural and non-structural measures to build a resilient society.

OYO Corporation

7 Kanda-Mitoshiro-cho, Chiyoda-ku, Tokyo 101-8486, Japan

URL: <https://www.oyo.co.jp/english/>

Contact: <https://www.oyo.co.jp/english/contacts/>

OYO Corporation, the top geological survey company in Japan established in Tokyo in 1957, is well known as one of leading companies providing cutting-edge technologies and measures for natural disasters such as landslides, earthquakes, tsunamis, and floods. Not just developing and selling measuring instruments related to disaster prevention, OYO also delivers a market-leading services in 3D ground/geological modeling and 3D exploration technologies.

Kokusai Kogyo Co. Ltd

2 Rokubancho, Chiyoda-ku, Tokyo 102-0085, Japan

URL: <https://www.kkc.co.jp/english/index.html>

Contact: overseas@kk-grp.jp

Kokusai Kogyo Co. Ltd. as a leading company of geospatial information technologies, has long been providing public

services with its comprehensive expertise to address real world needs and cutting-edge measurement technologies. Kokusai Kogyo Co. Ltd. helps rebuild “Green Communities,” which has been of our great concern in terms of “environment and energy,” “disaster risk reduction” and “asset management”. Kokusai Kogyo Co. Ltd. offers the advanced and comprehensive analyses of geospatial information for developing new government policies, maintaining and operating social infrastructures safe and secure, and implementing low-carbon measures in cities.

Influenced by the recent global climate change, extreme rainfall events have become more frequent worldwide and resultant hydro-meteorological hazards are creating more deaths and devastations particularly in many developing countries where effective advanced countermeasures are not readily available. Kokusai Kogyo Co. Ltd. is proud of its achievements in establishing resilient infrastructure systems and implementing effective monitoring/early warning systems in developing countries, which have long been helping reduce the risks from natural hazards.

Geobrugg AG

Aachstrasse 11, 8590 Romanshorn, Switzerland

URL: www.geobrugg.com

Contact: info@geobrugg.com

Swiss company Geobrugg is the global leader in the supply of high-tensile steel wire safety nets and meshes – with production facilities on four continents, as well as branches and partners in over 50 countries. True to the philosophy “Safety is our nature” the company develops and manufactures protection systems made of high-tensile steel wire. These systems protect against natural hazards such as rockfall, landslides, debris flow and avalanches. They ensure safety in mining and tunneling, as well as on motorsport tracks and stop other impacts from falling or flying objects. More than 65 years of experience and close collaboration with research institutes and universities make Geobrugg a pioneer in these fields.

Ellegi Srl

Via Petrarca, 55 I-22070 Rovello Porro (CO) Italy

URL: <http://www.lisalab.com/engl/?seze=1>

Contact: info@lisalab.com

Ellegi srl provides worldwide monitoring services and produces Ground Based synthetic aperture radar (GBInSAR) for remote measurement of displacements and deformations on

natural hazards and manmade buildings using its own designed and patented LiSALab system.

Its activities started in 2003 as a spin off project to exploit commercially the Ground Based Linear Synthetic Aperture Radars technology developed by European Commission’s Ispra Joint Research Centre and based on the results of more than 10 years of research. Since then Ellegi has industrialized and developed the core technology of the LiSALab system and latest LiSAMobile system represents the 5th generation of development.

In 2003 it was the first commercial company in the world to provide GBInSAR measurements of natural hazards and structure.

Ellegi srl offers:

- Displacement fields measurement, control and monitoring of the deformation caused by natural hazards, like landslides, rockslides, sinkhole, volcanic deformation in every operative condition, including emergencies,
- Structural strain fields measurement, control, monitoring and diagnosis of the deformation affecting buildings, bridges, viaducts, dams,
- GBInSAR monitoring systems, installation, management and maintenance in order to provide information about natural hazards or anthropic activity, that can generate or cause slopes failures or buildings instabilities.

In all the above-mentioned activities Ellegi srl uses the GBInSAR LiSALab technology that represents a real “break-through”.

Chuo Kaihatsu Corporation

3-13-5 Nishi-waseda, Shinjuku-ku, Tokyo 169-8612, Japan

URL: <https://www.ckcnet.co.jp/global/>

Contact: <https://www.ckcnet.co.jp/contactus/>

Chuo Kaihatsu Corporation (CKC) was founded in 1946, and has been aiming to become the “Only One” consultant for our customers. We engage in the hands-on work that will “Remain with the earth, Remain in people’s hearts, and Lead to a prosperous future”. We focus on road, river and dam engineering to flesh out industrial infrastructures specifically by means of geophysical/geotechnical/geological investigations, civil engineering surveys and project implementations. In recent years, we make significant efforts on earthquake disaster mitigation, sediment disaster prevention/mitigation and ICT information services. Many achievements of ours have already contributed to mitigation of natural disasters such as landslides, earthquakes and slope failures in Japan, Asia and the Pacific Region.

IDS GeoRadar S.R.L

Via Augusto Righi, 6, 6A, 8, Loc. Ospedaletto, Pisa, Italy, 56121

URL: <https://idsgeoradar.com/>

Contact: info@idsgeoradar.com

IDS GeoRadar, part of Hexagon, provides products and solutions, based on radar technology, for monitoring applications including landslides, rockfalls, complex structures, mining and civil engineering. The company is a leading provider of Ground Penetrating Radar (GPR) and Interferometric Radar solutions worldwide. IDS GeoRadar is committed to delivering best-in-class performance solutions and to the pursuit of product excellence, through the creation of application-specific, innovative and cost-efficient systems for a wide range of applications.

METER Group, Inc

2365 NE Hopkins Court, Pullman, WA 99163, USA

URL: metergroup.com/wlf5

Contact: bryan.wacker@metergroup.com

METER Group provides accurate, rugged, and dependable instrumentation to monitor moisture in all its phases within an unstable slope. METER specializes in instrumentation for near real-time monitoring of incoming moisture in the form of rain and weather. In addition, we provide real-time below-surface monitoring of existing moisture conditions like moisture content and soil suction which show how the soil profile is filling with water to saturation, including the transition to positive pore water pressure.

The ZL6 advanced cloud data logger works together with ZENTRA Cloud data software to simplify and speed up data collection, management, visualization, and alerting. Our well-published instrumentation is used worldwide in universities, research and testing labs, government agencies, and industrial applications.

For almost four decades, scientists and engineers have relied on our instrumentation to understand critical moisture parameters. We've even partnered with NASA to measure soil (regolith) moisture on Mars. Wherever you measure, and whatever you're measuring, rely on METER for accuracy, affordability, and simplicity that will make your job easier.

Asia Air Survey Co. Ltd

Shinyuri 21 BLDG 3F, 1-2-2 Manpukuji, Asao-Ku, Kawasaki, Kanagawa 215-0004, Japan

URL: <https://www.ajiko.co.jp/en/>

Contact: service@ajiko.co.jp

Asia Air Survey (AAS), as one of the leading engineering and consulting companies, has long been providing disaster prevention and mitigation services for over 65 years, particularly in the fields of landslide, debris flow, erosion control, etc. AAS is proud of being the inventor of Red Relief Image Map (RRIM), which is a cutting-edge 3D terrain visualization method allowing great geomorphological details to be visualized in one glance, thus has been used in various facets of disaster prevention and mitigation.

Kiso-Jiban Consultants Co. Ltd

Kinshicho Prime Tower 12 Floor, 1-5-7 Kameido, Koto-ku, Tokyo 36-8577, Japan

URL: <https://www.kisojiban.com/>

Contact: kisojiban-contactus@kiso.co.jp

Kiso-Jiban Consultants, established in 1953, is an engineering consulting firm especially well known in the field of geotechnical engineering. The areas of its comprehensive services are listed below:

- Geological and Geotechnical Survey
- Geotechnical Analysis and Design
- Disaster Prevention and Management
- GIS (Geographic Information Systems)
- Soil and Rock Laboratory Tests
- Instrumentation and Monitoring
- Geophysical Exploration and Logging
- Distribution of Geosynthetics Products

Much-talked-about new service is Kiso-SAR System allowing accurate estimation of both extent and rate of landslide movements based upon a comprehensive interpretation of InSAR results from geotechnical and landslide engineering viewpoint (see the one-page introduction of Kiso-Jiban Consultants Co. Ltd.). With Kiso-SAR system, the following pieces of important geotechnical information can be provided:

- (1) Extent of a deforming landslide mass (and the rate of its movement)
- (2) Consolidation buildup in soft clay underlying a fill
- (3) Deformation buildups induced by slope cutting.

Okuyama Boring Co. Ltd

10-39 Shimei-cho, Yokote City, Akita 013-0046, Japan

URL: <https://okuyama.co.jp/en/>

Contact: info@okuyama.co.jp

Okuyama Boring Co. Ltd. is proud of its achievements in various projects to help solve many landslide problems. The company has been offering services in geological surveys and analyses, developing rational countermeasures against various geotechnical problems as well as safe workflow diagrams, and providing necessary pieces of advice for ensuring safety during landslide countermeasure works. For this purpose, Okuyama Boring Co. Ltd. works on monitoring, observations, field surveys, numerical analyses, countermeasure works, etc. of landslides.

Kawasaki Geological Engineering Co. Ltd

Mita-Kawasaki Bldg, 2-11-15 Mita, Minato-ku, Tokyo108-8337, Japan

URL: <http://www.kge.co.jp/>

Contact: post-master@kge.co.jp

Kawasaki Geological Engineering Co. Ltd. as one of the leading members of SAAM Research Group, has proactively been involved in developing “Sustainable Asset Anchor Maintenance (SAAM, hereafter) System,” enabling easy maintenance of ground anchors. Its unique jack, weighing about half the weight of a conventional jack, together with a newly developed jig, can be applied to any type of anchor even with a short extra length, thus allowing for in situ lift-off tests on these anchors. The SAAM system also has an optional weight meter that can be installed after performing a lift-off test.

Nissaku Co. Ltd

4-199-3 Sakuragi-cho, Omiya-ku, Saitama 330-0854, Japan

URL: <https://www.nissaku.co.jp/>

Contact: survey@nissaku.co.jp

Nissaku Co. Ltd., founded in 1912 as a well drilling company, provides services for far-flung fields of not only groundwater exploitation but also measures for landslides. Having its rich expertise in these fields, Nissaku Co. Ltd. offers general reliable one-stop technical services including designs, investigations, analyses, constructions, and maintenances.

Full-color presentations from the above seventeen exhibitors focusing on their landslide technologies are shown on the following pages. Their cutting-edge technologies have of course been instrumental in the progress that we have made in landslide risk-reduction worldwide, and we want to exert even greater effort to aim high given the KLC 2020 as our new action goals. The International Consortium on Landslides seeks volunteers willing to support our activities introducing their brand-new technologies for landslide disaster mitigation in our international journal “Landslides,” full color books for WLFs, exhibitions at WLFs, etc. If you are interested in being engaged in supporting ICL activities, please contact the ICL secretariat < secretariat@iclhq.org > .

Stress / Speed Dual Control
Ring Shear Apparatus

ICL-2 type : High-Stress Landslide Simulator

ICL-2 type



MARUI & CO., LTD.

Web site : <https://www.marui-group.co.jp/en/>

E-mail : hp-mail@marui-group.co.jp

Address : 1-9-17 Goryo, Daito City,
Osaka Prefecture,
574-0064, Japan

Phone : 81-72-869-3201

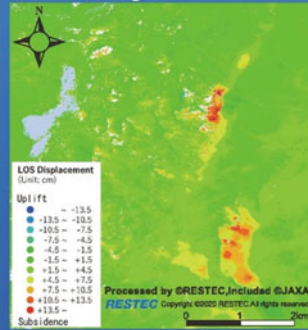
F a x : 81-72-869-3205

Geohazard Management

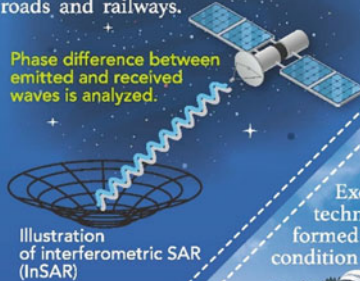
Response to natural disasters with various technologies from space to the surface

Remote Sensing Technology

Potential hazards around the globe are assessed by optical remote sensing and InSAR which can detect land-resources, topographic features, and ground deformation. Example of InSAR, shown below, is a new effective way to detect deformation of slopes along infrastructures such as roads and railways.



Phase difference between emitted and received waves is analyzed.



Landslide monitoring using InSAR

Integrated technologies and engineers-Application of spaceborne, airborne, and ground-based technologies for disaster risk reduction.

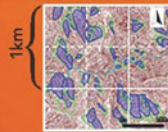
A team of 5,497 multidisciplinary experts

Excellent teams, covering advanced and wide range of technologies based on long-standing experiences, are formed to provide optimum solutions customized for each condition and needs.



AI Technology

Our AI technology helps quickly identify morphological features of past and current landslides.



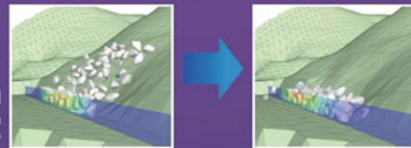
Near a volcano, our AI technology can help identify unstable masses of volcanic matters perching on the flanks of the volcano.
Data for machine learning: DEM and landslides identified by an expert



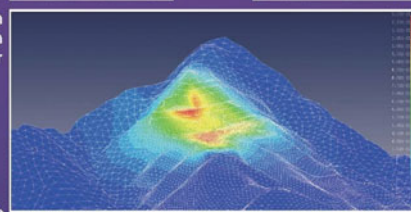
Extraction of landslide topography using AI technology

Numerical simulation

We can predict the extent of damage in the event of a disaster and the effectiveness of countermeasure works by numerical analysis.



Numerical simulation for slope excavation by R&D center



R&D center

State-of-the-Art Nippon Koei's R&D Center



NIPPON KOEI

Global Consulting Engineering Firm

Head Office 5-4 Kojimachi, Chiyoda-ku, Tokyo 102-8539, Japan

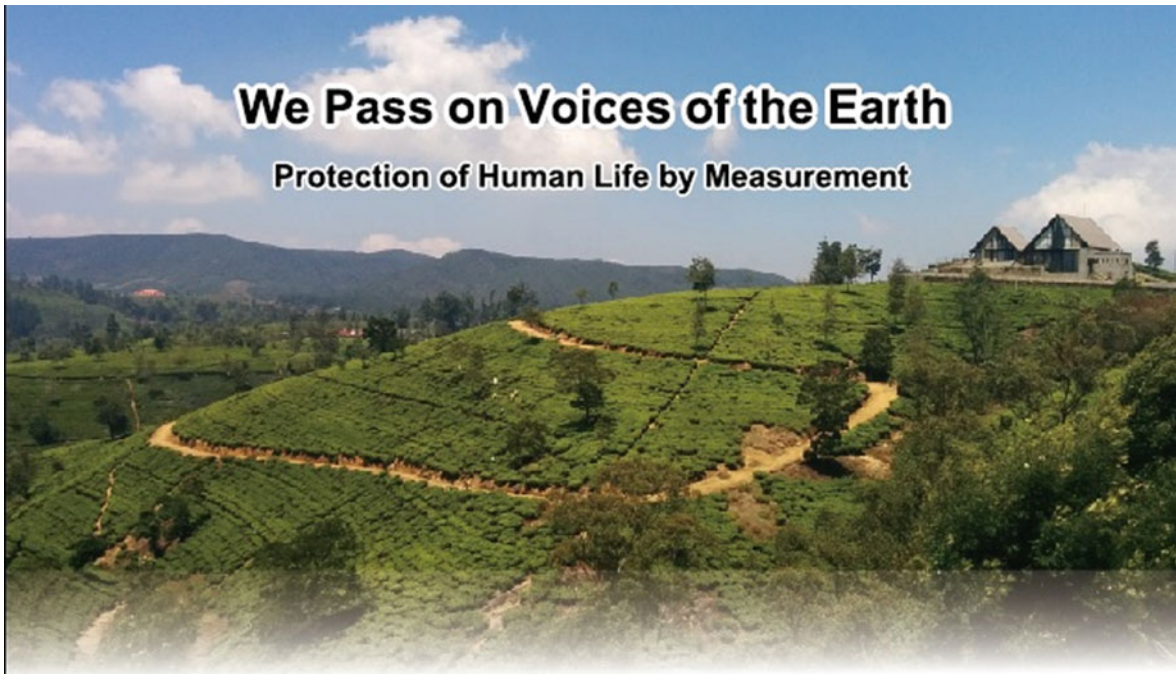
TEL +81-3-3238-8030

Website www.n-koei.co.jp/english



We Pass on Voices of the Earth

Protection of Human Life by Measurement



Measurement technology × Transmission technology

Early Warning System

Extensometer



Communication device



Multi-point Inclinometer



Alarm device



Rain gauge



Corporate Headquarters (Kochi)
65-3 Hongu-cho, Kochi-shi, Kochi 780-0945, Japan
TEL:+81-88-850-0535 E-mail : cs@osasi.co.jp
<http://www.osasi.co.jp/en/>

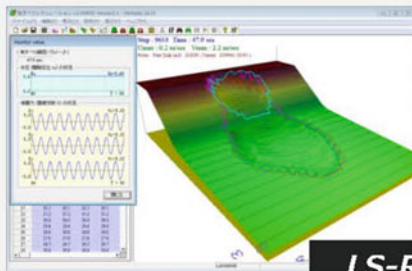
Tokyo Headquarters
Sumitomo Seimei Nishi-Shimbashi Building 4F,
1-10-2, Nishi-shimbashi, Minato-ku, Tokyo, 105-0003, Japan
TEL:+81-3-5510-1391 E-mail : cs@osasi.co.jp

GODAI KAIHATSU Co.,Ltd.

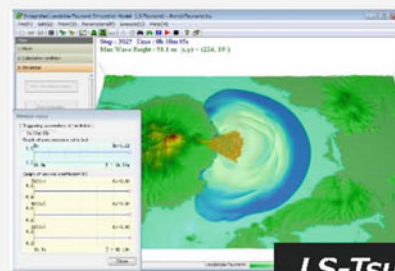
*Good Human Relation
& Harmony with Nature*



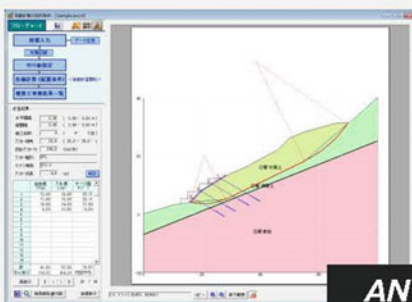
We have developed a variety of software related to the slope disaster prevention and social infrastructure, analysis, simulation, and monitoring.



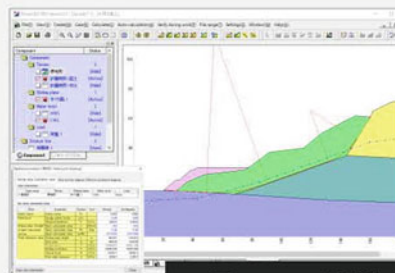
LS-RAPID



LS-Tsunami



ANCHOR



Power SSA PRO

◆ Address : 1-35 Kuroda, KANAZAWA-City, ISHIKAWA Pref. 921-8051, Japan
 ◆ Tel : +81-76-240-9587 ◆ Fax : +81-76-240-9585
 ◆ URL : <http://www.godai.co.jp/> ◆ E-mail : pp-sales@godai.co.jp



We aim to establish a sustainable country by various technology related to earth, water, and vegetation.



Consulting Services

Slope Disaster Management/
Forest Conservation and Afforestation/
Community Based Disaster Risk Reduction/
Disaster Risk Assessment Technology Transfer



Construction and Supervision

Construction of Landslide and Slope Disaster
Prevention Measures/
Countermeasures Against Aging Infrastructure



Research and Development

Slope Protection Technology/
Afforestation Technology/
Geospatial Information Technology/
3D Simulation Technology/
Laboratory Testing of Soil and Rocks

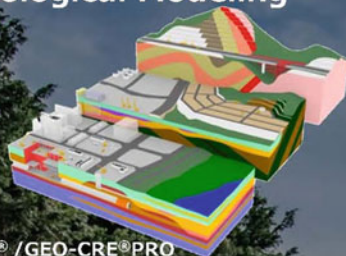
 **JAPAN CONSERVATION ENGINEERS & CO., LTD.**

3-18-5, Toranomon, Minato, Tokyo, Japan 105-0001
Tel: +81.3.3436.3673 E-mail: go_info@jce.jp URL <https://www.jce.co.jp/en>



**Find the best answer to the future
of people and the earth.
To realize a sustainable society.**

3D Geological Modeling



**GEO-CRE® /GEO-CRE®PRO
OCTAS® Modeler**

OCTAS Modeler is a system to support the utilization of subsurface information. It helps to grasp the positional relationship of the borehole logs and create various 3D models including borehole, soil, bearing layer, and terrain.

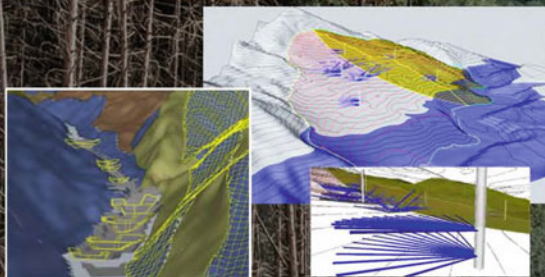


Inclinometer

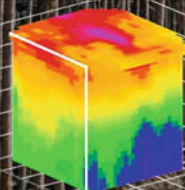


Clino-pole

Tilt sensor for Sediment disaster



3D Geophysical Survey



McSEIS-AT

McSEIS-AT is an epoch-making microtremor exploration system that can measure S-wave velocity structures in three dimensions.



oyo corporation

7 kanda, Mitoshiro-cho, Chiyoda-ku, Tokyo
101-8486, JAPAN
<https://www.oyo.co.jp/english/>

Copyright © 2020 OYO Corporation. All rights reserved

Green Communities

~Towards a better future,
for people and the environment~

Participations



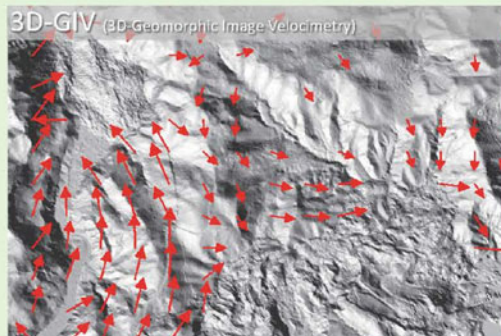
SENDAI FRAMEWORK
FOR DISASTER RISK REDUCTION 2015-2030



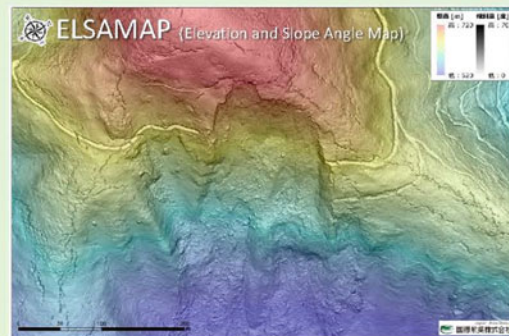
Japan Asia Group

KOKUSAI KOGYO

Kokusai Kogyo as a leading company of geospatial information technologies, has been contributing to the improvement of public services with advanced measurement technologies and a wide range of consulting technologies. Kokusai Kogyo supports the development of "Green Communities" representing the new era public concerns on "environment and energy," "disaster risk reduction" and "asset management". Kokusai Kogyo offers the advanced analysis of geospatial information consultancy for developing new government policies, maintaining and operating social infrastructures with safe and secure city planning, and building low-carbon cities.



3D-GIV can help grasp the ground surface displacements caused by natural phenomena such as landslides by analyzing differences between digital geomorphic images obtained through ad hoc Airborne Laser Surveys.



ELSAMAP is our cutting-edge 3D terrain visualization method allowing great geomorphological details to be visualized in one glance with gray-scaled slope inclinations and colored altitudes. ELSAMAP has been used to interpret micro-topographies, landslides and some other things.



Our Realtime Hazard Map reflects up-to-date information of soil natures and precipitations at landslide hazard sites, etc. that can constantly be changing, and evaluates area-wide hazard risk in real time.



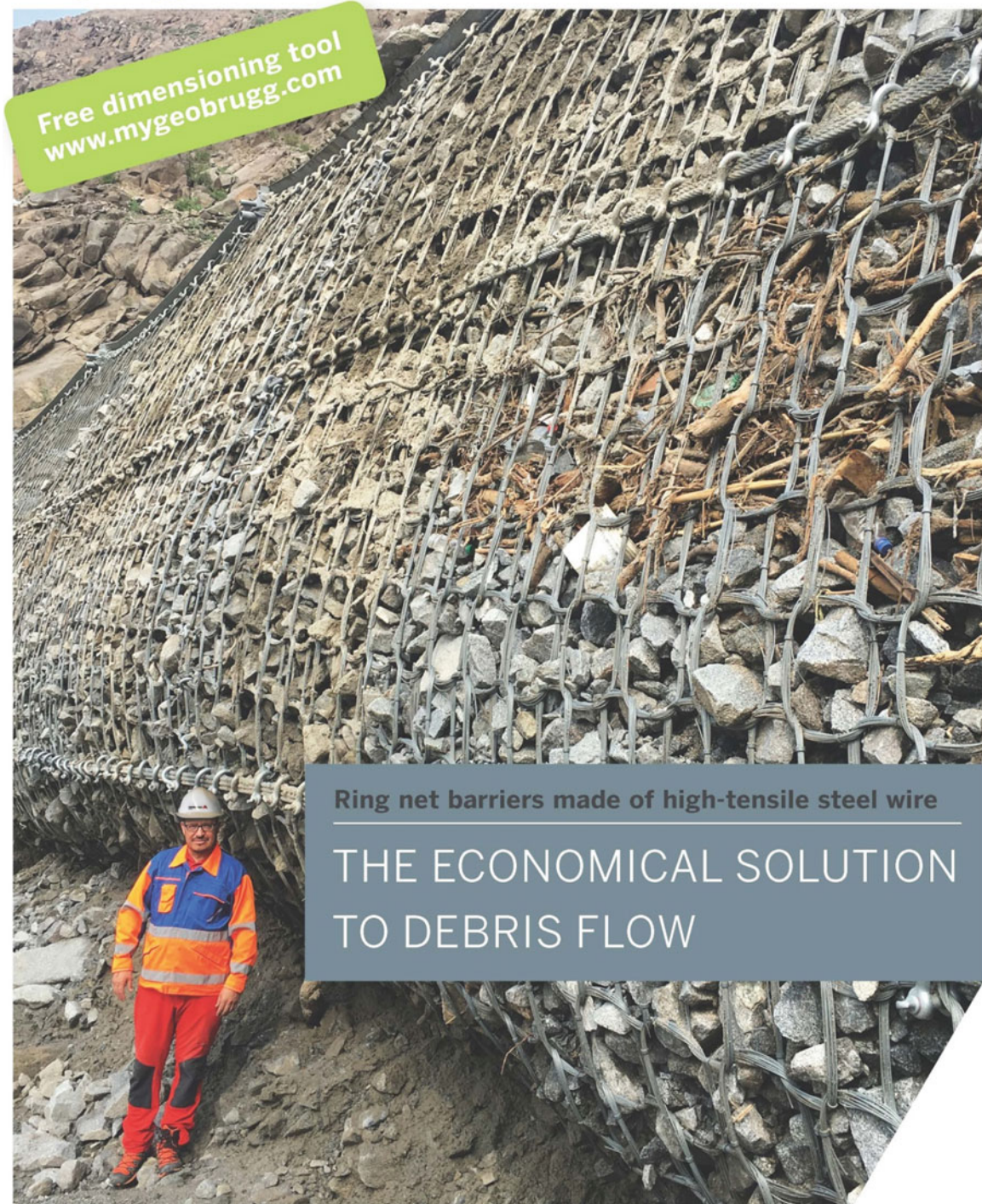
"shamen-net" is a total monitoring system integrating GNSS and other monitoring devices (Measurement precision: +/-1mm, on a real time basis)



www.geobrugg.com/debrisflow



Safety is our nature



Free dimensioning tool
www.mygeobrugg.com

Ring net barriers made of high-tensile steel wire

THE ECONOMICAL SOLUTION
TO DEBRIS FLOW



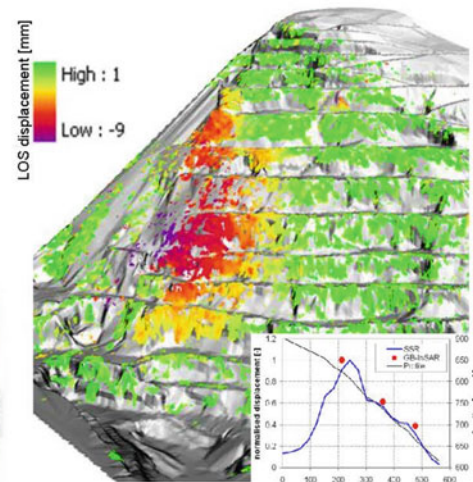
... A step ahead in monitoring structures and natural hazards ...

by Ground Based Interferometric Synthetic Aperture Radar LiSALab technology

Ellegi's provides services and products for remote sensing measurement of displacements and deformations of natural hazards and manmade buildings using a ground based SAR system, known as LiSALab system, in software production and system integration, production and developments of data acquisition, visualization and data-analysis systems.

LiSALab system at present is at its 5th generation of development since 2003.

One of the biggest point of strength of Ellegi is based on its high vertical integration. It can internally design, produce, sell, maintains and provide services and products using GBInSAR LiSALab technology, the customer can have all the answers.

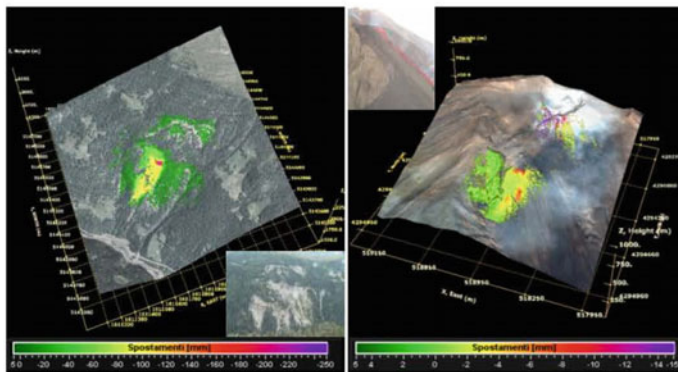


GBInSAR LiSALab technology quarry monitoring example and displacements' field comparison between the GBInSAR measurements and FEM model results.

Ellegi srl offers:

- **displacement fields measurement, control and monitoring** of the deformation caused by natural hazards, in every operative conditions, including emergencies;
- **structural strain fields measurement, control, monitoring** and diagnosis of the deformation affecting buildings, bridges, viaducts, dams, etc. etc.;
- **integrated monitoring systems** design, installation, management and maintenance in order to provide information about natural hazards or anthropic activity, that can generate or cause slopes or buildings instabilities.

Since 2003 Ellegi has provided services, systems and technologies in the world to the most important players in the monitoring sector.



GBInSAR LiSALab technology results in monitoring a slope affected by a landslide (left) and a volcanic slope affected by deformation (right).


Landslide or moving areas mapping and boundaries identification is made easy by GBInSAR LiSALab technology.

Ellegi srl

Via Bandello, 5 I-20123 Milano Italy
 Headquarters: via Petrarca, 55 I-22070 Rovello Porro CO Italy
 Tel. +39 02 9443 5051 Fax +39 +39 02 9443 5052
 info@lisalab.com - www.lisalab.com

Early Warning Monitoring System of Slope Failure using Multi-point Tilt Change and Volumetric Water Content

- CHUO KAIHATSU CORPORATION -

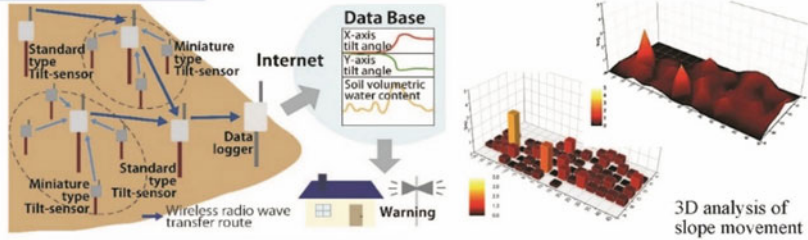


Objectives and Subjects

Research and develop a highly accurate, multi-point early-warning system for slope failure using low-cost tilt sensors

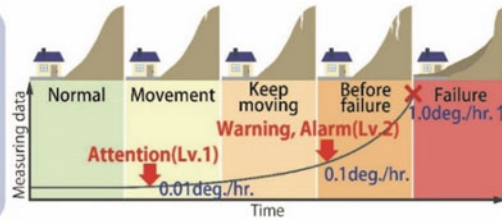
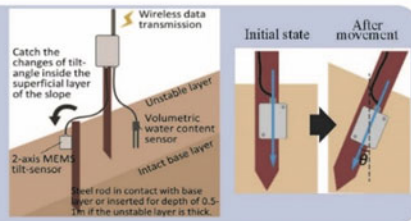
NETIS (MLIT) : KT-130093-A
 Japanese Geotechnical Society Award for Technology Development 2014
 The Society of Instrument and Control Engineers Award for Technology Development 2015
 NETIS (MLIT) Evaluation Promotion Technology from 2016

- Low-cost, easy-to-install tilt sensors.
 ⇒ **Realized low cost multi-point measurement.**
- Prediction of slope deformation by multi-point measurements.
 ⇒ **Realized high-precision, stable, slope failure early warning system.**



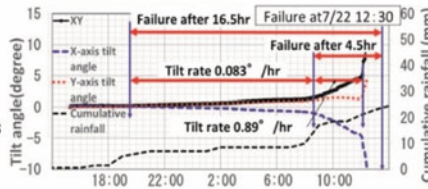
Accomplishments

Effective, rapid, and convenient installation of sensors by inserting a steel pole into the slope and affixing the sensor module.



Utilization example

At other sites, there were gradual tilt rate increases within a relatively short time before slope failures occurred; the rate increase, in a way, was inversely proportional to the remaining time before failure.



Early warning can be issued based on the relationship between tilt rate and remaining time to failure.

International Support

- Support pilot projects
- Promote an international standard
- Export of technology packages

Technical Services

- Early warning of slope failure
- Prevention of secondary disasters
- Assess pre-failure phenomena of slopes
- Dynamic monitoring of landslides in mountainous areas
- Application to Internet of Things and trends in Big data

Joint Research by Local Autonomies and Private Enterprise

- Secondary disaster prevention of cutting slope works
- Slope monitoring in densely populated areas
- Community participation in disaster-prevention education

Users

JICA, Local autonomies, Regional Bureaus of MLIT, General construction company etc.
 International : Taiwan, China, India, Australia, Sri Lanka, Pakistan, Bhutan etc.

Cooperation with Regional Bureau of MLIT to develop research results

- Slope failure prevention along roads
- Slope failure prevention along railway lines
- Monitoring of dam site wall slopes
- Monitoring of natural slopes

Places of use


To fulfill a role of early warning for disaster prevention by using the results of research and develop for natural slope, road works, cutting slope works, and rock fall.

Achievement (-2019)

Over 900 sets in Japan
Over 300 sets abroad

High-precision and stable early-warning system for slope failure.
 →Realized early-warning system based on spatial and temporal analysis of entire slope behavior.

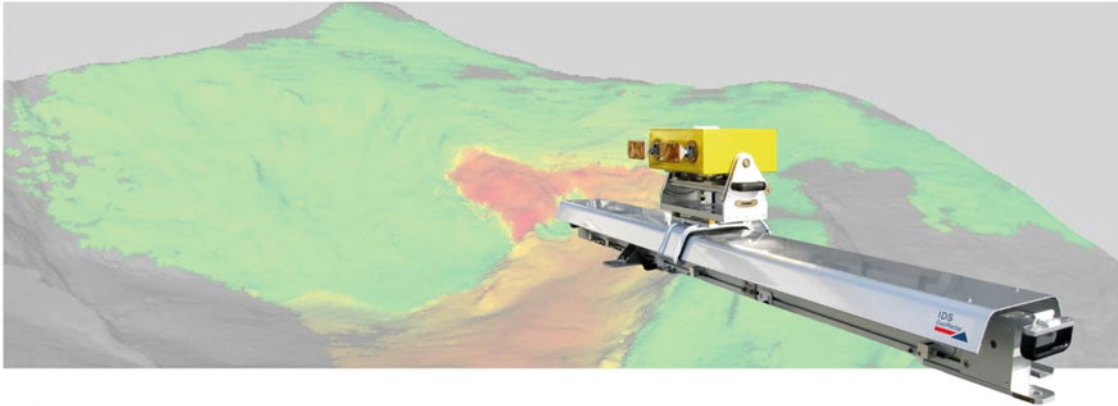
This R&D project is sponsored by Cabinet office of Japan
 Principal Investigator : Chuo Kaihatsu Corporation


 Cross-ministerial Strategic Innovation Promotion Program



IBIS FM - Natural Hazard Monitoring Solution

GB-InSAR System with Advanced Atmospheric Correction



IDS GeoRadar is nowadays the leader company in the Radar monitoring solutions applied to landslide monitoring, thanks to the combination of the highest performance radar technology with the most advanced data processing algorithm for the removal of atmospheric artifacts integral part of Guardian Software.

The unique IBIS-FM radar system accurately monitors multiple scales of displacements in real time, from early detection of slow movements to fast accelerations associated with slope collapse. The great operative range, up to 4500 m, allows to safely deploying the system in comfortably accessible areas, without exposing people and equipment to hazardous zones.

Fully automatic

The atmospheric correction procedure does not require any input from the user (does not need any stable area selection); it is a completely automatic software processing, not requiring advanced know-how to the user. The atmospheric compensation algorithm is based on hundreds of thousands of pixels automatically selected by the software and updated at each radar scan. It permits to achieve the best performances even in case of extreme or unstable atmospheric conditions.



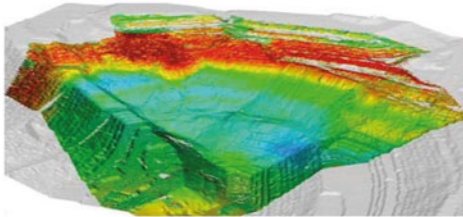
Advanced 3D atmospheric effects modelling

IDS GeoRadar algorithm for atmospheric correction offers unique capability able to model and remove complex atmospheric effects in extensive areas overcoming the limits of the standard linear model algorithms, providing very clean displacement maps in the most extreme atmospheric conditions environment.

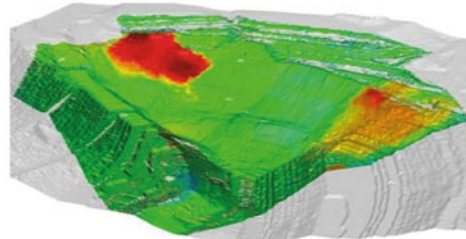


Slow and fast movement detection

IDS GeoRadar algorithm is able to distinguish very slow movement together with the faster ones providing the capability to measure in real time movements across four orders of magnitudes: from very fast movements (up to 150 mm/hour) to extremely low displacements (few mm/month).



Displacement map obtained with standard processing and standard atmospheric correction



Displacement map obtained with IDS GeoRadar Guardian atmospheric correction and processing



IDS GeoRadar Srl
Part of Hexagon
Via Augusto Righi, 6, 6A, B - 56121 Ospedaletto, Pisa, Italy
Tel: +39 050 89 34 100
info@idsgeoradar.com
www.idsgeoradar.com



METER
ENVIRONMENT

LANDSLIDE PREDICTION AND ALERTS **POSITIVE & NEGATIVE PORE WATER** **PRESSURE MONITORING**

DISCOVER NOW



For more information visit
metergroup.com/wlf5



ASIA AIR SURVEY CO.,LTD.

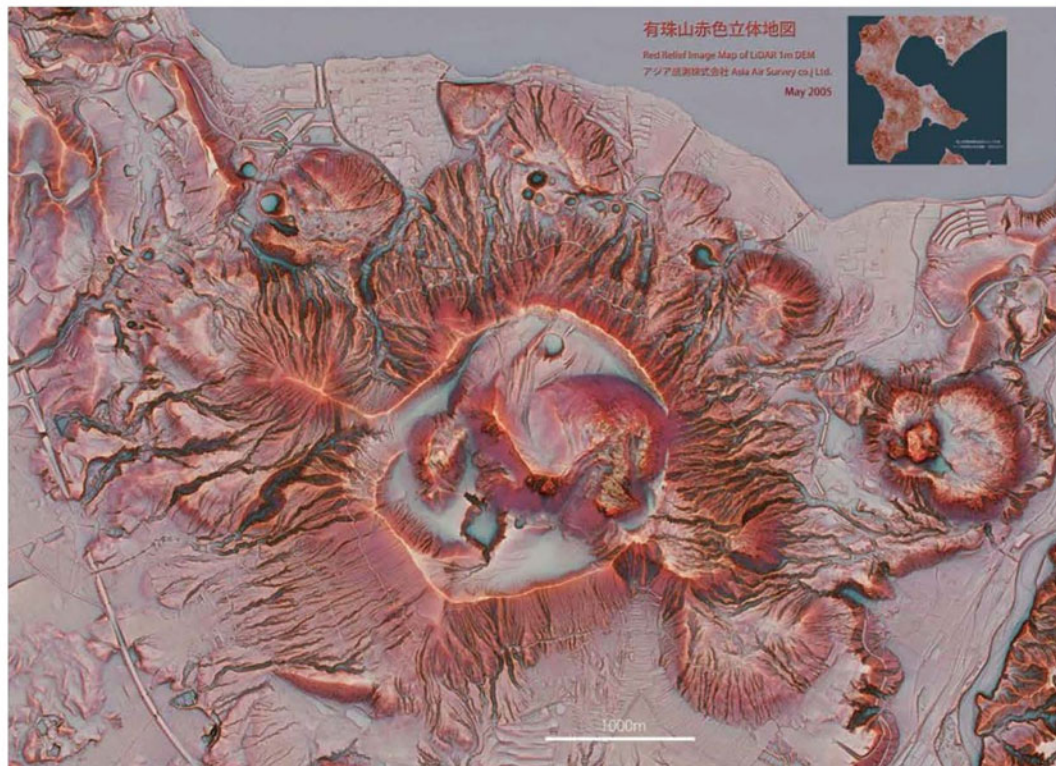
PIONEERING THE FUTURE

A novel 3D visualization technique

Red Relief Image Map (RRIM)

Developed by AAS, RRIM is a simple and effective tool for representing and interpreting ground surface features. The RRIM allows great geomorphological details to be visualized in one glance with a single map without any device, at any map scale, from any viewing angles without shades.

AAS provides one-stop services of RRIM.



RRIM of Mt.Usu, Japan, from 1m mesh Lidar data.

Contact:

Shinyuri 21 BLDG 3F, 1-2-2 Manpukuji, Asao-Ku, Kawasaki City, Kanagawa Prefecture, 215-0004, Japan

<https://www.ajiko.co.jp/en/>

email:service@ajiko.co.jp

Tel. +81-44-969-7510 Fax. +81-44-965-0029

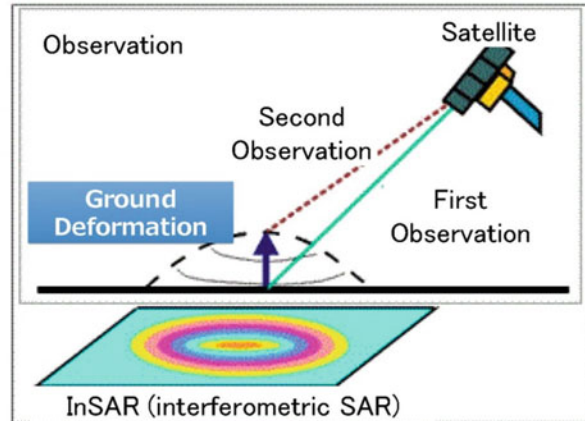
Kisojiban

Kiso-Jiban Consultants Co., Ltd.

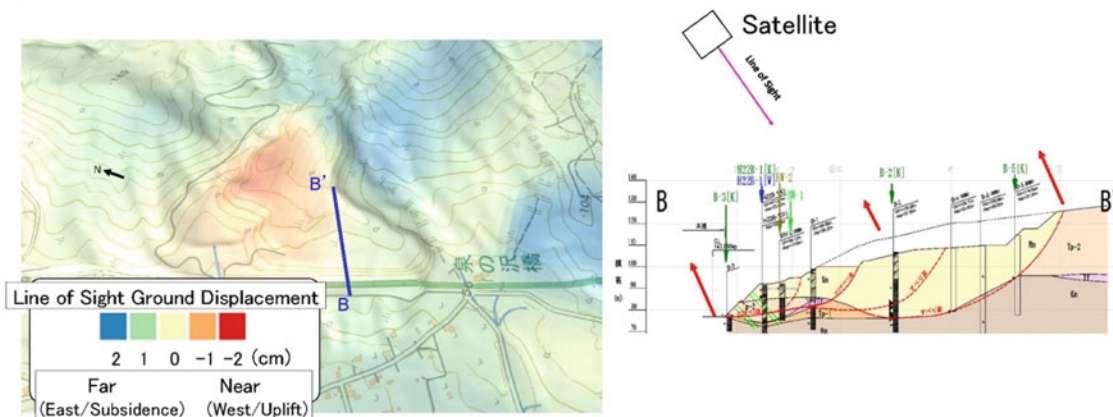
Monitoring Service for Landslide by Kiso-SAR System

What's SAR ?

SAR (Synthetic Aperture Radar) is a technique that utilizes interference of radio waves for precise determination of distance. InSAR (interferometric SAR), the phase of the received backscattered signal from two images of the same scene are used to measure path length differences with an accuracy of a few millimeters.



Ground Deformation Estimation in Landslides



Ground Deformation of Landslide Observed by Kiso-SAR System

Kisojiban

Kiso-Jiban Consultants Co., Ltd.
 Kinshicho Prime Tower 12 Floor,1-5-7
 Kameido, Koto-ku, Tokyo 136-8577, Japan
 Tel.: +81-3-6861-8800



Small & simple water drainage drilling system* for landslide disaster prevention

Simple & Small

- Simple structure.
- At a narrow space (0.3m×1.5m for guide rail, 0.8m×2.0m for drilling machine base).
- Lightweight equipment (Max. weight of drilling machine: 25kg).
- Easy installation of one operational well requires only 2 persons.

Quick & Short-term construction

- All pieces of equipment are man-portable.
- Preparation time for starting drilling is only 30 min.
- 50% reduction in construction time compared with conventional construction method.

Low cost & High effectivity

- Additional works (ex. scaffold or construction road) are not required.
- 50% reduction in construction cost compared with conventional construction method.
- About 30m long water drainage hole can be drilled in clayey and/or soft rock layers.

Safety & Environmentally friendly

- Small sound and low vibration.
- Construction yard is not required.



*Japanese utility model registration No.3186011



奥山ボーリング株式会社
Okuyama Boring Co.,Ltd.

<https://okuyama.co.jp/en/>

10-39 Shinmei-cho, Yokote-City, AKITA Pref. 013-0046, JAPAN

Sustainable Asset Anchor Maintenance System



What's "SAAM System"?

SAAM stands for "Sustainable Asset Anchor Maintenance".

SAAM Jack, only half the weight of a conventional jack, enables lift-off tests in various onsite conditions.

SAAM, thus, allows for easy maintenance of ground anchors.



SAAM Jack



SAAM System

SAAM-A (PAT No. 5971596)

Lift-off tests on anchors with a short extra length can be performed with a newly developed jig.



Installation of Inner Coupler



Removal of Wedge

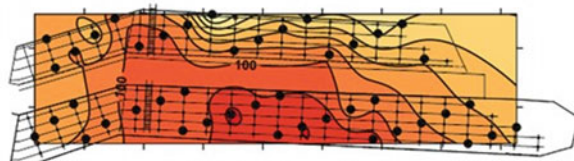
SAAM-L (PAT No. 5440772)

SAAM load cell can be attached to any anchors without loosening them.

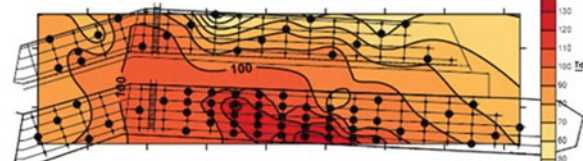


Load Meter

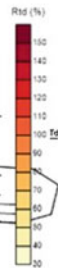
Planar Distribution of Anchor's Tensioning Force



Thinning Measuring for a quarter

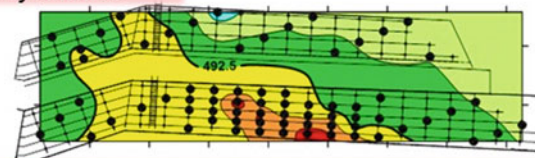


Additional Survey



Evaluation based on Soundness of Anchors

	Evaluation	Status	Coping example
0.9 Tys	E+	Risk of Breakage	Emergency measures
1.1 Ta	D+	Risk of Damage	Implementation of countermeasure work
Allowable anchor force (Ta)	C+	Exceeds the allowable value	Implementation of countermeasure work
Design anchor force (Td)	B+		Follow up
Tensile force when fixed (Pt)	A+	Good	
0.8 Pt	A-		
0.5 Pt	B-		Follow up
0.1 Pt	C-	Function deterioration	Implementation of countermeasure work
	D-	Dysfunction	Implementation of countermeasure work



SAAM 合同会社アンカーアセットマネジメント研究会
Society of Anchor Asset Management

川崎地質株式会社
Kawasaki Geological Engineering Co., Ltd.
Marketing & Sales Department
URL : www.kge.co.jp TEL : +81-3-5445-2077



Established in 1912

NISSAKU CO., LTD.

WELL DRILLINGS & CONSULTING ENGINEERS



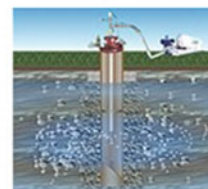
Geological Survey,
Construction
Consultancy Service



Civil Construction



Well Drilling



Well Rehabilitation



Facility Construction



Manufacturing and
Sales of Equipment



Overseas Business



Technology
Development

Head Office No. 199-3, Sakuragi-cho 4-chome, Omiya-ku, Saitama-shi, Saitama 330-0854, Japan

TEL : 048-644-3911 FAX : 048-644-3958

Branch Office : Sendai, Niigata, Jyoetsu, Tokyo, Nagano, Komatsu, Nagoya, Shizuoka, Osaka, Fukuoka,
Naha and Konosu (Saitama factory)

URL : <http://www.nissaku.co.jp/>

E-Mail : honsha@nissaku.co.jp



International Consortium on Landslides

	<h2>International Consortium on Landslides</h2> <p>An international non-government and non-profit scientific organization promoting landslide research and capacity building for the benefit of society and the environment</p> <p>President: Peter T. Bobrowsky (Geological Survey of Canada) Vice Presidents: Matjaž Mikoš (University of Ljubljana, Slovenia), Dwikorita Karnawati (Agency for Meteorology, Climatology, and Geophysics, Indonesia), Nicola Casagli (University of Florence, Italy), Binod Tiwari (California State University, USA), Željko Arbanas (University of Rijeka, Croatia) Executive Director: Kaoru Takara (Kyoto University, Japan), Treasurer: Kyoji Sassa (Prof. Emeritus, Kyoto University, Japan)</p>
	<p>ICL Full Members: Geotechnical Engineering Office, Hong Kong Special Administrative Region, China UNESCO Chair for the Prevention and the Sustainable Management of Geo-hydrological Hazards - University of Florence, Italy Korea Institute of Geoscience and Mineral Resources (KIGAM) University of Ljubljana, Faculty of Civil and Geodetic Engineering (ULFGG), Slovenia</p> <p>Albania Geological Survey / The Geotechnical Society of Bosnia and Herzegovina / Center for Scientific Support in Disasters – Federal University of Parana, Brazil/ Geological Survey of Canada / University of Alberta, Canada / Northeast Forestry University, Institute of Cold Regions Science and Engineering, China / China University of Geosciences / Chinese Academy of Sciences, Institute of Mountain Hazards and Environment / Tongji University, College of Surveying and Geo-Informatics, China / The Hong Kong University of Science and Technology, China / Shanghai Jiao Tong University, China / The University of Hong Kong, China / Universidad Nacional de Colombia / Croatian Landslide Group (Faculty of Civil Engineering, University of Rijeka and Faculty of Mining, Geology and Petroleum Engineering, University of Zagreb) / City of Zagreb, Emergency Management Office, Croatia / Charles University, Faculty of Science, Czech Republic / Institute of Rock Structure and Mechanics, Department of Engineering Geology, Czech Republic / Brown Coal Research Institute, Czech Republic / Cairo University, Egypt / Technische Universität Darmstadt, Institute and Laboratory of Geotechnics, Germany / National Environmental Agency, Department of Geology, Georgia / Universidad Nacional Autónoma de Honduras (UNAH), Honduras / Amrita Vishwa Vidyapeetham, Amrita University / Vellore Institute of Technology, India / National Institute of Disaster Management, India / Agency for Meteorology, Climatology, and Geophysics of the Republic of Indonesia (BMKG Indonesia) / University of Gadjah Mada, Center for Disaster Mitigation and Technological Innovation (GAMA-InaTEK), Indonesia / Parahyangan Catholic University, Indonesia / Building & Housing Research Center, Iran / Italian Institute for Environmental Protection and Research (ISPRA) - Dept. Geological Survey, Italy / University of Calabria, DIMES, CAMILAB, Italy / Istituto de Ricerca per la Protezione Idrogeologica (IRPI), CNR, Italy / DIA–Università degli Studi di Parma, Italy / University of Torino, Dept of Earth Science, Italy / Centro di Ricerca CERi - Sapienza Università di Roma, Italy / Kyoto University, Disaster Prevention Research Institute, Japan / Japan Landslide Society / Korean Society of Forest Engineering / National Institute of Forest Science, Korea / Korea Infrastructure Safety & Technology Corporation / Korea Institute of Civil Engineering and Building Technology / Slope Engineering Branch, Public Works Department of Malaysia / Institute of Geography, National Autonomous University of Mexico (UNAM) / International Centre for Integrated Mountain Development (ICIMOD), Nepal / University of Nigeria, Department of Geology, Nigeria / Moscow State University, Department of Engineering and Ecological Geology, Russia / JSC “Hydroproject Institute”, Russia / University of Belgrade, Faculty of Mining and Geology, Serbia / Comenius University, Faculty of Natural Sciences, Department of Engineering Geology, Slovakia / Geological Survey of Slovenia / University of Ljubljana, Faculty of Natural Sciences and Engineering (ULNTF), Slovenia / Central Engineering Consultancy Bureau (CECB), Sri Lanka / National Building Research Organization, Sri Lanka / Landslide group in National Central University from Graduate Institute of Applied Geology, Department of Civil Engineering, Center for Environmental Studies, Chinese Taipei / National Taiwan University, Department of Civil Engineering, Chinese Taipei / Asian Disaster Preparedness Center, Thailand / Ministry of Agriculture and Cooperative, Land Development Department, Thailand / Institute of Telecommunication and Global Information Space, Ukraine / California State University, Fullerton & Tribhuvan University, Institute of Engineering, USA & Nepal / Institute of Transport Science and Technology, Vietnam / Vietnam Institute of Geosciences and Mineral Resources (VIGMR).</p>
	<p>ICL Associates State Key Laboratory of Geohazard Prevention and Geoenvironment Protection (Chengdu University of Technology), China / Czech Geological Survey, Czech Republic / Department of Earth and Environmental Sciences, University Aldo Moro, Bari, Italy / Department of Sciences and Technologies, University of Sannio, Italy / Department of Earth and Environmental Sciences – University of Pavia, Italy / Geotechnical Engineering Group (GEG), University of Salerno, Italy / Niigata University, Research Institute for Natural Hazards and Disaster Recovery, Japan / Ehime University Center for Disaster Management Informatics Research, Japan / Tian-Shan Geological Society, Kyrgyzstan / Institute of Environmental Geoscience RAS (IEG RAS), Russia / Russian State Geological Prospecting University n.a. Sergo Ordzhonikidze (MGRI-RSGPU) / TEMPOS, environmental civil engineering Ltd., Slovenia / Institute of Earth Sciences – Faculty of Geoscience and Environment, University of Lausanne, Switzerland / Middle East Technical University (METU), Turkey / North Dakota State University, USA</p>
	<p>ICL Secretariat: Secretary General: Kyoji Sassa International Consortium on Landslides, 138-1 Tanaka Asukai-cho, Sakyo-ku, Kyoto 606-8226, Japan Web: http://icl.iphq.org/, E-mail: secretariat@iclhq.org Tel: +81-75-723-0640, Fax: +81-75-950-0910</p>